Proceedings of:

The Twelfth Annual Meeting

The American Society for Precision Engineering

October 5-10, 1997

Norfolk Marriott Waterside Hotel and Waterside Convention Center

Norfolk, Virginia

The American Society for Precision Engineering (ASPE) is a multidisciplinary professional and technical society concerned with research and development, design, manufacture and measurement of high accuracy components and systems. ASPE activities encompass relevant aspects of mechanical, electronic, optical and production engineering, physics, chemistry, and computer and materials science. Membership is open to anyone interested in any aspect of precision engineering.

Founded in 1986, ASPE provides a new focus for a diverse but important community. Other professional organizations have covered aspects of precision engineering, always as a sideline to their principal goals. ASPE is based on the core of generic concepts necessary to achieve precision in any application; independent of discipline, ASPE intends to be the focus for precision technology — and to represent all facets from research to application.

ASPE — The American Society for Precision Engineering
301 Glenwood Avenue, Suite 205
Raleigh, NC 27603
Phone (919) 839-8444 Fax (919) 839-8039

Preface

This book comprises the proceedings of the 1997 Annual Meeting. The contributions reflect the authors' opinions and are published as presented to ASPE, without change. Their inclusion in this publication does not necessarily constitute endorsement by the ASPE, or its editorial staff.

Individual readers of this book and nonprofit libraries acting for them are permitted to make fair use of the material contained in this book to be used in teaching or research; provided they copy said paper in total, as written by the author. Permission is granted to quote excerpts from the scientific or technical works in this book with proper acknowledgement of the source to include: the author's name, the book name, and the ASPE tag line. Reproduction of figures and tables is likewise permitted from the contents of this book, provided that the same acknowledgment of the same source and content is printed.

Any other type reproduction, systematic copying or multiple reproduction of any material in this book is expressly prohibited except with the written permission of the ASPE editorial staff, addressed to the Society's headquarters.

ISBN 1-887706-18-6

1997

American Society for Precision Engineering
301 Glenwood Avenue, Suite 205
Raleigh, NC 27603

Printed in the United States of America

Welcome Note

The American Society for Precision Engineering celebrates its Twelfth Annual Meeting this year in Norfolk, Virginia. The remarkable growth and success of the Society is reflective of the increasing importance of precision engineering in a wide variety of fields of endeavor, from manufacturing to microelectronics to basic science. The Society serves as a focus for precision engineers across all of these fields. The Annual Meeting has evolved into a premier international forum for the exchange of ideas and presentation of research results relating to precision engineering problems involving mechanical parts, electronic components, materials and material processing, metrology, controls, and system integration. Precision engineers and scientists from private industry, government laboratories, and universities meet to learn about the latest developments and to exchange ideas about the future directions of these technologies.

This year's meeting continues the tradition of offering two full days of tutorials presented by some of the foremost precision engineers and scientists in the world. Many participants cite the tutorial program as one of the most valuable features of the meeting. The technical sessions and poster presentations offer the latest research results in the areas of ultraprecision machining, metrology, controls, precision grinding, micro-positioning, material processing, design, precision transducers, surface profilometry, machine tool metrology, and error compensation. The commercial exhibit will provide attendees with the opportunity to view and discuss the latest precision engineering equipment, products, and services that are commercially available. The open forum will give attendees the opportunity to express their opinions and pose questions for discussion by the group, enhancing the exchange of information.

The conference organizing committee is proud to present the program for the Twelfth Annual Meeting of ASPE. We welcome your participation.

Welcome to Norfolk.

1997 ASPE Meeting Organizing Committee

Don A. Lucca, Chair, Oklahoma State University

Ekkard Brinksmeier, University of Bremen
John H. Bruning, Tropel Corporation
James F. Cuttino, University of Alabama
David A. Dornfeld, University of California at Berkeley
Thomas A. Dow, North Carolina State University
Chris J. Evans, National Institute of Standards and Technology
Anthony E. Gee, Cranfield University
Dong-Chul Han, Seoul National University
Andrew J. Hazelton, Nikon Research Corporation of America
Dan E. Luttrell, 3M Company
Toshimichi Moriwaki, Kobe University
Andrea H. Plain, Reflexite-Precision Technology Center
Richard L. Rhorer, National Institute of Standards and Technology
Paul I. Ro, North Carolina State University
Irving F. Stowers, Lawrence Livermore National Laboratory
Hy Dinh Tran, University of New Mexico
H. Frank van Beek, Delft University of Technology
Vellore C. Venkatesh, Nanyang Technological University
Wanjun Wang, Louisiana State University
Robert G. Wilhelm, University of North Carolina at Charlotte

Program

1997 ASPE Annual Meeting

Time	Sun., Oct. 5	Mon., Oct. 6	Tues., Oct. 7	Wed., Oct. 8	Thurs., Oct. 9	Fri., Oct. 10
8:00			Continental Breakfast			
9:00	Tutorials	Tutorials + Executive Forum	Keynote Address	Technical Session 2	Technical Session 5	Technical Tours
10:00	Break	Break	Break	Break	Break	
11:00	Tutorials	Tutorials + Executive Forum	Technical Session 1	Technical Session 3	Invited Papers	
12:00			Lunch + Committee Meetings	Awards Lunch + Business Meeting	Lunch + Roundtable Discussions	
1:00						
2:00	Tutorials	Tutorials + Executive Forum	Commercial Session	Technical Session 4	Technical Session 6	
3:00			Break		Break	
4:00	Break	Break	Poster Papers & Exhibits Hospitality Hour	Break	Technical Session 7	
5:00	Tutorials	Tutorials + Executive Forum		Poster Papers & Exhibits Hospitality Hour		
6:00			Open Forum			
7:00		Welcome Reception		Open Evening	Casual Dinner (Naval Officers' Club)	
8:00			Dinner (Nauticus)			
9:00						

1997 Annual Meeting
Contents

Preface . . . . . *ii*

Welcome Note—Organizing Committee . . . . . *iii*

Program . . . . . *iv*

Sponsor Members . . . . . *vi*

Cooperating Sponsors—Technical Exhibitors . . . . . *vii*

1997 Lifetime Achievement Awards . . . . . *viii*

Keynote Address/Forum/Commercial *1*

Technical Paper Index *2-11*

Technical Papers *15-532*

Authors Index *533-536*

Sponsor Members of the ASPE

3M Company
St. Paul, MN 55144
Contact: William J. Bryan
(612) 575-1465

ADE Corporation
Westwood, MA 02090-1806
Contact: Joe Petrie
(617) 467-3600

Bausch & Lomb
Rochester, NY 14692-0450
Contact: Michael J. Clark
(716) 338-8935

Brown & Sharpe
North Kingstown, RI 02852
Contact: David H. Genest
(401) 886-2358

Chardon Tool & Supply Company, Inc.
Chardon, OH 44024
Contact: Weldon Bennett
(216) 286-6440

Contour Fine Tooling, Inc.
North Swanzey, NH 03431
Contact: Jeffrey Tomlin
(603) 355-1080

Corning, Inc.
Corning, NY 14831
Contact: Dan E. Luttrell
(607) 974-3393

Cranfield Precision, Div. of Landis Lund
Cranfield, Bedford MK43 OJR, England
Contact: Keith G. Dobson
44-1234-752789

Dover Instrument Corporation
Westboro, MA 01581
Contact: Stephen L. Hero
(508) 366-1456

D.A.C. Vision
Carpinteria, CA 93013
Contact: John R. Keller
(805) 684-8307

Fabreeka International, Inc.
Stoughton, MA 02072
Contact: Robert P. Haley
(617) 341-3655

Federal Products Company
Providence, RI 02940
Contact: Frederick G. Parsons
(401) 784-3403

KLA-Tencor Instruments
Milpitas, CA 95035
Contact: Graham J. Siddall
(408) 875-3000

Lawrence Livermore National Laboratory
Livermore, CA 94550
Contact: Daniel C. Thompson
(510) 422-1915

Lion Precision
St. Paul, MN 55126
Contact: Don L. Martin
(612) 484-6544

MicroE, Inc.
Natick, MA 01760-1313
Contact: Robert W. Morgenroth
(508) 903-5000

Moore Tool Company
Bridgeport, CT 06607-0088
Contact: Kevin Uhlig
(203) 366-3224

New Way Machine Components, Inc.
Aston, PA 19014
Contact: Andrew J. Devitt
(610) 494-6700

Precitech, Inc.
Keene, NH 03431
Contact: Stephen C. Hobert
(603) 357-2511

Professional Instruments Company
Minneapolis, MN 55416
Contact: James Arneson
(612) 933-1222

Reflexite-Precision Technology Center
West Henrietta, NY 14586
Contact: Steven M. Scott
(716) 272-0309

RMB Miniature Bearings, Inc.
Ringwood, NJ 07456
Contact: Thomas Rudziensky
(201) 962-1111

Taylor Hobson / Pneumo
Keene, NH 03431
Contact: Ralph E. Murray
(603) 352-5242

Tropel Corporation
Fairport, NY 14450
Contact: John H. Bruning
(716) 388-3400

Zygo Corporation
Middlefield, CT 06455-0448
Contact: Carl A. Zanoni
(860) 704-5102

Cooperating Sponsors

Elsevier Science, Inc.

Photonics Spectra

Technical Exhibitors

ADE Technologies, Inc.
A-G-Davis/AA Gage
AlumiPlate, Inc.
Automated Precision, Inc.
Balance Dynamics Corporation
Bal-tec, Division of Micro Surface Engineering, Inc.
Center for Precision Metrology—University of N. C. at Charlotte
Chardon Tool
Contour Fine Tooling, Inc.
Dover Instrument Corporation
Fabreeka International, Inc.
Heidenhain Corporation
K&Y DIAMOND Ltd.
Lawrence Livermore National Laboratory
Lion Precision
MicroE, Inc.
Moore Tool Company
National Precision Manufacturing Institute
NEW WAY Machine Components, Inc.
Phase Shift Technology, Inc.
Precision Engineering Center—N. C. State University
Precitech, Inc.
Professional Instruments Co., Inc.
Queensgate Instruments Inc.
Taylor Hobson / Pneumo
Techmetals, Inc.
Technodiamant USA, Inc.
The Timken Company Specialty Tooling and Rebuild Business
TROPEL Corporation
VisiTec Microtechnik GmbH
WYKO Corporation
Zygo Corporation

1997 Lifetime Achievement Award

The 1997 ASPE Lifetime Achievement Award is presented to the trio of founders of Zygo Corporation: Paul Forman, Sol Laufer and Carl Zanoni. They met at Perkin Elmer where Paul was the Director of Optical Operations, Sol managed the Experimental Development Laboratory and Carl was a new staff physicist fresh from Princeton with a post-doc at Wesleyan University. Together they formed Zygo Corporation in 1970. Each brought a key skill to the organization and together they have guided it to be one of the worlds most successful metrology companies. Zygo designs, develops and markets high-performance laser-based noncontact electro-optical measuring instruments and manufactures precision optical components. Zygo became a public company in 1983.

Paul F. Forman

Paul received his BS in Optics in 1956 from the University of Rochester. After a brief stint at Bausch & Lomb, he began his successful association with Perkin Elmer Corporation in 1957. He held various engineering, program and corporate management positions including Director of Optical Engineering. He was program manager of the retroreflector array installed by Armstrong and the Apollo 11 team during the first moon landing. Paul served as CEO and Chairman of the Zygo Corporation from its inception in 1970 until 1993 and he is currently the Chairman of the Board.

Sol Laufer

Sol has been intimately associated with high precision optics during his entire professional career of approximately fifty years. Early on, he gained valuable experience working for 12 years with Professor E. Goldberg, once the Director of the Carl Zeiss Jena works. Sol joined the Perkin Elmer Corporation in 1966 where he designed special purpose equipment, tools and processes for the production of large precision optical elements requiring minimal operator skills and resulting in minimum waste. At Zygo, he directed the development and implementation of fabricating processes and equipment for a large variety of precision optical components. As a result of his leadership, Zygo has gained an international reputation for optical fabrication.

Carl Zanoni

Carl received his MA and PhD in Physics from Princeton and held a Post Doctoral Fellowship at Wesleyan University. He began his industrial career as a staff physicist at Perkin Elmer Corporation but left in 1970 to become a founding member of Zygo Corporation. Carl's experience has been in the design and development of electro-optical instrumentation and systems for 1) industrial laser metrology, 2) terrestrial and space born stellar and solar astronomy, 3) the generation of optical surfaces using ultra precise machine tools and 4) automatic optical polishing processes. As Vice President of R&D, his responsibilities cover all of Zygo's technical activities from design and development of surface and wavefront laser interferometer systems to the fabrication of one meter optics for laser fusion research.

Keynote Speaker

Dennis Coyne

Tuesday, October 7, 8:30 a.m.

Dennis Coyne is the Detector Chief Engineer for the LIGO project at the California Institute of Technology. Prior to LIGO, he worked on adaptive optics, pointing and tracking and servo-control systems, as a principal scientist for Kaman Sciences Corporation, and on product design and telephony at Bell Laboratories. He has an MSME from the University of California at Berkeley and was a Commonwealth Scholar at the University of Massachusetts.

"Precision Engineering in LIGO"

The Laser Interferometer Gravitational Wave Observatory (LIGO), a National Science Foundation sponsored project being performed jointly by the California Institute of Technology and the Massachusetts Institute of Technology, is among a new class of astronomical instruments designed to probe the universe using gravitational waves. Possible sources include coalescing binary compact systems (neutron stars and black holes), supernovae, rotating pulsars, and the stochastic background. In order to detect these cataclysmic astrophysical events, the initial LIGO detector must be capable of sensing a gravitationally induced strain of ~10^{-20} rms over a detection band of 40 Hz to 5 kHz and 10^{-21} rms in a few hundred Hz band near 100 Hz. Each initial LIGO interferometer is fundamentally a Michelson interferometer designed to detect differential motion between its arms as small as 10^{-18} m rms (1/1000 the diameter of a nucleus of an atom). Key precision engineering considerations for the LIGO detector include (1) high performance, vacuum compatible optical baffling, (2) precision GPS alignment of the 4km vacuum beam tube, (3) high reflectivity (1 ppm loss) multi-layer dielectric coatings, (4) optically flat (~lambda/1000 rms) surfaces, (5) test mass (mirror) mounts/attachments and substrates with high vibration Q (Qs on the order of 10^7), (6) laser frequency stabilization of ~1(mHz)/($\sqrt{Hz}$) at 100 Hz, (7) laser power stabilization of ~$10^{-7}/\sqrt{Hz}$ using an acousto-optic modulator, (8) vibration and acoustic isolation of -120 dB at 40 Hz with multiple stages of constrained layer damped springs and (9) low noise test mass (mirror) actuators (<1(pA)/($\sqrt{Hz}$)).

The fundamental limiting noise sources, the precision engineering challenges and the current status of the construction and R&D are discussed.

Executive Forum

Monday, October 6, 8:00 a.m.

Session Chair: John H. Bruning, Tropel Corporation

The purpose of the executive forum is to bring together executives and decision makers in a forum to discuss contemporary trends in management and technology in a casual environment with ample networking time. The one-day event will begin with an interactive morning session conducted by Hal Mather, a leading author and management consultant, on "Gaining a competitive edge through improved business logistics." The afternoon session will be devoted to the softer sides of management, industry trends and emerging technologies. This special session is designed to provide the executive with valuable business tips and technology trends along with the opportunity to interact with industry experts and peers.

Commercial Session

Tuesday, October 7, 1:30 p.m.

Session Chair: Dan E. Luttrell, Corning, Inc.

The commercial session will take place on Tuesday afternoon, in a special session where company representatives are invited to make brief presentations on new products associated with precision engineering. Conference participants will have the opportunity to hear about limitations of performance of existing approaches, new approaches relevant to precision engineering, and advances that can be expected in the future.

Open Forum

Tuesday, October 7, 7:00 p.m.

Session Chair: E. Clayton Teague, National Institute of Standards and Technology

The open forum was created to encourage dissemination of new and significant results, as well as observations on precision engineering subjects. All interested conference participants can sign up at the Conference Registration Table for short, informal presentations.

Technical and Poster Paper Index

The technical program for the 1997 ASPE Annual Meeting contains over 130 papers on precision engineering advances. Papers that lent themselves to significant verbal interaction, concise but important discoveries, or strongly visual or tactile subjects have been selected for the poster session. Authors will be present to discuss their work on Tuesday, October 7, from 3:30 to 5:00 p.m., and again on Wednesday, October 8, from 4:00 to 5:00 p.m.

Keynote Address

Tuesday, October 7, 1997
8:30 a.m. - 9:30 a.m.

Session Chair: Don A. Lucca (Oklahoma State University)

Precision Engineering in LIGO
D. Coyne (California Institute of Technology) . . . . . *page 15*

Session I
Metrology I

Tuesday, October 7, 1997
10:00 a.m. - 12:00 p.m.

Session Chair: Anthony E. Gee (Cranfield University)

1. ***AFM Based Nanoindentation as a Probe of Nanomechanics (Invited Paper)****
   P. Russell, K. F. Jarausch (North Carolina State University) and J. E. Houston (Sandia Nat'l Laboratories) . . . . . *page 19*
2. ***Potentials of X-tended View SEMs—Environment for the Micro Manufacturing World***
   S. Klein (Fachhochschule Lübeck), and M. Klein (VISITEC Microtechnik GmbH) . . . . . *page 21*
3. ***Interferometric Measurement of Absolute Dimensions of Cylindrical Surfaces***
   A. W. Kulawiec, J. F. Fleig, J. H. Bruning (Tropel Corporation) . . . . . *page 25*
4. ***Multi-step Form Metrology: Principles and Applications to the LIGO Pathfinder Optics***
   C. J. Evans, W. T. Estler (Nat'l Institute of Standards and Technology), P. J. Sullivan (KLA-Tencor), R. E. Parks (Optical Perspectives Group), and L. Shao (Tucson Optical Research Corporation) . . . . . *page 29*
5. ***Complex Surfaces — Applications and Generation by Diamond Machining***
   E. Brinksmeier, W. Preuß (University of Bremen) . . . . . *page 33*

**Extended abstract not available at press time.*

Poster Session

Tuesday, October 7, 1997
3:30 p.m. - 5:00 p.m.

METROLOGY

1. ***Virtual Reality Applied to Precision Manufacturing***
   R. Wilhelm, S. Patterson, D. Schmidt, K. Nagalla, B. Sethupathi, J. Kroll, O. Martin, N. Li (University of North Carolina at Charlotte) . . . . . *page 37*

SCANNING PROBE MICROSCOPY

1. ***A Tapping Stylus for Surface Topographical Measurement Using a Quartz Fork Resonator***
   T. Hatsuzawa (Tokyo Institute of Technology) . . . . . *page 41*

MACHINE TOOL METROLOGY

1. ***Rotary Axis Metrology***
   J. C. Ziegert, B. Sanders (University of Florida) . . . . . *page 45*
2. ***Linear Displacement Accuracy: A Comparison of National Standards***
   S. Badrawy, T. Schmitz (University of Florida), and D. Bernhard (Boeing Commercial Airplane Group) . . . . *page 49*
3. ***Second Order Terms Influence in Mathematical Models of Machine Tools Considering the Machine Temperature State***
   B. Di Giacomo, D. P. Vieira Sato, R. M. Martinez Orrego (University of São Paulo) . . . . . *page 53*
4. ***A New Error Separation Method for Measuring Angular Motion of a Spindle***
   W. Gao, S. Kiyono (Tohoku University) . . . . . *page 57*
5. ***Rapid Machine Volumetric Error Measurement and Compensation by a 5-Degree-of-freedom Laser System*****
   X. Chu, Q. Ma, K. Lau (Automated Precision, Inc.)
6. ***Assessment of Machine Tool Accuracy Using ISO "Guide to the Expression of Uncertainty in Measurement" (GUM)***
   J. D. Drescher (UTC-Pratt & Whitney) . . . . . *page 61*
7. ***A Model of the Tracking Errors of a Machine Tool Slideway***
   C. M. Daniel, J. W. Sutherland, W. W. Olson (Michigan Technological University) . . . . . *page 65*

COORDINATE MEASURING MACHINES

1. ***Engineering Applications of Geometric Metrology***
   M. J. Kaiser (Wichita State University) . . . . . *page 69*
2. ***A Study on Auto-measurement System of Coordinate Measuring Machine***
   Wang J., Liu S., Li Z., Zhang G. (Tianjin University) . . . . . *page 73*
3. ***A Laser Tracking Interferometer Based on a New Servo System***
   Fu J., Ding Y., Zhang G. (Tianjin University) . . . . . *page 78*
4. ***Form Error Assessment: Error Separation Method for the Calibration of Free-form Surfaces by Means of Coordinate Measuring Machines***
   D. Feautrier, P. Bourdet (LURPA, Ecole Normale Supérieure de Cachan) . . . . . *page 82*
5. ***Geometric Form Evaluation of Cone Based on the Minimum Zone Criteria***
   H. M. Kim (University of Michigan), and B. C. Lee (Korea Advanced Institute of Science and Technology) . . . . . *page 86*
6. ***An Efficient Calibration Technique for CMM Machines*****
   S. J. Lee (Yuan-Ze Institute of Technology), and Y. L. Pan, C. M. Chang (Chung-Shan Institute of Science and Technology)

***Abstract unavailable at press time.*

7. ***Applications of Surface Normal Measurements to Coordinate Metrology***
R. Edgeworth, R. G. Wilhelm (University of North Carolina at Charlotte) . . . . . *page 90*

8. ***Application of a Probe Pretravel Model in CMM Measurements***
Y. Shen, S. Moon (George Washington University) . . . . . *page 94*

SURFACE FINISH AND FORM

1. ***Optimizing the Phase Shift Steps for the Least-squares Algorithm in Phase Shift Interferometry for Engineering Surface Measurement***
Y. Wang, K. S. Moon (Michigan Technological University) . . . . . *page 98*

2. ***Study on Computational Geometry Approach to Minimum Circumscribed Circle***
Liu S-G., Yang F., Ma X-H. (Tianjin University) . . . . . *page 102*

3. ***Repeatability and Calibration of a Grazing Incidence Cylindrical Interferometer***
P. D. Knight, Jr., S. R. Patterson (University of North Carolina at Charlotte) . . . . . *page 106*

4. ***Development of a Roundness Profile Measurement System for Precision Rollers by V-block Method***
K. Mitsui, K. Goho, (Keio University) A. Hayashi (Nano Corporation) . . . . . *page 110*

5. ***A Method to Decouple the Compound Effect of Machine Error and Free-form Geometric Characteristics***
G. Lee, J. Mou (Arizona State University) . . . . . *page 114*

6. ***Systematic Error Removal in Interferometric Measurements of Cylindrical Form*****
J. F. Fleig (Tropel Corporation), and D. P. McClimans (Inti Electronics)

7. ***Information Content in Surface Metrology for Functional Correlations***
C. A. Brown, P. Hoch (Worcester Polytechnic Institute) . . . . . *page 118*

8. ***An In-line Digital Filtering Algorithm for Surface Roughness Profiles***
S. Hara (Nagaoka Univeristy of Technology), and T. Tsukada, K. Sasajima (Tokyo Institute of Technology) . . . . . *page 122*

9. ***Noise-insensitive Phase Unwrapping in Phase Shift Laser Interferometric Surface Measurement***
Y. Wang, K. S. Moon (Michigan Technological University) . . . . . *page 126*

SENSORS/NEW INSTRUMENTS

1. ***Traceable Diameter Measurements of Thin Wires***
O. Jusko, H. Bosse, G. Frase, F. Lüdicke (Physikalisch-Technische Bundesanstalt), and W. Tang (Harbin Institute of Technology) . . . . . *page 131*

2. ***High Precision Straight Motion and Measurement Technique Applying Optical Datum***
Mu Y., Wan D. A. (Tongji University), and Lin E. (Shanghai JiaoTong University) . . . . . *page 135*

3. ***System for the Measurement of Corneal Shape by Laser Deflectometry***
R. Díaz, A. Caballero, A. Muñiz, L. Ruíz, G. Ascanio (National University of Mexico) . . . . . *page 139*

4. ***Electrodeposition of Superconductor Thin Film and the Magnetoresistance Characterization for Magnetic Field Sensing Application***
A. Natarajan, W. Wang, E. Ma, (Louisiana State University), and R. N. Bhattacharya (National Renewable Energy Laboratory) . . . . . *page 143*

5. ***Evaluation of Thermistors as a Reference for Local Temperature Control***
K. M. Lawton, S. R. Patterson (University of North Carolina at Charlotte) . . . . . *page 149*

6. ***Investigation of Nonlinearity in High Accuracy Heterodyne Laser Interferometry***
V. G. Badami, S. R. Patterson (University of North Carolina at Charlotte) . . . . . *page 153*

7. ***Interferometric Measurement of Surface Microstructure in Engine Cylinder Walls***
D. J. Aziz (WYKO Corporation), and M. Kramer (General Motors Corporation) . . . . . *page 157*

8. ***Development of a Sophisticated Michelson-type Laser Interferometer Utilizing an Optical Thin Film for the Constant Phase Difference***
K. Miyazawa (Union Tool Co.), and K. Yanagi, S. Mishina (Nagaoka University of Technology) . . . . . *page 161*

***Abstract unavailable at press time.*

9. ***A New Method for Dynamic Balancing of Digital Head Drum (Ø 21.7 mm)***
Joe, Y-U, Yang, Y-W, Lee, J-K (DAEWOO Electronics Co., Ltd.) ..... *page 165*

10. ***Lateral Shearing Interferometer by Using Zone Plates***
T. Nomura, K. Kamiya, H. Miyashiro, S. Okuda (Toyama Prefectural University), and H. Tashiro, K. Yoshikawa, (Toyama University) ..... *page 169*

11. ***Fiber Optic Displacement Transducer with Nanometer Resolution Using AC-modulation***
D. Wang, Y. Alayli, M. Bonis, J. C. Henrio (Universitè de Technologie de Compiègne) ..... *page 173*

12. ***Nanometer Level Autofocus Air Gauge***
T. Thomas, C. Hamaker, J. Martyniuk, G. Mirro (Etec Systems, Inc.) ..... *page 178*

CONTROLS

1. ***Compensation of Hysteresis and Coupling Effect of Tube Scanner for Atomic Force Microscope*****
J. Y. Shim, H. Jung, D. G. Gweon (Korea Advanced Institute of Science and Technology)

2. ***Study on High Precision Cutting by Workpiece Referred Form Accuracy Control System— A Proposition of Double MTS Method***
N. Ohno, T. Yazawa, T. Kohno (Tokyo Metropolitan Institute of Technology), and Y. Uda (Nikon Corporation) ..... *page 183*

3. ***Design of a Linear Voice Coil Actuator for Fast Tool Servo Applications***
W. Greene, D. E. Schinstock (The University of Alabama) ..... *page 187*

4. ***Intelligent 3D-Free-Form Surface Cutting Toward High Precision and High Efficiency***
M. Mitsuishi, M. Hashiguchi, Z. Kiriyama, J. Li, T. Nagao (The University of Tokyo) ..... *page 191*

MACHINING

1. ***New Biarc Interpolation for Ultra-precision Aspheric Surface Machining***
M. Y. Yang, T. M. Lee (Korea Advanced Institute of Science and Technology), and J. Y. Lee, T. H. Kim, J. Y. Ha (Daewoo Heavy Industry) ..... *page 195*

2. ***Cutting Temperature and its Effect to Sub-surface Damage in Diamond Turning***
K. Horio, T. Kasai, K. Sekiguchi (Saitama University) ..... *page 199*

3. ***Experimental Investigation of Surface Roughness in Ultra Precision Cutting of a Plastic***
M. Saeki, H. Yasui, A. Hosokawa, S. Kondo (Kumamoto University) ..... *page 203*

4. ***Effects of Round-nosed Tools on Chatter in Diamond Turning***
A. Schaut, E. Marsh (The Pennsylvania State University) ..... *page 207*

5. ***Microcutting Phenomena of Monocrystalline Silicon with Large Nose Radius Diamond Tool***
A. Kanai, F. Inaba, M. Miyashita, R. Kato, T. Yokotsuka, S. Fujita, (Ashikaga Institute of Technology), and M. Daito (Nissin Machine Works) ..... *page 211*

6. ***Side Burr Generation Model in Micro-Grooving***
J. H. Ahn, H. S. Lim (Pusan National University) ..... *page 215*

7. ***On High Quality Turned Silicon Surfaces***
F. Z. Fang, V. C. Venkatesh (Nanyang Technological University) ..... *page 220*

8. ***Morphology and Topography of Chip Produced by Diamond Turning of Al-Mg Alloy for Mirrors***
R. G. Jasinevicius, A. J. Vieira Porto, J. G. Duduch (University of São Paulo) ..... *page 224*

9. ***Chip Dynamics in Diamond Turning***
B. H. Jared, T. A. Dow (North Carolina State University) ..... *page 230*

GRINDING

1. ***Combined Model of Ceramics Grinding***
L. Yin, I. D. Marinescu (Kansas State University), and T. Matsuo (Kumamoto University) ..... *page 234*

2. ***A Self-deformable Face Grinding Machine to Realize Some 0.1 μm Flatness for 8-inch Substrates***
M. Nakao, Y. Takashima, K. Ohta, Y. Hatamura (The University of Tokyo) ..... *page 238*

***Abstract unavailable at press time.*

3. ***A Local Grinding System for Wide and Flat Surface with a 3-Axis Negative Compliance Device***
K. Matsumoto, M. Nakao, Y. Hatamura (The University of Tokyo) . . . . . *page 242*

4. ***Experimental Verification of a Grinding Chatter Model***
B. R. Knapp, E. R. Marsh (The Pennsylvania State University) . . . . . *page 246*

5. ***A Model for Self-dressing of Resin Bound Grinding Wheels***
T. S. Kakumanu, M. H. Miller (Michigan Technological University) . . . . . *page 250*

6. ***The Effect of Workpiece Modulation on Surface Quality***
W. Qu, M. H. Miller (Michigan Technological University) . . . . . *page 254*

7. ***Grinding with Directionally Aligned SiC Whisker Wheel—Loading-free Grinding***
K. Yamaguchi (Nagoya University), I. Horaguchi (Toyota College of Technology), and Y. Sato (Aichi Industrial Research Institute) . . . . . *page 258*

8. ***An Application of 40 kHz Ultrasonic Vibration to Shear-mode Grinding of Silicon Wafers***
Y. Yoshida (Tokyo Diamond Tool), K. Imai, H. Hashimoto (Kanagawa Institute of Technology), Z. N. Sun (Harbin Institute of Technology), and Y. S. Lu (Northeastern University) . . . . . *page 262*

9. ***Surface and Subsurface Structure of Alumina After Ductile-mode Grinding***
I. Zarudi, L. C. Zhang (The University of Sydney) . . . . . *page 267*

10. ***In-process EDM Truing to Generate Complex Contours on Metal-bond, Superabrasive Grinding Wheels for Precision Grinding Structural Ceramics***
M. A. Piscotty, P. J. Davis, T. T. Saito, K. L. Blaedel, L. Griffith (Lawrence Livermore National Laboratory) . . . . . *page 271*

POLISHING

1. ***Figure Correction for Rotary Asymmetric Error by Linearly Arranged Segmented Pressurizing Polishing Machine***
K. Horio, T. Kasai, A. Matsuse (Saitama University) . . . . . *page 275*

2. ***Fabrication of New Collimating Optical Fibers Using Glass Slit-microferrules***
K. Koyabu, F. Ohira (NTT Opto-electronics Laboratories) . . . . . *page 279*

3. ***Rotating Lapping Machine with a Pneumatic Bearing Supported Lap***
G. Ascanio, C. Cava, R. Chicurel, R. Nava (National University of Mexico), and R. Reséndiz (DIBYASA) . . . . . *page 283*

4. ***Surface Contamination of Abrasive During Lapping***
A. W. Barylski (Technical University of Gdánsk) . . . . . *page 287*

MODELING

1. ***Model-based Precision Machining Simulation for the Prediction of Tool Life***
K. Maekawa (Ibaraki University) . . . . . *page 291*

2. ***An Orthogonal Cutting Stability Model with Variable Delay Length Due to Tool Motion***
T. B. O'Reilly, E. R. Marsh (The Pennsylvania State University) . . . . . *page 295*

3. ***Fuzzy Logic Modeling of Electrolytic Grinding Process***
K. G. R. Koteswara Rao, G. Kuppuswamy (Indian Institute of Technology) . . . . . *page 299*

4. ***An Adaptive Method for Predicting Residual Stresses Associated with Grinding Induced Phase Transformation***
M. Mahdi, L. C. Zhang (The University of Sydney)) . . . . . *page 303*

NOVEL/OTHER PROCESSES

1. ***Transient Response of Wire Electrode in Wire Electrical Discharge Machining***
H. Yamada, N. Mohri, K. Furutani (Toyota Technological Institute), and T. Magara (Mitsubishi Electric Corporation) . . . . . *page 307*

2. ***Three-dimensional Micro Forming Using Metal Jet***
K. Yamaguchi, K. Sakai, T. Yamanaka, T. Hirayama (Nagoya University) . . . . . *page 311*

DESIGN

1. ***Fabrication and Thermal Analysis of a Bellows Type Gas-liquid Phase-change Micro-actuator***
   S. Kato, T. Shintani (Nippon Institute of Technology) . . . . . *page 315*
2. ***Miniaturized Positioning Device for Precise Rotary Motion by Use of Piezoelectric Actuators***
   P. Dörrer (Fraunhofer Institute for Applied Optics and Precision Engineering) . . . . . *page 319*
3. ***Dynamic Accuracy Monitoring for the Comparison and Optimization of Fast Axis Feed Drives***
   O. Zirn (Mikron SA Agno), and S. Weikert (IWF-ETH) . . . . . *page 323*
4. ***Design and Characterization of Nanometer Precision Mechanisms***
   Y. Xu, P. D. Atherton, P. Rhead, T. R. Hicks, M. McConnell (Queensgate Instruments, Ltd.) . . . . . *page 328*
5. ***Preload Control in Ball Screw Using Piezoelectric Actuators***
   S. Fukada (Shinshu University) . . . . . *page 333*
6. ***Thin, Light-weight, Compact Pick-up Actuator for High Precision, Fast Access CD-ROM Devices***
   S. M. Kim, D. G. Gweon (Korea Advanced Institute of Science and Technology) . . . . . *page 337*
7. ***A Long Stroke and Ultraprecision XYθ Stage Using Simple Linear DC Servo Actuators***
   S. Q. Lee, D. G. Gweon (Korea Advanced Institute of Science and Technology) . . . . . *page 341*
8. ***Function Related Tolerance Theory and its Application to Needle-bar Motion Mechanism in a Sewing Machine***
   K. J. Chun, D. Y. Shin (Korea Institute of Industrial Technology) . . . . . *page 345*
9. ***A Study on Performance Improvement of Non-contact Type Seals for High Speed Spindle***
   B. C. Na (Korea Automotive Technology Institute), K. J. Chun (Korea Institute of Industrial Technology), and D. C. Han (Seoul National University) . . . . . *page 351*
10. ***An End Effector Using Parallel Mechanism for Scanning Electrical Discharge Machining***
    K. Furutani, K. Shibatani, N. Itoh, N. Mohri (Toyota Technological Institute) . . . . . *page 357*
11. ***Self Calibration for a Hexapod Coordinate Measuring Machine***
    C. C. Huang, J. C. Ziegert (University of Florida) . . . . . *page 361*
12. ***Three Parameter Solution of Time-varying Thermal Errors***
    T. Gim, J. Corbett, A. E. Gee (Cranfield University) . . . . . *page 365*
13. ***Relative Tolerances and Simplicity in High Precision Micro Drive Design*****
    A. Birkicht (Roulements Miniatures SA), and J N. Perkins (RMB Miniature Bearings, Inc.)
14. ***Load Capacity of an Externally Pressurized Air Bearing Used in Measuring the Power Drawn in Stirred Tanks***
    D. Palomino, G. Robles, G. Ascanio, E. Galindo (National University of Mexico) . . . . . *page 369*
15. ***Design of an Ultra Low Speed Straight Motion System Based on a High Viscosity Fluid Bearing***
    J. W. Spronck, P. F. A. M. van Putten, G. J. P. Nijsse (Delft University of Technology) . . . . . *page 373*
16. ***Comparison of Carbon Fiber, Alumina Ceramic and Aluminum Beams***
    A. J. Devitt, N. Sotiropoulos, J. Radice (New Way Machine Components, Inc.) . . . . . *page 377*
17. ***Estimation of Thermal Contact Resistance by Electrical Contact Resistance Measurement***
    K. Mizuhara, N. Ozawa (AIST, MITI) . . . . . *page 381*
18. ***Design of a Second Generation Nanometric Cutting Instrument***
    R. Hocken, R. Namperumal, P. Pereira, J. Lovingood, R. Edgeworth, A. Sharma, M. Holmes, B. Muralikrishnan (University of North Carolina at Charlotte) . . . . . *page 386*
19. ***A Flexible Alignment Fixture for the Fabrication of Replication Mandrels***
    J. F. Cuttino, D. E. Schinstock, M. W. Todd (The University of Alabama) . . . . . *page 390*
20. ***Low Cost Metrology of 6-Degree-of-freedom, Millimeter-range Stages***
    Y. Wu, J. F. Cuttino (The University of Alabama) . . . . . *page 394*
21. ***Development of a Long Range, Traction Drive Fast Tool Servo for Diamond Turning Applications***
    M. W. Todd, J. F. Cuttino (The University of Alabama) . . . . . *page 398*

***Abstract unavailable at press time.*

22. **FAUST and WAGNER: Machine Design and Process Simulation**
O. W. Fähnle, (TNO Institute of Applied Physics), and H. van Brug, C. J. van der Laan, H. J. Frankena (Delft University of Technology) . . . . . page 402

23. **Micropositioning of Linear Motion Table with Magnetic Bearing Suspension**
O. S. Kim, H. J. Ahn, D. C. Han (Seoul National University), Y. Joung (Samsung Electronics Co.), and I. B. Chang (Kangwon National University) . . . . . page 406

EDUCATION

1. **The Machinist's Role in a Modern High-precision Manuacturing Enterprise**
R. L. Rhorer, N. R. Copeland, C. W. Brooks, B. S. Dutterer (Nat'l Institute of Standards and Technology) . . . . . page 410

Session II
Metrology II

Wednesday, October 8, 1997
8:00 a.m. - 9:45 a.m.

Session Chair: Dan E. Luttrell (Corning, Inc.)

1. **Self-calibration of Interference Microscopes**
M. Kanai, W. Gao, I. Ogura, S. Kiyono (Tohoku University) . . . . . page 414

2. **A Model for Visualization of Roller Bearing Error Motion**
W. Holzhauer (The Timken Company) . . . . . page 418

3. **Geometric Error Calibration of Multi-axis Machines Using an Auto-alignment Laser Interferometer**
J. S. Chen (National Chung Cheng University) . . . . . page 422

4. **Precision Profile Measurement of Aspheric Surfaces by Improved Ronchi Test**
S. W. Kim, H. J. Lee (Korea Advanced Institute of Science and Technology), and S. E. Lim (Samsung Electronics) . . . . . page 426

5. **Surface and Form On-machine Metrology/Correction System for Ultraprecision Machining and Grinding**
G. Malkin (Precitech, Inc.) . . . . . page 430

Session III
CMMs

Wednesday, October 8, 1997
10:15 a.m. - 11:45 a.m.

Session Chair: Frederick G. Parsons (Federal Products Company)

1. **Development of Non-contact Measuring for 3D Micro Pattern in Semiconductor Wafer Using a New Optical Probe Implementing a High Performance Optical Window**
H. J. Pahk, W. J. Ahn (Seoul National University), and S. W. Cho (Halla Optical Engineering) . . . . . page 434

2. **Development of a 2D Probing System with Nanometer Resolution**
W. O. Pril, K. G. Struik, P. H. J. Schellekens (Eindhoven University of Technology) . . . . . page 438

3. ***The Calculation of CMM Measurement Uncertainty via the Method of Simulation by Constraints***
S. Phillips, B. Borchardt, D. Sawyer, W. T. Estler, D. Ward, K. Eberhardt, M. Levenson, M. McClain (Nat'l Institute of Standards and Technology), and B. Melvin, (ICAMP, Inc.) T. Hopp (ZigZag Inc.) and Y. Shen (G.W. University) . . . . . page 443

4. ***Thermal Responses of Coordinate Measuring Machines***
C. Nickels, T. Charlton (Brown & Sharpe Manufacturing Company) . . . . . page 447

Session IV
Cutting and Grinding

Wednesday, October 8, 1997
1:30 p.m. - 3:30 p.m.

Session Chair: Michele H. Miller (Michigan Technological University)

1. ***Research Challenges and Directions in Precision Machining of Hardened Steels (Invited Paper)****
M. A. Davies, Y. K. Chou, C. J. Evans (Nat'l Institute of Standards and Technology) . . . . . page 451

2. ***Precision Engineering and Statistics: Is There Any Common Ground?***
R. L. Rhorer (Nat'l Institute of Standards and Technology), and J. L. Rhorer (Iowa State University). . . . . page 452

3. ***Ultraprecision Grinding of High Aspect Ratio Microparts***
H. H. Gatzen, J. C. Maetzig, L. P. Ruhbach (Hanover University) . . . . . page 454

4. ***Direct Fabrication of Deep X-ray Lithography Masks by Micromechanical Milling***
C. Friedrich (Michigan Technological University), P. Coane, J. Goettert (Louisiana Tech University), and N. Gopinathin (Read-Rite, Inc.) . . . . . page 458

5. ***The Mechanism of Material Removal in Grinding and Polishing Silicon Mono-crystals on the Nanometer Scale***
L. C. Zhang, H. Tanaka, I. Zarudi (The University of Sydney) . . . . . page 462

6. ***A Basic Study on Nanometer Cutting of Brittle Materials***
K. Asamoto, K. Furutani, N. Mohri (Toyota Technological Institute) . . . . . page 466

Session V
Precision Positioning Systems

Thursday, October 9, 1997
8:00 a.m. - 10:00 a.m.

Session Chair: Andrew J. Hazelton (Nikon Research Corporation of America)

1. ***High-precision Magnetic Levitation Stage for Photolithography (Invited Paper)***
W. J. Kim, D. L. Trumper (Massachusetts Institute of Technology) . . . . . page 470

2. ***A Long Range Scanning Stage (The LORS Project)***
M. L. Holmes, R. J. Hocken (University of North Carolina at Charlotte), and D. L. Trumper (Massachusetts Institute of Technology) . . . . . page 474

3. ***A 3 DOF Z-tilts Micro Positioning System Using Electromagnetic Actuators with Air Bearings***
S. Q. Lee, D. G. Gweon (Korea Advanced Institute of Science and Technology) . . . . . page 478

**Extended abstract not available at press time.*

4. ***A 1/100 Machine Tool to Fabricate 1/100 Micro Parts***
K. Ishii, M. Nakao, Y. Hatamura (The University of Tokyo) . . . . . *page 482*

5. ***Assembly of Micro Systems in a Large-chamber Scanning Electron Microscope***
M. Weck, J. Hümmler, B. Petersen (Fraunhofer-Institute for Production Technology IPT) . . . . . *page 486*

Invited Paper
Emerging Technologies

Thursday, October 9, 1997
10:30 a.m. - 11:30 a.m.

Session Chair: Wanjun Wang (Louisiana State University)

1. ***Review of Non-destructive Measuring Methods for the Assessment of Surface Integrity (Invited Paper)***
G. Goch, B. Schmitz, J. Geerkens, M. Reigl, P. Sprongl, R. Ritter (University of Ulm) . . . . . *page 490*

Session VI
Controls

Thursday, October 9, 1997
1:30 p.m. - 3:00 p.m.

Session Chair: James F. Cuttino (The University of Alabama)

1. ***Six Axis Active Vibration Isolation and Payload Reaction Force Compensation System***
M. Williams (Integrated Solutions Inc.), and P. Subrahmanyan, D. L. Trumper (Massachusetts Institute of Technology) . . . . . *page 494*

2. ***Compensation of Dynamic Vibrations and Spindle-Runout***
M. Weck, R. Hilbing (Fraunhofer-Institute of Production Technology IPT) . . . . . *page 498*

3. ***In-process Active Balancing of High-speed Machine Tools****
S. W. Dyer (Balance Dynamics Corporation) . . . . . *page 502*

4. ***A New Zero-stiffness Magnetic Bearing for Vibration Isolation***
G. J. P. Nijsse, J. W. Spronck, M. H. A. Leenders, H. F. van Beek (Delft University of Technology) . . . . . *page 503*

5. ***Mechatronic Analysis and Design of High-precision Drives***
E. Kallenbach, E. Saffert, C. Schäffel (Technical University of Ilmenau), P. Maißer, H. Freudenberg (Technical University of Chemnitz-Zwickau), and J. Lückel, W. Kuhlbusch (University-GH Paderborn) . . . *page 507*

**Extended abstract not available at press time.*

Session VII
Novel Processes

Thursday, October 9, 1997
3:30 p.m. - 5:00 p.m.

Session Chair: Thomas Dow (North Carolina State University)

1. ***Current and Future Possibilities of Non-contact Nano Machining by Combination of Laser with Scanning Probe Technology (Invited Paper)***
   K. Dickmann, J. Jersch (Fachhochschule Münster) . . . . . *page 511*
2. ***Thermal Effects of Broad Beam Neutral Ion Machining***
   H. E. Fawcett (MicroE, Inc.), and T. G. Bifano, D. Wroblewski (Boston University) . . . . . *page 515*
3. ***Near-field Photolithography to Realize High Resolution Smaller Than Light Wavelength***
   S. Tanaka, M. Nakao, Y. Hatamura (The University of Tokyo) . . . . . *page 521*
4. ***High Efficiency Fine Boring in Single Crystalline Silicon Ingot by Electrical Discharge Machining***
   Y. Uno, A. Okada, Y. Okamoto (Okayama University), and Y. Yamada (KASEN USA Corp.) . . . . . *page 525*
5. ***Micro Devices Produced by Micro Robots***
   H. Aoyama (University of Electro-Communications), K. Mizutani, T. Miura, K. Murakami, F. Iwata (Shizuoka University) . . . . . *page 529*

**Extended abstract not available at press time.*

Technical Papers

Technical Papers

PRECISION ENGINEERING IN LIGO (LASER INTERFEROMETER GRAVITATIONAL-WAVE OBSERVATORY)

Dennis Coyne
California Institute of Technology
Physics Department, LIGO Project, Mail Code 18-34
Pasadena, CA 91125
818-395-2034; coyne@ligo.caltech.edu

The Laser Interferometer Gravitational Wave Observatory (LIGO)[1], a National Science Foundation sponsored project being performed jointly by the California Institute of Technology and the Massachusetts Institute of Technology, is among a new class of astronomical instruments designed to probe the universe using gravitational waves. Possible sources include coalescing binary compact systems (neutron stars and black holes), supernovae, rotating pulsars and the stochastic background (as a result of the big bang and the gravitational analog to the cosmic microwave background). In order to detect these cataclysmic, astrophysical events, the initial LIGO detector is designed to be capable of sensing a gravitationally induced strain of ~ 10^{-20} rms over a detection band of 40 Hz to 5 kHz and 10^{-21} rms in a few hundred Hz band near 100 Hz.

Each initial LIGO interferometer is fundamentally a Michelson interferometer (Figure 1). A gravitational-wave induces a small dilatational strain in one arm of the Michelson interferometer while simultaneously inducing a small strain of opposite sign in the other arm. The strain is manifested by the displacement of "test mass" mirrors in the arms of the interferometer. The interference of the light which is recombined at the beamsplitter transduces the differential strain into a phase measurement. The phase difference can be amplified by using long effective arm lengths. The arms of the LIGO interferometer have resonant (Fabry-Perot) cavities formed by super-polished and extremely low loss mirrors. These cavities effectively increase the physical length of the arms by a factor of ~ 50, i.e. photons on average experience ~ 50 bounces in the arm cavities.

All the optical components in the phase sensitive part of the interferometer are suspended as pendula to reduce the coupling to seismic and thermal noise and to provide a means to control the optical path lengths in the interferometer. A highly stabilized laser beam is injected into the two arms of the interferometer via a beamsplitter and servo-locked to the average length of the arms of the interferometer. The path lengths are maintained by servo systems to hold the light incident on the detector, placed at the antisymmetric port of the beamsplitter, at a dark fringe. LIGO is designed to detect differential motion between its arms as small as 10^{-18} m rms (1/1000 the diameter of a nucleus of an atom).

The Fabry-Perot cavities also enhance the light power used to sense the mirror displacement thereby reducing the effect of photon shot noise. To further increase the laser power, the light which propagates back toward the laser after recombination at the beamsplitter is reflected back toward the arms with the introduction of another beamsplitter; this is known as power recycling. The light from a frequency stabilized 10 W single frequency, single mode Nd:YAG laser is amplified to ~ 10 kW in the Fabry-Perot cavities in the LIGO system. The introduction of the recycling

1. A. Abramovici, et. al., "LIGO: The Laser Interferometer Gravitational-Wave Observatory", *Science*, v256, 325-333, April 1992.

mirror creates another cavity formed by the input test mirrors of the Fabry-Perot cavities and the beamsplitter. The cavities formed by the large optics (25 cm diameter), as well as additional optics used to spatially filter and frequency stabilize the light injected into the LIGO interferometer, have to be length controlled. In addition, the amount of light which leaks into higher order modes must be controlled by precise alignment of all of these optics.

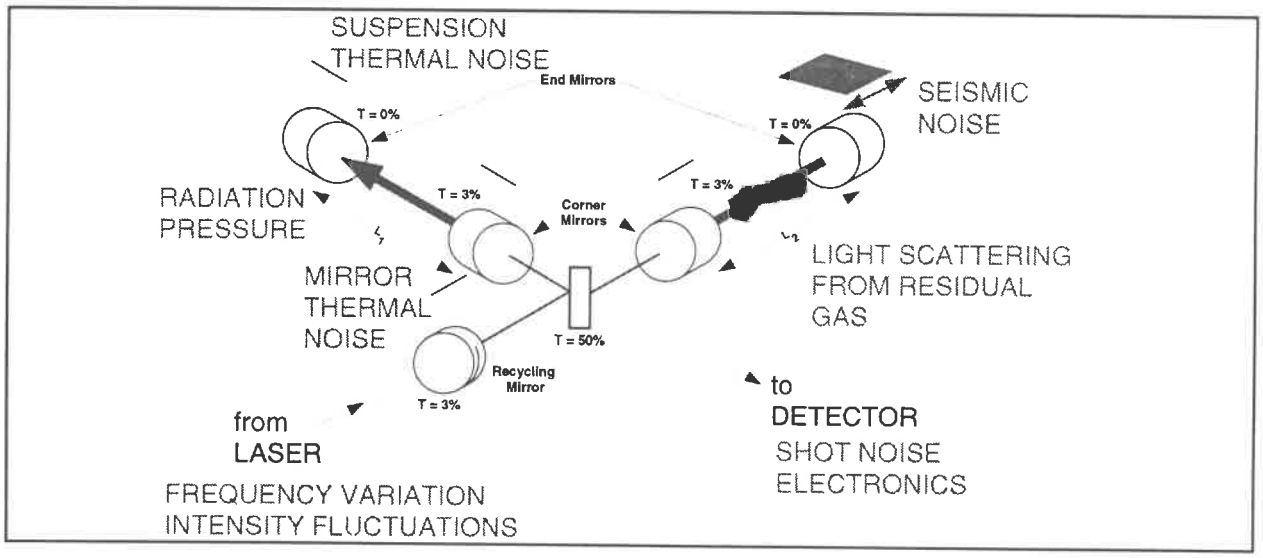

Figure 1: Basic Configuration and Principal Noise Sources

In order to mitigate the effects of laser amplitude fluctuations in the signal band (above shot noise), a modulation scheme is employed to shift the measurement to a higher frequency (~ 25 MHz). Feedback control systems correct the laser's emission frequency to match the TEM_{00} mode frequency of the highly stable, Fabry-Perot resonators. Length change measurement, and laser frequency error, are both accomplished with a radiofrequency phase modulation reflection scheme (also known as the reflection locking technique)[1]. The modulation of the beam is accomplished through the use of electro-optical phase modulating crystals (Pockel-effect phase shifters).

Key precision engineering considerations for the LIGO detector include:

- high performance, vacuum compatible optical baffling,
- precision GPS alignment of the 4 km vacuum beam tube,
- high reflectivity (1 ppm loss) multi-layer dielectric coatings,
- optically flat ($\lambda/1000$ rms) surfaces,
- test mass (mirror) mounts/attachments and substrates with high vibration Q (low loss) (Qs on the order of 10^7),
- laser frequency (λ = 1064 nm) stabilization of ~ 1 $(mHz)/(\sqrt{Hz})$ at 100 Hz with frequency separated servo-loops and a lock sequence from small reference cavities to finally the 4km Fabry-Perot cavities,
- laser amplitude stabilization of $\delta P/P \sim 10^{-7}/\sqrt{Hz}$ using an acousto-optic modulator,
- vibration and acoustic isolation of -120 dB at 40 Hz with multiple stages of constrained layer damped springs,
- low noise test mass (mirror) actuators ($< 1\,(pA)/(\sqrt{Hz})$), and

1. R. Drever et. al., Appl. Phys. B, 31, 97, 1983.

- precision alignment of the suspended optics (< 10 nrad) using wavefront sensing techniques

LIGO has several research testbeds used to verify design approaches and investigate interferometer control and response. The 40m Interferometer (Figure 2) is used principally to investigate displacement noise sources (seismic and thermal) and system level design considerations. The Phase Noise Interferometer (PNI) is used to investigate phase noise (photon shot noise and scattered light). The 40m Interferometer was recently reconfigured to include optical recombination (previously the signals from the two arms were combined electronically) and a revised modulation and control system in order to be more representative of the full scale system and to test models for the dynamics of length control. In the near future a recycling mirror will be added to complete the reconfiguration. A sensitivity of ~5 x 10^{-19} $(m)/(\sqrt{Hz})$ (or about ~ 10^{-20} $(strain)/(\sqrt{Hz})$) has been demonstrated in the 40 m prototype detector (Figure 3). If this same displacement sensitivity is realized on the full scale LIGO detector, then the comparable strain sensitivity would be ~ 10^{-22} $(strain)/(\sqrt{Hz})$, due to the longer cavity length.

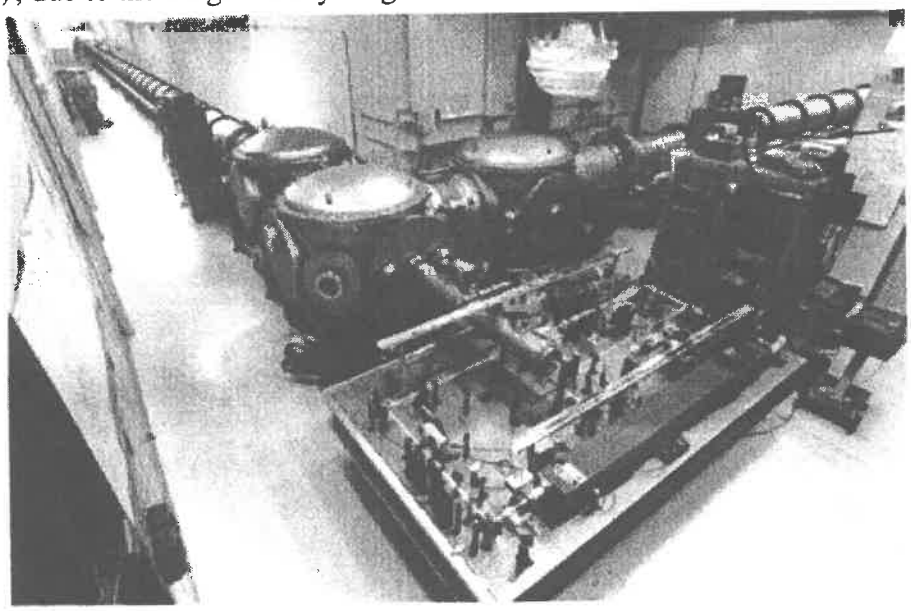

Figure 2: 40-meter Prototype Interferometer

The PNI, a Michelson interferometer with 5 meter long arms in a power recycled configuration, is used to develop and demonstrate the technology for the shot-noise limited interferometer operation at initial LIGO power levels to achieve the required phase sensitivity. Initial measurements with the recycled Phase Noise Interferometer showed that to achieve the measurement goals a system of automated alignment was needed using wavefront sensing techniques. The PNI operates with roughly 200 mW of input power (514 nm green light from an Argon laser source). The recycling factor of roughly 450 leads to approximately 90 W of circulating power in the recycling cavity. With this set of parameters, a phase noise sensitivity of roughly 3 x 10^{-10} $(rad)/(\sqrt{Hz})$ has been achieved, in good agreement with calculations. This very encouraging result is, to our knowledge, the highest phase sensitivity of any interferometer to date. Preparations are underway to convert to Nd:YAG

The fundamental limiting noise sources are quantitatively described and the precision engineering

challenges required to meet these demanding performance requirements are discussed.

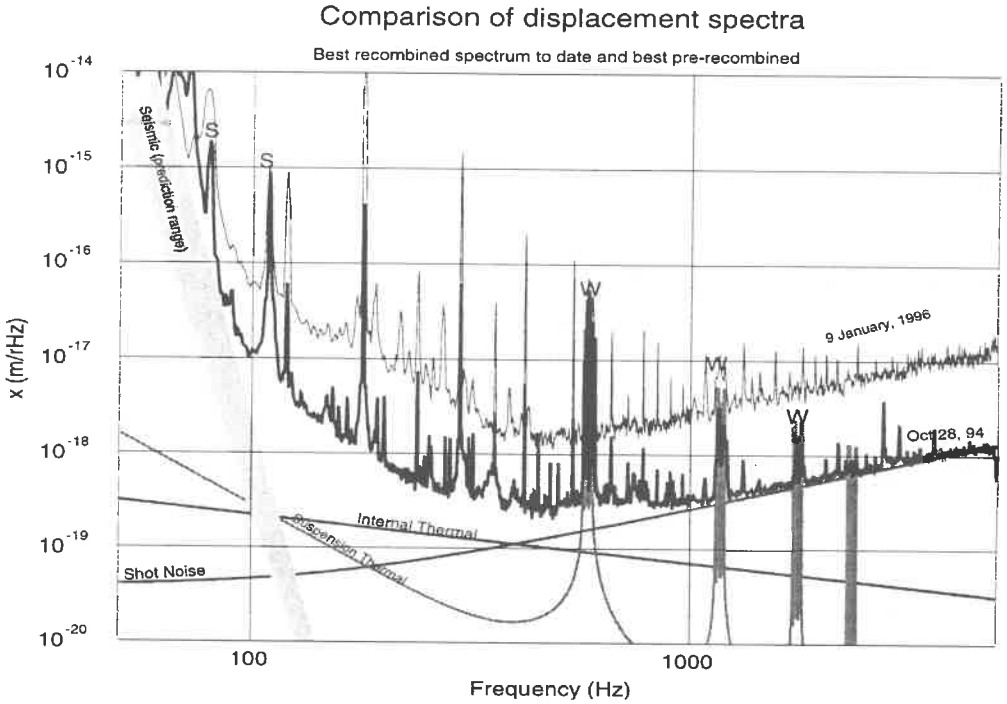

Figure 3: Displacement Sensitivity of the 40 Meter Prototype Interferometer

The LIGO project has a major construction effort underway at its two sites (Figure 4).The current status of the construction and concurrent R&D are also discussed.

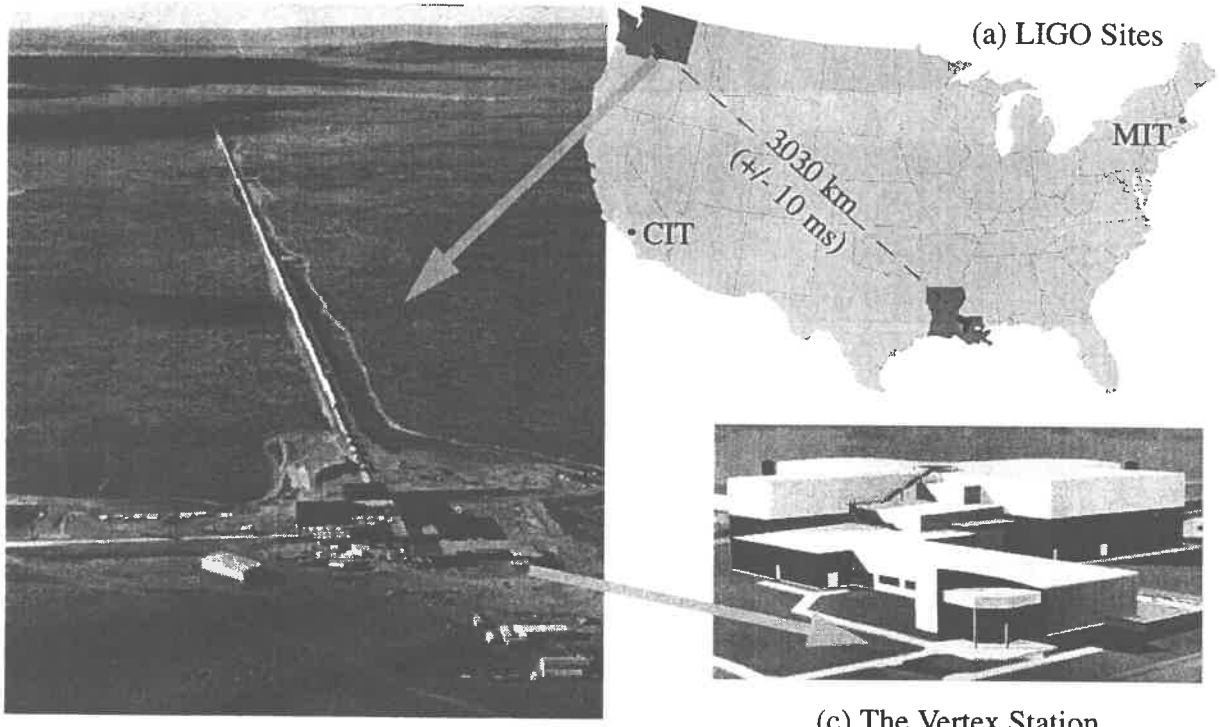

(b) The Hanford, WA Facility in Construction (6/97)

(c) The Vertex Station

Figure 4: The Hanford, WA Facility in Construction (June 97)

AFM Based Nanoindentation as a Probe of Nanomechanics

P.E. Russell*, K.F. Jarausch,* and J.E. Houston**
*Analytical Instrumentation Facility, North Carolina State University, Raleigh NC 27695-7531
**Department 1114, Sandia National Laboratories, Albuquerque NM 87185

The investigation of the mechanical properties of nanostructured materials is critical to the continuing development of thin film technology. A variety of nanoindentation techniques have been developed as tools to investigate the mechanical behavior of thin films.[1-4] In this study the interfacial force microscope (IFM)[2] and a specially equipped[5] atomic force mircoscope (AFM) were used to survey the mechanical response of 100nm thick Au films as a function of residual and imposed film stress. These techniques differ significantly from conventional nanoindentation techniques in their approach to force measurement, in-situ imaging capability, and analysis of load-displacement data.

An IFM and an AFM equipped with a stainless-steel cantilver and diamond probe[5] have been used to investigate the nano-mechanical properties of Au thin films. These systems share the same components as scanned probe microscopes (SPMs) and differ only in their approach to load sensing. The capacitive feedback system of the IFM sensor allows for quantitative measurement of the load applied while minimizing the sensor's compliance. The AFM measures the applied load by recording the deflection of a cantilever and is therefore a compliance based load sensor. The advantages and limitations of indentation with SPMs will be discussed in the context of other nanoindentation techniques.

As an example application,[6] the mechanical response of 100 nm thickpolycrystalline Au films deposited on various adhesion layers (Ti, Cr, Pt) on Si substrates was investigated. The mechanical response was consistent for a particular film-adhesion layer combination, however the values of effective elastic modulus and shear-stress threshold were found to vary by as much as a factor of two as a function of adhesion layer. The IFM measurements were found to correlate with the differences in residual stress resulting from the film-adhesion layer combination and were not found to correlate with the films' morphology or adhesion to the substrate. A new four-point bending device is being used to investigate the dependence of IFM nanoindentation measurements on imposed tensile and compressive stress. The observed dependence of the mechanical response on stress will be discussed in terms of possible mechanisms, identifying how the stress alters the measurement process and causes the variation of the films' mechanical response. These experiments suggest that the IFM and AFM used in nanoindenter mode have the potential for being able to measure thin film stress on a very local level.

This work was supported under DOE under Contract No. DE-AC04-94AL85000.

REFERENCES

1. G.M Pharr and W.C. Oliver, MRS Bulletin, July(1992)28.
2. S.A. Joyce and J.E. Houston, Rev. Sci. Instrum., 62(1991)710.
3. M. R. VanLandingham et al., J. Adhesion, 64(1997)31.
4. W.W. Gerberich et al, Acta. mater., 44(1996)3585.
5. Digital Instruments, Santa Barbara CA.
6. P. Tangyunyong et al, J. Adhesion Sci. Technol., 8(1994)897.

POTENTIALS OF X-TENDED VIEW SEMS - ENVIRONMENT FOR THE MICRO MANUFACTURING WORLD

Stephan Klein* and Martin Klein**

*Fachhochschule Lübeck, Department of Applied Natural Sciences, 23562 Lübeck, Germany
e-mail: klein@fh-luebeck.de
**VISITEC Microtechnik GmbH, 23936 Grevesmühlen, Germany
e-mail: visitec@t-online.de

ABSTRACT: This paper describes concept, features, and application of a new scanning-electron-microscope (SEM) called x-tended view - SEM (XV - SEM). In addition to investigating products of the macromechanical world which do not fit into conventional SEM´s vacuum chambers one of the XV - SEM´s main field of operation will be the support of micromechanical manufacturing processes in general. The paper is focused on this field. The need of optimum product properties leads to the necessity of assembling products containing different parts in the micromechanical as well as in the macromechanical world. After introducing the necessities leading to a new form of SEM the development, the concept, and the features of the LC SEM are described in detail.

INTRODUCTION

Although there is a big need of sensorical systems transmitting information of any process from the micro world into the operator´s macro world many sensorical systems common in the macroworld can not be used within the micromechanical world /HNS-94/. Optical microscopes are of limited use due to their small magnification and depth of focus (e.g. an optical microscope offers just a depth of focus of 2 µm at an enlargement of 100). Conventional SEMs offer a much better resolution and a better depth of focus but are limited in the size and weight of objects to be inspected because of the usually small vacuum-chambers. Conventional goniometer tables are usually built with a very high precision and for a load carrying capacity up to 20 kg. Especially a flexible tool allowing a visual control of any micro-mechanical manufacturing, assembling, or testing process has not yet been described. A large-chamber SEM as a suitable tool offering this visual control and to support these processes has been developed to open new fields of application to electron microscopy. There are also fields of application within the macroworld.

CONCEPT OF THE LARGE-CHAMBER SEM

The concept of the XV - SEM is based on an analysis of human behaviour /KLK-97, PAB-95/. Persons investigating a small object are taking these objects into their hand and turning them around (fixed eye, moved object), large objects are investigated by mooving around the object (fixed object, mooving eye). The main difference to conventional SEMs is the freely programmable positioning system allowing to move the electron optics to any point of the working space within a large vacuum chamber. This main

advantage offers a flexible view on large objects or manufacturing equipment of any form. It becomes possible to visualize objects and processes of the micromechanical world without a repercussion on the investigated objects with nearly no limitations of the objects in size and weight.

The new XV - SEM consists of four main subassemblies:

- electron-optics including PC-supported visualization-system,
- positioning system for electron optics,
- vacuum chamber including vacuum system with pumps, pipes, valves, pressure sensing equipment, vibration control system, and
- control-unit.

Fig. 3 shows the layout of the XV - SEM. The visualization system is PC-based comparable to systems used for conventional SEMs. The PC system is used for controlling the whole microscope, too.

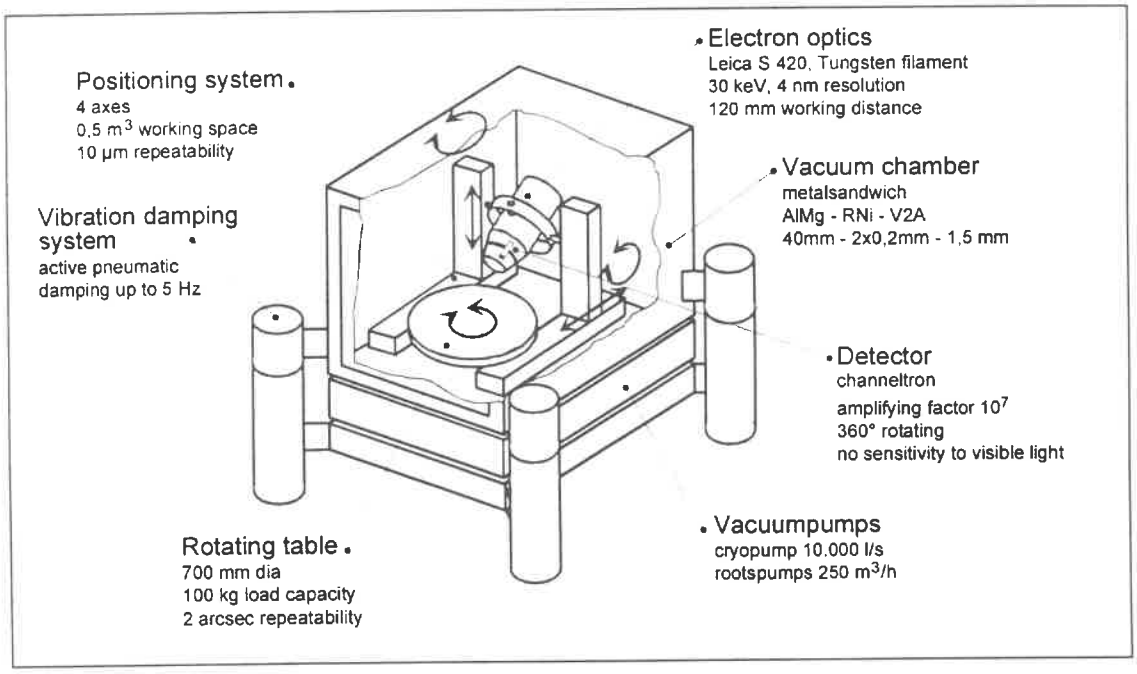

Fig. 1: View of complete LC SEM
(control unit and vacuum-system not displayed)

For positioning a body in a space six degrees of freedom are required. The positioning system allows the freely positioning of the electron optics within the chamber. Main requirements for the developed precision positioning system are according to /SLO-92/:

- accuracy
- repeatability,
- resolution, and for the special purpose here,
- operatability within the vacuum.

Two translatory axes and two rotary axes are moving the electron optics. In addition to the mechanical positioning system an electronic beam shift allows a movement of about ± 2 mm. Although the sixth axis is not necessary here, a rotating device for the channeltron detector at the end lens of the electron optics is installed for more comfortable work and the additional property of choosing arbitary directions of illumination by the operator. This device is the sixth axis of the positioning system. The positioning

system enables the user to investigate objects up to a size of 600 mm to 600 mm to 600 mm. A rotating device is carrying the object to be investigated. A mass of 100 kg is permitted for the objects.

The rectangular vacuum-chamber is made of aluminium with an overall wall-thickness of 40 mm. The material has been chosen because of its magnetical properties. In addition the chamber is plated with a special nickel alloy as a magnetic screen. The chamber offers a large front door opening. This allows a comfortable access to the working space and an easy installation of objects to be investigated or in situ testing equipment. In addition maintainance of the electron optics and the positioning system can be made easily. For the handling of heavy objects a lifting equipment is installed inside the chamber. Windows are integrated to allow a visual control of the equipment installed within the chamber. Time to pump the chamber to the required vacuum of 10^{-6} mbar is about one hour. Auxiliary pumps reach a pressure of 10^{-2} mbar and are turned off at this pressure. A cryo-pump is used as the main pump.

APPLICATION

As mentioned above, the new kinematics and the enlarged chamber open many new fields of application for electron microscopy. The three main fields of application for the XV - SEM are:

- microtechnology,
- macrotechnology, and
- in-situ testing.

Results of the investigations in these fields are described in /WEH-96/. Especially the assembly of microsystems is introduced in /WHP-97/. Fig. 2 shows the image of a mechanical drilled hole with a diameter of 20 µm.

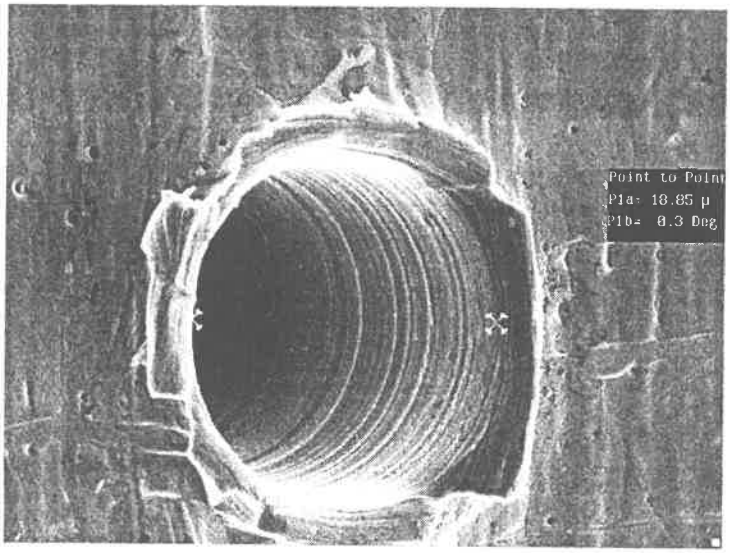

Fig. 2: Mechanical drilled hole (20 µm dia)

In addition to the visualization of objects element analysis is required for many applications of electron microscopy. For that purpose two systems can be integrated into the chamber:

- EDX - energy dispersive x-ray analysis, and
- WDX - wavelength dispersive x-ray anlysis.

Both systems are fixed closed to the electron optics and can be moved by the positioning system, too. Two additional linear stages allow the adjustment of the EDX - system.

RESULTS

The paper describes concept, development, and applications of a new scanning electron microscope. This microscope allows the flexible positioning of the electron optics within its enlarged vacuum chamber. The broad potential of the new XV - SEM can be described by the following main features:

- non-destructive analysis of large specimen
- cyclic investigation of expensive objects
  (use - investigation - use - investigation - use)
- comparative investigation of several objects under identical conditions
- integration of testing equipment for situ test of components and systems during operation
  - test of component operation
  - material testing
  - manufacturing technology
- integration of EDX and WDX analysis
- day-light observation of investigation
  (integration of laser-technology into chamber)
- simulation of space conditions
  (vacuum, radiation, temperature)

Adapting these potentials to the use within the field of micromanufacturing opens new fields of application for electron microscopy in testing and production of these processes and therefore helps improving their quality and productivity.

REFERENCES

/HNS-94/ Hatamura, Y., Nakao, M., Sato, T.: Construction of Nano Manufacturing World. Proc. 4th Int. Conf. on Micro Electro, Opto, Mechanical Systems and Components. Berlin, 1994, pp. 37 - 51.

/KLK-97/ Klein, M., Klein, St.: Adapting Human Behaviour for the Development of a New Scanning Electron Microscope. Proc. Int. Conf. on Micromechatronics for Information and Precision Equipment MIPE'97, Tokyo, Japan, 1997, pp. 324 - 328.

/PAB-95/ Pahl, G., Beitz, W.: Engineering Design. A Systematic Approach. 2nd ed. Berlin Heidelberg, New York: Springer 1995.

/SLO-92/ Slocum A. H.: Precision Machine Design. Englewood Cliffs: Prentice Hall, 1992.

/WEH-96/ Weck, M., Hümmler, J.: Beobachtung von Produktionsvorgängen mit einem Großkammer-Rasterelektronenmikroskop. wt-Produktion und Management 86, pp. 596 - 600, (1996).

/WHP-97/ Weck, M., Hümmler, J. Petresen, B.: Assembly of micro systems in a large-chamber scanning electron microscope. Proc. 12th Annual ASPE Meeting, Norfolk, Virginia, 1997.

Interferometric Measurement of Absolute Dimensions of Cylindrical Surfaces

Andrew W. Kulawiec, Jon F. Fleig and John H. Bruning

Tropel Corporation
60 O'Connor Road
Fairport, NY 14450

ABSTRACT

Recently, grazing incidence laser interferometry has been applied to the measurements of the surface form of cylindrical and other rotationally symmetric surfaces.[1-4] This particular technique uses high precision diffractive optical elements to produce wavefronts which precisely match the surface of a perfect cylinder. Deviations of a test cylinder from a perfect cylinder show up as phase differences in the interference pattern. Conventional phase shifting techniques are used to obtain accurate surface height data over the entire surface of the cylinder. Since the method is interferometric, the entire measurement is very rapid (less than 1 minute) and capable of sub-micron accuracy. Until now, measurements produced by this technique have been limited to measurements of deviations from a perfect cylinder. This paper presents a method by which measurements of absolute dimensions of the cylindrical surface can be made using grazing incidence interferometry. In particular, measurements of the average, maximum and minimum diameters can be made, as well as the radius of each point on the surface. A theoretical description of the method is given, as well as some experimental results. An additional method to extend the dynamic range of the measurement is also described.

1. INTRODUCTION

The optical layout of a grazing incidence cylindrical interferometer is given in Figure 1. A collimated beam of laser light is produced with a point source, typically the output of a single mode fiber, and a well-corrected collimating lens. This wavefront illuminates a first rotationally symmetric diffractive optical element. The first order diffracted light from this element is directed toward the part under test at a grazing angle and provides the test wavefront in the interferometer. The zero order diffracted light remains undeviated and serves as the reference wavefront. Light reflected off the part is again diffracted at the second diffractive optical element where it is recombined with the reference wavefront. A second lens forms an image of the part under test on a screen, where it is viewed with a CCD camera. The aperture located between the lens and the image plane is used to block unwanted diffracted orders. Inside or outside cylinders of different diameters and aspect ratios can be measured by using different diffracted orders from the same diffractive optical elements.

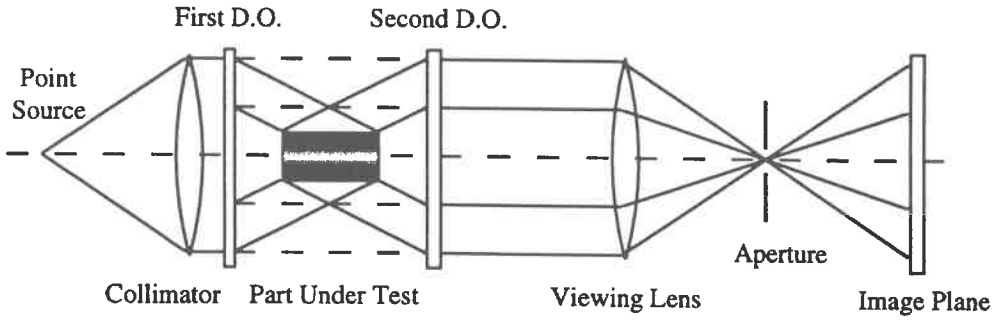

Figure 1. Optical layout of grazing incidence cylindrical interferometer.

The combination of the reflected test wavefront and the undeviated reference wavefront produces an annular fringe pattern indicative of form errors over the entire surface of the cylindrical part. Conventional phase shifting

interferometric techniques are then used to extract precise surface height information from the fringe pattern. The result is a three-dimensional surface map showing the deviations of the test cylinder from a theoretically perfect cylinder. This surface map contains many thousands of individual data points collected simultaneously. The data set can then be numerically analyzed in numerous ways to produce measures of cylindricity, roundness, straightness and taper. A sample measurement of a cylinder with significant form errors is shown below in Figure 2. This typical measurement report includes a three-dimensional surface plot, an unwrapped contour plot, a sample roundness and straightness trace taken from the locations indicated by the two cursors in the contour plot, and finally, various measurement parameters calculated from the entire data set.

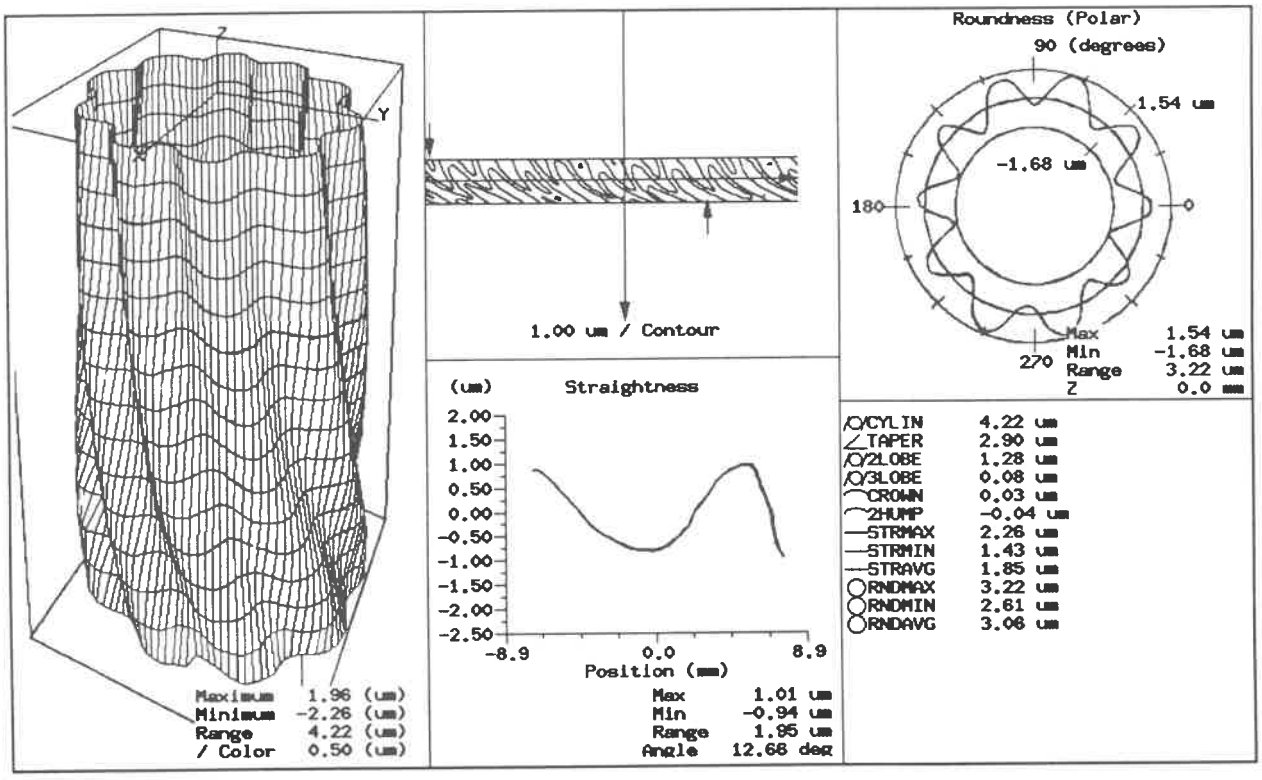

Figure 2. Sample measurement of a cylinder using the grazing incidence cylindrical interferometer.

The grazing incidence illumination produces a high reflectivity from parts with non-specular surface finishes. This permits the measurement of cylindrical parts produced by turning, grinding or honing operations. Furthermore, the grazing incidence geometry reduces the fringe sensitivity, or spacing between adjacent fringes in the interferogram, thereby permitting the measurement of surfaces with many wavelengths of form errors. The fringe sensitivity is typically designed to be 2-5 microns to accommodate most industrial parts.

2. THEORY

Until now, the method described above has only been used to determine form deviations of a test cylinder from a perfect cylinder. Interferometric measurements of the absolute diameter of a cylinder have not been possible. A secondary method such as contact, capacitance or air gauging has been required. However, it has been discovered that the data from the interferometric method does contain useful information regarding the diameter of the cylindrical part. In particular, the constant or average phase in the interferogram is directly related to the average radius of the part. A change in the radius of the part by exactly the fringe sensitivity will change the value of the constant phase term by one fringe.

This observation can be used to accurately measure the difference in radius (or diameter) of two different parts, assuming there has been no change in the instrument between measurements. However, the cyclical nature of interference fringes allows the constant or average phase of an interferogram to be determined only to within one fringe, or modulo 2π. A difference in the radius of two parts of exactly two fringes will appear identical to a difference of one fringe. Hence only relatively small differences in diameter can be determined. However, the uncertainty to which the phase in an interferometer can be measured is typically a small fraction of a fringe. This will result in a very accurate and repeatable measurement.

Using the above method, the absolute diameter of an unknown test cylinder can be determined by comparing the constant phase term of the interferogram with that from an interferogram from a master cylinder. The difference of the constant phase terms multiplied by the sensitivity is simply the difference in average radius of the two cylinders. If the average diameter of the master cylinder is previously known, then the absolute diameter of the test cylinder can be calculated. The radius at any point on the test cylinder can then be determined by combining the average diameter with the surface height map generated by the interferometer. Clearly, if the difference in average radii of the master and test cylinder is greater than one fringe, which is typically 2-5 microns, then a phase ambiguity occurs. Hence the dynamic range for diameter measurements is given by twice the sensitivity of the interferometer.

An extended dynamic range measurement can be made by using a two wavelength interferometric technique. In this particular configuration, the cylinder is measured simultaneously at two different sensitivities. This is done by fabricating diffractive optics with two concentric annular zones containing different grating pitches. Diffracted light from each zone illuminates the same surface at two different grazing angles, resulting in interference patterns of different sensitivities. The two measurements are combined to produce a measurement of the part at a much larger sensitivity (given by the ratio of the product and the difference of the two sensitivities). The constant phase term of this can be used in the same manner as before to determine the difference in average radius from the master, but with a much larger dynamic range. In essence, the addition of the second interference pattern resolves the 2π phase ambiguity up to the beat frequency of the two effective wavelengths.

3. MEASUREMENTS

In order to demonstrate the validity of this method and estimate its uncertainty, a set of five cylindrical parts were measured using the grazing incidence cylindrical interferometer and a contact gauge. The latter gauge is a contact instrument consisting of a motorized flat-ended probe with a distance measuring laser interferometer measuring the translation of the probe. The instrument is mounted on a granite surface plate, thereby permitting general thickness and distance measurements. The grazing incidence interferometer has a fringe sensitivity of 4 microns/fringe, resulting in a dynamic range of 8 microns for diameter measurements.

The parts chosen for this test were outside cylinders with a nominal diameter of 4.0 mm and a length of 15.0 mm. The cylindricity of each part was approximately 0.5 microns, thereby permitting reasonable measurements of average diameter with the contact gauge. In order to obtain repeatable measurements with the contact gauge, the parts were placed in a very shallow V-groove with a precision ground and polished flat top. The contact gauge was zeroed off the flat top prior to the placement of the parts in the V. This resulted in a constant offset of approximately 0.2 mm from the true diameter, but allowed repeatable and accurate measurements of the diameter differences.

Table 1 shows the results of measurements of these five parts on both the grazing incidence interferometer and the contact gauge. The constant phase terms are obtained from a least squares fit of the data to a set of orthogonal polynomials. The reported measurements are the average of four measurements for each part performed in a rotating order. The contact measurements are the average of nine separate measurements for each part, three each performed at three random locations on the part. The correlation coefficient of nearly 1.0 indicates an extremely high degree of correlation, as illustrated in Figure 3. Furthermore, the fitted slope parameter is less than 0.2% different than the theoretical value of 0.008 mm/fringe (twice the fringe sensitivity). The standard errors are calculated by taking the average of the standard deviation of each measurement divided by the square root of the number of samples taken for each part.

Part #	Constant Phase Term (fringes)	Contact Measurement (mm)
1	0.0076	3.8285
2	0.2915	3.8307
3	0.3350	3.8311
4	0.3692	3.8314
5	0.4148	3.8317

Correlation Coefficient	0.99987
Slope (mm/fringe)	0.007986
Y-Intercept (mm)	3.8284
X Standard Error (fringes)	0.0042
Y Standard Error (mm)	0.00010

Average Deviation (microns)	0.026
Standard Deviation (microns)	0.027

Table 1. Summary of comparison measurement results including regression analysis.

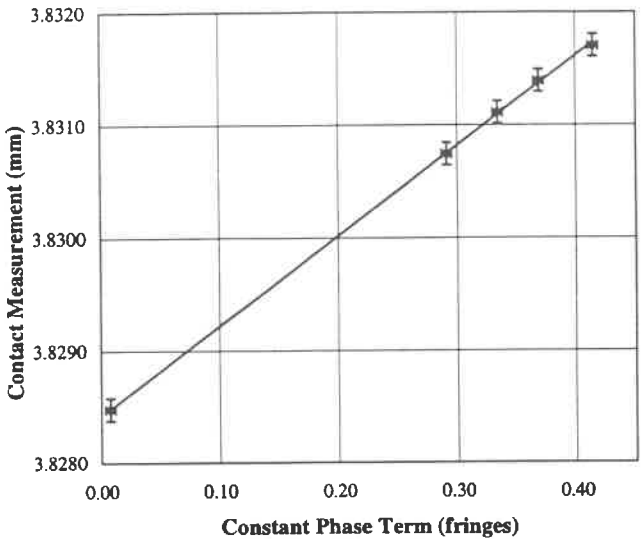

Figure 3. Plot of measured constant phase terms vs. contact measurements including a linear fit to the data.

The average deviation reported in Table 1 is computed by the following method. First, one part is chosen as the "master" cylinder. The diameter of every other part is then calculated from the differences in the measured constant phase terms, using the theoretical fringe spacing of 4 microns/fringe for radius. A difference from the contact method is then calculated for each part resulting in a measured deviation. The next part is then chosen as the master and the process is repeated. Finally, the absolute value of each measured deviation is taken and the average deviation is calculated. The standard deviation of this parameter is also given in Table 1. This value is indicative of the uncertainty in diameter one would achieve in using this method with only one part measured separately as the calibrated master cylinder.

4. CONCLUSIONS

The use of grazing incidence interferometry for the measurement of absolute diameter of a cylindrical surface has been demonstrated. This method, based on the measurement of the constant phase of the interferogram, has been shown to provide accurate and repeatable measurements of the average diameter of cylindrical surfaces. The results of this technique have been compared with measurements from a traditional contact gauge and show excellent correlation and stability. The method can also be extended to provide measurements of maximum and minimum diameters, as well as the radius of each point on the surface. Furthermore, a method to extend the dynamic range of the measurements has been proposed.

5. REFERENCES

1. T. Dresel, J. Schwider, A. Wehrhahn and S. Babin, "Grazing incidence interferometry applied to the measurement of cylindrical surfaces," Opt. Eng. **34**, 3531-3535 (1995).
2. S. Brinkmann, T. Dresel, R. Schreiner and J. Schwider, "Axicon-type test interferometer for cylindrical surfaces," Optik **102**, 106-110 (1996).
3. A. Kulawiec and J. Bruning, "Applications of diffractive optics to three-dimensional surface form measurements," 1996 Annual Meeting of the Optical Society of America, Rochester, NY.
4. N. Lindlein, R. Schreiner, S. Brinkmann, T. Dresel and J. Schwider, "Axicon-type test interferometer for cylindrical surfaces: systematic error assessment," Appl. Opt. Vol. **36**, No. 13, 2791-2795 (1997).

Multi-step form metrology: principles and applications to the LIGO Pathfinder optics

Chris J. Evans(1), Paul J. Sullivan(2), R. E. Parks(1,3), W. T. Estler(1) and L-Z. Shao(4)

(1) National Institute of Standards and Technology, Precision Engineering Division, Gaithersburg, MD 20899
(2) now at KLA-Tencor, Milpitas, CA
(3) Optical Perspectives Group, Tucson, AZ
(4)Tucson Optical Research Corp, Tucson, AZ

Prior to placing procurement contracts for the fabrication of optics for the Laser Interferometer Gravitational Wave Observatory (LIGO)[1], several vendors were contracted to produce demonstration optics. Eight such optics were measured at NIST using methods analogous to those used in a variety of areas of more conventional mechanical metrology. This presentation aims (i) to describe the measurements made and the results achieved; and (ii) to highlight the general aspects of the methods used and their relationships with other metrological methods.

The primary measurement method used at NIST was a multiply-redundant areal N-position averaging 3 flat test[2] - a combination of a 3D analog of multi-step spindle/roundness testing and the classical 3-flat test.

N-position areal 3-flat test

It is well known in the optical fabrication and testing community that coma in an optical surface can be removed from the tested wavefront simply by averaging two interferograms with the test object rotated 180 degrees about the optical axis. Freischlad et al[3] discuss the averaging of interferograms taken at different angular positions and note: *"The common fabrication errors astigmatism, coma and trefoil are completely eliminated by four orientations at 90º intervals"*.

The departure (from a flat, sphere, etc) of any arbitrary wavefront, A, of circular cross-section may be expressed as the well known linear combination of polynomial terms:

$$A(r,\theta) = \sum_{k,l} R_l^k(r)[a_l^k \cos k\theta + a_l^{-k} \sin k\theta] \qquad (1)$$

where the coefficients $a_l^{\pm k}$ specify the magnitude of each term while the trigonometric terms specify the angular part of the polynomial representation. Following usual practice, the $R_l^k(r)$ are the radial terms of the Zernike polynomials.

Evans and Kestner[2] proved that, for any surface described by Eqn (1) -- and for any $R_l^k(r)$ -- that the average of N measurements spaced at 360/N degree intervals reduces to zero all terms in the rotated member except those of order kNθ, where k is an integer. The practical utility of this proof may best be understood by considering a specific case. Suppose a flat is mounted in front of a Fizeau interferometer and tested at 5 positions 72 degrees apart. If the five measured

wavefronts are averaged, the result will contain*: all the departures from flatness of the reference surface mounted on the interferometer; rotationally invariant errors (k=0) in the flat under test; and terms from the flat in 5θ (k=1), 10θ (k=2). 15θ (k=3)...etc. Now if this averaged result is subtracted from the original measurement data, the non-rotationally invariant components in the reference and the flat under test (except those of order kNθ) have been separated. Now, if the five data sets are rotated back, in software, to a common origin and averaged, this represents a virtual rotation of the interferometer. Then using an analogous procedure we can identify the non-rotationally invariant terms in the test optic. Finally, with the non-rotationally invariant components removed, we can invoke the conventional 3-flat algorithm to solve for rotationally invariant terms and then sum the rotationally invariant and variant terms to obtain the surface departure of the flat under test and the reference flat.

For the measurements of the LIGO Pathfinder optics, we chose to test at 5 azimuthal positions. This decision was based on three considerations. First, we wished to minimize the number of positions to minimize the time taken, consistent with reaching the target uncertainty in the measurement. Second, we analyzed a database of measurements made over several years at NIST either comprising two NIST owned flats or of artifacts of similar quality submitted to NIST for measurement. We fit the data to Zernike polynomials up to 12θ and plotted the rms contributions as a function of azimuthal order[4]. Not surprisingly, the contribution decreases with increasing azimuthal order. For 4θ or higher, the contributions are significantly less than 1 nm rms. Further, we showed elsewhere[5] that using an odd value of θ results in a halving of the uncertainty arising at the harmonics of N.

Six LIGO Pathfinder optics were measured with 3 different NIST owned transmission flats using the N-position areal 3-flat test. Data was taken for both the 6 km radiussed surface (about 0.5 μm sag over a 150 mm aperture) and the flat, wedged surface, as well as in transmission. In addition, data was taken at 4 positions 40 mm off-axis. Not all possible measurements were made for all optics with all NIST transmission flats. Even so, large numbers of redundant "solutions" were available for each of the NIST owned transmission flats.

To assess the uncertainty of our measurement process, we chose to intercompare possible solutions for the NIST owned transmission flats. There were seven solutions for one flat and three for each of the other two. The maximum rms value for the difference between any two solutions for a given NIST owned transmission flat was less than 1 nm. All solutions were averaged to further reduce the uncertainty in the measurement of the NIST owned transmission flats. These resulting error maps are then subtracted from the original measurement to give maps of the Pathfinder optics.

Figure 1 shows two measurements of the curved surface (power removed) based on solutions for two different NIST owned transmission flats. The parameter agreement (approximately 20 pm rms) is remarkable.

Solutions for the reference surfaces used were also derived using an optimized version of Fritz's method[6] and a multiple averaging method[7]. Differences between the solutions are less than 1 nm rms.

* Ignoring typically second order errors arising from the imaging system, etc.

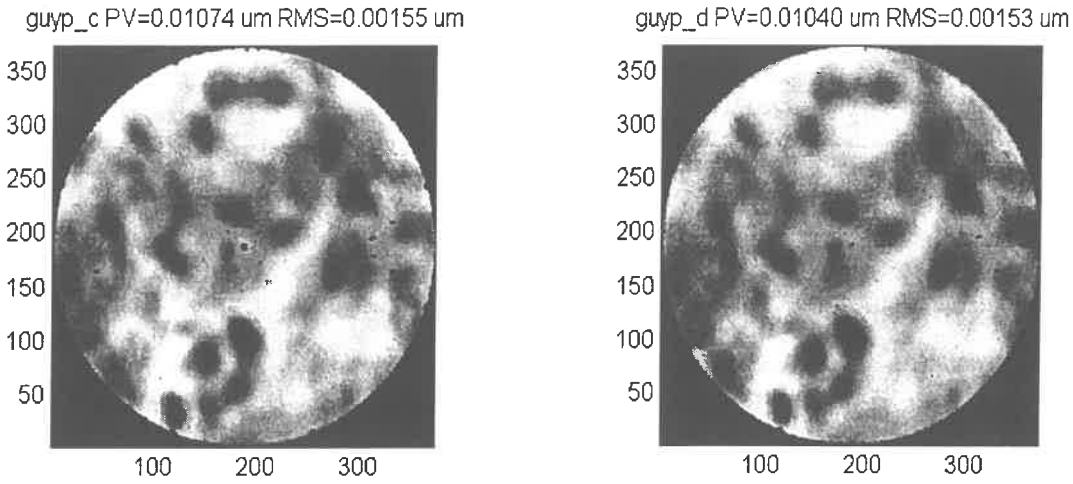

Figure 1: Independent measurement results for one Pathfinder optic on a 373 x 373 pixel grid.

Synthesized data

We have shown how, in multi-step measurements[8], if two measurements are made at angular orientations separated by 360/N degrees (where N is an integer >2), the remaining N-2 measurements can be synthesised; more generally, if n measurements are made, the remaining N-n may be synthesised. Either of these procedures will result in an increased uncertainty, assuming that, for a fixed angular position, the uncertainties are uncorrelated in θ and, for fixed θ uncorrelated between measurements. This is exactly analogous to the case where data is synthesized from n of N positions in a multi-position roundness test. An analysis of those uncertainties[9] show that, for n=2:

$$\frac{u_{n=2}}{u_{n=N}} = \sqrt{N}\sqrt{\frac{2}{3}N - 2 + \frac{7}{3N}} \approx \sqrt{\frac{2}{3}N}$$

for large N. For other values of n, the formulation given by Estler et al[9] allows the metrologist to trade-off required uncertainties and angular resolution with level of effort. In the 3D case (testing the LIGO optics) use of n-position generated data allowed us to check for uncertainties arising, for example, from a misalignment of the axis of rotation of the test optic with respect to the optical axis of the interferometer and from the rotation angle. Solutions obtained for the optics using data generation reveal no significant systematic uncertainties.

Concluding remarks

This paper has described the multiply redundant measurement procedures used at NIST to measure six of the LIGO Pathfinder optics. The data are internally consistent to better than 1 nm rms. Massive averaging has been used to reduce the statistically treated uncertainties to this level. Sources of uncertainty making contributions that are a reasonable fraction of a nanometer

rms include relocation errors, data processing, electrical noise and environmental effects. Test procedures were designed to identify systematic components, all of which were below 1 nm rms.

Acknowledgements

This material is based in part upon work supported by the National Science Foundation under the Cooperative Agreement with the California Institute of Technology, No. PHY-9210038. Any opinions, findings, and conclusions or recommendations expressed in this material are those of the author(s) and do not necessarily reflect the view of the National Science Foundation. Throughout the period during which the work was performed, the authors have benefited from the support of Caltech staff including D. Jungwirth (now at Hughes), W. Kells, G. Billingsley and S. Whitcomb. Many colleagues at NIST have made contributions, including E. P. Whitenton and M. L. McGlauflin.

References

[1] Spero R. E. and Whitcomb S. E. "The Laser Interferometer Gravitational-wave Observatory (LIGO)" Optics & Photonics News, v.6, no.7, pp35-39 (July 1995).
[2] Evans C. J. and Kestner R. N., "Test optics error removal" Applied Optics Vol 35 (1996) No 7, pp1015-21
[3] Freishlad K., Kuchel M., Schuster K. H., Wegmann U., and Kaiser W. "Real Time Wavefront Measurement with Lambda/10 Fringe Spacing for the Optical Shop" Proc SPIE Vol 1332 pp18-24, (1990)
[4] Evans C. J., Parks R. E., Sullivan, P. J. and Taylor J. S. "Visualization of surface figure by the use of Zernike polynomials" Applied Optics, Vol 34 (1995) No 34, pp7815-9
[5] Parks R. E., Evans C. J., Sullivan P. J., Shao L-Z. and Loucks B "Measurements of the LIGO Pathfinder Optics" SPIE Vol 3134 (1997) in press
[6] Fritz B. S. "Absolute calibration of an optical flat" Optical Engineering, Vol 23, 1984, pp379-83
[7] Creath K. and Wyant J. C. "Absolute measurement of surface roughness" Applied Optics, Vol 29 (1990) pp3823-7
[8] Parks R. E. , Shao L-Z. and Evans C. J. "Pixel based absolute topography test for three flats" Applied Optics, 1997, in press
[9] Estler W. T., Evans C. J., and Shao L-Z. "Uncertainty estimation for multi-position form error metrology" Precision Engineering (1997) in press

Complex Surfaces - Applications and Generation by Diamond Machining

E. Brinksmeier, W. Preuss
LFM Labor für Mikrozerspanung, University of Bremen, Germany

1. Introduction

Many innovative products require key components with complex and precise surfaces which have important optical or mechanical functions [1], e. g. diffractive optics, intra-ocular lenses, new car lightsystems, HDTV projection screens, sinewave mirrors, micromechanical and microoptical parts, fusion targets and many more. This spectrum of optical components can be devided into two classes: surfaces with continuously varying slope and structured surfaces with discontinuous features, e. g. steps and profiles, superimposed onto plano, aspheric or asymmetric envelope surfaces.

continuous surfaces

type of surface	machining operation	examples
plano	diamond turning (1 axis)	plano mirrors
conic, aspheric	diamond turning (2 axes)	aspherical molds and mirrors axicons, waxicons
mild asymmetric	fast tool servo	sinewave and ring mirrors with small amplitudes
deep asymmetric	fly-cutting (3 axes) ball-end milling (3 axes)	ring mirrors with large amplitudes deep asymmetric mirrors

OR 145e

discontinuous surfaces

type of profile	envelope surface	machining operation	examples
linear	plano	fly-cutting (1 axis)	gratings, prisms, precision steps
	asymmetric	fly-cutting (4-5 axes)	prisms on asymmetric surfaces
rotational symmetric	plano	diamond turning (1-2 axes)	Fresnel lenses, diffractive optical elements (DOE)
	aspheric	diamond turning (2 axes)	Fresnel lenses, DOE (e.g. intra-ocular lenses)
asymmetric	aspheric	fast tool servo	facetted mirrors
	asymmetric	fly-cutting (4-5 axes)	Fresnel zones on asymmetric surfaces

OR 146e

Fig. 1: Classification of diamond machining processes for the generation of continuous and discontinuous optical surfaces.

In the case of continuous optical surfaces, the degree of complexity of the diamond machining process increases with the number of numerically controlled axes. According to this definition, many aspherics and asymmetric surfaces are examples for complex surfaces. In the case of discontinuous optical surfaces, the complexity depends on the form and profile of discontinuous features and the degree of symmetry of the envelope surface. Figure 1 summarizes the types of surfaces and the diamond machining operations required for manufacturing with respect to increasing complexity. Typical applications are listed in the last column of figure 1. In this paper examples for complex surfaces will be given and appropriate precision machining processes will be discussed.

2. Diamond machining of sinewave ring mirrors

Sinewave ring mirrors are used in CO_2-laser resonators for generating specific cavity modes with high efficiency. These ring mirrors made of OFHC copper have a typical outer diameter of 80 mm and a ring width of 15 mm. The sinewave amplitude is a fraction of the CO_2-laser wavelength λ = 10.6 µm. The number of sinewaves varies between 30 and 60.

A machining concept well suited for the manufacture of these mirrors is the fast tool servo approach. This machining technique has been developed for the generation of non-rotational symmetric surfaces superimposed on rotational symmetric ones. This is achieved by adding a fast linear NC-axis carrying the tool which moves according to the angular position of the rotating workpiece. Thus, the workpiece spindle has to be equipped with an encoder. Several solutions differing in stroke amplitude and oscillation frequency have been realized so far [2, 3, 4]. The stroke of the first concepts using exclusivly piezoelectric transducers is restricted to several microns. Recently, long stroke fast tool servos have been built using piezos and linear motors [3] or air bearings and linear motors [4]. Maximum strokes up to 16 mm can be achieved now.

Alternatively, ring mirrors with virtually abitrary profile depths can be generated in a three axes diamond fly-cutting set-up. The workpiece is mounted on a rotary table which is placed on a linear slide and is slightly inclined to the fly-cutter plane. The linear slide is moved back and forth according to the angular position of the rotary table.

3. Diamond machining of deep asymmetric mirrors

Deep asymmetric surfaces which cannot be generated in a fast tool servo set-up can only be realized by three axes milling operations (see upper part of figure 2).

For the generation of asymmetric surfaces ball-end milling has been transferred to diamond machining. In order to overcome zero cutting velocity at the rotational axis of the tool, a pseudo ball-end milling tool has been designed [5]. Even glass was machined sucessfully using a diamond ball-end milling tool [6]. Surfaces with optical finish are attainable when appropriate small feed rates are applied.

To our knowledge torus milling, well known from conventional machining, has not yet been applied in diamond machining, although one should expect much shorter machining times compared with ball-end milling. However, the method is essentially restricted to convex shapes.

For the generation of large asymmetric surfaces single-point fly-cutting (SPFC) has been developed [7]. Large depths of cut and long tool live ensure the machining of parts with a large departure from rotational symmetry in tolerable machining times.

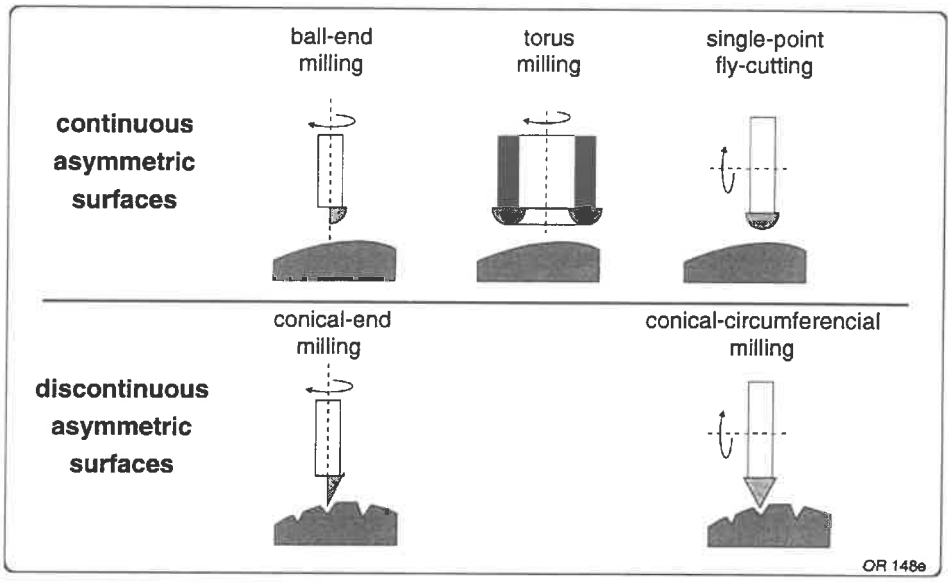

Fig. 2: Multi-axes milling operations for the generation of continuous and discontinuous asymmetric surfaces.

4. Diamond machining of Fresnel zones on asymmetric surfaces

An example from the automotive industry for the application of complex surfaces is given in figure 3. A typical rearlight lens of a motorcar contains refractive Fresnel prisms around its center and adjacent prisms for total internal reflexion. Traditionally, these structures are superimposed onto rotationally symmetric surfaces. The negative lens structure has to be diamond machined into a mold for injection molding.

Novel lens design will require Fresnel zones to be superimposed onto asymmetric surfaces with the additional requirement of continuously changing slopes within each individual zone. This machining task can be solved by conical-end or conical-circumferencial milling (see lower part of figure 2). While the first process requires four NC-axes, the latter process can only be realized with five NC-axes, since the cutter plane has to be positioned tangentially with respect to the local slope and the local direction of the groove. Currently both processes are developed in the LFM within a cooperative r&d-project with an industrial partner.

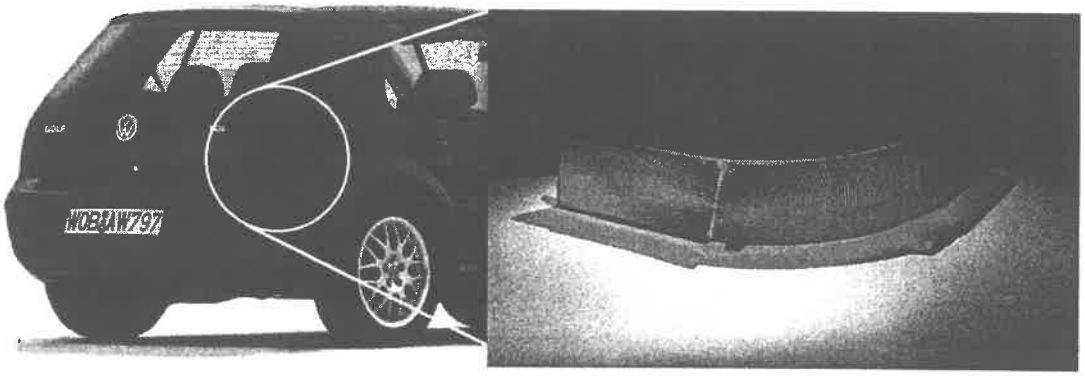

Fig. 3: Injection molded plastic lens with Fresnel zones for a car rearlight.

5. Inspection techniques

For the manufacture of complex surfaces the availability of appropriate surface inspection techniques is essential. Coordinate measuring machines are suited for testing the actual geometry of asymmetric parts. Atomic force microscopy is frequently applied for investigating texture and microroughness of the machined surfaces. The geometry of discontinuous surface features can often be analysed by white-light interferometry. Nevertheless, there is still a lack of measuring techniques for assessing the geometry and surface texture of grooves and prisms with steep slopes.

6. Summary

The complexity of a precision machining operation increases with decreasing number of symmetry elements of the surface to be generated. Hence, the manufacture of asymmetric surfaces requires at least three NC-axes. If discontinuous surface features are superimposed onto asymmetric surfaces even four or five NC-axes are needed.

In this paper examples for the increasing industrial demand of complex optical surfaces are presented. Existing multi-axes precision machining operations, e. g. fast tool servo and ball-end milling, are reviewed. New solutions for the diamond machining of large as well as discontinuous asymmetric surfaces, e. g. single-point fly-cutting and conical-end milling, are discussed. The demand for further improvement of inspection techniques for complex precision parts with discontinuous surface features has been emphazised.

7. References

[1] Brinksmeier, E; W. Preuß; J. Schmütz. „Manufacture of microstructures by diamond machining". Proceedings of 9th IPES / UME 4, 26.-30. Mai 1997, Braunschweig 1997: pp. 503-507.

[2] Falter, P. J; Th. A. Dow. „A diamond turning apparatus for fabrication of non-rotationally symmetric surfaces". Ultraprecision in Manufacturing Engineering, ed. by M. Weck and R. Hartel, Springer 1988: pp. 187-201.

[3] Weck, M; M. Pyra. „Diamond turning of non-symmetric laser optics". Proceedings of the ASPE 1990: pp. 59-62.

[4] Weck, M; H. Oezmeral; K. Mehlkopp; T. Terwei. „A long stroke fast-tool-servo with air bearings". Proceedings of 9th IPES / UME 4, 26.-30. Mai 1997, Braunschweig 1997: pp. 393-396.

[5] Takeuchi, Y; K. Sawada; T. Kawai. "Three-dimensional micromachining by means of ultraprecision milling". Proceedings of the 9th IPES / UME 4, 26.-30. Mai 1997, Braunschweig 1997: pp. 596-599.

[6] Takeuchi, Y; K. Sawada; T. Sata. "Ultraprecision 3D micromachining of glass". Annals of the CIRP Vol. 45/1, 1996: p. 401-404.

[7] Brinksmeier, E; W. Preuß. „Diamond machining of the 3m reflector of the KOSMA submillimeter telescope by a single-point fly-cutting process". Proc. 11th Annual Meeting ASPE, 9-14 Nov. 1996, Monterey, USA: pp. 56-61.

Virtual Reality Applied to Precision Manufacturing

R. Wilhelm, S. Patterson, D. Schmidt K. Nagalla, B. Sethupathi, J. Kroll, O. Martin, & N. Li
Center for Precision Metrology
Department of Mechanical Engineering and Engineering Science
University of North Carolina at Charlotte, Charlotte NC

Introduction

Working from many results in machine tool measurement and modeling, a long term research effort has been initiated to model machine tool behavior and machined parts at resolutions of one part per million and greater. A computer simulated or *virtual* machine tool is used to produce a *virtual* part. From the simulated machine tool behavior and simulated part, it is expected that estimates can be made of process capability.

In previous work, machine tool errors [1] and thermal behavior [2] have been studied and characterized in considerable detail. Many methods have been developed [3,4,5,6,7,8,9,10] for the modeling and compensation of both quasistatic and dynamic errors. Some effort has been made to characterize the statistical behavior of machine tool errors [11]. Correlation has also been established for turned workpieces and spindle behavior [12,13,14] and for simple features cut in milled workpieces [15]. The work reported here goes further by relating the measured behavior of the machine tool to variations found in prismatic part features that have been cut on the machine tool.

Machining simulation usually addresses nominal shape part[16] or details of the tool material interface [17] but not both. This can be explained by the great size disparity found in these approaches, with ratios on the order of one to ten thousand, and also the types of questions that have been addressed by the different simulations. Part shape prediction is typically used to validate tool path programs while simulation of the tool material interface is used to predict very local dynamic effects.

The shear size of detailed part shape predictions has been addressed in many respects by significant advances in ray casting and solid modeling technology [18, 19] and some mathematical aspects of the problem [20] have also been considered. Simulations of the tool material interface have become quite more sophisticated [21] but single process behaviors such as tool dynamics or fixturing are still the typical result from these simulations [22].

Approach

Our approach uses a detailed model of the entire part shape to broadly evaluate the effect of machining errors on part tolerances. This type of question has not been addressed previously in the literature, probably due to the complexity issues discussed earlier. We have defined a virtual part representation [23] to guide our simulation approach and found that a virtual part could also serve as a standard interface among many different types of machining simulations.

Just as one part may be influenced by many different manufacturing processes such as milling, lapping, cleaning, and metrology, the goal for virtual parts is a general purpose representation scheme that can be used with high precision for many different types of manufacturing simulations. More importantly, this representation should allow a variety of simulated manufacturing processes to simultaneously influence a part description similar to the influences found in actual manufacturing environments. For example, during a milling operation to generate a slot on a steel part, changes in ambient temperature may cause the part to grow while energy added to the machining center causes distortion in the spindle length and orientation. At the same time, coolant flow may be driving the part to shrink and quasi-static geometric errors in the machining center may be causing small motion errors as the tool moves through the work envelope.

Current machine simulation prototypes account for measured quasi-static errors, repeatability errors and some thermal error consideration. Standard machine tool testing techniques are used, as available, to measure machine behavior. Response curves and surfaces fitted to the measured data are then used to develop the simulators. Solid modeling technology is used to create virtual parts from the machining simulations. Virtual metrology techniques are used to sample the virtual parts and evaluate tolerances.

For example, in a typical simulation cycle, a preconfigured machine simulator is used along with a solid model of the stock or blank material that is machined to arrive at a finished part. Tool geometry and cutting paths are predefined. The solid model of the workpiece is located relative the origin of the machine tool simulator. Using this information, the machine simulator computes error motion at small steps along the cutting path to locate and orient the simulated tool. At each step, the volume of the tool is compared to the volume of the workpiece. When the two volumes intersect, a subtraction operation is used to modify the solid model of the workpiece in a similar manner to actual machining. The simulation continues until the entire cutting path has been exhausted.

Once a machining simulation is completed, a solid model of the finished workpiece, or virtual part, remains. These models are currently developed using machining step sizes of 10 to 100 micrometers. For parts occupying a cube with ten centimeter sides the virtual part occupies between 100 megabytes and one gigabyte of mass storage.

The virtual part is then evaluated using sampling techniques and computational metrology algorithms. In our current efforts, very dense sample patterns are developed using ray-casting techniques and no modeling of measurement uncertainty is implemented.

Figure 1 shows one of the earliest virtual parts produced at UNC Charlotte and results generated from the study - the plot indicates flatness variations in a range of six micrometers for a part machined for a gear pump. The magnitude and shape of the variations are very consistent with actual parts machined in the UNC Charlotte manufacturing labs. Similar results have been achieved for contours and holes.

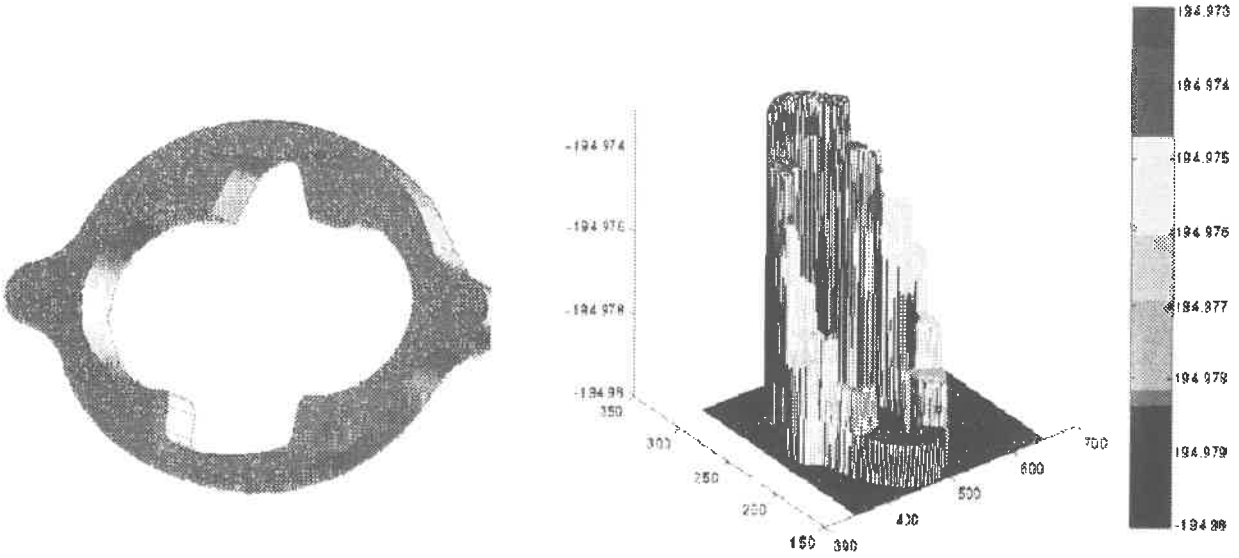

Figure 1: Virtual part and form variation for planar feature, with flatness tolerance, machined from an iron casting.

Discussion

An approach for very high resolution simulation of machining behavior has been developed and an initial prototype has been implemented. A virtual part is used as a standard interface among several different types of machining simulations. This approach is very demanding computationally but provides the flexibility needed to address feature interactions that occur during machining, measurement, and use. Figure 2 shows a very simple example of this.

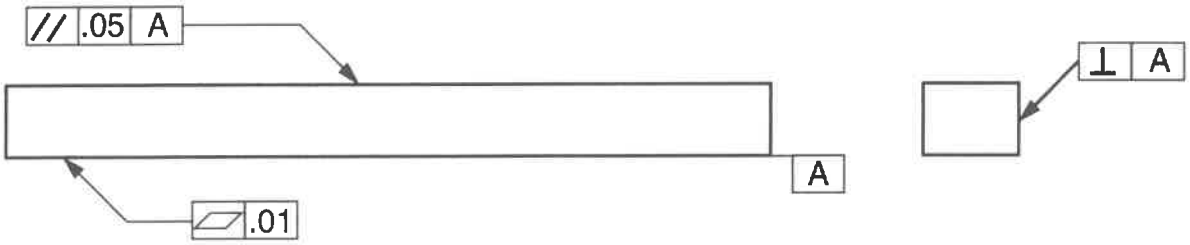

Figure 2: Simple example of interacting features where machining result for one surface may influence the machining result for another surface.

Additional error behaviors due to machine, material, and tool properties are now under development. A measurement system for rapid characterization of machine errors is also being designed. Extensions to solid modeling are under development to address the large surface and volume details that are generated in the simulations.

References

(1) Kline, E.R., Accuracy of Large Machining Centers, Proceedings of the CIRP Conference on Precision Engineering and Manufacturing System, Sept. 1991.

(2) Bryan, J.B., "International Status of Thermal Error Research", Annals of CIRP, Vol. 39, No. 2, 1990.

(3) Chen, J.S., Yuan, J.X., Ni, J. and Wu, S.M., "Real-time Compensation for Time-variant Volumetric Errors on a Machining Center", Transactions Of the ASME, Vol. 115, 1993.

(4) Donmez, M.A., Blomquist, D.S., Hocken, R.J., Liu, C.R. and Barash, M.M., "A General methodology for Machine Tool Accuracy Enhancement by Error Compensation", Precision Engineering, Vol. 8, No. 4, 1988.

(5) Hocken, R.J., Simpson, J.A., Borchardt, B., Lazar, J., Reeve, C., and Stein, P., "Three Dimensional Metrology", Annals of CIRP, Vol. 26, No. 2, 1977.

(6) Kiridena, V.S.B., Ferreira, P.M., "Kinematic Modeling of Quasistatic Errors of Three-Axis Machining Centers", International Journal of Machine Tools and Manufacturing, Vol. 34, No. 1, 1994.

(7) Okushima, K., Kakino, Y., Higashimoto, A., "Compensation of Thermal Displacement by Coordinate System Correction", Annals of CIRP, Vol. 24, No. 2, 1975.

(8) Schultschik, R., "The Components of Volumetric Accuracy", Annals of CIRP, Vol. 26, No. 1, 1977.

(9) Soons, J.A., Theuws, F.C. and Schellekens, P.H., "Modeling the Errors of Multi-Axis Machines: A General methodology", Precision Engineering, Vol. 14, No. 1, 1992.

(10) Zhang, G., Ouyang, R., Liu, B., Hocken, R.J., Veale, R., and Donmez, M.A., "A Displacement Method for Machine Geometry Calibration", Annals of CIRP, Vol. 37, No. 2, 1988.

(11) Donmez, M.A., Liu, C.R., Barash, M.M., Mirski, F., "Statistical Analysis of Positioning Error of a CNC Milling Machine", Journal Of Manufacturing Systems, Vol. 1, No. 1, 1981.

(12) Kakino, Y., Yamamoto, Y., and Ishii, N., "New Measuring Method of Rotating Accuracy of Spindles", Annals of CIRP, Vol. 22, No. 1, 1973.

(13) Sawabe, M., and Fujinuma, N., "Influence of Radial Motion on Form Error of Workpiece in Turning", Annals of CIRP, Vol. 27, No. 1, 1978.

(14) Vanherck, P., Peters, J., and Siddall, G., "Spindle Error Motion", in Technology of Machine Tools, Vol. 5: Machine Tool Accuracy, Hocken, R.J., ed., NTIS Doc. No. UCRL-52960-5, Oct. 1980.

(15) R.G. Wilhelm, N. Srinivasan, F. Farabaugh, and R. Hocken, "Part Form Errors Predicted from Machine Tool Performance Measurements", Annals of CIRP, 46/1:471-474, 1997.

(16) J.H. Oliver and E.D. Goodman. Direct dimensional NC verification. *Computer Aided Design.* 22(1):3-9, 1990.

(17) R.E. DeVor, W.J. Zdeblick, V.A. Tipnis, and S. Buescher. Development of Mathematical Models for Process Planning of Machining Operations. *Transactions of the North American Manufacturing Research Institute of SME*, pages 395-401, 1978.

(18) J.P. Menon and D.M. Robinson. High performance NC verification via massively parallel Raycasting: Extensions to new phenomena and geometric domains. PED Concurrent Engineering - 1992 Winter Annual Meeting of the American Society of Mechanical Engineering, 59:179-194, 1992.

(19) S. Boussac and A. Crosnier. Swept volumes generated from deformable objects application to NC verification. *Proceedings of the 1996 13th IEEE International Conference on Robotics and Automation*, 2:1813-1818, 1996.

(20) J.P. Menon and H.B. Voelcker. Toward a comprehensive formulation of NC verification as a mathematical and computational problem. *PED Concurrent Engineering - 1992 Winter Annual Meeting of the American Society of Mechanical Engineering*, 59:147-164, 1992.

(21) S.N. Melkote, S. M. Athavale, R. E. DeVor, S. G. Kapoor, and J. J. Burkey. Prediction of the Reaction Force System for Machining Fixtures Based on Machining Process Simulation. *Transactions of the North American Manufacturing Research Institute of SME*, Vol. 23, 1995.

(22) R.G. Wilhelm, The Industrial Electronics Handbook, chapter on Virtual Manufacturing Environments, David Irwin, editor, CRC Press, 1997.

(23) R.G. Wilhelm and K.C. Nagalla. Computer Representation of Virtual Parts.*Proceedings of the Symposium on Virtual Reality in Manufacturing Research and Education*, University of Illinois at Chicago, Chicago IL, Oct 7-8, 1996.

A Tapping Stylus for Surface Topographical Measurement Using a Quartz Fork Resonator

Takeshi Hatsuzawa

Precision and Intelligence Laboratory
Tokyo Institute of Technology
4259 Nagatsuta-cho, Midori-ku, Yokohama 226 JAPAN

1.Introduction

A new stylus for surface topographical measurements by using a quartz fork resonator of watches has been developed. The stylus can be applied for a measurement range between AFMs and conventional stylus profilometers. So far, an SPM system based on the quartz fork is developed by Goch. et al.[1-3], however, it uses an acoustic aerodynamic interaction between a vibrating leg and the surface, the resolution of horizontal measurements is not sufficient. The tapping stylus solved this problem by using an AFM cantilever fixed at one end of the fork. Also, as the fork is brought closer in order to tap the surface periodically, measurement reliability is improved by realizing a semi-contact measurement system. In this paper, principle of measurement, construction of the system and results of the measurements are shown.

2.Principle of the tapping stylus

A quartz fork is driven by a TTL level electronic circuit. When the fork is brought close to the surface shown in figure 1, one of the leg is tapping the surface periodically, resulting in the output voltage amplitude decrease of the driving circuit. Since the resonant status is changed by the tapping period , the maximum output voltage becomes a function of distance. Figure 2 is the relationship obtained during a fork travel of forward to a gaugeblock surface and then back from the surface. Since it has a little hysteresis between 0.1 to 0.2 μ m, the fork works as a gap sensor with a fine sensitivity in this region. Together with an x-y scanner, a surface profiler can be constructed by a vertical position control system so that it keeps the height of the fork to be constant.

3.Construction of measurement system

A servosystem shown in figure 3 is constructed to control the distance between the fork leg and the surface to be constant. Elimination of displacement measurement instrument for AFMs such as optical lever or strain gauges makes the system very simple, since the driving circuit itself works as a gap sensing circuit. The topographical information can be obtained from the voltage to piezo controller, since it imitate the surface on a constant gap just like an STM. A piezodriven x-y scanner with

travelling lengths of 8 μ m are used together with the vertical piezo actuator of the same traveling length. A watch quartz fork with a resonant frequency of 32.718kHz is used for the tapping stylus after stripping the protection can, however, it has an unsuitable chamfered corner for the work as a high resolution stylus. To improve the horizontal resolution, an Olympus AFM cantilever with a 4 μ m pyramidal tip is bonded by an epoxy glue beside the leg, which is shown in photo 1. An outlook of the profilometry system by the tapping stylus is shown in photo 2.

4.Example of the measurement

Two of the measurement examples are shown in figures 4 and 5. A measurement result of a line-and-space of an EB(electron beam) resist with a pitch of 3 μ m and a thickness of 0.3 μ m is compared with those of an optical profilometer(Wyco RST-plus) and an SEM micrograph in figure 4. The optically obtained profile has overshoots at the edges of artifacts, because the reflective condition changes rapidly at the boundary of the EB resist and silicon surface. As the tip of the AFM cantilever is not so long nor thin enough to measure high steps, narrower grooves are observed in the tapping profilometry. A measurement was attempted by using a conventional profiler, however, a typical stylus force of 4mN destroyed the EB resist completely. A measurement time of 30min is necessary for a 71×71 points profilometry, since the quartz response is fairly slow.

A result of a optical grating with a pitch of 1.7 μ m and a height of 0.19 μ m is shown in figure 5. As the height of the grating is lower than that of EB resist, the shape of peaks and valleys is more distinctive than that of figure 4. From those results, the vertical resolution of the tapping stylus is estimated to a several nm and horizontal resolution is some dozens of nm. No scratch is observed after the measurements, which indicates very little tapping force of the stylus.

5.Discussion

A tapping stylus has been developed for precise surface measurements. Some of the problems to be solved are as follows.

1)Low step response time of the quartz resonator, resulting in slow measurement time.

2)Resonant disturbance by the bonded cantilever.

3)Deterioration of quartz resonator by the surface electrode oxidation and peering off.

Those can be improved by faster driving circuits, creating an all-in-one stylus with a thin needle.

References

1)G.Goch, R.Volk and H.Kunzmann: Contactless Surface Measurement with a Acoustic Sensor, Annals of CIRP, 43, 487/490(1994)

2)P.Gunther, U.C.Fischer and K.Dransfeld: Scanning Nearfield Acoustic Microscopy, Appl. Phys., B-48, 89/92(1989)

3)M.Weinmann and F.Assumus: Akustische Flachenprofilerfassung unter Verwerdung von Schwingquarzen als Sensoren – ein neuartiges Oberflachenprufverfarhren. VDI Berichte. 939. 453/458(1992)

Figures and Photos

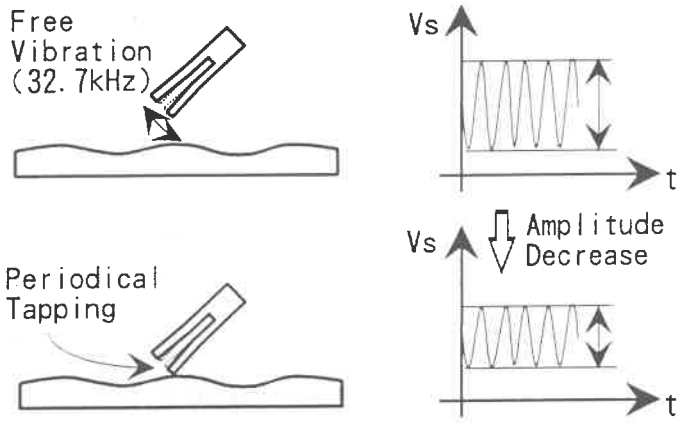

Figure 1. Principle of the tapping stylus.

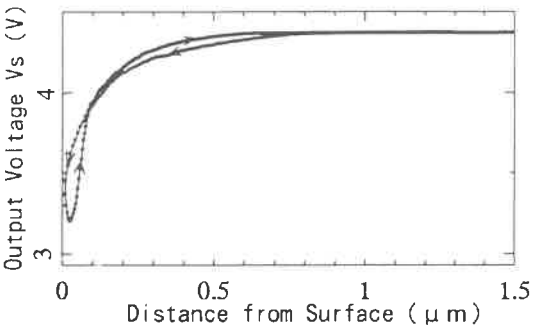

Figure 2. An output voltage hysteresis curve for a forward and back path.

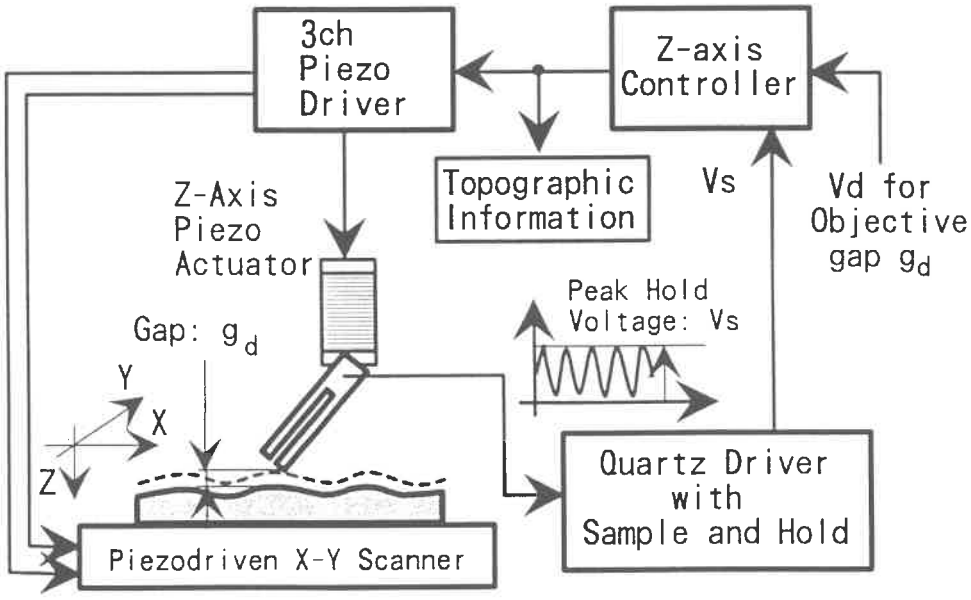

Figure 3. Schematic construction of the measurement system.

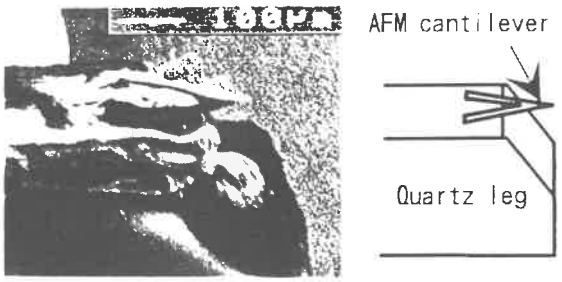

Photo 1. An SEM micrograph of the AFM cantilever bonded to the quartz leg.

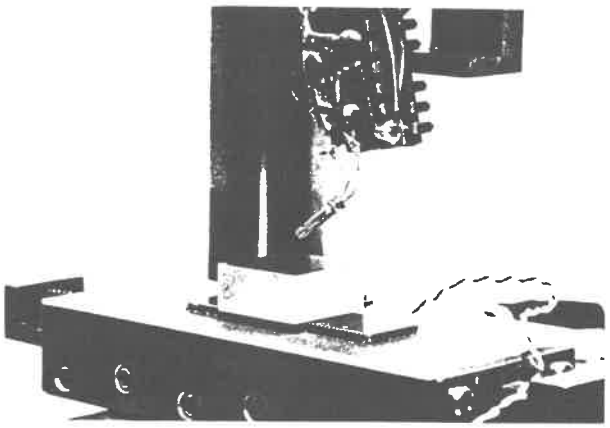

Photo 2. Outlook of the tapping stylus measurement system.

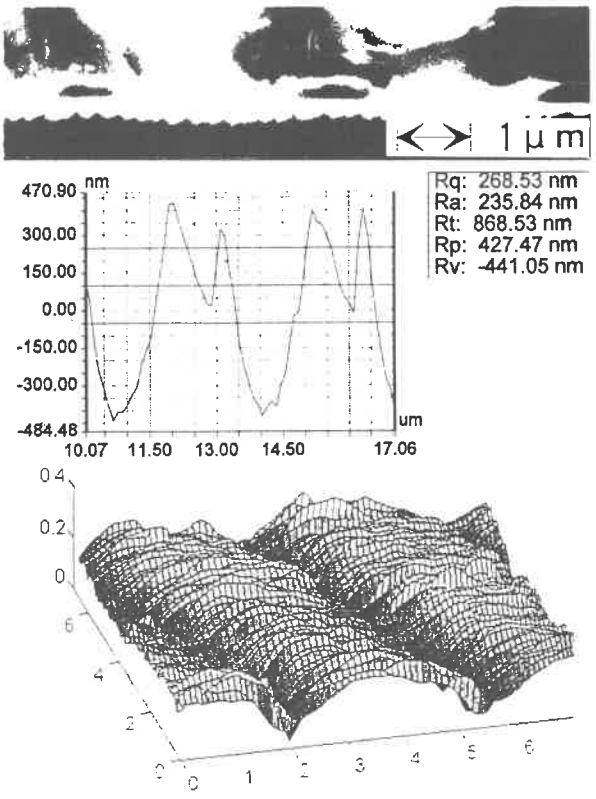

Figure 4. A measurement example of an EB resist pattern with a pitch of 3 μ m and a thickness of 0.3 μ m. Top: SEM micrograph, middle: cross-section by an optical profilometer(Wyco RST-plus), bottom: 3D image by the tapping stylus.

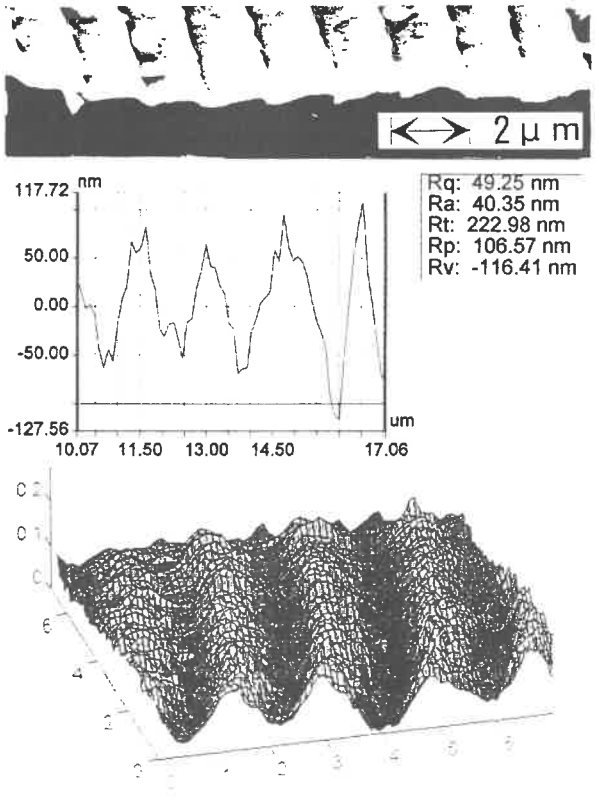

Figure 5. a measurement example of a diffraction grating with a pitch of 1.7 μ m and a height of 0.19 μ m. Top: SEM micrograph, middle: cross-section by an optical profilometer(Wyco RST-plus), bottom: 3D image by the tapping stylus.

ROTARY AXIS METROLOGY

John C. Ziegert
Benjamin Sanders

Machine Tool Research Center
University of Florida
Gainesville, FL

1.0 Introduction

Methods for measuring the parametric errors of rotary axes in machine tools have been developed and documented in previous publications including the ASME B5.54 national standard [1] and the ANSI/ASME B89.3.4M national standard[2]. These rotary axis parametric errors include three components of translational motion and three components of angular motion, which, in general, are functions of the nominal angular position of the rotary axis. The translational errors consist of two radial and one axial component. The orientation errors consist of a commanded angle error, or angular displacement error, and two tilt errors.

The translational errors are associated with particular points on the moving body. The existence of angular error components causes the translational errors to be different at each point on the body. For this reason, it is necessary to specify the point to which the translational errors are referred. Any comparison between methods for measurement of rotary axis translational parametric errors must be corrected to reflect motions of the same point.

In addition to the parametric error functions, errors in the position and alignment of the nominal axis of rotation relative to the other machine axes will result in separate error effects. Even a theoretically perfect rotation about an axis other than the one represented in the part program will produce errors of form in the finished workpiece as the actual rotation differs from what is expected. The position and alignment of the rotary axis with respect to the other machine axes is defined by the coordinates of two points along its average axis of rotation. The six parametric error functions describe motions which are departures from a pure rotation about this average axis of rotation.

Rotary axis parametric errors are traditionally measured with capacitance gage nests, precision rotary tables or optical polygons, and angular interferometers. This paper describes a method for measurement of all of the errors of rotary axes in a single setup using the laser ball bar (LBB). The results of the proposed method are compared to results obtained using traditional instrumentation. Previous reports [3,4] have described the working principal of the LBB, and its application to the measurement of parametric error motions of linear axes as well as spindle thermal drifts. Using the methods described here, the LBB is shown to be a useful tool for measurement of rotary axes of four and five axis machining centers.

2.0 Measurement Method

The experiments described in this report were conducted on a Cincinnati Milacron Maxim 500; a four axis horizontal milling machine. The rotary B-axis is defined by a rotation of the workpiece pallet about a vertical axis (parallel to the machine Y-axis). The B-axis is not a continuous machining axis, but rather a discrete indexing axis. Rotation requires that the pallet lift up (moving parallel to the Y-axis) from its supports, rotate (about an axis parallel to the machine Y-axis) to a discrete angle given in one degree increments and then lower to its new working position.

2.1 B5.54 Measurements

Measurements were taken by Rangarajan Sourirajan of the University of North Carolina at Charlotte in accordance with the ASME B5.54 specification. A precision artifact having a pair one-inch diameter spheres separated by approximately 76mm was mounted on the table and nominally aligned with the assumed axis of rotation (Figure 1). The balls were adjusted to lie within ±5 microns of the average center of rotation. A nest of two precision LVDT sensors was mounted to the spindle for measurement of the motion of the balls in two directions nominally in line with the machine X and machine Z axes, respectively. Three data sets were taken for one full revolution of each ball at 30 degree increments. Ball eccentricity was removed from the data by filtering the once-per-rev component. The results were averaged over the three runs and normalized against the first data point, which was at a commanded angle of B=0°. The large axial motion present during actuation prevented measurement of axial error motions. No instrumentation was available for measurement of angular displacement error.

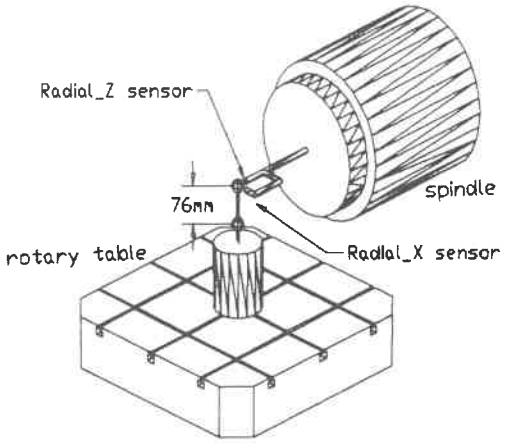

Figure 1. B5.54 Measurement setup.

2.2 LBB Measurements

The three base sockets of the LBB measurement system were clamped directly to the pallet of the machine (Figure 2). No special effort was made to ensure the alignment of the sockets to each other or to the machine. The LBB measurement system calculates the location of its measurement frame with respect to the machine reference frame, so no precision alignment or orientation is required.

A primary measurement socket was placed in the spindle tool holder. The coordinates of the tool point with respect to the pallet were measured at each rotary position. The spindle socket was then moved to two new locations by moving the X and Y axes. For each of these tool locations, the coordinates of the tool point with respect to the pallet were measured at each rotary position. The spindle was software locked and restrained with a mechanical clamp to prevent rotation.

At each rotational position, a tool frame of reference is constructed by taking cross products of the vectors between the measured locations of the three tool sockets to build a right handed orthogonal coordinate system whose axes are nominally aligned with the machine axes. The coordinate transformation between the LBB frame and the tool frame at each rotational position is then computed. Using these transformations, it is possible to compute the tool frame coordinates of arbitrary points in the moving LBB frame. In order to facilitate comparison with the B5.54 data, the tool frame coordinates of two virtual spheres fixed on the pallet centerline, and at the same height as those used in the B5.54 tests, were computed at each rotational position. The location of the sphere centers in the plane normal to the axis of rotation was found by an iterative search procedure which removed any eccentricity in the resulting motion. A line joining these two virtual sphere centers defined the average axis of rotation. Deviations of the center locations relative to the initial position in the X, Y, and Z directions were then computed.

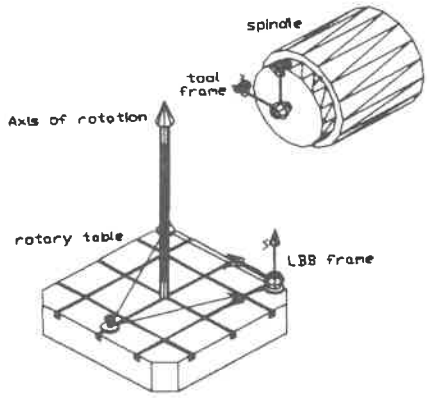

Figure 2. LBB setup for measurement of Maxim 500 rotary axis.

Motions of the virtual sphere centers in directions normal to the average axis of rotation are radial error motions. Motions parallel to the average axis of rotation are axial error motions. Tilt motions are computed by dividing the difference in radial error motions at two different axial positions by the distance between the points. This data is then compared directly with the results of the B5.54 measurements.

3.0 Experimental Results

Data for the LBB method was collected during a single four hour period using one setup and following the procedure outlined in Chapter 3 to generate three complete data sets. Data for the ASME B5.54 method was collected on a different day in a similar time frame. All measurements were taken at the cold state of the machine. A comparison of radial and tilt error motions for the two methods are shown in Figure 3 through Figure 8. All data represent the average of three runs.

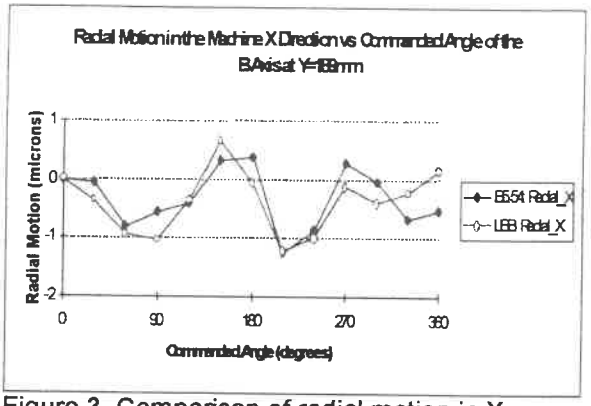

Figure 3. Comparison of radial motion in X direction at Y=189mm

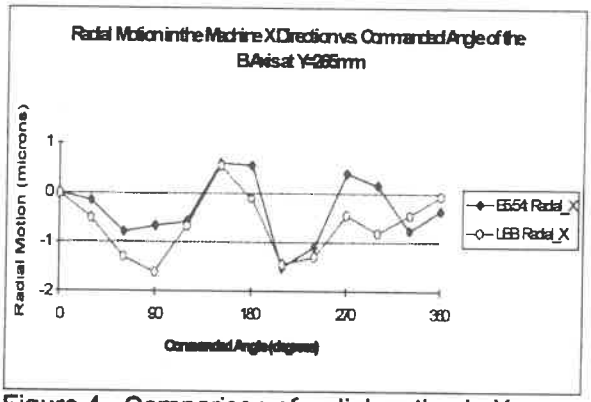

Figure 4. Comparison of radial motion in X direction at Y = 265mm.

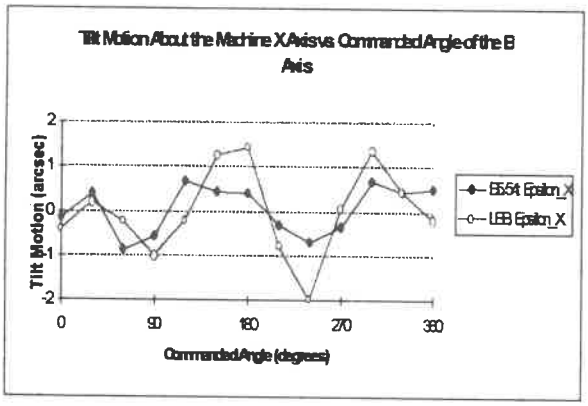

Figure 5. Comparison of tilt motion about X axis.

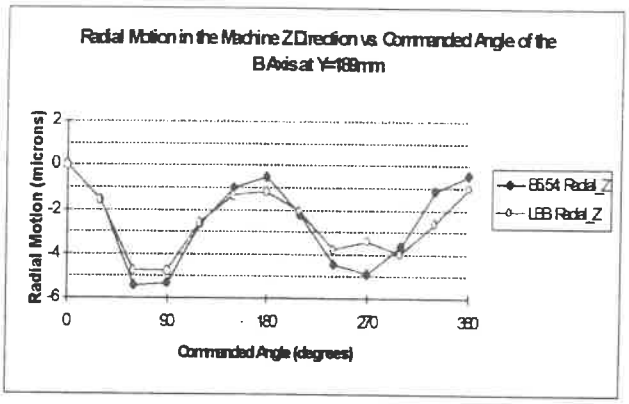

Figure 6. Comparison of radial motion in Z direction at Y = 189m

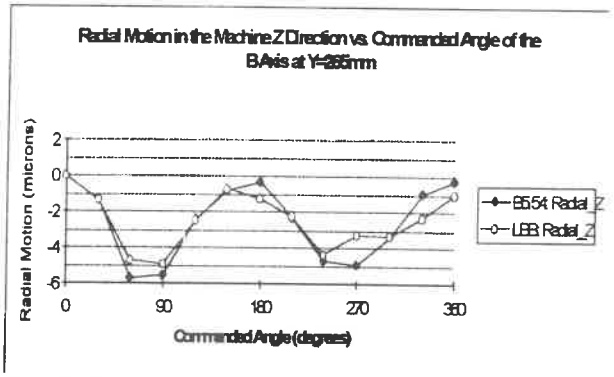

Figure 7. Comparison of radial motion in Z direction at Y = 265mm

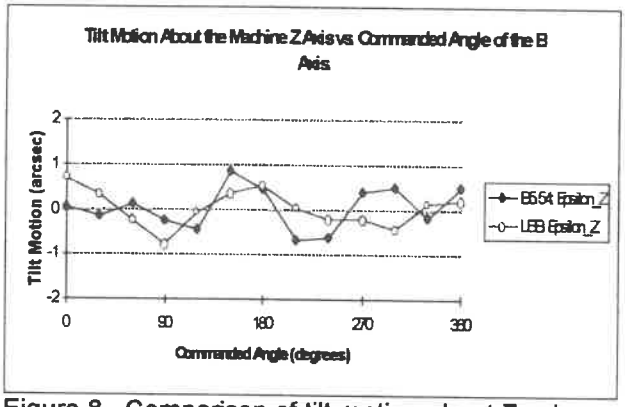

Figure 8. Comparison of tilt motion about Z axis.

In addition to the error components shown above, two additional error components were extracted from the LBB measurement data. These are the axial error motion and the angular displacement accuracy. Although no instrumentation was available for measurement comparisons, the results of the LBB measurements are reported here for the sake of completeness.

Axial error motions are determined by computing the projection of the vector from the

original tool position (B=0°) to the measured tool position in the direction of the average axis of rotation. This is a "face motion" at the radius of the tool position. To find the effective motion of a point on the centerline, the motion must be corrected using the tilt data found above. The results are shown in Figure 9.

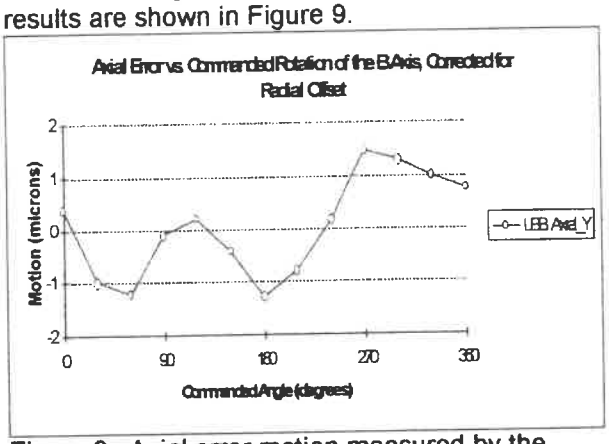

Figure 9. Axial error motion measured by the LBB.

The measured angle of rotation is found by calculating the angle between two vectors emanating outwards, normal to the axis of rotation, to a point on the tool at the B=0° and the B=Q_i positions. The angle between the two vectors is the measured angle of rotation. The commanded angle is subtracted from the measured angle to find the angular positioning error. The results of this measurement are shown in Figure 11.

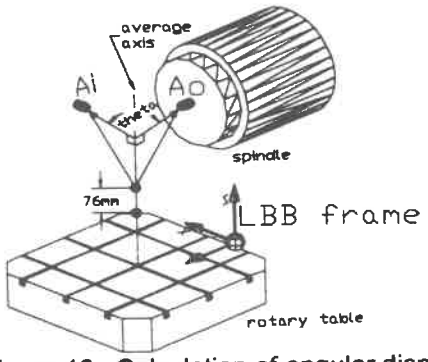

Figure 10. Calculation of angular displacement error.

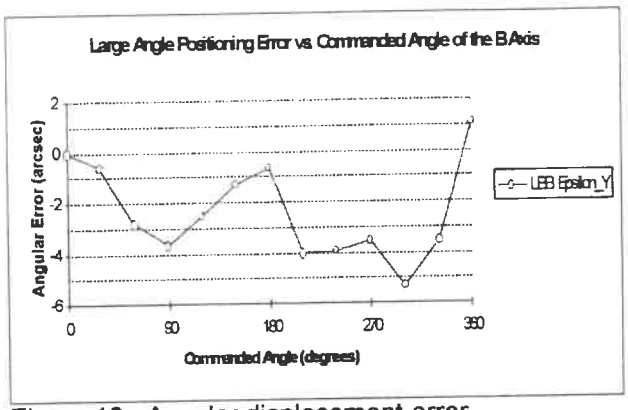

Figure 10. Angular displacement error measured by LBB.

4.0 Conclusions

The measurements taken by the LBB agree with the conventional methods to within an acceptable tolerance. The LBB method produced a comparable result inexpensively and with simple setups requiring no precision artifacts. The LBB method is capable of measuring all six parametric errors of rotary axes with a single instrument and setup. In addition, the absolute location and orientation of the average axis of rotation can be obtained from the LBB measurements.

Acknowledgements: This work was supported in part by grants from the National Science Foundation.

References

1. ASME B5.54, "Methods for Performance Evaluation of Computer Numerically Controlled Machining Centers," New York, NY, 1992.
2. ASME B89.3.4M, "Axes of Rotation: Methods for Specifying and Testing," New York, NY, 1985.
3. Mize, C.D., "Design and Implementation of a Laser Ball-Bar Based Measurement Technique for Machine Tool Calibration," Master's Thesis, University of Florida, 1993.
4. Ziegert, J.C., Mize, C.D., "The Laser Ball Bar: A New Instrument for Machine Tool Metrology," Precision Engineering, Vol. 16(4), pp. 259-267, 1994.

Linear Displacement Accuracy: A Comparison of National Standards

Dr. Ing. S. Badrawy*, T. Schmitz*, Dr. D. BernhardΨ
*Machine Tool Research Center, University of Florida, Gainesville, FL 32611; and ΨBoeing Commercial Airplane Group, Seattle, WA 98124
Keywords: ASME B5.54, VDI/DGQ 3441-3445, positioning accuracy, laser interferometry

Introduction

In an effort to standardize the assessment of the accuracy of machine tools by both builders and users, many countries have drafted and adopted performance evaluation standards for machine tools. Two prominent examples are the German VDI/DGQ 3441-3445[1] and the U.S. ASME B5.54 Standard, "Methods for Performance Evaluation of Computer Numerically Controlled Machining Centers."[2] These national acceptance tests differ in both terminology and method, but either could feasibly be used to qualify the same machine tool. The purpose of this paper is to investigate the specific topic of linear displacement accuracy for single axes and compare the results obtained by following both the German and U.S. standards.

Linear Displacement Tests

Differences between the VDI and the B5.54 include both testing procedure and data evaluation. The B5.54 outlines its test for Linear Displacement Accuracy (LDA) in Section 5.5. This section describes one displacement test comprised of 3 consecutive measurements of a set of bi-directional, sequentially spaced points along a line parallel to the machine axis using a laser interferometer. The analysis of the data includes correcting the laser reading for ambient temperature, pressure and humidity and the scale reading for thermal expansion, calculating the error as the corrected machine reading (CMR) minus the corrected laser reading (CLR) and averaging first the 3 forward measurements and then the 3 reverse measurements. The average forward and reverse errors are then plotted versus the axis position to find the maximum reversal error and the linear displacement accuracy. A typical B5.54 LDA plot is shown in Fig. 1.

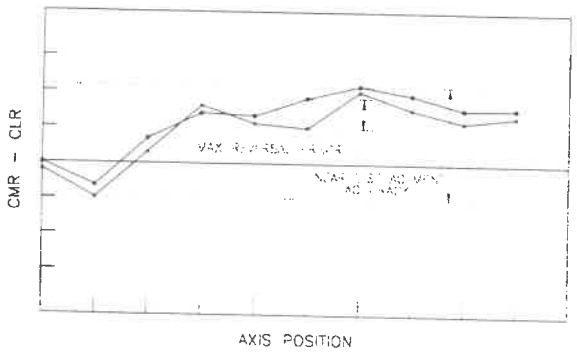

Figure 1: Typical B5.54 LDA Plot

To determine the linear displacement accuracy using the VDI, 5 consecutive bi-directional measurements are required. Additionally, irregular spacing of the measurement points is specified. From these measured points the displacement accuracy, P, the positioning variation, P_s, the deviation of the position, $\bar{x}$, and the reversal error, U, can be determined.

The Gaussian frequency distribution of the error of a measurement point at the position i is shown in Fig. 2. The reversal error, U_i, is defined as the distance between the means of the forward and reverse directions. This error is determined at the position i using Eq. 1.

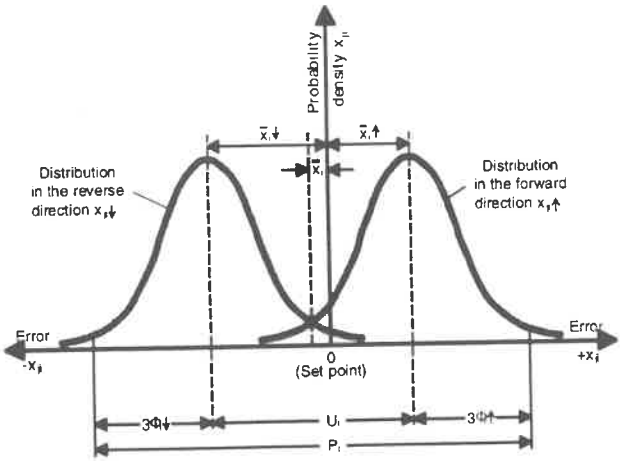

Figure 2: Error Distribution for Measurement Point i

$$U_i = |\bar{x}_i\downarrow - \bar{x}_i\uparrow| \quad (1)$$

The positioning variation, P_s, describes the random error at the measurement position i with a confidence level of 99.7% or 6σ. It is determined by multiplying the arithmetic average, s_i, of the standard deviation in the forward and reverse directions by 6 (Eq. 2).

$$P_{si} = 6 \cdot s_i \quad (2)$$

$$s_i = \frac{s_i\downarrow + s_i\uparrow}{2} \quad (3)$$

$$s_i\downarrow;\uparrow = \sqrt{\frac{1}{n-1}\sum_{j=1}^{n}(x_{ji}\downarrow;\uparrow - \bar{x}_i\downarrow;\uparrow)^2} \quad (4)$$

$$P_i = U_i + P_{si} \quad (5)$$

The displacement accuracy, P_i, contains the positioning deviation, the reversal error and the positioning variation (systematic and random errors). It is given in Eq. 5.

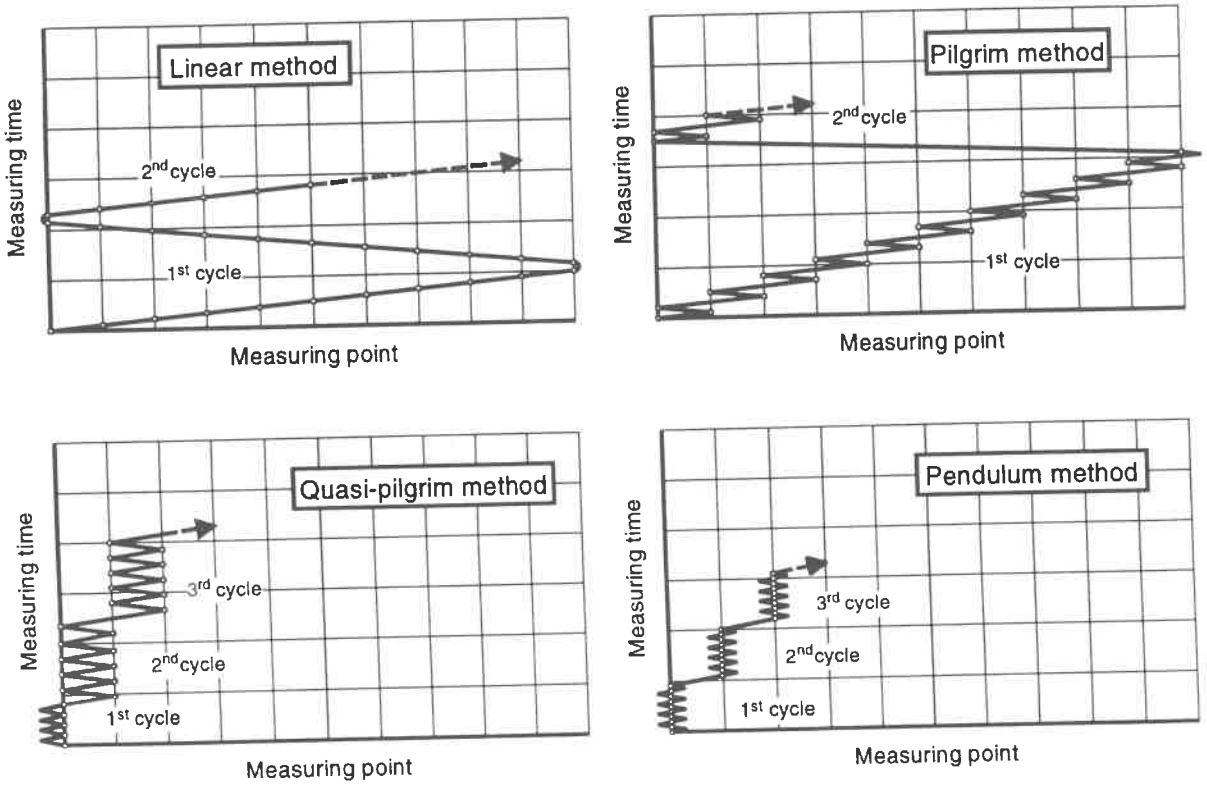

Figure 3: VDI/DGQ Test Methods to Evaluate Linear Displacement Error

The VDI permits the use of four different test methods to determine the linear displacement accuracy: the Linear, Pilgrim, Quasi-pilgrim and Pendulum tests (see Fig. 3). Each of these tests is bi-directional and taken along a line parallel to a machine axis. Note, however,

that each method uses a different strategy to reach the measurement points from the forward and reverse directions.

Experimental Results

At the onset, it should be noted that the purpose of these tests was not to evaluate or qualify the performance of a machine tool, but rather to compare the results of the predicted linear displacement accuracy using two different national acceptance tests. Therefore, the testing methods have been tailored to suit this specific purpose.

Measurements were taken directly at the scale of an axis powered by linear drives (the Z-axis of a machine tool designed and constructed at the UF-MTRC). The test set-up is shown in Fig. 4. This method was chosen to directly assess the differences between the two standards by minimizing the geometric and dynamic errors associated with measuring at the tool point, especially reversal errors due to the Abbe' offset and, therefore, decrease the possible non-repeatability of the axis motions.

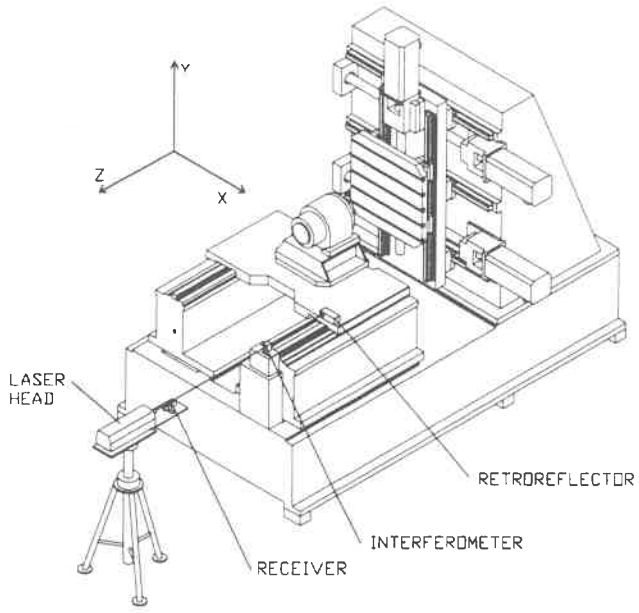

Figure 4: Test Set-up

The results of tests completed at a velocity of 150 in/min and an acceleration of 3 m/s^2 are shown in Figures 5 and 6. It can been seen that the five tests give surprisingly different results. The B5.54 predicts an LDA of 170 µin with maximum reversal error of 20. The VDI tests show two separate results. The Linear and Pendulum tests predict a linear displacement accuracy of about 325 µin and a reversal of 50, while the Pilgrim and Quasi-pilgrim tests give a displacement accuracy of roughly 500 µin and a reversal of 300. These differences can be attributed to three key factors. First, and perhaps most obvious, the VDI tests show a larger total error band due to the inclusion of the standard deviation. Second, unlike the B5.54, the VDI does not specify a correction for scale thermal expansion. Instead, only the actual laser and scale readings are used and any temperature correction must be provided by the machine tool controller. Therefore, this systematic error is included in the VDI measurements and increases the linear positioning inaccuracy. [A slight linear trend is also still apparent in the B5.54 data because, although the machine scale readings were corrected for thermal expansion, room temperature was used and not a measurement taken directly at the linear encoder. The scale's proximity to the heat generated by the linear drive suggests that the temperature at the scale was slightly higher than ambient conditions causing a small thermal expansion of the Z-axis scale.] Third, while the VDI Linear and Pendulum tests show agreement with the B5.54, the Pilgrim and Quasi-Pilgrim give quite different results. An initial explanation for these differences is based on the fact that the B5.54, Linear and Pendulum tests are point-to-point measurements, while the other two tests may better simulate the machining process by following a back-and-forth motion.

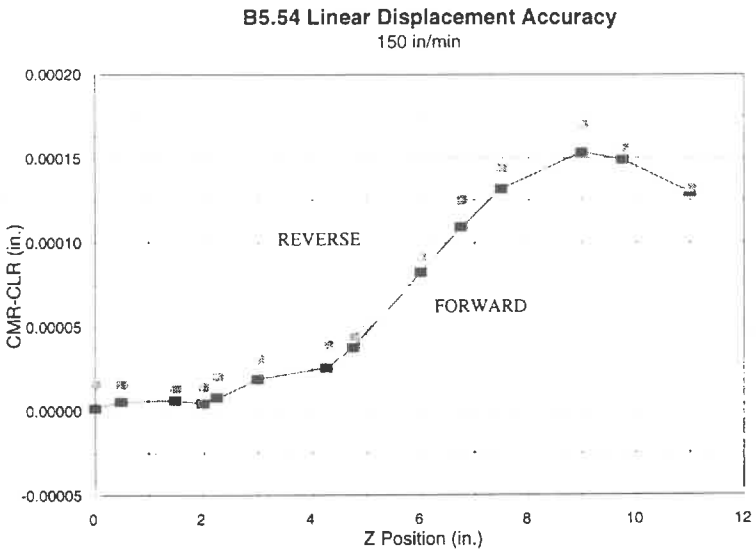

Figure 5: B5.54 LDA Plot

Conclusions

The linear displacement accuracy tests of two different national standards, the U.S. ASME B5.54 and the German VDI/DGQ 3441-3445, have been compared and experimental results obtained. These results show that the B5.54 will predict a better absolute linear displacement accuracy for a given machine tool than the VDI. The three principal reasons for this are: 1) the VDI displacement accuracy plot includes the statistical deviation of the error, 2) the VDI does not correct for thermal expansion of the machine scales, and 3) the Pilgrim and Quasi-Pilgrim tests use a back-and-forth rather than a point-to-point sampling strategy. As a final note, more testing will be necessary to validate these initial results, especially the differences noted with the Pilgrim and Quasi-Pilgrim tests, and also to investigate the influence of feedrate and acceleration on the final results.

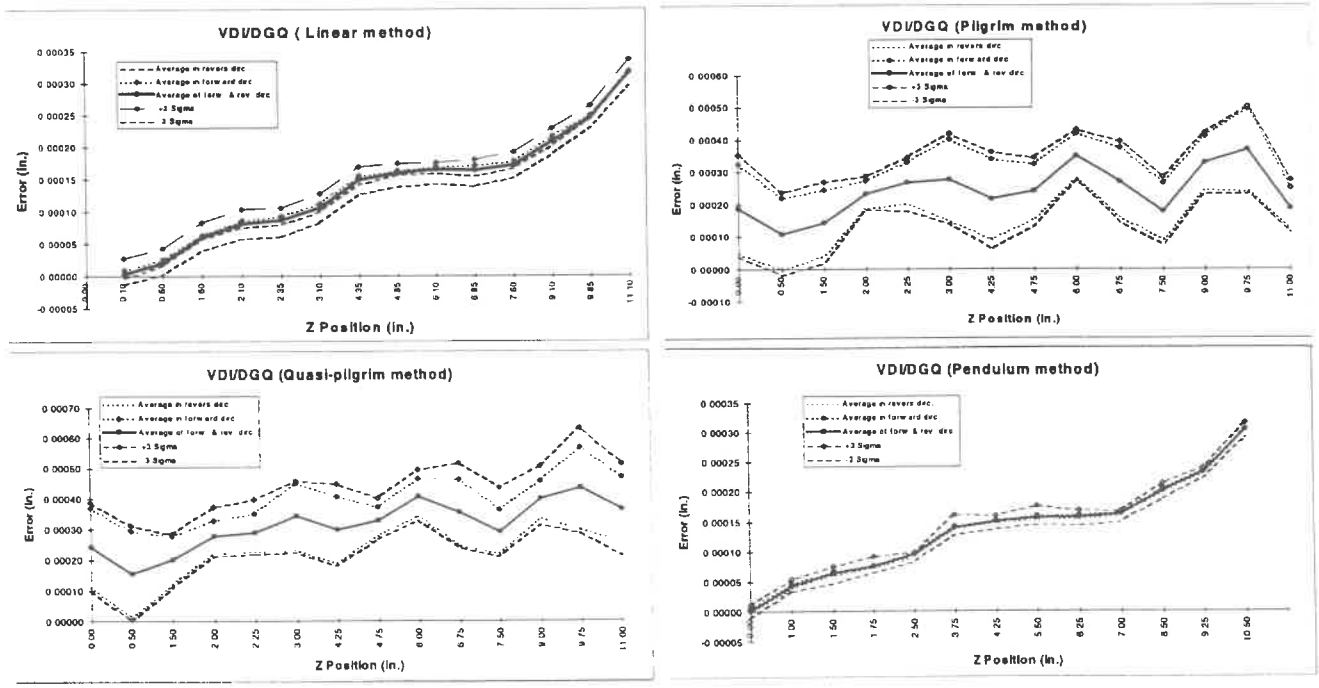

Figure 6: VDI/DGQ Test Results

References

1. VDI/DGQ 3441-3445: Statische Prüfung der Arbeits- und Positionsgenauigkeit von Werkzeugmaschinen/ Grundlagen. Düsseldorf: VDI-Verlag, 1977.

2. American National Standard ASME B5.54-1992, "Methods for Performance Evaluation of Computer Numerically Controlled Machining Centers", American National Standards Institute, New York, NY, 1992.

SECOND ORDER TERMS INFLUENCE IN MATHEMATICAL MODELS OF MACHINE TOOLS CONSIDERING THE MACHINE TEMPERATURE STATE

Benedito Di Giacomo, Denise Pizarro Vieira Sato*, Roxana M. Martinez Orrego*
** Assoc. Prof. , * Ph.D. Students - Dept. for Mech. Eng. - Eng. School of São Carlos
University of São Paulo - Brazil, e-mail : satodeni@sc.usp.br and rox@sc.usp.br

Introduction

The quality of a machine tool is related to its capability of generating mechanical components with form and dimensions identical to the planed geometry. The errors of the machine structure influence the correct position between the tool and the piece. Consequently, this position error, called volumetric error too, affects the accuracy of the manufactured piece. Beside this, the machine structure suffers, when it is working, several temperature states, that affect the volumetric error as well as the piece dimensions. Many models have been developed for characterizing, determining and compensating the machine tools errors. Generally, these models do not consider second order terms because of their very small magnitudes, but under certain conditions, particularly for high precision machines and for machines with high performance, these terms can become significant.

The objective of this work is the evaluation of the influence of second order terms in the error models of machine tools, considering the error in different temperature states. Two models were used to achieve this goal. First, the errors were adequately replaced by their mathematical functions in the volumetric error equations obtained from a machine model in which the second order terms were not considered; and second, the same mathematical functions were introduced in the volumetric error equations that contain terms of second and higher order. The two models were compared in several machine temperature states.

Machine Modeling

The significance of the second order terms was evaluated modeling a CNC cylindrical grinding machine with the Homogeneous Transformation Technique [1], [2]. This technique was used because of its versatility for describing the real and actual spatial relation between the machine components. The modeled machine and the several coordinate systems associated to its elements are shown in the figure 1. The tool path, with respect to the reference system 0, is given by the systems 1,2 ,3 and 4 and it can be written as the matrix

$$T_{tool}={}^{0}T_{1}.{}^{1}T_{2}.{}^{2}T_{3}.{}^{3}T_{4} \quad (1)$$

The piece path is described, with respect to system 0, by the adequate combination of the systems 5, 6 and 7 in the matrix

$$T_{piece} = {}^{0}T_{5}.{}^{5}T_{6}.{}^{6}T_{7} \quad (2)$$

and finally, the relative position error between the tool and the piece is obtained from the equation:

$$E_{total}=T^{-1}{}_{tool}.T_{piece} \quad (3)$$

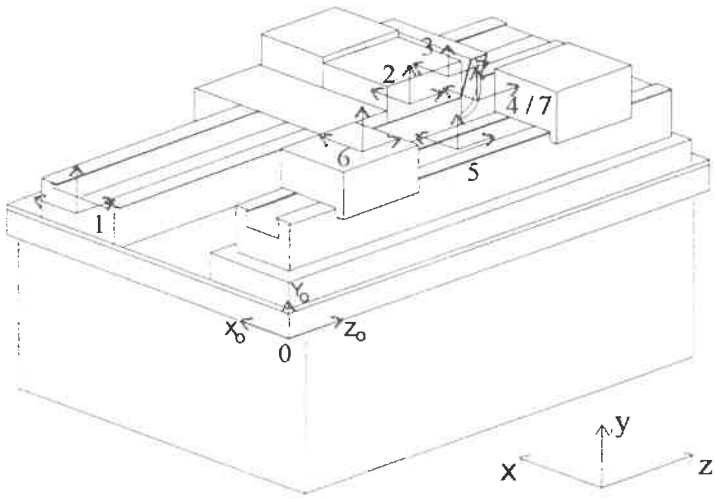

Figure 1: Coordinate systems in the CNC cylindrical grinding machine

The tool of the modeled CNC cylindrical grinding machine moves in the plane XZ. The components of the error in this plane are the elements $E_{total}[1,4]$ and $E_{total}[3,4]$ (Ex and Ez receptively) of the matrix E_{total}. The most important displacement of the grinding wheel occurs in the X direction in which the main piece dimension: the diameter is defined. In the Z direction the piece tolerances are greater than in the X direction. The components Ex and Ez of the machine error in the plane XZ, without considering the terms of second or higher order, are given by the following expressions:

$$Ex = \delta_x(x) + \delta_x(z) - \varepsilon_z(z) \cdot Y12 + \varepsilon_y(z) \cdot (Z12 + Z23) + \varepsilon_y(x) \cdot Z23 \quad (4)$$

$$Ez = \delta_z(z) + \delta_z(x) - \varepsilon_y(z) \cdot (x - X12 + X23 - X34) - \varepsilon_y(x) \cdot (X23 - X34) + \varepsilon_x(z) \cdot Y12 \quad (5)$$

where
$\delta_i(j)$ are translation errors in the direction i due to the displacement in the direction j; $\varepsilon_i(j)$ are rotation errors about the axis i due to the displacement in the direction j; Xkl, Ykl, Zkl are offsets between the coordinate systems k and l in the directions X, Y and Z respectively and x and z are the coordinates in these directions.
It can be noted, that there are not second order terms or terms of higher order in the equations 4 and 5. They all were eliminated during the multiplications of the matrices. If these terms are not simplified, the error in the plane XZ is given by the expressions 6 and 7 as follow

$$\begin{aligned} Ex' = {} & \delta_x(x) + \delta_x(z) + \delta_z(x) \cdot \varepsilon_y(z) + \delta_z(x) \cdot \varepsilon_x(z)\ \varepsilon_z(z) + \\ & (-\varepsilon_y(x)\,\varepsilon_y(z) + \varepsilon_x(z)\,\varepsilon_y(z)\,\varepsilon_z(x) - \varepsilon_x(z)\,\varepsilon_y(x)\,\varepsilon_z(z) - \varepsilon_z(x)\,\varepsilon_z(z) + \varepsilon_y(x)\,\varepsilon_y(z))\ X23 + \\ & (-\varepsilon_x(z)\,\varepsilon_y(z)\,\varepsilon_z(x) + \varepsilon_x(z)\,\varepsilon_y(x)\,\varepsilon_z(z) + \varepsilon_z(x)\,\varepsilon_z(z))\ X34 + (\varepsilon_x(z)\,\varepsilon_y(z) - \varepsilon_z(z))\ Y12 + \\ & (\varepsilon_y(z) + \varepsilon_x(z)\,\varepsilon_z(z))\ Z12 + (\varepsilon_y(x) + \varepsilon_y(z) - \varepsilon_x(x)\,\varepsilon_x(z)\,\varepsilon_y(z) + \varepsilon_x(x)\,\varepsilon_z(x) + \\ & \varepsilon_x(z)\,\varepsilon_y(x)\,\varepsilon_y(z)\,\varepsilon_z(x) + \varepsilon_x(x)\,\varepsilon_z(z) + \varepsilon_x(z)\,\varepsilon_z(z) - \varepsilon_y(x)\,\varepsilon_z(x)\,\varepsilon_z(z))\ Z23 \end{aligned} \quad (6)$$

$$\begin{aligned} Ez' = {} & \delta_z(z) + \delta_z(x) - \varepsilon_y(z)\,(x - X12 + X23 - X34) - \varepsilon_y(x)\,(X23 - X34) + \varepsilon_x(z)\,Y12 - \delta_x(x)\,\varepsilon_y(z) + \\ & \varepsilon_x(z)\,\varepsilon_z(x)\ (X23 - X34) + (-\varepsilon_x(x)\,\varepsilon_x(z) - \varepsilon_y(x)\,\varepsilon_y(z) + \varepsilon_x(z)\,\varepsilon_y(x)\,\varepsilon_z(x) - \\ & \varepsilon_x(x)\,\varepsilon_y(z)\,\varepsilon_z(x))\ Z23 \end{aligned} \quad (7)$$

Calibration

The value and the behavior of the machine error budget is obtained through the calibration of their individual errors. The calibration of each geometric error of the CNC cylindrical grinding machine has been made using a Displacement Laser Interferometer System and an electronic level (for Roll). Each geometric error was measured until its stabilization, experimenting different temperature states. The readings were taken at discrete points along the travel (forwards and backwards) of the X and Z axis.
It was necessary to develop a software for monitoring all the measurement process. A computer stored automatically the data from the laser system (or the electronic level) together with the temperature variations indicated by temperature sensors (thermocouples) placed in heat points of the machine.

Data Analysis and Discussion

After processing the data obtained with statistical methods, a curve fitting for each geometric error in each temperature state evaluated has been made. In a general way, the curves obtained have a polynomial behavior. The influence of the second order terms in the analysis of the total error was studied through the comparison of the components Ex and Ez calculated by the two models described previously through

the equations 4 and 5 and 6 and 7, respectively. For space reasons, in this abstract is analyzed only the error in the direction that defines the piece main dimension (X direction).
The errors that appear in the equations 4, 5, 6 and 7 were replaced by their respectively mathematical functions. Surfaces representing the difference (Ex' - Ex), for several temperature states, were calculated and traced as shown in the figure 2 and 3.

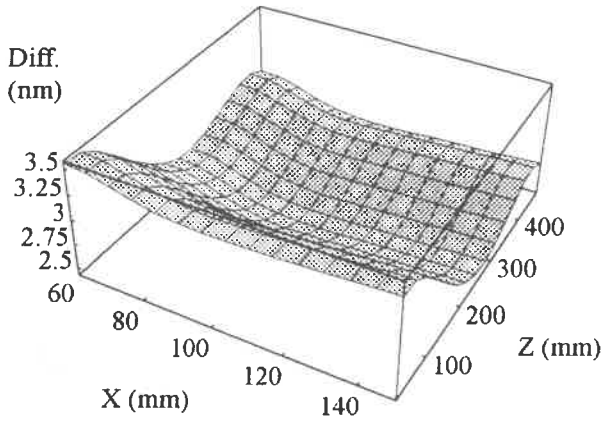

Figura 2: Difference (Ex'-Ex) after 1:30 hours

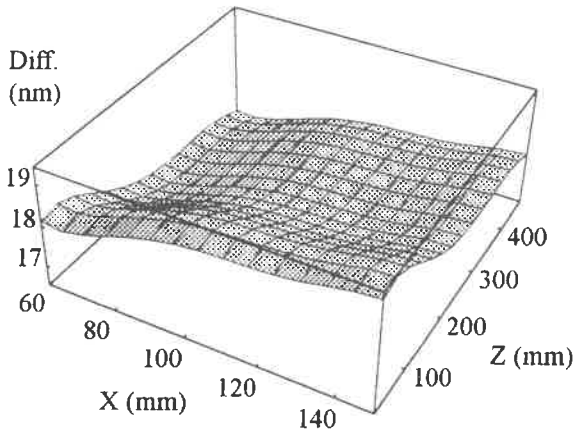

Figura 3: Difference (Ex'-Ex) after 18 hours

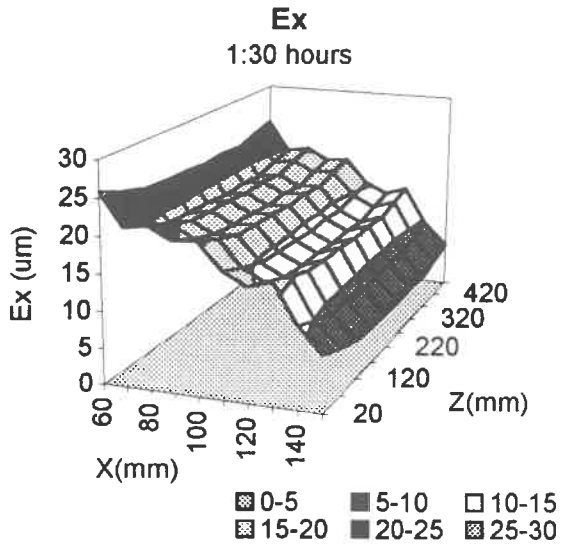

Figure 4: Error in the X direction measured after 1:30 hours of turning on the grinding wheel

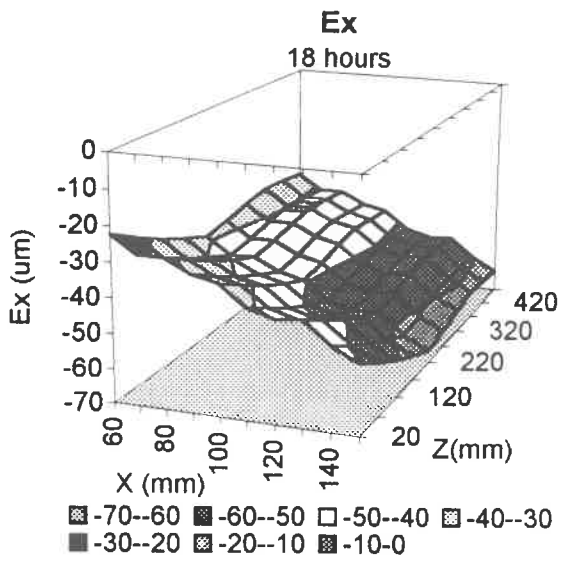

Figure 5: Error in the X direction measured after 18 hours of turning on the grinding wheel

The surface shown in figure 2 was calculated replacing in the equations 4 - 7 the error curves obtained after 1:30 hours of turning on the grinding wheel and making the difference (Ex'-Ex). It was noted, that the Ex becomes stable in a period of 18 hours. The difference between the two models, using the curves obtained when the errors attained the stability, is represented by the surface shown in figure 3. In a general way, the differences are very small, between 0,4 and 18 nm. Surfaces traced for intermediary temperature states showed that (Ex'-Ex) grows when the machine temperature increases. The same trend was found observing the absolute value of Ex, i.e the difference between the two models are larger for increasing Ex absolute values, see figures 4 and 5.

According to the results of this analysis, the influence of the second and higher order terms is still insignificant for the evaluation of the machine error behavior in all the temperature states observed. However, for determining the error components in any position and temperature state, it is necessary to express them as a function of position and temperature variation. With the introduction of the temperature vector increases the number of mathematical operations that should be made to obtain the error final equations. This increment of operations entails a greater error propagation which certainly could hide the improvement achieved with the inclusions of all the terms in the machine model.

Conclusions

This work had as objective the analysis of the influence of the second and higher order terms in the determination of the error of machine tools during its warm-up period. The major difference, 18 nm, was found when the temperature and the machine error were stables. This value can be considered as insignificant for a machine that reaches an error of 80 microns in the X direction. Therefore , the second and higher order terms can still be eliminated without affecting the results of the machine error analysis. This procedure simplifies the mathematical manipulation when the error is calculated.

Another results of this work (not included in this abstract) showed that there is no major differences between the inclusion of the error functions in the rotation and translation matrices before their mathematical manipulation and the inclusion of the functions directly in the final equations.

Acknowledgment

The Authors would like to thank the financial support received from FAPESP (process number: 94/ 5765-2) and from CNPq for the development of this work.

References:

[1] Donmez, M.A.; Blomquist, D.S.; Hocken, R.J.; Liu, C.R.; Barash,M.M. *A general methodology for machine tool accuracy enhancement by error compensation.* Precision Engineering, v. 8, n 4, 1986.

[2] Paul, P.R. *Robot manipulators: Mathematic, Programming and Control.* Mit Press, Chapters 1, 2 and 3, p. 9-83, 1981.

[3] Di Giacomo, B., Pereira, P.H., Abackerli, AJ. *Thermal errors calibration and modeling of a cylindrical grinding machine CNC,* Proceedings of the ASPE, v. 14, p. 223-228, 1996.

[4] Kiridena, V.S.B, Ferreira, P.M. *Kinematic modeling of quasistatic of three axis machining center,* Int. Journal of Mach. Tools Manufact., n 34, p. 85-100, 1994

[5] Kiridena, V.S.B, Ferreira, P.M. *Parameter estimation and model verification of first order quasistatic error model for three axis machining center,* Int. Journal of Mach. Tools Manufact., n 34, p. 101-125, 1994

[6] Di Giacomo, B., Martinez Orrego R.M., Vieira Sato, D.P. *An exploratory study about the second order errors in mathematical models of coordinate measuring machines*, METROCAL 97, Santiago de Chile, Marz 1997.

A New Error Separation Method for Measuring Angular Motion of a Spindle

Wei GAO and Satoshi KIYONO
Department of Mechatronics, Faculty of Engineering, Tohoku University, Sendai, 980-77 JAPAN

ABSTRACT

This paper presents a new error separation method for measuring angular motion of a spindle. In this method, two angle probes, separated with a small angular distance, are fixed around a cylindrical workpiece mounted on the spindle. The probes are used to detect the inclination of axial generators of the workpiece. The angular motion and the local surface slope can be obtained from the output data of the two sensors. An optical sensor consisting of two angle probes with high resolution and stability were developed to realize the proposed error separation method. The experimental results of angular motion measurement confirmed the effectiveness of the new method.

Key Words : measurement, spindle, error motion, angular motion, error separation, angle probe

1. INTRODUCTION

It is important to measure error motions of machine tool spindles accurately. The error motion of a spindle can be classified into the radial motion, the angular motion and the axial motion[1]. To identify the total error motion, it is necessary to accurately measure the three error motions simultaneously. Accurate measurement of the axial motion can be easily realized by detecting the displacement of the face center of the spindle axis. However, it is difficult to measure accurately the radial motion and the angular motion. Generally, the radial motion is measured by detecting the relative displacement in the radial direction between a displacement probe and a spherical master fixed on the spindle. The angular motion is calculated from the radial motions measured at two positions along the axis of the spindle. The measurement accuracy of the radial motion, and then the angular motion, is affected by the roundness error of the spherical master. To realize accurate measurement of the radial motion and the angular motion, it is necessary to separate the error motion from the roundness error.

Several error separation methods[2], including the method proposed by the authors[3], have been developed for accurate radial motion measurement. Theoretically, the angular motion can also be accurately calculated from two radial motions measured by the error separation methods. However, in practice, a lot of sensors have to be used, and the electrical and mechanical matching of the sensors is much difficult. In addition, the relative positions of the sensors are also difficult to adjust. For these reasons, the error separation methods are thought to be limited to the radial motion measurement.

In this paper, we propose a new error separation method specifically suited to the angular motion measurement, and construct an optical sensor to realize the new method. Experiments are also been performed to investigate basic performances of the optical senor, and to confirm the effectiveness of angular motion measurement.

2. PRINCIPLE OF ANGULAR MOTION MEASUREMENT

The principle of the error separation method for angular motion measurement of a spindle is shown in Figure 1 schematically. The fixed coordinate axes XYZ are also plotted in this figure. Two angle probes, separated with a small angular distance, are fixed around a cylindrical workpiece mounted on the spindle, and can scan the workpiece while the workpiece is rotating. The probes are used to detect the inclination of the axial generators of the workpiece. The detecting points A and B of the two probes are set on the same circumference that is perpendicular to the spindle axis. The output data of the two probes consist of the same angular motion and the local surface slopes with an interval of the probe distance. Using the technique of the error separation method of straight profile measurements [4], we can obtain the angular motion and the local surface slope with the accuracy of the angle probes. For simplicity, the sampling interval is chosen to be equal to the probe distance in the following discussion.

Let the local surface slope of the workpiece be $r'_Y(\theta_n)$, and the angular motion of the spindle be $e_a(\theta_n)$, where θ_n is the rotation angle of the workpiece. The output $\tau_A(\theta_n)$ of the angle probe 1 and the output $\tau_B(\theta_n)$ of the angle probe 2 can be expressed as:

$$\tau_A(\theta_n)=r'_Y(\theta_n)+e_a(\theta_n), \quad (1)$$

$$\tau_B(\theta_n)=r'_Y(\theta_{n+1})+e_a(\theta_n). \quad (n=0,1,...N) \quad (2)$$

Where, N is the sampling number in one revolution.

The differential output to canceling the angular motion term can be obtained as follows:

$$\begin{aligned}\Delta\tau(\theta_n)&=\tau_B(\theta_n)-\tau_A(\theta_n)\\ &=r'_Y(\theta_{n+1})-r'_Y(\theta_n).\end{aligned} \quad (3)$$

By using $\Delta\tau(\theta_n)$, $r'_Y(\theta_n)$ can be given by

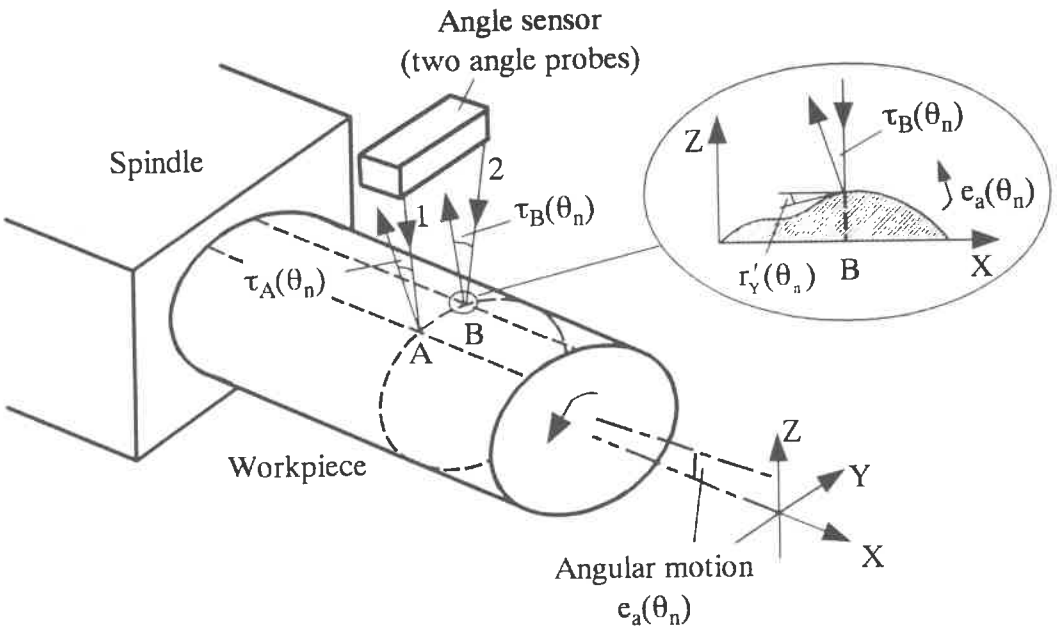

Figure 1 Principle of angular motion measurement

$$r'_Y(\theta_{n+1}) = r'_Y(\theta_n) + \Delta\tau(\theta_n). \quad (4)$$

As a result, the angular motion can be evaluated as:

$$e_a(\theta_n) = \tau_A(\theta_n) - r'_Y(\theta_n). \quad (5)$$

3. EXPERIMENT

3.1 Optical sensor

An angle sensor was developed to realize the proposed method of angular motion measurement. A schematic view of this sensor is shown in Figure 2. As can be seen in this figure, the sensor consists of two angle probes with an angular distance of 7.2°. The angle probes utilize the principle of autocollimation. A laser diode was used as the light source, and two position sensing detectors were used as the photo detectors. The sensor was made so compact (110mm × 70mm) that it can be easily used in on-machine measurements.

Figure 3 shows the stability of the angle sensor tested over a term of 50 seconds. The sample was a cylindrical workpiece with a diameter of 80mm. The angle probes can be seen to have a stability of ±0.05 arcsec. The variation of the differential output is also in the same level.

The outputs of the probes were monitored when angular motion $e_a(\theta)$ was introduced by titling the cylindrical workpiece sinusoidally around Y-axis. Figure 4 shows the outputs of the probes and the differential output. It can be seen that the angular motion is correctly captured by the two probes, and is canceled in the differential output.

3.2 Angular motion measurement

Figure 5 shows the results of angular motion measurement. Two repeated results are plotted in the figure. The workpiece was mounted on a ball bearing spindle that was driven by a servo motor. The measured angular motion shown in Figure 5(a) can be seen to be approximately 80 arcsec., and the local

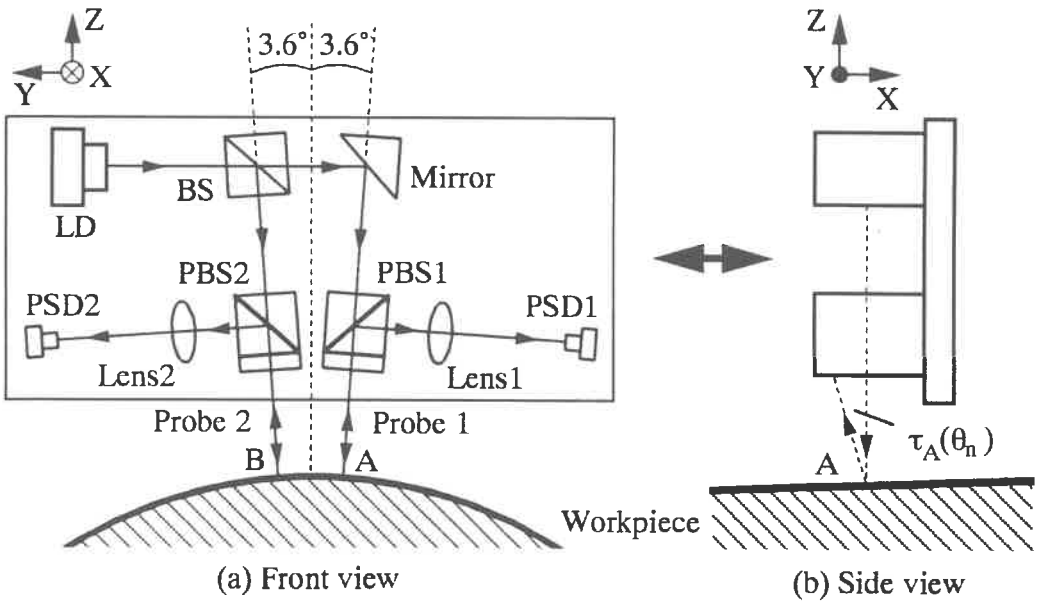

Figure 2 Schematic view of the optical sensor

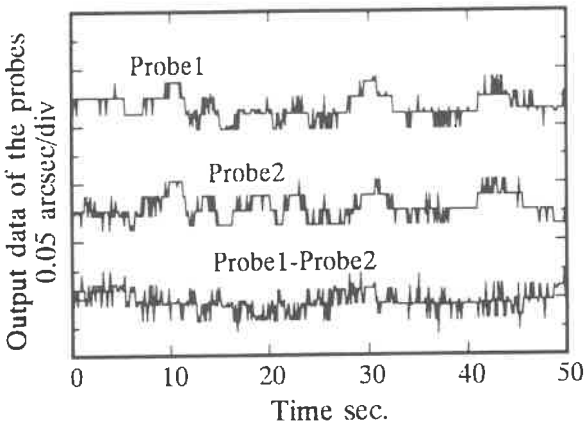

Figure 3 Results of stability test

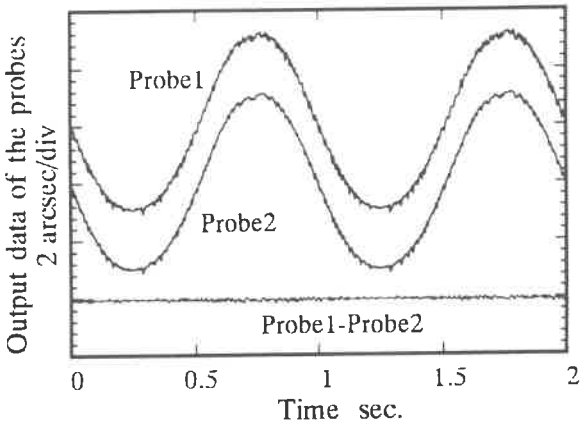

Figure 4 Angular motion cancellation in the differential output

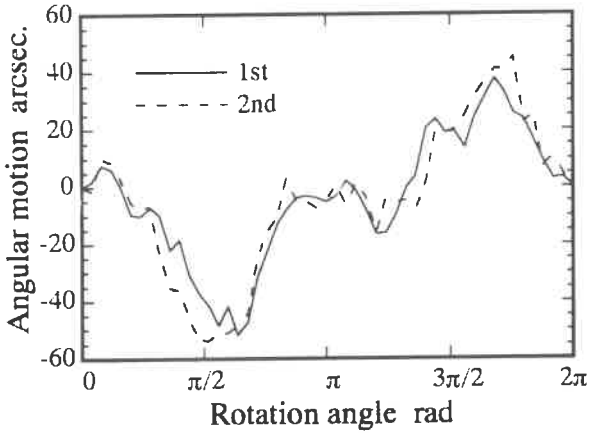

(a) Measured angular motion of spindle

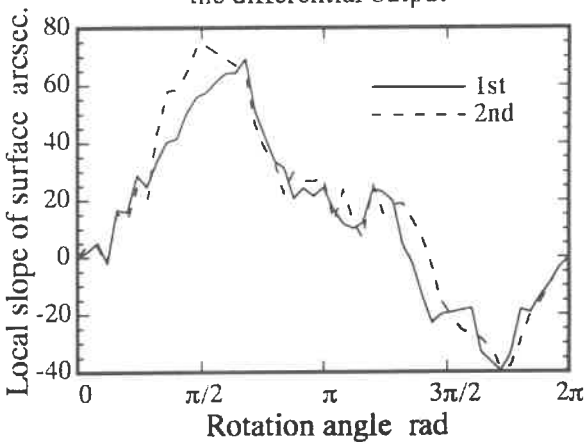

(b) Measured local slope of surface

Figure 5 Results of angular motion measurement

slope of the surface shown in Figure 5(b) is about 120 arcsec.

4. CONCLUSIONS

1) A new error separation method for angular motion measurement has been proposed.

2) An optical sensor has been constructed to realize the proposed method.

ACKNOWLEDGMENT

Financial support was provided by the Mechatronics Scientific Foundation and Grant-in-Aid for Scientific Research of The Ministry of Education of Japan.

REFERENCES

[1] Unification Document Me: Axes of Rotation, Annals of the CIRP, Vol. 25, No. 2, (1976), pp. 545-564.

[2] D. J. Whitehouse: Some theoretical aspects of error separation techniques in surface metrology, Journal of Physics E: Scientific Instruments, Vol. 9, (1976), pp. 531-536

[3] W. Gao, S. Kiyono and T. Sugawara: Nano-metrology of roundness and spindle error, Proc. of ASPE 11th, (1996), pp.163-166.

[4] S. Kiyono and W. Gao: Profile measurement of machined surface with a new differential method, Precision Engineering, Journal of the ASPE, Vol. 16, No. 3, (1994), pp. 212-218

Assessment of Machine Tool Accuracy Using ISO "Guide to the Expression of Uncertainty in Measurement," (GUM)

J.D. Drescher (United Technologies, Corp. - Pratt & Whitney, Div.)

Abstract

On-machine probing has been used for years. But industry is still looking for methods of calibration that give accurate values of measurement uncertainty to minimize the need for independent correlation. This paper introduces a method of calculating volumetric accuracy based on an interpretation of the "Guide to the Expression of Uncertainty in Measurement" [1]. It provides a way to include uncorrected, systematic errors in estimates of measurement uncertainty. The expected value of the systematic error and the variance of the systematic error are calculated. The variance of the systematic errors is combined with the non-systematic errors for a standard uncertainty. The accuracy is expressed as a linear combination of the average systematic error and the expanded uncertainty for each direction. The model is applied to a 5-axis laser hole driller with a fixed focal point, BAXYZF configuration. The expected value of the systematic error is the average of all errors calculated at grid points using equations derived from the homogenous transformation matrices (HTM's) for this machine [2]. Equal weighting is given to each point. The "zero" point for all geometric and parametric error vectors is chosen at the center of the working volume. This is where the machine axes are referenced to the laser focal point. Results are compared to those of a common error budget combinatorial rule and with inspection data. This leads to a discussion about the difference between machine tool accuracy and process capability.

Introduction

Rules for combining errors to predict process capabilities and methods of translating overall process requirements into elemental requirements need further development. Several researchers have contributed [3, 4, 5, 6, 7]. One obstacle to a standardized method for analyzing the machine tool or measuring machine component of the process is the difficulty in verification. The machine (or CMM) calibration is one of several factors that go into estimates of process capability (or measurement uncertainty). Considering the machine tool, correlation of machine tool accuracy with overall process results requires that:

- other errors be physically eliminated. Or,
- machine tool accuracy be defined to include the other process errors. Or,
- conservative estimates be made to "cover" the errors that are not included in the estimates (rules of thumb).

All three approaches can be found in the literature. The first two constitute the deterministic approach [8]. This is the trend but it is not easy to implement widely. The third approach is unsatisfactory but probably most common.

More fundamentally, a difficulty lies in dealing with systematic errors such as machine geometry. Estimates of positioning or measurement uncertainty are desired as a qualification of the machine without regard for the particular parts or features to be produced or inspected within the calibrated working volume. However, for a certain set of test parts or features, the systematic errors by definition do not contribute to variation. Furthermore, when a part is in production and an independent inspection feedback loop is in place, systematic errors are often corrected (though not always with an understanding of the error sources). For example, a squareness error might be "corrected" with a linear offset to maintain a diameter tolerance on a cylinder. Or an offset might be added to a part probing routine to improve correlation with post-process inspection when the actual error is in the calibration of an artifact used on the machine. While these practices can be confusing and inefficient in small batch manufacturing, the point is, they make it difficult to predict machine tool accuracy or measurement uncertainty.

This leads to the conclusion that models to relate estimates of uncertainty to actual performance should really include a time-based component which takes into account feedback loops with independent measurements and the relative magnitudes of systematic and non-systematic components of uncertainty. To clarify this discussion a term is introduced. "First piece machine tool accuracy" is an estimate of the bounds on accuracy which a machine can produce within its working volume without regard to the actual part or other process details such as fixturing, tooling, and operating methods. Many other definitions could follow with qualifiers based on the amount of process information available and the level of corrections applied (e.g. limited volume, first piece accuracy; full volume, linearly corrected accuracy; part specific, terminal accuracy; etc.).

The latter definitions might be interesting topics for production research. However, this paper deals only with what is defined here as "first piece machine tool accuracy." Therefore, the uncorrected, systematic errors must be included in the estimate of measurement uncertainty or machine tool accuracy. For an error budget at a design stage, it may be reasonable to assume zero expected value for systematic errors and treat them mathematically as equivalent to other, independent non-systematic errors. However, for a given machine, there is bias which is not included in these estimates of uncertainty [9].

Machine Tool Accuracy vs. Measurement Uncertainty

The ISO "Guide to the Expression of Uncertainty in Measurement" [1] provides rules for combining elemental error sources of measuring equipment to estimate measurement uncertainty. It has been used to estimate axis positioning accuracy and repeatability as well as uncertainty of geometric and parametric machine tool errors from measurement results [10]. It may also be used to estimate volumetric positioning accuracy of a machine tool. However, certain interpretations are needed:

1 Measurement uncertainty is a range of values in which the measurand is expected to exist in relation to any single measurement. It depends on the individual sources of uncertainty and the sensitivity of the measurement result to each source. Machine accuracy is the range of dimensions a finished feature is expected to have in relation to the target dimension. This depends on the individual machine error sources and the sensitivity of the machining result to each source.

2 The measurement uncertainty is not equal to the range in a set of measurements because unknown yet fixed quantities affect the result. For example, a simple gage system includes a master whose length is not known. The uncertainty for the master is taken as the uncertainty of the system used for its calibration. The actual length of the master does not change but the uncertainty in its length contributes to the system's measurement uncertainty. Machine accuracy is not equal to dimensional variation because systematic machine tool errors exist.

3 In measurement, the distinction between known and unknown systematic errors is not usually needed. If a systematic error is known, measurement results can usually be corrected by that value. Unknown systematic errors are usually characterized by an expected value of zero and a range, or probability distribution. These errors are therefore treated mathematically the same as non-systematic errors. In estimating machine accuracy, the known, systematic errors are troublesome.

Calculations and results

For the purposes of this discussion, systematic errors are functions of controlled variables. In addition, these variables are the same each time a certain feature of each part is produced. Systematic errors then, are functions of position, its time derivatives, and offsets determined by tooling. Non-systematic errors are functions of other variables. For example, environmental temperature error is considered non-systematic. Although air temperature may be controlled, the temperature, as recorded each time a certain feature is produced, may vary quite randomly between the controlled limits. For the ABXYZF, fixed focal point laser hole driller, table 1 summarizes the errors considered. Measurements included 5 bi-directional runs. Squareness values were obtained from ballbar tests. Errors of the rotary axes were neglected.

Table 1: Error terms included in the calculation [10]

Systematic error terms	Non-systematic error terms
Linear positioning accuracy, E (bi-dir. syst. deviation)	*Positioning repeatability*, R (bi-dir., includes reversal)
Straightness, (Defined similar to E)	*Straightness repeatability*, (Defined similar to R)
Roll, Pitch, Yaw as appropriate, (Defined similar to E)	*Roll, Pitch, Yaw repeatability*, (Defined similar to R)
Squareness	*Environmental Temperature Variation Error*, ETVE

GUM recommends that corrections be applied to measurement results for known significant systematic effects. However, it also recognizes this is not always feasible "because of the unacceptable expense that would be incurred in calculating and applying an individual correction, and in calculating and using an individual uncertainty, for each (measurement value)." The recommendation of Annex F is to compute a mean correction as:

$$\bar{b} = \frac{1}{t_2 - t_1} \int_{t_1}^{t_2} b(t)dt \qquad (1)$$

Where b is the known, systematic error defined for the parameter, t, over the range of interest from t_1 to t_2.

The systematic error is calculated for each axis direction at each (x,y,z) coordinate using the following equations derived from the HTM's for the BAXYZF machine. Notation follows [2]. All translational error terms are measured through the center point (or corrected to the center). The machine has a left-hand coordinate system.

$$E_x(x,y,z) = \delta_x(x) + \delta_x(y) + \delta_x(z) - Y\,\varepsilon_z(x) + Z\,[\varepsilon_y(x) + \varepsilon_y(y)\,] - Y\,\alpha_{xy} - Z\,\alpha_{xz} \quad (2)$$

$$E_y(x,y,z) = \delta_y(x) + \delta_y(y) + \delta_y(z) - Z\,[\varepsilon_x(y) - \varepsilon_x(x)\,] - Z\,\alpha_{yz} \quad (3)$$

$$E_z(x,y,z) = \delta_z(x) + \delta_z(y) + \delta_z(z) - Y\,\varepsilon_x(x) \quad (4)$$

The expected value of systematic error in the x-direction is calculated from the numerical equivalent of equation (1):

$$\overline{E}_x = \frac{1}{N^3}\sum_{i,j,k}^{N}\left(E_x\right)_{i,j,k} \quad (5)$$

Equation 5 assumes a uniform probability regarding the position of the X-axis throughout its range. Similar equations are applied for Y and Z directions.

GUM also requires calculation of the variance associated with the mean correction according to:

$$u^2\left(\overline{b}\right) = \frac{1}{t_2 - t_1}\int_{t_1}^{t_2}\left[b(t) - \overline{b}\right]^2 dt \quad (6)$$

This is accomplished numerically as well using the results of equations 2-4 in equation 7.

$$u^2\left(\overline{E}_x\right) = \frac{1}{N^3}\sum_{i,j,k}^{N}\left[\left(E_x\right)_{i,j,k} - \overline{E}_x\right]^2 \quad (7)$$

The standard uncertainty for each direction is calculated as the squareroot of the sum of the variances for each term of equations 2-4 with the addition of the term from equation 7 and the ETVE term. For the x-direction:

$$u^2\left[E_x(x,y,z)\right] = u^2\left[\delta_x(x)\right] + u^2\left[\delta_x(y)\right] + u^2\left[\delta_x(z)\right] + \overline{Y}^2u^2\left[\varepsilon_z(x)\right] + u^2(Y)\overline{\varepsilon}_z^2(x) + \overline{Z}^2\left\{u^2\left[\varepsilon_y(x)\right] + u^2\left[\varepsilon_y(y)\right]\right\} \quad (8)$$
$$+ u^2(Z)\left[\overline{\varepsilon}_y^2(x) + \overline{\varepsilon}_y^2(y)\right] + \overline{Y}^2u^2\left(\alpha_{xy}\right) + u^2(Y)\overline{\alpha}_{xy}^2 + \overline{Z}^2u^2\left(\alpha_{xz}\right) + u^2(Z)\overline{\alpha}_{xz}^2 + u^2\left(\overline{E}_x\right) + u^2\left(ETVE_x\right)$$

Uniform distributions are assumed for uncertainties of parametric errors and axis offsets with bounds equal to the measured repeatabilities and axis ranges respectively. Table 2 summarizes the results. Values are scaled.

Table 2: Calculated results (scaled)

(mm)	X-direction	Y-direction	Z-direction
Exp. Value of Sys. Error	0.000187	-0.00013	4.72E-05
Variance of Exp. Value	0.001583	0.000619	0.000578
Standard uncertainty	0.00231	0.00111	0.00193
Estimate of Uncertainty	0.000187+/-0.00462	-0.00013+/-0.00222	4.72E-05+/-0.00386

For comparison purposes the expected machine error was also calculated according to:

$$\frac{1}{2}\left(\sum e_i + \sqrt{\sum e_i^2}\right) \quad (9)$$

For equation 9, no distinction was made between systematic and non-systematic errors. For example, the term for linear accuracy included the range of all measured values. Offsets were taken as the maximum distance from the center of the working volume and multiplied by the total range of angular errors for those terms. ETVE was taken as the total range for each axis direction. The results are as follows. Values are scaled.

Table 3: Commonly used "error budget" calculations using the same data as Table 2

(mm)	X-direction	Y-direction	Z-direction
Equation (9)	+/-0.00315	+/-0.00283	+/-0.00445

Inspection results were also obtained. True position of drilled holes was separated into X and Y directions. Z direction positioning error was not measured directly. Hole diameter is the related feature. Z direction error is not easily derived from this because other factors influence the diameter. Table 4 summarizes inspection data from approximately 300 holes made soon after the metrology was performed on the machine.

Table 4: Inspection data from approximately 300 measurements. Values are scaled

(mm)	X-direction	Y-direction
Average error	0.0003	-0.0006
Std. Uncertainty	0.0022	0.0029

Conclusions

A simple method is proposed to define "first piece machine tool accuracy" which offers a solution to the problem of dealing with known, uncorrected, systematic errors. The expected value of the systematic error and its variance are calculated assuming uniform probability of position throughout the working volume. Results are compared to the most common calculation method as well as to inspection data. For this single case, results of the proposed calculation are mixed; both conservative and less than conservative with respect to both the inspection results and the other method.

Discussion

The definition for "expected value of systematic error" is open to interpretation. We could imagine giving added weight to error values calculated near the center of the working volume for example. With information about parts we would probably limit consideration to a subset of the working volume. It may even be reasonable to make calculations of systematic error using the point-to-point positions of a CNC program. The datum point for calculations is also important. Either measuring or machining a feature involves a relative move. The error at a point is not absolute. The calculations of expected systematic error might include all possible relative moves. This is an interesting option because for every error value there is an equal magnitude error of opposite sign. The expected value of systematic error would be zero.

The mean variance of the systematic error due to its actual determination is neglected in the calculations. According to ISO GUM, Annex F, equation F.7.c, this is the RMS value of uncertainty in the determination of systematic error at each position where the error is calculated. This term was considered as composed of the variations in each error used to calculate systematic error at each point (i.e. the repeatability of positioning accuracy, etc.). Because these were the non-systematic terms included in the calculation of standard uncertainty, the uncertainty in determination of average systematic error was assumed zero.

From the overall process point of view, the uncertainty in determination of the average systematic error should probably include the other sources of error in the process. For the machine considered, these are dominated by the ability to reference the laser beam to the machine coordinate system. A Helium-Neon pilot beam, assumed to be colinear with the cutting beam, is turned on and the axes are positioned to obtain maximum intensity through a hole in a tooling block. It is safe to say an analysis of the entire process to include the operating methods, part fixturing and inspection machine in addition to the positioner would yield an estimate of uncertainty to encompass all the measured results.

References

[1] ISBN 92-67-10188-9, 1993, "Guide to the Expression of Uncertainty in Measurement," **ISO**

[2] Hocken, R.J., 1995, "Machine Metrology," **ASPE Tutorial**

[3] Donaldson, R.R., 1980, "Error Budgets," **Technology of Machine Tools**, Vol. 5, sec. 9, pp. 1-14

[4] Shen, Y.L., Duffie, N.A., 1993, "Comparison of Combinatorial Rules for Machine Error Budgets," **Annals of the CIRP**, pp. 619-622

[5] Dorndorf, U., Kiridena, V.S.B., Ferreira, P.M., 1994, "Optimal Budgeting of Quasistatic Machine Tool Errors," **Transactions of the ASME (Jrnl of Engrg. Ind.),** Vol. 116, pp. 42-53

[6] Thompson, D.C., 1989, "The Design of an Ultra-Precision CNC Measuring Machine," **Annals of the CIRP**, Vol. 38/1, pp. 501-504

[7] CIRP STC <<Me>> Working Party on 3DU, 1978, "A Proposal for Defining and Specifying the Dimensional Uncertainty of Multi-Axis Measuring Machines," **Annals of the CIRP**, Vol. 27/2, pp. 623-630

[8] Bryan, J.B., 1993, "The Deterministic Approach in Metrology and Manufacturing," **Proceedings of the 1993 International Forum on Dimensional Tolerancing and Metrology**, pp. 161-166

[9] Hazelton, A.J., 1995, "On-Machine Acceptance of Machined Components," **Proceedings of the ASPE**, pp. 420-423

[10] Hocken, R.J., 1997, "ASME B5.57M - Methods for Performance Evaluation of Computer Numerically Controlled Lathes and Turning Centers," **ASME Draft Standard** v.9.0

A Model of the Tracking Errors of a Machine Tool Slideway

Cecil M. Daniel, John W. Sutherland and Walter W. Olson

Department of Mechanical Engineering - Engineering Mechanics
Michigan Technological University, Houghton, MI 49931

INTRODUCTION

Customers are demanding ever higher levels of dimensional accuracy for machined components. Some factors affecting accuracy are related to the machining process (tooling, workpiece and fixturing) and others are related to the machine tool. Often, the accuracy of the machine tool is a limiting factor in achieving higher dimensional accuracy in machined components [Kiridena & Ferreira, 1994]. Hocken [1980] emphasized the importance of developing a mechanistic understanding of the systematic errors of a machine tool. A mapping between component level attributes (design parameters / manufacturing inaccuracies) and error behavior is thus required. As a step toward achieving this, a mechanistic understanding of the angular and positional errors of a slideway (single machine axis) is obtained based on the force system and contact deformations of the slideway. An analytical model of the tracking errors of a slideway is then developed in this work.

There are six error motions associated with the six degrees of freedom possible for the saddle of a machine slideway. Three of these are translational errors δ_x, δ_y and δ_z, and the others are angular α, β and γ as shown in Figure 1. The combined influence of these errors cause three components of the tracking error viz., e_x, e_y and e_z in the three axis directions at the cutting point.

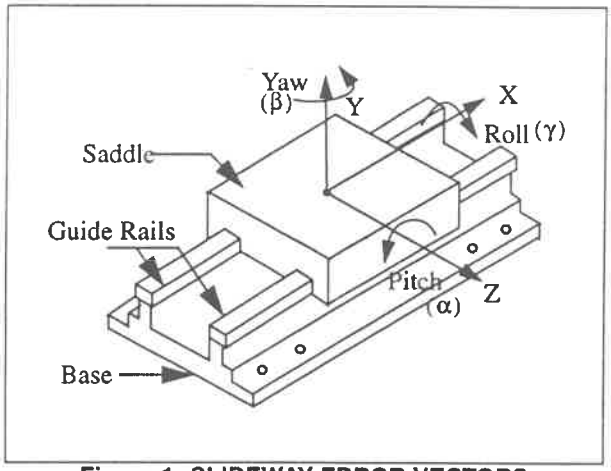

Figure 1: SLIDEWAY ERROR VECTORS

SLIDEWAY FORCE SYSTEM

During a machining operation, a complex force system acts on each slide of a machine tool. The force system influences slideway tracking error by affecting both contact deformation and geometry of contact between the slide and guide. Sliding joints have finite stiffness in different directions and permit linear and angular deflections when forces act on them. These deflections manifest themselves as joint errors and affect the tracking accuracy of the slideway. Slideway reaction forces are distributed forces that act along the length of the guideways. The shape and magnitude of the distributed force may be obtained through a finite element analysis of the structure by constraining nodes at the interface between slide and guide. The reaction force often applies very high pressure locally at small "contact patches" at the joint interface. Hence in this work the distributed reactions are modeled as concentrated forces acting at discrete contact patches.

Figure 2 illustrates the force system that exists on a slideway during a machining operation. The applied forces include the components of the cutting force in three orthogonal directions, F_x, F_y and F_z the force on the lead screw nut F_l in the direction of motion and the gravity forces due to the slide and workpiece, W_s and W_w respectively. The center of gravity of the workpiece is positioned at a distance 'd' and 'e' in the X and Z directions from the origin O of the reference co-ordinate frame. Location of point O has been chosen such that the moment due to R_1 is zero. The reaction forces acting on the slideway are the vertical (R_1, R_2, R_3) and horizontal (F_1, F_2) forces applied by each guide rail on the slide, friction forces f_1 and f_2 at the slide / guide interface. F_{pre} is the known reaction due to gib preload. Rigid body analysis may be performed to predict the reaction forces on the slideway. To make the problem statically determinate, one vertical reaction force (R_1) is considered on one of the guideways and two reactions (R_2, R_3) on the other. The seven unknown reaction forces may then be computed from the conditions of static equilibrium using Eqs. (1) through (7).

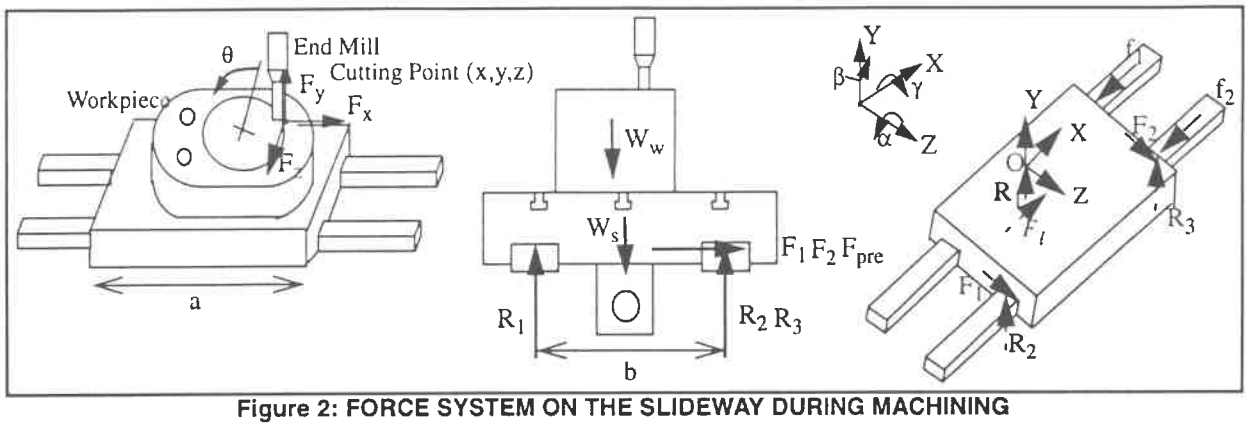

Figure 2: FORCE SYSTEM ON THE SLIDEWAY DURING MACHINING

$$\Sigma F_x = F_x + F_l + f_1 + f_2 = 0 \quad (1)$$

$$\Sigma F_z = F_z + F_1 + F_2 = 0 \quad (2)$$

$$\Sigma F_y = F_y + R_1 + R_2 + R_3 + W_w + W_s = 0 \quad (3)$$

$$-b(R_2) - b(R_3) - z(F_y) + y(F_z) + \frac{b}{2}(W_s) + e(W_w) = 0 \quad (4)$$

$$\frac{b}{2}(F_l) - b(f_2) + \frac{a}{2}(F_1) - \frac{a}{2}(F_2) + z(F_x) - x(F_z) = 0 \quad (5)$$

$$-\frac{a}{2}(R_2) + \frac{a}{2}(R_3) - y(F_x) + x(F_y) - d(W_w) = 0 \quad (6)$$

$$f_1 = \mu(R_1) \qquad f_2 = \mu(R_2 + R_3 + F_{pre}) \quad (7)$$

Eqs. (1-7) were used to compute reaction forces and Figure 3 shows predicted reactions as a function of tool position (θ in Figure 2) during a pocket milling operation.

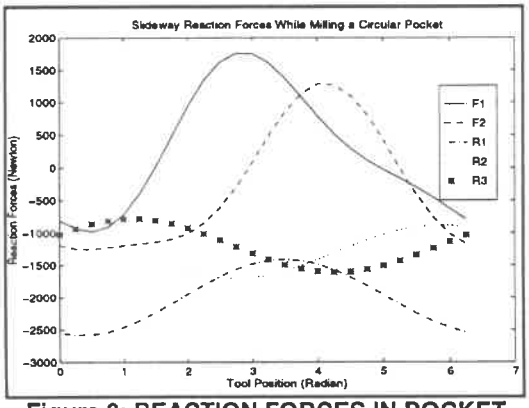

Figure 3: REACTION FORCES IN POCKET MILLING

Reactions F_1 and F_2 influence the yaw behavior, while R_1, R_2, and R_3 could potentially influence the roll and pitch behavior of the slideway.

FORCE SYSTEM INFLUENCE ON ERRORS

Force based joint deformations occur at the contact surfaces of the slideway and have been extensively studied by researchers Levina [1967] and Furukawa & Moronuki [1987]. As with any generated surface, the joint surfaces in a slideway are imperfect and exhibit waviness and flatness deviation. Due to this, only a small part of the apparent area of contact actually supports a load. Elastic deformations occur at the roughness peaks and waves of these patches of contact and may cause deflection and angular errors in the slideway. Levina [1967] likens the behavior of slideway contact surfaces under load to that of flexible washers inserted between parts in contact. He further estimates that for a lathe, contact deformations (including deflection of gibs) account for 80-90% of the total elastic displacement between tool and spindle. Analytical methods to estimate contact stiffness of slideways often depend on empirical formulae or a finite element analysis of objects with imperfect mating surfaces. An experimental method is used here to determine contact stiffness of the slideway in various directions.

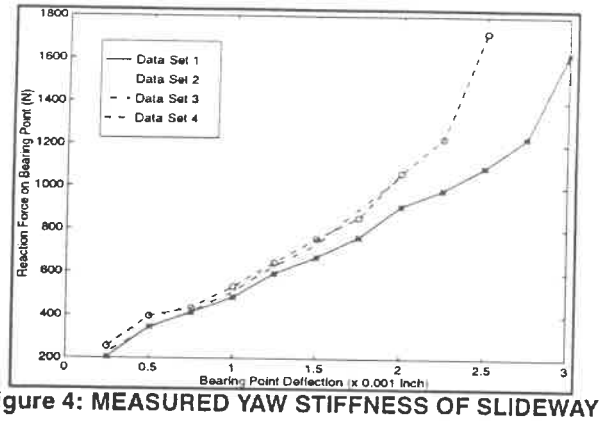

Figure 4: MEASURED YAW STIFFNESS OF SLIDEWAY

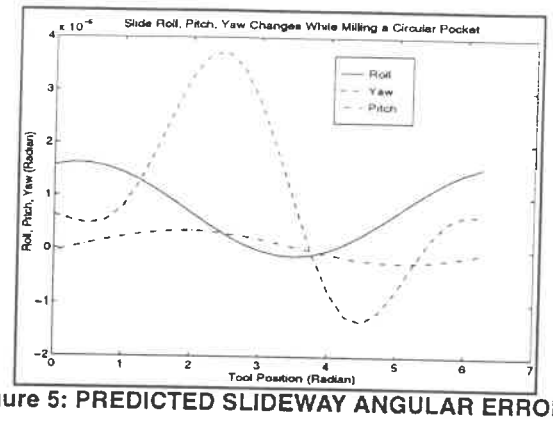

Figure 5: PREDICTED SLIDEWAY ANGULAR ERRORS

By applying a known horizontal couple (moment) to produce reactions F_1 and F_2 in Figure 2, a yaw error was obtained and measured. Reaction forces F_1 and F_2 were computed and Figure 4 shows a plot of reaction force versus measured deflection at the two dominant bearing points in the yaw direction at different points in the travel. The slideway stiffness in the yaw direction may now be computed. Similar experiments may be performed by applying couples in other directions and measuring the deflections. For a given slideway geometry, variation of angular errors due to force based deflections were computed for the case study of pocket milling explained in the previous section. Figure 5 illustrates the variation of roll, pitch and yaw due to joint contact deformation.

SLIDEWAY TRACKING ERROR MODEL

Coordinate transformations may be used to obtain a mapping between geometric errors of slideway parts (saddle, base, guide rails), misalignments at the sliding joint and the tracking error. Homogenous transformation matrices (HTM) are used to move from one co-ordinate frame to another. The positional error $\delta(x)$ and angular errors $\alpha(x)$, $\beta(x)$ and $\gamma(x)$ vary with saddle position and may be described by an n^{th} order polynomial [Kiridena & Ferreira, 1994] in x and represented in general form by:

$$\alpha(x) = \sum_{1}^{n} A_n x^n \; ; \qquad \beta(x) = \sum_{1}^{n} B_n x^n \; ; \qquad \gamma(x) = \sum_{1}^{n} C_n x^n \; ; \qquad \delta(x) = \sum_{1}^{n} D_n x^n \tag{8}$$

Figure 6 illustrates a steelway slide and the equivalent kinematic chain that may be used for analysis. Four coordinate frames F_1, F_2, F_3, F_4 are used to move through the chain. Three HTMs are used to transform vectors from frame F_1 to frame F_4. Two of the HTMs model the geometric inaccuracies of the slideway parts (base, guideways, and saddle). The third HTM models the positional and angular errors occurring at the sliding joint. Using the approach illustrated in Ferreira and Liu [1986], and modeling the angular and positional errors as linear functions and neglecting second order error terms, the tracking errors in terms of the basic dimensions and geometric deviations of the slideway are given by:

$$e_x = -b_2(\alpha_1 + \alpha_2) + c_2(\beta_1 + \beta_2) \; -b_1\alpha_1 + c_1\beta_1 + \Delta a_1 + \Delta a_2 + x(-b_2A_1 + c_2B_1 + D_1) \tag{9}$$

$$e_y = a_2(\alpha_1 + \alpha_2) \; -c_2(\gamma_1 + \gamma_2) + a_1\alpha_1 - c_1\gamma_1 + \Delta b_1 + \Delta b_2 + x(a_1A_1 - c_1C_1 + \alpha_1) + x^2\left(\frac{1}{2}A_1\right) \tag{10}$$

$$e_z = -a_2(\beta_1 + \beta_2) + b_2(\gamma_1 + \gamma_2) \; -a_1\beta_1 + b_1\gamma_1 + \Delta c_1 + \Delta c_2 + x(-a_2B_1 + b_2C_1 + \beta_1) + x^2\left(\frac{-1}{2}B_1\right) \tag{11}$$

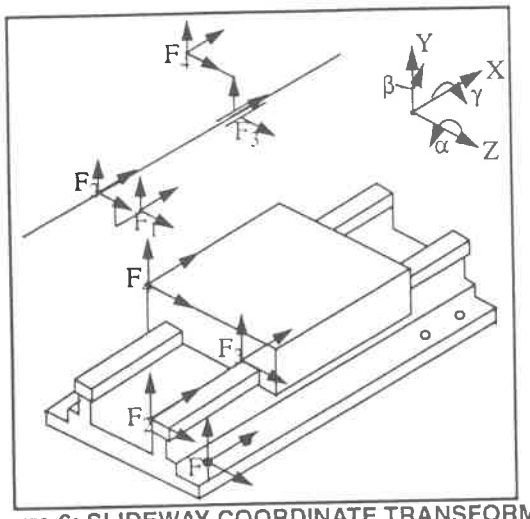

Figure 6: SLIDEWAY COORDINATE TRANSFORMS

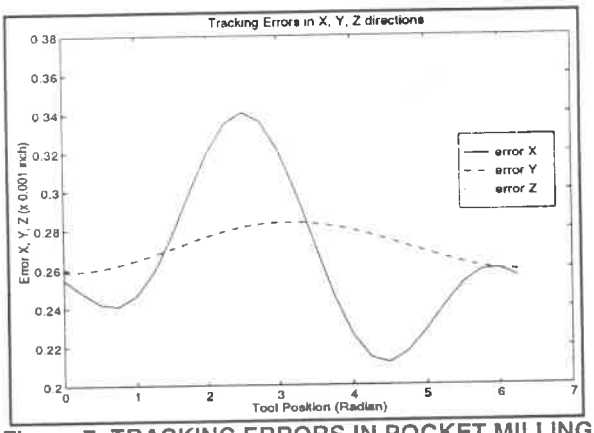

Figure 7: TRACKING ERRORS IN POCKET MILLING

Using Eqs. (9-11), the tracking errors of the slideway may be computed for given geometric errors in the slideway parts and known angular errors. Using co-ordinate transforms, similar error models may be derived for cases where roll, pitch and yaw errors are given by higher order polynomials. Using this approach for the case study of milling, Figure 7 shows predicted tracking errors of the saddle as a function of tool position during the milling operation. For this case, slideway design dimensions for the computation were from Setco [1990] and values for the shape errors of slideway parts were modified from Ferreira & Liu [1986]. For the particular case study, the maximum tracking errors in the X, Y and Z direction at the saddle are 0.00034, 0.00028 and 0.00038 inch (9, 7 and 10 μm) respectively. Depending on the workpiece, some or all of these components may be in sensitive directions and may contribute to the surface error of the machined workpiece. A designer may use the model for error budgeting, or to choose robust design dimensions to minimize tracking errors in sensitive directions.

CONCLUSIONS

A model for the tracking errors of a machine slideway has been presented. The model uses known geometric errors of the slideway parts and measured contact stiffness to estimate the cartesian errors in the three directions. Specific findings include:

- There exist finite stiffness that may be measured in various directions for a machine slideway.
- Guideway reaction forces may be predicted for a given slide geometry provided the applied forces are known.
- Tracking errors of a slideway may be estimated based on geometry deviations and contact stiffness of the joint.

REFERENCES

Ferreira, P. M., and Liu, C. R., "An Analytical Quadratic Model for the Geometric Error of a Machine Tool," Journal of Manufacturing Systems, Vol. 5, No. 1, 1986, pp. 51-63.

Furukawa, Y., and Moronuki, N., "Contact Deformation of a Machine Tool Slideway and Its Effect on Machining Accuracy," JSME International Journal, Vol. 30, No. 263, 1987, pp. 868-874

Hocken, R. J., and Machine Tool Task Force, "Technology of Machine Tools, Vol. 5, Machine Tool Accuracy," 1980, UCRL 52960-5, Lawrence Livermore Laboratory, University of California, Livermore, CA.

Kiridena, V. S. B., and Ferreira, P. M., "Kinematic Modeling of Quasistatic Errors of Three Axis Machining Centers," Int. J. Mach. Tools Manufact., Vol. 34, No. 1, 1994, pp. 85-100.

Levina, Z. M., "Research On The Static Stiffness of Joints In Machine Tools," Proceedings of the 8 th. Intl. M.T.D.R. Conference, Part 2, Sep. 1967, pp. 737-758.

Setco Catalog # 287, "Precision Hardened Steelway Slides," Setco Sales Co., Cincinnati, OH 45233.

Slocum, A. H., "Precision Machine Design," Prentice Hall Co., 1992.

Engineering Applications of Geometric Metrology

Mark J. Kaiser

Department of Industrial and Manufacturing Engineering
Wichita State University, Wichita, KS 67260–0035
Email: kaiser@ie.twsu.edu

Abstract. Geometric metrology represents an approach to metrological analysis based on the notion of a separation functional and the underlying geometric structure representing the problem. In [1], the separation functional was defined, described, and a formal framework presented for the evaluation of shape measures based on this functional. A generalized compliance test and a global measure of shape difference was described to determine the shape variability between the perfect form and manufactured artefect. In the current work, the computation of tolerance measures and application examples based on the separation functional are now described. Separation measures are calculated for several classes of manufactured objects, including a convex polygonal perfect form and measurement data described by a simple polygonal region, and an incomplete data set such as commonly occurs with keyways, flats, and partial arcs. Separation functionals for tubular objects which include cylindrical and rectangular artefacts, bored tubes, and parallel surfaces with different diameters, and a generalized class of three–dimensional objects are computed. The techniques of geometric metrology are also applied to complex part geometry, straightness, flatness, and the positional tolerance problem.

As one moves from the nominal engineering design (the blueprints) to the manufacturing process, the control of variability becomes a major production concern. Variability arises from the physical processes used to make and assemble parts, and tolerancing and metrology serve as the primary tools to control such variation. The control of variation is important to the quality of the part produced as well as its functional performance. The control of variation is also directly related to cost reductions during manufacturing, since a low variability process will promote less re–work and reduce scrap. Methods to control, reduce, quantify and understand the causes of variability is thus fundamental to every production process.

Typical manufactured products are specified in terms of their nominal (ideal) shapes and material properties, and when designed, dimensional tolerances are assigned to specify allowable variations. Tolerance is generally a function of the manufacturing process, and the accepted values of tolerance are normally dictated by the desired functional requirements of the end product. The application (functional requirement) determines the design (form) as well as the relevant features of the form, e.g., high–speed gyroshafts require fine axis alignment, experiments to compute the Avogadro number require a perfectly spherical silicon ball, high performance six–cylinder engines require cylindricity to prevent sticking and premature wear, etc. In this instance form refers to the macro–characteristics of components such as flatness, circularity, cylindricity, sphericity, ... as distinct from the micro–characteristics such

with an analytic equation describing Φ. The form functional f_Φ can be computed in closed-form for a few special cases [1].

In the poster presentation of this material, computational results will be shown for several examples where the methodology of geometric metrology is applied. The diversity of the examples (planar, tubular, and three–dimensional objects; complex part geometry; straightness and flatness; and positional tolerance) indicate that the approach of geometric metrology can address a wide range of problems.

References

[1] Kaiser, M. J., "Geometric metrology I. Separation functionals in tolerance assessment," *Journal of Franklin Institute: Engineering and Applied Mathematics*, to appear.

A Study on Auto-measurement System of Coordinate Measuring Machine

Wang Jianli Liu Shugui Li Zhen Zhang Guoxiong
College of Precision Instrument&Opto-Electronics Engineering,
Tianjin University, Tianjin, P.R. OF CHINA

Abstract: An auto-measurement system of CMM is designed in this paper. It can analyze the IGES files and distinguish the feature of workpiece. It can automatically plan the measuring path and check collision. It can convert the measuring path file to the DMIS file and automatically control the measurement.

Key word: CAD CMM automatic measurement expert system

1 Introduction

Coordinate measuring machine(CMM) is specially becoming the major inspecting equipment in quality data acquisition and quality control in automatic manufacture industry. With the development of the CIMS, the requirement of integration and automation for CMM increase, so the research of auto-measurement system of CMM is processed by many college. The main problems of it are the following three: most CAD system is designed to drawing not manufacture and measuring, the file format don't support the measurement path planing, how to transform the CAD date to the CMM is first problem, how to plan the measure path of CMM to avoid the collision between the CMM and part is the second problem, how to use the measure path file to control measurement of CMM is the third problem. In this paper, these three problems will be solved.

2 General Design

The whole system consists of the follow parts: feature distinguish expert system, the workpiece coordinate calculate system, the measurement path planning expert system, the collision avoiding checking system, the system of conversion from measuring path file to DMIS(date measuring interface system) file, the system of interface between operator and computer, the system of interface between expert and computer.(Fig. 1)

Feature distinguish system is an expert system, which can finish putting forward the measuring information and distinguishing features of workpiece and the relation between them from the CAD file IGES (Initial Graphics Exchange Specificifications). IGES is a neutral CAD data transformation medium that was created by the National Bureau of Standards. The worpiece coordinate calculation system can finish the dimension and coordinate calculation of workpiece. The measuring path planning block is an expert system, which can finish the measuring path planning, probe tip selection and measuring point distribution. The collision avoiding checking block is a system which can check whether the measuring path of measuring tip collide the workpiece and machine. DMIS file conversion system can convert the measuring path to DMIS file. DMIS provides a standard for the bidirectional communication of inspection data between a computer system and inspection equipment. The specification is a vocabulary of terms which establishes a neutral format for inspection programs and inspection results data. We can control the measuring motion of CMM through the DMIS file.

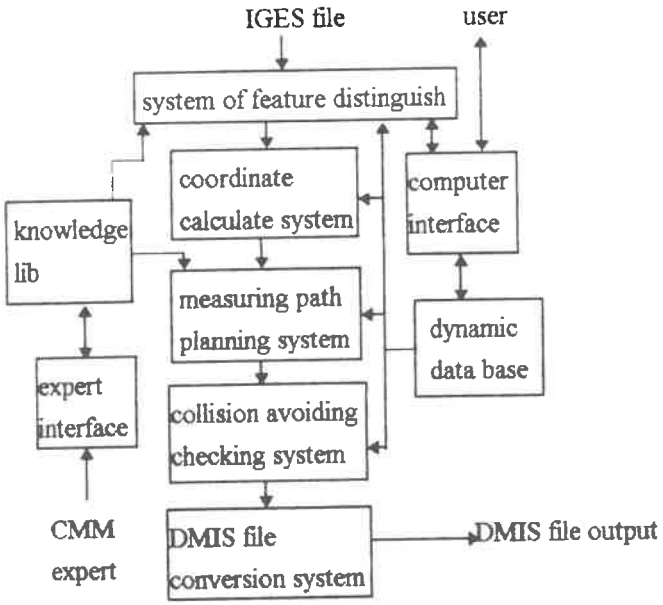

fig. 1 CMM automatic measurement system general design

The interface between operator and computer is designed in order that the operator can control the process of measuring. The interface between expert and knowledge lib in order to expand the knowledge lib. The integrate data structure and the integrate dynamic database is adopted during those seven parts in order to convert data between the whole system conveniently.

The whole system which is designed by C++ can run in the environment of WINDOWS. The auto-measurement system integrate the CAD system, inspect system, calculate system and symbol process system, so the system involves lots of techniques. Some key techniques are explained in this paper.

3 the key techniques study

3.1 data structure

Oriented object technique has advantage of abstract, inherit and envelope, so this technique is applied to design the data structure and data lib in this system. The workpiece measurement information can be expressed as follows:

```
CLASS part 1{
    CLASS element 1;
    CLASS  element 2;
     ... ...
    CLASS  element n;
    FUNCTION  operate function();
}
CLASS element 1{
    UNION element feature;
    FLOAT dimension tolerance;
```

FLOAT form and position tolerance;
STRUCT coordinate of feature point;
FUNCTION operate function();
}

3.2 the foundation of oriented object expert system

There are three parts in IGES file, the first is geometry entity, the second is explain entity, the third is structure entity. Those three parts construct the information of part though logistic relation. So the distinguish of feature information must be basis on those basic information and their logistic relation. which can be taken as these steps:

1. Confirm the each part meaning of IGES files.
2. Setup the rules of view disparate and feature distinguish.
3. Distinguish the feature from the IGES file on basis of rules. If it can not distinguish from IGES file it must be input by the operator though the interface.

The measuring path planning system must complete those jobs: the selection of measuring base plane, the selection of measuring probes, the number of measuring point on basis of the measurement precision, the selection of the measuring path and the optimization of the measuring path.

The oriented object expert system can be designed as following(fig. 2).

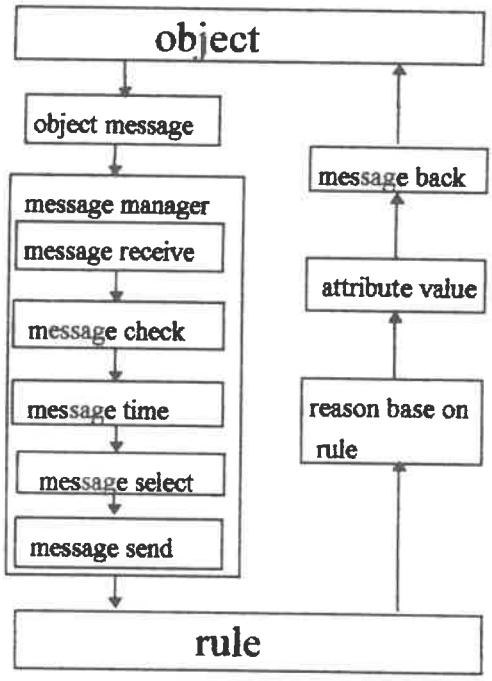

fig. 2 oriented object expert system

The rule of the knowledge lib can be expressed as follow:

rule::=IF condition THEN conclusion::=<attribute1, attribute2… …>is <value1,value2,.....>

Message is the control instruct which can operate the object, message manager is in charge of the receive of message, the send of message and the checking of message. It has some feature in the path planning system as follows:

1 The message can directly send to the receiver.

2 The message can send lots of objects.

3 The message can guild the direct of the object transmission

The oriented object reason algorithm is as follows:

1 Load the object class and open the knowledge lib.

2 Send the message by the outer.

3 The message manager receive the message.

4 Check the message, if it is OK, then continue, else go to step 2.

5 Start the message timer.

6 Go to the message matching(find the name of message, if success then put the name of message in the data lib and continue else go back and go to step 2.

7 Send the inner message from the object.

8 Load the rules.

9 Reason by the rules. Seek the attribute value of the object, then seek the name of each sub-object, and put the name of it into the data lib, go to step 10, if the name not exist, seek the supper-object, and put the name of it into the data lib, go to step 9.

10 Send the message according to the rules.

11 Select the message by the message manager.

12 Seek the sub-object which is a recurrence procession of message base on the message drive. If successful go to step 13, else go to step 12. If all the sub-objects are sought unsuccessfully, print the reason is fail.

13 The reason end.

From the above algorithm we can see that the oriented object reason machine is a reason machine base message, the message control the reason according rules, which is the only hub connecting the message.

3.3 the algorithm of avoiding collision

During the measurement of CMM, the most dangerous thing is the collision between measuring probe and workpiece, so the checking of avoiding collision must be carried after the path planning. In this paper, an algorithm named "the method of space occupy survey" is put forth.

1 The two normal measuring probe is sampled to the segment lines(fig. 3).

2 Calculate the plane of measuring probe movement from one measuring point to the second point.

3 Read the element from the feature solider of workpiece, if all of the elements are checked, then go to step 5.

4 Check whether the plane of the measuring probe movement intersect the space of element occupy. If intersect, then quit the checking and display "collision occur", else redo step 3.

5 No collision and quit.

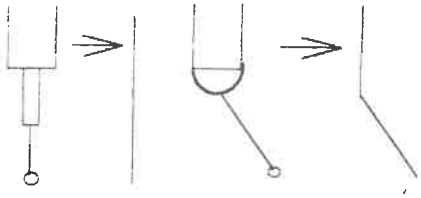

fig. 3 measuring probe abstract

4 Conclusion

From the design of this system, we can see:

1. It is reasonable that we can integrate the CAD and inspect system by the IGES.
2. We can design the expert system using C++.
3. We can integrate the express of measuring information in the whole system using the technique of oriented object.
4. The automatic measurement system of CMM has metric of high intelligent, the method of design can be spread to other automatic instrument.

References

1 H. Y. Herman et al, "Computer aided programming of CMMs", Proc. of Int. Symp. on Automation and Robotics in Production Eng., May 24-27, 1988, Xi'an, P.R.China

2 W. Evershein et al, "Automatic generation of part programs for CNC-coordinate measuring machine linked to CAD/CAM systems", Annals of CIRP, vol. 35, no.1, 1986, pp.341-345

3 P.H.Gu, "A knowledge-based inspection process planning system for coordinate measuring machine", Journal of intelligent Manufacturing, 1994

4 Theodore H. Hopp, "CAD-Directed Inspection", Annals of CIRP, Vol. 33/1/1984, pp.357-361

5 Martin Prinz et al, "From CAD-Based Kinematic Modeling to Automated Robot Programming", Robotics & Computer-Integrated Manufacturing, Vol. 12, No.1, 1996, pp. 99-109

6 P.Gu et al, "Object-oriented product modelling for computer-integrated manufacturing", INT.J. Computer Integrated Manufacturing, 1994, Vol. 7, No.1, pp.17-28

7 Richard J. Mayer et al, "Plan generation strategies for a knowledge-based automated process planning system", INT. J. Computer Integrated Manufacturing, 1995, Vol.8, No.6, pp.399-410

A Laser Tracking Interferometer Based on a New Servo System

Fu Jiyou Ding Yao Zhang Guoxiong
College of Precision Instrument & Opto-electronics Engineering
Tianjin University, Tianjin 300072, China

Abstract: A laser tracking interferometer based on a new direct drive servo system is introduced in this paper. In the new tracking system, the electric current signal from a position error detector drives the coil in a magnetic field and a reflecting mirror stuck on the coil will rotate certain angle to keep aiming at the target retroreflector. This simplified system obtains high response speed and costs much less. Experiments show that the servo system can track the object with the speed 5m/s as well as the acceleration 10m/s^2. By using several such tracking interferometers, a moving corner retroreflector mounted on CMM has been tracked and the two dimensional coordinate values of the object have been given.

Key words: Laser Tracking Interferometer Servo System

1 Introduction

Among the various coordinate measuring techniques, laser tracking systems based on interferometry have the potential for continuously producing noninvasive and highly accurate measurement over a large work volume of calibrated machine [1] [2]. When laser interferometer is applied for target tracking, the accuracy and response speed of servo system play an important role. Traditionally, each servo system is quite complex, including positional error detector, motor controller, motor, transmission shaft, bearing, gimbals and mirror. To achieve high accuracy and reliability during tracking process, the mechanical parts should be manufactured highly precisely and the design of motor controller is difficult. As the result, each tracking system is expensive and the tracking speed is not high. To overcome these problems, we put forward a new laser tracking interferometer with a suspension filament rotatable mirror and realized 2D coordinate measurement.

2 Single-beam Laser Tracking Interferometer

A schematic diagram of a single-axis laser tracking mirror positioning servo mechanism is shown in Figure 1.

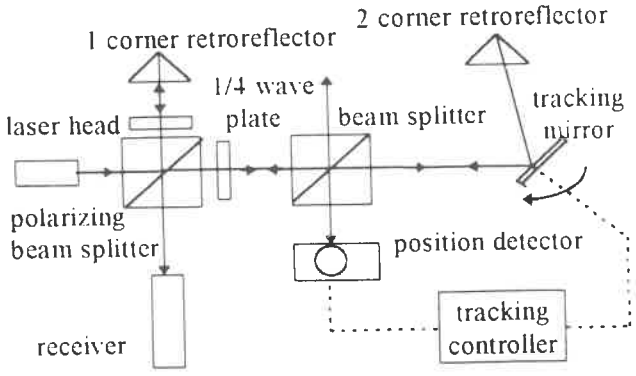

fig.1 schematic diagram of a laser tracking interferometer

Two orthogonally polarized beams are emitted by the laser head. The reference beam is diverted to a receiver by a polarizing beam splitter (PBS) through a quarter wave plate and corner retroreflector (1).

The measuring beam proceeds the PBS, a quarter wave plate and the beam splitter (BS) and is directed by the tracking mirror to a retroreflector(2) located on a moving target. The returning beam from the retroreflector goes parallel to the incoming beam and enters the BS from the opposite direction. The beam that passes through BS is reflected by PBS and emerges into the receiver. The beam that reflected by BS is transmitted to a two-quadrant detector, which detects the deviations of the returning bean from the center. The resulting error signal drives the servo system that adjusts the angle of a single-axis mirror gimbal. Thus the beam can reach in any direction on a plane by the single-axis tracking mirror servo system.

The rotation of the mirror must be adjusted very accurately in order to obtain the desired accuracy and repeatability of the tracking interferometer. As the rotatable mirror is light, a suspension filament can be used as a spindle to support the mirror and make it rotate freely. Referring to the structures of filament galvanometers and optical oscilloscopes, a rotatable mirror based on a suspension filament is designed [3].

3 Design of the Rotatable Mirror and its Servo Control System

3.1 make the rotatable mirror and its actuator

According to electromagnetic theory, an electrified coil in a magnetic field will be rotated by Lorentz effect. If the electrical current is put into a coil mounted on a rack by two filaments in a magnetic field, the coil will rotate until its electromagnetic torque balances the filament reaction torque. Once a mirror is stuck on the coil, it has been modified into a rotatable mirror. Thus, a tracking mirror system will be made following these steps:

1. Choose a precision filament galvanometer, save its permanent magnet and coil. Increase the height of the rack and choose a filament suitable for the mirror.

2. Weld one end of a copper slice on the upper end of the coil and the other on the filament.

3. Stick one reflective mirror on the copper slice and the other mirror on the opposite of the copper slice to avoid the unbalance of the rotated part in the tracking period.

The tracking mirror system is shown in Figure 2.

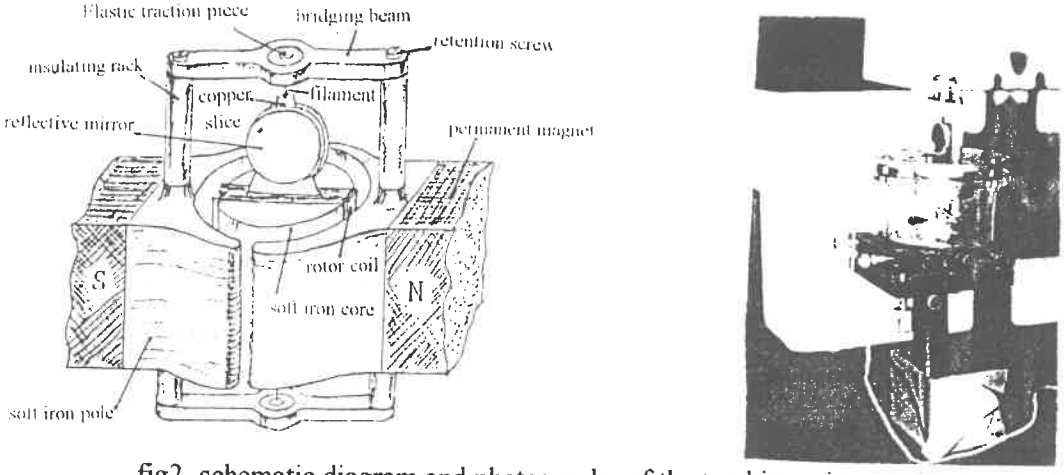

fig2. schematic diagram and photography of the tracking mirror

The advantages of the structure lie in:

1. High rotating accuracy. The tightly stretched filament serviced as the spindle has very litter radial displacement, much less than the ordinary mechanical shaft.

2. Small volume and moment of inertia conductive to achieve good dynamic features.

3. Free of friction and clearance conductive to long use and simple maintain.

4. Easily be made and controlled and very cheap.

3.2 the characteristics of the tracking mirror

The open-loop dynamic characteristics of tracking mirror can be described by the third order model expressed by transfer function M(s). The block diagram representation of the model is shown in Figure 3. where input drive torque T(s) applied to the mirror is equal to $U_{in}(s)*(NAB/SL+R)$ and $U_{in}(s)$ input drive voltage. N the coil number. A the coil area. B the magnetic stiffness. L the self-inductivity. R the coil resistance. J total inertia (coil plus mirror). K_t spring constant of the suspension filament. K_d the damping coefficient. θ(s) the rotation angle.

$$M(s) = \frac{\theta(s)}{U_{in}(s)} = \frac{NBA}{JLs^3 + JRs^2 + (K_t L + NBAK_d)s + K_t R} \qquad (1)$$

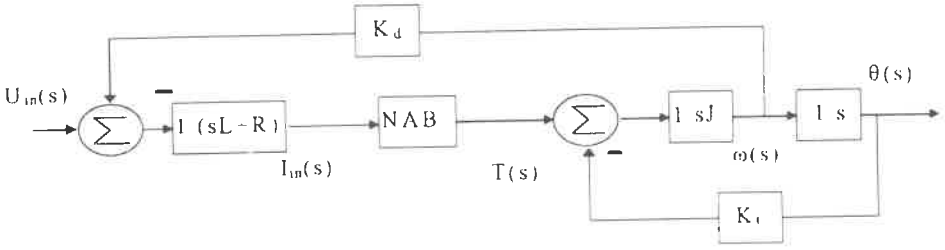

fig.3 block diagram representation of the tracking mirror

After the transfer function is confirmed by the actual open-loop magnitude and phase Bode plot. a close loop control system is designed as shown in Figure 4. where preset position P(s) determined by the ducell detector drives the tracking mirror system and R(s) is PD controller in order to achieve high dynamic response speed.

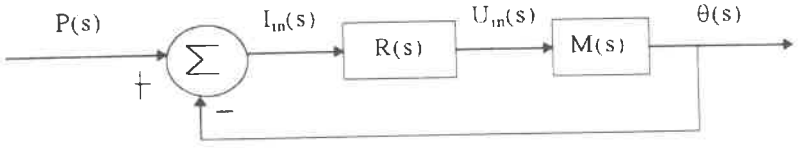

fig.4 block diagram representation of the close-loop tracking mirror system

3.3 the electronic circuit of the servo control system

The mirror control circuit includes the following parts: position sensing processor. amplifier/correction. triangle wave generator. tracking/scanning mode controller. power amplifier. power supply. (fig.5)

If the laser beam is interrupted by some disturbing objects in the measurement area. the rotatable mirror can no longer track the object. The scanning mode is used to regain laser beam contact with the retroreflector [4]. If the photocurrent of the two cells are both low (no laser beam reaches on the ducell surface). the multiplexer will switch to the triangle wave generator and the output of multiplexer goes to the power amplifier to drive the rotatable mirror. Once one of the two cells put out high photocurrent. the multiplexer will switch to PD controller and the mirror restore its tracking status.

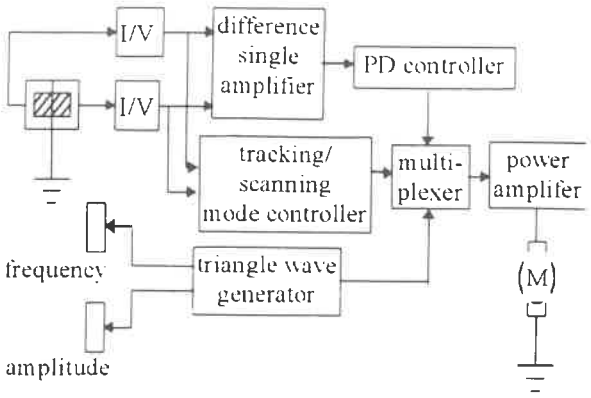

fig.5 the mirror control circuit

4 Experiments and Conclusion

The target retroreflector moved by a CMM has been tracked by the new tracking mirror system. Figure 6 shows the waveform of the control voltage fed on the tracking mirror coil during the tracking status. The waveform change shows the feedback voltage to suppress the interference produce by CMM and other factors. Experiments have proved that the system can track continuously and rapidly the target retroreflector located 400mm away from the tracking mirror with speed 5m/s and acceleration 10m/s^2. By using several such new tracking interferometers, multi-beam laser tracking interferometer system for two dimensional coordinate measurement has been established. The readings of the interferometers have been stored and processed by a computer and the 2D coordinate values of the object can be given.

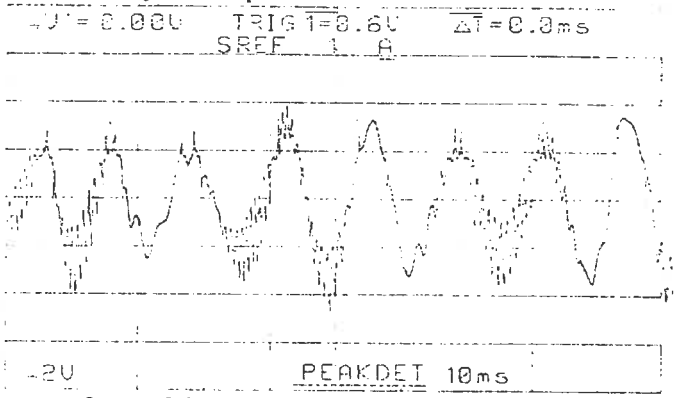

fig.6 the waveform of the tracking mirror coil during the tracking status

References

1. K. Lau, R.J. Hocken, W.C. Haight , "Automatic laser tracking interferometer system for robot metrology" . Precision Engineering, 1986, 8(1):3-8

2. Osamu Nakamura, Mitsuo Goto, "Four-beam laser interferometry for three-dimensional microscopic coordinate measurement", Applied Optics, 1994, 33(1):31-36

3. Fu Jiyou, "Multi-beam Laser Tracking Interferometer System for Flexible Coordinate Measurement", Ph.D. thesis, Tianjin University, China, June, 1997

4. Theo A.G.Heeren, Frans E.Veldpaus, An optical system to measure the end effector position for on-line control purpose, Int. J. Robotics Res., 11(1):53-63, 1992

FORM ERROR ASSESSMENT: ERROR SEPARATION METHOD FOR THE CALIBRATION OF FREE-FORM SURFACES BY MEANS OF COORDINATE MEASURING MACHINES

D. Feautrier, P. Bourdet
LURPA, Ecole Normale Supérieure de Cachan
61, av du Pdt Wilson 94235 CACHAN CEDEX FRANCE

Abstract:

The calibration of free-form surfaces by means of Coordinate Measuring Machines requires the use of high accuracy devices. The problem is that the accuracy of today's CMMs is of the same order as the form errors of the surface of the artifact to calibrate. It is then impossible to ensure that a calibration is accurate enough. We propose a contribution to this problem by establishing a general method that is relevant for all types of surfaces and allows to separate the errors of a CMM from the error of a free-form surface. It is based both on a strategy equivalent to a multi-reversal of the artifact and on a numerical method for the identification of the surface of the artifact.

Keywords: error separation, free-form, CMM, calibration

1. Introduction

The problem of free-form surfaces identification is not new. Our concern is the measurement of free-form standards by means of coordinate measuring machines (CMM). The complexity of such a problem comes from a simple thing. We want to measure a part, the form errors of which are of the same order as the form errors of the device used to calibrate it. As one of today's key issues is to reduce the uncertainties arising at each level of the «chevron of traceability», reversal techniques, by their ability to separate errors, seem useful to help us solve our problem. The method we are proposing generalizes the concept of error separation. As a result, it allows to improve the calculation of form errors of complex surfaces. We performed experiments in order to test our theory. The results are given in the last section of this paper and the discussion is open concerning the possible improvements.

2. Dimensional measurements, error compensation and separation: state of the art

In general, the analysis of form errors of a surface with respect to a reference surface, starts with the analysis of the errors of the measuring device [1] used to perform the measurement. For the time being, error compensation methods are as numerous as different though their initial goal is the same. In order to develop new methods, and to clarify the terms used to qualify the existing methods, a state of the art was made by S. Sartori and G.X. Zhang [2]. In general, the problem can be summarized as follows: How can the function allowing to transfer curvilinear coordinates of points given by the CMM to the true coordinates be established in a cartesian reference system ? To solve this problem, two types of techniques exist, i.e. calibration and self-calibration techniques. Calibration techniques consist in the direct comparison of distances measured on artifacts by means of CMMs, with the same distances calibrated by standard organizations. Self-calibration techniques consist in the comparison of measurements made on an un-calibrated artifact in several locations of the working volume of a CMM. Then, one has to verify the consistency of the measurements and check wether the calibration is still correct. In both cases, each measurement is used to figure out the desired component of the machine errors at discrete locations of the working volume in accordance with the error model chosen. In the case of a solid modeling of the CMM, it generally takes into account 18 geometrical error functions. Even though they have proved their efficiency, their cost and time of experimentation make those methods difficult to implement. This is why between the two types of techniques, we have interested ourselves into self-calibration techniques since the calibration of the artifacts is not required. A state of the art as well as a proposition of classification of these techniques were made by C.J. Evans [3]. These techniques are generally based on the change of sign or on the shifting of one of the sources of error between two measurements. By means of simple equation systems modeling the measurement recordings, the error separation is possible. Nevertheless, all error separation techniques are not equivalent since they give either a full or a partial knowledge on both the instrument and the artifact or only a knowledge on one of the two errors.

We want to measure and determine the shape of free-forms by means of a coordinate measuring machine (CMM). As we show later in more details, this problem is a lot more difficult than the straightedge reversal for obvious reasons, the first of which is that CMMs are composed of three theoretically perpendicular linear axes. Nevertheless, we use, in our method, a local modeling of the errors close from for the one used for the straight edge reversal or the three flat test.

3. Proposed method

3.1. Assumptions

The theory actually relies on the following hypothesis. Consider that both the part and the machine temperature and humidity are stabilized enough to meet standards requirements. It implies that we can assume that both the part and the machine geometries are stable with respect to time. Assume now that when the part is moved within the working volume of the CMM, the low increase of its temperature along with the displacement of air in the CMM's room does not change its geometry as well. Nevertheless it is well known that if we measure a part in different positions in the measuring volume, the data sets of points obtained will not be the same with respect to a local reference system. In spite of no external influence but the part's position, the results of the measurements are different when plotted in a 3-D cartesian reference system. Since, according to the above assessment, the part's geometry does not change, the differences between the data sets of points only come from the CMM. The CMM actually acts like a prism that distorts the image of the test part. Suppose it is possible to calculate the global error e_{ij} at a point i of the surface for a position j of the part in the working volume of the CMM. Then suppose we calculate the global error e_{ik} at the same point i of the surface for a position k of the part. The difference $e_{ij} - e_{ik}$ gives the variation of the machine error between those two positions for the same point of the part. By precisely controlling the displacement of the part between all positions, one can in theory make a 3D-mapping of the variation of the machine error within its working volume. We use this concept to separate the machine errors from the part errors. The desired result is at first to get the knowledge of the part errors. The idea of a controlled displacement of the part is used to measure the same points on the surface again and again for each position. It allows to compare coherent (though distorted) data sets of points.

3.2. Experimental technique

The technique developed in the following sections requires to model the errors both locally and globally. The local modeling is used to set the equation system eventually allowing the separation of the errors and the global modeling is used to locate the reference surface with respect to the cloud of points. As for the resolution, we use both models alternatively.

3.2.1 Local modeling

Here we consider each point separately and model the global error along the theoretical normal vector as follows. The global error at each point is the standard output of the measuring of a part. We made the assumption that it is the result of two sources of error defining the respective positions of three surfaces (figure 1).

- e_i , global error due to both the machine and the part error, between a measuring point M_i and its corresponding theoretical point M_{thi} along the normal vector $\vec{n}_i$ of the reference surface,
- e_{pi} , part error resulting from the measurement of a part having errors with respect to its nominal shape, with an **errorless** CMM,
- e_{mi} , machine error resulting from the measurement of the **same** part with a **non-corrected** CMM[1].

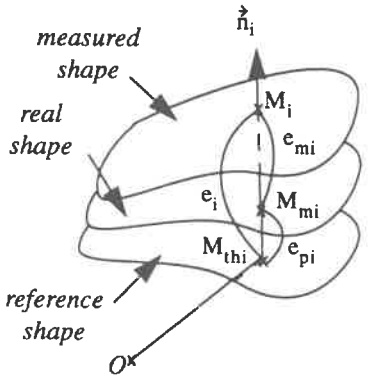

$$e_i = e_{mi} + e_{pi}$$

Fig. 1 Local view of each shape

1. figure 1 results from the **superposing** of two views (the *measured shape* is in reality the same as the *real shape).* The difference is a consequence of the representation in a **unique** cartesian coordinate system of,
coordinates of points acquired with a perfect CMM (*real shape*)
coordinates of the **same** points of the **same** surface (*measured shape*) acquired with a «**curvilinear**» (non-corrected) CMM and plotted in a cartesian coordinate system.

Given a set of errors e_i, for each measured point, our goal is to quantify each error e_{pi} and e_{mi} that represent the contributions of both the errors of the part and the machine respectively to the global measurement errors.

3.2.2 Displacement method

The next step consists in building a system of equations as a function of the errors defined above, i.e. e_i, e_{pi}, e_{mi}. We adopt the following strategy. Let us take the example of a 2D profile (figure 2). For each measured point M_i, we calculate the deviations e_i (the method of calculation lies on the small displacement torsor concept, see next section).

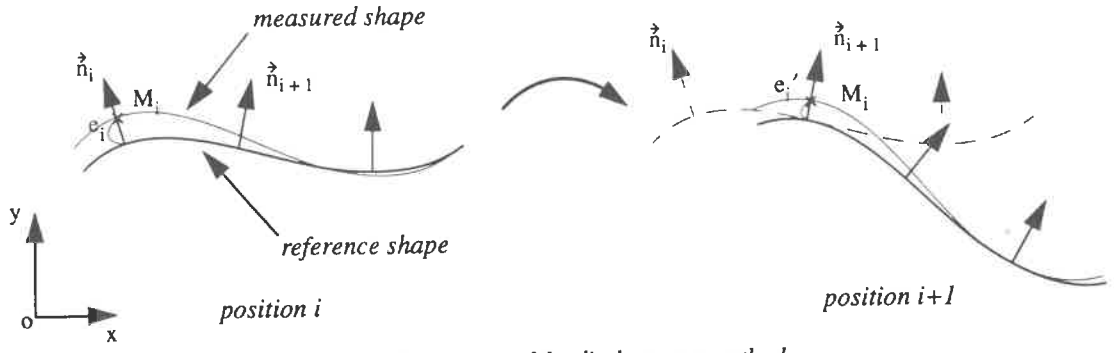

Fig. 2 Illustration of the displacement method

The following linear system is then carried out in accordance with the formalism used in equation 1,

$e_1 = e_{m1} + e_{p1}$ .... (equ. 1)

$e_i = e_{mi} + e_{pi}$ .... (equ. 2)

$e_n = e_{mn} + e_{pn}$ (equ. 3)

This system has n equations and 2n unknowns. At this point, we need to increase the number of equations. We use an external device able to move the part in the (x, y) plane. It is possible to move the part in an other position such that point M_i takes the position that the point M_{i+1} had in the first position in the working volume of the CMM and also such that $\vec{n}_i \sim \vec{n}_{i+1}$, and so on for the other points. For each position we recalculate the optimized deviations with respect to the nominal shape, so that each point participates to the considered errors, each position only giving one new equation of the kind,

$e_i' = e_{mi+1} + e_{pi}$ (equ. 4)

In addition, it is necessary to introduce displacements such that normal vectors are reverted locally (this is why it is a reversal technique) and then we can write equations of the kind,

$e_i'' = e_{mi} - e_{pi}$ (equ. 5)

It is then possible to estimate e_{pi} and e_{mi} for each measuring point by inverting a displacement matrix.

3.2.3 Global modeling

The error of the measured shape with respect with the reference shape is defined by a set of deviations e_i along the theoretical normal vectors $\vec{n}_i$. As a result, the position of the reference with respect to the clouds of measured points has a great importance. We have to find the best-fit location of the reference for each position of the part in the reference system. This problem can be solved by the use of the *small displacements torsor concept* [4]. The SDT concept consists in a multi-step method. A first arbitrary reference surface position allows to calculate a set of initial deviations ζ_i between the cloud of measured points and this initial reference position. Because they take into account an a priori position of the reference surface, these deviations are not optimum. For each considered point, a formula using the torsor tool allows to express the global small displacement to give to the reference surface such that the new calculated deviations e_i are optimum. We optimize the deviations using a least square fitting method because it is generally robust.

4. Experiment set-up and results

To gain time, we carried out our experiments on 2D profiles. To perform them we used a CMM as well as an external device allowing translations in the (x, y) plane and a rotation with respect to the z axis. We did not use correction matrices so that the errors, except for the scale errors, were magnified. None of the point coordinates were compensated, the raw data only were used to run our algorithms. The CMM then had errors of about $7\mu m$ in its working volume. Two simple profiles were used to verify our technique. First of all, we wanted to identify a portion of an ellipse. The shape was designed on a CAD/CAM software and machined by means of our milling center. We then measured a section of the profile using the method we

described in the previous sections. We verified that the error separation was possible, but also that the form errors were of the order of a few hundredths of a millimeter. To make sure that the method worked, we decided to do the same experiment on a roundness standard, a 40 mm ring the theoretical form error of which is less than a micrometer (we checked it on a roundness measuring device (Talyrond)). The ring is first measured in 18 equally spaced points. The measured deviations we then get are far from our objective. The ring is then moved in accordance with the principle describe above. This strategy allowed to separate the part errors from the machine errors several time. Two experimental results are given (see the bold broken lines showing the part error after separation, in Appendix A). Given the repeatability error of our CMM ($\pm 1 \mu m$) the results are satisfying. The results also show that some points have their errors divided by three. In general, points with large errors before separation have the biggest error decrease after separation.

5. Conclusion

Thanks to the experiments, we are able to validate our error separation technique, which allows us to get the form error of free-form surfaces. Nevertheless, in the method, an important assessment was made. We supposed that the scale errors of each axis are the same. The consequence is that proportions change in the same order of magnitude in the three directions, which guarantees a stability of the reference shape used to calculate the deviations in each position of the part. In case the assessment above is not made, we think the knowledge of the absolute scale error of one axis calibrated by an external reference is enough to calculate the relative scale errors of the two other axes. We could then calculate the theoretical deformation of the reference as a function of the location of the part in the working volume of the CMM and eventually correct the final results as well. We also would like to validate the displacement strategy in order to obtain the best information on the errors. From now on, we know that in theory for a given set of n measured points, n + 1 positions of the part are enough to operate the separation. Nevertheless, we know that the choice of the set of positions is not unique. This choice should take into account the minimization of the uncertainties of position of the reference shape and eventually allow to improve the error separation. Finally we are testing the method on more complicated artifacts.

References

1. Soons, J.A., Theuws, F.C., and Schellekens, P.H., Modelling the errors of multi-axis machines: a general methodology, Precision Engineering, Vol. 14, 5-19, 1992
2. Sartori, S. and Zhang, G.X., Geometric error measurement and compensation of machines, Annals of the CIRP, volume 44/2/1995, 617-634, 1995.
3. Evans, C.J., Hocken, R.J., and Estler, W.T., Self-calibration: reversal, redundancy, error separation, and «absolute testing», Annals of the CIRP, volume 45/2/96, 617-634, 1996.
4. Bourdet, P., Mathieu, L., Lartigue, C., and Ballu, A., The concept of the small displacement torsor in metrology, Proceedings of the International Euroconference on Advanced Mathematical Tools in Metrology, 110-122, 1995.

Appendix A: Experimental results

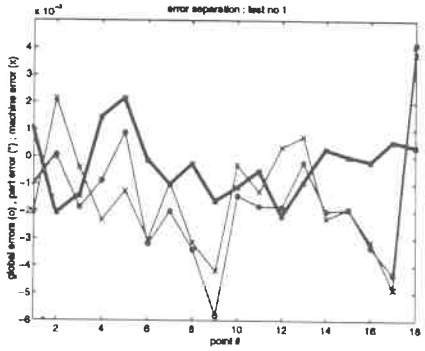

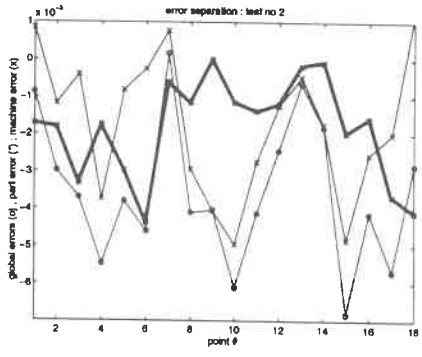

GEOMETRIC FORM EVALUATION OF CONE BASED ON THE MINIMUM ZONE CRITERIA

Hyung Min Kim
Graduate student
Department of Mechanical Engineering and Applied Mechanics
University of Michigan
Ann Arbor MI48109

Byung-Chai Lee
Associate professor
Department of Mechanical Engineering
Korea Advanced Institute of Science and Technology
Taejon Korea 305-701

ISO definition for form tolerances requires the form error of a geometry to be less than some specific limit. Most inspectors measure form tolerances as the minimum zone solution which minimizes the maximum deviations between the measured points and the estimated feature. Current Coordinate Measuring Machines (CMMs) measure the form error based on the least square method, which minimizes the sum of the squared errors between the measured points and the estimated feature, possibly resulting in some overestimations on the errors.
The form evaluation algorithm for the conical geometry developed in this paper computes the minimum zone solution based on the ISO standards, which is inherently a nonlinear optimization problem with local minimums. The developed algorithm consists of two phases. The first phase is to find good initial values for the cone geometry. Disregarding the angular components of the measured data points, 3-D data points are mapped into 2-D data points. From the 2-D points, least square line can be fitted and the tolerance zone with respect to the line can be calculated. Comparing the tolerance zone, the cone axis which has the smallest tolerance zone can be obtained. With these information, initial values for the cone geometric factors can be fixed. The second phase is to search geometric factors for the minimum zone cone with the initial values from the first phase. The problem is formulated as a constrained nonlinear optimization problem, which finds two nearest coaxial cones locating all the measured data points between the two cone, which satisfy the ISO minimum zone criteria. At each phase, the nonlinear constrained optimization problem is solved by the sequential quadratic programming (SQP).
Using the adequate initial values from the first phase of the present algorithm, the minimum zone solution can be efficiently and conveniently obtained. Lots of numerical examples are presented in the paper, which show that this cone evaluation algorithm meets the ISO requirements and that the present algorithm is reliable and efficient for the geometric evaluation of cone.

Key words : cone, minimum zone, least square, ISO

1. Introduction

ISO definitions for form tolerances requires the form error of a geometry to be less than some specific limit for basic geometric shapes such as line in 2-D and 3-D, plane, circle, sphere, cone, etc. According to the ISO definitions for form tolerance, geometric form tolerance is measured as the maximum deviations between measured data points [1]. But most Coordinate Measuring Machine (CMM) measures form tolerance based on the least square method, in which the tolerance is the squared sum of deviations measured from each data point. Using the least square method, for some basic geometries, searching for final geometry can be described by a system of linear equations, for which, direct analytical solutions are possibly obtained [2,4,5]. But for most geometries, to find out final geometric shapes is a nonlinear problem, for which several optimization techniques have been used for the final geometries [2,6,7,8,9,10,11,12,13]. Also, in the least square method, as the deviations are squared, this squared sum can lead to inexact geometric information from the data points.
Based on the minimum zone method, searching for best geometry which describes prescribed geometry exactly from the measured data points can be described as a nonlinear optimization problem in which maximum deviation from the prescribed geometry should be minimized. As the deviations from each data point are Euclidean distances, these deviations are nonlinear and to find out the prescribed geometry is quite a nonlinear process also. This process can be described by the following nonlinear optimization problem, in which the maximum deviation is the objective function.

$$\min\left\{\left|(deviation)_{\max}\right|+\left|(deviation)_{\min}\right|\right\}$$

subject to

$$(deviation)_i \le (deviation)_{\max}$$

$$(deviation)_i \ge (deviation)_{\min}$$

For the cone geometry, there were some researches to find out best cone geometry based on the least square method [3,16,17,18], but there were quite few researches based on the minimum zone method because of its nonlinearity and complexity of the geometry compared to other basic geometries.

In this paper, based on the ISO minimum zone method, overall formulation as a constrained optimization problem to find out cone geometry from the measured data points is presented and to obtain robustness of the algorithm, fixing initial values for the geometric factors in a systematic way also presented. For the efficiency of the algorithm in case of large number of measured data points, data reduction scheme is also developed. Suggested nonlinear optimization problem was solved by the Sequential Quadratic Programming (SQP).

2. Formulation

Cone can be represented by the following equations (Figure 1) [14,15].

$$C: D \subset R^6 \rightarrow P(R^3)$$

$$C(l_3, m_3, x_0, y_0, \phi, t_0) = \left\{\mathbf{x}: \cos\phi \left\| (\mathbf{x}-\mathbf{x_0}) \times \mathbf{a} \right\| + \sin\phi (\mathbf{a}(\mathbf{x}-\mathbf{x_0})^{\mathrm{T}}) - t_0 = 0 \right\}$$

$$x(\theta, t) = (r_0 - t\tan\phi)\cos\theta$$

$$y(\theta, t) = (r_0 - t\tan\phi)\sin\theta$$

$$z(\theta, t) = t$$

For the cone shape, the minimum number of geometric elements is six, which are $l_3, m_3, x_0, y_0, \phi, t_0$.

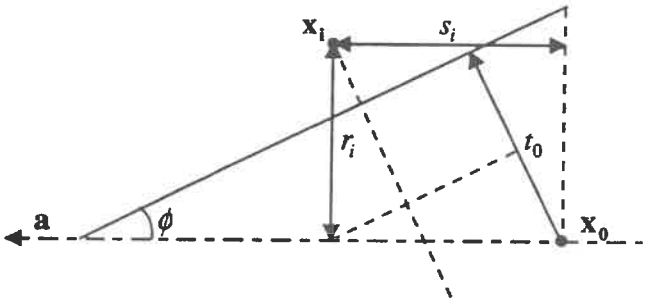

Figure 1 Parametrization of cone

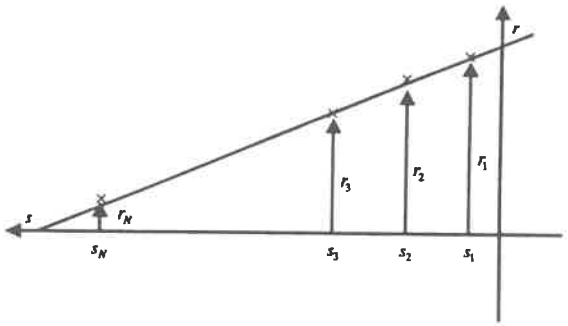

Figure 2 Mapping 3-D distance into 2-D distance

The deviation of a point from the cone surface can be formulated as follows.

$$d = r\cos\phi + s\sin\phi - t_0$$

From the parameters above and definition of deviation, the objective function based on the minimum zone criteria is as follows.

$$f(x_0, y_0, l_3, m_3, \phi, t_0) = \left|\max d_i\right| + \left|\min d_i\right| \quad i = 1,2,...,N$$

Also, objective function based on the least square criteria is as follows.

$$f(x_0, y_0, l_3, m_3, \phi, t_0) = \sum_{i=1}^{N} d_i^2 \qquad i = 1,2,...,N$$

Here, N is the number of data points.

3. Form evaluation algorithm

Form evaluation algorithm of cone can be divided into two part; the first part is to fix initial values for the geometric elements of the cone shape and the second part is to find out final optimal cone shape with the initial values from the first step, which is to solve a nonlinear constrained optimization problem. Because of the nonlinearity of the formulation, when solving the optimization problem, initial start points for the design variables can be important in

view of the local convergence property. In the first part, systematic way of finding out initial values would increase the robustness of the algorithm.

- *Part one : Fixing initial values for the cone geometric factors*

1) Calculate center of the data points and shift all the data as follows.

$$(X_i - \Delta X, Y_i - \Delta Y, Z_i - \Delta Z)$$

Here, though there can be some variations depending on data, the shifting amounts are as follows.

$$(\Delta X, \Delta Y, \Delta Z) = (XCENTER, YCENTER, ZMIN)$$

2) Calculate distances from the center axis and the base plane with respect to all the data points and map these two values into 2-D plane (Figure 2).

3) Find out least square line for the two variables in 2). If the 2-D line is $r = as + c$, in which r and s are the distances from the center axis and the base plane, a and c are as follows [2].

$$a = (N\sum s_i r_i - \sum s_i \sum r_i) / [N\sum s_i{}^2 - (\sum s_i)^2]$$

$$c = (\sum r_i - a\sum s_i) / N$$

4) Fix initial values for the geometric factors from the slope and origin information from the above line.

- *Part two : Getting final cone shape from the constrained optimization formulation*

The concept of this part is to find out nearest possible two concentric cones, between which all the data points are located.

1) Based on the 2-D line from the first part, sort all the data points according to the activeness of the data point.
2) Discard redundant data points which are in the middle of the tolerance zone, i.e. less active.
3) With the initial values from the part one, solve the nonlinear constrained optimization problem.

4. Test results

In addition to the measured data from a commercial coordinate measuring machine, lots of artificial data were generated by the following equations with some tolerances.

$$x(\theta, s) = (r_0 - s\tan\phi)\cos\theta = (t_0 \sec\phi - s\tan\phi)\cos\theta$$

$$y(\theta, s) = (r_0 - s\tan\phi)\sin\theta = (t_0 \sec\phi - s\tan\phi)\sin\theta$$

$$z(\theta, s) = s$$

Current algorithm is validated with least square method for the same data sets. The first part of the algorithm was implemented in the least square method also for the comparison of the conicity which can be defined as follows.

$$(conicity) = h_t = \left|(e_i)_{\max}\right| + \left|(e_i)_{\min}\right|$$

Table 1 Deviations evaluated by commercial S/W and present algorithm

Data sets	Deviations	
	commercial S/W (D_c)	Present algorithm (D_p)
1	0.0396	0.0388
2	0.1090	0.0870
3	0.2328	0.1866
4	0.2489	0.1918
5	0.4045	0.3451

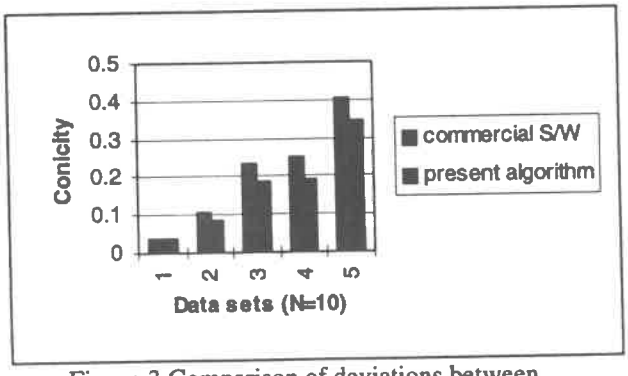

Figure 3 Comparison of deviations between commercial S/W and present algorithm

5. Conclusion

Geometric form evaluation algorithm for 3-D cone was presented. The algorithm meets ISO criteria which requires minimum tolerance zone for the measured data. In the first part of the algorithm, new algorithm to determine initial values of the geometric factors for the next step was introduced. Constrained optimization formulation to determine 3-D cone shape from the initial values was presented also. Lots of number of data sets were validated for the robustness of the algorithm based on the conicity, which is the minimum tolerance zone.

Table 2 Deviations evaluated by Least Square method and Minimum Zone method (present)

Number of data points	Deviations	
	Least square (D_{LS})	Present algorithm (D_{MZ})
6	0.106	0.006
10	0.252	0.204
20	0.733	0.636
30	1.006	0.740
40	0.823	0.739
50	0.759	0.559
60	0.865	0.691
70	0.754	0.566
80	0.843	0.787
90	1.381	0.761
100	1.044	0.895
120	0.925	0.639
140	0.926	0.557
160	1.377	0.831
180	0.982	0.244
200	0.974	0.309

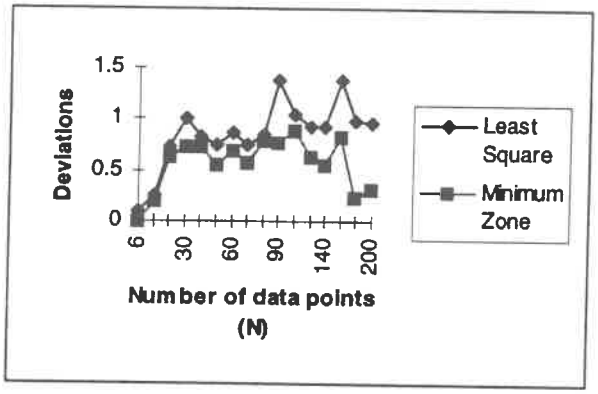

Figure 4 Comparison of deviations between the least square algorithm and present algorithm

References

[1] ISO, Technical Drawings - Geometrical Tolerancing - Tolerancing of Form, Orientation, Location and Run-out - Generalities, Definitions, Symbols, Indications on Drawing, *International Standard Organization*, 1983, ISO 1101-1983(E)

[2] T. Murthy and S. Abdin, Minimum Zone Evaluation of Surfaces, *Int. J. Mach. Tool Des. Res.* , 1980, vol.20, pp.123-136

[3] A.B.Forbes, Least-Squares Best-Fit Geometric Elements, *NPL Report DITC 140/89*, pp.16-28

[4] N.-H.Kim and S.-W.Kim, Geometrical Tolerances : Improved linear approximation of least squares evaluation of circularity by minimum variance, *Int. J. Mach. Tools Manufact*, 1996., vol. 36, No.3, pp.355-366

[5] N.-H.Kim, Evaluation of form tolerances by normal least squares, 1996, *KAIST Ph.D. dissertation*

[6] D.G.Chetwynd, Applications of Linear Programming to Engineering Metrology, *Proc. Instn. Mech. Engrs.* , 1985 , vol.199 No.B2, pp.93-100

[7] M.S.Shunmugam, Comparison of Linear and Normal Deviations of Forms of Engineering Surfaces, *Precision Engineering*, 1987, vol.9, No.2, April, pp.96-102

[8] P.Dhanish and M.Shunmugam, An algorithm for form error evaluation - using the theory of discrete and linear Chebyshev appriximation, *Computer Methods in Applied Mech. and Engng.* , 1991, vol.92, pp. 309-324

[9] T.Kanada and S.Suzuki, Evaluation of minimum zone flatness by means of nonlinear optimization techniques and its verification, *Precision Engineering*, 1993, vol. 15, pp. 93-99

[10] K.Carr and P.Ferreira, Verification of form tolerances Part I : Basic issues, flatness, and straightness, *Precision Engineering*, 1995, vol. 17, pp. 131-143

[11] K.Carr and P.Ferreira, Verification of form tolerances Part II : Cylindricity and straightness of a median line, *Precision Engineering*, 1995, vol. 17, pp. 144-156

[12] S.Huang, et al, A new minimum zone method for evaluating straightness errors, *Precision Engineering*, 1993, vol. 15, pp. 158-165

[13] J.-Y.Lai and I.-H.Chen, Minimum zone evaluation of circles and cylinders, *Int. J. Mach. Tools Manufact.* , 1996, vol. 36, No. 4, pp.435-451

[14] G.T.Anthony, et al, Chebyshev best-fit geometric elements, *NPL report DITC 221/93*

[15] G.T.Anthony et al, Parametrization of Geometric Form Part III and IV: theory and calculations, *National Physical Laboratory*, EUR 13517EN, pp.1-53

[16] T.Tsukada, et al, A new technique for evaluating conical taper form errors, *Bull. Japan Soc. Prec. Engng.* , 1988, vol.22, No. 1, pp.32-36

[17] T.Tsukada, et al, A verification technique of minimum zone conical taper form, *Bull. Japan Soc. Prec. Engng.* , 1988, vol.22, No.3, pp. 211-215

[18] T.Tsukada, et al, Method for evaluation of form errors of conical tapered parts, *Precision Engineering*, 1988, vol. 10, No.1, pp.8-12

Applications of Surface Normal Measurements to Coordinate Metrology

Robert Edgeworth and Robert G. Wilhelm
Center for Precision Metrology
Department of Mechanical Engineering and Engineering Science
The University of North Carolina at Charlotte
9201 University City Blvd., Charlotte, NC 28223-0001

Introduction

Surface normal measurements have been available with scanning Coordinate Measuring Machines since the 1970s. Recent publications indicate that touch trigger probes which are capable of accurately measuring surface normals will be available commercially in the short term. This paper discusses uses of surface normal data to enhance and extend the capabilities of point probing Coordinate Measurement Systems. Measurement repeatability and probing speeds can be increased for point probing systems by using an analog probe. The reliability of measurements using CMMs can be improved by probing error detection such as might occur when the measurement surface is obscured by dirt or burrs. Computational reliability can be increased by including surface normal data in fitting algorithms. We will discuss the benefits of surface normal measurements to the evaluation of functional surfaces. The time required to reverse engineering parts can be decreased by applying automatic feature recognition. Finally the uncertainty of surface evaluation can be controlled through the use of adaptive sampling.

Probing Error Detection

A probe which collects both point and surface normal information effectively doubles the information content of each CMM sample. We can apply this extra information to detect and reject erroneous measurements due to burrs, dirt or contact with adjacent surfaces. By comparing the reported surface normal with the nominal surface normal for each inspection point test for large deviations and reject potentially spurious data points. In this manner we can sharply constrain the shape and location of objects that will interfere with the measurement process. This method would be particularly effective in identifying obstructions that lie outside of the plane, such as is the case with burrs (Figure 1). For measurement of intricate parts with small surfaces such as cutting tools, the surface normal measurement could be used to recognize the surface contacted by the touch probe. This data could be then used to drive subsequent probing operations to ensure that all surfaces of interest are measured. Such a measurement technique could be of particular use in locating the trailing edges of airfoils.

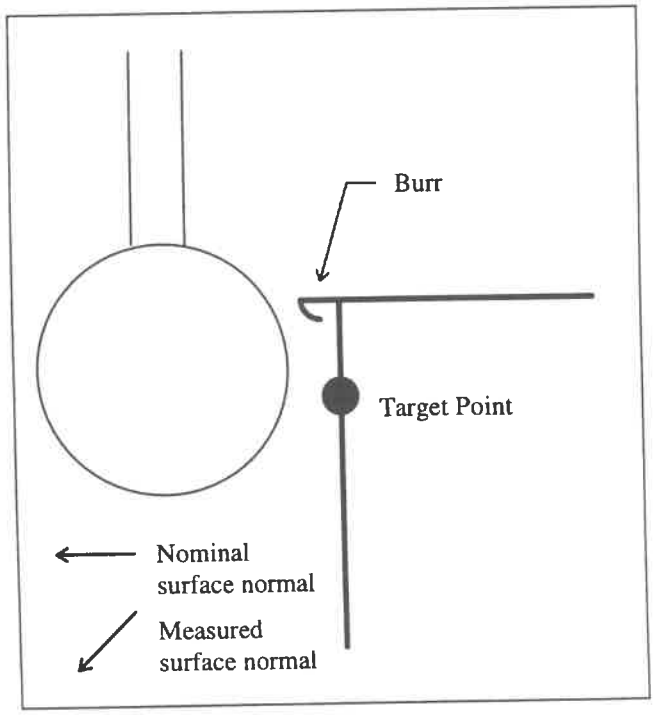

Figure 1: Detection of probing error using testing of surface normals

Reverse Engineering

Aoyama et. Al. [1, 2] has shown that surface normal data can be used to automate recognition of prismatic features such as planes, cylinders, spheres, and toroids. As well, he shows how surface patches can be generated using points and surface normals to reverse engineer sculptured surfaces. These features could be used to develop a product which would allow the online development of a solid model from a physical part with minimal operator intervention. The feature recognition capabilities can also be used to streamline the manual CMM measurement process by automatically computing fits of prismatic features.

Functional Surface Evaluation

Functional surfaces, such as airfoils for turbine engines or blades for ship propellers are quite difficult to measure in a manner that provides meaningful feedback regarding conformance of the part to design intent. Ye, et. Al. [3] note that "*physical constraints for functional surface design frequently involve only surface normals*". This is a direct result of the fact that the momentum transfer between the medium and surface is proportional to the cross product of the fluid velocity vector and the surface normal vector. Measuring the manufactured surface normals would allow the part conformance to the original design intent be directly evaluated. Furthermore, a more direct relation between part measurements and performance could be established, allowing improvements to the cost and efficiency of these sculptured surfaces. At present, there are no standards for specifying surface normals or directly applying tolerances, so there is considerable work which would need to be done to consistently apply this methodology.

Robust Fitting

Computing least squares fits using surface normal as well as point data would allow fits to be computed with fewer samples than the minimum required with only point data, due to the extra information content available. In the presence of form errors, it was shown [4] that substitute geometry parameters found using surface normal data would produce identical results to point based least-squares fits with the exception of cases where the least-squares fit produced degenerate results. When the point based least-squares fit calculation produced degenerate results, the surface normal fit would generate results that was either significantly better or worse than the point based fit. By using both types of fits users could identify cases of degenerate fit calculations that cannot otherwise be identified and take corrective action to prevent erroneous results to be accepted.

Adaptive Sampling

The deviation from the nominal surface normal direction at a point gives an indication of the local position errors about that point. The difference between the measured and nominal surface normal at each point is literally the rate of change of position error at the point. Combining the position and surface normal errors for pairs of points allows us to develop a cubic polynomial estimating the position error between the samples. The uncertainty of this estimate is dependent upon the measurement uncertainty of the point and surface normal results and increases linearly with the distance between samples.

If we initially sample a surface at the boundaries of the region of interest we can use this interpolation process to identify areas that have large deviations and command the measuring machine to sample these regions. A new prediction of the surface errors is then developed in the form of a cubic spline. The resampling process is repeated in a iterative fashion until the stopping criteria are satisfied [5]. Figure 2 shows how the use of an interpolating curve fitted with surface normal and position data at pairs of measurement points can be used to determine the location of subsequent sampling positions required to produce a complete evaluation of a surface. The solid lines indicate the true form of the surface being measured, as taken from an exhaustive measurement of the feature using UNCC's metrology facilities. The dashed lines show the interpolation model's estimation of the surfaces errors, based upon the information available at the sampling points represented by squares. As the deviation between the lines decreases, the

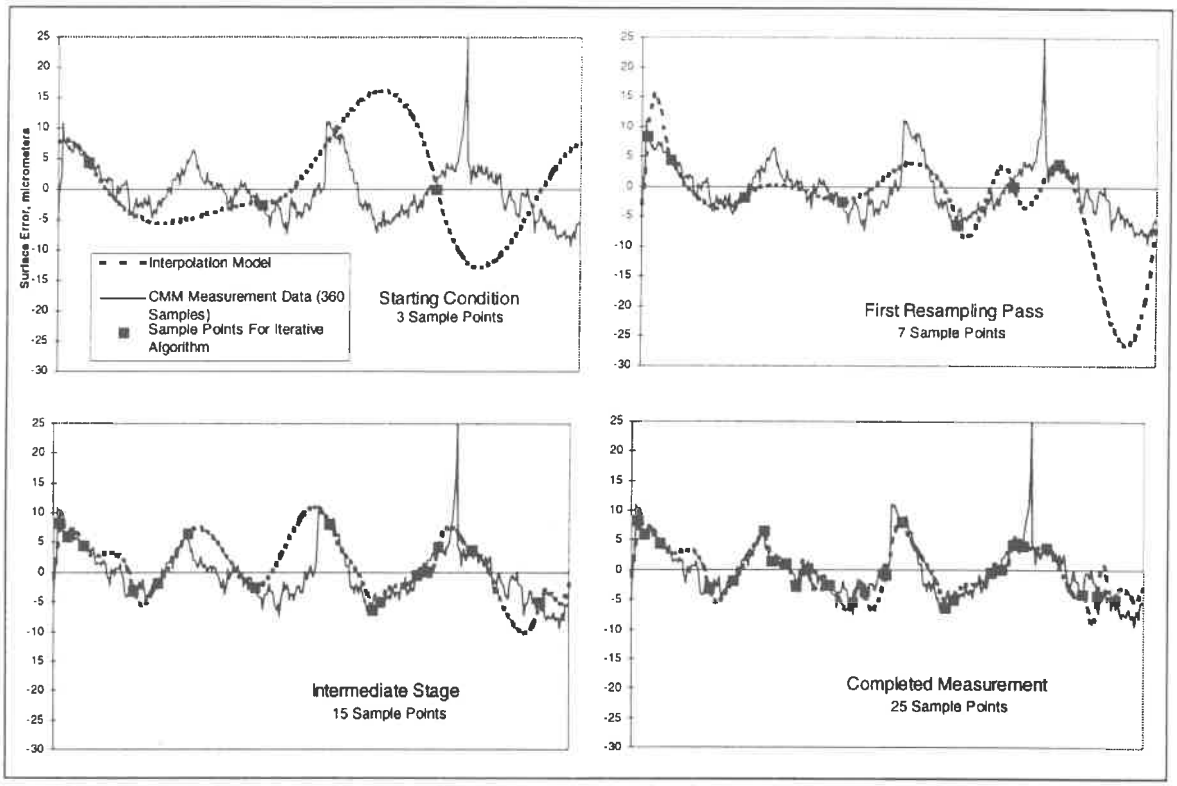

Figure 2: Convergence of the adaptive sampling process to an extensive 360 point measurement with only 25 samples.

quality of the measurement increases. The algorithm selects successive measurement points based upon the magnitude of the errors predicted by the interpolating curve. The figure shows how the accuracy of the measurement increases with each iteration of the measurement process, until the stopping criteria is finally satisfied.

This adaptive sampling process can be applied to any part geometry, is manufacturing process independent and requires no operator intervention. Since measurement time is minimized for conforming parts the cost of inspection over a part life cycle will be optimized.

Improved Repeatability and Increased Probing Speed

Using an analog probe head it is possible to improve the repeatability of single point measurements by holding the probe head stationary and averaging the reported values from the probe head and machine scales over a brief period of time [6]. This technique can be further improved by recognizing that the dominant type of errors that will be removed are dynamic errors of the machine and that these errors can be modeled as a damped simple harmonic motion. Instead of sampling over a constant time frame and averaging, which can give skewed results for harmonic motions, we sample at a rate much faster than the highest natural frequency of the measuring machine until either a known multiple of oscillations have passed or the amplitude of vibration drops below a threshold value. In this manner, maximum reduction of dynamic effects are produced in a minimum time regardless of the probe configuration, probing direction, probe position in the measuring volume and other factors which affect the natural frequency of the measurement system.

Sampling in this manner would require more time than standard touch trigger probing. Since the dynamic behavior of the machine would no longer be critical to measurement accuracy, the extra sampling time

could be compensated for by increasing the machine velocity during the probing stage. Instead of driving very slowly for a short period of time to allow the machine to stabilize, probing could be performed at the maximum speed which would allow the machine to decelerate to a stop while still within the linear range of the probe head. Consider a machine with a dynamic probe range of 0.5 mm and deceleration capability of 0.1 g (0.98 m/s^2). A probing approach speed of 31 mm/s would be possible, almost 4 times the typical probing speed of 8 mm/s. It is likely that a machine configured to operate in this manner could sample at a sustained rate of 4-5 points per second.

Conclusions

Our investigations have shown that surface normal data could be used to enhance and extend the capabilities of coordinate measuring machines in a wide variety of ways. At present, surface normal measurement capabilities are only available on machines that are designed to scan surfaces by keeping the probe stylus in constant contact with a part while moving along a predetermined path. These machines are quite expensive, typically 2-5 times the cost of a similarly sized point probing coordinate measuring machine. Most of the extra cost of scanning machines is a result of the stiffness and control requirements necessary to scan accurately. There are commercially available contact probes which can generate surface normal measurements that could be mounted on a point probing coordinate measuring machine for less than ten thousand dollars. It is clear to the authors that a point probing CMM configured to measure surface normals would greatly enhance the capabilities of coordinate measuring machines while adding very little extra cost to the users of the machines.

Acknowledgments

This work has benefited greatly from the exceptional research environment provided by the Precision Engineering Laboratory at The University of North Carolina at Charlotte and the Cameron Center for Applied Research. This material is based upon work supported by the National Science Foundation under Grant No. DMI-9457168 and by the University Research Associates Fellowship program at UNC Charlotte.

References

1. Aoyama, H. and Kishinami, T. "A Proposition of and Interpolation Form Defined by Position Vectors and Unit Normal Vectors", International Journal Japan Society of Precision Engineering, 25, 3, (1991), 239 - 241.
2. Aoyama, H. and Inasaki, I., "Surface Classification and Model Construction Based on Processing Position Vectors and Unit Normal Vectors", Transactions of NAMRI/SME, 24, (1996), 211 - 216
3. Ye, X., Jackson, T. R. and Patrikalakis, N. M., "Geometric Design of Functional Surfaces", Computer Aided Design, 28, 9, 741 - 752
4. Edgeworth, R. And Wilhelm, R. G., "Substitute Geometry from Position and Surface Normal Information", 1996 ASPE Proceedings, 229 - 232
5. Edgeworth, R. And Wilhelm, R. G., "An Iterative Approach to Profile Evaluation using Interpolation of Measured Positions and Surface Normals", Fifth International CIRP Seminar on Computer Aided Tolerancing, 1997, 253-264
6. Renishaw plc, SP600M Analogue Measurement Probe Beta Site Installation and Integration Guide, 1994

APPLICATION OF A PROBE PRETRAVEL MODEL IN CMM MEASUREMENTS

Yin-Lin Shen, Sungho Moon
George Washington University
Washington, DC

Introduction

This paper discusses the practicality issues of implementing a pretravel model for kinematic touch trigger probes with straight styli on coordinate measuring machines (CMMs). Typical kinematic touch trigger probes include Renishaw TP2-5 way and TP6 probes. Pretravel, mainly caused by bending deflection of the stylus, accounts for the majority of probe errors. Pretravel errors are highly repeatable but can be adversely influenced by force variations encountered in different probe approach directions [1,2]. A pretravel model based on the derivation of the trigger force (probing force at the triggering instant) has been developed [3,4]. It has been shown that only sparse probing data (e.g., 30 points) are needed to accurately identify the key model parameters so the model can be used to correct pretravel errors in CMM measurements using vertically-oriented probes with straight styli. The model has also been extended to non-vertical probe orientations when indexable probe heads are used on CMMs [5].

The trigger force model includes six trigger force equations (in six azimuthal regions) and one of the six trigger forces, for $-60°<\phi-\phi_0<0°$ in vertical probe orientation, is shown as follows [3,4]

$$F_p = \frac{F_s + W - 6F_t \sin\alpha}{(\cos\theta + 2\frac{L}{T}\sin\theta\cos\phi) - 2\sin\theta\sin\phi\tan\alpha} \tag{1}$$

where F_p: trigger force, F_s: spring force setting, F_t: threshold force level, W: weight of stylus structure, ϕ_0: tripod phase angle, α: kinematic support angle, T: tripod leg size, L: stylus extension length, ϕ and θ are azimuthal and polar angles representing the probe approach direction. Treating the stylus as a cantilevered beam, the magnitude of the projection of the 3D pretravel vector along the trigger force direction can be described as

$$\delta_{pt} = \frac{F_p(\sin\theta)^2 L^3}{3EI} \tag{2}$$

where δ_{pt}: model predicted pretravel, E: modulus of elasticity of the stylus shat material, and I: moment of inertia of the stylus shaft. We use r_e (effective radius of stylus shaft) to represent the effect of I, where $I=\pi r_e^4/4$). Equations 1 and 2 constitute the pretravel model for vertically-oriented probes with straight styli.

One of the six trigger force equations in the general case (including vertical and non-vertical orientations of probes with straight styli) is shown as follows

$$F_p = \frac{F_s + W\cos\theta_w - 6F_t\sin\alpha - W\sin\theta_w(2\frac{L_w}{T}\cos\phi_w - 2\tan\alpha\sin\phi_w)}{(\cos\theta + 2\frac{L}{T}\sin\theta\cos\phi) - 2\tan\alpha\sin\theta\sin\phi} \tag{3}$$

where θ_w: probe orientation, L_w: center of gravity of the stylus structure, and ϕ_w: tripod phase angle defined in general case (known after ϕ_0 in vertical case is identified). Pretravel model in general orientation can be derived by using this trigger force model and the cantilever beam treatment.

One key issue is: Can we use the model parameters identified in vertical orientation to predict pretravels in general orientation? If the answer is yes, then we can predict pretravels in arbitrarily-oriented touch trigger probes with straight styli with only 30 points in vertical case. This would be a cost-effective approach to implement the pretravel model. Another key issue is: Is it reasonable to assume that all parameter values, except ϕ_0 and r_e, are known? (For example, can users measure F_s accurately?) We also implement the vertical model using a nonlinear optimization approach. These issues have been investigated and the results and findings are reported in this paper.

Experimental probe pretravel in various probe orientations

Figure 1 shows the pretravel behavior associated with three probe orientations: (a) 0° (vertical orientation), (b) 45°, and (c) 90° (horizontal orientation). The data in these experiments were obtained using a TP2-5way probe with a 50 mm stylus extension and a 6 mm diameter stylus ball sampling a 10 mm diameter test ball (reference ball). In each case the mean and standard deviation (sd) of probe pretravel at 311 positions over 10 repetitions have been shown, representing the deterministic pretravel and the repeatability of the probe performance. The 311-point sampling strategy in the three probe orientations are also shown in Figure 1. In this paper, the averaged pretravel is used in testing the effectiveness of the pretravel model in that the model accounts for the systematic behavior but not the

repeatability errors. The test ball center used in calculating the pretravels is not the sphere fit of the 311 points. The common practice is to fit the 311 probing points to a sphere so the center of the test ball can be calculated. This practice does not reveal the correct test ball center and thus an incorrect pretravel behavior is obtained. It has been found that the actual test ball center deviate significantly (up to 10 μm in tested cases) from the sphere-fit center [6]. A synthesized data approach has been used to find the test ball center in preparing the plots in Figure 1.

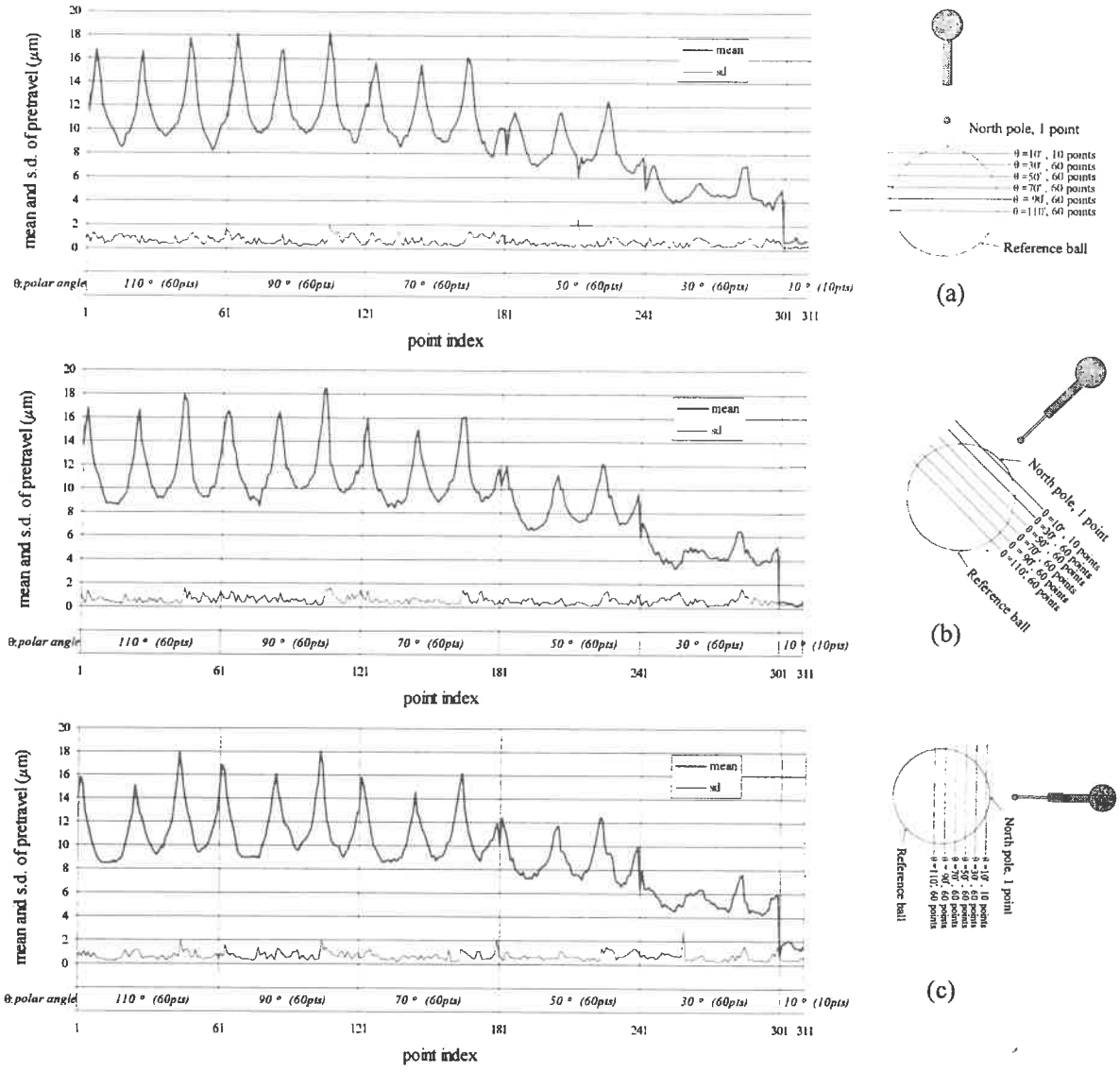

Figure 1. Mean and standard deviation of pretravel with probe orientation at 0°, 45°, and 90°

The cost-effective approach

Figure 2 shows the flowchart of implementing the general case pretravel model by using 30 points of probing data in vertical orientation. Prediction results of vertical case is shown in Figure 3a, r_e=1.30 mm, ϕ_0=10.61°, and the mean and standard deviation of the prediction errors are 0.4 μm and 0.56 μm. The following parameter values have been used in calculating r_e and ϕ_0: F_s=156 gm, F_t=0, W=2.6 gm, L=59 mm (50 mm extension and a 9 mm stub), T=5 mm, α=41°, the test ball radius R_0=5 mm, and E=200 GPa. We then use r_e=1.30 mm, ϕ_0=10.61°, L_w=24 mm, and θ_w=45° or 90° in the general model to predict pretravels in probe orientations at 45° and 90°. Results are shown in Figures 3b and 3c. The standard deviation (sd) of the prediction errors is in the range of 0.6 μm. Ten sets of 30 points of data are used and the results shown in Table 1.

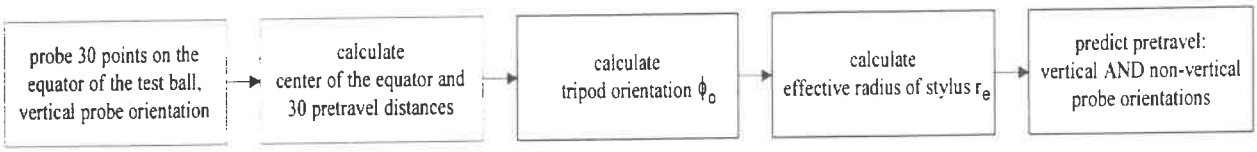
probe 30 points on the equator of the test ball, vertical probe orientation
calculate center of the equator and 30 pretravel distances
calculate tripod orientation ϕ_o
calculate effective radius of stylus r_e
predict pretravel: vertical AND non-vertical probe orientations

Figure 2. Flowchart implementing the cost-effective approach of the pretravel model

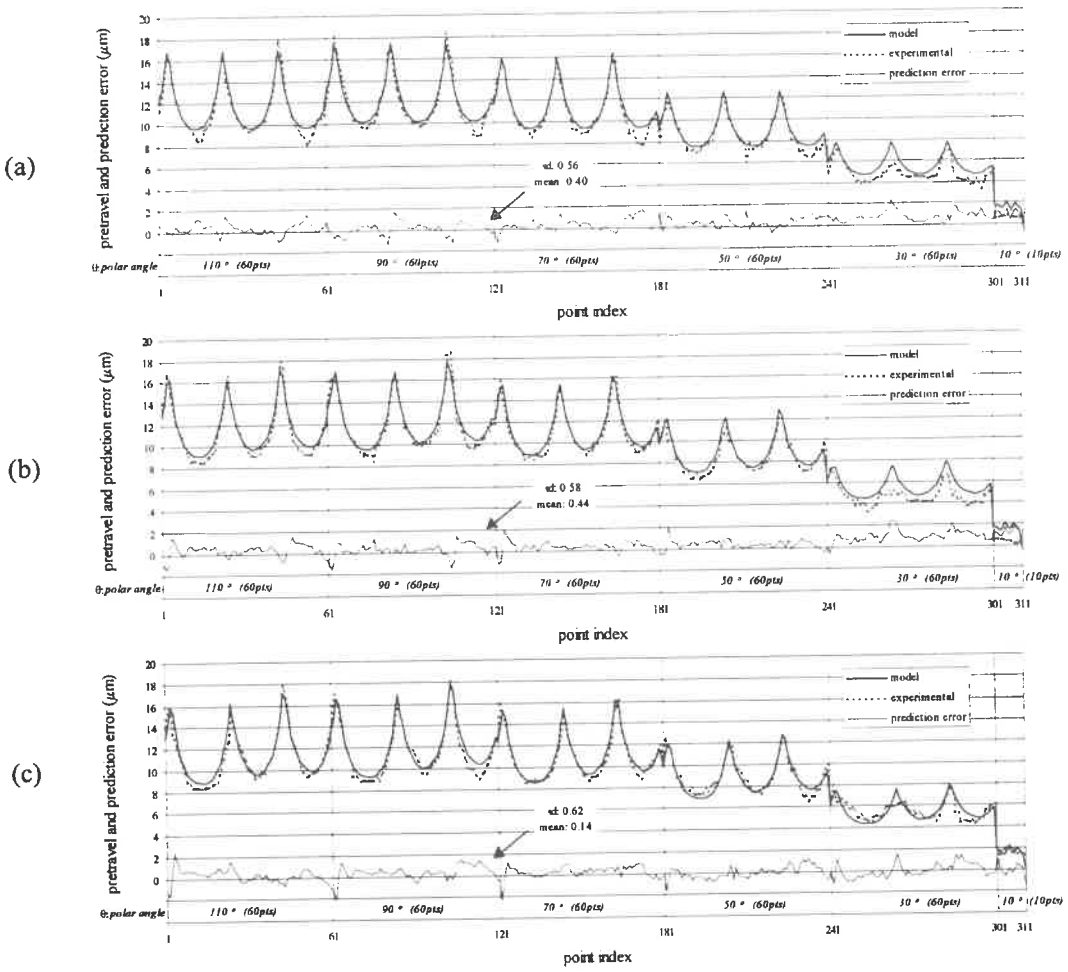

Figure 3. Comparison of model and experimental pretravel at 0°, 45°, and 90° probe orientations

Fs value issue

To measure F_s accurately may be a difficult task. In the previous testing case, an accurate F_s value (156 gm) was used. We repeat the tests by using two inaccurate F_s values: 20% off its actual value, i.e., we use F_s value as 124 gm and 187 gm in the tests. Results are shown in Table 2: r_e values vary according to F_s values. We then use the incorrect r_e and F_s values to predict general case pretravels. The finding is that the model still performs reasonably well in all three orientations, see Table 3. On the other hand, users of the probes usually set F_s by turning an adjustment screw. The F_s value can be determined with a table correlating F_s and the number of turns.

Phase angle issue

It has been shown in Table 1 that the tripod phase angle can be determined with the 30 equatorial data. However, more accurate information on this phase angle can improve the prediction effectiveness of the model because the tiny mismatch between the model and experimental pretravels can be reduced.

Nonlinear optimization approach

We have developed a nonlinear optimization computer program in implementing the pretravel model in vertical

orientation. The hypothesis is: Can we identify F_s, R_0, ϕ_0, r_e, and the test ball center by least-squares fit the model and the experimental data (48 points). We found the F_s and r_e attenuate each other, so F_s value can not be accurately identified with this approach. Actually the optimal F_s value is found to be dependent on the initial guess of F_s. In addition, the test ball center cannot be accurately identified perhaps due to the noise embedded in the data set.

Table 1. Results of model tests from 30 points of probing data (10 tests)

Data set	r_e (mm)	ϕ_o (°)	Standard deviation of prediction error (μm)
1	1.30	10.57	0.56
2	1.30	10.64	0.56
3	1.31	12.78	0.65
4	1.31	12.67	0.60
5	1.30	11.15	0.56
6	1.30	11.62	0.56
7	1.29	11.09	0.54
8	1.29	11.30	0.52
9	1.31	13.53	0.65
10	1.30	12.96	0.59

Table 2. Model parameter r_e with incorrect F_s values

θ_w	F_s (gm)	r_e (mm)
0°	124	1.22
	156	1.30
	187	1.35

Table 3. Results of model tests using incorrect F_s and r_e values

θ_w	F_s (gm)	Standard deviation of prediction error (μm)
0°	124	0.56
	156	0.56
	187	0.56
45°	124	0.56
	156	0.58
	187	0.61
90°	124	0.60
	156	0.62
	187	0.66

Probe approach speed issue

A probe approach speed of 7.5mm/sec was used in the experimental data shown in this paper. We have conducted experiments using various speeds in vertical orientation situation in our lab and the results indicate the pretravel pattern and magnitude are not affected when the speed ranges from 7.5 mm/sec to 15 mm/sec (15 mm/sec is the highest measurement speed recommended by the CMM vendor).

Summary

A number of practicality issues of implementing a pretravel model for kinematic touch trigger probes commonly used on CMMs have been discussed in this paper. It has been shown that only 30 points of probe calibration data in vertical probe orientation can be used to identify the essential model parameters so general-case pretravels can be accurately predicted when such probes are connected to an indexable probe head. We also discussed the parameters needed to implement the cost-effective approach. We are developing and testing pretravel model for kinematic touch trigger probes with offset stylus and we will report the results and findings.

Acknowledgments

This work was supported in part by the National Science Foundation under Grant No. DMII-9624966 and DMII-9308648. We thank Stephen Liebold of the George Washington University for the investigation on the probe approach speed issue. We thank the Computational Metrology Group of the National Institute of Standards and Technology for useful discussions and the experimental data provided by Bruce Borchardt.

References

[1] Butler, C., 1991, An Investigation into the Performance of Probes on Coordinate Measuring Machines, *Industrial Metrology*, Vol. 2, pp. 59-70.

[2] Estler, W.T., Phillips, S.D., Borchardt, B., Hopp, T., Witzgall, C., Levenson, M., Eberhardt, K., McClain, M., Shen, Y., and Zhang, X., 1996, Error Compensation for CMM Touch Trigger Probes, *Precision Engineering*, Vol. 19, No. 2/3, pp. 85-97.

[3] Shen, Y., Zhang, X., 1997, Pretravel Compensation for Vertically-Oriented Touch Trigger Probes with Straight Styli, *International Journal of Machine Tools and Manufacture*, Vol. 37, No. 3, pp. 249-262.

[4] Shen, Y., Springer, M.E., A Robust Model for Touch Trigger Probes in Coordinate Metrology, accepted for publication to the *ASME Transactions Journal of Manufacturing Science and Engineering*, to appear.

[5] Shen, Y., Zhang, X., 1997, Modeling of Pretravel for Touch Trigger Probes on Indexable Probe Heads on CMMs, *Intl. J. of Advanced Manufacturing Technology*, Vol. 13/4, pp. 206-213.

[6] Shen, Y., Moon, S., 1996, Sampling Plan for Point-To-Point Prove Performance Test on Coordinate Measuring Machines, *Proceedings of the 1996 ASPE Annual Meeting*, pp. 247-252, Monterey, CA.

Optimizing the Phase Shift Steps for the Least-Squares Algorithm in Phase Shift Interferometry for Engineering Surface Measurement

Yiding Wang and Kee S. Moon
Department of Mechanical Engineering and Engineering Mechanics
Michigan Technological University
Houghton, MI

ABSTRACT

The general least-squares method commonly used in the data processing for phase shift interferometry (PSI) usually suffers badly from the inaccurate movement of phase shift steps as well as other disturbances. The loss of accuracy is extremely serious when the matrices in obtaining the least-squares solutions are ill conditioned. In this paper, the accuracy of the least squares method is analyzed and the optimal phase shift steps are suggested. It offers a method to select the phase shift steps for the least squares evaluation in phase shift interferometry.
Keywords: Phase-Shift Interferometry, Least -Square Algorithm, Error, Optimizing.

INTRODUCTION

Phase shift interferometry (PSI) in the precision measurement of ultra-smooth engineering surfaces is a well established method. PSI electronically records a series of interferograms while the reference phase of the interferometer is changed. The wave front phase is encoded in the variation in the intensity pattern of the recorded interferograms and a simple point-by-point calculation recovers the phase [1]. Generally, the existing algorithm for the analysis of PSI interferograms can be classified into two basic categories: temporal and spatial. Temporal phase-measurement techniques require a phase-stepping process and use a minimum of three fringe patterns to solve for three unknowns in the interference equation. Spatial method uses only one interferogram but requires a large number of fringes. Numerous temporal phase-measurement techniques are summarized in [2], which includes three-step algorithms, least-square algorithms, Carre algorithms, averaging 3+3 algorithms Hariharan algorithm, etc. Each algorithm has its own edges and shortcomings in resisting some particular kinds of system errors. The least-squares solution for a series of N interferograms was first discussed by Bruning et al. [1] and more rigorously by Greivenkamp and Morgan [3] [6]. A generalized phase-shifting interferometry was proposed which is based on the least squares algorithm principle[4]. However, the accuracy of the least squares algorithm suffers badly from the phase shift mis-calibration when the matrices in the calculation are ill conditioned. The choice of the phase shift steps is usually arbitrary and no guidelines are currently available. The optimal phase shift steps are suggested in this paper based on simulation.

PRINCIPLES AND ERROR ANALYSIS OF LEAST SQUARES ALGORITHM FOR PSI

For typical phase shift interferometry, the measured intensity at a given location in the interferogram varies as a sinusoidal function of the reference phase with three unknowns:

$$I_k(x,y) = I_0(x,y)\{1+\alpha(x,y)\cos[\phi(x,y)+\psi_k]\} \tag{1}$$

where $I_0(x,y)$ is the mean intensity, $\alpha(x,y)$ is the fringe contrast, $\phi(x,y)$ is the phase distribution to be measured and $I_k(x,y)$ and ψ_k are the intensity and the relative reference phase ($k=0,1,...,N-1$). This equation can be rewritten in a different form:

$$I_k = a_0 + a_1\cos(\psi_k) + a_2\sin(\psi_k) \tag{2}$$

where: $a_0=I_0(x,y)$, $a_1=I_0\alpha(x,y)cos(\phi(x,y))$, $a_2=-I_0\alpha(x,y)sin(\phi(x,y))$. Eq. (2) is in the proper form for a generalized least-squares fit to the measured intensities $I'_k(x,y)$ at each location. The squared difference between the measured intensities and the intensities predicted by eq. (2) for a choice of the three unknowns a_0, a_1 and a_2 is:

$$E = \sum_{k=0}^{N-1}(a_0 + a_1\cos(\psi_k) + a_2\sin(\psi_k) - I'_k)^2 \tag{3}$$

This error is minimized by differentiating with respect to each of the three unknowns and equating these three results to zero:

$$A(\psi_k)\,a = b(\psi_k) \tag{4}$$

where: $A(\psi_k) = \begin{bmatrix} N & \sum_{k=0}^{N-1}\cos(\psi_k) & \sum_{k=0}^{N-1}\sin(\psi_k) \\ \sum_{k=0}^{N-1}\cos(\psi_k) & \sum_{k=0}^{N-1}\cos^2\psi_k & \sum_{k=0}^{N-1}\cos\psi_k\sin\psi_k \\ \sum_{k=0}^{N-1}\sin(\psi_k) & \sum_{k=0}^{N-1}\cos\psi_k\sin\psi_k & \sum_{k=0}^{N-1}\sin^2\psi_k \end{bmatrix}$, $b(\psi_k) = \begin{bmatrix} \sum_{k=0}^{N-1} I'_k \\ \sum_{k=0}^{N-1} I'_k\cos\psi_k \\ \sum_{k=0}^{N-1} I'_k\sin\psi_k \end{bmatrix}$, $a = \begin{bmatrix} a_0 \\ a_1 \\ a_2 \end{bmatrix}$

The three unknowns can be solved by:

$$a = A^{-1}(\psi_k)\,b(\psi_k) \tag{5}$$

Therefore, the phase can be obtained by:

$$\phi = -\text{atan}\frac{a_2}{a_1} \tag{6}$$

Repeating this calculation for all the measured points, we can obtain $\phi(x,y)$.

In actual measurement, there always exist small phase steps error as well as the intensity measurement errors. Sometimes, these errors can be greatly amplified to make the results extremely biased owing to the solving process. A problem is called to be ill-conditioned if small changes in the data can produce large changes in the solution. For equation (4), suppose that the measurement errors cause the small variation of the coefficients matrix δA and δb, and suppose the error of the solution is δa. Therefore eq. (4) can be written as:

$$(A+\delta A)(a+\delta a) = b+\delta b \tag{7}$$

Based on matrices manipulation principles, the following results can be obtained (5):

$$\frac{\|\delta a\|}{\|a\|} \le \frac{cond(A)}{1-cond(A)\frac{\|\delta A\|}{\|A\|}}\left(\frac{\|\delta b\|}{\|b\|}+\frac{\|\delta A\|}{\|A\|}\right) \tag{8}$$

where $cond(A) = \|A\|\|A^{-1}\|$ is the condition number of the coefficients matrix and $\|\ \|$ means the

norm of the matrix. Eq.(8) shows the relationship between the relative solution error and the relative error in A and b, together with the key role played by the condition number. Once A is given, *cond(A)* is fixed and solutions will exhibit sensitivity to perturbations in the data regardless of the computer round-off error. Usually, the bigger the condition number is, the more likely that the equation is ill conditioned. For ill-conditioned problems, iterative refinement and scaling method [5] can be employed to improve the accuracy of the solution. However, these methods are too involved and not appropriate for the large amount of data in PSI technique. The only effective means of preventing or controlling ill-conditioning is in the choice of A itself.

OPTIMAL PHASE SHIFT STEPS FOR THE LEAST-SQUARE ALGORITHMS IN PSI

In order to optimize the selection of the phase shift steps to avoid the ill condition of the problem, a computer simulation program is developed to calculate the condition number of matrix A for different values and different numbers of phase shifts and then try to find the phase shift steps that make the condition number the smallest. In the simulation, we assume that all the phase shift steps are equal. Figure 1 illustrates the result of the simulation for three-step phase shift PSI.

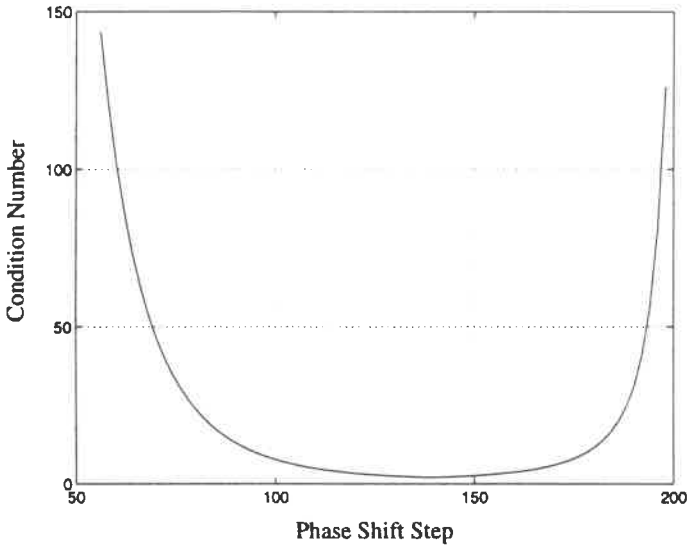

Fig. 1. Condition Number VS. Phase Shift Step for Three Step Method

It is found that when the phase shift step is 120.6°, there is a minimum condition number of 2.025. A sample of the results of the searched optimal phase shift steps for different number of phase shifts is documented in table 1.

Table 1: Optimal Phase Shift Steps for Different Number of Phase Shift

Number of Steps	Three	Four	Five	Six	Seven	Eight
Optimal Phase Shift Steps	120.6°	90°	72°	60°	51.3°	45°
Condition Numbers	2.205	2.000	2.000	2.206	2.009	2.000

A careful observation of a lot of the optimal phase shift steps as well as the condition number plots indicates that the optimal phase step are always centered at $2\pi/N$, where N is the number of the phase shift step. (The reason that there are several optimal phase shift steps which are not exactly equal to $2\pi/N$ is due to the round-off errors in the simulation). Therefore, the optimal phase shift step for least square algorithm in PSI is $2\pi/N$. In this case, all of the off-diagonal terms in matrix A are zero, and a simple solution for the wave front phase can be obtained by:

$$\phi(x, y) = \operatorname{atan} \frac{-\sum_{k=0}^{N-1} I_k \sin\psi_k}{\sum_{k=0}^{N-1} I_k \cos\psi_k} \tag{9}$$

Another observation by examination of the optimal phase shift plots for a lot of different phase shifts is: as the number of the phase shift steps increase, the condition numbers are generally decrease respectively. This is consistent with the findings in [4]. Usually, 10 steps are enough to produce good matrix. For more than 10 phase steps, it is appropriate to choose the phase shift step to be 90^o and it is usually not risky to choose the phase shift steps between 0.2π~0.8π for these cases. A point that should be kept in mind is that increasing the number of phase shift steps also increase measurement uncertainty. Therefore a careful comparison of the trade-off should be made before making the decision for how many phase shift steps are going to be used.

CONCLUSION

The errors that result from the ill-condition of the matrices in least squares algorithm for phase shift interferometry are analyzed. A simulation program is developed to find the optimal phase shift steps in PSI. It is suggested that for small number ($N<10$) of phase shift steps, the optimal step should be $2\pi/N$. Increasing the number of phase shift steps usually produce good matrices and in these cases, the phase shift should be chosen between 0.2π~0.8π according to the convenience of the instruments and it is good to choose the optimal phase shift step to be 90^o in these cases.

REFERENCES:

1. J. H. Bruning, et al., "Digital Wavefront Measuring Interferometer for Testing Optical Surfaces and Lens." Applied Optics. Vol. 13. No. 11. (1974). pp. 2693-2703.
2. D. Malacara, ed. Optical Shop Testing. Second Edition. (1992) John Wiley & Sons, Inc.
3. J. E. Greivenkamp, "Generalized Data Reduction for Heterodyne Interferometry." Optical Engineering. Vol. 23. (1984) pp. 350-352.
4. G. Lai and T. Yatagai., "Generalized Phase-Shifting Interferometry." Journal of the Optical Society of America. A. Vol. 8, No. 5, (1991). pp. 822-827.
5. I. S. Duff, A. M. Erisman and J. K. Reid, Direct Methods for Sparse Matrices. Oxford Science Publications. (1986).
6. C. J. Morgan, "Least-Squares Estimation in Phase-Measurement Interferometry." Optics Letters. Vol. 7. (1982). pp. 368-370.
7. J. Schwider, et al., "Digital Wavefront Measuring Interferometry: Some Systematic Error Sources." Applied Optics. Vol. 22, No. 21, (1983). pp. 3421-3432.

Study on Computational Geometry Approach to Minimum Circumscribed Circle

Liu Shu-gui Yang Fang Ma Xin-hui
(Tianjin University, P.R.China,300072)

Abstract: In this article the problems of Minimum Circumscribed Circle(MCC are investigated using computation geometry approach. A principle is presented to delete points which is useless to the algorithms. In the end, some experiments are done to certify them.

The analysis and design of geometric algorithms in the past two decades have resulted in the new discipline of Computational Geometry. Through development of efficient data structure and algorithm, Computational Geometry has provided solutions for many geometric problems which could not be solved by classical approaches.
In geometric problems inspection data are usually not amenable to efficient computations. Computational Geometry is useful to reshape these problems such that efficient algorithms can be developed and exalt solution can be arrived in reasonable time. In this article the problems of Minimum Circumscribed Circle(MCC) are investigated using computational geometry approach.

1.0 foreword

The problem of MCC is very common and useful in science. It can be described by the view of Operational Research: in search of a center of circle, which must fit for the following equation:

$$\min_{i} \max_{p \in S} [(x_i - x_0)^2 + (y_i - y_0)^2]$$

In practical application, we can use MCC to arrange the public sites, such as Police Station and hospital. Let it be the center of circle, to certify the inhabitant of certain region can reach them. In measuring field, the MCC is one of approaches of evaluating roundness. Also it can be used in
many other fields.
In MCC problem, there exists two serious defaults in previous methods:

1.The theory of function approximation is usually applied, which can only reach a approximate result of the center, not the truth value.

2.Because inspection data are usually not amenable to efficient computations, the time complexity of algorithms isn't very content.

An efficient approach is Optimization Method. It can calculate the exalt result. However, time complexity isn't improved.

2.0 About Computational Geometry

Computational Geometry is a new subject which developed in recent 20 years. It mainly study on the algorithms of geometric problems, and was named by M.I.Shamos in 1975 at first. An fundamental viewpoint of Computational Geometry is: the classical geometry are usually

unfitted for efficient algorithms. To avoid this, the useful parts for algorithms should be distinguished from all to build efficient algorithms.
Till now Computational Geometry has been applied to many aspects. For example, Computer Aided Design, Computer Graph Science, Modeling Recognition, Skeleton Theory etc.

2.1 Hull

As a base tool of Computational Geometry, hull is defined as follows: the least polygon including all the sampling points. In short, we use a large elastic to round a series of sampling points, formed a polygon, which is the hull.

2.2 The farthest point Voronio Diagram

The farthest point Voronio Diagram is an important concept of Computational Geometry. as figure 1 shows, every point i on hull has a farthest region V(i), and any points in V(i) is farthest away from point i, while nearer to other points on hull that i.

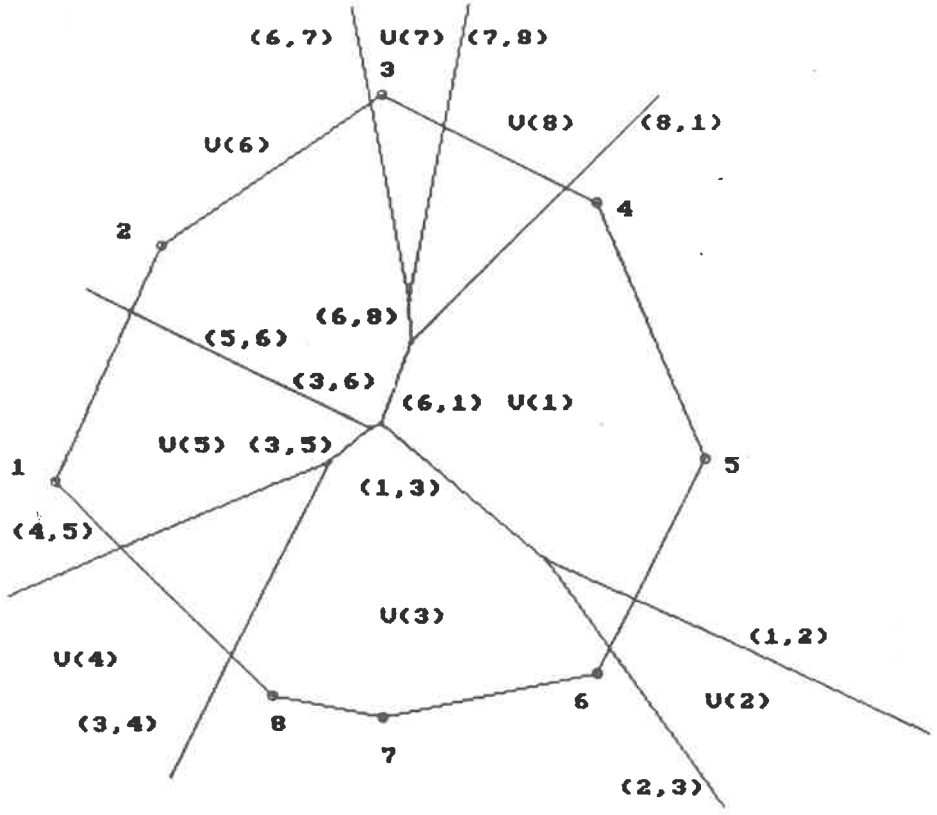

figure 1

2.3 Using Computational Geometry solve the MCC problem

Theorem 1: The point which is possible on the MCC must on hull
We can demonstrate Theorem1 according to the following facts:
As figure 2 shows, supposing a point A which isn't on the hull, but possible on MCC, then we can find a center. The redius is the distance from center to the point. Other points should be on or inside the circle.

We can draw a tangent of the circle. All other points should be on the same side of tangent. And now, connected any other two points and point A. The angle must be less than 180 degrees. Thus the point A must be on hull. Obviously this is conflicted with the previous suppose. So theorem is valid.

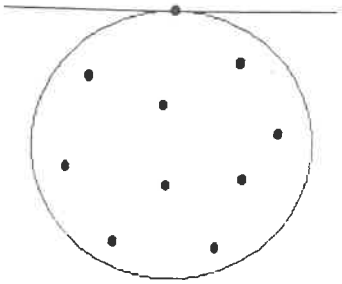

figure 2

According to theorem 1, the points inside the hull could be deleted , because they ate useless for MCC. By this step we usually take account of one third of all sampling points. However, when the amount of sampling points are very large, still there are many points we have to consider. Now a principle of deleting useless points on hull is presented. Through it the amount of points can be reduced further.

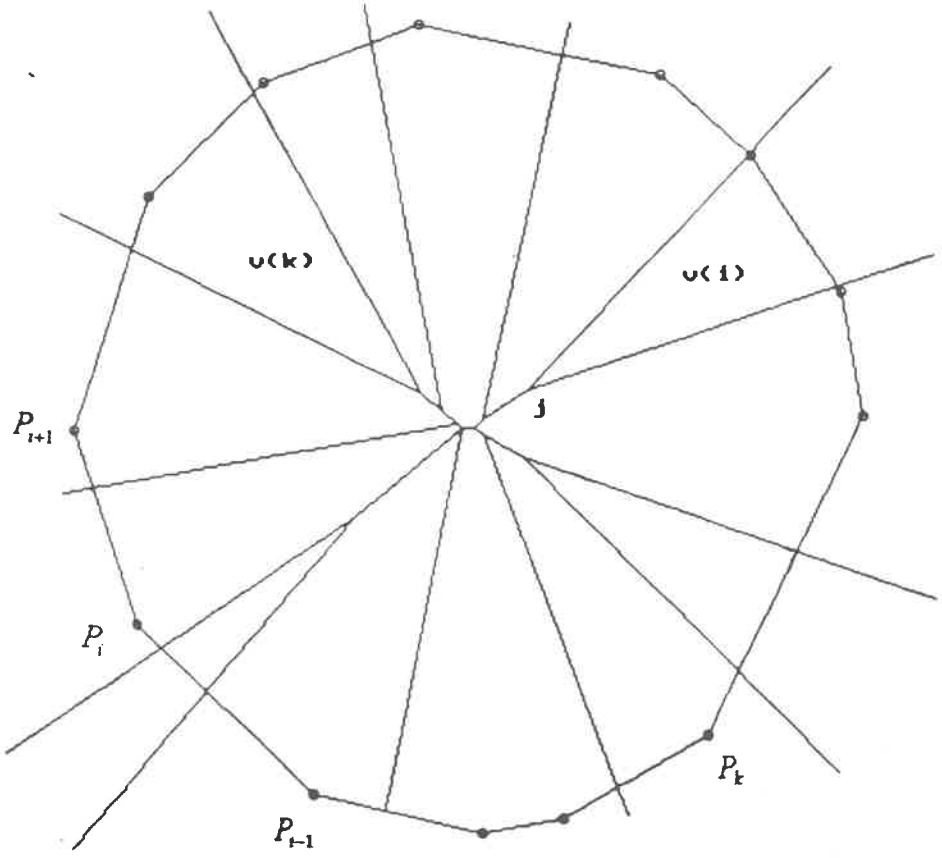

figure 3

Figure 3 shows the sampling points and the farthest point Voronio Diagram. For point P(i), the perpendicular of edges P(i-1)P(i) and P(i)P(i+1) intersect to a point J. V(i) is the farthest region of P(i). Then, supposing P(i) is a point of MCC, we must find a center, which is farthest away from P(i). In fact J is the center. R(ij) is the radius of MCC.

Now we define a radius used to compare with R(ij). Let the measuring center as a point, checking out a farthest sampling point. These two points distance is comparing radius R(c). As we know, R(c) must be less than the real radius of MCC.

If R(ij) < R(c), R(ij) must be less than the real radius of MCC. P(i) could not be on MCC. It is also means: although P(i) is possible to be a point of Circumscribed Circle, the circle isn't the minimum. So we can delete P(i).

The R(c) can be revised again and again till no points are deleted. It is, after a cycle is finished, we get the distance between measuring center and farthest point.

3.0 Conclusion

On the basis of above theories, the author made programs in C language. Very satisfied resulted are achieved. By comparison with the Optimization Method, the following achievement have been gained:

1.The results are completely same as Optimization Method, which demonstrated the validity of Computational Geometry Method.

2.The deletion of unnecessary points are introduced. No more than one tenth of the original input data are useful to MCC#, while all the others are deleted. Time complexity is four~five times lower than Optimization Method. Table 1 shows the comparison between the amount of all sampling points and the possible points for MCC after deletion. In some groups only three points are left, it is no doubt the complexity decreased greatly.

Table 1

Group No.	1	2	3	4	5	6	7	8	9	10
total amount of sampling points	125	125	125	125	125	125	125	60	60	60
possible amount for MCC	5	6	9	7	3	4	10	4	3	6

Table 2 shows the comparison of computing time between two method:
Computational Geometry and Optimization Method.

Table 2 unit: S

Group No.	1	2	3	4	5	6	7	8	9	10
Optimization Method	14.1	13.3	12.3	14.8	15.7	11.2	10.8	15.0	10.9	13.7
Computational Geometry	3.0	3.0	3.3	3.2	4.1	2.9	2.8	3.6	3.4	3.3

Now we can conclude: Computational Geometry Approach solved the MCC problem successfully from a new viewpoint. It reduced the time of algorithm greatly, improve the efficiency meantime.

[Reference]

1. M.I.Shamos, Computational Geometry
2. Kewei Lai, A Computational Geometry Approach to Geometric Tolerancing,
Dept. of Mechanical Eng. Northwestern University.
3. Fang Yang, Study on Computational Geometry Approach to roundness, Paper for Master degree of Tianjin University.

Repeatability and Calibration of a Grazing Incidence Cylindrical Interferometer

P. Douglas Knight, Jr., Steve R. Patterson
Department of Mechanical Engineering and Engineering Science
University of North Carolina at Charlotte, Charlotte, N.C. 28223

1. Introduction

Grazing incidence interferometry has successfully been used for the measurement of flat surfaces. [1,2] The advantage was that a grazing incidence beam did not require a highly reflective surface and had a much larger dynamic range than normal incidence interferometry. Recent advances in grazing incidence interferometry have led to the development of techniques for the measurements of surfaces with a cylindrical form. [3,4] From this work, the Tropel Corporation has developed the Cylinder Master 25, which quickly measures cylindrical and tapered parts to find form, cylindricity, taper, and other metrological attributes of both OD and ID components.

The basic operation of the CM25 is shown in Figure 1. A nominally plane light wave is incident on a binary phase grating (DOE1) of eight micron pitch. This grating is composed of concentric circles that diffract the first order beam (test beam) at an angle of about 4.5°. The binary grating is manufactured such that the intensity of the zero order (reference beam) and first order beam are equal in order to maximize contrast in the resulting interferogram. The test beam is then reflected from the part and recombined with the reference beam by DOE2. The two beams, now parallel, interfere and the resulting interferogram is captured at the image plane by a CCD camera. Therefore any variations in the part being measured from the cylinder mapped in the space between DOE1 and DOE2 by DOE1 will result in a path difference of the test beam that shows up as a phase difference in the interferogram. This phase difference can be fitted using cylindrical polynomials to give the form of the cylindrical part.

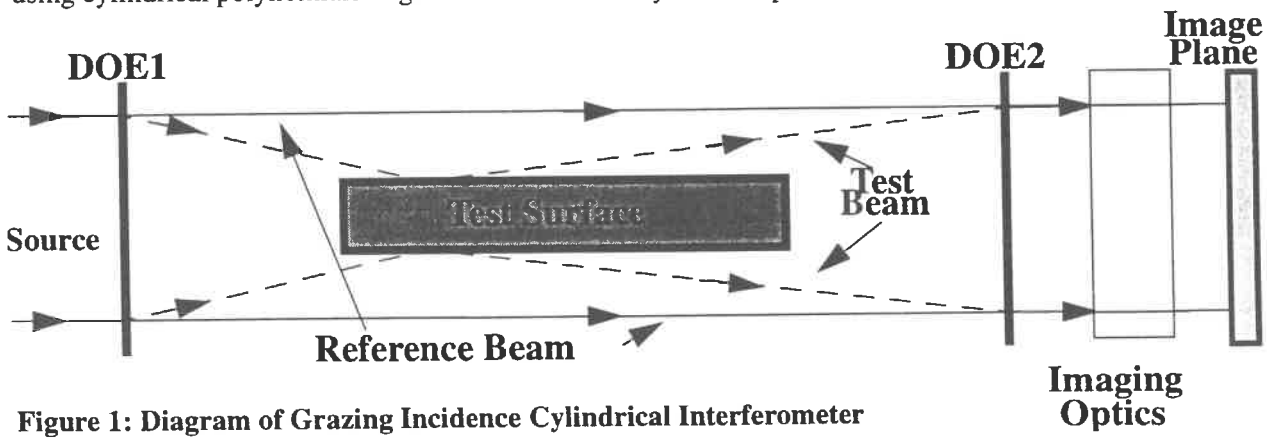

Figure 1: Diagram of Grazing Incidence Cylindrical Interferometer

3. Repeatability of a Grazing Incidence Cylindrical Interferometer

3.1 TVE Measurements

The TVE (Thermal Variation Error) test was performed in the Metrology Lab of the University of North Carolina at Charlotte which is temperature controlled at 20° C ± 0.1° C. Initially a TVE test was executed where the part being measured, a 20 x 50 mm pin gage, was handled without gloves while placing the gage on the fixture of the CM25. The machine was set on repeat mode and allowed to run for approximately 24 hours. Graphical results from this TVE tests are shown in the Figure 2 and the standard devia-

tion of the cylindricity TVE data was 0.0115 um for all of the data. The standard deviation for trial number 400 to 941 is 0.0053 um.

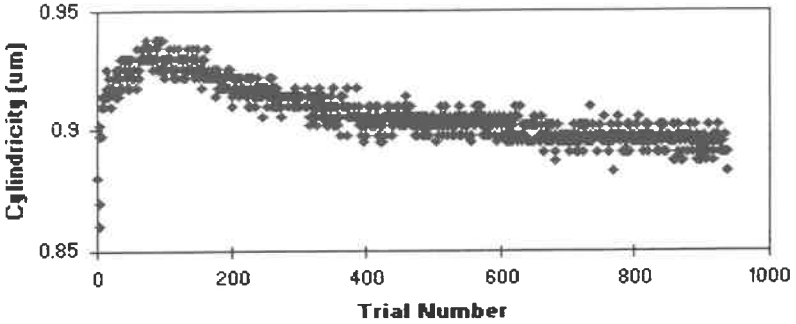

Figure 2: TVE test of cylindricity vs. Trial Number of approximately 24 hours with the part handled before the test occurred.

Next, three different TVE tests were performed using the same ring gage for measurement. For these tests, the part was not handled between each of the tests and not handled for 24 hours before the beginning of this set of TVE tests. The machine was again placed in repeat mode and allowed to run for approximately 24 hours. Different wait time TVE tests were performed to determine if the wait time between measurements affected the standard deviation value for cylindricity. The standard deviations from the TVE tests are shown in Table 1. An F-test was performed that concluded the difference in the standard deviations of cylindricity for different wait times was not statistically significant.

Wait Time (s)	20	60	120	300
σ (um)	0.0042	0.0037	0.0039	0.0042

Table 1: Standard deviation of Cylindricity for TVE tests with varying wait time between trials

3.2 Repeatability with Part Repositioning

A test was conducted to measure the repeatability of the instrument when the part was repositioned between measurements. The part was repositioned after each measurement by placing the part at a different place on the fixture for each test and then realigning the part parallel to the instrument's optical axis. Four different repeatability tests of thirty trials each were performed; two with pin gages and two with ring gages. The pin gages had nominal sizes of 20 x 51 mm and 5 x 51 mm and the ring gages had nominal sizes of 0.5" x 19 mm and 0.5" x 13 mm. The test results are shown in Tables 2a and 2b. F tests were performed that found differences in standard deviations for cylindricity and taper are not significant for differing pin and ring gages but the standard deviations are significant when comparing pin to ring gage measurements.

	20x51 mm Pin Gage	
Statistic	Cylindricity (um)	Taper (um)
Mean	0.9104	-0.0597
σ	0.0700	0.0274
	5x51 mm Pin Gage	
Statistic	Cylindricity (um)	Taper (um)
Mean	0.0903	0.3754
σ	0.0633	0.0285

Table 2a

	0.5"x19 mm Ring Gage	
Statistic	Cylindricity (um)	Taper (um)
Mean	1.3896	0.2547
σ	0.0331	0.0136
	0.5"x13 mm Ring Gage	
Statistic	Cylindricity (um)	Taper (um)
Mean	1.0457	-1.0587
σ	0.0397	0.0108

Table 2b

Table 2a: Repeatability with part repositioning of two different diameter pin gages
Table 2b: Repeatability with part repositioning of two different length ring gages

4. Factors Affecting Calibration of Instrument

Systematic errors of the instrument are manifested as biases to metrological attributes calculated for the part being measured. The measurement of taper and twolobe of a part are two terms that are offset due to repeatable components of systematic error. To rid the machine output of this measurement bias, a calibration routine involving reversals is implemented that is derived from classic reversal techniques that change the sign of one of the components of error.[5]

The first set of calibration tests were performed using the two ring gages of different heights previously used for the part repeatability measurements. Twenty instrument calibration measurements for each part were recorded. The calibration routine involved measuring the part initially, rotating it 90 degrees, remeasure, and then flipping the part 180 degrees for the final measurement. The top grating did not change position when a different ring gage was calibrated. The CM25 then calculated the repeatable taper and twolobe systematic components of error from these measurements. The results from the two sets of calibration are shown in Table 3a and 3b. T tests were performed comparing the means of systematic taper and twolobe for different length ring gages. These were found to be significantly different when using ring gages of different heights. The standard deviations for the ring gage calibrations are consistent with the calculated standard deviations using propagation of errors through the calibration technique at a significance level of 5%.

	13 mm Gage	
Statistic	**Taper (um)**	**Twolobe (um)**
Mean	**0.0211**	**0.0343**
σ	**0.0069**	**0.0123**

Table 3a

	19 mm Gage	
Statistic	**Taper (um)**	**Twolobe (um)**
Mean	**0.0409**	**0.1718**
σ	**0.0060**	**0.0053**

Table 3b

Table 3a: Calibrated repeatability components of systematic error for a 0.500" x 13 mm ring gage
Table 3b: Calibrated repeatability components of systematic error for a 0.500" x 19 mm ring gage

Another set of calibration measurements were made using two pin gages with different height fixtures. The calibration experiment presented in the previous paragraph used two different ring gages that kept the position of the top grating the same but used a different part of the grating and therefore a different part of the beam for the calibration of each respective ring gage. By using two gages of equal heights and different diameters, the same part of the grating and therefore the same part of the beam would be used for the calibration of each gage by suitably adjusting the position of the upper grating. Therefore the only effective difference from the previous calibrations (with respect to the instrument) would be the position of the top grating. Two different fixtures were available, one with a height of 21.0 mm above the bottom grating and the other with a height of 49.5 mm above the bottom grating. Using the equation, $\tan \theta = \Delta r / \Delta d$, where θ is the angle the first order beam is diffracted by the gratings, Δr is the differential radius of two different pin gages, and Δd is the differential height of two fixtures, two pin gages were selected for calibration based on the differential height of the two available fixtures. The two pin gages used for this set of calibration measurements had a diameter of 0.876" for the fixture with height 21.0 mm above the bottom grating and 0.700" for the fixture with height 49.5 mm above the bottom grating. The results of the calibration are presented in Tables 4a and 4b. T tests were performed on this set of calibrated systematic taper and twolobe error means and found to be statistically different when the same part of the beam and grating are used and the only systematic change is the position of the top grating. The standard deviations for the pin gage calibrations are also consistent with the calculated standard deviations using propagation of errors through the calibration technique at a significance level of 5%.

	0.700" pin gage			0.876" pin gage	
Statistic	Taper (um)	Twolobe (um)	Statistic	Taper (um)	Twolobe (um)
Mean	0.3214	0.2720	Mean	0.2846	0.2502
σ	0.0247	0.0300	σ	0.0246	0.0096

Table 4a Table 4b

Table 4a:Calibrated repeatability components of systematic error for a 0.700" x 51.2 mm pin gage
Table 4b:Calibrated repeatability components of systematic error for a 0.876" x 51.2 mm pin gage

5. Conclusions

When initially handled, the TVE measurements of a part seemed to level off at a cylindricity of 0.895 um. This is close (within 10 nm) to the mean cylindricity of the part measured during the other TVE tests. The initial variations in part cylindricity are thought to be caused by the temperature of the part stabilizing and the temperature of the enclosure surrounding the part itself stabilizing. Because the standard deviations of the different wait times between measurements for the TVE tests were not significantly different, the wait time between measurements does not affect the standard deviation of the TVE test.

The standard deviation in measured cylindricity and taper was not significantly different for both ring gages with different heights and for pin gages with different diameters when the part was repositioned between measurements. Neither the height of a ring gage nor the diameter of a pin gage affected the variance of a part measurement. The standard deviation of measuring a part with repositioning was small but statistically different for both cylindricity and taper when using a pin gage as opposed a ring gage for testing. Therefore the standard deviation for measuring ID parts as opposed to OD parts was statistically different but the difference was only about 30 nm for cylindricity and 15 nm for taper. This difference may have been a function of a more enclosed air path for the ring gages (for the light beam while within the ring) as opposed to the pin gages which were only surrounded by the instrument enclosure.

For the calibration tests, the t tests concluded that the means of the instrument calibration for taper and twolobe were different when using different height ring gages. This leads to the conclusion that the part of the grating used and/or the part of the beam used for the calibration does affect the calibrated machine error. For the pin gages on different height fixtures, the t-test showed statistically different taper and twolobe instrument calibration values when the top grating changed position. The reported machine calibrated error depends on either the position of the top grating, instrument zoom, or error in the calibration artifact. Future testing will be performed to elucidate the calibrated error dependencies.

References

1. Salsbury, James G., "Laser measurements at Cummins Engine," Quality, (Feb. 1994).
2. Birch, K.G., "Oblique incidence interferometry applied to non-optical surfaces," J. Phys. E Vol 6 (10), 1045-1048 (1973).
3. ATP Project Brief 95-01-0022, "Non-contact optical metrology of complex surface forms for precision industrial manufacturing," General Competition (July 1995).
4. Dresel, Thomas et al, "Grazing incidence interferometry applied to the measurement of cylindrical surfaces," Optical Engineering, Vol 34, pp. 3531-3535 (1995).
5. Evans, Chris J., Hocken, Robert J., and Estler, W. Tyler, "Self-Calibration: Reversal, Redundancy, Error Separation, and "Absolute Testing," CIRP Annals, Vol. 45/2,(1996).

Development of a Roundness Profile Measurement System for Precision Rollers by V-Block Method

Kimiyuki Mitsui*, Kenji Goho* and Akira Hayashi**

* Department of Mechanical Engineering, Keio University
3-14-1 Hiyoshi, Kohoku-ku, Yokohama, 223, Japan
** Nano Corporation, 5-12-5 Kugahara, Ota-ku, Tokyo 146, Japan

Introduction

Cross-section roundness profile measurement is generally considered a significant procedure in the processing of parallel rollers requiring the highest quality in dimensional accuracy. Such rollers, intended for use in high precision mechanical stages of ultra-precision machine tools, are usually chosen out of a batch of uniform rollers that have undergone cross-section roundness tests. This becomes a difficult procedure due to the fact that such rollers show extremely small dimensional error, resulting in expensive and time consuming measuring methods or, in most cases, the ignorance of the procedure itself.

A variety of methods are categorized as roundness measurement, with each having its merits and drawbacks. Diameter measurement is a simple and highly accurate method, yet cross-sections, which have uniform diameter in all directions, can not be detected from this method. Other methods such as radius measurement enable uniform-diameter detection, though drawbacks such as the difficulty of setting the roller perfectly vertical to the rotation table, the eccentricity caused by rotation axis error, etc., effect the resolution of the method.

The V-block method enables enlargement of the parameters, which construct the cross-section profile of a cylindrical workpieces. The drawback of this method at the time was that the profile was approximated into a distorted circle of a single order, thus reducing the accuracy of the resultant profile. For this reason the V-block method was long known as just a simple method for roundness measurement giving approximate profile. [1]-[2]-[4]

We have already reported about the principle, hardware system configuration and basic experimental results of roundness profile measurement method based on V-block. [3] Results of our later study will be reported in this report.

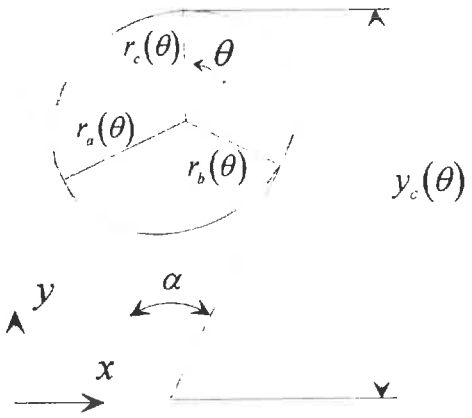

Fig. 1 Measuring principle

Measuring principles

Figure 1 illustrates the cross-section of a cylindrical workpiece placed in a V-block with a taper angle of α. The cross-section of a cylindrical workpiece can be looked upon as a periodic function with a period of 2π, and thus its radius r(θ) can be expressed in a Fourier series as shown in equation(1).

$$r(\theta) = r_0 + \sum_{k=1}^{\infty}(A_k \cos k\theta + B_k \sin k\theta) \tag{1}$$

By arranging the measured yc(θ) values into a Fourier series, the resultant Fourier coefficients, Ak and Bk can be easily calculated using equation (2). [3]

In reality, the maximum order of the Fourier coefficients required to fully reconstruct a cross-section will run to infinity, thus making it impossible to mathematically analyze such coefficients. Yet in most cylindrical workpieces lumps of high order tend to show small amplitude, making it possible to effectively analyze coefficients to a certain order N, and yet obtain the original distorted shape.

$$y_c(\theta) = \left(1 + \frac{1}{\sin\frac{\alpha}{2}}\right) r_0 + \sum_{k=2}^{\infty}\left\{1 + \frac{\cos k\left(\frac{\pi}{2} + \frac{\alpha}{2}\right)}{\sin\frac{\alpha}{2}}\right\}(A_k \cos k\theta + B_k \sin k\theta) \tag{2}$$

System layout of the apparatus

Figure 2 shows system layout of the proposed measuring system. All parts of the apparatus were processed from SUJ2 steel composite. The parallel roller is enlarged first by a V-block, and furthermore by a measuring bar which acts as a lever. The V-block is cut out of a 10mm thick SUJ2 steel composite block, and the taper angle is set at 14 degrees. The measuring bar enlarges the yc value to 5 times at measuring position. A capacitance type displacement sensor with a sensitivity of 0.01 μm, was used for measurements.

The rotation of the roller is given by a miniature DC motor. These two are coupled with a thin piano wire, thus eliminating the influence of unexpected eccentricity to the roller.

The output of the capacitance type displacement sensor is recorded by an FFT analyzer, which is triggered by a pulse signal emitted from a rotary encoder attached to the motor. The data recorded by the FFT is transferred to a personal computer, where it is analyzed to reconstruct the measured profile.

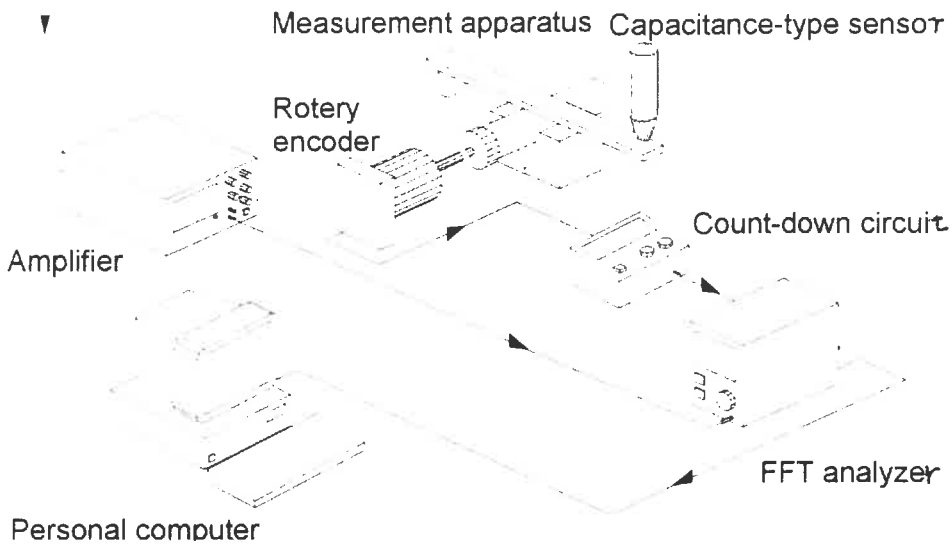

Fig. 2 System layout of apparatus

Experimental results

Figure 3 illustrates analyzed results obtained from 230 roller samples measured with our proposed method. In figure 3 a) the vertical and horizontal axis respectively represent base radius deviation and roundness of the measured rollers. In Fig. 3 b), c) the horizontal axis represents roundness (3 b) and base radius deviation (3 c) respectively, while the vertical axis gives the number of samples found in that value range. These results showed that while all rollers satisfied the requirements of the applied standard, for applications such as use in high precision mechanical stages, the classification of these rollers based on roundness and base radius give hope for miraculous improvement in movement accuracy of such devices.

Conclusions

In this reports, the measuring principle and set-up of the roundness profile measurement system based on a V-block method are described, followed by analyzed results of 230 sample rollers classified according to roundness and base radius deviation.

References

[1] T. Nakata and A. Yamamoto. "Out-of-roundness measurement method for cylindrical processed workpieces", Journal of The Japan Society for Mechanical Engineering, Vol. 53. No. 367. PP. 159-163 (I 950). (in Japanese)

[2] S. Yonezu. "Extension of the V-block 3 point method", Journal of The Japan Society for Precision Engineering. Vol. 19, No. 8, PP. 307-311 (1953). (in Japanese)

[3] K. Goho, K. Mitsui and A. Hayashi. "Development of a roundness measurement system for parallel rollers based on a V-block double enlargement device", Proceedings of The Third International Symposium on Measurement Technology and Intelligent Instruments, PP. 432-437 (1996).

[4] R. Yamada. K. Yanagi and T. Shimizu. "Out-of-roundness measuring apparatus by the V-block method for precisely ground shaft using small laser beam". Journal of The Japan Society for Design Engineering, Vol. 30, No. I, PP. 26-32 (1995).

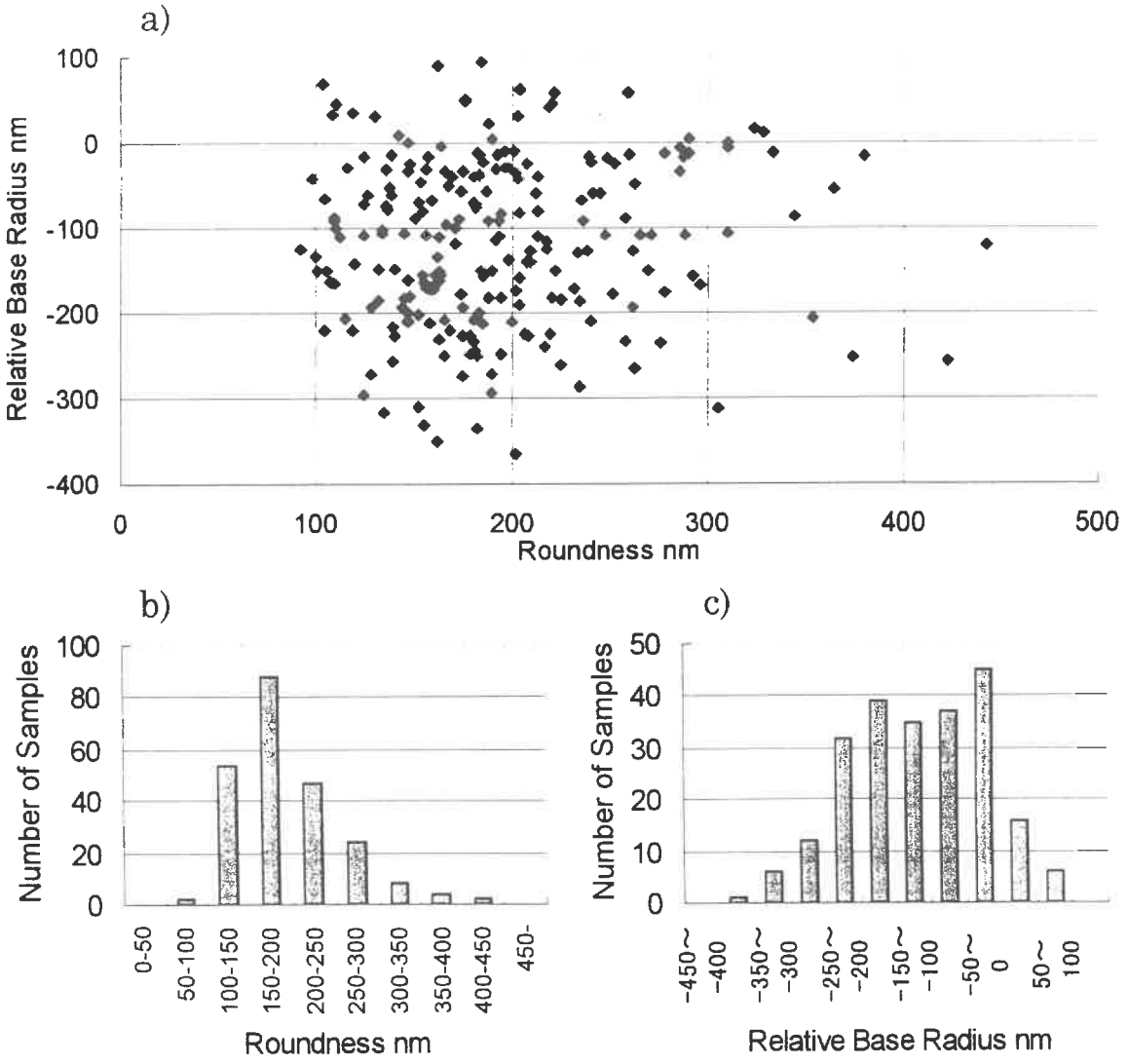

Fig. 3 Analyzed results

A METHOD TO DECOUPLE THE COMPOUND EFFECT OF MACHINE ERROR AND FREE-FORM GEOMETRIC CHARACTERISTICS

G. Lee , J. Mou
Department of I&MSE
Arizona State University
Tempe, AZ 85287

ABSTRACT

One of the prominent sources for measurement errors is due to the imperfection of a measuring device and the compound effect of its imperfection with geometric characteristics of a measured feature. A method is therefore needed to identify and decouple the effect of compound errors. If this can be done, then the collected data can be properly adjusted and a more meaningful analysis result can be drawn. In this paper, the issues of measurement errors identification and reduction for machine calibration and dimension measurement, deal with uniform bicubic B-spline surface feature, are discussed.

1. INTRODUCTION

There are sources of errors in any manufacturing equipment and measuring system. The error sources include imperfect mechanical structures, the errors in control systems, and the environmental disturbances [1]. A variety of techniques were developed to deal with the machine error modeling and compensation as well as the uncertainty in inspection [2, 3, 5]. However, there are several issues still remain unsolved. One of those issues is the measurement error that resulted from the compound effect of machine errors and geometric characteristics of the measured surfaces [4]. The major premise of compound measurement error identification and reduction was described in that paper. The results also showed that the compound effects of measurement along the normal direction to the surface are much smaller than that of measurement along any single axis that is a result of easy programming. In this paper, a method is presented to discuss the issue of measurement errors identification and reduction in dimensional measurement of sculptured surfaces.

Sculptured surfaces can be mathematically described in several ways. In this paper, the proposed algorithm based on bicubic B-spline surfaces is demonstrated for its simple and superior design properties [6]. A uniform cubic B-spline surface is composed by uniform cubic B-spline patches. Let u and v be the principal parameters defining the principal directions in a bicubic B-spline patch $r_{ij}(u,v)$. Let a defining vector q_{ij} be $q_{ij} = (x_{ij}, y_{ij}, z_{ij})$ and M be the cubic B-spline coefficient matrix. If (m+2)(n+2) defining vectors, $q_{-1,-1}$, $q_{-1,0}$, …, $q_{-1,n}$, $q_{0,-1}$, $q_{0,0}$, …, and $q_{m,n}$, are given, the patch can then be expressed as $r_{ij}(u,v) = UMQ_{ij}M^{T}V^{T}$, with $0 \le u \le 1$, $0 \le v \le 1$, and i, j = 0, 1, …, n-2, where $U = [u^3\ u^2\ u\ 1]$, $V = [v^3\ v^2\ v\ 1]$, m, n ≥ 2, $r_{ij}(u,v) = (x(u,v)_{ij}, y(u,v)_{ij}, z(u,v)_{ij})$, $\phi(u,v)_{ij} = UMQ_{ij}^{\phi}M^{T}V^{T}$, $\phi = x, y, z$, and

$$M=\frac{1}{6}\begin{bmatrix} -1 & 3 & -3 & 1 \\ 3 & -6 & 3 & 0 \\ -3 & 0 & 3 & 0 \\ 1 & 4 & 1 & 0 \end{bmatrix}, Q_{i,j}=\begin{bmatrix} q_{i-1,j-1} & q_{i-1,j} & q_{i-1,j+1} & q_{i-1,j+2} \\ q_{i,j-1} & q_{i,j} & q_{i,j+1} & q_{i,j+2} \\ q_{i+1,j-1} & q_{i+1,j} & q_{i+1,j+1} & q_{i+1,j+2} \\ q_{i+2,j-1} & q_{i+2,j} & q_{i+2,j+1} & q_{i+2,j+2} \end{bmatrix}, Q_{i,j}^{\phi}=\begin{bmatrix} \phi_{i-1,j-1} & \phi_{i-1,j} & \phi_{i-1,j+1} & \phi_{i-1,j+2} \\ \phi_{i,j-1} & \phi_{i,j} & \phi_{i,j+1} & \phi_{i,j+2} \\ \phi_{i+1,j-1} & \phi_{i+1,j} & \phi_{i+1,j+1} & \phi_{i+1,j+2} \\ \phi_{i+2,j-1} & \phi_{i+2,j} & \phi_{i+2,j+1} & \phi_{i+2,j+2} \end{bmatrix}$$

2. MEASUREMENT ERRORS ASSESSMENT

If the inspection process was designed to take measurement along the normal direction that is normal to the ideal feature surface, we can assume: (1) $N = r_{ij}(u_0,v_0) = (x(u_0,v_0), y(u_0,v_0), z(u_0,v_0))$ is a nominal point being measured on the (i,j)th surface patch; (2) a unit vector w is chosen to indicate the probe approach direction; and (3) there are machine errors (δ_x, δ_y, and δ_z) in all x-axis, y-axis and z-axis. First, w can be calculated in a right-hand system as:

$$w=\begin{bmatrix} w_x & w_y & w_z \end{bmatrix} = \left(\frac{\partial r}{\partial u}\times\frac{\partial r}{\partial v}\right) \Big/ \left|\frac{\partial r}{\partial u}\times\frac{\partial r}{\partial v}\right| \qquad (1)$$

where $\frac{\partial r}{\partial u}=\left(\frac{\partial U}{\partial u}\right)MQM^TV^T\Big|_{u=u_0} = \left[\frac{\partial x(u,v_0)}{\partial u} \quad \frac{\partial y(u,v_0)}{\partial u} \quad \frac{\partial z(u,v_0)}{\partial u}\right]_{u=u_0}$ and $\frac{\partial r}{\partial v}=UMQM^T\left(\frac{\partial V}{\partial v}\right)^T\Big|_{v=v_0} = \left[\frac{\partial x(u_0,v)}{\partial v} \quad \frac{\partial y(u_0,v)}{\partial v} \quad \frac{\partial z(u_0,v)}{\partial v}\right]_{v=v_0}$ are the tangent vectors at point N along u-curve and v-curve, respectively.

Suppose the (m+1)(n+1) defining vectors, q_{ij}, of the bicubic B-spline net are known from the inverse transformation of the CAD data. According to Eq.1 and the generalized algorithm, we may find that:

(a) $\mathbf{N} = [x(u_0,v_0) \quad y(u_0,v_0) \quad z(u_0,v_0)]^T$;

(b) $\mathbf{N}_1 = [x(u_0,v_0)+d*w_x \quad y(u_0,v_0)+d*w_y \quad z(u_0,v_0)+d*w_z]^T$;

(c) $\mathbf{P}_1 = [x(u_0,v_0)+d*w_x+\delta_x \quad y(u_0,v_0)+d*w_y+\delta_y \quad z(u_0,v_0)+d*w_z+\delta_z]^T$;

(d) $\mathbf{P}_f = [x(u_{Pf},v_{Pf}) \quad y(u_{Pf},v_{Pf}) \quad z(u_{Pf},v_{Pf})]^T = [x(u_0,v_0)+c*w_x+\delta_x \quad y(u_0,v_0)+c*w_y+\delta_y \quad z(u_0,v_0)+c*w_z+\delta_z]^T$;

(e) $\mathbf{N}_f = [x(u_{Nf},v_{Nf}) \quad y(u_{Nf},v_{Nf}) \quad z(u_{Nf},v_{Nf})]^T = [x(u_{Pf},v_{Pf})-\delta_x \quad y(u_{Pf},v_{Pf})-\delta_y \quad z(u_{Pf},v_{Pf})-\delta_z]^T$.

where (d) and (e) can be calculated by letting $\mathbf{P}_f = r_{ij}(u_{Pf},v_{Pf}) = U_{Pf}MQ_{ij}M^TV_{Pf}^T$ and solving the three unknowns, u_{Pf}, v_{Pf}, and c, from the three equations where $U_{Pf} = [u_{Pf}^3 \; u_{Pf}^2 \; u_{Pf} \; 1]$ and $V_{Pf} = [v_{Pf}^3 \; v_{Pf}^2 \; v_{Pf} \; 1]$. The actual machine errors should be expressed as: $\delta_x = x(u_{Pf},v_{Pf}) - x(u_{Nf},v_{Nf})$; $\delta_y = y(u_{Pf},v_{Pf}) - y(u_{Nf},v_{Nf})$; $\delta_z = z(u_{Pf},v_{Pf}) - z(u_{Nf},v_{Nf})$.

Simulation analysis is conducted to illustrate the effect of the compound measurement error in measuring a bicubic B-spline surface. Suppose the surface defining net of a uniform bicubic B-spline surface is given as $q_{i,j} = [i/2 - j/2 \; (3.125 - (i/2 - 0.75)^2 + (-j/2 + 0.75)^2)]$ where i, j = -1, 0, 1, ..., 4. The bicubic B-spline surface (see Figure 1) is then composed by the 9 patches of r_{ij} where i, j = 0, 1, 2. In order to clearly compare the difference of the compound effects on the same base, let's assume the default value of the approach distance d = 2 mm (0.07874 in.) and the machine errors at point N have the same magnitudes as $\delta_x = \delta_y = \delta_z$ = 127 μm (0.005 in.) with a repeatability in a Normal distribution $N(0, \sigma_r^2)$ where $3\sigma_r$ = 5.08 μm (0.0002 in.). For a systematic comparison based on a stepwise width, there S_n points may systematically be sampled on the uniform bicubic B-spline surface. Suppose the sample size S_n = 9, according to a uniform sampling strategy, a set of the nominal points on the surface may be sampled at u = 0.5 and v = 0.5 on each bicubic B-spline patch. The measured error (Δx, Δy, and Δz) due to the compound effects are first determined and then compared with assigned machine errors (δ_x, δ_y, and δ_z). The measurement errors are either enlarged or dwindled. The results also show that the compound effect of machine related and geometric related errors could be largely biased and significantly degrade the accuracy of any measurement. Hence, the analysis results could be misled based on the measuring data without considering these compound effects.

3. MEASUREMENT ERRORS REDUCTION

Since the effects of machine errors are compound, it is impossible to identify the magnitude of δ_x, δ_y, and δ_z from a single measurement at each nominal point. Therefore, a different measurement procedure is proposed. For a 3-D measurement, at least three repetitive measurements are needed in order to identify the magnitude of δ_x, δ_y, and δ_z at each measuring point. The geometric analysis of the measuring behavior of each approach when measuring a designed nominal point $N = r_{ij}(u_0,v_0) = (x(u_0,v_0), y(u_0,v_0), z(u_0,v_0))$ on the workpiece is described in Section 2. If the other two associated nominal measurement points are selected to be very close to N and, therefore, the difference between δ_x, δ_y, and δ_z at all three measuring points can be assumed negligible. From the previous algorithm, yields

$$r_{ij}(u_{Pfk},v_{Pfk}) = U_{Pfk}MQ_{ij}M^TV_{Pfk}^T, \; k = 1, 2, 3; \tag{2}$$

$$[x(u_{Pfk},v_{Pfk}) \quad y(u_{Pfk},v_{Pfk}) \quad z(u_{Pfk},v_{Pfk})]^T = [x(u_{Nfk},v_{Nfk})+\delta_x \quad y(u_{Nfk},v_{Nfk})+\delta_y \quad z(u_{Nfk},v_{Nfk})+\delta_z]^T, \; k = 1, 2, 3; \tag{3}$$

with $0 \le u_{Pfk} \le 1$; $0 \le v_{Pfk} \le 1$; and i, j = 0, 1, ..., n-2, where $U_{Pfk} = [u_{Pfk}^3 \; u_{Pfk}^2 \; u_{Pfk} \; 1]$ and $V_{Pfk} = [v_{Pfk}^3 \; v_{Pfk}^2 \; v_{Pfk} \; 1]$. Then, since there are nine unknowns from the system of nine equations, the machine error $[\delta_x \; \delta_y \; \delta_z]^T$ at N with u_{Pfk} and v_{Pfk}, k = 1, 2, 3, could be solved by using Eq.2 and Eq.3.

To ensure a systematic performance for a surface patch measurement, we may arrange the relative positions of three measuring points as those shown in Figure 2. In this arrangement, we need to determine an angle α and a radius R_s to locate the other two associate nominal measurement points, M_{ij2} and M_{ij3} for a designed nominal point M_{ij1}. The criteria for choosing the suitable α and R_s are (1) to make the range (the triangle) of $\Delta M_{ij1}M_{ij2}M_{ij3}$ as

small as possible to ensure that the δ_x, δ_y, and δ_z are the same within the triangle area, and (2) to make the range large enough in order to identify the magnitudes of δ_x, δ_y, and δ_z efficiently. The parameter coordinates u and v of M_{ij1}, M_{ij2}, and M_{ij3} can be determined as $M_{ij1} = (u_1,v_1) = (R\cos(\alpha), R\sin(\alpha))$; $M_{ij2} = (u_2,v_2) = (R\cos(\alpha + 120°), R\sin(\alpha + 120°))$; $M_{ij3} = (u_3,v_3) = (R\cos(\alpha + 240°), R\sin(\alpha + 240°))$. Accompanying the three determined point, a variation of Newton's method could be used to solve the nonlinear equations of Eq.2 and Eq.3 for decoupling the compound effect.

Suppose the finally probe contact points for all three measurements are located at $P_{f1} = (x_{Pf1}, y_{Pf1}, z_{Pf1})$, $P_{f2} = (x_{Pf2}, y_{Pf2}, z_{Pf2})$, and $P_{f3} = (x_{Pf3}, y_{Pf3}, z_{Pf3})$, respectively. However, the three measuring points may be interpreted by the machine controller as follows $N_{f1} = (x_{Nf1}, y_{Nf1}, z_{Nf1}) = P_{f1} - (\delta_{x1}, \delta_{y1}, \delta_{z1})$; $N_{f2} = (x_{Nf2}, y_{Nf2}, z_{Nf2}) = P_{f2} - (\delta_{x2}, \delta_{y2}, \delta_{z2})$; and $N_{f3} = (x_{Nf3}, y_{Nf3}, z_{Nf3}) = P_{f3} - (\delta_{x3}, \delta_{y3}, \delta_{z3})$; where $(\delta_{x1}, \delta_{y1}, \delta_{z1})$, $(\delta_{x2}, \delta_{y2}, \delta_{z2})$, and $(\delta_{x3}, \delta_{y3}, \delta_{z3})$ are the machine errors in M_{ij1}, M_{ij2}, M_{ij3}. If the distance between the three points is small enough, we may assume $\delta_x = \delta_{x1} \cong \delta_{x2} \cong \delta_{x3}$, $\delta_y = \delta_{y1} \cong \delta_{y2} \cong \delta_{y3}$, and $\delta_z = \delta_{z1} \cong \delta_{z2} \cong \delta_{z3}$. To any feature of a uniform bicubic B-spline surface, yields

$$x_{Nfk} + \delta_{xk} = U_{Pfk} M Q_{i,j}{}^{x} M^T V_{Pfk}{}^T, \; k = 1, 2, 3; \tag{4}$$

$$y_{Nfk} + \delta_{yk} = U_{Pfk} M Q_{i,j}{}^{y} M^T V_{Pfk}{}^T, \; k = 1, 2, 3; \tag{5}$$

$$z_{Nfk} + \delta_{zk} = U_{Pfk} M Q_{i,j}{}^{z} M^T V_{Pfk}{}^T, \; k = 1, 2, 3. \tag{6}$$

By solving the nine equations of Eq.4 through Eq.6 together, a more accurate value of δ_x, δ_y, and δ_z can be determined for machine errors identification and reduction.

Simulation analysis is also conducted to illustrate the effectiveness of the analytical model derived for decoupling the compound effect and identify the actual magnitude of the machine related errors, δ_x, δ_y, and δ_z. According to the criteria for choosing the suitable α and R_s, we set R_s = 3.81 mm (0.15 in.) and randomly choose an α (say 25°). In addition to the same data shown in Section 2, we allow the machine errors δ_x, δ_y, and δ_z to have Normal distributions in both accuracy, $N(0, \sigma_a^2)$, and repeatability, $N(0, \sigma_r^2)$, for this simulation analysis. Eq.4 through Eq.6 were solved simultaneously by a variation of Newton's method.

For a machine where $3\sigma_a$ = 127 μm (0.005 in.) and $3\sigma_r$ = 5.08 μm (0.0002 in.) for δ_x, δ_y, and δ_z, the results show that on an average about 81% of the compound effects on the x-axis, y-axis, and z-axis can be decoupled. The results also show that the effectiveness of the decoupling algorithm is depended on the ratio of the accuracy to the repeatability of a measuring machine. Nevertheless, the measurement error resulted from machine related error and the geometric characteristics of the measured feature can be reduced significantly.

Simulation analysis is also used to examine the sensitivity of the derived algorithm when subjected to various size of $\Delta M_{ij1} M_{ij2} M_{ij3}$ and ratio R_{ar} of the accuracy to the repeatability of a measuring machine. Since α may not be a significant factor to the range of $\Delta M_{ij1} M_{ij2} M_{ij3}$, we may randomly pick a value for α (say 25°) during the simulation. Examples are then demonstrated for on-machine probing with R_s = 2.54, 3.81, or 5.08 mm (0.1, 0.15, or 0.2 in.) and $R_{ar} = \sigma_a / \sigma_r$ = 10, 25, or 50. Thus, for a machine where accuracy is $3\sigma_a$ = 127 μm (0.005 in.), its repeatability may have $3\sigma_r$ = 12.7, 5.08, or 2.54 μm (0.0005, 0.0002, or 0.0001 in., respectively) for each of δ_x, δ_y, and δ_z. Total of 100 points with random accuracy and repeatability is first randomly sampled for each case. Decoupling algorithm is then applied to each sample point. To guarantee a robust comparison, the ratios of the decoupled errors are calculated with the absolute form and the root mean square error form, $R_{(ABS)}$ and $R_{(RMSE)}$ [4]. The simulation results are shown in Table 1. The result shows that (1) both $R_{(ABS)}$ and $R_{(RMSE)}$ have similar results, (2) the assumption of a larger R_s could lead to a better decoupling result is verified, and (3) R_{ar} has significant effect on the performance of the decoupling algorithm.

4. CONCLUSIONS

In this paper, an innovative method was presented to discuss the issues of compound measurement error identification and reduction in dimension measurement on uniform bicubic B-spline surface feature. The measurement method and error classification for both the machine related and surface geometry related measurement error were discussed. Generalized analytical models were derived to identify and assess the compound effect of both types of errors. Simulation analyses were then used to show that neither of the errors resulted from the measuring device and geometric characteristics of measured features can be neglected and their effects are compound with one another.

A novel measurement procedure was also proposed for data sampling and analytical models, and then derived to mathematically decouple the compound effect. As the compound effect of machine related error and geometric characteristics was decoupled, the measurement error can be significantly reduced. Therefore, a more accurate information about the machine error can be derived and, thus, the modified sampling data on machine error can then be used to derive a more accurate and more meaningful result on precision inspection, as well as machine error modeling and compensation processes.

5. REFERENCE

1. ANSI/ASME B89.1.12M-1990, 1990, Methods for Performance Evaluation of Coordinate Measuring Machines, ASME, New York.
2. Busch, K., Kunzmann, H., and Waldele, F., 1985, "Calibration of Coordinate Measuring Machines," *Precision Engineering*, Vol. 7, pp. 139-144.
3. Donmez, M. A., Blomquist, D. S., Hocken, R. J., Liu, C. R., and Barash, M. M., 1986, "A General Methodology for Machine Tool Accuracy Enhancement by Error Compensation," *Precision Engineering*, Vol. 8, No. 4, pp. 187-196.
4. Lee, G., J. Mou, and Y. Shen, 1997 "An Analytical Assessment of Measurement Uncertainty in Precision Inspection and Machine Calibration," *International Journal of Machine Tools and Manufacture*, Vol. 37, No. 3, pp. 263-276.
5. Mou, J., and C. R. Liu, 1992, "A Method for Enhancing the Accuracy of CNC Machine Tools for On-machine Inspection," *Journal of Manufacturing Systems*, Vol. 11, No. 4, pp. 229-237.
6. Yamaguchi, F., 1988, Curves and Surfaces in Computer Aided Geometric Design, Springer-Verlag, New York.

Table 1 The Decoupled Ability with Different R_s and R_{ar}

		R_{ar} =10			R_{ar} =25			R_{ar} =50		
		x	y	z	x	y	z	x	y	z
R_s = 2.54mm	$R_{(ABS)}$	33.2%	36.2%	29.7%	75.5%	75.0%	71.7%	87.6%	87.6%	86.3%
	$R_{(RMSE)}$	32.8%	36.5%	26.4%	75.5%	73.9%	69.9%	87.7%	87.3%	85.1%
R_s = 3.81mm	$R_{(ABS)}$	56.5%	56.6%	51.6%	83.5%	81.8%	79.9%	91.4%	91.7%	90.0%
	$R_{(RMSE)}$	56.9%	56.2%	50.3%	83.0%	81.8%	78.4%	91.2%	91.6%	89.4%
R_s = 5.08mm	$R_{(ABS)}$	68.6%	66.0%	64.5%	87.5%	86.1%	84.9%	94.0%	93.6%	93.2%
	$R_{(RMSE)}$	67.5%	67.1%	62.6%	87.0%	86.2%	83.8%	93.8%	93.5%	92.6%

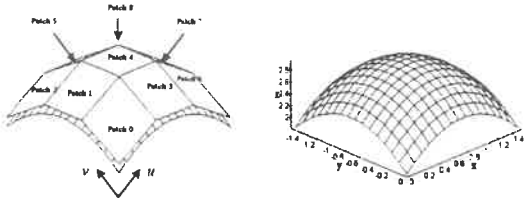

(a) composited patches and surface (b) composited surface only

Figure 1 Example of a Bicubic B-spline Surface from the Surface Defining Net

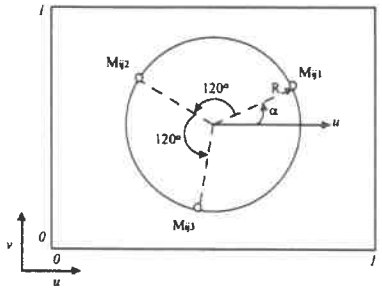

Figure 2 An Example of M_{ij1} with its Two Other Auxiliary Points

Information Content in Surface Metrology for Functional Correlations

Christopher A. Brown, Pierre Hoch
Surface Metrology Laboratory
Mechanical Engineering Department
Worcester Polytechnic Institute
Worcester, MA 01609-2280 USA

Introduction

The objective of this study is to propose and perform a preliminary investigation of a method for determining the information content of topographic characterization parameters.

There are many topographic characterization parameters, both standard and non-standard, which can be used to investigate functional correlations, i.e., correlations with the surface production or surface performance. Frequently it is not clear how to chose topographic characterization parameters that will elucidate the functional correlations. The information content can serve as an aid to selecting topographic characterization parameters, which will have a good likelihood of establishing functional correlations in surface metrology.

Nowicki (1985) proposed one means of selecting parameters, or at least excluding parameters. The approach was to test, for a variety of surfaces, which parameters were well correlated. The regression coefficients for several parameters were presented in a cross correlation matrix. In this way it is obvious which parameters are well correlated. In a situation where a limited number of parameters could be used to characterize a surface, Nowicki proposed it would not be advantageous to select two parameters, which were well correlated. The point is that well correlated parameters contain essentially the same information about the surface topography. Brown and co-workers have also investigated parameter correlations for limited types of surfaces with the same objective (Brown et al. 1990, Terry and Brown 1997).

The approach here is to present a concept for assessing the information content of a topographic characterization parameter. A method is presented, for quantifying the information content of a parameter, based on the number of different surfaces that a given value of a certain parameter can define. This method is tedious. A qualitative approach to the method, avoiding the tedium of the quantitative approach, is discussed.

Methods

The information content has been developed in other applications, notably design, based on the probability of achieving a desired result (Suh 1990). The basic principle is to compare the number of possible surfaces with the number of surfaces that can satisfy the topographic characterization parameter.

$$I = \ln (1/p) \qquad [1]$$

The information content is I and p is the probability that a certain parameter can be used to identify the surface as defined by the topographic data set used to calculate the parameter. When the natural log is used the units on information are nats.

$$p = n/N \qquad [2]$$

The number of possible surfaces is N. The number of surfaces that satisfy N and will have the same value for a certain topographic characterization parameter is n. N is a function of the sampling

intervals, the lengths of the sides of the topographic data set, vertical resolution and the vertical range. The number of samples in each nominally horizontal direction (x,y) is the length of that side of the data set divided by the sampling interval. The vertical range divided by the vertical resolution (z) is the number of possible elevations at each measured position. Therefore

$$N = z^{xy} \qquad [3]$$

The value of N is specific to the structure of the data set, i.e., the dimensions, sampling interval and resolution. For typical topographic data sets this tends to be extremely large numbers as x and y may be 512 and z can be greater than 4,000. However large, N is finite. Clearly not all the data sets as defined above are physically possible. Further refinement is possible, based on consideration of thermodynamics of materials, to reduce N and make it more realistic, although that is not pursued here.

The value of n must be equal to or less than N. If n and N are equal, then the information content for that parameter is zero (ln 1). The smaller n is, with respect to N, the more restrictive the parameter in terms of the number of possible topographic data sets, and the larger the information content. The total possible information content increases with respect to N. This is logical, because for large values of N, there is more information available.

In order to determine n a program was written to generate every possible data set, for a given structure, and then the roughness average, Ra (ASME B46.1 – 1995) for each possibility was evaluated. Due to the large computational times, small data sets were selected. Also because of computational limitations the Ra was not calculated from a mean line, but from the center reference line. Therefore the values of Ra tend to be larger than they would be if the mean line had been used. The Ra and values are normalized with respect to the largest value calculated for that data structure.

The data sets are profiles, 8 points (x), or samples, long. The vertical resolution was varied to include, or resolve, 8, 16, 20, 24 and 28 possible elevations (z). Since it is a profile, y=1. The value of N can be calculated to range from about 1.6×10^7 to about 13.8×10^{11}.

Results and Discussion

The number of possible data sets described by a value of Ra, depends not only on the size, or structure of the data set, but also on the value of Ra. Fig. 1 shows the distribution of n, the number of data sets described by the same Ra values as a function of the Ra value and the number of elevations. For 8 elevations the maximum number of Ra values is about 4.5×10^6, and for 28 the maximum is about 1.7×10^{10}. In both cases the maximums occur for a normalized Ra slightly over 0.5.

The information content is shown in Fig. 2 for the maximum Ra as a function of the number of elevations. The maximum Ra is the value of Ra, which describes the greatest number of possible data sets, therefore the results in Fig. 2 represent the worst case, or lowest information content. The information contents increase as the number of elevations increase, from less than 1.5 nats to greater than 3 nats. Based on the number of possible elevations the maximum possible information content can vary from 16.6 nats for 8 elevations to 26.7 nats for 28 elevations. The increase in information content of Ra with respect to the number of possible elevations in the data sets is due in part to the increased information inherent in a data set with better vertical resolution.

In the definition of information applied here, for the purpose of selecting characterization parameters, large information contents are desirable. A notable difference between this approach and that used by Suh, and a potential point of confusion, is that in Suh's axiomatic design method it is desirable to

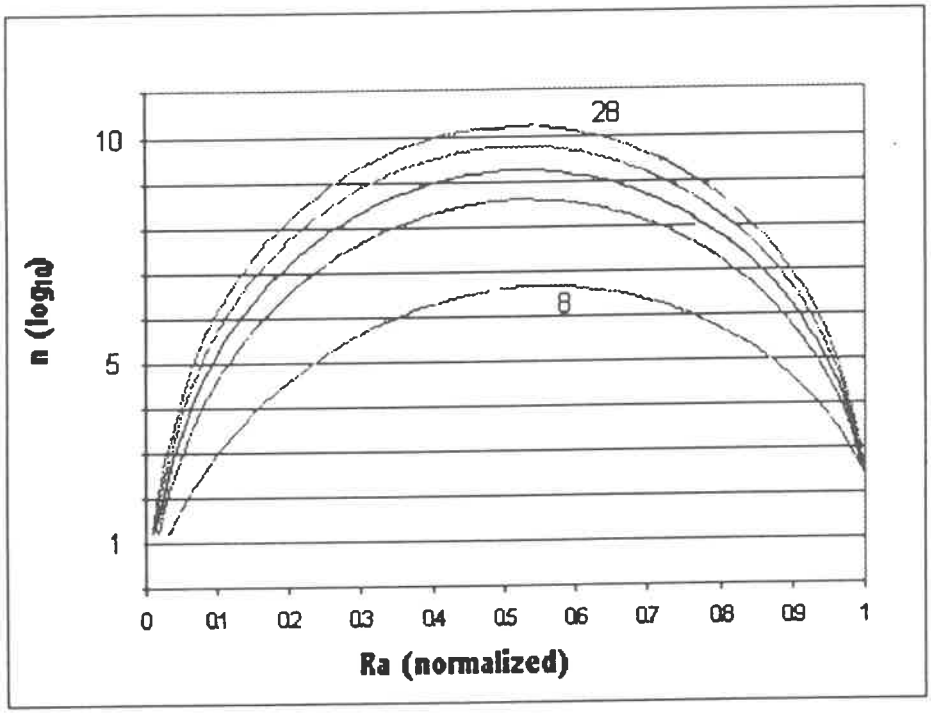

Fig. 1. The number of data sets which can be described by the same Ra, as a function of Ra. The data sets are profiles 8 points long, with 8, 16, 20, 24 and 28 elevations.

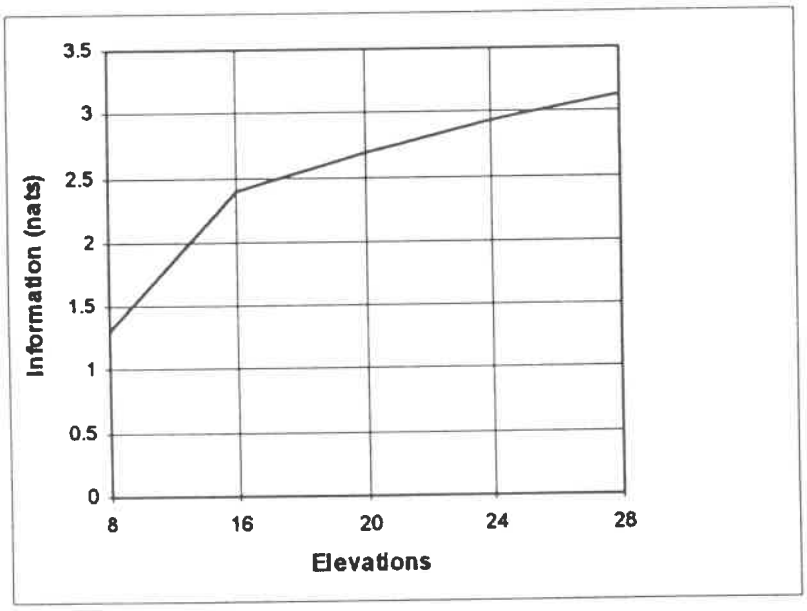

Fig. 2.The information content for Ra in a profile 8 points long as a function of the vertical resolution, given in terms of the number of elevations.

minimize the information content in a product or manufacturing system. Intuitively this follows as the less one needs to know to produce or use something, the easier it will be to do it. The purpose of a characterization in surface metrology is to provide information about the surface, therefore higher information contents are desirable for the characterization parameters. How to integrate these two approaches to information content, for use in design and in surface metrology, is the subject of further work.

This method for determining the information content is computing time intensive, and therefore awkward to apply. The potential could be developed currently in two ways: one by extrapolation to customary sized data sets from smaller data sets for which the information content can be calculated in a reasonable time; and two by identifying qualitative rules which could be applied to larger data sets. Extrapolation from the current results is not immediately obvious. More work will need to be done. Furthermore, for selection of parameters, comparisons must be applied, so calculations must be made for other parameters besides Ra.

Rules for applying the concept of information content qualitatively could be developed by considering factors, which would tend to increase the number of data sets described by a parameter. For example, discounting the complications introduced by filtering and leveling, Ra is insensitive to the order in which the points appear in a data set, and therefore should have a smaller information content than a parameter which is influenced by both the order and value of the points. In analyzing 3D data, some analysis methods are insensitive to the order of the data rows, these parameters potentially have lower information than a parameter, which is sensitive to the position of the rows.

When two or more topographic characterization parameters are used to describe a data set, there may be a method for assessing the additional information that the additional parameters bring. The correlation coefficients between the parameters (Nowicki 1985) are an indication of the redundant information.

Conclusions

1. The concept of information content of topographic characterization parameters can be applied quantitatively to small, model topographic data sets.
2. The information content in a data set varies with the size, or resolution, of the data set.
3. The information content of Ra varies with the size, or resolution, of the data set.
4. The information content of Ra is a function of the value of Ra.

References

1. ASME B46.1 – 1995, Surface Texture (surface roughness, waviness, and lay), An American National Standard, American Society of Mechanical Engineers, New York (1996).
2. Brown,C.A., Dauw,D.F., Savary,G. "Comparison of Fractal and Conventional Topographic Analysis of Electric Discharge Machined Surface Topography on Ceramics," Surface Engineering: Current Trends and Future Prospects S.A. Meguid, ed., Elsevier Applied Science, London (1990) 39-51.
3. Nowicki,B., Multiparameter representation of surface roughness, Wear (1985) 102: 161-176.
4. Suh,N.P. The Principles of Design, Oxford Press, New York (1990).
5. Terry,A.J., Brown,C.A. "A comparison of topographic characterization parameters in grinding," Annals of the CIRP (1997) 46/1 479-500.
6. Whitehouse,D.J., Handbook of Surface Metrology, Institute of Physics Publishing, Bristol (1994).

An In-line Digital Filtering Algorithm for the Surface Roughness Profiles

Seiichiro Hara*, Tadao Tsukada** and Kazuyuki Sasajima**

*Nagaoka University of Technology, Niigata, Japan

**Tokyo Institute of Technology, Tokyo, Japan

1. Introduction

A profile achieved by applying the low pass filter to the traced profile is called the primary profile(P)[1], and the roughness profile obtained by applying the high-pass filter to the primary profile(P) is called the roughness profile(P). According to ISO/DIS 11562[1], a phase correct filter (Gaussian digital filter) should be provided. In general, the batch processing of the Gaussian digital filter is widely used for the roughness profile(P).

The batch processing is performed after the whole measured data of the traced profile are stored in the computer memory. Therefore, not only long processing time is required after the measurement, but also a large size memory is demanded because a very small sampling space is adopted for the low-pass filter. Considering these problems, a desirable solution is a data processing system in which a traced profile is filtered in real time like an analogue filter.

In this report, a new filtering algorithm is developed to obtain one item of filtered data within each sampling interval by a contact stylus instrument. The authors call this algorithm the "in-line digital filter"

2. Gaussian digital filter

With a wavelength λ, the exact transfer function (amplitude-transmission characteristics) $H_L(\lambda)$ of the Gaussian filter is described by the following formula[4].

$$H_L(\lambda) = \exp\left\{-\pi\left(\alpha\,\lambda_B/\lambda\right)^2\right\} \tag{1}$$

where λ_B is cut-off wavelength described in general form. As $H_L(\lambda)$ is 50% at $\lambda=\lambda_B$, α=0.4697.

Figure 1 shows the processing time t required to obtain one item of filtered data (the time from reading the traced data, computing them and storing the filtered data into the memory by using Intel DX4 100MHz as MPU). The error ΔH of the transfer function is defined as the difference of the transfer function by discrete calculation from eq. (1) and the absolute maximum of the ΔH is expressed by ΔH_{max}. The processing times t in Fig. 1 are shown within the allowable limit ΔH_{max}=2.5% which was presented in the previous reports[2)3)]. The Gaussian convolution filter was computed by using such convolutions[3] as $\lambda_B/\Delta x \geq 12$ and $2N_g\Delta x/\lambda_B=0.9$. The processing time t of the Gaussian filter increases radically as $\lambda_B/\Delta x$ increases. Therefore some contrivances are required in order to make t smaller.

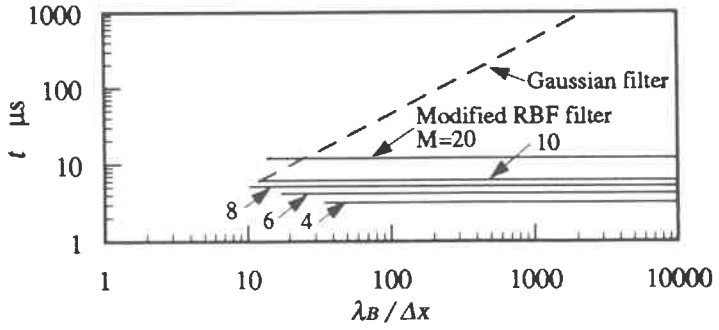

Fig. 1 Processing time to obtain one filtered data

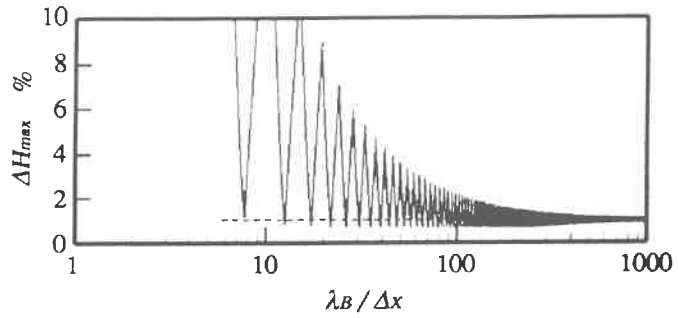

Fig. 2 ΔH_{max} of the RBF filter

There are some methods of digital filtering such as FFT or Burt's method[5], although it is very hard to apply these methods to "in-line processing". In this report, running-box-function (RBF) filters[6][7] is discussed because this filters has a similar transfer function to that of the Gaussian filter and are expected to have the ability of fast processing.

3. Running-Box-Function(RBF) filter

The RBF filter which is a iteration of running averages of succeeding N data in each step is considered. In order to diminish the number of multiplications, the output data is obtained by multiplying the data in the final step by the coefficient $1/N^M$. The number N_p of data to obtain one item of output data is given by $N_p=MN-(M-1)$. The requirement that N_p should be odd in order to obtain the output data at the positions correspond to an input data is satisfied by making M even.

The transfer function $H_L(\lambda)$ is given as follows when Δx is very small[7].

$$H_L = \left\{\sin(\pi W_x/\lambda)/(\pi W_x/\lambda)\right\}^M \tag{2}$$

W_x in eq. (2) is a length of profile for averaging which is decided for $H_L(\lambda_B)$ to become 50%.

The weighting function is the triangular form for M=2 and approaches the Gaussian distribution as M increases. The transfer function of discrete filter is described as follows by using the Fourier cosine transform of the weighting function.

$$H_L(\lambda) = \left[\sin(\pi N \Delta x/\lambda)/\left\{N \sin(\pi \Delta x/\lambda)\right\}\right]^M \tag{3}$$

Letting N_O be N satisfying the condition of $H_L(\lambda_B)$=50%, the following formula is defined.

$$\left[\sin(\pi N_O \Delta x/\lambda_B)/\left\{N_O \sin(\pi \Delta x/\lambda_B)\right\}\right]^M = 0.5 \tag{4}$$

N_O is approximated by the following formula.

$$N_O = a\,\lambda_B/\Delta x + b\,\lambda_B \cdot \Delta x \tag{5}$$

For example, a=0.228 and b=2.03 for M=8, a=0.319 and b=1.45 for M=4. Let N be the integer nearest to N_O. Then N is expressed as follows by using the Gaussian mark [ ].

$$N = \left[N_O + 0.5\right] \tag{6}$$

Figure 2 shows an example of the relation between $\lambda_B/\Delta x$ and ΔH_{max} of eq. (3) for M=8. The dotted line presents ΔH_{max} of eq. (2) which is the convergent value when Δx approaches to zero. ΔH_{max} is locally smaller than the convergent value. It is because ΔH_{max} becomes minimum at the point where the cut-off value is slightly shifted from λ_B. However the shifted value is smaller than $\lambda_B/500$ for the example of Fig. 2. ΔH_{max} increases when the

shifted cut-off value $\Delta\lambda_B$ occurs due to unconformity of N with N_O. Therefore, it is necessary to reduce $\Delta\lambda_B$ in the region of small $\lambda_B/\Delta x$.

4. Modified Running Box Function filter

An ability to reduce $\Delta\lambda_B$ is expected by appropriately combining the steps of the different number N_m of data with those of the N data. N_m is the number of data in m-th step and is given by (N+1) or (N-1) in this report. The steps of (N+1) or (N-1) data are called the modified steps, and this filtering method is designated as the modified RBF filter in this report.

The transfer function $H_L(\lambda)$ is

$$H_L(\lambda) = \prod_{m=1}^{M} h_m$$
$$h_m = \sin\left(\pi N_m \Delta x\ \lambda\right) \Big/ \left\{N_m \sin\left(\pi \Delta x\ \lambda\right)\right\} \tag{7}$$

The data in the final step is multiplied for averaging by the following coefficient C.

$$C = 1 \Big/ \prod_{m=1}^{M} N_m \tag{8}$$

N_p should be odd according to the reason stated above. Supposing that the number of the modified steps is q, this requirement is satisfied sufficiently by making both of M and q be even. For example, in the case of M=8 and N=3 (this condition corresponds to $\lambda_B/\Delta x \gg 12$), the solid lines in Fig. 3 show the relation between ΔH_{max} and (N_O-N) of the modified RBF filter which consists of an appropriate combination of modified steps replacing N with N_m=N-1 or N_m=N+1. The dashed lines illustrate a portion of Fig. 2 of the RBF filter.

N of the RBF filter changes at the position marked with the symbol ●. ΔH_{max} increases as N is shifted from N_O. On the other hand, for the modified RBF filter, N_m changes at many positions indicated by the symbol ○. The ΔH_{max} of the modified RBF filter is greatly reduced in comparison with that of the RBF filter.

It is evident from Fig. 2 that ΔH_{max} decreases as $\lambda_B/\Delta x$ increases. In order to simplify the application of the modified RBF filter, the condition applied to small $\lambda_B/\Delta x$, e.g. N=3, may be utilized over the whole range of $\lambda_B/\Delta x$. Table 1 presents the conditions corresponding with the symbols of ○ in Fig. 3. From eq. (7), it is known that the modified step is allowed to be situated at any step in sequence of M-steps. Figure 4 shows the relation between $\lambda_B/\Delta x$ and ΔH_{max} calculated by using the conditions of Table 2. The ΔH_{max} is considerably smaller than that of the RBF filter shown in Fig. 2 and converges to the value of dashed line in the region of $\lambda_B/\Delta x$>60.

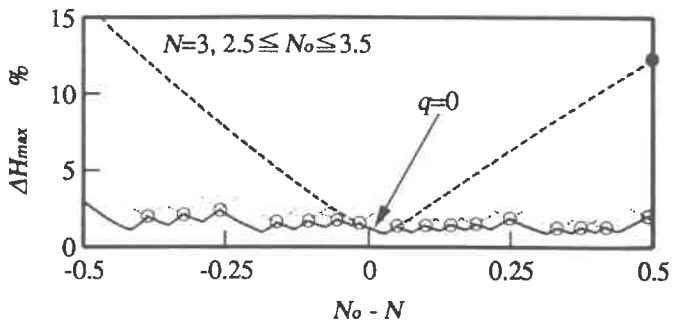

Fig. 3 Relation between N-N_O and ΔH_{max}

Because the processing time t of the RBF filter depends only on M as shown in Fig. 1, this filter is especially effective for the high-pass filter using the very large $\lambda_B/\Delta x$. This filter has an advantage over the gaussian filter concerning the processing time even when these filters are used as an low-

Table 1 N_m of the modified 8-step RBF filter

q	Range of N_O-N over	up to	Number of steps modified by N_m=N-1	N_m=N	N_m=N+1
4	-0.500	-0.385	4	4	0
6	-0.385	-0.323	5	2	1
8	-0.323	-0.262	6	0	2
2	-0.262	-0.160	2	6	0
		:			
		:			
8	0.418	0.491	3	0	5
4	0.491	0.500	0	4	4

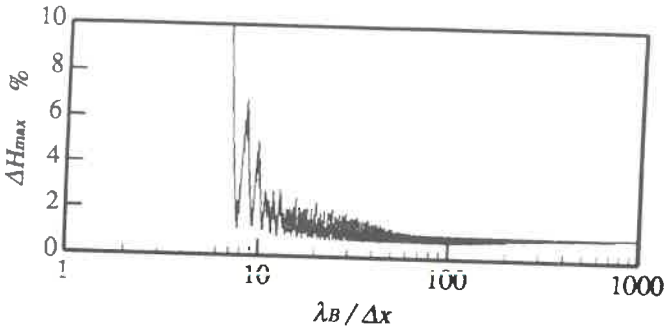

Fig. 4 ΔH_{max} of the modified 8-step RBF filter

pass filters to eliminate the short wavelength signals.

Consider using the modified RBF filter as the low-pass filter of short cut-off, it is desirable that Δx be larger. Allowable $\lambda_B/\Delta x$ becomes minimum when M=8[2]. Therefore M=8 is considered to be a suitable condition.

For the high-pass filter which is applied to the condition of large $\lambda_B/\Delta x$, the 4-step RBF filter may be sufficient[3].

4. Conclusions

The following conclusions were reached.

(1) In the Gaussian convolution, the processing time t increases as $\lambda_B/\Delta x$ increases. In contrast, t of the RBF filter does not depend on $\lambda_B/\Delta x$ and becomes remarkably shorter. Therefore, this filter is suitable for the fast processing.

(2) The modified RBF filter was newly developed in order to reduce the error of transfer function for small $\lambda_B/\Delta x$ and it was found that the 8-step modified RBF filter is suitable as a low-pass filter to eliminate short wave length signals.

(3) The 4-step RBF filter is sufficient as a high-pass filter which is applied in the region that $\lambda_B/\Delta x$ is large.

References

1) ISO/DIS 11562-1994: Metrological characterization of phase corrected filters and transmission bands for use in contact instruments.

2) S. Hara, T. Tsukada and M. Ito : The Conditions to Apply the Phase Corrected Filter to Traced Profiles for Roughness profiles (2nd Report) (in Japanese), Jour. Japan Soc. for Precision Engineering, **62**, 7, (1996)953.

3) S. Hara, T. Tsukada and M. Ito : The Conditions to Apply the Phase Corrected Filter to Traced Profiles for Roughness profiles (1st Report) (in Japanese), Jour. Japan Soc. for Precision Engineering, **62**, 4, (1996)501.

4) ISO 468-1982, Surface roughness — Parameters, their values and general rules for specifying requirements.

5) P. J. Burt: Fast Algorithms for Estimating Local Image Properties, Computer Vision, Graphics and Image Processing, **21**, (1983)368.

6) W. M. Wells : Efficient Synthesis of Gaussian Filters by Cascaded Uniform Filters, IEEE Trans. Pattern Analysis and Machine Intelligence, **PAMI-8**, 2, (1986)234.

7) D. J. Whitehouse: Handbook of Surface Metrology, Inst. Physics Publ., London, (1994)283.

NOISE-INSENSITIVE PHASE UNWRAPING IN PHASE SHIFT LASER INTERFEROMETRIC SURFACE MEASUREMENT: A WAVELETS BASED METHOD

Yiding Wang and **Kee S. Moon**
Department of Mechanical Engineering and Engineering Mechanics
Michigan Technological University
Houghton, MI

ABSTRACT

For phase shift laser interferometric surface measurement, the manipulation of the obtained phase shift data usually results in a set of principal values of inverse tangent function. The measured surface can be reconstructed from these values through phase unwrapping algorithm. This process is often degraded by a combination of surface defects and measurement noise, resulting in improper phase reconstruction. In this paper, a denoising technique which is based on wavelets transformation method is proposed. This method utilize nonlinear operation in the wavelet domain and accomplish tasks which are not possible by traditional linear or Fourier approaches. Simulations show that this method can effectively reduce the risk of false detection of phase change caused by noise and provide a noise-insensitive phase unwrapping algorithm.

PRINCIPLES FOR PHASE SHIFT LASER INTERFEROMETRIC MEASUREMENT

In phase-shift laser interferometric system, the interferogram pixel intensities are given by:

$$I_i(x,y) = I_0(x,y)\{1+\gamma(x,y)\cos[\theta(x,y)+\phi_i]\} \quad (1)$$

where: $I_i(x,y)$ is the intensity at a pixel of the ith interferogram, $I_0(x,y)$ is the average intensity, $\gamma(x,y)$ is the intensity modulation, $\theta(x,y)$ is the phase of the wave front being measured, and ϕ_i is the reference beam phase shift.

For the commonly used four phase-shift technique, the phase shifter moves three steps, each step corresponding to a $\pi/2$ phase shift. Solving for θ leads to:

$$\theta(x,y) = \operatorname{atan}\left(\frac{I_4 - I_2}{I_1 - I_3}\right) \quad (2)$$

The surface height can be calculated by:

$$h(x,y) = \frac{\lambda}{4\pi}\theta(x,y) \quad (3)$$

where λ is the wave length of the laser beam.

In this process, the solutions of atan() contains the principal values between $-\pi/2$ and $\pi/2$, a discontinuity exists for every phase change of π. The result is represented as a saw tooth profile. Therefore, unwrapping algorithms are needed to reconstruct the surface from these calculated principal values. This is usually accomplished by detecting the phase jump from $\pi/2$ to $-\pi/2$. In actual measurement condition, if the measurement noise or surface defects are big, there is a risk that phase unwrapping algorithm can false detect the phase jump from $\pi/2$ to $-\pi/2$, resulting in misrepresentation of the reconstructed surfaces.

Figure 1. is an interferogram for a clean plane surface along with its reconstructed surface. It is evident that in the case which no noise is introduced into the interferogram, the unwrapped surface can accurately reconstruct the original surface. Figure 2 is an interferogram with added noise which has a signal to noise ratio (S/N) of 7 along with its reconstructed surface. In this case, some false detections of the phase jumps from $\pi/2$ to $-\pi/2$ occur and propagate into the following data processing routine, resulting in a biased representation of the measurement surface. Figure 3 is the interferogram of a plane surface with the added noise which has a signal to noise ratio (S/N) of 20. In this case, the noise does not cause false detection of the phase jumps from $\pi/2$ to $-\pi/2$, which means the signal is strong enough to overcome the effect of noise in surface reconstruction. However, the reconstructed surface contains the manipulated noise content, resulting in the decrease of the accuracy of the algorithm.

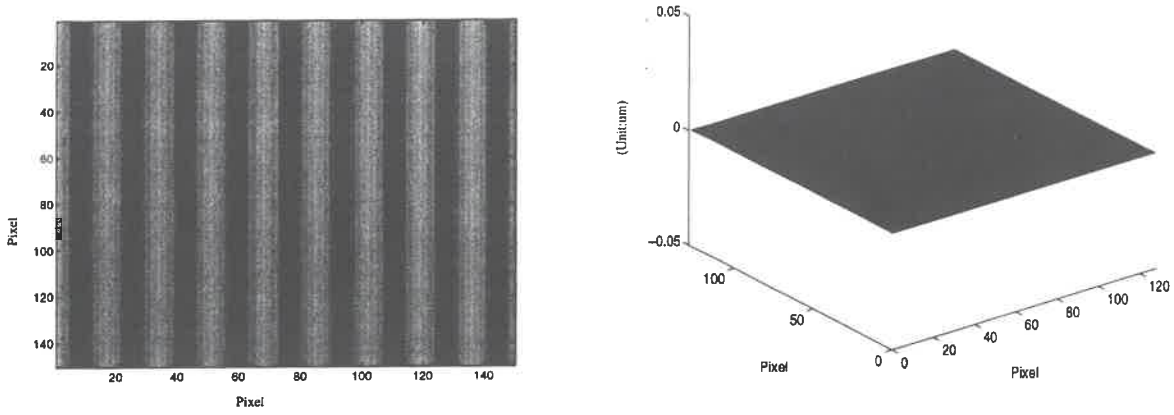

FIG. 1. INTERFEROGRAM OF A PLANE SURFACE WITHOUT NOISE VS. THE RECONSTRUCTED SURFACE

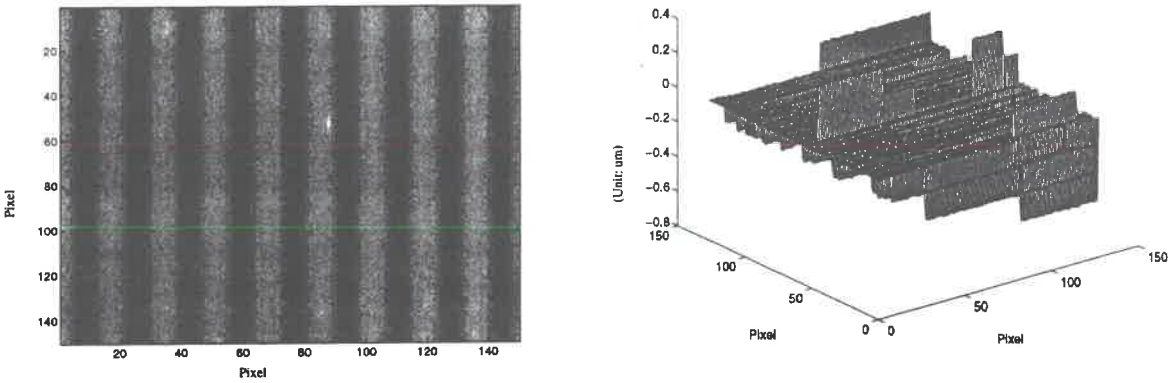

FIG. 2. INTERFEROGRAM OF A PLANE SURFACE WITH NOISE VS. THE RECONSTRUCTED SURFACE (S/N=7)

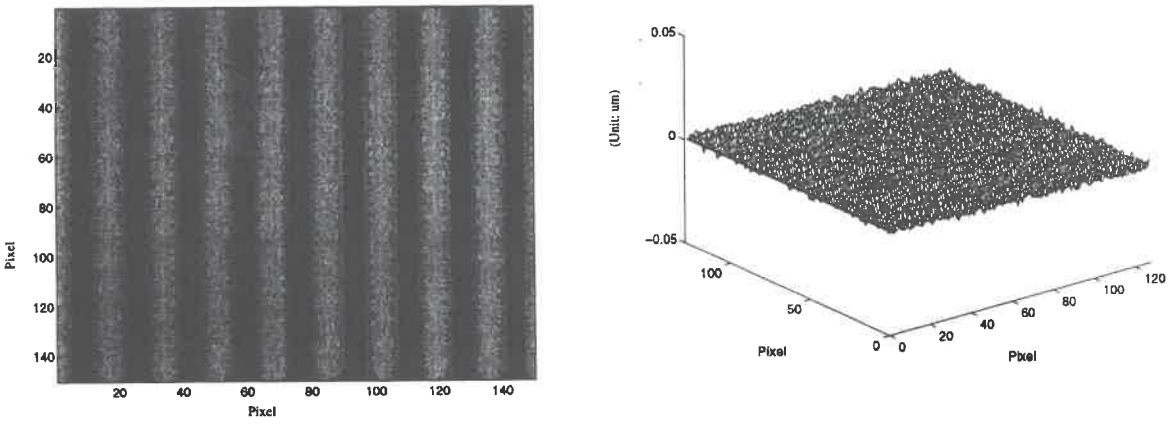

FIG. 3. INTERFEROGRAM OF A PLANE SURFACE WITH NOISE VS. THE RECONSTRUCTED SURFACE (S/N=20)

Besides the four-frame technique, lots of phase shift strategies exist to extract the measurement phase from

the interferograms. The most popular ones are three-frame technique, five-frame technique, Carre technique, "2+1" technique, "N+1" technique [2]. Each algorithm has its own edges and shortcomings in reducing a particular kind of errors. Generally, the more the phase shift are made, the more the effect that random factors have on the unwrapped phase. Denoising for the interferograms is critical for any phase shift technique and a problem-independent denoising algorithm is needed.

WAVELET METHOD FOR DENOISING OF INTERFEROGRAMS

The wavelets method has been finding more and more applications in engineering practices due to its significant advantages over the traditional signal processing techniques. The wavelets transform is a tool that cuts up data or functions or operations into different frequency components, and then studies each component with a resolution matched to its scale. The wavelet transform has the following format which is similar to the Fourier transformation and provides a time-frequency description of the signal [15].

$$\left(T^{wav}f\right)(a,b) = |a|^{-\frac{1}{2}}\int f(t)\,\psi\left(\frac{t-a}{b}\right)dt \tag{4}$$

The functions $\psi^{a,b}$ are called "wavelets"; the function ψ is sometimes called "mother wavelet." As a changes, the $\psi^{a,0}(s)=|a|^{-1/2}\psi(s/a)$ cover different frequency ranges (large values of the scaling parameter $|a|$ correspond to small frequencies or large scale $\psi^{a,0}$, small values of $|a|$ correspond to high frequencies or very fine scale $\psi^{a,0}$. Changing the parameter b allows us to move the time location center: each $\psi^{a,b}(s)$ is localized around $s=b$.

The wavelets transformation can be used in the denoising of noisy signals [14]. Suppose we are interested in a function $f(t)$ on the unit interval $t \in [0, 1]$ and we have $n=2^{J+1}$ data $y_i = f(t_i) + \sigma z_i$, $i=1,\ldots, n$; here the t_i are equispaced and the z_i a white noise. For recovery of $f(t)$ from the noisy signal, the following three steps are performed:

(1) Perform the pre-conditioned, interval-adapted, pyramid wavelet filtering of Cohen, Daubechies, Jawerth and Vial to the data $\beta_{J+1,k} = \frac{y_k}{\sqrt{n}}$, yielding noisy wavelet coefficients, $w_{j,k}$, $j=j_0,\ldots,J$, $k=0,\ldots,2^j-1$.

(2) Apply the soft-threshold nonlinearity $\eta_t(w) = \mathrm{sgn}(w)\,(|w|-t)$ to the noisy empirical wavelet coefficients, with threshold $t = \frac{\sqrt{2\log(n)}}{\sqrt{n}}\sigma$, yielding estimates $\hat{\alpha}_{j,k}$.

(3) Set all wavelet coefficients $\hat{\alpha}_{j,k} = 0$ for $j>J$, invert the wavelet transform, producing the estimate $\hat{f}(t)$, $t \in [0, 1]$.

This behavior is very different from traditional linear methods of smoothening, which achieve noise suppression only by broadening features significantly.

SIMULATION RESULTS

The wavelet denoising procedure discussed above is applied in the denoising of four-frame phase shift laser interferometric measurement system. The obtained interferograms are first denoised before performing phase unwrapping and reconstruction. For ease of illustration, the results of denoising one scan line is given. As a comparison with fig. 2, the scan line is picked up from the interferogram of fig. 2. The wavelet denoising procedure is performed and the results are illustrated in fig. 4. It is evident that the noise content in the interferogram has been effectively suppressed. No false detection of phase jump occurs as in figure 2. The RMS error of the reconstructed scan line after denoising is 2.2nm. Figure 5 is the reconstruction of a scan line with a scratch of 40 nm in depth. It is seen that this scratch can be clearly reconstructed.

CONCLUSIONS

This paper addresses the problem of the errors caused by the noise in the phase shift laser interferometric measurement. It has been shown that false detection of the phase jump from $\pi/2$ to $-\pi/2$ can occur and cause the biased reconstruction of the measurement surface when the signal to noise ratio is not big enough. The nanoscale measurement capability of the interferometric methods is greatly affected in the presence of noise. A new denoising technique based on wavelet transformation is proposed. Simulation of denoising of a scan line in the interferogram shows that this method can effectively suppress the noise and accurately reconstruct the surface. This procedure is robust and works well in the presence strong noise. It is not problem dependent and therefore requires minimal skill in application. This algorithm can be easily used in the phase shift laser interferometer measurement method.

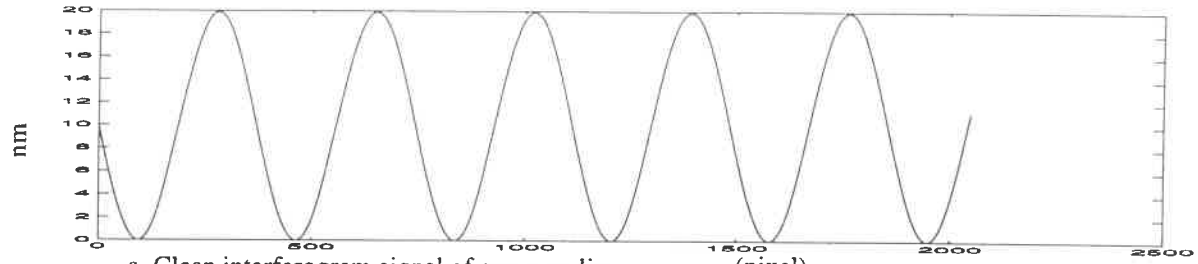

a. Clean interferogram signal of one scan line

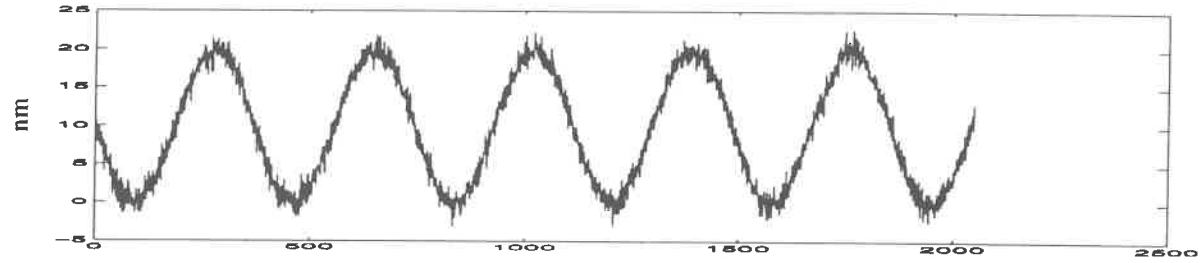

b. The signal in a. with added noise.

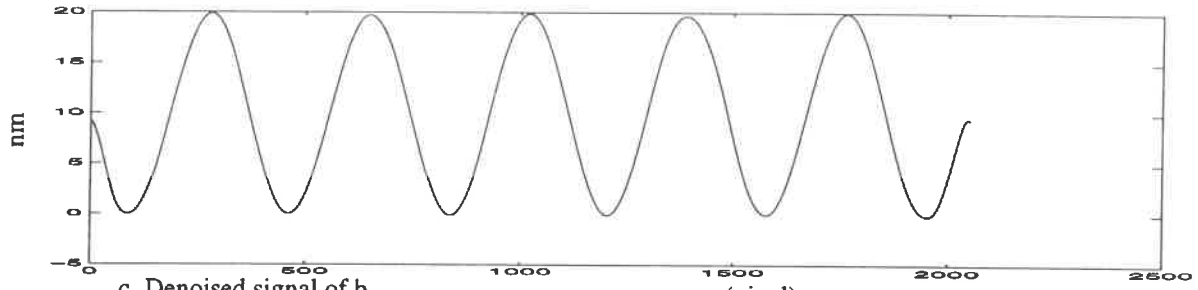

c. Denoised signal of b.

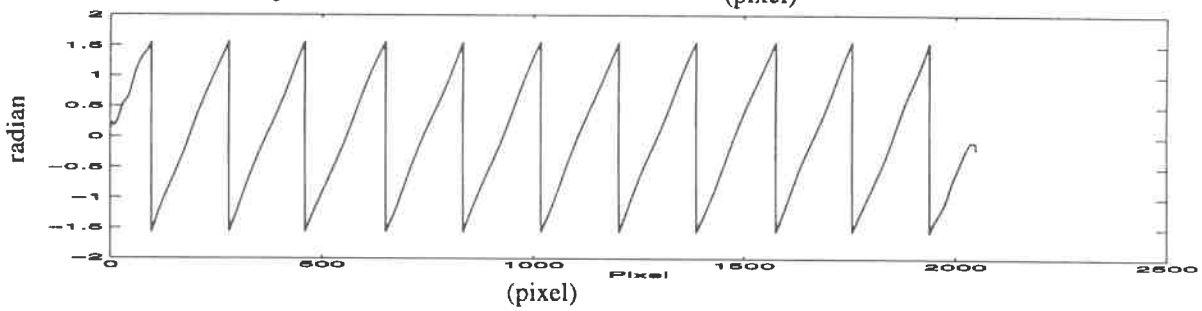

d. Wrapped phase of the denoised signal from four phase-shift interferograms.

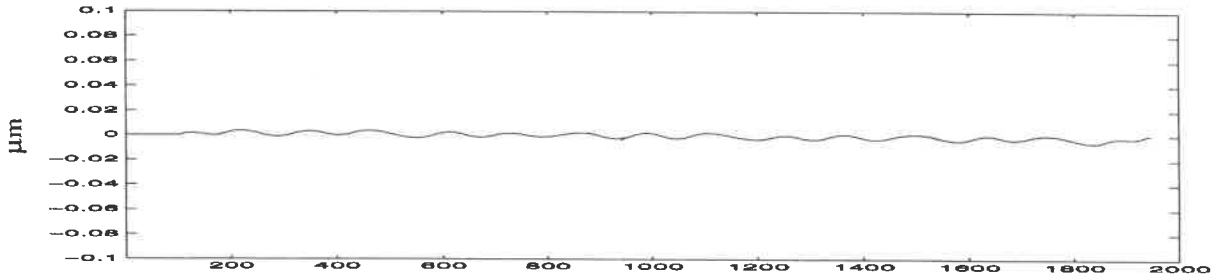

e. Reconstructed one scan line of the surface after denoising.

FIG. 4. WAVELET DENOISING OF ONE SCAN LINE FOR MEASURING A PLANE SURFACE BY PHASE SHIFT LASER INTERFEROMETRY

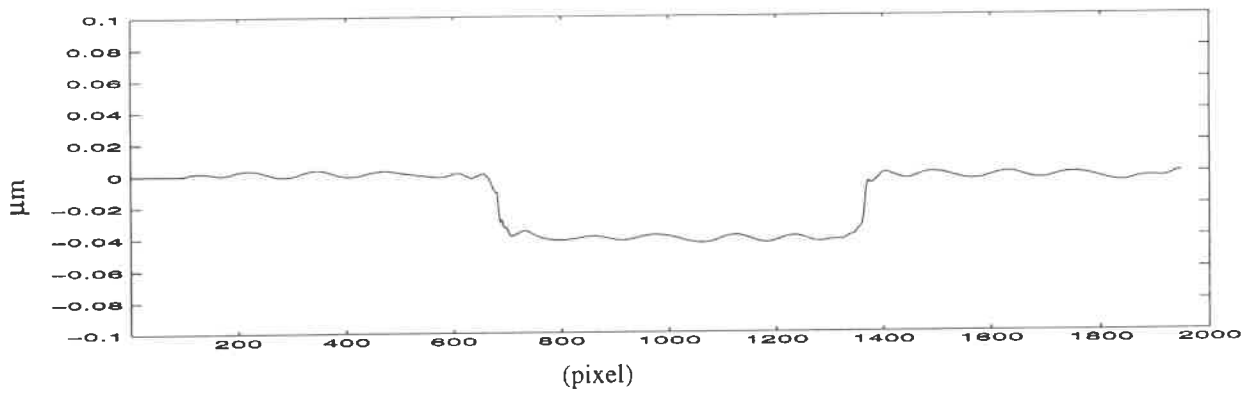

FIG. 5. RECONSTRUCTION OF A SCAN LINE WITH A SCRATCH OF 40nm IN DEPTH USING WAVELETS DENOISING METHOD

REFERENCES

1. J. H. Bruning, D. R. Herriott, G. H. Gallagher, D. P. Rosenfeld, A. D. White and D. J. Brangaccio, "Digital Wavefront Measuring Interferometer for Testing Optical Surfaces and Lenses." *Applied Optics*, Vol. 13, No. 11, 1974, pp. 2693-2703.

2. K. Creath, "Temporal Phase Measurement Methods," in *Interferogram Analysis*, D. Robinson and G. T. Reid, eds. Institute of Physics, University of Reading, Berkshire, UK, 1993, pp. 95-140.

3. J. Schwider, R. Burow, K. -E. Elssner, J. Grzanna, R. Spolaczyk and K. Merkel, "Digital, Wave-front Measurement Interferometry: some systematic error sources." *Applied Optics*, Vol. 22, No. 21, 1983, pp. 3421-3432.

4.J. V. Wingerden, H. J. Frankena and C. Smorenburg, "Linear Approximation for Measurement Errors in Phase Shifting Interferometry." *Applied Optics*, Vol. 30, No. 19, 1991, pp. 2718-2729.

5. C. Ai and J. C. Wyant, "Effect of Piezoelectric Transducer Nonlinearility on Phase Shift Interferometry." *Applied Optics*, Vol. 26, No. 6, 1987, pp. 1112-1116.

6. Y. Cheng and J. C. Wyant, "Phase Shifter Calibration in Phase-Shifting Interferometry." *Applied Optics*, Vol. 24, No. 18, 1985, pp. 3049-3052.

7. C. P. Brophy, "Effect of Intensity Error Correlation on the Computed Phase of Phase-Shifting Interferometry." Journal of the Optical Society of America. Vol. 7, No. 4, 1990, pp. 537-541.

8. P. Hariharan, B. F. Oreb and T. Eiju, "A Simple Error-Compensating Phase Calculation." *Applied Optics*, Vol. 26, No. 13, 1987, pp. 2504-2507.

9. Y. Surrel, "Design of Algorithms for Phase Measurements by the Use of Phase Stepping." *Applied Optics*, Vol. 35, No. 1, 1996, pp. 51-60.

10. J. A. Quiroga and E. Bernabeu, "Phase-unwrapping Algorithm for Noise Phase-map Processing." *Applied Optics*, Vol. 33, No. 29, 1991, pp. 6725-6731.

11. E. J. Salisbury, K. S. Moon and J. W. Sutherland, "Nano-Surface Texture Measurement Using Laser Interferometry and Image Synthesis." *Manufacturing Science and Engineering*. PED-Vol. 68-1. ASME, 1994.

12. S. M. Pandit, N. Jordache and G. A. Joshi, "Data -dependent Systems Methodology for Noise-insitive Phase Unwrapping in Laser Interferometric Surface Characterization." Journal of The Optical Society of America. A/ Vol. 11, No. 10. pp.2584-2592.

13. S. M. Pandit and G. A. Joshi, "Image Enhancement: A Data Dependent Systems Approach." *Transactions of the ASME, Journal of Engineering for Industry*. Vol. 116, pp. 247-252. 1994.

14. D. L. Donoho, "Nonlinear Wavelet Methods for Recovery of Signals, Densities, and Spectra from Indirect and Noise Data." Proceedings of Symposia in Applied Mathematics. pp. 173-205. 1993.

15. I. Daubechies, *Ten Lectures on Wavelets*. Philadelphia: SIAM. 1992

TRACEABLE DIAMETER MEASUREMENTS OF THIN WIRES

O. Jusko, H. Bosse, G. Frase, F. Lüdicke, W. Tang[†]

Physikalisch-Technische Bundesanstalt
Braunschweig, Germany

[†]Harbin Institute of Technology
Harbin, China

1. INTRODUCTION

Throughout the wire industry the problem of diameter traceability has become very important. So far, there is no established measurement technique for diameter measurements, which delivers low measurement uncertainties and is traceable to national standards. But traceability is an important criterion for an ISO 9000 accreditation, which is aimed by the whole industry.

The most established measurement technique in industry for diameter measurements of wires of diameters below approx. 0,5 mm is (laser-) light diffraction. Diffraction based instruments supply quite reproducible results and generally have very fast data analysis capabilities, making them suitable for in-process control. The disadvantage of present diffraction based instruments is the lack of a known measurement uncertainty and traceability.

PTB therefore is a partner in a joint European project (ABSODIAM = ABSOolute DIAMeter measurement of wires) with the aim to improve the techniques of diffraction based instruments with respect to stability and measurement uncertainty. This includes improvements of the theory on which the diffraction analysis in the instrument software is based.

2. COMPARISON MEASUREMENTS

The measurement possibilities and uncertainty of the diffraction method should be investigated. Therefore comparison measurements were performed.

A choice of about 50 wires with diameters between 0,1 mm and 0,5 mm from different sources was acquired for the comparison measurements. Under them were gauge wires (manufacturers: Mahr, Pampel, Messwelk) and weaving wires (Sprint Metal). About the same number of wires was acquired from a further manufacturer (Feinmeßtechnik).

Gauge wires are produced to deal as dimensional standards for example for thread gauging. Therefore it was assumed that their quality is high. For their application it is necessary that their nominal diameter value is valid within narrow bounds. Most gauge wires are made from hardened steel with an additional surface lapping process. The steel-type is not resistant to corrosion, therefore they are shipped with a cover of grease and must be re-greased after use. The hardened steel prevents plastic deformation while handling or measuring with mechanical contact. Gauge wires are shipped as small straight cut pieces of about 25 mm to 45 mm length. Such pieces were used for the measurement as shipped.

Weaving wires are produced by a drawing process. It is known that their surface finish is of high quality. This is also a demand for their final application. Weaving wires are produced from non-corrosive steel and can therefore be handled and shipped without further cover grease. Weaving wires are shipped on reels. Cut pieces are therefore not as straight as gauge wires. For the measurements pieces between 50 mm and 300 mm were cut.

2.1 Check of Wire Quality

There is no standard procedure for the assessment of wire quality. It was therefore decided to inspect their surface by microscopy. Although a light microscope might have sufficient resolution for this task, a scanning electron microscope was chosen. Its larger depth of focus is helpful for imaging the whole three-dimensional wire semi-cylinder in a single micrograph.

The micrographs were performed with a Philipps standard SEM, operating with an acceleration voltage of 10 kV.

From the micrographs can be deduced that the surface quality of the weaving wires is generally of superior quality compared to the gauge wires. This will be demonstrated by two examples.

Fig. 1 shows a typical weaving wire. The surface is smooth with only a low density of flat protrusions. Some traces of the drawing process (drawing die finger print) are visible.

Fig. 2 shows a typical gauge wire. There are also some axial traces but they do not dominant the texture. More apparent are the large number of protrusions or out-broken material. Generally this is not the surface of dimensional standard of high local reproducibility. Yet, it was decided to include also such wires, because of the need of hardened steel artifacts for mechanical contact measurements.

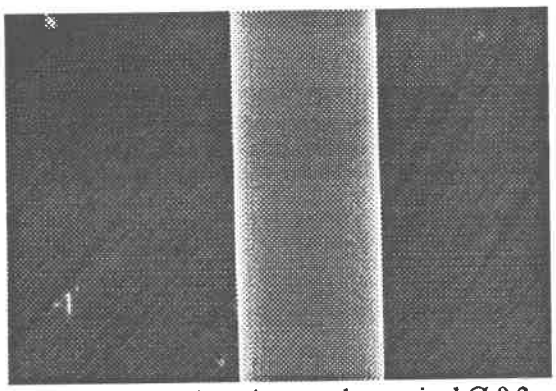

Fig. 1 weaving wire micrograph, nominal ∅ 0,2 mm

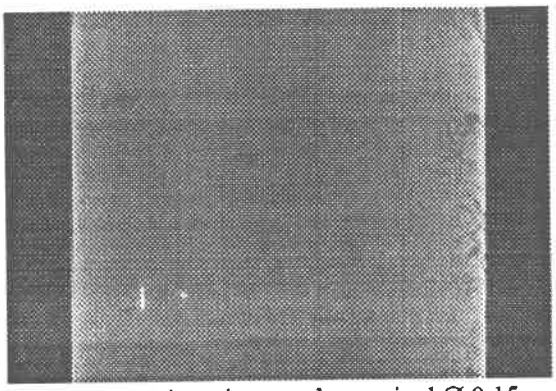

Fig. 2 gauge wire micrograph, nominal ∅ 0,15 mm

2.2 Measurement Equipment

For the measurements PTB's dimensional standard instruments were used. Under them are the 'INCO' and the 'EOMS'.

The Abbe Length Interference Comparator (INCO) is a one-dimensional diameter measurement system following the comparator principle [1]. Its construction obeys Abbe's principle and the reference, a cadmium spectral-lamp, is directly traceable to the national length standard. The diameter measurement works by utilizing the three-body method. Wire measurements are possible down to 0,15 mm diameter.

The EOMS is a new electron optics based two-dimensional metrology prototype system of the PTB [2]. The EOMS consists of a very low-energy electron microscope combined with a two-dimensional X-Y-stage equipped with laser-interferometry in high-vacuum.

The comparison was made to the results of the Diffraction Analysis System ('DAS'), a commercially available diffraction-based wire diameter measurement instrument (manufacturer: KJM GmbH, Germany).

2.3 INCO measurements

The wires under test were firmly mounted by two screws in a distance of about 6 mm. Both sides of the wire were contacted with the touching element. The touching force amounted between 15 µN and 50 µN. All wires were measured in two different orthogonal polar orientations and about 5 repeat measurements were performed. Each single measurement lasted about a full day, including thermal conditioning.

In case of the hardened steel samples, i.e. the gauge wires, the reproducibility of single point repeat measurements was high, about 50 nm to 150 nm. But because of the bad surface quality of the gauge wires, diameter measurement results at randomly chosen positions varied up to about 1 micrometre for the wires with the worst surfaces.

The measurement results of the weaving wires showed a lower reproducibility for single point repeat measurement, but a more stable statistics for randomly chosen positions.

2.4 DAS measurements

Weaving wires were clamped by the standard air-pressure clamps of the DAS. For wires with diameters of more than 0,2 mm the position is held firmly by the clamps. The reproducibility of the wire position was quite low. The diffraction pattern was used to check for a suitable position.

The gauge wire pieces were too short for the air-pressure clamps. Therefore a special wire holder was built, similar to the calibration sample holder of KJM, which fits into the slit of the optics setup of the DAS. The wire is fixed by two screws which press onto rubber plates in contact with the wire. The wire holder can be put out and in of the DAS without significantly influencing the position of the wire with respect to the optical system.

For the measurements of this workpackage nothing except the measurement range was adjusted in DAS system. Especially the factory-shipped correction constants in the software were not touched.

2.6 EOMS Measurements

Wire measurements with the EOMS follow this principle: The edge of the left side of the wire is approximately moved to the center of the scanning area of the electron beam and the resulting SEM-image is stored. Then the X-Y-stage is moved until the right edge of the wire is approximately centered. Again a SEM image is stored. The precise position of the wire edges in the image is calculated by applying an edge finding algorithm. The distance between both positions can be read from the laser-interferometer.

3. Results

Table 1 lists the measured diameter values (in µm) derived with the DAS and the INCO for the chosen wires. A measurement uncertainty for the INCO-measurement is given.

Wire	nominal dia.	INCO	uncertainty	DAS	difference
M1	200	199,9	0,2	199,6	-0,3
M2	500	500,5	0,3	499,6	-0,9
M3	150	150,2	0,2	149,7	-0,5
P1	150	150,0	0,2	149,5	-0,5
P2	300	300,4	0,2	300,2	-0,2
MW	200	199,8	0,1	199,8	0,0
SM1	200	199,8	0,1	199,9	0,0
SM2	300	299,2	0,1	299,3	0,1

Table 1: measured diameter values (in µm) for a choice of wires

Table 2 lists five test series of a diameter measurement with the EOMS system for a selected wire (Sprint Metall 0,2 mm). The 'position' parameter indicated different image positions while measuring. Its variation shall deal as an indicator for the reproducibility of the system.

Position	series 1	series 2	series 3	series 4	series 5	mean	std. dev.
1 (0 µm)	200,939	200,940	200,935	200,942	200,948	200,941	0,005
2 (20 µm)	200,987	200,980	200,982	200,979	200,972	200,980	0,005
3 (40 µm)	200,972	200,967	200,959	200,976	200,966	200,968	0,007
4 (60 µm)	200,948	200,940	200,937	200,942	200,934	200,940	0,005
5 (80 µm)	200,951	200,955	200,963	200,960	200,956	200,957	0,005
mean	200,959	200,956	200,955	200,960	200,955		
std. dev	0,019	0,017	0,020	0,018	0,015		

Table 2: EOMS instrument measured diameter values (in µm) for a selected wire (SM1)

Table 1 shows nice corresponding diameter values of both measurement devices for wires with sufficient quality. In some cases the agreement is worse. These are generally wires of very bad quality. It is therefore important to have wires of satisfying quality available for further measurements. The larger deviation for the 500µm wire is explainable by the bad quality of the diffraction pattern in the DAS for larger objects.

The absolute EOMS measurement data values in table 2 are about 1 µm higher than the corresponding values for the same wire of table 1. But the difference in the axial positions of the wire was not determined. Therefore diameter variations may responsible for the difference. The low standard deviation of the different series is already quite promising.

4. Conclusions and Outlook

The achieved results are already quite promising and proof that current diffraction based instruments are suitable for high precision measurements. But the current limits of the diffraction method could not be reached, because the quality of industrially available wires is just too low. Therefore the comparison will be rerun with custom-produced high quality wires. The running project ABSODIAM includes the development of a optically and mechanically more stable diffraction instrument and of advanced analysis diffraction theory to be put implemented into the software of the instrument. The measurement uncertainty will also benefit from those improvements. The final aim is a diffraction-based measurement technique, which can be utilized in the same way and with a known low measurement uncertainty (i.e. about 50 nm to 100 nm) in national standard laboratory and in a production line in industry.

5. Acknowledgments

Part of this work was supported by the EU under contract number SMT4-CT95-2042

6. References

[1] F. Lüdicke, and H.J. Rademacher, Bestimmung von Maß und Form an Zylindern, PTB-Mitteilungen, 6 (1989)

[2] H. Bosse, W. Häßler-Grohne, A new Instrument for Pattern Placement Calibration Using an Electron Beam Probe, Proc 9th IPES / UME-4, Braunschweig 1997

HIGH PRECISION STRAIGHT MOTION AND MEASUREMENT TECHNIQUE APPLYING OPTICAL DATUM

Mu Yunjun*, Lin Enhao**, Wan De-an*
*Department of Mechanical Engineering, Tongji University, Shanghai, P. R. China
**Department of Mechanical Engineering, Shanghai JiaoTong University, P.R. China

A highly accurate straightness datum is critical to high precision alignment and measurement of straightness and flatness. Laser beam is expected to be ideal straightness datum in case the beam drift caused by the thermal deformation of the laser tube and the environment disturbance can be controlled within desired limits. For this purpose, a device of direction stabilization of laser beam drift is developed. The scheme is showed in figure 1.

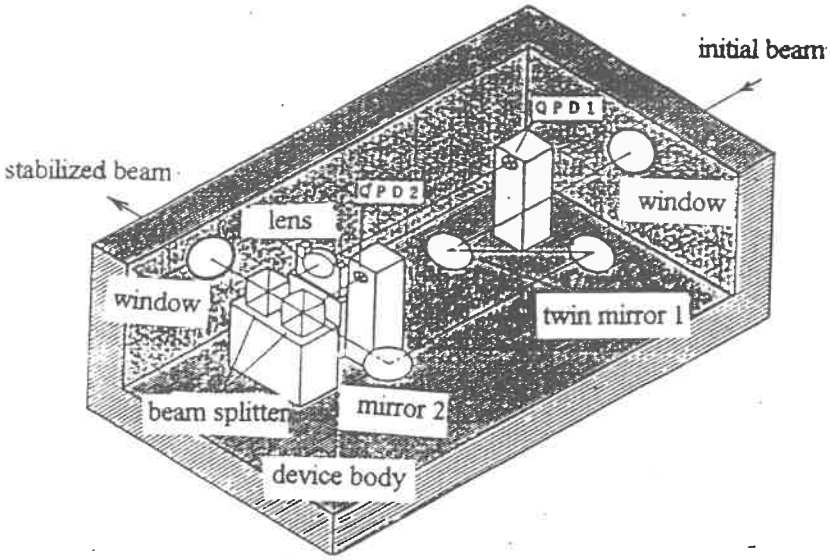

Fig. 1 Scheme of direction stabilization of laser beam drift

At beam splitter, one column of beam goes through lens and reach QPD1, which can only detect the angular drift rather than positional drift because of the centering act of the lens. The angular drift signal is fed back to the piezo-actuator which adjusts the rolling angles of mirror 2 so that the angular drift is compensated; The other column of beam goes directly to QPD2, which only detects the positional drift because the angular drift has been compensated. In the same way, the signal from QPD2 is fed back to compensate the positional drift through driving the piezo-acutors which adjust the position of twin mirror 1.

To reduce the disturbance factor of atmosphere fluctuation, we design a sliding pipe, which is able to maintain a vacuum of 0.01 atm in 2-3 hours, to protect the outside laser beam.

Figure 2 shows the effect of the stabilization device. Experimental results show that angular drift of less than 2×10^{-8} rad and positional drift of less than 3nm can be maintained by the stabilization device.

In order to realize straight motion at the highest level of accuracy, a theoretical method is introduced

which is aimed to precisely control the five freedom of a moving table: vertical, horizontal, pitch, roll, and yaw angles, by using 3 parallel laser beams. A more practical device using 2 parallel beams as datum is developed, its scheme is showed in figure 3. The device can be used to measure and compensate the error of straight motion. QPD1 and QPD2 are mounted in the same horizontal holder with distance of 70mm. QPD1 and QPD2 can make minute displacements along horizontal and vertical direction so as to compensate the related straight motion error. The compensation is realized by the act of piezo-actuator 1 and piezo-actuator 2, which receive feedback signals from QPD1 and QPD2 .

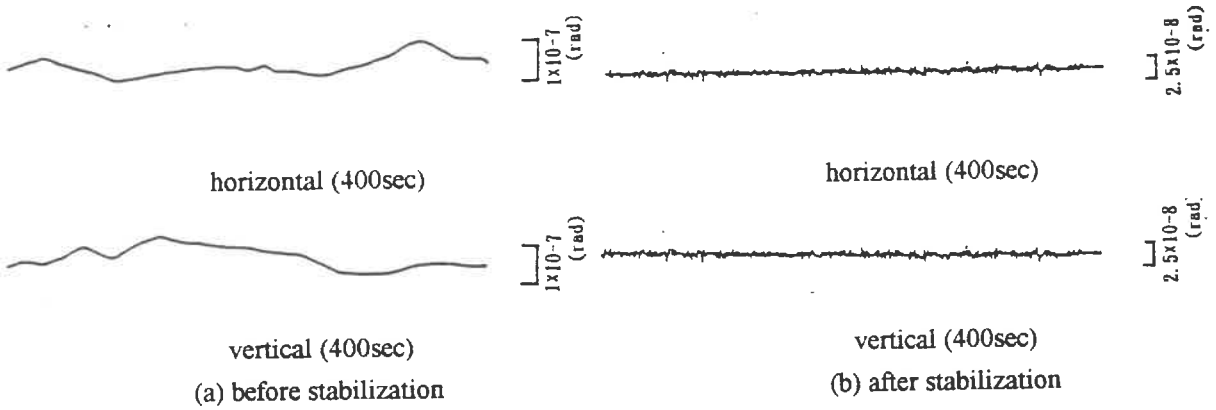

Fig. 2 Beam drift before and after stabilization process

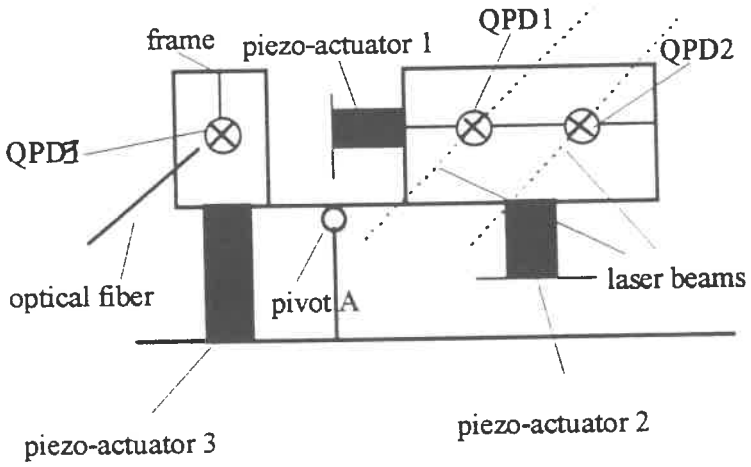

Fig. 3 Straight motion device with 2 parallel beams as datum

The whole frame mounted with QPD1, QPD2, piezo-actuator 1, and piezo-actuator 2 can roll around pivot A. The static rolling error of the moving object can be detected by QPD3 with a novel method called "static pluming method". The method detects the static rolling angle error through measuring the relative displacement between the axis of optical fiber probe and QPD3. The signal from QPD3 is processed and fed back to piezo-actuator 3, which control the rolling angle around Pivot A so as to compensate the rolling error. The method make it convenient to adjusting parallel degree of the two beams, which can be controlled

within 0.1arcsec. Fig. 4 show the relative displacements with the compensation of the rolling angle error. In practical measurement, we detected the dynamic rolling angle error utilizing the two adjusted parallel beams as datum.

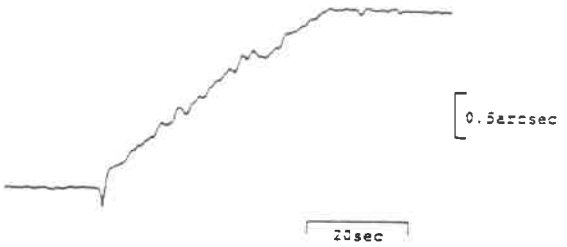

(a) Relative displacement corresponding to the rolling angle error of the moving object measured by the clinometer

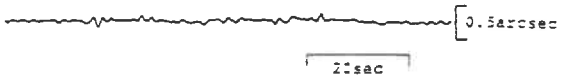

(b) Relative displacement in the case of the compensation of the rolling angle error

Fig. 4 Relative displacements before and after the compensation of the rolling angle error

Fig. 5 shows the output of QPD1 and QPD2 in the horizontal direction when the two columns of beams have an unparalleled error of 0.8arcsec. After adjusting, the unparalleled error can be controlled within 0.1arcsec, which is showed in figure 6. Apparently, the two highly parallel beams can be satisfactorily used as measurement datum of high precision straight motion , straightness, and flatness.

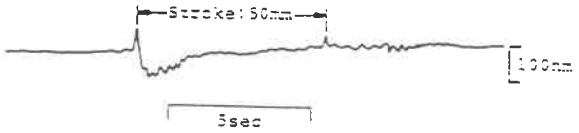

Output of QPD(1) in the horizontal direction

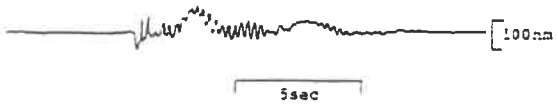

Output of QPD(1) in the horizontal direction

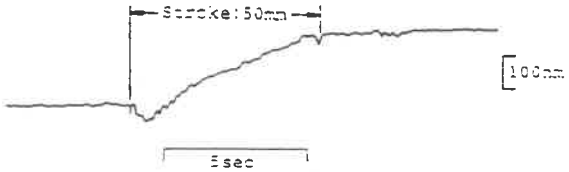

Output of QPD(2) in the horizontal direction

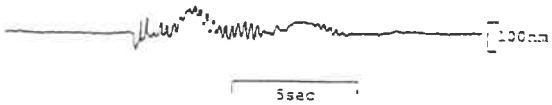

Output of QPD(2) in the horizontal direction

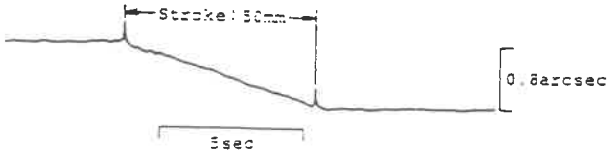

Differential output between outputs of QPD(1) and QPD(2)

Fig. 5

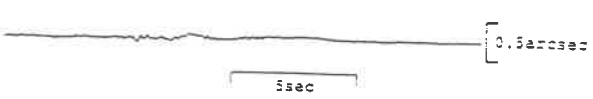

Differential output between outputs of QPD(1) and QPD(2)

Fig. 6

With the straight motion and measurement device, we successfully separated the horizontal displacement, the vertical displacement, and the dynamic rolling angle error of straight motion. The accuracy of displacement is within 10nm, the accuracy of the dynamic rolling error is 0.03arcsec.

To demonstrate the effect of the straight motion and measurement device, the form error of a disc was measured by using two parallel beams as datum. A eddy current sensor was used to scan the disc face. The measurement results were showed in figure 7. The results showed that the flatness of the left disc part is 0.44 μ m/25mm, the flatness of the right part is 0.18 μ m/25mm. The height difference between two side of the hole is 0.32 μ m/20mm. By contrasting the results of the first and second measurement, it can be seen that the results have highly repeated consistence. The accuracy of the method can get to 0.02 μ m.

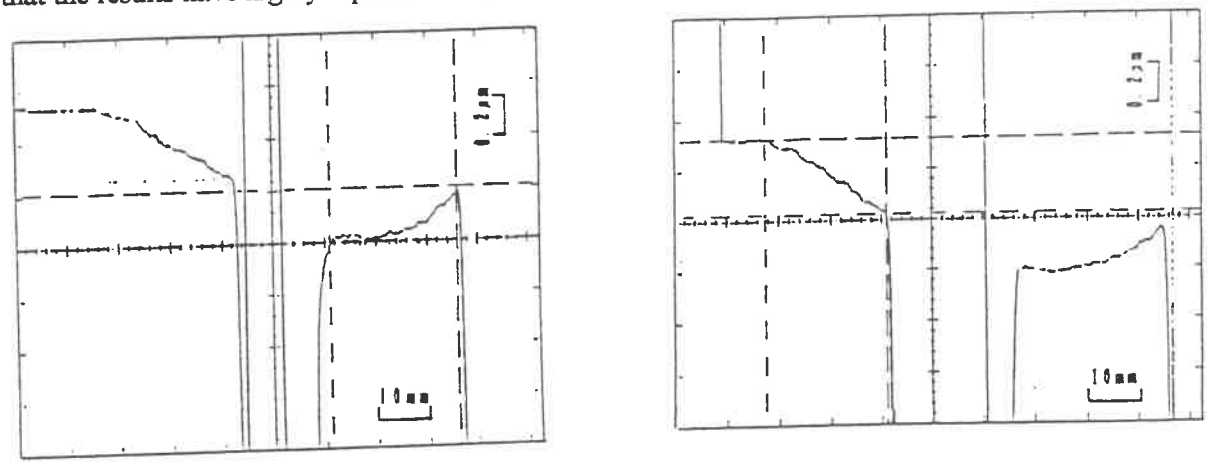

first measurement　　second measurement

Fig. 7　Measurement results of a disc

The high precision straight motion system has been applied successfully for measuring the motion accuracy of precision machines and the straightness and flatness of computer discs, optical flats and straightedges, etc. at a high level of accuracy.

References

1　E. Zhang, et al, Study on Laser Fiber Alignment System and its Applications, 7th IPES 1993

2　Shoichi Shimada, et al, Direction Stabibkzed Laser Beam for Straightt Datum, 7th IPES 1993

3　Wan De-an, et al, An Analytical Study of Directional Stability of Laser Beam in the Air, MDEA 1992

4　Wan De-an, et al, Basic Experimental Investigation On the Laser Beam Stability in the Method of Laser Datum, Xith ICPR 1991

5　Naoya Ikawa, et al, Laser Beam as a Straight Datum and its Application to Straightness Measurement on Nanometer Level, Annals of the CIRP, 37-1, 1988

6　Hisayuki Aoyuama, et al, An Ultraprecision Straight Motion System, JPES Vol 54, 3, 1988

7　Tani, et al, Development of Optical Measurement fro the Straightness of Granite Bed Using Laser Beam Datum, JSME, 592, 1995

8　Nakamura, et al, Laser Interferometric Calibration, Precision Engineering, 1993, 15(1)

SYSTEM FOR THE MEASUREMENT OF CORNEAL SHAPE BY LASER DEFLECTOMETRY

Rufino Díaz, Alberto Caballero, Abdul Muñíz, Leopoldo Ruiz and Gabriel Ascanio
Center of Instruments, National University of Mexico, A.P. 70-186, Mexico DF 04510

Abstract

The design of a system for measurement of corneal shape and its topography is presented. The measurement is carried out by scanning the cornea with a laser beam which displaces describing a spiral trajectory, which is produced by two components: linear and radial. Linear component is produced by means of a linear actuator and radial component by moving a prism by means of a DC motor.
The prototype will be tested to evaluate the scan system by using the same detection scheme used for the measurement of the cornea. Results of characterization will be compared to those obtained with a previous system.

Introduction

The treatment of several ophthalmic diseases demands correct knowledge of the corneal shape, whether to know the disease evolution or the effect of surgical intervention. Usually, by measuring the spacing and deformations of the reflected image of a set of bright rings some information about the corneal shape may be deduced. This method, however, has some limitations. Today there are some work to improve the evaluation but it is not fully reliable.

As an attempt to improve the measurement of the corneal shape and give to the physician a powerful tool, we propose to apply the laser deflectometry principles used for Optical Testing, to the measurement of the corneal shape. We call this method: Laser Keratopography. The idea is to scan the cornea with a low power He-Ne laser beam. From the direction of the reflected beam, the normal to each point of incidence is derived. Having this information, it is possible to evaluate the shape of the cornea and its topography.

It is necessary to take into account two important considerations:
a) The total exposition time of the retina to the laser beam must be very low, in order to satisfy the requirements of the Laser Safety Standards [1], and avoid eye damage. This can be done by using a low power He-Ne laser (power ≤ 1 mW), and doing all measurements in a very short time. Furthermore, it would be useful to give to the beam a small divergence, avoiding the great energy concentration on the retina.
b) The eye performs a complicated sort of involuntary movements, therefore measurements must be done as fast as possible.

Description

Rosete-Aguilar and Díaz-Uribe [2] proposed a method for testing spherical surfaces in which the scanning of the surface is done by means of a laser beam keeping a fixed point during the scan; this point has to be coincident with the center of curvature of the surface.
Figure 1 shows the experimental setup of the equipment, which consists of the following systems: Optical, mechanical, control and electronics.

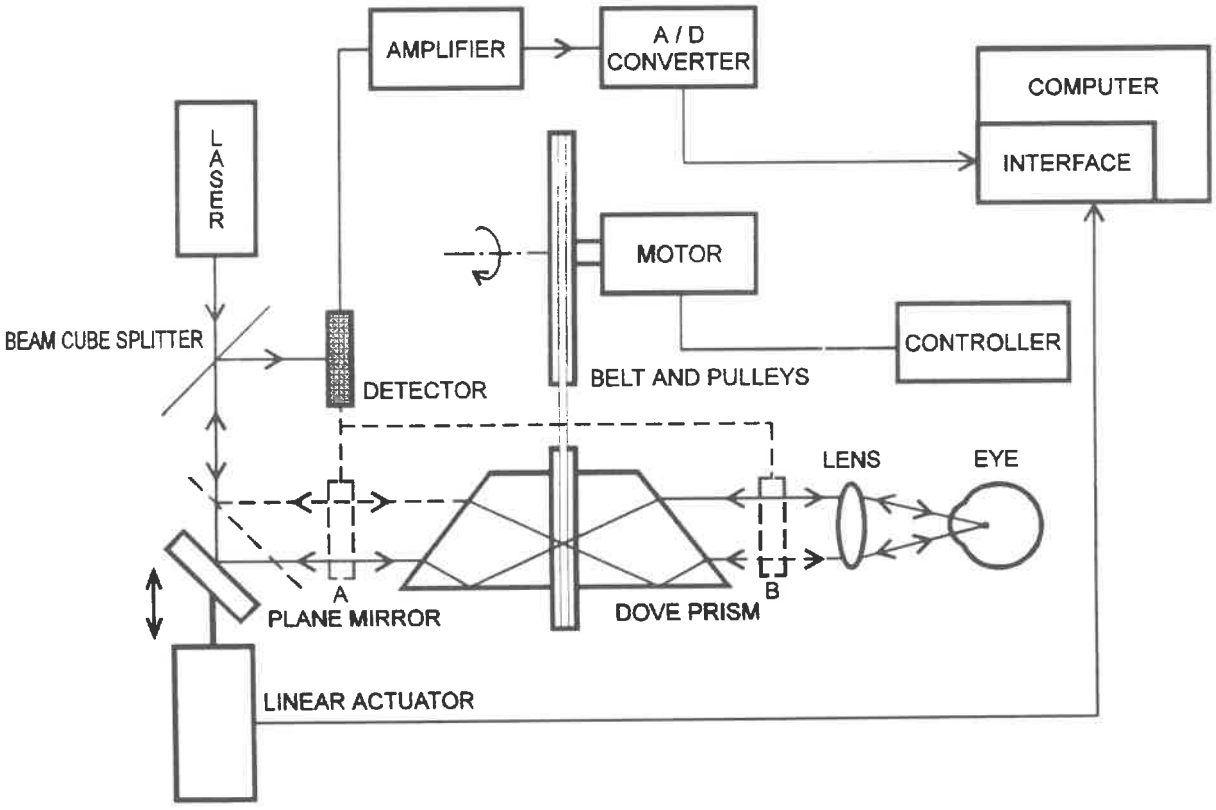

Figure 1 Experimental setup of the system for measurement of corneal shape.

In the optical system a laser beam is partially transmitted through a cube beam splitter and strikes on a 45 degrees plane mirror. This mirror lies on a linear pneumatic actuator of single effect which displaces laterally a laser beam, generating one of the two components. To produce the other component (radial), the beam is incident on a DOVE prism which rotates at a fixed angular speed . As is well known [3], if the prism is rotated, the output beam rotates at the twice of the prism angular speed. Finally, the beam pass through a positive lens in order to convert the transversal movement to an angular one. Every time the beam is directed to the focal point of the lens.

In order to measure the shape on a cornea, it must placed in such a way that its center of curvature and the focus of the lens coincides. Therefore, the reflected beam goes back along the same path, but now it is partially reflected by the beam splitter to the position sensing detector with the following characteristics:

Model :	United Detector Techologies SC-50
Sensing diameter:	50 mm
resolution:	20 μm in a 10 mm diameter
	140 μm from 10 to 50 mm diameter

The detector signal is transmitted to an 301 DIV amplifier of United Detector Techologies and the data adquisition is carried out by a Lab-40 interface with up to a 10 kHz sampling rate, connected to a computer.
The scanning describes a spiral trajectory by means of two components produced by the mechanical system. A linear actuator produces the first scanning component displacing laterally the laser beam. On the other hand, the radial component is generated by the motion of a DOVE prism, which rotates by means of a motor coupled to an arrangement of timing belt-pulleys.
In a previous system [4] the spiral trajectory was generated by the lateral displacement of the mirror by means of crank shaft mechanism and a motor. The radial component was produced with a motor which moves the prism by using two straight teeth gears. Although the operating conditions were very different from those used in this work, this system presented a low precision due to the gear backlash as well as mechanism motion to produce the lateral displacement.

The characteristics of the new mechanical system are presented as follows:

Linear actuator

Type:	single effect
Inlet pressure:	2.8 to 6 bar
displacement:	40 mm
force:	185 N @ 6 bar

Motor

Supply:	6 VDC, 1.5 A
speed:	8000 rpm

Timing belts:

Material:	Nylon covered fiberglass reinforced neoprene
pitch:	5.08 mm
pitch lenght:	614.7 mm
width:	9.5 mm

Pulleys:

Material:	Aluminum alloy
pitch:	5.08 mm
pitch diameter:	48.5 mm and 116.43 mm (amplification rate 2.38)

Experimental setup

In order to characterize this new design, the tests will be carried out based in the experimental setup diagram as shown in figure 1. The position sensing detector will be placed after the mirror and the prism (positions A and B in the figure 1), so that the scanning component can be independently studied. Errors generated by the motion of two mechanism can be determined. One of the test consist in displacing only the linear actuator to analize the lateral displacement and the other one consists on moving the DOVE prisms so that the radial component can analized. In this way the position of the beam going through the scanner will be measured each ms or even each 100μs. This will allow us to have a complete characterization of the real movementns of the system. In operation the position sensing detector will be placed after the beam splitter.

Aknowledgements

This project has part of its financial supports from the CONACYT under Grant no. 2120-PA. It has also the enthusiastic cooperation of Wilfredo Martínez.

Conclusions

The prototype design of system for measurement of corneal topography has been completed. This design has been developed taken into account a previous system, which was chracterized by using a high quality optical sphere as test surface. Results shown that the concept was novel having some limitations as the testing time and resolutions which must be improved in this new design.

References

[1] D.H. Sinley and B.J. Freasier, *Evaluation of optical radiation hazards*, Appl.Opt. **12**, 1973, p.p. 1-24.
[2] M. Rosete-Aguilar and R. Díaz-Uribe, *Profile Testing of Spherical Surfaces by Laser Deflectometry*, Appl. Opt. **32**, No. 25 (1993), p.p. 4690-4697
[3] E. Hetch, OPTICS, 2nd. edition, Adisson-Wesley, New York (1989).
[4] R. Díaz-Uribe and P. Anaszkiewiecz, *Laser Deflectometry Keratopography*, Proc. of the Int. Conf. on Optics in Life Sciences, Elsevier, The Nederlands (1993).

ELECTRODEPOSITION OF SUPERCONDUCTOR THIN FILM AND THE MAGNETORESISTANCE CHARACTERIZATION FOR MAGNETIC FIELD SENSING APPLICATION

A. NATARAJAN *, W. WANG *, E. MA *, R. N. BHATTACHARYA **

*Microsystems Engineering Team (μ-SET), Department of Mechanical Engineering
Louisiana State University, Baton Rouge, LA 70803

**National Renewable Energy Laboratory, 1617 Cole Boulevard, Golden, CO 80401

ABSTRACT

Preliminary experiments have been conducted to study the feasibility of using the magnetoresistance property of $Tl_1Ba_2Ca_2Cu_3O_x$ (Tl-1223) high-T_c superconductor (HTS) for magnetic field sensor applications. The HTS film has been successfully electroplated and patterned using photolithography. The effect of magnetic field (H) on the R-T behavior of the patterned Tl-1223 HTS was investigated at temperatures near its T_c. The magnetoresistance behavior R (H,T) in the temperature range of 100 K - 105 K was tested for magnetic fields up to 0.5T. It is found that the magnetoresistance effect is more significant at temperatures very close to T_c and the $Tl_1Ba_2Ca_2Cu_3O_x$ (Tl-1223) high-T_c superconductor (HTS) is not very suitable for weak magnetic field detection because of its low magnetoresistance in low magnetic field. Other types of the HTS need to be investigated for such an application.

INTRODUCTION

It has been demonstrated that electrodeposition can be used to fabricate high temperature superconductors (HTS) [1-7]. This process has tremendous practical potential in the fabrication of planar and non-planar electronic devices and micro-sensors. Electrodeposition is a low-cost process and has the ability to deposit conductors or conductor-coated insulators of any shape. The short coherence lengths, anisotropy of electronic structures and low carrier densities of high-T_c oxide superconductors have not made them suitable for conventional superconducting electronic devices. However, these properties have been utilized to fabricate other devices such as magnetic field sensors.

An increase in electrical resistance with the application of a weak magnetic field in high-T_c superconductors, has been reported [8-9]. This property was utilized in the fabrication of a bulk magnetoresistive sensor using YBCO superconductor by Nojima et al. [10]. These sensors were reported to exhibit a much higher sensitivity as compared with the traditional Hall Effect or semiconductor sensors, especially at low fields. In this paper, we report an attempt to fabricate a magnetic field microsensor based on Tl-1223 HTS. The property of magnetoresistance R(H,T) in some Tl oxide based HTS has been studied [11-15].

EXPERIMENTAL

The BCCO precursor films doped with Ag were obtained by co-electrodeposition of the constituent metals using nitrate salts dissolved in dimethyl sulfoxide (DMSO). The substrates

were single crystal MgO coated with 300 A° Ag. A typical electrolyte bath for depositing BCCO films consisted of 0.137 M $Ca(NO_3)_2 \cdot 4H_2O$, 0.376 M $Ba(NO_3)_2$, 0.067 $Cu(NO_3)_2 \cdot 5H_2O$ and 0.003 M $Ag(NO_3)$ dissolved in 390 ml of (DMSO) solvent. All chemicals were of Analar or Puratronic grade and were used as received. A conventional three-electrode cell was employed. The silver coated ceramic substrate was used as the working electrode. The reference electrode was Ag (pseudo-reference) and the counter electrode was Pt gauze. A pulsed potentiostatic mode was employed to deposit the films and the potential cycle was 10 s at -4.0 V followed by 10 s at -1.0 V. Film depositions were performed at room temperature with minimal stirring, thus assuring the process occurred in the diffusion-limited regime. A Princeton Applied Research potentiostat/galvanostat Model 273A with an IBM PC AT computer interface was used for controlling the pulsed-potential electrolysis and to monitor the current and voltage profiles. A number of electrodeposition runs were conducted with different electrolyte compositions to optimize the composition of the as-deposited film. Inductively coupled plasma (ICP) spectrometry was used to analyze the composition of the electrolyte and the precursor films.

The electrodeposited precursor films were thallinated, using a two-zone anneal which employs a separate Tl source zone and a sample zone within a flowing O_2 ambient [6]. The samples were inserted and heated to 860° C. The Tl source was kept initially at a low temperature of 685° C for 24 min. and then increased to 728° C and held at this temperature for 34 min. X-ray diffraction analysis was carried out on the post-annealed films.

The annealed samples were patterned using a photolithography process to create the microsensor. A positive photoresist was spun-coat on the samples and exposed using UV-rays employing an optical mask. The exposed samples were then developed using a positive photoresist developer. An acid etch was employed to etch the regions of the film under the resist that were removed during the developing process. The unexposed resist was stripped to leave behind a wire pattern of the HTS sensor.

The superconducting transition temperature of the films was determined by the resistance-temperature (R-T) measurement at a constant current in a four-point probe configuration. Contacts to the film and the patterned sensor were provided using Ag wires and Ag paint. A bias current of 10 μA was used to evaluate the R-T behavior and determine the T_c at ambient (H = 0). The magnetoresistance measurements were performed by initially applying a magnetic field perpendicular to the applied current (H || c axis of the film) and measuring the R-T behavior, by ramping the temperature between 77 K and 120 K. This was repeated for each value of the applied field up to 0.5 Tesla. The desired magnetoresistance plots were then obtained from these curves by fixing a temperature and plotting R as a function of the applied fields and repeating this for various temperatures within the measured range.

RESULTS AND DISCUSSION

The electrolyte bath composition was optimized to produce BCCO precursors of the desired ratio. A ternary diagram showing how the electrolyte compositions were adjusted in order to reach the desired film composition is presented in Fig.1. The composition of the optimized electrolyte bath as measured by ICP analysis was 57.26 atom % Ba [$Ba(NO_3)_2$], 27.11 atom % Ca as [$Ca(NO_3)_2 \cdot 4H_2O$], 14.72 atom % Cu as [$Cu(NO_3)_2 \cdot 5H_2O$] and 0.9 atom % Ag as [$Ag(NO_3)$]. The composition of the precursor films deposited from this bath (in terms of ratio of

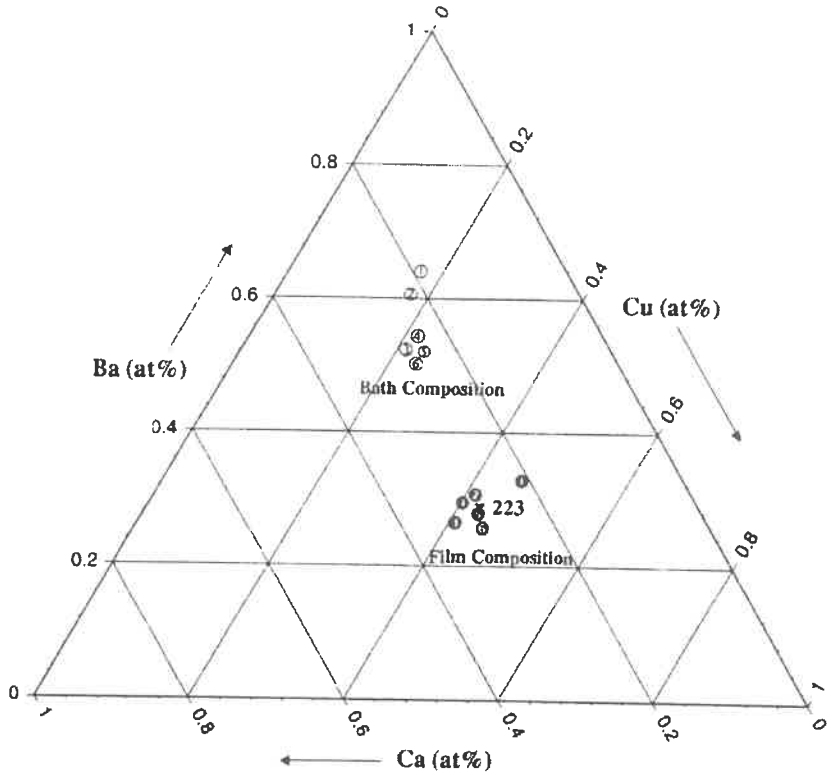

Fig. 1. A ternary diagram showing the electrolyte composition map to the film composition.

the constituent elements Ba/Ca/Cu/Ag) was 1.917/2.121/2.962/0.2 ($Ba_{1.92}$ $Ca_{2.12}$ $Cu_{2.96}$ $Ag_{0.2}$). The deposition bath contains 3mM Ag(NO3).

A representative X-ray diffraction of the annealed Tl-1223 film deposited on 300° A Ag/MgO shown in Fig. 2 indicates a phase-pure c-axis oriented $Tl_1Ba_2Ca_2Cu_3O_x$ phase. Further analysis at the HTS/ceramic interface did not detect any Ag.

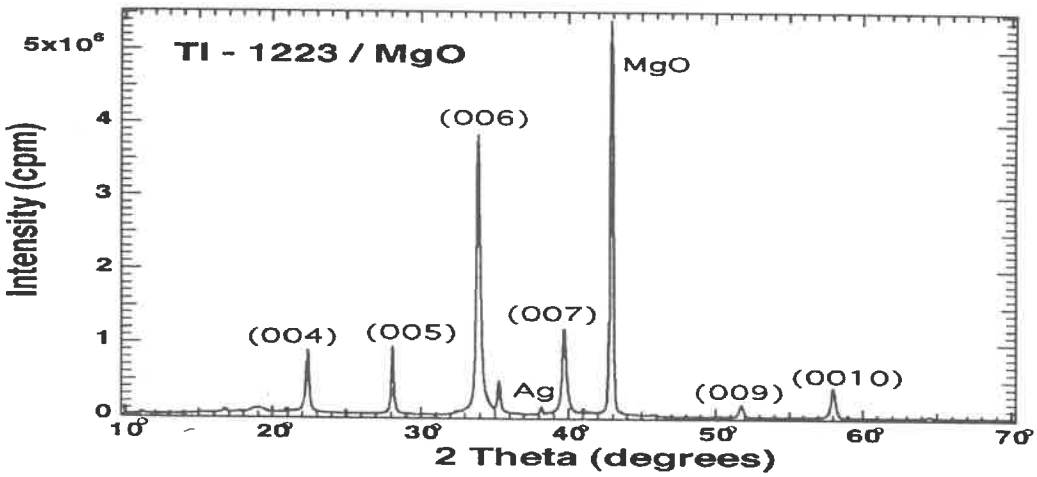

Fig. 2. X-ray diffraction data of an annealed Tl-1223 film (1.2 μm thick) deposited on 300 A° Ag/MgO.

The resistance-temperature (R-T) measurement carried at ambient (0 Tesla), with a bias current of 10 μA, identified the critical temperature (Tc) to be ~ 105 K as shown in Fig. 3. The 300 A° Ag used as a conducting layer appears to have dispersed away from the interface into the film during the annealing process. Hence the magnetoresistance properties measured for the Tl-1223 based sensor were free from any potential interference by this conducting layer

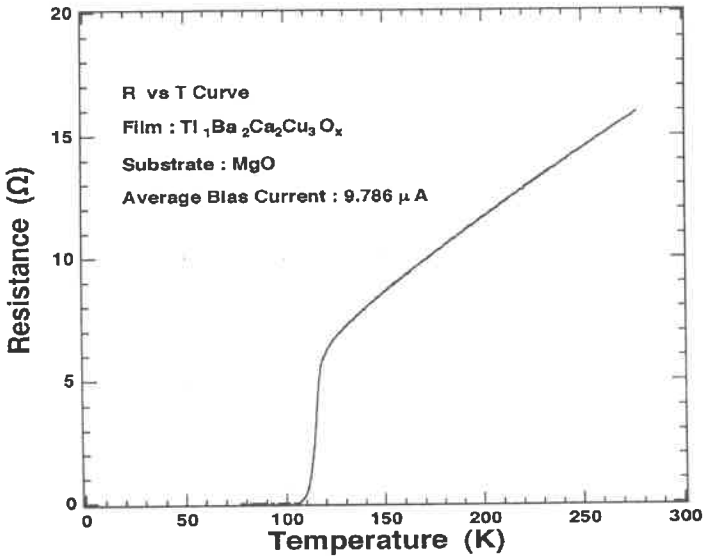

Fig. 3. The resistance - temperature curve of annealed Tl-1223 film deposited on 300A° Ag/MgO

The Tl-1223 HTS sensor, after the process of patterning, is shown in Fig. 4. The meandered shape of the wire increases the total length and reduces the cross-sectional area of the HTS without having to increase the size of the ceramic substrate. This enables an increase in the measured magnetoresistance assuming a constant resistivity for bare and patterned HTS films. The pattern shown in Fig. 4 has a total wire length of 29 mm, a wire width and spacing of 200 μm each, and a film thickness of 1.2 μm. This scales the resistance measurements by a factor of about 60 when compared to an unpatterned HTS film on a similar ceramic substrate. The rectangles at both ends of the wire were used as contact pads for current and voltage connections. A second stage lithography could also be employed to evaporate Ag over these pads.

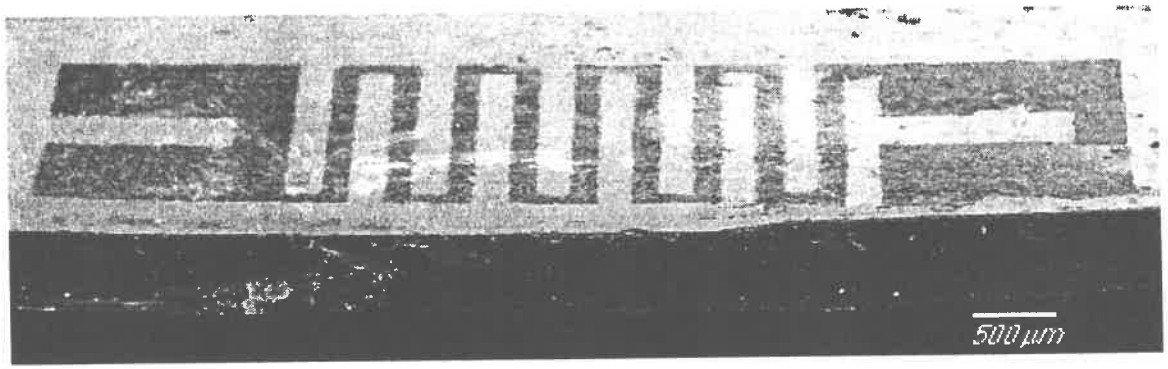

Fig 4. SEM image of a patterned T1-1223 microsensor fabricated on a MgO ceramic substrate.

Fig. 5 shows the effect of applied magnetic fields on the R - T behavior of the patterned T1-1223 HTS. The magnetic field was applied perpendicular to the applied current (H || c axis of the film) and the R-T plots were obtained using a bias current of 10.0 mA in this case. The magnetic field was increased up to 0.5 Tesla.

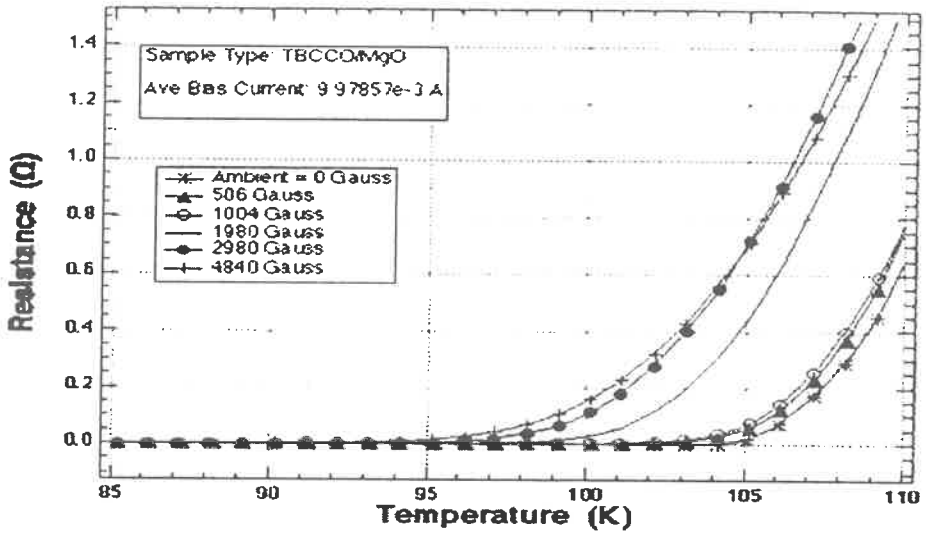

Fig. 5. The effect of applied magnetic fields on the R -T behavior of the patterned T1-1223 HTS

By fixing a temperature on the x-axis and moving vertically up the graph, the R(H) plots could be obtained for each such fixed temperature. Fig. 6 shows the magnetoresistance behavior for the Tl-1223 sensor for temperatures between 100 K and 105 K . In this range, the change in resistance is observed to be significant compared to other temperature ranges ($\Delta R = R_H$ [at H field]- R_0 [at zero field]). When this change is evaluated as [$\Delta R/ R_i$], it implies an extremely large value of resolution, when R_i is close to R_0 as is the case between 100 K and 105 K.

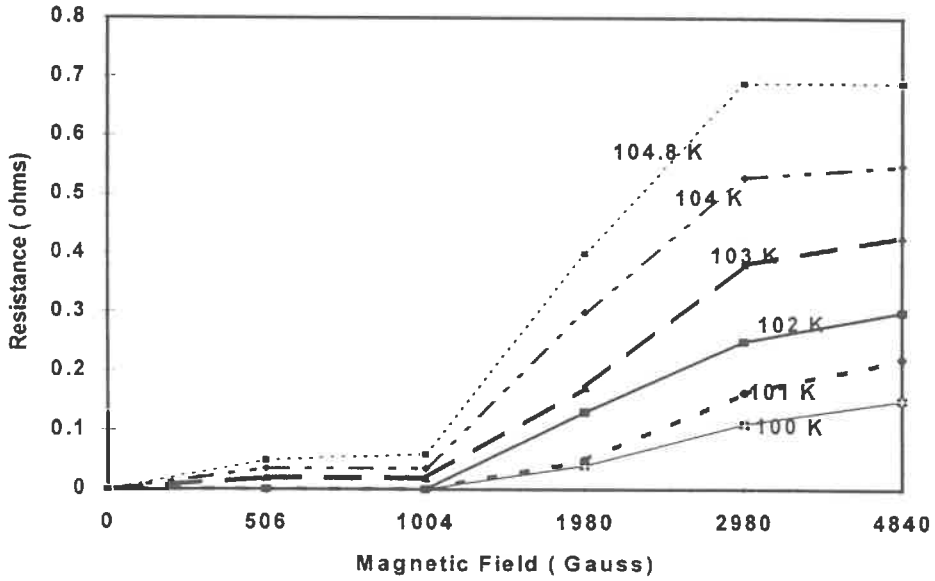

Fig. 6. Magnetoresistance behavior for the Tl-1223 HTS sensor for temperatures between 100 K and 105 K .

It is observed that the magnetoresistance behavior of the fabricated Tl-1223 films display very little increase in resistance for temperatures up to 100 K. When the temperature rises, these curves show a steeper variation with the increasing fields. Similar effects in other Tl based HTS were reported [12] although these studies were also extended to higher magnetic fields.

CONCLUSIONS

In conclusion, we have fabricated a prototype magnetic field microsensor using $Tl_1Ba_2Ca_2Cu_3O_x$ (Tl-1223) high-T_c superconductor (HTS). R-T plots of the Tl-1223 films revealed reproducible superconducting behavior even after a wet, chemical photolithography process. The effect of magnetic field on the R-T behavior of the patterned Tl-1223 HTS was investigated at temperatures near its T_c. The magnetoresistance behavior R (H,T) in the temperature range of 100 K - 105 K was plotted for magnetic fields up to 0.5T. The increase in resistance was more significant at temperatures very close to T_c.

Initial results of Tl based HTS as a magnetic field sensor in the low magnetic fields seem promising. The simplicity and low cost of the electrodeposition proces combined with the capability of superior control of geometry using photolithography techniques are noteworthy. The fabrication of thinner sensor wires to increase the R (H,T) is being investigated. Detailed magnetoresistance studies are in progress to understand the R (H,T) curves obtained for the Tl-1223 HTS.

ACKNOWLEDGEMENT

This work is supported by the Louisiana Education Quality Support Fund (LEQSF) under the contract number, LEQSF(1995-98)-RD-A-13.

REFERENCES

1. D. J. Zurawski, P. J. Kulesza and A. Wieckowski, J. Electrochem. Soc. v 135, p 1607 (1988).
2. M. Maxfield, H. Eckhardt, Z. Iqbal, F. Reidinger and R. H. Baughman, Appl. Phys. Lett. v 54, p 1932 (1989).
3. P. Slezak and A. Wiekowski, J. Electrochem. Soc. v 138, p 1038 (1991).
4. R. N. Bhattacharya, P .A. Parilla, A. Mason, L. L. Roybal, R. K. Ahrenkiel, R. Noufi, R .P. Hellmer, J. F. Kwak and D. S. Ginley, J. Mater. Res. v 6, p 1389 (1991).
5. R. N. Bhattacharya, P. A. Parilla, R. Noufi, P Arendt and N. Elliot, J. Electrochem. Soc. v 139, p 67 (1992).
6. R. N. Bhattcharya, A. Duda, D. S. Ginley, J. A. DeLuca, Z. F. Ren, C. A. Wang, J. H. Wang, Physica -C v 229, p 145 (1994).
7. R. N. Bhattacharya, P. A. Parilla and R. D. Blaugher, Physica -C v 211, p 475 (1993).
8. H. Nojima, S. Tsuchimoto and S. Kataoka, Jap. J. Appl. Phys. v 27, p 746 (1988).
9. J. M. Rowell, IEEE Trans. Magn. v 25, p 759 (1989).
10. H. Nojima, H. Shintaku, M. Nagata and S. Kataoka, IEEE Trans. Electron Devices,v 139, p 576 (1992).
11. T. W. Clinton, A. W. Smith, J. L. Peng, M. Eddy, R.L. Greene, C. J. Lobb, Physica-C v 235-240 pt 2, p 1375 (Dec 1994).
12. C. M. Fu, V. V. Moshchalkov, W. Boon, E. Rosseel, M. Baert, Y. Bruynseraede, Liu-RS, J. Alloys. Comp. v 195 n 1-2 , p 651 (1993).
13. C. Hohn, A. Dascoulidou, O. Maldonado, T. Zetterer, A. Freimuth, Physica-C v 191 n 3-4 , p 354 (1992).
14. G. A. Kapustin, B. B. Tolkachev, Yu. A. Cherushev, L. D. Shustov, Physica-C v 190 n 4, p 549 (1992).
15. A. Poddar, P. Mandal. K. Ghosh-Ray, A. N. Das, B. Ghosh, P. Choudhury, S. K. Lahiri, Physica-C v 159 n 3 , p 226 (1989).

EVALUATION OF THERMISTORS AS A REFERENCE FOR LOCAL TEMPERATURE CONTROL

Kevin M. Lawton, Steven R. Patterson
University of North Carolina at Charlotte
Center for Precision Metrology
Charlotte, NC

Introduction

Thermistors can be effective sensors for precision temperature measurement and control once it is established that their stability is suitably good. Thermistors have merits of low cost and high sensitivity. Thermal resistors are made of metal oxide materials that change resistance with temperature in a logarithmic form. Glass-bead thermistors have a protective glass coating that helps stabilize the semiconductor bead and protect it from the environment.

The relative stability of four commercially available glass-bead thermistors has been analyzed since May 1996 in order to determine if thermistors have sufficient stability to be used as feedback sensors for milliKelvin temperature control. The thermistors have a nominal resistance of 12.5 kΩ and sensitivity of -4.5%/°C at 20°C. High-precision digital multimeters (with scanner cards) were used to perform two-wire measurements of the thermistor resistances. The thermistors are nested together inside several layers of thermal resistance and capacitance which are held at nominal 20°C with a temperature-controlled, recirculating air chamber. Air temperature stability is typically better than 0.1°C over a week. The combination of the insulation and the thermal mass provide filtering for high-frequency deviations of the air temperature.

Data Analysis

The raw resistance data taken of the thermistors is manipulated through several stages in order to compute the relative drift numbers. First, the average temperature of the four thermistors is computed using nominal coefficients given by the manufacturer. The difference between the average temperature and each thermistor temperature is computed as a function of time. Each set of the four differences becomes the dependent variable for four sets of linear regression analysis. A constant, a relative sensitivity, and a temperature derivative sensitivity are computed for each thermistor to minimize the residuals. The independent variables are taken to be the difference between the average temperature and 20°C, and the temperature derivative computed as: [ΔTavg/Δt]. The temperature derivative and the corresponding slope compensate for the fact that the thermistors see slightly different temperatures over the measurement cycle due to delays between each measurement.

The weighted averages of the relative sensitivities of the thermistors are computed from the data sets over the time of study. A new independent variable is computed by subtracting the product of the weighted sensitivities and the [Tavg(t) - 20] independent variable. This removes the effects of the relative sensitivities on the fit variable and leaves only a constant to be determined from the residuals. The weighted

averages are used in this step because it is assumed that the sensitivities of the thermistors remain constant over time, and the weighted averages are the best estimate of the sensitivities.

If there were no deterministic drift of the two-wire measurement system over the time of the test, the constants computed from the previous step could be used to determine the relative drift of the four thermistors. Two high-stability reference resistors were measured with the test thermistors and can be used to track the drift of the scanner card used in the multimeters to multiplex the channels. The relative drift between the reference resistors was converted to an equivalent temperature and used to characterize drift in the scanner card. A linear regression analysis is used to determine the sensitivity coefficients that best correlate the computed thermistor constants and the relative drift of the reference resistors. Subtracting the product of the sensitivity coefficients and the equivalent drift of the reference resistors from the above fit constants best removes the effects of the scanner drift.

The corrected relative drift of each thermistor is computed as the difference between each fit constant and the average of the constants for each thermistor over the entire study. The RMS drift is computed as the root of the average squared difference of the corrected constants and the average constant, for each data set. Another linear regression analysis is used to fit a slope through the corrected RMS drift over the time of the study to determine the overall trend for the relative drift of the thermistors.

Results

The average uncorrected RMS drift of the constants of the thermistors over the 60 week study is 90 μK, with a standard deviation of 64 μK (Figure 1). The peak to peak drift was in band of approximately 700 μK (Figure 2). The average corrected RMS drift of the constants over the 60 week study is 57 μK, with a standard deviation of 26 μK (Figure 1). The peak to peak corrected drift is in band of approximately 300 μK (Figure 3). The average maximum shift in corrected constant from the first week for each thermistor over the 60 weeks is 180 μK with a standard deviation of 53 μK. The uncertainty associated with each of the fitted thermistor constants is 28 μK. The slope of the RMS drift over time is statistically insignificant.

Conclusions

The relative stability measured in this study is sufficient to warrant glass-bead thermistors for use in the proposed experiment requiring milliKelvin stability. Since the thermistors were not compared to an absolute standard, we cannot determine the absolute drift of the group of thermistors. However, in many cases the relative stability of multiple feedback sensors is of greater importance than their absolute stability.

Earlier work at NBS[1] provided an average absolute drift rate for a large number of bead thermistors (at 30°C) of approximately 200 μK/100 days (840 μK/60 weeks), but with lower precision than the study here. Median drift rates were reported to be zero within the experimental error of the study. Another study[2] reported average absolute drift rates of approximately 100 μK/100 days (420 μK/60 weeks). The best beads were reported to have had zero drift within the experimental error of the study (20 μK/100 days, or 84 μK/60 weeks).

The nature of the relative drift of the thermistors in this study does not suggest the linear trends of the average absolute drift in the other two studies, but is similar to a flat trend with some oscillation about the mean. Therefore, it is somewhat difficult to compare the results of the studies. However, the relative drift in this study is consistent with the absolute drift of the most stable beads in the other two studies, in that there is no statistically meaningful drift rate in the data.

By comparing the corrected and uncorrected drift (Figure 3 and Figure 2) of the thermistors, it can be seen that the drift of the two-wire resistance measuring instrument contributed significantly to the overall drift numbers. By removing the scanner drift, the overall drift numbers were reduced by about a factor of 2. However, if relative stability no better than ½ milliKelvin were required, glass-bead thermistors can be used directly with commercial two-wire instrumentation, with no correction for instrumentation drift.

References

[1] S. D. Wood, B. W. Mangum, J. J. Filliben, and S. B. Tillet. An Investigation of the Stability of Thermistors. *Journal of Research of the NBS*, 1978, **83(3)**, 247-263.

[2] T. J. Edwards. Observations on the Stability of Thermistors. *Rev. Sci. Instrum.*, 1983, **54(5)**, 613-617.

Figure 1: RMS Drift vs. Time

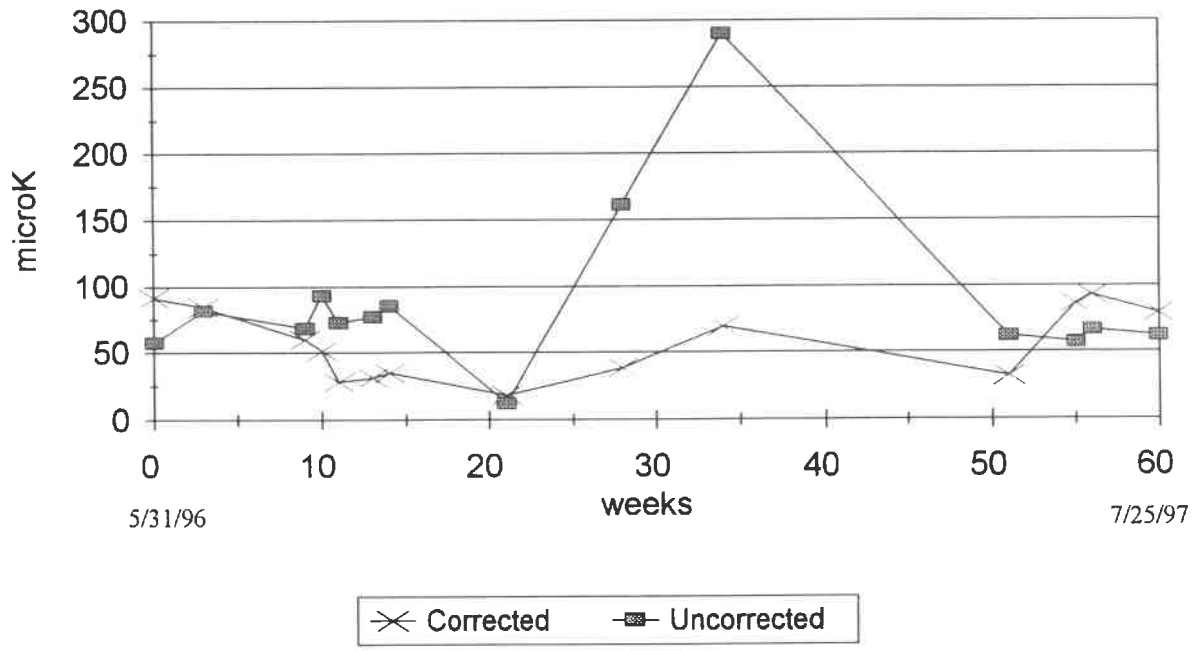

Figure 2: Thermistor Drift vs. Time
Constant(week i) - Average(Constant i)

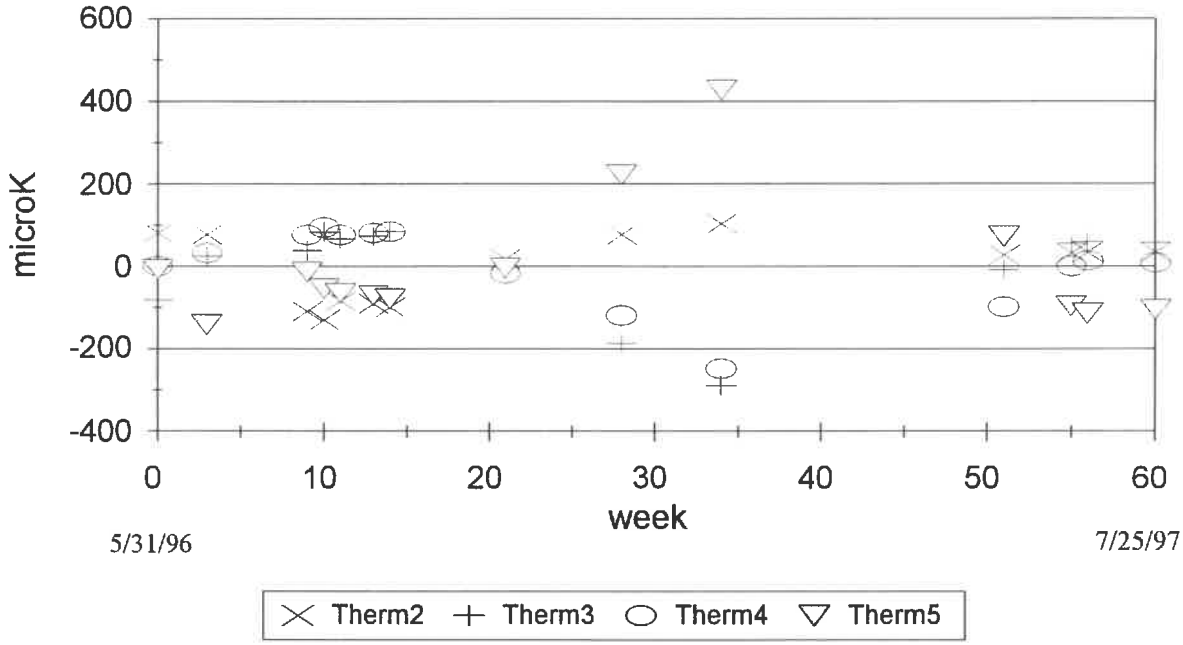

Figure 3: Corrected Drift vs. Time
Constant(week i) - Average(Constant i)

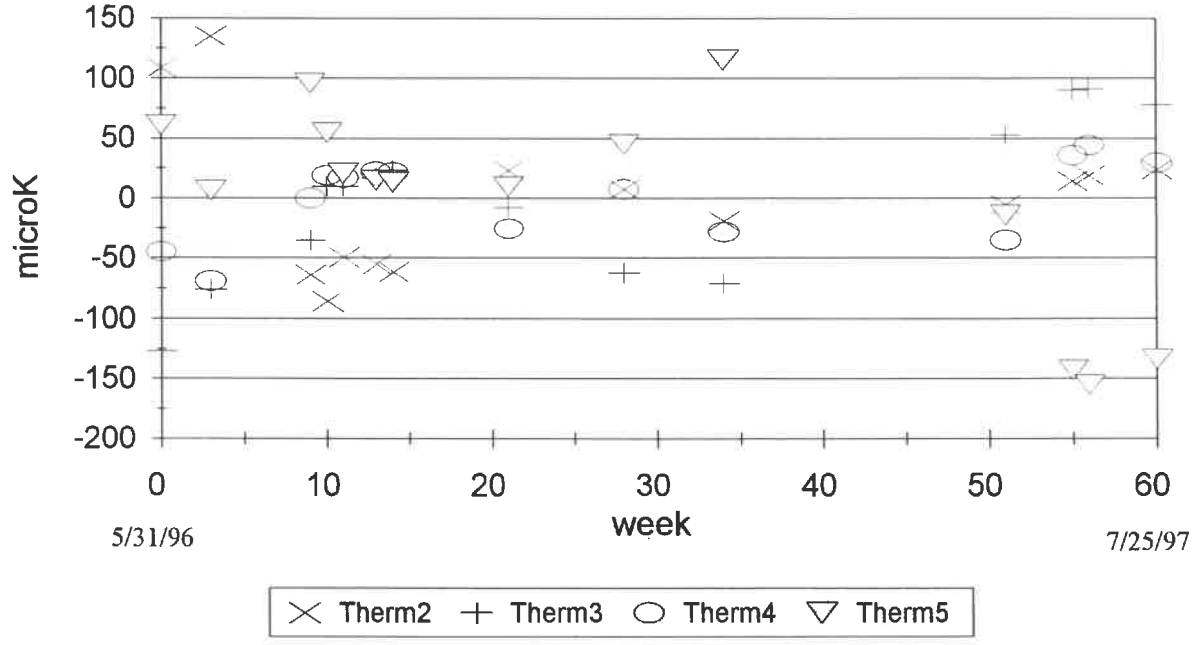

INVESTIGATION OF NONLINEARITY IN HIGH ACCURACY HETERODYNE LASER INTERFEROMETRY

V.G. Badami, S. R. Patterson
Center for Precision Metrology
Department of Mechanical Engineering and Engineering Science
University of North Carolina at Charlotte, Charlotte, NC 28223

Introduction

Optical heterodyne interferometry forms the basis of metrology and control in numerous high precision applications. In polarization encoded laser heterodyne interferometry, the input beam consists of two orthogonally polarized beams of slightly different frequencies. In an ideal interferometer, the two beams separate and travel in pure form in the two arms of the interferometer. On recombination, the optical path difference between the two paths is carried as phase information relative to some reference by the heterodyne signal. This heterodyne signal has a frequency equal to the difference in frequencies of the input beams. In practice, these beams are contaminated by the leakage of a small quantity of one beam into the path of the other. This phenomenon is known as beam mixing and can be attributed to imperfect components, elliptically polarized input beams and misalignment While the attainable resolution has been steadily become higher with improved signal processing techniques, the achievable accuracy is limited by nonlinearity inherent to the system to about 5 nm.

The nonlinearities predicted by Quenelle [1] were first demonstrated experimentally by Sutton [2] who measured 5 nm peak-to-peak variation in the nonlinearity. In addition to the nonlinearity predicted by Quenelle with a periodicity of one cycle per 2π change in optical path length, he also observed a smaller nonlinearity at the second harmonic (hereafter referred to as first-order and second-order nonlinearity respectively). Further experimental investigation along with analysis of the sources of nonlinearity have been performed by a number of investigators [3-6]. Some attempts have been made to compensate and/or cancel first-order nonlinearity and have met with varying degrees of success [7,8].However, for extremely high-accuracy interferometry (accuracy in the 0.1 nm regime) it is necessary to consider the effects of the second-order term and any higher order terms that may occur.

High accuracy interferometry requires the minimization of the effects of both first and second order mixing. The work presented here is an effort in that direction. This paper describes a experimental setup for the measurement of these nonlinearities which allows for intentional beam mixing in a controlled fashion. This is accompanied by a theoretical development that relates the various experimental parameters. Experimental results are presented as a verification of the model developed. At the present time only first-order errors are addressed, the treatment of second-order errors being the subject of future work.

Theory

The interferometer system shown schematically in Figure 1 has been modeled using the Jones calculus [9]. The system consists of interferometer composed of a polarizing beam splitter (PBS) and two retroreflectors. A retarder has been introduced into the input beam to induce mixing. The azimuthal angle of the retarder φ, can be varied to vary the induced mixing. The model also considers the effects of PBS leakage terms, α_{12} and α_{21}(which take into account the undesirable intensity leakage of Beam 2 into the intended path of Beam 1 and vice-versa respectively) and the effect of azimuthal angle of the analyzer θ, used to combine the beams at the output. The ellipticity and orthogonality of the two beams emerging from the laser head and angular alignment of the interferometer have been omitted as the contributions of these errors are negligible relative to the induced ellipticity.

Neglecting DC and quasi-DC terms, the output intensity I_{rel}, observed after the recombining analyzer is given by

$$I_{rel} = 2\Re\{(\Gamma_0 e^{i\Delta\phi} + \Gamma_1 + \Gamma_2 e^{-i\Delta\phi}) E_1 \overline{E}_2 e^{i\Delta\omega t} \quad (1)$$

where $\Delta\phi$ is the change in optical path length between the two arms of the interferometer, E_1 and E_2 are the amplitudes of the two input beams and $\Delta\omega$ is the frequency difference between them. Each of the terms in (1) may be further expanded as follows

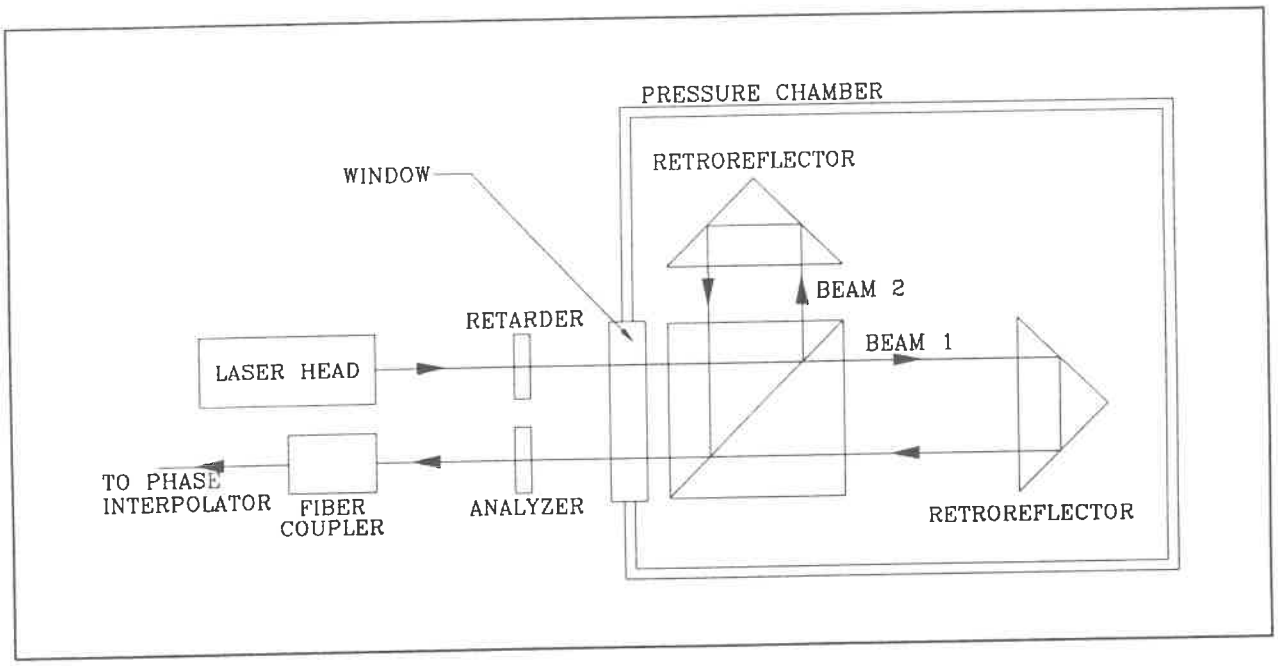

Figure 1. Schematic of interferometer configuration and experimental setup

$$\Gamma_0 = 1 + \frac{z}{\sin 2\theta}\left[(\alpha_{21} - \overline{\alpha}_{12}) - \cos 2\theta(\alpha_{21} + \overline{\alpha}_{12})\right] - z^2(\overline{\alpha}_{12}\alpha_{21}) \quad (2)$$

$$\Gamma_1 = (\alpha_{12} + \overline{\alpha}_{21}) - \frac{z}{\sin 2\theta}\left[\left(|\alpha_{21}|^2 - |\alpha_{12}|^2\right) - \cos 2\theta\left(|\alpha_{12}|^2 + |\alpha_{21}|^2 + 2\right)\right] - z^2(\overline{\alpha}_{12} + \alpha_{21}) \quad (3)$$

$$\Gamma_2 = \overline{\alpha}_{21}\alpha_{12} + \frac{z}{\sin 2\theta}\left[(\alpha_{12} - \overline{\alpha}_{21}) + \cos 2\theta(\alpha_{12} + \overline{\alpha}_{21})\right] - z^2 \quad (4)$$

where z is given by

$$z = \frac{\overline{q}}{p} \quad (5)$$

and p and q are parameters that completely describe the retarder in the input beam whose Jones matrix is given by

$$J_{retarder} = \begin{pmatrix} p & q \\ -\overline{q} & \overline{p} \end{pmatrix} \quad (6)$$

Γ_0 forms the basic heterodyne signal while Γ_1 and Γ_2 are the amplitudes of the nonlinearities with periodicity of one and two cycles per 2π of optical path length change respectively.

Examination of Γ_1 shows that the bulk of the first order error may be nulled by careful alignment of the analyzer about a nominal 45°. The $\cos 2\theta$ dependence of the bulk of the first-order nonlinearity and the $\sin 2\theta$ dependence of the base signal and the second-order nonlinearity imply that the first-order nonlinearity may be attenuated by analyzer rotation without substantially affecting the base signal or the magnitude of the second-order

Experimental Setup

In order to verify the above model, a means of producing optical path changes equivalent to a small fraction of the wavelength is required. Rather than use controlled mechanical displacement as a means of producing this change, the pressure scan method of Sutton [2] has been used. In this technique changes in pressure are used to vary the refractive index of the medium and hence its optical density. An interferometer with unequal arm lengths subjected to changes in optical density records a net change in optical path length. This change is a product of the change in refractive index and the path imbalance.

The setup is shown schematically in Figure 1. The two retroreflectors are rigidly attached to the two faces of the PBS. The path imbalance is set by using suitable spacers in the mounting of the retroreflectors. In the present setup the path imbalance is approximately 7.9 mm. This produces an optical path length change of approximately 5λ (3000nm approx.) for a pressure change of approximately 90 kPa (13 psi). The entire interferometer assembly is mounted inside a pressure chamber whose pressure can be varied under computer control. The pressure can be varied in increments corresponding to an optical path change of approximately λ/16. The pressure in the chamber is monitored using a pressure transducer. The temperature of the air inside the chamber as well as that of the interferometer body are monitored using thermistors. The input beam from a two frequency HeNe laser first passes through a λ/4 retarder whose azimuthal angle can be varied. The beam then enters the chamber through a window. The output beam exits the pressure chamber through the same window and passes through a polarizer whose azimuthal angle can be varied. This is followed by a fiber coupler which launches the beam into a multi-mode fiber for transport to the phase measuring electronics.

A typical data run consists of two scans, a forward scan with increasing pressure and a reverse scan with decreasing pressure. At each point in the scan, the phase, pressure and temperature of the air and interferometer body are recorded under computer control. The acquired data is then subjected to a multi-variate regression with pressure and temperature being the independent variables. The deviation of the raw data from the best fit to these variables is then displayed as the nonlinearity.

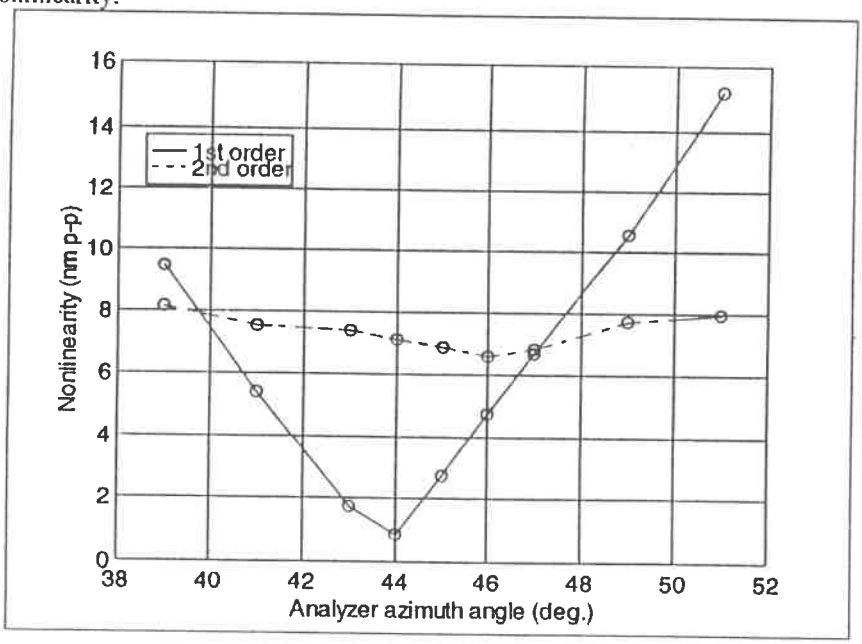

Figure 2: Variation of nonlinearity with analyzer orientation

Results

In order to verify the effect of analyzer alignment, a series of scans was made with the analyzer azimuthal angle being varied in approximately 2° increments about a nominal 45°. The λ/4 plate in the input beam was held at a fixed azimuthal angle of 10° throughout. Figure 2 shows a plot of the magnitudes of the coefficients for the first and second order nonlinearity as a function of analyzer azimuth angle. The analyzer angle are known to within

and second order nonlinearity as a function of analyzer azimuth angle. The analyzer angle are known to within approximately 1°. It can be seen that there is a sharp and well defined minimum at a nominal 45° for the first order term. It is not certain that this is the most reduction that can be obtained as it is quite possible that there exist a lower minimum between the data points obtained.

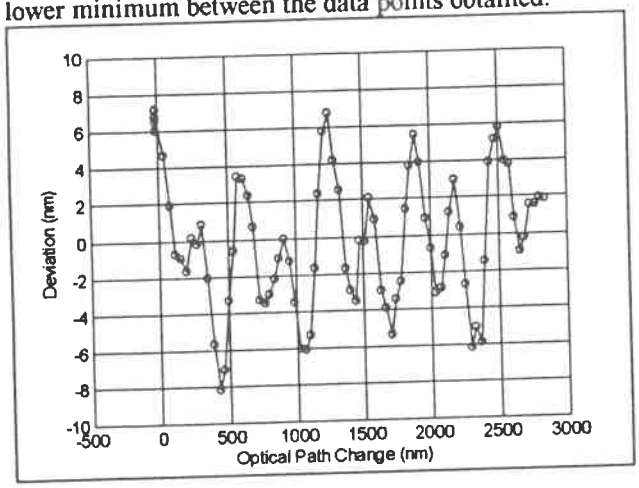

Figure 3: First and second order nonlinearity (41°)

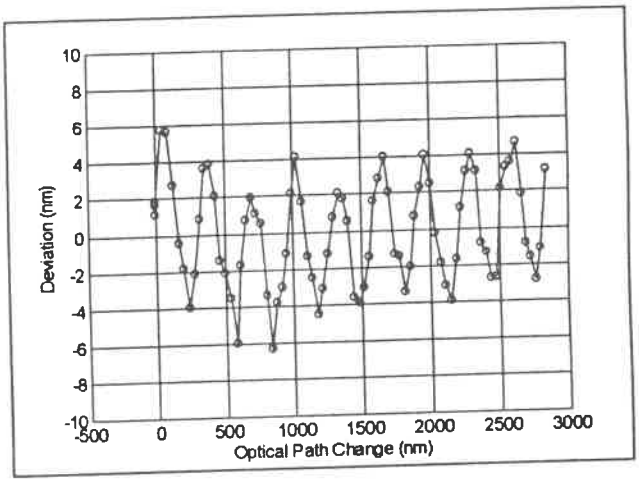

Figure 4: Dominant second-order nonlinearity (44°)

Figure 3 and 4 show two such scans (only forward scans are shown for clarity) with analyzer orientations 3° apart. Deviation is shown in units of equivalent displacement, while the ordinate shows the change in optical path length. Figure3 shows both the first and second order nonlinearity while in Figure 4 the second-order nonlinearity dominates. Fourier analysis of the two scans shows that the scan in Figure 3 has first and second order nonlinearities at the level of 5.41 nm and 7.51 nm peak-to-peak respectively. The corresponding numbers for the scan in Figure 3 are 0.87 nm and 7.07 nm. Comparison of the two sets shows that small changes in angular alignment (3°) about the nominal 45° can produce an order of magnitude reduction of the first-order nonlinearity while leaving the second -order nonlinearity virtually unaffected. This result bears out the predictions of Equation 3 and thus provides a simple control on the magnitude of the first-order nonlinearity.

References

[1] Quenelle, R., "Nonlinearity in Interferometric Measurements," *Hewlett-Packard J.*, **34**, No. 4, 10(1983).

[2] Sutton, C. M., "Non-linearity in length measurement using heterodyne laser Michelson interferometry," *J. Phys. E: Sci. Instrum.*, **20**, 1290 (1987).

[3] Bobroff, N., "Residual errors in laser interferometry from air turbulence and nonlinearity," *Appl. Opt.*, **26**(13), 2676(1987).

[4] Rosenbluth, A. E., and Bobroff, N., "Optical sources of nonlinearity in heterodyne interferometers," *Precision Engineering* **12**(1), 7 (1990).

[5] De Freitas, J. M., and Player, M. A., "Polarization effects in heterodyne interferometry," *J. Mod. Opt.*, **42**(9), 1875(1995).

[6] Wu, C., and Su, C., "Nonlinearity in measurements of length by optical interferometry," *Meas. Sci. Technol.*, **7**, 62(1996).

[7] Hou, W., and Wilkening, G., "Investigation and compensation of the nonlinearity of heterodyne interferometers," *Precision Engineering* **14**(2), 91(1992).

[8] Patterson, S. R., and Beckwith, J., "Reduction of systematic errors in heterodyne interferometric displacement measurement,"

[9] Azzam, R. M. A., and Bashara, N. M., Ellipsometry and Polarized Light, Amsterdam:North-Holland, 1977.

INTERFEROMETRIC MEASUREMENT OF SURFACE MICROSTRUCTURE IN ENGINE CYLINDER WALLS

David J. Aziz[1] and Martin Kramer[2]

[1]WYKO Corporation
2650 E. Elvira Rd., Tucson, AZ 85706

[2]General Motors Corporation
GM Powertrain Group
895 Joslyn Ave., Pontiac, MI 48340

Abstract

This paper describes the application of optical interferometry to the non-destructive inspection of engine cylinder surface microstructure. A description of the technique, its application to engine cylinders, and measurement results are included.

Introduction

The surface microstructure of engine cylinders is typically generated with a honing machine, and is critical to engine performance. Roughness, bearing ratio, and peak-count calculations are all used to analyze the surface structure. Engine cylinder surface analysis tools have primarily consisted of stylus instruments for two-dimensional height measurements, and video and fax-film systems, which allow measurement of the angles, but not the depths, of the grooves in a honed surface.

Interferometric optical profilers are often used for the measurement of surface microstructure (1-3), and have been applied to the measurement of the engine cylinder surfaces (4). This technique is both non-contract and non-destructive. There are several measurements possible with the three-dimensional measurement obtained with this technique that cannot be performed with stylus, fax-film, or video systems. This includes true volumetric calculations, as well as full characterization of groove angle, spacing, and depth in honed surfaces. New metrics in the evaluation of honing machine performance are possible, including detection of inconsistencies between the upward and downward strokes.

Measurement System

The WYKO InSight™ 2000 has been developed for in-situ measurement of cylinder wall microstructure. By providing a true three-dimensional measurement of the surface, this system can show hidden surface attributes for evaluation of manufacturing processes. A vertical scanning coherence sensing technique is used to provide a height resolution of 10 nm or less and a height measurement range of up to 500 microns (5-8). This gives the resolution and range necessary to measure honed, machined, and other surfaces. The system accommodates engine cylinders between 65 and 150 mm in diameter, and inspects from the top of the cylinder to a depth of 150 mm. Measurement of a typical honed surface takes less than 30 seconds, and provides a three-dimensional profile of a 0.9 mm x 1.2 mm region. Multiple data sets can be combined to increase the measurement region (field-of-view) without reducing the resolution.

Measurement Results

The WYKO InSight 2000 provides all standard surface roughness and bearing-ratio parameters, including Ra (Average Roughness), Rz (Average Profile Height), Rpk (Reduced Peak Height), Rk (Core Roughness Depth), Rvk (Reduced Valley Depth), Mr1 (Peak Material Component), and Mr2 (Valley Material Component). Furthermore, a number of parameters are available that can only be obtained with a true three-dimensional measurement. This includes surface volume, calculation of bearing-ratio parameters using three-dimensional, rather than two-dimensional, data, and the depth, spacing, and angle of grooves in a honed surface.

As described above, the InSight 2000 produces a three-dimensional measurement of the surface of an engine cylinder wall. Several plots and parameter values are shown in Figures 1–5, and many other visualization methods and parameters are available with the system. In each figure, a best-fit surface (a cylinder for this case) has been subtracted from the raw data. This removes the waviness, or surface shape, from the data, leaving only the surface roughness for analysis.

Figure 1 shows a contour plot of a plateau honed engine cylinder, where increasing height is represented by lighter shading. The deep cuts made during the honing process are visible as dark gray or black areas (depending on their depth). Both automated and manual measurements of the predominant honing angles are displayed in this figure. The automated measurement uses the power spectrum of the measured data, while the manual measurement reflects the angles of the cursors visible in the contour plot of Figure 1.

Figure 2 shows a three-dimensional plot of the cylinder wall, as well as several roughness parameters. The depth scale for this sample is shown on the right of the 3-D plot. The plot may be rotated, zoomed, and even inverted, to observe specific surface attributes or regions.

Figure 3 shows a plot of the bearing ratio curve for this cylinder, as well as the values Htp, Rk, Rpk, Rvk, Mr1, and Mr2. One of the three-dimensional measurement results is shown in Figure 4. The volume below a plane is calculated, and the portions of the cylinder wall below this surface are displayed. The volume as a function of the plane depth below the top of the sample is shown on the right of Figure 4.

Figure 5 shows the stylus analysis feature of the InSight 2000. The three-dimensional data are separated into several hundred two-dimensional traces, each of which is then filtered with the desired stylus filter (e.g. Gaussian). A variety of parameters are calculated for each of the traces. The mean value of each of these parameters over all the traces is displayed on the right side of Figure 5. On the left side of Figure 5, the parameters for a single trace are displayed. The position of the cursor in the contour plot of Figure 5 determines which trace is to be analyzed.

Conclusion

A vertical scanning coherence sensing technique can be used to measure the surface microstructure of an engine cylinder. A system has been designed that allows this technique to be applied to in-situ engine cylinders. The resulting three-dimensional measurement allows sophisticated analysis of the surface.

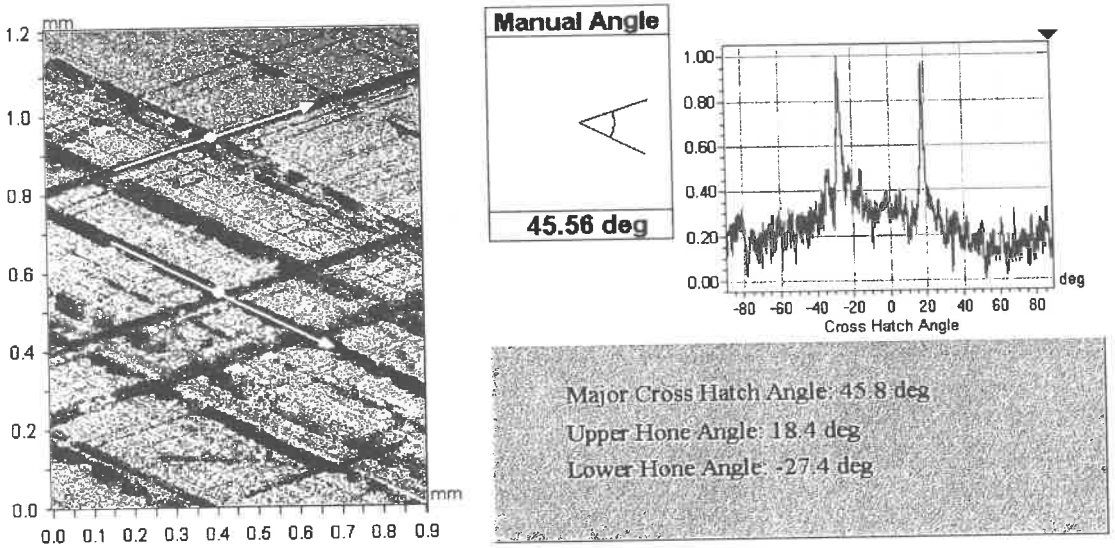

Figure 1. Contour map and crosshatch analysis of a plateau honed engine cylinder.

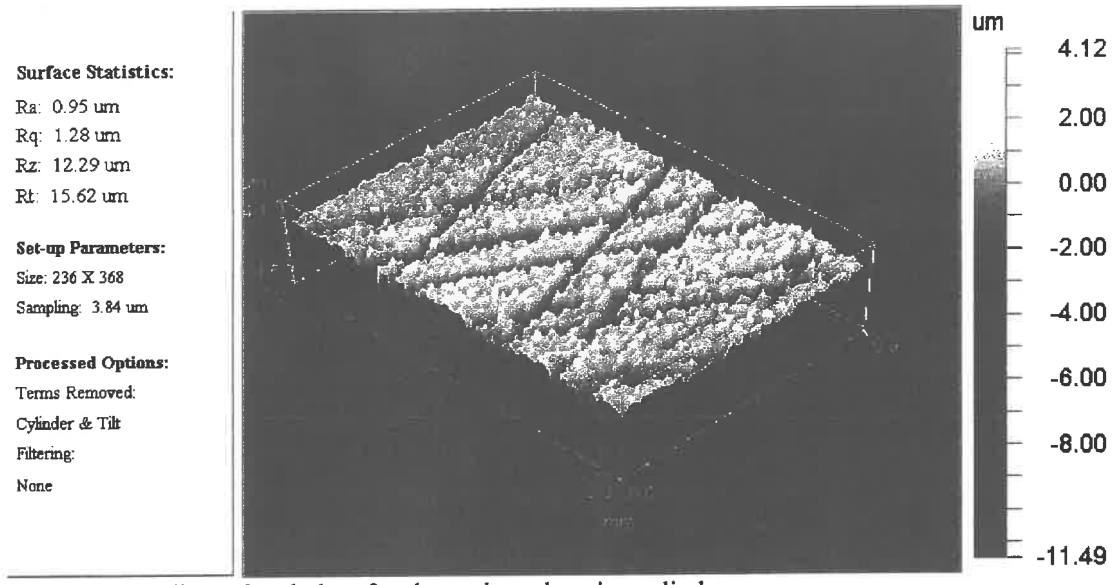

Figure 2. Three-dimensional plot of a plateau honed engine cylinder.

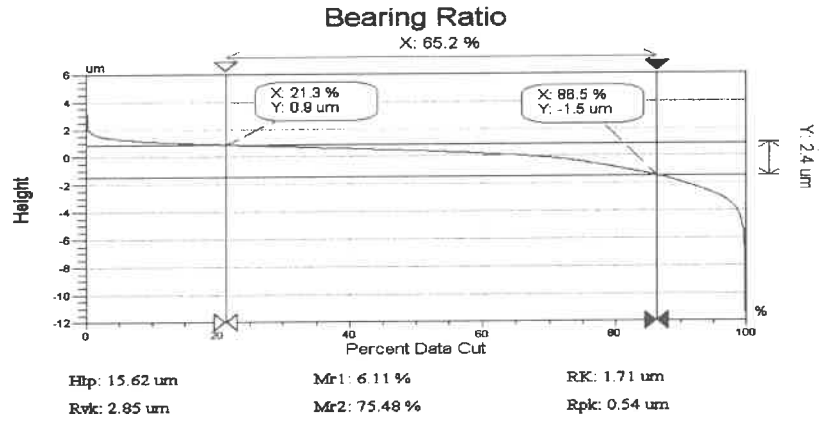

Figure 3. Bearing ratio of a plateau honed engine cylinder.

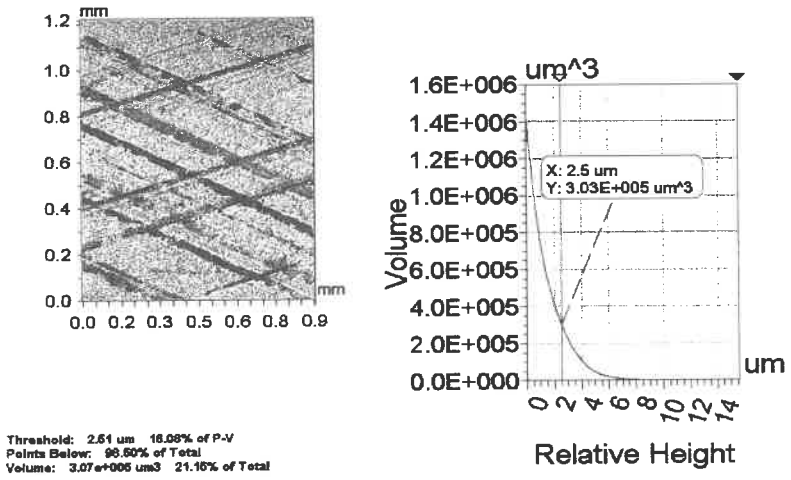

Figure 4. Volumetric analysis of a plateau honed engine cylinder.

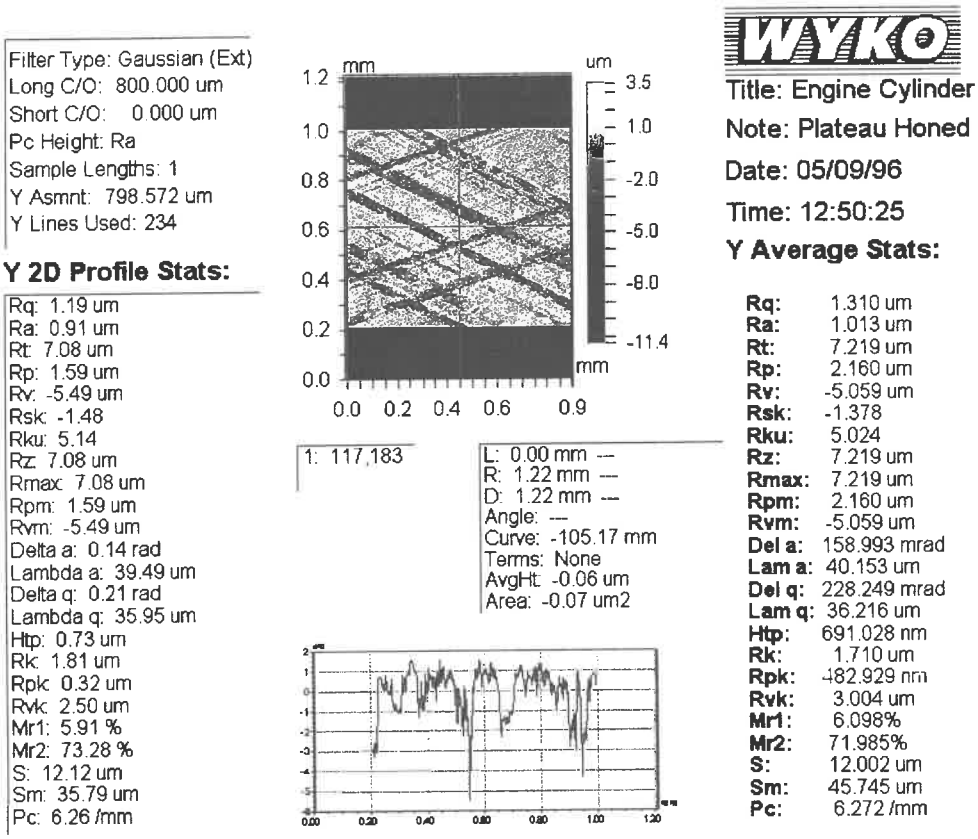

Figure 5. Stylus analysis of a plateau honed engine cylinder.

References

1. B. Bhushan, J.C. Wyant and C.L. Koliopoulos, "Measurement of surface topography of magnetic tapes by Mirau interferometry", Appl. Opt., 28:1489-1497, 1985.
2. J.C. Wyant, "Optical profilers for surface roughness," Proceedings of the Society of Photo-Optical Instrumentation Engineers, 525, 174-180, 1985.
3. J. C. Wyant and K. Creath, "Advances in Interferometric Optical Profiling," Int. J. Mach. Tools Manufact. Vol. 32, No.1/2, 5-10(1992).
4. D. Aziz, B. Guenther, and J. C. Wyant, "Computerized Interferometric Measurement of the Microstructure of Machined Surfaces," 1996 International Workshop on Interferometry, (1996).
5. G. S. Kino and S. Chim, "Mirau Correlation Microscope," Appl. Opt. 29, 3775-3783 (1990).
6. T. Dresel, G. Hausler, and H. Venzke, "Three-dimensional sensing of rough surfaces by coherence radar," Appl. Opt. 31(7):919-3925, March 1992.
7. P. J. Caber, "An Interferometric Profiler for Rough Surfaces," Appl. Opt. 32(19):3438-3441, July 1993.
8. J. C. Wyant, "Computerized Interferometric Measurement of Surface Microstructure," Proc. SPIE Vol. 2576:122-130, (1995).

Development of a sophisticated Michelson-type laser interferometer utilizing an optical thin-film for the constant phase difference

MIYAZAWA. Kimio *. YANAGI. Kazuhisa** and MISHINA. Satoshi **

* Union Tool Co. . Kamitogari. Nagaizumi-tyou. Suntou-gun. 411. JAPAN

** Nagaoka University of Technology. Kamitomioka. Nagaoka-city. 940-21. JAPAN

1. Introduction

Wavelength of light has been the standard for length measurements and the optical interferometry based on the wavelength has been most reliable method for the length measurement. Michelson-type interferometer using a single wavelength laser is most fundamental one because of its simple optical configuration. A laser beam is basically divided into reference and measuring beams. And the two beams combines together to produce the interference waves depending on the optical path of the measuring beam. In this Michelson-type interferometer. the two interference signals with $\pi/2$ phase difference are needed to judge the displacement direction. In order to obtain those signals the polarization techniques have been preferably applied. However. polarization interferometer requires additional optical components such as polarizing beam splitters. quarter-wave plate and corner-cube prisms. From this point of view. we have tried to invent a simple and sophisticated Michelson-type laser interferometer composed only of a frequency-stabilized laser of linear polarization. an ordinary beam splitter. a corner-cube prism for the measuring beam. and another specific beam splitter to produce the two essential interference waves. This paper describes the optical function of the latter beam splitter to provide with the constant phase difference between the final two waves. Numerical simulation indicates that such a beam splitter is realizable.

2. Optical configuration and measurement principle

Figure 1 shows a schematic of the modified Michelson-type laser interferometer which we propose. As to a light source the frequency-stabilized laser of linear polarization is applied and its polarization change through the optical path is not taken into consideration. The laser beam is divided purely into two beams in orthogonal directions by the first beam splitter. One of the two beams is used for measuring the displacement of an object. The measuring beam is reflected by a corner-cube prism and then combines with another beam at the second beam splitter to produce the consequential interference waves. The reference and measuring beams E_f and E_m just before entering into the second beam splitter are expressed by the following formulae.

$$E_f = A_f \exp\left\{i\left(\omega t - 2\pi \ell_f / \lambda + \phi_f\right)\right\} \tag{1}$$

$$E_m = A_m \exp\left\{i\left(\omega t - 2\pi \ell_m / \lambda + \phi_m\right)\right\} \tag{2}$$

where. A is amplitude . λ is wavelength. ω is angular frequency. ϕ is initial phase, ℓ is total optical path between the two beam splitters. The subscripts f and m denotes reference and measuring beams respectively.

At the second beam splitter each beam is divided again into two beams. The reflection part will be indicated hereafter by subscript r and the transmission part by subscript t. If the incident beam axes are perfectly crossing at a point, output interference waves from the beam

splitter are optical combination of the reference and the measuring beams. Each output wave power can be transformed into an electric current by a photodiode. The final two signals from the photodiodes *a* and *b* can be written as follows.

$$I_a = E_a^{\,2} = E_{mt} + E_{fr}^{\,2} \tag{3}$$

$$I_b = E_b^{\,2} = E_{mr} + E_{ft}^{\,2} \tag{4}$$

I_a and I_b are interference fringe signals based on the object displacement and they are expected to be sinusoidal form under the constant speed displacement. In order to judge the direction of the displacement and to measure the phase of interference signal precisely, it is usually needed that the phase difference between the two sinusoidal signals is $\pi/2$. If the second beam splitter is composed of optical thin-film, it may be possible to induce certain phase shift for both reflected and transmitted waves by multiple-reflection and transmission characteristics at the interfacial optical film.

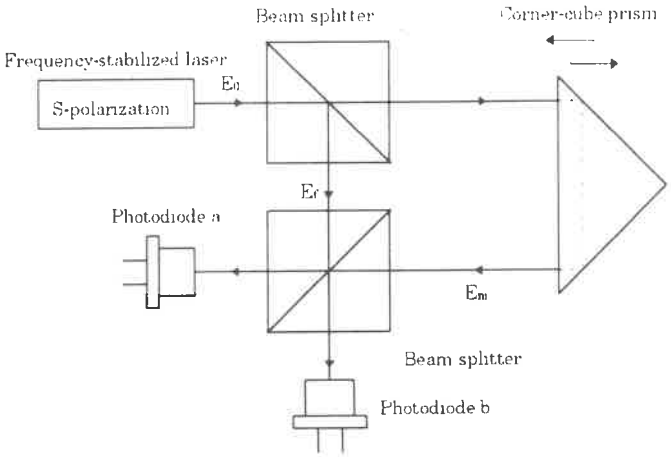

Fig.1 Modified Michelson-type laser interferometer

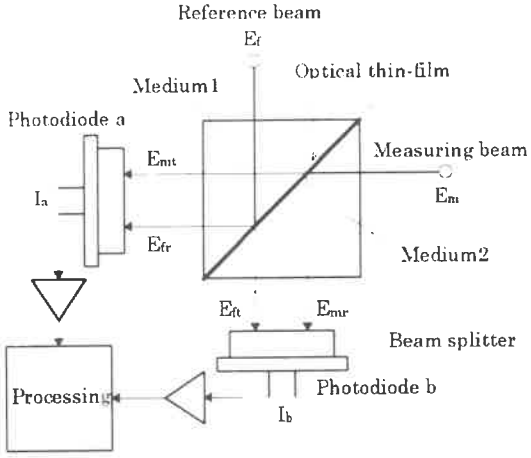

Fig.2 Optical combination of the two beams at the second beam splitter

3. Multiple-beam interference and final interference signals

In this study, only the case of a single layer of imperfect conductor is dealt with. Being based on the theory of multiple-beam interference illustrated in Fig.3, the amplitude reflectance and transmittance for the film can be drawn as follows.

$$Z_r = \frac{r_0 + r_1 e^{-2i\delta}}{1 + r_0 r_1 e^{-2i\delta}} = R_r + iX_r \tag{5}$$

$$Z_t = \frac{t_0 t_1 e^{-i\gamma}}{1 + r_0 r_1 e^{-2i\delta}} = R_t + iX_t \tag{6}$$

where, r and t are Fresnel's coefficients at the interfaces and are determined by optical constants of composing mediums and incident angle θ_0 of the original wave. δ is relative phase difference between adjoining reflected waves (e.g. C and C') caused by the film thickness h, and γ is the phase lag at B for the first transmitted wave. They are given by the following equations.

$$\delta = \frac{2\pi}{\lambda_0} n_1 h \cos\theta_1 \tag{7}$$

$$\gamma = \frac{2\pi}{\lambda_0} n_1 h \frac{1}{\cos\theta_1} \tag{8}$$

For a better interpretation of eqs. (5) and (6), they can be expressed in terms of complex number as follows.

$$\rho_r = \sqrt{R_r + X_r}\ , \quad \beta_r = \tan^{-1}(X_r / R_r) \tag{9}$$

$$\rho_t = \sqrt{R_t + X_t}\ , \quad \beta_t = \tan^{-1}(X_t / R_t) \tag{10}$$

where, ρ and β are amplitude coefficient and phase shift derived from optical constants of mediums, thickness, and optical properties of incident wave.

Discriminating the mediums in the second beam splitter by subscripts 1, 2 and indicating the transmitting direction by their sequence, eqs. (3) and (4) are reexpressed by the following equations.

$$I_a = K_{11}\left[1 + K_{12}\cos\left\{(2\pi/\lambda)\cdot(\ell_m - \ell_f) + \phi_f + \phi_m + \beta_{r1} - \beta_{t21}\right\}\right] \tag{11}$$

$$I_b = K_{21}\left[1 + K_{22}\cos\left\{(2\pi/\lambda)\cdot(\ell_m - \ell_f) + \phi_f + \phi_m + \beta_{t12} - \beta_{r2}\right\}\right] \tag{12}$$

where, K is amplitude coefficient as a function of A and ρ.

The final phase difference between the optical intensities I_a and I_b detected by the photodiodes a and b can be simplified as follows.

$$\Delta\theta = \beta_{r1} + \beta_{r2} - \beta_{t12} - \beta_{t21} \tag{13}$$

In this modified interferometer, it is desirable that the value of $\Delta\theta$ becomes just $\pm\pi/2$ and the fluctuation of K is as little as possible because it causes the phase measurement error.

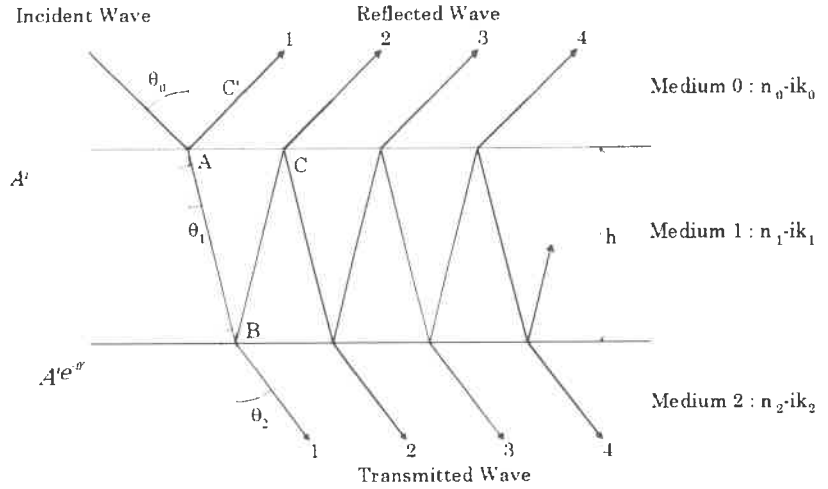

Fig.3 Multiple-reflection and transmission geometry

4. Numerical simulation

Letting the light beam source be a single frequency He-Ne laser of S-polarization, the intensity transmittance and the phase difference by eq. (13) were calculated for some kinds of optical thin-films by varying their thickness. Figure 4 shows the calculated results for the case that the film is inserted between two glass prisms(n=1.51). When the medium 1 is air(n=1.0), the calculated results are turned to Figure 5. In the calculations, optical constants of the materials under consideration were referred from References (3) and (4) .

The simulation results indicates that the phase difference of $\pm\pi/2$ could be achieved by selecting an appropriate film material and adjusting its thickness.

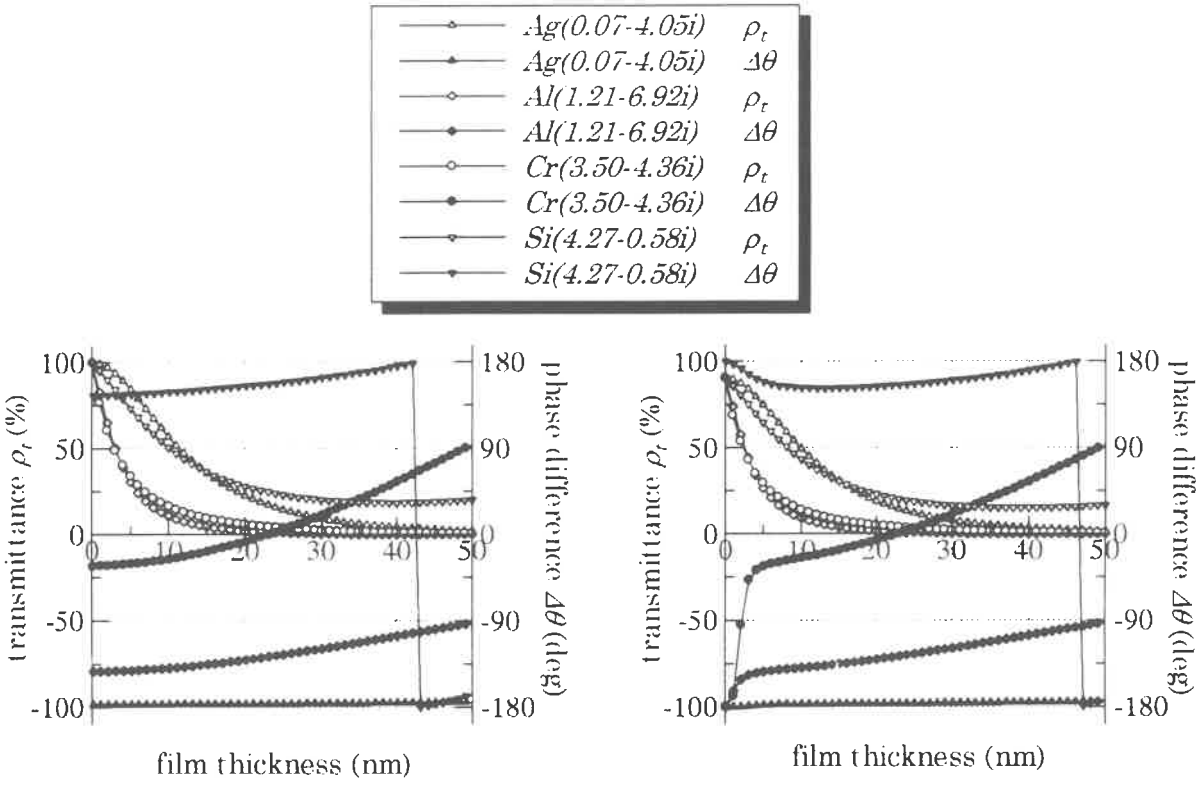

Fig.4 Numerical simulation of transmittance and phase difference
Glass(n=1.51) / Metal / Glass(n=1.51)

Fig.5 Numerical simulation of transmittance and phase difference
Air(n=1.0) / Metal / Glass(n=1.51)

5. Concluding remark

A modified Michelson-type laser interferometer was proposed. in which two interference signals with $\pi/2$ phase difference are to be automatically generated from the reference and measuring beams using only one beam splitter composed of an optical thin-film.

Revealing the phase shifts of the reflected and transmitted parts of each beam. the phase difference between the final two signal was formulated. It is concluded from the calculated results that the above mentioned condition can be empirically obtained.

Reference

(1) Eugene Hecht. Alfred Zajac. OPTICS. Addison-Wesley Pub. Co.. 1974.
(2) Miles V.Klein. Thomase E.Furtak. OPTICS (second edition). John Wiley & Sons. Inc.. 1986.
(3) Pankove. Jacques I.. Willardson. Robert K.. Beer. Albert C.. Optical properties. Academic Press. 1984.
(4) Palik. Edward D.. Handbook of optical constants of solids / edited by Edward D. Palik, Academic Press. 1985.

A New Method for dynamic balancing of Digital Head Drum(Φ 21.7 mm)

Joe, Yeo-Uk; Yang, Yun-Won; Lee, Jin-Koo
DAEWOO Electronics Co., Ltd.
Seoul, Korea

Introduction

A drum unit in a video cassette recorder(VCR) represents a mechanism which, when rotated, facilitates a magnetic head to play back and record a digital signal onto a magnetic tape. When the Digital Head Drum is assembled, the weight unbalance may be remain. This unbalance cannot be neglected since it often causes the vibration of the overall chassis and the burring effect of the image[1]. The vibration from the unbalance often makes the camcorder users feel uncomfortable because the vibration is transferred to the hand when the camcorder is used[2]. This vibration can be even more serious problem in the camcorder with a microphone. In this regard, it is of great significance to achieve an accurate and efficient dynamic balancing to reduce any ill vibration effect. However, methods used in industries are trial and error approaches rather addressing the vibration itself by using mathematical models.

In this paper, the vibration caused by an unbalanced mass is analyzed using a mathematical model. A new method for balancing is suggested. It is intended that this proposed method can simplify the process of obtaining the dynamic balancing while conducting only one measurement step along with a compensation of the system after the drum assembly. The new method is verified using an LDV(Laser Doppler Vibrometer).

Modeling of dynamic characteristic of the digital drum

Due to the high rotational speed , i.e. 9000rpm, and the low inertia, dynamic balancing is essential. To achieve dynamic balancing, it is necessary to analyze and model, namely dynamic characteristic of the drum.

Assumption In the modeling, there are many elements which influence the dynamic characteristic such as ; the shape of the rotary drum(upper drum), the effect of the bearing and bending of the shaft and so on. However, there are some features which we know. For instance ① the shaft and lower drum are fixed, ② the torsional natural frequency is high, ③ the magnitude of the unbalance force by the unbalance mass is very small and ④ the bending rigidity is relatively smaller than twisting rigidity. As results, the torsional vibration has a negligible effect on dynamic characteristic; the bending of the shaft is the most dominant factor in relation to the dynamic characteristic of the Drum.

Suggestion we decide to model the shaft bending as its dynamic modeling and verify this modeling by measuring the bending deflection.

A suggestion of balancing method based on modeling

We suggest a new balancing method based on our modeling. Our suggestion is to add a compensation mass to the upper drum so that the deflections due to the unbalance mass and the compensation mass will cancel resulting in dynamic balancing of the system. In Fig. 2, if P is the force caused by unbalance mass(m), the shaft will be bended to Δ, then a compensation mass($m0$) is added in order to make $P0$ which makes the shaft bended to Δ in

the opposite direction.

$$\delta = \frac{Fa \cdot a^2}{6EI}(3L-a) + \frac{Fb \cdot b^2}{6EI}(3L-b) = \frac{P}{6EI(a-b)}\left\{a^2(c-b)(3L-a) + b^2(a-c)(3L-b)\right\} \cdots (1)$$

The equation (1) is the deflection δ caused by the unbalance mass m and (2) is the deflection $\delta 0$ caused by the compensation mass $m0$.

$$\delta 0 = \frac{F0a \cdot a^2}{6EI}(3L-a) + \frac{F0b \cdot b^2}{6EI}(3L-b) = \frac{P0}{6EI(a-b)}\left\{a^2(d-b)(3L-a) + b^2(a-d)(3L-b)\right\} \cdots (2)$$

In other words, after measuring the deflection δ, and we add a compensation mass on motor's back yoke in order that the deflection $\delta 0$ may be almost the same as δ.

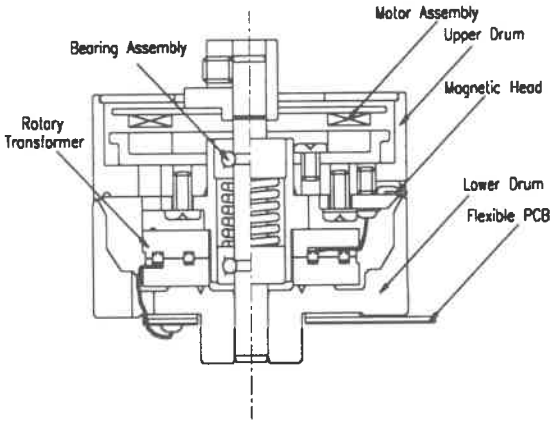

Fig. 1 Digital Head Drum

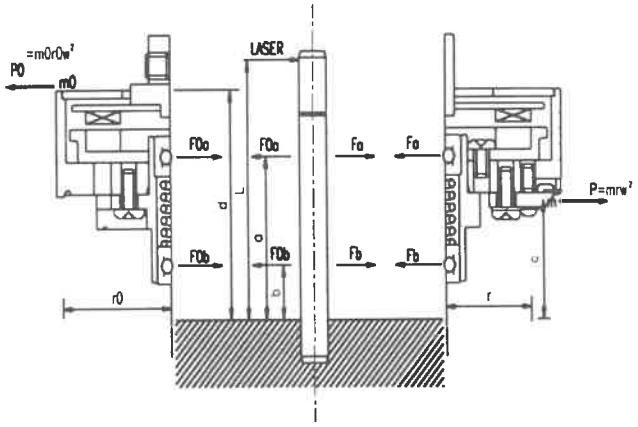

Fig. 2 A suggestion of balancing method based on our modeling

Measurement of dynamic characteristic

The LDV(Laser Doppler Vibrometer) was used as the method to measure and verify our model and also as a new method for balancing. This system was used due to ① its ability to measure at real rotational speed as a non-contact device, ② the high sampling frequency(above 1 kHz), ③ the high accuracy and resolution of the measurement and ④ its ability to make the experiment more convenient and reliable.

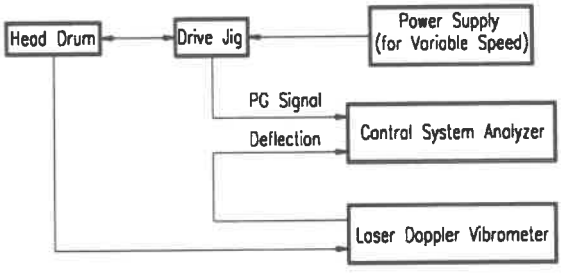

Fig. 3 The scheme of the experiment

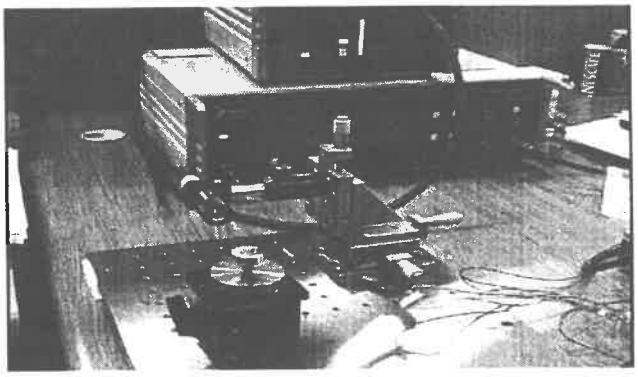

Fig. 4 The photo of the experiment

Results of the experiment

In order to measure the deflection by the unbalance mass we set up the experiment as in Fig. 4. The laser was focused onto a point on the shaft(Fig. 2) and the relevant readings obtained. We then experimented in two ways. These will be explained as follows.

The verification of our modeling We made an experiment to verify our modeling using a known unbalance mass. In Fig.6, the drum speed, the amount of deflection and the position of the unbalance mass are measured. In Fig. 7, the calculated data is derived from equation (1). This experiment shows that the data produced by our modeling was approximately equal to that of the measured.

Constants	data
a(fixed)	12.1 mm
b(fixed)	5.2 mm
c(given)	9.27 mm
d(fixed)	13.22 mm
L(fixed)	17.87 mm
m(given)	0.203g
r(given)	6.2 mm
m0(calculated)	0.048g
r0(fixed)	10.3 mm
E(fixed)	21,200 kgf/mm²
I(fixed)	1.3737 mm⁴

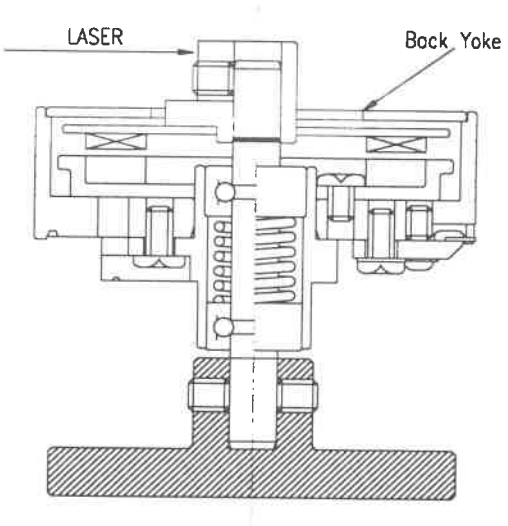

Fig. 5 The jig and data(from Fig. 2) for verifying our modeling

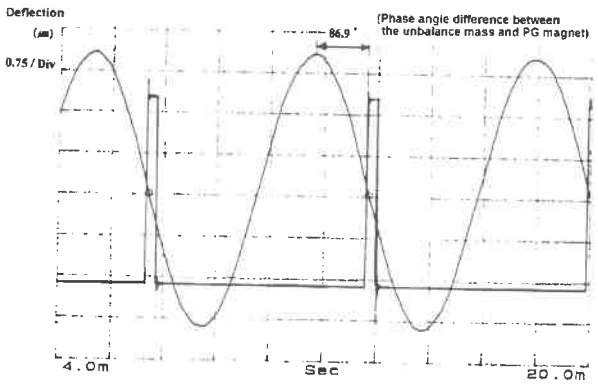

Fig. 6 The measured signal from Analyzer

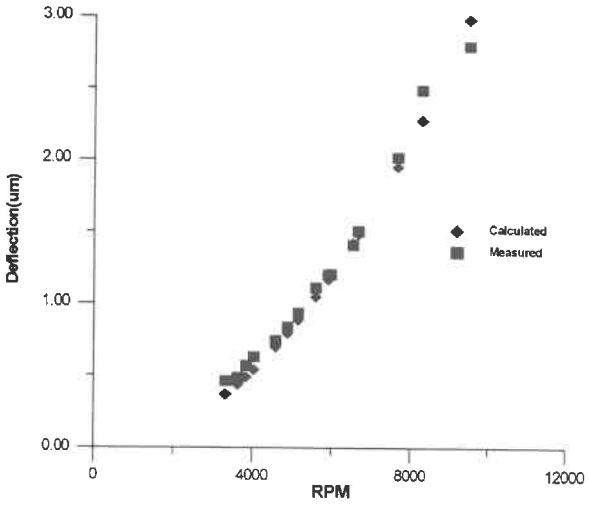

Fig. 7 The comparison with calculated(eq. 1) and measured data in Fig. 5

Application to a real drum We then applied the suggested balancing method to a drum which had not been previously measured to determine the magnitude of its unbalance weight. If we refer to the table in Fig. 5, only the calculated data is required for balancing. The calculated data is derived from equation (2). With reference to Fig. 9, by using the suggested method for balancing, it was possible to significantly reduce the deflection by unbalance mass.

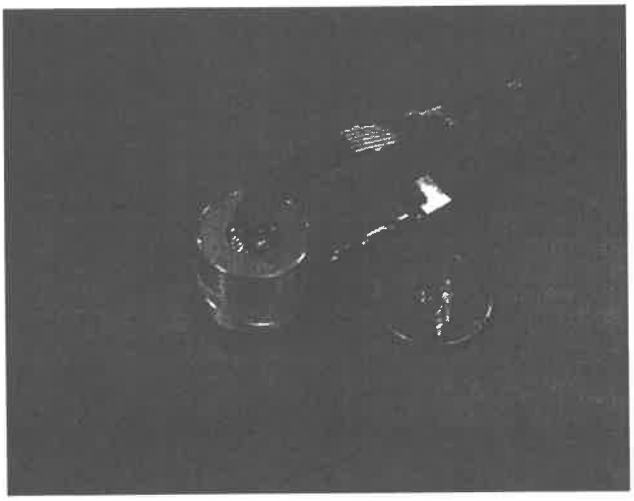

Fig. 8 The photo of the real drum

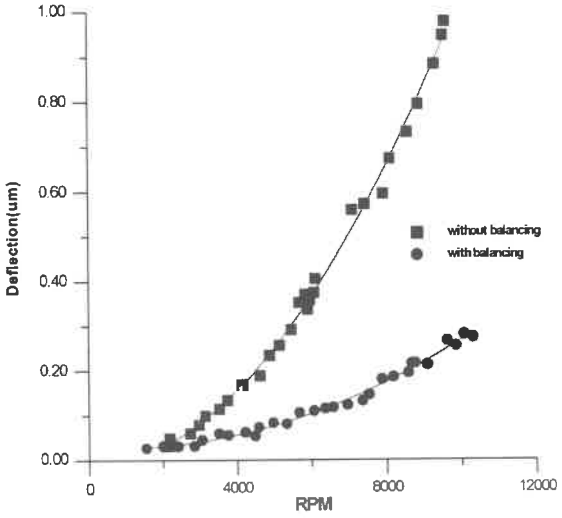

Fig. 9 The Application to a real drum with and without balancing

Conclusion

We suggest a modeling of the drum and balancing method in order to produce the Digital Head Drum economically and productively. The modeling of its dynamic characteristic has been realized along with the new and simple balancing method. To show how this method works, a dynamic characteristic experiment based on our suggestion using LDV(Laser Doppler Vibrometer) was performed. With experiment results, we showed that the data calculated by modeling of the shaft bending with unbalance mass was almost the same as the data acquired by the experiment. And we applied to a real drum, the effect was verified. With this proposed method, after assembling the drum, it would require only one measurement process and one compensation of the system to obtain dynamic balancing.

References

[1] Kohuo et al.,"Mechanism for Balancing a Rotary Magnetic Head Apparatus", *United States Patent*, Patent Number 5,051,852, Sep. 24, 1991

[2] *Nikkei Mechanical*, no. 472 pp. 22-46 1996. 1.22.

LATERAL SHEARING INTERFEROMETER USING ZONE PLATES

Takashi Nomura[1], Kazuhide Kamiya[1], Hiroshi Miyashiro[1],
Seiichi Okuda[1], Hatsuzo Tashiro[2], and Kazuo Yoshikawa[2]
1. Toyama Prefectural University, Kosugi-machi, Toyama, 939-03, Japan
2. Toyama University, Gofuku, Toyama, 930, Japan

Abstract

A common path lateral shearing interferometer with a minimum number of optical components has been developed. Because the interferometer is little affected by mechanical vibrations and air turbulence, it can be mounted on an ultra-precision lathe and can be used to measure the shapes of workpieces. A plane parallel glass plate is used to shear the wavefront under test in the interferometer. To analyze the interference fringes obtained by the interferometer precisely, a fringe scanning method using a slight tilt of the glass plate is used. Zone plates which are computer generated holograms are used in order to measure spherical and aspherical surfaces with the interferometer. A spherical mirror and a parabolic concave mirror were measured with the interferometer. The spherical mirror was also measured by a Fizeau interferometer in order to compare the error with that measured by the lateral shearing interferometer. The experimental results agreed well with those measured by the lateral shearing interferometer.
Keywords: lateral shearing interferometer; on-machine measurement; zone plate; fringe scanning method; shape measurements of an aspherical surface

Introduction

A zone-plate interferometer[1] is one kind of common-path interferometers and is little affected by mechanical vibrations and air turbulence. Taking advantage of this feature, we developed two types of zone-plate interferometer that could be mounted on an ultra-precision lathe.[2,3] However, it was expensive to produce the interferometers because the configurations were complex. Therefore it was necessary to investigate simple and inexpensive interferometers which could be widely used as interferometers for use on a lathe. Yatagai et al. proposed a lateral shearing interferometer[4] which employed a fringe scanning method using a piezoelectric-driven mirror in order to measure the interference fringes obtained by the interferometer precisely. The interferometer is, however, affected by mechanical vibrations and air turbulence because it is not a common path type. To eliminate this disadvantage, we developed a common path lateral shearing interferometer with a minimum number of optical components. A wavefront under test can be sheared by a single parallel flat or a slightly wedge shaped plate.[5] The method is simple and inexpensive. In the lateral shearing interferometer we developed, therefore, a plane parallel glass plate is used to shear the wavefront under test. A fringe scanning method using a slight tilt of the glass plate is used to measure the fringes obtained by the interferometer precisely. To produce a compact and light weight interferometer, Shakher et al. proposed a shearing interferometer using holo-lenses which are made by the interference between diverging spherical and plane wavefronts.[6] In the interferometer we developed, zone plates which are computer generated holograms are used to produce a compact interferometer for measuring spherical and aspherical surfaces.

Lateral shearing interferometer

Figure 1 shows a schematic diagram of the common-path lateral shearing interferometer. A laser beam

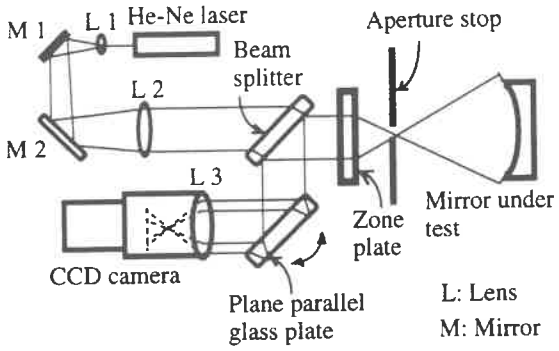

Fig. 1 Schematic diagram of a lateral shearing interferometer.

collimated by the lenses 1 and 2 becomes a spatially coherent plane wavefront beam and illuminates a zone plate. The beam is diffracted at the zone plate and goes to the mirror being tested. In the interferometer two zone plates are used. One zone plate is used to determine the design position of the mirror being tested. The other zone plate is used to measure the error in the shape of the mirror. The first zone plate is made in such a way that the first order diffracted light beam converges at the vertex of the mirror surface. The diffracted light beam reflected from the vertex of the mirror is diffracted at the zone plate and nominally recollimated. The recollimated light beam is reflected at the beam splitter and goes to a plane parallel glass plate. The glass plate is used to shear the wavefront of the recollimated light, that is, lateral shearing interference fringes are produced by the optical path difference between the wavefront reflected from the front surface of the parallel glass plate and that from the rear surface. When the mirror being tested is located at the design position, null interference fringes are obtained. After the mirror has been placed at the design position, the zone plate is replaced with the other zone plate to measure the error in the shape of the mirror. The zone plate is made in such a way that the first order diffracted light beam converges on the optical axis and travels in a direction perpendicular to the surface of the mirror under test and illuminates the entire surface of the mirror. The light is reflected from the mirror, is diffracted at the zone plate, and is nominally recollimated. Extraneous light beams are blocked out almost completely by the aperture stop located at the focal point of the zone plate.

The wavefront under test may be expressed as $W(x,y)$, where (x,y) are coordinates of a point of measurement P. When this wavefront is sheared in the x-direction by an amount S, the sheared wavefront at the same point is $W(x\text{-}S,y)$. The resulting optical path difference $\Delta W(x,y)$ at P between the original and the sheared wavefronts is $W(x,y)\text{-}W(x\text{-}S,y)$. When S is small the optical path difference is written as

$$\Delta W(x,y) = W(x+S,y) - W(x,y) \cong \left(\frac{\partial W}{\partial x}\right) S = n\lambda$$

where λ is the wavelength of the light source and n is the order of the interference fringe. The interferogram obtained by the lateral shearing interferometer represents the derivative of the aberration in the laterally sheared direction of the wavefront under test. By integrating the phase distribution, the shapes of cross-sections of the mirror under test in the laterally sheared direction are obtained. To get the two dimensional wavefront shape, integration is performed in two mutually perpendicular directions; that is, in the x-direction and y-direction. Because the mirror under test is mounted on the chuck of the lathe and revolves on the axis of the lathe spindle, the mirror can be measured at one position and then measured again when the mirror has revolved through 90 degrees. Consequently, mutually perpendicularly sheared interferograms can be obtained. The shapes of the mirror cross-sections in the two directions are calculated independently. The center line parallel to the y-axis is used for comparing relative heights in the shape of the cross-section in the x-direction.

The fringe scanning method[7,8] is applied to analyze the fringes precisely. A slight tilt of the glass plate produces an optical path difference between the two wavefronts, that is, the wavefront reflected from the front surface of the glass plate and that from the rear surface, and gives a change in the phase of the fringes. Four laterally sheared fringe patterns are obtained by a CCD camera. The phase distribution of the fringe pattern is analyzed from these four patterns. After the mirror has revolved through 90 degrees in the counterclockwise direction, the same analyses are performed from the

four interferograms obtained at this position. The integration calculations of the analyzed phases are performed along the mutually perpendicular sheared directions. Consequently the error in the shape of the mirror under test is obtained by these calculations.

Experiments

To investigate the validity of the interferometer shown in Figure 1, two metallic concave mirrors were measured. One was a concave spherical mirror with a diameter of 100 mm, a radius of curvature of 500 mm, and a thickness of 30 mm. The other was a concave parabolic mirror with a diameter of 50 mm, a focal length of 70 mm, and a thickness of 60 mm. These mirrors had been manufactured on an ultraprecision lathe in advance and were reattached to the chuck of the lathe. Optically plane parallel glass plates with a diameter of 50.0 mm and a thickness of 3.00 mm were used as the substrates of the zone plates and as the plate used to shear the wavefront under test. The zone plates used for the experiments were manufactured with an instrument, consisting of an ultraprecision lathe and an Ar laser with a wavelength of 458 nm.[9] The zone plates were manufactured by the following procedure: (1) The glass plates were coated with photoresist so that they could be used as photographic plates. (2) The photographic plates were mounted in the chuck of the lathe and rotated. (3) Grating lines were drawn on the plates by exposing them to a beam from an Ar laser mounted on the lathe. (4) The photoresist exposed to the laser beam was removed by development. (5) The entire surfaces of the plates were coated by SiO_2. (6) The plates were submerged in a solvent and the unexposed photoresist and its SiO_2 coating were removed, leaving behind the SiO_2 coated on the exposed grating lines. Therefore, the zone-plate gratings have a binary phase structure. (7) The back surfaces of the zone plates were coated by SiO_2 to prevent reflections from the surfaces.

Experimental results

Four interferograms of the concave spherical mirror were obtained with this lateral shearing interferometer in which the wavefront was sheared in the x-direction. In the measurement, phase shifts were introduced in steps of $\pi/2$ between each interferogram. The image data of the interferograms consists of 512×512 pixels and 256 levels of gray scale data. Similarly, another four interferograms of the mirror were obtained with the interferometer in which the wavefront was sheared in the y-direction. The phase distribution analyzed by the fringe scanning method is shown in Figures 2 (a) and 2 (b). After the phase unwrap procedure of the phase distribution[8] had been carried out of the phase distributions were integrated along the two sheared directions. The error in the shape of the mirror under test was analyzed from the results. Figure 3 shows the error in the shape of the concave spherical mirror as measured by the lateral shearing interferometer. The length of the shear was 22.4 mm and the analyzed diameter was 76 mm. The peak to valley value obtained by this interferometer was 3.20 λ, where λ is the wavelength of the light source (633 nm). The spherical mirror was measured by a Fizeau interferometer for comparison with the experimental results as measured by the lateral shearing interferometer. In the Fizeau interferometer the fringe scanning method using a piezoelectric-driven reference mirror was used. Figure 4 shows the error in the shape of the mirror as measured by the Fizeau interferometer. The peak to valley value obtained by the Fizeau interferometer was 3.23 λ inside the 76 mm diameter circle. These results agreed well with those obtained with the lateral

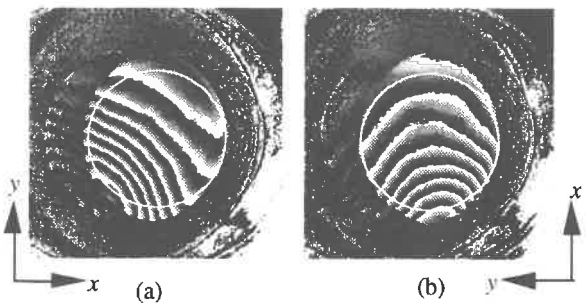

Fig. 2 Phase distribution of the concave spherical mirror as obtained by the lateral shearing interferometer. (a) Phase distribution in the x-direction and (b) phase distribution in the y-direction

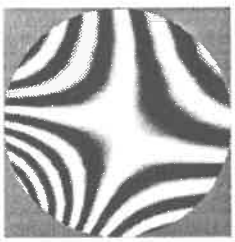

Fig. 3 Contour map indicating the error in the shape of the concave spherical mirror. The contour map was obtained by analyzing the lateral shearing interferogram. The difference in height between adjacent contour lines is 316 nm.

Fig. 4 Interferogram obtained with a Fizeau interferometer.

shearing interferometer. The concave parabolic mirror was also measured by the lateral shearing interferometer. The length of the shear was 11.2 mm and the analyzed diameter was 38 mm. The peak to valley value obtained by this interferometer was 0.33 λ.

Conclusions

A common path lateral shearing interferometer with a minimum number of optical components was developed to measure the errors in the shape of mirrors on an ultraprecision lathe. In the interferometer, zone plates are used to measure spherical and aspherical surfaces, an optically plane parallel glass plate is used to shear the wavefront under test, and a fringe scanning method using a slight tilt of the glass plate is used to measure the fringes obtained by the interferometer precisely. Two metallic concave mirrors were measured with the interferometer. One was a spherical mirror and the other was a parabolic mirror. The spherical mirror was measured by a Fizeau interferometer for comparison with the results measured with the lateral shearing interferometer. The error in the shape of the spherical mirror as measured by the lateral shearing interferometer agreed well with that measured by the Fizeau interferometer. A parabolic mirror was also measured by the lateral shearing interferometer. Interference fringes obtained by the interferometer were little affected by air turbulence in the optical paths and by machine vibrations.

Acknowledgments

We would like to thank Prof. T. Kohno and Mr. T. Yazawa of the Tokyo Metropolitan Institute of Technology, Mr. F. Kobayashi of Fuji Photo Optical Co., Ltd., and Mr. T. Shimizu of Nachi-Fujikoshi Co., Ltd. for their support.

References

1. Smartt, R.N., "Zone plates interferometer," Appl. Opt. , 1974, 13(5), 1093-1099.

2. Nomura, T., Yoshikawa, K., Tashiro, H., Suzuki, M., Kobayashi, F., and Usuki, M. "Shape measurement of workpiece surface with zone-plate interferometer during machine running," Prec. Eng., 1993, 15(2), 86-92.

3. Nomura, T., Kamiya, K., Miyashiro, H., Tashiro, H., and Yoshikawa, K. "Zone-plate interferometer for measuring the shape error of mirrors with large numerical aperture and steep asphericity," Opt. Rev., 1996, 3(1), 34-37.

4. Yatagami, T., and Kanou Y. "Aspherical surface testing with shearing interferometer using fringe scanning detection method," Opt. Eng., 1984, 23(4), 357-360.

5. Murty, M. V. R. K., "The use of a single plane parallel plate as a lateral shearing interferometer with a visible gas laser source," Appl. Opt., 1964, 3(4), 531-534.

6. Schaher, C., Godbolr, P. B., and Gupta B. N. "Shearing interferometer using holo-lenses," Appl. Opt., 1986, 25(15), 2477-2478.

7. Burning, J.H., Heriot, D.H., Gallagher, J.E., Posenfield, D.P., White, A.D., and Brangaccio, D.J. "Digital wavefront measuring interferometer for testing optical surface and lens," Appl. Opt., 1974, 13, 2693-2703.

8. Malacara, D. Optical shop testing, New York, Wiley, 1992, 501-513.

9. Nomura, T., Kamiya, K., Miyashiro, H., Yoshikawa, K., Tashiro, H., Suzuki, M., Ozono, S., Kobayashi, F., and Usuki M., "An instrument for manufacturing zone-plates by using a lathe," Prec. Eng., 1993, 16(4), 290-295.

Fibre optic displacement transducer with nanometer resolution using ac-modulation

D. Wang, Y. Alayli, M. Bonis and J.C. Henrio

Division Machines, Systèmes et Procédés, Université de Technologie de Compiègne
BP 649, 60206 Compiègne Cedex (France)
tel: (33) 3 44 23 45 18 ; Fax: (33) 3 44 23 52 29 ; email: wangdanp@utc.fr

Abstract

This paper describes an accurate noncontacting fibre optic ac modulated measurement system capable to the measuring the displacement of a reflecting surface with nanometer resolution. The light source feed circuit was designed in order to reduce drift. The technique of modulation and demodulation was used to obtain a greater stable linear measuring range with high resolution. The results of calibration show that the sensitivity of the fibre optic transducer is 0.06 $V.\mu m^{-1}$. The random noise level has been reduced to less than 3 nanometers over a dynamic bandwidth of 500 Hz and 2 nanometers over a dynamic range of 100 Hz.

Keyword : Displacement, fibre optic, calibration, dynamic range

Introduction

Fibre optic displacement transducers have the well-known of permitting measurements to be performed without direct mechanical contact, nor interaction force, between the transducer and the object to be measured. Moreover, their insensitivity to external eletromagnetic disturbances has been pointed out by several authors.[1,2,3] Two distinct ways are used to measure displacements using fibre optic transducers : either by interferometric sensing or with intensity-based transducers. The interferometer is the most accurate device, because of its high resolution and stability of measurement. For example, the extrinsic Fabry-Perot fibre optic interferometer (EFPFOI)[4,5] has been used to measure displacements with subnanometer resolution. Nevertheless, the associated EFPFOI demodulating procedure involves fringe counting to recover relative displacement ; therefore, its precision and stability depend on the wavelength of the light. On the other hand, the transduction mechanism of the intensity-based transducer uses the modulation of light power transmitted between the reflecting surface and the receiving fibres, which is proportional to the varying space between the fibre tip and the target.[6,7,8,9] The associated optics and signal processing are much simpler than for an interferometric transducer. Moreover, an incoherent light source is suitable for reflective intensity-modulated fibre optic transducers. Since incoherent light sources are used and the power of light reflected is proportional to the signal measured, the principles of radiometry are applicable in investigating the intensity modulation.

The major problems existing in nanometer order displacement measurement are the drift in the system output and high noise levels, which cause the resolution to deteriorate. The drift is due mainly to the light source. This effect may be reduced with the aid of a reference voltage.[7] In previous work[10], using a dc current fed light source, the sensor resolution was limited by low frequency parasites due to the electronic circuit. The use of ac modulation with appropriate

filtering enables this problem to be overcome, and to increase the accuracy and the signal-to-noise ratio of the system.
In this paper, a fibre optic displacement transducer with an ac modulated and stabilised light source is presented. It permits resolutions of the order of a nanometer for proximity displacement measurements. The principle of the system, experimental results, the calibration set-up, and potential applications are presented and discussed.

Principle of operation

The principle of the reflective intensity-modulated fibre optic transducer is shown in Fig. 1. The probe consists of two, respectively emitting and receiving, fibre optic bundles. The target object is illuminated by the emitting fibers. The measurement relates the displacement of the target object to the amount of light reflected back into the bundle of receiving fibres[1]. A LED is used as the light source. It is illuminated through an electronic circuit fed with a reference voltage to prevent power drift. Amplitude modulation is used to provide an AC light source that significantly improves the signal to noise ratio over a wide bandwidth including static, by narrow band filtering of the output. A photodiode is used as a detector of the optical signal modulated by the displacement. The photodiode is connected to low input noise operational amplifiers in a current to voltage configuration. High precision amplifiers are used to achieve the desired resolution. A voltage output signal which contains the displacement information is obtained by ac demodulation and a signal processing module.
Because of the stabilisation and ac modulation, the drift generated by the light source is reduced to a minimum level, and accordingly the resolution of the system is increased.

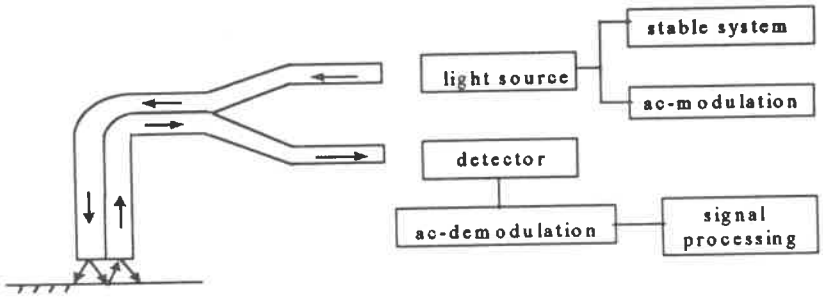

Fig. 1. Schematic principle of the fibre optic displacement transducer with ac modulation

Experiment and results

A schematic view of the set-up used to calibrate the transducer is shown in Fig. 2. The calibration was performed by detecting the displacement of a mirror moved by a low voltage piezoeletric translator (LVPZT) over a 15 μm range. The movement was measured with a heterodyne laser interferometer (ZYGO AXIOM 2/20) with a resolution of 1.25 nm. The LVPZT was mounted on an anti-vibration table and driven by a voltage controller. The expansion of the ceramic was detected using a built-in strain gauge sensor (SGS). Signal acquisition was performed using a two channel (OROS) PC board and softwares supplied by the company ACOVIB. The laser interferometer output was recorded in a PC through a RS 232 interface.

Fig. 3 shows the response of the fibre optic displacement transducer. Displacements are generated by the LVPZT and measured with the AXIOM 2/20 interferometer. The response of this transducer is fairly linear over the investigated range of 10 μm. The sensitivity is 0.06 $V.\mu m^{-1}$.

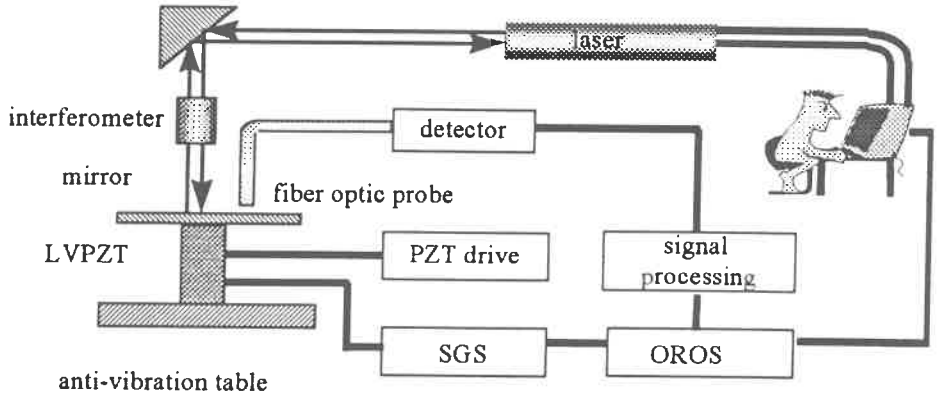

Fig. 2 Calibration system of the fibre optic displacement transducer

The fibre optic ac modulated displacement transducer was tested with dynamic bandwidth of 100 Hz and 500 Hz respectively. These may be tuned according to the domain of utilisation. Fig. 4(a) shows the spectrum of the response of the LVPZT driven by a sine wave signal at 60 Hz, with a displacement amplitude of 2 μm. The signal output of the SGS at the detected frequency of 60 Hz is 70 dB higher than the maximum noise voltage. Fig. 4(b) presents the spectrum of the fibre optic transducer output to the same 4 μm displacement of the LVPZT, with a dynamic bandwidth of 100 Hz. The signal voltage of the fibre optic transducer is 95 dB higher than the maximum noise level.

Fig. 5(a) shows the spectrum of the response of the LVPZT to a sine wave signal of 325 Hz with a displacement of 4 μm, while the spectrum of the fibre optic transducer with a response dynamic bandwidth of 500 Hz is shown in figure 5(b). The output signal of the transducer is 85 dB higher than the noise level.

The noise signal is presented in Fig. 6, recorded over ranges of 100 Hz and 500 Hz respectively. The static noise amplitude corresponds to about 2 nanometers peak-to-peak with the bandwidth of 100 Hz, Fig. 6(a), and to about 3 nanometers p-p in the case of 500 Hz, Fig.6(b).

All the above measurements were performed at the temperature of 296 K.

Conclusion

An ac modulated fibre optic displacement transducer has been described. It was designed to measure small displacements, mechanical vibrations and surface profiles without contact. The drift of the intensity of the light source was considerably reduced by using a feed circuit with a reference voltage. The amplitude modulation technique was used to increase the signal to noise ratio to more than 90 dB for a 4 μm range, and to expand the dynamic measuring range of the transducer up to several hundred Hertz. The response of the transducer shows good linearity over the domain tested. This transducer has a high sensitivity over a wide dynamic bandwidth.

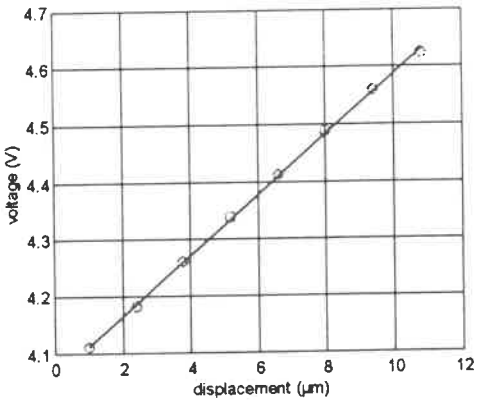

Fig. 3 Static response of the fibre optic displacement transducer

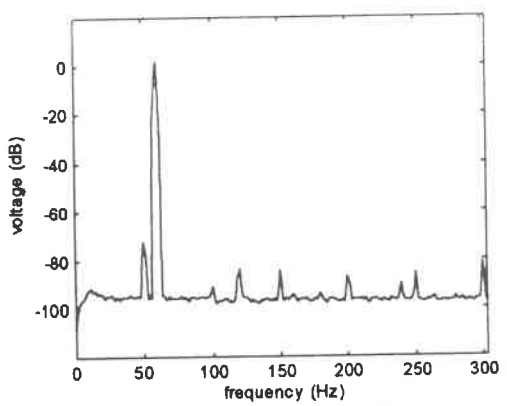

(a) Response of the LVPZT

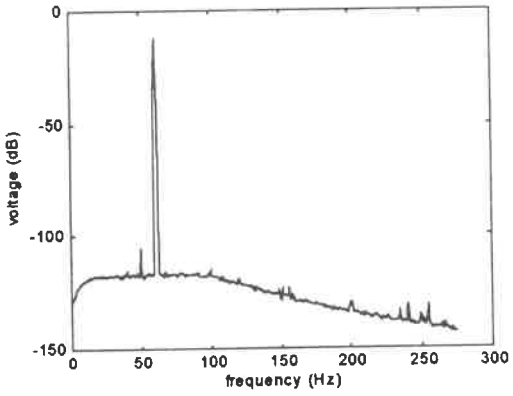

(b) Response of the transducer with filtering at 100 Hz

Fig. 4 Response to a sinus signal input at 60 Hz

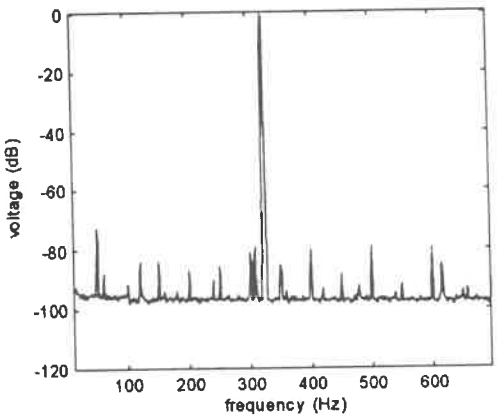

(a) Response of the LVPZT

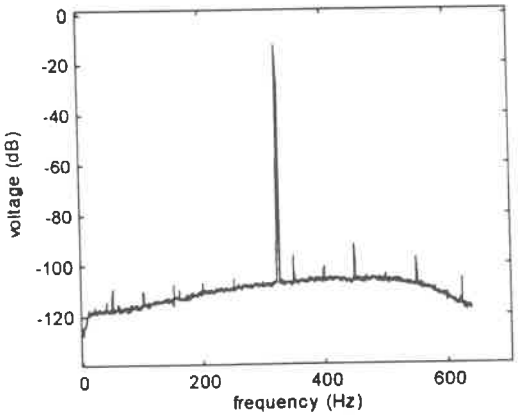

(b) Response of the transducer with filtering at 500 Hz

Fig. 5 Response to a sinus signal input at 325 Hz

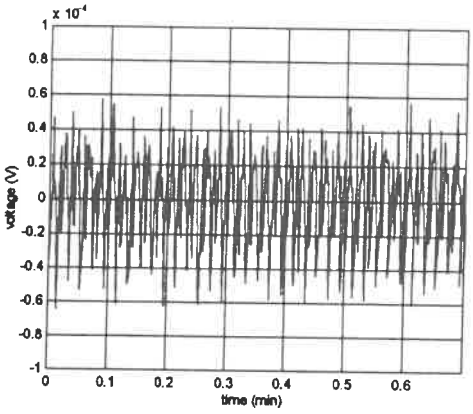

(a) bandwidth of 100 Hz

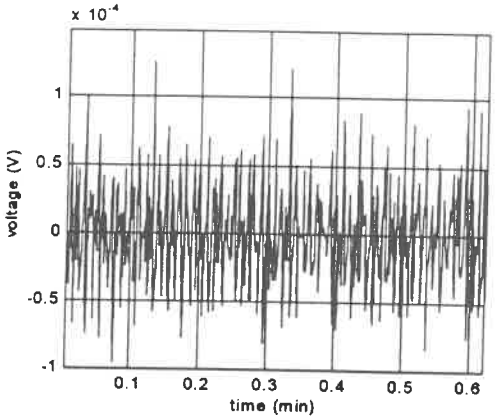

(b) bandwidth of 500 Hz

Fig. 6 Static noise of the fibre optic displacement transducer

Acknowledgements

Particular thanks are due to our colleague V. Nautet for his help in signal processing.

References

1. C. Lin and R. Chang, Fibre optic displacement sensors for the measurement of a vibrating object, Precision Eng., **16**, 4, 302-306, 1994.
2. R. P. Main, Fibre optic sensors future light, Sensor Review, July 1985.
3. C. M. Davis, Fibre optic sensors : an overview, Opt. Eng. **24**, 2, 347-351, 1985.
4. K.A. Murphy, M.F. Gunther, A.M.Vengsarkar, R.O.Claus, Fabry-Perot fibre optic sensors in full-scale fatigue testing on an F-15 aircraft, Appl. Opt., **31**, 4, 431-433, 1992.
5. D. Wang, X. Zheng, Interference optic fibre displacement sensor, Report of the state natural science fund item (In Chinese), 5, 1994.
6. L. Heogenboom, G. Hull-Allen, S. Wang, Theoretical and experimental analysis of a fibre optic proximity probe, SPIE **478**, Fibre optic and laser sensors II, 46-57, 1984.
7. R.O. Cook, C.W. Hamm, Fibre optic lever displacement transducer, Appl. Opt., **18**, 19, 3230-3241, 1979.
8. D. Wang, Y. Alayli, M. Bonis, An ultra-precision optical fibre optic displacement sensor, Proc. IMEKO, Copenhague, 101-106, 1996.
9. G.Z. Wang, A. Wang, R.G. May, R.O. Claus, Self-referenced fibre optic sensor for microdisplacement measurement, Opt. Eng., **34**, 1, 240-243, 1995.
10. D. Wang, Y. Alayli, M. Bonis, Design and modelling of a fibre optic displacement sensor with nanometer resolution, Proc. 9th IPES, Braunschweig, **1**, 90-92, 1997.

NANOMETER LEVEL AUTOFOCUS AIR GAUGE

Tim Thomas, Chris Hamaker, Jerry Martyniuk, Gene Mirro
Etec Systems, Inc.
9100 SW Gemini Drive
Beaverton, OR 97008

Introduction

High-performance UV lithography systems require a means of accurately controlling the distance between the last optical element and the surface to be exposed. Modern systems are using large numerical aperture lenses with a narrow depth of focus, requiring focus control to better than 0.1 micron and with a target distance of several millimeters. The accuracy of a focus control system can be no greater than the accuracy of the distance sensor. Also, this sensor must not appreciably damage, heat, cool, or contaminate the target surface and must not expose the photoresist. The sensor must be insensitive to the properties of the surface to be exposed. Some of these properties are: dielectric constant, electrical resistance, thin film effects, and reflectivity. A pneumatic system meeting the above requirements has been developed. See Figure 1. A source of constant air flow supplies two parallel air paths, referred to as *reference* and *measurement*. The reference path has a fixed resistance to air flow. The measurement path has a flow resistance, which is a strong function of the distance between the lens and the target surface. By measuring the relative flow rates in the two paths, the distance to the target surface can be determined. Air flow rate is measured using a hot wire anemometer operated in a constant-temperature bridge. Long-term accuracies of 0.1 micron and noise of 10 nanometers peak-to-peak in the DC to 100 Hz range have been achieved.

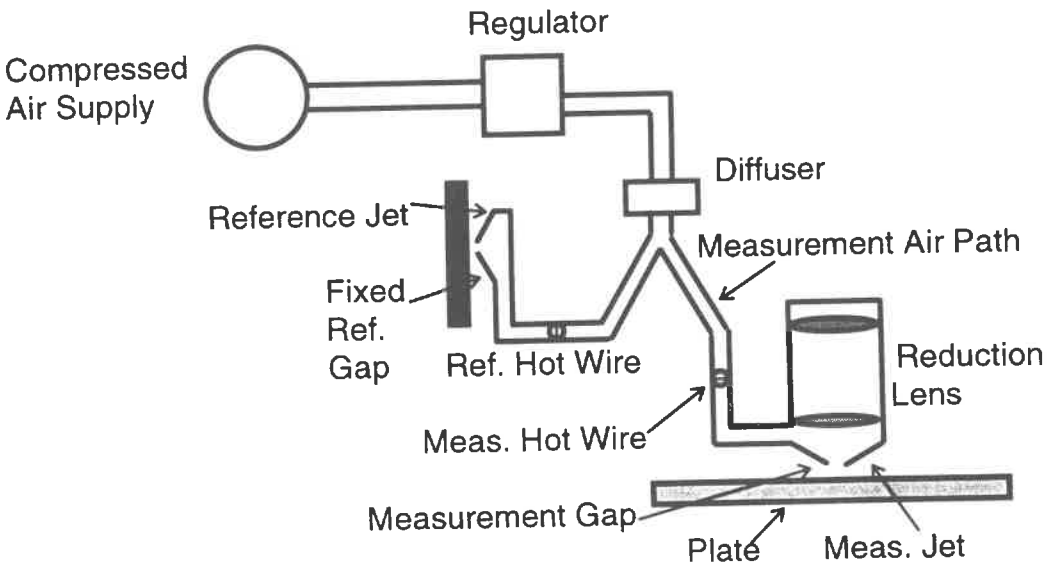

Figure 1. Overview of air gauge pneumatic design.

Pneumatic-electrical model

An electrical distributed model for noncompressible flow in pipes and orifices was developed that relates the fundamental properties of air flow, pipe geometry, and orifice resistance to the electrical quantities of capacitance, inductance, and resistance. These properties are modeled using the time-independent Navier-Stokes equation.

The maximum frequency in the desired bandwidth of the focus sensor can be expressed in terms of an acoustic wavelength in air. Because the focus sensor contains tubes whose length is an appreciable fraction of this

wavelength, an accurate model must include lossy transmission lines, which requires a distributed element analysis. This model was run in PSPICE, and the resulting frequency and time domain responses were in excellent agreement with measured data.

Transmission line equivalents

The two primary transmission line parameters, the characteristic impedance Z_0 and the propagation constant g, are given for fully developed Poiseuille flow as:

$$Z_0 = \sqrt{\frac{R_s T}{2\pi^2 a^4}}\left\{\sqrt{\sqrt{1+\left(\frac{8\mu}{\rho a^2\omega}\right)^2}+1}+j\sqrt{\sqrt{1+\left(\frac{8\mu}{\rho a^2\omega}\right)^2}-1}\right\} \qquad \gamma = \sqrt{\frac{1}{2R_s T}}\left[\sqrt{\sqrt{1+\left(\frac{8\mu}{\rho a^2\omega}\right)}-1}+j\sqrt{\sqrt{1+\left(\frac{8\mu}{\rho a^2\omega}\right)}+1}\right]$$

where a = the pipe radius, R_s = gas constant = 2.87×10^6 cm^{2}sec^{-2}K^{-1}, T = temperature (degrees K), μ = viscosity = 1.8×10^{-4}gm/cm-sec, and ρ = air density = 1.29×10^{-3}gm/cm^3.

Our system can be modeled reasonably well by using seven transmission line sections. See Figure 2. A different section is required each time the tube branches, changes size, or encloses a sensor. The response time of the system is proportional to the cross-sectional area of the tubes. However, if the cross-sectional area is decreased, tube resistance increases in a parabolic relationship. As the tube resistance becomes comparable with the sense nozzle resistance, the settling time lengthens. Also, to maximize the frequency of tube resonances, the tube length must be shortened. This will create additional benefits in lowering the tube capacitance.

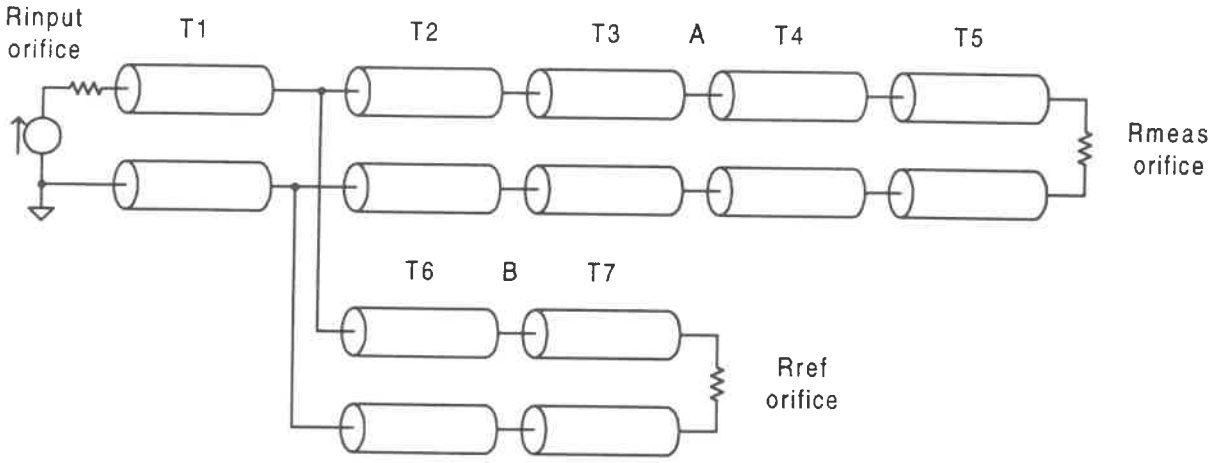

Figure 2. Electrical transmission line analog of the air gauge.

Hot wire anemometer modeling

Even though the pneumatic electrical analog was demonstrated favorably, there was still the issue of time constants innate in the actual hot wires and their surroundings. To estimate this response time, we generally follow the treatment of Lomas.[1] Assuming that radiation effects are negligible, the one-dimensional equation governing heat transfer from the hot wire as a function of position x along the wire and time t is given by

$$A\frac{\partial}{\partial x}\left(k_s\frac{\partial T_s}{\partial x}\right)+\frac{I^2\rho_r}{A}-\rho\, cA\frac{\partial T_s}{\partial t}-\pi\, dh\left(T_s-T_f\right)=0$$

where A = wire cross-sectional area, k_s = wire thermal conductivity coefficient, T_s = wire temperature, T_f = temperature of the fluid, I = wire current, ρ_r = resistivity of the wire, ρ = density of the wire material, c = specific heat of the wire material, d = wire diameter, and h = coefficient of convective heat transfer. The value for h is dependent on the fluid velocity v. The terms in this equation represent respectively the heat losses via conduction at the ends of the wire, the rate of Joule heating, the rate of heat storage from warming of the wire, and the rate of convective cooling by the fluid. Generally, T_s and $\rho_r = \rho_0[1+\alpha(T_s-T_0)]$ are functions of x; here a is the

temperature coefficient of resistivity and ρ_0 is the resistivity at a reference temperature T_0. However, if the heat loss is primarily due to convection (large wire aspect ratio), then T_s is constant except near the ends. In this case, and for fluid flows sufficiently high that Kramer's law for the velocity dependence of the convective cooling is valid, then the time constant is approximately

$$\tau = \frac{\rho c A l \left(\overline{R}_s - R_f\right)}{I^2 \alpha R_f R_0}$$

where l is the length of the wire and $\overline{R_s}$, R_f, and R_0 are the resistances of the wire at temperatures T_s, T_f, and T_0, respectively. The values of the relevant parameters for the anemometer design described in this abstract are given in Table 1. With these values, the estimated value for t is about 0.9 ms. Thus, the intrinsic response of the hot wire is fast compared to the pneumatic time constants of the system and does not limit performance.

Table 1. Design parameters for platinum-coated tungsten hot wire with 100K temperature rise.

Parameter	Value
ρ	19.3 g-cm^{-3}
c	0.133 J-g^{-1}-K^{-1}
A	1.1×10^{-7} cm^2
k_s	0.73 W-cm^{-1}-K^{-1}
l	1.5 mm
I	23 mA
α	0.0048 K^{-1}
R_0	6 Ω
$\overline{R_s}$	8.8 Ω
R_f	6 Ω
v	15 cm-s^{-1}

Heat loss mechanisms

To maintain the efficiency of the hot wire in measuring air flow, it is important that the Joule heating is dissipated primarily through convection. The other possible mechanisms are conduction through the ends of the wire and radiation. We can determine the relative magnitudes of the various terms by solving the heat transfer equation for T_s in the steady state and computing the values. Assuming that the temperature of the end points of the wire remains at T_f, the solution is of the form

$$T_s - T_f = \frac{K_2}{K_1}\left[\frac{\cosh\left(\sqrt{|K_1|}\, x\right)}{\cosh\left(\sqrt{|K_1|}\, l/2\right)} - 1\right] \quad \text{where} \quad K_1 = \frac{\alpha I^2 R_0 - \pi dhl}{A k_s l} \qquad K_2 = -\frac{I^2 R_f}{A k_s l}$$

The solution is valid for negative values of K_1. With the parameters from Table 1, the average temperature rise above ambient is approximately 98K, and the convective and conductive cooling mechanisms account for about 75 and 24%, respectively. The remaining 1% is lost through radiation, as calculated using the Stefan-Boltzmann equation.

The remaining concern is that the convective losses are due to self-convection rather than from the forced fluid flow. In this case, a poor signal-to-noise ratio would be expected. There are several criteria that may be used to determine whether the flow is adequate. One such criterion for the lower limit of flow comes from the condition that self-convection accounts for less than 10% of the total cooling. This condition is met if $\mathrm{Re} > 2.2\mathrm{Ra}^{0.418}$ where Re and Ra are the Reynold's and Rayleigh numbers, respectively. In this design, the left and right sides evaluate to 0.044 and 0.0028, respectively, so the cooling of the hot wire is indeed due primarily to the air flow.

One final issue needs to be considered. The model assumes that the supports for the hot wire remain at the temperature of the fluid. Because heat is being conducted into these supports from the hot wire, some mechanism must be provided for removing this heat. Typically, the fluid flow is adequate for this. However, if a significant drop in flow occurs, then the supports themselves may begin to heat. Since their thermal mass is much greater than that of the hot wire, the response time for them to attain equilibrium can be quite large. To minimize these effects, the thermal conductivity and thermal mass of the supports can be increased. In this way, transient drops in flow will cause relatively small changes in the support temperature and the recovery time will be short.

Electronic design

The purpose of the hot wire electronics is to convert the voltages and currents from the hot wires into an output voltage that is linearly related to the distance between the lens nosepiece and the plate (the target). The primary

components of the electronic design are shown in Figure 3. The hot wire constant temperature bridge holds the hot wire mean temperature at a constant value well above room temperature. As air flow across the hot wire increases, the amount of power required to maintain the hot wire temperature increases, and the voltage out of the bridge circuit increases. Since the hot wire temperature does not vary, the thermal time constant of the hot wire is not a primary limiting factor in the speed of response of this circuit. A separate bridge is needed for each hot wire.

The differential amplifier removes signals that are common to both hot wires. This helps to eliminate responses to acoustic noise, air source flow variations, environmental variations, power supply noise, and other common-mode error sources. The variable gain stage is used to boost the level of the differential signal to the degree required by the linearizer stage. The linearizer compensates for nonlinear response from two sources: the flow resistance of the measurement leg, which is inversely proportional to the third power of the distance from the lens to the target, and the transfer function of the hot wire/bridge combination. The resulting output voltage is linear over the focus height range of 30 to 100 microns, and the gain is 0.25 volts per micron. The cable driver is designed to drive a long cable without the usual stability problems associated with capacitive loading of an op amp.

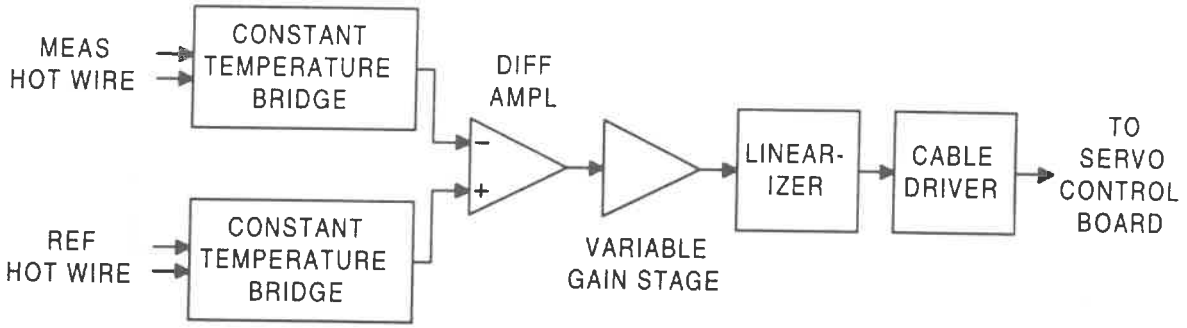

Figure 3. Block diagram of air gauge focus sensor.

Overview of the hot wire constant temperature bridge

See Figure 4. Rhw represents the resistance of the hot wire. As the current through Rhw increases, the temperature of the hot wire increases, and the resistance Rhw increases. A1 is an amplifier with very high DC gain. A1 will tend to make its two input voltages equal. This occurs if the ratio of R1 to R2 is equal to the ratio of R3 to Rhw. As the output voltage of A1 increases, the current through the hot wire increases, the hot wire resistance increases, and the ratio of R3 to Rhw decreases. If the R values have been chosen properly, A1 will be able to manipulate the ratio of R3 to Rhw until it is equal to the ratio of R1 to R2. Since Rhw has a unique value for a given hot wire temperature, this circuit in effect controls the hot wire temperature by controlling the hot wire resistance.

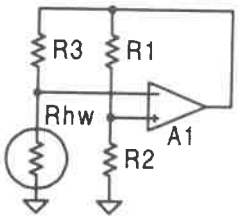

Figure 4. Simplified hot wire constant temperature bridge.

If we now cause air to flow across the hot wire, its temperature will tend to decrease, causing Rhw to decrease. This will cause the output of A1 to increase, causing the current through the hot wire to increase, causing the hot wire temperature to increase, causing the hot wire resistance Rhw to increase. Therefore, A1 will tend to keep the hot wire resistance and temperature constant, regardless of the air flow across the hot wire. However, as air flow increases, the voltage at the output of A1 must increase to keep the hot wire at the proper temperature. Therefore, the voltage at the output of A1 will be roughly proportional to the air flow across the hot wire. In this way, a hot wire can be used as an anemometer (a device for measuring air flow).

Mechanical design

The distance from the vertex of the last optical element in the Etec reduction lens to the focal plane is only 0.92 mm. The sensor is designed to work within this limited space. The measurement jet, as shown in Figure 1, is designed to form an air-tight seal and cavity with the reduction lens. Air enters this cavity and escapes at the measurement gap. The unique shape of the measurement jet is a result of the limited space available and lens geometry.

Acoustic disturbances can be significant sources of sensor noise. To minimize the sensitivity of the sensor to acoustic disturbances, the reference and measurement air paths have been designed to be geometrically matched. Acoustic disturbances should be nearly identical in phase and amplitude when reaching the hot wires, and all acoustic disturbances will appear as common-mode signals at the differential amplifier input. As a result, acoustic disturbances will be largely rejected by the differential amplifier.

The length and diameter of the air passages determines the sensor's fluid capacitance, resistance, and inertance. The tube lengths were made as short as conveniently possible to improve the fluid step response.

The thermal response of the hot wire has two primary thermal time constants. When a large step input occurs, the sensor first responds very rapidly (the response of the hot wire) and then slowly reaches steady-state (the response of the support needles). The support needle thermal response was improved by increasing its mass. Further improvement was made by fabricating the support needles from pure silver and applying a coating of gold plating directly to the silver. The hot wire is attached to the support needle using indium-silver alloy solder. Figure 5 illustrates the hot wire probe and Figure 6 illustrates the sensor assembly.

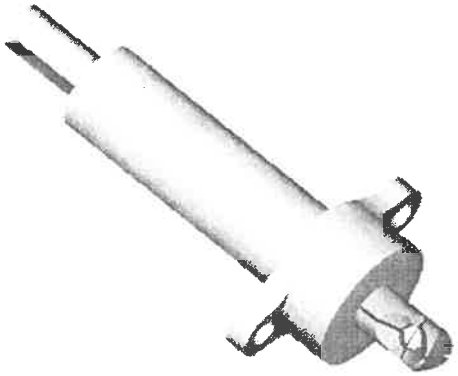

Figure 5. Hot wire probe assembly.

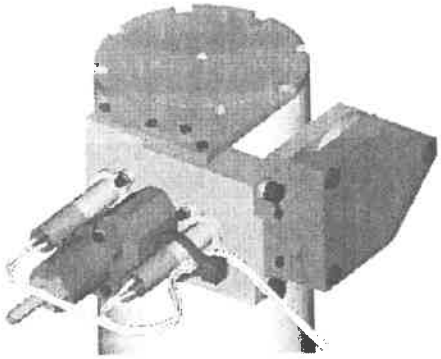

Figure 6. Completed sensor.

Trademarks
Etec is a registered trademark of Etec Systems, Inc.
All other trademarks are the property of their respective owners.

[1] Charles G. Lomas, *Fundamentals of Hot Wire Anemometers*, (Cambridge University Press, Cambridge, 1986), pp. 55–83.

Study on High Precision Cutting by Workpiece Referred Form Accuracy Control System

-A Proposition of Double MTS Method -

Naohiro Ohno[1]*, Takanori Yazawa[1], Tsuguo Kohno[1], Yutaka Uda[2]
[1]Tokyo Metropolitan Institute of Technology, [2]Nikon Corporation
*Present Address Konica Corporation

1. Introduction

There continues to be ever increasing demand for more precision cutting by single point diamond turning. We proposed Workpiece-Referred Form Accuracy Control system (=WORFAC) and have confirmed an effectiveness of this method[1]. It is the direct control method of the relative displacement between cutting tool and workpiece used by in-process measurement. Since the displacement sensing is based on the workpiece surface, for the precise controlled cutting, the first reference surface with a good quality is essential.

In this study, we propose Double Micro-Tool Sarvo (=D-MTS) method and confirmed it's good function by experiments.

2. Principle of D-MTS

In the WORFAC, relative motion of the workpiece and cutting tool point is controlled in process measurement instead of trying to control all the mechanical elements. The principle of the WORFAC is shown in Fig.1. If the tool-holder receded in the distance from the workpiece, change of the relative displacement between tool-holder and the workpiece surface is measured by the gap sensor which is attached on the tool-holder, and the micro tool servo (=MTS) push out the tool by the same amount, and vice versa.

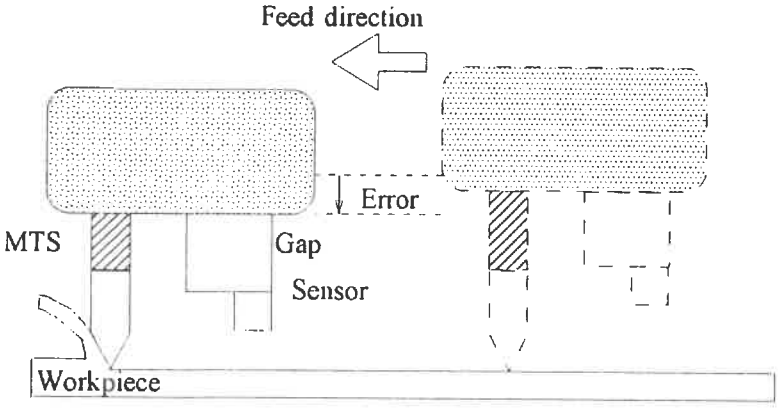

Fig.1 Principle of WORFAC

As for the cylindrical turning[2], it was found that the WORFAC is effective for the face turning[1]. However, two problems lie in it to realize all the surface into high accuracy.

The measurement of the displacement sensor is based on the workpiece surface. For the controlled cutting, the precise reference surface is essential. However, because of the distance between the sensor and the tool, the first reference surface can not always be controlled. This is the first problem.

The second problem is copying the form error of the first non-controlled surface on the controlled cutting surface. In the WORFAC, only the relative motion between the sensor and workpiece is controlled by the information of gap sensor. If the first reference surface has an error, the sensor regards the error as the change of relative displacement. So, the controlled surface will have the same error, i.e. an error on the first reference surface

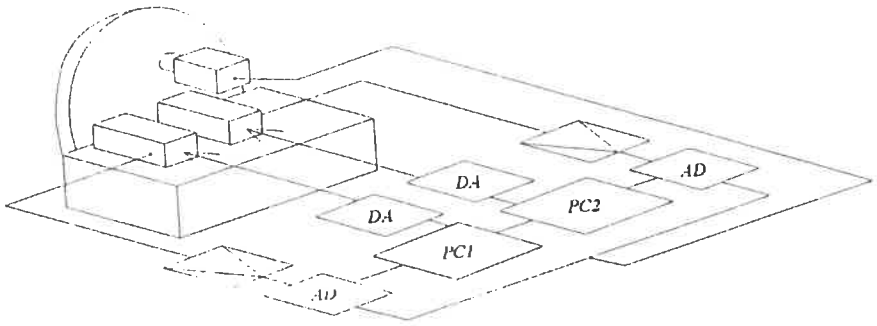

Fig.2 System of D-MTS Experiment

is copied on the controlled surface.

In the previous report[3], it was shown that, in the case of cutting from the center to outside, the second problem can be solved by devising the positioning of the sensor and the tool.

To solve the first problem, we propose here D-MTS method, in which two MTSs and one gap sensor are used. Fig.3 shows that the first MTS(=MTS-a), the second MTS(=MTS-b) and the gap sensor are all attached to the same feed table. x_s and y_s are offsets of X- and Y-axis respectively between cutting point of MTS-a and sensing point of the sensor . The offset from MTS-a to MTS-b of X-axis is x_s, and that of y_s is 0. The MTS-a and the sensor make up the ordinal WORFAC system. In Fig.3, it is shown that controlled cutting surface by WORFAC is accurate enough to use it as a controlled reference surface. So, the sensor measures the change of relative displacement only as shown in Fig.4. If the same signal is used to control both MTS-a and MTS-b simultaneously which is started the cutting from the rotational center, the central part of the flat workpiece is can be accurately cut by MTS-b. If the depths of cut of the first and the second tools are in coincidence, an accurately controlled surface can be made to all over the workpiece.

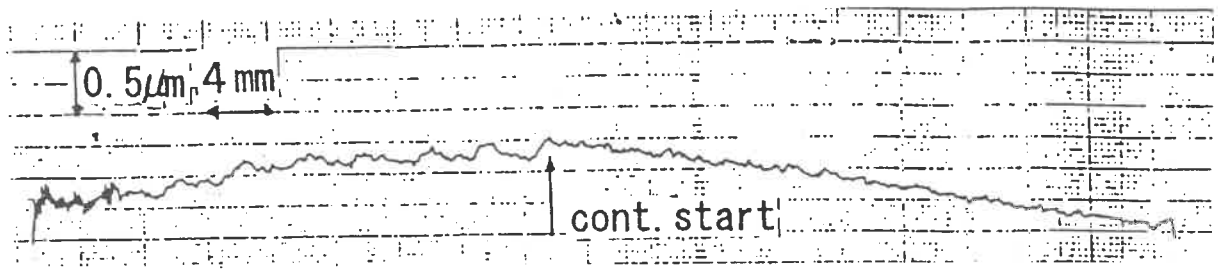

Fig.3 Controlled cutting surface by WORFAC

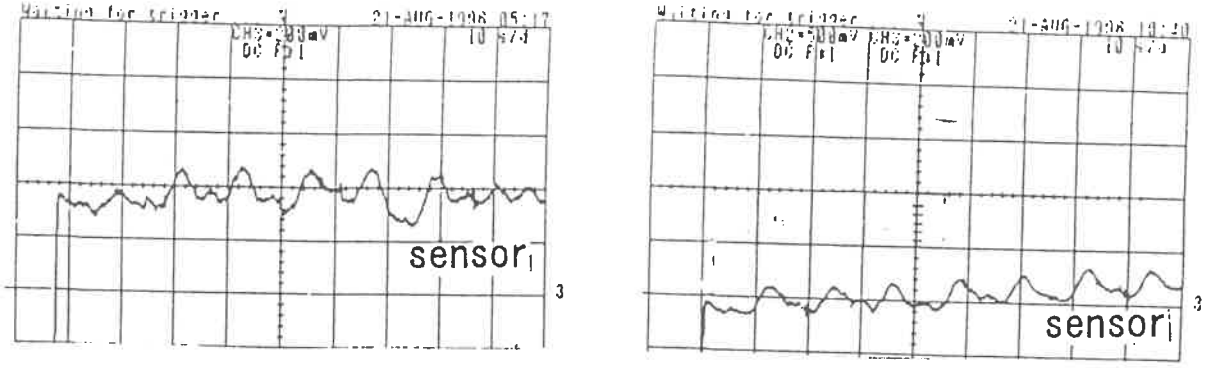

(a)sensor signal of the non-controlled surface (b)sensor signal of the controlled surface

Fig.4 In-process measurement signal

3. Experiment

The results of D-MTS experiment are shown in Fig.5. The surface by non-controlled cutting has some errors due to the feed screw. In the case of the same depths of cut by MTS-a and MTS-b as shown in Fig.5(b), accurately controlled surface is made to all over the workpiece. If they are not in coincidence, a step error will be attributed on the finished surface. However, if the depth of cut of MTS-b is lager than that of MTS-a, controlled MTS-b over-cuts the surface made by MTS-a. Let r_{M2} is a radius of the controlled surface by MTS-b and r_w is a radius of the workpiece as shown in Fig.6. The relation of r_{M2}, r_w and y_g is represented by

$$(r_{M2}/r_w)^2+(y_g/r_w)^2=1. \qquad (1)$$

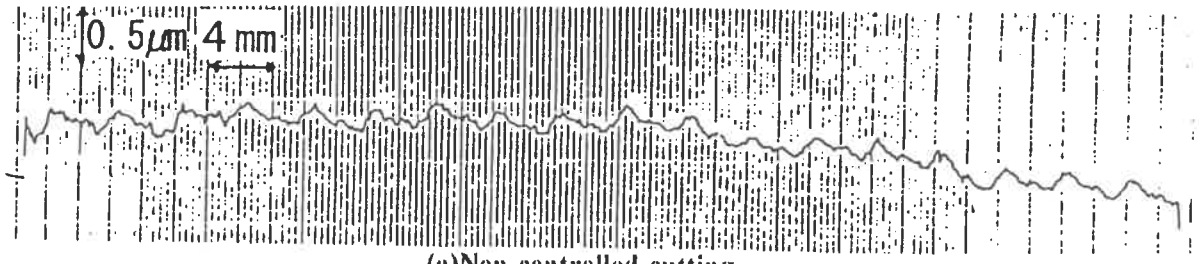

(a)Non-controlled cutting

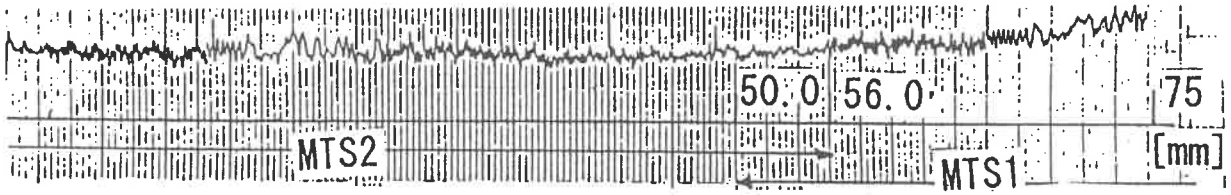

(b)Controlled cutting

Fig.5 experiment of the D-MTS

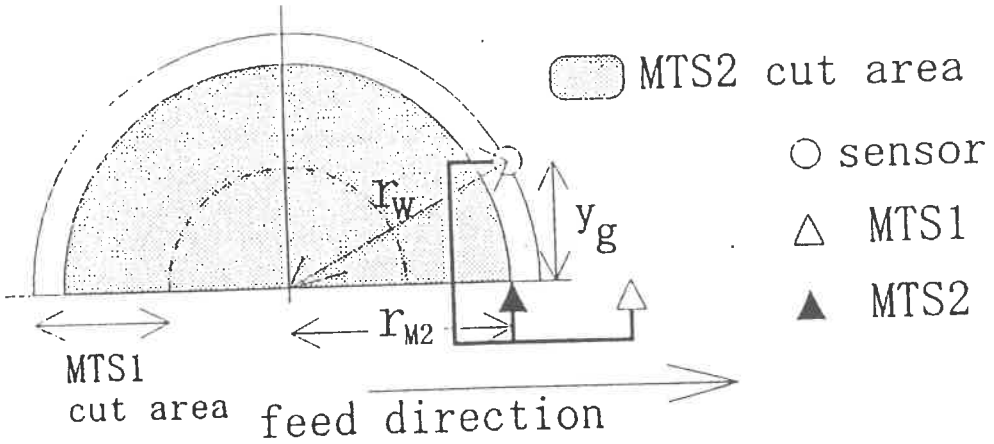

Fig.6 Area of the controlled surface by the second MTS

If y_g is 40 percents of r_w or less, the controlled surface diameter made by MTS-b only is more than 75% of full workpiece.

4. Conclusion

To solve the probrem of the WORFAC, the double Micro Tool Servo (=D-MTS) system was proposed and tested experimentally. The experiment showed the first reference surface of good quality could be obtained. If the depths of cut of the first and the second tools are in coincidence, accurately controlled surface can be made to all over the workpiece. In the different case, step error is attributed to it on the finished surface. But, if the offset between the cutting point of the MTS-a and the sensor can be holded to 40 percents or less for a radius of the workpiece, the controlled surface size will be 75% or more by MTS-b only.

References

[1]T.Kohno, et al.: Precision Engineering, P.9, Vol.11, No.1, 1989

[2]T.Kohno, et al.: Accuracy Improvement of Machine Tool by Workpiece-Referred Control, ASPE Annual Meeting '92, P.376,1992

[3]T.Yazawa, et al.: Accuracy Improvement of Machine Tool by Workpiece-Referred Control (4th Report), ASPE Annual Meeting '95, P.151

DESIGN OF A LINEAR VOICE COIL ACTUATOR FOR FAST TOOL SERVO APPLICATIONS

Wade Greene and Dale E. Schinstock
The University of Alabama
Tuscaloosa, Alabama

Introduction

A linear voice coil (Figure 1) has been proposed as the actuator in an extended range Fast Tool Servo (FTS). Many non-axisymmetric parts are currently fabricated in Diamond Turning Machines (DTM) using piezoelectric FTS designs to actuate the diamond tool. However, several problems exist with using a piezoelectric actuator including limited range of motion and hysteresis.

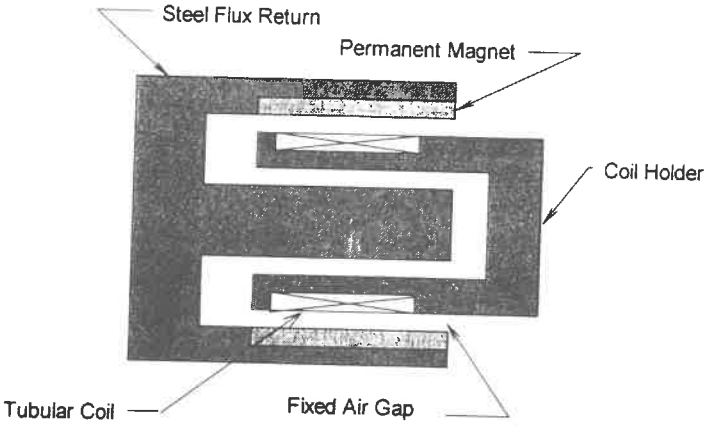

Figure 1. Linear voice coil actuator schematic.

The linear voice coil offers a greater range of motion than piezoelectric actuators, while providing high bandwidth and resolution. The high bandwidth is a result of high power to mass ratios. These actuators have a low armature mass and thus can produce high accelerations. The low mass of the actuator-tool assembly poses a problem however, because it adversely affects the disturbance force. Since the uncontrolled plant has poor disturbance rejection properties, the controller must incorporate compensation that will improve the disturbance rejection of the closed loop system. Another significant problem associated with voice coil actuator is that they can generate considerable heat. This abstract examines the feasibility of using a linear voice coil actuator for FTS applications. The goal of the system is to obtain a 1mm range of travel at 50 Hz.

System

Figure 2 shows a prototype system developed at The University of Alabama, Department of Mechanical Engineering. The prototype uses a model LA13-12-000A linear voice coil actuator manufactured by *BEI Sensors and Systems Company*. The performance data for this coil is shown in Table 1.

Table 1. Performance data of a *BEI* LA13 voice coil.

Continuous stall force (F_{CS})	7.12 N(1.6 lb.)
Force constant (K_F)	10.45 N/amp(2.35 lb./amp)
Stroke	± 3.12 mm (0.125 in.)
Weight of coil assy.	14.2 g(0.5 oz.)
Weight of field assy.	102.1 g(3.6 oz.)

The coil that was selected for the prototype model is smaller and less powerful than one that would be used for a long range FTS. The amplifier chosen for the prototype system is a *Copley Controls Corporation* DC-Servo Amplifier, model 201. It is a high frequency pulse width modulated switching amplifier that offers a maximum current of 3 amps. The high switching frequency of 26 kHz allows operation with low inductance motors. It also allows amplifier bandwidths that are well beyond servo frequencies and consequently will not degrade position servo stability or performance.

A simple flexural bearing was constructed to provide the linear movement of the system. Analysis was performed on the voice coil/flexure system to determine the modes of vibration and whether they would affect the performance of the system. The first mode of vibration was found to be at 15 Hz with the mass attached.

A capacitance gauge sensor is used to detect the position of the system for feedback into the computer. The advantages of using a capacitance gauge over that of other analog sensors are good resolution and non-contacting measurements of position.

The computer controller consist of a Pentium 120 MHz computer with a 16 bit data acquisition card *(Computer Boards* model: CIO-DAS1602/16). The total noise for the ADC and capacitance gauge is approximately 58 nm. The computer and card together produce a time delay from the time the ADC reads the data, runs the control calculations and then outputs the control voltage. The time delay was calculated to be two sample periods of the ADC (0.4 milliseconds).

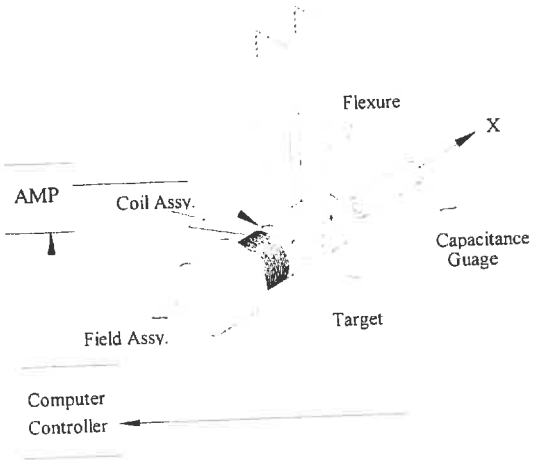

Figure 2. Linear voice coil actuator test system.

Control

FTS applications require direct contact of the tool with the workpiece, resulting in significant disturbances on the tool. For this reason, the dynamic stiffness of the system must be large. The dynamic stiffness is the inverse of the position response to disturbance forces. The difficulty with using a voice coil actuator for such an application is that the moving mass is small which decreases the dynamic stiffness. Also, the stiffness of the flexure bearing must be kept small to allow the voice coil to achieve the desired displacements.

System identification was conducted on the amplifier to determine its contribution to the system dynamics. The bandwidth of the amplifier is over 2 decades past the desired closed loop position response. For this reason the amplifier dynamics are left out of the controller design, but were added to the model for computer simulations and frequency response models.

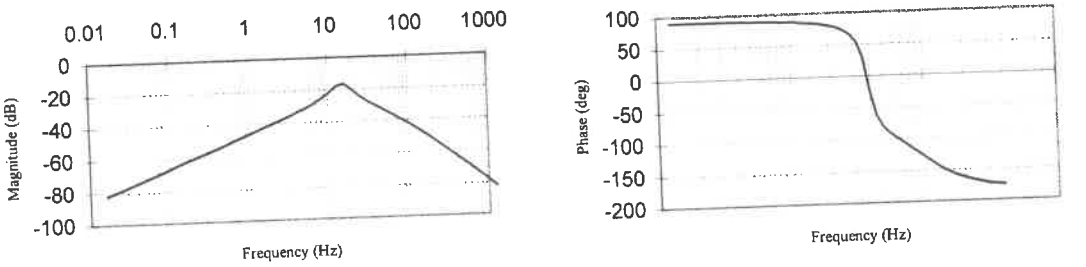

Figure 3. Position frequency response to a disturbance input to the tool.

The plant for the system produced two imaginary poles that are just to the left of the imaginary axis on the root locus. By using a PID controller the zeros from the controller were placed on top of the poles from the plant. The gains for the controller were chosen by setting the position bandwidth of the system at 100 Hz.

Typical production diamond tool forces are on the order of 0.05N [1]. Using the diamond tool forces and the peak of the disturbance introduced to the system (see Figure 3), the resulting error is approximately 45 μm at 15 Hz. This is an unacceptable error. The peak in Figure 3 is decreased by increasing the mass of the coil and tool and by increasing the spring rate of the flexure. However, the small coil used in the prototype is not large enough to drive a significantly large mass and high spring stiffness.

A command feedforward controller was added to the system to improve the magnitude and the phase of the system. The objective of command feedforward control is to modify the command input to the system in such a way that the performance of the system is improved by reducing or eliminating phase errors. The general form of the feedforward control uses the inverse of the plant transfer function (see Figure 4).

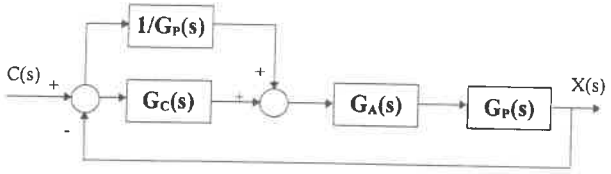

Figure 4. Block diagram of feedforward controller.

Testing

Testing was performed on the system using both the PID controller with and without feedforward. Each controller scheme was tested at different frequencies ranging from 1 to 200 Hz to determine the frequency response. The command used was a 76 μm (3 microinch) 20 Hz sine wave. Figure 5 shows the frequency response for the modeled system and the actual system. The results of the model closely matched the experimentally developed transfer function.

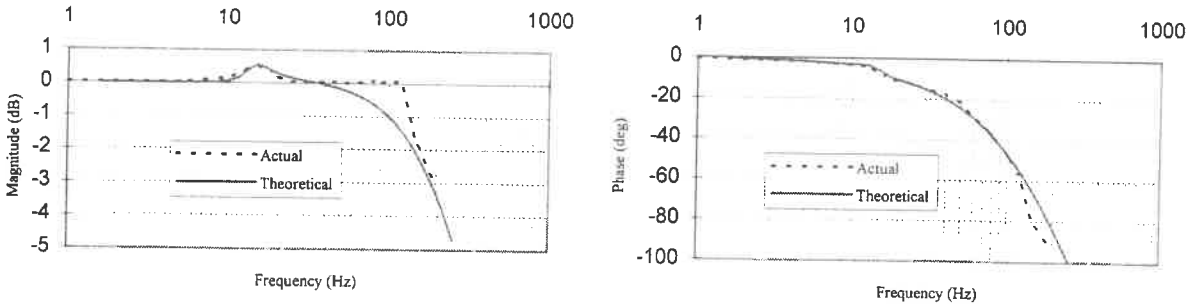

Figure 5. Closed loop frequency response comparing the actual to the theoretical system.

The feedforward controller was tested to determine the frequency response. Figure 6 shows the actual test data for both the feedforward and the non-feedforward controller schemes. Adding feedforward control improves the magnitude at 20 Hz but shifts the resonant peak to 100 Hz, and is amplified by 1.3 dB at resonance. The phase is much flatter with feedforward control with the phase decreased by 17 degrees at 50 Hz.

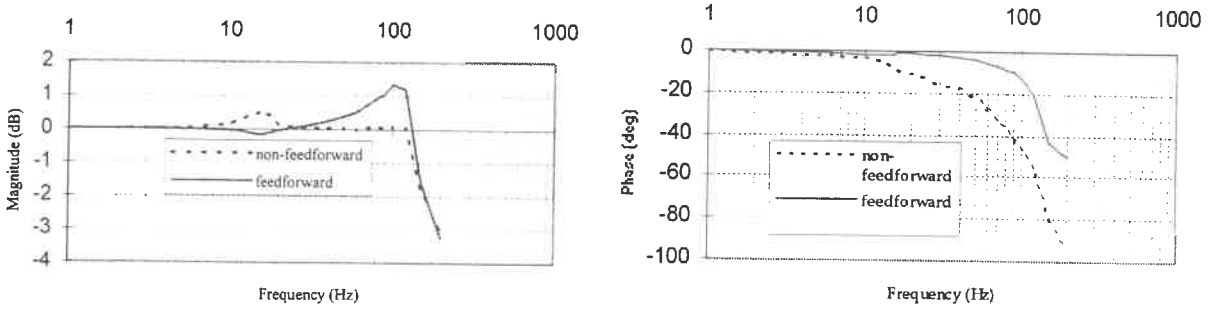

Figure 6. Frequency response of feedforward and non-feedforward controller.

Feasibility of using a Voice Coil for FTS applications

The prototype system studied is incapable of rejecting disturbances and providing the range of motion necessary for FTS systems. The major drawbacks to the system are the underpowered voice coil and limited mass and dynamic stiffness to reject the disturbances. With present technology, can a system be built that could be used for an FTS? This section of the paper examines a theoretical model using a larger and more improved system.

A larger voice coil actuator was selected that should provide sufficient power to operate the system (see Table 2). A flexural bearing system is still used but the spring constant will need to be increased to support the weight of the new coil and also to increase the stiffness of the system.

Table 2. Performance data for a *BEI* LA90 voice coil.

Continuous stall force (F_{CS})	289 N(65 lb.)
Force constant (K_F)	35 N/amp(7.9 lb./amp)
Stroke	± 14.5 mm(0.57 in.)
Weight of coil assy.	0.72 kg(1.57 lb.)
Weight of field assy.	15.9 kg(35 lb.)

Using the same design methology developed for the prototype system, a model was developed for the new system. The flexure bearing was designed to increase the spring constant to 350 kN/m or 2000 lb./in. (the spring constant for the prototype is 336 N/m or 1.92 lb./in.). A PID controller with a bandwidth of 300 Hz is used for the system to give a pole-zero cancellation. The closed loop frequency response of the position is shown in Figure 7. It is assumed that a laser interferometer and better data acquisition card will be used for the new system. This combination should reduce the error from noise and give an extended range of the feedback sensor.

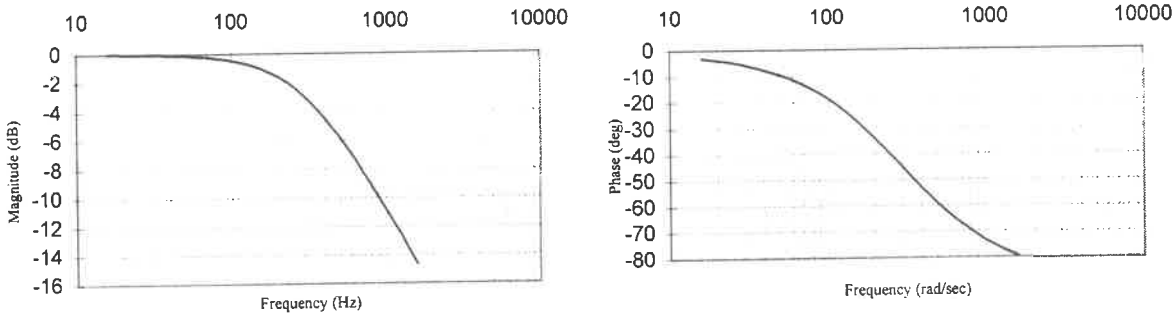

Figure 7. Closed loop frequency response of the new system.

The more powerful voice coil will enable the use of a larger mass and spring stiffness to improve the disturbance rejection properties. The force needed to actuate the new coil 1 mm is 173.5 N or 39 lb. The increase in mass of the system is due to the larger and heavier coil.

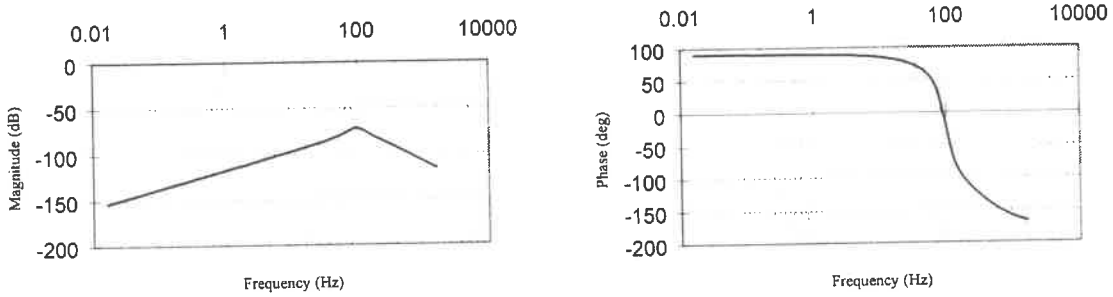

Figure 8. Position frequency response to a disturbance input to the tool for the new system.

The disturbance peak for the new system is approximately -72 dB at 100 Hz (see Figure 8). By using the diamond tool forces outlined earlier this will result in an error of approximately 72 nm. This system has greatly reduced the error from the disturbance input.

Conclusions

The feasibility of using a voice coil for FTS application has been examined. A prototype was built as proof of the concept. The performance of the prototype was improved by using a PID and feedforward control. Knowledge obtained from the prototype was used to model a voice coil system capable of meeting performance goals. Using the more powerful voice coil, the stiffness and mass of the system can be increased, thus increasing the disturbance rejection properties. Simulations show that the new system will be able to achieve the desired range, with an error less than 100 nm.

References

[1] J. Schaefer, C. Arcona, T.A. Dow, G.M. Moorefield II, K. Falter, and R.L. Rhorer Diamond point tool force measurement in a production environment. Proceedings from the ASPE 1996 Annual Meeting, pp 412-415.

Intelligent 3D-Free-Form Surface Cutting toward High Precision and High Efficiency

Mamoru Mitsuishi, Makoto Hashiguchi, Zenkichi Kiriyama, Li Junqi and Takaaki Nagao
Department of Engineering Synthesis, Faculty of Engineering
The University of Tokyo
Hongo 7-3-1, Bunkyo-ku, Tokyo 113, Japan
mamoru@nml.t.u-tokyo.ac.jp
http://www.nml.t.u-tokyo.ac.jp/~mamoru

1. Introduction

The authors have developed a system using a machining center equipped with a multi-axis force sensor for 2 and half dimensional end-milling which has real-time machining state judgement capability, adaptive control capability by modifying the feed speed and the spindle speed, and the high efficiency cutting capability by avoiding chatter vibration [1, 2]. This paper proposes a real-time cutting state judgement method for the flank milling using a ball and a square-endmill. Experimental results for adaptive control to achieve high quality cutting is also presented.

2. Related work

Many researchers have discussed chatter vibration in machine tools, starting Merritt[3], Tlusty[4] and Tobias[5]. In particular, Sato, et al. [6] have discussed the multiple regenerative effect in chatter vibration. Concerning the 3D-free-form surface cutting, Yamazaki, et al. [7] have developed a system where feed speed can be controlled in real-time, maintaining the cutting force constant by referring to the geometrical model of a workpiece. In the system it is possible to change the geometrical shape of the workpiece in real-time. It is also possible to calculate the metal removal rate. Feed speed is controlled to maintain the cutting force constant with an assumption that the cutting force is proportional to the metal removal rate [8]. The system, however, is not monitoring the cutting state in real-time.

Concerning the cutting state monitoring, there are many researches to detect chatter vibration, tool wear and tipping. In particular, Moriwaki, et al. [9] report the possibility to estimate the amount of the tool wear using the physical model and the cutting force per unit area of cut which is calculated from the observed cutting force. Kasashima, et al. [10] propose a method where normal cutting, tool breakage and eccentricity of the tool can be detected using the discrete wavelet trasformation method.

Concerning open-architecture machine tools, there are several projects by Pritschow[11], Altintas[12] and Koren[13]. Pritschow, et al. have been developing an open-architecture CNC based on the OSACA specification. Altintas et al. have realized adaptive control using a machine tool with an open-architecture controller. Koren, et al. are discussing the relation between the controller architecture and the cycle time. Our system is implemented based on the open-architecture CNC for real-time control.

3. System construction

The developed system consists of (a) a machining center with open-architecture CNC, (b) CAD system which can be accessible from a machining center and data-base and can generate the tool path quasidynamically, and (c) the data-base which presents the relation between cutting conditions and results. The information from the multi-axis force sensor is fed back to the real-time controller and the spindle speed and the

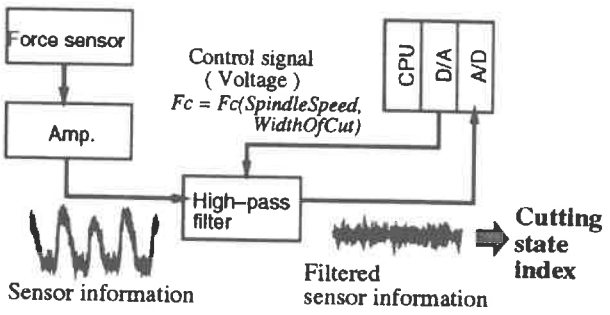

Fig.1 Calculation of cutting state index

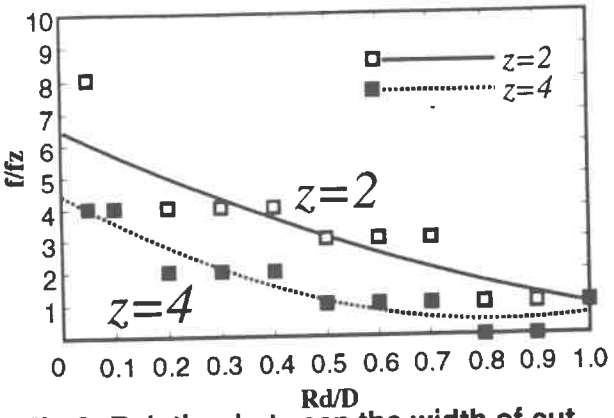

Fig.2 Relation between the width of cut and maximum frequency with more than -30dB

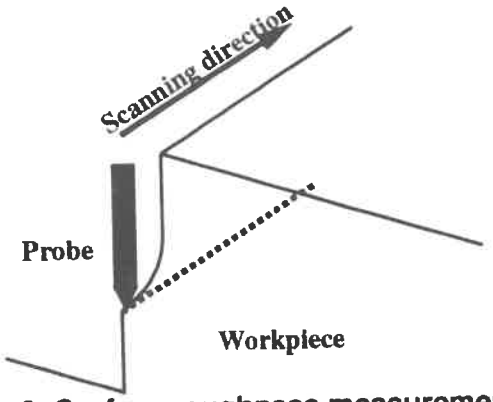

Fig.3 Surface roughness measurement

feed speed can be controlled for adaptive control.

4. Calculation method of a cutting state index

4.1 Calculation of the cutting state index

(a) Cutting state index

The authors propose a "cutting state index" obtained by the following sequence. High frequency components are extracted by applying a high-pass filter for one directional cutting force. The cutting state index is determined to represent the magnitude of the high frequency components. To calculate the index, cutting force components perpendicular to the feed direction is used. Y directional cutting force components are, for example, used if the feed direction is X direction in the coordinate frame of the cutting tool. To use the multi-axis force, each component is used for calculating index and the information from each axis should be integrated.

(b) Features of the cutting state index

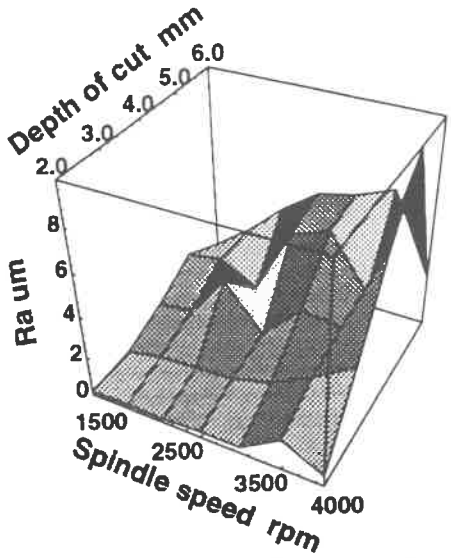

Fig.4 Measured surface roughness

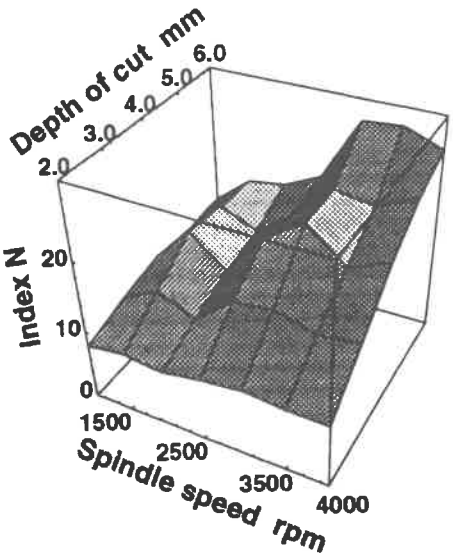

Fig.5 Cutting state index

The basic idea to calculate the cutting state index proposed in this paper is the same as the judgement method of cutting state using "force vector locus" for the full immersion cutting [14] because the high frequency force components are extracted. The features of the calculation method are as follows: (i) The calculation method is independent of the shape of the force vector locus. (ii) The method is applicable to the flank milling. (iii) It is not necessary to prepare a set of data like digital FFT. (iv) Measuring period need not be restricted to one tool rotation time.

(c) Utilization of the high-pass filter and the calculation of the cutting state index

Table 1 Cutting conditions

Workpiece	Aluminum alloy (JIS: A2017)
Cutting tool	Ball endmill (ϕ8, 2 teeth)
Cutting type	Down cut
Spindle speed	1,000 – 4,000 rpm
Width of cut	2.0 mm ($R_d/D = 0.25$)
Depth of cut	2.0 – 6.0 mm
Feed per tooth	0.025mm/tooth
Coolant	Wet
Sampling freq.	20kHz
Cut-off freq.	$f_c = 4.0 \times f_z$

In the system, cutting force information detected at the multi-axis force sensor is amplified by strain amplifiers and it is sent to the high-pass filter. Extracted high frequency data is sent to the A/D converter to calculate the cutting state index on CPU board.

High frequency cutting force data during one tool rotation are used to calculate their root mean square. The value is used as a cutting state index I.

$$I = \sqrt{\frac{\sum_{i=0}^{n-1}(F_i - \bar{F})^2}{n}} \qquad (1)$$

4.2 Determination of the cut-off frequency of the high-pass filter

Determination of the cut-off frequency for high-pass filter is the crucial problem to calculate cutting state index. Band-pass filter might be effective if the self-exciting frequency of the total machining system is known because components in the frequency could be tested to detect the cutting state. However, it is rather difficult to identify the self-exciting frequency because there are so many parameters which depend on a machine tool, a cutting tool and a workpiece. Therefore, high-pass filter was prepared where components with higher frequency compared with the dominant frequency in stable cutting state could be passed. The cut-off frequency f_c is determined as proportional to the spindle speed as follows:

$$f_c = K \times f_z \qquad (2)$$

where f_z can be calculated as

$$f_z = \frac{N \times z}{60}. \qquad (3)$$

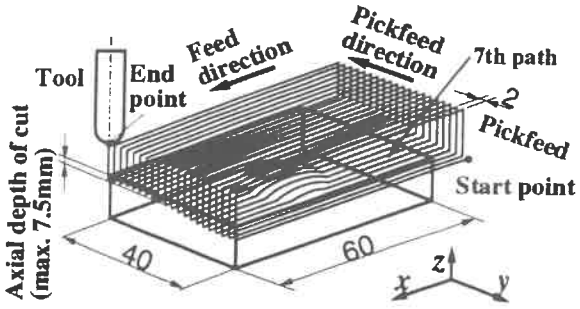

Fig.6 Tool path in an experiment

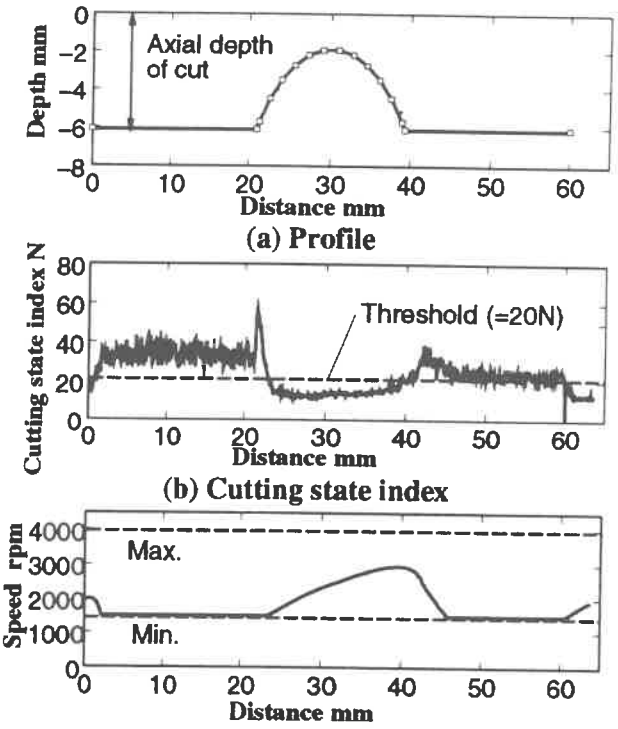

Fig.7 Experimental data in adaptive control (the 7th path)

N and z are spindle speed and the number of teeth, respectively. K in eq. (2) is determined using the physical model of cutting.

Cutting force in stable cutting for square endmilling was calculated using the physical model of cutting. Dominant frequency for the stable cutting was obtained by applying FFT to the calculated cutting force. In Fig.2, the horizontal axis shows ratio between the width of cut R_d and the tool diameter D. The vertical axis shows the ratio between the frequency f and f_z, where f shows the maximum frequency with power spectrum more than -30dB. f/f_z is selected as K. For example, $K = 4$ if the cutting tool is 2-flute square endmill with diameter ϕ10 and the width

of cut R_d is 2.0mm. Curves in Fig.2 were drawn using least square method. They are described as

$$\frac{f}{f_z} = 2.5\left(\frac{R_d}{D}\right)^2 - 8.0\left(\frac{R_d}{D}\right) + 6.4 \quad (4)$$

and

$$\frac{f}{f_z} = 5.7\left(\frac{R_d}{D}\right)^2 - 9.5\left(\frac{R_d}{D}\right) + 4.4 \quad (5)$$

for $z = 2$ and $z = 4$, respectively.

4.3 Relation between the cutting state index and the surface roughness

To evaluate the cutting state index calculation method, the relation between the cutting state index and the surface roughness R_a was measured. The cutting state index was calculated using eq. (1). The surface roughness was measured as shown in Fig.3. Fig.4 and Fig.5 show the measured surface roughness and the cutting state index, respectively. From these figures it is clear that the proposed cutting state index well represents the surface roughness. If the depth of cut is large the surface roughness becomes large. The cutting conditions in the experiments are shown in Table 1.

5. Adaptive control experiments

Using the cutting state index discussed above, adaptive control experiments were performed for the 3D-free-form surface as shown in Fig.6. The goals of the control are to reduce the cutting time and to improve the cutting surface. By controlling the spindle speed and the feed speed, the cutting state index was maintained to be constant. In the experiment, the threshold value of the cutting state index was set as 20N. Furthermore, the spindle speed and the feed speed were proportionally controlled to maintain the feed per edge constant. As shown in Fig.7, the feed speed was maintained low while the axial depth of cut was large, and on the contrary, the feed speed was high while the axial depth of cut was small. The measured cutting time for adaptive control was 270 second compared with 258 second for the non-adaptive control. The cutting time could not be reduced.

6. Conclusions

The authors have proposed a real-time cutting state judgement method for the flank milling. From the experiment, it was proved that the cutting state index well represents the surface roughness. Using the cutting state index and the open-architecture capability of the system, 3D-free-form surface was cut adaptively controlled to realize the high surface quality.

References

[1] Mitsuishi,M., et al., "A Practical Machining Condition Determination Strategy Using Multi-Axis Force Information," *Annals of the CIRP*, 45/1, pp.373–376, 1996.

[2] Mitsuishi,M., et al., "An Open Architecture CNC CAD-CAM Machining System with Data-Base Sharing and Mutual Information Feedback," *Annals of the CIRP*, 46/1, pp.269–274, 1997.

[3] Merritt,H.E., "Theory of Self-Excited Machine Tool Chatter," *ASME J. Eng. for Industry*, pp.447-454, Nov. 1965.

[4] Tlusty,J., et al., "Experience with Analysis of Machine Tools Against Chatter," *Proc. 9th MTDR Conf.*, Pergamon Press, 1968.

[5] Tobias,S.A., "Schwingungen an Werkzeugmaschinen," *Carl Hanser Verlag*, München, 1961.

[6] Kondo,Y., Kawano,O. and Sato,H., "Behavior of Self-Excited Chatter due to Multiple Regenerative Effect," *ASME, J. Eng. for Industry*, 103, 3, pp.324–329, Aug. 1981.

[7] Yamazaki,K., et al., "Real Time Model Reference Adaptive Control of 3-D Sculptured Surface Machining," *Annals of the CIRP*, 40/1, pp.479–482, 1991.

[8] Yamazaki,K., et al., "Autonomous Process Planning with Real-Time Machining for Productive Sculptured Surface Manufacturing Based on Automatic Recognition of Geometric Features," *Annals of the CIRP*, 44/1, pp.439–444, 1995.

[9] Moriwaki,T., et al., "Milling State Recognition Based on Dynamic Cutting Force Model (1st Report, Parameter Identification by Optimization Method and Estimation of Tool Wear)," *J. JSME*, C, vol.61, no.586, pp.418–424, 1995.

[10] Kasashima,N., et al., "Detection of Tool Failure in Milling Process Using Discrete Wavelet Transform," *J. JSME*, C, vol.61, no.583, pp.468–474, 1995.

[11] Pritschow,G., et al., "Open System Controllers – A Challenge for the Future of the Machine Tool Industry," *Annals of the CIRP*, 42/1, pp.449–452, 1993.

[12] Altintas,Y., et al., "A Hierarchical Open-Architecture CNC System for Machine Tools," *Annals of the CIRP*, 43/1, pp.349–354, 1994.

[13] Koren,Y., et al., "Real-Time Open Control Architectures and System Performance," *Annals of the CIRP*, 45/1, pp.377–380, 1996.

[14] Mitsuishi,M., et al., "Real-time Machining State Detection Using Multi-axis Force Sensing," *Annals of the CIRP*, 41/1, pp.505–508, 1992.

NEW BIARC INTERPOLATION FOR ULTRA-PRECISION ASPHERIC SURFACE MACHINING

Min Y. Yang[1], Taik M. Lee[1], Jae Y. Lee[2], Tae H. Kim[2] and Jae Y. Ha[2]
[1]Korea Advanced Institute of Science and Technology, Taejon, KOREA
[2]Daewoo Heavy Industry, Changwon, KOREA

ABSTRACT

This work is concerned with a new biarc interpolation method in which a segment span is composed of two circular arcs and the location of the maximum interpolation error is fixed. The newly developed biarc meets the given tolerance more precisely, performs faster calculation, and generates less NC code blocks(about 60%) in comparison with existing biarcs

KEY WORDS Aspheric Surface, Ultra-precision, Interpolation, New Biarc

1. INTRODUCTION

Nowadays, as consumer electronics, information, and aero-space industries grow, the demand for aspheric lenses in CD players, camcoders, and optical instruments has increased drastically. The aspheric lens has various shapes according to its application and often requires tens nanometer order of form accuracy. To obtain such ultra-precision products, the error caused by the path of the cutting tool, influence of the cutting force, inaccuracy of the feed drive system, pressure fluctuations in the air network, and so on must be minimized.[1]

In this paper, a new biarc interpolation method, in which a segment span is composed of two circular arcs and the location of the maximum interpolation error is fixed, is proposed to minimize the error induced by the path of the cutting tool and to decrease the calculating time of interpolation.

In general, CNC machine tools carry out only linear, arc, and spline machining, such that the path for aspheric surface, expressed by a complicated equation, must be interpolated. Interpolation of the aspherical surface path must precisely meet the allowable tolerance. Linear interpolation of the aspheric surface path for CNC machining generates an enormous amount of NC code to satisfy the extremely small tolerance, and produces scallops on the machined surface due to the acceleration and deceleration of the tool during each linear motion. Spline interpolation is also not suitable to ultra-precision, because the error of interpolation is calculated not in an analytical manner but in an iterative manner and thus requires more time. On the other hand, arc interpolation generates less NC code than linear interpolation does and produces continuous 1st differential values at the connection points of each arc to eliminate scallops. Also, arc interpolation of an aspheric surface path can be solved analytically, and thus requires much less calculation time than spline interpolation.

In biarc methods, the most widely used form of arc interpolation, six requirements are needed to generate two arcs in a segment span[2]. While five requirements are commonly used to enforce continuity of the 1st differential values at arc connecting points, the 6th requirement varies depending on the proposed method[2][3]. In general, the existing methods have the following drawbacks.

① The location of maximum error isn't considered (See Fig.1 (a)), such that a large amount of calculation is needed to locate the maximum error and to meet the tolerance exactly.

② It is inefficient. If the radius of curvature of the real curve increases along the path, as shown in Fig.1, the radius of the first arc should be sufficiently small and the second sufficiently large as in Fig.1(b) to decrease the maximum error value. However, existing biarc methods don't consider this resulting in a greater maximum error.

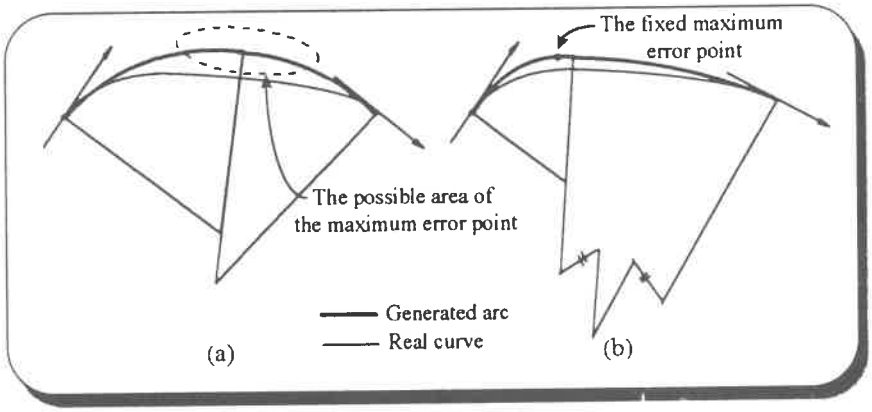

Fig. 1 (a) The existing biarc (b) The new biarc

2. NEW BIARC INTERPOLATION

In the new biarc interpolation method, the arc of the new biarc which contains the maximum error point is divided into two arcs at the maximum error point. Thus, the new biarc is temporarily divided into three arcs(S_1, S_2, S_3) to consider the location of the maximum error (See Fig.2).

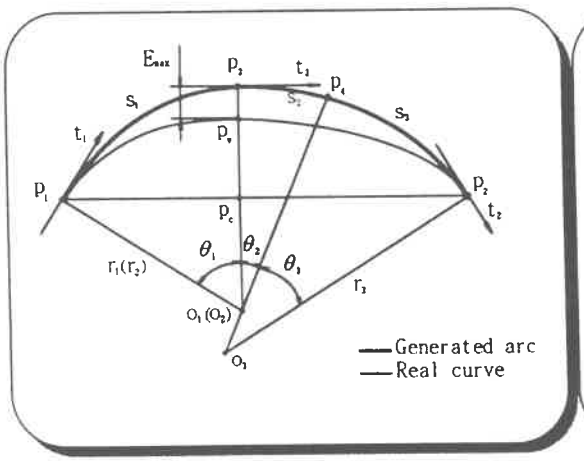

Fig.2 Geometric configuration of the new biarc divided into three arcs.

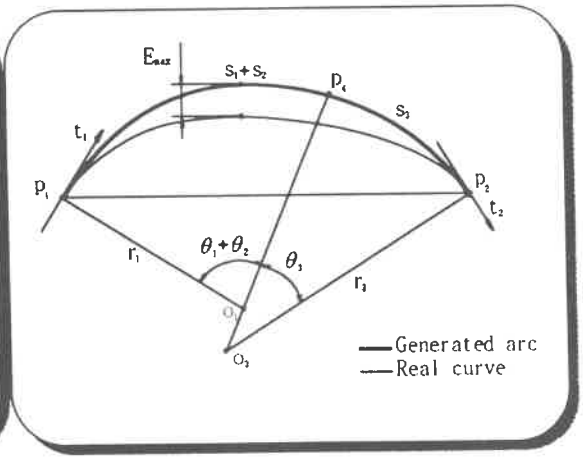

Fig.3 New biarc combined into two arcs.

The first arc(S_1) is generated from the start knot point(P_1) to the position(P_3) where the maximum error occurs. If a junction P_3 exists on the normal vector at the point P_v which is the farthest point from the chord P_1P_2 and its tangential direction runs parallel with the chord P_1P_2, the maximum error exists at the junction P_3.

To support the above hypothesis, the error between the original curve and generated arc at arbitrary position

(P_a) is analyzed as given below.

$$|error| = r_1 - \sqrt{x^2 + f^2(x)} \qquad (1)$$

$$|error|' = -\frac{x + f(x)f'(x)}{\sqrt{x^2 + f^2(x)}} \qquad (2)$$

Thus, the extremum satisfies the equation

$$x + f(x)f'(x) = 0 \qquad (3)$$

The above equation can be rewritten as

$$\frac{f(x)}{x} f'(x) = -1 \qquad (4)$$

In equation (4), $\frac{f(x)}{x}$ means the slope of O_1P_a. The extremum exists at a position where the tangent vector at a point on the original curve is perpendicular to the radial direction from the corresponding point on the generated arc, in other words, where the normal vector at a point on the original curve passes through a center of the generated arc. Therefore, junction P_3 has the maximum value of the interpolation error and knot P_1 has the minimum value of that in Fig.2. These results are the same to the right side that will be generated .

To generate the second(S_2) and third arc(S_3), six requirements are needed.

① The second arc(S_2) must pass through point P_3.

② The secend arc(S_2) must have tangent vector parallel with the chord P_1P_2 at point P_3.

③ The third arc(S_3) must pass through point P_2.

④ The third arc(S_3) must have tangent vector parallel with the chord P_1P_2 at point P_2.

⑤ The two arcs must have a point of common tangency.

⑥ The radius(r_2) of the second arc(S_2) is equal to the radius(r_1) of the first arc(S_1)

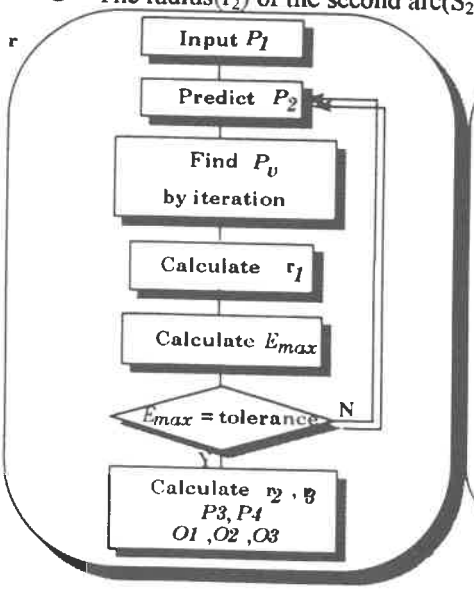

Fig.4 Flow chart for the new biarc.

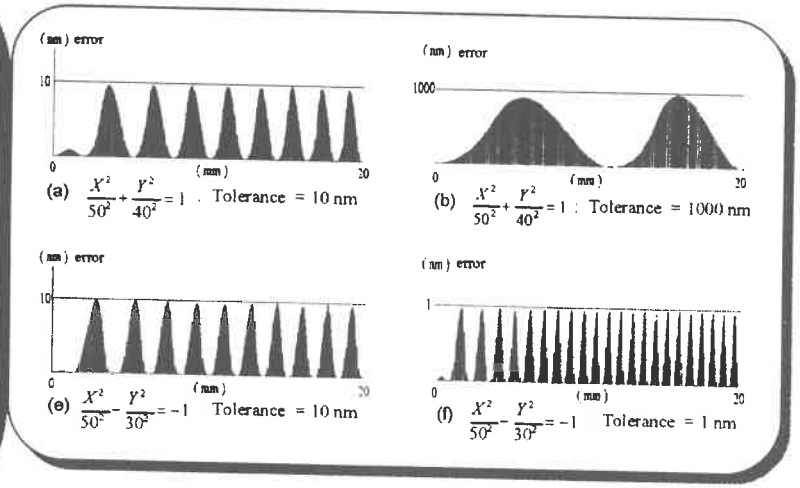
(nm) error
(mm)
(a) $\frac{X^2}{50^2} + \frac{Y^2}{40^2} = 1$. Tolerance = 10 nm
(b) $\frac{X^2}{50^2} + \frac{Y^2}{40^2} = 1$: Tolerance = 1000 nm
(e) $\frac{X^2}{50^2} - \frac{Y^2}{30^2} = -1$ Tolerance = 10 nm
(f) $\frac{X^2}{50^2} - \frac{Y^2}{30^2} = -1$ Tolerance = 1 nm

Fig.5 Error map between the new biarc and various aspheric profiles.

According to the above process, three arcs are generated between two knots as shown in Fig.2 and the first and second arcs of identical radii are combined into one to complete the new biarc interpolation (See Fig.3).

The advantage of the new biarc method is that the maximum error can be calculated without error iteration in contrast with general arc interpolation methods. Therefore, it is easy to make the error meet the allowable tolerance by controlling the terminal knot P_2 (See Fig.4).

3. RESULT

The error maps for various aspheric profiles show that new biarc meets the given tolerance precisely (See Fig.5). In the comparison with existing biarcs, the new biarc generates less NC code blocks(about 60%)

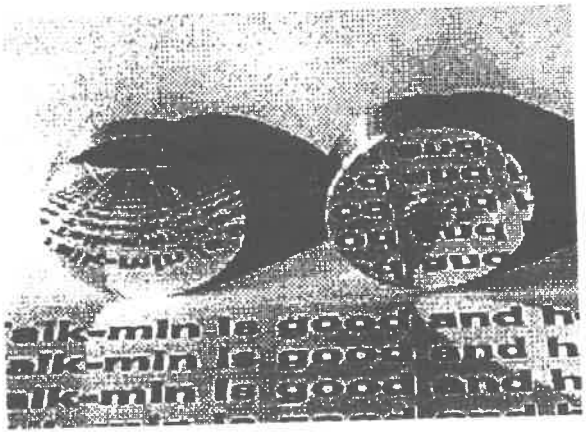

Fig.6 Machining example of aspheric surfaces using new biarc interpolation.

Figure 6 is the example of convex and concave aspheric surfaces machined by the ultra-precision machine of Daewoo Heavy Inustry.(Surface roughness : Ra 11nm)

4. CONCLUSION

In conclusion, the new biarc interpoltion method with the following chracteristics was developed.

① The new biarc in which the location of the maximum interpolation error is fixed meets the given tolerance precisely and fast.

② the new biarc generates less NC code blocks(about 60%) in comparison with existing biarcs due to the efficient location of the maximum error.

The proposed new biarc can be expected to improve the precision and productivity of aspheric surfaces.

REFERENCE

[1] A.I.Minaev, 'Methods of increasing the finishing accuracy of specular surfaces of optical elements by diamond turning',the Optical Society of Ameria, 1991, pp.501-504

[2] K.M.Bolton, 'Biarc curves', CAD, Vol.7, 1975, pp.89-92.

[3] D.B.Parkinson and D.N.Moreton, 'Optimal biarc-curve fitting', CAD, Vol.23, 1991, pp.411-419.

Cutting temperature and its effect to sub-surface damage in diamond turning

Ken-ichiro Horio, Toshio Kasai, Kazuhiro Sekiguchi
Saitama university
255 Shimo-okubo, Urawa, Saitama, 338, Japan

1. Introduction

As conventional metal cutting there are some factors which are sensitive to the processes in diamond turning. In Fig.1 an idea about relation between the factors and the parameters in diamond turning is shown. We have done some works concerning to subsurface damage after diamond turning though our apparatus was limited to a fly cutting.

In this work we focused temperature of the workpiece. We have tried to evaluate the temperature during the process and to investigate its effect to sub-surface damage.

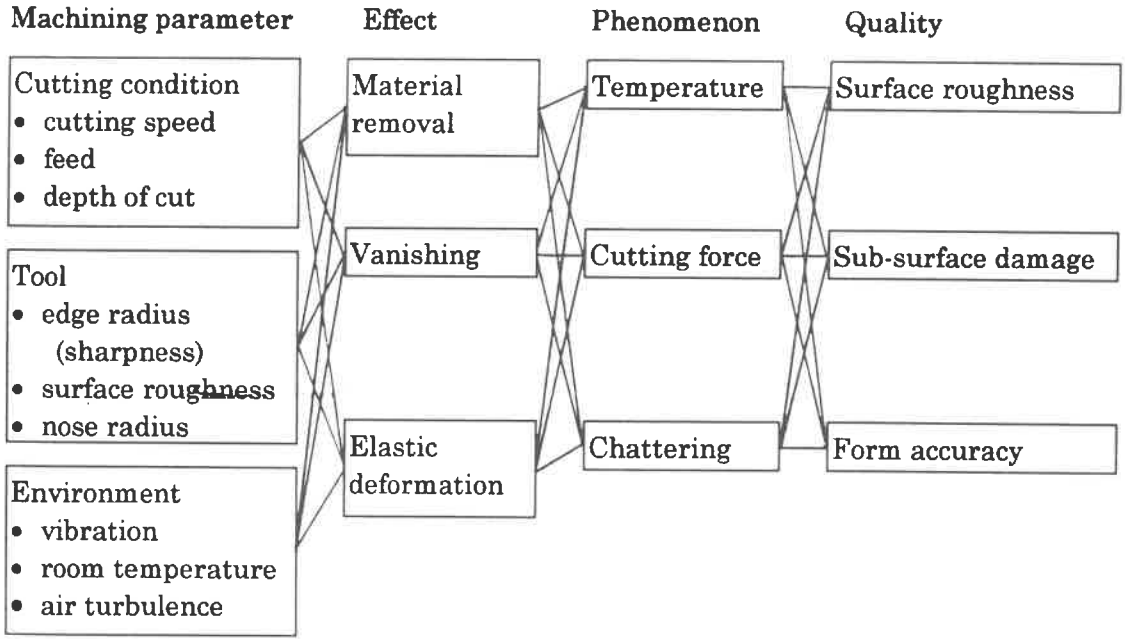

Fig.1 Process factors in diamond turning

2. Experiments

2.1. Temperatures at cutting point

At first we tried to measure the temperature at the cutting point. We made a special workpiece (Fig.2) which was laminated aluminum, insulator, copper, insulator and aluminum in

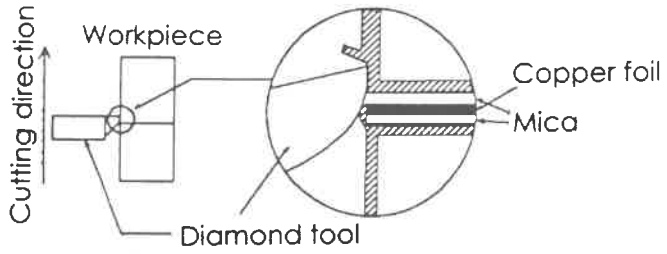

Fig.2 Sample configuration for measurement of the temperature at cutting point

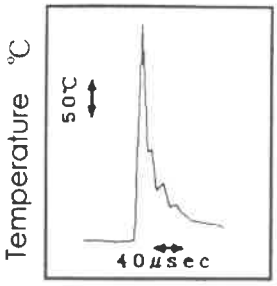

Fig.3 Example of the temperature at the cutting point

this order. When fly cutting with single crystal diamond tool on the usual cutting condition, the flowed aluminum chip might cover the copper surface, which composed thermocouple to measure the temperature. An example of experimental result is shown in Fig.3. It shows steep rise and descent of the temperature at the cutting point during very short period.

Table 1 Machining condition

Material	Aluminum alloy
Tool	Single crystal diamond (Sharp , Dull)
Apparatus	Fly cutting
Cutting speed	600m/min
Feed	5 μ m/rev
Depth of cut	5 μ m
Coolant	Oil mist

We tried to measure on both dry and oil mist sprayed conditions. Table1 shows experimental condition. The result is shown in Table 2. The measured values were distributed 250 to 400 degrees centigrade. However we could not find the difference between dry and wet conditions as the distribution is rather large.

Table 2 Measuring results of the temperatures at the cutting point

condition	number of trial	average	maximum	standard deviation
Dry	4	255℃	343℃	92℃
Wet	9	294℃	407℃	82℃

2.2. Average temperature of workpiece

We changed the measuring points from the cutting point to the backside of thin workpiece to measure the average temperature of workpiece. Because the measurement at the cutting point is not so reliable nor stable. Aluminum plates of around 0.5mm thickness were used which is suitable to our deformation method to evaluate the residual stress distribution. The ordinary thermocouple was set in a column on which the workpiece is set (Fig.4). The column is made of the same material as the sample. As shown in Fig.5, though values of the temperature are less than 1 degree centigrade, we can easily find the difference of lubricant condition (dry or wet) or tool edge condition (sharp or dull).

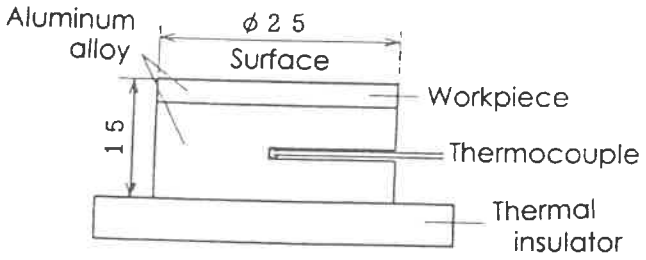

Fig.4 Sample configuration for average temperature measurement

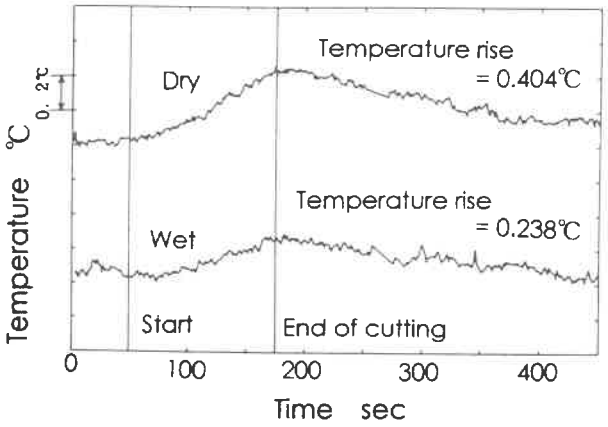

Fig.5 Experimental results of temperature changing

2.3. Residual stress measurement

As mentioned above the thin workpiece was used. Thus when the workpiece was removed from the chuck after machining, it tends to bend. By repeating the measurement of the curvature and slight etching of the workpiece surface, we could know the residual stress distribution along normal direction of the surface. We always use this technique to evaluate them[1]. The procedure is shown in Fig.6.

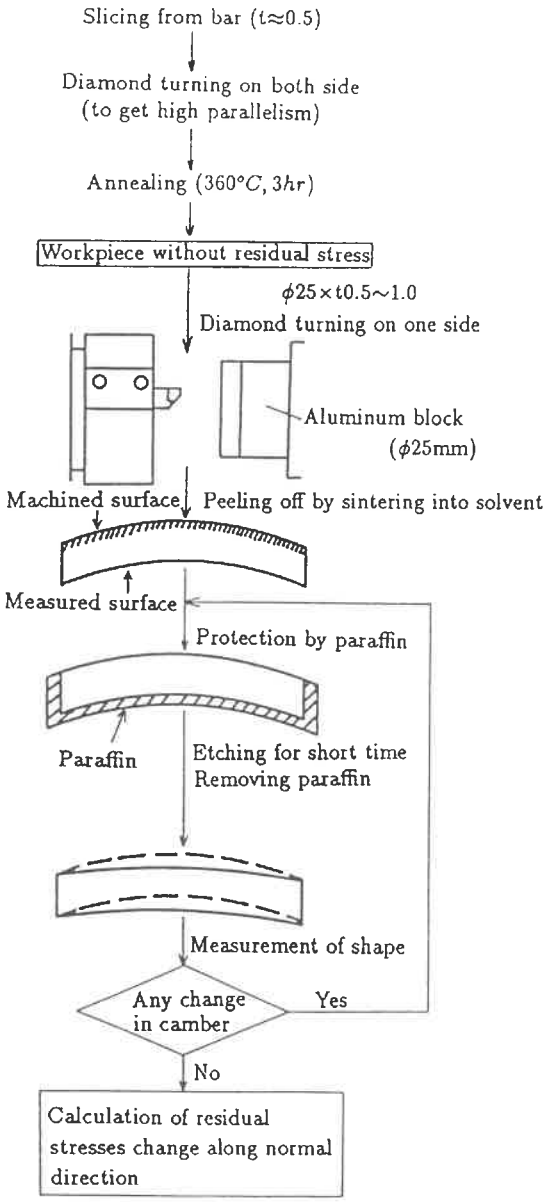

Fig.6 Procedure of evaluating residual stress distribution

If you cut with a dull tool or on dry condition, the temperature is rather higher and the residual stress is existed on deeper position. Though the stresses are mostly compression, however, it sometimes may become tensile stress under the dry condition and with the dull tool.

3. Discussions

3.1. Heat influx

By the data of the temperature such as Fig.5, we derived heat influx which flows into the sample through surface. The heat energy is thought to be generated by the cutting action. The way of the

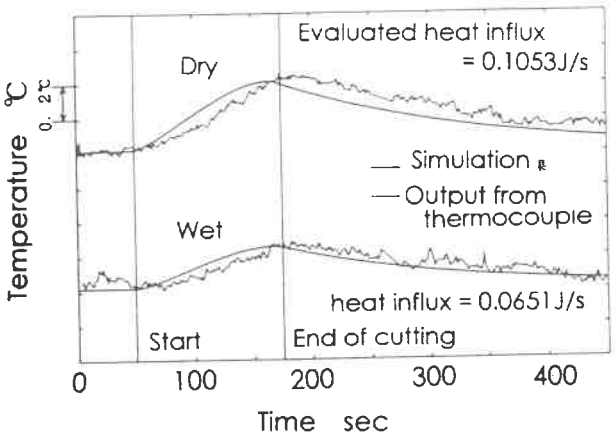

Fig.7 Comparison of the simulation and the experiment for temperature chang-ing during cutting

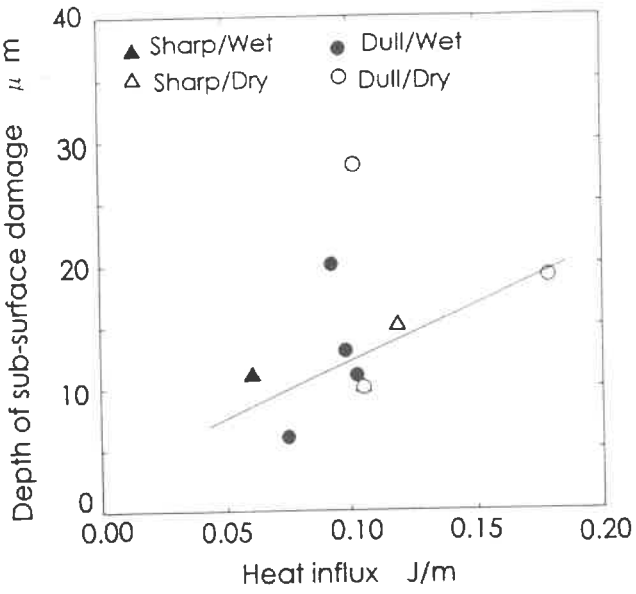

Fig.8 Influence of heat influx to sub-surface damage

evaluation is converse problem analysis. Finite element calculation for heat conduction was done with various heat influx conditions. In the case of the most fit data to the experimental result, the value is thought to an appropriate heat influx. Fig.7 shows an example. In each case those amount were evaluated.

3.2. Effect of the heat to sub-surface damage

Fig.8 shows the relation between calculated heat influx and the depth of sub-surface damage. If you cut with a dull tool or on dry condition, the temperature is rather higher and the residual stress is existed on deeper position. The cause of these seems to be related to the friction between tool and workpiece, the spring back of the workpiece, the material removal, the chip formation or the vanishing.

[1] Horio K., Kasai T., Ogata Y., 1992, Influence of machining parameters to residual stresses remaining in diamond cut surfaces, Proc. 1992 ASPE Annual Meeting: 61-64

Experimental Investigation of Surface Roughness in Ultra Precision Cutting of a Plastic

Morihiko SAEKI, Heiji YASUI, Akira HOSOKAWA and Sumihisa KONDO
Department of Mechanical Engineering & Materials Science, Kumamoto University
2-39-1 Kurokami, Kumamoto 860, JAPAN

1. INTRODUCTION

The ultra precision plastic components have recently been increasingly used as the industrial parts of the equipments and machines such as over head projector, compact disk player, projection TV, copy machine and so on. When ultra precision plastic components are mass-produced by molding process, those can cost lower than direct cut components, though ultra precision molds are very expensive. In small lot production, however, those cost higher depending on expensive mold. Specially, the component of large scale is too expensive to be produced by molding process because its ultra precision mold is usually difficult to be manufactured naturally. Accordingly, in manufacturing of the ultra precision plastic component of large scale and/or small lot, the direct ultra precision cutting of the raw plastic is strongly requested. But there have been the inadequate researches on ultra precision cutting of plastics [1].

The present research aims to clear the influence of cutting conditions on the surface roughness formed by ultra precision cutting of plastics. For the purpose, polymethyl methacrylate plastic (PMMA) which is easier to be cut than Poly carbonate plastic or ZEONEX [2] is face-turned at various cutting conditions with single diamond bite attached on the ultra precision turning machine. Then the face-turned PMMA surfaces are observed with a Normarski differential interference microscope and measured with AFM (NanoScope Ⅲ). Based on the results obtained, the influence of the cutting fluid supply, bite nose radius and cutting speed on the surface roughness is investigated.

2. EXPERIMENTAL PROCEDURE

The face-turning of PMMA square plate of $10\text{x}10\text{mm}^2$ glued to Aluminum disk of ϕ95mm is executed by two different nose radii of single diamond bites attached on the ultra-precision turning machine (Toshiba machine corp. ULC-100A). The main cutting conditions are listed in **Table 1**. The physical and mechanical properties of PMMA are shown in **Table 2**. To clear the effect of the cutting fluid supply on the surface roughness, the experiments are carried out in dry and wet face-turning. The face-turned PMMA surfaces are observed with a Normarski differential interference microscope and the surface roughness are measured with AFM (NanoScope Ⅲ). The measuring length used for comparing with the roughness is 100μm.

Table 1 Physical and mechanical properties of PMMA

Absorption of water	0.30%
Transmittance	93%
Heat deformation temprature	363K
Tensile strength	72.5MPa
Elongation	10%
Vickers hardness	29

Table 2 Cutting conditions

Nose radius	r	0.4 or 4mm
Rake angle	α	0°
Relief angle	β	7°
Cutting speed	V	0.8 - 6.3m/s
Feed rate	f	0.67 - 30μm/rev
Depth of cut	d	1μm
Cutting fluid		Kerosene

3. EXPERIMENTAL RESULTS AND DISCUSSION

3.1 Effect of cutting fluid supply

Figure 1 shows the Normarski microscope photographs of PMMA surfaces formed by dry and wet face-turning at three different feed rates with two different nose radii of diamond bites. At feed rates of f = 5.3μm/rev for the bite of r = 0.4mm and f = 10μm/rev for the bites of r = 0.4mm and r = 4mm, the feed marks corresponding with feed rates can be found clearly in case of both dry and wet face-turning. At f = 5.3μm/rev for r = 4mm and f = 0.67μm/rev for r = 0.4mm and r = 4mm in dry face-turning, there are a lot of irregular grooves which are different from feed marks. At the same feed of f = 0.67μm/rev for r = 0.4mm and r = 4mm in wet face-turning, on the other hand, there are no marks found on the PMMA surface. From the result, the cutting fluid is considered to make an important contribution on the formation of ultra smooth surface in the cutting of PMMA.

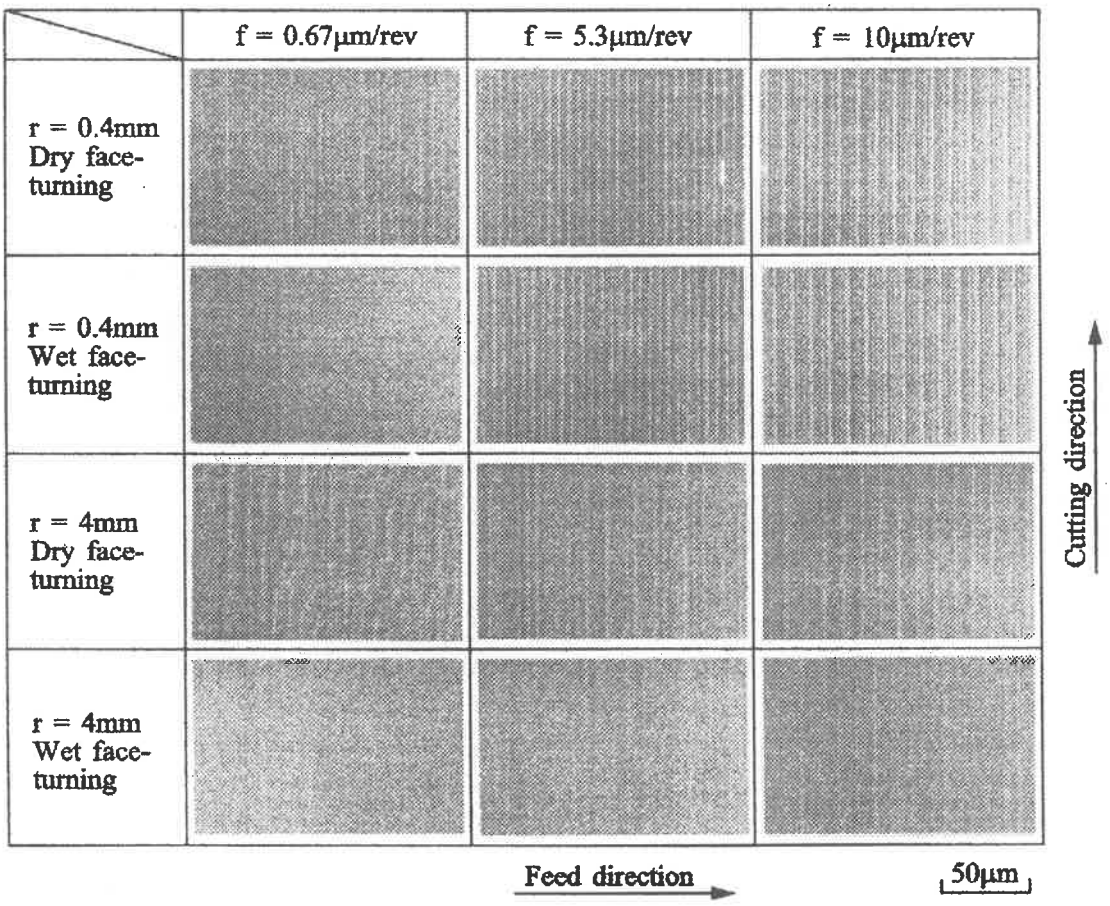

Figure 1 Normarski microscope photographs of PMMA surfaces formed by dry or wet face-turning [d = 1μm, V = 6.3m/s].

Figure 2 shows the AFM image of PMMA surface formed by wet face-turning under the cutting conditions of d = 1μm, V = 6.3m/s, f = 0.67μm/rev and r = 4mm. From the image, it is clear that the ultra smooth surface of about 8nm (Rmax) in surface roughness is formed by ultra precision cutting of PMMA.

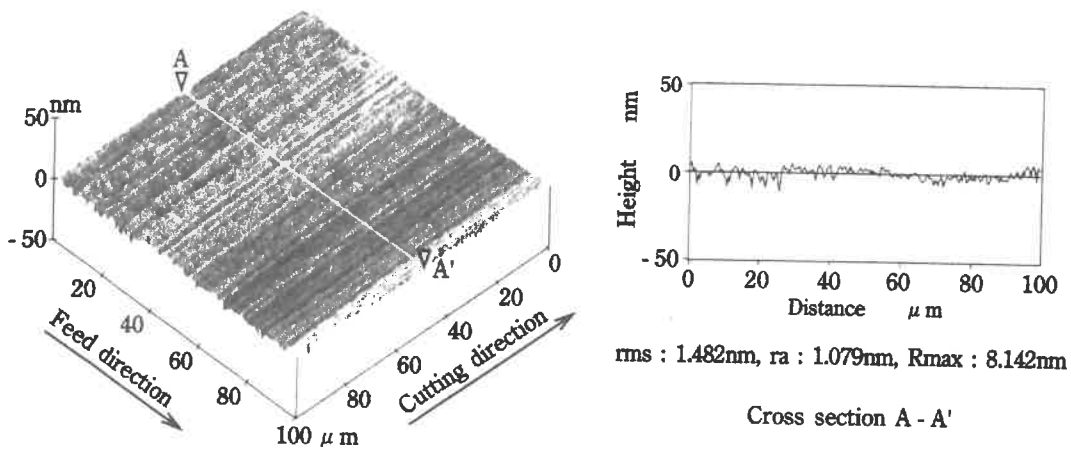

Figure 2 AFM image of PMMA surface formed by wet face-turning under the cutting conditions of d = 1μm, V = 6.3m/s, f = 0.67μm/rev and r = 4mm.

3.2 Influence of bite feed rate

Figure 3 shows the relationship between the surface roughness Rmax measured in bite feed direction and feed rate. Each plot shows the average value of the surface roughness measured at ten different places with AFM. The dotted lines show the surface roughness obtained from the theoretical equation, $R_{th}=(f^2/8r)$. It is found from the figure that the relationship between the surface roughness and feed rate is classified into three types depending on the range of feed rate; that is, 1) the first range for faster feed rate than a critical one, 2) the second range from the critical feed rate to the limiting feed rate and 3) the third range for later feed rate than the limiting one. In the first range, the surface roughness improves along with the theoretical curves. In the second range, with the decrease of feed rate, the surface roughness decreases gradually and finally converges to a limiting surface roughness of about 9nm (Rmax). In the third range, the limiting

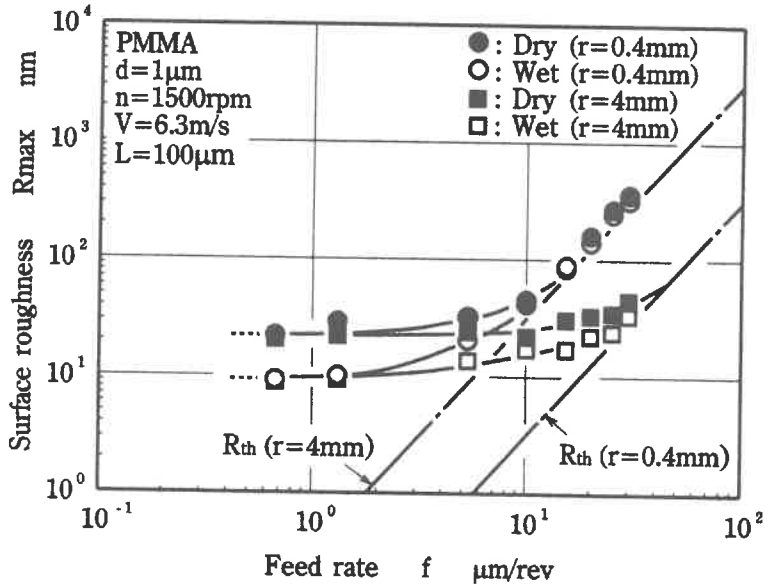

Figure 3 Relationship between surface roughness and feed rate

surface is kept all over the range. The limiting surface roughness formed by wet face-turning is much smoother than dry face-turning. The influence of nose radius on the limiting surface is little. The limiting feed rate becomes faster for large nose radius.

3.3 Influence of cutting speed

Figure 4 shows the relationship between the surface roughness and the cutting speed. The cutting speed ranges from 0.5m/s to 6.3m/s. The cutting conditions used in the experiments, however, are within the third range of the feed rate. It is obvious that the cutting speed and the nose radius have little influence on the limiting surface roughness.

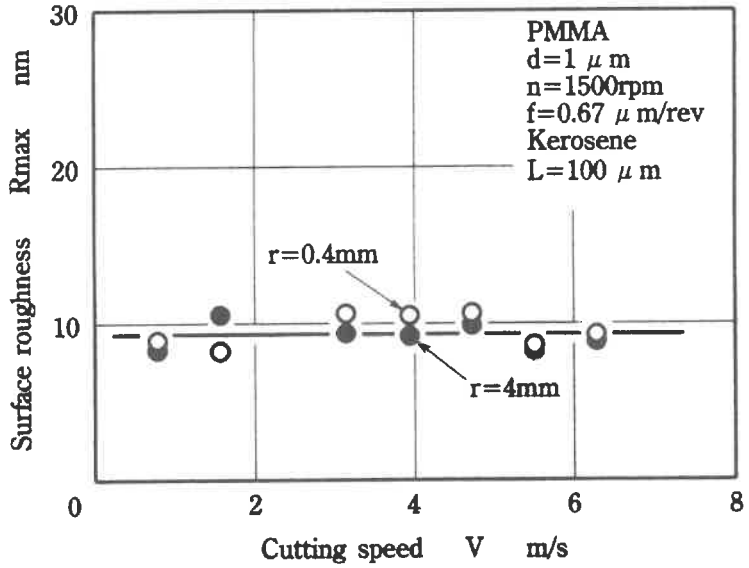

Figure 4 Relationship between surface roughness and cutting speed in wet face-turning.

4. CONCLUSIONS

To clear the influence of cutting conditions on the surface roughness formed by ultra precision cutting of plastics, the polymethyl methacrylate plastic is face-turned with ultra precision turning machine and its surface roughness is investigated.

The main conclusions obtained are as follows;

1) The cutting fluid supply makes an important contribution on the formation of ultra smooth surface in the cutting of plastic.
2) The surface roughness improves in the range of faster feed rate than a limiting one as the feed rate is slow. Below the limiting feed rate, the limiting surface roughness of about 9nm (Rmax) is kept.
3) The cutting speed and the nose radius has little influence on the limiting surface roughness.

REFERENCES

1) Kenji Hirakawa, Akira Kobayashi, Toshio Kasai, "Ultra-Precision Cutting of Plastics", Proc. of Japan Soc. for Precision Engg. Spring Annual Meeting, 1984, 75-78.
2) Morihiko Saeki, Heiji Yasui, Akira Hosokawa, Sumihisa Kondo, "A Study on Ultra Precision Diamond Turning of Plastics", Proc. of Japan Soc. of Mechanical Engg. Spring Annual Meeting, 1997, 208-209.

Effects of Round-Nosed Tools on Chatter in Diamond Turning

Adam J. Schaut, Eric R. Marsh
The Pennsylvania State University
University Park, PA

Chatter is a problem that has plagued machinists and machine tool designers throughout the years. Chatter not only affects the surface finish but also the dimensional accuracy, tool wear and the cost of the manufacturing process since the chatter marks are difficult to remove.

Chatter is caused by a relative motion between the machine tool and the workpiece. This causes oscillations of the tool that grow due to feedback between the current and previous positions of the cutting tool. The oscillations create undulations on the surface of the workpiece. If the relative motion between the tool and the workpiece grows, the cutting operation is unstable and chatter develops. According to Stepan, regenerative chatter is the most common instability in machining processes [1].

In an attempt to better understand the effects of regenerative chatter in the turning process a Single Degree Of Freedom (SDOF) simulation model was developed. The model uses a round nosed diamond tool as the cutter. This type of tool geometry is typical of that used in turning of parts where surface finish is critical. For numerical efficiency a parabolic profile is used to model the round nosed diamond tool. This approximation restricts the depth-of-cut to where the parabolic profile is close to circular, a condition met with typical diamond tool nose radii and depths-of-cut. The simulation model utilizes a fourth order Runge-Kutta (RK-4) method to calculate the response for the first few time steps, and then a Adams-Moulton predictor-corrector scheme is used for the remaining time steps. The predictor-corrector scheme was implemented to increase the speed of the simulation and to eliminate chip area interpolation necessary with the RK-4 method.

The machine tool structure is modeled as a mass, spring, damper system as shown in Figure 1. The previous pass of the cutting tool is illustrated by the term $x(t-\tau)$ where τ is the delay term from the rotation of the workpiece. The term $x(t)$ represents the current pass of the workpiece.

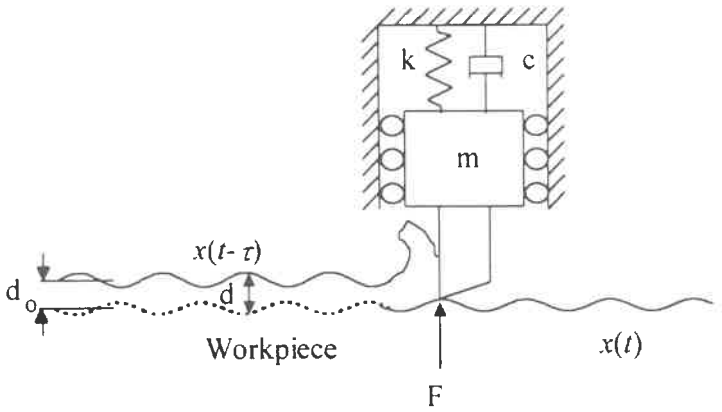

Figure 1 Single degree of freedom chatter model

The governing Equation Of Motion (EOM) for this model is as follows:

$$m\ddot{x} + c\dot{x} + k(x - h) = -\lambda K_c A \qquad \text{Equation 1.}$$

where, m = mass (kg)
c = damping (N-s/m)
k = stiffness (N/m)
h = depth-of-cut (m)
λ = fraction of the cutting force transmitted to the tool in the direction of motion
K_c = specific cutting energy (N/m^2)
A = chip area removed during machining (m^2)

The chip area in this equation is a function of the tool path history and its current position. The simulation program calculates the amount of chip area that is removed at each time increment which in turn is used in the forcing function of Equation 1. The chip area calculation is based on multiple passes of the workpiece. As chatter develops the amount of previous passes needed in the chip area calculation increases. This can be seen in Figure 2 in which two previous passes are required to accurately describe the amount of chip area that is removed. The amount of chip area removed is depicted by the bold lines.

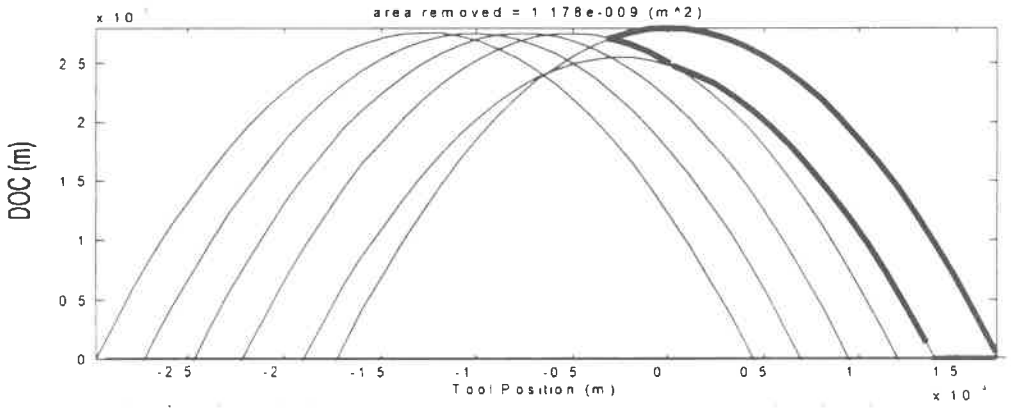

Figure 2 Chip area formulation for multiple tool passes

The tool parameters for this simulation are based on a single degree of freedom flexure designed to examine the behavior of the cutting model as seen in Figure 2. This flexure only allows motion of the tool in and out of the workpiece. The design criteria and physical parameters can be found in Yantek [3]. The fraction of the force transmitted in the normal direction (λ) was taken to be 0.3 as recommended by Lucca [4]. The process was simulated for machining of 6061 aluminum with a specific cutting energy of $1x10^9$ N/m^2. According to Lucca et. al. the amount of force transmitted to the tool and the specific cutting energy is not constant in the machining process, but varies with the depth of cut [4]. Reference [4] also provides plots of these parameters versus the depth-of-cut. This information was included in the simulation program by computing an average chip thickness for each revolution of the workpiece and applying correction factors to K_c and λ based on the plots provided in the literature.

The simulation model was then compared to experimental data. The data were collected on a Moore 3 diamond turning machine. An impact hammer was used to apply a disturbance to the tool in the normal direction. The acceleration and displacement of the tool were then measured using an accelerometer and a capacitance probe. A typical plot from testing is shown in Figure 3 for a depth of cut of 38.1 μ m. This data was then compared to the simulation program results.

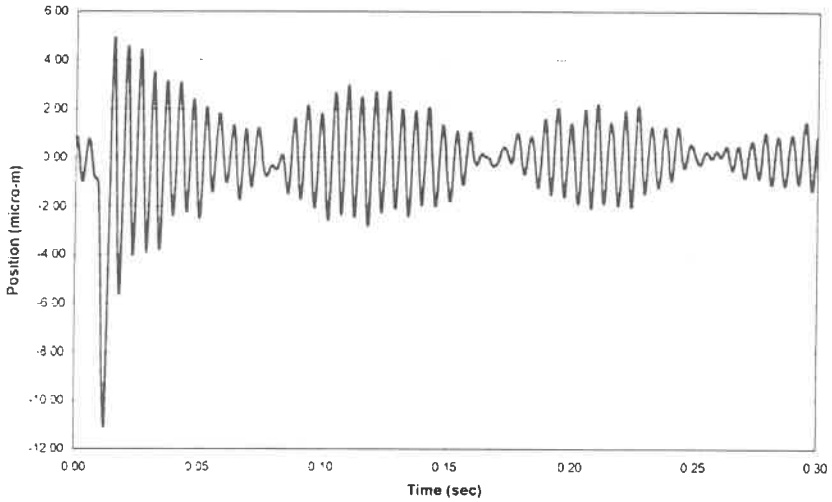

Figure 3 Experimental data given a transverse impact force

The impact force that was used to excite the flexure was curve fit to find an analytic function describing the impact force which was then input into the simulation program. The program was allowed to reach steady state, and then the impact was simulated. Figure 4 shows the result from the simulation program given the impact force. Upon comparing Figures 3 and 4, the results of the simulation program compare quite well to the experimental results.

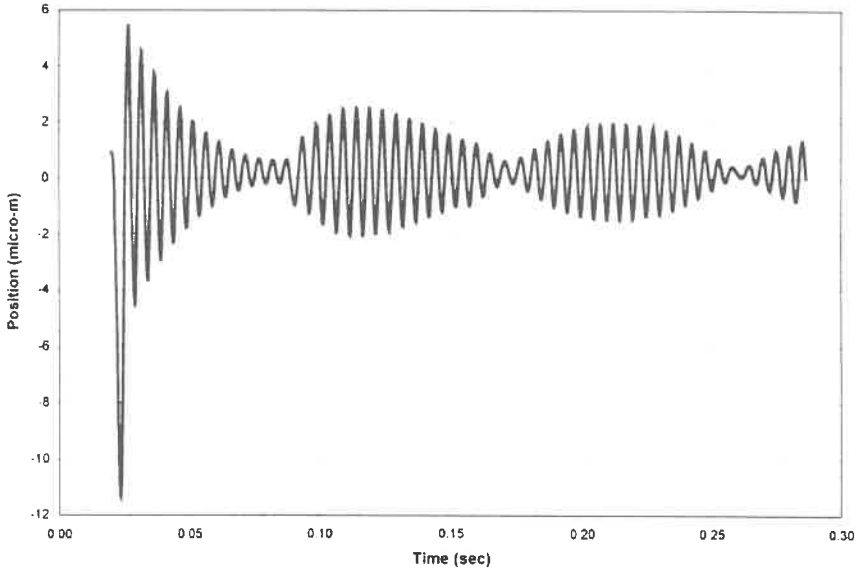

Figure 4 Simulation program plot with K_c and λ correction factors

In the future, the simulation program can be used to modify cutting parameters to determine the onset of chatter for a particular configuration. Once the chatter limit is found, the tool parameters can be modified to determine their effect on chatter. This will aid in determining the optimum design of the cutting tool in a turning process.

The simulation program can also be used to create a stability diagram for various spindle speeds as previously presented in the literature [2]. This would involve increasing the depth-of-cut until chatter occurs for various spindle speeds, and investigating the possibility of stability lobes. This could then be compared to Tlusty's stability diagram for the SDOF turning process.

References

[1] **Stepan, G.** Retarded Dynamical Systems: Stability and Characteristics, an Introduction. Cambridge University Press, 1970.

[2] **Tlusty, J.** "Machine Dynamics". In King, R. I. (ed.), Handbook of High Speed Machining Technology, New York, Chapman and Hall, pp. 48-143, 1985. "Machine Dynamics", Chapter 3. McMaster University.

[3] **Yantek, D.** "Chatter and Process Damping in Diamond Turning". Masters Thesis, Pennsylvania State University, 1996.

[4] **Lucca, D., Rhorer, R.** "Energy Dissipation and Tool-Workpiece Contact in Ultra-Precision Machining", Tribology Transactions, Vol 37, pp. 651-655, 1994.

Microcutting Phenomena of Monocrystalline Silicon with Large Nose Radius Diamond Tool

*A. Kanai, F. Inaba , M. Miyashita, , R. Kato, T. Yokotsuka, S. Fujita and M. Daito**

Ashikaga Institute of Technology, 268 Omae, Ashikaga 326, Japan
*Nissin Machine Works, 300 Aritama-nishi, Hamamatsu 431-31, Japan

1. Introduction

One of the field which is looking forward to development of ultraprecision grinding technology of brittle materials including ductile mode grinding technology is the field of 12-14 inches wafer processing for LSI in near future. In that field several ten million wafers are produced per month. It means that the grinding technology for the silicon wafer industry has to be ultra-precise and also mass-productive at the same time.
High productivity in grinding is achieved with high peripheral speed of grinding wheel or/and large wheel depth of cut. Several micron in wheel depth of cut is permissible for ductile mode grinding of brittle materials under the condition that protrusion height distribution of active grains is controlled within less than ductile-brittle transition value in uncut chip thickness[1][2]. A large wheel depth of cut requires coarse abrasives on a wheel which can be protruded much higher than the wheel depth of cut.

The many test results of cutting of silicon with a diamond tool[3][4]have been reported since the ductile mode grinding technology of brittle materials was proposed. Those tests were conducted with a diamond indentor or a small nose radius diamond tool which had a sharp and small cutting edge. The cutting tests with large nose radius diamond tools which give cutting width of several ten micron at least for depth of cut of few hundred nanometer at most are required to provide basic data to development of ductile mode grinding technology of brittle materials with coarse abrasives.

The present paper describes test results of microcutting of monocrystelline silicon with diamond tools with nose radius of 40 mm which give cutting width of 180 μm for depth of cut of 100 nm. The workpiece is a silicon wafer of 6 inches in diameter. The surface features of cutting grooves or surface roughness with a stylus profilometer, surface image with a scanning electron microscope(SEM) and Nomarski microscope are investigated for depth of cut which changes continuously from zero to several hundred nanometer.

2. Experimental details

The material used in the present test was a monocrystalline silicon wafer of 6 inches in diameter which was finished with polishing in device grade. The crystal orientation of the wafer surface was (100). The surface along the orientation-flat was [220]. A diamond tool with nose radius of 40 mm was used as a cutting tool. The negative rake angle was adopted for extension to grinding with a diamond wheel as a tool with multi-cutting edges. The rake angle of -30° and -60° was selected. The nose radius of 40 mm engraved groove with the width of 180 μm for depth of cut of 100 nm.

Microcutting tests were conducted on a ultraprecision surface grinding machine of Nissin HPG-1[5] with high stiffness and high feed resolution. It is a T-shaped grinding machine and has a X slide for a work spindle and a Z slide for a wheel spindle. Both the work and the wheel spindle is supported by hydrostatic bearings in a horizontal plane. They are orthogonal to each other. The slides are supported by linear bearing guideways and driven by a force-operated hydraulic linear actuator controlled by NC system with a linear laser scale with resolution of 10 nm as a feedback position sensor. The workpiece was fixed on a vacuum chuck of the work spindle. The diamond tool was rigidly mounted on the head stock of the wheel spindle.

A scheme for microcutting is shown in Figure 1. A rotational speed of the workpiece was 150 revolutions per minute. A feed rate of the workpiece on the X slide was 75 mm/min or 0.5 mm per workpiece revolution and a infeed rate of the diamond tool on the Z slide was 2.5 μm/min or 17 nm per workpiece revolution. A trail of the diamond tool on the silicon wafer or a microcut groove is a spiral starting at the outer periphery of the wafer. A depth of cut continuously increases from the periphery to the center of the wafer and nominally by 17

nm a revolution. A width of cut increases as the depth of cut does. Figure. 2 is a section of the microcut groove measured with a stylus profilometer, Talystep. The width of cut is 340 μm for the depth of cut of 300 nm.

The microcut groove on the line O-A and O-B shown in Figure 1 was investigated with Talystep, a field emission scanning electron microscope and a Nomarski microscope. O-A is parallel to the orientation flat and O-B is 45 degrees to O-A. The cracking thresholds were studied from a surface roughness in R_a and R_t, and SEM images in relation to a rake angle of the diamond tool and a crystal orientation along the cutting groove. The amount of depth of cut and the surface roughness were acquired from the section profile measured with Talystep as shown in Figure 2.

3. Test results and discussions

A Nomarski microscope image shown in Figure 3 was a portion of the spiral microcut groove on O-B microcut with the diamond tool which has the rake angle, θ of -30°. The depth of cut, t ranges from 285 nm to 420 nm which are in the vicinity of crack initiation. The cracking thresholds can be observed between t of 340 nm and 370 nm. Figure 4 is the high magnification images of the groove observed with SEM. The cutting direction is along a vertical one in the pictures. The surface shown in Figure 4a which was cut in depth of cut of 60 nm had many streaks copied from the cutting edge of the diamond tool along the cutting direction, however no crack. In Figure 4b for the depth of cut of 370 nm many fine lines in a fine pitch were observed along the direction perpendicular to the cutting one. Some small cracks along the fine line appeared. This kind of cracks could be more clearly observed in Figure 4c for the depth of cut of 390 nm. In Figure 4d a large crack was generated. The surface roughness of the groove is shown in Figure 5 in relation to depth of cut. The roughness in both R_a and R_t is almost constant in a range of less than 340 nm in depth of cut. The value in R_a is about 8 nm and the one in R_t is about 80 nm. The roughness R_a along the cutting direction was a little better than the above and the roughness R_t was much better. From the larger depth of cut than 340 nm the roughness changed rapidly for the worse. This means that under the condition of depth of cut less than 340 nm the microprofile of the cutting edge was copied to the silicon surface and chips were removed in ductile mode. The crack initiation threshold is estimated to be 340 nm for this cutting condition. The cutting width for 340 nm in depth of cut was 363 μm. This phenomena in the roughness characteristics correspond to the surface features shown in Figure 4.

The surface of the groove along O-A had the roughness shown in Figure 6. It is estimated that the crack initiated from the deptn of cut of 200 nm which is about two third of the one along O-B. The cutting width for the depth of cut of 200 nm was 270 μm. The SEM images of the groove along O-A are shown in Figure 7.

The test results on the diamond tool with a rake angle of -60° are shown in Figure 8 and 9. The surface roughness of the microcut groove was almost same as the roughness in the case of rake angle of -30°. The roughness data along O-B could not acquired for larger than 350 nm in depth of cut.

The test results that a crack initiation threshold was 200 nm for the cutting width of 270 μm showed the possibility for monocrystalline silicon to be ground in ductile mode with a coarse abrasive diamond wheel.

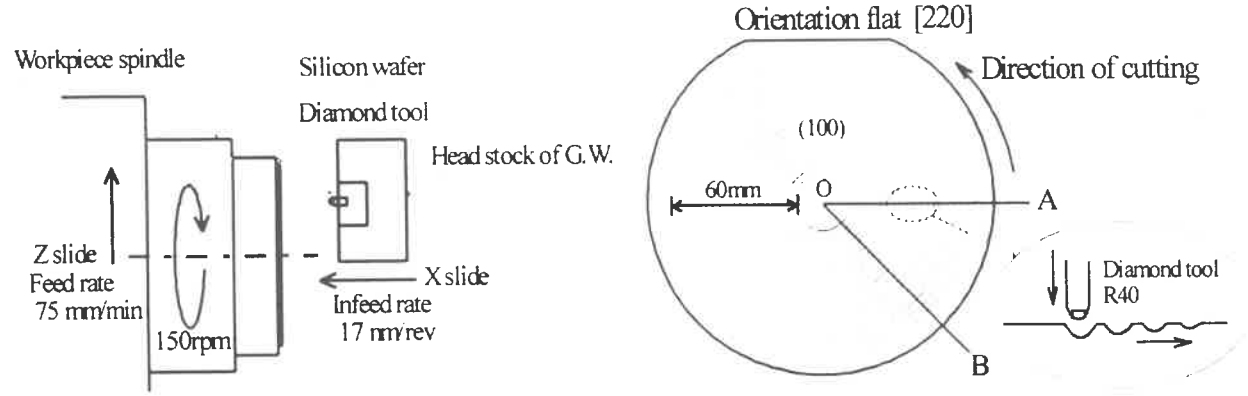

Fig. 1 Scheme of microcutting

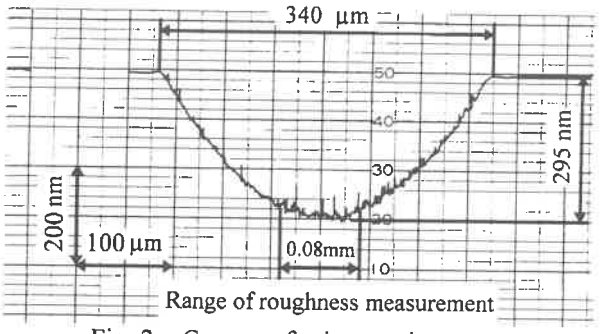

Fig. 2 Groove of microcutting

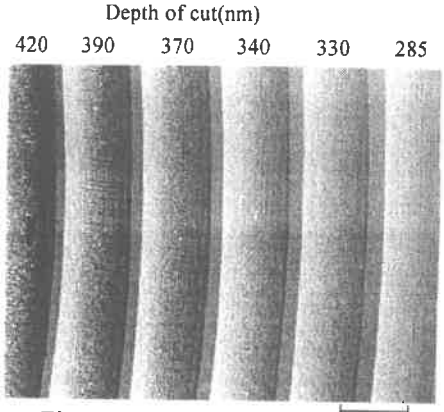

Fig. 3 Cutting grooves

(a) t=60nm, SEM ×10000

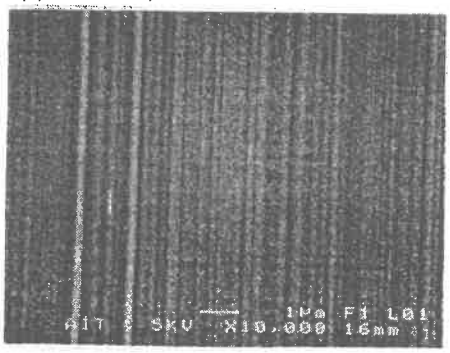

(b) t=370nm, SEM ×10000

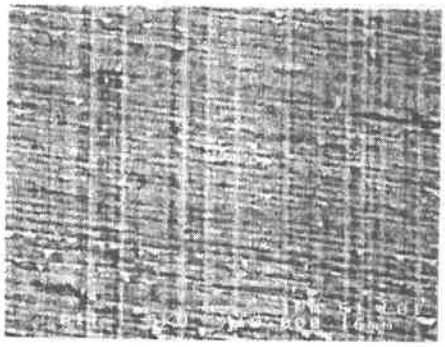

(c) t=390nm, SEM ×10000

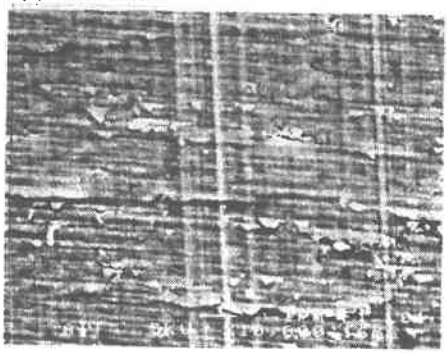

(d) t=420nm, SEM ×10000

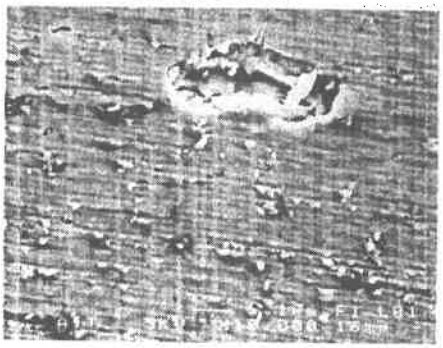

Fig. 4 SEM images of microcut groove surface (θ =-30˚, O-B)

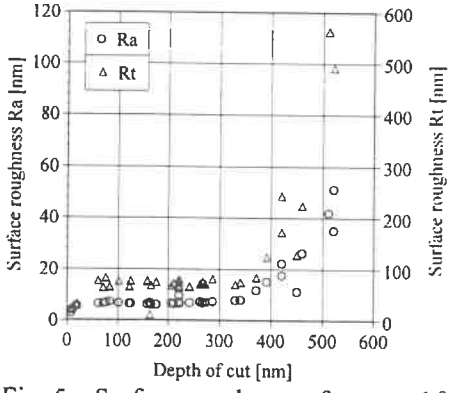

Fig. 5 Surface roughness of groove (θ =-30˚, O-B)

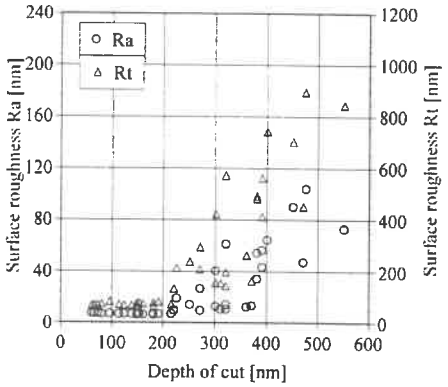

Fig. 6 Surface roughness of groove (θ =-30˚, O-A)

(a) t=60nm, SEM ×10000

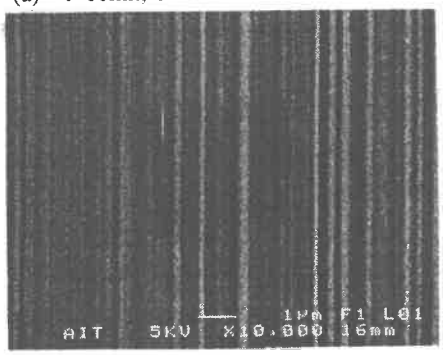

(b) t=160nm, SEM ×10000

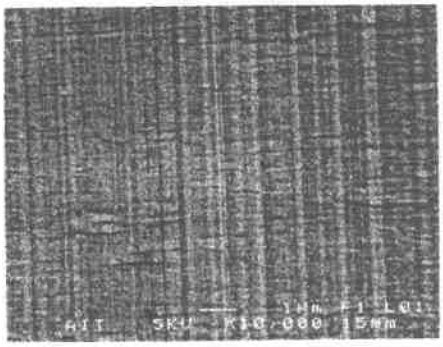

(c) t=190nm, SEM ×10000

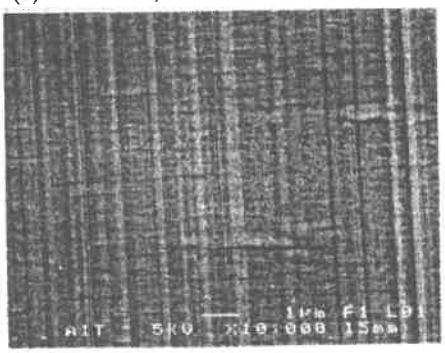

(e) t=220nm, SEM ×10000

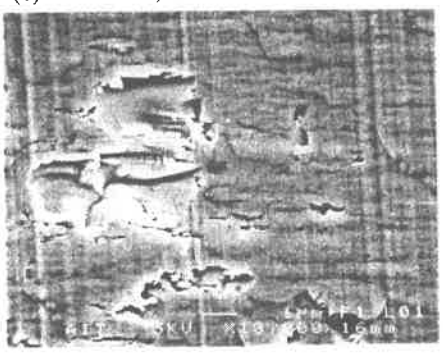

Fig. 7 SEM images of microcut groove surface (θ =-30° , O-A)

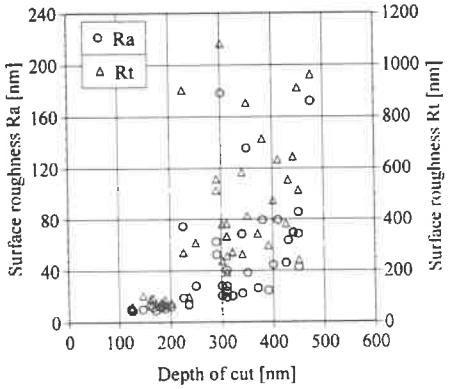

Fig. 8 Surface roughness of groove (θ =-60° , O-A)

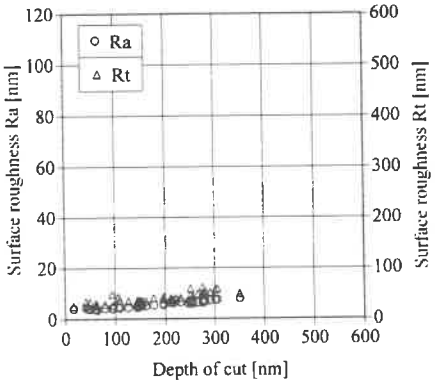

Fig. 9 Surface roughness of groove (θ =-60° , O-B)

4. References

1) A. Kanai et al. :Proposal of High Productivity in Ductile Mode Grinding of Brittle Materials, ASPE, (1996)
2) A. Kanai et al. :Control of Grain Depth of Cut in Ductile Mode Grinding of Brittle Materials and Practical Application, ISAAT, World Scientific(1997)
3) C. K. Syn et al. :Ductile-Brittle Transition of Cutting Mode in Diamond Turning of Single Crystal Si and Glass, ASPE/IPES, (1989)
4) B. V. Tanikella et al. :Controlled Microcutting Tests on Single Crystal Silicon, ASPE, (1996)
5) M. Daito et al. :Design Strategies of an Ultraprecision Surface Grinding Machine for Ductile Mode Surface Finishing of Brittle Materials, ASPE, (1994)

Side Burr Generation Model in Micro-Grooving

Jung-Hwan Ahn, HanSeok Lim
Pusan Natational University, Pusan, Korea

1. Introduction

Fresnel lens and lenticular lens are typical slimmed optics which are composed of various shapes of micro groove on a flat surface. In order to meet such optical requirements as reflectivity and refractivity, dies for optics should be machined very precisely not only in shape but also in surface by a single crystal diamond tool. A big problem in the diamond precision machining is side burr generated in the edge of micro-groove[1].

Many studies on burr have been conducted. Gillespe tried to explain the side burr using bulging mechanism by the high hydrostatic pressure around a round tool edge [2]. The burr estimate, however, is too small because the effect of depth of cut on the burr is not included in his model. Nakayama et al. experimentally investigated the side burr length according to depth of cut and concluded that it is closely related to the shear strain rate of chip[3].

In this study, a side burr generation model is proposed based on a side shear plane and an extended deformation area due to the tool edge radius effect in micro-cutting. Through comparision of the burr thickness estimates with the measured one for three workpiece materials, it was shown that the proposed burr model works well and the effect of a tool edge radius on side burr is well described in the model.

2. Side burr generation model

Fig.1 shows conceptually the effect of hydrostatic pressure on generating side burr in the 2-dimensional cutting. The material inside of C-C′ line is considered to be plastically deformed along the principal shear plane. But the material outside of C-C′ line, particularly near the edge, experiences the side shear deformation, perpendicular to the cutting direction, due to the hydrostatic pressure as well as the principal shear deformation. That is a cause of side burr generation.

Fig.2 shows a simplified side burr generation model based on the concept explained above. Plane ADH is assumed a boundary surface, on the C-C′ line of Fig.1, where the y-directional hydrostatic force is equal to the material resistance to side shear deformation and no side shear occurs.

Plane APED is assumed as a side shear

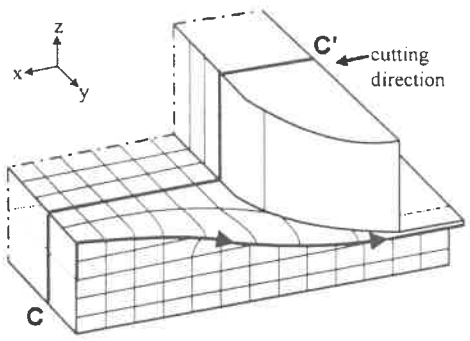

Fig. 1 Generation of side burr[3]

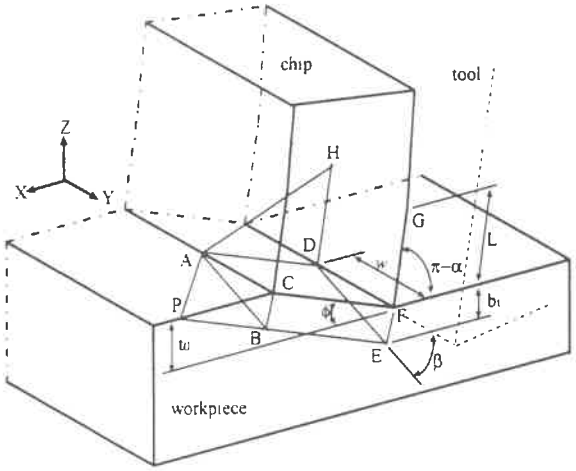

Fig.2 Schematic diagram of a side burr generation model

plane along which side shear deformation occurs. The distance from $\overline{AD}$ to the edge, w, is defined as a side shear deformation width which means the maximum side shear deformation zone. The side shear angle, β, between plane APED and plane ACFD can be calculated on the assumption that the total energy consumption in side burr generation might be minimized.

2.1 Calculation of side shear angle

The total energy in side burr generation is a sum of the shear deformation energy (ΔW_U) along the side shear plane APED and the friction energy(ΔW_F) along the tool-chip contact surface DFGH. That is:

$$\Delta W_{sideburr} = \Delta W_U + \Delta W_F \qquad (1)$$

Fig.3 shows how to find out a proper side shear plane along which the total deformation energy is minimized. If an infinitesimal element △PQS of a unit thickness in side shear zone is about to be sheared in the direction of new shear plane, i.e., $\beta+d\beta$, it should be deformed to △P'QS before

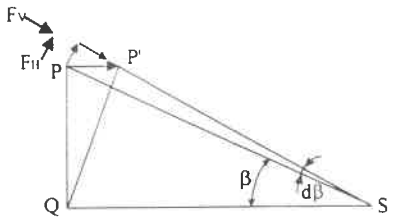

Fig.3 Additional deformation for the change of side shear angle

shearing. This can be done by a proper combination of F_v, F_H. The deformation energies $\Delta W_{U1}, \Delta W_{U2}$ by F_V, F_H are expressed respectively as following:

$$\Delta W_{U1} = k_0 w^2 / 2\tan\beta \qquad (2)$$

$$\Delta W_{U2} = \sigma_e w^2 / 4\cos^2\beta \qquad (3)$$

where k_0 is a yielding shear stress and σ_e is a yielding tensile stress[4]. Assuming ΔW_{U1}, ΔW_{U2} are uniform all over the side shear zone, the total side shear deformation energy ΔW_U is expressed as following:

$$\Delta W_U = (\Delta W_{U1} + \Delta W_{U2}) \cdot Volume(APEDFC)$$
$$= \sigma_e w^2 \left\{ \frac{k_0}{\sigma_e} \frac{1}{2\tan\beta} + \frac{1}{4\cos^2\beta} \right\}$$
$$\cdot \left\{ \frac{t_0}{\sin\phi} + \frac{1}{3} \frac{w \cdot \tan\beta \cdot \cos\phi}{\tan\phi} \right\} \qquad (4)$$

Assuming that the friction stress distribution is bilinear on the surface DFGH and □DFGH is deformed to □D'F'G'H' as shown in Fig.4, ΔW_F is expressed as following:

$$\triangle W_F = \frac{1}{12} k_0 w L \left[w\tan\beta + \frac{2L}{\sin\beta} \right] \qquad (5)$$

Applying Von-Mises' yielding criterion, $k_0/\sigma_e = 1/\sqrt{3}$, to equation (4) and (5) and letting $L = t_0 = 1$, equation (1) is rearranged as equation (6)

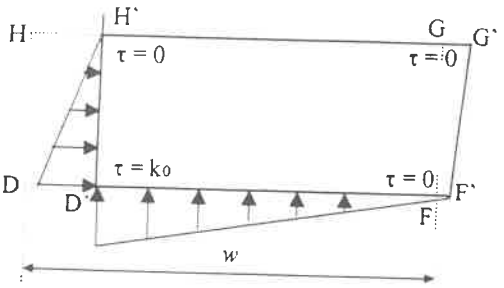

Fig.4 Stress distribution on tool-chip contact surface

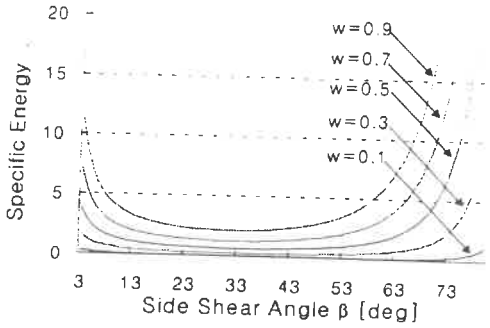

Fig.5 Estimates of specific energy

$$\frac{\triangle W_U + \triangle W_F}{t_0 \sigma_e} = w^2 \left[\frac{1}{2\sqrt{3}\tan\beta} + \frac{1}{4\cos^2\beta} \right] \cdot \left[\frac{1}{\sin\phi} + \frac{w\tan\beta\cos\phi}{3\tan\phi} \right] + \frac{1}{12\sqrt{3}} w^2 \tan\beta + \frac{1}{6\sqrt{3}} \frac{w}{\sin\beta} \quad (6)$$

Fig.5 shows variations of specific deformation energy with ϕ =30 deg, w = 0.1~0.9. A suitable side shear angle with minimum shear energy is about 27~29 deg with slight deviation depending on w.

2.2 Estimation of burr thickness

A side shear deformation width is determined from the condition that the resultant shear force on the side shear plane and on the tool-chip contact surface should be equal to the hydrostatic force acting on ADH plane. That is

$$\left\{ \frac{t_0 w}{\sin\phi \cdot \cos\beta} + w^2 \tan\beta \right\} k_0 = \frac{\sigma_e t_0^2}{2\tan\phi} \quad (7)$$

Once the side shear angle and the side shear deformation width are obtained, burr thickness, b_t, can be calculated geometrically through equation (8).

$$b_t = w\tan\beta \quad (8)$$

The ratio of burr thickness to depth of cut comes to equation (9).

$$b_t / t_0 = 0.2 \sim 0.3 \quad (9)$$

The estimate is considered too small for micro-cutting. It may be because the tool edge radius effect is not taken into consideration.

2.3 Modification of a burr thickness model

In micro-cutting, as shown in Fig.6(a), a relatively large edge radius, R, compared to depth of cut causes a large compressive force, F_c, resulting in a wide and deep plastic deformation zone up to several times as deep as the depth of cut, t_0, under the tool edge.

Expanded plastic deformation zone due to a tool edge radius is simplified as a triangular zone with an effective depth of cut, h_p, depicted in Fig.6(b). h_p is assumed to be:

$$h_p = k_p \cdot t_0 \quad (10)$$

where k_p is a deformation expansion coefficient dependent on workpiece materials and R/t_0.

Replacing t_0 in equation (7) with h_p results in equation (11).

$$\frac{k_p t_0 w}{\sin\phi \cdot \cos\beta} k_s + w^2 \tan\beta k_s = \sigma_e k_p^2 \frac{t_0^2}{2\tan\phi} \quad (11)$$

Therefore, a new burr thickness model is expressed as equation (12).

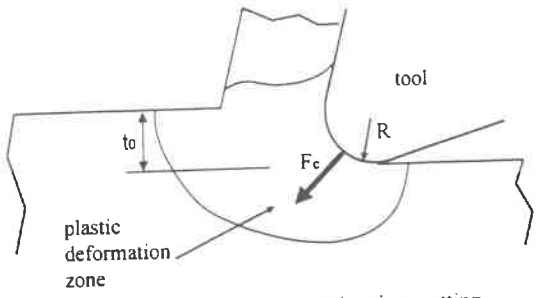

(a) Plastic deformation zone in micro-cutting

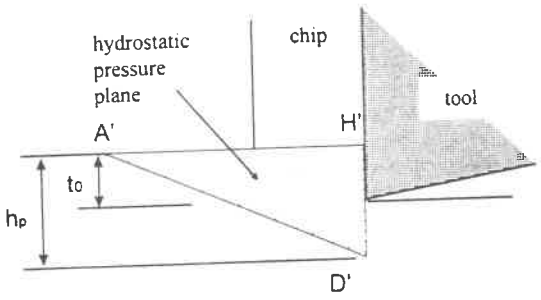

(b) Simplified hydrostatic pressure plane

Fig.6 Extension of plastic deformation zone due to tool edge radius in micro-cutting

$$b_f = t_0 k_p \tan\beta \left(\frac{\sqrt{1-\frac{1}{2}\left(\frac{\sigma_e}{k_0}\right)\sin 2\beta \sin 2\phi} - 1}{2\sin\phi\sin\beta} \right) \quad (12)$$

Fig.7 shows the burr thickness estimates from equation (12) with $k_p = 2$. Burr thickness decreases slowly with the increase of principal shear angle and is more affected by the change of side shear angle. Burr thickness is expected to be 1.3 to 2 times the depth of cut.

3. Experimental verification of burr thickness model

In order to compare the estimate of burr thickness with its actual measurements, diamond cutting experiment was conducted with brass, aluminium and copper plates

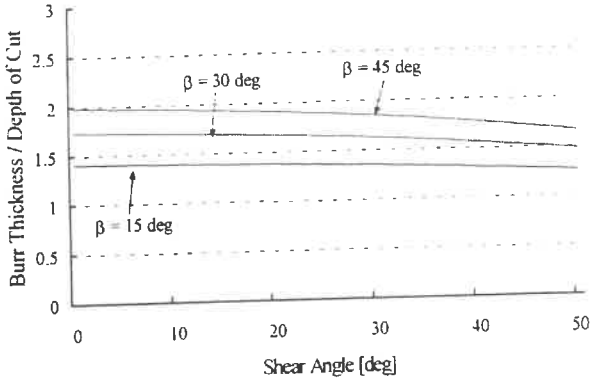

Fig.7 Burr thickness estimates(k_p=2)

0.5mm thick, groove angle of 50 deg. and depth of cuts of 2 to 12μm.

Fig.8 shows microscopic photographs of the cross section of burr for a brass plate. It is shown that burr thickness increases and the root of burr gets smoother and stronger with the increse of depth of cut.

Fig.9 shows the burr thickness measurements for three workpiece materials: brass, aluminium and copper. Thick line shows estimates from the proposed burr thickness model with $k_p = 2$. The measured values are higher for copper and lower for brass than the estimate. The estimate fits quite well for aluminium.

The difference of burr thickness due to material is considered to be caused by material characteristics such as ductility, yielding stress, fracture and etc. Therefore, the deformation expansion coefficient need to be adjusted depending on materials. The adjustments based on the results in Fig.9 are made as following: $k_p = 1.17$ for brass, 2.35 for aluminium and 3.76 for copper. It says that the more ductile materials causes the larger plastic deformation. Therefore, materials with some brittleness, like brass, are thought to be

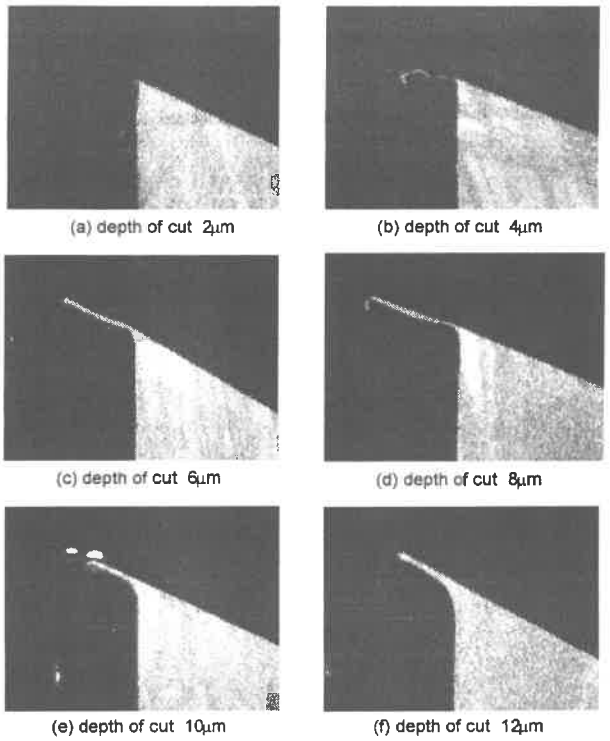

Fig.8 Microscopic photographs of burr shapes(brass)

more suitable for micro-grooving in view of burr.

4. Conclusion

1. A side burr generation model based on a side shear plane is developed.
2. Without a tool edge radius effect, probably the case in conventional cutting, burr thickness is estimated only 0.2 to 0.3 times the depth of cut.
3. Burr thickness in micro-cutting can be well estimated, ranging from 1.3 to 2.0 times the depth of cut, from the extended burr model with a tool edge radius effect.
4. Burr thickness measurements from the machined specimens are 0.9 to 1.2 times the depth of cut for brass, 1.7 to 2.2 times for aluminium and about 3 times for copper

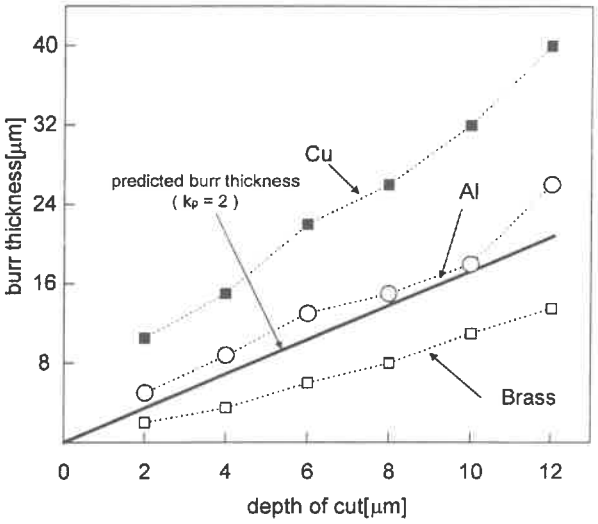

Fig.9 Comparision of burr thickness estimates and measurements with three material

5. Reference

[1] JungHwan Ahn, HanSeok Lim, David A. Dornfeld, Burr and shape distortion in micro-grooving of optical components, Proc. ASPE, Vol.14, 1996, pp496-499

[2] L.K. Gillespie, P.T. Blotter, The Formation and Properties of Machining Burrs, J. of Eng. for Ind.,Trans. of ASME, Feb., 1976, pp66-74

[3] Kazuo Nakayama and Minoru Arai, Burr Formation in Metal Cutting, Ann. of CIRP, vol. 36, no.1, 1987, pp33-36

[4] Sung-Lim Ko, David A. Dornfeld, A Study on Burr Formation Mechanism, J. of Eng. Mat. and Tech.. Trans. of ASME, Vol.113, Jan., 1991, pp75-87

ON HIGH QUALITY TURNED SILICON SURFACES

F. Z. Fang and V. C. Venkatesh
Nanyang Technological University
Singapore 639798 Email: mfzfang@ntu.edu.sg

Abstract A threshold barrier of 1 nm surface roughness for diamond turning of aluminum, a soft and ductile material, has been suggested by McKeown. This same result has been obtained now for silicon, a hard and brittle material. Surfaces of 1 nm roughness were obtained and three novel techniques are proposed in this paper. The surface integrity was studied in detail by using Atomic Force Microscope, Scanning Electron Microscope, and Stylus Surface Instrument. The diamond tool sharpness has a considerable influence on the machined surface, therefore a novel technique—brightness modulation for measuring accurately the edge of the cutter was proposed. Mirror surfaces were assessed by another novel technique--a measure of their reflectivity. A third technique, single grit diamond machining was carried out. It supplies a experimental evidence for verifying the obtained high quality turned surfaces. Results show that turning has an excellent prospect in machining brittle materials, especially as it has industrial applications.

Keywords: mirror surfaces, diamond turning, brittle materials, single grit machining

1. Introduction

Brittle materials can be hard (Si, Ge, and glass) or soft (ZnSe, ZnS, and GaAs). It is more difficult to turn the hard and brittle materials than the soft and ductile materials, and it is relatively difficult in them to turn silicon material. Mckeown [1] has indicated a best surface finish of 1 nm by diamond turning of aluminum. The authors have been able to go a step further and obtain this order of finish with silicon surfaces. In addition, silicon constitutes 90% of all semiconductor materials [2]. It is expected that, in future, silicon-on-insulator (SOI) wafer will be applied to power electronic devices. The bonding of silicon wafers and the thinning of one side of the bonded wafer play an important part in the production process of SOI wafers [3].
Mirror surface machining has recently been the focus of attention [4-6]. Diamond turning as a technique for producing optical quality surfaces on brittle materials such as quartz crystal, silicon, and germanium using an ultra-precision machine has been reported. Diamond turning of brittle material silicon has resulted surface roughness of Rmax=40 nm [7].
In the recent study, experiments were carried out using an Precitech Ultra-precision Machine to get the nanometric mirror surfaces. A single crystal diamond tool with a rake angle of 0 degree was used to turn monocrystalline silicon. The surface integrity was studied in detail by using Atomic Force Microscope, Stylus Surface Instrument, and Scanning Electron Microscope. Three new techniques were proposed in this paper. Results show that turning has an excellent prospect in machining brittle materials, especially as it has industrial applications.

2. Turning of silicon surfaces

Obtaining mirror surfaces needs a ultra-precision machine with a very high accuracy, especially the high feed resolution of the two slideways is needed to meet the requirements of machining spherical or aspheric surfaces [8]. In this experiment, an ultra-precision turning machine (Precitech's Optimum 2800), with a feed back resolution of 8 nm, was used for machining.
During the turning silicon, a number of cutting conditions were tried out to get the best surface. At a depth of cut of 1 um, feed rate of 4 mm/min, and a speed of 400m/min, a mirror surface of Ra=5.9 nm was obtained; decreasing this feed rate 10 times to 0.4 mm/min has a dramatic effect--a roughness value of Ra=1.0 nm (Fig.1). By analyzing the figure 1, the distance between two scratches is seen to be just equal to the feed of per revolution.

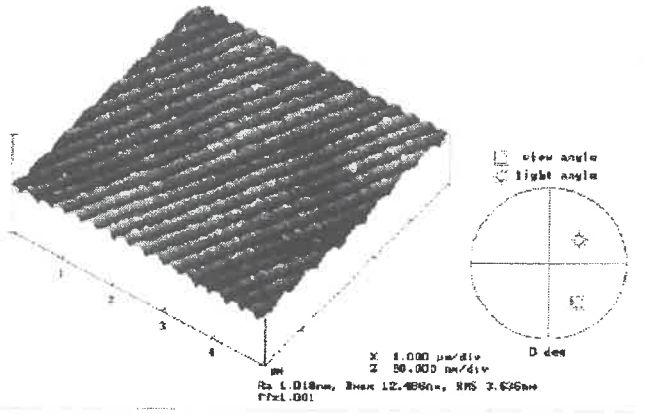

Fig. 1 AFM micrograph of turned silicon surfaces

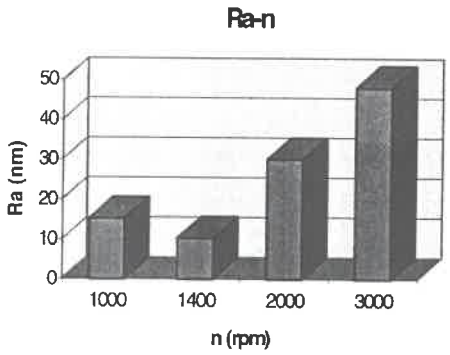

Fig. 2 Surface roughness Ra with variation of n

Variation of roughness Ra with spindle speed can be seen in Fig. 2, and the optimum cutting speed should be selected. Fig. 3 shows the wear on a single crystal diamond tool.

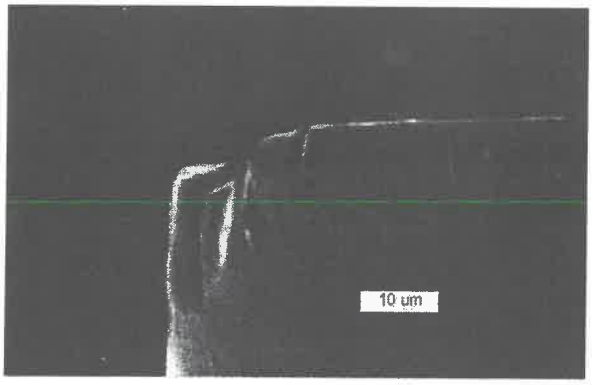

Fig. 3 SEM micrograph of cutter wear

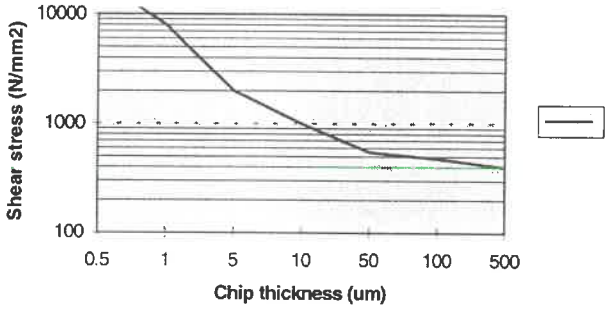

Fig. 4 Relationship between chip thickness and shear stress

High precision solid tool machining demands tools that can produce very fine chips. When chip thickness becomes less than about 1 um, the shear stress in both the work material and cutter increases sharply and becomes very large, resulting in rapid tool wear. Fig. 4 shows this relationship [1]. The reason for this is that with depths of cut less than 1 um, the distribution of movable dislocations in the metal crystals approaches zero and cutting forces have to overcome the very large atomic bonding forces within the crystals. This is where we move from single point machining to the use of grinding in which fine abrasive grains are used to remove initially large chips, but in finishing cuts, fine chips of the workpiece material. The cutting edge of the grains are subjected to very high pressure and temperature through the release of this high density energy. The abrasive grains thus wear rapidly. Nevertheless, in grinding, continuous machining is possible because as the grains are sheared at these high stresses, new edges are formed in a quasi-random manner. Thus the ground surface exhibits a quasi-random distribution of peaks and valleys. Mirror machining or truly specular finish cannot be got by grinding. It can only be generated by the same continuous cutting edge as in single point machining [1].

3. Brightness modulation—a measure of the cutter edge

Characterizing the diamond tool edges is interesting for many reasons, including research, quality control in tool manufacturing, and seletion of tools from inventory. Since a sharp tool has an edge radius below the optical diffraction limit, there is a significant challenge in developing an effective yet simple measurement method. Fig. 5 shows the variation of roughness Ra with edge radii. The diamond tool sharpness has a considerable influence on the machined surfaces. A new technique generates a graphical representation of the grey levels within the image (fig. 6). From the figure, the edge of the diamond cutter can be measured easily.

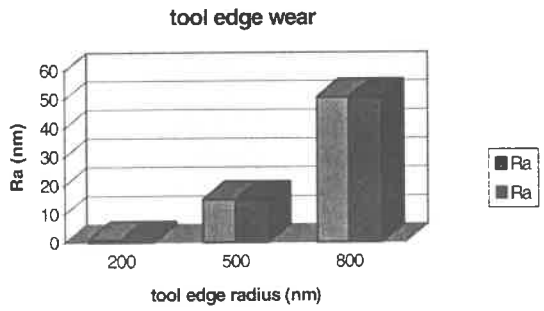

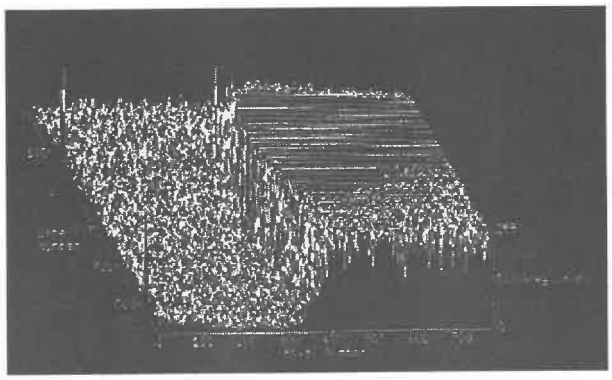

Fig. 5 Variation of roughness Ra with edge radii Fig. 6 Graphical representation of the grey levels with the image

4. Reflectivity of silicon surfaces

A novel approach in this paper is to measure the reflectivity of mirror surfaces. This is done by measuring brightness, better known scientifically as lightness. Lightness is an achromatic dimension necessary to describe the three dimensionality of colour, the other two dimensions being hue and saturation. Hue and saturation taken together is known as chromacity. Chroma Meters (Colorimeters) provide highly accurate measurements of both lightness and chromacity. Gloss could be a good indicator of surface characteristics. Gloss is a subjective term used to describe the relative amount and nature of mirror like reflection. Extremely fine surfaces have very low lightness values. Over a hundred surfaces were measured so as to get a simple relationship about the lightness. We got L=3.18 and 6.05 for feeds of 0.4 mm and 4 mm. For silicon surfaces, the lightness L has a linear relationship with roughness Ra (Fig 7) given by:

$$L=117.2Ra \qquad (1)$$

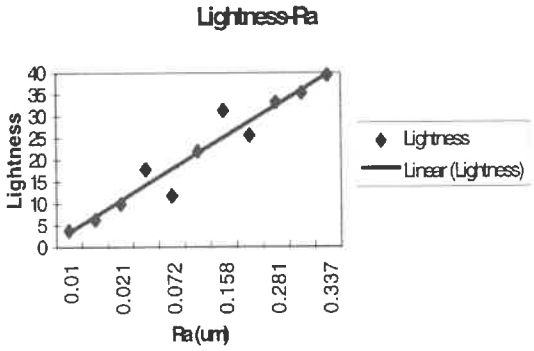

Fig. 7 Relationship between the lightness and roughness

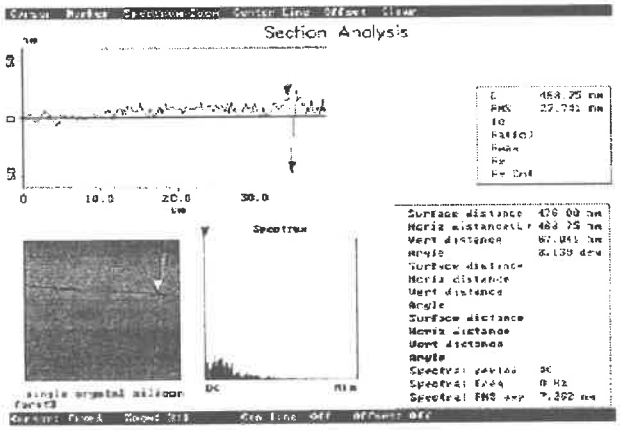

Fig. 8 Pile up on single crystal silicon

5. Single grit machining

Single grit machining often known as single point scratching, constitutes a useful method of understanding the mechanics of machining brittle materials as we can get fundamental information on the interaction between the abrasive and the work material. It is well known that brittle materials deform plastically when the depth of cut is very small. This depth of cut is known as the critical depth of brittle-ductile transition dc, when the cutting mode changes from brittle mode to ductile mode. Single grit machining was done on single crystal silicon. We got the AFM micrograph as shown in Fig. 8. It confirms that single crystal silicon has a similar performance with soft materials such as aluminum under ductile mode conditions.

6. Conclusion

Diamond turning of the brittle material Si has been studied, and the surface roughness of Ra=1.0 nm, Rmax=12.4 nm has been obtained on Precitech Ultra-precision Machine. New techniques were used to make a breakthrough in the silicon turning.

(1) Turned surfaces, when viewed under the Atomic Force Microscope and the Scanning Electron Microscope, barely reveal any marks, fractures, and ductile scratch.

(2) A novel technique brightness modulation is proposed in this paper. It simplifies measurement of the diamond cutter edge.

(3) The nanometric mirror surfaces were assessed by measuring their reflectivity, better known as lightness, gloss, or brightness.

(4) The scratch of silicon surfaces is sectioned on an AFM. A double pile up indicates that it has a similar performance with soft materials under ductile mode.

(5) Compared to several inspection methods, AFM and SEM were rated to be suitable for inspecting nanometric mirror surfaces.

Finally, analysis on the cutting parameters, the edge radius of cutter and the wear of cutter was made to confirm silicon mirror surface turning as a process for industry.

Reference

1. McKeown, P.A., 1995, High precision manufacturing in an advanced industrial economy, Lecture at GINTIC, NTU. Singapore.

2. Venkatesh, V.C., Inasaki, I., Tonshoff, H.K., Nakagawa, T.,Marinescu, I.D., 1995, Observations on polishing and ultraprecision machining of semiconductor substrate material, Annals of the CIRP, Vol. 44/2, pp. 611-618.

3. Yuan Z.J., Lee, W.B., Yao, Y.X., Zhou, M., 1994, Effect of crystallographic orientation on cutting forces and surface quality in diamond cutting of single crystal, Annals of the CIRP, Vol. 43/1, pp. 39-42.

4. Konig, W., Berktold, A., Koch, K. F., 1993, Turning vs Grinding -A comparison of surface integrity aspects and attainable accuracies, Annals of the CIRP, Vol. 44/1, pp. 39-43.

5. Paul, E., Evans, C. J., Mangamelli, A., McGlauflin, M., 1996, Chemical aspects of tool wear in the single point diamond turning, Journal of Precision Engineering, Vol. 18/1, pp. 4-19.

6. Blackley, W S., Scattergood, R.O., 1991, Ductile regime model for diamond turning of brittle materials, Journal of Precision Engineering, Vol. 13/2, pp. 95-102.

7. Shibata, T., Fujii, S., Makino, Eiji, E., Ikeda, M., 1996, Ductile-regime turning mechanism of single-crystal silicon, Journal of Precision Engineering, Vol. 18/3, pp. 129-137.

8. Fang, F.Z., Zhang, Y.Q., Yuan, Z. J., Research on enhancing in-process measuring system precision of ultra-precision turning machines, SPIE, Vol. 2394, pp. 247-250.

MORPHOLOGY AND TOPOGRAPHY OF CHIP PRODUCED BY DIAMOND TURNING OF *Al-Mg* ALLOY FOR MIRRORS

R. G. Jasinevicius, Arthur J. V. Porto, J. G. Duduch

Escola de Engenharia de São Carlos (**EESC**) -Universidade de São Paulo (**USP**) -
Departamento de Engenharia Mecânica (**SEM**) - LAMAFE
P.O. Box 359CEP 13560-970 - São Carlos - SP - Brazil
(AJVPORTO@SC.USP.BR)

Abstract

The undestanding of the machining process cannot be realized and determined only by the examination of the final characteristics of the machined surface. The characterization of machining chips using electron microscopy is of great relevance to better comprehend the phenomena occurring in the separation process. The morphological and topographic characteristics of chips can provide relevant insight into the interaction that occurs along the cutting edge and material.This work will be based on a critical observation through Scanning Electron Microscopy of chips produced by single point diamod turning focusing the interaction between the cutting edge radius and the uncut chip thickness. The surface roughness seems to be little affected by decreasing the infeed rate to submicron range. It was observed that the shear plane angle seems to be different across the width of the chip. This difference is represented by wrinkles on the thin edge of the chip which appears to indicate a higher shear plane angle. Therefore, another series of exeperiment was carried out to observe the behaviour of the mechanism of chip formation with fixed feedrates and different depths of cut. It was observed that the mechanism of chip formation was a little different from the former.

Keywords: Ultraprecision, Diamond tool cutting edge, Chip topography, Aluminium, Scanning Electron Microscopy

1. INTRODUCTION

Metal cutting chip formation process has a distinguished aspect concerning its extremely high strain rate (10^3-10^6 s^{-1}) as large strain is imposed in a small deformation zone. During the interaction between the tool cutting edge and the uncut chip thickness, there is a temperature rise due to deformation process. This heat generated in flow zone is due the creation and annihilation of point defects and dislocations (Black, 1979). It is assumed by some authors (Asai & Kobayashi, 1991) that the temperature in the surface of the chip and consequently in the vicinity of the cutting edge is higher, exceeding the melting temperature of the Al alloy, and probably, sufficiently high to increase the superficial temperature of the workpiece. The thermal effect due to this interation is the thermally reduced yield strength. This phenomenum is dependent on the specific cutting energy along with an increased shear stress (Liu & Dornfeld, 1996) with the decreasing of the chip thickness across the width of the chip at dimensions of the order of submicrometer.

Another important aspect reported by Polvani et al. (1987) is that materials including OFHC copper and 6061-T6 Aluminium exibit an exponentially increasing hardness near surfaces which have been diamond turned. In single point diamond turning, the undeformed chips have non uniform hardness depending on the profile of effective chip thickness (Liu and Dornfeld, 1996). The nature of the increasing hardness tendency depends on the tool edge sharpness or radius (r). According to Yuan et al. (1996), the plastic deformation is directly proportional to the cutting edge radius, the larger the tool edge radius the larger the

dislocation density on the surface and subsurface of the workpiece. This effect is related with the interaction bettwen the cutting edge and cutting conditions.

This work will be based on a critical observation of chips produced by single point diamod turning by the point of view of the interaction between the cutting edge radius and the uncut chip thickness. The surface roughness seems to be little affected by decreasing the infeed rate to submicron range. It was observed that the shear plane angle seems to be different across the width of the chip. This difference is represented by wrinkles on the thin edge of the chip which appears to indicate a higher shear plane angle. Therefore, another series of exeperiment was carried out to observe the behaviour of the mechanism of chip formation with fixed feedrates and different depths of cut. It was observed that the mechanism of chip formation was a little different from the former.

2. EXPERIMENTAL PROCEDURE

The workpieces material prepared for the testing was a polycrystalline Al-4,03%Mg Alloy cylinder 20 mm in diameter and 20 mm height. The average grain size of this alloy was aproximately 100 μm. The workpieces were stress relief for 3 hours at 380 °C following instructions of the manufacturer. These specimen were diamond turned using facing cuts on a Rank-Pneumo ASG 2500 Diamond Turning Machine. A 0° rake angle and clearance angle of 12° diamond tool with nose raidus Rp = 0,762 mm was used in all tests and the spindle speed was 1000 rpm. The workpieces recieved 5 rough cuts with f = 20 μm/rev and depth of cut ap =10 μm to plain the surface. The experiment was devided in two parts. The first part, the feed rate was kept constant and equal to 10 μm/rev. The nominal depth of cut was then varied from 0.5 μm, 1.0 μm and 3.0 μm giving nominal values of width of cut in the range of 26.94 - 66 μm. The second part of the cutting tests were carried out kepping the nominal depth of cut constant at dc = 10 μm, this value represents a theoretical chip width $W = (2\ dc\ Rp)^{1/2} = 123.45$ μm (Blake, 1988). The feed rate f was varied with the following values: 0.5 μm/rev, 1.0 μm/rev and 3.0 μm/rev in order to observe the chip thickness produced by cutting at micrometer and submicrometer scale. The chips were collected and then mounted on a standard specimen holders and were observed in a Scanning Electron Microscope (SEM).

A natural diamond tool is used as cutting tool. The diamond cutting tool was first observed in a Scanning Electron Microscope to have a estimative of the cutting edge radius. To inspect the cutting edge it was necessary a metalization coating due to the extremely high conductivity of diamond, the gold film layer deposited was 20 nm thick.. The cutting edge was estimated to be smaller than 100 nm through SEM observation.

3. RESULTS AND DISCUSSION

The first part of tests the surface roughness varied from 7.7, 7.8, 8.7 nm Ra with a $\sigma = \pm$ 0,1 nm, respectively. All Aluminium alloy chips produced by the diamond turning process can be considered as flow type continuous chips. The geometrical profile of the chip cross section area varies in thickness from zero at the tool nominal center to a maximum at the top of the uncut shoulder

However, as the depth of cut is decreased and reachs the same order of the cutting edge radius, the material, which is removed as chip, will actually be removed by a tool (round part of the cutting edge) with an effective rake angle more and more negative up to where the rake angle is so negative that no chip formation will occur and the plowing mechanism will take place. Because of that, it could be assumed that there is a change in the tension state envolved in the chip formation mechanism. Part of the chip (thinner part) is under compressive stress (highly negative effective rake angle) and the thicker part under tensile stress (nominal rake angle). Kita (1982) has considered that the increase in the compressive stress on the shear plane hinders the breakdown of chips and makes it easier to get a continuous chip even though the tool has a large negative rake. The magnitude of these stress

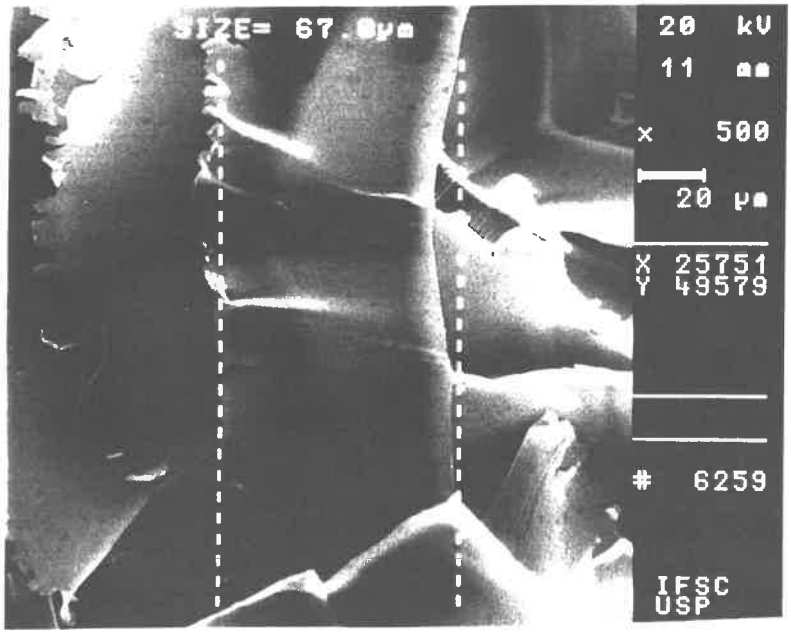

(a)

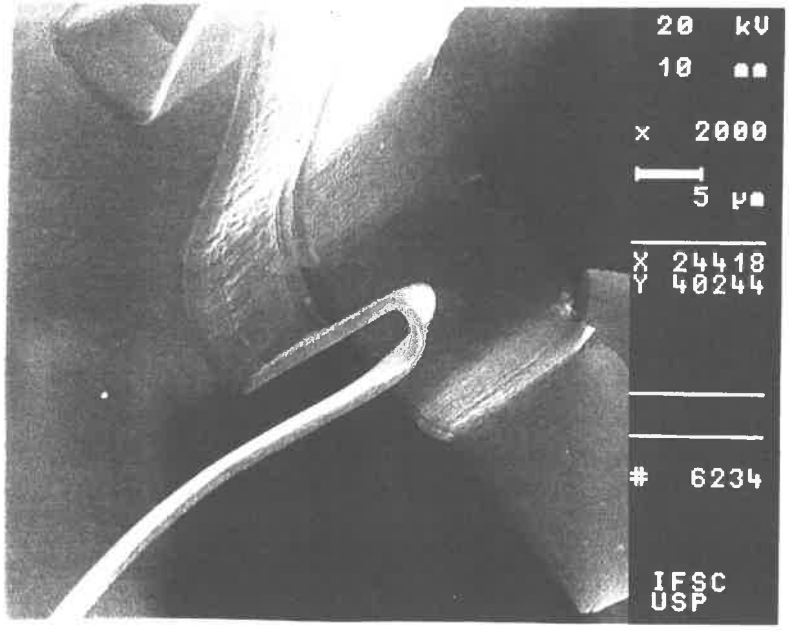

(b)

Figure 1. Chips produced in the first part of experiments; (a) small cracks are formed on the thin edge of the chip; (b) longitudinal crack tears the chip in two ribbon-like pieces.

would depend upon the uncut thickness of cut. When the uncut chip thickness is kept constant (10 μm/rev) and the depth of cut is increased, the tensile stress (from the thicker part of the chip) acting on the thinner part of the chip, under compressive stress, turns to be strong suficiently to iniciate cracks, so the chip thin edges will present small cracks as can be observed on Figure 1 (a). This might occur because the thickness on the thin edge of the chip is not

This cutting condition mantain the theoretical width of cut constant equal to 123,45 μm.

The chip shown in Figure 2 depicts a diferent feature from the typical chips produced. As can be seen, the thin edge of the chip presents a wrinkle, similar to what was observed by other authors like Blake and Scattergood (1986) and

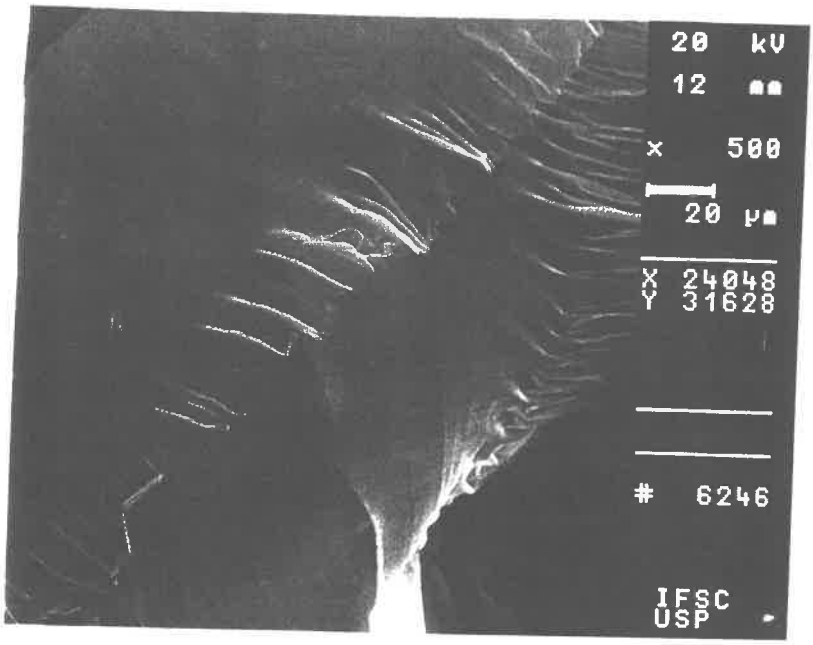

Figure 2. Chip showing aparently two shear plane angle. The thinner part seems to be longer than the opposite part.

suficcient to to resist to the tensile stress exerted by the thicker part. When the depth of cut is decreased, the stress field acting on the chip will take place on a smaller width of cut, so it will be concentrated on smaller and thicker cross sectional area. It was observed in the chip produced an existance of a longitudinal crack which tears apart the chip in two ribbon-like pieces, and the thin edge detaches from the other part of the chip as can be seen in Figure 1 (b). It should be noted that the edge cracks appears in this case, but in a smaller extent.

The chips produced with nominal depth of cut of 10 μm and decresing feedrate are now presented. The second part of tests the surface roughness varied from 7.2, 7.3, 7.7 nm Ra with a $\sigma = \pm 0{,}1$ nm, respectively.

Asai and Kobayashi (1990) under different cutting conditions and tool geometry. Apparently, this part of the chip is longer than the thicker part, suggesting that the shear angle is higher here. Asai and Kobayashi have demonstrated that this difference exists and calculated a higher value of the shear angle for the thin edge.

Therefore if the approach proposed by Asai and Kobayashi (1990) is close evaluated it is possible to think in another form. The Figure 3 shows a proposed two-dimensional view of the chip formation process. In this machining approach, the tool has a tool edge radius r and rake angle γ. As can be seen in the general view of the cutting approach, the depth of cut is divided in two parts. The first part, $\mathbf{ap_1}$, means

that the chip is formed with uncut chip thickness larger than the tool edge profile, so the chip formation mechanism is govern by the nominal value of the rake angle (γ_{nom}). In the second part, **ap2** , the depth of cut is of same order of the cutting edge radius, so the chip will be removed by a tool with a more and more large negative rake angle (γefn) as the depth of cut as well as the uncut chip thickness are being decreased, this angle is formed with round part of the cutting edge (Figure 3 (a)).

It is known that shear angle decreases as the depth of cut is decreased (the so called "size effect") and/or negative rake angles tools are used. The wrinkle formed based on this cutting approach, taking as reference to analysis the lateral view of the approach (Figure 3 (b)), considers that the shear angle is smaller because at this dimension of the uncut chip thickness and depth of cut, the cutting mechanism at which the chip is formed might be governed by the highly negative effective rake angle (Lucca et al. 1991, Lucca and Seo, 1993).

When the uncut chip thickness become of the same order of or smaller than the cutting edge radius there is a change in the microgeometry of cut. In this case, the effective tool rake angle will be that on the round part of the edge which, consequently, becomes more and more negative as the uncut chip thickness is decreased. This results in a decrease in the shear angle and, therefore, an "increase" in the shear plane area, so the heat generated due to creation and annihilation of point defects and dislocations along with recovery process may exerted a reduction in the flow stress. Because of the small area of the shear plane at uncut chip thickness in the submicrometer range, there is, apparently, a faster material flow to offset the slower material flow on the thicker portion close the shoulder of the chip. This is considered because the lamella spacing will be smaller at the thinner part and there must be, quantitatively, more lamellae being formed in a more extended length.

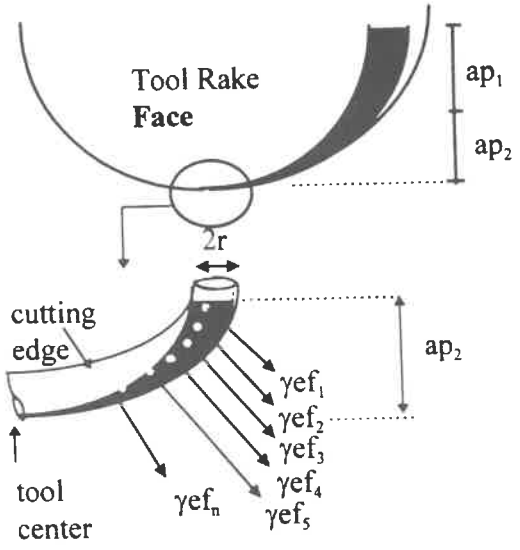

(a) Front view at a depth of cut ap_2 of the same order of the cutting edge radius

$a_{p1} > r\,(1 + \text{sen}\,\gamma)$ r : cutting edge radius
$a_{p2} \leq r\,(1 + \text{sen}\,\gamma)$ γ : Rake angle

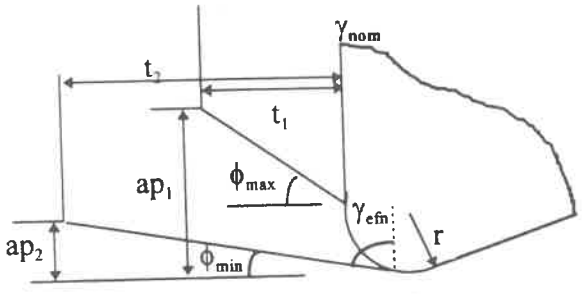

(b) Lateral view showing the effect of decreasing the depth of cut on shear angle.

Figure 3. Proposed approach for the chip formation process.

4. CONCLUSIONS

This work presented a preliminary study concerning topography and morphology of chip diamond turned of a Al-Mg Alloy. The model suggested in this paper has to be more deep explored through techniques such as Transmision Electron Micrsocopy to see if there is a real relationship bettwen the deformation process along the chip width and the concentraion of defects. This will be the subject of a future work. It was showed that there is a very low difference in surface roughness despite of the submicrometer range of feed rate at the tests caried out.

5. REFERENCES

Asai, S.,Kobayashi, A. "Observation of Chip Producing Behaviour in Ultraprecision Diamond Machining and Study on Mirror-like Surface Generating Mechanism", Precision Engineering, Vol. 12(3):137-143, 1990.

Black, J.T. "Flow stress model in metal cutting", Trans. ASME, J. of Engg. for Industry, Vol. 101, pp. 403-415, Nov. 1979.

Blake,P.N., Scattergood,R.O.,"Chip topography of diamond turned ductile metals". Proc. SPIE, Vol.676, pp.96-103, 1986.

Evans, C., Polvani, R., Postek, M., Rhorer, R., "Some observations on Tool Sharpness and Sub-Surface damage in Single Point Diamond Turning", in Proc. of SPIE, Vol.802, pp. 52-66, 1987.

Kita, Y., Ido, M., Kawasaki, N., "A study of metal flow ahead of tool face with large negative rake angle", ASME, J. of Engg. for Industry, Vol.104 (3): pp. 319-325, Aug. 1982.

Liu, J.J., Dornfeld, D.A., "Modeling and Analysis of Acoustic Emission in Diamond Turning", Journal of Manufacturing Science and Engineering, Vol.116(2):199-207, 1996.

Lucca, D.A., Rhorer, R.L., Komanduri, R."Energy dissipation in the ultra-precision machining of copper". Annals of the CIRP, Vol. 40 (1): 69-72, 1991

Lucca, D.A., Seo, Y.W., "Effect of tool edge geometry on energy dissipation in ultraprecision machining" Annals of the CIRP, Vol. 42(1): 83-86. 1993.

Drescher, J.D., Dow, T.A., "Tool Force Model Development for Diamond Turning", Precision Engineering, Vol. 12 (1):29-35, Jan.1990.

Ramalingam, S., Black, J.T. , "An Electron Microscopy Study of Chip Formation" Metallurgical Trans, Vol.4: pp. 1103-1112, Apr. 1973.

Yuan, Z.J., Zhou, M., Dong, S., "Effect of diamond tool sharpness on minimum cutting thickness and cutting surface integrity in ultraprecision machining", J. of Mat. Proc. Techn. vol.62, pp.327-330, 1996.

Chip Dynamics in Diamond Turning

B. H. Jared and T. A. Dow
Precision Engineering Center, North Carolina State University, Raleigh, NC

Key Words: Chip dynamics, diamond turning

Introduction

In recent years, university and industrial research has provided a wealth of information concerning the material deformation processes involved in diamond turning. Since most of this work has focused on the region near the cutting zone, a study of chip dynamics has been initiated to develop an understanding of the behavior of chips as they move away from the cutting zone and the workpiece surface.

Complementary research in conventional machining has demonstrated the correlation between chip geometry and motion and cutting parameters such as depth of cut, cutting speed, and tool geometry. Due to the small tool forces and small chip thicknesses, it is expected that phenomena which play a negligible role in conventional machining will affect the behavior of chips produced in diamond turning. Therefore, experiments have been conducted to determine the effects of cutting speed, depth of cut and tool geometry on chip motion in diamond turning.

Plated Copper Experiments

The first set of experiments were performed on a plated copper workpiece with a 292 mm outside diameter. A 90° dead sharp tool with a 0° rake angle was plunged into the workpiece at a constant z-axis position on a Nanoform 600 diamond turning machine. The infeed rate for each test was varied to insure that plunging of the tool into the workpiece occurred over no more than 2/5 of a rotation of the workpiece. Thus, a constant thickness chip was created during a majority of each test. Figure 1 shows that chip radius of curvature increased with cutting speed for a depth of cut of 50 μm and an infeed of 125 μm/rev. An increase in radius of curvature with cutting speed has also been documented in conventional machining research [1]. Figure 2 shows that the radius of curvature increased and then decreased with increasing depth of cut for a cutting speed of 1.53 m/sec and an infeed of 625 μm/rev. Although enough data was not collected here to establish a significant trend, work in conventional machining has shown that chip radius of curvature will increase with increasing depth of cut [2].

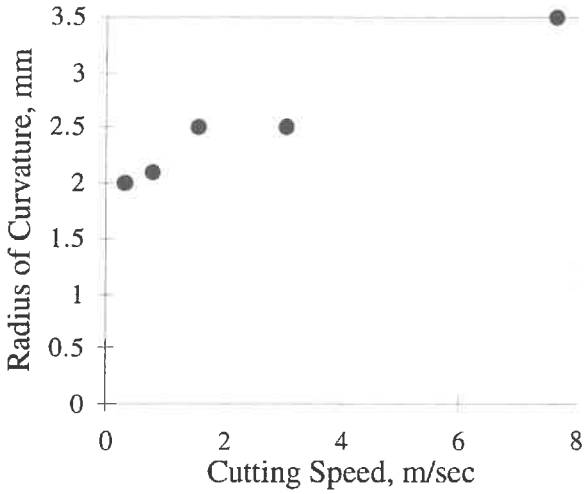

Figure 1: Chip Radius of Curvature vs. Cutting Speed

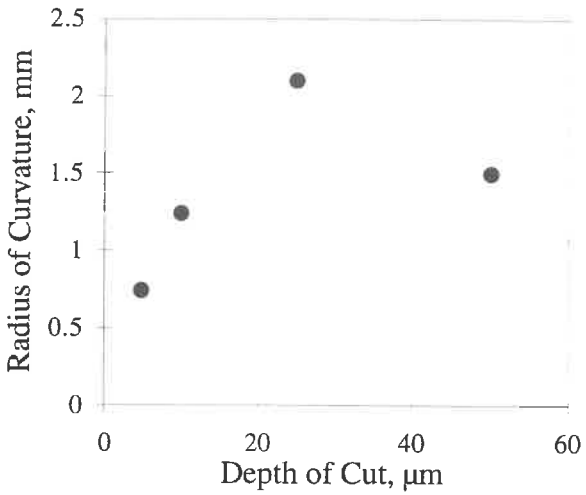

Figure 2: Chip Radius of Curvature vs. Depth of Cut

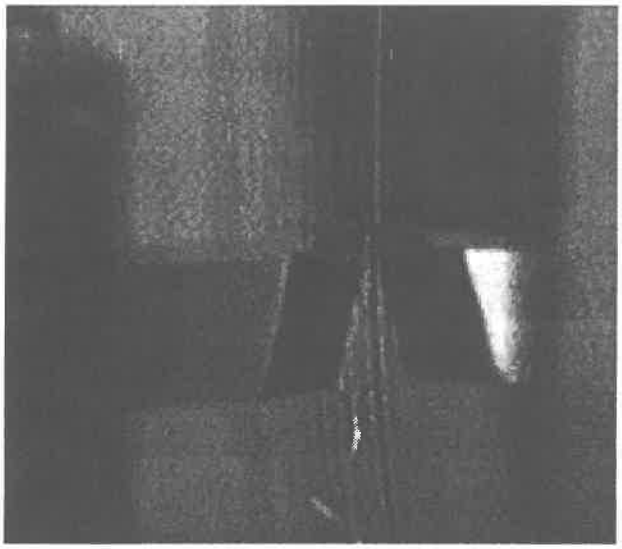

Figure 3: Chip Generated at 0.765 m/sec

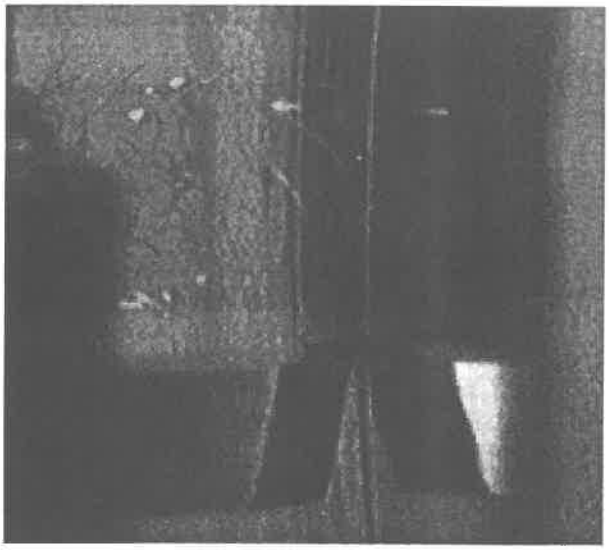

Figure 4: Chip Generated at 7.65 m/sec

Figures 3 and 4 show images of chips generated by a 50 μm depth of cut and a 125 μm/rev infeed. The chip in Figure 3 was produced using a 0.765 m/sec cutting speed, while Figure 4 shows a chip produced by a 7.65 m/sec cutting speed. Figure 3 shows the chip falling off of the tool face in the direction of the workpiece rotation. This behavior was repeated throughout the cutting experiments due to the small rake face area of the dead sharp tool and the low chip stiffness. The chip in Figure 4 provided the only exception to this behavior. Instead of moving with the workpiece velocity, it moved in the opposite direction and became entangled with itself above the tool face. Such motion was not observed with cutting tests below 7.65 m/sec. Thus, a velocity affect must be present to induce such a dynamic response.

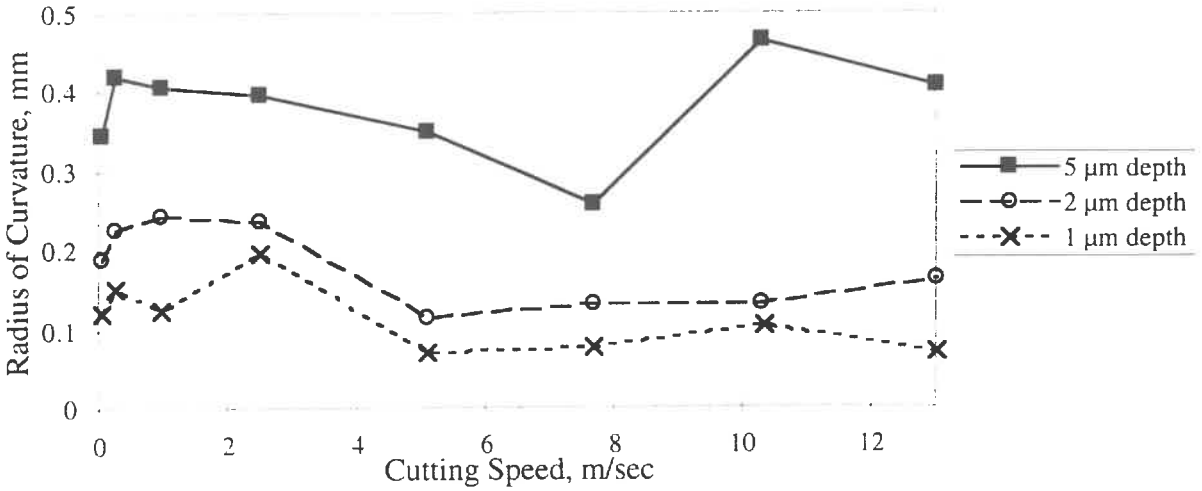

Figure 5: Chip Radius of Curvature vs. Cutting Speed (1-5 µm depth)

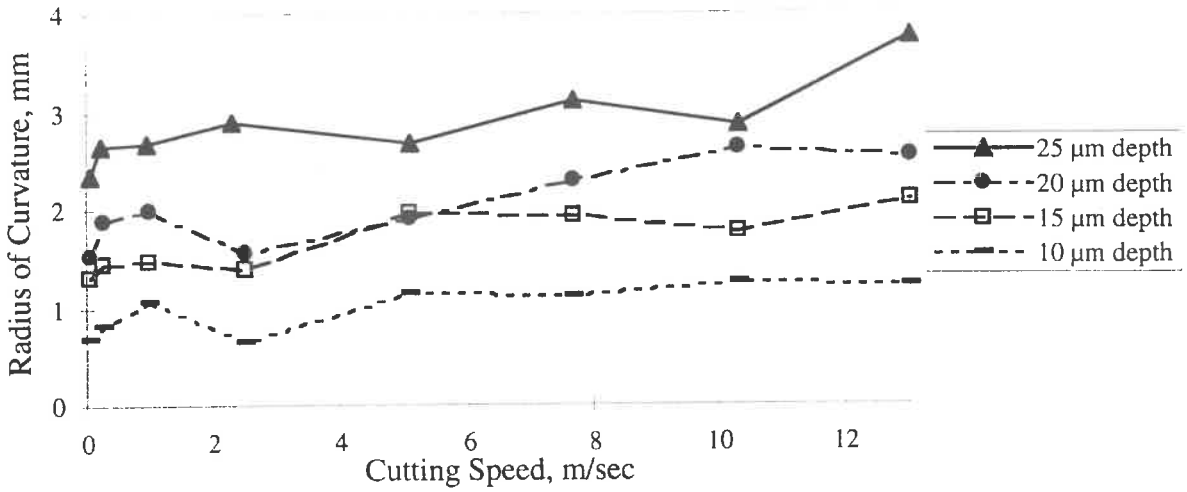

Figure 6: Chip Radius of Curvature vs. Cutting Speed (10-25 µm depth)

6061-T6 Aluminum Experiments

Plunge cut experiments have also been performed in 6061-T6 aluminum using a round nose tool with a 1.524 mm nose radius and a 0° rake angle. The tests were performed at a constant x-axis position on an ASG 2500 diamond turning machine. Cutting depths ranged from 1 µm to 25 µm, while the cutting speed was varied from 0.045 m/sec to 13.0 m/sec. The infeed rate was varied according to the spindle speed and the cutting depth to insure that plunging of the tool occurred over no more than 1/5 of a rotation of the workpiece. During the remainder of the part rotation, the chip thickness was constant.

Figures 5 and 6 show chip radius of curvature verses cutting speed for varying depths of cut. As observed in the plated copper tests, chip radius of curvature increased with increasing depth of cut. The effect of cutting speed, however, was not as significant as that of cutting depth, and did not follow the trends observed in conventional machining. Figure 5 shows that for small depths of cut, the radius of curvature increased, decreased and then increased again as the cutting speed was increased. For the larger depths of cut, shown in Figure 6, however, chip radius of curvature followed the expected trend of increasing with increasing cutting speed.

Conclusions

A study of the dynamic motion of chips produced in diamond turning has been initiated. The correlation of chip behavior observed in diamond turning with that described in conventional machining literature has begun as the effects of cutting parameters such as cutting speed, depth of cut, and tool geometry are all being investigated. Initial experiments indicate that chip behavior in diamond turning does not follow the same patterns and trends demonstrated in conventional machining.

References

1. Lee, D., "The Effect of Cutting Speed on Chip Formation Under Orthogonal Machining", *Journal of Engineering for Industry*, v. 107, Feb. 1985, pp. 55-63.
2. Hahn, R., "Some Observations on Chip Curl in the Metal-Cutting Process Under Orthogonal Cutting Conditions", *Transactions of the ASME*, May 1953, pp. 581-590.

COMBINED MODEL OF CERAMICS GRINDING

Ling Yin & Ioan D. Marinescu
Dept. of Industrial & Manufacturing Systems Engineering
Kansas State University, Manhattan, Kansas 66506

Tetsuo Matsuo
Faculty of Engineering, Kumamoto University, Kumamoto 860, Japan

In grinding of ceramics, five models of material removal have been established. They are called the brittle fracture, the ductile regime grinding, the pulverized regime grinding, the double fracture, and the semi-ductile grinding [Bifano et al., 1991; Zhang et al., 1994; Marinescu 1996; Zhong et al., 1995]. In these models little information exists on the interrelations between the temperature effects of grinding heat and the chip formation mechanisms. Due to grinding heat and forces, the phenomenon of the recrystallization of fragmentized ceramic crystals during grinding ceramics has been insufficiently emphasized in the past. The present paper describes a new material removal model of ceramics grinding on an emphasis of a thermo-mechanical action between diamond abrasives and ceramic workpieces based on single-point diamond abrasive grinding experiments of ceramics with different microstructures and theoretical analyses.

SINGLE-POINT DIAMOND GRINDING OF CERAMICS

Figure 1 shows the schematic set-up of the test. A natural diamond grain was welded by metal bond regardless of its orientation on the top of a small cylinder. The cylinder was further mounted on the periphery of an aluminum disk of 170mm in diameter and 20mm in thickness. Then the test was set on a surface grinder as a grinding wheel and grinding experiments were carried out with no lubricant. The ceramic workpiece was bonded on a piece of steel which was magnetically clamped on the table of the machine. Wheel surface speed was 27.1m/s, table speed was 0.16m/s, and grain depth of cut was 10μm.

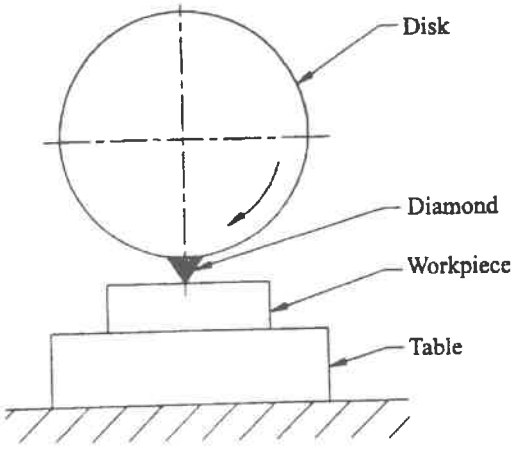

Figure 1. Schematic diagram of single-point diamond grinding experiments

Four alumina specimens which differed in grain size and purity were analyzed using a polarizing microscope. Specimen 1 was formed from a polycrystalline alumina with 95% purity. Most of the grains were columnar in shape. The average grain size was 42μm×15μm and the maximum grain size was 96μm×24μm. Specimens 2 and 3 were formed from the polycrystalline alumina with 97% and 99% purity respectively, with xenomorphic-granular grain shapes and the average grain sizes of about 6μm to 15μm and 6μm to 20μm respectively. The microstructure of Specimen 4 was very different from those of Specimens 1, 2 and 3. Specimen 4 was made from the polycrystalline alpha-phase alumina doped with chromium for the purpose of solution strength, with cryptocrystalline and amorphous structures.

When polycrystalline ceramics were ground with single-point diamonds, the materials were removed almost entirely by transgranular and integranular fracture accounting for the surface appearances, as shown in Figure 2. The sizes of fractured grains in Specimen 1, as shown in Figure

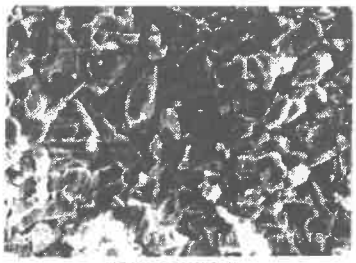

Figure 2(a)

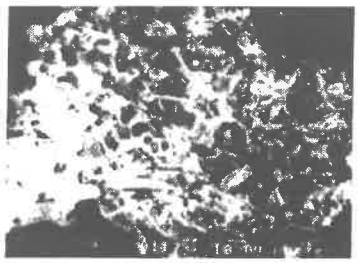

Figure 2(b)

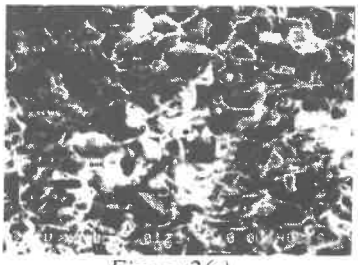

Figure 2(c)

Figure 2. SEM-photographs of the transgranular and intergranular fracture of the polycrystalline ceramics (a) Specimen 1, (b) Specimen 2, and (c) Specimen 3

2(a), were bigger than that of the fractured grains in Specimens 2, as shown in Figure 2(b), and 3, as shown in Figure 2(c), along the grain boundaries.

The photograph of the ground surface of the cryptocrystalline and amorphous ceramic shows the strongly different appearance as compared with the transgranular and intergranular fracture in polycrystalline alumina by single-point diamond grinding. Figure 3 shows an electron

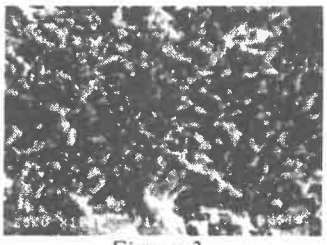

Figure 3

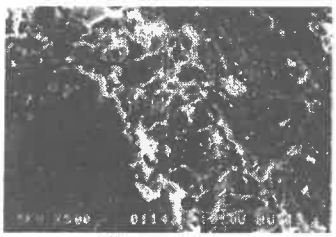

Figure 4(a)

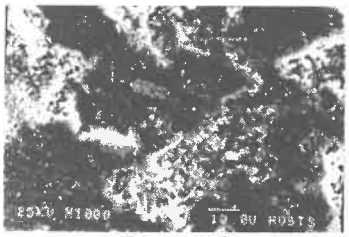

Figure 4(b)

Figure 3. SEM-photograph of the microparticle cluster fracture of the cryptocrystalline and amorphous ceramic in Specimen 4

Figure 4. SEM-photographs of the dense layers of deformation, microcracks and debris in the grooves (a) in the polycrystalline ceramic, (b) in the cryptocrystalline and amorphous ceramic

micrograph of the ground surface of Specimen 4. The faceted region shows where the material was removed due primarily to microparticle cluster fracture.

When the single-point diamond was acting heavily on the ceramic workpieces, both the polycrystalline ceramics and the crytocrystalline and amorphous ceramic were deformed and damaged extensively, forming the dense layers of deformation as shown in Figure 4. From these pictures, it is found that many clastic chips were produced and some of them were smashed into the powder chips. Furthermore, many residual microcracks were generated under the ground groove of the polycrystalline ceramics, as shown in Figure 4(a); but fewer microcracks were present under the scratched groove of the cryptocrystalline and amorphous ceramic, as shown in Figure 4(b). In Figure 4, in the bottom of the ground grooves, there was an abundance of cracked ceramic crystals. Some of the fragments would be released from the ceramic surfaces in the form of the chips, and some of the cracked ceramic crystals took the form of a dense fragmentation layer in which the fragmentized ceramic crystals had a regenerating tendency, i.e., recrystallization.

ANALYSES OF CHIP REMOVAL MECHANISMS

Surface Cracks During the grinding process, an abrasive acts upon a workpiece surface with an action resembling the behavior of a spherical or a v-shaped indenter which indents the surface when heating effects are not considered. The deformation and fracture patterns observed for normal contact with a Vickers pyramidal indenter were studied [Evans, 1984]. Directly under

the indenter is a zone of plastic deformation. Two principal crack systems emanate from the plastic zone: median/radial and lateral cracks. Median/radial cracks are usually associated with strength degradation, and lateral cracks with material removal. The crack formation process can be considered to result from outward forces exerted by the plastic zone on the surrounding elastic material. These outward forces develop because volume is considered in the plastic flow. Accommodation of the indentation volume thus causes a virtual expansion of the plastic zone. Above a critical normal load, stresses in the plastic zone will generate fracture damage in the form of lateral and median crack systems.

Micro-Plastic Deformation Plastic deformation of crystal includes slip dislocation and twinning. Dislocation motion is the most important mechanism of plastic deformation and twinning, and is also the most important mechanism of plastic deformation in crystalline materials. For example, alumina does not exhibit dislocation mobility at ambient temperatures. However, deformation of the single crystals at temperatures of 1200°C or higher shows that appreciable slip can occur on the {0001} basal plane [Davidge, 1979].

During grinding the process, it is the grinding forces and heat which cause the plastic deformation of polycrystalline ceramics. In fact, the temperatures in the near surface regions of grinding are expected to get quite high, exceeding 1000°C during chip formation [Koepke et al., 1977], with the highest temperature of abrasive grains in grinding reaching 1400 °C [Ueda et al., 1985]. The high temperatures result in dislocation slipping of the polycrystalline ceramics. It has been demonstrated that the dislocation multiplication produced on the ground surface of ceramics proves that plastic deformation occurs in the process of ceramics grinding by TEM [Yin, 1990].

Recrystallization During the process of ceramics grinding, it is also the thermo-mechnical action of grinding forces and heat which leads to the framentized ceramic crystals to recrystallize around the contacting region between the diamond abrasives and the ceramic workpiece. The action of grinding forces produced a number of surface cracks in the bottom of the contacting region between the abrasives and the ceramic workpiece. When the forces acted continually, the fractured surface crystals were further damaged to form debris or powders. The very small powders which had a larger surface tension grew gradually, i.e., recrystallized. The fragmentized material recrystallized easily because of the result of the stress action in the fractured zone, where some of the cracked mechanical energy changes into the surface energy of the comminuted particles spontaneously [Wang, 1982]. The temperatures at which the recrystallization occurs are at about half of the absolute melting temperatures of the crystals [You, 1983]. Based on this, the recrystallizing temperatures of ceramics should be higher than 1000°C. The grinding temperatures are approximately of the magnitude that cause many ceramics to recrystallize.

Generally, the recrystallization undergoes two phases [You, 1983]. In the first phase, many micro particles accumulate together to form supercrystals or subcrystals. In the second phase, the recrystallized crystals grow gradually and interfere with each other to form the polymorphous crystals. During the grinding process, due to the interactions of high local temperatures, and cooling from air and grinding fluids, there is not enough time for the accumulating microparticles to regenerate into complete crystals. In fact, the recrystallization during ceramics grinding only undergoes the first phase [Yin et al., 1987]. It has been proved that the recrystallization and amorphous layers exist on the ground ceramic surface [Yin, 1990].

DEVELOPMENT OF A MATERIAL REMOVAL MODEL IN CERAMICS GRINDING

According to the above experiment and analyses, a comprehensive material removal model in ceramics grinding can be proposed as shown in Figure 5. The deformation of ceramics grinding may be divided into three regions:

Region I (Brittle Region): is located in front of the diamond edge. When diamonds grind ceramics with a certain depth of cut, the initiation and propagation of medial, lateral and radial cracks on the surface and under the surface impacted by the forces of the diamonds produce intergranular and transgranular fracture of ceramics. Fractured ceramics are extruded by the abrasives to lead to brittle fracture of ceramics. Fractured ceramics are extruded by the abrasives to lead to brittle fragmentation and finally to form the particle and lump shaped chips.

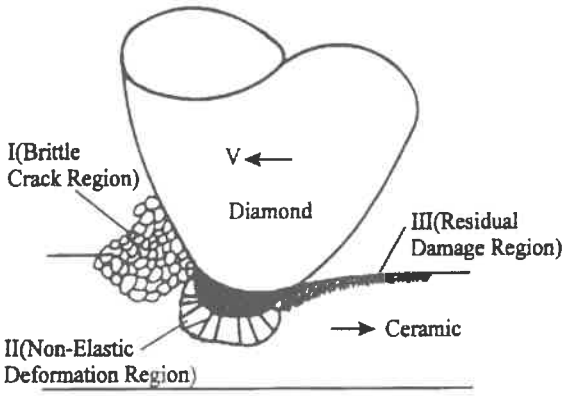

Figure 5. Development of the new model for material removal in ceramics grinding

Region II (Non-Elastic Deformation Region): is located under the diamond abrasive. In this region, the phenomena of plastic deformation, crack clustering, and recrystallization are included. The closed confining pressure field is produced and the grinding temperatures are high, sometimes exceeding 1000°C due to the severe friction between the abrasive and the ceramic. The high temperatures cause brittle ceramics to become semibrittle. Accompanying the microplastic deformation, the ceramic is severely fractured and a large number of microcracks are generated. In Region II, the fragments and powders of the ceramic which have larger surface tension forces are regenerated gradually and recrystallized.

Region III (Residual Damage Region): is located behind of the diamond. In this region, because the grinding forces of the diamond gradually reduce, recrystallized ceramic crystals, a number of microcracks, and residual stresses remain on the ground surface. In the unloading process of grinding forces, the residual stresses restrain the propagation of cracks. However, just before the diamond moves away from the surface, the residual stresses cause the growth of lateral cracks, i.e., microcracks are produced. After the diamond has moved away completely, the residual microcracks would continue to propagate and form debris.

REFERENCES

Bifano, T., T. Dow and R. Scattergood, (1991), ASME Trans., J. of Eng. for Ind., vol. 113, 184.

Davidge, R. W., (1979), Mechanical Behavior of Ceramics, Cambridge University Press, Cambridge.

Evans, A. G., (1984), Fracture in Ceramic Materials- Toughening Mechanisms, Machining Damage, Shock, Park Ridge, NJ.

Koepke, B.G., and R. J. Strokes, (1977), "Grinding Damage in Ceramics," Proc of SEM's International Tool & Manufacturing Engineering Conference, USA, 145.

Maklin, S., and J.E. Ritter, (1989), ASME Trans., J. of Eng. for Ind., vol. 111, 167.

Malkin, S., and T. W. Hwang, (1996), Annals of the CIRP, vol. 45(2), 1.

Marinescu, I.D., (1996), "Double-Fracture Model in Lapping of Ceramics," Proc of 1996 ASPE Spring Topical Meeting: Precision Grinding of Brittle Materials, Maryland, 88.

Ueda, T., A. Hosokawa and A. Yamamoto, (1985), ASME Trans., J. of Eng. for Ind., vol. 107, 127.

Wang, J., (1982), An Introduction of Stress Mineral, Geological Publishing House, Beijing.

Yin, L., and Z. Liu, (1987), "Grinding of Ceramics: Mechanisms of Surface Formation," Proc of the 6th International Conference on Production Engineering, Osaka, 299.

Yin, L., (1990), Investigation of Mechanisms and Technologies of Engineering Ceramics, Ph.D. Thesis, Huazhong University of Science & Technology, Wuhan, 147.

You, Z., (1983), Metamorphic Action and Microstructure. Geological Publishing House, Beijing.

Zhang, B., and T. Howes, (1994), Annals of CIRP, vol.43(1), 305.

Zhong, Z., and V.C. Venkatesh, (1995), Annals of the CIRP, vol. 44(1), 339.

A Self-Deformable Face Grinding Machine to Realize Some 0.1 μm Flatness for 8-inch Substrates

Masayuki NAKAO, Yasuhiro TAKASHIMA, Kazushige OHTA and Yotaro HATAMURA
The University of Tokyo, Faculty of Engineering, Department of Engineering Synthesis
7-3-1 Hongo, Bunkyo-ku, Tokyo 113, Japan

1. Introduction

Information processing devices employed thin substrates, such as silicon wafers, glass lithography masks, ceramic circuit boards and glass display boards. Competitive manufacturing of such devices requires large but ultra-flat substrates with surface flatness in the order of 0.1 μm per 200 x 200 mm. But various factors interfere with grinding of such substrates ; the grinding force deforms the rotary bearing ; irregular thermal expansion bends the column ; the table is pitching along the linear guide ; consequentially, conventional grinding produces convex substrate surfaces with flatness of about 10 μm. Some studies show that a thicker column or a more rigid hydrostatic linear guide reduces tool positioning error. Such passive methods are effective, but even the most expensive one cannot realize a zero positioning error.

An active method can realize the zero positioning error. For examples, sensors detect structural deformation of the column, and actuators compensate for it. The machine looks self-deformable. Besides the deformation, its computer which knows all the "cause and effect" of environmental variables to tool positioning can precisely control the latter by measuring the former [1]. To realize ultra-flatness using the autonomous control, the authors designed, fabricated, and evaluated a "self-deformable face grinding machine".

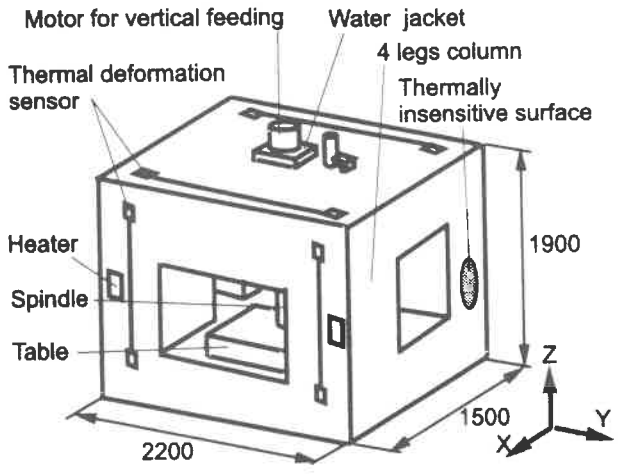

Fig. 1 schematic view of the self-deformable face grinding machine

2. Design of self-deformable face grinding machine

We designed the self-deformable face grinding machine as follows: i) The requirement was set to "flatness of the ground workpiece is 0.1 μm per 200 x 200 mm". ii) The following functions were analyzed to meet the requirement : "force-induced deformation compensation", "thermal deformation compensation", "bearing fluctuation compensation", and "zero-deformation fixturing". iii) The elementary works were decomposed from their functions such as displacement sensing or fine actuating. iv) An individual mechanism was proposed for each work such as strain gauges or piezo elements. v) A structural component was developed for each mechanism. vi) The total system was synthesized using all components.

Figure 1 shows a schematic view of the total system of the machine. Its structure would passively reduce tool positioning error by higher rigidity and thermal insensitiveness. Further, the changeless structure would help the active controllability with less detecting variables or narrower controlling range. For example, to make the "thermal deformation compensation" easier, the machine is composed of a 4-legs column structure which deforms symmetrically, and a thermally insensitive column surface which makes uniform temperature distribution.

Figure 2 shows a conceptual sketch using individual mechanisms [2]. In this paper, we will address the following main mechanisms : two actuating mechanism of a "spindle attitude control mechanism" and a "table attitude control mechanism", and two sensors of a "thermal deformation sensor" and a "wheel tilt sensor".

3. Development of structural components

Two main actuating mechanism use multi-layered piezo elements for fine positioning. For instance, a 20mm-long piezo elements generate a 10 μm displacement with up to 3.5 kN force under 100 V. Strain gauges attached on thin plates (see Figure 2) compose a feedback signal of the displacement. The feedback control makes the piezo elements displacement independent of the voltage history, positioning vertical feeding direction (Z) height with a 10 nm resolution and tilt with 0.1 μrad. In addition, the control makes the machine infinitely stiff ; the piezo elements expand over the same volume as the force-induced shrinkage of the other components [3].

The thermal deformation sensor is made of Invar ma-

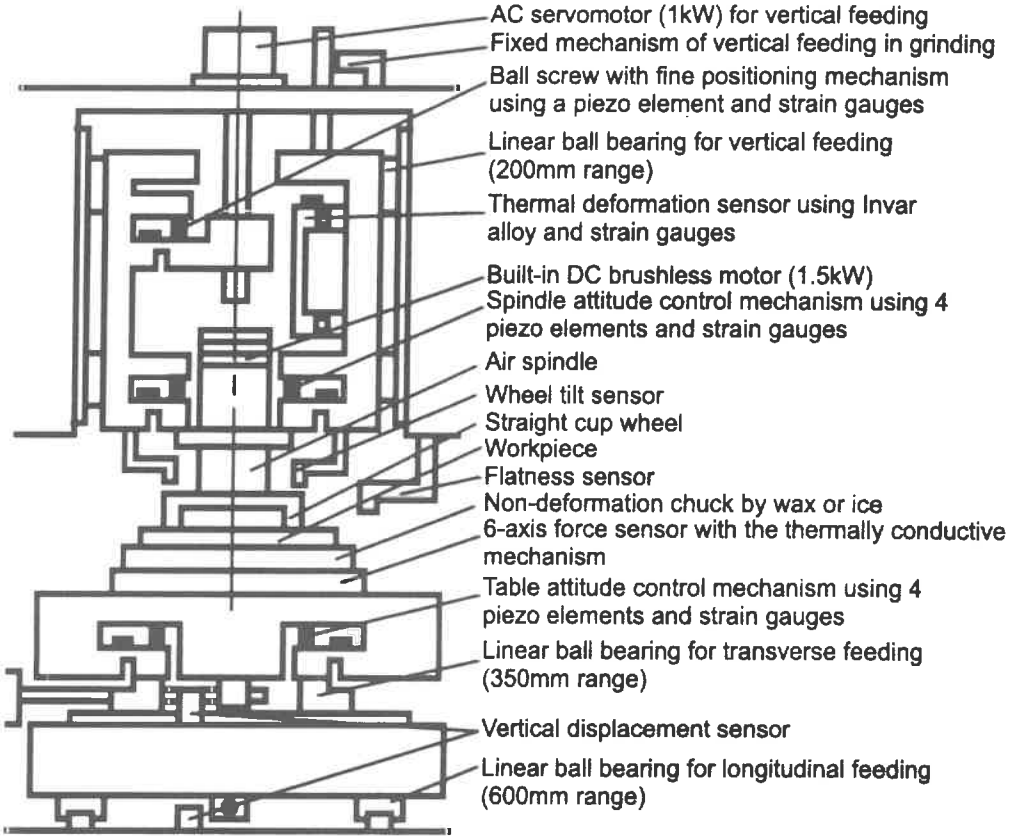
AC servomotor (1kW) for vertical feeding
Fixed mechanism of vertical feeding in grinding
Ball screw with fine positioning mechanism using a piezo element and strain gauges
Linear ball bearing for vertical feeding (200mm range)
Thermal deformation sensor using Invar alloy and strain gauges
Built-in DC brushless motor (1.5kW)
Spindle attitude control mechanism using 4 piezo elements and strain gauges
Air spindle
Wheel tilt sensor
Straight cup wheel
Workpiece
Flatness sensor
Non-deformation chuck by wax or ice
6-axis force sensor with the thermally conductive mechanism
Table attitude control mechanism using 4 piezo elements and strain gauges
Linear ball bearing for transverse feeding (350mm range)
Vertical displacement sensor
Linear ball bearing for longitudinal feeding (600mm range)

Fig. 2 a conceptual sketch of the self-deformable face grinding machine

terial ; the metal machine expands as the temperature increases, but the sensor doesn't ; strain gauges on the sensor measure the deformation caused by the discrepancy of the thermal expansions. The sensor can detect the expansion with a 0.1 μm resolution per 1,300 mm of length of the legs. The wheel tilt sensor is composed of four capacitance displacement sensors. The gap between the wheel and the sensor is always free from debris or mists because the air flow exhausted from the spindle works as an air seal. The sensor can detect Z height with a 10 nm resolution and tilt with 0.03 μrad.

4. Evaluation of self-deformable face grinding machine

4.1 Force-induced deformation compensation In order to produce ultra-flat surfaces using a straight cup wheel in face grinding, it is most important to keep the wheel surface normal to the spindle axis. Otherwise the tilted wheel makes a curved surface on the workpiece.

Figure 3 shows normal grinding force history ; the force history indicates that the upward pushing force in the wheel initially increases as the wheel engages the workpiece, keeps constant, and decreases toward the end ; Figure 4 shows that the force pushed the wheel upward to 3 μ m and the moment declined it front-upward to 12 μ rad. Figure 5 shows ground surface profiles : convex curvatures of 2.5 μm in the transverse feeding (Y) direction and those of 2.0 μm in the longitudinal feeding (X) direction. The profiles were measured while they were still fixed on the table. The high rigidity of the machine, which is high in Z direction to 70 N/μm but is not so high in Y rotation to 2 Nm/ μrad, improves surface flatness from about 10 μm to 2.5 μm. But only the passive mechanisms can't make some 0.1 μm flatness.

Next we kept the wheel flat by the wheel tilt sensor and the spindle attitude control mechanism. Figure 6 shows the attitude of the wheel under the control ; the wheel kept to the initial Z position within $\pm$ 0.5 μm and kept flat within $\pm$ 2 μrad. Figure 7 shows surface profiles ground under the control : convex curvatures of 0.8 μm in the Y direction and 0.6 μm in the X. Through our grinding experiences, 8-inch size substrates can be produced with a 0.5 μm flatness except a 5mm-wide edge area.

4.2 Thermal deformation compensation The wheel tilts when the column deforms irregularly. For example, under room temperature variation of 16 degrees, the front side legs expand by about 70 μm more than the back

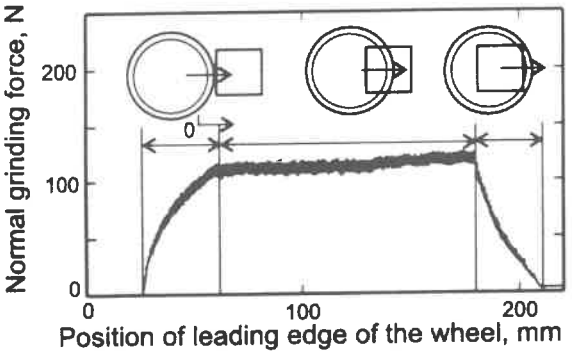

wheel : SD #325 bronze bonded (ϕ 220x w5 mm), spindle rotation : 1500r.p.m, depth of cut : 5 μ m, workpiece : glass (150x150x7mm), feed rate : 200mm/min, grinding coolant : water soluble type flowed from the spindle center.

Fig. 3 Normal grinding force in grinding without the wheel attitude control

side legs : the wheel translates upward by 14 μ m and tilts front-upward by 16 μ rad, which is comparable to tilts in grinding shown in figure 4. In addition to room temperature variation, the motor coolant flow variation induced 2 μ rad and the spindle rotation did 4 μ rad. We would suffer various thermal deformations ;only a 5μ rad tilt of the ϕ220 mm wheel would degrade flatness by 0.5 μ m.

To compensate for the deformation, heaters on the column legs (see Figure 1) was effective in addition to the spindle attitude control mechanism [1]. Figure 8 shows that the wheel tilts by 5 μ rad when the heaters on two front (or back) side legs expand by 30 μ m.

But a passive method is more cost-effective than an active method. Figure 9 shows the difference of the thermal expansions of the legs without / with the thermally insensitive surface made of a 10 mm thick foamed plastic. Figure 9 indicates that the insensitive surface improved the thermal expansion to only about 30 %. We

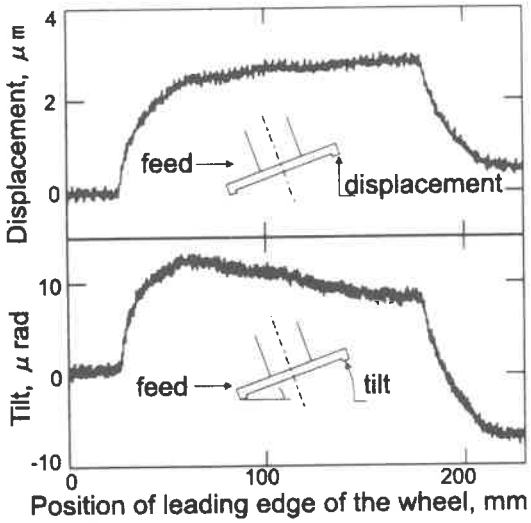

Fig. 4 Displacement and tilt of the wheel in grinding without any control

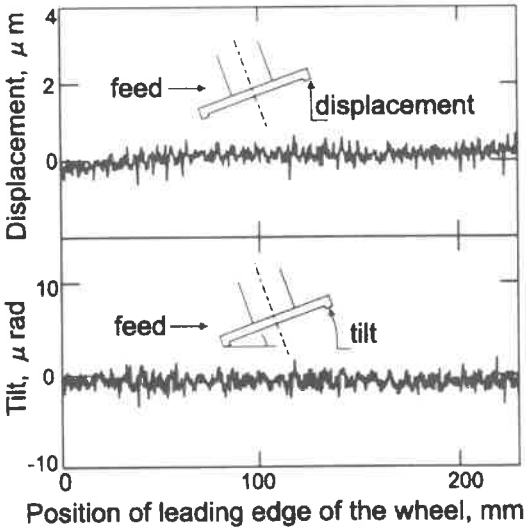

Fig. 6 Displacement and tilt of the wheel in grinding with the wheel attitude control

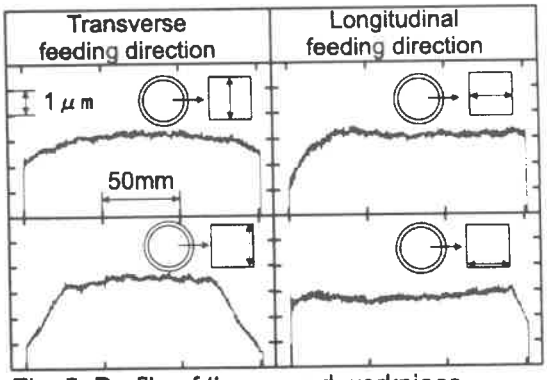

Fig. 5 Profile of the ground workpiece in grinding without any control

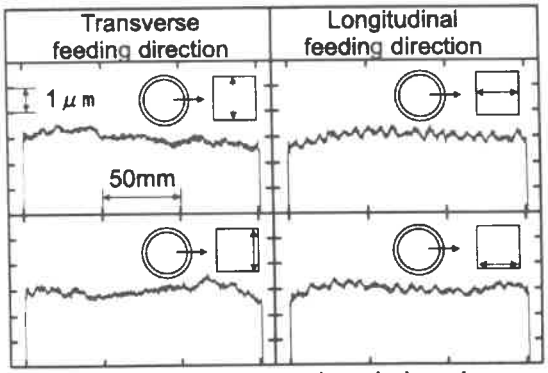

Fig. 7 Profile of the ground workpiece in grinding with the wheel attitude control

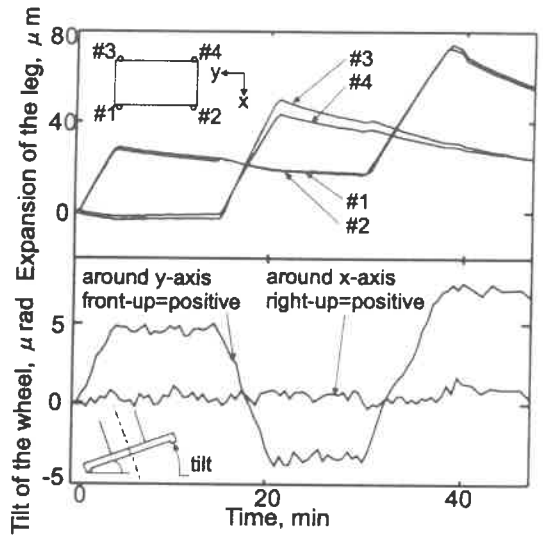

Fig. 8 Tilt of the wheel induced by expansion of the legs of the column

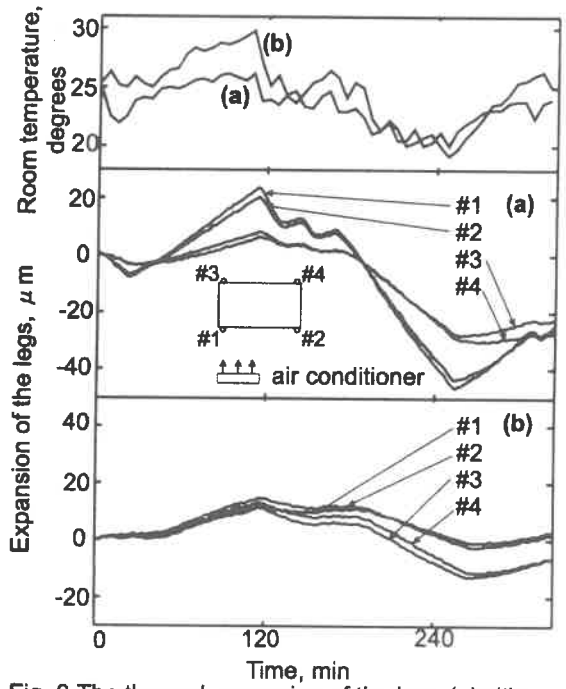

Fig. 9 The thermal expansion of the legs (a)without / (b) with thermally insensitiv surface

can neglect the thermal deformation of the column with the thermally insensitive surface.

4.3 Bearing fluctuation compensation The flatness is also affected by a Z height deviation caused by the linear ball bearing of the table. Figure 10 shows the non-compensated Z height deviations on the top and the compensated ones on the bottom. Each shows five measured deviations. The former indicates that the waviness had

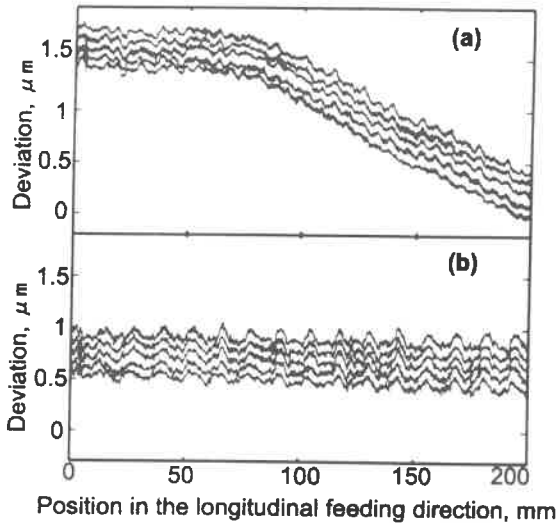

Fig. 10 (a) Z height deviations measured five times that are caused by the linear ball bearing of the table, (b) the compensated ones with the table attitude mechanism

large repeatability, but the roughness looked like spikes did small repeatability. Because the interval of the spikes is twice of the ball diameter, the roughness should be caused by irregularity of ball movement from the loose return groove to the tight preloaded slider groove. When some spikes in the former and no spikes in the latter happen unfortunately, the compensated roughness made worse as indicated in Figure 10.

The measured Z height deviation over a 200 x 200 mm area is about 1.5 μm. We can compensate it using the table attitude mechanism within $\pm$ 0.05 μm the waviness and within $\pm$ 0.1 μm the roughness.

5. Conclusion

To produce some 0.1 μ m flatness on the 8-inch substrates of information processing devices, we designed, fabricated, and evaluated a "self-deformable face grinding machine". The machine executes an active, knowledge-based, self-deformable control using sensors, actuators and computers. The machine improves the flatness of ground substrate surfaces up to 0.5 μm under the control. Further improvement from 0.5 μ m to 0.1 μ m will be realized by some developing mechanisms which weren't described in this paper : a ball bearing with a retainer or a zero-deformation chuck with ice.

We thank THK Co., Ltd. for fabricating the machine.

Reference

[1] Hatamura, Y., et al., CIRP Ann. 42-1, 549-552, 1993
[2] Nakao, M., et al., CIRP Ann. '96, 397-400, 1996
[3] Matsumoto, K., et al., ASPE Ann. '96, 476-481, 1996

A Local Grinding System for Wide and Flat Surface with a 3-Axis Negative Compliance Device

Kiyoshi MATSUMOTO, Masayuki NAKAO and Yotaro HATAMURA
Department of Engineering Synthesis, Faculty of Engineering, The University of Tokyo
7-3-1 Hongo Bunkyo-ku Tokyo 113, JAPAN

1. Introduction

Machining process to obtain a wide and flat surface in short time is highly required in many industrial fields; silicon wafers, magnetic disk substrates, ceramic substrates for computers and optical flats. Usually whole lapping method is employed for this processing, but it is inefficient from view points of process time and material cost. The authors challenge local grinding to obtain a wide and flat surface in short time.

Generally, to increase preciseness of tool position control, rigidities of frame, chuck and tool of a grinding system have to be reinforced. This causes increases of size, mass and complexity of the system. The authors make an another approach. By employing a negative compliance device, it is possible to compensate deformation of the grinding system caused by machining force.

The authors previously proposed a force sensor with actively controlled compliance.[1] With this sensor, it is possible to achieve negative compliance. We applied this sensor to a local lapping/grinding system with a water driven turbine motor.[2] Through the experiment of grinding a silicon wafer, it was confirmed that grinding error was reduced to 60 %. But there was a deviation in distribution of the grinding force on the tool. To increase preciseness of tool position control, it is necessary to control the tool not only in one direction but also in two moment-directions. The authors developed an improved 3-axes negative compliance system, and applied it to a local grinding system.

2. Analysis of grinding process

Fig. 1(a) shows schematic of conventional grinding process. If a grinding tool is controlled so as to follow a prescribed trajectory, the resulting surface does not retain the desired accuracy. The grinding force deforms the mechanical elements such as the tool, the workpiece and the structural frame. This results in grinding error by spring-back.

Fig. 1(b) shows schematic of grinding process with negative compliance. To compensate spring-back, a negative compliance device generates additional depth of cut. When initial depth of cut is Z, grinding force F, spring-back S and grinding error E are described as follows.

$$F_0 = -\frac{Z}{Cd} \quad (1), \qquad S_0 = Cs \cdot F_0 \quad (2), \qquad E_0 = S_0 \quad (3),$$

Cd is dynamic compliance, and defined as a ratio of (grinding force)/(cutting depth). Cs is static compliance of the grinding system. When Cz is employed as compliance to generate additional depth of cut Zc, grinding force F, spring-back S and grinding error E are given as follows.

$$Zc_1 = -Cz \cdot F_0 \quad (4), \qquad F_1 = \frac{Z + Zc_1}{Cd} = \frac{Z - Cz \cdot F_0}{Cd} \quad (5),$$

$$S_1 = Cs \cdot F_1 \quad (6), \qquad E_1 = S_1 - Zc_1 \quad (7),$$

Fi is a geometric series. If Cz is within the range of $-Cd<Cz<Cd$, grinding force Fi converges to a certain value, and F, S, Zc and E are given as follows.

$$F_\infty = \frac{Z}{Cd + Cz} \quad (8), \qquad S_\infty = Cs \cdot F_\infty \quad (9), \qquad Zc_\infty = -Cz \cdot F_\infty \quad (10),$$

$$E_\infty = S_\infty - Zc_\infty = (Cs + Cz) \cdot F_\infty = \frac{Cs + Cz}{Cd + Cz} \cdot Z \quad (11),$$

Equation (11) shows that the grinding error can be zero regardless of the cutting depth Z if Cz is set to -Cs. This means that if the static compliance of the grinding system

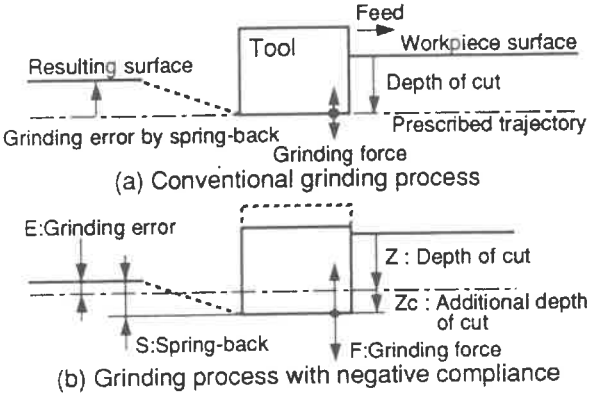

Fig.1 Schematic of grinding process

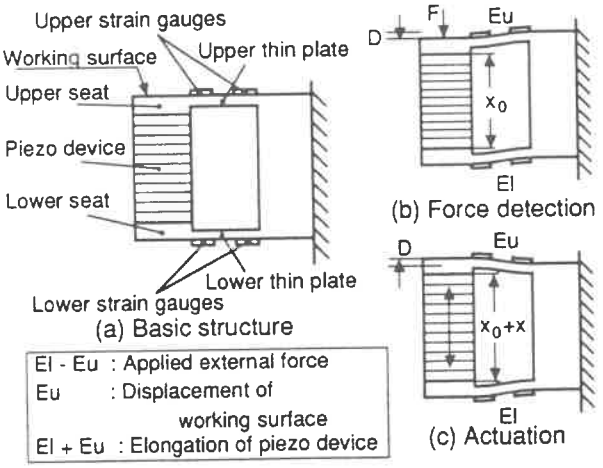

Fig.2 Structure and deformations of sensing unit

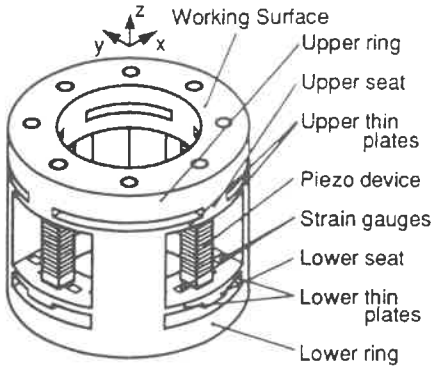

Fig.3 Ring-shape active force sensor

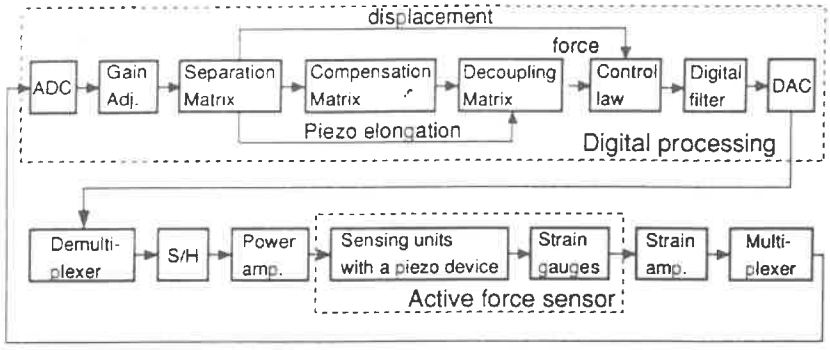

Fig.4 Block diagram of sensing and actuating system

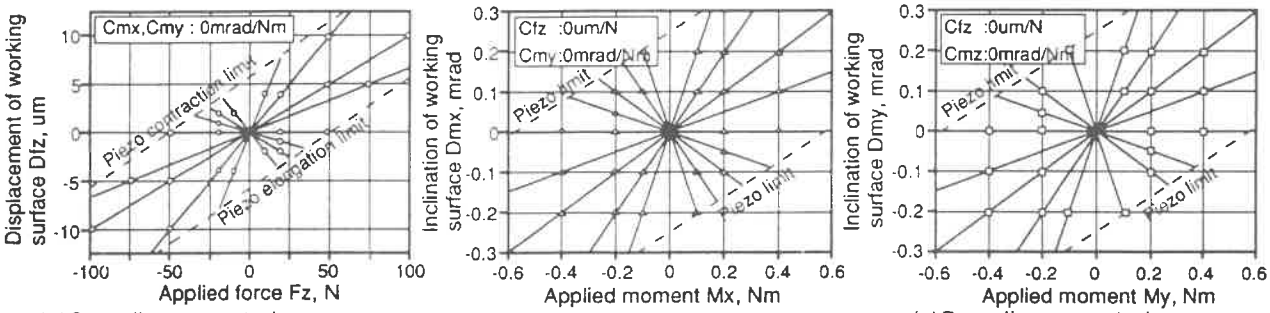

Fig.5 Compliance control operation

Cs is measured precisely, an error free grinding system can be achieved.

3. Development of a 3-Axes negative compliance system

3.1 Structure of a ring-shape active force sensor

This Fig. 2(a) shows structure and deformations of a sensing unit. A pillar is composed of upper/lower seats, and a piezo device which is glued between the seats. This pillar is movable and connected to a fixed pillar by a pair of parallel thin plates. On the surface of the thin plates, strain gauges are glued which detect their deformations.

External force applied onto the working surface causes displacement (Df) as shown in Fig2(b), and it is detected by the strain gauges. Elongation of the piezo device generates displacement of working surface (Da) as in Fig2(c), and it is detected by the strain gauges similarly. The active force sensor uses superposition of these deformations. Assuming that the signs of Eu and El are positive as shown in the case of Fig. 2(c). Eu-Eu is proportional to the applied external force, and is not affected by the elongation of the piezo device. Eu, Eu+El are proportional to the displacement of the working surface and the elongation of the piezo device respectively .

Fig. 3 shows structure of the ring-shape active force sensor. Between upper and lower ring, 4 active sensing units are located at every 90 degrees. Each unit can detect force and actuate. By calculation of the outputs from 4 units, force in the direction of z (Fz) and moments around the x and y axes (Mx, My) can be obtained. By actuation of the piezo elements in 4 units, displacement in the direction of z (Dfz) and inclinations around the x and y axes (Dmx, Dmy) can be generated. The lower ring is fixed to frame or base, and a machining tool is attached to the upper ring.

3.2 Sensing and actuating system

Fig. 4 shows a block diagram of the sensing and actuating system. The output signals from strain amplifiers are converted to digital form, being processed in a computer. Control signals are converted to analog form, and drives the piezo devices in the sensing units through power amplifiers. In digital processing session, the separation matrix is used to separate force, displacement and piezo elongation information. The compensation matrix is used to reduce mutual interference with force information Fz, Mx and My. The decoupling matrix removes interference with force information due to actuation.

Fig. 5 shows performance of compliance control operations. The compliance can be changed within the working range of the piezo devices. As shown in Fig5(a), the rated value of force Fz is about -50N ~ 50N when compliance Cfz is set to zero. As shown in Fig5(b) and (c), the rated value of moments Mx and My are about -0.6Nm ~ 0.6Nm when compliance Cmx and Cmy is set to zero. The resolutions of force and displacement information

were estimated to be less than 0.5%.

4. Grinding experiment

4.1 Experimental system

Fig. 6 shows the experimental system. A surface grinding machine is used as feed mechanism. Straight cup wheel is employed as grinding tool, and is rotated by a water driven turbine. The pressure of water fed to water inlet is about 3 MPa, and nominal rotation speed is 10000 r.p.m. Rotation shaft which connects the turbine and the grinding tool is suspended by a dynamic water pressure bearing. The ring-shape active force sensor is installed between the turbine and the feed mechanism in z direction. An 8-inch silicon wafer is glued to the table base by hot wax. The table base is fed in x direction. The static compliance Cs of this system is measured to be 0.257 um/N at the center of the table base.

Fig. 7 shows nominal experimental conditions. Diameter of the straight cup wheel is 30mm. Metal bonded grains on the wheel is #2000. Feed rate is fixed at 100 mm/min. Bandwidth of the digital servo system to control the compliance is set at about 10 Hz. DC gain is about 60 dB. Grinding forces Fz, Mx, My and displacements of the sensor Dfz, Dmx, Dmy are measured when grinding over a trapezoid shape. Nominal height of the trapezoid shape is 10um, lengh is 80mm. As for attitude of the wheel, the inclination and the compliance around y-axis (Dmy and Cmy) are fixed at -0.1mrad and 0mrad/Nm respectively, so that leading edge of the wheel can always be used for cutting.

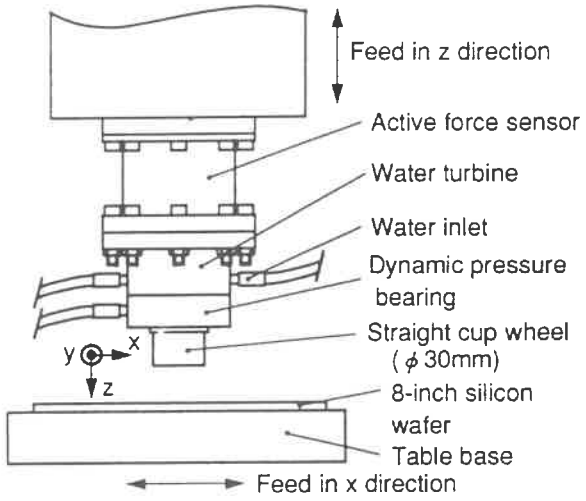

Fig.6 Experimental system

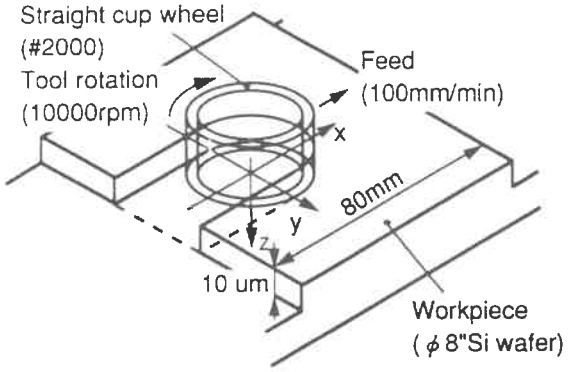

Fig.7 Experimental conditions

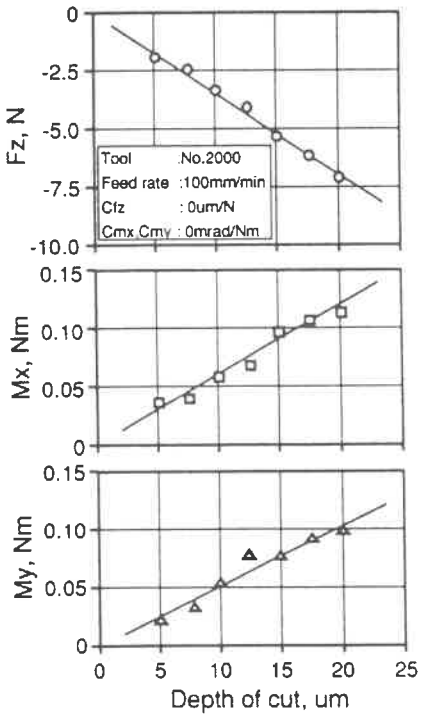

Fig.8 Depth of cut vs. grinding force

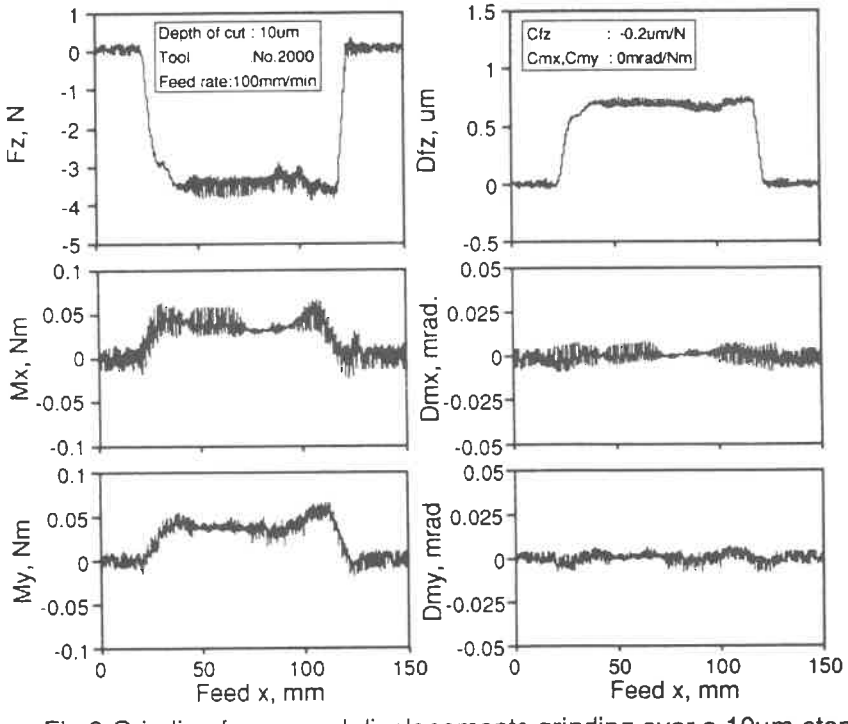

Fig.9 Grinding forces and displacements grinding over a 10um-step

4.2 Measurement of the dynamic compliance Cd

Grinding forces are measured under the condition that all the compliance is set to zero. Fig. 8 shows cutting depth vs. grinding forces. The forces are in proportion to the cutting depth. The dynamic compliance in z-axis Cd is estimated to be 2.80um/N. The dynamic compliance Cd is 10 times greater than the static compliance Cs.

4.3 Grinding experiment with negative compliance

In this experiment, we measured reactive force when grinding over a trapezoid shape of 10um high. Fig. 9 shows an example of grinding forces and displacements. The compliance Cfz is set at -0.2um/N. The grinding force Fz is about 3.5N, and the sensor generates deformation of 0.7 um to reduce the grinding error. The inclination around x-, y-axis Dmx, Dmy are almost zero.

Due to the analysis in section 2, the grinding error will be zero when the compliance Cfz is set at -Cs, i.e. -0.257 um/N. Fig. 10 shows compliance Cfz vs. grinding error under the condition that compliance Cmx and Cmy is set to zero. The error is minimum when the compliance Cfz is -0.3um/N. There is deviation in the error according to the position y. The error at the left edge of feed path is 0.2um higher, while that at the right edge is 0.2um lower. This derives from deviation in distribution of the grinding force. The moment Mx represents this deviation, so negative compliance around x-axis is introduced.

Fig. 11 shows compliance Cmx vs. grinding error under the condition that the compliance Cfz is set to -0.3um/N, and Cmy to zero. The error is minimum when the compliance Cmx is -0.3mrad/Nm. The error is less than 0.1um.

Fig. 12 shows resulting surface profile when the compliance Cfz is changed. The compliance Cmx and Cmy is zero. Length of a trapezoid shape is 30 mm. Grinding error increases at the end of feed. It probably derives from change of the static compliance Cs at edge of the base.

5. Conclusions.

A local grinding system with a 3-axis negative compliance device was proposed. By analysis of grinding process, the condition to minimize grinding error was shown. 3-Axes negative compliance system with a ring-shape active force sensor was developed, and its performance was confirmed. Through experiment of grinding a silicon wafer, it was confirmed that grinding error was reduced to 0.1um.

[1] K. Matsumoto, et al., A Trial of Force Sensor with actively controlled Compliance, Proc. ASPE Spring Topical Meeting on Mechanisms and Controls for Ultraprecision Motion, ASPE, Tucson, USA, (1994)

[2] K. Matsumoto, et al., Local Lapping System to Obtain Wide and Flat Surface with Actively Controlled Force Sensor, Proc. 1996 ASPE Annual Meeting, ASPE, Monterey, USA, (1996)

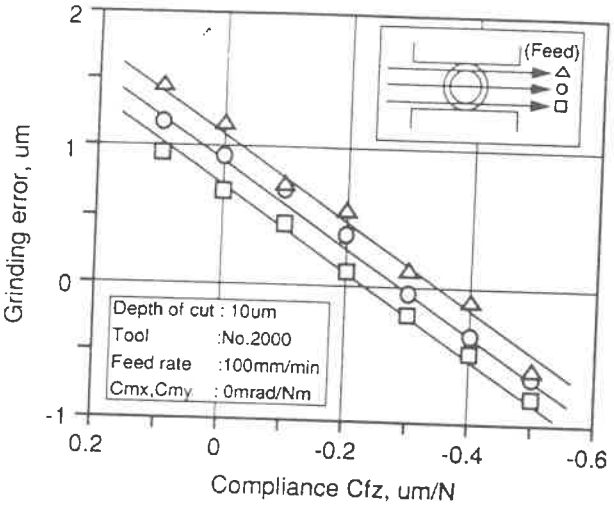

Fig.10 Compliance Cfz vs. grinding error

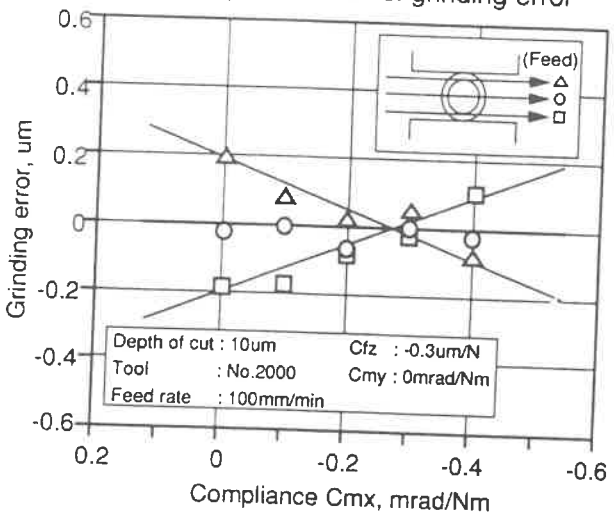

Fig.11 Compliance Cmx vs. grinding error

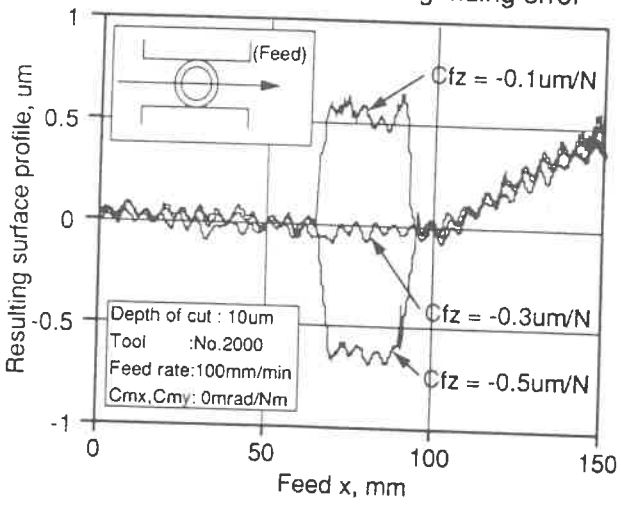

Fig.12 Resulting surface profile

Experimental Verification of a Grinding Chatter Model

Byron R. Knapp, Eric R. Marsh
The Machine Dynamics Research Lab
The Pennsylvania State University
University Park, PA

Introduction:

Grinding has long been used in the precision production environment where surface finish and geometric tolerances cannot be met with traditional cutting operations. With the introduction of 'near net shape' technology and the increasing demand for precision components, much larger demands will be placed on grinding performance. Once regarded as a finishing operation with low material removal rates, advances in abrasive technology and machine design will allow grinding to become the primary operation with large removal rates.

A major concern in any material removal process is the occurrence of chatter which causes relative motion between the tool and the workpiece. As a result of this motion, the workpiece surface will contain undesirable undulations and, in some cases, surface damage. In addition, the increased cutting forces associated with chatter lead to accelerated tool wear.

Many researchers have proposed different mathematical models in order to predict the occurrence of chatter. Several models of chatter have been developed for cutting processes (i.e., turning, milling, boring, etc.) including the two degree of freedom model proposed by Tlusty and Ismail [1]. However, there are several fundamental differences between cutting and grinding operations. For example, as opposed to a turning tool, grinding wheels contain many grains that are randomly spaced radially and around the periphery of the wheel. In addition, those grains can rub, plow, or cut the workpiece surface depending on wear, normal grinding force (F_n), and dress conditions. Furthermore, the development of lobes on both the wheel and the workpiece introduces a second feedback loop into the depth of cut which does not exist in the traditional cutting models. Because of these differences, cutting models cannot be applied to the grinding process.

Since the first grinding model by Hahn [2], several mathematical models have been devoted to predicting stability in grinding and the onset of chatter, but they lack published experimental verification. Recently, Thompson [3, 4] continued the development of his own doubly regenerative grinding chatter model but did not correlate it to experimental results. Verification of any mathematical model is necessary in order to determine if all the dominant parameters are correctly modeled. Once a grinding model is verified, its application in precision production grinding will increase the understanding of this

'black art' while improving cycle times and thus productivity. Unfortunately, experimental verification of grinding models is difficult to obtain and published verification is virtually non-existent. It is the aim of this work to compare Thompson's model to experimental results obtained from cylindrical plunge grinding tests.

The Model:

Two categories of chatter exist; forced and self-excited. Forced chatter is directly related to the wheel rotational frequency and can be caused by wheel imbalance, offset, or some other rotating imbalance in the machine. Vibrations independent of the wheel rotational frequency often correspond to a natural frequency of the grinding machine and are termed self-excited. Self-excited chatter will decay over time for a stable process and increase over time for an unstable one. Unstable, self-excited chatter, or regenerative chatter, causes lobing to occur on the wheel (wheel regenerative) or the workpiece (workpiece regenerative), or both. For example, *Figure 1* illustrates how regenerative chatter produces lobing in the workpiece.

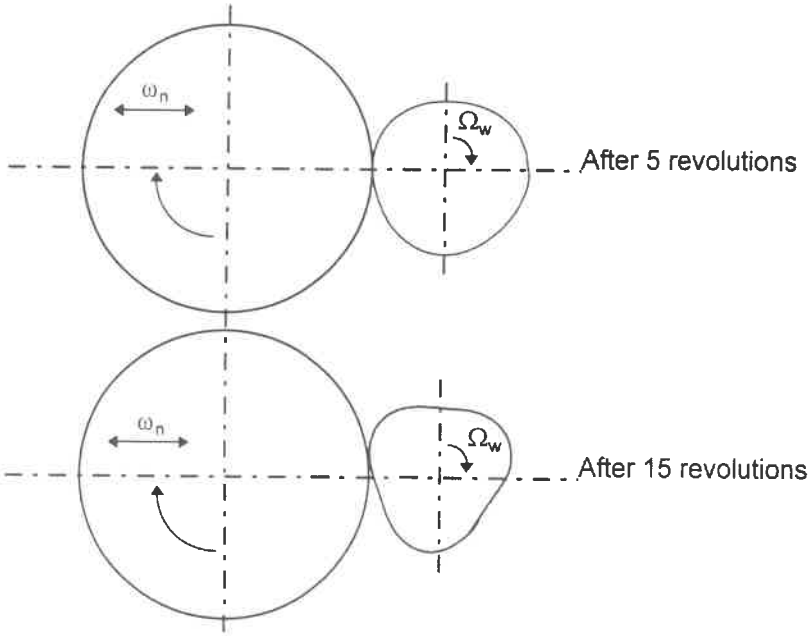

Figure 1. Workpiece regenerative chatter (after Salmon [5]).

The dominant mode of the machine is a horizontal vibration at ω_n = 18 Hz and the workpiece rotational frequency is Ω_w = 6 Hz (360 rpm) which eventually causes 3 lobes on the workpiece. Once the lobes form on the workpiece, they act as feedback into the system and can cause unstable vibration of the machine.

Thompson's model for regenerative chatter [3], shown in *Figure 2*, assumes a harmonic normal force, F_n, which may increase (decrease) over time according to the exponential growth (decay) index, α. Only the dominant mode of the machine is modeled by the effective m, c, and k, and Hertzian contact is neglected. Experimental verification of the model will help determine the relevance of these assumptions. Thompson solves the governing equations according to this model and proposes a triple iterative process for analyzing the growth of chatter.

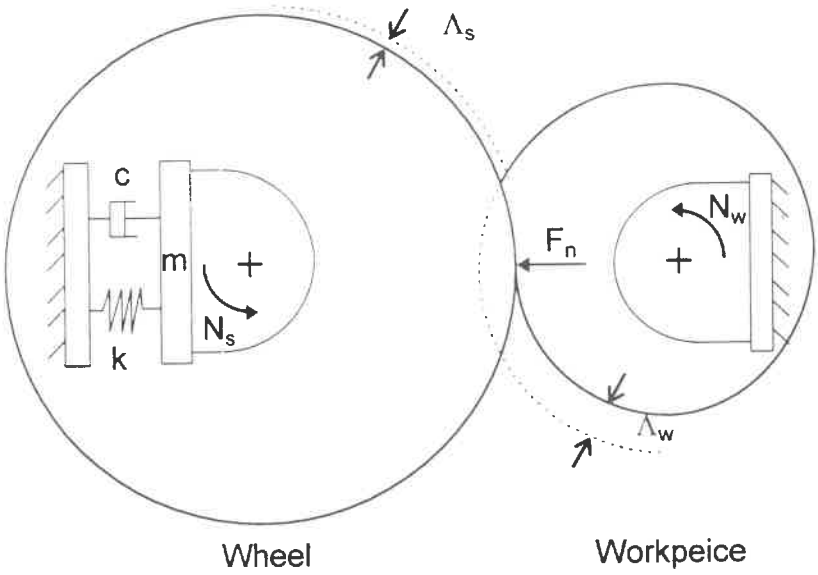

Figure 2. Grinding chatter model (after Thompson).
$F_n = F_o e^{\alpha t} \text{ Sin } \omega t$

c	:	machine damping	m	:	equivalent machine mass
F_o	:	initial force	t	:	time
F_n	:	normal grinding force	α	:	exponential growth index
k	:	machine stiffness	Λ_s	:	wheel wear rate
N_s	:	wheel rotation rate	Λ_w	:	material removal rate
N_w	:	workpiece rotation rate	ω	:	chatter frequency

Verification:

The experiments were conducted as part of a joint investigation of several contributors to the Machine Dynamics Research Lab at Penn State. A Weldon 1632 cylindrical grinder with an Aluminum Oxide wheel was used to grind ANSI 8620 steel. The machine vibration was monitored during the process with several Kistler accelerometers. Measurement of the wheel spindle vibration was obtained with a Lion Precision capacitance gage. The dynamic characteristics of the grinder were obtained using experimental modal analysis, and the grinding process parameters were inferred from several grinding

tests. An exploration of the effects of several grinding parameters was made to determine the important variables in chatter and how they compare to the results of the triple iterative analysis proposed by Thompson.

Future Work:

The results of this study help relate theoretical predictions of grinding instability to actual conditions. Modifications of the model based upon these results will be made to insure accuracy. The model will then be applied in the production environment in order to supplement operator experience with experimentally proven theory, drastically reducing the time to manufacture and thus the cost to grind. In addition, the model will be used to monitor the stability of the grinding process which will decrease manufacturing time while increasing quality.

References:

[1] **Tlusty, J. and Ismail, F.** "Basic Non-Linearity in Machining Chatter." *Annals of the CIRP.* Vol. 30, No. 1, 1981, p. 299.

[2] **Hahn, R.S.** "On the Theory of Regenerative Chatter in Precision-Grinding Operations." *Trans. ASME*, Vol. 76, No. 1, 1954, p. 593.

[3] **Thompson, R.A.** "On the Doubly Regenerative Stability of A Grinder: The Theory of Chatter Growth." *Journal of Engineering for Industry*, Vol. 108, May 1986, p. 75.

[4] **Thompson, R.A.** "On the Doubly Regenerative Stability of A Grinder: The Mathematical Analysis of Chatter Growth." *Journal of Engineering for Industry*, Vol. 108, May 1986, p. 83.

[5] **Salmon, S.C.** Modern Grinding Process Technology. McGraw-Hill, Inc.: New York. 1992. p. 152.

Keywords:

Grinding Chatter, Grinding Experimentation, Precision Cylindrical Grinding.

A Model for Self-Dressing of Resin Bound Grinding Wheels

Thrinath S. Kakumanu, Michele H. Miller
Michigan Technological University
Houghton, MI 49931

1 Introduction

The multiple cutters of a grinding wheel give grinding advantages over single point cutting, especially for machining hard work materials. While a single point tool will quickly dull and require re-sharpening, a grinding wheel distributes wear over many cutters and is capable of replenishing itself. Ideally, grinding wheel wear will occur fast enough to supply fresh cutting edges but slow enough to permit long wheel life and good machining accuracy. Understanding wheel wear and optimizing it is crucial to achieving good performance in the grinding of brittle materials.

For grinding brittle materials resin binders tend to perform better than metal binders. Their greater compliance puts more grits in contact with the workpiece and their lower hardness causes faster wear and more self-dressability. Both effects occur simultaneously, and it is unclear which effect is more important in terms of ductile grinding performance or if both contribute equally. In this paper we focus on the wheel wear and self-dressing of resin bound wheels.

2 Self-Dressing Process

Tang et al. observed two dominant wear mechanisms for resin bound wheels: grit pullout for blocky diamonds and grit fracture for friable diamonds [1]. Focussing on grit pullout as the primary mechanism, we develop a model to describe the self-dressing process and to predict the growth of the cutting force. Self-dressing, a beneficial result of wheel wear, is a grit replenishment and wheel sharpening process. The cutting process causes sharp abrasive grit edges to wear. As a grit's wear plateau area increases, friction between the grit and workpiece increases causing an increase in the cutting force. When this cutting force exceeds the binder strength, the abrasive grit is pulled out of the binder matrix. The pullout of worn abrasive grits exposes fresh grits with sharp cutting edges.

Starting with a sharp dressed wheel, the overall grinding force will increase as the cutting grains dull. The force levels off and reaches an equilibrium when grits pull out and get replenished at a steady rate. The equilibrium force is significant in determining the surface finish of the workpiece and wear of the grinding wheel.

3 Model

Figure 1 outlines an algorithm that was developed to model the self-dressing phenomenon in plunge grinding. The algorithm initially estimates the number of cutting grits involved in the process. Then, it calculates grit forces over the entire wheel circumference as a function of wear plateau area (assumes one cutting edge per grit). It adds all the grit forces to get a total for one wheel revolution. Next, by comparing each grit force to a preset threshold force, it determines whether any grits would pull out of the binder. It then replaces pulled out grits with sharp grits that have a small wear plateau area.

The rate of self-dressing is influenced by: (1) the relationship between grinding infeed and number of active grits; (2) the relationship between grit sharpness and cutting force; (3) the relationship between binder hardness and the force required to pull a grit out of the binder.

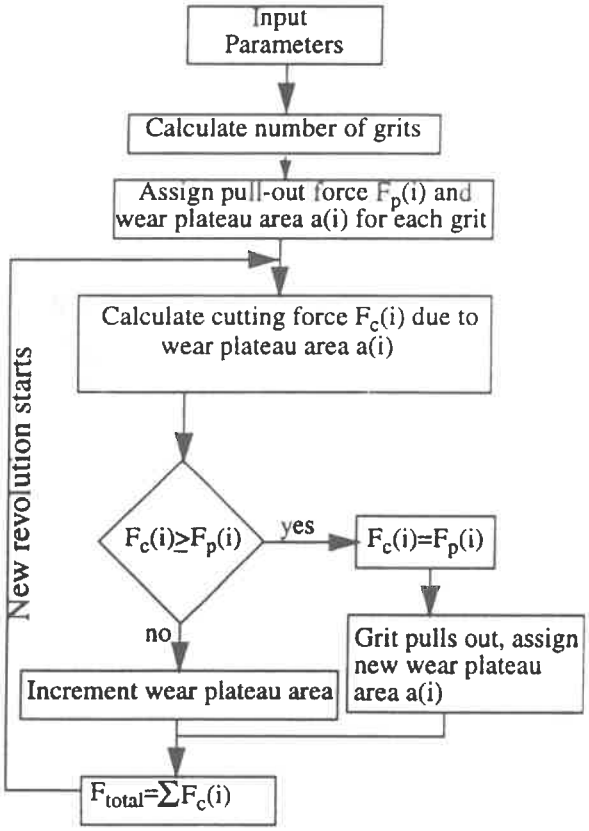
Input Parameters
Calculate number of grits
Assign pull-out force $F_p(i)$ and wear plateau area a(i) for each grit
Calculate cutting force $F_c(i)$ due to wear plateau area a(i)
New revolution starts
$F_c(i) \geq F_p(i)$
yes
$F_c(i)=F_p(i)$
no
Grit pulls out, assign new wear plateau area a(i)
Increment wear plateau area
$F_{total}=\sum F_c(i)$

Figure 1: Flow chart for the self-dressing model

Effect of Infeed on Number of Cutting Grits Infeed rate affects the cutting force and therefore the rate of self-dressing. Increasing the infeed will increase the number of cutting grits and the force per grit. In our simplified model we neglect the change in grit force and consider only the impact on number of cutting grits. Based on the kinematics of plunge grinding, the number of cutting grits n_g changes with infeed according to [2]:

$$n_g = 0.52\frac{w}{r_g}(f_v l)^{0.6} d^{0.4} \qquad (1)$$

where,

d = infeed per revolution
w = width of grinding wheel
f_v = abrasive volume fraction
r_g = grit radius
l = wheel circumference

Effect of Wear Plateau Area on the Cutting Force According to Davis et al. [3], the normal grinding force has three components: (1) force on the flat wear plateau areas of the grits; (2) force on the curved portions of the grits; (3) force on the ploughing grits. For simplicity, we neglect the second and third components, and assume the normal force on one grit is related to work hardness as follows:

$$F_n = aH_w \qquad (2)$$

where,

a = wear plateau area,
H_w= hardness of the workpiece

The tangential force is related to the normal force by:

$$F_t = \mu F_n \qquad (3)$$

Therefore,

$$F_t = \mu H_w a \qquad (4)$$

Wear plateau area a depends on the shape of the grit. Assuming a spherical grit, the wear plateau area is a circle. Defining the radius of the wear plateau as r_1, then the area is:

$$a = \pi r_1^2 \qquad (5)$$

Therefore the tangential cutting force is given by:

$$F_t = \pi \mu H_w r_1^2 \qquad (6)$$

Here, μ depends on the type of abrasive and workpiece material used. Based on [4], a value of 0.44 was used in our model. The tangential cutting force then becomes,

$$F_t = 1.3816 H_w r_1^2 \qquad (7)$$

Effect of Binder Hardness on Pull-out Force Pull-out force is defined as the force required to remove an abrasive grit from the binder matrix. In modeling the self-dressing phenomenon, measuring pull-out force for each abrasive grit is a significant task [5]. To derive this force, two parameters of the wheel were given importance--binder hardness and grit size. Assuming the abrasive grit as spherical and half embedded in the binder, the pull-out force was approximated as:

$$F_p = 2\pi r_g^2 Y_b \qquad (8)$$

where Y_b is the yield strength of the binder.

4 Parametric Study

Results of the self-dressing model were studied to understand the effect of several different parameters. Figure 2 describes the effects of depth of cut, binder hardness, and workpiece hardness on the growth and stabilization of the cutting force. As infeed increases, the rate of force growth (slope) increases as well as the equilibrium force. The higher force is due to the larger number of cutting grits at high infeeds. Figure 2 also shows that harder work materials and harder binder materials lead to higher grinding forces.

5 Summary and Conclusion

The model presented here describes the self-dressing process and its effect on cutting force. It provides a qualitative picture of the effect of key grinding parameters. To improve the model, assumptions associated with wear rates and grit pull-out force will be further refined. Experiments will soon be conducted to assess the model's validity. In addition, more research is needed to relate the equilibrium force to the grinding performance. Given a desired equilibrium force, this model provides guidance in selecting infeed rate and binder hardness.

References

1. Tang, J., K. Syoji and D. Dornfield, "Diamond Wheel Wear Sensing with Acoustic Emission," *Proceedings of the ASPE Spring Topical Meeting,* Vol. 13, pp. 109-114, 1996.

2. Miller, M. H. and T. A. Dow, "Modeling the Wheel/Work Interface in Precision Grinding," *Proceedings of the ASPE Annual Meeting*, pp. 101-104, 1994.

3. Davis, C. E. and C. Rubenstein, "Reciprocating Plunge Surface Grinding with Diamond Abrasive Wheels," *Int. J. Mach. Tool Des. Res.*, Vol. 12, pp. 165-177, 1972.

4. Reinhart, *Proceedings of the International Industrial Diamond Conference*, Industrial Diamond Information Bureau, London, Vol. 2, p.19, 1967.

5. Peklenik, J. and H. Opitz, "Testing of grinding wheels," *Proc. 3rd Int'l MTDR Conference*, Pergamon Press, London, pp. 163-177, 1963.

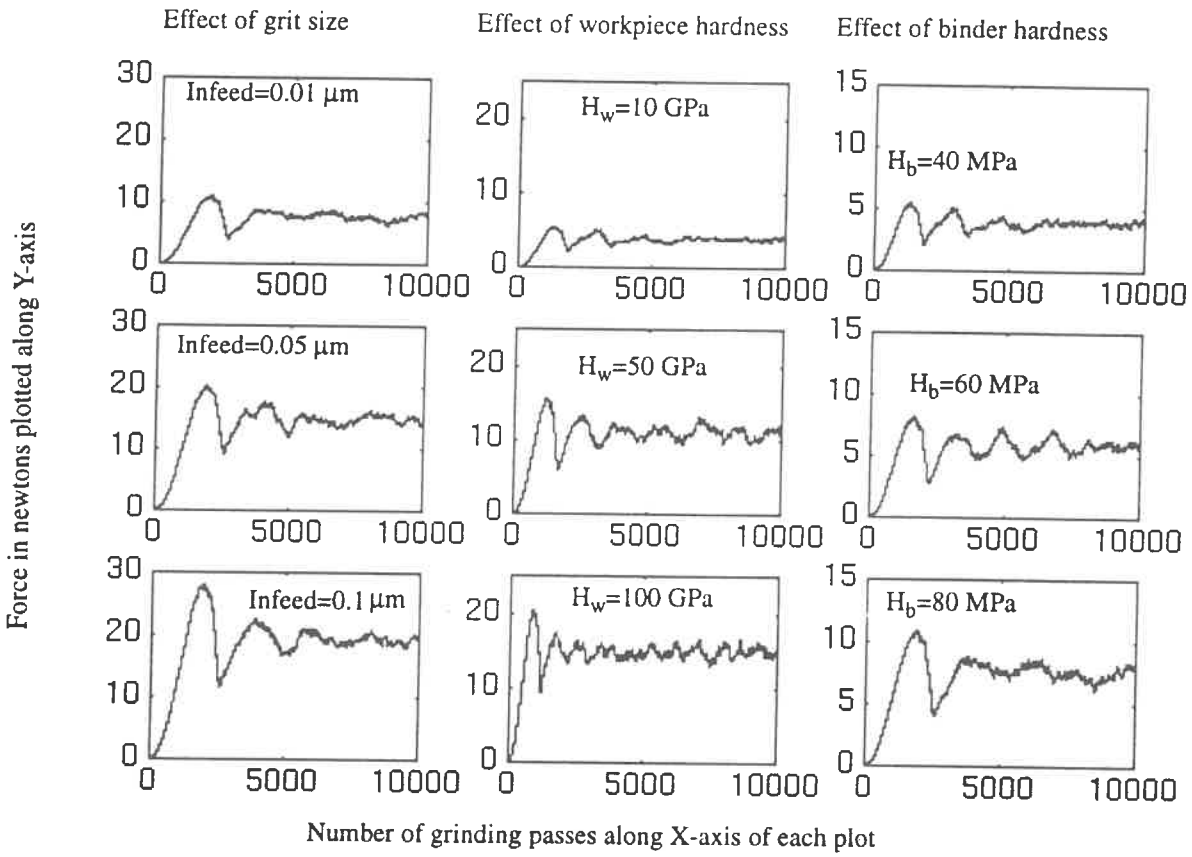

Figure 2: Effect of various parameters

THE EFFECT OF WORKPIECE MODULATION ON SURFACE QUALITY

Weimin Qu, Michele H. Miller
Department of ME-EM
Michigan Technological University
Houghton, MI 49931

1 Introduction

Ductile regime grinding is an enabling technology in the manufacture of ceramic components because it produces accurate shapes deterministically and without fracture. However, the process requires very small chip thicknesses which limit material removal rates (MRR) and consequently economic viability. Some researchers have taken advantage of ultrasonically-assisted machining to increase the MRR since the modulation can reduce the cutting forces. Moriwaki [1] achieved a seven times increase in critical depth of cut for single point machining of glass and credited the improvement to a reduction of frictional force on the tool rake face. However, the cutting speed was quite low--1.5m/s. With the much higher cutting speed of grinding and the short time of each abrasive/work interaction, it is uncertain whether high frequency vibration would have a similar effect on grinding performance.

In this paper we investigate the effect of workpiece modulation on grinding surface fracture. We also investigate the mechanisms by which modulation impacts ground surface quality.

2 Experiments

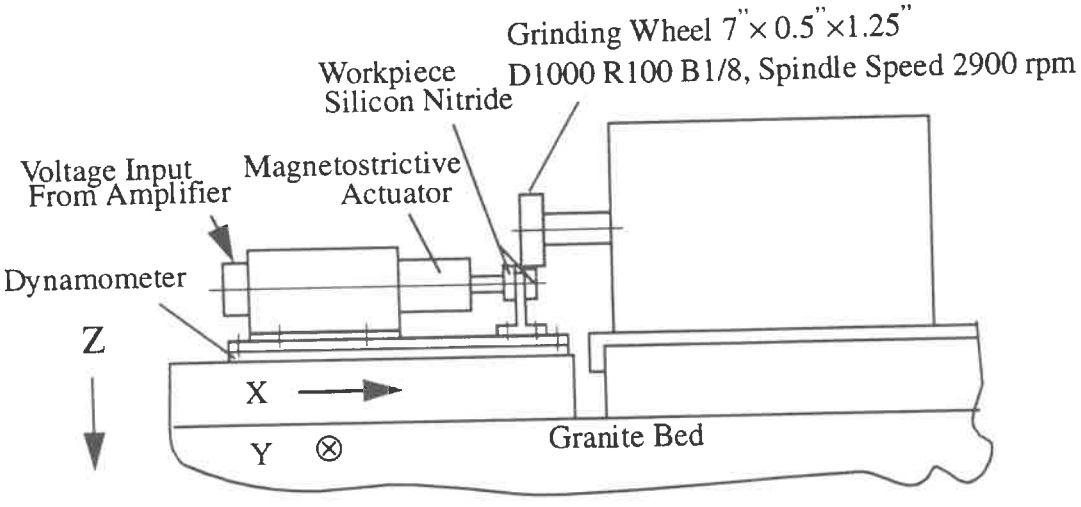

Figure 1: Schematic illustration of the surface grinder with the actuator

Experiments were conducted to assess the effect of modulation on the ground surface. Figure 1 shows a schematic illustration of the surface grinder with a magnetostrictive actuator. The work-

piece is silicon nitride and excited to vibrate in the crossfeed (or X) direction. Table 1 describes the experimental conditions.

Table 1: Experimental conditions

Spindle speed	2900 rpm
Cutting speed	29000 mm/s
Feedrate	13 mm/s
Depth of cut	0.015 mm
Workpiece	silicon nitride
Modulation frequency	2000 Hz
Modulation amplitude	2.2 μm
Grinding wheel	D1000 R100 B1/8

When the surfaces are ground, for each 15 μm depth of cut, the grinding wheel passes the workpiece four times. Figure 2 shows a surface ground with modulation, and Figure 3 shows a surface ground without modulation. Comparing the two figures, the surface ground with modulation has fewer scratches and less visible fracture.

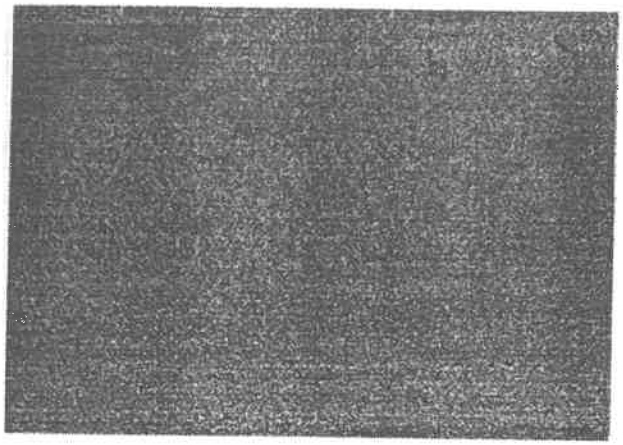

Figure 2: Surface texture with modulation(100X)

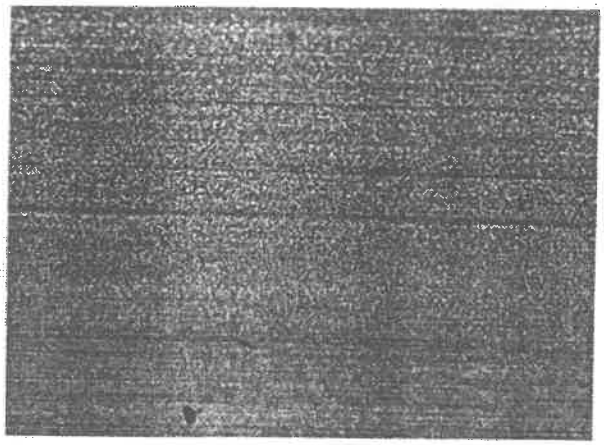

Figure 3: Surface texture without modulation(100X)

Surface profilometer traces confirm that the surface in Figure 2 has lower roughness than the surface in Figure 3. Table 2 summarizes the measurements.

Table 2: Surface roughness comparison

	Ra (μm)
with modulation	0.25
without modulation	0.39

3 Theory

Experiments demonstrate that high frequency modulation can improve the surface quality. To optimize the effect of modulation, we need to understand the mechanism behind its influence on

surface quality. Researchers have observed that high frequency modulation has the following effects:

(a) reduction of the effective friction force between workpiece and cutting tool [2-6];
(b) reduction of the effective yield strength of the workpiece [4,5];
(c) self-dressing of the cutting grits [7];
(d) reduction of surface temperature or better coolant penetration conditions [7,8].

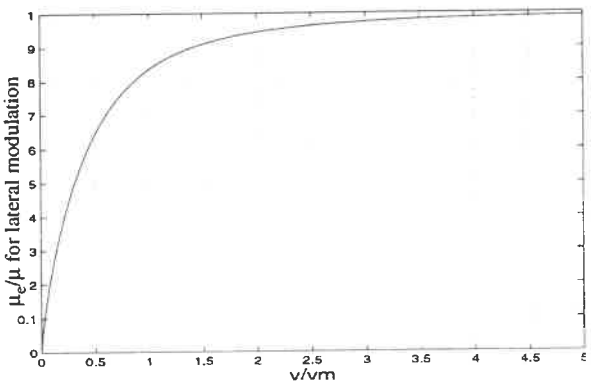

Figure 4: Reduction in friction coefficient as a function of velocity ratio

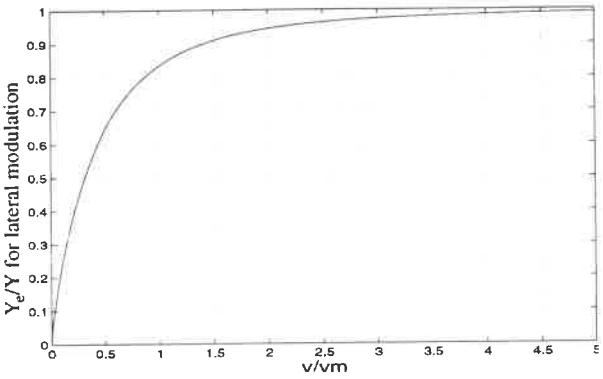

Figure 5: Reduction in flow stress as a function of velocity ratio

First, we consider the friction between the workpiece and a cutting grit under lateral modulation. According to [6], the vector of instantaneous friction force is constant in magnitude (independent of velocity magnitude) and in the direction opposite to the relative velocity. The lateral modulation thus redirects some of the frictional force to the lateral direction thereby reducing the component in the primary sliding direction. The primary direction component cycles between a nominal value (the value it would have without modulation) and some lower value. When averaged over time, the primary direction component is lower than the nominal value, and the lateral direction component is zero. The amount of reduction of the average or effective friction μ_e with respect to the nominal μ depends on the ratio of the cutting velocity v and the modulation velocity v_m. Figure 4 shows the variation in friction coefficient ratio μ_e/μ with speed ratio v/v_m. According to Figure 4, modulation has little effect on friction when the sliding velocity is much greater than the modulation velocity. For the experimental conditions described in Section 2, in which the cutting speed was approximately 1000 times the modulation velocity (v = 29 m/s and v_m = 0.0276 m/s), the reduction in friction is only 0.02%. Even with a higher modulation frequency of 20 kHz and larger modulation amplitude of 10 μm, the friction reduction would only be 0.07%.

Second, we consider the lateral modulation effect on the reduction of the effective yield strength. The cutting force is approximately equal to the work material's flow stress multiplied by the tool area projected into a plane perpendicular to the cutting direction. In the presence of lateral modulation, the instantaneous cutting velocity changes in direction and magnitude. However, for a work material whose flow stress is independent of cutting velocity and for a cutting grit whose projected area is independent of cutting direction, the instantaneous cutting force changes in direction but not magnitude. Similar to the friction effect described above, some of the cutting force is redirected into the lateral direction. The average force in the primary cutting direction is,

therefore, lower than the nominal force. In other words, the material appears to have a lower flow stress. The reduction in this effective flow stress Y_e with respect to the nominal Y depends on v/v_m as shown in Figure 5. Considering the velocity ratio in our experiments (or even one achieved by ultrasonic modulation), Figure 5 indicates that the flow stress effect is negligible.

Regarding the third possible explanation for improved ground surface quality, Colwell found that 10 kHz vibrations inhibited the build up of debris on the grinding wheel [7]. In the honing of steels, Markov found that 18 kHz vibrations permitted better coolant penetration [8]. Further experiments are needed to test the validity of these explanations.

4 Summary

From an experimental study of the modulation grinding of silicon nitride we found that grinding with modulation reduces surface roughness and fracture. Analysis shows that two of the possible explanations for improved surface quality--reduced effective friction and reduced effective flow stress--are invalid. Additional experiments that focus on the wheel condition and workpiece temperature will be conducted.

References

[1] Moriwaki, T., E. Shamoto and K. Inoue, "Ultraprecision Ductile Cutting of Glass by Applying Ultrasonic Vibration," *Annals of the CIRP*, Vol. 41, No. 1, pp. 141-144, 1992.

[2] Astashev, V. K., "Effect of Ultrasonic Vibration of a Single-Point Tool on the Process of Cutting," *Journal of Machinery Manufacture and Reliability*, No. 3, pp. 65-70, 1992.

[3] Moriwaki, T. and E. Shamoto, "Ultrasonic Elliptical Vibration Cutting," *Annals of the CIRP*, Vol. 44, No. 1, pp. 31-34, 1995.

[4] Cornier, A. "Turning Assisted by Non Conventional Process," *Bulletin Du Cercle D'setudes Des Msetaux*, Vol. 16, No. 4, pp. 5.1-5.16, 1992.

[5] Markov, A. I., *Ultrasonic Machining of Intractable Materials*, Illife Books, London, 1966.

[6] Nazarenko, A. F. and E. G. Topilin, "Study of vibrations effect on friction," *Journal of Friction and Wear*, Vol. 15, No. 4, pp. 36-39, 1994.

[7] Colwell, L. V. "The effects of high-frequency vibrations in grinding," *Transactions of the ASME*, pp. 837-846, May, 1956.

[8] Markov, A. I. and P. A. Ermak, "Ultrasonic diamond honing of steels," *Vestnik Mashinostroeniya*, Vol. 62, No. 4, pp. 52-55, 1982.

Grinding With Directionally Aligned SiC Whisker Wheel

– Loading-free Grinding –

Katsumi YAMAGUCHI*, Iwao HORAGUCHI** and Yutaka SATO***

* Department of Mechanical Engineering, Nagoya University,
Furo-cho, Chikusa-ku, Nagoya 464, Japan
** Toyota College of Technology, Eisei-cho 2-1,
Toyota-shi, Aichi–ken 471, Japan
*** Aichi Industrial Research Institute,
Nishishinwari, Hitotsugi-cho, Kariya-shi, Aichi-ken 448, Japan

1. Introduction

In a previous work [1], the authors developed a SiC whisker grinding wheel with its whiskers aligned normally to the grinding surface. Using this new type of grinding wheel, a surface finish of 16 nmRmax (1.5 nmRa) roughness was successfully produced in hardened die steel. The SiC whisker is characterized by its small size and high aspect ratio, for example, a diameter of 1 μm with a length of 40~50 μm. This high aspect ratio helps the whisker to bond strongly and to be difficult to tear out from the grinding wheel surface. These unique characteristics may lead to longer durability and finer grinding over the conventional grain-bonded grinding wheel.

An anticipated weak point of the SiC whisker grinding wheel is that it is apt to load because the whiskers cannot be renewed in the grinding process as the abrasive grains can in conventional grinding wheels.

In the present research, a simple method to prevent loading is proposed, named "Loading-free grinding". In this method, a grinding fluid mixed with a small amount of very fine abrasive grains is used. The authors investigated the effects of the size and content of grains added to the grinding fluid on grinding characteristics. The ground surface and the wheel surface were observed under scanning electron microscope to verify the action of the grains in the grinding fluid.

2 Experimental Detail

2.1. Loading-free grinding

In this experiment, loading-free grinding is proposed, by which loading may be completely prevented. The principle of the loading-free grinding is illustrated in Fig. 1, where it is supposed that the grinding fluid brings the grains into the contact surfaces, and the grains strike the adhered chips and the binder. By this motion, the grains may tear out the grinding chips adhered to whiskers and abrade the binder in the process, hence improving grinding efficiency.

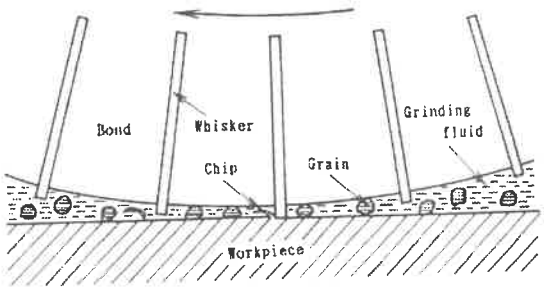

Fig. 1 Principle of loading–free grinding

2.2. Grinding wheel, fluid and workpiece

The grinding wheel used in the experiments is composed of SiC whisker as the abrasive and phenol resin as the binder. The whiskers were mixed with phenol at a ratio of 14% in volume. The whiskers were aligned

unidirectionally using the method reported in the previous paper [1]. Then the mixture was baked at a controlled temperature at a maximum 180°C for 30 hours. The prepared material was then cut into smaller blocks and fixed by epoxy binder on a cup-shape holder to align the whiskers in the direction normal to the grinding surface as demonstrated in Fig. 2. Next, parallel grooves were provided on the grinding wheel surface to facilitate the removal of grinding chips from the grinding surface.

The grinding fluid was soluble type (JIS W2-1), in which alumina (WA) grains of 0.4 ~ 1.2 μm in diameter are mixed to prevent the wheel from loading.

The workpiece for the grinding test was hardened die steel SKD11 of Rockwell hardness HRC60, with an initial surface roughness of about 1.5 μmRa.

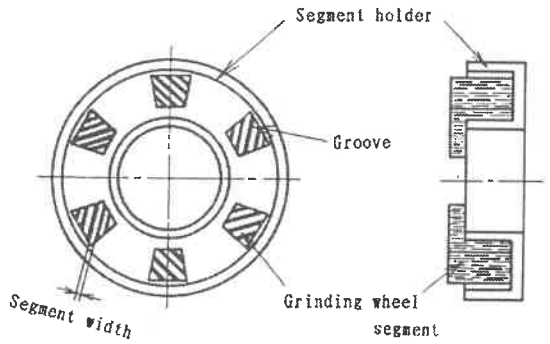

Fig. 2 Grinding wheel.

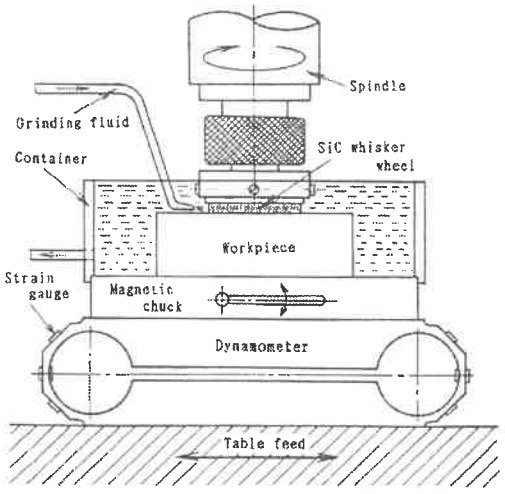

Fig. 3 Experimental set-up.

2.3. Experimental apparatus

The apparatus used for grinding experiments was a CNC vertical milling machine as illustrated in Fig. 3. The cup-shape grinding wheel was fixed on the machine spindle. The grinding was performed in the grinding fluid. The grinding test was done under a constant grinding load. Fig. 4 shows a SEM micrograph of the surface of the grinding wheel after grinding. The arrow indicates a representative tip of an aligned whisker, while the boxed X shows some whiskers clogged with chips.

To measure the ground volume from the workpiece, micro-Vickers indentations were marked on the work surface. The ground volume was measured from the changes in diameter of Vickers marks. As for the wear of grinding wheel, the Vickers indentations were marked on small pieces of brass, which were inserted in the segments. The experimental conditions are summarized in Table 1.

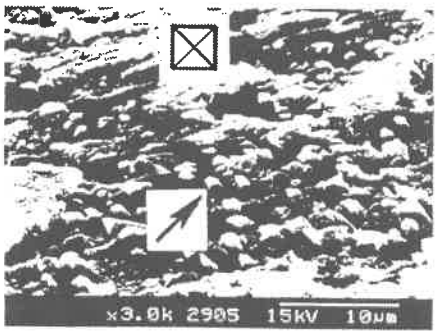

Fig. 4 SEM micrograph of grinding wheel structure

Table 1 Experimental conditions

Experimental apparatus	CNC milling machine
Grinding conditions	Wheel speed: 50 m/min
	Load: 400 N
	Feed: 35-42 mm/min
Grinding wheel	Wheel diameter: 50 mm
	Whisker content: 14 vol%
	Segment width: 1.5-8 mm
Specimen	Die steel SKD 11 (HRC 60)
Abrasive grain	Material: Al_2O_3 (WA)
	Grain size: 0.4-1.2 μm
	Concentration in fluid: 0-0.5 wt%
Grinding fluid	Soluble type (JIS W 2-1)

3 Characteristics of Loading-Free Grinding

3.1. Effect of grain size

The results of surface finishes are compared for different sizes of WA grains in Fig. 5. The initial surface roughness was about 1.5 μmRmax and the concentration of WA grains in the fluid was 0.25%wt. The surface roughness Rmax is plotted against the traverse cycles of the grinding wheel. From this figure, it is noticeable that, with grains of 0.6 μm size or 1.2 μm, a surface finish can be obtained faster than with the finer grains of 0.4 μm in size. This means that the grains equal to or just smaller than the whisker diameter are the best in improving the anti-loading or the grinding efficiency.

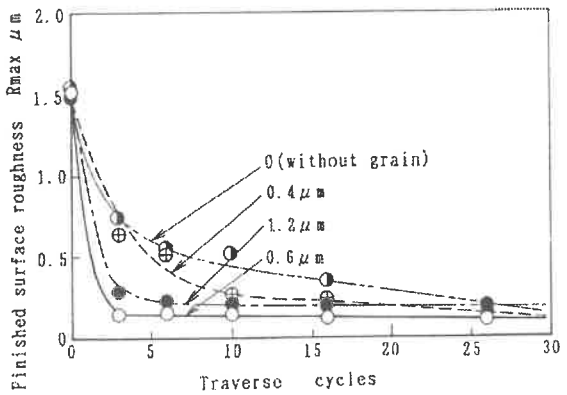

Fig. 5 Effect of WA grain size
(Concentration: 0.25wt%,
Segment width: 1.5mm)

3.2. Effect of grain concentration

The effect of grain concentration on anti-loading was investigated using alumina grains of 0.6 μm size. The material removal rates from the workpiece and wear of grinding wheel were shown in Fig. 6. The removal rate from the workpiece was found to increase, first, sharply with the increase in grain concentration, and then to saturate at a concentration around 0.25%wt. As for the grinding wheel, the wear rate always increases at an extremely slow rate. Hence, a WA grain concentration of 0.25%wt was found to be the most suitable and sufficient ratio for anti-loading.

The scanning electron microscopy of the wheel surface, shown in Fig. 7, indicates that a low concentration of grains can remove the grinding chips, which allows the whiskers to protrude on the wheel surface so as to improve the anti-loading.

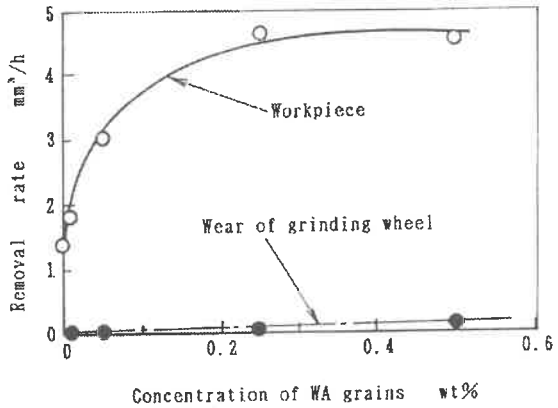

Fig. 6 Removal rates with different grain concentrations. (Grain size: 0.6 μm)

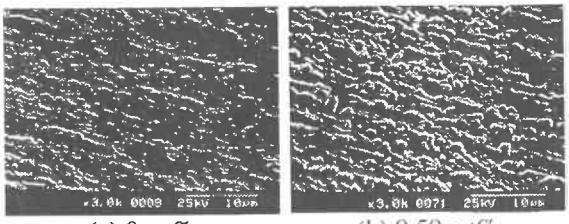

(a) 0 wt% (b) 0.50 wt%

Fig.7 Effect of abrasive grain concentrations on loading.

3.3. Grinding ratio

In Fig. 8, the ground volume of the workpiece and the wear of the grinding wheel are compared in two cases with and without anti-loading grains. The grinding rate is increased 10 times with the addition of grain to the grinding fluid, and the wear of the grinding wheel is increased. However, the grinding ratio is increased from 1000 to 6000 for two cases of grinding without and with anti-loading grains, respectively.

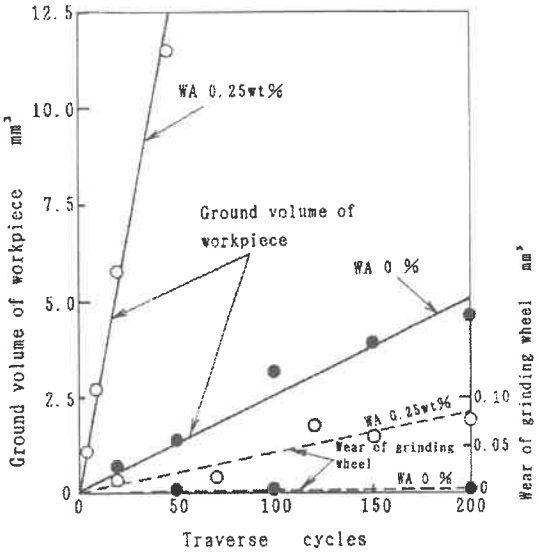

Fig.8 Grinding characteristics
(Grain size: 0.6μ m)

3.4. Ground surface observation

Fig. 9 shows AFM photographs of the ground surfaces for two cases; a) the surface obtained without using anti-loading grains, where a roughness of 16 nmRmax (1.5 nmRa) could be accomplished; and b) the surface obtained by applying anti-loading grains. The latter surface has a roughness of maximum 100 nmRmax (10 nmRa).

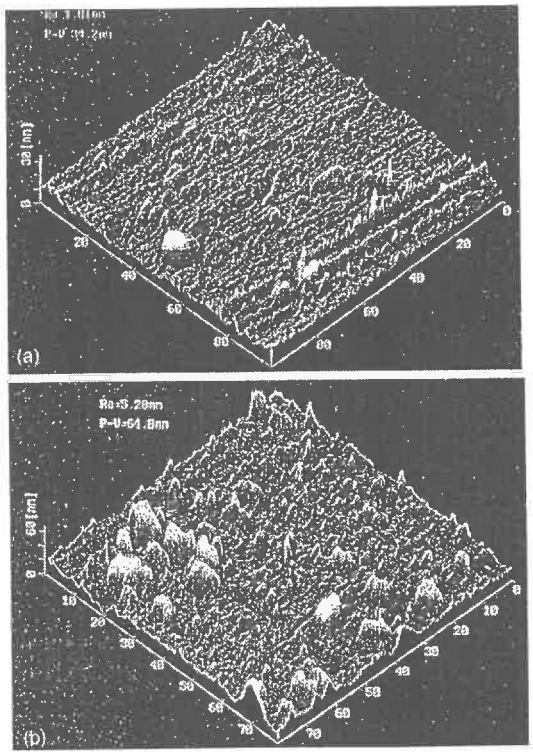

Fig. 9 AFM micrographs of ground surfaces.
(a) Without anti-loading
(b) With anti-loading (WA 0.25 wt%)

4 Conclusions

The results of this work are as follows:

1) A loading-free grinding is proposed in this paper. The loading problem in grinding with SiC whisker grinding wheel has been successfully resolved by this method.
2) The addition of a small amount of fine abrasive grains to the grinding fluid works as an anti-loading agent that can remarkably increase grinding efficiency.
3) The optimum grinding efficiency can be obtained by using anti-loading grains just smaller than the whisker diameter.
4) The concentration of 0.25%wt of anti-loading grains is quite sufficient. A higher concentration results in greater grinding wheel wear without improving the grinding efficiency.

References

[1] K. Yamaguchi and I. Horaguchi. Development of directionally aligned SiC whisker wheel. Precision Engineering, vol.17, no.1 (1995) 5–9.

AN APPLICATION OF 40kHz ULTRASONIC VIBRATION TO SHEAR-MODE GRINDING OF SILICON WAFERS

Y. Yoshida *, K. Imai**, H. Hashimoto**, Z. N. Sun○, Y. S. Lu○○
*Tokyo Diamond Tool, ** Kanagawa Institute of Technology
○Harbin Institute of Technology, ○○Northeastern University
1030 Shimo-ogino Atsugi-shi, 243-02 JAPAN TEL0462-41-1211 FAX0463-93-5440

Introduction

Previous papers [1),2)] reported shear-mode grinding of various brittle materials using #3000 grit metal bond diamond straight wheels. In those experiments, it was shown that: (1) After a number of passes, the normal grinding force reached an approximate steady state: (2) During grinding, the wheel surface roughness and cutting performance were invariant, and wheel truing and dressing were not carried out.

From these experimental results, the shear-mode grinding force criterion was defined as the steady, invariant grinding force that is a repeatable deterministic function of shear-mode grinding conditions including materials and grinding wheels.

The criterion can usefully be applied to design a high precision shear-mode grinding machine by determining its compliance, and enables shear-mode grinding of various brittle materials without any in-process dressing.

The cup wheels can manufacture large surfaces efficiently and the surface accuracy is stable. However, the criterion isn't sufficiently defined yet using cup wheels. Because the contact area between the wheel and work increases, there are many problems such as the supply of coolant and the occurrence of grinding heat in the cup wheel. The ultrasonic vibration helps the supply of coolant between the wheel and work. Usually ultrasonic vibration was applied to high efficiency machining of hard and brittle materials with brittle-mode.

In this paper, the application of 40kHz ultrasonic vibration to shear-mode grinding is described. However, shear-mode grinding was expected to be possible in using fine grit and ultrasonic vibration of small amplitude. And it is performed in order to realize shear-mode grinding of sixteen inch silicon wafers, which are expected to be manufactured in the twenty-first century.

Experimental method

In experiments, metal bond cup wheels were used on a reconstructed surface grinding machine (Okamoto PSG-52DX) with a Professional Instrument's "Block-Head" type 4R. The ultrasonic spindle was installed under the air spindle. The frequency of the ultrasonic vibration is 40 kHz and the amplitude is 2 μm. Batches of 10×25mm silicon wafers (100 surface) were ground with ("ultrasonic vibration grinding") and without ultrasonic vibration ("conventional grinding"), with various diamond grits, #170~#3000. The wheel rotation was changed to 1000 and 2000 rpm, the table speed was

changed to 50～150mm/min and the depth of cut was changed 0.5～4 μ m/pass.

The schematic illustration of the grinding machine is shown in Figure 1 and the grinding conditions are shown in table 1.

Definition of the grinding force

The grinding force contains the high frequency ingredient of 40 kHz. Therefore, to examine grinding force in this paper, we joined an amplifier to a dynamometer and examined the value which is output by the digital oscilloscope and the pen recorder in the comparison. As a result, the

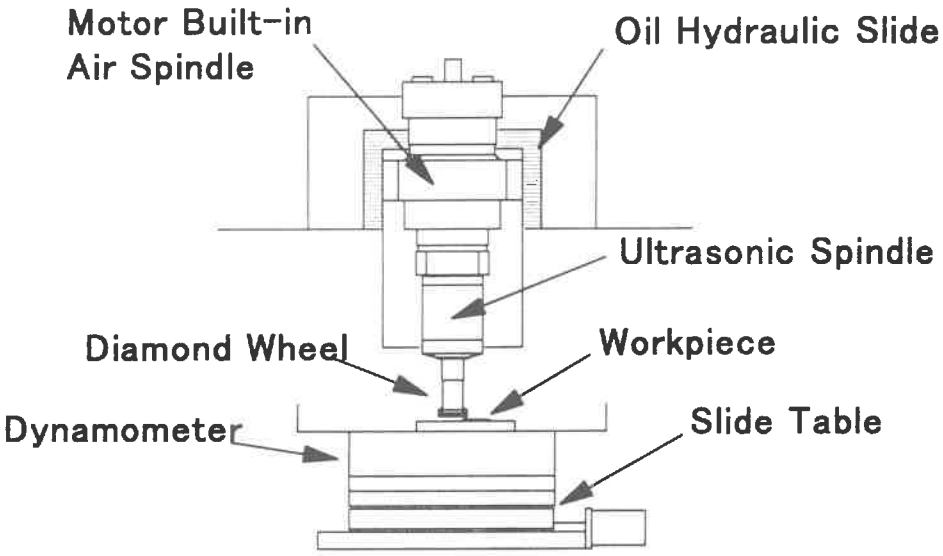

Figure 1 Schematic Illustration of The Grinding Machine

Table 1 Experimental Equipment and Grinding Conditions

Grinding machine	PSG-520DX (Okamoto Machine Tool)
Air spindle	BLOCK-HEAD Type 4R (Professional Instruments)
Slide table	Twinkler 5000 (THK)
Dynamometer ／Charge Amplifier	TYPE 9257A ／ TYPE 5007 (KISTLER)
Work piece	Silicon 10×25×2mm (100 surface)
Diamond wheels ϕ 42-1w (cup type)	SD#170 P 75 M SD#1000 P 75 M SD#3000 P 75 M

Ultrasonic Spindle

Frequency	40kHz
Amplitude (wheel surface)	2 μ m

Grinding Conditions

Wheel Rotation (Peripheral Speed)	1000, 2000 rpm (2.2, 4.4 m/s)
Table Speed	50, 100, 150 mm/min
Depth of Cut	0.5, 1, 2, 4 μ m/pass

corrugation which corresponds to 40 kHz and the high frequency ingredient of about 4 kHz were observed by the oscilloscope. In the pen recorder, it was found that the value which is equivalent to the integration value which contains these high frequency components was put out. There are a few changes, though we found that grinding force according to depth of cut was measured using the dynamometer and the pen recorder. Therefore, in this paper, we defined the value which was registered by the pen recorder as being the grinding force value.

Experimental results

Changes in normal grinding forces are shown in Figure 2, grinding conditions are as follows: Wheel rotation: 2000rpm (2.2m/s), table speed: 100mm/min,and depth of cut: 1 μm/pass. In the figure, white marks show conventional grinding, and black marks show grinding with ultrasonic vibration. Brittle-mode surface was produced by #170 and #1000 grit wheels with ultrasonic vibration. Then the normal grinding forces were lower than normal grinding force by conventional grinding. But a #3000 wheel produced a high normal grinding force by grinding with ultrasonic vibration. The normal

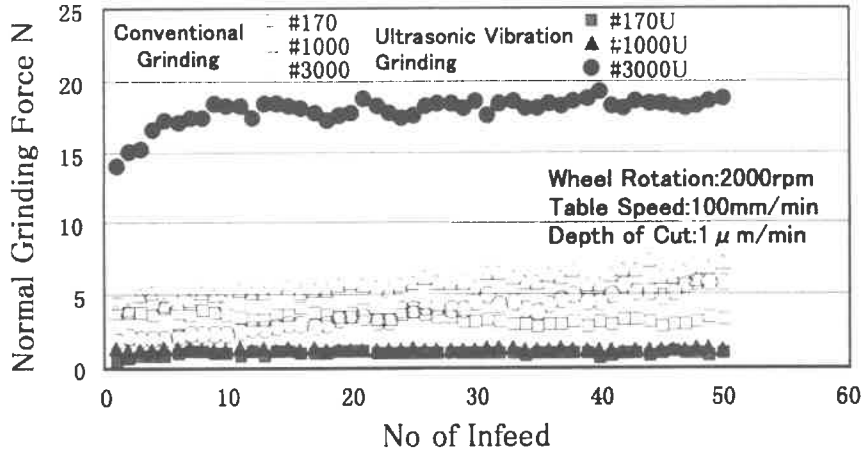

Figure 2 Comparison of normal grinding forces of various grit size

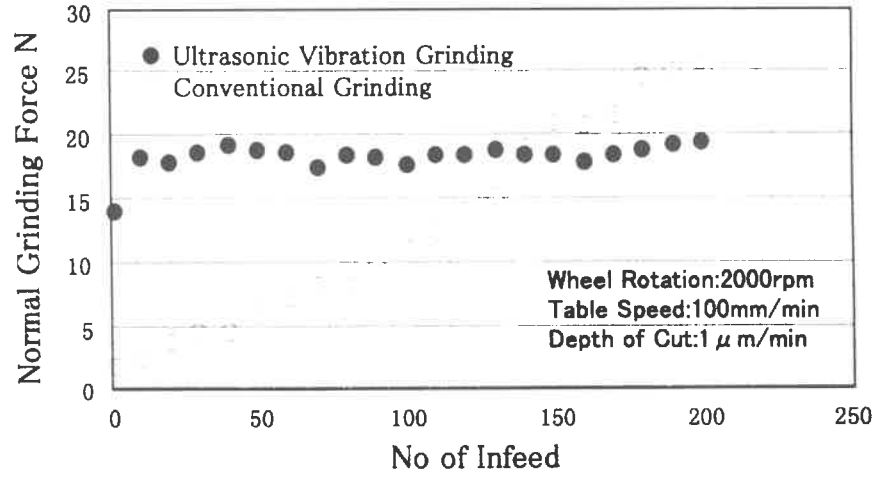

Figure 3 Comparison of normal grinding forces with a #3000 grit wheel

grinding forces by conventional grinding with #1000 and #3000 grit wheels increased with passes, but they were stable in grinding with ultrasonic vibration. In the shear-mode grinding, the condition of the wheel surface changed and the normal grinding force rose with an increase in the number of passes.

However, because there is little change of the wheel surface in grinding with ultrasonic vibration, we think that the normal grinding force will change very little. With a #3000 grit wheel, in case of ultrasonic vibration grinding, the tangential grinding force was stable and smaller than with conventional grinding. The value was about 1/5 in comparison with conventional grinding. This fact is extremely favorable in shear-mode grinding with a cup wheel.

Comparison of change of the normal grinding force with and without ultrasonic vibration under 200 passes is shown in Figure 3. The normal grinding force of conventional grinding increased with passes and exceeded the value, produced by ultrasonic vibration grinding. On the other hand, the normal grinding force of grinding with ultrasonic vibration showed comparatively high value, but it was quite stable.

The micrographs of the ground surfaces with various grinding conditions and various grit sizes are shown in Figure 4. Ground surfaces by both grinding methods in #170 grit wheel were approximately brittle-mode. With a #1000 grit wheel, the ground surfaces by conventional grinding were approximately shear-mode. On the other hand the surfaces by ultrasonic vibration grinding were intermingled with shear-mode and brittle-mode. We consider that the ground surface of conventional grinding was affected by the grinding heat, but the ground surface of ultrasonic vibration grinding was little affected by the grinding heat according to the observation results of the micrographs. When using #3000 grit wheel, we could produce shear-mode surfaces in any condition.

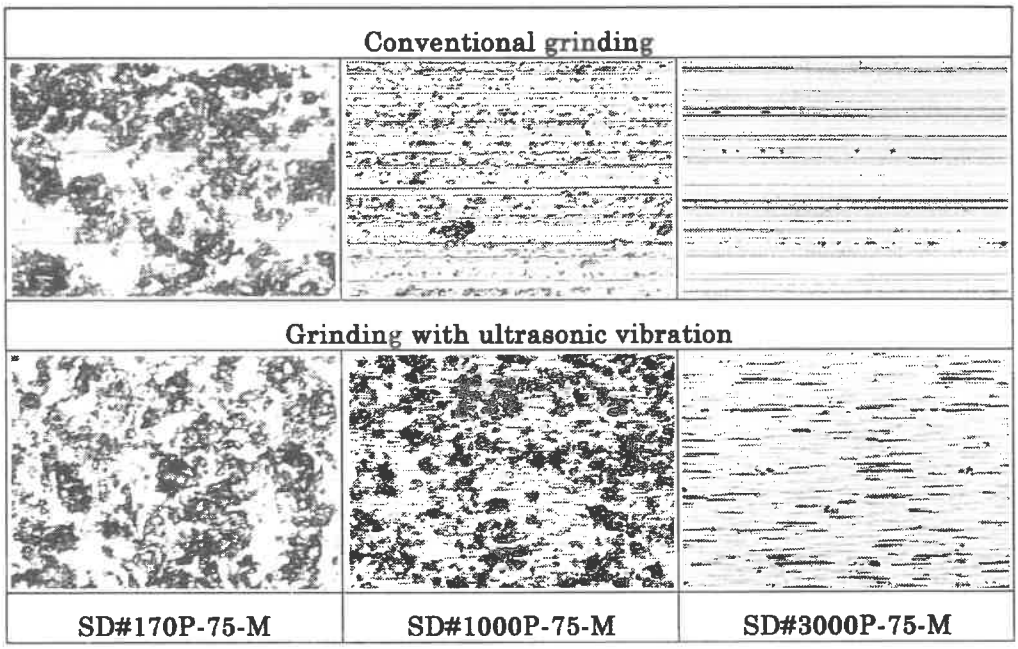

Figure 4 Micrographs of ground surfaces with various grit size and both grinding methods

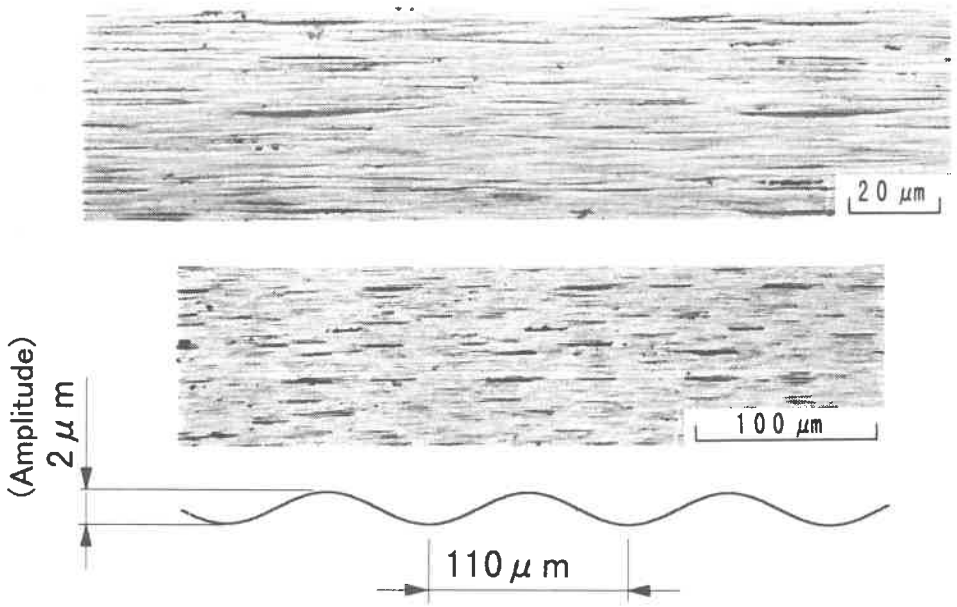

(The shift distance with 1 period at a individual grit)

Figure 5 Micrographs of grinding streaks and the track of theoretically calculated individual grits

The grinding streaks which were shown in the micrographs agree with the track of theoretically calculated individual grit. We think the streak was produced by rough or worn-out grit. It is necessary to produce finer streaks; therefore, the magnitude of the individual grit machining unit needs to be small.

Conclusions

We found the following in silicon wafer grinding with ultrasonic vibration:

① Under various conditions, with and without ultrasonic vibration, shear-mode surface can be produced with #3000 grit diamond cup wheels.

② The grinding force was kept dramatically stable during many repeated passes in grinding with ultrasonic vibration.

③ It is possible to produce a smoother surface by using a finer diamond grit with ultrasonic vibration grinding.

These experimental results show great potential for using ultrasonic vibration in manufacturing next generation sixteen-inch silicon wafers.

Reference

1) H. Hashimoto, K. Imai, 10th Proc. ASPE, (1995)171

2) H. Hashimoto, J. Takeda, K. Imai, K. Blaedel, Int. JSPE, 27,2 (1993)95.

SURFACE AND SUBSURFACE STRUCTURE OF ALUMINA AFTER DUCTILE-MODE GRINDING

I. Zarudi and L. C. Zhang[1]

Department of Mechanical and Mechatronic Engineering, The University of Sydney, NSW 2006, Australia

1. Introduction

Alumina is known as a material of low density with high temperature strength and high resistance to wear and corrosion. These properties make it attractive to industry for producing electronic and optical components that require high quality of surface and damage-free subsurface. Fortunately, the recent application of ultra-precision grinding [1-2] has made it possible to produce surfaces with high integrity. However, the formation mechanism of the subsurface structure has not been well understood yet and its correlation with grinding conditions has not been fully established. As pointed by the research group in the University of Sydney, the structure of subsurface plays a crucial role in affecting the properties of a ground component and microcracks may exist in the subsurface even if the ground surface is absolutely microcrack-free.

The purpose of this work is to gain an understanding of the formation mechanism of the surface and subsurface structures of alumina in ultra-precision grinding.

2. Method

The materials used for study were alumina with average grain diameters of 1 μm and 25 μm. The grinding experiments were conducted on an ultra-precision surface grinder, Minini Junior CF CNC M286. A diamond grinding wheel of SD4000L75BPF(diameter 305 mm, peripheral speed 27 m/s) was used. The depth of cut was fixed at 100 nm but the table speed was varied from 0.02 m/min to 1 m/min. A water based coolant Syntilo 3 (99 % water, 1 % mineral oil) was used.

Topography of the ground surfaces was explored by means of High Resolution Scanning Microscope (HRSEM) JSM-6000F. The surface roughness was measured by Atomic Force Microscope (AFM) and the subsurface structure of specimens was studied on Transmission Electron Microscope (TEM) EM 430. Detailed procedure can be found in Ref. [3].

3. Results and Discussion

3.1 *Overall features of ground surfaces*

The surface topography of ground alumina is shown in **Fig.1**. Mirror surfaces were obtained under all the table speeds used. Plastic grooves were clearly seen on the ground surface, suggesting the ductile mode of material removal. However, some pits were also observed. The

[1] **Author for correspondence**

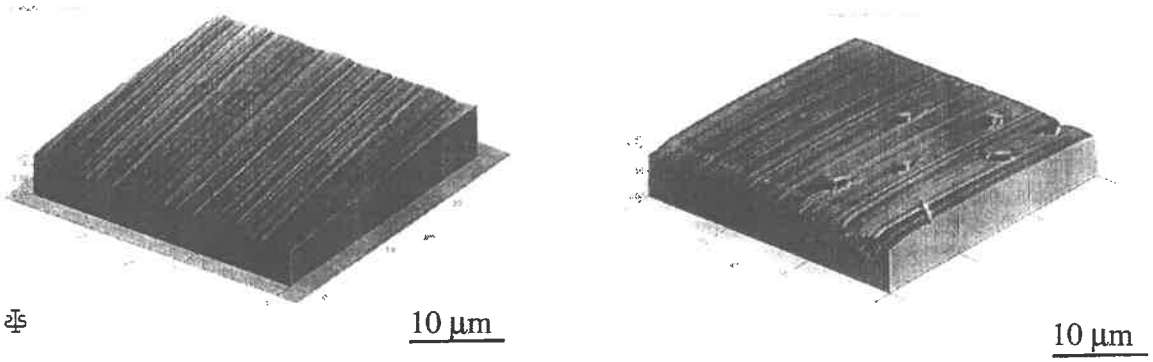

(a) (b)

Fig.1 Surface topography after ultra-precision grinding (Table speed 0.02 m/min): (a) The 1 μm-grained alumina; (b) The 25 μm-grained alumina.

variation of Rms roughness *vs* table speed for both types of alumina is shown in **Fig.2**. It is clear that Rms roughness increased with the increase of table speed. For the 1 μm-grained alumina Rms roughness increased from 30 nm to 50 nm with the increase of table speed from 0.02 m/min to 1 m/min. For the 25 μm-grained alumina the effect was more pronounced and Rms roughness varied from 33 nm to 90 nm. Clearly, Rms roughness was affected by pits on the surface. The surface covered by pits was determined by the technique of image analysis, as shown in **Fig.3**. It is obvious that the surface covered by pits decreased significantly with the decrease of table speed, i.e., with the decrease of the uncut chip thickness. Furthermore, the surface covered by pits in the 1 μm-grained alumina (1.5 % for table speed 0.02 m/min) is less compared with those in the 25 μm-grained alumina (5 % for the same table speed).

To study the nature of pits we explored their topography by HRSEM. As shown in **Fig.4,** the central part of a pit resembles the cross-section of pores that were formed during specimen processing. The peripheral part of the pit possesses the characteristics of fracture.

The fracture around the pit can be explained by the effect of pore on the grinding process. A pore in the material can act as a stress raiser and promote microcracking near its

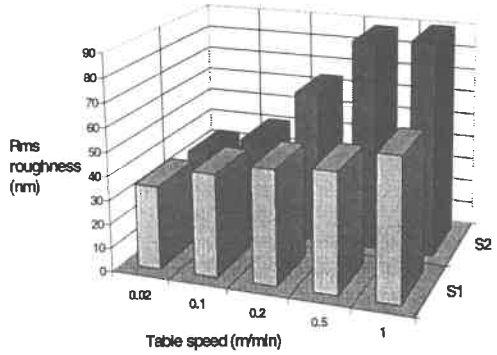

Fig.2 Effect of table speed on Rms roughness in: (S1) The 1 μm-grained alumina; (S2) The 25 μm-grained alumina.

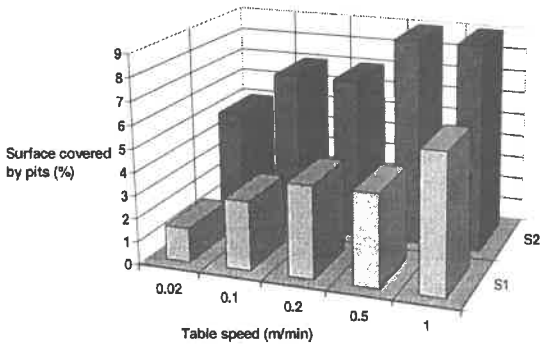

Fig.3 Effect of table speed on surface covered by pits in: (S1) The 1 μm-grained alumina; (S2) The 25 μm-grained alumina.

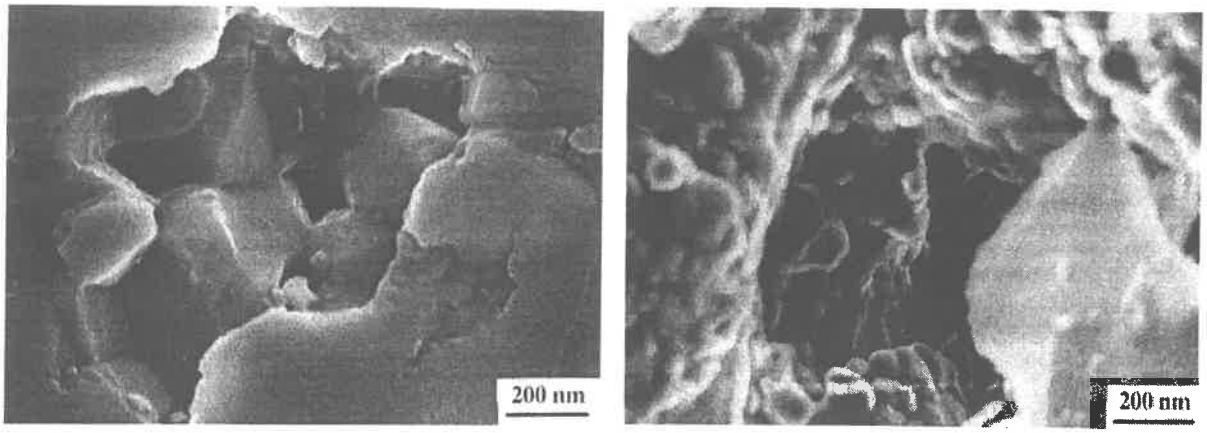

(a) (b)

Fig.4 Topography of a pit in: (a) The 1 μm-grained alumina; (b) The 25 μm-grained alumina.

edge during the abrasive cutting of grinding wheel. It is worth to note that the fractured surface area of the 25 μm-grained polished alumina was 18 %, this is much higher then that of the ground 25 μm-grained alumina (9 %). This means that ultra-precision grinding can generate better surface quality compared with ordinary polishing.

3.2. *Subsurface structure*

Before ultra-precision grinding, the damaged subsurface layer induced by specimen preparation (conventional grinding) was determined so that this initially damaged zone could be removed completely during the subsequent ductile-mode grinding. Thus in all the cases below the subsurface structures were purely caused by grinding.

Figure 5 showes that ductile-mode grinding created a layer with an extremely high density of dislocations, which was immediately beneath the ground surface. This layer spread to the depth of 100 nm to 150 nm under the surface depending on table speed. Following this, a zone with a much lower density of dislocations appeared. Dislocations could be

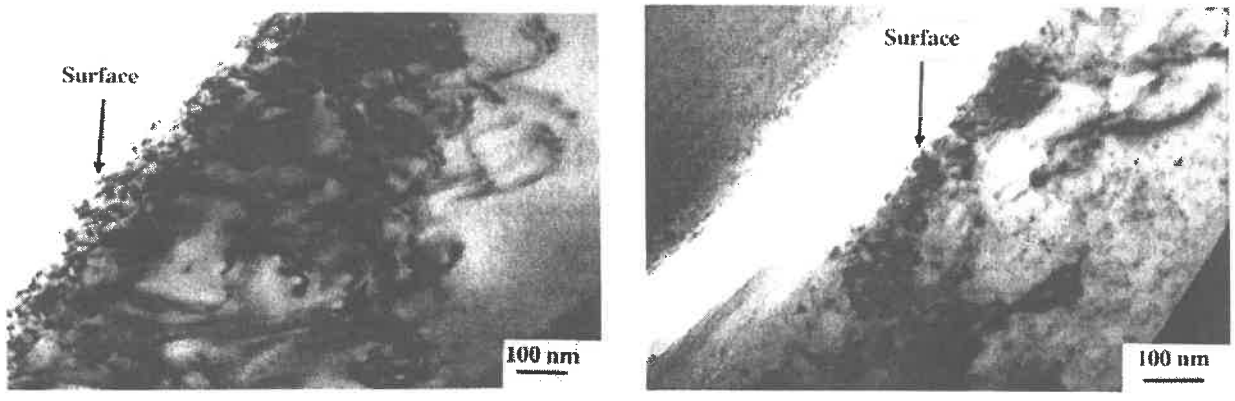

(a) (b)

Fig.5 Subsurface structure in alumina after ductile-mode grinding. (Table speed 1 m/min): (a) The 1 μm-grained alumina; (b) The 25 μm-grained alumina.

distinguished easily there. The depth of the second zone was also dependent on table speed and varied from 150 nm to 500 nm.

3.3 *Microcracks*

Microcracks were observed only in the vicinity of pit edges, which neither radial no lateral cracks. The microcracking-free behaviour in the first layer can be explained by the nucleation of sufficient number of twin and slip systems that satisfy von Mises criterion [4]. The second zone had less than five independent slip and twin systems and thus microcracking should be highly possible there. However, this is inconsistent with the above experimental observations. Such phenomenon can be explained by the possibility of microcracking due to the pile-up of dislocations on an active slip plane. The threshold effective resolve shear stress (τ_s) for cracking could be determined by [5]:

$$\tau_s^2 = \frac{3\pi}{8}\left[\frac{\gamma\mu}{(1-\nu)L}\right]$$

where γ is fracture surface energy, μ is shear modulus, ν is Poisson's ratio, and L is the length of pile-up. Considering the length of pile-up of 150-500 nm (i.e. penetration depth of dislocation in grinding), we can see that for such a small pile-up length the nucleating of microcracks usually does not occur. It is also worth to note that the interaction of different slip systems was a rear event here and could not create microcracks.

4. Conclusions

(1) Ductile-mode of material removal was obtained in ultra-precision grinding of different types of alumina, featuring mirror surfaces with Rms roughness in the range of 30 nm to 90 nm.

(2) The nature of pits on ground surfaces is related to pores in the bulk material.

(3) The subsurface structure of alumina after ductile-mode grinding is composed of a layer with high dislocation density in the surface vicinity followed by a layer with much lower dislocation density.

(4) The ductile-mode of material removal is possible due to initiation of more than five independent slip and twin systems in the first layer. The possible explanation of the absence of microcracks in the second layer is the small length of pile-ups that can not create sufficient stress for microcracking.

(5) No radial and lateral microcracks were detected in the whole subsurface area after grinding.

References

1. Zarudi and L. C Zhang, in: *Advances in Abrasive Technology*, L. C. Zhang and N. Yasunaga, ed. 33 (World Scientific, Singapore, 1997).
2. H. Suzuki, N. Wajima, M. S. S. Zahmaty, T. Kuriyagava, K. Syoji, in: *Advances in Abrasive Technology*, L. C. Zhang and N. Yasunaga, ed. 116 (World Scientific, Singapore, 1997).
3. I. Zarudi and L. C. Zhang, Proc. of 10-th ASPE Annual Meeting, 165 (1995).
4. R. Von Mises, *Math. Mech.*, **8**, 161 (1928).
5. T. Hagan, *J. Mat. Sci.*, **14**, 2975 (1979).

IN-PROCESS EDM TRUING TO GENERATE COMPLEX CONTOURS ON METAL-BOND, SUPERABRASIVE GRINDING WHEELS FOR PRECISION GRINDING STRUCTURAL CERAMICS*

Mark A. Piscotty, Pete J. Davis, Theodore T. Saito, Kenneth L. Blaedel, Lee Griffith
Lawrence Livermore National Laboratory
7000 East Ave Livermore, CA 94551 USA
510-422-2052 / 510-423-1460 fax
markp@llnl.gov

1. INTRODUCTION

The demand and use of precision grinding of structural ceramics continue to increase as the worldwide advanced ceramic industry surpasses $20 billion in sales [1]. Included in this industry are engineering structural ceramics, electronic ceramics, bioceramics and others. These materials are used in applications such as engine components, casting and extrusion dies, bearings, medical implants, nozzles, thermal insulators, and more. Along with the variety of ceramic applications comes a broad range of precision requirements, which in turn leads to various required processes to accommodate a spectrum of specifications. A process for grinding ceramic components to micrometer tolerances was employed and further developed at Lawrence Livermore National Laboratory for two separate grinding projects.

2. PROCESS DESCRIPTION

The grinding methodology was developed for a variety of ceramic grinding processes including creep-feed and cylindrical grinding. Figure 1 shows a schematic with the major components of the grinding machine used to creep-feed grind flat ceramic components. An in-situ EDM rotating graphite electrode is used to profile metal bond grinding wheels and both the electrode and the grinding wheels are mounted on air-bearing spindles [2]. The rotating electrode has separate truing surfaces, for coarse and fine profiling. In turn, the profile that is imparted onto the grinding wheel may have multiple, complex features for coarse stock removal and finish detailing.

2.1 Creep-Feed Grinding

One application which greatly benefits from adoption of this methodology is creep-feed grinding of precision grooves in flat BeO substrates. Figure 2

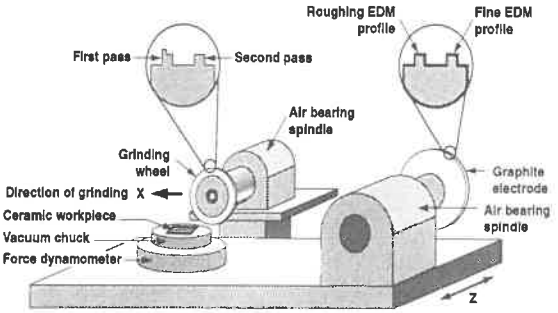

Fig. 1. Creep-feed grinding process schematic with in-situ EDM wheel profiling.

shows a photograph of a ground 1 cm x 4 cm x 0.2 cm BeO component. Most tolerances are ± 1 μm, including the periodic spacing among the grooves. In addition to meeting dimensional specifications, it is necessary to maintain surface roughness and sub-surface damage below levels that significantly affect the material properties and component performance [3].

Figure 3(a) shows a close-up photograph of the profiled grinding wheel approaching four BeO workpieces held in a vacuum chuck, which is mounted on a 3-axis, strain-gage force dynamometer. The machine tool is temperature controlled to ± 0.5 C and air-bearing spindles support and drive the grinding wheel and graphite electrode.

Low pressure aqueous grinding fluid is used with the option of applying high pressure fluid to

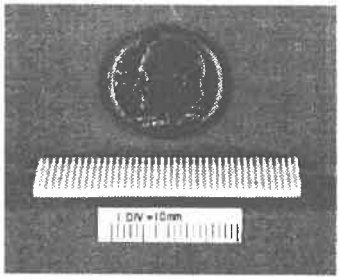

Fig. 2. 4 cm x 1 cm x 0.2 cm BeO substrate.

*This work was performed under the auspices of the US Dept. of Energy by LLNL under Contract W-7405-Eng-48

continuously clean the wheel surface. Figure 3(b) shows the graphite electrode about to profile the metal bond, grinding wheel. For this particular process, a CBN grinding wheel, mounted on the same spindle as the diamond grinding wheel, is used to profile the graphite electrode. Table 1 provides typical process parameters for the creep-feed grinding.

Fig. 3(a). Creep-feed grinding of BeO.

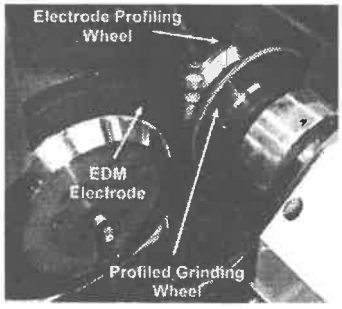

Fig. 3(b). EDM profiling of grinding wheel.

Table 1. Creep-feed process parameters.

Parameter	Description
Grinding wheel	SD1000, N100 M, 18 cm Ø
Workpiece	BeO
EDM electrode	Poco Graphite (1 µm grain size)
Wheel speed	105 m/sec
Feed rate	7.5 cm/min

2.2 Cylindrical Grinding

Another application that utilizes this process methodology is cylindrical grinding of structural ceramic engine components. These multi-featured components have typical tolerances down to a micrometer. Figure 4 shows a photograph of one of the zirconia components.

Some of the critical features to note regarding

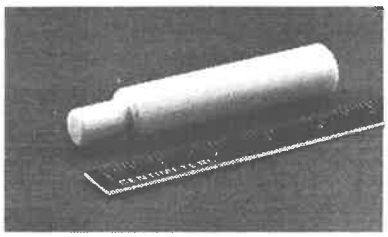

Fig. 4. Ground zirconia component.

this geometry are cylindricity to within 1.5 µm, a specified radius of curvature on the right side of the component, a chamfer edge on the left side and a minimum shoulder internal corner radius.

The process procedure is similar to that for creep-feed grinding except that the workpiece is rotated in a spindle mounted collet, instead of mounted on a traversing table. In this case, in-situ profiling of the EDM electrode is performed using a single-point tool mounted on the machine. The profiled electrode is used to EDM profile the grinding wheel.

Figure 5 shows a photograph of the grinding machine and shown are the grinding wheel spindle and the workpiece spindle that rotates the workpiece and the EDM electrode. Also shown are the ceramic workpiece and the single point tool used to profile the electrode. Table 2 presents the nominal process parameters used in this particular application.

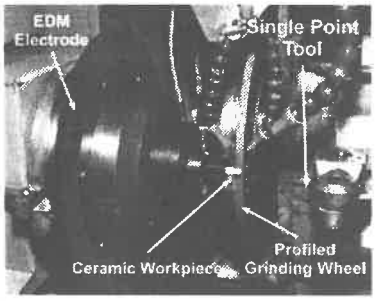

Fig. 5. Cylindrical grinding machine tool.

Table 2. Nominal process parameters for cylindrical grinding using EDM profiled grinding wheels.

Process Parameter	Description
Grinding wheel	15-25 µm, cast iron bond, 30 cm Ø
Workpiece	Al_2O_3, Si_3N_4 and Al_2ZrO_3
EDM electrode	Poco Graphite (1 µm grain size)
Wheel speed	25 m/sec
Workpiece speed	150 rpm

3. PROCESS ANALYSIS

3.1 Grinding Wheel Wear

Understanding and controlling wheel wear is an essential factor in determining both the level of achievable precision and the economics of the grinding process [4]. To facilitate this understanding, an instantaneous grinding ratio (volumetric material removed/volumetric wheel wear) test procedure was developed to examine the changes in grinding ratio over time. To circumvent the problem of directly measuring small changes in wheel dimensions, measurements of witness grinds were used.

Figure 6 shows a schematic of the instantaneous grinding ratio method using cylindrical grinding. A workpiece is rotated in a spindle and a grinding wheel grinds with only half of the available bond surface, leaving the unused portion intact. Shallow witness grinds, with both the 'unused' and the worn portions of the wheel, are performed on available workpiece areas after each successive grind. This produces a measurable artifact for step height differences between the worn and unused wheel surfaces.

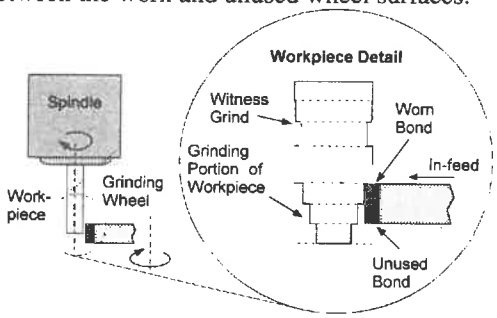

Fig. 6. Instantaneous grinding ratio schematic.

Figure 7 shows an image of a typical ground workpiece from such a test. On the left are shown the grinding steps and on the right is one of the witness grinds used to measure wheel wear. Figure 8 is a plot of data obtained for a particular grinding wheel for different workpiece materials.

3.2 Sub-surface Damage

Investigation of the presence of residual damage, including sub-surface damage (SSD) [5], and its effect on workpiece material properties is being investigated. Transmission electron microscopy (TEM) analysis was used to examine the SSD. Figure 9 shows a typical TEM of a BeO surface using

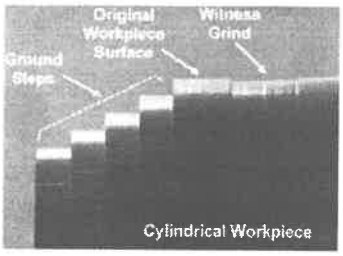

Fig. 7. A typical workpiece ground during an instantaneous grinding ratio test.

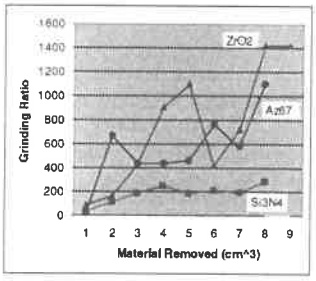

Fig. 8. Instantaneous grinding ratio data for various materials. Wheel: 15-25 µm, cast iron bond.

grinding conditions shown in Table 1 and a wheel traverse speed of 5.1 cm/min. This workpiece showed a significant number of cracks between and through grains to depths of 10 µm or more. A sample ground at 0.7 cm/min showed essentially no cracks, but had a larger number of dislocations near the surface. We surmise that the more catastrophic damage of cracks may significantly affect the thermal and mechanical properties of the component.

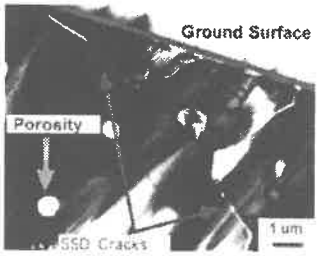

Fig. 9. TEM image of a ground BeO surface with wheel traverse speed of 5.1cm/min.

Another type of grinding test was conducted to investigate the effect of residual damage on the modulus of rupture (MOR) values of zirconia-alumina (ZrO_2-Al_2O_3) bars. Three groups of bars were machined, then tested in a 4-point flexure [6]. The first group was loose abrasive polished (0.5 µm diamond), the second was ground with a 25 µm diamond abrasive, bronze bond wheel, and the third was ground with a 100 µm diamond abrasive, bronze bond wheel. Figure 10 shows a plot of the

MOR values for the three cases and indicates that the polished and the fine ground parts had statistically similar MOR values, while the coarse ground parts exhibited a reduction of MOR by a factor of approximately 3.

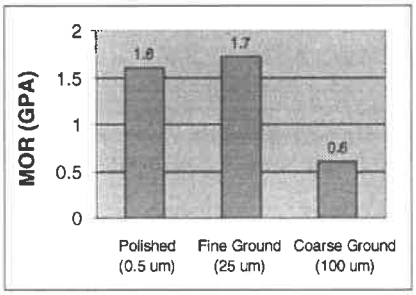

Fig. 10. MOR values as a function of grit size. ZrO_2-Al_2O_3 MOR bars.

4. DISCUSSION

The economic advantages of instituting an on-machine EDM profiling process for precision grinding can be substantial for a number of reasons. Integrating the entire process on one machine reduces operator set-up and tear-down times over multiple-machine procedures. Using a single machine tool reduces capital equipment expense and decreases required floor space. However, one of the largest economic incentives of such a procedure is that performing all the machining and grinding on one machine can significantly improve part accuracy leading to improved yield. Equally important is the versatility to generate complex profiles in grinding wheels, which can reduce the number of passes required to grind a given component.

Control of wheel wear is essential to controlling the accuracy of the grinding process. Traditional grinding ratio tests typically require substantial grinding, with a single 'integrated' grinding ratio value as the result. The instantaneous grinding ratio tests discussed here allow the user to capture wheel wear information throughout the life of the wheel. The data shown in Figure 8 all show a sharp increase in grinding ratio after the first few grinding steps. The initial low grinding ratios are the result of the softer, recast layer generated on the wheel surface during EDM profiling, which wear quickly relative to the bulk bond matrix. To maintain dimensional accuracy, the user must be aware of how the wheel wears over time and optimize the wheel profile and EDM parameters to account for the recast layer.

The residual SSD imparted in the ceramic workpiece is often as important to the customer as is compliance with geometric specifications. As higher performance demands are placed on ceramic components, changes of 10 – 15% in mechanical properties can become crucial. In one test, we noted a 3 times decrease in modulus of rupture values for coarse ground parts over polished or fine ground parts. This has significant implications regarding component reliability and time between failures. Further research will continue at LLNL to investigate the thermal and mechanical SSD effects on ground ceramic components.

5. SUMMARY

A generalized precision grinding process is under development at Lawrence Livermore National Laboratory to use EDM profiled, metal-bond, superabrasive grinding wheels to economically fabricate ceramic components. The two applications reported here include creep-feed grinding of 0.5 mm wide grooves in BeO substrates and cylindrical grinding of various ceramic components with micrometer tolerances. Resultant sub-surface damage and grinding ratios were investigated to optimize grinding conditions for maximum yield and wheel life.

6. REFERENCES

[1] Mayer, J.E., "Structural ceramics tell you their optimum grinding condition," Abrasives Magazine, pp 14-18, June/July 1997.

[2] Suzuki, K., "On-machine electro-discharge trueing for metal bond diamond grinding wheels for ceramics," NIST Special Publication 847, Editor – Said Jahanmir, July 1993.

[3] Green, D.J., "Critical microstructure for microcracking in Al2O3-ZrO2 composites," J.Am.Ceram.Soc., 65, pp 610-614, 1992.

[4] Mindek, R.B., "A study of the wheel wear and thermal limitations in creep-feed grinding...", PhD Dissertation, Univ. of Connecticut, 1996.

[5] B.Zhang, "Subsurface evaluation of ground ceramics," Annals of CIRP, Vol 44/1/1995.

[6] "Standard test method for flexural strength of advanced ceramics at ambient temperature," ASTM Standard C 1161-90, December, 1990.

Figure correction for rotary asymmetric error by linearly arranged segmented pressurizing polishing machine

Ken-ichiro Horio, Toshio Kasai, Atsuhiro Matsuse
Saitama university
255 Shimo-okubo, Urawa, Saitama, 338, Japan

1. Introduction

For example, in a field of optical components or semiconductor wafers there is no bounds for demand of high performance. In some cases we will have to mass-produce those high quality articles which has both smooth surface and high form accuracy. In the mass production yield rate of these should be rather high. One solution for dealing with those is advancing the final figuring process. However it is not effective nor economical in some cases. The other solution is adding a special figure correction process to the ordinary final process. Of course, in this case, you should have some degree of yield rate from the ordinary final process and have some inferior articles just below the border. Unless this condition is satisfied, the adding process is not effective nor economical. Our aim of the work is for this kind of figure correction technology.

2. Advantage of segmented tool method

In the previous work[1] we proposed the effectiveness of using multiple small tools in the polishing for figure correction. Fig.1 shows the comparison between (usual) small tool method and segmented tool one. In the small tool method you should scan a tool over the sample and control dwelling time at each position to compensate material removal amount. On the contrary, in the segmented tool method the compensation is done by supply of pressure to each piston. There are two

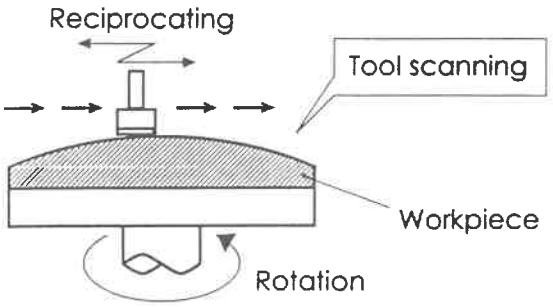

(a) Small tool method

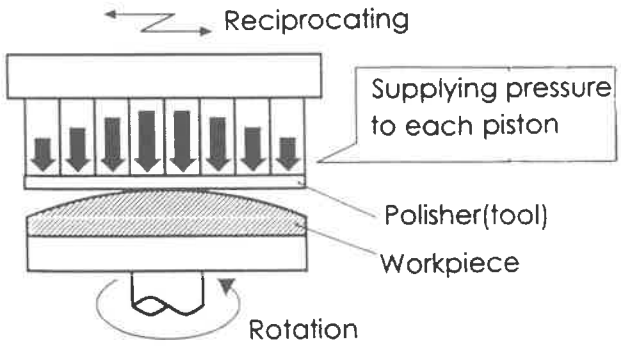

(b) Segmented tool method

Fig.1 Comparison of principle between small tool method and segmented tool one

way of the compensation; one is by amount of pressure and the other is by time with constant pressure, though the time is easier to be controlled.

Because you can expect several times efficiency with 10 small tools in compare of single tool. We also stated linearly arranged segmented tools is more practical or effective than two-dimensionally arranged segmented tools which has some difficulty in pressuring or supplying abrasives.

On the contrary linearly arranged tool is hard to compensate the rotary asymmetric error because the apparatus should be moved with more than two degrees of freedom (if you use two-dimensional, one degree is enough) and the one degree tends to be rotary movement in easier design. So in the previous work results were limited to rotary symmetric figures.

3. Strategy for correction of asymmetric error

In this work, we tried to treat asymmetric error by rotary movement. Fig.2 shows the principle. In the figure correction process the radial position is always detected by the encoder and orders of pressuring were sent dependent on the position. The figure correction is based on dwelling time control of each tool. The strategy is integration of material removal by each tool and consideration of overlapping with each other. In this case the difference of radial position of each tool also should be considered.

4. Asymmetric Figure Correction by Prototype Machine

We made a prototype apparatus to demonstrate and prove the idea. Fig.3 shows the configuration of the system. It has ten segmented tools which is linearly arranged and can be moved linearly as one body along the same direction of the line. Workpiece is fixed on the rotary table with a rotary encoder. Fig.4 shows the tool arrangement and its capability to cover an area over the sample (experimental result). We developed a program to control each electro-magnetic valve for pressurizing a piston by the signal from the encoder and the information about the figure deviation

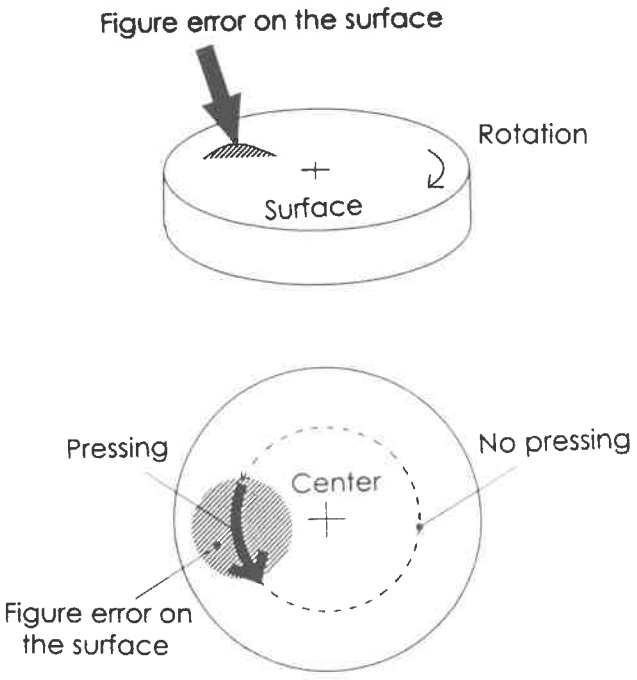

Fig.2 Principle of the figure correction for asymmetric error

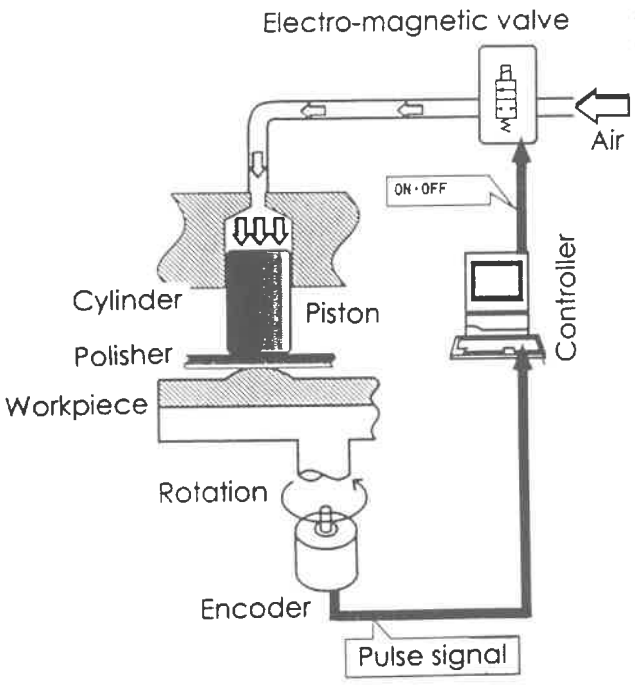

Fig.3 Conceptual figure of the proto-type apparatus

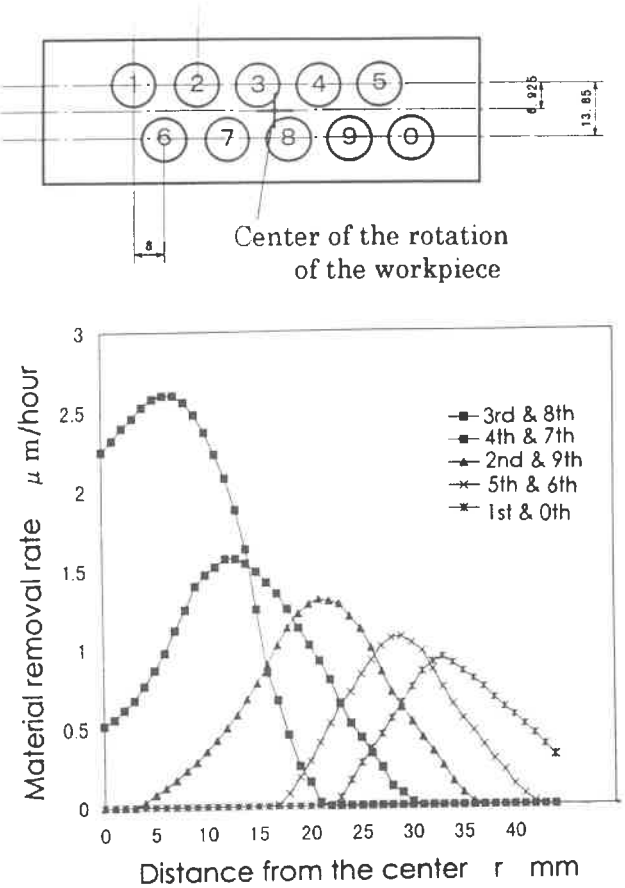

Fig.4 Arrangement of the tools in the prototype machine and its covering area

(where should be removed).

For the example, we tried to get a cylindrical concave which is rotary asymmetric with this rotary movement apparatus. Fig. 5 shows the result. Work material was BK7 (optical glass). Though the initial shape of the sample was spherical convex, we could get a shape like cylindrical concave by polishing combined with cerium dioxide powders and artificial leather polisher. Fig.6 shows the sectional shape along the two main directions (generator and diameter) of the cylinder. You can find difference of those.

5. Conclusion

Though our prototype is mechanical polishing apparatus, the idea can be applied to other complicated process as it is under rule of dwelling time only. The applicable area we think are manufacturing of aspheric optical (glass) components, planarization during semiconductor process, or precision molding die for plastic optical components and flatness improvement in wafers for

semiconductor or quartz crystal.

[1] Horio K., Kasai T., 1993, Figure Correction by Segmented Pressurizing Polishing Machine, Proc. 1993 ASPE Annual Meeting: 268-271

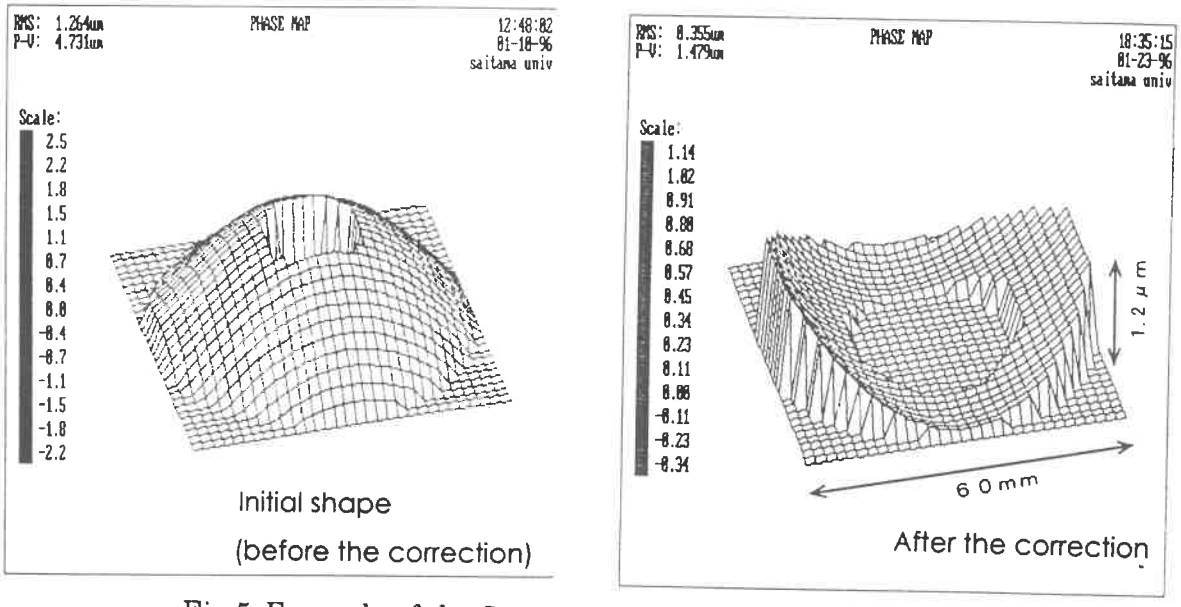

Fig.5 Example of the figure correction to a cylindrical concave

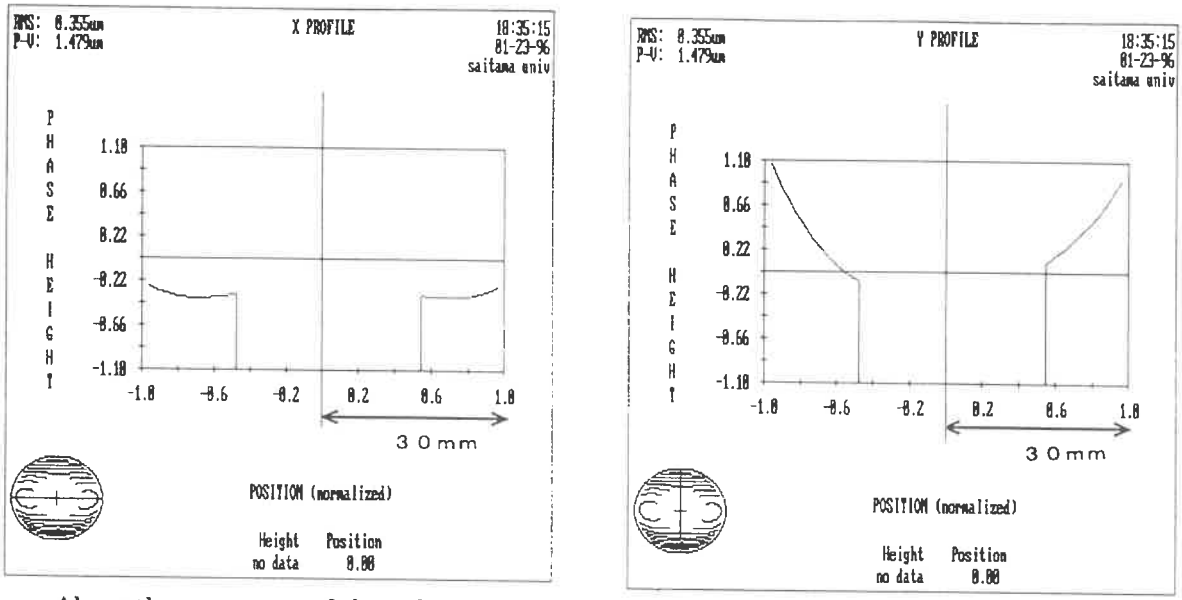

Along the generator of the cylinder

Along the section of the cylinder

Fig.6 Sectional shapes of the corrected sample

Fabrication of new collimating optical fibers using glass slit-microferrules

Kunio KOYABU and Fumikazu OHIRA
NTT Opto-electronics Laboratories, Nippon Telegraph and Telephone Corporation
3-9-11, Midori-cho, Musashino-shi, Tokyo 180 Japan

1. Background

Efficient input of light beams into optical fibers and output from fibers is important for optical communications. Methods where optical lenses are placed in front of the end surfaces of optical fibers have been widely used to improve input and output efficiency. However, it is difficult to align lenses to optical fibers and the parts making the joint are too big. To overcome these problems, a new structure in which a piece of graded-index (GI) fiber is fused and connected to the end of a single-mode (SM) fiber, has been proposed and evaluated[1]. This structure overcomes the problems of the difficult fabrication and the excessive volume, but creates new problems in that the optical characteristics are affected by the heating process and the irregular length of the GI fibers from the cleaving. Therefore, we propose a new collimating optical fiber that uses glass slit-microferrules. We have fabricated such a fiber and evaluate its optical characteristics.

2. Structure and principle of the collimating optical fiber

In the proposed collimating optical fiber (C-fiber), a piece of GI fiber with a regular length is placed in contact with an end surface of a SM fiber inside a glass slit-microferrule(Fig. 1), and they are fixed together with ultraviolet (UV) glue. A C-fiber transforms a divergent light beam into a collimated beam that exits the end surface of the C-fiber. To collimate light beams, the length of a piece of GI fiber should be $(2n+1)p/4$, where p is the period of a sine-curve and n is an integer, because a light beam from a SM fiber propagates along the trajectory of a sine-curve in a GI fiber.

3. Fabrication process and advantages of C-fibers

The fabrication process of the C-fiber is shown in Fig. 2. First, the coat of the SM fiber is removed and the bare part of the SM fiber is cleaved to a length of 6-7 mm. Then, the bare part of the SM fiber is set into a glass slit-microferrule. The slit-microferrule is a glass tube with a slit formed by dicing, and it has an outer-diameter of 0.25 mm, an inner-diameter of 0.126 mm and a length of 10 mm. Next, a piece of GI fiber is set into the opposite side of the glass slit-microferrule from the SM fiber, and UV glue is applied to the interface between the two fibers through the slit. The glue is then hardened by exposure to UV light, fixing the two fibers and the glass slit-microferrule together. After that, the GI fiber and the glass microferrule are polished until the GI fiber reaches the desired length.

This fabrication process offers the advantages of a short process with only four steps, a simple fabrication without two-fiber positioning, no damage to the optical characteristics from a heat treatment and good reliability in the optical characteristics because the GI fibers can be polished.

4. Experimental results

In the design of C-fibers, it is important that the periods of the sine-curves are clear when light beam are propagating inside the cores of GI fibers. Figure 3 shows the relation between the length of GI fibers with cores of 50 and 80 μm and the divergent angle of the outgoing light beam. The period of the sine-curve for 50 μm is 1.1 mm and for 80 μm it is 1.4 mm. Table 1 shows the specifications of fabricated C-fibers with 50-μm and 80-μm cores, and Fig. 4 shows a fabricated C-fiber with a 50-μm core.

The relation between the traveling distance and the light-beam diameter when a beam leaves a C-fiber is shown in Fig. 5. The outgoing beam diameter ($1/e^2$) of a C-fiber with a 50-μm core is less than 0.3 mm at a traveling distance of 6 mm and the divergent angle is 2.5 degrees. Our experimental results showed that the divergent angles of these C-fibers were about one-quarter those of conventional SM fibers. Results for the C- fibers with 80-μm cores were better than with the 50-μm cores, which suggests that the larger the core of a GI fiber, the better the optical characteristics.

Figure 6 shows the contours and the distributions of an outgoing light beam from a C-fiber with a 80-μm core at traveling distance of 0.5 mm and 5.5 mm. At 0.5 mm, the contour consisted of various circles with the same center position and a good Gaussian distribution was obtained. The contours and the distribution at 5.5 mm were almost as good. Thus, fabricated C-fibers have good optical characteristics that change little while traveling a certain distance.

Figure 7 shows the relation between the C-fiber interval and optical coupling loss when two C-fibers were placed with various positioning errors. For small C-fiber positioning errors, the optical coupling loss simply worsened as the intervals of the C-fibers became larger. For some of the larger C-fiber positioning errors, though, coupling losses had local peaks while one of the C- fibers moved. It appears that for small fiber positioning errors, the input (detection) C-fiber will always be placed in the outgoing light beam at any intervals, however, for larger positioning errors, the input C-fiber may not be placed in the outgoing light beam for short intervals, but comes into the outgoing light beam as the interval widens.

With the experimental C-fiber, we achieved non contact connecting with 3-dB coupling losses for 0.5-mm intervals between C-fibers with a 50-μm core and for 1-mm intervals with an 80-μm core.

5. Conclusions

We have proposed and fabricated C-fibers made using a glass slit-microferrule. In this structure, a piece of GI fiber with a regular length is connected to the end of an SM fiber inside of a glass slit-microferrule and they are fixed together with UV glue. The fabricated C-fibers had good optical characteristics because of the short and easy fabrication without heating treatment. Non contact optical connection using the C-fibers was achieved.

Reference

[1] W. L. Emkey and C. T. Jack, " Analysis and Evaluation of Graded-Index Fiber-Lenses ", Journal of Lightwave Technology, VOL. LT-5, NO. 9, Sep., pp. 1156-1164, 1987.

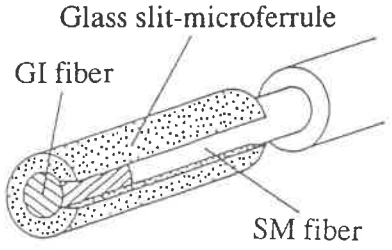

Fig.1 Structure of collimating optical fiber using glass slit-microferrule

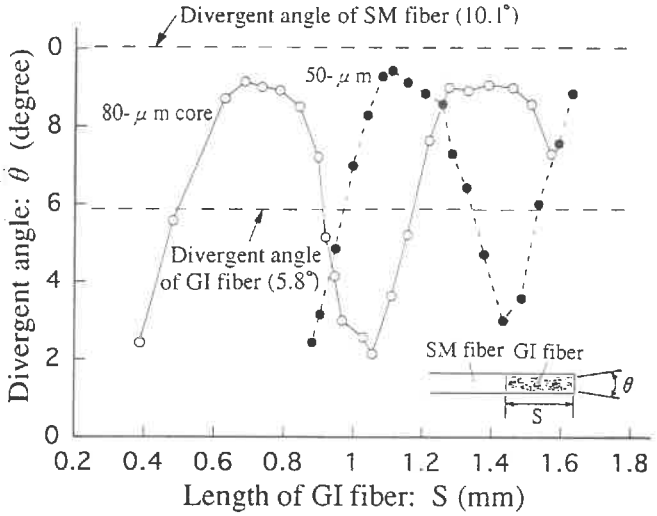

Fig. 3 Relation between length of GI fiber and divergent angle of outgoing light beam

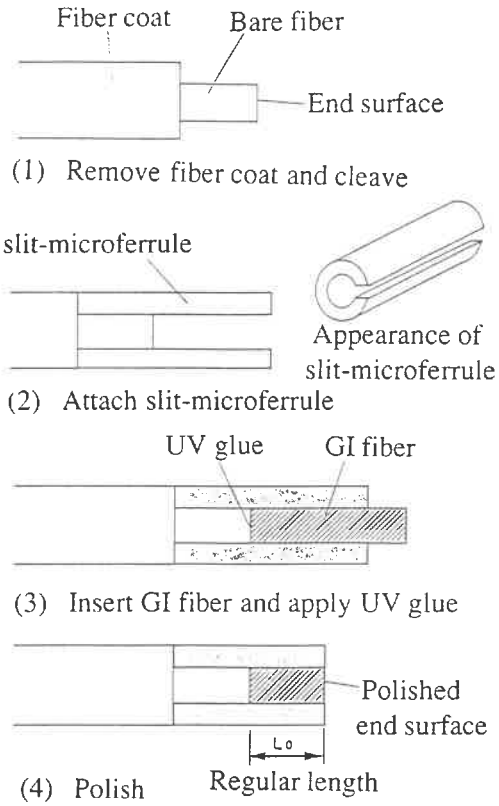

Fig. 2 Fabrication process of C-fiber

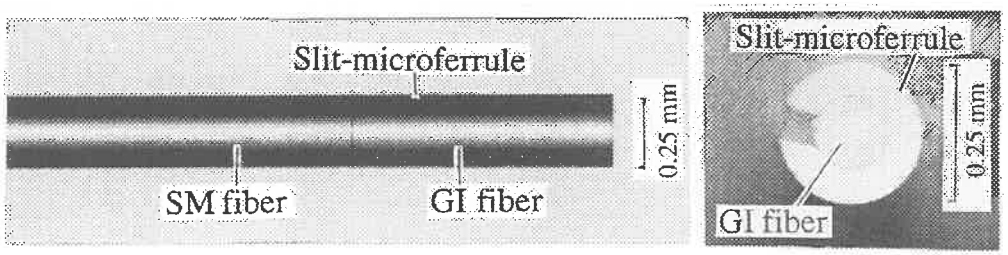

(a) Side view (b) End view

Fig. 4 Fabricated C-fiber

Table 1 Specifications of fabricated C-fibefs

Core diameter of GI fiber	Length of GI fiber	Core diameter of SM fiber	Outer-diameter of C-fiber
50 μm	0.85 mm	6 μm	0.25 mm
80 μm	1.1 mm		

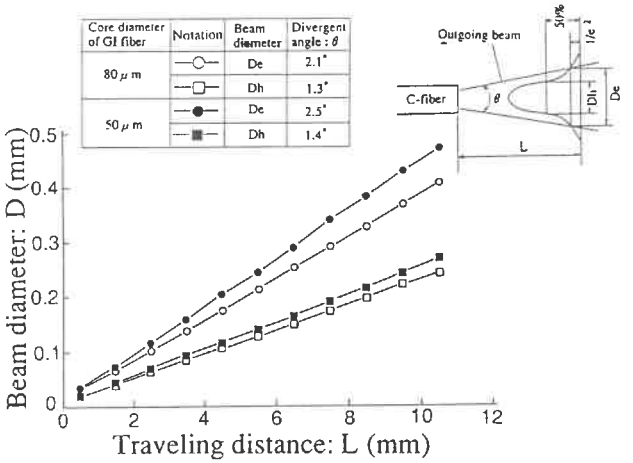

Fig. 5 Relation between beam diameter and traveling distance of outgoing beam from C-fibers

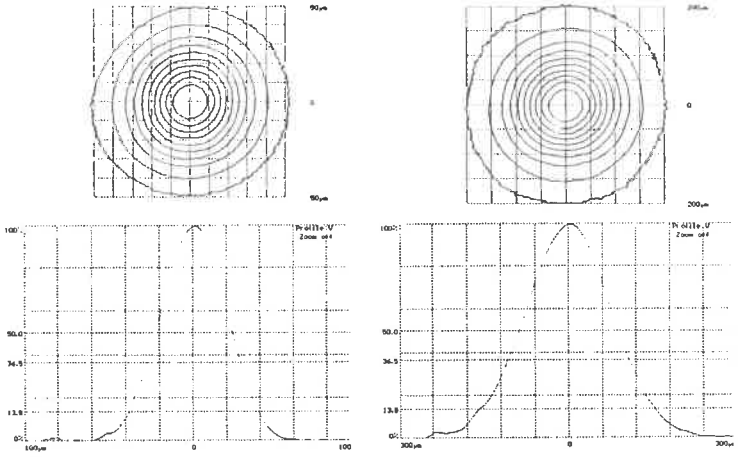

(a) Traveling distance: 0.5 mm (b) Traveling distance: 5.5 mm

Fig. 6 Contour and distribution of a light beam from a C-fiber with an 80- μ m core

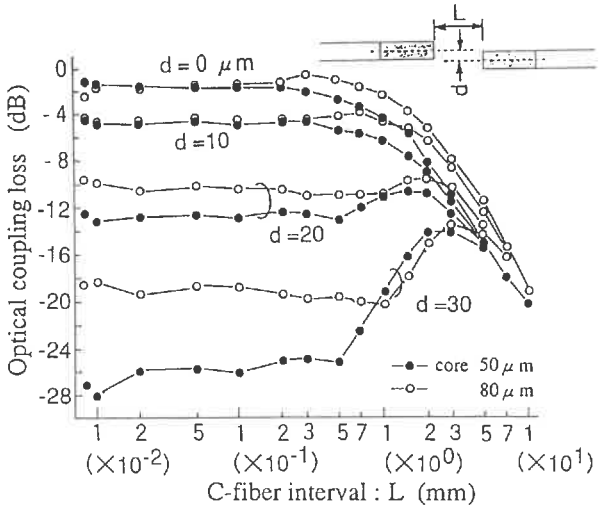

Fig.7 Relation between C-fiber interval and optical coupling loss

ROTATING LAPPING MACHINE WITH A PNEUMATIC BEARING SUPPORTED LAP

Gabriel Ascanio[(1)],Carlos J. Cava[(1)], Roberto U. Reséndiz[(2)], Ricardo Chicurel[(3)] and Rigoberto Nava[(1)]
(1) Centro de Instrumentos, UNAM, A.P. 70-186, Mexico, DF 04510
(2) DIBYASA, Indiana 260-704, Cd. de los Deportes, Mexico, DF 03710
(3) Instituto de Ingeniería, UNAM, Mexico, DF 04510

Abstract

The development of a prototype rotating lapping machine is presented. In order to improve the flatness and finish of the workpiece, a pneumatic bearing has been used to support the lap. Many factors such as stability and high load capacity were taken into account to design the bearing. With respect to the kinematics, lapping is characterized by the type of relative motion of the lap and work surface. The lap rotates around the machine axis. The workpiece holder can also rotate resulting in a rotational and translational relative motion.

Introduction

Lapping is regarded as the oldest method of obtaining a fine finish, and is extensively used in the engineering world in applications such as the finishing of gauge blocks and flats for checking production parts. Lapping is an abrasive process carried out by means of loose abrasive in which the role of the cutting points is played by grains finding momentary support by the laps. Lapping has four main purposes: to obtain a superior accuracy as to dimensions, to correct shape imperfections. to obtain smooth polished surfaces and to improve the fit between surfaces. The purpose of using a pneumatic bearing is to damp out vibrations that can have a negative effect on the surface quality. No reports of the applications in lapping machines were found in the literature so that the concept appears to be novel.

Description of the system

In the rotating lapping machine dicussed in this paper, a rigid structure supports the mechanism and the drive system, which consist of the lap, the pneumatic bearing and the motor. The lap used in this equipment is a 12 inches diameter and 1 inch thick plate made of ASTM 30 soft cast iron [1] and the conditioning rings are 4¼ inches cylinders made of AISI 4140 steel. The composition of cast iron is 3.25% C and 2% Si with Brinell Rockwell Hardness of 80. A soft material is used in accordance with the fact that the lap should always be softer than the material to be lapped in order to avoid charging the workpiece, and cutting of the lap itself [2]. Harder laps will often cause glazing and scratching while softer laps cause a loss of flatness and paralellism and will produce grayer finishes. Care was taken to make the plate heavy enough so that it would not distort in use. Workpieces to be lapped are supported by three holders mounted over

the lap at 120° between holders. The frictional force can be varied by using weights mounted on the workpiece holders. In this prototype, the abrasive and liquid are manually supplied.

The pneumatic bearing consists of two complementary conical parts. This geometry allows axial and radial loads in the same plane. The pneumatic bearing has two elements: one static (lower) and the other floating (upper) [3]. The clearance between the two elements is 2.8×10^{-5} m, when pressurized air is introduced at 490 kPa.

The drive system consists also of a ½ hp 4 pole induction motor coupled to a gear speed reducer with 5.1 ratio, so that the maximum rotational speed is 350 rpm. The lapping speed is controlled by means of a frequency changer which is directly connected to the motor. Normally, lapping equipment operates at a fix lapping speed, which is of the order of 250 rpm [2], however, in this prototype testings at different speeds will be possible. Othe operating conditions that will be varied are the abrasive size and lapping pressure to determine their effect on the stock removal rate [4,5]. Figure 1 shows a diagram of the rotating lapping machine and the conical air bearing.

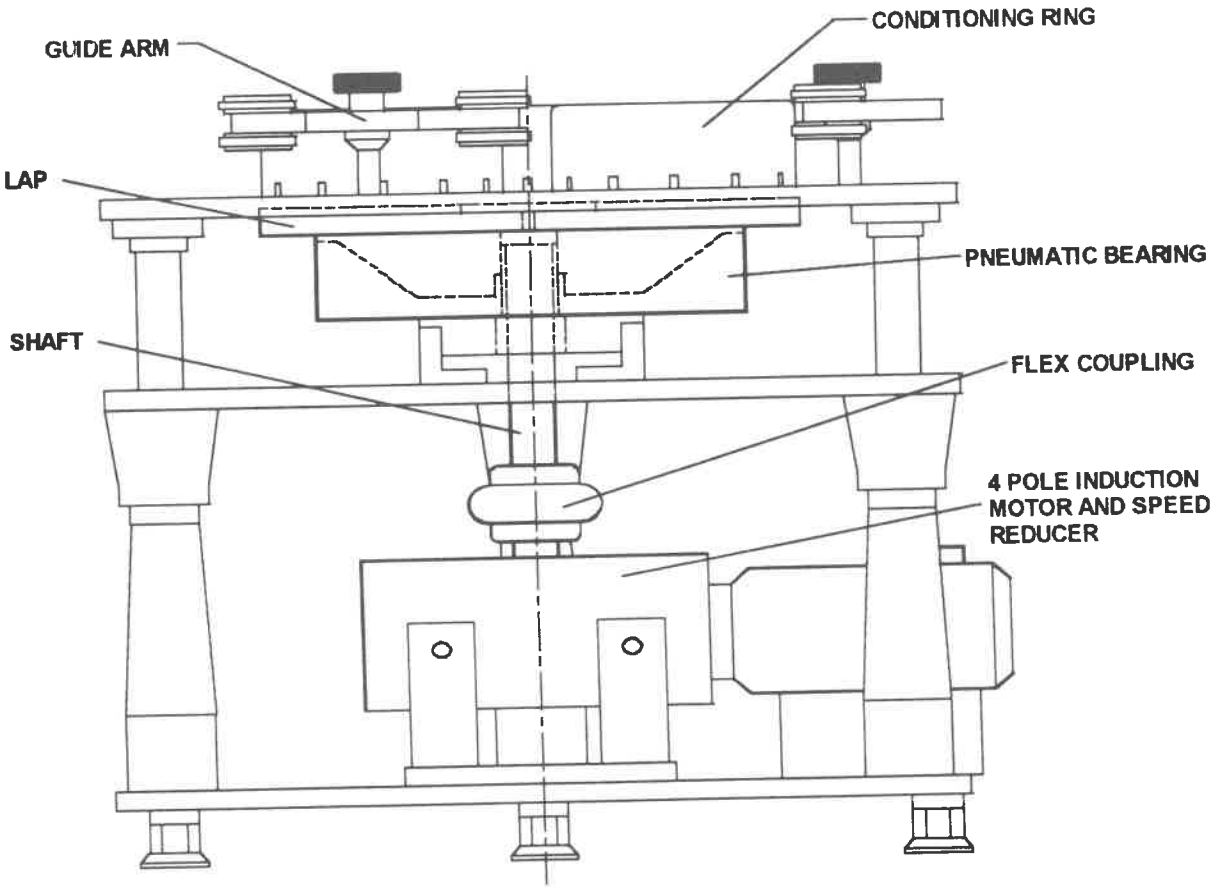

Figure 1 Rotating lapping machine with a pneumatic bearing

Kinematics of lapping machine

In the present lapping machine, the workholders rotation is induced by the drag exerted by tha lap. A fundamental problem arises is the calculation of the rate of such induced rotation as a function of the lap´s angular velocity.
Following Matsunaga [5], the problem can be solved by assuming a constant pressure distribution, P, and friction coefficient, μ, over the contact area between the workpiece and tha lap. Then the friction force per unit area at any point is μP and its direction is along the relative velocity vector.

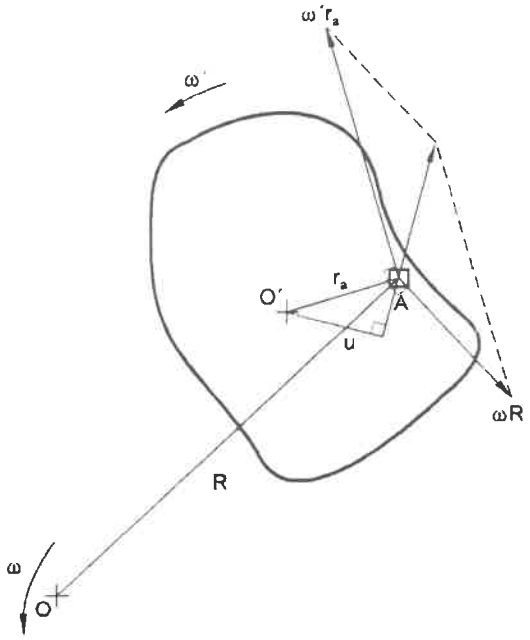

Figure 2 Velocity diagram of an arbitrary shape

Figure 2 is a diagram in which O represents the lap's axis and O' the workholder's axis. A workpiece of arbitrary shape is shown. The angular velocity of lap and workpiece are ω and ω' respectively. Other symbols are defined in the figure. Any point of the workpiece such as A has a velocity relative to a coincident point on the lap which is made up of two components: ωR in a direction perpendicular to OA and $\omega' r_a$ in a direction perpendicular to O'A. The resultant is in the direction of the friction force at that point. u represents the moment arm of such friction force about O'. The total moment on the workpiece is obtained as

$$M = \int\int_A \mu P u \, dA$$

In the above equation, u may be expressed in term of appropiate coordinates of the point A and the velocities ω and ω'. Upon carrying out the integration and setting M = 0, the desired relation between ω and ω' is obtained.

Test setup

In order to determine the effect of lapping pressure on the stock removal rate, five ½ inch diameter test pieces made of AISI 1045 steel quenched and tempered will be used. This test consists in placing each test piece using different loads so that the lapping pressure will be 1, 2, 3, 4 and 5 kg/cm². It must be taken into account that the test will be done by using a 5 μm white alumina compound and grease as vehicle. This compound will be continuously fed between the lap and the workpiece during the lapping operation. Plots of stock removal rate (Q) versus the pressure (P) will be prepared.

On the other hand, the effect of abrasive size on the stock removal rate will be studied by using five different mesh size white alumina compounds. Likewise, a ½ inch diameter probe will be lapped at a fix lapping speed and pressure. Also, plots of stock removal rate (Q) versus the mesh size will be prepared.

Conclusions

The prototype design of a Rotating Lapping Machine with a Pneumatic Bearing has been completed and about 60% of the parts have been constructed. Tests are being planned to compare flatness and roughness of lapped surfaces produced by this machine with those produced by a conventional machine. Also the effects of lapping pressure and abrasive size on the stock removal rates will be investigated.

References

[1] Lynah, P., Metals Handbook, vol. 3

[2] *Grinding and lapping compunds*, http:/www.mfginfo.com/mfg/lapvalve/lapartical.htm, United States Products, Co., Pittsburgh, PA, 1995.

[3] Resendiz, R., et-al, *Chem.Eng.Tech.* **14** (1991), p.p. 105-108.

[4] Kackzmarek, *Principles of machining by cutting, abrassion and erosion*, Peter Pergrinus, Lt., Warsow, Poland.

[5] Matsunaga M., *Fundamental Studies on Lapping*, Report of the Institute of Industrial Science, University of Tokyo, Japan, 1966.

SURFACE CONTAMINATION OF ABRASIVE DURING LAPPING

Adam W. BARYLSKI
Technical University of Gdańsk, Faculty of Mechanical Engineering
G. Narutowicza 11/12, 80-952 Gdańsk, Poland

1. Introduction

The high demands required today by design engineers for machine parts and tools necessitates very precise machining. The lapping process leads to a surface with low roughness and high precision. The topographical structure of the surface after lapping is very advantageous for sliding joints because of the high lubricant retention ability, as well as in non-sliding joints because of the high load - carrying ability. The range of lapped materials is very wide. This situation requires the use of natural and artificial abrasive materials and mainly such materials as micrograins of alumina, silicon carbide, boron carbide and diamond. Solid and liquid carriers distribute the micrograins on the surface of the lapping tool and the chemical active components make the machining more intensive [1].

One of the main disadvantages of lapping is the contamination of machined surfaces by micrograins of the abrasive material. The micrograins embedded into the machine surface during coarse lapping enter the „machining" zone during fine lapping. During service, contaminated surfaces are objected to excessive wear [3,5].

Since surface contamination is harmful and the methods of removal of the embedded micrograins are ineffective, the intensity of the contamination should be reduced as much as possible during the lapping process. The indentation of abrasive material into a machined surface should be considered as an element of general behaviour of abrasive micrograins including position of the micrograins, their size, shape as well as the physical and mechanical properties of the machined material and the lapping tool. The pressure and the lapping speed are also important.

2. Test Conditions

In the present investigation, surfaces contaminated by abrasive micrograins have been studied with an electron microscope and a microanalyzer. The combination of microscopy with X-ray analysis permits the study of secondary electron images and the X-ray images of the same spot on the sample [2,4,5]. The statistical size of abrasive slurry micrograins was estimated by means of an automatic image analysis (TV image analysis). The workpiece samples were made of spheroidal cast iron Zs55003 (2.6% C, 2.59% Si, 0.51% Mn, 0.15% P, 0.034% S, 0.15% Cu, hardness 1903 - 1942 MPa).

The samples were lapped in a special device with a planetary kinematic system. The paths of machined elements were of epicycloidal shape with almost constant speed of sample with respect to the lapping tool. The lapping disks were made of ferritic spheroidal cast iron Zs35022 (3.5% C, 2.3% Si, 0.51% Mn, 0.10% P, 0.045% S, 0.15% Cu, hardness 1491 - 1521 MPa).

3. Results

Tests were done in stages. In the first stage, the X-ray and spot analyses were carried out for the evaluation of intended micrograins with respect to the structural components of cast iron. In the second stage, the influence of lapping parameters such as pressure p, speed v and time t, on the contamination intensity were found. Complementary tests included the evaluation of the influence of micrograins size and concentration in the abrasive slurry as well as the method of cleaning the surface following lapping. Changes of radiation line intensity of specific elements in the X-ray analysis are equivalent to the changes of their concentration (Fig. 1).

Changes of radiation line intensity of specific elements in the X-ray analysis are equivalent to the changes of their concentration. At the same time the characteristic radiation intensity SiKα and FeKα were recorded at a sampling interval of 5 μm. The pulse counting time was 10 s. The results of the contaminated surface analyse were related to the radiation value of non-contaminated surfaces of similar roughness.

Due to the fact that in the spot method the relative error depends on the number of analysed spots, the subsequent tests were based on the surface distribution analysis of the elements. Statistical test have proved that the distribution of number of indented abrasive micrograins observed in particular fields of analysis follows a Poisson distribution [1)]. After estimating surface distribution for silicon it has been found that the concentration of indented abrasive micrograins is smaller for longer machining times.

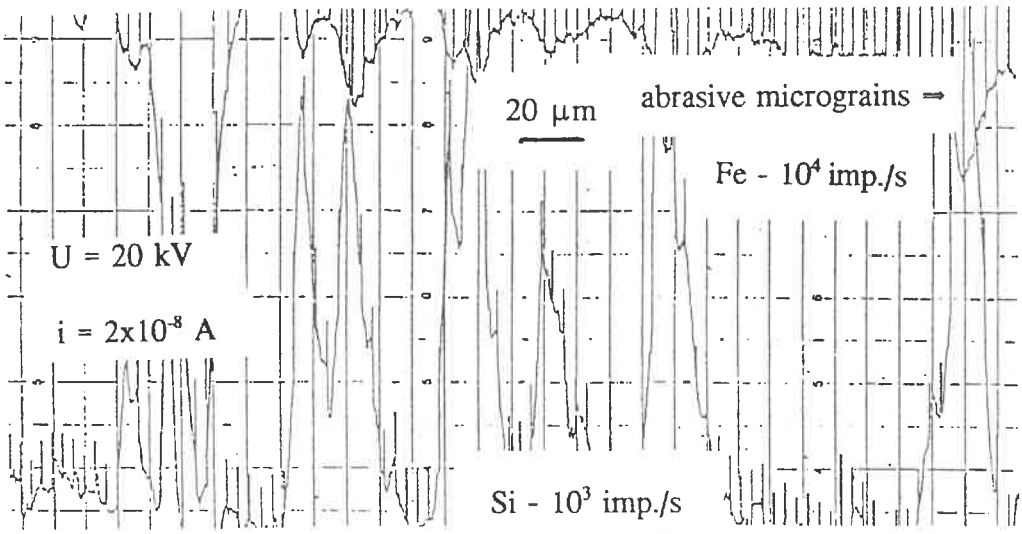

Fig.1. The linear distribution of Si and Fe on the surface of Zs55003 cast iron

Tests of intended micrograins have shown log-normal distribution for the micrograin size. Depending on the tested factors the mean value E(d) of the indented micrograins size with respect to expected values of abrasive slurry micrograins amount to 30-60%. As well as surface analysis for the distribution of elements, secondary electron images have also been made. These observations show that surface contamination with micrograins of size E(d) > 30 μm. is very rare. The fragments of micrograins, a result of their cracking and chipping, penetrate into pearlite and ferrite as well (Fig.2). An increase in penetration or micrograins into the graphite border and into the ferrite envelope has been observed. The microphotographic analysis also shows that the micrograin shape is subjected to changes approaching isometric form where the rounding radius at the corners and the aspects angles are icreased. The

influence of the packing factor B of the micrograin in the machining zone (Fig.3) and the micrograin size of cast iron contamination intensity have also been analysed [1].

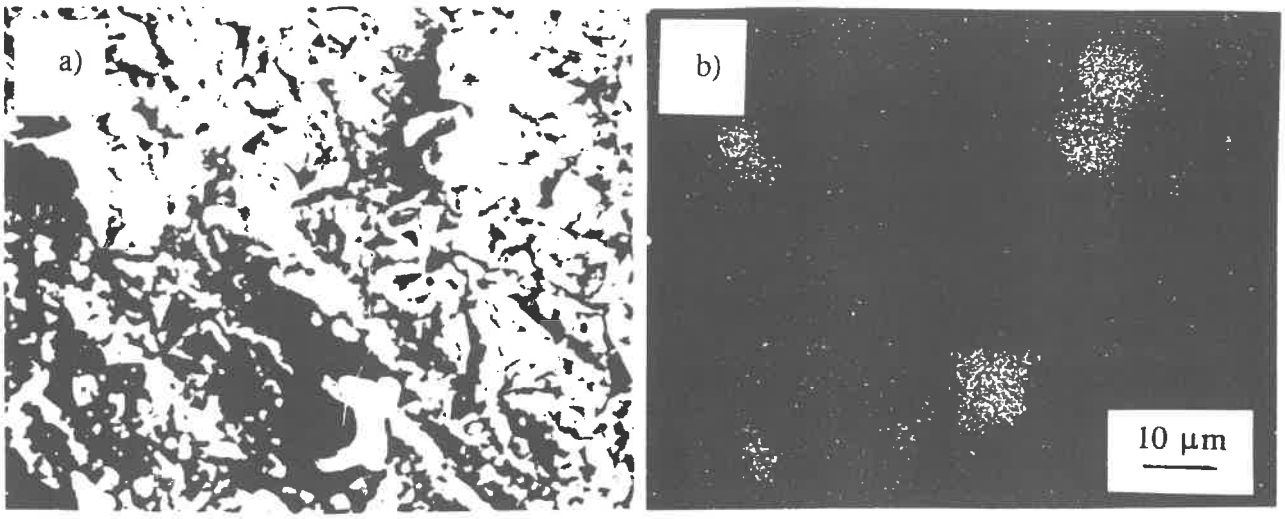

Fig.2. Microphotograph of Zs55003 cast iron: a) SEM, b) SiKα (U = 25 kV, JSM-35C)

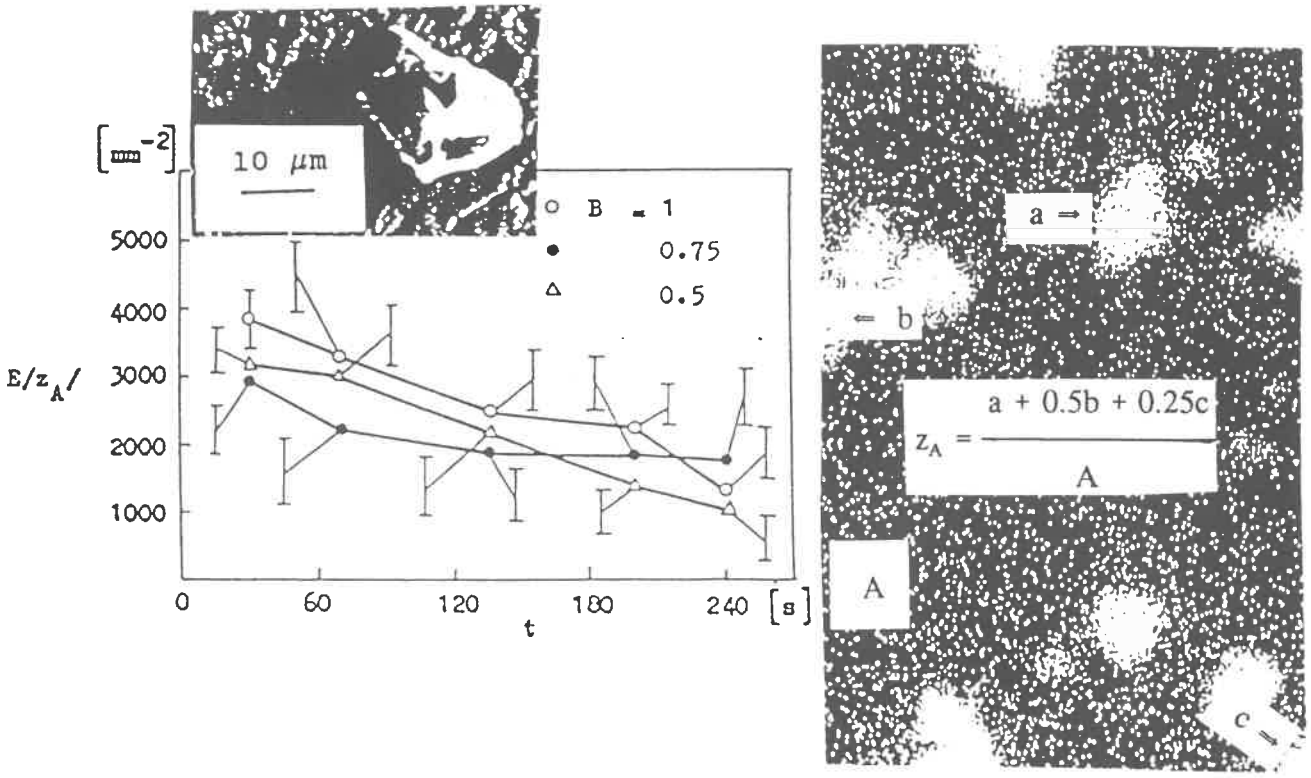

Fig.3. The effect of abrasive material packing factor B and the lapping time t on the concentration of micrograins contamination the surface of Zs55003 cast iron (silicon carbide 800, p=0.19 MPa, v=0.46 m/s)

4. Conclusions

The following conclusions can be formulated on the basic of the test that have been carried out:

- The effects of surface contamination with abrasive material can be reduced by prolonged time of lapping and by decreasing the micrograin packing in the machining zone in the beginning, or by reduction of unit pressure and lapping speed. During the lapping process the dispersion of abrasive micrograins increases where as the load by a single micrograin and its penetration dept into the machined material is reduced.
- The distribution of size for silicon carbide micrograins indented into the machined surface is log-normal. The same type of distribution is typical for the characteristic radiation value SiKα defined in the cast iron surface after lapping.
- For greater micrograin number in the abrasive slurry, the concentration of cast iron contamination micrograins is reduced.
- There are no significant differences in intensity of surface contamination by silicon carbide micrograins after lapping and cleaning (manual or ultrasonic).
- The number of micrograins indented into cast iron surface per individual microscopic field of view has a Poisson distribution with relatively great variance, where as the number of micrograins of defined size are characterizes by a Poisson distribution of relatively small variance.
- Contamination of any particular structural components of the cast iron is relatively uniform [1].

References

1. Barylski, A.: Sc. Bull. of Gdańsk Tech. Univ., 491 (1992), 3-196
2. Barylski, A.: Pract. Met., 25 (1988), 349-355
3. Misra, A.: Finnie, I.: Wear, 65 (1981), 359-373
4. Read, S.J.: Electron Microprobe Analysis, Cambridge Univ. Press, 1975
5. Ronen, A., Malkin, S.: Wear, 68 (1981), 371-389
6. Takowitz, H.: Practical Scanning Microscopy, Plenum Press, New York, 1975

MODEL-BASED PRECISION MACHINING SIMULATION FOR THE PREDICTION OF TOOL LIFE

Katsuhiro Maekawa
Department of Mechanical Engineering, Ibaraki University
4-12-1 Nakanarusawa, Hitachi 316, Japan

INTRODUCTION

Tool life is of particular importance in metal machining since it influences machining economics and product quality: in particular, flank wear or a change in the shape of the edge directly leads to a geometrical error in the finished machining of a product. Taylor's tool life equation has been extensively used to estimate the cutting performance of a tool; however this requires a long series of wear tests entailing the extensive examination of variables such as cutting speed, feed, tool geometry and work material, which is time-consuming, wasteful of materials and expensive. A comprehensive, scientifically-based approach should be adopted to overcome these disadvantages; it is desirable to predict a tool-life diagram based on a wear characteristic equation in conjunction with a numerical simulation of the machining process.

The present paper describes a model-based machining simulation system for the prediction of tool life. Briefly discussing the system and the wear characteristic equation to be used, the way in which the wear of a P20 carbide tool develops with cutting time when a 0.46%C steel is machined in air at practical cutting speeds is demonstrated. The simulation results are then compared with experiments.

A MODEL-BASED MACHINING SIMULATION SYSTEM

Figure 1 shows the overall structure of a model-based machining simulation system for the prediction of tool life. The purpose of the concept is to obtain the maximum possible output of information on a given machining process using the smallest amount of experimental data. Initially required are finite element assemblage, cutting parameters and material properties. Neither contact stress nor tool temperature is prerequisite for the prediction of tool wear. A time-incremental analysis of the machining process based on a finite element analysis yields not only the progress of tool edge wear but also the changes in cutting forces, tool temperature, stress and strain distributions and chip morphology.

The core of the analytical method comprises finite element elastic-plastic and thermal analyses. In principle the following elastic-plastic constitutive equation and energy equation are solved simultaneously:

$$\dot{\sigma}_{ij} = \left[\frac{E}{1+\nu} \left(\delta_{ik}\delta_{jl} + \frac{\nu}{1-2\nu}\delta_{ij}\delta_{kl} \right) - \alpha^* \frac{9G^2}{\bar{\sigma}^2(3G+H')} \sigma'_{ij}\sigma'_{ij} \right] \dot{\epsilon}_{kl} \tag{1}$$

$$\dot{\theta} + v_j\theta_{,j} - K\theta_{,kk} = Q/\rho C \tag{2}$$

Equation (1) is the tensor expression for isotropic hardening materials obeying the Mises yield criterion and the Prandtl-Reuss flow rule, where $\dot{\sigma}_{ij}$ is the Jaumann rate of Euler stress, $\dot{\epsilon}_{kl}$ is the velocity strain, σ'_{ij} is the deviatoric component of Euler stress and $\bar{\sigma}$ is the equivalent stress; E, G, H' and ν are Young's modulus, the shear modulus, the work hardening rate and Poisson's ratio, respectively; δ_{ij} is the Kronecker delta; $\alpha^* = 0$ for elastic deformation and $\alpha^* = 1$ for the plastic state. In Eq. (2) θ is the temperature, $\dot{\theta}$ is the time derivative of temperature, v_j is the

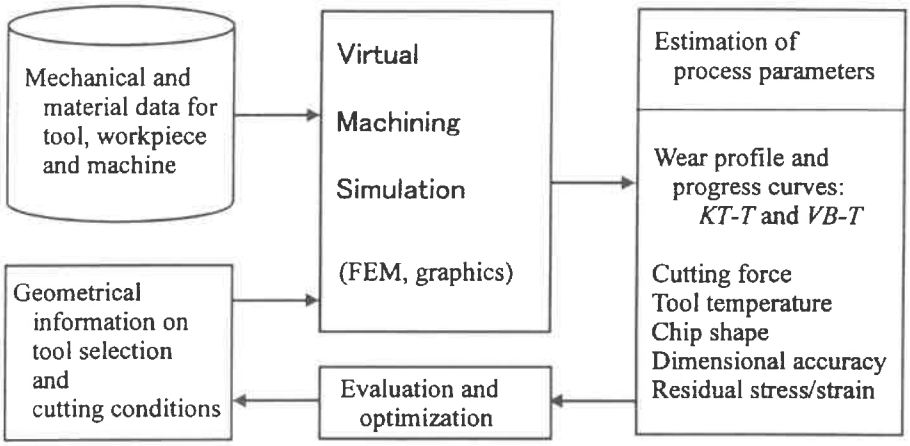

Fig. 1 Model-based machining simulation system for tool life prediction.

velocity, K is the thermal conductivity, Q is the internal heat generation, ρ is the density and C is the specific heat.

The finite element method can be employed to solve Eqs. (1) and (2) under the appropriate cutting geometry, material property and friction boundary conditions. The analysis applies to two-dimensional steady-state machining for which the iterative convergence method (ICM) is proposed. A review can be seen elsewhere [1, 2]. Since the tool is not rigid during machining its shape must be changed as both crater and flank wear develop. This can be done using an incremental method. When wear rate is estimated using a wear equation (see Eq.(5)) together with the temperature and normal stress obtained it is assumed that the tool wears away at the wear rate during a specified time increment, leading to slight changes in the shape of the edge. The ICM is repeated for the modified tool shape and information on chip geometry and flow stress within the chip is utilised as initial values at the subsequent interval. A steady state is also assumed at every time step so that the time does not correspond to the real machining time.

Good material property data are essential to the analysis. The uniaxial flow stress $\bar{\sigma}$ (MPa) of the workpiece is empirically expressed as a function of the strain $\bar{\epsilon}$, strain rate $\dot{\bar{\epsilon}}$ and temperature θ (°C) according to

$$\bar{\sigma} = \mathrm{A}(10^{-3}\dot{\bar{\epsilon}})^{\mathrm{M}}\mathrm{e}^{\mathrm{k}\theta}(10^{-3}\dot{\bar{\epsilon}})^{\mathrm{m}}\left[\int_{\theta,\dot{\bar{\epsilon}}\equiv h(\bar{\epsilon})} \mathrm{e}^{-\mathrm{k}\theta/\mathrm{N}}(10^{-3}\dot{\bar{\epsilon}})^{-\mathrm{m}/\mathrm{N}}d\bar{\epsilon}\right]^{\mathrm{N}} \tag{3}$$

where the coefficients A, M and N vary with temperature and k and m are constants. These values are obtained from Hopkinson bar tests [3]. Friction conditions at the chip-tool and workpiece-tool interfaces are expressed as

$$\tau_t = k[1 - \exp\{-(\mu\sigma_t/k)^{\mathrm{n}}\}]^{1/\mathrm{n}} \tag{4}$$

where τ_t is the friction stress, σ_t is the normal contact stress, k is the shear flow stress and μ and n are constants. The coefficients are obtained from split tool tests [4].

Tool wear characteristics are a key factor in the present study, being formulated as

$$\frac{1}{\sigma_t}\frac{\mathrm{d}W}{\mathrm{d}L} = \mathrm{C}_1 \exp\left(\frac{-\mathrm{C}_2}{\theta}\right) + \mathrm{C}_1' \exp\left(\frac{-\mathrm{C}_2'}{\theta}\right) \tag{5}$$

Equation (5) combines a thermally-activated adhesion model with a temperature-dependent abra-

sion model [5] and describes both crater and flank wear, where dW/dL is the wear rate per unit area, θ is the tool temperature (K) at the interface and C_1, C_2, C_1' and C_2' are constants to be determined for a combination of tool and work materials.

PREDICTED WEAR OF A CARBIDE TOOL IN STEEL MACHINING

The following case is typical: a 0.46%C plain carbon steel is orthogonally machined with a P20 carbide tool in air at a feed of 0.2 mm and cutting speeds of 100 and 200 m/min. The tool has a rake angle of 0° and a clearance angle of 4°. Table 1 lists the material properties measured and used in the simulation, including the values of the constants in Eqs. (3)–(5). The simulation programme installed on a UNIX workstation was interactively employed; it takes less than 10 minutes to obtain a wear progress curve together with a graphic presentation of other quantities such as chip shape and temperature distribution, as shown in Fig. 2.

Figure 2 shows a simulation result at a cutting speed of 100 m/min for (a) a sharp tool and (b) a worn tool when flank wear reaches a length of 0.6 mm. Due to the development of crater wear on the rake face a more curled chip is obtained. There is a marked difference in temperature distribution around the flank of the edge whereas no substantial changes can be seen on the rake face. The flank temperature rises to 700 °C when machining the steel with the worn tool. Plots of the depth of the crater and the width of the flank wear land at each time-increment yield the wear progress curves shown in Fig. 3.

Table 1 **Mechanical and thermal constants used in simulation**

Flow stress: $A=1350\exp(-0.0011\theta)+120\exp\{-0.00006(\theta-275)^2\}$, $M=0.036$,
$N=0.17\exp(-0.001\theta)+0.09\exp\{-0.000015(\theta-340)^2\}$, $k=0.00014$, $m=-0.0024$
Young's modulus $E=206$ GPa; Poisson's ratio $\nu=0.3$; Friction: $\mu=1.6$, $n=1.0$;
Tool wear: $C_1=11.98$ MPa^{-1}, $C_2=21950$ K, $C_1'=7.80\times10^{-6}$ MPa^{-1}, $C_2'=5300$ K

	Thermal conductivity K $Wm^{-1}K^{-1}$	Density ρ kg m^{-3}	Specific heat C J $kg^{-1}K^{-1}$
Workpiece (0.46%C steel)	46.1	7840	502
Insert (carbide P20)	66.9	11200	356
Shank (0.55%C steel)	36.0	7750	461

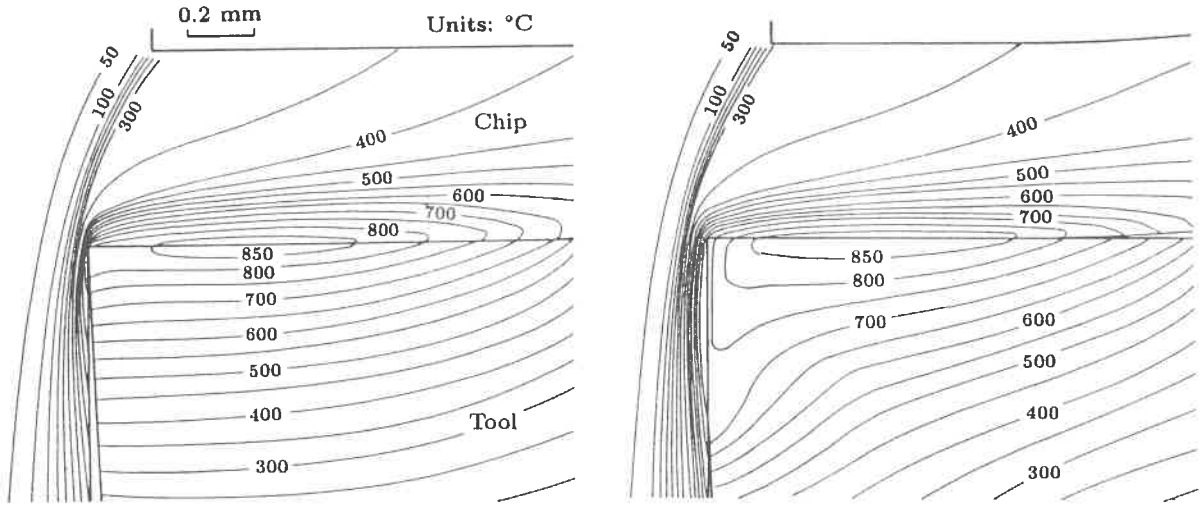

(a) Sharp tool (b) Worn tool with flank wear land of 0.6 mm

Fig. 2 Comparison of predicted chip shape and cutting temperature when machining 0.46%C steel with P20 tool at feed of 0.2 mm and cutting speed of 100 m/min.

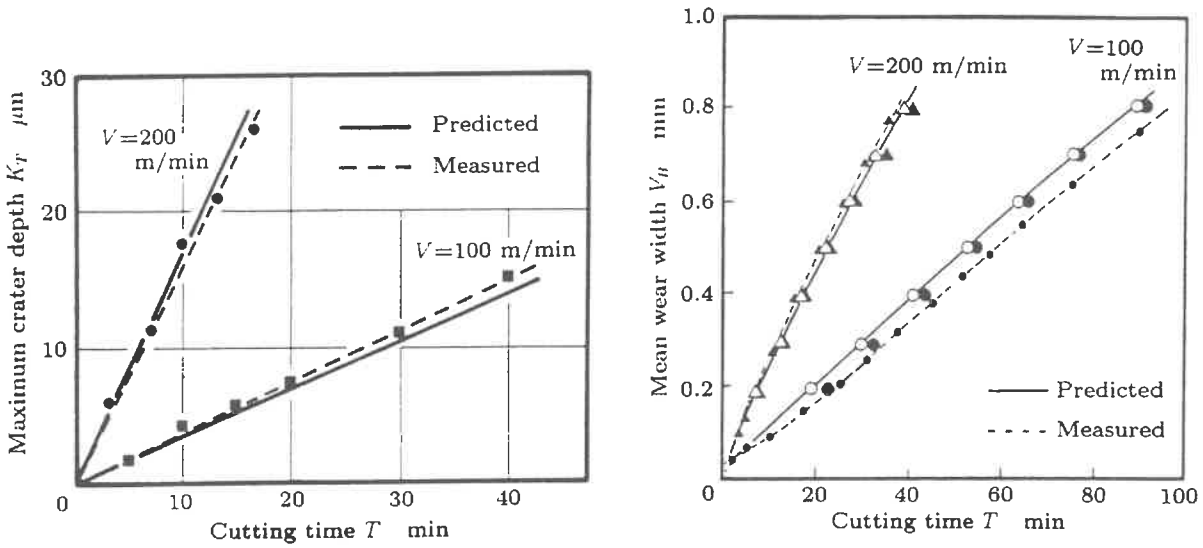

(a) Crater wear (b) Flank wear

Fig. 3 Comparison of predicted tool wear progress curves with experiment: cutting conditions are the same as those in Fig. 2.

Figure 3 shows variations in tool wear as a function of time: (a) maximum crater depth and (b) mean flank wear width at cutting speeds of 100 and 200 m/min. The solid lines show the prediction and the dashed lines the experiment. Cutting experiments were conducted in the semi-orthogonal turning of a steel bar of ϕ150–200×300 mm. The tool geometry was set at (0°, 0°, 6°, 6°, 15°, 15°, 0.5mm), tool shank dimensions were 30×30 mm and its overhang was 30 mm, which allows a stable cutting state without tool vibration. Reasonable agreement between the prediction and the experiment can be seen although an initial flank wear width of 0.03 mm is postulated in the simulation.

CONCLUSIONS

The present paper proposes a numerical method for the prediction of tool life in precision machining, in which an existing finite element model [2] is extended to cope with the deterioration of a cutting edge. A numerical simulation based on a wear characteristic equation is carried out to show how the wear of a cutting tool is developed with increasing cutting time. As a result tool life can easily be obtained in conjunction with changes in other quantities including cutting force, tool temperature and stress and strain in the work material. The applicability of the proposed method is shown by comparison with experiments when machining a 0.46%C steel with a P20 carbide tool under controlled laboratory conditions.

Acknowledgments – The author would like to thank Professor T. Kitagawa, Department of Mechanical System Engineering at Kitami Institute of Technology, Japan, for his valuable comments.

REFERENCES

[1] Usui, E. and Shirakashi, T., On the art of cutting metals – 75 years later, ASME Publ. PED–7 (1982) 13–35.

[2] Maekawa, K., Shirakashi, T. and Obikawa, T., Proc. Instn Mech. Engrs, Journal of Engineering Manufacture, B 210 (1996) 233–242.

[3] Shirakashi, T., Maekawa, K. and Usui, E., Bull. Japan Soc. Prec. Engng, 17 (3) (1983) 161–172.

[4] Maekawa, K., Kitagawa, T. and Childs, T.H.C., Proc. 2nd Int. Conf. on Behaviour of Materials in Machining, York, UK, Nov. 14–15 (1991) 132–145.

[5] Kitagawa, T., Kubo, A. and Maekawa, K., Proc. 23rd Leeds–Lyon Symposium on Tribology, Leeds, UK, Sept. 10-13 (1996).

AN ORTHOGONAL CUTTING STABILITY MODEL WITH VARIABLE DELAY LENGTH DUE TO TOOL MOTION

Thomas B. O'Reilly, Eric R. Marsh
The Pennsylvania State University
University Park, PA

Background

Regenerative chatter in machine tools occurs when irregularities in the surface of the part being machined grow with each pass of the tool. This is a severe problem in manufacturing industries which results in poor surface finish, poor dimensional accuracy and increased tool wear. Once chatter marks have developed in a workpiece they are very difficult to remove due to the regenerative effect which occurs as the tool cuts the material. The chatter marks left by previous passes of the tool cause the structure to vibrate in such a way that chatter marks of larger amplitude are produced with each pass. In some cases it is faster and easier to scrap the part and start over resulting in lost time and material.

Complicating the stability analysis for most types of machining processes is the fact that the forcing function that the tool experiences is related to both the current position of the tool and the profile of the surface that is being removed. This in turn is related to the position of the tool the last time it passed over that part of the surface. As a result, time delay terms appear in the equations of motion.

Figure 1 shows a typical model used to predict the onset of chatter in orthogonal, or plunge cutting, as would be performed on a lathe. This model only accounts for motion of the tool into and out of the workpiece. Most existing models used to predict the chatter limit, such as the one presented in Tlusty [4], are based on this type of analysis. For a model of this type with constant spindle speed the length of the delay term in the equations of motion is constant.

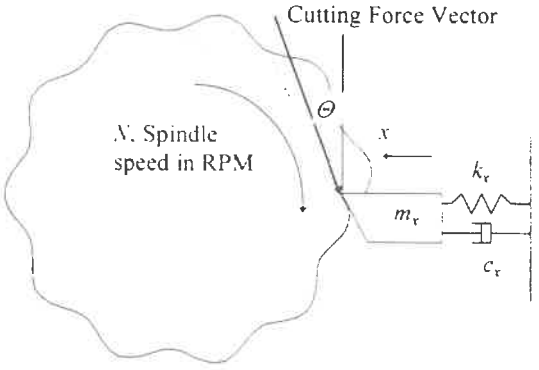

Figure 1. Diagram of a workpiece and cutting tool on a single degree-of-freedom spring/damper system.

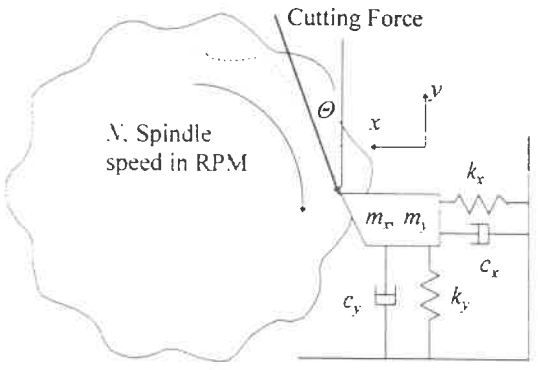

Figure 2. Diagram of a workpiece and cutting tool on two degree-of-freedom spring/damper system.

As part of research sponsored by the National Institute of Standards and Technology a new model of chatter has been developed which accounts for the motion of the tool in both the x- and y-directions as shown in Figure 2.

Analytical Model

The system was first examined using an analytical model. The two degree-of-freedom model used in this study assumes that the cutting force proportional to the area of the chip, and neglects the steady-state offset induced by the mean cutting force. In addition the stiffness and damping are assumed to be linear.

The equations of motion are:

X-direction: $m_x\ddot{x} + c_x\dot{x} + k_x x = -\alpha F$ where: $\alpha = \sin\Theta$ **(1)**

Y-Direction: $m_y\ddot{y} + c_y\dot{y} + k_y y = -\beta F$ where: $\beta = \cos\Theta$ **(2)**

Cutting Force Approximation:

$$F = bC(x(t) - x(t-\tau)) \quad \textbf{(3)}$$

Where b is the width of the cut, C is a material dependent cutting stiffness term, and τ is the length of time since the tool last passed over this point on the workpiece. For the single degree-of-freedom case this amount is fixed and is given by:

$\tau = 60 / N$ where N is the spindle speed in RPM.

For the two degree-of-freedom model the amount of the delay is not constant due to the motion in the y-direction. Because constant delay terms are much easier to deal with, it is necessary to convert the equations of motions to a form in terms of arc length, u, defined as follows:

$$u = Vt + y$$

where V is the linear velocity of the tool relative to the workpiece, and t is time. After performing this transformation the equations of motion can be written as:

X-direction:

$$m_x\left(\frac{du}{dt}\right)^2 x''(u) + c_x\frac{du}{dt}x'(u) + k_x x(u) = -\alpha bC(x(u) - x(u - d\pi)) \quad \textbf{(4)}$$

Y-direction:

$$m_y\left(\frac{du}{dt}\right)^2 y''(u) + c_y\frac{du}{dt}y'(u) + k_y y(u) = -\beta bC(x(u) - x(u - d\pi)) \quad \textbf{(5)}$$

Terms such as x', y' indicate derivatives with respect to arc leng . rather than time. The delay term is now the constant length $d\pi$, where d is the workpiece diameter, rather than a varying length of time. In these equations:

$$\frac{du}{dt} = V + \dot{y} \approx V$$

Since $\dot{y}$ should be small compared to V the system is linearized by neglecting the $\dot{y}$ term.

The tau-decomposition method (presented in Hsu [1], Lee [2] and Stepan [3]) was then used to examine the stability of this system and produce the stability chart shown in Figure 3. On this plot the straight horizontal line is based on the results of Tlusty [4], who derived the stability limit for a single degree-of-freedom model. The lower lobed line was produced using the tau-decomposition method and a single degree-of-freedom model of the system. The upper lobed line was produced by the two degree-of-freedom model described above. In all three cases the system parameters in the x-direction are the same.

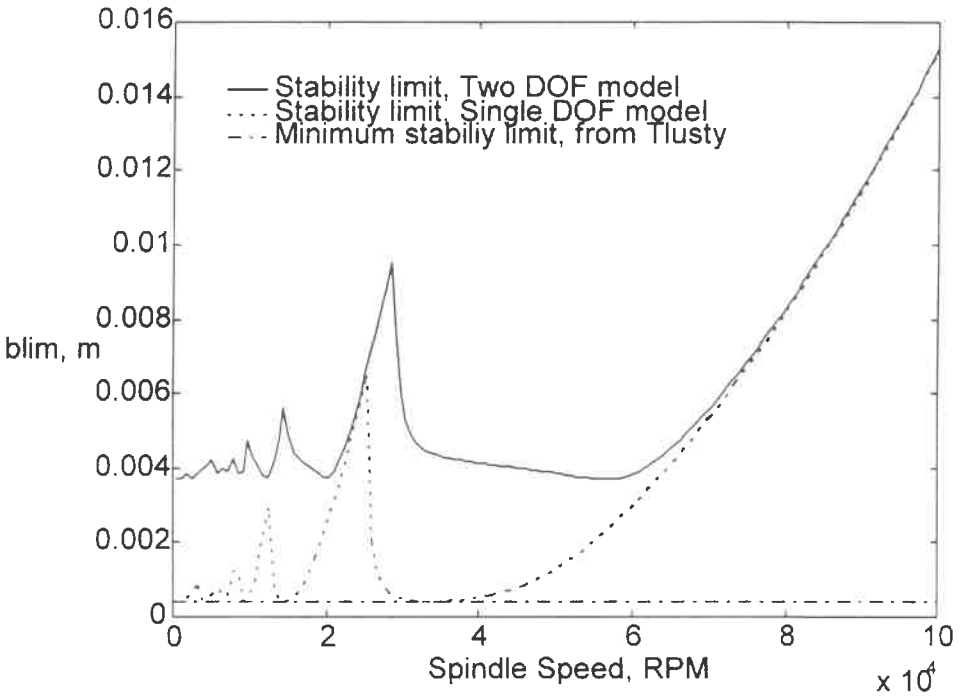

Figure 3. Two degree-of-freedom stability chart.

Numerical Simulation

A numerical simulation of this system was written to examine the dynamics of the cutting process under a variety of conditions. Using this simulation, the effect of different ratios between the x- and y-direction stiffness and natural frequencies was studied to determine its impact on the stability of the system and on the types of tool motions seen during cutting. The

simulatic. can also be used to numerically generate stability charts for comparison to the simplified analytical model and experimental data.

Experimental Work

A two degree-of-freedom flexure was designed and constructed to experimentally test this model. The stiffness of the flexure is much lower than the stiffness of the machine tool base. Therefore the dominant dynamics of a tool mounted in the flexure are due to the compliance of the flexure. In this way the behavior of the cutting tool approximates the model used to develop the stability predictions above.

Orthogonal cuts of different widths were made using a steel tool mounted in this flexure. Cutting tests were performed under a variety of conditions to study the effect that varying speeds and feed rates have on the system.

Conclusions

The initial results obtained using the model of chatter described above suggest a large gain in stability over a single degree-of-freedom model. Although this effect has not been verified experimentally, experimental data shows some effects that are worth investigating, some of which may be due to the *y*-direction motion. It is possible that the simplifications made in the system model are not appropriate, in which case the model may be overestimating the stability of the actual process. A more complete examination of the system, including the nonlinearities related to the delay term, is being performed using numerical models. In addition, more detail may be included such as a more comprehensive model of the cutting force, and the effect of the curvature of the workpiece.

To verify this more comprehensive model an experimental stability chart will be produced using the flexure. These results will also be compared to existing experimental stability charts found in the literature.

References

1. Hsu, C. S. "Application of the Tau-Decomposition Method to Dynamical Systems Subjected to Retarded Follower Forces," Journal of Applied Mechanics, June 1970, pp 259-266.

2. Lee, M. S., and C. S. Hsu. "On the τ-Decomposition Method of Stability Analysis for Retarded Dynamical Systems," SIAM Journal on Control, Volume 7, 1969, pp 242-259.

3. Stepan, G. Retarded dynamical systems: stability and characteristic functions, Longman Scientific & Technical , Essex, UK, 1989.

4. Tlusty, J. Machine Dynamics (1985). In King, Robert I. (ed), Handbook of High Speed Machining Technology (pp. 48-143). New York, Chapman and Hall.

FUZZY LOGIC MODELING OF ELECTROLYTIC GRINDING PROCESS

K. G. R. Koteswara Rao, G. Kuppuswamy
Indian Institute of Technology
Madras, INDIA

Key words : Electrolytic Grinding, Machinability Assessment, Fuzzy logic, Modeling and Simulation

Introduction

Electrolytic Grinding, one of the precision processes, is a material removal process by both mechanical and electrolytic actions. The process employs an electrically conductive metal bonded wheel on the anodic workpiece with an electrolyte introduced in the electrode gap. Due to numerous interacting variables involved, the mathematical modeling is very difficult to be formulated for process analysis. The nature of such machining responses are largely probabilistic rather than deterministic [1].

Need for fuzzy logic approach

Fuzzy logic modeling is based on mathematical theory combining multivalued logic, probability theory and Artificial Intelligence methods and can be used to tackle complex problems. The main advantage of Fuzzy logic analysis is that there is no need to establish a mathematical model. Fuzzy modeling is based on fuzzy set theory and the linguistic statements expressed mathematically which corresponds to the analysis of a human expert. Fuzzy systems base their decisions on inputs and outputs in the form of linguistic variables. The variables are tested with IF-THEN rules, which produces one or more responses depending on which rules are asserted. The response of each rule is weighed according to the degree of membership of it's inputs and the centroid of the responses is calculated to generate the appropriate output [2&3]. Typically the input variables for the face grinding process are feed force and current density, the output variables being material removal rate or grinding time and surface roughness.

Experimental details

The experimental set up shown in Fig.1, consists of an electrolytic diamond wheel (type D6A2C) of diameter 150 mm run at 3000 rev/min. and 120 double oscillations per minute with a stroke of 6 mm. A 12V d.c. supply was used. The electrolyte was a solution of 15 % wt. NaNo3 in water. WC tool bit (K20 grade) was face ground [4].

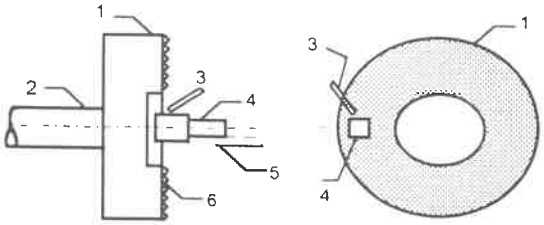

1. Metal bonded Grinding Wheel (Cathode)
2. Insulated Spindle
3. Electrolyte Supply
4. Work (Anode)
5. Work Table
6. Abrasive Particle

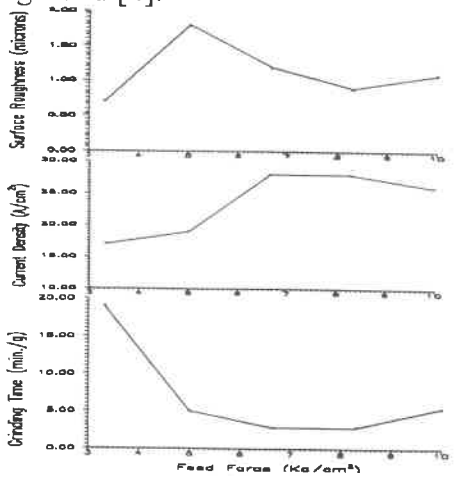

Fig 1: Electrolytic Grinding process and experimental results

Fuzzy logic modeling

The basic steps involved in the fuzzy logic analysis are as follows[5]:

1: Defining inputs and outputs

First, the ranges for the variables are identified, that represent the relevant conditions of the given process. The range of values that inputs and outputs may take is called the universe of discourse or dimension.

2: Fuzzify the inputs and outputs

Then meaningful linguistic statements are selected for each variable and expressed by appropriate fuzzy sets. The fuzzification for the feed force and current density are given in the Table 1 and Figs. 2 & 3 represent the fuzzy membership values for these variables.

Table 1: Fuzzification of the input variables

Feed force (kg/cm^2):

Fuzzy variable		Crisp Input Range
Very Low	(VL)	0-4
Low	(L)	2-6
Medium	(M)	4-8
High	(H)	6-10
Very High	(VH)	8-12

Current Density (A/cm^2):

Fuzzy variable		Crisp Input Range
Low	(L)	0-15
Medium	(M)	7.5-22
High	(H)	15-30

The change of states, like very low to low, is assumed to be continuous rather than abrupt and are represented by the set of overlapped triangles. Fuzzy memberships are assigned to the output variables just as for input variables and these are given in the Table 2 .

Table 2 : Fuzzification of the output variables

Grinding Time (min./g):

Fuzzy variable		Crisp Input Range
Extremely Low	(XL)	0-6
Very Low	(VL)	3-9.5
Low	(L)	6-12
Medium	(M)	9.5-15
High	(H)	12-18
Very High	(VH)	15-22
Extremely High	(XH)	18-25

Surface Roughness (microns):

Fuzzy variable		Crisp Input Range
Very Low	(VL)	0-0.6
Low	(L)	0.3-0.9
Medium	(M)	0.6-1.1
High	(H)	0.9-1.4
Very High	(VH)	1.1-1.7
Extremely High	(XH)	1.4-2.0

3: Create a fuzzy rule base

Table 3 refers to the fuzzy rule base matrix and these had been developed by heuristic guidelines of the analyst based on the experimental results, and represents the knowledge base.

Table 3 : Fuzzy rule matrix

F.F→ C.D↓	VL	L	M	H	VH
L	G.T:XH S.R:VL	G.T:H S.R:L	G.T:L S.R:M	G.T:XL S.R:H	G.T:L S.R:XH
M	G.T:VH S.R:VL	G.T:M S.R:L	G.T:VL S.R:M	G.T:XL S.R:VH	G.T:L S.R:XH
H	G.T:H S.R:L	G.T:M S.R:M	G.T:XL S.R:H	G.T:VL S.R:VH	G.T:L S.R:XH

F.F - Feed Force
C.D - Current Density
G.T - Grinding Time
S.R - Surface Roughness

4: Defuzzify the output

The inputs and outputs to the fuzzy rule base are fuzzy variables. The final step is defuzzification of the output for the given inputs into a crisp value. This is normally computed by either Fuzzy-OR method or centroid method of defuzzification on the fired rules.

Case Example:

For a feed force of 7.3 Kg/cm^2 removal and current density of 25 A/cm^2, the grinding time estimate is to be computed. By fuzzification, feed force comes under two categories, namely Medium and High fuzzy sets with 0.33 and 0.69 membership values respectively. Current Density comes under the High category with membership value 1.0.

Two rules are fired from the knowledge base rule matrix:

1)IF Feed force IS Medium (0.33) AND Current Density IS High (1.0)
THEN Grinding time IS eXtremely Low.

2)IF Feed force IS High (0.69).AND Current Density IS High (1.0)
THEN Grinding time IS Very Low.

First the firing strengths of the rules are determined from the two rules by the conjunction or minimum operator and these represent membership values in the corresponding fuzzy sets.

For rule 1) : $0.33 \wedge 1.0 = 0.33$ of category eXtremely Low (XL) of Grinding time

For rule 2) : $0.69 \wedge 1.0 = 0.69$ of category Very Low (VL) of Grinding time

Final output value of the Grinding time is obtained by the centroid method of defuzzification as follows.

The strength values or the fuzzy set memberships of the output after firing of the rules are used to fill in the concerned triangular membership functions of the output parameter to that strength level in the fuzzy sets diagram. So category Extremely Low (XL) is filled up to 0.33 and Very Low (VL) is filled up to 0.69 as shown in the Fig.4. These truncated figures are aligned and the centroid of that overlapped figure gives the output value of 4.8 min./gm. Similarly surface roughness value for the given inputs is 1.3 microns as given in Fig. 5.

Figs. 6&7 represent the output estimate surface for grinding time and surface roughness respectively based on similar computations. Figs. 8&9 represent the two dimensional views having one input variable fixed. Thus the method becomes a simulation tool for further process analysis.

Conclusions

The fuzzy logic inference methodology for modeling of Electrolytic Grinding Process appears to be a more meaningful alternative to the traditionally known methods for predicting output estimates quantitatively. The methodology presented is suitable in principle to any arbitrary machining problem provided that the associated knowledge base could be incorporated appropriately.

References

1) Iwata K Murotsu Y and Fujii S. A Probabilistic Approach to the Determination of the Optimum Cutting Conditions. ASME J. of Engg. for Ind., 1972, November, 1099-1107.
2) Zadeh L.A. Fuzzy sets. Informat. Contr., 1965, vol. 8, 338-353.
3) Schwartz D.G., Klir G.J., Lewis III H.W. and Ezawa Y. Applications of Fuzzy sets and Approximate Reasoning. Proceedings of the IEEE, 1994, April, 482-498.
4) Kuppuswamy G. Wheel variables in electrolytic grinding. Tribol. Int., 1976, **9(1)**,. 29-32.
5) Martin McNeill F., Thro E. 'Fuzzy Logic-A Practical Approach'. AP Professional, 1996.

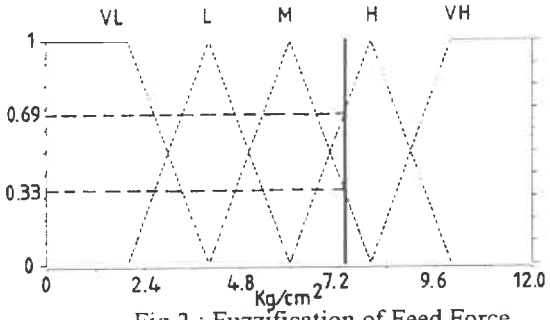

Fig 2 : Fuzzification of Feed Force

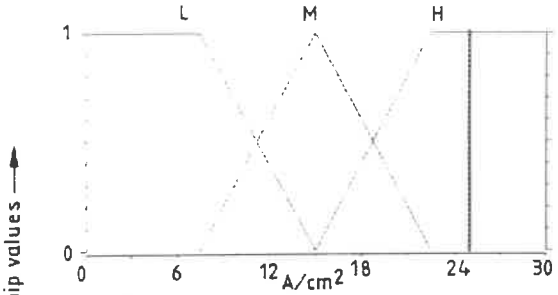

Fig 3 : Fuzzification of Current Density

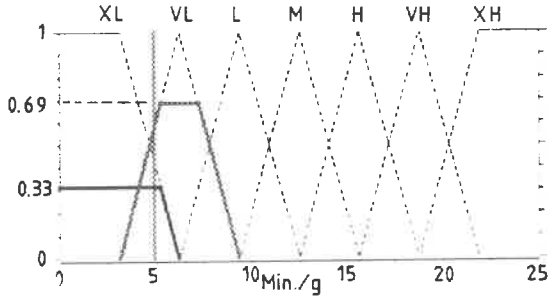

Fig 4 : Defuzzification of Grinding Time

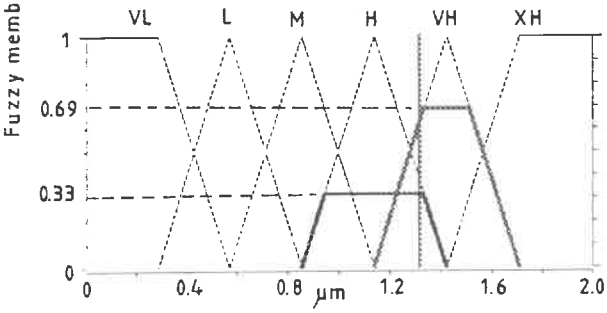

Fig 5 : Defuzzification of Surface Roughness

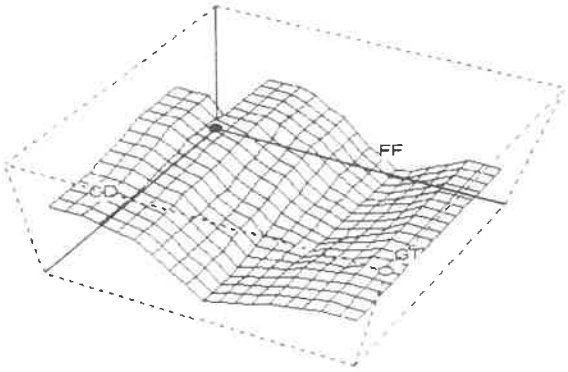

Fig 6 : 3-D View of the output against inputs (For Grinding Time)

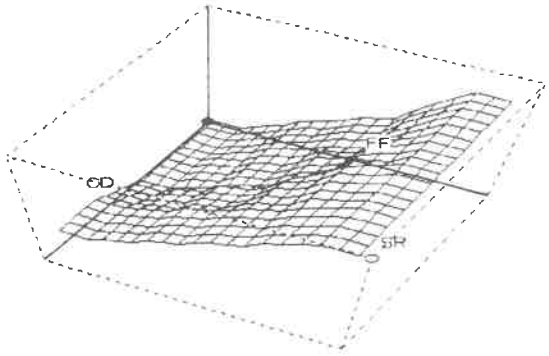

Fig 7 : 3-D View of the output against inputs (For Surface Roughness)

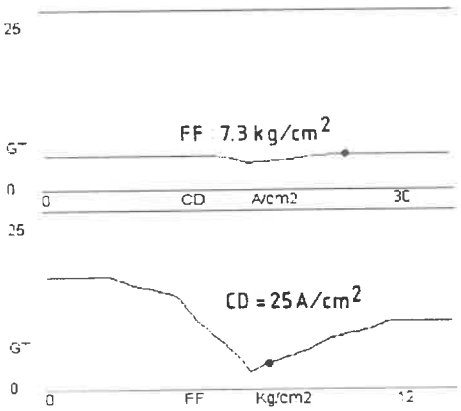

Fig 8 : 2-D View of the output against inputs

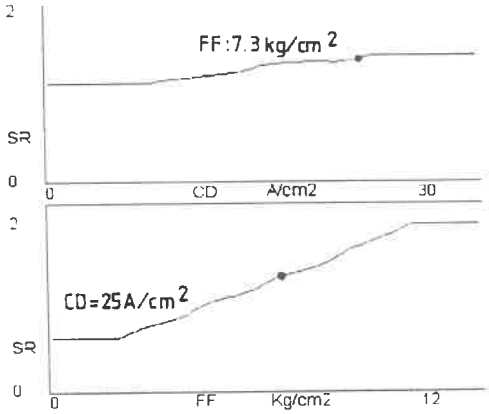

Fig 9 : 2-D View of the output against inputs

AN ADAPTIVE METHOD FOR PREDICTING RESIDUAL STRESSES ASSOCIATED WITH GRINDING INDUCED PHASE TRANSFORMATION

Mofid Mahdi and L. C. Zhang
Department of Mechanical and Mechatronic Engineering
The University of Sydney, NSW 2006, Australia

Abstract

This paper developed an efficient adaptive method to simulate the thermal residual stresses of grinding, particularly those associated with phase transformation when the workmaterial was subjected to a critical grinding temperature variation. The change of workpiece properties was modelled as a function of grinding temperature history to account for the surface hardness and volume increase during phase transformation. It found that if the properties of a workpiece is temperature-independent, the residual stresses in both the grinding direction and that perpendicular to it are tensile. The maximum residual stress in this case is about 1.25 times the initial yield stress of the material and is not affected by the further increase of the input heat flux generated by grinding. When the material properties are temperature-dependent, however, the increase of the surface hardness due to phase transformation will raise the level of the maximum residual stress to about 2.7 times the original yield stress. The volume growth associated with phase change plays an important role in the formation and nature of residual stresses.

NOTATIONS

Cr_{700}	the cooling rate at 700°C
Hv	Vickers hardness
l_a	relative peak location of a heat flux ($2\zeta a/L_c$), see Fig 1
M	martensite
P_e	Pecklet number ($vl/2\alpha$)
q	heat flux per unit grinding width
q_a	peak value of the heat flux
T	temperature rise with respect to ambient temperature T_∞
v	moving speed of the heat source, see Fig 1
Y	yield stress of the workmaterial
α	thermal diffusivity
σ	stress tensor

Subscripts

x,y,z	x-, y-, and z-directions, see Fig. (1)
y	yield
∞	room temperature

1. INTRODUCTION

The rapid heating and cooling in a grinding process may cause phase transformation and thermal plastic deformation in a workpiece and in turn introduce substantial residual stresses. The present study aims to develop an efficient adaptive approach to investigate the grinding residual stresses of phase transformation with the aid of the finite element method taking into account the property changes of workpiece materials due to phase transformation.

2. MODELLING

As shown in Fig. 1, the deformation of a workpiece subjected to a surface grinding operation is considered as a plane-strain problem. The heat generated by grinding is approximated by a triangular heat source moving along the positive direction of x-axis on the workpiece surface [1].

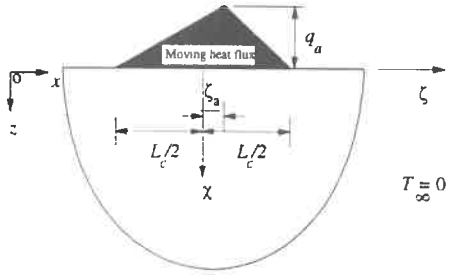

Fig. 1 Thermal grinding model

2.1 Material Properties

When a workmaterial experiences a critical temperature change in grinding, phase transformation will take place [1-2]. To study the residual stresses of phase transformation by the finite element method, We propose the following constitutive model for the EN23 steel alloy to describe the irreversible

deformation induced by martensite transformation. The variation of martensite hardness, Hv, can be determined by the steel composition directly [3-4], i.e.,

$$H_V = 463.2376 + 21.0 \log(Cr_{700}) \quad (1)$$

The yield stress of martensite, σ_y, is calculated by

$$\sigma_Y = 80.0 + 2.7544\ H_V \quad (2)$$

The yield stress of the workmaterial surface undergoing phase transformation is treated as a weighted average quantity based on the martensite percentage formed and original yield stress, Y. To demonstrate the grinding temperature history a typical transient surface grinding temperature is considered in relation to heat source movement (Fig. 2).

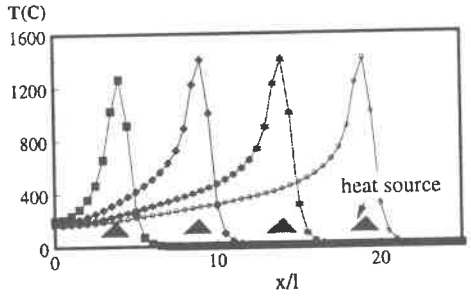

Fig. 2 Typical surface temperature (q_a=80 MW/m^2, l_a = 0.25, Pe_∞ = 1)

The figure indicates that the surface temperature approaches the steady state in a short time. For the surface layer in the vicinity of the ground surface, (z=0), the progress of the martensite yield stress profile has a strong relation to heat source (see Fig. 3).

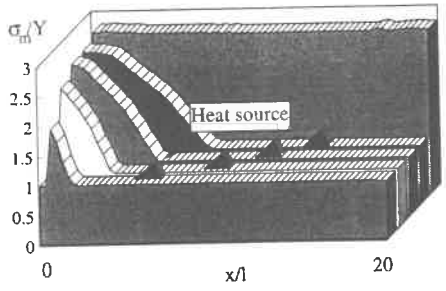

Fig. 3 Typical surface yield stress *vs* heat source movements (q_a=80 MW/m^2, l_a = 0.25, Pe_∞ = 1)

In an early stage, the development of martensite phase creates a hardened zone. It is clear that the surface yield stress increases to a level of 2.8 Y as more martensite formes.

According to the above understanding, an adaptive algorithm is built up, see Fig. 4, to account for the general change of material properties and perform the nonlinear calculations based on the grinding conditions,

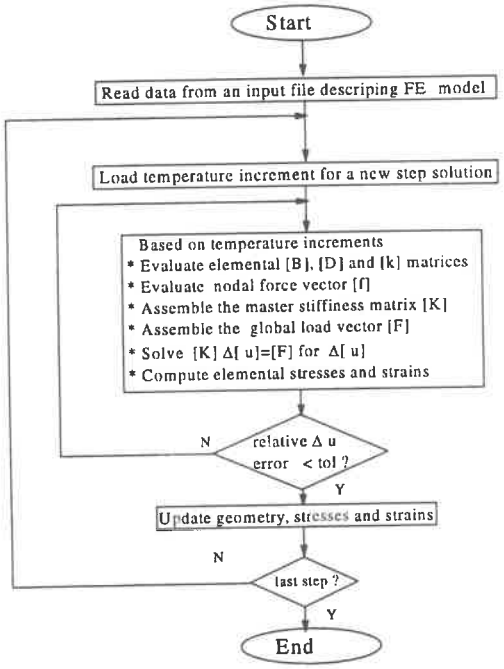
Start
Read data from an input file descriping FE model
Load temperature increment for a new step solution
Based on temperature increments
* Evaluate elemental [B], [D] and [k] matrices
* Evaluate nodal force vector [f]
* Assemble the master stiffiness matrix [K]
* Assemble the global load vector [F]
* Solve [K] Δ[u]=[F] for Δ[u]
* Compute elemental stresses and strains
N
relative Δ u error < tol ?
Y
Update geometry, stresses and strains
N
last step ?
Y
End

Fig. 4 An adaptive algorithm

When grinding conditions are not critical, the yield stress is constant. The results of developed algorithm are compared with those calculated by ADINA code [5] for the same grinding conditions and show close agreement in terms of the maximum residual stresses for different grinding conditions (Fig.5).

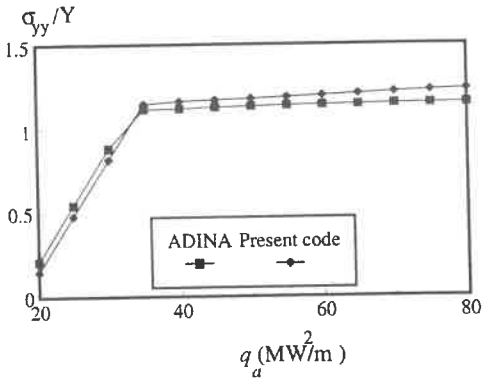

Fig. 5 Residual stresses (ADINA *vs* present code) (q_a=80 MW/m^2, l_a = 0.25, Pe_∞ = 1)

3. RESULTS AND DISCUSSION

Figure 6 compares the variation of residual stresses with surface hardening. In the case of surface hardening, stresses σ_{xx} and σ_{yy} are both tensile with a maximum of 2.6 times the initial yield stress of workpiece material. Therefore the hardening effect results in a higher tensile stresses since the yield stress of martensite is higher. The variation of residual stresses near the surface is nearly linear for both stresses but with a rapid change at the onset of phase transformation. At a higher depth, the residual stresses are similar for both cases regardless of surface hardening. This indicates that the residual stresses within the martensite zone is directly related to martensite depth. On the other hand, the permanent volume growth of martensite is restrained by the part without transformation thus results in compressive residual stresses (Fig. 7). The effects of the surface hardening and the volume growth are combined and considered in Fig. (8). The combination results in higher magnitudes of residual stresses regardless of their nature.

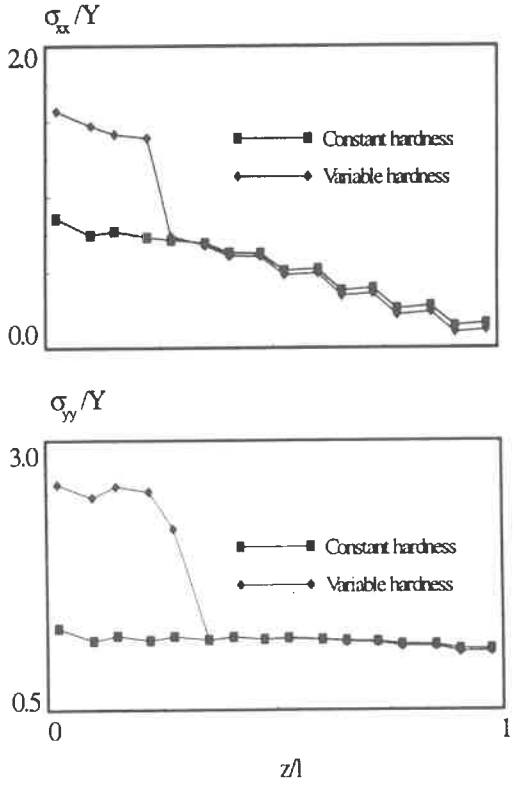

Fig. 6 Typical residual stress distribution *vs* effect of surface hardening (q_a=80 MW/m^2, l_a = 0.25, Pe_∞ = 1)

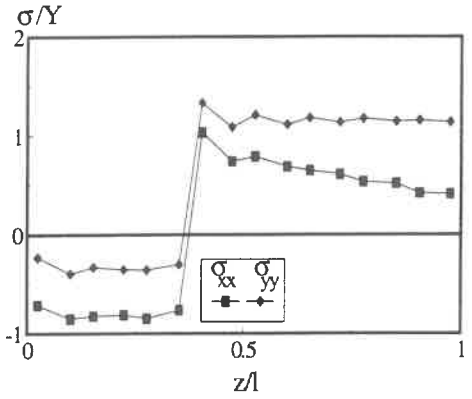

Fig. 7 Residual stress distribution *vs* effect of volume growth (q_a=80 MW/m^2, l_a = 0.25, Pe_∞ = 1)

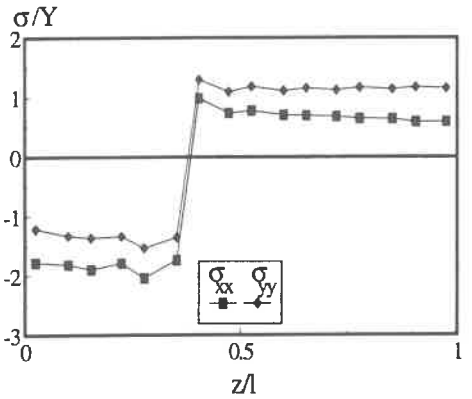

Fig. 8 Residual stress distribution *vs* effect of volume growth and surface hardening (q_a=80 MW/m^2, l_a = 0.25, Pe_∞ = 1)

4. CONCLUSIONS

A mathematical material model and a feasible adaptive algorithm have been developed for studying the residual stresses of grinding induced by phase transformation. Analysis can be carried out at the resolution of integration points. It concludes that

(1) the developed algorithm is a useful and stable tool,

(2) the workmaterial composition is a key factor in determining the phase change and the associated constitutive relations, and

(3) the volume growth and surface hardening dominate the transition of residual stresses from compressive to tensile.

Acknowledgment- The finical support from ARC Small Grant to the present study is appreciated. ADINA code was used for grinding temperature calculations.

REFERENCES

1 M. Mahdi and L. C. Zhang, The finite element thermal analysis of grinding processes by ADINA, Computer & Structure, **56**, (2/3) 313-320 (1995).

2 L. C. Zhang and M. Mahdi, Applied mechanics in grinding, part IV: grinding induced phase transformation. *Int. J. Mach. Tools Manufact.*, **35** 1397-1409 (1995).

3 British Iron and Steel Research Association, *The mechanical and physical properties of the british standard on steels*, Vol.2, Pergamon Press ,Oxford, UK (1969).

4 M Atkin BSc, B Met,FEM , *Atlas of Continuous Cooling Transformation diagrams for Engineering Steels*, Market Promotion Department, British Steel Corporation, BBC Billet, Bar and Rod Products, Sheffield, UK (1977).

5 ADINA R & D, inc, *Theory and modelling guide.* Report ARD 92-5, ADINA R & D, inc, December, (1992).

Transient Response of Wire Electrode in Wire Electrical Discharge Machining

Hisashi Yamada, Notake Mohri, Katsushi Furutani
Toyota Technological Institute, Nagoya 468, Japan
Takuji Magara
Mitsubishi Electric, Corp., Nagoya 461, Japan

1. Introduction

In wire electrical discharge machining (wire-EDM), fine machining with high accuracy can be realized since a fine thread wire is used as a tool electrode. Recently, there is a demand of higher accuracy in the manufacture of fine products. Thus, it is necessary to restrain the vibration of a wire caused by a force received in wire-EDM.

A numerous number of works have been done concerning the vibration of the wire electrode in steady state based on long term observation [1][2]. However, there are few papers discussing the transient behavior of a wire electrode forced by each discharge which moves discontinuously on the wire electrode. The authors investigated the randomness of wire displacement caused by concentrated force at a certain point during a thin plate cutting. It is found that an averaged external force acts on the wire electrode as an exciting force or a restraint force according to the direction of the wire movement at the moment when discharges occur. This is the reason why the amplitude of the wire vibration changes randomly [3].

In the analysis of wire vibration in steady state, wire can be approximated as a string . However, the force caused by electrical discharge acts on the wire intermittently, very locally and longitudinally. Thus, in order to analyze the wire vibration in detail when the force caused by discharge acts on the wire, it is necessary that the transient phenomena are to be investigated.

In this paper, in the discussion of transient vibration of the wire, we represent the wire as a beam under a constant tensile force. The vibration process of the wire is considered using experimental results right after voltage is supplied between the wire electrode and the workpiece.

Table 1 Experimental conditions

Wire electrode	ϕ0.200mm, brass
Wire guide	Internal diameter: ϕ0.205mm
Work piece	Steel 1mm and 20mm in thickness
Pulse setting	Open-circuit voltage ui: 80,150V
	Peak current of discharge ie: 145A
	Discharge duration te: 0.7μs
Distance between two support guides: L	80mm
Tension of wire: T	9.5N
Wire winding rate	145mm/s
Working fluid	Deionized water(Conductivity:15μS)
	Flow rate: upper 1.0l/min,lower 0l/min

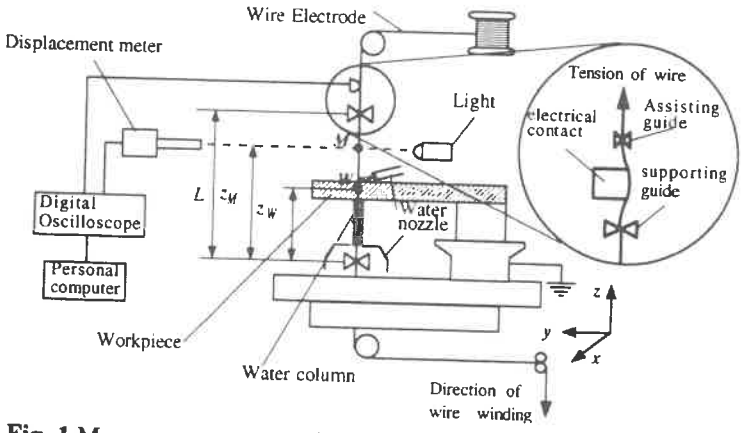

Fig. 1 Measurement system for wire vibration in wire-EDM

2. Wire vibration caused by single discharge

Before dealing with the vibration caused by continuous discharges, firstly it is necessary to investigate the response of wire electrode to a single discharge. Therefore, the transient response of the wire to a single discharge is observed. The measurement system is shown in Fig. 1 and the experimental conditions are shown in Table 1. The wire electrode is supported by an upper and a lower supporting guides, winded downward at a constant speed, and stretched by tensile force. It is bent by electrical contacts for supplying machining pulse voltage and assisting guides as shown in Fig. 1. Both of the supporting guides are made up of diamond having a hole with a clearance of 5mm, so that it enables the wire to pass through. The workpiece plate of stainless steel with 1mm in thickness is cramped at the height of the center between two supporting guides, so that the center is located approximately at the center of the workpiece in vertical direction.

The displacements of the wire electrode are measured with an optical displacement meter (OPT-FOLLOW 7100C, YA-MAN Corp., Frequency bandwidth: 500kHz). The measuring location is set up at M, so that the measured displacement is not disturbed by

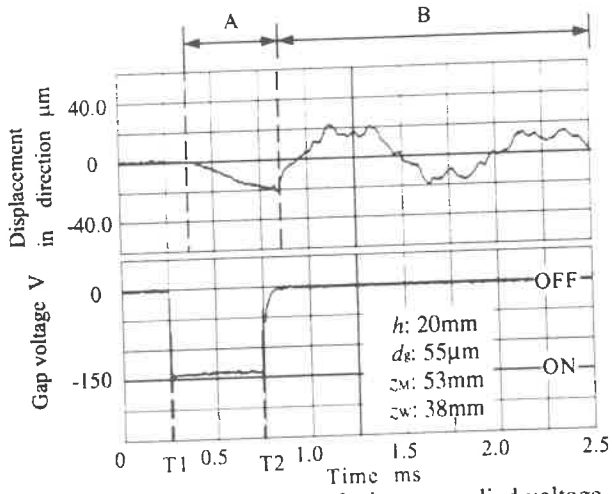

Fig. 2 Transient response of wire to supplied voltage and discharge

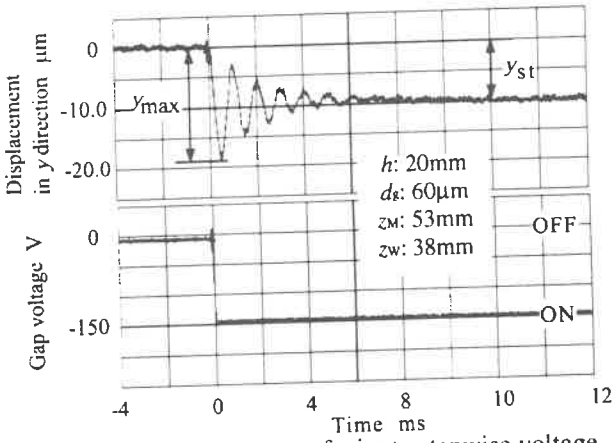

Fig. 3 Transient response of wire to stepwise voltage

flushing deionized water as working fluid. Fig. 2 shows an example of transient displacement of wire at the measurement point M and machining voltage. They are obtained just after the voltage is supplied to the gap between the wire electrode and the workpiece. In Fig. 2, T1 shows the time when voltage is supplied and T2 shows the time when an electrical discharge occurs. In the wave form of displacement, it can be observed that part A and B are affected by supplied voltage and discharge, respectively. There is a certain delay in the displacement wave form from the change of voltage. This is due to the wave propagation from the discharge point to the measurement point. Judging from the direction of wire displacement, it can be considered that the wire is attracted toward the workpiece after T1 and repulsed away from workpiece after T2. Their forces which act on the wire just after the voltage is supplied will be discussed in the following sections.

3. Influence of electrostatic force on wire electrode

3.1 Transient response to supplied voltage

In the above experiment, a discharge occurs just after the wire starts moving towards the workpiece. In order to investigate only the influence of the supplied voltage on displacement of the wire, the gap distance d_g between the wire electrode and the workpiece is set so that it would not lead to discharge. Fig. 3 shows displacement of the wire and amplitude of voltage just after stepwise voltage is supplied. In Fig. 3, the response of wire can be observed as an indicial response to the supplied voltage. The displacement of the wire cannot be observed in case of the experiment with the gap of air. As the dielectric constant of air is one-eightieth as that of water, this force which drives the wire can be considered to be electrostatic force.

3.2 Discussion on electrostatic force

In order to evaluate the electrostatic force quantitatively, the final displacement in steady state y_{st} shown in Fig. 3 will be compared with the displacement calculated on a model of electrostatic field. In the calculation of the electrostatic force, the wire and the workpiece are assumed to be a cylinder and a plane, respectively. The influence of edge portions at the top face and the bottom face of workpiece can be neglected. Then, a static displacement y_{st} is calculated as a deflection of the wire caused by the electrostatic force which acts uniformly on the wire in the region limited to the thickness of the workpiece.

The relation between calculated wire displacement and the gap distance d_g is shown in Fig. 4 with the measurement results for different supplied voltages and for different thicknesses of workpiece. The observing height z_M for workpiece thickness h=1mm is 48mm and 53mm for h=20mm. The height of the workpiece z_W is 38mm for both cases. In Fig. 4, the plotted points and the curves show the measured results and the calculated results, respectively. The measured results are fairly close to the calculated results. Therefore, the input to the wire system can be considered to be an electrostatic force just after the gap voltage is supplied. In this experiment, the electrostatic force acting between the wire and the plain was obtained by the observation of transient response of the wire displacement. Also the magnitude of electrostatic force during the machining of a groove can be obtained.

By looking at the transient part of displacement in fig. 3, from time 0 to the wave diminished to y_{st}, two following points are known. One is that the period of the vibration applies closely to the first normal mode. The other is that the maximum transient displacement y_{max} is approximately twice the value of final displacement y_{st}. Therefore, the displacement can be considered to show

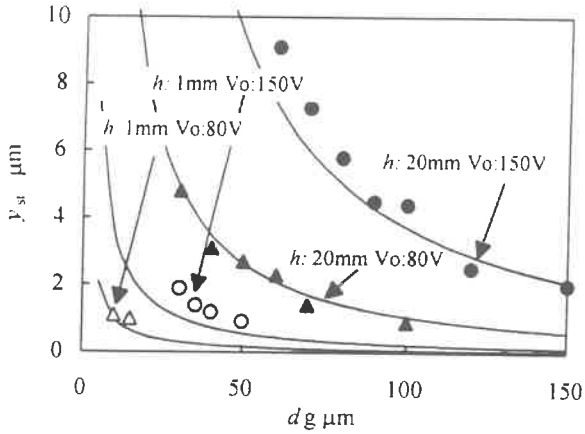

Fig. 4 Static displacement of wire caused by electorostatic force

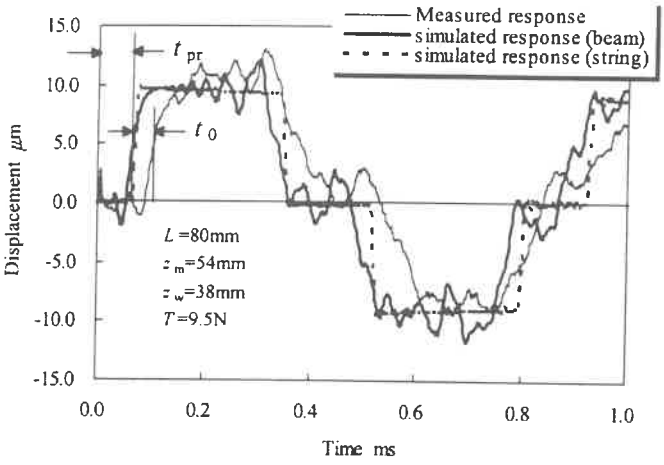

Fig. 5 Simulated response and measured response to impulsive force

the transient response to the step function of supplied voltage. Under the condition affected by an electrostatic force, the instantaneous decrease of the gap distance, right after voltage is supplied, becomes a primary factor which causes a discharge.

4. Vibration of beam under constant tensile force

In this chapter, the force which acts on the wire caused by a discharge is discussed. Just after the discharge occurs, the material of the workpiece melts at the discharge point and fluid surrounding the discharge point vaporizes. In this moment, the pressure caused by the vaporization removes the melting portion and then a discharge crater generates. Since the acting period of the pressure is shorter than the period of lower vibration mode, the pressure can be considered as an impulsive force. By looking at the period of part B in Fig. 2, it can be seen that the response wave to the impulsive force after discharging is different from the response wave form assumed in a vibration system of a string. The bending stiffness on the wire vibration is taken into consideration for the investigation of vibration system and the impulsive force.

4.1 Equation of wire vibration

It is supposed that the wire vibration system during machining is to be comprised of an elastic beam under a certain tensile force, damping force and an external force $F(z,t)$. The equation of motion in this vibration system can be written by

$$EI\frac{\partial^4 y}{\partial z^4} - T\frac{\partial^2 y}{\partial z^2} + \rho A\frac{\partial^2 y}{\partial t^2} + c\frac{\partial y}{\partial t} = F(z,t) \quad (1)$$

where $y(z,t)$ is the displacement of the wire, E is Young's modulus, I is the moment of inertia, ρ is the density, A is the cross-section area and c is the damping coefficient under the consideration of water viscosity. The first term of equation (1) shows the force affected by stiffness. If the stiffness can be disregarded, it will be an equation for a string. From now on, the vibration system in which stiffness of the wire is considered is called a "beam model" and the vibration system in which stiffness is disregarded is called a "string model".

4.2 Numerical simulation of the wire

The numerical simulation based on equation (1) is calculated using the finite differences method under the condition that both ends are fixed.

It is assumed that influence of wire winding rate (0.145m/s) on the displacement response can be neglected because the wire winding rate is much slower than the propagation speed (187m/s).

Regarding the above vibration system, it is assumed that the impulsive force caused by a single discharge acts on a wire very locally. It is defined that a rectangular impulse of a magnitude F_0 and period t_1 acts on an element of the wire at the height of the workpiece (z_w=38mm). The response of the wire displacement to the impulse is observed at the observing height (z_M=54mm). The initial conditions are given y=0 for all elements. In the numerical simulation, a distance interval of Δz=0.1mm in z-direction and a time interval of Δt=10ms were used.

4.3 Estimation of impulse caused by a discharge

In order to evaluate the availability of the model for the wire vibration, first, the simulated results are compared to the measured wave forms of the response to a single discharge. Then, an impulse caused by a discharge will be determined so that the calculated response corresponds to the measured response. The conditions of the simulation are shown in Table 2. In the experiment, the workpiece (h=1mm) thickness and the magnitude of supplied voltage

Table 2 Parameters in simulation of wire vibration

Young's modulus: E	N/m^2	9.6×10^{10}
Moment of inertia: I	m^4	7.854×10^{-17}
Tension of wire: T	N	9.5
Density: ρ	kg/m^3	8.53×10^{3}
Cross-section area: A	m^2	3.14×10^{-8}
Damping coefficient: c	m/(kg s)	0.05
Distance between two support guides: L	m	0.08

(80V) is set in order to disregard the influence of an electrostatic force.

The response in the experiment and the simulation are shown in Fig. 5. In the figure, the thin solid line, the thick solid line and the dotted line show the experimented result, the simulated result of the beam model and the simulated result of the string model, respectively. The simulated results of the beam model and the string model show that the wave form of higher frequencies and the reflected waves are represented clearly in the beam model. Thus, the condition of the supporting guides and the impulse which acts on the wire can be evaluated using the method above.

Since the observing point is offset from the discharge point, the simulated response at the observing point will not exactly be synchronized to the instance of the discharge meaning there is a time in delay t_{pr} as shown in Fig. 5 for the wave propagation. In the experiment, the observed response delays furthermore -t_0- as shown in Fig. 5. This is due to the time required to generate pressure on the wire after the discharge.

5. Consideration of transient behavior of wire electrode

As a result, after the gap voltage is supplied, the transition of wire behavior (a) to (d) in Fig. 6 follows the below:

(1) At the moment the voltage is supplied stepwise between a wire electrode and a workpiece, the wire is attracted to the workpiece. The transient response of the wire represents the indicial response to electrostatic force which is distributed uniformly on the wire.

(2) As the result of the attracting force, the gap between the wire and the workpiece becomes narrow. It leads to the occurrence of discharge.

(3) Just at the occurrence of discharge, the attractive force disappears. After a certain interval, an impulsive force acts on the wire very locally, and the wire is deformed locally where the impulsive force is received.

(4) The wave of displacement propagates toward the both ends with time. Thus, the displacement of the wire is observed as an impulse response, with the initial condition of the wire just before the discharge occur.

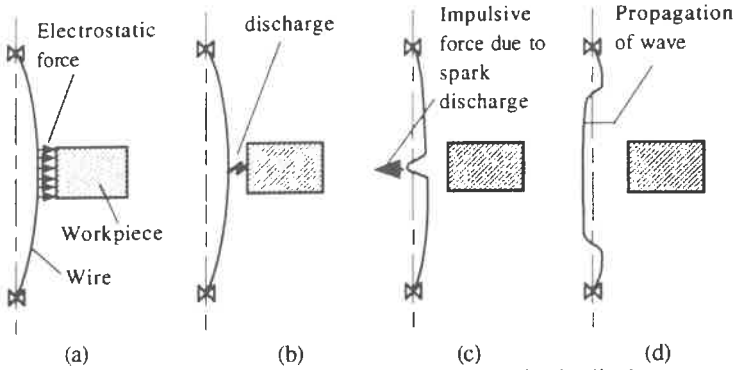

Fig. 6 Typical behavior of wire electrode in single discharge

6. Conclusions

In this paper, the influence of pressure caused by each discharge and the influence of an electrostatic force on wire displacement are investigated under a mechanical model supposing the tool electrode to be a beam under a certain tensile force. The obtained conclusions are as follows:

(1) The response in experiments is fairly close to the impulse response simulated with the beam model of the wire.

(2) Owing to small gap between electrode and workpiece, this electrostatic force acts on the wire electrode as a uniformly distributed load along the wire. The displacement of the wire induced by the electrostatic force is considered as the indicial response to applied stepwise voltage. The initial position for the impulse response to the following discharge is given by the displacement.

These considerations of the wire response to the exciting force caused by a single discharge helps us to investigate the primary factors of the wire vibration by continuous discharges in wire-EDM. Consequently it will lead to the precision machining in the future.

Acknowledgment

The authors wish to thank to Mr. Tamio Takawashi of Mitsubishi Electric Corp. for his helpful suggestions.

References

[1] K.Horio, et al.: The study of wire behavior in wire EDM (1st report) -Wire vibration and discharge phenomena-, J. Jpn. Soc. Electrical Machining Eng., VOL.14, No.28, pp.30-41(1981)

[2] W.Dekeyser: Knowledge-based system for wire-EDM, Ph.D. Thesis, K.U. Leuven, Belgium, pp.6-25 (1988) 6

[3] H.Yamada, et al.: Modal analysis of wire electrode vibration in wire-EDM, Int. J. Electrical Machining, No. 2, pp.19-24(1997)

THREE–DIMENSIONAL MICRO FORMING USING METAL JET

Katsumi Yamaguchi, Katsuhiko Sakai, Takashi Yamanaka, Takao Hirayama

Department of Mechanical Engineering, Nagoya University
Furo-cho, Chikusa-ku, Nagoya, 464-01 JAPAN

1. Introduction

In recent years, various micromachining processes have been developed to meet the demands for micro machines. It is well known that small sensors or micro parts are produced by a silicon fabrication process [1][2]. LIGA, laser assisted etching and 3–dimensional photo fabrication processes have also been developed to produce various microcomponents [3]–[7]. However, 3-dimensional parts cannot be formed by these processes, and the material is limited to silicon or plastics. In this study, the authors developed a method to form micro parts by a metal jet. This method is similar to an ink jet printer. A thin layer is first formed by molten metal jet ejected through a nozzle and a second layer is formed on the first layer. The repetition of this process produces the 3-dimensional parts. In this research, the basic performance of the metal jet head is examined, and some examples of 3-dimensional forming and a 3–dimensional circuit made by fusible alloy and Pb-Sn alloy are shown.

2. Principle of ejecting metal-jet drops

Figure 1 is an illustration of the metal-jet head used. A metal drop is ejected from the nozzle by a piezoelectric actuator. This device is very different from a ink jet printer head in various points. The density of the metal, for example, is much greater than that of ink, and the metal surface tension and metal-to-nozzle wettability are different from those of ink. Further, the melting point of alloy metal is too high for the layer type piezoelectric actuator. Thus, great care was taken to avoid these problems in the design of the metal jet head. For example, the actuator is protected against thermal damage by insulators and heat radiator.

The metal drops was generated as follows. The metal alloy is melted in an electrically heated tank which is mounted above the nozzle, and the molten alloy is supplied to the chamber by gravity. The chamber has a diaphragm which connects to the piezoelectric actuator. This actuator is driven by the signal from a pulse generator through a high-capacity amplifier. The nozzle diameter is 0.2 mm and the metal drop ejected is about 0.30 to 0.40 mm in diameter. In this experiment, fusible alloy (Bi–Pb–Sn–Cd–In) and solder (Pb–Sn alloy) were used with a melting point of 47°C and 183°C, respectively.

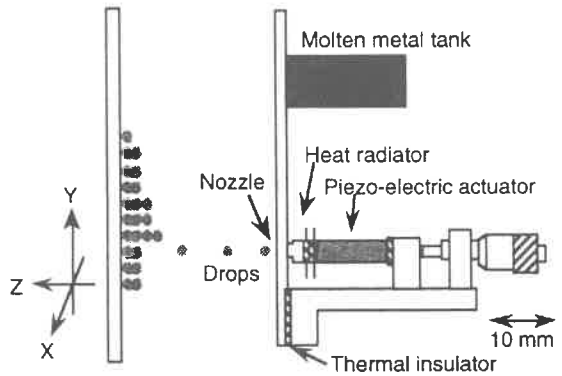

Fig. 1 Schematic illustratration of metal–jet head and principle of 3–dimensional forming

3. Performance of metal-jet head

Voltage, pulse frequency applied to the actuator and the temperature of molten metal are the parameters greatly affecting the size, speed, shape, stability and reproducibility of ejected drop or dot on the base plate. Therefore, suitable conditions have to be found to produce a model for good accuracy. First, the shape of a flying fusible alloy drop is investigated. Figure 2 shows a continuous shot of the drop observed by a high-speed video system. The time interval of shots was 0.001 second. The drop seems to be oval and stable during the flight. One drop is ejected by one pulse signal. From these frames, the initial speed of drops was estimated, and shown in Fig. 3. The speed of drops can be controlled by the voltage applied to the actuator. Second, the accuracy of "printing" on the base plane was studied. Metal dots are ejected in line onto the base plane. Figure 4 is an image of the adhered dots under scanning electron microscope. The size and intervals of the dots are almost uniform. For example, the mean diameter of drops is 403±14 μm, and positional error is within ±13 μm.

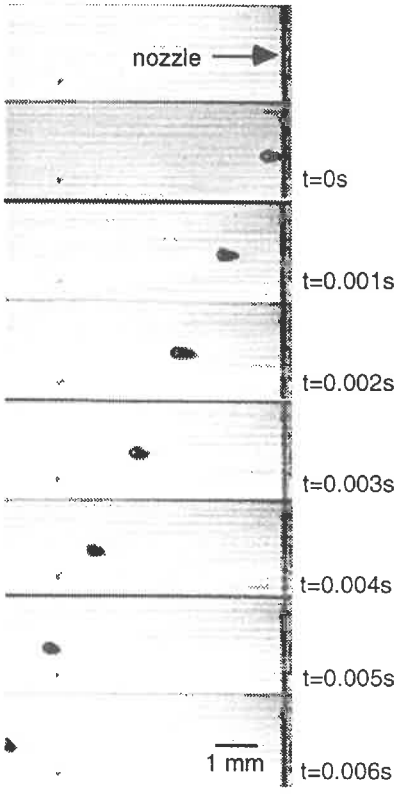

Fig. 2 Flight of a metal drop taken by high speed video system.

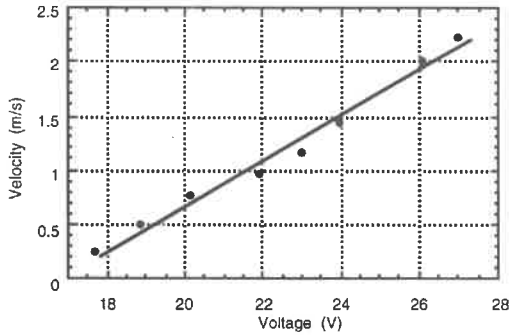

Fig. 3 velocity of metal drop

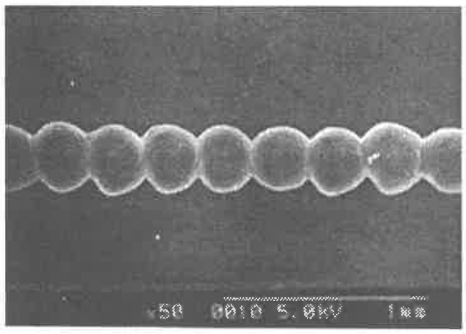

Fig. 4 SEM image of the metal dots on the base plane

4. 3–dimensional forming

Typical examples of a 3–dimensional model made by fusible alloy and solder are shown in Fig. 5 and 6. Models are formed by the layer-by-layer technique described in the previous section. Figure 7(a) presents an SEM image of the model surface, which is seen to have many small dimples. Although a few vacancies remain in the cross section shown in Fig. 7(b), the metal dots are very densely packed. To confirm this, the bulk density of the models was measured by the Archimedes method. The bulk density changes from 8.4 to 9.2 $g \cdot cm^{-3}$ as shown in Fig. 8. The density of the fusible alloy is 9.4 $g \cdot cm^{-3}$, so the maximum packing rate reaches 98%.

Figure 9 shows the coil of solder formed in the transparent resin. The alloy dots are connected with each other to assure electric conductivity. Therefore, this model can be used as an electrical circuit. This method can be applied to the production of the functional gradient material. A typical sample is shown in Fig. 10. The concentration of the metal and resin changes continuously in the middle of the model.

It can be easily recognized that this process has a wide variety of applications in the forming of micro components, electric circuits and functional gradient material.

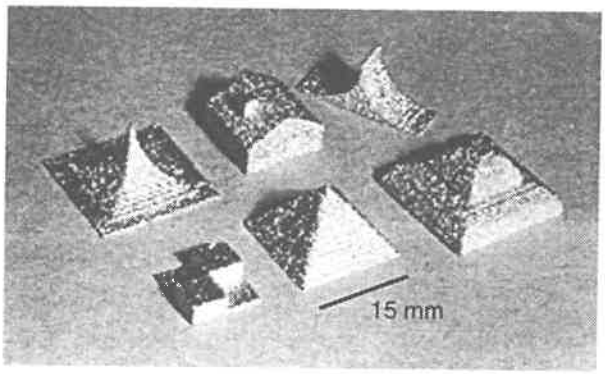

Fig. 5 Typical examples of 3–dimensional model made by fusible alloy

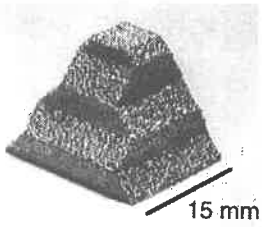

Fig. 6 3–dimensional model made by solder

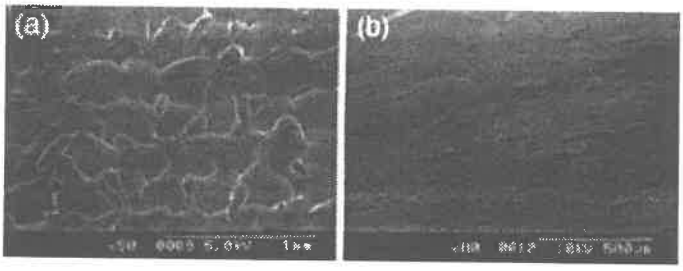

Fig. 7 (a) SEM image of the layer surface and (b) cross-sectional image of the specimen

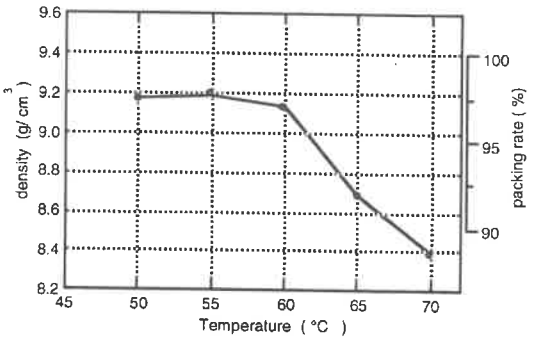

Fig. 8 Bulk density of the models

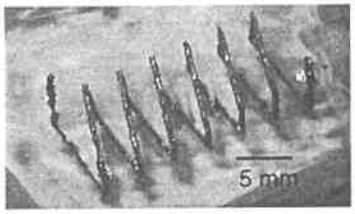

Fig. 9 Coil in the transparent resin

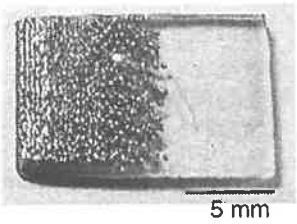

Fig. 10 Functional gradient material

5. Conclusion

1) A metal-jet prototype system was developed and its performance was shown. 2) 3-dimensional models, electric circuits and functional gradient materials were successfully produced. 3) The highest packing rate of the metal is 98%.

6. Acknowledgments

The authors would like to thank Mr. K. Nunome for setting up the experimental equipment and Mr. M. Yamasaki for cooperation in conducting the experiments.

7. References

[1] M. Mehregany, K. J. Gabriel and W. S. N. Trimmer, Integrated Fabrication of Polysilicon Mechanisms, *IEEE Trans. Electron Devices*, 1988, **35(6)**, 719.

[2] L. S. Fan, Y. C. Tai and R.S. Muller, Integrated Movable Micromechanical Structures for Sensors and Actuators, *IEEE Trans. Electron Devices*, 1988, **35(6)**, 724.

[3] W. Ehrfeld, The LIGA Processes for Microsystems, *Micro System Technologies 90, Proceedings of 1st International Conference on Micro Electro, Opto, Mechanic System and Components*, 1990, 521.

[4] J Mohr, C. Burbaum, P. Bley, W. Mentz and U. Wallrabe, Movable Microstructures Manufactured by the LIGA Processes as Basic Elements for Microsystems, *Micro System Technologies 90, Proceedings of 1st International Conference on Micro Electro, Opto, Mechanic System and Components*, 1990, 529.

[5] H. Guckel, K. J. Strobis, T. R. Christenson, J. Klein, S. Han, B. Choi, E. G. Lovell and T. W. Chapman, Fabrication and Testing of the Planer Magnetic Micromotor, *Journal of Micromechanics and Microeng.*, 1991, **1(3)**, 135.

[6] B. Frazier, J. W. Babb, M. G. Allen and D. G. Taylor, Design and Fabrication of Electroplated Micromotor Structures, *Proc. of ASME Winter Annual Meeting.*, 1991, **DSC32**, 135.

[7] K. Yamaguchi, T. Nakamoto and P. Abraha, Consideration on the Optimum Condition to Produce Micromechanical Parts by Photo Polymerization using Direct Focused Beam Writing, *Proc. of 6th International Symposium on MHS*, 1995, 71.

FABRICATION AND THERMAL ANALYSIS OF A BELLOWS TYPE GAS-LIQUID PHASE-CHANGE MICRO-ACTUATOR

Shigeo KATO and Tadashi SHINTANI
Nippon Institute of Technology,
Miyashiro, Saitama 345, Japan

1. Introduction

New inching mechanisms to inspect the human body or to repair thin pipings have been searched.

There are flexible inching mechanisms which are able to inch in pipings by imitating the creeping motion of earthworms. We have fabricated a metal bellows type gas-liquid phase-change micro-actuator for the engine of the flexible inching mechanism. When a liquid is vaporized, the volume of the phase-changed gas is more than 100 times that of the liquid. Gas-liquid phase-change actuators are thermal engines that utilize the large change in volume that occurs during a phase-change. [1],[2]

By using a metal bellows, a thin and long actuator has been obtained. Furthermore, the stretching and shrinking motion of the metal bellows actuator can be utilized for the inching motion of the flexible inching mechanism.

This paper presents a fabrication and thermal analysis of a metal bellows type gas-liquid phase-change micro-actuator.

2. Characteristics of the fabricated actuator

A cross section of the fabricated metal bellows type micro-actuator is shown in Fig. 1. The bellows is made of nickel. Its dimension is 6.8 mm in outer diameter, 3.8 mm in inner diameter, and 20.4 mm long. It has a volume of 536 μl for operating liquid. The operating fluid is non-chlorine perfluorocarbon ($C_5H_{11}NO$), because its vaporizing temperature, though higher than the human body, is still only 50 °C and its latent heat for vaporization is only 1/22 that of water. Consequently, the energy needed for vaporization is very low. The operating liquid is heated by a heater 0.1-mm thick made of coiled constantan wire with an electrical resistance of 12 Ω. The elasticity of the bellows is almost linear in the displacement less than 2.5 mm. The gauge pressure in the bellows is 0.04 MPa when the displacement of the bellows is 2.5 mm.

An electrical power of 5.88 W is supplied

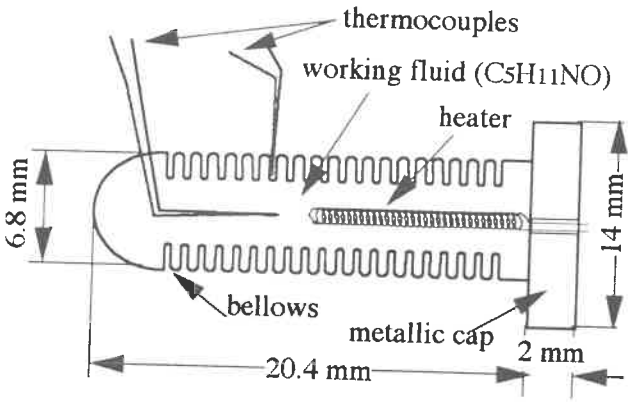

Fig. 1 Metal bellows type gas-liquid phase-change actuator

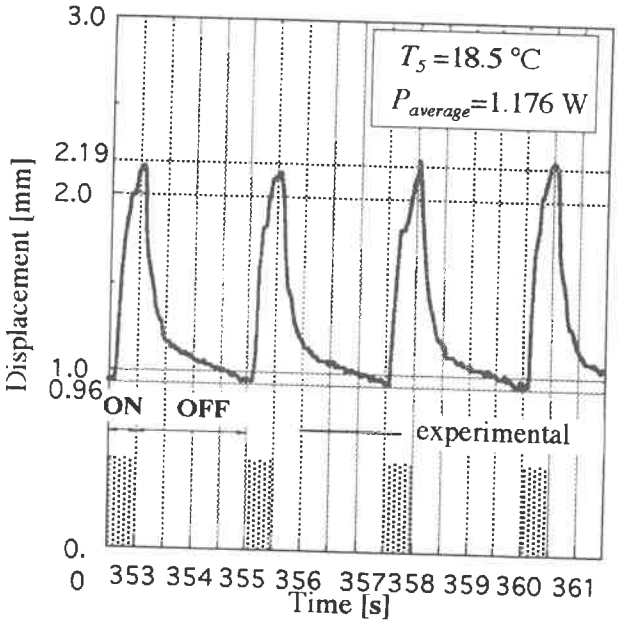

Fig. 2 Continuous stroke motion (Average power is 1.176W)

within 0.5 seconds to the heater and it is cut in the interval of 2 seconds. This operation is repeated. The maximum displacement of the piston gradually increases. After 60 seconds, the maximum displacement reaches 2.19 mm and the minimum displacement reaches 0.96 mm. This motion is shown in Fig. 2.

Thus, this actuator was confirmed to have a reciprocating motion with a 1.23-mm stroke at an average power of 1.176 W.

Next, the electric power was given continuously. The displacement of the bellows increases according to the power. However, if the power decreases to 1.17 W, the stroke of the piston freezes at the length of 0.81 mm. The performance of the actuator is considered to be thermally critical. In this case, the ambient temperature (T_5) is 18 °C, the temperature of the outer wall of the bellows is 29.2 °C, and the temperature of the operating liquid at 1 mm from the heater is 33 °C.

3. Mathematical model of the actuator

In order to simulate the actuator, we needed to create a mathematical thermal model of the actuator. A model of the actuator is shown in Fig. 3. The temperature distribution is very complicated. However, we simply considered four thermal elements receiving the heat and their temperature changes. These are (1) the heater, (2) the operating liquid near the heater (boiling temperature zone), (3) the operating liquid near the casing, (4) the bellows and a metallic cap. If we select only one liquid for the operating fluid, we cannot explain why vaporization starts 0.2 seconds after power is supplied. The heat capacity, the temperature, and the heat transfer area of the element-i are C_i(J/K), T_i(°C), and A_i(m^2), respectively. The heat flow rate and the heat transfer coefficient from element-i to element-(i+1) are q_i(W), and h_i(W/m^2 K), respectively. The heat flow rate to the heater is q_H(=5.88 W). The heat flow rate for vaporizing is q_V(W). The heat flow rate when the vaporized gas is re-liquefied and the liquefying area are q_L(W) and A_L(m^2), respectively. Simultaneous differential equations of the thermal model are solved by the Runge-Kutta method.

3.1 Under power supply (from start to vaporization)

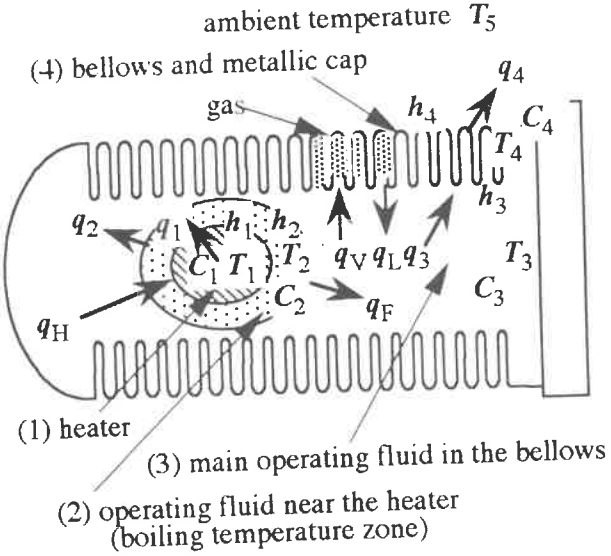

Fig. 3 Thermal model of the metal bellows type gas-liquid phase-change actuator

When power is supplied to the heater, the operating liquid near the heater quickly vaporizes. For the period from the start till vaporization occurs, the heat balances of the four thermal elements are represented by next four differential equations. t represents the operating time.

$$C_1 \frac{dT_1}{dt} = q_H - q_1 = q_H - A_1 h_1 (T_1 - T_2) \quad (1)$$

$$C_2 \frac{dT_2}{dt} = q_1 - q_2 = A_1 h_1 (T_1 - T_2) - A_2 h_2 (T_2 - T_3) \quad (2)$$

$$C_3 \frac{dT_3}{dt} = q_2 - q_3 = A_2 h_2 (T_2 - T_3) - A_3 h_3 (T_3 - T_4) \quad (3)$$

$$C_4 \frac{dT_4}{dt} = q_3 - q_4 = A_3 h_3 (T_3 - T_4) - A_4 h_4 (T_4 - T_5) \quad (4)$$

3.2 Under power supply (after the vaporization)

When the temperature of the operating liquid near the heater reaches the boiling temperature (T_b=50 °C), vaporization is assumed to start from the sidewall of the heater. Eqs. (2) and (3) are changed to Eqs. (5) and (6), respectively.

$$C_2 \frac{dT_2}{dt} = 0 \quad (5)$$

$$C_3 \frac{dT_3}{dt} = q_2 - q_3 + q_L$$
$$= (A_2h_2 + A_Lh_L)(T_b - T_3) - A_3h_3(T_3 - T_4) \quad (6)$$

$$q_1 - q_2 = A_1h_1(T_1 - T_b) - A_2h_2(T_b - T_3) = q_V + q_F \quad (7)$$

The zero in Eq. (5) shows that temperature T_2 maintains the boiling temperature, and $(q_1 - q_2)$ is obviously not equal to zero as Eq. (7). The term q_F in Eq. (7) is the heat flow rate that is used to spread the vaporizing temperature zone (the operating liquid near the heater). Supposing that β is a constant less than 1, it is assumed that terms q_V and q_F can be represented as follows.

$$q_V = \beta (q_1 - q_2) \quad (8)$$

$$q_F = (1 - \beta)(q_1 - q_2) \quad (9)$$

Increasing of the vaporizing temperature zone is represented as

$$(T_b - T_3) \frac{dC_2}{dt} = q_F = (1 - \beta)\ (q_1 - q_2) \quad (10)$$

The mass per unit of time of the vaporizing fluid (kg/s) is represented as

$$m_V = \frac{q_V - q_L}{H_b} \quad (11)$$

where H_b is the latent heat for vaporization (kJ/kg K) of the operating fluid.

4. Estimation of the heat transfer coefficients

Using the heat transfer areas shown in Table 1 and critical power of 1.17W, some heat transfer coefficients have been estimated.

When power of the heater is critical, the heat transfers between each thermal element are static. Consequently, following equations are obtained.

$$q_1 = q_2 = q_3 = q_4 = q_H = 1.17 \text{ (W)} \quad (12)$$

$$A_1h_1 (T_1 - T_2) = q_H \quad (13)$$

$$A_2h_2 (T_2 - T_3) = q_H \quad (14)$$

Table 1 Simulation data

Heat Transfer Area	A_1=63.5 $\times 10^{-6}$ m^2 A_2=78.4 – A_3=1377 A_4=2025 A_{L2}=270
Heat Capacity	C_1=5.97 $\times 10^{-3}$ J/K C_2=1.27 $\times 10^{-3}$ – C_3= – 0.951 C_4=2.546
Heat Transfer Coefficient	h_1 =648 W/m^2 K h_2 =648 h_3 =224 h_4 =52 h_L =25
Ratio of Heat Flow Rate for Vaporization	β=0.06

$$A_3h_3 (T_3 - T_4) = q_H \quad (15)$$

$$A_4h_4 (T_4 - T_5) = q_H \quad (16)$$

We have considered that T_2 is at a boiling temperature of 50 °C as mentioned and T_5 is 18 °C. Under these conditions, we obtained that h_2 is 648, h_3 is 224 and h_4 is 52 (W/m^2 K). However, we can not obtain only h_1 by these equations.

Calculation of the heat transfer coefficient h_1

We calculated the heat transfer coefficient h_1 as natural convection from a 0.1-mm horizontal hot column. The Nusselt number Nu is represented as

$$Nu = 1.03\ B_1\ Ra^{0.25} \quad (17)$$

where B_1 is a constant (=0.46) depending on the Prandtl number (=12.14). Ra is the Rayleigh number, and is 27.9 in this case. By substituting these values into Equation (17), we have Nu=1.108. Finally, we obtain h_1=648 (W/m^2 K) from the Nusselt number.

The heat transfer area for liquefying A_L is an area (A_{L2}=270 mm^2) if the displacement is as large as H= 2 mm. However, if the displacement of the piston decreases, the area where the gas and liquid come in contact with each other may

decrease due to the capillary phenomenon. If the displacement is zero, then area A_L may be zero. Consequently, we assume that area A_L is related to displacement H and is represented as

$$A_L=A_{L2}(\frac{H}{H_2})^N \quad (18)$$

where H_2 shows a displacement of 2-mm.

The heat transfer coefficient for liquefying h_L is assumed to be h_L= 25(W/m^2 K) and the value of N is 5, because this value enables the minimum displacement of the piston to reach H=0.96 mm .

5. Simulation of the displacement of the piston

We simulated the displacement of the actuator using the values β=0.06, because this value enables the displacement of the piston to reach H=2.19 mm of the maximum displacement.

The relationship between volume V (μl) of the vaporized gas and displacement H (mm) is represented as

$$V=22.05\,H \quad (19)$$

The relationship between the pressure in the rubber membrane P (MPa) and the displacement H (mm) is represented as

$$P=0.101+0.016H \quad (20)$$

The pressure and the volume are represented as

$$PV=M_V\,R\,T_b \quad (21)$$

where M_V and R are the mass of the gas in the rubber membrane and the gas constant of the operating fluid, respectively.

Because the molecular weight of C5H11NO is 310, from Eqs. (19), (20), and (21), the relationship between the displacement H and the mass of the gas M_V(kg) is represented as

$$H(0.101+0.016\,H)=4.072\times10^5\,M_V \quad (22)$$

If we know the mass of the gas, we obtain the displacement of the piston by Eq. (22).

The simulation of the continuous reciprocating movement of the piston is shown in Fig. 4 by the gray line. It is confirmed that

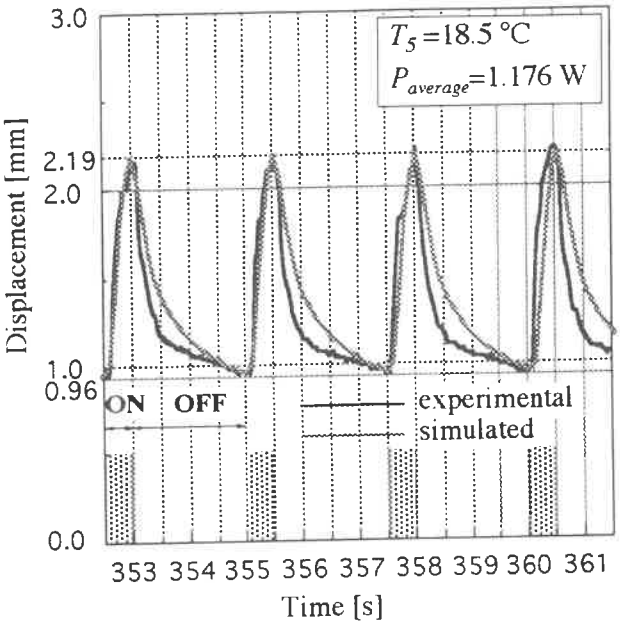

Fig. 4 Continuous stroke motion
(Average power is 1.176W)

continuous reciprocating movement of the piston with a 1.23-mm stroke can be simulated.

6. Conclusions

(1) We fabricated a metal bellows type gas-liquid phase-change micro-actuator that is 6.8 mm in diameter and 20.4 mm long, and that has a volume of 536 μl for the operating liquid. The operating fluid is C5H11NO.

(2) By dividing the operating fluid into two thermal elements, we could make a simple mathematical model for the gas-liquid phase-change micro-actuator.

(3) By experiment and simulation, the actuator was confirmed to reciprocate continuously with a 1.23-mm stroke at an average input power of 1.17W.

Reference

[1] H. Mizoguchi, M. Ando, T. Mizuno, T. Takagi, and N. Nakajima: Proc. of Micro Electro Mechanical Systems '92, Design and Fabrication of Light Driven Micropump, pp. 31-36.

[2] S. Kato: Proc of ASPE, Fabrication and Thermal Analysis of a Gas-liquid Phase-change Micro-actuator, pp. 332-335.

MINIATURIZED POSITIONING DEVICE FOR PRECISE ROTARY MOTION BY USE OF PIEZOELECTRIC ACTUATORS

Peggy Dörrer

Fraunhofer Institute for Applied Optics and Precision Engineering
Jena, Germany

Introduction

With increasing miniaturisation, more accurate positioning systems for precise handling and for examining components for quality are required. Such high accuracy requirements can be met by piezoelectric actuators, easily producing displacements on the order of submicrons by voltage control. However, in applying such actuators it is difficult to realize a rotary motion.
At the Fraunhofer Institute in Jena new positioning devices for precise rotary motions have been developed, driven by piezoelectric multilayer actuators. The deformation of one actuator generates a precise linear motion, which is transformed to rotary motion by an elastic hinge. This elastic hinge constitutes the pivot point of the whole positioning system. Due to the use of such a mechanism an angular resolution of 0.025 seconds of arc could be proved for the first developed device and for a second miniaturized device with a volume of 2.3 cm^3, as well.

First design

For the first design, work was centered on the development of a new piezoelectric positioning system with high accuracy for generating a slow step by step rotary motion of a rotary table (rotor) /1/.
The general idea contains three driving elements: the first (1), which is not necessary in all cases, positions the rotor (5) at a certain height; the second (2), brings the stator (4) into contact with the rotor (5), and the third (3), generates the true rotary motion. All driving elements used are piezoelectric multilayer actuators. The first driving elements (1), for positioning. the rotor at a fixed height, exist as three rectangular columns protruding from the stator base plate to surround the adjustable holder of the stator (4). Each contains a piezoelectric actuator for varying the height of the column. The displacement of each piezoactuator is transmitted by an arrangement of elastic hinges, which enlarges the range for adjustment from 28 µm to 200 µm. A similar mechanism is used for bringing contact between the adjustable holder of the stator (4) and the rotor (5). The maximum adjustment of the stator height is 200 µm, as well.

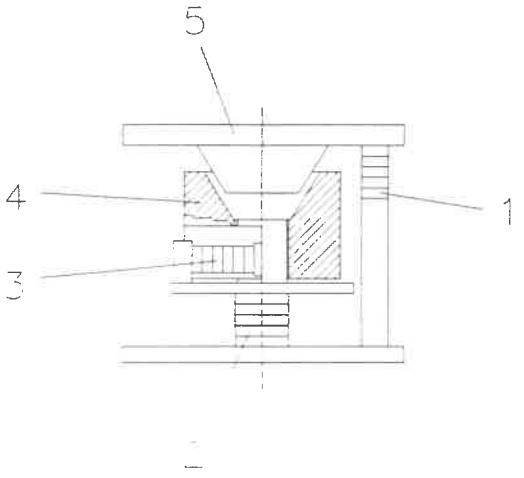

Fig. 1: Structure

The horizontally arranged piezoactuator (3) generates a variable linear motion, transformed by an elastic hinge into a rotary motion of the adjustable holder of the stator (4).
For driving this positioning system, a special electronic device has been developed, consisting of two parts: a logical part for generating the chronological sequence and an analogical part for driving each actuator.
The measured minimum rotary motion is 0.025 seconds of arc and the maximum angular step is 104 seconds of arc. For measuring the rotational motion, two plane reflectors are mounted on the rotor, the measuring reflector and the reference reflector. In addition, the measuring set-up contains a laser, an interferometer, and an analyser for calculating the angle around which the two reflectors are rotated. The angle is determined from the difference in path length of the light beams.

Design of the miniaturized positioning system and its improvements upon the first design

Because the first design has some disadvantages in industrial application: for example, large volume of the whole, relatively slow operation and restriction of operation to only one position, there is a demand for a miniaturized positioning system, which can work in different positions.
The miniaturized positioning system is based on a stator which is surrounded by a tubular rotor. With exception of the piezoelectric actuators, the stator of the positioning system, depicted in figure 2, consists of only one piece having three layers; the middle layer for rotary motion generation and two outer layers for clamping,. To produce the layers the stator is given two horizontal slits, guaranteeing a clear separation of rotary motion and clamping function. The clamping layers are identically constructed and include an extra structure, due to the manufacturing of the three layers as one mechanical piece, which however has no influence on clamping function. The whole stator shape, including the microstructures, is produced by electrodischarge machining. By this process very complicated shapes can be manufactured with minimal tolerances. The diameter of the presented positioning system is 12 mm, but, in the area of the clamp shoes, it is some micrometers greater. The height of the stator is 10 mm and the volume of this miniaturized instrument with rotor is 2.3 cm^3.

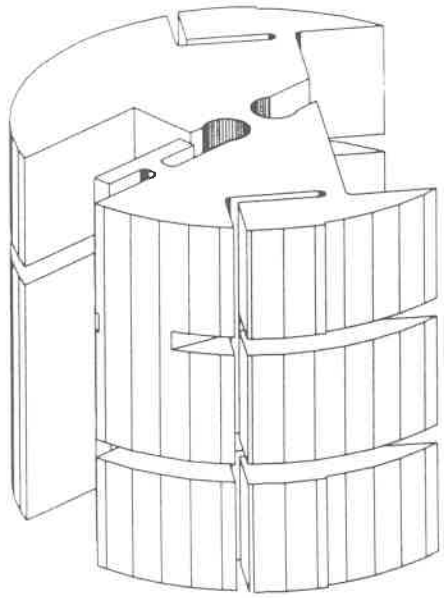

Fig. 2: Stator

Both clamps contact the rotor when there is no power consumption. Starting the operational sequence the piezoelectric actuator of the lower clamp is controlled by a voltage up to 150 V releasing this clamp from the rotor. Then an extension of the piezoelectric actuator in the middle layer causes a rotary motion of the upper layer which is still clamped to the rotor, rotating the rotor. To enable further rotation of the rotor, the lower clamp secures the position of the rotor again while the upper clamp releases. The piezoactuator in the middle layer can return back to its original position without rotating the rotor and the process can begin again. In this way a step-wise rotary motion of the rotor is generated without limiting range of rotation.
To avoid complicated micro-assembly techniques in general, the mechanical body of the positioning device consists of only one piece and there is no need for additional conventional bearings. The only assembly involves attaching the actuators. The simple structure of this miniaturized positioning device has the additional advantage of minimized sensitivity to vibrations.

Details of design

For generating the rotary motion a transfer of the linear motion of the piezoelectric actuator is necessary.
Elastic hinges give the possibility to change the type and direction of motion generated. In order to prevent tribological and assembly problems and to ease manufacturing with small tolerances, an elastic hinge has been chosen to constitute the pivot point of the whole positioning instrument. The measurements on the first instrument show, that the motion generation by means of piezoelectric actuators and the transformation and transmission of this motion by elastic hinges guarantees a very high angular resolution. Figure 3 presents the mechanism, which generates the rotary motion. The highest stiffness is along the vertical y-axis. The ratio between the width of the hinge to the diameter of the rounded end of the slit creating the hinge determines the ratio between the stiffness in the y-direction to the stiffness of rotation around the elastic hinge.

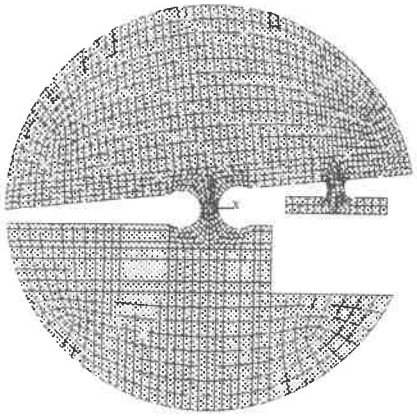

Fig. 3: Layer for generating rotary motion

The concept of clamping is based on the idea that at all times one clamp is active as in linear positioning systems like /2/ and /3/. In case of no power consumption both clamps clamp on to the rotor surrounding the stator. Therefore, the miniaturized positioning instrument is usable in any position.
Figure 4 shows the functional structure of one clamp containing a multilayered piezoelectric stack. When a voltage is applied the clamp shoes move inwards and are disengaged from the rotor. The pivot point for this motion is again an elastic hinge. The sort of clamping is influenced by the clamp shoes, the actuator and its distance to the pivot points and, as well, the surrounding rotor. The size of the gap between the clamp shoes and the rotor is very critical to the performance of the miniaturized positioning system.

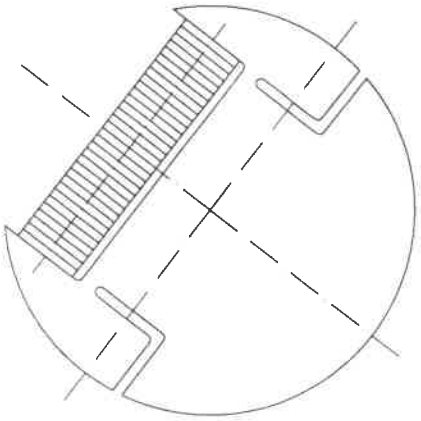

Fig. 4: Functional structure of clamp

Control

There are different possibilities for operational sequence. One will be explained here:
With no power consumption both clamps contact the rotor. After releasing clamp 1 the actuator for movement generation extends causing a rotary motion of clamp 2 and the rotor. Now clamp 1 contacts the rotor again and clamp 2 releases. In the next step, the contraction of the actuator for movement generation causes a rotary motion of clamp 2 without rotating the rotor. Such a cycle realizes a rotary step motion of the tubular rotor. The successive repetition of this cycle generates an unlimited step-wise motion of the rotor. The following figure shows the control for such a cycle.

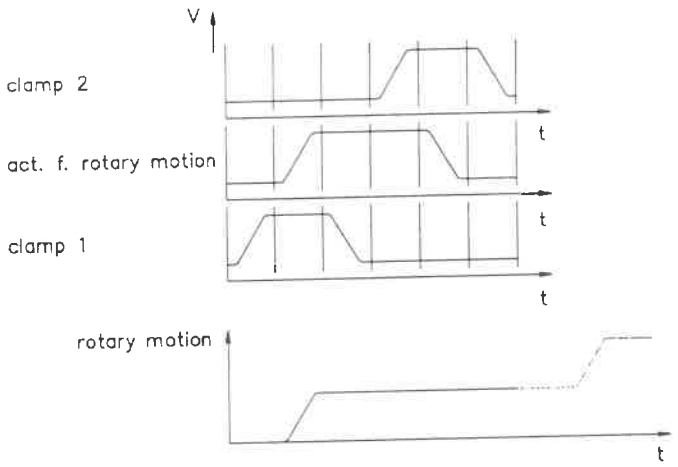

Fig. 5: Control of the actuators and generation of rotary motion

Measurement

The measuring set-up contains a laser, an interferometer and an analyser. For measuring the angular resolution the piezoelectric actuator for generating rotary motion was controlled by a triangular voltage. The measurement results are shown in figure 6 on the right. Every step is 0.025 seconds of arc high, which reflects exactly the angular resolution of used measurement set-up. That means there is no measurable reduction of displacement resolution of piezoactuator by the mechanism with elastic hinge.

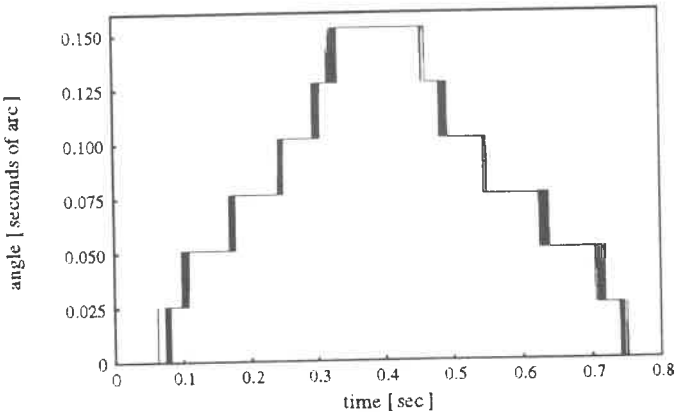

Fig. 6: Measurement of angular resolution

Conclusion

The miniaturized positioning device has been developed for high accuracy positioning of objects for handling and examination, for adjustment and quality control and for precise alignment of sensors. Due to the clamping without power consumption it is a long-time stable adjusting device. It can be coupled with linear positioning systems.

References

/1/ Portius, P.; Wehrsdorfer, E.: Piezoelectrically Driven Rotation Stepper Motor for High Resolution Movings. Proc., 4th Int. Conference on New Actuators (Actuator 94), Bremen, June 1994, pp. 183 - 185

/2/ Burleigh Instruments, US Patent 3,902,084

/3/ Philips Electronics N.V., European Patent EP 0 592 030 A1

Dynamic Accuracy Monitoring for the Comparison and Optimization of Fast Axis Feed Drives

O. Zirn,S. Weikert***
**Mikron SA Agno, Lugano, Switzerland
*Inst. of Machine Tools and Mfg.(IWF-ETH), Zürich, Switzerland

Abstract:

Based on the milling path verification via a 2-D incremental measuring grid, high speed machine tools as well as serially coupled high dynamic feed axis drives can easily be investigated and optimized. Supported by the Swiss machine tool industry, a method for the identification and the optimization of the accuracy and dynamic performance of fast axis feed drives has been developed. The exemplary comparison of a direct driven as well as a ball screw driven milling and engraving machine elucidates the obtainable improvements by this method.

Keywords:

Drive, Optimization, Measurement

1 Introduction

The successful application of the high speed machining process requires feed axis drives and machine structures capable of driving the tool at adequate feed rates along the milling path.
The efficient design and optimization of the machine tool must be based a model concerning all significant influences in the design phase and a suitable dynamic accuracy monitoring for the set-up and acceptance test.
Finite Element- (FE-) models [1] allow exact modeling but require suitable software tools that are not generally available in today's machine tool industry. The verification of he FE-models requires frequency analysis results from the prototype or comparable machine structures with known boundary conditions.
For the present investigation the application of the incremental 2-D-measuring grid in combination with a model of flexibly coupled discrete masses has proven to be advantageous. It yields useful results with moderate effort.

2 Modeling of high speed machine tools

Figure 1 shows the body structure of two exemplary state of the art high speed machine tools. Both machine types detach the X- and the Y-axis to obtain optimum acceleration capabilities. This represents a basic boundary condition for the successful application of direct drives.
Serial machine principles for 3 or more machining dimensions require at least one cinematic chain of feed axes. In the presented examples (figure 1) the vertical Z-axis is attached on the slider (a)) or the column (b)) of the Y-axis. The Y- and Z-axis machine structure can't be realized with infinitive stiffness and thus must be considered as a system of flexibly coupled masses.

The division of the structure in two equal masses is a helpful approximation for a wide range of cases. The ball screw drive as well can be modeled as two flexibly coupled masses [4].

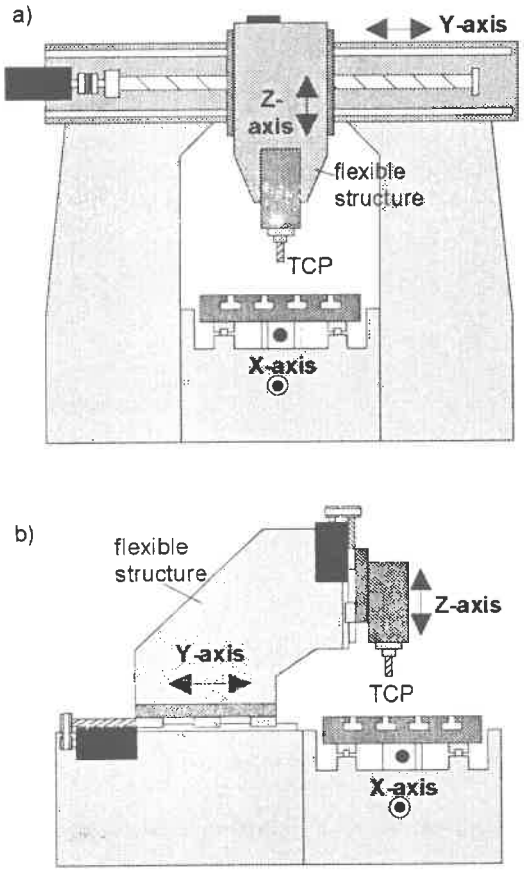

Figure 1: Typical axis arrangement of HSM machine tools with serial kinematics

A ball screw drive with a belt gearing can be modeled as a system of three flexibly coupled masses (see figure 2).
The complete model of the machine tool is shown in figure 2. The dynamic performance of the Z-axis will not be considered in this contribution.
The block diagram including the nonlinear influences of reluctance, friction and input saturation is shown in figure 3.

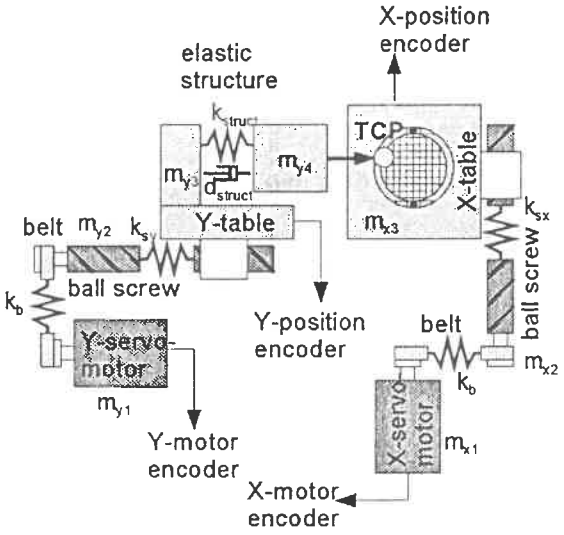

Figure 2: axis and flexible structure model

In this contribution an exemplary high speed milling and engraving machine tool, based on machine principle b) in figure 1 is investigated and optimized using the above (figure 2) shown machine model and the 2-D-measuring grid. The main technical data and the model parameters are shown in table 1. Most of the model parameters can be gathered from the components data sheets. The other parameters can be calculated or estimated basing on the machine's construction data.

parameter list	Y-axis	X-axis
table or structure mass m [kg]	250	50
stroke L [mm]	250	400
ball screw pitch h_s [mm]	10	10
ball screw stiffness k_s [N/m]	$154 \cdot 10^6$	$154 \cdot 10^6$
belt stiffness k_b [N/m]	$350 \cdot 10^6$	$350 \cdot 10^6$
structure eigenfrq. ω_{oS} [rad/s]	157	>1500
structure damp. d_{struct} [Ns/m]	9200	-
motor friction F_{R1} [N]	150	150
screw friction F_{R2} [N]	150	150
slider friction F_{R3} [N]	100	60
maximum force F_{max} [N]	8050	8050
reluctance force F_{rel} [N]	40	40
m_1 [kg]	319	319
m_2 [kg]	125	125
m_3 [kg]	138	150
m_4 [kg]	138	-
electrical time lag T_{elr} [s]	$2 \cdot 10^{-4}$	$2 \cdot 10^{-4}$
delay time T_{dead} [s]	$1.5 \cdot 10^{-4}$	$1.5 \cdot 10^{-4}$

Table 1: machine data and model parameters

Usually the relative damping of screw and belt is smaller than 5 % and therefore negligible. The machine structure damping can be higher and will be considered in the model.
The structure spring constant k_{struct} is much smaller than the spring constant of the belt k_b or the screw k_s. In this case the eigenfrequency ω_{oS} of the machine structure can be approximated by:

$$\omega_{oS} \approx \sqrt{k_{struct} \cdot \frac{m_{1y} + m_{2y} + m_{3y} + m_{4y}}{(m_{1y} + m_{2y} + m_{3y}) \cdot m_{4y}}} \qquad (1)$$

where m_{1y} is the motor mass, m_{2y} is the mass of the half screw, m_{3y} is the half screw and the half structure mass as well as m_{4y} is the other half of the structure mass.

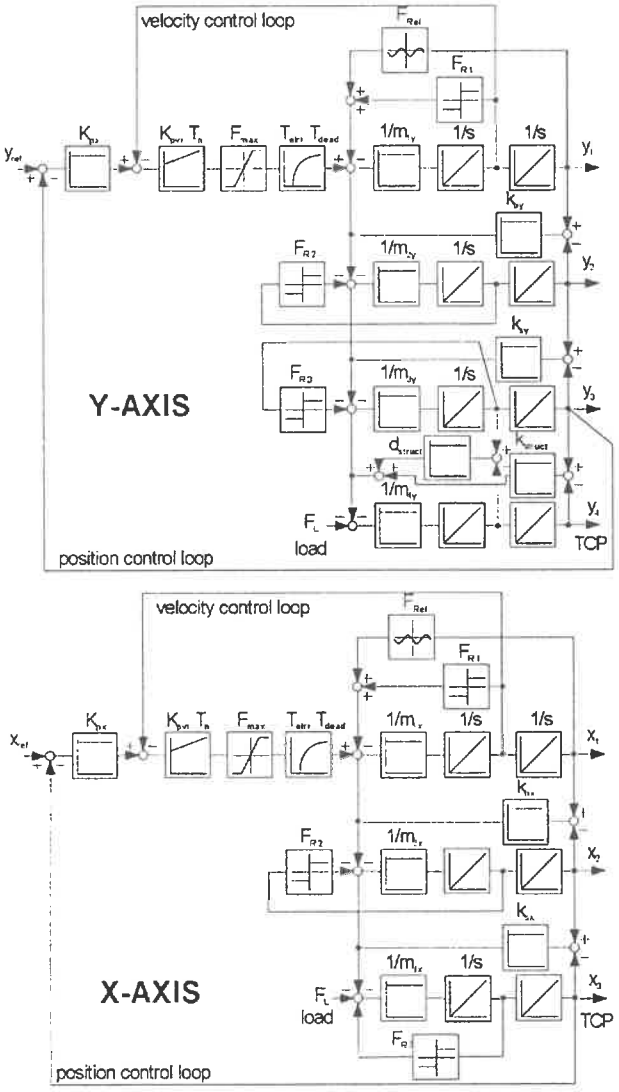

Figure 3: Block diagram of X- and Y-axis with ball screw drives

3 Analysis of tool trajectories

The measuring grid [2] (figure 4) is well suited for observing the relative planar motion of two bodies.

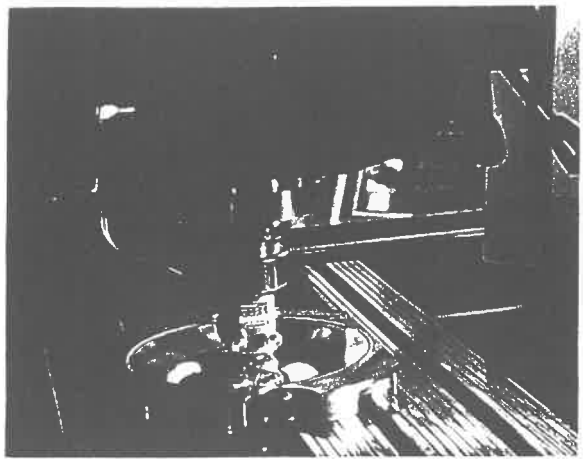

Figure 4: 2-D incremental measuring grid

The grid plate carries two line grids orthogonal to each other. A scanning head, mounted in the tool center point (TCP) also equipped with orthogonal line grids simultane-ously lights the grid and observes the reflected light. The signal picked up is interpolated in 1024 intervals by the measuring circuit which results in a resolution of 5 nm. A PC is then used for storing and further processing the recorded data. The maximum speed is 24 m/min, which can be altered by reducing the resolution.

Figure 5 shows the measured tool trajectories at a YX-corner (upper figure) and a XY-corner (lower figure). The reference speed is 10 m/min with a reference acceleration limit of 1 m/s^2. The controller gains are the drive builders default values (table 2):

controller gains	Y-axis	X-axis
position gain K_{px} [1/s]	83	83
velocity gain K_{pv} [Ns/m]	350000	350000
integrator time constant T_n [s]	0.003	0.003

Table 2

This measurement shows clear that the controller gains of the machine tool axes are to high and lead to oscillations of the X-table and an overshoot of the Y-axis in combination with the flexible structure.

Computer based simulation with the nonlinear machine model in figure 3 allows a fast optimization of the controller gains (table 3).

controller gains	Y-axis	X-axis
position gain K_{px} [1/s]	50	50
velocity gain K_{pv} [Ns/m]	250000	160000
integrator time constant T_n [s]	0.003	0.003

Table 3

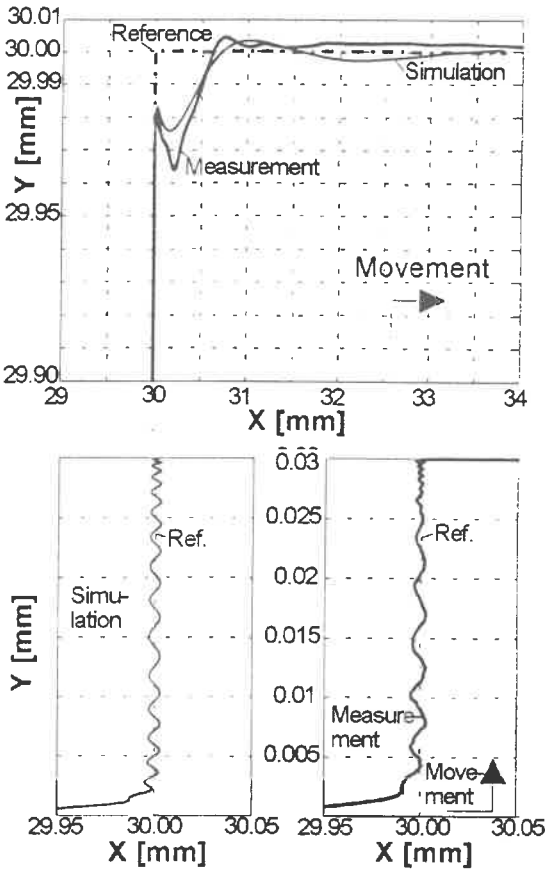

Figure 5: Comparison of the path deviation (measured and simulated tool trajectories)

Simulation results and the monitored path using the controller gains in table 3 are shown in figures 6a, 6b. The comparison of measurement and simulation shows good agreement. Deviations are caused by the different initial conditions of the simulation as well as estimation errors of parameters and the simplification. Although the nonlinear machine model (fig.3) is well suited for the design and the analysis of high speed machine tools in combination with the measuring grid.

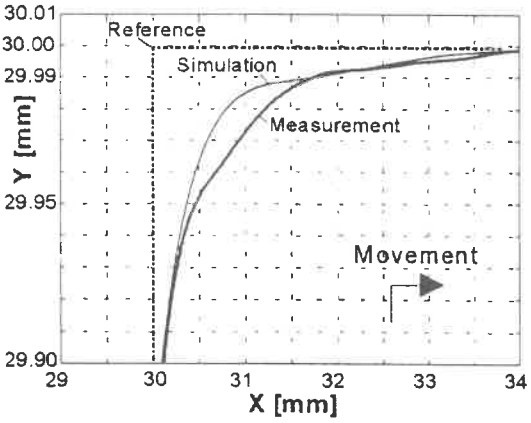

Figure 6a: TCP-path with moderate controller gains (2-D- grid measurement and simulation, 10 m/min reference speed)

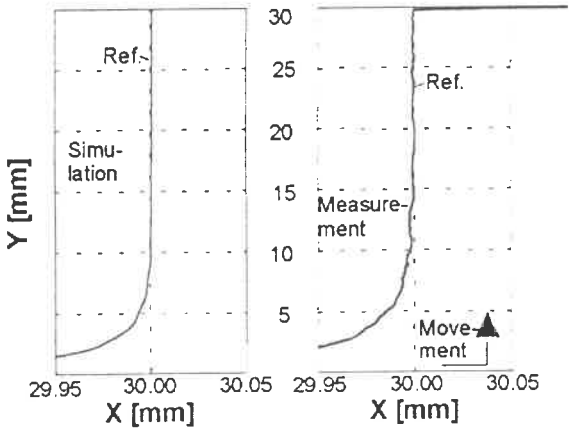

Figure 6b: TCP path with moderate controller ains (2-D-grid measurement and imulation, 10 m/min reference speed)

4 Direct Drive

The same milling and engraving machine type has been equipped with direct drives in the X- and Y-axis. The tecnnical data and the model (figure 7) parameters are shown in table 4.

parameter list	Y-axis	X-axis
table mass m [kg]	250	50
stroke L [mm]	250	400
structure eigenfrq. ω_{oS} [rad/s]	157	>1500
slider friction F_R [N]	60	60
maximum force F_{max} [N]	2200	2200
reluctance force F_{rel} [N]	10	10
m_1 [kg]	142	67
m_2 [kg]	125	-
electrical time lag T_{elr} [s]	$2 \cdot 10^{-4}$	$2 \cdot 10^{-4}$
delay time T_{dead} [s]	$1.5 \cdot 10^{-4}$	$1.5 \cdot 10^{-4}$

Table 4

The direct driven X-axis yields very high controller gains (see table 5), while the flexible structure causes a significant overshoot of the direct driven Y-axis, even with moderate gains. The simulated and measured tool trajectories are shown in figure 8.
For the investigated machine tool, the direct drive itself will not increase the dynamic performance [2]. Further efforts to increase the structure (column) stiffness will be necessary.

controller gains	Y-axis	X-axis
position gain K_{px} [1/s]	67	67
velocity gain K_{pv} [Ns/m]	500000	10000
integrator time constant T_n [s]	0.002	0.0025

Table 5

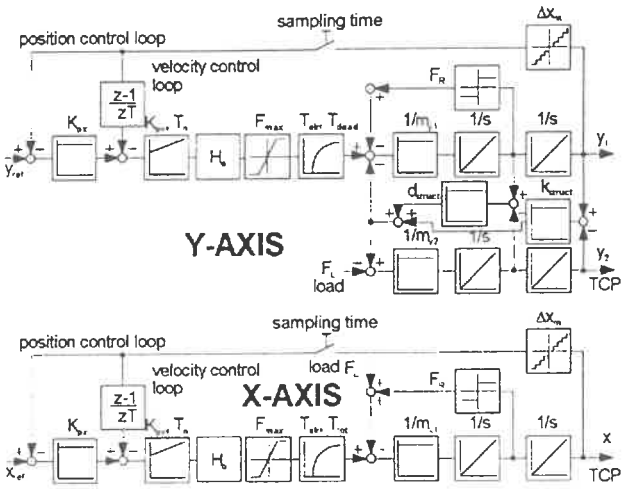

Figure 7: Block diagram with direct drives

The comparison of measurement and simulation shows good agreement also in this case. Therefore the model in figure 7 is suitable to assess the controller gains for the design and setup of direct driven machine tools.

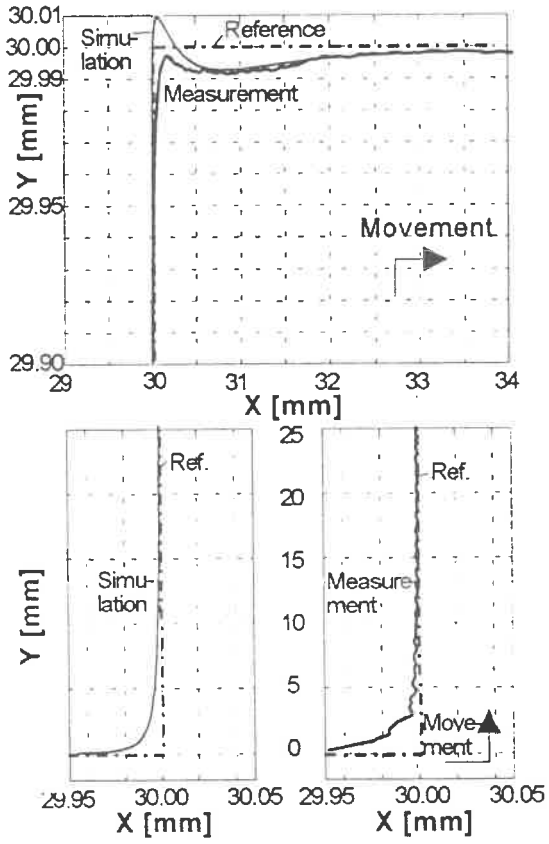

Figure 8: path monitoring of a direct driven machine

5 Performance limitation by structure flexibility

For high speed machine tools, the flexible structure becomes a very important design parameter. Figure 9 illustrates the simulation results for the position gain of direct drive and ball screw drive vs. eigenfrequency. This shows clear that stiff structures are an essential supposition for machine tools to benefit from the advantages of the direct drive.

The dotted curve in figure 9 shows the theoretical limit for the direct drive position gain depending on the structure's eigenfrequency. This represents a comprehensive design aid for the development of high dynamic machine tools.

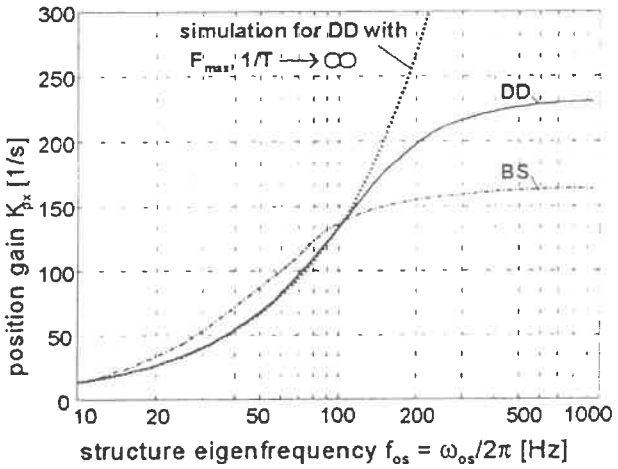

Figure 9: Position gain vs. eigenfrequency of direct drive (DD) and ball screw drive (BS)

6 Conclusion

The 2-D-measurement grid in combination with the presented model of the machine tool permits a fast monitoring and optimization of the machine tool performance. The exemplary investigation of a milling and engraving machine shows clear that the possibilities of tuning the performance of serial kinematics by using direct drives are restricted by reason of the high requirements on structural stiffness. Therefore the recently developed parallel kinematics (e.g. Hexaglide etc.) with small masses, stiff structures (struts) and high eigenfrequencies are the suitable machine principles for highest requirements on dynamic machine performance.

Acknowledgments

This project was supported by the Swiss Commission for the Promotion of Applied Research (KTI) and by the partners Heidenhain (CH) AG, ALMAC SA, ETEL SA, MIKRON AG.

Literature

[1] Bianchi, G.; Paolucci, F.; Van den Braembussche, P.; Jovane, F.: *Toward Virtual Engineering in Machine-Tool Design*. Annals of the CIRP Vol. 45/1/1996: 379-382.

[2] Zirn, O.; Weikert, S.; Rehsteiner, F.: *Design and Optimization of Fast Axis Feed Drives Using Nonlinear Stability Analysis*. Annals of the CIRP Vol. 45/1/1996: 363-366.

[3] Zirn, O.; Weikert, S.; Rehsteiner, F.: *Design and Optimization of Fast Axis Feed Drives Using Nonlinear Stability Analysis*. Annals of the CIRP Vol. 45/1/1996: 363-366.

Design and Characterisation of Nanometer Precision Mechanisms

(Paper II)

Y. Xu, P. D. Atherton, P. Rhead, T. R. Hicks, and M. McConnell
Queensgate Instruments Ltd. Waterside Park, Bracknell, RG12 1RB, UK

To meet the ever increasing precision required of positioning and scanning devices, Queensgate Instruments is developing a NanoPositioning technology, the technology of moving and measuring with subnanometer precision, which helps researchers and manufacturers in the production of some of the most advanced products in use today. NanoPositioning products are developed by combining Queensgate's piezoelectric and NanoSensor technology into multi-axis positioners with the ability to position with sub-nanometeric accuracy. The positioners are composed of a series of stages, called NanoMechanisms, including single axis stages, x-y stages, tilting stages and yaw stages etc.. The combinations of these stages can provide three, four, five or six degree of freedom positioning units. The nano-mechanisms are all driven by piezoelectric actuators and their positions are monitored by capacitance sensors which are of noise level < 0.005 $nmH_z^{-1/2}$ and linearity < 0.01%. The outputs of the sensors are used as feedback signals to form closed loop controls. Each stage consists of a linear flexure system machined from a single Super Invar block using EDM. The NPS 3000 controller system features the use of Digital Signal Processor technology to produce a high performance servo loop, with up to 21 bit resolution. Advanced digital algorithms reduce the effect of mechanical resonances greatly improving settle times. The working bandwidth can be controlled by computer and loop parameters be defined by the user for performance optimization.

The design philosophy and some technique considerations in the development of NanoMechanism have been introduced in the previous papers[1,2]. In this paper, the characterisation of the positioning systems is discussed and the performance details measured from these NanoMechanisms are presented. To know what the NanoMechanisms are really doing at the subnanometer level, systematic characterization has to be carried out using advanced metrological technologies. The specifications have to be carefully defined and the measuring methods be chosen properly.

Noise measurements

As it was discussed in the paper (I)[1], the measuring and positioning resolution is directly related to the noise level of the system. For a closed loop stage system, internal sensors are used for reading the actual position of the stage and providing feedback signals to the control loop. The noise measured from the sensors is the measuring noise which can not be considered as a true representation of the actual stage position, because the measuring noise includes both sensor noise and position noise. The sensor noise could be of the same level as the positioning noise, or even higher, depending on the bandwidth with which the sensor noise is measured. To monitor stage position and provide feedback signal to the controller, the internal sensor has to have a working bandwidth much higher than the stage bandwidth, which is mainly limited by the open loop resonant frequency of the mechanism. Normally, the noise level goes up as the working bandwidth increases. Both sensor noise and piezo drive noise[2] in the loop will be transferred into actual displacement by the piezo actuator driven by the controller. Usually, the sensor noise is much higher than the piezo drive noise. However it can only be transferred into actual stage displacement partially because the stage working bandwidth is much lower than sensor's working bandwidth and it does not respond to the high frequency noise. Therefore, the position noise is normally lower than measuring noise. To measure the stage noise directly requires

a sensor which should have a noise level of tens pico meter or less at a working bandwidth of a few kHz. The position noise level can be worked out indirectly by measuring the noise level from HV output of the controller. This voltage noise will be charged on piezo actuator and transferred into motion noise of the stage. By calibrating the converting factor between voltage value of HV and the stage motion, the actual position noise of the stage can be calculated.

Non-linearity, hysteresis .

Non-linearity and hysteresis are motion errors along the moving axis. To assess those static motion errors, the stages are calibrated using a Zygo ZMI 1000 interferometer combined with a Nanosensor[3] (capacitance sensor). After a stage is built, it is firstly calibrated against a laser interferometer and the linearity errors are measured as shown in Figure 1 (curve *a*) (the data of Figure 1 is from NPS-X-15F). Based on the initial scanning data, the internal capacitance sensors are linearized digitally to fourth order. Then, a NanoSensor is used to measure the residuals down to subnanometers. A linearity < 0.01 % can be achieved without extra effort, as shown in Figure 1 (curve *b*). Expanding the scale of the curve *b*, a plot of hysteresis error of the system is generated, as shown in Figure 2. The residuals of curve *b* is mainly limited by hysteresis, drift and noise. Subtracting the 'down' scan from the 'up' scan gives the amplitude of the hysteresis error. For the NanoMechanisms, the hysteresis errors are normally controlled less than 0.005 %, i.e. less than 0.5 nm over 10 μm.

Parasitic motions

The parasitic rotations affect the positioning accuracy due to Abbe errors. These are measured using an auto-collimator with resolution of 0.1 μrad. For single axis stages the rotation error is normally controlled within 0.1 μrad/μm about the axis of maximum error and significantly less about the other axes (< 1 μrad over whole travelling range).

In some applications the out-of-plane motion of the x-y stage is important.. The out-of-plane motion is measured using a capacitive NanoSensor. In this case, the sensor is mounted parallel to the assumed x-y plane, so that the parasitic motions in the z axis will be monitored. The working area of the target electrode has to be much larger than that of probe to avoid the influence of boundary effects when the probe moves laterally relative to the target. Figure 3 shows a two dimensional profile of the out-of-plane motion of NPS-XY-100A stage over a scanning range of 100 μm x 100 μm. The peak-to-peak residuals of the out-of-plane motion from best fit plane is measured as less than twonanometers which includes the effects of measurement noise and nonlinear drift, leading to an estimation of about one nanometer for out-of-plane motion. The out-of-plane motion of the *x-y* stage is mainly caused by the distortions due to driving forces. The testing results indicate that the stiffness of NPS-XY-100A stage in the *z* axis has been designed high enough to withstand parasitic forces.

Dynamic response

In open loop, a stage can be simply considered as a mass – spring – damping second order linear system. The response of the stage is generally dominated by the stage resonant frequency, which mainly depends on the mass of the moving part and the stiffness of the system. It has a translation function

$$G(s) = \frac{1}{\frac{1}{\omega_n^2}s^2 + \frac{1}{\omega_n Q}s + 1} \qquad (1)$$

Where ω_n is the resonant frequency and Q is the amplification factor. The Q value depends on the energy loss in the system or damping. For the closed loop case, the dynamic characteristics of the system are determined by both functions of controller and mechanical properties of stage. Figure 4 shows a block diagram of a closed loop PID control model of the NanoMechanisms.

The settling time is used as an important criterion which characterises the dynamic properties of a closed loop system. The shorter the settling time, the faster the stage can move. Settling time is defined as the time taken for stage to move and settle down within a certain percentage of the command step, (usually 2 %). For a step response the settling time is composed of two parts: the time for slewing and the time for ringing to settle down. For large signals the settling time mainly depends on slew-rate, and the slewing time dominates. With small signals the ringing time dominates. The small signal settling time mainly depends on PID parameters, and mechanical damping in the stage helps greatly to improve the settling speed. In most applications, the stage is driven with a series of small step signals and so the small signal settling time is the main concern. The small signal settling time is measured through a snapshot of a 500 nm step response. The time for stage to settle down to within 10 nm (2 % of the step), or sometimes 5 nm or even 2 nm for some special applications, is taken as the settling time of the stage. Figure 5 (curve *a*) is a typical step response of the NPS-Z-15A, which has a small signal settling time of 1.6 ms for settling down to 2 % of the command position.

Sometimes, the loading mass can have a big influence on dynamic performance of the system, especially for the stages of compact size. To avoid the problem, the Queensgate digital controller is so designed that the PID parameters can be easily defined by users and therefore it possible to optimize the performance in situ.. Curve *a* in Figure 5 is measured from an unloaded stage under the control of optimized PID parameters, curve *b* shows how the performance was influenced by a 100 g mass loaded onto the stage, and re-optimized PID parameters gives back a desired step response as curve *c*.

Conclusion

To build an ultra precision positioning stage of nanometer or even subnanometer metrological capability, many metrological and design concepts have to be considered carefully. Those mainly include noise, linearity, hysteresis, Abbe errors (linear and rotational parasitic motions), dynamic characteristics and stability. The NanoMechanisms are designed with all these issues in mind and built and characterized with most advanced techniques. The initial results of systematic assessment have shown that their performance is well under control at nanometer level or below.

Reference

1. Ying Xu, Paul D Atherton, Thomas R. Hicks and Malachy McConnell, Design and Characterisation of Nanometer Precision Mechanisms (Paper I), *Proceedings of ASPE 1996 Annual Meeting*, Monterey.
2. Thomas R. Hicks, Paul D Atherton, Ying Xu, and Malachy McConnell, *The NanoPositioning Book*, Queensgate Instruments Ltd, 1997
3. NanoSensor is a trade mark for the capacitance sensors of Queensgate Instruments Ltd

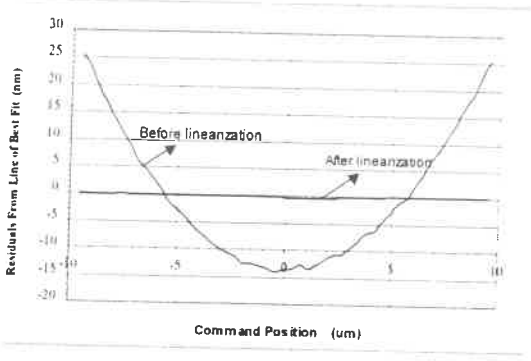

Figure 1 Linearity errors

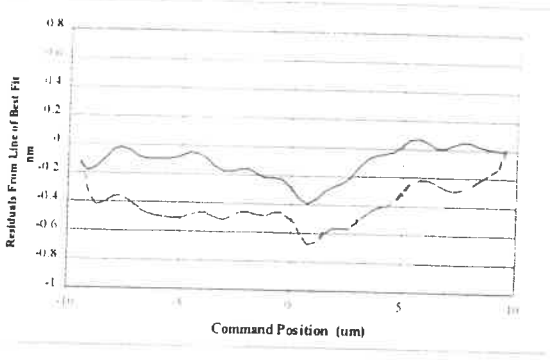

Figure 2 Hysteresis error

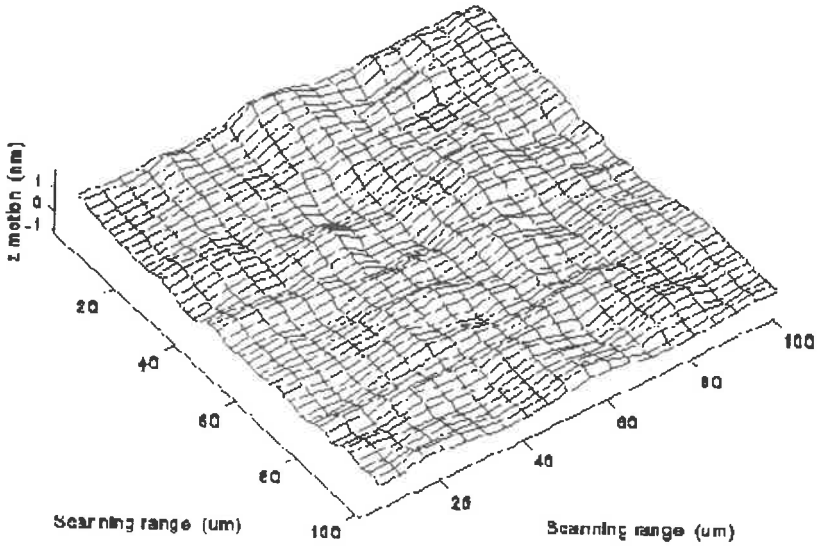

Figure 3 Out-of-plane parasitic motion of x-y stage

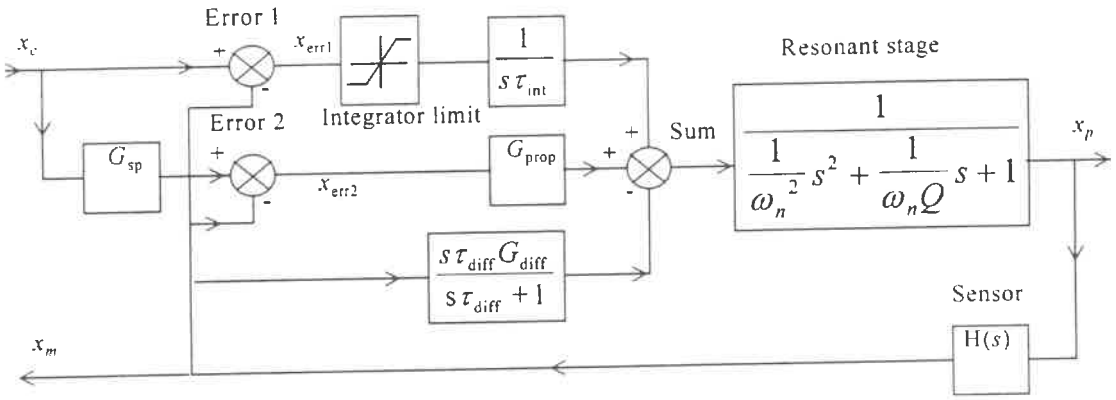

Figure 4 A block diagram of closed loop control

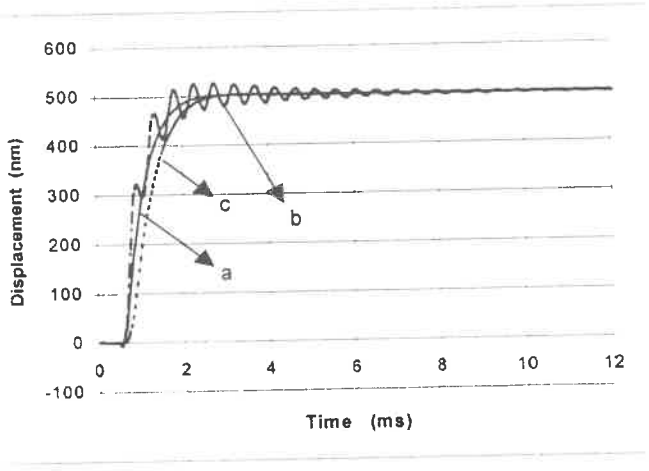

Figure 5 Step response of NPS-Z-15A

PRELOAD CONTROL IN BALL SCREW USING PIEZOELECTRIC ACTUATORS

Shigeo Fukada
Department of Mechanical Systems Engineering
Shinshu University
500 Wakasato, Nagano 380 JAPAN

1. Introduction

Ball screws are usually used in the preloaded condition. The preload serves to eliminate the backlash of nuts and to improve their stiffness. On the other hand, the preload also has negative effects: it increases friction loss, which results in more heat generation, causing thermal expansion of the screw shaft and accuracy deterioration[1)2)]. Although the preload has these advantages and drawbacks, the existing ball screws used are under constant preload. Therefore, it is desirable that the preload be controlled: increased when the load is heavy and the speed is low; decreased when the load is slight and the speed is high. This study proposes a method of controlling the preload of ball screws using piezoelectric actuators (PEA). The expansion of the PEA is so slight that the stiffness of each part must be painstakingly designed to transform the expansion into the force efficiently. In this report, first, the force generating characteristics of the PEA are considered fundamentally using a simplified model; next, manufacture and testing of the preload controllable ball screw are examined.

2. Principle

The concept of the preload controllable ball screw is shown in Fig. 1. The ball screw is the double-nut type, and PEAs are inserted between the nuts. The preload is controlled by PEAs to change the distance between the double nuts. In order to eliminate the hysteretic effect of PEA, the actual preload is sensed by load cells for feedback control.

A statical model for the mechanism of preload control is described in Fig. 2. The PEA is modeled as a combination of a generator of displacement δ_p and an elastic element of stiffness K_2. Fig. 3 shows the characteristics of the PEA used in this study. If the expansion of the PEA is not restrained, it will generate a displacement of 16 μm for the applied voltage of 100 V. On the other hand, if the expansion is completely restrained, it will generate a force of 4 kN. However, in actual practice, the displacement of PEA is absorbed into other elastic elements, so that the generated force is reduced.

In the model of Fig. 2, the generated force F is given by the following equation.

$$F = K_0\left(\delta_0 + \delta_p + \delta_d\right) \qquad (1)$$

where δ_0 is the displacement of initial preloading, and δ_d represents the change in the distance between the

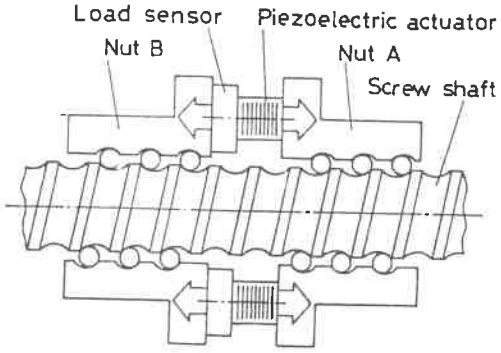

Fig. 1 Basic concept of preload control

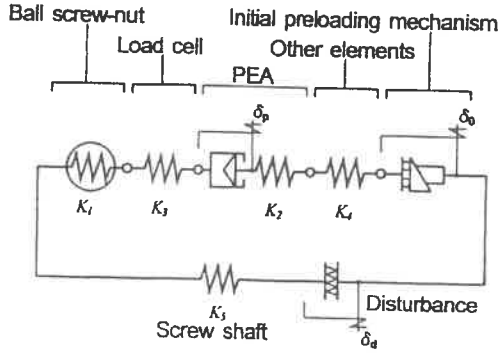

Fig. 2 Principle of preload control

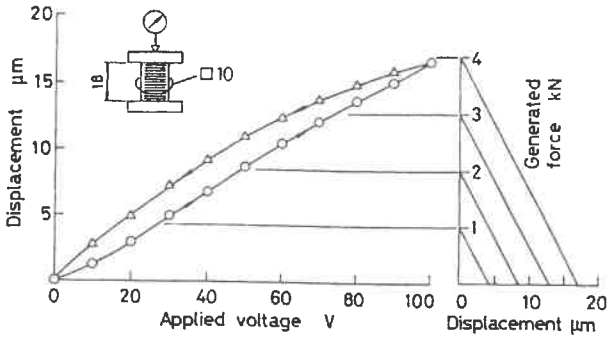

Fig. 3 Characteristics of piezoelectric actuator

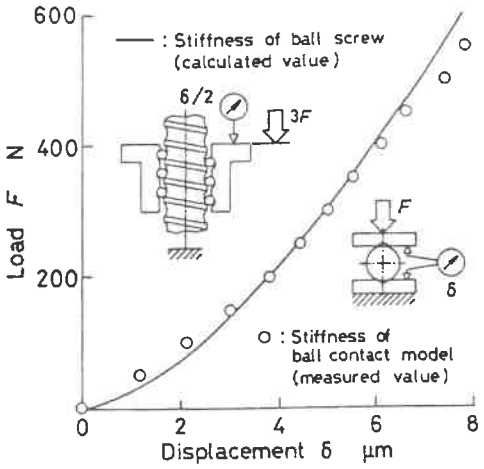

Fig. 4 Stiffness of ball screw

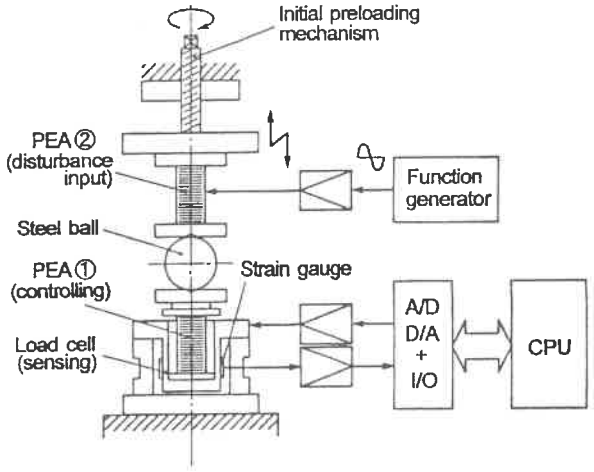

Fig. 5 Experimental set up for simplified model

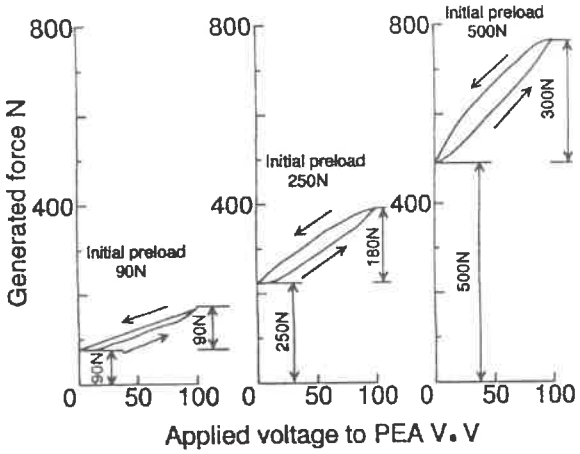

Fig. 6 Initial preload and force generation

nuts caused by the lead error of the screw shaft, which acts as the disturbance for the preload control system. K_0 in eq. (1) means the combined stiffness of the mechanism, given as follows.

$$\frac{1}{K_0} = \sum_{i=1}^{5} \frac{1}{K_i} \qquad (2)$$

K_1 in Fig. 2 represents the stiffness between the screw shaft and the nuts through circulating balls. Because the characteristics of K_1 are ruled by Herzian contact, it is nonlinear as shown in Fig. 4. The solid line in the figure represents the stiffness of the ball screw used in this study[3]. The stiffness, as seen in the slope of the curve, becomes larger as the applied load increases, so that the manipulated range of the preload becomes wider with the increase of the initial preload.

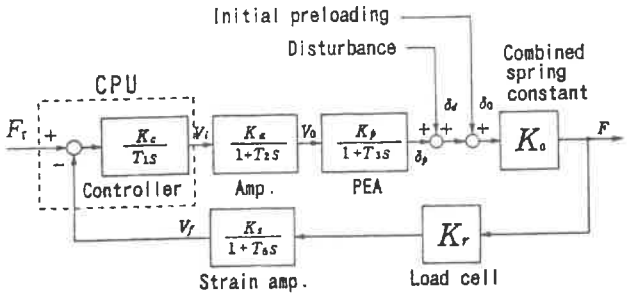

Fig. 7 Block diagram of control system

3. Experiments on simplified model

3.1 Statical characteristics First, a compact preloading unit, which consists of a PEA (□10×18 mm) and a cylindrical load cell with strain gauges, is manufactured for trial. To evaluate the preloading unit, simplified experiments are performed as shown in Fig. 5. The stiffness of the practical ball screw is simulated by a "single ball model". The measured stiffness of the model is similar to the ball screw as shown in Fig. 4. To simulate the disturbance in Fig. 2, another PEA is set serially to the preload control unit.

Fig. 6 shows the generated force as the function of applied voltage to the PEA. The force at this point is not controlled with feedback, so that the characteristics show hysteretic effects. It is shown in the figure that the manipulating range of the preload is enlarged by the increase of the initial preload because of the nonlinearity of the stiffness mentioned above. The range of preload control is about 300 N with an initial preload of 500 N.

3.2 Control system The generated force is sensed by the load cell, and the sensed signal is fed back to the controller. Fig. 7 shows a block diagram of the control system. The controller with integral operation is realized by 16 bits digital CPU. The sampling time T_1 is 2 ms. The parameter K_c is tuned to 1.4 V/V.

Fig. 8 shows the closed loop response of the control system to the step input of reference F_r. The resolution of preload control is finer than 5 N, and the system responds without hysteresis.

3.3 Dynamic response Fig. 9 shows the frequency response of the closed loop system: (a) is the response to the reference input. The band width of the system is limited to 10 Hz even though the PEA must have a dynamic range wider than 10 kHz. The cause of the limitation lies in the low pass filter in the strain amplifier, the cut off frequency of which is 10 Hz.

Fig. 9 (b) is the response to the disturbance input. The disturbance is given by applying a sinusoidal voltage of 12 V amplitude to the PEA② in Fig. 5. The preload control system responds to the dynamic input to resume the disturbance of 5 Hz.

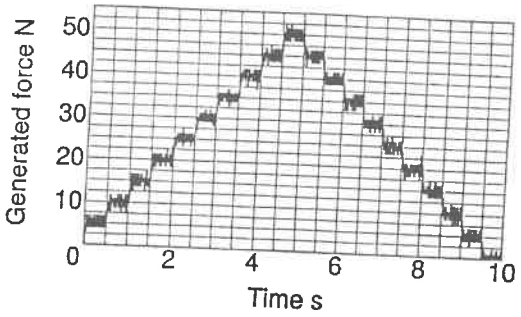

Fig. 8 Step response of preload control system

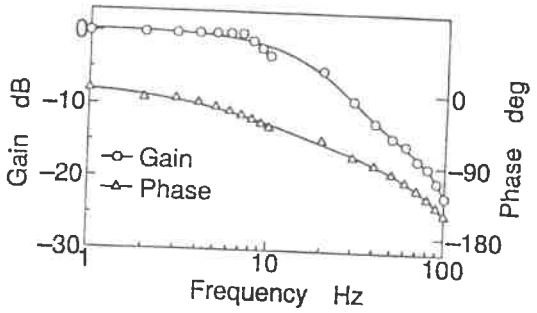

(a) Response to reference input

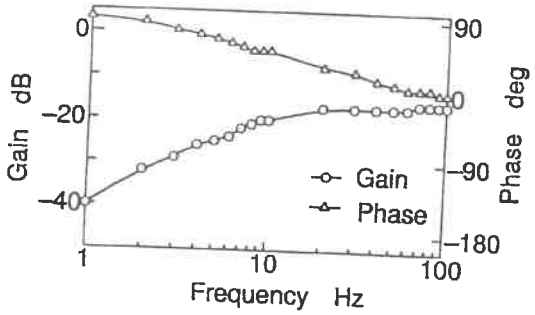

(b) Response to disturbance input

Fig. 9 Frequency response

4. Preload controllable ball screw

4.1 Structure On the basis of the results of the above simplified experiments, a preload controllable ball screw is constructed as shown in Fig. 10. Three preloading units are set on the nut flange so as to surround the screw shaft symmetrically; then they are inserted between the double nuts of the ball screw. The outer diameter of the screw shaft is 32 mm, the lead is 5 mm, and the circuit of ball circulation is 2.5×2. Micrometer heads are used as the initial preloading

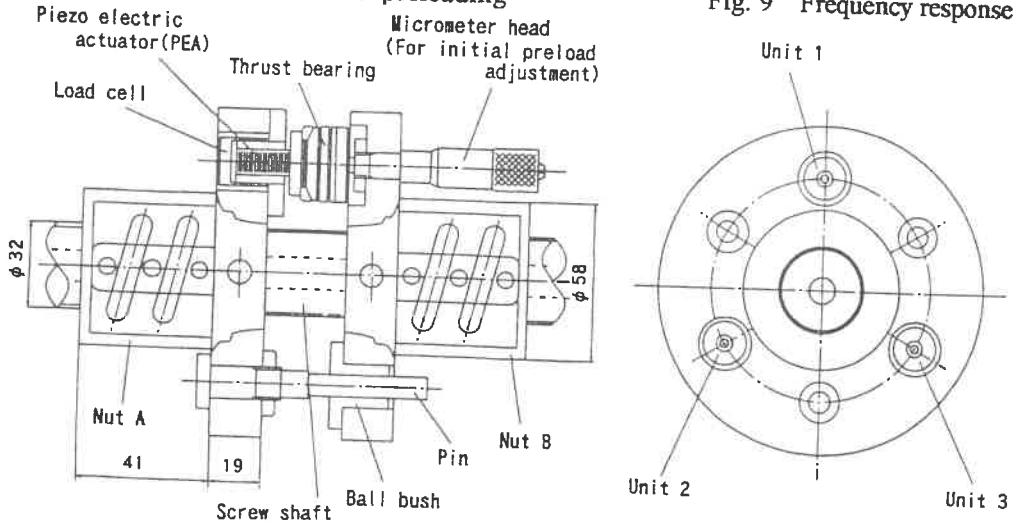

Fig. 10 Construction of preload controllable ball screw

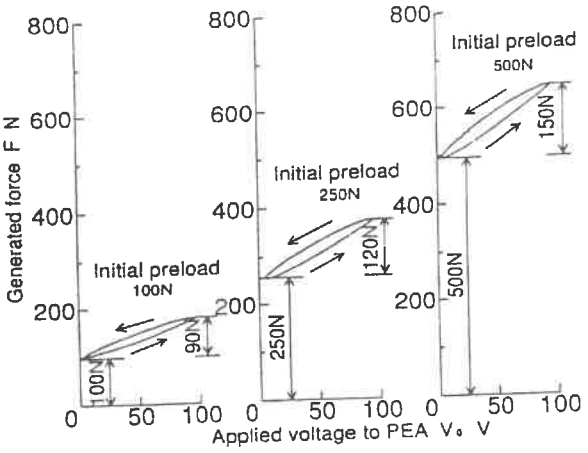

Fig. 11 Initial preload and force generation

device. A thrust ball bearing with spherical washer is inserted between each micrometer head and the preload unit so as to prevent the misalignment. To fix the phase between the nuts, three pins guided by ball bushes are inserted through the nut flanges.

4.2 Performance First, the range of generated force is tested without feedback control, similar to the experiments of Fig. 6. Fig. 11 shows the generated force per preload control unit as the function of the applied voltage to the PEA. The range of preload control is 150 N with an initial preload of 500 N, or a total range of 450 N for three units. The actual range per unit is smaller than the result on the simplified model. The actual mechanism in Fig. 10 includes some elements with low stiffness, such as the thrust ball bearings or micrometer heads, which are not assumed in the simplified model, so that the combined stiffness K_0 in eq. (1) is smaller than in the simplified model.

Next, the preload is controlled with feedback system as shown in Fig. 7. The experiments are performed on the ball screw while it is rotating with an actual speed of 60 rpm, while the driving torque (drag torque) is measured instantaneously. Fig. 12 shows the results. (a) shows the applied voltage to the PEAs, and (b) shows the generated force of each unit. The initial preload is 500 N per unit, and the desired value of preload is 600 N. After feedback control starts, the applied voltages are regulated so as to keep the preload at 600 N. Variation of the preload caused by rotation is eliminated by the preload control. Fig. 12 (c) shows the driving torque of the ball screw. The torque changes at the same time as the preload is increased. These results mean that preload control in ball screw is possible using PEA, and that this preload control is available to change the driving condition dynamically or actively.

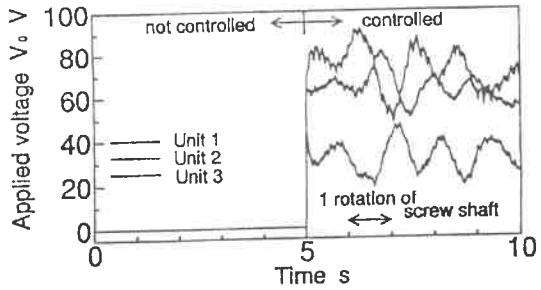

(a) Applied voltage

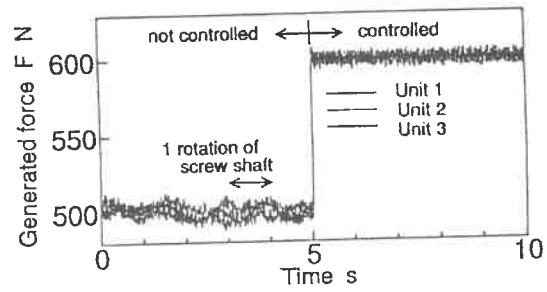

(b) Generated force

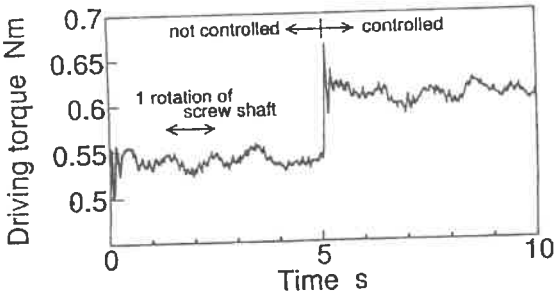

(c) Driving torque

Fig. 12 Performance of preload control

5. Conclusions

(1) A method of controlling the preload of ball screw is proposed using PEAs, and a compact preloading unit is manufactured for trial.

(2) Experiments on the simplified model show that the control range of the preload is about 300 N with an initial preload of 500 N.

(3) The preload controllable ball screw is constructed using the preloading units, and the availability of the preload control is confirmed experimentally.

References

1) J. Otsuka, S. Fukada et al.: A Study of Thermal Expansion of Ball Screw, Bull. JSPE, 17, 4 (1983) 273.
2) N. Obuchi and J. Otsuka: Study of Friction Torque of Ball Screw, Bull. P.M.E. (Tokyo. Inst. Tech.), No. 61(1988)1.
3) NSK Ball Screw Catalog, CAT. No. 3101 (1993).

Thin, Light-weight, Compact Pick-Up Actuator for High Precision, Fast Access CD-ROM Devices

S. M. KIM, D. G. GWEON

Dept. of Mechanical Engineering
Korea Advanced Institute of Science and Technology

Abstract

For a conventional pick-up actuator, the magnets are used separately to the coarse actuator and the two axis actuators. That is, a magnet and yoke assembly is mounted on the moving part which becomes heavy. But in this study the proposed thin, light-weight, compact pick-up actuator is designed to mount only one magnet and yoke assembly for the coarse actuator and two axis actuators to reduce the moving part mass, and the teflon coating was done to the guide to reduce friction, which results in the significant decrease in seek time. For the optimally designed pick-up actuator, the tickness and the seek time was obtained below 10mm and 15msec, respectively. The parasitic resonances due to the wire suspension supporting the optical head are attenuated using the modal strain energy method.

1. Introduction

The small sized optical disk drive with short seek time capability is generally applied to the multi-media devices and computers. To reduce the seek time, the optimal design study for the moving coil actuator was being done.[1],[2] However, the optimal design was mainly focused to the coarse actuator. The usual pick-up actuator used the magnet separately on the coarse actuator and two axis actuators. That is, a magnet and yoke assembly are mounted on the moving part, which leaved the moving part heavy. But in this study the proposed thin, light-weight, compact pick-up actuator is designed to mount only one magnet and yoke assembly on the coarse actuator and two axis actuators to reduce the moving part mass, and the teflon coating was done to the guide to reduce friction. The moving coil actuator is designed via the optimal design including the coarse actuator and two axis actuators.

2. Structure of the moving coil actuator

The proposed pick-up actuator is shown in Fig.1. As can be seen from the Fig.1, a fixed magnet and yoke assembly is used for the coarse and two-axis actuators. For the coarse actuator, teflon coating was processed on the guide to reduce friction. The optical head is supported by four wire suspensions. From this optimal design, the pick-up actuator can be made with less than 10mm thickness and light weight.

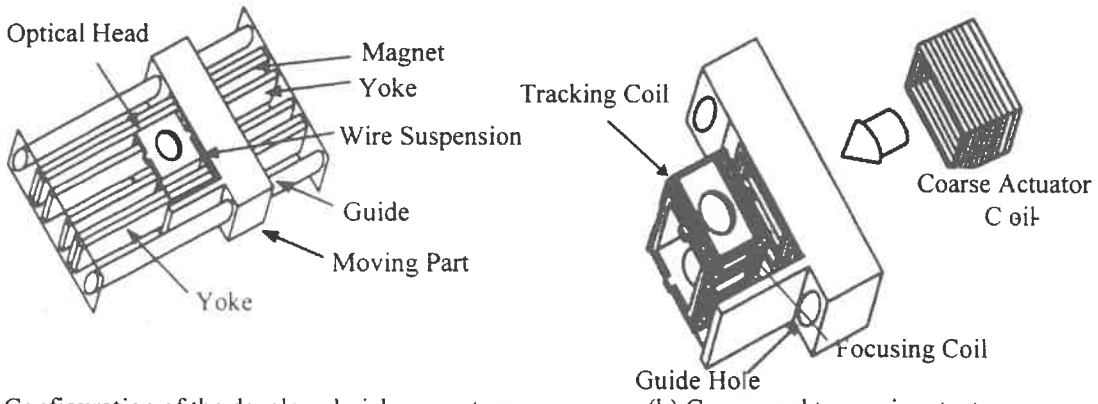

(a) Configuration of the developed pick-up system (b) Coarse and two-axis actuators

Fig. 1 Structure of the pick-up actuator

3. Optimum design of the pick-up actuator for fast access

The optimal design parameters of pick-up actuator are the dimensions of moving part, the coarse actuator coil, the focusing/tracking coil, the optical head, the magnetic flux density. The cost function in the optimal design is to minimize the mass of the optical head and the moving part. The constraints of the optimal design are the 1st natural frequency (higher than 25Hz), 1Hz sensitivity (1mm/V), 200Hz sensitivity (50μm/V) and Q-value (lower than 8dB).

Hence, the proposed pick-up actuator is optimally designed to satisfy the constraints minimizing the cost function. To get 15msec average seek time[3](1/3 full stroke), the coarse actuator drive force F_s and the required force F_n are given as below.

$$F_s = BLnI \tag{1}$$

$$F_n = M_t\left[L_s\left(\frac{\tau_a}{T_{av}}\right)^2 + \mu(v)g\right] \tag{2}$$

where

B : magnetic flux density at air gaps
L : coil length in the air gaps
n : number of coarse actuator coil turns
I : coarse actuator coil current
M_t : total mass
L_s : access full stroke
T_{av} : average seek time (1/3 full stroke)
g : gravitational acceleration

$\tau_a = \dfrac{\beta_m + \frac{1}{3}}{\sqrt{\beta_m}}$ β_m : minimum speed factor (from $\dfrac{\partial F_n}{\partial \beta} = 0$)

$\mu(v)$: friction coefficient of teflon coating for velocity

From the equation(2) the minimum value of F_n is calculated for the given average seek time. The actuator is optimally designed so that F_s has the minimum value of F_n, which is ultimately the same approach to minimize the actuator size. The total mass M_t from the equation(1) covers the coil mass determined by the number of coil turns and coil length in equation(1). M_t also includes the optical head mass. Therefore it is impossible to obtain the F_n and F_s directly. That is, F_s can be calculated numerically. Figure 2 shows the flow chart in the optimization program.

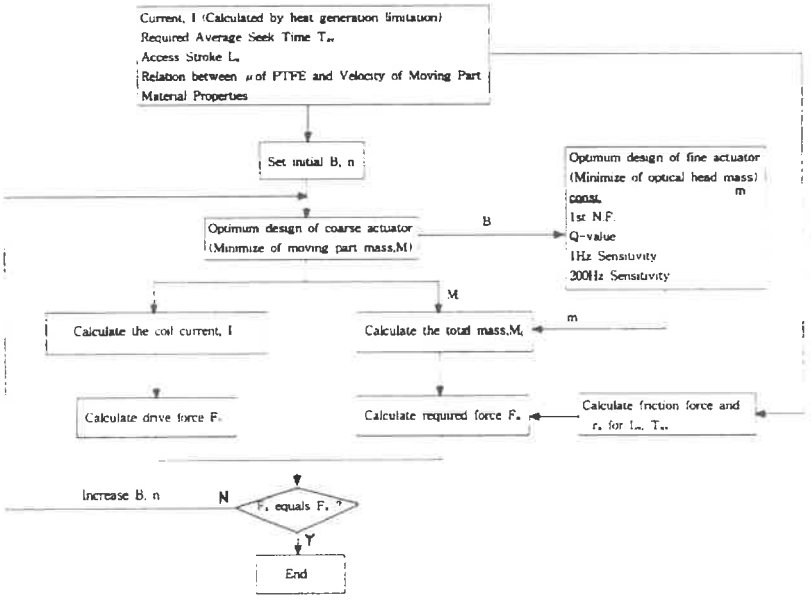

Fig. 2 Flow chart for the developed actuator design

From the fig.2, the initial small values of B, n are arbitrarily selected. The design parameters and F_s are calculated satisfying the cost function and constraints. If F_s is not equal to F_n, iterations are repeated so that F_s is converged to F_n by increasing the infinitesimal amount to B and n. Figure 3 shows the relationship between the speed factor and average seek time with respect to the M_t of 15 g and L_s of 32 mm. As can be seen, the minimum average seek time is obtained when β value is 0.16.

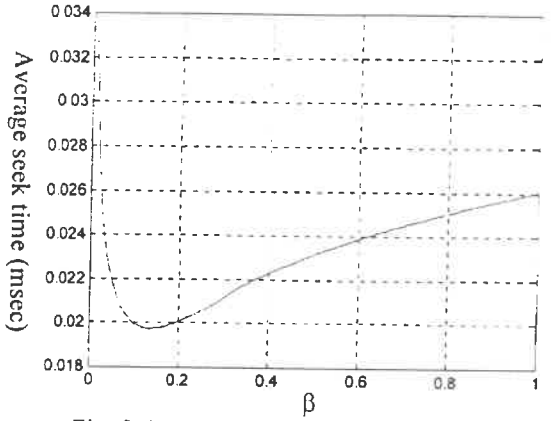

Fig. 3 Average seek time vs. speed factor

4. Vibration and damping analysis of wire suspension

From the fig.4 assuming a quarter of the optical head mass is supported by each wire suspension, the parasitic resonances of wire suspension is attenuated by the viscous damping material.

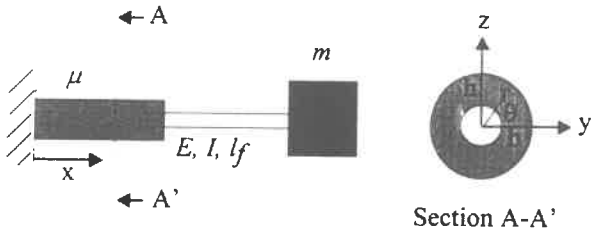

Fig.4 A wire spring modelled as cantilever beam

In the Fig. E, I, and l_f are representing the elastic modulus, moment of inertia, length of the suspension, while m and μ represent a quarter of optical head mass and the dynamic viscosity of viscous damping material, respectively. Also, h represents the gap between the wire suspension and the damping material. The damping ratio can be obtained using the modal strain energy method[4]. The beam's transverse displacement with respect to each mode can be expressed as follows.

$$Z_i(x,t) = Z_i(x)\, e^{j\omega_i t} \tag{3}$$

The beam's damping ratio in each mode can be written as equation(4).

$$C_i = \frac{1}{2}\left(\frac{W_{diss}}{2\pi W_{total}}\right) \tag{4}$$

where W_{diss} represents the dissipated energy by the damping material during one cycle vibration while W_{total} represents the total energy stored to the beam during resonance. Using the equation (3), W_{total} can be calculated as given in equation (5).

$$W_{total} = \left| \frac{1}{2}\rho \int_0^{l_f} \left(\frac{\partial Z_i}{\partial t}\right)^2 dx \right| \tag{5}$$

where $l_f \rho$ represents the mass of wire suspension. Using the transverse displacement, $Z_i(x,t)$, beam's longitudinal displacement, $\delta_i(x,t)$, can be obtained as below.

$$\frac{\partial \delta_i(x,t)}{\partial x} = -r\sin(\theta)\frac{\partial^2 Z_i(x,t)}{\partial x^2} \tag{6}$$

Assuming the dissipated energy is caused by the shear deformation of damping material which appears to the surface of wire suspension, the dissipated power is writen as follows.

$$\Pi_{diss} = \frac{\mu \omega_i r}{l_f} \left| \int_A \delta_i \dot{\delta}_i d\theta dx \right| \tag{7}$$

From the equation (7), the dissipated energy can be obtained as below.

$$W_{diss} = \left| \Pi_{diss} \right| \frac{\pi}{\omega_r} \tag{8}$$

Hence the damping ratio can be calculated using the equations(4), (5), and (8). The vibration and damping analysis of the wire suspension using the modal strain energy method and the optimization algorithm in fig.2 are used to design optimal pick-up actuator.

Table 1 lists the performances of the optimal-designed actuator when T_{av} is 15msec. The performances listed in the Table 1 satisfy all the optimization constraints.

Table 1

1st natural frequency (tracking)	27.74 Hz	Q-value (focusing)	6.16 dB
Q-value (tracking)	8 dB	1Hz sensitivity (focusing)	6.47 mm/V
1Hz sensitivity (tracking)	5.72 mm/V	200Hz sensitivity (focusing)	126.6 μm/V
200Hz sensitivity (tracking)	112.2 μm/V	Magnetic flux density (B)	5100 Gauss
1stnatural frequency (focusing)	27.74 Hz	Total mass (M_t)	1.48 g

Figures 5 and 6 show the frequency responses to the direction of focusing direction with and without damping, respectively. In fig.6 many parasitic resonances are happened within the 30 kHz range. However, these parasitic resonances are fully attenuated due to the damping ratio using the modal strain energy method, as can be seen from the fig.6.

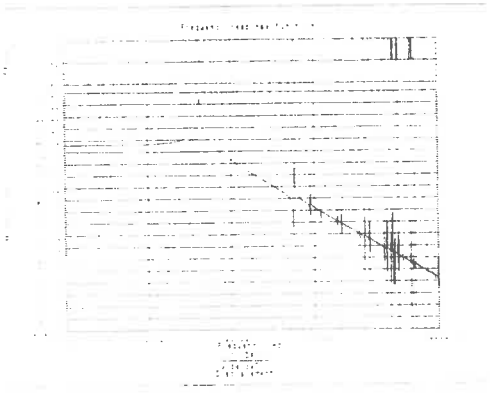

Fig.5 Frequency response without damping

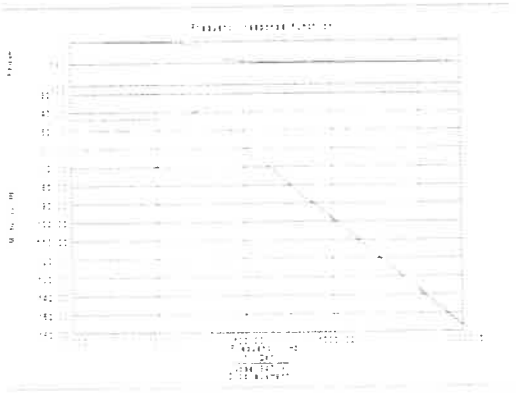

Fig.6 Frequency response with damping

5. Conclusions

For the proposed pick-up actuator in this study a fixed magnet and yoke assembly are used to the coarse and two axis actuators. This structure makes it possible to design the thin, light-weight, compact pick-up actuator with thickness of less than 10mm. Using the optimal designed pick-up actuator fast seek can be possible that the average seek time is less than 15msec. The parasitic resonances due to the wire suspension supporting the optical head are attenuated using the modal strain energy method.

REFERENCES

[1] Tetsu Yamamoto, Takashi Yumura and Hiroo Shimegi, *Proc. SPIE*, Vol.695, pp.153-159(1986)

[2] J. Arthur Wagner, *IEEE Trans. on Magnetics*, Vol.Mag-19, No.5, pp.1686-1688(1983)

[3] F. R. Hertrich, *IBM J. Res. Develop.*, Vol.9, pp.124-133(1965)

[4] Marsh, E. R. and Slocum, A. H., *J. of ASPE*, Vol.18, No.2/3, pp.103-109(1996)

A Long Stroke and Ultra Precision XYθ Stage Using Simple Linear DC servo Actuators

Sung-Q Lee and Dae-Gab Gweon
Dept. of Mechanical Engineering
Korea Advanced Institute of Science and Technology
373-1 Kusung-Dong, Yusong-Gu, Taejon, 305-701, Korea

Abstract

A XYθ stage which has a long stroke and ultra precision resolution without extra fine servo is proposed. The characteristics of the stage are symmetry, simple servo principle, and inherently infinite resolution. it has three linear actuators and three air bearings which are radially disposed with 120 degrees pitch, so that it has symmetry. And a linear actuator is the type of VCM, so that it has simple servo mechanism. Moreover, with the use of air bearings, it has no friction or wear allowing the chance of infinite resolution.

1. Introduction

A dual servo stage (coarse servo and fine servo) has been popular for the wafer positioning purpose. However, this has complex structure and control scheme. Therefore, a XYθ stage which has a long stroke and ultra precision resolution without extra fine servo - more over rapid response - is proposed. Recently, many kinds of systems are published to meet the purpose of long stroke and ultra precision resolution-for example friction drive, dual servo system in which coarse/fine servo work together and surface motor using BLDC type motor. However, though these systems meet the purpose, a friction drive has low bandwidth, a dual servo system has complex structure and control algorithms, and a surface motor has complicated motor. Therefore, a Long Stroke and Ultra Precision XYθ Stage Using Simple Linear DC servo Actuators is presented.

2. Characteristics of System

Symmetry

Figure 1. shows the configuration and prototype photo of the proposed system. The stage consists of three linear actuators and three air bearings. Three linear actuators are attached at the upper plate symmetrically and disposed radially with 120 degrees pitch, and so does the air bearings. Actuation force is induced by the moving coil type voice coil motor (VCM). From the combination of three actuators, x, y and θ motions can be obtained. Especially, the stage will be rotated when each actuator produces the same force. With this configuration, working space becomes the shape of 10mm diameter circle. By virtue of symmetrical configuration, this system is under low thermal effects and appropriate to the precision system.

Simple Servo

Figure 2. shows the cross section of the linear actuator. Actuation force is induced by moving coil type voice coil motor (VCM) as mentioned above. Since moving coil type VCM has lighter moving mass than that of moving magnet type, the moving coil type is preferable. Each actuator has permanent magnets which produce the Z-directional magnetic flux and a moving coil which cross the permanent magnets. As in figure 2, two permanent magnets are placed to look each other in order to make the same directional force when the closed coil has different current direction. By the Fleming's Left Hand Rule, each actuator simply produce actuation force.

$$F_{act} = nBil$$

where n is the number of coil turns, B, air gap flux, i, current, l, coil effective length. It is noticeable that since there are no ripples or nonlinearity of magnetic flux, high precision position control can be possible as well as high speed. By the way, like usual rotary motor, since it has also back emf, it need care to derive the transfer function from voltage input to output speed.

In this system, 2BB ferrite permanent magnet of maximum residual flux is 4,100 gauss is used. Therefore at operating point flux is about 3500 gauss. Coil of 0.5 diameter is wound 480 turns. l, effective length is 50mm. Therefore, one actuator of this system can exert following actuator force at rated 1 ampere(A),

$$F_{act} = 480(\text{turns}) \times 0.35(\text{T}) \times 1(\text{A}) \times 0.05(\text{m}) \times 2(\text{two sides})$$
$$= 16.8\ (\text{N})$$

The specifications of proposed system are summarized in Table 1

Total range	10mm diameter circle
Linear Actuator	
Permanent Magnet	
Quantity	6 EA(2EA/1actuator)
Material	Ferrite type, 3500 gauss
Coil	
Number of turns	480
Size	0.5mm diameter
Rated Current	1 ampere
Rated Actuation Force	16 N
Air gap	7mm
Air bearing	
Type	Annular type (Ro=30mm, Ri=12mm)

Table 1. Specification of Proposed System

Inherently infinite resolution

Three air bearings are used to guide the stage. Each bearing is attached to the upper plate and supports the moving part. The stage can move XY-direction freely and is under constraint in Z-direction to reduce the Z-direction movement and tilting. Because of air bearing, the stage does not have friction and wear, so that ultra precision control can be possible. Also, like other servo motors, this system has inherently infinite resolution but is restricted by the measurement

device or digital quantization. Therefore, without extra fine servo, structure and control scheme is simple and ultra precision resolution can be obtained.

3. Dynamics of this system

Figure 3 shows the schematic of three directional actuation mechanism. Each linear actuator exert actuation force are same and can be obtained by the following equation

$$F_{act} = nBil = k_s\, i$$

where trust constant $k_s = nBl$.

The dynamics of the system can be expressed by the following matrix equations:

$$\boldsymbol{M}\ddot{\boldsymbol{x}} = \boldsymbol{T}\boldsymbol{k}\boldsymbol{i}$$

$$\boldsymbol{L}\dot{\boldsymbol{i}} + \boldsymbol{R}\boldsymbol{i} = \boldsymbol{V} - \boldsymbol{k}\boldsymbol{T}^{T}\dot{\boldsymbol{x}}$$

$$T = \begin{bmatrix} 1 & -1 & -1 \\ 0 & 1 & -1 \\ 1 & 1 & 1 \end{bmatrix}$$

Where $\boldsymbol{M}$ = diag(M, M, J) is the mass and inertia matrix, $\boldsymbol{x}$ = [x, y, θ]^T stage position vector, $\boldsymbol{k}$ = diag(k_s, k_s, k_s) the trust constant matrix, $\boldsymbol{L}$ = diag(L, L, L) the coil inductance matrix, $\boldsymbol{R}$ = diag(R, R, R) the coil resistance matrix, $\boldsymbol{i}$ = [i_x, i_y, i_θ], the current vector, $\boldsymbol{V}$ = [v_x, v_y, v_θ] the input voltage vector, T the transformation matrix linearized at θ=0 degree.

It is noticeable that the $\boldsymbol{k}$, $\boldsymbol{L}$, $\boldsymbol{R}$, matrix has the value because of the symmetrical design of the system.

4. Conclusion

A XYθ stage which has long stroke and ultra precision resolution without extra fine servo is proposed. The characteristics of stage are symmetry, simple servo principle, and inherently infinite resolutio. In detail, it has three linear actuators and three air bearings which are radially disposed with 120 degrees pitch, so that it has symmetry. And a linear actuator is the type of VCM, so that simple servo mechanism can be obtained. Moreover, with the use of air bearings it has no friction or wear. To control the system it need to derive the dynamics of proposed system and is derived. In the future, closed loop control may be performed with laser interferometer feedback.

References

[1] Alexander H. Slocum, 1992, "Precision Machine Design", Prentice-Hall.

[2] S.A.Nasar and L.E.Unnewehr, 1983, "Electromechanics and Electric Machines", John Wiley and Sons.

[3] Yuichi Okazaki, Shin Asano and Takayuki Goto, 1991, "Dual-servo Mechanical stage for continuous positioning" Int. JSPE Vol.27, No.2, pp172-173.

[4] Rodney Kendall, Sam Doran and Erwin Weissmann, 1991, "A servo Guided X-Y-theta Stage for Electron beam lithography", J. Vac. Sci. Technol. B9(6), Nov/Dec.

[5] Yoshiyuki Tomita , Yasushi Koyanagawa and Fumiaki Satoh, 1996, "A Surface Motor-driven Precise Positioning System" ,Precision Engineering, Vol.16, No.3, pp184-191.

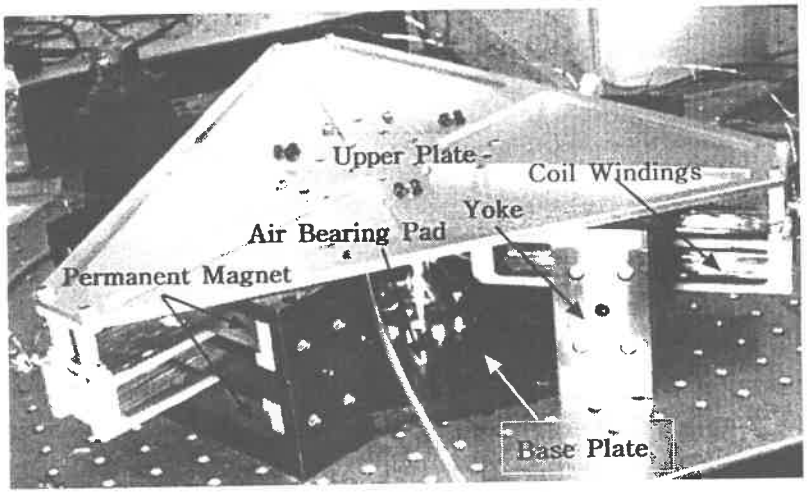

Fig. 1 Prototype of Proposed System

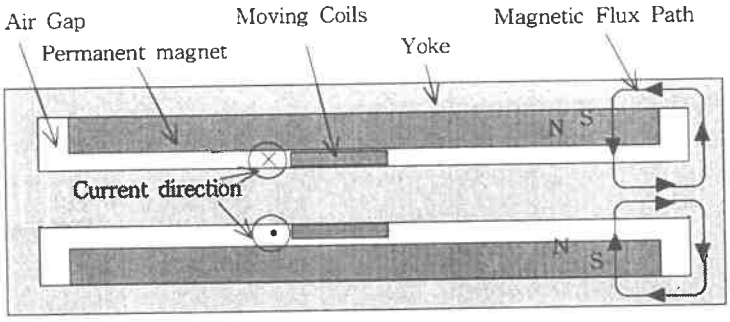

Fig. 2 Cross Section of Linear Actuator

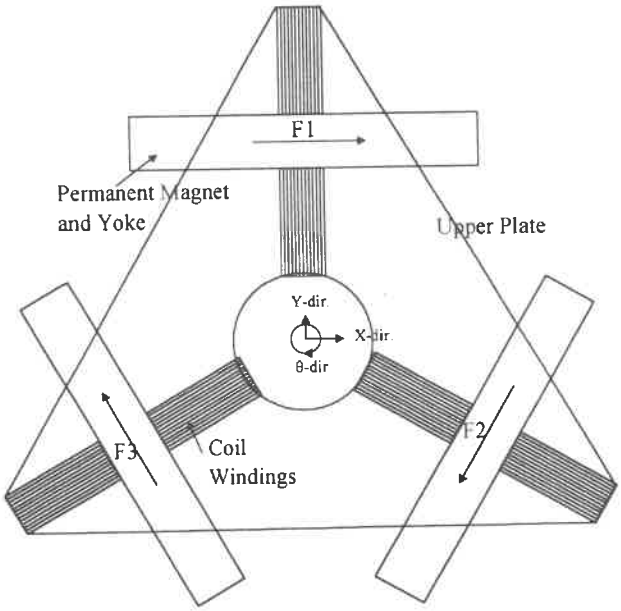

Fig. 3 Principle of Three Actuator Combination

Function Related Tolerance Theory and Its Application to Needle-Bar Motion Mechanism in A Sewing Machine

Keyoung Jin Chun, Dae Young Shin

Korea Institute of Industrial Technology
San 17-1, HongChonRi, IbJangMyun,
ChonAnSi, Chung Nam 330-820
KOREA

1. Introduction

In order to apply a tolerance theory to needle-bar motion mechanism (NMM) of an industrial lock stitch sewing machine, kinematic and sensitivity analysis are carried out. From a kinematic analysis, three constraint equations are obtained, which is later used to derive a mathematical expression of the sensitivity coefficient. Furthermore, a locus of a needle's extremity is obtained, and a dominant factor ('blade point') for stitch making is found. From a sensitivity analysis, the sensitivity coefficient of each design variable is represented as a mathematical expression by use of the implicit differentiation. Thus, the exact value of each sensitivity coefficient can be obtained. Then, it is discussed that how design variables have effects on this dominant factor, which interrelations between each design variable exist, and how tolerance values are effectively allocated to design variables in consideration of machining and/or assembling difficulties within the domain of allowable errors of the machine's function.

From the above results, the motion of NMM is characterized, and well distributed tolerance values to design variables might be determined by a function related tolerance theory for better machine designs.

2. Kinematic analysis of NMM

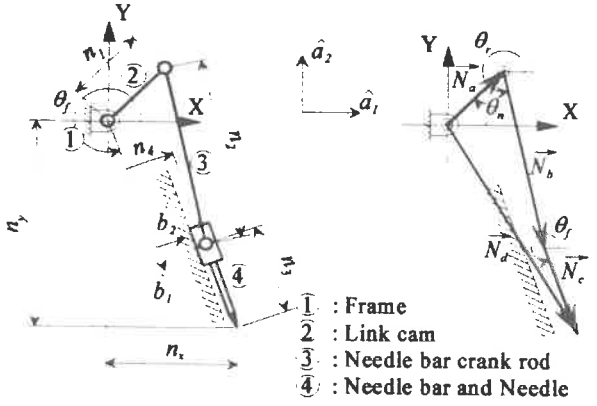

Figure 1. Needle bar motion mechanism

NMM is a slide crank mechanism as shown in *Figure 1.* The reference system is the Cartesian coordinate system. There are two unit coordinate vectors on a frame.

One is $(\hat{a}_1,\hat{a}_2)$ directed along the X and Y coordinate axes. The other is $(\hat{b}_1,\hat{b}_2)$ which defines the sliding plane S of a follower. Here, $\hat{b}_1$ is parallel to the sliding plane S.

NMM is composed of the link cam (driver), the needle bar crank rod (coupler), the needle bar and needle (follower) and the body (frame) as shown in *Figure 1*. The input of NMM is a rotational angle θ_n of the link cam and the output of NMM is a periodic movement (n_x,n_y) of the needle's extremity. NMM has five constants $(n_1,n_2,n_3,n_4,\theta_f)$, one independent variable θ_n and three dependent variables θ_r,n_x,n_y. Here, θ_f and n_4 define the sliding plane of the follower.

There is a closed loop $(\vec{N}_a+\vec{N}_b+\vec{N}_c-\vec{N}_d=0)$ as shown in *Figure 1*. As Cartesian components on $\hat{a}_1$ and on $\hat{a}_2$ in this loop are equal to zero, four constraint equations are given as

$$\begin{aligned} g_1 &\equiv n_1\cos(\theta_n)+n_2\cos(\theta_r)+n_3\cos(\theta_f)-n_x \\ &=0 \\ g_2 &\equiv n_1\sin(\theta_n)+n_2\sin(\theta_r)+n_3\sin(\theta_f)-n_y \\ &=0 \end{aligned} \quad (1)$$

As $(\vec{N}_a+\vec{N}_b)\bullet\hat{b}_2=n_4$ in *Figure 1*, another constraint equation is given as

$$\begin{aligned} g_3 &= n_1\sin(\theta_n-\theta_f)+n_2\sin(\theta_r-\theta_f)-n_4 \\ &=0 \end{aligned} \quad (2)$$

From *Equation (1)* and *(2)*, the equations of three dependent variables θ_r,n_x,n_y are derived as

$$\theta_r=\theta_f+\sin^{-1}\left[\frac{n_4-n_1\sin(\theta_n-\theta_f)}{n_2}\right] \quad (3)$$

$$\begin{aligned} n_x &= n_1\cos(\theta_n)+n_2\cos(\theta_r)+n_3\cos(\theta_f) \\ n_y &= n_1\sin(\theta_n)+n_2\sin(\theta_r)+n_3\sin(\theta_f) \end{aligned} \quad (4)$$

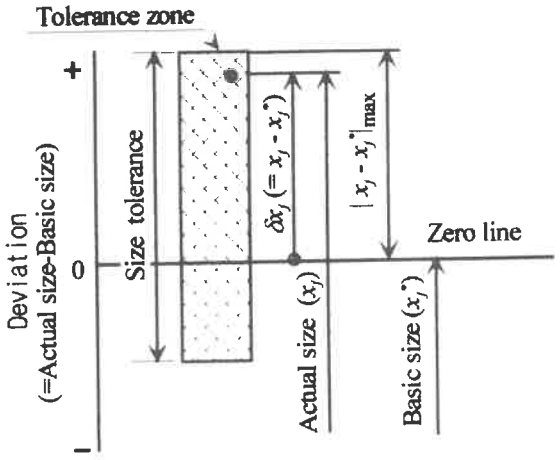

Figure 2. Basic Size, deviation and tolerance in the ISO system (by ISO 286-1:1988(E))

3. Sensitivity analysis for Tolerance

The actual size (x_j) on machine design is never able to be made as the basic size (x_j^*) as shown in *Figure 2*. Thus, the actual size of a design variable always involves a deviation from the basic size. Also this deviation of each design variable necessarily makes some response errors on dependent variables.

Assuming that dependent variables $\underline{y}:D^m\rightarrow R^n$ have derivatives of all orders everywhere in $\underline{x}\in D^m$, dependent variables $\underline{y}$ can be expanded by Talor expansion near $\underline{y}(\underline{x}^*)$ as

$$y_i(\underline{x})=y_i(\underline{x}^*)+\sum_{j=1}^{m}S_{i,j}(x_j-x_j^*)+R_i \quad (5)$$

where $S_{i,j}=\partial y_i/\partial x_j$, R_i is the remainder term.

In *Equation (5)*, if $\underline{x}$ is sufficiently close to $\underline{x}^*$, $R_i \ll y_i(\underline{x}^*) + \sum_{j=1}^{m} S_{i,j}(\underline{x}^*)(x_j - x_j^*)$. So, the remainder term can be neglected in *Equation (5)*. Hence, a change in y_i at $\underline{x}^*$ (denoted as δy_i) is rearranged as

$$\begin{aligned} \delta y_i &\approx \sum_{j=1}^{m} S_{i,j}(\underline{x}^*)\delta x_j \\ &\approx \sum_{j=1}^{m} S_{i,j}(\underline{x}^*)(x_j - x_j^*) \end{aligned} \tag{6}$$

where δx_j is a small change in $x_j^* \left(\delta x_j = x_j - x_j^*\right)$, $\delta y_i = y_i(\underline{x}) - y_i(\underline{x}^*)$ and $S_{i,j}(\underline{x}^*)$ is a sensitivity coefficient matrix, which express the sensitivity of i^{th} dependent variable to a small change in j^{th} design variable.

3.1. Maximum response error of dependent variable

When each design variable $\underline{x}$ has a deviation $\delta\underline{x}$, the response error of a dependent variable can be derived from *Equation (6)* as

$$\begin{aligned} |\delta y_i| &\approx |S_{i,1}(\underline{x}^*)(x_1 - x_1^*) + \cdots + S_{i,m}(\underline{x}^*)(x_m - x_m^*)| \\ &\le |S_{i,1}(\underline{x}^*)||x_1 - x_1^*| + \cdots + |S_{i,m}(\underline{x}^*)||x_m - x_m^*| \end{aligned} \tag{7}$$

where $|x_j - x_j^*|$ is the deviation's magnitude of j^{th} design variable.

From *Equation (7)*, it becomes clear that the maximum response error (MRE, $|ME_i|$) of a dependent variable is made when the deviation's magnitude of each design variable is maximum. That is,

$$\begin{aligned} |ME_i| \approx\ & |S_{i,1}(\underline{x}^*)||x_1 - x_1^*|_{max} + \cdots \\ & + |S_{i,m}(\underline{x}^*)||x_m - x_m^*|_{max} \end{aligned} \tag{8}$$

where $|x_j - x_j^*|_{max} \left(= max\{|x_j - x_j^*|\}\right)$ is the deviation's maximum magnitude of j^{th} design variable, and $|ME_i|$ is the MRE of i^{th} dependent variable.

3.2. Procedure for allocation of tolerance

If response errors of dependent variables were successfully derived from maximum deviations of design variables in § 3.1, it might be practicable to reversely allocate tolerances to satisfy with a limit of response error (LRE, $|LE_i|$) of the dependent variable. An allocating procedure of tolerances is introduced here.

First, assuming that every dependent variable has the same maximum deviation in order to simplify a procedure to allocate tolerances, this same maximum deviation is set as an assumed allowable deviation (α) of design variables and can be derived as

$$\begin{aligned} |LE_i| &\approx |S_{i,1}(\underline{x}^*)|\alpha + \cdots + |S_{i,m}(\underline{x}^*)|\alpha \\ \therefore \alpha &\approx \frac{|LE_i|}{\sum_{j=1}^{m} |S_{i,j}(\underline{x}^*)|} \end{aligned} \tag{9}$$

However, as each design variable has its characteristics, it is need to adjust maximum deviation of each design variable to satisfy with its own characteristics. In adjusting process, the maximum response error ($|ME_i|$) is less than or equal to the limit of response error ($|LE_i|$) as

$$|ME_i| \le |LE_i| \tag{10}$$

Then, the maximum deviation of the h^{th} design variable ($|x_h - x_h^*|_{max}$) can be obtained from changing maximum deviations of other design variables arranging *Equation*

(9) and *(10)* as

$$|x_k - x_k^*|_{max} \le a + \sum_{k=1}^{k-1} \frac{|S_{i,k}(x^*)|}{|S_{i,k}(x^*)|}(a - |x_k - x_k^*|_{max}) + \sum_{l=k+1}^{m} \frac{|S_{i,l}(x^*)|}{|S_{i,p}(x^*)|}(a - |x_l - x_l^*|_{max}) \quad (11)$$

3.3. Sensitivity coefficient matrix of NMM

NMM has four design variables $\underline{\xi} = [n_1, n_2, n_3, n_4]^T$ which are independent each other, and three dependent variables $\underline{e}(\underline{\xi}) = [\theta_r, n_x, n_y]^T$. Here, $\underline{e}$ is the function of $\underline{\xi}$.

There are four constraint equations as shown in *Equation (1)* and *(2)* in NMM. These equations can be rearranged as

$$\underline{g}(\underline{e}, \underline{\xi}) = 0 \quad (12)$$

where $\underline{g} = [g_1, g_2, g_3]^T$.

Equation (12) can be differentiated with the design variables $\underline{\xi}$ by using the chain rule, and a sensitivity matrix is derived as

$$[r_{\gamma\varepsilon}] = -[v_{\alpha\beta}]^{-1}[s_{\varepsilon\mu}] \quad (13)$$

where $v_{\alpha\beta} = \partial g_\alpha / \partial e_\beta$, $r_{\gamma\varepsilon} = \partial e_\gamma / \partial \xi_\varepsilon$, $s_{\varepsilon\mu} = \partial g_\varepsilon / \partial \xi_\mu$, and $[v_{\alpha\beta}]$ is a nonsingular matrix.

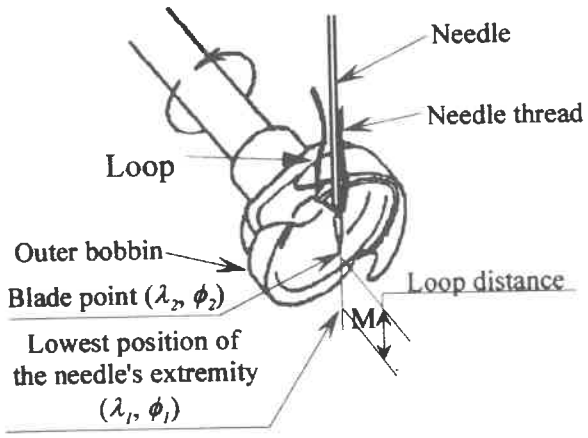

Figure 3. Blade point

A principal function of NMM is to make loops of needle threads. A loop making is influenced by the blade point and the loop distance M as shown in *Figure 3*. Here, the loop distance M is a distance between the lowest position (λ_1, ϕ_1) of the needle's extremity and the blade point (λ_2, ϕ_2). Namely,

$$M = \{(\lambda_2 - \lambda_1)^2 + (\phi_2 - \phi_1)^2\}^{1/2} \quad (14)$$

A loop distance M can be differentiated with the design variables $\underline{\xi}$ as

$$\frac{\partial M}{\partial \xi_i} = \frac{(\lambda_2 - \lambda_1)}{M}\left(\frac{\partial \lambda_2}{\partial \xi_i} - \frac{\partial \lambda_1}{\partial \xi_i}\right) + \frac{(\phi_2 - \phi_1)}{M}\left(\frac{\partial \phi_2}{\partial \xi_i} - \frac{\partial \phi_1}{\partial \xi_i}\right) \quad (15)$$

where $\left(\frac{\partial \lambda_1}{\partial \xi_i}, \frac{\partial \phi_1}{\partial \xi_i}\right)$ is a sensitivity of (n_x, n_y) at the lowest position and $\left(\frac{\partial \lambda_2}{\partial \xi_i}, \frac{\partial \phi_2}{\partial \xi_i}\right)$ is a sensitivity of (n_x, n_y) at the blade point in a locus of the needle's extremity.

4. Applications and Results

4.1. Kinematic analysis of NMM

n_1	n_2	n_3	n_4	θ_f
15.4 *mm*	48.5 *mm*	108.4 *mm*	0.0 *mm*	270°

Table 1. Nominal sizes of an example model

The nominal sizes of the feeding control mechanism from an example model as tabulated in *Table 1*.

While the link cam rotates, the value of the needle's extremity (n_x) always is zero, and the locus of the needle's extremity (n_y)

is shown in *Figure 4*. The needle's extremity is moving downward during $360^\circ \le \theta_n \le 270^\circ$, is moving upward during $270^\circ \le \theta_n \le 90^\circ$, and is moving downward again during $90^\circ \le \theta_n \le 0^\circ$. Thus, the needle's extremity is in the lowest position $(\lambda_1 = 0.0\,mm, \phi_1 = -172.3\,mm)$ at $\theta_n = 270^\circ$. In case of the example model, the loop distance M is about *2.2 mm*. Thus, the blade point occurs at $\theta_n = 243^\circ$ from the analysis.

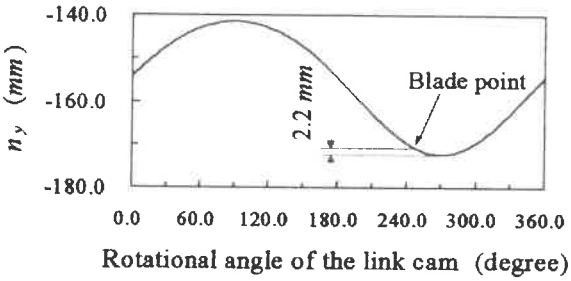

Figure 4. Motion of the needle's extremity(n_y)

4.2. Sensitivity analysis of NMM

ξ_i	n_1	n_2	n_3	n_4
$\partial\lambda_2/\partial\xi_i\ (mm/mm)$	0.00	0.00	0.00	1.00
$\partial\phi_2/\partial\xi_i\ (mm/mm)$	-0.82	-1.01	-1.00	0.15

Table 2. Sensitivity coefficients of the blade point (λ_2, ϕ_2)

ξ_i	n_1	n_2	n_3	n_4
$\partial M/\partial\xi_i\ (mm/mm)$	0.18	-0.01	0.00	0.14

Table 3. Sensitivity coefficients of the loop distance M

A sensitivity analysis of the blade point and the loop distance M is investigated here. A sensitivity coefficient matrix (from *Equation (13)*) at the blade point (λ_2, ϕ_2) and that (from *Equation (15)*) at the loop distance M are shown in *Table 2* and *Table 3*.

In order to allocate tolerances of the design variables $\underline{\xi} = [n_1, n_2, n_3, n_4]^T$, this paper arbitrarily chooses a limit of response errors (LREs) as follows.

CONDITION 1 : The LREs of λ_2 and ϕ_2 on the blade point (λ_2, ϕ_2) are *0.15 mm* each other.

CONDITION 2 : The LRE of the loop distance M is *0.11 mm*.

From *Table 1*, the nominal sizes of design variables n_3 is larger than the others. In general case, the bigger size of machine part, the more difficult to get the precise tolerance values. Thus, we try to make larger maximum deviations of n_3.

An assumed allowable deviation (α) for λ_2 is *0.15 mm*, α for ϕ_2 is *0.05 mm*, and α for M is *0.33 mm*, which are calculated by *Equation (9)*. Because α for ϕ_2 is the smallest value, it is safe to use the sensitivity coefficients of ϕ_2 in order to satisfy with above two CONDITIONs.

In order to make larger maximum deviations of n_3 within LRE of ϕ_2, maximum deviations of $n_1(=0.03\,mm)$, $n_2(=0.04\,mm)$ and $n_4(=0.04\,mm)$ are arbitrarily set smaller than $\alpha(=0.05\,mm)$ of ϕ_2. Thus, maximum deviation of $n_3(=0.08\,mm)$ is obtained from *Equation (11)*.

When above determined maximum deviations of design variables are applied to

Equation (4), the worst responses of (n_x, n_y) are represented in *Figure 5*.

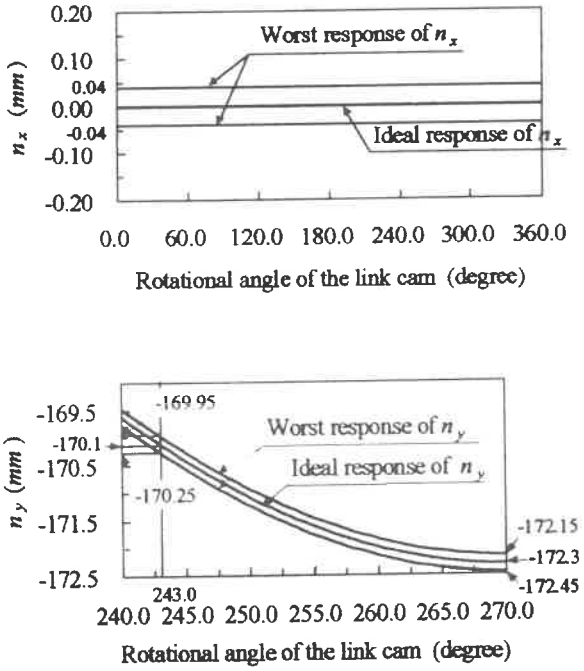

Figure 5. Motion of the needle's extremity when the maximum deviations of design variables are considered

As shown in *Figure 5*, the maximum deviation of λ_2 is ± 0.04 *mm*, that of ϕ_2 is ± 0.15 *mm*, and that of the loop distance M(= *2.2 mm*) is about zero. Thus, above two CONDITIONs are satisfied.

5. Conclusions

Machine's function related tolerance theory is studied here by using kinematic and sensitivity analysis.

From the kinematics and sensitivity analysis, motions of a machine could be characterized, and maximum deviations of dependent variables might be predicted when the tolerances of design variables are applied. Inversely, maximum deviations of dependent variables might be determined for tolerance allocation when the a limit of response error of the dependent variable is preset. Therefore, this tolerance theory might be very useful to machine designs, whose functions are much related to kinematics like sewing machines, robots, etc..

References

1. Hartenberg R. S., and Denavit J., Kinematic Synthesis of Linkages, McGraw-Hill, New York, 1964, 315-320
2. L. F. Knappe, A technique for analyzing MECHANISM TOLERANCES, Machine Design, 1963, 25, 155-157
3. R. E. Garrett, and Allen S. Hall, Jr., Effect of Tolerance and Clearance in Linkage Design, Trans. ASME J. Engng Ind., Series B, 1969, 91, 198-202
4. J. Chakraborty, Synthesis of Mechanical Error in Linkage, Mechanism and Machine Theory, 1975, 10, 155-165
5. M. Choubey, and A. C. Rao, Synthesizing Linkages with Minimal Structural and Mechanical Error Based upon Tolerance Allocation, Mechanism and Machine Theory, 1982, 17(2), 91-97
6. Keyoung Jin Chun, Dae Young Shin, "A Study on Feeding Control Mechanism Analysis of Industrial Lock Stitch Sewing Machine", Proc ASPE, 1996, 300-305

A Study on Performance Improvement of Non-Contact Type Seals for High Speed Spindle

Byung Chul Na*, Keyoung Jin Chun, Dong-Chul Han*****

*Korea Automotive Technology Institute, 74 Yongjong-ri Pungse-myon, ChunAnSi ChungChongnam-do 333-910, KOREA
**Korea Institute of Industrial Technology, San. 17-1, HongChonRi, IbjangMyun, ChonAnSi, 330-820, Korea
***Seoul National University, Seoul 151-742, KOREA

1. Introduction

High speed spindle requires special type of sealing mechanism that prevents a leakage of oil jet or oil mist lubrication system[1]. In the previous study[2], protective collar type labyrinth seal and air jet type seal show more preferable for non-contact types sealing mechanisms working with oil mist or oil jet fluids. Minimum clearance of protective collar type labyrinth seal should be located between inlet side wall and collar, while its size should be minimized taking into account thermal expansions and deflection of the spindle. Therefore this clearance is minimum distance not to be close together physically.

Current work emphases on the investigation of the air jet effect on the protective collar type labyrinth seal. To improve the sealing capability of conventional labyrinth seal, air jet is injected against the leakage flow. In this study, both of numerical analysis by CFD(Computational Fluid Dynamics) and experimental measurements are carried out to verify sealing improvements.

Gas or liquid has been used as a working fluid for most of non-contact types seals including the labyrinth seal[3]. However, it is more reasonable to regard two phase flow because oil mist or oil jet are used for high speed spindle's lubrication. In this study, working fluid is regard as two phases that are mixed flow of oil and air phase. Both of turbulence and compressible flow model are also introduced in a CFD analysis to represent an isentropic process[4,5]. Estimation of non-leaking property is determined by amount of pressure drop in the leakage path. Sealing effect of the leakage clearance and air jet magnitude are studied for various parameters in experiment.

2. Structure of sealing enhancement mechanism

Fig. 1 shows a schematic geometry of an applied seal model. It has a combined geometry of a protective collar type and an air jet type seal. Protective collar that makes a minimum clearance between collar and cavity wall is located at the inlet side of cavity. Then air is injected against leakage flow in the minimum clearance. The isentropic process in the clearance is increased because a clearance is reduced by blocking air jet. It makes enhanced sealing performance along with increasing pressure drop. A clearance reduction effect can be expected in this model even though the clearance can not be close together physically anymore. Fig. 2 shows an effect of clearance reduction by a restrict jet. When the air jet is injected into the minimum clearance, the jetting air reduces an effective leakage clearance. This model can achieve excellent sealing performance even though a rotating spindle and cavity has wide leakage clearance unavoidably. In addition, it can control sealing performance by adjusting the jetting air.

3. Performance testing device

An experimental device is constructed to

test sealing performances as shown in Fig. 3. This device has oil mist generating nozzles to make oil mist lubrication environments. Resolution of pressure measurement is 1 Pa. Leakage clearance is adjustable and capable of close together to 0.01 mm. Sixteen air jet nozzles are installed to the circumference direction for the restrict air jet. Precision pressure sensor(measuring resolution of 1Pa) and regulator are installed at the inlet side of the device to measure and control of leakage pressure. A pressure manipulator supplies high-pressure air to the sixteen nozzles.

4. Testing method and conditions

The pressure drops between inlet and outlet are measured at the speed of 0, 1000, 2000, 3000 rpm to find initial turbulence effects. This test is to find effects of jetting air and spindle rotation speeds without any leakage for the initial turbulence effect. Diameter of collar is 98mm and end clearance is 2mm. Face clearances between collar and wall are adjustable to 0.25mm, 0.5mm, 0.75mm, 1.0mm, 1.25mm and 1.5mm to find clearance effects on leakage flow. For measuring pressure drops, jetting pressures are adjusted to 9.8KPa, 19.6KPa, 29.4KPa, 39.2KPa, and 49.0KPa to find air jetting effects on constant leakage pressure. Initial leakage pressures are ranged from 10Pa to 200Pa to find an initial leakage effect on constant jetting pressure. The estimation of non-leaking property is determined by the amount of pressure drop in the leakage path.

5. Results and discussion

Fig. 4 indicates effect of spindle rotation on constant jetting pressure. This figure is only one case of leakage clearance at 0.25mm while total experiment varies it from 0.25mm to 1.5mm by a clearance adjusting screw. The result shows that rotation speed is not so much affect to pressure drop. Because of a low density of working fluid, turbulence is fully developed at the beginning of test by air jet and spindle rotation. Therefore increase of circumference direction of rotation speed is not so much affect to pressure drop.

Fig. 5 shows an effect of jetting pressure on constant leakage pressure. In this case, the clearance is 0.5mm. Leakage pressure, represented here, is proportional to the leakage flow. That means a constant leakage flow occurs at constant leakage pressure at the same geometry. The result shows that increase of jetting pressures increase total pressure drops. Thus, sealing performance is improved by the restrict jet. This is very effective way of sealing enhancement in oil mist lubrication system.

Fig. 6 shows an effect of leakage pressure on constant jetting pressure. It shows that a quantity of pressure drop increases between inlet and outlet by restricts jet when it has constant leakage pressure. As shown in dot line of Fig. 6, jetting 39.2 KPa of restrict jet generates 2.1 KPa of total pressure drop where the initial pressure drop(the same as leakage pressure) remains as 0.08 KPa.

Fig. 7 shows an effect of leakage clearance on a constant jetting pressure. If a leakage clearance becomes larger, pressure drops decrease, which representing poor sealing performances in ordinary non-contact type seals. However, this figure shows a inverse behavior that increase of clearance makes bigger pressure drop at clearance of 0.25mm and 0.5mm because of effect of jetting air amount. As a diameter of jetting nozzles are 1.0 mm, leakage clearance of 0.25mm is not enough to send a restrict jet. However, in the case of 0.5mm leakage clearance, effects of restrict jets become dominant to generate pressure drops. Therefore, the restrict jet can achieve good sealing performance although a spindle lubrication system has large leakage clearance inevitably.

Fig. 8 shows an effect of jet nozzle number(4 to 16) on constant leakage pressure. For an ideal case, line source jet is preferable than any number of point source. However, the line source jet is impossible to practical cases. Therefore the effect of jet point number is

investigated as a practical design factor. The effect of jet nozzle number is almost proportional to pressure drop in the range of testing condition. Increase of jet nozzle number means an increase of jet flow, thus, sealing performance is improved until it reaches to line source jet condition.

6. Comparison of CFD Analysis

Boundary conditions are fitted to the testing equipment, and assuming a divided geometry into 16 segment, and each segment has one jetting nozzle. Both of the turbulence and compressible model are introduced in adiabatic condition at 20 °C. The initial condition for comparing with experiments is 0.75mm of leakage clearance and 0.08KPa of leakage pressure where leakage flow rate is 1.3 l/s and corresponding inlet velocity is 0.536m/s. Jet pressures are applied to 9.8KPa, 19.6KPa, 29.4KPa and 39.2KPa as same as the experiment and their flow rates on each nozzle correspond to 0.16l/s, 0.22l/s, 0.27l/s and 0.33l/s respectively. Jet velocity is calculated according to jet flow rate and applied to CFD analysis as jet velocity.

Fig. 9 shows pressure distribution without air jet conditions. This figure show that pressure drop mostly occurs at the entrance of minimum clearance between cavity and collar. Therefore, sealing is achieved by flow that passes through the minimum clearance undergoing an isentropic process. Fig. 10 shows pressure distribution of air jet applied model. This figure show that pressure drop mostly occurs in the minimum clearance near the jet point. It means reductions of leakage clearance by restrict jet are made and flow undergoes more isentropic process. The applied model generates 1.8KPa of pressure drop while no air jet condition generates 0.042KPa of pressure drop. As same results of the experiments, the CFD analysis shows the applied model has excellent sealing performances compare to protective collar type seals without air jetting.

Fig. 11 shows comparison of experiment and CFD results at the condition of 0.75mm clearance and 0.08KPa leakage pressure. It compares the relative behaviors of pressure drops for the CFD analysis and experiments. Here, CFD results are fitted to experiments by introducing a flow coefficient(0.5). As seen in the Fig. 11, behaviors of pressure drop in experiments and simulation are well match with each other. It verifies an improvement of sealing capability by the restrict jet.

7. Conclusion

This paper offers a way of performance improvements of labyrinth seal used in a high speed machining center. Performance improvements are verified by experiments and the CFD analysis. An applied model has a combined geometry of a protective collar type and air jet type. Effects of sealing improvement are explained as decreasing of leakage clearance by air jetting. Their sealing characteristics are investigated through experiments of a special testing device. Jet flow, which affects sealing characteristics, should be large to achieve an enhanced sealing. Rotation speed does not affect so much to sealing characteristics on this experimental condition. The restrict jet can achieve good sealing performances although a spindle lubrication system which has large leakage clearance inevitably. Increasing jet nozzle number improves sealing characteristics until it reaches to line source condition. The CFD analysis considers turbulence, compressible and two phase flow to simulates a leakage flow of oil mist lubrication system. Behaviors of pressure drop in experiments and simulation are well match with each other. It verifies an improvement of sealing capability by the restrict jet.

References

1. "Seals and Sealing HANDBOOK 2nd Edition", Trade & Technical Press Limited, 1986
2. Byung Chul Na, Keyoung Jin Chun, Dong-Chul Han, "Analysis of Seal Leakage Characteristics for High Speed Spindle", The 6th International Symposium on Pheonomena and Dynamics of Rotating Machinery, Vol. 1, pp. 542-551, Feb., 1996
3. Rhode, D. L., Ko, S. H., and Morrison, G. L., "Numerical and Experimental Evaluation of a New Low-Leakage Labyrinth Seal," AIAA Paper 88-2884, July 1988.
4. "PHOENICS Traning Course Notes CHAM TR/300", CHAM Limited, 1990
5. Partankar,"Numerical Heat Transfer and Fluid Flow", Spalding, 1980

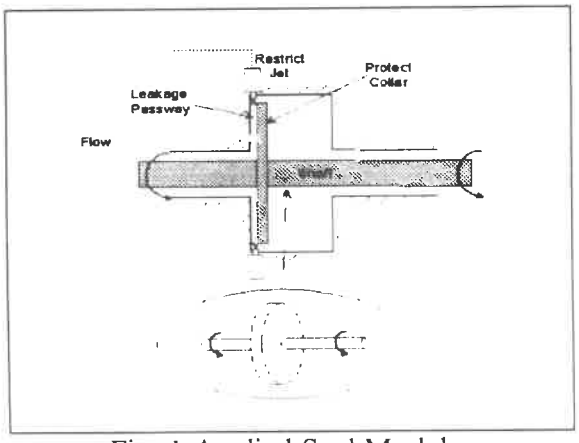

Fig. 1 Applied Seal Model

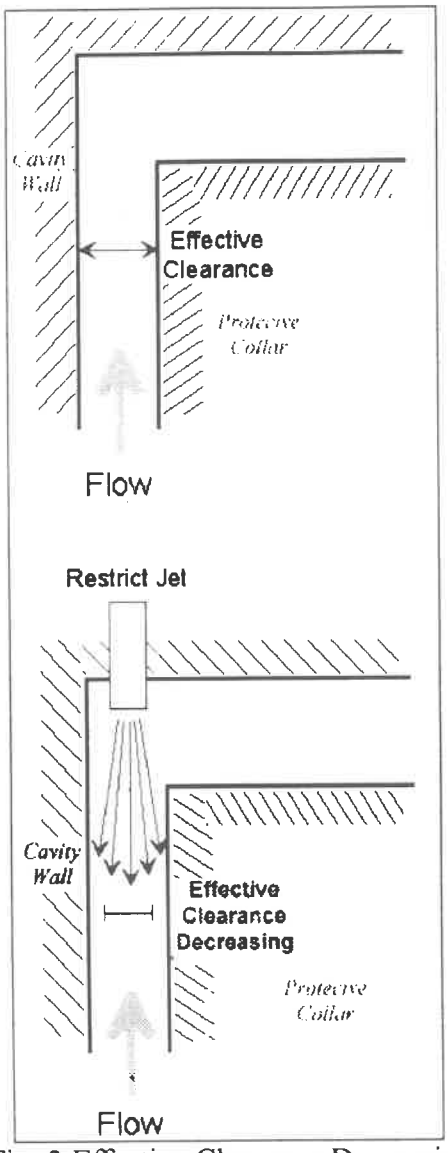

Fig. 2 Effective Clearance Decreasing

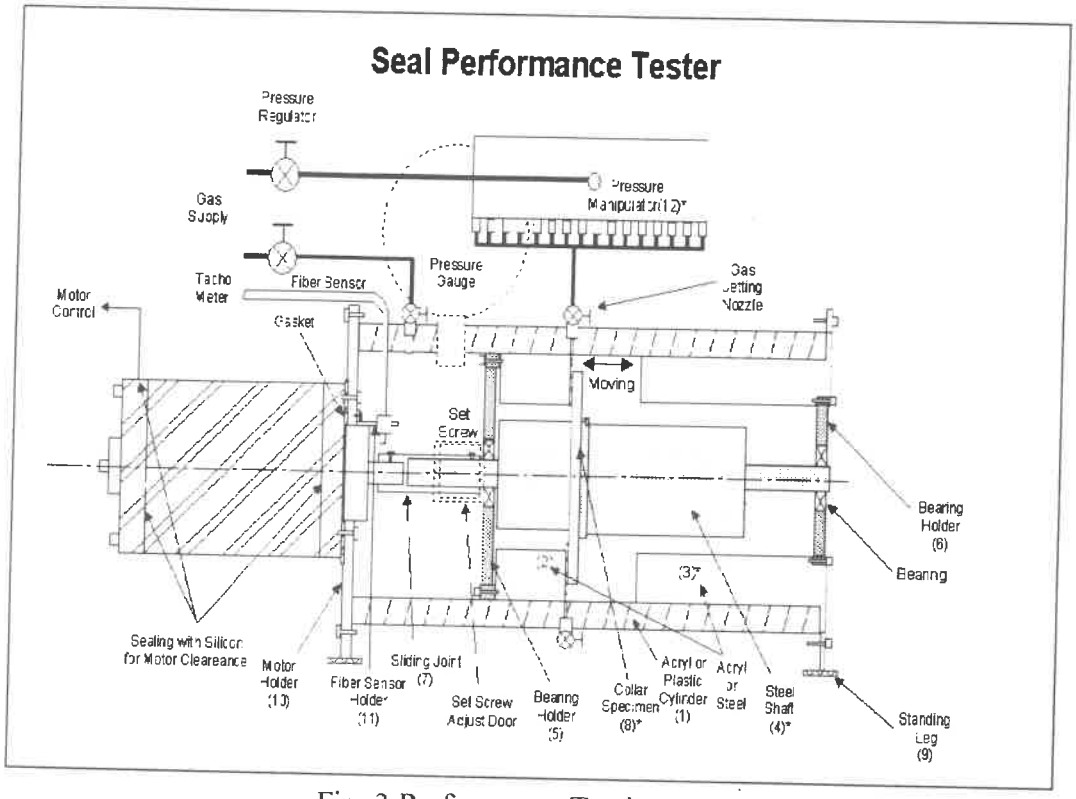

Fig. 3 Performance Testing Device

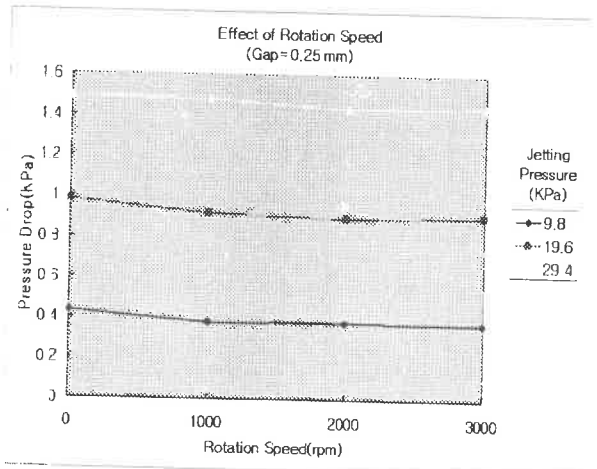

Fig. 4 Effect of Rotation Speed

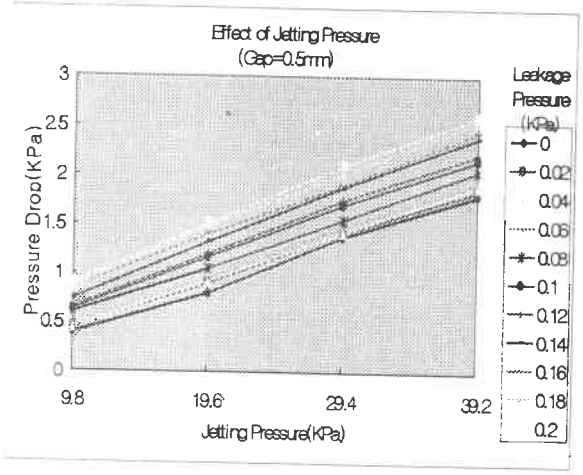

Fig. 5 Effect of Jetting Pressure

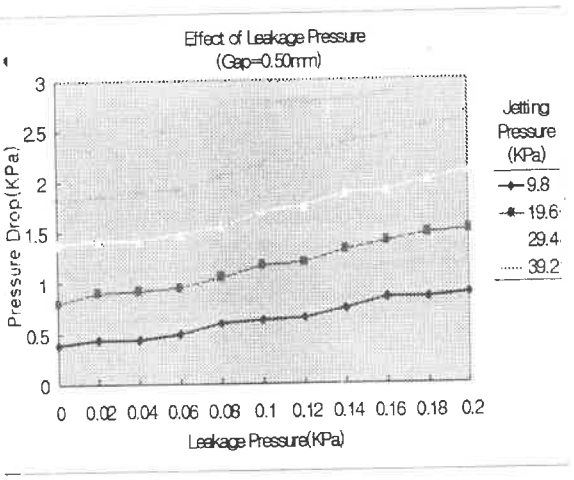

Fig. 6 Effect of leakage Pressure

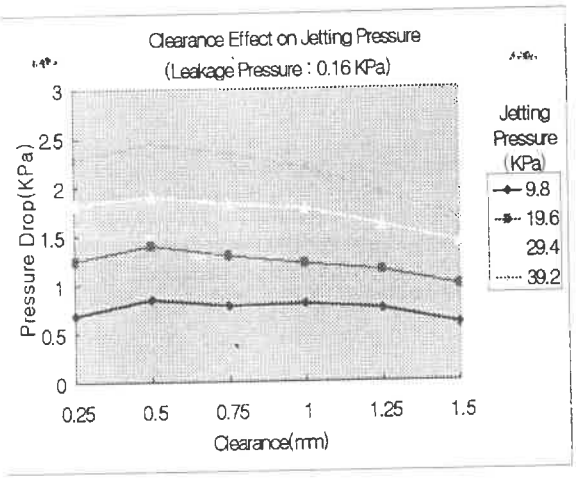

Fig. 7 Effect of Clearance

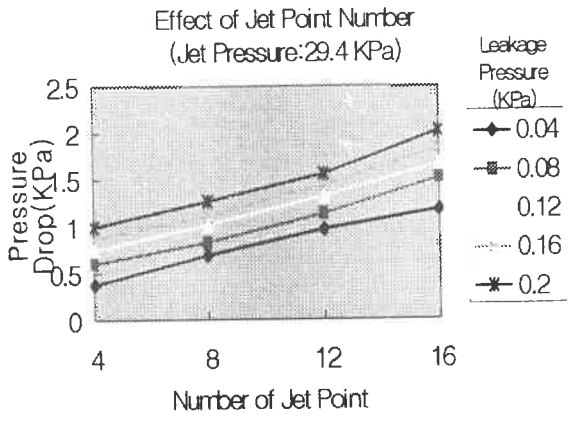

Fig. 8 Effect of Jet Point Number

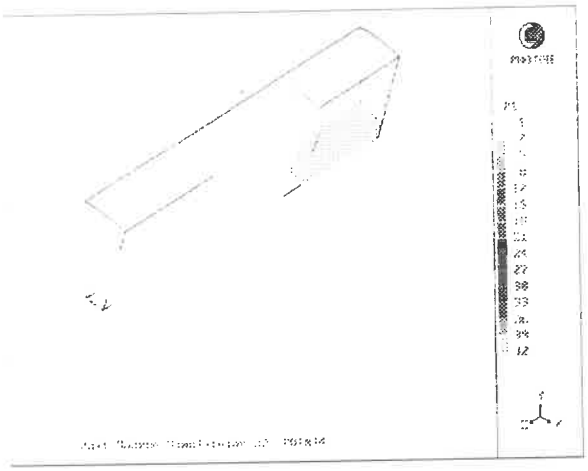

Fig. 9. Pressure Distribution without Air Jet

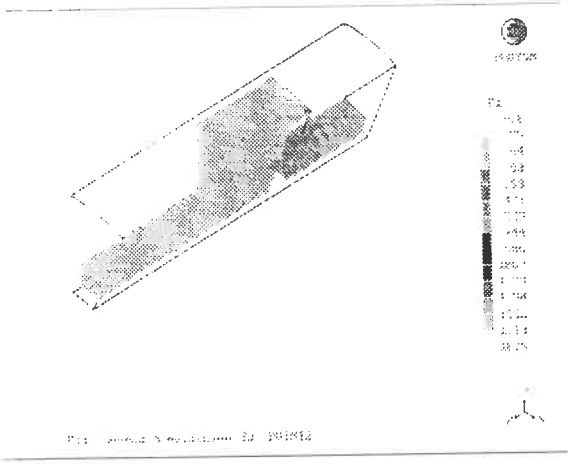

Fig. 10. Pressure Distribution with Air Jet

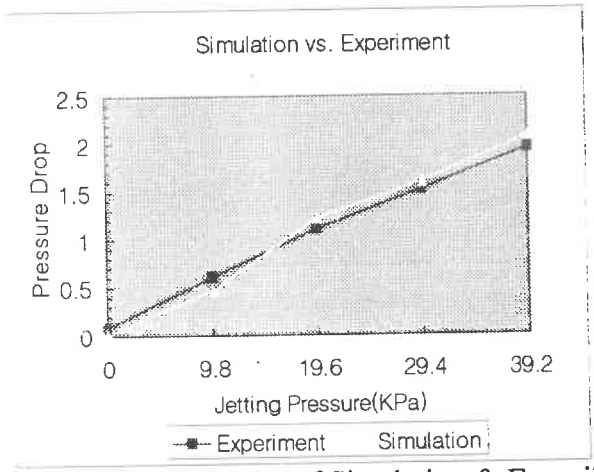

Fig. 11 Pressure Drop of Simulation & Experiment

An End Effector Using Parallel Mechanism for Scanning Electrical Discharge Machining

Katsushi FURUTANI, Kazuhiro SHIBATANI*, Naoki ITOH** and Naotake MOHRI
Toyota Technological Institute
12-1, Hisakata 2-chome, Tempaku-ku, Nagoya 468 JAPAN, e-mail: furutani@toyota-ti.ac.jp
* *Tsubakimoto Chain Co.* at present, ** *Toyoda Machine Works, Ltd.* at present

1. Introduction

The electrical discharge machining (EDM) method by scanning an electrode with a primitive shape is proposed to machine a complex shapes in a short time[1)2)]. Hereafter, this method is called the scanning EDM.

In order to make machining systems flexible, an EDM robot has been proposed[3)]. In this system, an end effector is necessary to obtain high response. Conventional end effectors for EDM have only one degree of freedom (DOF) in the feeding direction[4)].

On the other hand, many parallel mechanisms have been studied recently[5)]. Since they have multiple DOF, high response and high stiffness, they satisfy the requirements for the end effectors for EDM[6)].

In this paper, an end effector with a parallel mechanism for the scanning EDM is proposed. Then the structure and control method are described. Finally, some results of the scanning EDM are discussed by comparing the motion accuracy of the end effector with its machining accuracy.

2. Parallel mechanism for EDM

2.1 Structure

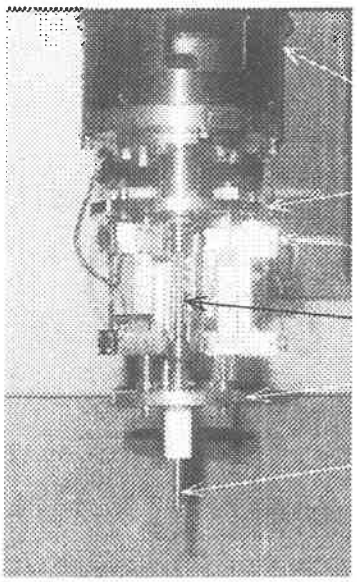

Fig. 1 Appearance of end effector with parallel mechanism

Fig. 1 shows an appearance of a prototype. It consists of a base plate, a stage, three Inchworm[7)] devices performing as links and a constraint link.

This end effector measures ϕ 182 × 228 mm. The whole device and the stage weight 6 kg and 2 kg, respectively.

The clamp B and the bottom end of a shaft of each inchworm device are connected with the base plate and the stage with ball joints, respectively. A spline shaft used for the constraint link restricts the motion of the end effector to three DOF. The upper end of the spline shaft is connected with the base plate directly and the lower end, with the stage through a universal joint. Therefore, the end effector can tilt around the x and y axes and it can also move in the z direction.

The Inchworm device measures 120 × 30 × 64 mm and weights 0.8 kg. The shaft of the Inchworm device can move for 30 mm. The piezoelectric elements in the clamps deform 30 μm and that in the driver deforms 40 μm at the applied voltage of 600 V. In order to support the stage in case of turning off the power, the clamps release the shafts with the diameter of 10 mm

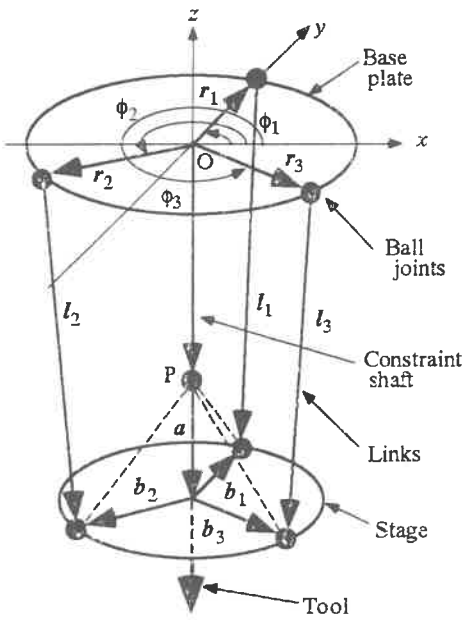

Fig. 2 Geometrical arrangement of links, stage and base plate

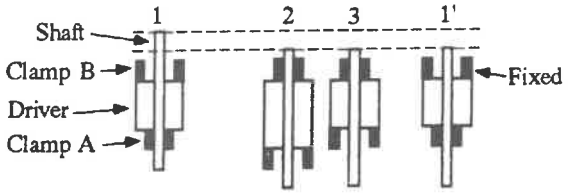

(a) Motion of Inchworm device

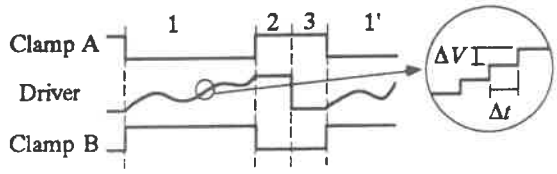

(b) Driving signal

Fig. 3 Driving method by hybrid mode

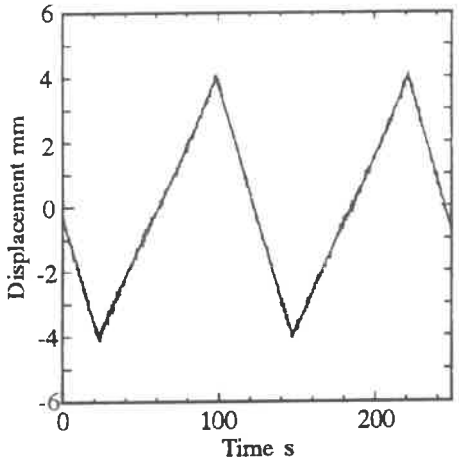

Fig. 4 Coarse motion by step mode

in case of applying the voltage to the piezo. The clamps can hold the shafts up to 30 N.

Potentiometers with the measurement range of 50mm and the straightness of 3% are used to measure the displacement of the shafts of the Inchworm devices.

2.2 Inverse problem

In general, the inverse motion of the Stewart platform type parallel mechanism can be easily calculated by using the geometrical relation. Fig. 2 illustrates a geometrical relation of this end effector. The origin of the coordinates system is the center point of the base plate O. Each solid circle indicates a ball joint with two DOF. The point P indicates a universal joint.

The position and the inclination of the stage are represented by the vector $\mathbf{d}$ and the normal vector of the stage $\mathbf{n} = (n_x, n_y, n_z)$.

The position vector of each link $\mathbf{l}i$ can be calculated by

$$\mathbf{l}_i = R(\mathbf{a} + \mathbf{b}_i) + \mathbf{d} - \mathbf{r}_i \qquad (1)$$

where the vectors $\mathbf{a}$, $\mathbf{b}_i$, $\mathbf{r}_i$ are known.

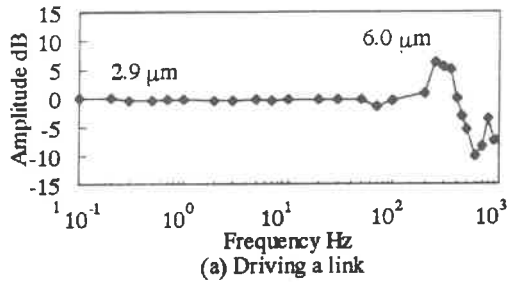

(a) Driving a link

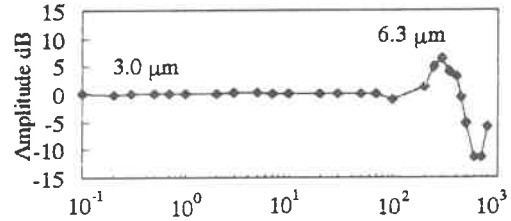

(b) Driving 3 links

Fig. 5 Frequency response by linear mode

2.3 Driving method

This end effector is driven by the hybrid mode which is a combination of the step mode and the linear mode as shown in Fig. 3. In the step mode, the shaft is driven by the original operation of the Inchworm mechanism. The shafts are positioned roughly. In the linear mode, the piezo for the driver is deformed continuously to displace the stage. The clamps A of all Inchworm devices grasp the shafts and the clamps B of all Inchworm devices release them during the linear mode. The high response can be obtained within a steplike movement in the step mode. The stage is mainly driven by the linear mode during precise positioning or EDM. The shafts are driven by the step mode in coarse motion. When the shaft reaches a reference position, they are driven by the linear mode again.

2.4 Motion performance of end effector

Fig. 4 shows a displacement of the stage by the step mode. The reference position is given every 0.5 mm in the PTP (point to point) control. The stage moves downward faster than upward because of the gravity. The step of the stage is 10 μm in case of the voltage amplitude of the driver of 400 V and the driving frequency of 100 Hz. The positioning accuracy of the stage in the step mode is restricted to ±30 μm due to the noise from the potentiometers.

Fig. 5 shows the frequency response in which the response curves for one device driving and three devices synchronously driving by linear mode are indicated. The amplitude of 3 μm at 0.1 Hz is indicated as 0dB. In both cases, the resonance

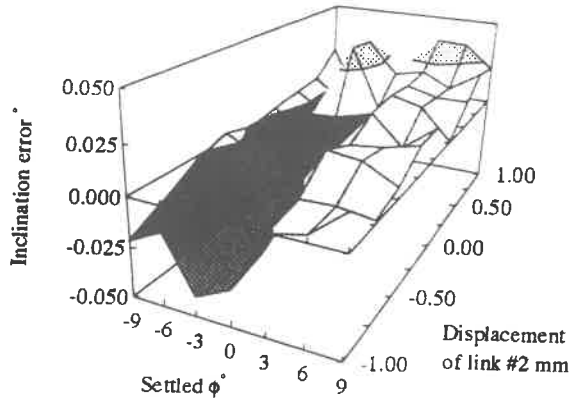

(a) Inclination

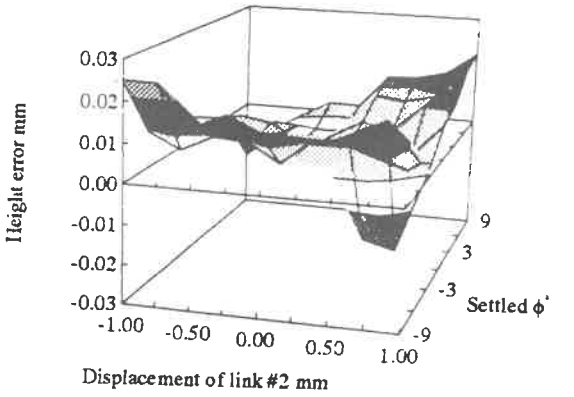

(b) Height

Fig. 6 Positioning error of end effector

frequency is 250 Hz. Therefore, the applicable frequency range is up to 200 Hz as shown in Fig. 5. This end effector driven by the linear mode has enough frequency range for EDM. The clamps grasp the shafts without slip during these experiments.

2.5 Positioning accuracy

Since the displacement range by the linear mode is 10 μm, the motion accuracy in the step mode affects the machining accuracy more than that in the linear mode. The motion accuracy in the step mode is measured as follows.

Fig. 6 shows the positioning errors in height and inclination which are the difference between the calculated position and the measured one. The instructed inclination of the stage is changed with every 3° from -9 to 9° and the length of one of the links is changed from -1 to 1 mm around the calculated length based on the instructed inclination. In this paper, the length of the links in the forward problem is calculated by the repetitive calculation by Newton method. In all cases, the motion errors are less than ±0.04° in inclination and ±0.03 mm in height along the z direction. The error of the potentiometers of 30 μm yields the motion errors.

In case of mounting the electrode with the length of 100 mm on the stage, the positioning error of the top of the electrode becomes less than ±0.09 mm.

3. Scanning EDM

3.1 System configuration

Fig. 7 shows the system configuration for the scanning EDM with the parallel mechanism.

The path of the electrode is controlled by PTP with the position and inclination data of the stage (P/I data). The driving signals are supplied through amplifiers for the piezos. The electrode is controlled according to the forward/ backward signal (F/B signal) decided by comparing the average supply currents with a certain reference current. The electrode moves to the next reference position in case of the forward signal and reverse to the previous reference position in case of the

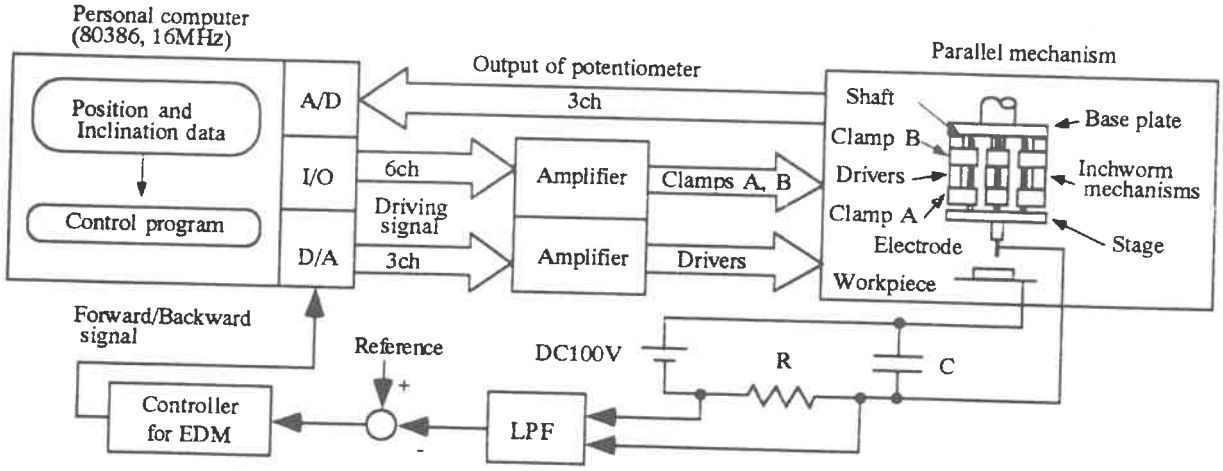

Fig. 7 System configuration of scanning EDM with parallel mechanism

backward signal in order to reduce the machining error and to avoid a short-circuited. state. The displacement direction of the shaft is decided according to the current position and F/B signal. The F/B signal has the priority to the P/I data for stable EDM.

3.2 Machining grooves

In order to compare the machining accuracy with the motion accuracy, grooves are machined on AISI 304 stainless steel plates.

The discharge circuit used in the experiments consists of the capacitor of 1 μF and the resistance 168 Ω. The gap voltage is settled to 100 V. A tungsten rod of 1.0mm in diameter is used for an electrode. The driving frequencies are settled to 25 Hz for the step mode and 150 Hz for the linear mode.

The reference points are given at every 0.1 mm for the straight grooves and at every 2° for the circular groove. After the electrode is scanned along the whole part of the groove, the stage is driven by 0.1 mm in the z direction.

Fig. 8 (a) shows a result of machined crosslike groove of 5mm in length. The machining time is approximately 30 minutes. The width and the average depth of the grooves are 1.10 mm and 0.58 mm, respectively. Though the settled angle between two grooves is 90.0°, the actual angle is 90.8°.

Fig. 8 (b) shows a result of machined circular groove when the center line of the electrode draws a circle of 5 mm in diameter. The machining time is approximately 70 minutes. The outer and the inner radiuses are 3.210 mm and 2.015 mm, respectively. The average depth of the groove is 0.31 mm. The roundness is 0.142 mm for the outer circle and 0.126 mm for the inner circle. The distance between the centers of the outer and the inner circles is 0.043 mm. Since the machining accuracy by conventional EDM is approximately several micrometers and the machining accuracy is less than the motion accuracy measured in Section 2, the machining accuracy depends on the motion accuracy.

4. Conclusions

The end effector with three DOF by using a parallel mechanism is developed and applied to EDM.

The following conclusion can be drawn through the experiments:

(1) The accuracy of machined grooves is less than the motion accuracy. The surface modification with silicon is demonstrated.

(2) This end effector has an enough frequency range for EDM. The frequency range in linear mode is up to 200Hz.

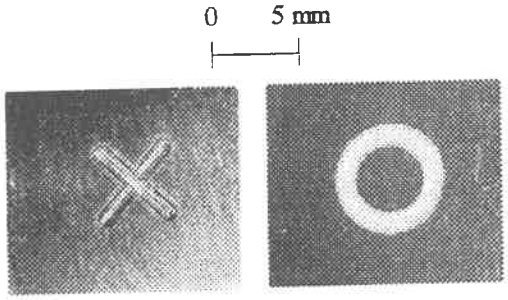

(a) Cross (b) Circle

Fig. 8 Examples of machined shapes

Acknowledgment

The authors wish to thank to the Ceramic R&D Dept. of Denso Corp. for providing the piezoelectric elements and Mr. N. Andoh who graduated from Toyota Technological Institute for their helpful cooperation. This study is financially supported by the Die and Mold Technology Promotion Foundation, Amada Foundation for Machine Tool Technology, Tokai Foundation for Technology, OSG Fund and Grant-in-aid for Scientific Research (A) (1) (06555041) and (C) (2) (07650155) of the Ministry of Education, Science, Sports and Culture, Japan.

References

1) T. Kaneko et al.: Improvement of 3D NC Contouring EDM Using Cylindrical Electrode, Proc. Int. Sympo. Electro Machining 9, Nagoya, Japan, pp. 49-52 (1989).

2) K. Furutani et al.: 3D Profile Generation by Dot-Matrix Method Using Miniaturized Electrode Feeding Devices, Proc. 11th Ann. Meeting of Am. Soc. Prec. Eng., pp. 86-90 (1996).

3) T. Narikiyo et al.: Control System Design for Macro/ Micro Manipulator with Application to Electro-discharge Machining, Proc. IEEE/ RSJ/ GI Int. Conf. Intelligent Rob. Syst., 2, pp. 1454-1460 (1994).

4) D. Kremer et al.: Effects of Ultrasonic Vibrations on the Performances in EDM, Ann. CIRP, 38, 1, pp. 199-202 (1989).

5) R. S. Stoughton et al.: A Modified Stewart Platform Manipulator with Improved Dexterity, IEEE Trans. Rob. Autom., 9, 2, pp. 166-173 (1993).

6) K. Furutani et al.: Miniaturized Electrode Feeding Devices Using Piezoelectric Elements, Proc. Int. Symp. Electro-machining, pp. 621-628 (1995).

7) Burleigh Instrum. Inc.: Inchworm catalog.

SELF-CALIBRATION FOR A HEXAPOD COORDINATE MEASURING MACHINE

Chin-Chou Huang, John C. Ziegert
Machine Tool Research Center, University of Florida, Gainesville, FL

1. Introduction

Typically a conventional coordinate measuring machine (CMM) uses serial kinematic linkages, each providing a single degree of freedom. The configuration may be a bridge type or cantilever construction. In order to achieve high accuracy measurements, the conventional CMM must be placed in a temperature-controlled environment to minimize the structural distortion due to thermal gradients in the machine elements. Therefore, the total cost for the machine itself and the creation and maintenance of the required working environment is a significant economic issue for CMM users.

An alternative is the hexapod coordinate measuring machine (HCMM) as shown in Figure 1. This machine uses a parallel structure in which light weight telescoping struts are used to reduce the moving masses typically in the conventional CMMs. The HCMM is designed to self calibrate and compensate for thermally induced changes in its own elements. Thus the requirements for temperature control in the operating environment are greatly reduced.

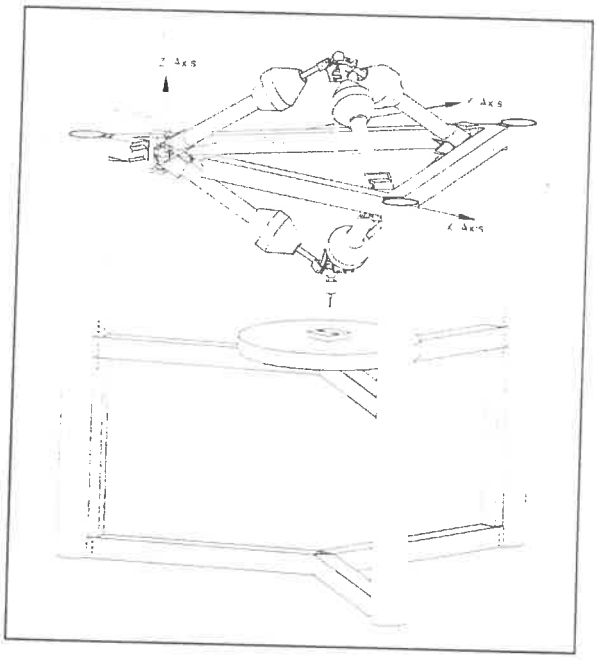

Figure 1 The hexapod coordinate measuring machine

This five degree of freedom HCMM we are now constructing is composed of six telescoping struts with laser interferometric displacement measurement and a single fixed-length center rod . The six telescoping struts are mounted in pairs, with one pair at each of three spherical joints around the base of the machine. The configuration of the machine resembles two tetrahedrons which share a common base and whose apex points are connected by the fixed rod. The laser interferometers measure the length changes of each strut. However, in order to calculate the coordinates of the probe, it is necessary to know the absolute length of each strut and the distance between the three base joints. Thus there are nine kinematic parameters to be determined in the calibration process, the three base lengths and the initial lengths of the six struts.

This paper presents a method to find the initial strut lengths and the base joint locations without adopting any external artifacts or measurements. During calibration the measuring probe is moved to a number of different positions within the measuring volume. For each position, the center rod length is assumed to remain constant. The length is calculated based on an initial guess of the machine kinematic parameters. A non-linear least squares problem is then formulated to search for the values of the base locations and initial strut lengths which minimize the variation in the computed center rod length. The entire calibration procedure can be completed within several seconds after the final movement of probe. Therefore, it is possible to correct in real time the thermally induced changes in the strut lengths and the base positions.

2. HCMM performance

The maximum and minimum strut lengths are 762 and 1270 mm respectively. The expected HCMM system performance was outlined by Jokiel [1] as follows:

1. Overall accuracy: ±2.2 to ±5.3 μm.
2. Workspace: A cylindrical volume 381 mm in diameter and 381 mm in height.
3. Speed: Maximum constant probe speed of 762 mm/sec. Strut extension speed of 635 mm/sec.

3. Kinematic Modeling

The origin of the world coordinate system is placed on one of the base sphere centers, BS1. The x axis lies along a line connecting two base sphere centers. The plane passing through the three base spheres is chosen as the x-y plane. The BS2 has coordinate of (r,0,0) and BS3 is located at (b,h,0).

Because of the telescoping strut design, each of the six struts may change its length to satisfy the kinematic constraint when the center rod is moved from one position to the other. Let's say the *k*th strut, with its initial (or starting) length of a(k), has a length change of S(k,i) at the *i*th configuration. At this instant its absolute length is expressed as $l(k,i) = a(k) + S(k,i)$ where k=1,..,6 and i=1,..,m. The initial length a(k) is a constant value and the length change S(k,i) will vary from configuration to configuration. The centers of the upper and lower spheres, P_u and P_l can be represented as:

$$P_u(i) = f(a_1, a_3, a_5, r, b, h, S(k,i)) \qquad P_l(i) = f(a_2, a_4, a_6, r, b, h, S(k,i))$$

Therefore, the center rod length can be calculated as:

$$Lc = \sqrt{(P_{u,x} - P_{l,x})^2 + (P_{u,y} - P_{l,y})^2 + (P_{u,z} - P_{l,z})^2} = f(a_1, \ldots, a_6, r, b, h, S(k,i))$$

4. Measurement

For the calibration of a conventional CMM, the measurement process is time consuming, laborious, and prone to human error. In contrast, the measurement process for the HCMM is simply movement of the center rod to a number of different positions within its work volume, and recording the displacement reading in each strut. Therefore, this calibration procedure is called "self-calibration" since no external measurement device is required. Data collection is quick and easy. However, it is necessary to minimize the number of measurement, because we assume that there is no thermal effect during the calibration process. If too many measurements are used, could the time required may allow significant thermal deformation in the structure.

We will show that the self-calibration process is very sensitive to the level of measurement noise. The measurement noise may include the modeling imperfection or measurement error from the laser interferometer. To eliminate or minimize the effect owing to measurement noise, then, becomes one of the most difficult problems in the parameter identification. In general, the magnitude of the noise itself is quite small, but its effect on the estimation accuracy may be rather significant. To minimize the effects of the inevitable noise on the results of estimation, the selection of measurement configurations becomes important

5. Identification

Because of the incorrect nominal values, measurement noise and modeling error, the calculated center rod length from the model will not have the same value at each pose. Therefore, an algorithm called *reference residual* is used in the HCMM calibration procedure. It is formulated as follows: $e_i = Lc_r^2 - \hat{Lc}_i^2$ where Lc_r is an assumed value for the center rod value which is an approximate guess. It is not necessary for this value to be known exactly and it will be treated as the tenth kinematic parameter which needs to be identified. The objective is then to find a set of parameters including the Lc_r to minimize the reference residual, e_i. The least-squares method can be expressed as

$$\text{Minimize} \sum_{i=1}^{m} e_i^2 \qquad \textbf{Equation 1}$$

Since Equation 1 is highly non-linear, one method to solve it is to linearize this equation. At the *i*th configuration of the HCMM, by using the Taylor expansion, the reference residual can be written as:

$$e_i = e_i\Big|_{A_o} + \frac{\partial e_i}{\partial a_1}\Big|_{A_o} \Delta a_1 + \cdots + \frac{\partial e_i}{\partial r}\Big|_{A_o} \Delta r + \frac{\partial e_i}{\partial b}\Big|_{A_o} \Delta b + \frac{\partial e_i}{\partial h}\Big|_{A_o} \Delta h + \frac{\partial e_i}{\partial Lc_r}\Big|_{A_o} \Delta Lc_r + \textit{higher order terms}$$

where vector A_o is the nominal value for parameters $\{a_1, \cdots, a_6, r, b, h, Lc_r\}^T$.

Suppose that the center rod is placed into *m* poses, this provides a vector of E which is written as

$$E = E_o + J\Delta A + \textit{higher order terms} \qquad \textbf{Equation 2}$$

where J is referred as Jacobian matrix. If the nominal values of A_o are close enough to the true values, the higher order terms in Equation 2 can be ignored. In this case the objective function of Equation 1 can be rewritten as:

$$\text{Minimize } f = (E_o + J\Delta A)^T (E_o + J\Delta A) \qquad \textbf{Equation 3}$$

Using the iterative linear least-squares method, the minimum value of f can be obtained

$$\Delta A = (J^T J)^{-1} J^T E_o$$

During each iteration the nominal parameter values are updated as

$$A_{new} = A_{old} + \Delta A \qquad \textbf{Equation 4}$$

This procedure is iterated until the largest value in vector ΔA is less than the desired tolerance.

6. Calibration Simulation

A computer simulation of the self calibration process has been implemented. The flowchart for the calibration simulations is shown in Figure 2. The approach taken during the course of the identification simulations was as follows. The measurement strategy and number of poses were decided first. The initial HCMM configuration was given as shown in Table 1. The center rod motion then was created by using the measurement strategy. The HCMM inverse kinematic model then was applied to these center rod positions to generate the strut length change data, followed by a check of the strut displacements to ensure all the motions are within the working space of the HCMM. The strut length changes and actual center rod position coordinates for each pose were then saved in a file, with 14 place decimal accuracy. We assume there is no thermal effect on the HCMM during the calibration process. A uniformly distributed random noise was superimposed on the strut length changes before saving to the data file.

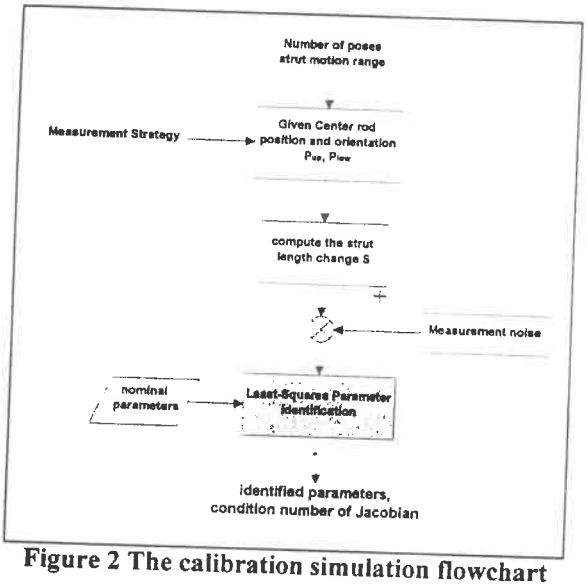

Figure 2 The calibration simulation flowchart

Table 1 The true kinematic parameters (mm)

a1	a2	a3	a4	a5	a6
1016	1016	1016	1016	1016	1016
r	b	h		Lc	
1600	800	$800\sqrt{3}$		856	

The programs to generate measurement data and to implement the least-squares identification method were written and run in MATLAB on a Windows 95 based Pentium 200 personal computer. When the calibration procedure was completed, the lower sphere position at each pose was estimated by applying the identified kinematic parameters and the data of the stored strut length changes in the forward kinematic model. The lower sphere position errors were determined by comparing these estimated lower sphere positions and the stored exact lower sphere positions.

The symbols used in the simulation are as follows. The number of poses is "m". The error value used for the ten nominal parameters in the HCMM model was "δA". The measurement uncertainty is represented by Un. The measurement strategy types are "$Strg$". After the calibration procedure is completed, the identified parameter errors δa_1, ..., δa_6, δr, δb, δh, and δLc are represented as "δA_{rms}" which is found by taking the root mean square of all ten parameter errors. The magnitude of lower sphere position error at each pose is "$|\delta P|$". The condition number of identification Jacobian is "$Cond(J)$" which is the value of the maximum singular value of the Jacobian matrix divided by the minimum singular value of the Jacobian matrix.

In our iterative least-squares algorithm each entity in the Jacobian matrix was calculated analytically by taking the partial derivative of the objective function. The iterative procedure was terminated when the maximum value in parameter update vector, ΔA, became less than 2.54×10^{-14} m.

6.1 Measurement Strategy Five measurement strategies have been examined through computer simulation, where the center rod motion locus is shown in Figure 3. The calibration results are shown in Table 2.

Table 2 Comparison of measurement strategies

	Strg 1	Strg 2	Strg 3	Strg 4	Strg 5
δA_{rms}	not identifiable	not identifiable	60.4μ m	53.3μ m	1.7μm
cond(J)	ill conditioned	ill conditioned	11540	12917	303
	m=200	noise:±0.254μm	initial δA= 12.7mm		

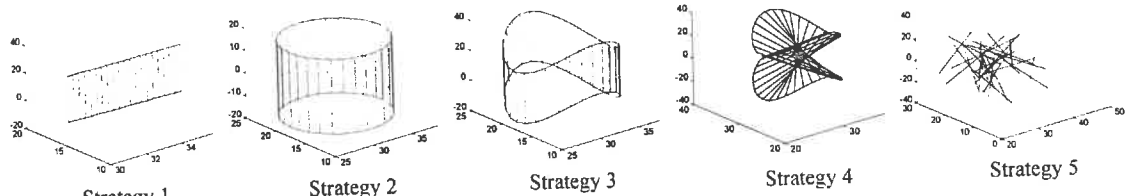

Figure 3 Measurement Strategy

6.2 Pose Selection Each pose set has a sensitivity level for the measurement noise so that using a different pose set would yield different calibration results. To present the noise sensitivity of a pose set, one widely used index is the condition number of the Jacobian matrix J. Figure 4 shows the calibration results of a thousand simulations. One can observe from the simulation results that a pose set with smaller condition number does not guarantee that the calibration results will be better than for a pose set with a higher condition number. However, comparing the upper boundaries of condition numbers one can see the trend toward pose sets with smaller condition numbers having smaller a upper bound in position errors. If one draws a straight line above all the points in Figure 4, one can see the trend. From the above simulation we found that the position error varied from a maximum of 33μm (cond=1100) to a minimum of 0.337μm (cond=393). However, for a randomly selected pose set the calibration result has a large possibility of being located in the region of the mean value from 1000 simulation results. Thus we choose to use the mean value and its standard deviation of the 1000 simulation results to represent the overall calibration results.

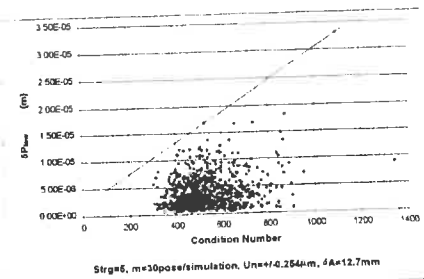

Figure 4 Calibration Results of 1000 Simulations

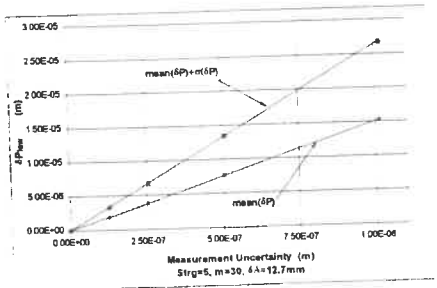

Figure 5 HCMM Accuracy vs. Measurement Noise

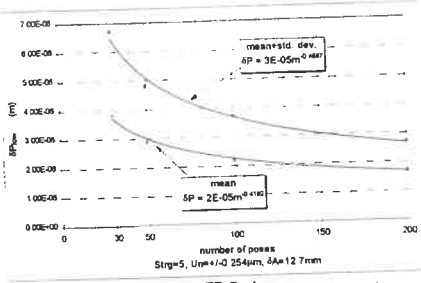

Figure 6 HCMM Accuracy vs. Number of Poses

6.3 Effect of Measurement Uncertainty This simulation was repeated using different levels of measurement uncertainty. The results are shown in Figure 5.

6.4 Effect of Number of Poses Figure 6 shows the calibration results obtained using an increasing number of poses.

7. Conclusion

A good measurement strategy will determine the quality of the parametric identification results. In some cases, the parameters may be unidentifiable from a given pose set such as the straight line or circular motion. The best measurement strategy of those tested is random selection. Furthermore, it has been found that not all of the pose sets selected from the random strategy obtained acceptable calibration results. A good calibration result should be obtained when the pose set is least sensitive to measurement noise. It has been shown that increasing the number of poses and reducing the measurement error are two methods to improve the calibration quality. The most significant factor that will improve the calibration quality is the pose set selection. Thus the condition number of the identification matrix can be used as an important indicator, but not an absolute reference, during the selection of the poses. The condition number computed from the experiment can be used to refer back to the simulation tables and estimate the quality of the pose set, and suggest a level of confidence in parameter identification.

References

1. Jokiel, B., "Analysis of a Parallel Architecture Coordinate Measuring Machine," Master's Thesis, University of Florida, 1996.

Three Parameter Solution of Time-varying Thermal Errors

T Gim*,**, J Corbett** and A E Gee**

* Machine Tool R&D Center, Daewoo Heavy Industries, Ltd.
601-3, Namsan-dong, Changwon, Kyungnam, 641-090, Korea (on leave at ** 1994-97)
** School of Industrial & Manufacturing Science
Cranfield University, Cranfield, Bedford, MK43 0AL, UK

Introduction

Errors in machine tools are generally classified as being time or spatially dependent. Thermal errors are strongly dependent on the continuously changing operating conditions of a machine and its surrounding environment, which account for as much as 70% of workpiece inaccuracy, according to Bryan [1]. Uniform temperature rises or stable temperature gradients, which produce time-invariant thermal errors, are considered to be rare in ordinary shop floor environments. Time-varying (dynamic) thermal errors in machine tools, as the result of the effects of continuous temperature variations, had not been investigated satisfactorily, so compensation techniques using empirical correlations had been the main research subject [1,2]. In respect of applications-related design considerations, it was decided that a prime objective of this study should be the development of a simple, yet systematic, physically meaningful modeling method of time-varying thermal errors using appropriate thermal parameters.

Modeling Thermal Errors by Three Parameters

It was considered that accurate analysis of thermal deformation should accommodate the distributed nature of physical and material properties, and afterwards a lumped model might be employed as viable approximation. The distributed nature makes problems difficult because governing equations are complex. From a metrological point of view, we sample frequently the behavior of an object at discrete points considered to be interesting, so that the overall behavior can be described sufficiently with less effort and resource. This is appropriate for the case of thermal error problems of machine tools and coordinate-measuring machines. Errors occurring in machine movement are often measured at discrete points along the path of the movements. Thus, a point-wise description of thermal errors is reasonable in a metrological sense and difficulties in analyzing a distributed system will be overcome. Overall behavior can be obtained by interpolation between points of interest.

In Figure 1, there are several points on the body, denoted by P_i, which are assumed to be points of interest for this particular body. Points P_1 to P_5 are located on the surface of the body, P_6 is between the surface and its center, and P_7 is at its center. Each point has its own response under thermal loadings. This response at a particular time can be accurately described as a block diagram shown in Figure 2. From the theoretical analysis of simple machine elements such as bars, beams and cylinders, and extensive finite-element simulation data for a straightedge subject to room temperature variations [3], three thermal parameters, i.e. time-delay, time-constant and

gain, were identified to obtain a precise description of the thermal deformation of a point of a machine body. A heat input will cause a movement of point P_i to another position, and it has three components in a Cartesian coordinate system. During the movement, four types of process-elements, including processes due to those three thermal parameters, are acting, i.e. a delay element, first-order element, gain element and positive feedback element. This block diagram is the result of analyses done so far.

g: gravitational acceleration
$\mathbf{F}_1$, $\mathbf{F}_2$: external forces
T: temperature
q_b: heat flux at boundary
q_r: radiation at boundary
q_c: convection at boundary
n: outward normal coordinate
T_b: known temperature at boundary

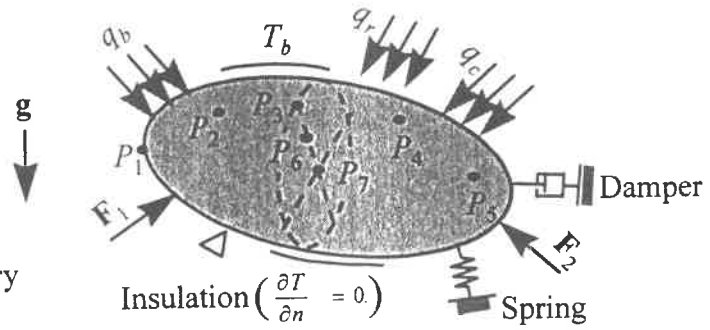

Figure 1 Body subject to external forces and thermal loadings

By definition, a delay or dead-time element causes the effect of an output to be delayed a finite time. In heat-transfer processes there is a transportation delay of heat flux. Point P_6 at the center will experience a greater time delay than points on the surface. This effect is particularly significant for a material having a low thermal diffusivity such as granite. A body having small dimensions and a moderate thermal diffusivity will not exhibit a significant time delay, and the effect of a delay element can be ignored. Thermal environments also affect the magnitude of time delay. Time delay, ranging from fractions of seconds to hours, depends on the location of the point of interest with respect to heat sources and material properties. Thermal environments generally vary with time, and thus time delay varies with time too.

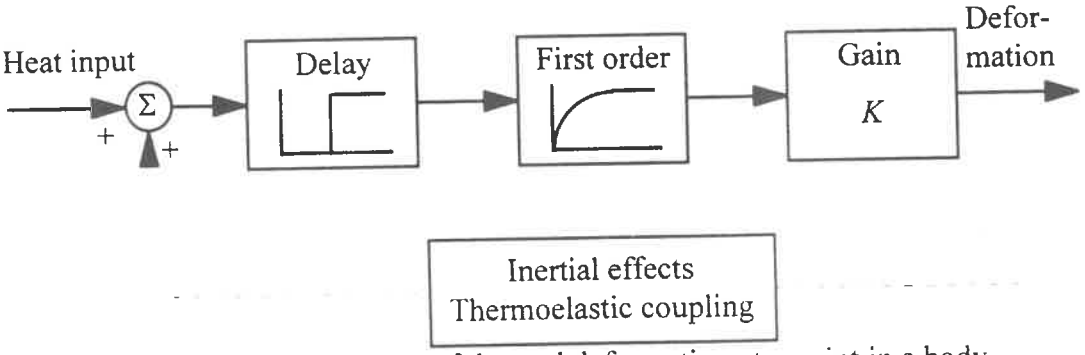

Figure 2 Block diagram of thermal deformation at a point in a body

A first-order element is well recognized in terms of thermal deformations, and characterized by its time-constant. A particular characteristic of a first-order element thermal deformation process is a very large time-constant in comparison with electrical or servo systems, i.e. of the order of hours to several days. Correspondingly, steady-state responses are not of great use for the problems of thermal deformations. It is understood that several factors are acting simultaneously to form the time-constant, i.e. the heat capacity of a body, its size and the thermal environment.

The thermal environment generally varies with time, and thus the time-constant varies with time too.

A 'gain element' is defined as converting changes in temperature to corresponding displacements in which coefficient of thermal expansion plays a principal role in this process. A body with a high thermal expansion coefficient will generally exhibit a high gain. Another important factor in this process is the constraint conditions of the body and they affect the distribution of the gain of each point significantly. A freely-expanding body will have a uniform distribution of the gain both throughout its surface and inside, whereas a constrained one will exhibit significant changes in gain. Finally, thermal environments also affect gain. The thermal environment generally varies with time, and thus gain varies with time too.

As a further element, there is the effect of positive feedback related to two physical phenomena, i.e. inertial effects and thermo-elastic coupling. Inertial effects are associated with the rate of change of strain rate. If an engineering component is stationary (or in a state of uniform motion) and external forces are applied gradually, then inertial effects are negligible. This applies to the case of machine tool components. Thermo-elastic coupling is related to strain rate. A process involving high strain rate, such as tensile testing, produces heat even though there are no heat inputs, but machine tool components do not generally involve such high strain rates. In elastic bodies undergoing non-inertial loading, it is observed that strain rate is always small compared with the rate of change of temperature, and thus we can discard the positive feedback element for this problem. In conclusion, thermal deformation of a body can be understood accurately with a point-wise delay-plus-first-order process, and thus thermal errors can be described by several delay-plus-first-order processes of points of interest in a machine structure.

Refinement of Point-wise Description Method

As a first step, a governing equation of thermal deformation of a point at a particular time will be obtained., then the transfer function G of thermal deformation process is obtained using Figure 2:

$$G = \frac{Ke^{-t_D s}}{1 + \tau s} \tag{1}$$

where K is the gain of the gain element; t_D is the dead time of the time-delay element, t is the time-constant of the first-order element and s is the Laplace variable. This transfer function is equivalent to the following first-order differential equation:

$$\tau \frac{du}{dt} + u = KF_{th}(t - t_D)H(t - t_D) \tag{2}$$

where u is the displacement of a point in a body caused by temperature rise; $F_{th}(t)$ denotes a time-varying thermal loading; $H(t)$ is the Heaviside unit step function. Because system parameters are varying with time due to continuously changing thermal environments and some finite number of sampling points will be involved, the governing equations of the thermal

deformation of a body can be effectively analyzed by employing a state-space analysis method. One benefit of using Equation 2 is that it provides flexibility in choosing system input when analyzing the thermal behavior of a machine, because it describes the input-output characteristics. If the heat input to a machine component is chosen to be the spindle speed, then the gain has a unit of the form [(thermal deflection)(spindle speed)-1].

Evaluation of Thermal Parameters

Completion of this approach was made by presenting the methods by which the three thermal parameters can be evaluated. The first method employs analytical tools based on simplifying assumptions about the shape and boundary conditions of machine components. The second method was to apply numerical techniques to complex machine components. Lastly, the three thermal parameters can be easily identified using popular parameter identification techniques which can be applied to time-varying cases by their recursive forms.

Direct experimental evaluation of the thermal parameters using a full-scale model was investigated using a single-point diamond turning research machine at Cranfield university. The experimental test of thermal errors and parameter evaluation using the test data was performed on the aero-static spindle unit because the main function of the machine is the facing of thin disks. Before the test, the expected thermal deformation of the spindle unit was calculated analytically. In order to identify time-varying system parameters quantitatively, some modified recursive least-squares methods were employed. They were, however, found to be sensitive to noise in the measurement data. The experiment implied that, under constant thermal and operating environment, the time-varying characteristics of the parameters can be neglected because they gave nearly equal thermal parameters under the same heat input conditions.

A scaled physical test model method was investigated regarding its use as a design test method. Also, it can be regarded as an indirect evaluation method of the three thermal parameters employing smaller scaled models as a feasible solution when dealing with large machine tool structures. It was found that there were some problems in directly applying similarity rules in thermal processes. These are due to the very large increases in the heat transfer coefficient and much smaller time scale for test models. This was overcome by using the inverse proportional relationship between the time-constant and heat transfer coefficient.

References

1. Bryan, J.B. (1990), "International status of thermal error research", Ann. CIRP, Vol. 39, No. 2, pp. 645-656
2. Weck, M., McKeown, P., Bonse, R. and Herbst, U. (1995), "Reduction and compensation of thermal errors in machine tools", Ann. CIRP, Vol. 44, No. 2, pp. 589-598
3. Gim, T. (1997), *Modelling and Evaluation of Time-varying Thermal Errors in Machine Tool Elements*, PhD Thesis, Cranfield University, Cranfield, Bedford, MK43 0AL, UK

Load Capacity of an Externally Pressurized Air Bearing Used in Measuring the Power Drawn in Stirred Tanks

David Palomino M.[1], Guillermo Robles M.[1], Gabriel Ascanio G.[1], Enrique Galindo F.[2]

[1] Departamento de Diseño Mecánico, Centro de Instrumentos, UNAM.
A. P. 70-186, Ciudad Universitaria, México D. F. 04510, MEXICO.
Phone: +52 (5) 622 8654, Fax: +52 (5) 622-8620.
[2] Departamento de Bioingeniería, Instituto de Biotecnología, UNAM.
A. P. 510-3, Cuernavaca, Morelos, 62250. MEXICO.

Abstract

In order to predict the load capacity of an externally pressurized air bearing, an analysis of the air flow through the clearence formed between its components is carried out. The dimensionless Reynolds' equation which describes the movement of fluid in the bearing is solved numerically to obtain the pressure distribution neglecting the curvature effects and assuming isothermal compressible flow. The load capacity is also calculated by numerical integration over the total surface wetted by the air. An experimental device was constructed to carry out experimental measurements. The pressure supplied was measured at different loads and these results were compared with the numerical ones obtaining maximum differences of roughly 9%.

Introduction

The rotating machinary is used extensively in diverse applications as power stations, marine propulsion, aircraft engines, machine tools, automobiles, mixing systems, ultraprecision equipment, etc., and is supported generally by one or more bearings which play a vital rol in determining the behavior of the rotating system under action of both static and dynamic loads. In order to design a system, it is neccesary to know the types of bearings and the performance characteristics associated with each one of them. A type of bearing commonly used today is the air bearing that has many advantages as to reduce the power loss, to support relatively high load even without spin, are free of friction due to the air film generated by the compressed air, compared with oil bearing have less heat generation, low contamination and high accuracy [1,2]. This paper presents results of the load capacity in an externally pressurized air bearing obtained by means of the wetted surface and the pressure supplied.

Description

The bearing, sketched in fig. 1, consist of two components [3]. The static one is a dish provided with a conical cavity in its upper surface and a shaft passing through its center. The dynamic part is a conical shaped disc provided with a cylindrical hole in its center so that it can freely rotate around the shaft of the static component. Pressurized air is supplied in the static component, is expanded by nozzles discharging along of three shallow circular channels and, finally, is distributed on its surface. The channels allow the bearing to have a higher load capacity and help to distribute the air to all its parts. The air flows through the clearance existing between both

components of the bearing exerting a thrust force and keeping the dynamic part, together with its load, floating by means of an air cushion during the power drawn measurements. The air gets out finally to the atmosphere. The shaft of the static part have also nozzles that distribute air on its surface and both components have never any contact.

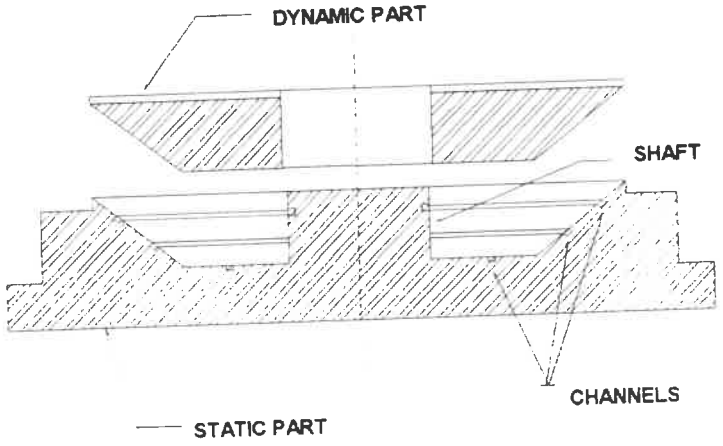

Fig. 1. Scheme of the pneumatic bearing

Theoretical Analysis

The governing equation which describes the characteristics of the pneumatic bearing can be obtained theoretically modeling the movement of fluid film. This equation was derived by Reynolds [4] for an isothermal compressible fluid and is presented as follows with the geometry shown on the fig. 2:

$$\frac{\partial}{\partial x}\left(\frac{\rho h^3}{\mu}\frac{\partial p}{\partial x}\right)+\frac{\partial}{\partial y}\left(\frac{\rho h^3}{\mu}\frac{\partial p}{\partial y}\right)=6\left[u_0\frac{\partial}{\partial x}(\rho h)+v_0\frac{\partial}{\partial y}(\rho h)\right]+12\frac{\partial}{\partial t}(\rho h) \qquad (1)$$

where p, ρ, μ, and h are the pressure, density, viscosity and film thickness, respectively; and u_0 and v_0 are the velocities in the x and y directions, respectively.

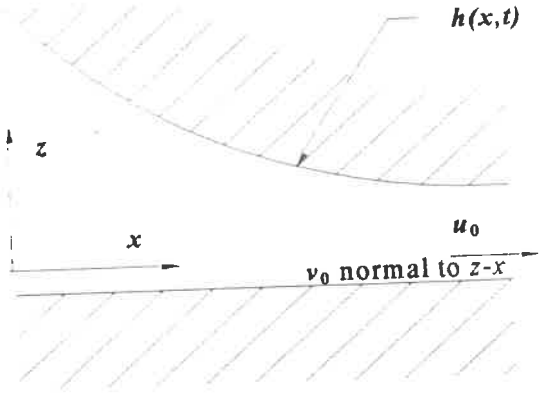

Fig. 2. Flow channel of lubricant

By introducing the ideal gas equation and assuming viscosity constant, steady state and static conditions, the Reynolds equation (1) is reduced to:

$$\frac{\partial}{\partial x}\left(ph^3\frac{\partial p}{\partial x}\right)+\frac{\partial}{\partial y}\left(ph^3\frac{\partial p}{\partial y}\right)=0 \tag{2}$$

The discharging pressure p_o on the channels is obtained by means of the inlet pressure p_s and the adiabatic coefficient γ assuming a isentropic process [5]:

$$p_o = p_s\left(\frac{2}{\gamma+1}\right)^{\gamma/(\gamma-1)} \tag{3}$$

The following dimensionless variables are used to generalize the solution, being p_a, L and c the atmospheric pressure, reference length and clearance, respectively [6].

$$P=\frac{p}{p_a},\qquad X=\frac{x}{L},\qquad Y=\frac{y}{L},\qquad H=\frac{h}{c} \tag{4}$$

By substituting in equation (2) it is transformed in:

$$\frac{\partial}{\partial X}\left(PH^3\frac{\partial P}{\partial X}\right)+\frac{\partial}{\partial Y}\left(PH^3\frac{\partial P}{\partial Y}\right)=0 \tag{5}$$

The boundary conditions are $P=P_o/P_a$ at each outlet of nozzles or channel, $P=1$ at the outlet to the atmosphere, and $P(X)=P(X+2\pi)$ as a periodicity condition.

The load capacity supported by the bearing is obtained by integrating the pressure distribution over the total surface A wetted by the air:

$$\overline{F}=p_a\int P\,dA \tag{6}$$

A computational code was elaborated by using an iterative scheme of finite differences where the value of pressure at each node is determined succesively up to satisfy a given tolerance. These results are shown in fig. 3 where it can be observed an exponential growth.

Experimental Measurements

Experimental measurements to determinate the static load supported by the bearing were carried out. Pressurized air at distinct pressures was supplied up to lift up the load together with the dynamic part. A tangential force was applied to the dynamic part to permit free spin and to verify the floating. Pressure measurements were taken with a Bourdon manometer up to raise each load. These results are shown in fig. 3, together with the numerical ones presenting the same behaviour.

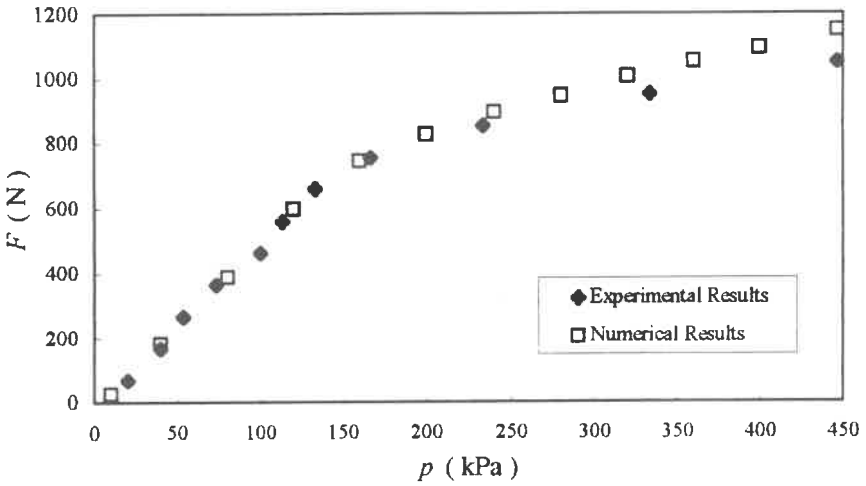

Fig. 3. Comparison between calculate and experimental results

Conclusions

The numerical calculations and experimental measurements present differences lesser than 9%. These differences are due to the limitations in the static model and to the nonuniformity of the load applied that causes instabilities and friction between the static and dynamic parts. A dynamic model will be solved in the future to obtain the dynamic characteristics and a better approximation between experimental and calculated results.

Thus, numerical and experimental load capacity results in an externally pressurized pneumatic bearing were presented in this paper with an acceptable approximation making a good prediction of the bearing performance.

Acknowledgment

This project was partially supported by funds from DGAPA-UNAM grant No. IN-503295.

References

1. Gross, W. A., *Fluid Film Lubrication*, New York, Wiley (1980).
2. Goodwin, M. J., *Dynamics of Rotor-Bearing System*, Unwin Hyman LTD, London (1989).
3. Reséndiz, R., Martínez, A., Ascanio, G., Galindo, E., "A new pneumatic bearing dynamometer for power input measurement in stirred tanks", *Chem. Eng. Tech.*, **14**, (1991). 105-108.
4. Reynolds, O., "On the theory of lubrication and its application to Mr. Beauchamp Tower's experiments, including an experimental determination of the viscosity of olive oil". *Phil. Trans. Roy. Soc. London*, **177**, pt. 1, (1886). 157-234.
5. Currie, I. G., *Fundamental Mechanics of Fluids*, Mc Graw-Hill Book Company, USA, 1974.
6. Han, D., Park, S., Kim, W., Kim, J., "A study on the characteristics of externally pressurized air bearings", *Precision Eng.*, **16**, (1994). 164-173.

Design of an Ultra Low Speed Straight Motion System Based on a High Viscosity Fluid Bearing

J.W. Spronck, P.F.A.M. van Putten and G.J.P. Nijsse
Delft University of Technology, Laboratory for Micro Engineering,
Mekelweg 2, 2628 CD Delft, the Netherlands
Tel. +31-15- 2781824; fax +31-15-2781887, E-mail J.W.Spronck@WbMT.TUDelft.NL

Abstract

An ultra low speed straight motion system is described. The system consists of a fine stage on top of a coarse stage. The coarse stage consists of a moving beam, a base plate and a side plate, separated by a thin grease film. The coarse stage must realize a very smooth motion within the control capabilities of the fine stage. The measurement results show that the proposed system can be used to establish a very constant low speed motion. More research has to be done to optimize the coarse stage.

Introduction

How to design a simple nanometer straight motion system that provides for a constant velocity in the range from 1 µm/s to 1 mm/s, over a travel range of approximately 100 mm?

The mechanical setup can be described as a fine stage on top of a coarse stage.

The coarse stage must realize a very smooth linear motion within the control-capabilities of the fine stage.

The fine stage (not drawn or discussed in this paper) has been equipped with piëzo-actuators to realize a fast tracking relative to a straightness reference standard. The range of the fine stage is a few micrometers.

This paper describes the mechanical design and the first measurement results of the coarse stage. The working principle of the coarse stage is shown in figure 1.

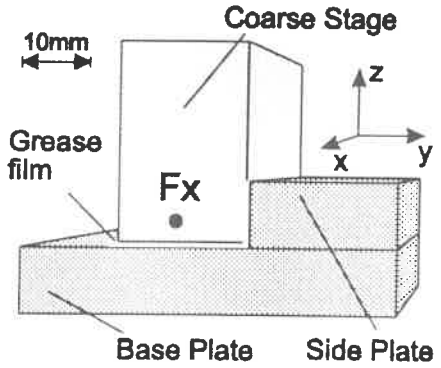

Fig. 1. The coarse stage is supported by a grease bearing on a base plate. Fx is the driving force in the x-direction.

1. The design concept of the coarse stage

The design of the coarse stage has been simplified to a great extent by the multifunctional use of grease. We used grease named *Kilopoise 0001* (a product of Rocol ltd., UK). The film thickness between the stage and the base plate is approximately 20 micrometer.

The most important advantages of grease in relation to the motion of the stage are:

1. The damping characteristic of the grease lubrication provides for a simple linear relation between the driving force *Fx* and velocity *Vx*;
2. High frequency deviations from the ideal momentary position and high frequency straightness errors that are normally caused by surface roughness and vibrations of the bearing, are eliminated to a great extent by the grease.

The most important advantages of grease in relation to the bearing of the stage are:

1. A very low cost lubricant and bearing with a high damping ratio is achieved;
2. The bearing provides high stiffness at high frequencies and almost zero stiffness at very low frequencies;
3. Easy and low cost assembly of the bearing.
4. No special requirements are needed for the bearing surfaces.

The overall advantages of the bearing are:

1. Very compact design;
2. Low cost;
3. Flexible design

The overall disadvantages of the bearing are:

1. The thickness of the grease-layer is not critical but must be controlled within certain limits. Stick slip and the roughness of the bearing surfaces affect the smooth motion.
2. Grease is a non-Newtonian fluid. The apparent viscosity depends on the shear rate and shear amplitude.
3. The viscosity of the grease depends on the temperature.

2. Physical model

The rheological behavior of greases in a lubricated bearing is a complex problem.
Grease is a non-Newtonian colloidal system. When subjected to oscillatory shearing of a certain amplitude, the grease exhibits a non-linear response in the output signal. The *Kilopoise 0001* grease used exhibits a high apparent viscosity at low shear rates and a low apparent viscosity at high shear rates. The viscosity also depends on the shear amplitude. The exact behavior has to be determined experimentally.
A linear model of the bearing has been derived to predict the behavior of the bearing.

The bearing can be described as a damper. The differential equation of a mass-damper system is:

$$m \cdot \ddot{x} + c \cdot \dot{x} = Fx,$$

where x is the deplacement of the stage, Fx is the force applied to the stage, m is the mass of the stage and c is the damping constant.
The damping constant depends on the geometry of the fluid film and the viscosity that is assumed to be constant in this idealized model.

$$c = \frac{l \cdot w}{h} \cdot \eta.$$

Here, l is the bearing length, w is the bearing width; h is the fluid film thickness and η is the coefficient of viscosity.
The viscosity of the grease used is 0,25 Kilopoise (in SI units: 25 kg/ms) at 25^0 C. The linear model of the bearing behaves like a low-pass filter.

3. The experimental setup and results

Experiments have been performed to obtain information on the following:

1. What is the relation between the driving force and the velocity of the stage?
2. How smooth is the displacement in x-direction? This should be within the control capabilities of the piëzo-driven fine stage.
3. How smooth are the straightness errors? For the same reason as mentioned above they must be within a few micrometers.

A laser interferometer was used for all displacement, velocity and straightness measurements.

3.1 Translation measurement; force-velocity

The experimental setup for the translation measurement is shown in figure 2.

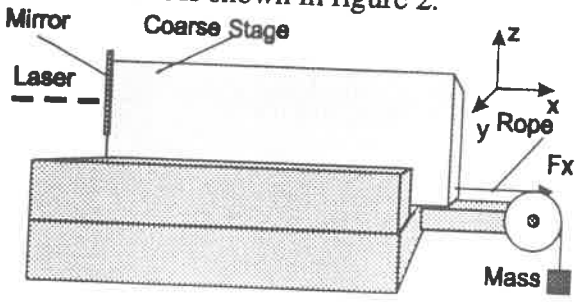

Fig. 2. Scheme of the experimental setup for measurements in the x-direction. A steel slider placed against two steel beams, separated by a thin film (20um) of grease. The force is applied by a variable mass hanging on a rope

During the very first experiments, the stage was pushed by hand. The results are represented in figure 3 and 4.

Table 1. The average Speed(AVG dx/dt in µm/s) by applying different forces. The relation between speed and force is linear within 10%.

Force	0	1,8	2,8	3,8	4,8	5,8
AVG dx/dt	0	76,5	128	180	228	282

In figure 5 we see the response of the stage when the driving-force is changed instantly from 2,8 N to 0 N. In the experimental setup a force in the range from 1,8 to 5,8 N gave a velocity from 76,5 to 282 µm/s. Results are shown in table 1.

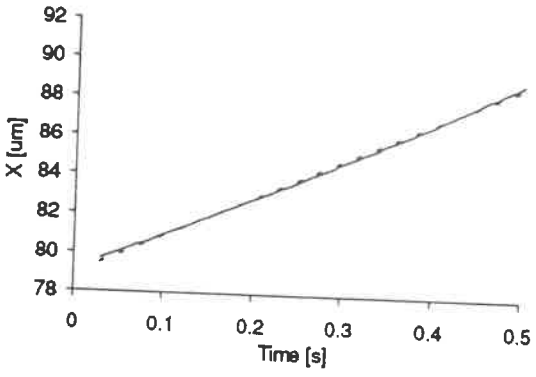

Fig. 3. Hand-driven x translation(from 80 to 140 µm in 2.5 seconds) and ideal position line (dashed). The deviation from the ideal position is less than 1 µm.

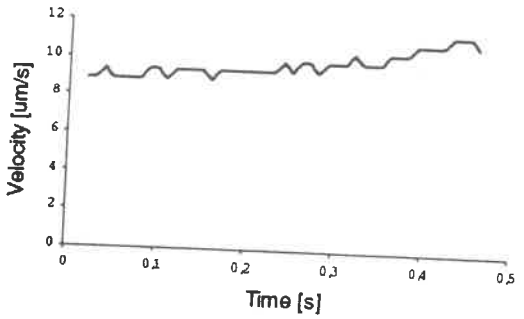

Fig. 4. Hand driven velocity vs. time for the first 0.5 seconds. The velocity is about 10 µm/s. The velocity error is less than 2 µm/s. The high frequent changes are due to the limited resolution of the laser.

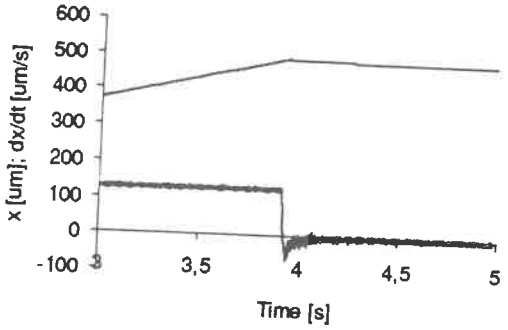

Fig. 5. A step in the applied force from 2,8 to 0 Newton. The step is generated by lifting the weight instantly.

3.2 Translation measurement: straightness

The experimental set-up for the straightness measurements is shown below.

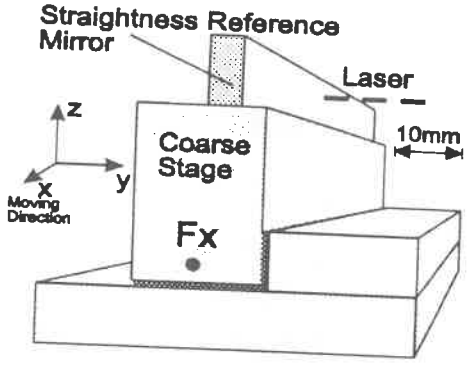

Fig. 6. Straightness measurements setup. A zerodur straightness reference mirror is placed on top of the stage. The distance between stage and laserinterferometer is measured while moving the stage.

During 120 seconds, the movements in the y-direction have been measured. The stage has moved over a distance of 9 mm in the x-direction.

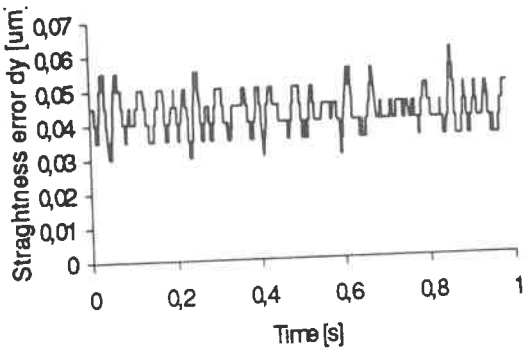

Fig. 7. Plot of the straightness error during the first second. The speed in the x-direction is 75 um/s. The straightness error is about 30 nm over a distance of 75 µm.

The straightness error over the distance of 9 mm is 0,14 µm.
The behavior of the stage in the z-direction is assumed to be similar.

3.3 Repeatability and drift

The behavior of the bearing is not constant over a few days. The film thickness decreases slowly to a constant value. Different loads on top of the bearing also influence the film thickness. The film thickness should be controlled to solve this problem. Another problem is that the temperature of the grease raises due to internal friction. This results in a lower constant of viscosity, which influences the relation between the velocity and the applied force.
When the driving force is turned off, the velocity drops to zero instantly and seems to stay zero. Position measurement showed that the stage is moving 2 µm in 10 minutes.

4. Comparison of the measurement results with the physical model.

From the measurement results we can conclude that the bearing behaves as a low-pass filter.
The stiffness of the bearing in the x-, y- and z-direction is high for high frequencies and low for low frequencies.
For small steps in the applied load, the physical model is satisfying. High steps could show the non-linear behavior, but are not needed in this application.
For a specific velocity range, one should measure the bearing characteristics experimentally to derive the damping constant.

5. Conclusions

The performance of the course stage is very promising. One should be aware that no special construction tools or materials were used.
1. The relation between the driving force and the velocity of the stage is linear within 10 %.
2. The smoothness of the displacement in the x-direction and the straightness errors are within tenths of nanometers.
3. More research has to be done to derive a non-linear physical model for grease-film bearings.

The piëzo driven top stage is under development and is expected to compensate the remaining tracking errors.

References

[1] A. Cameron, *The Principles of Lubrication*. Longmans, London, 1966
[2] B. Pugh, *Practical Lubrication*. Newnes-Butterworth, London, 1970

COMPARISON OF CARBON FIBER ALUMINA CERAMIC AND ALUMINUM BEAMS

Drew Devitt, Nick Sotiropoulos, Josh Radice
New Way Machine Components, Inc.
Aston, PA 19014

Carbon fiber composites have made a dramatic influence in the space and aero space industries. Lower weight, high strength, stiffness and controllable coefficient of thermal expansion of carbon fiber are several of the technical properties that could be employed with advantage in precision structures for metrology or manufacturing applications. The purpose of this paper is to help evaluate this potential.

To this end, we acquired an aluminum beam, a ceramic beam, and manufactured a carbon fiber beam in our shop using resin transfer molding. It should be noted that the aluminum beam had no machining on its surfaces and was not anodized. The composite beam was designed with unidirectional fiber, balanced with the resin to have near zero coefficient of thermal expansion. All three beams were 2.5 inches square with a .250 inch wall thickness and 21.5 inch length.

Three basic tests were performed on the rams: bending strength, thermal distortion, and dynamic analysis. The tests and their results are described below.

		DYNAMIC CHARACTERISTICS		THERMAL DISTORTIONS		BENDING STRENGTH	
	BEAM MASS (grms)	FIRST NATURAL FREQUENCY	DAMPING FUNCTION	AXIAL GROWTH (micro-inch)	BENDING (sensor C) (micro-inch)	DEFLECTION (2 ½ lb LOAD) (micro-inch)	DEFLECTION (5 lb LOAD) (micro-inch)
CERAMIC	3495	3350	.12%	47	182	131	261
ALUMINUM	2110	1295	.20%	201	133	413	829
CARBON FIBER	1135	1275	1.4%	88	687	637	1273

BENDING STRENGTH

The test beams were held in a vise 5 inches wide resulting in a cantilever of 16.5 inches. Two and a half pound and five pound loads were applied to the end of the beam. Measurements were taken using a capacitance probe and a steel gage block attached to the underside of the beam. Results are listed on the right side of the above summary table. The carbon fiber deflected the most and also took a noticeably longer time to return to zero after the loads had been removed. This lag may be attributed to micro deformations of the epoxy along the fiber interface which may also be responsible for the excellent damping. Unfortunately it is not advantageous in this application. It should be noted that this composite was designed for low coefficient of thermal expansion, not for high stiffness.

THERMAL DISTORTION TEST

Deflection in micro-inches

BEAM	SENSOR	LIGHT ON 3 minutes	LIGHT OFF 3 minutes	LIGHT OFF 6 minutes	LIGHT OFF 9 minutes
CERAMIC	A	70	70	35	13
	B	47	44	37	34
	C	182	82	30	16
ALUMINUM	A	-97	48	43	39
	B	201	212	207	205
	C	133	1	11	17
CARBON FIBER	A	-608	-314	-218	-147
	B	88	61	48	39
	C	687	394	291	231

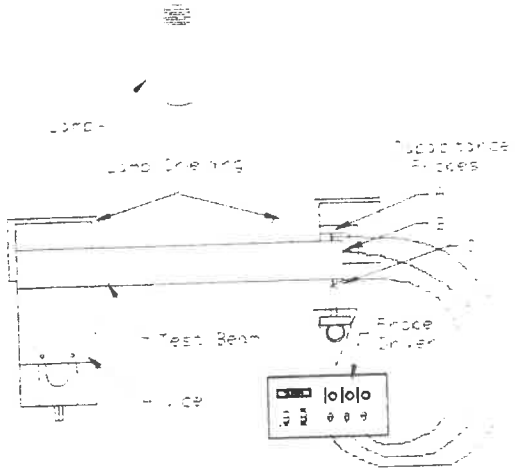

This test was performed on a large granite surface plate. Five inches of each tube was held in a vice and steel gage blocks were attached to the rams as indicated in the diagram to provide a conductive surface for the capacitance probes. The capacitance probes measured displacements caused by thermal distortions. The probes and vise were shielded from a 200 watt light placed 12 inches from the surface of the beam. In all three cases dimensional distortions were evident within 5 seconds of exposure to the light. It is likely that the black carbon fiber absorbed more energy than the white ceramic or reflective aluminum. It should be noted that in practice aluminum is hard coated or anodized dark gray or black. Thus, a more representative test would have been to use an aluminum beam treated in this manner because of the specific interest in determining actual responses to radiant heat inputs. It also would have been interesting to have outfitted the beams with temperature sensors as the heat conductivity of the materials certainly affected in the distortion patterns.

The carbon fiber beam showed a low axial growth but exhibited a warp much larger than expected. The ceramic beam also warped more than expected but was the most stable in the axial direction. The ceramic beam was the easiest to maintain good reference zero's when testing. While testing the aluminum beam care had to be taken to keep body heat or breath away from the beam as they would have an immediate dimensional effect. The conductivity of aluminum appeared to help minimize warping by equalizing temperature gradients quickly.

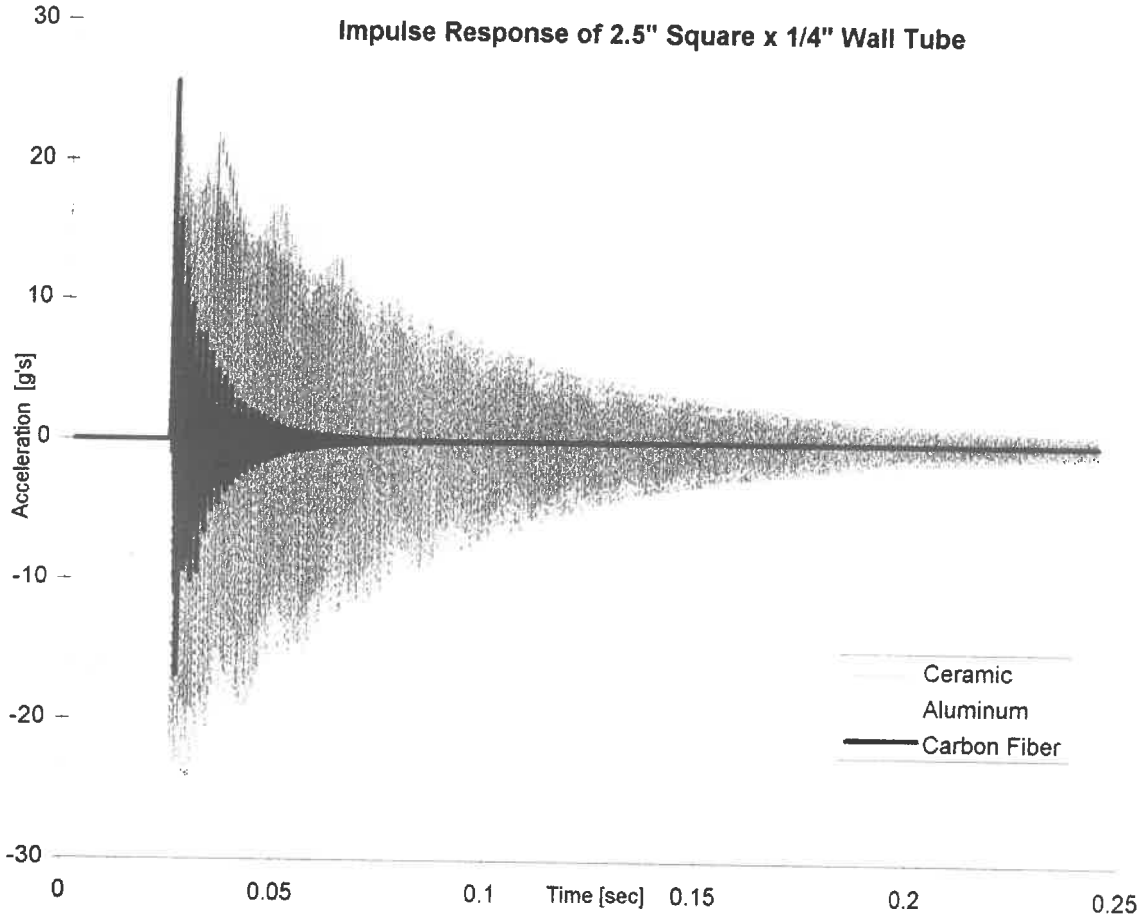
Impulse Response of 2.5" Square x 1/4" Wall Tube
30
20
10
0
-10
-20
-30
Acceleration [g's]
0
0.05
0.1
Time [sec]
0.15
0.2
0.25
Ceramic
Aluminum
Carbon Fiber

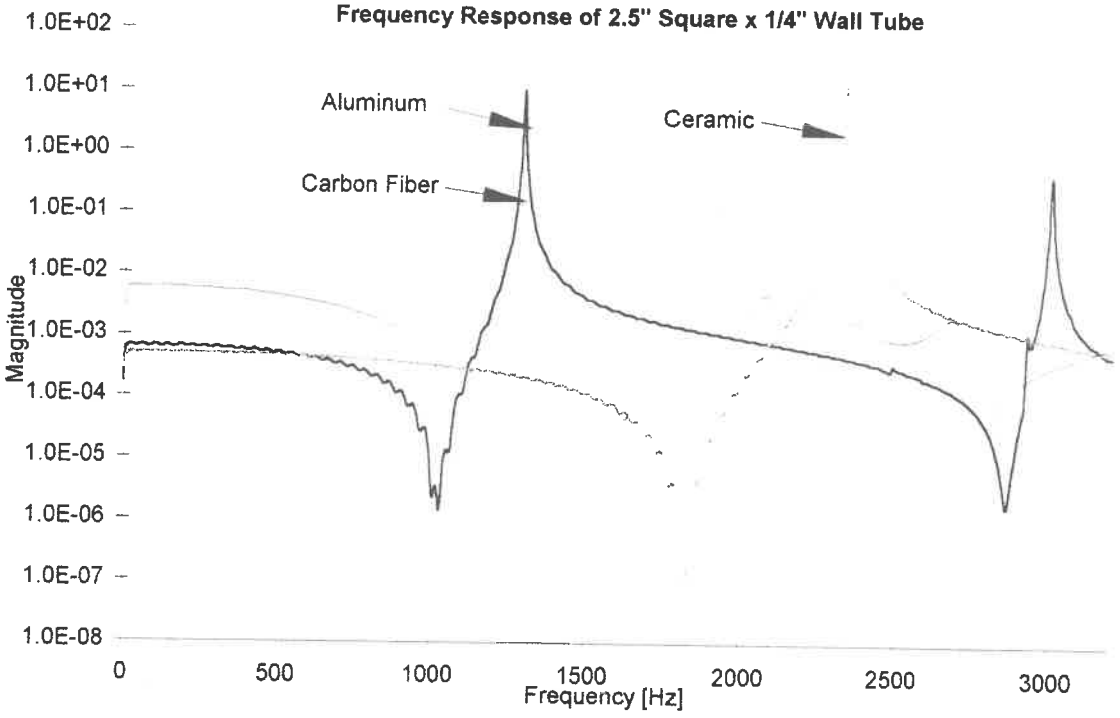
Frequency Response of 2.5" Square x 1/4" Wall Tube
1.0E+02
1.0E+01
1.0E+00
1.0E-01
1.0E-02
1.0E-03
1.0E-04
1.0E-05
1.0E-06
1.0E-07
1.0E-08
Magnitude
Aluminum
Ceramic
Carbon Fiber
0
500
1000
1500
2000
2500
3000
Frequency [Hz]

DYNAMIC ANALYSIS

The dynamic characteristics of the three beams were measured using an impact hammer, an accelerometer, and a dynamic signal analyzer. Each ram was hung from surgical tubing and exited using the impact hammer. The resulting accelerometer response was measured. From these tests, the natural frequencies and damping can be evaluated.

The first natural frequency of the carbon fiber was almost the same as the aluminum, although its second natural frequency was much lower. We suspect this was due to an out of square or diaphragm type vibration of the side wall. The unidirectional fiber orientation was selected for simplicity of obtaining a low coefficient of thermal expansion in the axial direction. It is expected that bi-directional or multi-directional fiber orientations will improve the second and higher natural frequencies. A higher fiber content combined with bi-directional or multi-directional components should significantly increase static stiffness and the first natural frequency.

The first natural frequency of the ceramic was significantly higher than both the aluminum and the carbon fiber. As expected though, the ceramic had the lowest damping function. The carbon fiber damping function was very high with vibration decays approximately seven times faster than the aluminum. This should result in faster setting times and excellent dynamic performance.

SUMMARY

Carbon fiber shows promise in large part to its light weight and high damping. If increased thermal stability and bending stiffness can be achieved, carbon fiber could become an attractive design material for precision engineers.

We recognize moisture absorption as another potential source of distortion for carbon fiber and so we will have information on stabilizing carbon fiber against moisture absorption on our poster.

Our thanks for their contributions to our project:

Dr. Eric Marsh
Dept. of Mech.Engrg.
Penn State University

and

Dr. Suresh G. Advani
Dept. of Mech.Engrg.
Center for Composite Mfg.
Univ. of Delaware

Estimation of Thermal Contact Resistance by Electrical Contact Resistance Measurement

Kiyoshi Mizuhara and Norimitsu Ozawa
Mechanical Engineering Laboratory, AIST, MITI
1-2 Namiki, Tsukuba, Ibaraki, 305 JAPAN

1. Introduction

Thermal deformation of machine tools is very important problem for the working accuracy. To solve this problem, it is necessary to analysis of temperature distribution and thermal displacement of the machine tool structure. Particularly, study of the thermal behavior on contact surfaces of the machine tool is essential. In general, there are two kinds of contact surfaces between structural components of machine tool; two components are fixed by bolt - nut or any clamping device, and two components are sliding with each other. In this paper, we discuss about the former contact surface and a method to evaluate the characteristics of the thermal contact resistance (hereinafter called the thermal resistance) on the contact surfaces has been studied. Since the thermal resistance is greatly influenced the contact conditions of contact surfaces, the electrical contact resistance (hereinafter called the electrical resistance) has been used to investigate the contact conditions. Several factors are affecting the electrical resistance on contact surfaces e.g. (1) surface roughness, (2) waviness of contact surfaces, (3) contact pressure between contact surfaces, and (4) substances existing on contact surfaces. As these factors also influence on the thermal resistance on contact surfaces, it is assumed that a correlation exists between the thermal resistance and the electrical resistance on contact surfaces. A number of research works not only the thermal resistance but also the electrical resistance have been carried out, [1), 2), 3), 4)] however, there are no research on the correlation between two resistance. From the point of view, this paper first describes the results of experiment of the electrical resistance on contact surfaces and, then, the results of the thermal resistance measurement. Finally, correlation between the electrical resistance and the thermal resistance will be discussed.

2. Experimental set-up and procedure

Figure 1 shows the experimental set-up for the thermal resistance measurement and test specimens. For the observation of changes in the electrical and thermal resistance caused by contact pressure, a standard pressure indicator with nominal weight and the hydraulic power loading device were used in increasing/decreasing the contact pressure, and the applied load was detected by a load-cell and indicator. As shown in this figure, the test specimens are cylindrical form (50 mm in diameter and 50 mm long) and end surfaces of each specimen are machined to serve as contact surfaces. Three types of contact surface were used: lapped surface (steel), ground surface (steel), and scraped surface (cast iron). Profile of the contact surface of test specimens is shown in Figure 2. As presented the figures, ground surface is the best surface waviness and lapped surface has the best surface roughness. To investigate the effects of lubricant, measurement of resistance were carried out under the following two condition: DRY (the contact surfaces were washed by benzine) and WET (oil was injected between contact surfaces washed by benzine). The total initial loading of 64N on the contact surfaces included weights of the test specimen, the heat source, the heating block and the load cell. Consequently, initial contact pressure was 0.03MPa. All experiments were carried out in a temperature controlled room within 20 $\pm$ 0.5 degrees.

In case of the thermal resistance measurement, as shown in Figure 1, heat source is heated using a heating block provided with four thermoelements. The heat flow from the heat source passes through the contact surface between two specimens. Temperature of the heat source was controlled by means of regulating the DC power supply in accordance with the output of the thermal recorder. The thermal recorder is monitored the heat source temperature measured by thermistors embedded in the heat source. The thermal resistance on the contact surfaces was measured using copper-constantan thermocouples inserted into four holes (S_1, S_2, S_3, and S_4) of the specimens. And output signals of thermocouples were transmitted via digital thermometers to an analog computer for calculation using the extrapolation method.

Since the electrical resistance to be measured is very small value, thus, we used a double bridge. Current and voltage terminals for the double bridge were connected to the same holes (S_1, S_2, S_3, and S_4) of the specimens instead of the thermocouples. Since the electrical resistance is not stable immediately after loading, measurements were made after the output signal saturated. The electrical resistance was measured while the load applied on the contact surfaces were

increased from 0N to 2942N(contact pressure 1.53MPa) in increments 490N, and also unloaded by the same increments. Three consecutive measurements as described above were conducted for each contact surface.

3. Experimental results and discussions

3.1 The electrical resistance Figure 3 and 4 represented the experimental results of relationship between the electrical resistance and contact pressure under loading in DRY and WET conditions of ground specimen. The electrical resistance decreased with increasing the contact pressure. The results clearly demonstrated that expansion in real contact area due to the contact pressure caused reduction of the electrical resistance. Value of the electrical resistance in WET contact condition, Figure 4, is about 1/5 of DRY contact condition shown in Figure 3. Various researches have been carried out concerning the electrical resistance of thin oil film.[4), 5), 6)] These researches indicate that the electrical resistance of oil film thickness equal to the oil molecule became to approximately zero based on the tunnel effect. It is evident that the electrical resistance reduction on WET condition is caused by the tunnel effect. In addition, the electrical resistance increased with increasing frequency of load application, and contact pressure at 1.53 MPa it becomes about 5 times the value taken from the first measurement. This phenomenon are interpreted by the fact that; (1) current flowing through a very small contact area during measurement, (2) microscopic electric discharge, (3) contact parts suffer change in quality (such as oxidation), and (4) as result of formation of certain material between the substrate metal and the contact parts. Figure 5 show the effect of finished surface on the electrical resistance under DRY contact condition. As this figure shows, the rougher the surface, the lager the electrical resistance, and more susceptible to the contact pressure.

3.2 The thermal resistance Figure 6 presents relationship between the thermal resistance and the contact pressure under DRY and WET contact conditions. Effect of the contact pressure and the lubricant are similar to the experimental results of the electrical resistance, however variation caused by the frequency of load application is obviously small values. Expansion of real contact area and existence of the oil cause the reduction of the thermal resistance. On the other hand, for the analysis of the different behavior between the electrical and thermal resistance on the load application frequency, further investigation is necessary. Figure 7 shows the relationship between the thermal resistance and the finishing methods. Behavior of the thermal resistance is approximately same in the case of the electrical resistance shown in Figure 5.

4. Correlation between the thermal resistance and the electrical resistance

Figure 8 shows the relationship between the thermal and electrical resistance for DRY and WET conditions at contact pressures of 0.53MPa and 1.53 MPa respectively. As is clear from the figure, the thermal and electrical resistance can be represented by a linear relationship on log-log curves independent of contact pressure, surface roughness and contact conditions (DRY and WET). In other words, it has been verified by experiments that the relationship between the thermal and electrical resistance changes exponentially. By representing the thermal and electrical resistance in terms of R_T and R_E respectively, the thermal resistance R_T is given by the following equation,

$$R_T = 0.35\, R_E^{\,0.74}$$

5. Conclusions

From the measurements of the thermal and electrical resistance under the same conditions, we led to the following conclusions:

(1) The electrical resistance is small value for combinations of test specimens having less surface roughness, and tends to decrease with increasing contact pressure. The rate of change in the resistance value against contact pressure decreases for combinations of test specimens having smooth surfaces. For WET conditions, the electrical resistance is smaller, and is less influenced by contact pressure and surface roughness than in DRY conditions.

(2) In case of the thermal resistance, effect of the contact pressure and the lubricant exhibited a tendency similar to the electrical resistance.

(3) The resistance due to the frequency of load application represented obvious difference between the electrical and thermal resistance. Analysis of the phenomenon is a future subject.

(4) The relationship between the thermal and electrical resistance is exponential, irrespective of contact and surface conditions. Therefore, measurement of the electrical resistance, which is easy to carry out, makes it possible to estimate the thermal resistance.

References

1)Weills, N. D. and Ryder, E. A., Trans. ASME 71(1949)259

2)Kouwenhovent, W. B. and Potter, J. H., Weld. J., 27(1948)515

3)Uppal, A. H. and Probert, S. D., Wear., 15(1970)271

4)Holm, R., Electrical Contact, Springer-Verlag(1967)

5)Tamai, Y., J. of JSLE, 11-3(1957)115, (in Japanese)

6)Wilson, R. H., Proc. Roy. Soc., A212(1952)450

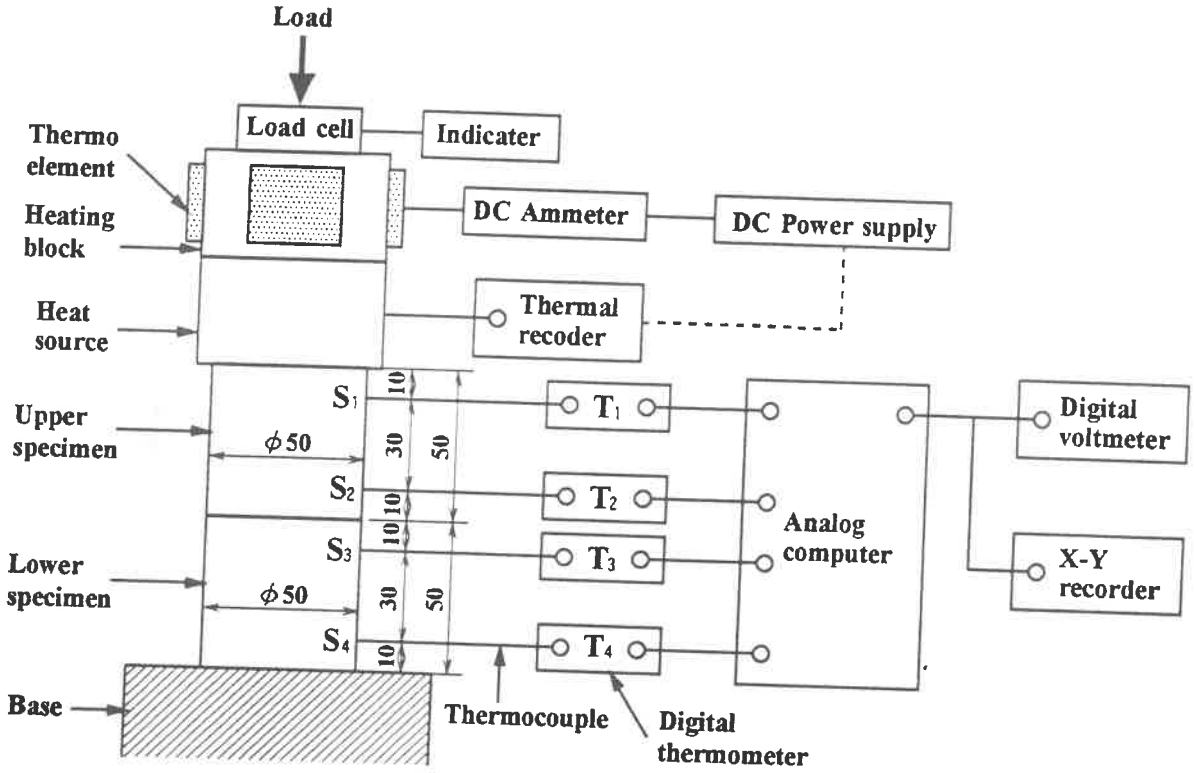

Fig.1 Experimental set-up and test specimens

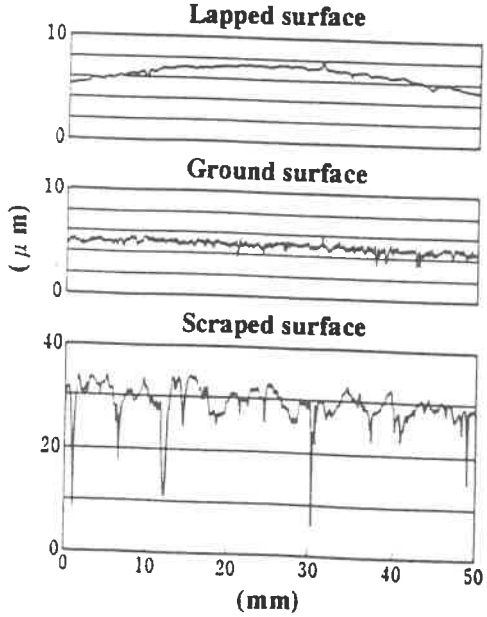

Fig.2 Profile of test specimens

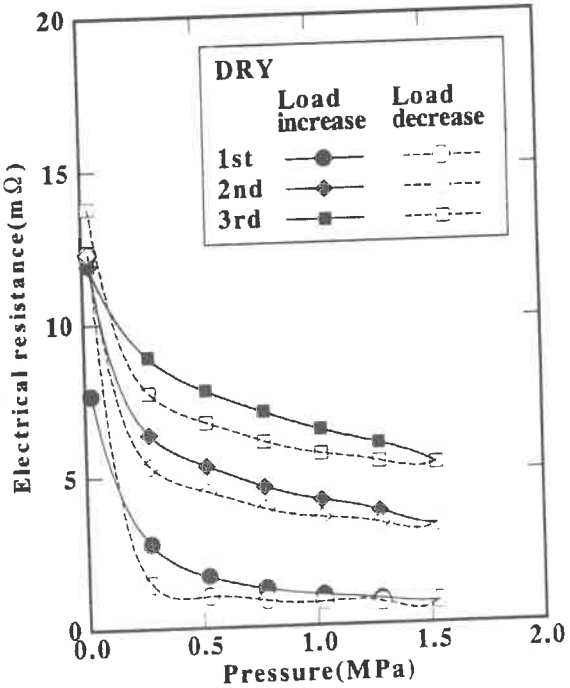

Fig.3 Relationship between pressure and electrical resistance (DRY) (Ground - Ground surface)

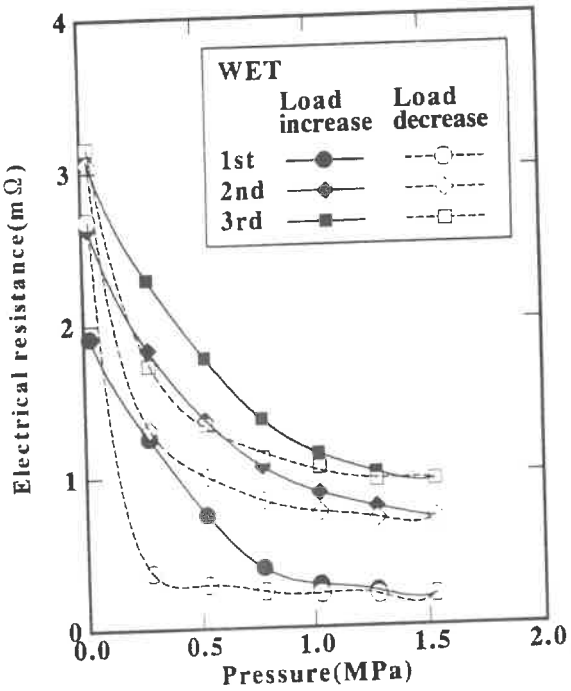

Fig.4 Relationship between pressure and electrical resistance (WET) (Ground - Ground surface)

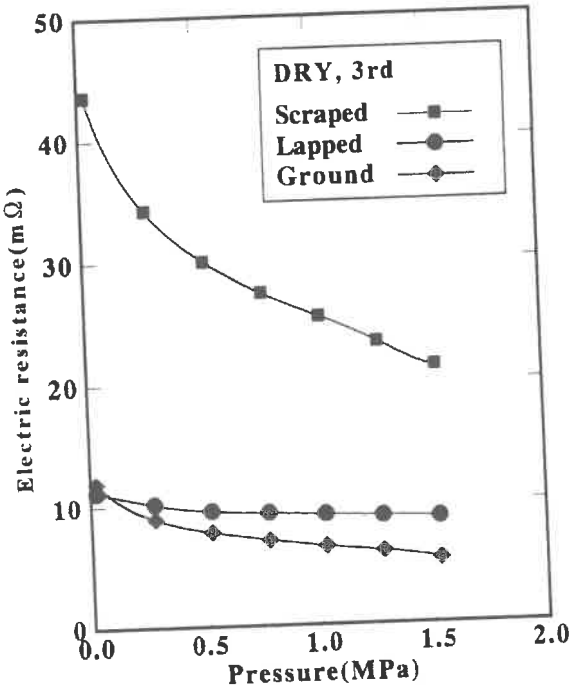

Fig.5 Relationship between finished surface and electrical resistance (DRY, 3rd)

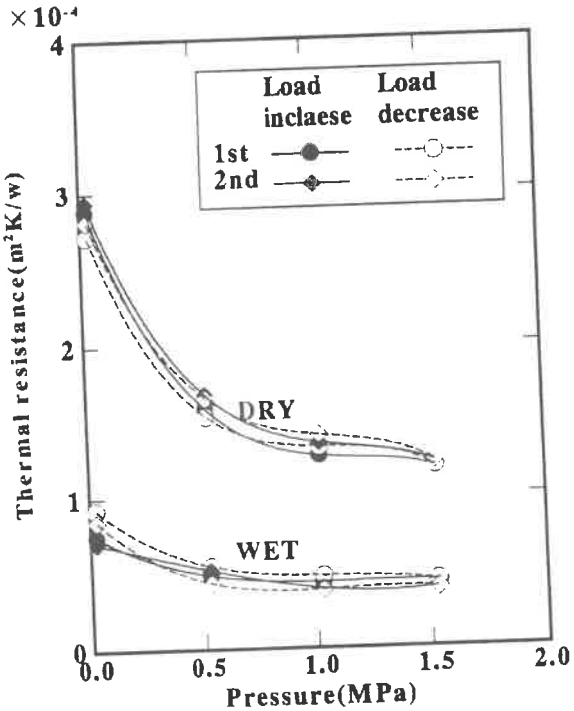

Fig.6 Relationship between pressure and thermal resistance (DRY and WET) (Ground - Ground surface)

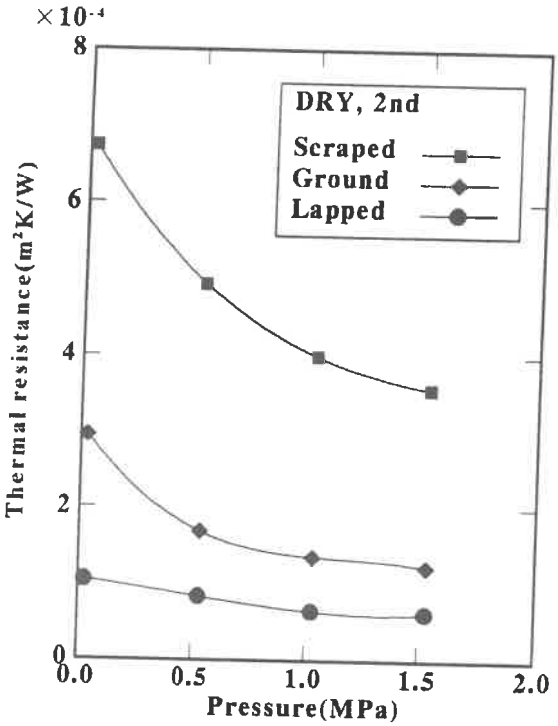

Fig.7 Relationship between finished surface and thermal resistance (DRY) (Ground - Ground surface)

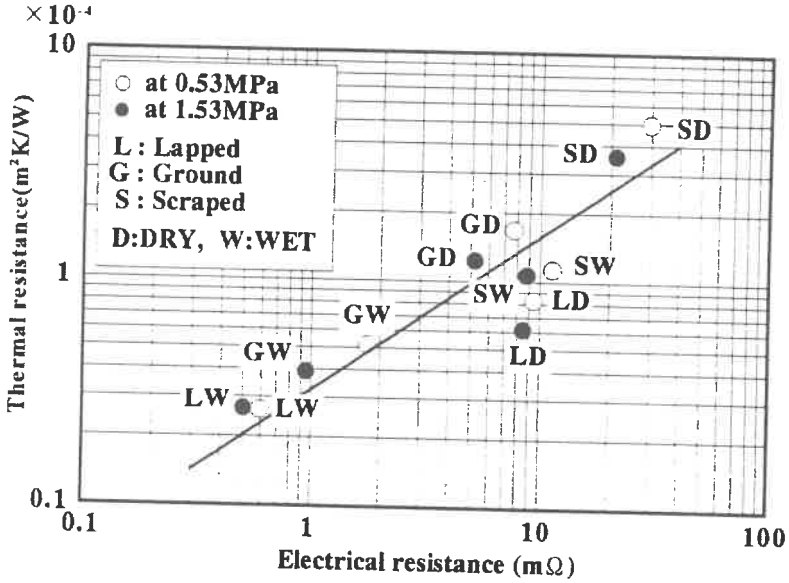

Fig.8 Relationship between electrical and thermal rssistance

DESIGN OF SECOND GENERATION NANOMETRIC CUTTING INSTRUMENT

Robert Hocken, Ramesh Namperumal, Paulo Pereira, John Lovingood, Robert Edgeworth, Aditya Sharma, Michael Holmes, Balasubramaniam Muralikrishnan.
Center for Precision Metrology
University of North Carolina at Charlotte, NC -28223

INTRODUCTION

There is an ever increasing demand for manufacturing to dimensions in the nanometric range with subatomic level smoothness without residual stress and metallurgical defects. To achieve this, Single Point Diamond Turning (SPDT) can be used [1][2].

SPDT machines which can provide sub-micrometer level accuracy are commercially available. These instruments have been used successively to study the ultra-precision machinability of copper [2], mechanism of micro-chip formation [3], mechanical energy involved in micro-machining [4]. But the study of machining in the nanometric range requires a new generation of instruments since it is beyond the control range achievable by commercially available diamond turning machines. A first generation instrument which can achieve cutting at nanometric range was built at the Center for Precision Metrology at UNCC [5]. A second generation instrument was designed and built as a team project for a graduate-level instrument design course. This report describes the design of the second generation nanometric cutting instrument developed to investigate the mechanics of nanometric cutting.

CONCEPTUAL DESIGN

The basic principle of operation of the instrument is a single point diamond planer as shown in the figure. The cutting movement is provided to the sample mounted at the end of piezoelectric (PZT) tube, with the tool being held stationary. The infeed and crossfeed cutting motions are provided by the axial and lateral displacement of the piezoelectric tube scanner respectively. The feed motions are measured using a capacitance probe mounted to the PZT tube scanner. In order to study the mechanics of micromachining the cutting and thrust force are measured using two single axis force transducers attached to the tool holder.

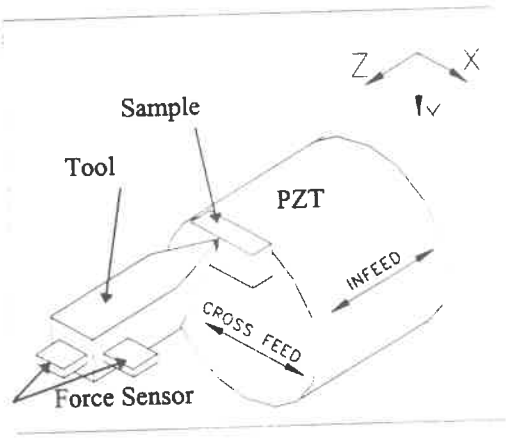

Figure 1 Principle of Operation

General considerations for the development of the instrument are dictated by various parameters depending on the intended functions. For example the instrument (1) should provide ability to measure forces in milli-newton range [1], (2) should provide a maximum of 2μm depth of cut and a maximum of 10μm length of cut, (3) should have

measurement resolution of cutting motions in the order of 0.1nm using a capacitance probe, (4) should have a stiffness of 1.8×10^7 N/m (10^5 lb./in), a typical value for the cutting instruments of this type [1], (5) should be completely vacuum compatible with all the components composed entirely of non-magnetic materials to allow observation within Scanning Electron Microscopy (SEM), (6) should be thermally stable for usage at normal room temperature environments, (7) overall outer dimensions should be less than 8 inches in diameter with center at the observation point (tool tip) accessible for observations inside a SEM.

INSTRUMENT DESIGN

To meet the above design requirement the nanometric cutting instrument, NanocutII as shown in figure 2 has been designed and built. The instrument has four modules namely:

(1) The sample holder and sample mount,
(2) PZT and capacitance probe assembly,
(3) Tool holder and force sensor assembly,
(4) Fine positioning system.

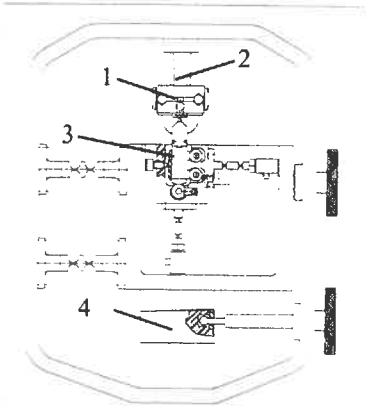

Figure 2 Assembly Drawing

SAMPLE HOLDER AND SAMPLE MOUNT

This module consists of a sample holder and a sample mount or kinematic mount. The workpiece which is 5x5x10mm is glued at the top of the sample holder as shown. The sample holder made of Aluminum is provided with angular flexure by cutting a slit. This flexure is designed to provide a tilting adjustment up to 10^{-5} radians for the sample along X axis. Tilting arrangement enable the face of sample to be aligned with PZT axis during cutting tests. The tilting can be provided by adjusting the two alignment screws provided. The function of the sample mount is to provide a repeatable mounting of the sample onto the PZT assembly. The sample mount is designed using two flats (of hot pressed SiC), a V groove (of hot pressed SiC) and three SiC balls of 6.35mm (1/4") diameter. The preload, calculated to meet the minimum stiffness requirement, was 5N on each of the balls. Such preload force was achieved by three O rings arranged in such a way to provide easy access while assembling.

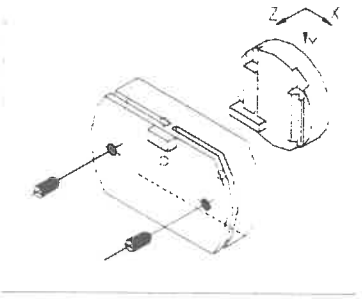
Figure 3 Sample Holder and Sample Mount

PZT AND CAPACITANCE PROBE ASSEMBLY

The PZT tube scanner mounted at the back of sample mount is used to provide cutting motions for the sample. By controlling the voltage applied to the quadrants of the PZT tube, displacements in two orthogonal directions can be achieved. A PZT tube suitable for providing 2μm depth of cut (Z) and 10μm length of cut (X) was chosen for

the purpose. The capacitance probe attached to the end of the PZT tube is used to measure the Z motions of the sample. The functional requirements of the PZT-capacitance probe assembly are, (1) to be thermal stable during operation, (2) fixing the target and setting the gap of 1μm for capacitance probe are to be easily achievable.

In order to ensure that the heavy electric field due to the high voltage applied to the PZT tube does not affect the capacitance probe, the capacitance probe was shielded using a thin macor tube. For thermal stability the cap probe is glued to the macor tube at only one end (at sample end) and the other end of the macor tube is glued to the outer disc. A 15mm x 15mm silicon wafer at the end of the sample mount serves as the cap probe target.

TOOL HOLDER AND FORCE SENSOR ASSEMBLY

The components of the tool holder and force sensor assembly are shown in figure 3. A single point diamond tool is brazed at the end of brass tool shank. The tool can be moved in the Z direction by rotating an eccentric cam with 0.5mm eccentricity. The tool can be moved in X direction using the two other indexing cams to make many cuts over the entire length of the sample. Two force sensors to measure cutting (X axis) and thrust (Z axis) forces are mounted to the tool assembly through circular flexures as shown. These double notch circular flexures made of beryllium copper are used to decouple the Z and X axis force measurement systems.

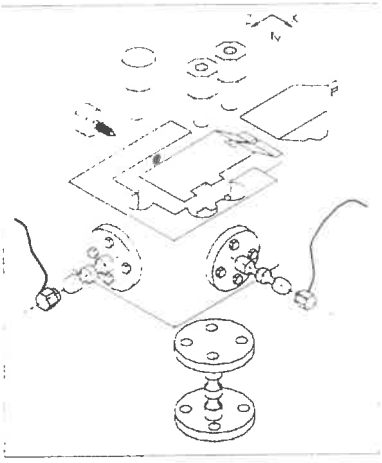

Figure 4 Tool Holder and Force Sensor Assembly

FINE POSITIONING SYSTEM

The function of fine positioning system is to provide a Z axis fine adjustment up to 50μm and Y axis fine positioning up to 500μm microns. These Z and Y axis fine adjustments are required during the tool-sample contact establishment procedure as described in the next section. Fine positioning in Z and Y axis is provided by means of wedges and four dual-axis flexures attached to the subframe. The flexures have a notch thickness of 1mm and are arranged on one side of the instrument to reduce the overall size (Refer to Figure 2).

THERMAL COMPENSATION

Since the structural loop is composed of different materials, thermal compensation of the loop is needed to keep the gap between the tool and sample constant. This was done by matching the thermal expansion of outer frame (Stainless steel grade 316) and the inner components. The material of inner components were carefully chosen and a block of aluminum was added so that the total expansion matched that of outer frame.

INSTRUMENT OPERATION

The actual cutting operation starts with establishing the tool-sample contact. For this, the tool is first brought close to the sample by using the eccentric cam provided in the tool holder assembly. Using this coarse positioning, the tool can be brought within 10μm with visual (light microscope) observation. Then the sample is vibrated at some suitable frequency and the tool is moved closer to the sample using the fine positioning system. The output of the thrust force sensor is monitored with a lock-in amplifier. Once the tool comes in contact with the sample, the force sensor output signal will correspond to the oscillation frequency of the sample. If the penetration depth is well within the elastic limit (say less than 1nm) , no damage will be caused to the sample by this procedure. Once the tool-sample contact is established, cutting motions are provided to the sample by controlling the voltage applied to the PZT tube.

CONCLUSION

A second generation nanometric cutting instrument prototype was designed and fabricated. The main challenge for the design of the instrument was to comply with stiffness, overall size, thermal stability requirements and component material selection. The design has many new features and improvements over the first generation nanometric cutting instrument including better sample and tool access, better stiffness and thermal stability.

REFERENCES

1. Moriwaki, T, "Machinability of Copper in Ultra-Precision Micro Diamond Cutting", Annals of CIRP 38, 1, 1989.
2. Woirgard, J. and Dargenton, C. J., " A new proposal for design of high-accuracy nano-indenters" Measurement Science and Technology. 6 (1995), 16-21.
3. Von Turkovich, B. F., and Black., J. T, "Micro-machining of Copper and Aluminum Crystals", Transactions of ASME, Journal of Engineering for Industry, February 1970.
4. Lucca, D. A., and Seo, Y. W., "Effect of tool edge geometry on the resulting forces and energies in the orthogonal flycutting of TeCu", Annals of CIRP 42, 1 ,1993.
5. Balasubramaniam, S., "Design of Nanometric Cuting Instrument", Masters thesis, University of North Carolina at Charlotte, 1995.

A FLEXIBLE ALIGNMENT FIXTURE FOR THE FABRICATION OF REPLICATION MANDRELS

James F. Cuttino
Dale E. Schinstock
Michael W. Todd
Department of Mechanical Engineering
The University of Alabama

ABSTRACT

A Flexible Alignment Fixture (FAF) has been developed to align a multi-piece replication mandrel for fabrication on a precision diamond turning machine (DTM). The fixture allows six degrees of motion of the workpiece relative to the spindle of the DTM. These degrees of freedom are necessary to remove error motions in the mandrel that are introduced during successive assembly/disassembly steps executed during fabrication of the mandrel. Requirements for small depths of cut necessitate that the axis of the mandrel be aligned with the axis of rotation of the chuck to within 25 μm error. Using conventional diamond turning methods, however, the minimum error motion obtained is often as high as 100 μm, rendering the mandrel useless.

The *FAF* replaces the vacuum chuck on the DTM and is used to precisely align the axis of the mandrel to the axis of the DTM. The fixture utilizes a hexapod arrangement to provide high stiffness, reduced error, and simple construction. The flexure has been used to realign a mandrel for the fabrication of an optic for NASA's X-ray Calibration Facility (XRCF), reducing the error motion of the mandrel from over 100 μm to less than 8 μm. Parts fabricated with the flexible alignment fixture show visible improvements in surface finish over parts cut on the original vacuum chuck.

INTRODUCTION

NASA uses precision diamond turning technology to fabricate replication mandrels for its X-ray Calibration Facility (XRCF) optics. As shown in Figure 1, the XRCF optics are tubular, and the internal surface contains a parabolic profile over the first section and a hyperbolic profile over the last. The optic is fabricated by depositing layers of gold and nickel on to the replication mandrel and then separating the resulting shell from the mandrel. Since the mandrel serves as a replication form, it must contain the inverse image of the surface. Figure 1 shows the components of the fabrication mandrel that are necessary to facilitate mounting, handling, and polishing during the fabrication process. More information concerning the replication mandrels has been documented by Fawcett and Engelhaupt [1993].

The difficulty in aligning the mandrel comes from the fabrication steps which it undergoes. The mandrel is rough machined and heat-treated prior to diamond turning. After diamond turning, silicon rubber separators that are undercut in radius by 3 mm (0.12") are inserted between the two end caps of the mandrel to allow the plating to wrap around the ends (to prevent flaking). The mandrel is then plated with a nickel-phosphor alloy using an electroless nickel process. At this point, the separators are removed and the mandrel is reassembled for the final cut on the DTM. The mandrel is measured for profile and finish, and polished to achieve an acceptable surface finish.

Wrapping the plating around the edges helps to prevent flaking, but it also destroys the alignment surfaces between the parts of the mandrel that insure that the axes of the parts are coincident. Several mandrels have been realigned by trial-and-error methods, consuming significant amounts of setup time. When the mandrel studied in this paper was reassembled, multiple efforts resulted in a minimum radial error motion of 100 μm. Since 50 μm of nickel plating was to be removed, and a minimum plating thickness of 25 μm was to remain on the part, the radial error motion had to be reduced to less than 25 μm. The mandrel was therefore unusable in its current state.

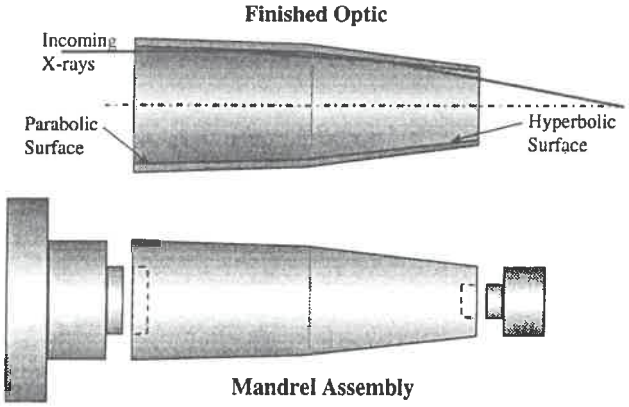

Figure 1: Geometry of XRCF Optical Surface and Replication Mandrel

DESIGN OF FIXTURE

To provide the motion necessary to align the mandrels, the *Flexible Alignment Fixture*, or *FAF*, was designed to replace the vacuum chuck normally used on the DTM. The design goals were to allow for linear displacements of 250 μm and rotations of 0.003 radians at the platform of the alignment fixture (over a 8" long mandrel, 0.003 radians results in an equivalent translation of one end of 600 μm, or 0.024").

The design utilizes a six-legged hexapod arrangement to provide full flexibility and high stiffness. Figure 2 is a conceptual drawing of the *FAF* mounted on a diamond turning machine. The fixture has a base that mounts directly to the spindle bearing and a platform suspended by the six legs. The workpiece is mounted directly to the platform.

Since the required motion was very small, the flexure was designed to rely on deformation of the legs rather than joints to allow relative motion of each leg. The stress was calculated for each leg based on a maximum deflection, and the legs were designed to provide a factor of safety of 8 to 10. The legs were threaded on each end and screwed directly into the base and the platform, and preloading was achieved by lowering the platform towards the base, thus introducing a bending moment in each leg.

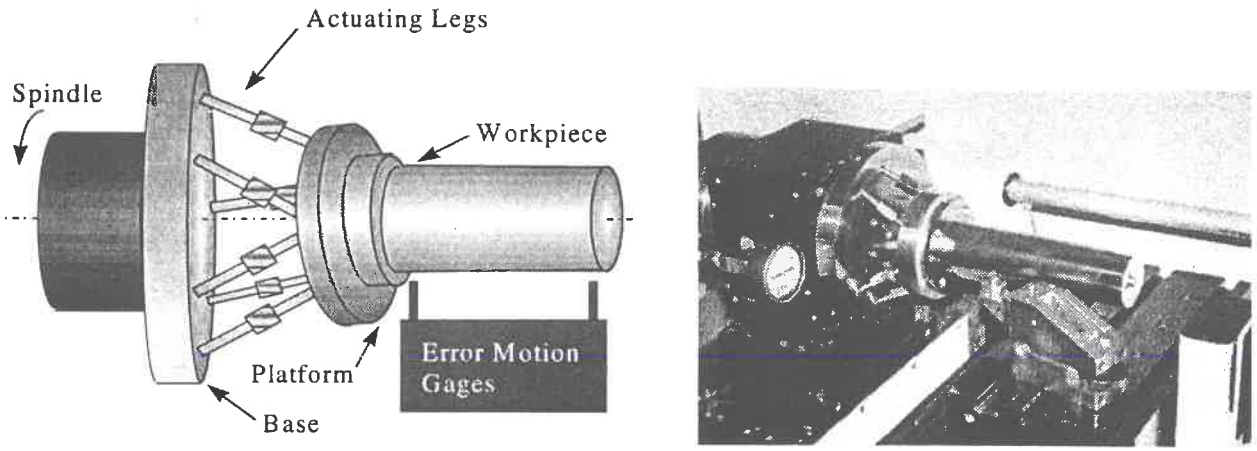

Figure 2: Flexible Fixture on a Lathe Spindle

The legs of the *FAF* utilized a differential pitch arrangement to provide high-resolution motion. A 3/8-24 UNF thread was machined on the portion of the leg inserted into the base of the *FAF*, and a 7/16-20 UNF thread was machined on the end inserted into the platform. This differential pitch in the screw provides a linear displacement of 210 μm per turn of the leg. In order to facilitate assembly of the *FAF*, the legs were fabricated in two sections joined in the middle by a hex nut. The legs were fabricated from AISI 410 stainless steel and were heat treated for additional strength.

EXPERIMENTAL RESULTS

The vacuum chuck of the DTM was replaced with the *FAF* for testing. When mounted on the original equipment vacuum chuck, the test mandrel had a minimum error motion of 100 μm, which was only achieved after significant effort to align the mandrel pieces. Mounting the mandrel on the *FAF* provided the necessary freedom to align the axis of the mandrel to that of the DTM spindle. Once mounted, the error motion was measured by two dial indicators at four equally spaced rotations of the spindle to determine the proper adjustment. By placing the indicators at determined positions along the axis of the mandrel, two measurements at each of the four rotational positions provided the necessary error motion information. A kinematic analysis was conducted on the hexapod to provide the necessary corrections while minimizing leg adjustment so that stresses in the legs would be minimized. The resulting analysis was programmed into MATLAB to facilitate adjustments on the fixture. To adjust the *FAF*, the measurement values from the dial indicators were input into the kinematic program and the required leg rotations were output. With the *FAF*, the same mandrel was aligned to within 8 μm error motion with minimal effort, representing a 92% reduction in the error. The 8 μm error was significantly less than the target requirement of 25 μm.

There were several measures for success in the project. The most important was the ability to diamond turn the mandrel without penetrating the nickel plating. If the turning process penetrated the nickel plating, the mandrel would be scrapped. Other measures of success were the surface finishes and *form* errors (low frequency errors) that were achieved using the *FAF*. Although surface finish and form can be altered by post-polishing, this process is expensive and time consuming. A goal of the project was therefore to achieve surface finishes and form errors that were comparable to or better than those turned using the conventional DTM chuck. The mandrel cut on the *FAF* was therefore compared to one that had been successfully aligned on the vacuum chuck without the *FAF*. The two tests were conducted at a slide feedrate of 3 mm/min (0.05 mm/s) and a spindle speed of 1000 rpm (17 Hz).

Visual inspection of the surface finish on the mandrel cut on the *FAF* surprisingly showed significant improvement over the finish of the mandrel cut on the vacuum chuck. This conclusion was verified using a WYKO *Topo-2D/Topo-3D* surface interferometer. Figure 3 shows the surface profiles of the benchmark and *FAF* mandrels over a range of 1.32 mm. As shown in Figure 3a, the mandrel cut on the vacuum chuck has several components of error. The scan appears to consist of three fundamental components with wavelengths of approximately 0.25 mm, 0.05 mm, and a high frequency noise with wavelength of around 0.001 mm (measured along the axial direction). Based on the feedrate, the surface components had frequency components of 0.2 Hz, 1 Hz, and 50 Hz respectively. The rms amplitude of the error was 19.3 nm. A complex mounting configuration unfortunately prohibited more than one scan of this specimen.

Several traces were taken of the mandrel cut with the *FAF*. Figure 3b shows one trace which is representative of all of the traces taken. A significant discrepancy was realized in the amplitudes of the error, which ranged from an rms value of 17 nm to 60 nm. Since only one trace was made of the benchmark mandrel, the amplitude data is considered inconclusive. The trace shown in Figure 3b has an rms amplitude of 20.9 nm and shows an error component with a 1 Hz frequency (wavelength = 0.05 mm) superimposed on a very low frequency trend (possibly not even periodic) that continues outside the scan range of the interferometer. While the discrepancies in the results require further investigation, it appears that using the *FAF* actually reduced the 0.2 Hz and 50 Hz error motions seen in the benchmark mandrel. More data obtained from the mandrel cut on the conventional chuck may show similar form amplitudes, so the form error data (low frequency component) are not considered conclusive at this point. The elimination of the 50 Hz component in the mandrel cut on the *FAF* explains the visible improvement in surface finish on the part.

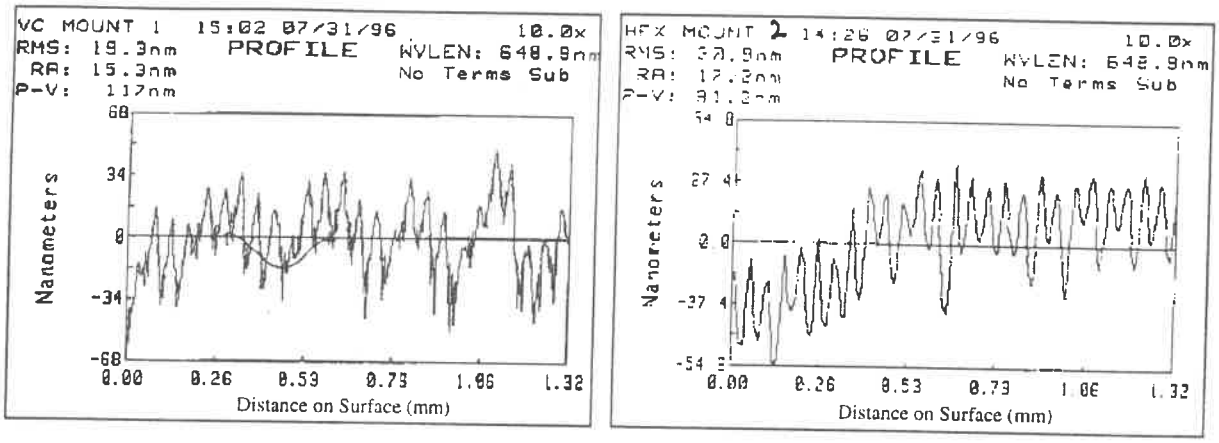

a) Mandrel cut on Vacuum Chuck

b) Mandrel Cut on *FAF*

Figure 3: Surface Profiles of Mandrels

Both parts are currently being measured using a *Long Trace Profilometer* to determine the actual error in each part. The preliminary results above, however, seem to indicate that the hexapod may help to reduce the error motion while salvaging the part.

CONCLUSION

A six-degree-of-freedom Flexible Alignment Fixture (*FAF*) has been developed to adjust the position and orientation of a workpiece on a diamond turning machine spindle. The device uses a hexapod design and kinematic analysis to reposition the workpiece. The designed range of motion allows for displacements of 250 µm and changes in orientation of 0.003 radians.

A fabrication mandrel for NASA's XRCF project, which was unusable due to alignment problems, has been salvaged using the *FAF*, which was able to reduce the error motion from 100 µm to 8 µm. The *FAF* also greatly reduces the effort necessary in insuring the alignment of the mandrel components prior to cutting. Preliminary results indicate that improved surface finish may be an added benefit to using the *FAF*. Pending results from a long trace profilometer will yield more information on the effectiveness of the *FAF*.

ACKNOWLEDGEMENTS

Sincere thanks go to NASA's Marshall Space Flight Center and to Dr. David L. Lehner, Mr. William D. Jones, Mr. John Cernosek, and Mr. Kent Bachelor for their input and support on this project.

REFERENCES

Fawcett, S.C., and D. Engelhaupt, 1993, "Production of X-Ray Optics by Diamond Turning and Replication Techniques," *Proceedings of the American Society for Precision Engineering*, Volume 8, pp. 95-98.

LOW-COST METROLOGY OF 6-DEGREE-OF-FREEDOM, MILLIMETER-RANGE STAGES

Yan Wu and James F. Cuttino
Department of Mechanical Engineering
The University of Alabama

This abstract describes a new low-cost metrology system for 6-degree-of-freedom millimeter-range stages. The objective of this measurement system is to achieve metrology resolution in the sub-micrometer regime. Toward this end, the performance characteristics of the sensors used in the metrology system are analyzed and evaluated experimentally.

1. Introduction

Microscanning mechanisms are becoming more common for a variety of applications including STM imaging[1], optical lithography with step-and-repeat cameras[2], and scanning test stands for magnetic read/write head research[3]. Conventional means for detecting the three-dimensional (3-D) behavior of a scanning stage typically use capacitance gages and/or laser interferometers. However, these instruments can be very complex, expensive and difficult to set up. Simpler and less expensive metrology systems are not only desirable for research, but also beneficial for industrial applications

This article describes the development of a low-cost method for conducting non-contacting, three-dimensional metrology in the sub-micrometer regime. The system uses three four-quadrant photo detectors to detect the positions of incident beams from three laser diodes attached to the measurement target. The system is designed to measure position and orientation of a multi-degree-of-freedom stage within ±1 mm travel. The total cost of the system is less than $1000.

In our previous work[4], we discussed the detailed kinematic analysis of the system including working envelope and error budget prediction. In this paper, we present the theoretical analyses and experimental results of performance characteristics of the laser diode / photo detector pair.

2. Description of Metrology System

The metrology concept is illustrated in Figure 1. The system uses 3 photo detectors mounted in specified orientations as position-sensitive detectors. Each of the photo detectors has four quadrants that measure the intensity of light landing on that particular quadrant. Three laser diodes are mounted to the object being measured and project their beams onto the photo detectors. As the body being measured moves in space, the corresponding positions of the incident beams are measured by the photo detectors. Using kinematic relationships developed at The University of Alabama, position and orientation information of the object is calculated from the output currents of the photo detectors.

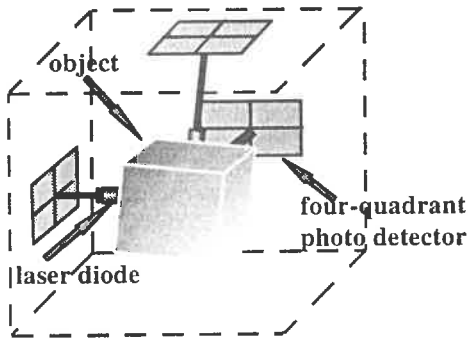

Figure 1: System Configuration

The error budget presented by Prather, Cuttino, and Schinstock[4] shows the dependence of the system performance on the ability to accurately locate the incident laser beam on the photo detector. This paper describes work being conducted to characterize the diode/detector performance.

3. Sensor performance evaluation

A four quadrant photo detector was selected to be the position sensor because of its high resolution and low-cost[5]. Assuming the light spot to be circular and of uniform intensity, the position of the beam can be calculated from the measured output currents of each of the photo-detectors using the following relationships:

$$\sin^{-1}\left(\frac{2S_x}{d}\right)+\frac{2S_x}{d}\sqrt{1-\left(\frac{2S_x}{d}\right)^2}=\frac{\pi}{2}\frac{(i_1+i_4)-(i_2+i_3)}{(i_1+i_2+i_3+i_4)} \quad \text{(a)}$$

and

$$\sin^{-1}\left(\frac{2S_y}{d}\right)+\frac{2S_y}{d}\sqrt{1-\left(\frac{2S_y}{d}\right)^2}=\frac{\pi}{2}\frac{(i_1+i_2)-(i_3+i_4)}{(i_1+i_2+i_3+i_4)} \quad \text{(b)}$$

As depicted in Figure 2, S_x and S_y are horizontal and vertical deviations of the light spot from the center of the detector. i_1, i_2, i_3 and i_4 are the average currents of quadrants I, II, III, IV, respectively. d is the diameter of the light spot.

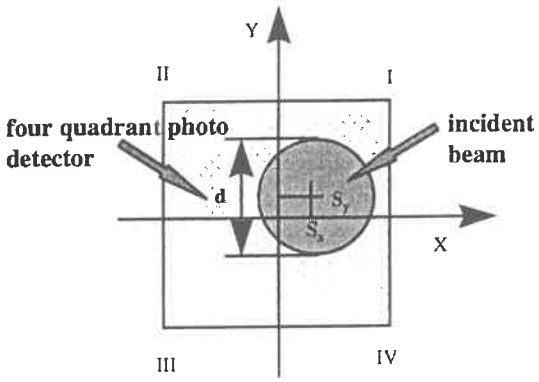

Figure 2: Geometric Definition for Beam on Photo Detector

Equations (a) and (b) can be expanded in series to yield solutions for S_x and S_y. These expressions are given by

$$S_x = \frac{d}{2}\left(\frac{Z_x}{2} + \frac{Z_x^3}{48} + \frac{13Z_x^5}{3840} + O(Z_x^6)\right) \qquad (c)$$

and

$$S_y = \frac{d}{2}\left(\frac{Z_y}{2} + \frac{Z_y^3}{48} + \frac{13Z_y^5}{3840} + O(Z_y^6)\right) \qquad (d)$$

where Z_x and Z_y are

$$Z_x = \frac{\pi}{2}\frac{(i_1+i_4)-(i_2+i_3)}{(i_1+i_2+i_3+i_4)} \text{ and } Z_y = \frac{\pi}{2}\frac{(i_1+i_2)-(i_3+i_4)}{(i_1+i_2+i_3+i_4)}.$$

For some applications, the first order solution is accurate enough[6]. We found that a fifth order solution reduced errors to less than 1μm for ±0.78 mm travel, but a higher order fit is required to improve the resolution to sub-micron levels.

Equations (a) and (b) are based on several assumptions. First, the light spot must be within the range of the active surface of the photo detector so that none of the beam falls outside of the detector. Second, the shape of the light spot is assumed to be circular. This is not valid for most laser diodes or when the incident beam is not perpendicular to the photo detector. Finally, the intensity distribution is assumed to be uniform, although the distribution is actually Gaussian. All of these assumptions are directly related to the performance characteristics of the system.

4. Experimental Procedure

A test stand has been built to characterize the performance of the photo detector and laser diode pairs. Shown in Figure 3, the test stand consists of a Dover X-Y air bearing stage controlled by a personal computer. A Zygo AXIOM 2/20 laser measurement system is used to give the actual position of the stage. The laser diode is fixed above the stage, and the photo detector is mounted on the stage. By moving the stage, the output from the photo detector can be mapped and the stability of the laser diode characterized.

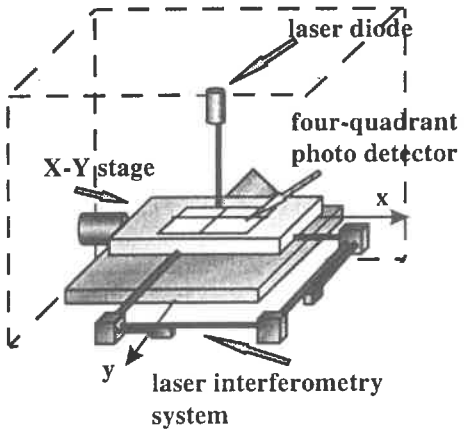

Figure 3: Laser diode /Detector Mapping

As illustrated in Figure 4, three experiments were conducted to test the performance of the position sensor. The first experiment measured sensor stability. Experiment 2 tested the ability of the diode/detector pair to measure position. Experiment 3 measured the effect of a non-uniform, asymmetric laser beam on the system. This non-symmetric beam is shown in Figure 4.

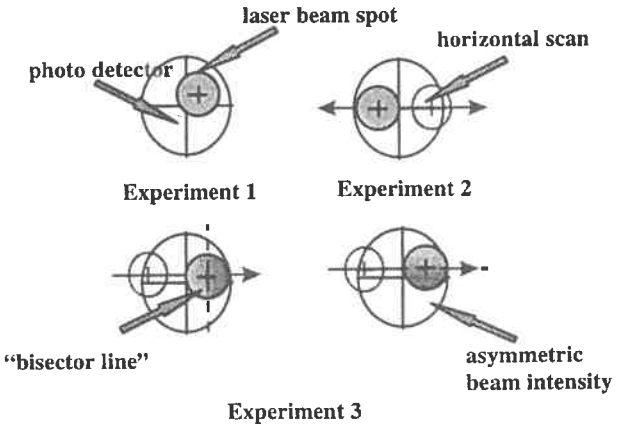

Figure 4: Experiment Design

The purpose of the first experiment was to test the stability of the sensor signal by keeping the laser beam at a fixed position on the photo detector. The beam diameter d is 3.2 mm. The data sampling rate is 210 Hz. Figure 5 shows that the error signal is 10 μm over of period of 6 seconds. The magnitude of the error signal was reduced to half in later experiments after the test stand was isolated from ambient light source. This result shows the need for either optical

filtering or signal processing to achieve sub-micron resolution.

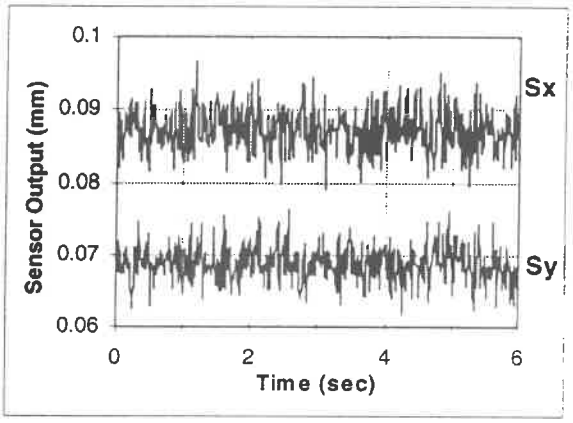

Figure 5: Result from Experiment 1 Showing Sensor Output Stability

In the second experiment, the stage was moved forward and backward along the X direction in order to let the laser beam scan across the active area of photo detector. The sensor output was compared with the output from the laser interferometer which has a measurement resolution of 1.25 nm. The laser diode was fixed throughout the experiment.

In Figure 6, the outputs from the photo detector and the laser interferometer are compared. Curve X is the laser interferometer output. Curve S_x represents the calculation result using equation (c) based on the measurements of the photo detector output currents. The curves show excellent agreement within the noise on the detector. To better compare the two signals, the calculated sensor output was plotted as a function of the stage position in Figure 7. Within the range of ±1.3 mm, the curve is a nominally straight line with unity slope. The mapping is very repeatable as seen by the multiple passes in Figure 7. This shows that errors can be removed from the system through calibration. Experiment 2 shows that equations (c) and (d) are valid for the positioning device and that the output is repeatable.

In experiment three, the effect of the intensity distribution on the sensor output was tested. It is common that the intensity distribution of commercial laser diodes is not central symmetric. The laser diode used in this experiment was visibly asymmetric, with one half darker than the other and the "lighter" and "darker" sides bisected with an imaginary line through the center of the beam. To measure the effect on this system, we first put the "bisector line" perpendicular to the scanning direction. Then we put the "bisector line" parallel to the scanning direction. This is shown in Figure 4.

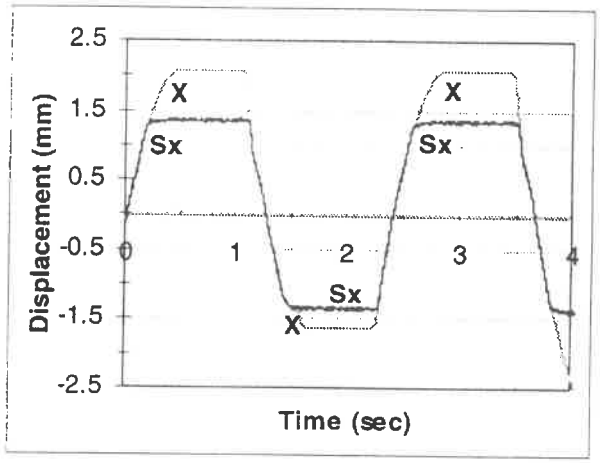

Figure 6: Result from Experiment 2 Showing Horizontal Scan Across Photo Detector

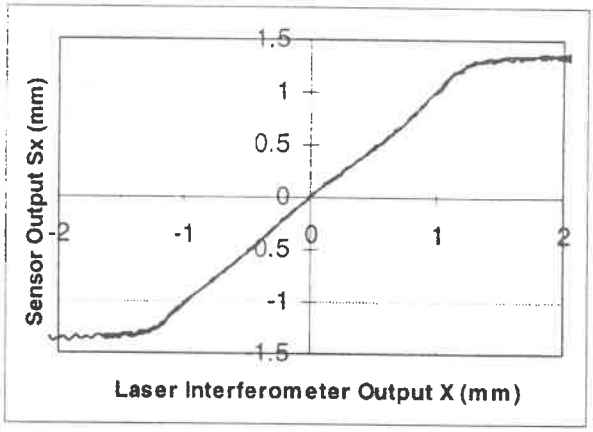

Figure 7: Sensor Output as a Function of the Stage Position in Experiment 2

The experiment results are shown in Figure 8 and Figure 9 respectively. These figures show that the intensity distribution of the incident laser beam has a great effect on the performance of the system. However, a linear relationship between the sensor output and actual displacement is still realized as long as the intensity distribution is symmetric along the scanning direction. This can be easily proven mathematically. A further implication is that the incident beam does not need to be uniform in intensity, but it is essential that the beam intensity is symmetric about the center in order to get two dimensional measurement from the photo detector and laser diode pairs. In this case, a calibration process before measurement is highly recommended since equation (a) and (b) is no longer valid theoretically. This form of calibration is routine in the AFM (atomic force microscopy) industry[7] and should be applicable in this case as well.

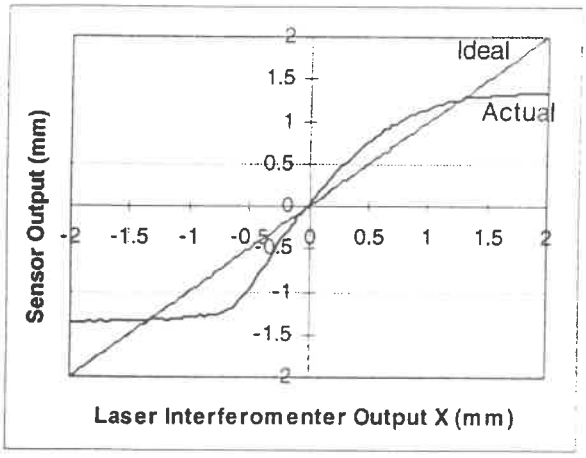

Figure 8: Experiment 3 Results when Bisector Line is Perpendicular to Travel

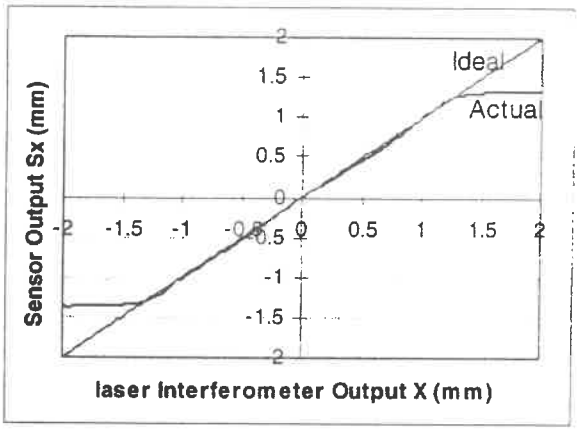

Figure 9: Experiment 3 Results when Bisector Line Parallel to Travel

5. Conclusion

The proposed metrology system will provide cost-effective, three-dimensional, non-contacting measurement in millimeter-range motion. The measurement quality of the system depends on the performance of the four-quadrant photo detector and laser diode pairs which are used as position sensors in this system. To evaluate the performance of the sensors, a test stand has been built and a series of experiments have been conducted at the Metrology and Precision Engineering Laboratory (MAPEL) at the University of Alabama.

Experimental results show that the proposed metrology system is not only feasible, but it also has great promise for achieving high resolution. The objective of future work is to optimize the performance of the position sensor by trying different kinds of laser diode and photo detector pairs.

References

[1] Holmes, M., R. Hocken, and D. Trumper, 1996, "A Long - Range Scanning Stage Design," *Proceedings of The American Society for Precision Engineering*, Vol. 14, pp. 322-327.

[2] Nakamura, Osamu and Nitsuo Goto,1994,"Four-beam Laser Interferometry for Three-dimensional Microscopic Coordinate Measurement", *Applied Optics*, Vol. 33, No.1, pp. 31-36

[3] Schults, S., "Five Degree of Freedom Scanning Test Stand for Magnetic Read/Write Head with 1 nm Resolution," *Proceedings of the ASPE Spring Topical Meeting*, Vol. 11, April 1995

[4] Prather, M. J., J. F. Cuttino, and D. E. Schinstock, "Three-dimensional Metrology Frame For Precision Applications," *Proceedings of the 1996 American Society for Precision Engineering Conference*, Vol.14, pp. 668-671.

[5]Constant A. J. Putman et al., "A detailed analysis of the optical beam deflection technique for use in atomic force microscopy," *Applied Physics*, Vol. 72, July, 1992, pp. 6-12.

[6]Anssi J. Mäkynen, Juha T. Kostanovaara, and Risto A. Myllyä, 1994, "Tracking Laser Radar for 3-D shape Measurements of Large Industrial Objects Based on Time-of -Flight Laser Range Finding and Position-sensitive Detection Techniques," *IEEE Transactions on Instrumentation and Measurement*, Vol.43, No.1 Feb. 1994, pp. 40-49.

[7] Neill P. D'Costa and Jan H. Hoh, 1995, "Calibration of optical lever sensitivity for atomic force microscopy," *Review of Scientific Instruments*, Vol. 66, Oct. 1995, pp. 5096-5097

DEVELOPMENT OF A LONG RANGE, TRACTION DRIVE FAST TOOL SERVO FOR DIAMOND TURNING APPLICATIONS

Michael W. Todd and James F. Cuttino
Department of Mechanical Engineering
The University of Alabama

Introduction

Fast Tool Servos (FTS's) have allowed Single Point Diamond Turning Machines (DTMs) to become more versatile in the range of applications for which they are used. One major limitation of the FTS, however, is that the range of motion is typically less than 400 micrometers due to limitations in actuator range and precision. The goal of this work is to extend the range of motion of FTS's to enable the fabrication of more complex optics with deep, non-axisymmetric features. Target characteristics are a range of motion of one millimeter at 50 hertz.

Selection of Traction Drive Configuration

The main objective of this research is to increase the range of motion of the FTS. Several potential designs were considered which could meet this objective including a voice coil approach, hydraulic arrangement, and piezoelectric (PZT) designs. Along with range and frequency of motion, other factors considered were stiffness, manufacturability, and controllability. The traction drive configuration was selected because of virtually unlimited range and the mechanical advantage gained through the pinion radius. Traction drives represent a compromise between the high stiffness but limited range of PZT actuators and the low stiffness, larger displacement voice coil actuators. Traction drives in larger systems have been proven capable of providing submicron position accuracy [1,2].

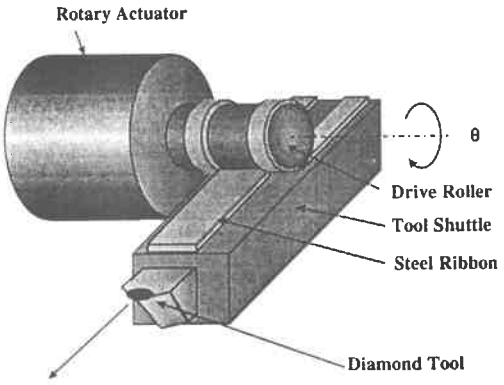

Figure 1: Traction Drive Servo

Figure 1 displays the actuation scheme used in the work. The torque from the rotary actuator is transferred to a linear force on the tool shuttle through a steel ribbon that is wrapped around the shaft and attached to the tool shuttle. This design minimizes excessive normal loads and slipping in a typical friction drive system. It also simplifies the suspension design since the shuttle does not need to resist normal forces from the driver roller. The preload between the ribbon and the shaft is adjusted by increasing or decreasing the tension in the ribbon.

Suspension of the Tool Shuttle

A principal challenge in the long-range FTS development is designing a bearing system that provides the necessary motion with sufficient stiffness and accuracy. Conventional cantilever

flexure bearings could not be used because they would have to be excessively large to provide the desired range of motion while maintaining stresses low enough to avoid fatigue. Conventional annulus flexure bearings are too restrictive on the axial motion as well. Therefore, a new type of flexure design, shown in Figure 2 and Figure 3, was developed. The rolling action of the flexures allows improve compliance in the axial direction, and the flexures support loads in the transverse directions through shear as shown in Figure 3.

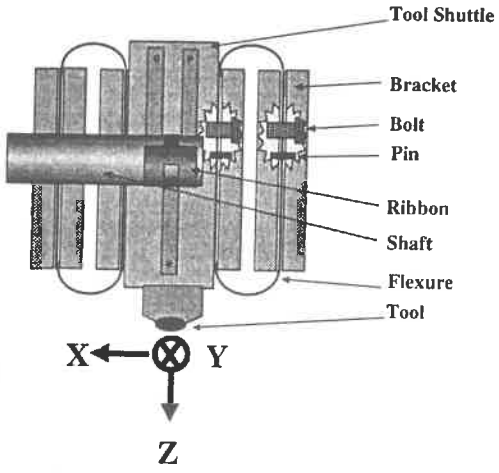

Figure 2: Flexure Design

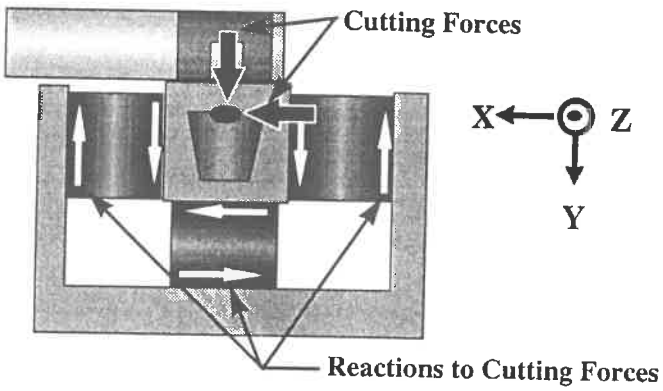

Figure 3: Forces on Flexures

Complex geometry and loading conditions of the flexures prevented closed form analysis of the flexures, so an empirical study was conducted using Finite Element Analysis (FEA). The FEA analysis was performed using ALGOR software. Only one flexure was modeled for each case due to symmetry. The loads on the flexure were varied and the displacements were obtained to prove that stiffness was linear. Then each of the flexure dimensions was changed to see its effect on flexure stiffness. The stresses were also computed using an input displacement.

The FEA analysis allowed development of various trends that helped in the design of curved flexures. Figure 4 shows that force is linear with respect to displacement for loading in the X, Y, and Z directions, so curved flexures will not produce any significant nonlinearities. Also, the Y-direction still maintains the highest stiffness, while the Z-direction is much more compliant. The effects of the flexure dimensions on stiffness were also examined. For all of the following trends one dimension was changed while the others were held constant. Parameters that were varied were flexure thickness, flexure height, and radius of curvature. Figure 5 shows the flexure dimensions of interest. Figure 6 shows that stiffness increases with respect to flexure thickness in a cubic trend. Figure 7 shows that increasing flexure height increases stiffness. This effect is

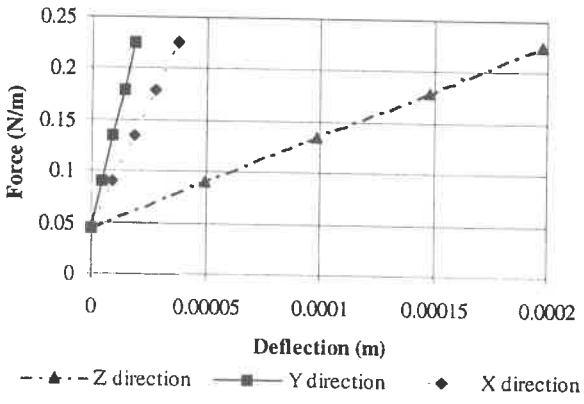

Figure 4: Force vs. Deflection

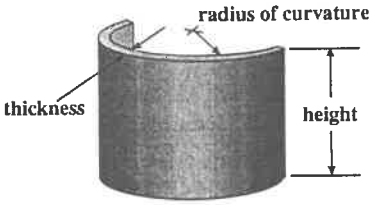

Figure 5: Flexure Dimensions

linear for the X- and Z-directions, but the effect is quadratic for the Y-direction. Increasing the radius of curvature also increases flexure stiffness. This effect is great at first, but the returns diminish with increasing radius. These trends demonstrate that stiffness in the Y-direction is most affected by changes in flexure dimensions, which is beneficial since that is the direction of the cutting force. The Z stiffness is least affected by changes in dimensions which is desirable since the stiffness in that direction should come from the actuator rather than the flexures. Knowledge about these trends and information concerning the tool forces encountered in diamond turning [3] can be used to design curved flexures that are well suited for long range FTS applications.

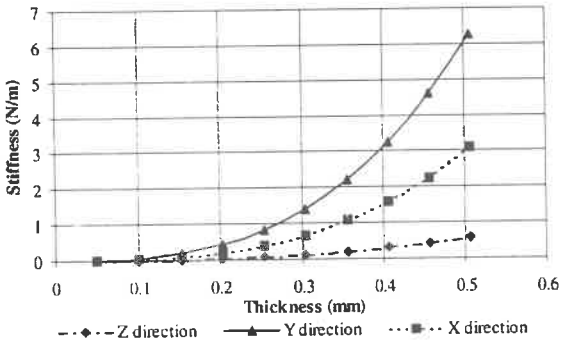

Figure 6: Effect of Thickness on Flexure Stiffness

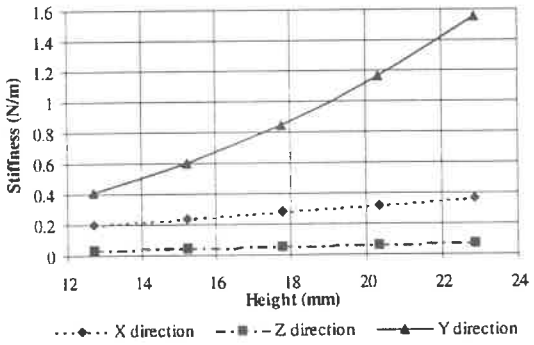

Figure 7: Effect of Flexure Height on Flexure Stiffness

Trends were also developed for stress so that the flexures could be designed to avoid plastic deformation or fatigue failure. Stress is linear with respect to displacement for X-, Y-, and Z-directions. For a given displacement, the lowest stress occurs for the smallest possible thickness and the shortest radius of curvature which still give the desired stiffness. The principal advantage of the curved flexures is that they can be made more compact than flat flexures for the same loads and displacements.

Prototype Device

The prototype device shown in Figure 8 was constructed for testing. A PID control algorithm was used to control the device. The computer sent a voltage out through the 12 bit D/A on a Computer Boards CIO DAS1602/16 card that was amplified using a Copley Controls Model 200 motor amplifier. The output of the amplifier was connected to a BEI model RA16-06 rotary actuator, and the position was read using an LVDT. The position was fed back to the computer through the 16 bit A/D on the Computer Boards card. A block diagram of the FTS control system is shown in Figure 9. The mass of the tool shuttle was 150 grams. The axial stiffness of the flexures was 3500 N/m, and the maximum torque of the rotary actuator was 0.07768 N-m.

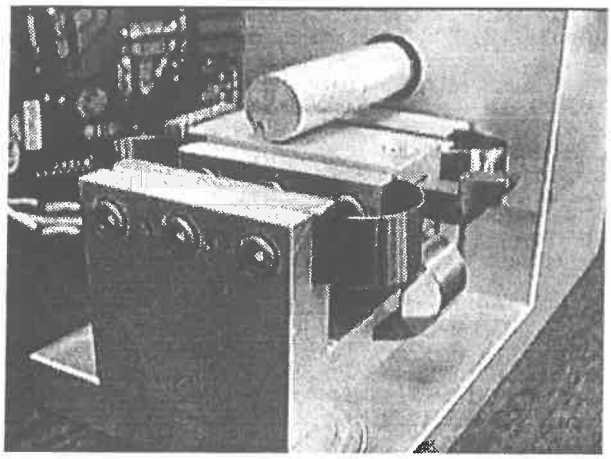

Figure 8: Prototype Traction Drive FTS

The system behaved as an underdamped second order system with a natural frequency of 21 hertz. The system easily generated a one millimeter amplitude up to 20 hertz. After the natural frequency, there was some attenuation and increased phase lag as expected. Work is currently being conducted to optimize PID gains for minimum error and maximum disturbance rejection. The preliminary results indicate that the traction drive will be capable of the desired range and frequencies.

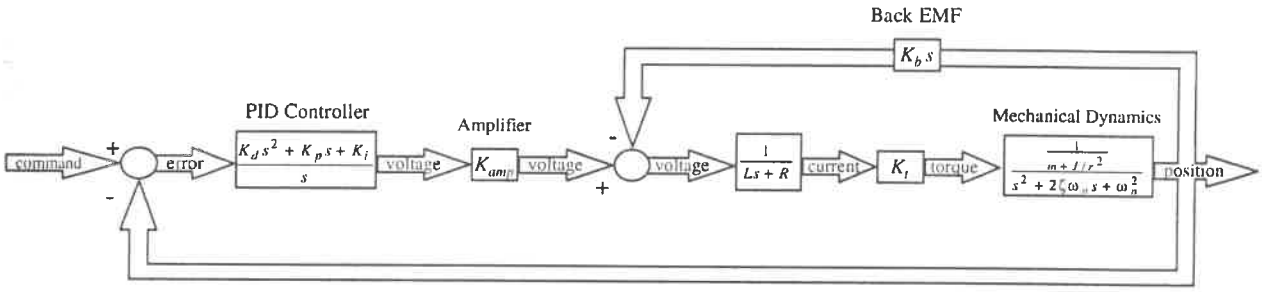

Figure 9: Block Diagram of the Prototype FTS System.

Conclusions

A prototype FTS based on a traction drive configuration has been constructed at The University of Alabama. Tests done on the device indicate that the traction drive is feasible for long-range FTS applications. A new flexure configuration has also been investigated using finite element analysis and experimental verification. Results from the study indicate that extended linear motion can be obtained from the new flexure design without significantly reducing stiffness. A second prototype device is currently being constructed using information that has been learned from the work conducted to date.

Acknowledgments

Special thanks go to NASA's Marshall Space Flight Center for support of this project.

References

1. Slocum, A. H., *Precision Machine Design*, Englewood Cliffs, NJ: Prentice-Hall, 1992.
2. Rao, G. S. and P. I. Ro, "Submicrometer control of a traction drive using state feedback and estimation," *Precision Engineering*, 17, (2), April 1995, 124-130.
3. Drescher, J. D. and T. A. Dow, "An Empirical Tool Force Model for Precision Machining," *Proceedings from ASPE 1996 Annual Meeting*, November 1996, 500-505.

FAUST AND WAGNER: MACHINE DESIGN AND PROCESS SIMULATION

O.W. Fähnle+, H. van Brug#, C.J. van der Laan# and H.J. Frankena#

+ TNO Institute of Applied Physics, P.O.Box 155, 2600 AD Delft, The Netherlands
# Delft University of Technology, Dept. of Applied Physics, Optics Research Group, Lorentzweg 1, 2628 CJ Delft, The Netherlands

ABSTRACT

Based on the same functioning principle, two new fabrication techniques, FAUST (Fabrication of Aspherical Ultraprecise Surfaces using a Tube; Patent pending) and WAGNER (Wear-based Aspherics Generator using a Novel Elliptical Rotator, Patent pending) have been developed. Their functioning principles have been described in detail in previous papers[1-3]. Both combine the self-correcting character of traditional load-controlled grinding and polishing with features of high precision machine tools, featuring an advantageous error propagation factor between tool shape and generated surface shape. Shaping and finishing are carried out on the same machine, improving the eventual shape accuracy. The machine designs of two tools based on FAUST and WAGNER are presented and first tests with the tool based on WAGNER are discussed. Finally, an accuracy analysis is presented with which the influences of tool misalignments can be simulated together with a process simulation of the production process. The obtained results can be used for compensation.

1. FUNCTIONING PRINCIPLE

Let a radial section (r in the range of $\Delta \le r \le r_m$) of a rotationally symmetric convex or concave surface of revolution $f(r)$ be intersected by a plane that is parallel to the y_r axis and that contains the points $P_\Delta = \{\Delta, 0, f(\Delta)\}$ and $P_m = \{r_m, 0, f(r_m)\}$ (the function $f(r)$ describes the cross-section of the surface in a plane which contains its axis of symmetry) [Fig.1]. The intersection curve between the surface and this plane is located in the x, y plane and will in the following be referred to as the *Shape*. Positioning this *Shape* above a rotating workpiece at an off-axis distance Δ and with a fixed angle α, given by

$$\alpha = \arctan\left(\frac{f(r_m) - f(\Delta)}{r_m - \Delta}\right), \tag{1}$$

with respect to the r axis, it can be used for production. Therefore, for the generation of a radial section $\Delta \le r \le r_m$ of the surface, the shape of the intersection curve (the *Path*) is given by[1]

$$x(r) = \frac{f(r) - f(\Delta)}{\sin\alpha} \qquad \text{and} \qquad y(r) = \sqrt{r^2 - \left(\frac{f(r)}{\tan\alpha} + \frac{\Delta f(r_m) - r_m f(\Delta)}{f(r_m) - f(\Delta)}\right)^2}. \tag{2}$$

Consequently, it is possible to generate all kinds of concave and convex, on- and off-axis surfaces of revolution. The shape of the generated surface depends on the shape of the intersection curve as well as on the angle between tool and surface. It is hence possible by varying the angle α to use the same *Path* for the generation of different kinds of surfaces. While FAUST uses a line-contact between tool and workpiece along the *Shape*, WAGNER is applying a point-contact. Both, FAUST and WAGNER apply load-controlled grinding and polishing.

2 FAUST

A tool based on FAUST is currently being constructed. Within the stiff geometrical frame of a milling machine a state-of-the-art air bearing spindle (with an absolute rotational error of 50 nm) is used to rotate the workpiece (e.g. BK7) around a vertical axis. A tubular element T [Fig.2] that has a non-circular cross-section in a plane that is parallel to the x, y plane is fixed above the workpiece in such a way that the f and the z axis intersect and form the required angle α. The surface is processed

using a machining band that is guided along the lower rim of the tubular element applying a line-contact with the workpiece in the x, y plane. A circular element D that is rotating around an axis parallel to the z axis is driving the band and pressing it radially outwards by the use of an elastic element R (e.g. a rubber ring). That way the machining band is following the non-circular cross-section of the tubular element and tool and workpiece are in line-contact along the required *Shape*.

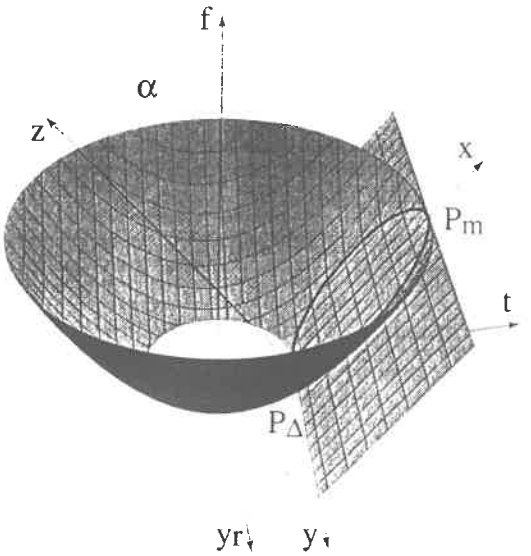

Fig.1 Functioning principle of FAUST and WAGNER and definition of the y_r, t, f system of coordinates of the workpiece and the y, x, z system of coordinates of the *Shape*.

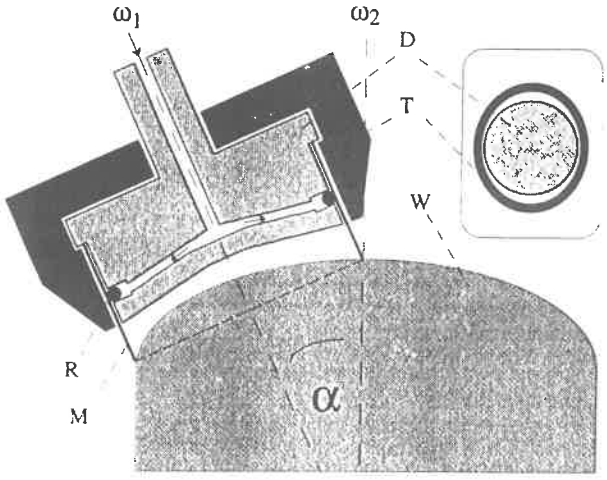

Fig.2 FAUST tool design: T indicates the fixed tubular element, M the machining band, W the workpiece and D a rotating circular element that is driving the band and pressing it by the use of the elastic element R (e.g. a rubber ring) radially outwards against T. (the inset shows a top view)

The tool has one translational degree of freedom such that the *Shape* moves parallel to the f axis down into the material. In order to achieve this the loaded tubular element has a translational degree of freedom along an axis that is located in the x, z plane and that has an angle α-σ with respect to the f axis (the angle σ depends on α and on the ratio between tool wear and workpiece wear[1]). As FAUST applies a load controlled process, it enables loose abrasive ductile grinding and subsequent bowl-feed polishing to generate aspherical surfaces.

3 WAGNER

A small tool is mechanically guided by the use of a tool-path shaping element and is applying a point-contact along the *Path*. As the machining process is load controlled and the relative speed between the loaded tool and the workpiece varies along the *Path*, the wear is not constant along the tool path. Therefore, a mechanical stop is applied to ensure that the process stops in the x, y plane where the *Shape* is located (at $z = 0$). Based on WAGNER, a tool was built capable of producing all kinds of on- and off-axis conic surfaces (surfaces of revolution with conic sections as generators)[2,3]. The tool-path shaping element is based on a geometrical effect using three pins of the same radius r_a [Fig.3]: if a pin P is rotated around the two fixed pins F_1 and F_2 and at the same time is pressed radially outwards by the use of a spring against a belt of constant length l that is encircling all three pins, the center of P follows a geometrically perfect ellipse in the x, y plane. In this way, an elliptical *Path* is generated that is determined by the distance e between F_1 and F_2 and by the inner length l of the belt. The center of this ellipse is positioned at the rotary axis R of the tool-path shaping element and the three pins are located parallel to the z axis. The rotary axis R must have a diameter of $\delta < 2r_a$ in order to avoid contact with the belt. Adjusting the line ε through the two points F_1 and F_2, either parallel to the y axis or parallel on the x axis all kinds of off- or on- axis conic surfaces can be generated[3] not requiring an in-process tool-path control. In order to enable the production of different scales of the same surface, a pantograph is used that is mechanically connecting the points

P, *R* and *S*. The pantograph is rotating in a plane parallel to the *x*, *y* plane around its fixed reference point *R*. Its stiff construction [Fig.3] allows the use of the pantograph to drive the pin *P* as well as to guide *S* along a scaled version of the path of *P*. The arm ξ is fixed to *R* and is rotating with a constant angular speed. Therefore, the points *P* and *S* are accelerated along their tool-paths, thereby avoiding the generation of cycloids. The machining is carried out at *S* using fixed abrasive load controlled point-contact grinding and polishing using a small cylindrical machining-head that is rotating around its axis of symmetry. The machining head can translate along an axis parallel to the *z* axis. It is pressed against the workpiece surface by the use of a spring and is machining the surface until it reaches the mechanical stop. The machining head is then rotating along the required *Shape* in the *x*, *y* plane. The *Shape* accuracy is thus given by the rigidity of F_1 and F_2 with respect to the workpiece coordinate system, by the accuracy of the belt length (which depends on its longitudinal elastic constant), by the accuracy of r_0 and by the accuracy of the scaling factor of the pantograph. A positioning inaccuracy of the rotary axis R with respect to the center of the generated ellipse does not affect the production. As relatively slow rotational speeds ($\omega_1 \approx \omega_2 \approx$ 1Hz) and small forces (*P* is pressed with about 20 N outwards against the belt and the machining head is pressed with about 10 N against the workpiece surface) are applied and the tool will be used within the stiff geometrical frame together with a state of the art air bearing spindle for the workpiece rotation, highest accuracy levels can be expected.

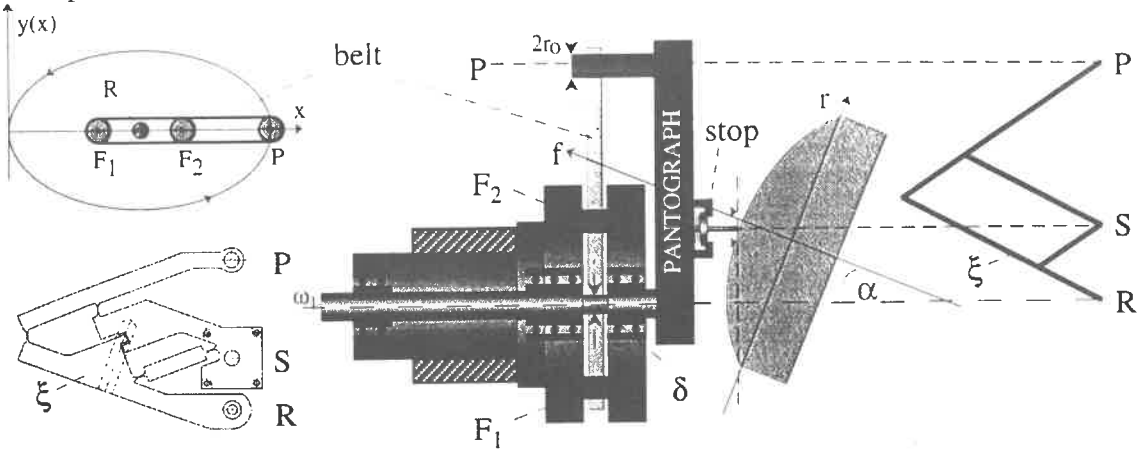

Fig.3 Sketch of a tool based on WAGNER for the generation of conic surfaces. The pantograph consists of a 15 mm thick aluminium plate comprising 4 pivot holes that are generated by electric discharge machining enabling a play-free movement of the pantograph.

In order to demonstrate the possibility to generate a smooth surface applying WAGNER, a first test was carried out implementing the tool on a not state-of-the-art milling machine that was poorly isolated from vibrations and other mechanical disturbances and that comprised a conventional workpiece spindle. The amplitude of the machine vibrations that causes distortions to the *Shape* was measured to be 5-10 µm at 1Hz corresponding to the rotary speed of the tool. The surface (glass, BK7, with r_m=70 mm) was microground using cup wheels having a diameter d = 10 mm, using 1 µm loose abrasive diamonds, an oil-based slurry and tin as cup wheel material. Once a smooth surface was achieved, the process was stopped and it was measured to have an average roughness of R_a= 4.15 nm. The fitted conic surface, a hyperboloidal surface, is within the adjustment accuracy of the angle α. The shape inaccuracy of the fitted conic surface of 9.7 µm *PV* (standard deviation σ = 4.89 µm) with respect to the measured surface can be explained by the amplitude of the machine vibrations. Consequently, future experiments will be carried out on a better grinding machine using a more appropriate type of belt and better allignment possibilities.

4 DISCUSSION

Likewise a curve generator that uses a cup-wheel to generate spherical surfaces of revolution, FAUST and WAGNER are characterized by their three degrees of freedom: the rotation of the workpiece

around its symmetry axis, the rotation of the tool along the *Shape* and the translation of the *Shape* parallel to the *f* axis down into the material. Both FAUST and WAGNER are generating the *Path* mechanically in advance not requiring an in-process control of a complicated tool path. It is not necessary to achieve the same shape accuracy for the *Shape* as is required for the workpiece: there is an advantageous error propagation factor between the shape of the intersection curve and the workpiece that depends on the angle α[1]. The shape accuracy of the generated surface depends on the shape accuracy of the *Shape* as well as on its accurate position and orientation with respect to the workpiece. Therefore, an isolation from vibrations and temperature changes is required. On the other hand, a tool based on WAGNER or FAUST is less sensitive to external mechanical disturbances than a precision grinding machine, because the tool is hold against the workpiece by pressure and can move sideways along its translational degree of freedom. Unlike a curve generator, WAGNER and FAUST split the functioning elements of the machining of the surface, the positioning of the *Shape* and the generation of the *Path*. Consequently, they can be used to compensate each other. It is e.g. possible for known inaccuracies of the tool-path shaping element and for known small positioning inaccuracies of the *Shape* with respect to the workpiece, to compensate for these already in the design stage of the tool-path shaping element. A numerical analysis tool has been written, where shape errors of the generated surface due to all kinds of tool misalignments (e.g. lateral errors along the *x*, *y*, *z* and *r* axes, *Shape* inaccuracies (e.g. caused by guidance inaccurasies) or rotations of the *Shape* around the *x*, *y*, *z r* and *f* axes) can be simulated. The obtained results can be used to compensate e.g. by adjusting the *Path*. Besides, for FAUST a machining process simulation has been developed to simulate the in-process generation of the surface shape as well as the shape of the cross-section of the machining band. This simulation is based on Preston's law[4] and uses as starting point a rectangular band cross-section with a thickness δ in the *x*, *y* plane and a spherical workpiece surface. The band is rotating along the *Shape* and has only partly contact with the surface. The loaded tubular element can move along an axis z_σ that is located in the *x*, *z* plane and has an angle σ with respect to the *z* axis that depends on the ratio between tool and workpiece wear[1]. The ratio between ω_1 and ω_2 is assumed to be constant. A point τ located on the machining band is given in the y_r, r, z_σ coordinate system by a vector [Eq.2]

$$\tau(n,r)=\begin{bmatrix}\cos(\sigma)(x(r)+nd\sin(\phi))\\(y(r)-nd\cos(\phi))\\\sin(\sigma)(x(r)+nd\sin(\phi))\end{bmatrix} \qquad \text{with: } \tan(\phi)=\frac{\dfrac{\partial y(r)}{\partial r}}{\dfrac{\partial x(r)}{\partial r}}, \qquad (3)$$

$Nd = \delta$, $\Delta \le r \le r_m$ and $0 \le n \le N$ (d denotes the size of the contact area between band and surface at τ). The distances along the z_σ axis between the points τ and the corresponding surface points (the surface being machined in the same coordinate system) determine how many points along the band are worn away during one iteration step. The amount of local tool and workpiece wear is then determined, taking into account the local relative speed between band and surface together with the amount of the band surface that is in contact with the surface. That way the cross-section of the band and the surface shape being generated are simulated. This can be used to minimise the amount of *Shape* inaccuracy caused by the band thickness[1]. This process simulation can also be adjusted to determine the cross-section of the wall of a small cup-wheel as it is used within WAGNER.

References

1. O.W. Fähnle, H. van Brug, C.J. van der Laan and H.J. Frankena, "Loose abrasive line-contact machining of aspherical optical surfaces of revolution," Appl.Opt. **36**, 4483-4489 (1997)
2. O.W. Fähnle, H. van Brug, C.J. van der Laan and H.J. Frankena, "The generation of on-axis and off-axis conic surfaces of revolution by applying a tubular tool", Appl.Opt. **36**, 4490-4496 (1997)
3. O.W. Fähnle, H. van Brug and H.J. Frankena, "Fabrication technique for the production of on- and off-axis conic surfaces of revolution", accepted for "Optical Manufacturing and Testing II", SPIE Annual Meeting, 1997
4. F.W. Preston, J.Glass Technol. **11**, 124 (1927)

Micropositioning of a Linear Motion Table with Magnetic Bearing Suspension

Oui-Serg Kim*, Hyeong-Joon Ahn*, Yoon Joung**,
In-Bae Chang*** and Dong-Chul Han****

* Graduate Student, Dept. of Mech. Design and Production Eng., Seoul National University, Korea
** Production Engineering Center, Samsung Electronics Co., Suwon, Korea
*** Dept. of Precision Mechanical Eng., Kangwon National Univ., Chuncheon, Korea
**** Dept. of Mech. Design and Production Eng., Seoul National University, Korea

Abstract

This paper presents a design and performance of the 6 D.O.F. linear motion table with a magnetic bearing suspension. The linear positioning of the table with a 150 mm stroke is driven by a brushless DC linear motor and the other attitudes of the stage are controlled by the analog PD controller with magnetic bearing actuators. Each magnetic bearing unit which consists of 3 electromagnets ,3 capacitance probes and 3 backup bearings affords controlled forces by detecting the air gap between the probes and guideways.

A current integration type capacitance probe amplifier is equipped on the upper plate of the table so that the probe line to the probe amplifier can be shorter therefore the problems due to the stray capacitance and noise can be reduced.

From the pitch-yaw errors measured by the autocollimator, the vertical and horizontal straightness errors of the table are derived that they are maintained below 1 μm over 100 mm stroke. The positioning accuracy of the linear motion is maintained below ± 1 μm and the repeatability error is below 1 μm.

Keywords : magnetic bearing, linear motion table, straightness, micropositioning, capacitance probe

1. Introduction

In the semiconductor manufacturing systems, there are growing demands for the ultra precision equipments and especially the linear positioning system is essential. In the linear positioning system, the driving and support mechanisms determine the accuracy, so various positioning mechanisms are under way on the development. Although the magnetically levitated system with attractive type electromagnetic force is originally unstable, the feedback control plant can stabilize. The magnetic bearing is a lubricant-free system, so it can be used in the vacuum or clean room environment which can be usually encountered in the semiconductor manufacturing procedures.

In this paper, the magnetically levitated linear motion table system is developed for the probe station. The probe station analyze the wafer/substrates at the final manufacturing stage of the wafers. This station has an X-Y table, microscope, vertical positioning stage for the probes and so forth. The exchange of the already existed X-Y table into the magnetically levitated table system gives the higher positioning accuracy, reduces the friction and enables the system to be free for the contamination by lubricant. Furthermore, it can eliminate the fine attitude positioning mechanisms for the roll-pitch-yaw of the wafer, because the magnetically levitated system can not only levitate the table but also control the fine attitude in the range of nominal clearance.

There are a few researches on this system. Trumper[1], Kuzin[2] and Joung[3,4] developed the linear motion table with magnetic bearings. Tieste[5] investigated the frequency response and Eisenhaure[6] suggested precision design schemes on magnetically suspended table system.

This paper describes the design and performance test of a 5 D.O.F. linear motion table with magnetic bearing suspension. The 150 mm stroke brushless DC linear motor is used to drive the table and it's position is detected by the optical type linear scale. The table consists of platen and four magnetic bearing unit. Each magnetic bearing unit is composed of three electromagnets and three capacitance sensors. The performance of the table system is verified by autocollimator for the attitudes and by laser interferometer for the linear positioning.

2. System Design

Table System Fig. 1 shows that the schematics of the table system composed of six guideways, four bearing units, a table body, a linear motor, a linear scale, a sensor amplifier for twelve sensor probes and a wafer holder.

Each bearing unit consists of three electromagnets and three plate type capacitance sensor probes.

They are embedded in the bearing holder in three directions and molded as shown in Fig. 2. The specifications of the electromagnet actuator are similar to Joung[4]'s

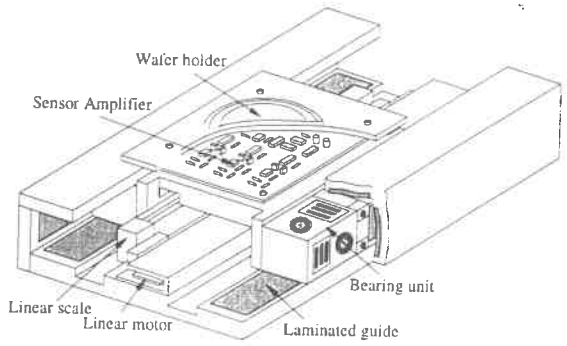

Fig. 1 Schematics of the table system

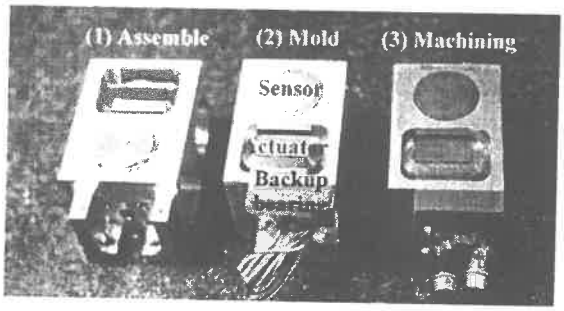

Fig. 2 Magnetic bearing units

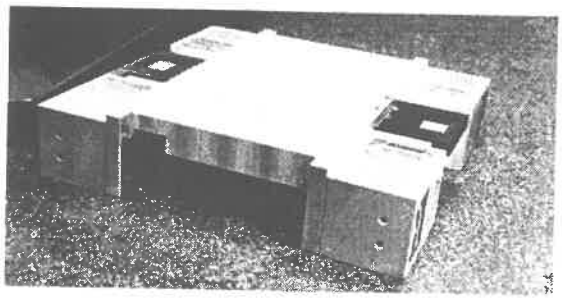

Fig. 3 Assembled table body

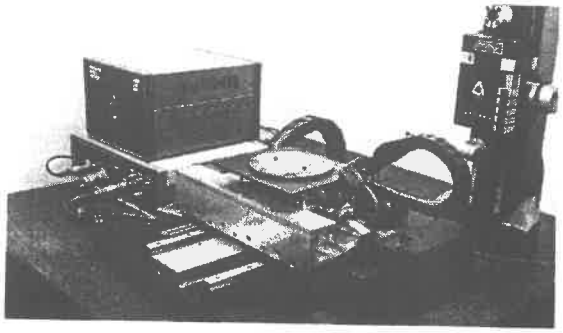

Fig. 4 X-Y micropositioning stage for probe station

Four magnetic bearing units are attached to the table body as shown in Fig. 3. The table is assembled with the guideways, linear motor and linear scale. The guideways are made of laminated silicon steel in order to reduce the hysterisis problems of the target material. The sensor amplifier for the twelve capacitance probes is assembled on the table body to eliminate the stray capacitance and noise problems. The wafer holder is finally attached on the table as in Fig. 4. In this figure, the other linear motion axis(Y-direction) of the X-Y linear motion table system is supported by the commercial LM guide.

Sensors[6] Twelve capacitance sensors are used to feedback the 5 D.O.F. displacement signal of the table to the controller. Configurations of sensor and guard electrodes are optimized experimentally and numerically[7]. The guard electrode enclose the sensor electrode and the triaxial cable is used so that the stray capacitance can be reduced. The two signals from the sensors at the opposite direction are electrically subtracted by operational amplifiers to get the table displacement of one direction with minimizing the baseline drift and nonlinearity. The sensor amplifier based on the charge transfer principle consists of CMOS analog switches and a current integration amplifiers. This amplifier has a 4 MHz sampling frequency and can remove the effects of stray capacitance with switched guard method. The basic circuit diagram is shown in Fig. 5 and the steady state output equation of this amplifier is very simple as given in equation (1).

$$V_{so} = -C_x V_c f R_f \qquad (1)$$

Here, the C_x is the unknown sensor capacitance, V_c is the charge voltage, f is the sampling frequency, R_f is the feedback resistor .

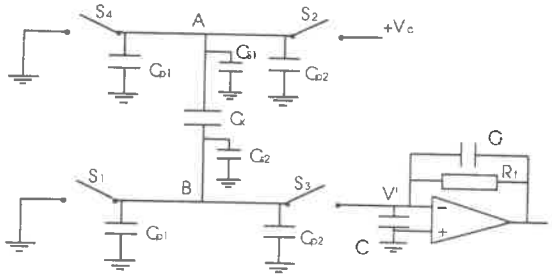

Fig. 5 Basic circuits of the sensor amplifier

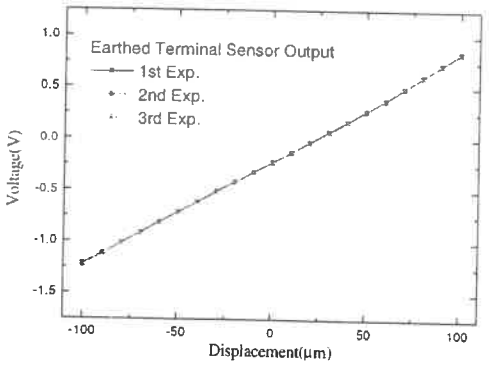

Fig. 6 The calibrated data of one sensor

Fig. 6 shows the calibrated results for one sensor probe. The linearity of this sensor/amplifier system is below 0.03 % over 200 μm range and has a 1 mV/μm sensitivity.

Controller Fig. 7 shows the control loops of the table system. The six signals from the sensor amplifiers are transmitted to the six analog PD controllers which have offset adjustment, PD and lead compensations, low pass filter circuits and current amplifiers[3]. The circuit board is shown in Fig. 8.

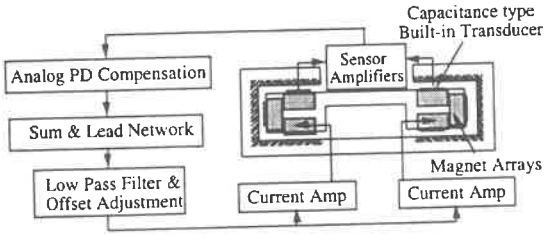

Fig. 7 Block diagram of the control system

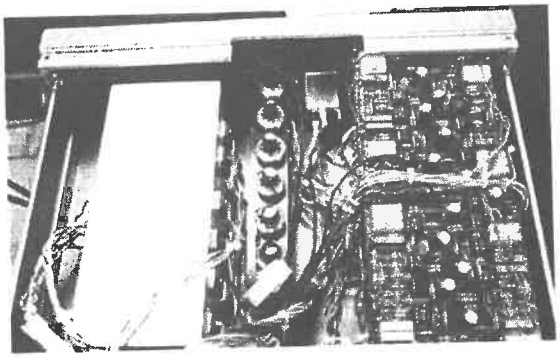

Fig. 8 Controller system with current amplifiers

Linear motor & Linear scale To get 150mm stroke of the table, linear brushless D.C. motor is used which has simple structure and has no contact nature. Normag BLC04-18 motor with 15 lbs of moving force has no attraction force in any other axis except driving axis so that the motor gives no disturbance force to the magnetic bearings. RSF MSA6703 linear scale with 10 ㎛ of grating period shows good performance to use in position feedback system of 0.05 ㎛ resolution.

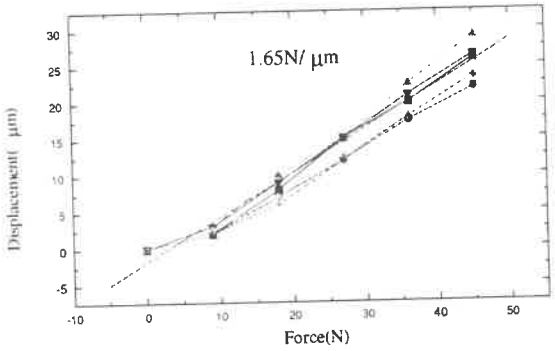

Fig. 9 The stiffness of the table

3. Experimental Results

The performances of the linear motion table are measured by three types of test schemes.

Table Stiffness The stiffness of the table is measured to 1.65 N/μm by adding the mass at the top of the table up to 45 N range and shown in Fig. 9.

Straightness of the Table The straightness of the table is indirectly measured with the autocollimator system. The autocollimator can measure the pitch and yaw motion of the table and by using the conversion equation (2), the vertical and horizontal straightness of the table can be attained. To compensate the measured data, the incremental angular method and the least square fit is used.

$$L[\mu m] = 4.8l[m] \cdot \theta[\sec] \qquad (2)$$

In the equation (2), the L means the displacement of horizontal and vertical direction respectively, θ is the measured angle data and l is the travel length of each step.

Fig. 10 shows the experimental set-up and Fig. 11 shows the vertical and horizontal straightness error graphs. In the straightness error graphs, the maximum errors are remained below 1 μm over the 100 mm stroke range in each direction.

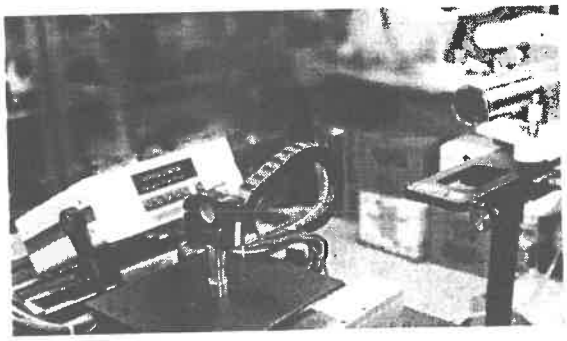

Fig. 10 Experimental set-up for straightness measurement

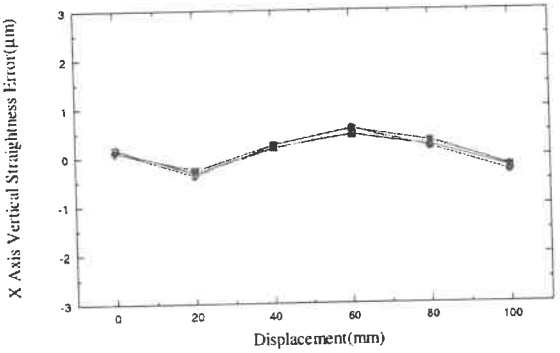

(a) Vertical straightness error of the table

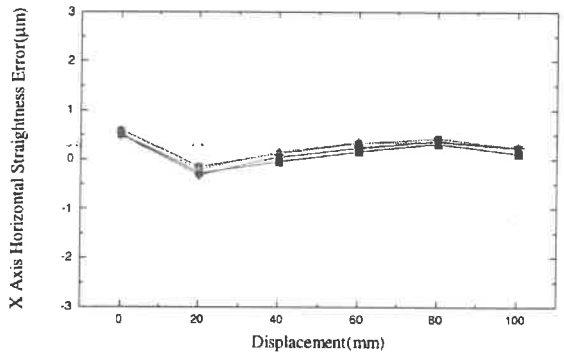

(b) Horizontal straightness error of the table

Fig. 11 Straightness error of the table system

Repeatability of the Table The positioning accuracy of the table is affected not only by the linear motor system but also by the bearing support conditions and linear scale accuracy. And the accuracy of the system is measured by the laser interferometer system. The experimental set-up is shown in Fig. 12. Fig. 13 (a) shows the positioning error of the table that it is remained below ± 1 μm over a 60 mm range. Fig. 13 (b) shows the repeatability error of the table. The table goes forward to 20 mm and back to the initial position that the repeatability error is measured to 3 times. The repeatability error is remained below 1 μm at the both ends and middle position for the full stroke

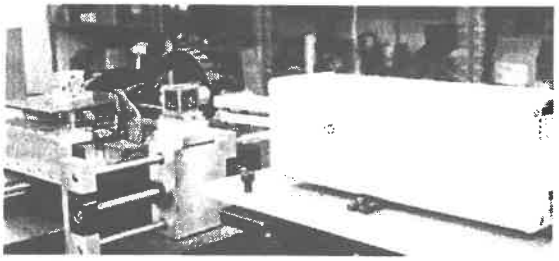

Fig. 12 Experimental set-up for the positioning error measurement

4. Conclusion

The electromagnetically levitated linear motion table system is developed for 6" wafer prove station and the performances of the table are measured.

With current integration type capacitance sensor and PD controller for magnetic bearings,advanced levitation performance can be achieved so that metrology of linear motion table is well performed.

Acknowledgments

This work was funded by Samsung Electronics Co. and supported in part by Turbo & Power Machinery Research Center and Institute of Advanced Machinery & Design in Seoul National University.

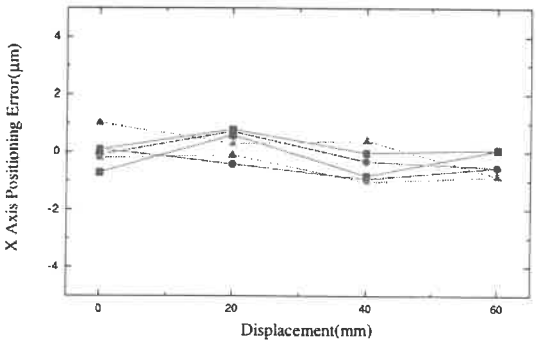

(a) Positioning accuracy of the table

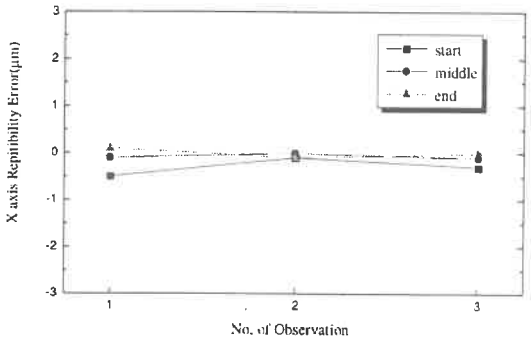

(b) Repeatability error of the table

Fig. 13 Positioning error of the table with longitudinal direction

References

[1] M.E.Williams, D.L.Trumper, "Precision magnetic bearing six degree of freedom stage", *3'rd Int'l Symp. on Magnetic Suspension Tech.*, July, 1995, pp.453.

[2] A.Kuzin, "Precision magnetically suspended XY stage", 4'th Int. Symp. on Magnetic bearings, 1994, 177-182

[3] Y.Joung, S.C.Jung, I.B.Chang, D.C.Han, "An experimental study on the high-precision linear motion table with magnetic bearing suspension", *Proceedings of ASPE 10'th Annual Meeting*, Oct., 1995, pp.328.

[4] Y.Joung, H.J.Ahn, O.S.Kim, I.B.Chang and D.C.Han "A Study on a High-Precision Linear Motion Table with Magnetic Bearing Suspension", *Proceedings of ASPE 11'th Annual Meeting*, Oct., 1996, pp.328.

[5] K.Tieste, K.Popp, "Dynamical behavior of a linear maglev support unit for fast tooling machines", 4'th Int. Symp. on Magnetic Bearings, 1994, 269-274

[6] D.Eisenhaure, A.Slocum, A.R.Hockney, "Magnetic Bearings for Precision Linear Slides", *1'st Int. Symposium on Magnetic Bearings*, 1988, pp. 67.

[7] H.J.Ahn, " A Study on a Cylindrical Capacitance Displacement Sensor for the Measurement of small rotor motion", M.D. diss., Seoul National University, 1997, Seoul, Korea

THE MACHINIST'S ROLE IN A MODERN HIGH-PRECISION MANUFACTURING ENTERPRISE

Richard L. Rhorer, Nathan R. Copeland, Charles W. Brooks, and Brian S. Dutterer
Fabrication Technology Division
National Institute of Standards and Technology, Gaithersburg, MD 20899

It has been suggested that as better systems are developed for controlling manufacturing processes, the need for the skilled machinist will decrease. The authors of this paper argue there will be an increasing role in high-precision manufacturing enterprises for people with the skills of the precision machinist.

Introduction

The role of the machinist in modern manufacturing is rapidly changing. Some manufacturing experts have suggested that in the future we will need good machine operators, but that many of the tasks traditionally handled by the skilled machinists will become automatic. An example is in the set-up of machining processes. In the past we have often relied on the experience and skill of a machinist to select the speeds and feeds best suited for a job. Tables of data were available to provide a starting point on speeds and feeds, but often a skilled machinist could greatly reduce the time and expense of optimizing a process by applying his experience to refine "book values" in particular situations. Computer Numerical Controllers (CNCs) in the future will probably have automatic speed and feed setting capabilities with appropriate sensors providing feed back from the actual process. An operator will simply have to push the "go" button and the system will adjust itself to the correct speed and feed to eliminate chatter and minimize tool wear.

As the CNCs and "virtual manufacturing systems" become better, will there eventually be no need for the skilled machinist? We think there will always be a need for the skilled machinist. And, this need for the skilled machinist will increase as industry moves to smaller lot sizes and as shops continually upgrade with new equipment. The machinist's traditional roles of making prototype parts and trouble shooting production equipment will increase, plus there will be new roles. In future manufacturing enterprises the skilled machinist's role will include participating with engineers and managers on teams which are developing new manufacturing processes. Therefore, in addition to many of the traditional skills, the next generation machinist will need some new skills.

Needed Machinist Skills

There are many things that have changed for the working machinist in the last three decades. Although machine tools have not significantly changed in appearance, even in the last hundred years, a modern precision machinist has to understand and be able to operate a machine tool through a computer based controller. Knowledge and skills of using computers, as well as the more traditional knowledge of manufacturing processes, are required by the modern machinist. We think it is very important that the "feel" that comes from making a part by hand not be lost in the training of the modern machinist. Table I lists some of the skills that we think a modern precision machinist should have as compared to a machinist of thirty years ago. In Table II, we have listed some of the skills that we think a modern precision machinist should retain even though they are not needed every day. The authors are seeking suggestions to add to the list.

TABLE I -- How Machinist's Skills have Changed

Skills taught and used 30 years ago	Skills used in modern shop
did layout work on bolt circles, etc.; used dividers, rulers, etc.; used drill press for holes	use readout on milling machine to produce bolt circle or use CNC machine
on lathes, used 4-jaw chucks, soft jaws	use 6-jaw adjustable chucks, collets
used scales and dials on milling machines to position work, had to deal with backlash	now never concerned with backlash, use readouts or CNC machines
used basic math, geometry, and trig, and had to do arithmetic quickly and accurately by hand	in addition to traditional math, use CAD/CAM (any hand calculations are done with calculator)
dimensions were always in inches	now mix metric and English units, and must know ANSI Y14.5
performed handwork using chisel, file, scraper at times to produce precision surface	only handwork done now is deburring
there was little need for communication skills	now need to read technical reports, be able to write about complicated machines and processes, be able to give good lectures and lead discussions
needed to know how to measure complicated parts with hand measuring tools (mikes, height gages, bore gages, etc.)	now need to be able to use CMMs in addition to using many of the traditional hand measuring tools
needed to make hand sketches	now use computers to make drawings
needed knowledge and skill to cut special threads on a lathe by changing lead screw gears	now use CNC lathes and program any thread, need programming skills

TABLE II -- Skills to Maintain

In addition to all the modern skills needed we recommend that the precision machinist of the future be taught the following skills that were common in the past but are in danger of being lost in the future.

-- be able to center a part in a four jaw chuck
-- be capable of producing a flat surface with a hand file
-- be able to accurately position a slide that has backlash
-- be capable of making hand drawings and sketches
-- cut special threads on a manual lathe by changing lead screw gears
-- modify previously machined parts, machine parts in place
-- indicate vise square with machine motions, tram machine spindle

Machinist's Role in New Equipment Installation

Even more in a modern shop than in times past, new machine tools have to be installed and brought up to speed very rapidly. In a large shop a "new machine department" may handle all the details and the production department simply takes over a turn-key operation. In many smaller shops, and in research shops like our shop at National Institute of Standards and Technology (NIST), the machinist plays a significant role in the installation of a new machine tool. For example, we have installed a new high speed milling machine at NIST and one of the authors (Brian Dutterer) has been involved since the very early stages of this project. This new machine was purchased for doing machining process research and to provide a new support service capability for our shop. As the lead machinist on this project, Brian participated at every stage of the project. The details of the machinist role are described in Table III. This project proceeded smoothly and achieved its goals in a large part because of a skilled machinist's involvement. We recommend this approach for a shop of any size--the skilled machinist can make the project move more rapidly and smoothly.

TABLE III -- Machinist's Contributions to a New Machine Installation

Step in the "new machine tool" project	The role of a Skilled Machinist in this project
Justification of new machine tool	a. help define current work and jobs that are difficult or impossible: small hole drilling, thin wall, high speed b. define advantages of 4-axis machine
Preparing specifications for the new machine tool	a. check specifications for air and electrical requirements b. read and review specifications
Ordering the new machine tool	a. consider what options would make the machine more useful in our shop b. help review bids
Specify tooling	a. research tools needed for jobs intended for the machine and talk to tool suppliers b. help order tooling
Delivery of the new machine tool	a. aid in preparing utilities and new area for machine b. answer questions regarding new machine needs
Installation of the new machine tool	a. aid in proper placement of machine tool b. monitored installation for potential problems with machine c. aid in leveling and machine start up
Acceptance testing of the new machine tool	a. set-up fixtures for ball-bar test and help perform ASME B5.54 tests (by participating in these tests gain knowledge that will allow monitoring of accuracy during life of machine) b. answer questions and report results of acceptance testing to management
First parts fabricated on the new machine tool	a. prepare fixtures, blanks and part programs for some of the first parts from machine b. measure parts
Develop an efficient system of making parts in a job shop environment with the new machine tool	a. work with management to develop a scheduling approach for new machine b. explain new machine to high level management and visitors

Communication Skills and Certification

Another vital skill for the modern machinist is the ability to communicate with a broad range of fellow workers and customers. The machinist has to work in a more diverse workplace than ever before--diverse not only in working with people of different races and cultural backgrounds, but diverse in constantly changing work place situations such as new equipment and new experimental management approaches. For example, historically the precision machinist might learn from one mentor, but now the precision machinist is more likely to learn the basics in the environment of a community college, and work under many different managers during his career. To be successful he or she has to not only know how to make the parts, but must be able to tell others how the parts were made, and communicate with a variety of scientists and engineers concerning requirements and methods of fabrication. The precision machinist or instrument maker of the future will come much closer to the professional levels, which suggests that there may be a benefit for a "certification" program.

The certification of engineers, such as Professional Engineers (PE) licenses issued by states, usually involves passing a written test. For certifying precision machinists (or we would propose the title "Instrument Maker") there will be a need for some form of hands-on testing, in addition to some form of written test. An idea for a hands-on certification test could be adapted from the approach used by the Vocational Industrial Club of America (VICA) in the skills competition events. Contestants are given a drawing of a part and then allowed a given length of time to make the part. The contestants are graded on the number of features of the part that are within tolerance. In a similar vane, for a certification test, the actual fabrication of a special part could be required. This would be in addition to some form of written test verifying advanced skills, such as metrology.

We view the idea of having a certified machinist, or certified instrument maker, to be an advantage. A certified instrument maker could be relied upon to have the necessary skills of a traditional machinist plus have the advanced skills needed for working in the field of precision engineering.

Conclusions

The role of the precision machinist has changed in the past thirty years, and will continue to change. We propose that in the future the precision machinist will:

1. be a key member of teams developing and implementing new technology,
2. take a leadership role in acquiring and implementing new machine tools,
3. need to acquire computer expertise and advanced communication skills, and
4. need to work hard at maintaining traditional "hands-on" skills.

If the American Society for Precision Engineering (ASPE), or any other organization implements a certification program, we suggest that the program include a "hands-on" component as part of the certification criteria. We propose using the title "Certified Instrument Maker" if such a program is instituted.

Acknowledgments

We include a memorial recognition of Donald S. Blomquist. As the Chief of the Automated Production Technology Division, Don was a strong advocate of the project to install the new high speed mill used as an example in this paper. This machine had just recently become operational prior to Don's accidental death on July 3, 1997.

Self-Calibration of Interference Microscopes

Masaya KANAI, Wei GAO, Ichiro OGURA, Satoshi KIYONO
Department of Mechatronics, Faculty of Engineering
Tohoku University, Sendai, 980-77, Japan

ABSTRACT

The present study introduces a self-calibration method that does not require references or additional sensors to detect derivative function in order to yield a calibration curve for an interference microscope. Two specimens were used to realize the self-calibration technique. One specimen was an inclined flat surface that produces a continuous flow of calibration values. The calibration curve was derived from the difference between two measurements obtained before and after a small shift in the Z-direction. The other was a step specimen. The derivative function can be evaluated from the data obtained from the upper and lower regions of the step specimen. The results of the two specimens showed good agreement, suggesting that the proposed self-calibration technique provides an effective and reliable means of calibrating an interference microscope.

1. INTRODUCTION

Interferometric microscopes have long been used in quantitative characterization of a surface structure [1]. As a result of recent advances in phase detection techniques, interference microscopes can achieve extremely high vertical resolution [2]. However, the accuracy of interference microscopes is affected by some inherent systematic errors [3]. In particular the linearity error (deviation from a linear calibration line) of the microscope output is much larger than the resolution level. To assure accuracy of interference microscopes, the linearity error must be calibrated accurately [4]. In addition, due to the variable characteristics of linearity error with respect to the measurement conditions, the microscope should be calibrated in situ frequently to address changing conditions. The conventional calibration method requires an accurate calibration reference which is difficult to be obtain in practice. Thus, in situ calibration cannot be easily performed using the conventional method.

A self-calibration method that does not require a calibration reference has been proposed for displacement or angle sensors [5 - 7]. However this method is too large to apply to a calibration system for a restricted space because a lever system that multiplies the input to the reference side sensor is required in this method. Thus, this method is not appropriate for in situ calibration of an interference microscope.

The present paper proposes a new self-calibration method that has been specifically designed for use with an interference microscope. The proposed method does not require an extra lever system or partner sensor and can be easily applied in situ calibration. Calibration results for a commercially available interference microscope [8] are also presented.

2. PRINCIPLE

Figure 1 shows a schematic diagram of the calibration target, which is a scanning white light interferometer that employs a new spatial frequency domain analysis technique [2].

After passing through an objective lens, the light from the white light source is divided into two beams by a beam splitter in a Mirau-type objective. The transmitted beam propagates to the test surface, and the reflected beam propagates to an internal reference surface. These beams are then reflected back to the beam splitter and interfere with each other. The interference beam is received by a CCD video camera in which

each pixel corresponds to a small area of the surface.

The test surface is scanned by moving the objective in the Z-direction using a piezo-electric transducer (PZT) . As the objective scans, the optical path difference (OPD) of the interferometer is varied, and the sequence of interference intensity data frames are detected and stored by the CCD camera. The data of each pixel, which represent the variation in intensity as a function of the scanning position, are transformed into the frequency domain by Fourier analysis. The relative surface height of each point of the test surface can then be obtained by calculating the phase slope with respect to the angular wave number [2].

Because the sampling position is decided by the scanning PZT, nonlinear motion of the PZT will greatly affect the linearity of the interferometer. For example, although this microscope has a vertical resolution of 0.1 nm with a maximum vertical range of 100 μm, the assured accuracy is only 1.5 % of the vertical range [8].

Assume the calibration curve of the interferometer is described by function f(z) as shown in Figure 2. f(z) can be generally expressed as the sum of a straight line with a slope of 1 that connects both ends of the calibration range and the deviation g(z) from the straight line :

$$h = f(z) = z + g(z) . \qquad (1)$$

Here, g(z) is called the linearity error. Let the displacement output of the interferometer at sampling position z_i be m_i, and that at position $z_i+\Delta z$ be m_{+i}. If the inverse function of f(z) shown in Figure 3 is given by

$$h_i = m_i ,$$

$$f^{-1}(h_i) = h_i - b(h_i) , \quad (i = 1, 2, \dots , n) \qquad (2)$$

where n is the sampling number, the derivative of b(h) at the discrete i-th sampling point can be written as

$$b'(h_i) = 1 - \Delta z / \Delta m_i , \qquad (3)$$

where $\Delta m_i = m_{+i} - m_i$.

If Δz is given, b(h) can be obtained by integration of $b'(h_i)$. If Δz is not given, Δz can be calculated as follows:

$$\Delta z = \{1/(ns)\} \Sigma \Delta m_i(z_{i+1} - z_i)/(z_n - z_1) \qquad (4)$$

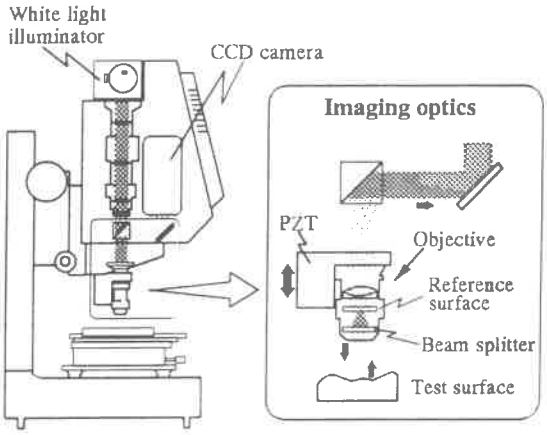

Figure 1 Schematic of microscope

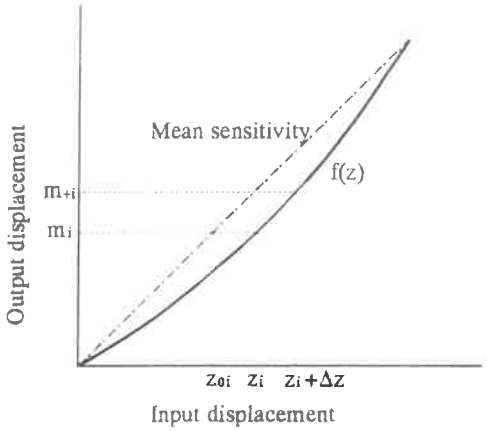

Figure 2 Calibration curve

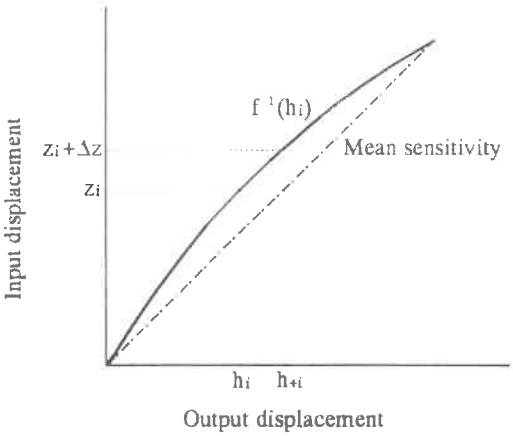

Figure 3 Inverse function of calibration curve

3. EXPERIMENT

3.1 Methods to obtain m_i and m_{+i}

Two methods are employed to obtain m_i and m_{+i}.

In Method 1, an inclined flat surface, which can give a continuous change in the input value z_i over the calibration range from z_1 to z_n, is used as the specimen as shown in Figure 4. If the inclined specimen is shifted a small distance Δz in the Z-direction, the same Δz can be applied to all points of z_i. Therefore, m_i and m_{+i} in Equation (3) can be obtained from the data measured before and after Δz.

As shown in Figure 5, Method 2 employs a step specimen, for which the step-height is assumed to be Δz. In this case, m_i and m_{+i} can be obtained from the data acquired from the upper and the lower regions of the step specimen, respectively. The evaluation accuracy can be improved by averaging the data of the upper or lower regions. To obtain m_i and m_{+i} over the calibration range from z_1 to z_n, the step specimen must be moved n times in the Z-direction with an interval of approximately Δz. Measurement is repeated at each position.

3.2 Experimental results

The calibration results obtained using Methods 1 and 2 are shown in Figures 6 (a) and (b), respectively.

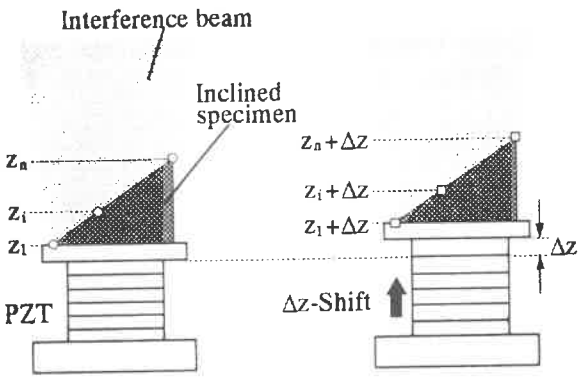

Figure 4 Principle of Method 1

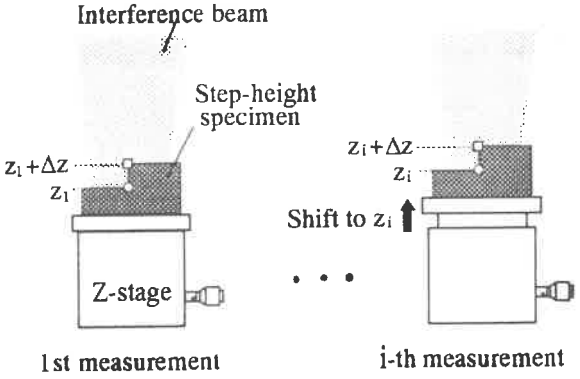

Figure 5 Principle of Method 2

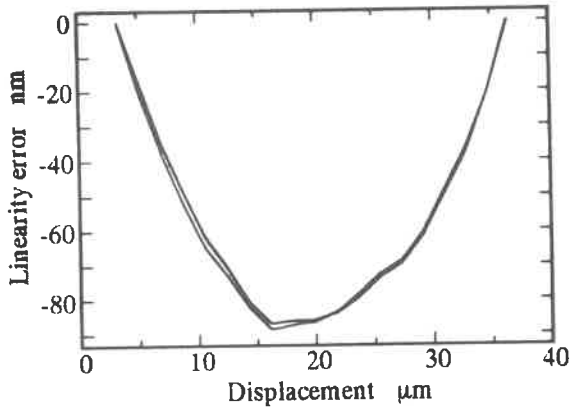

(a) Results of Method 1

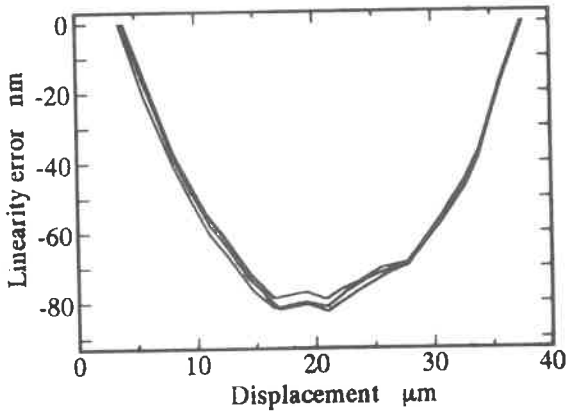

(b) Results of Method 2

Figure 6 Calibration results by two methods

The abscissa represents the position of the specimen in the Z-direction, which is calculated from the output of the interference microscopes. The results of three repeated calibrations are shown in each figure. The repeatability error of the three measurements in Figure 6 (a) was approximately 3 nm, and that in Figure 6 (b) was approximately 6 nm. Figure 7 shows the results obtained by fitting the average values of the three results with a fourth-order polynomial. The repeatability error, which was estimated by the root-mean-square value of the deviation associated with each measurement result from the fitting curve, was approximately 2.5 nm for each of the methods. The difference between the two fitting curves of the two methods was approximately 8 nm. These results confirmed the reliability of the proposed calibration method. The linearity error was approximately 80 nm, which is approximately 0.2 % of the calibration range of 40 μm.

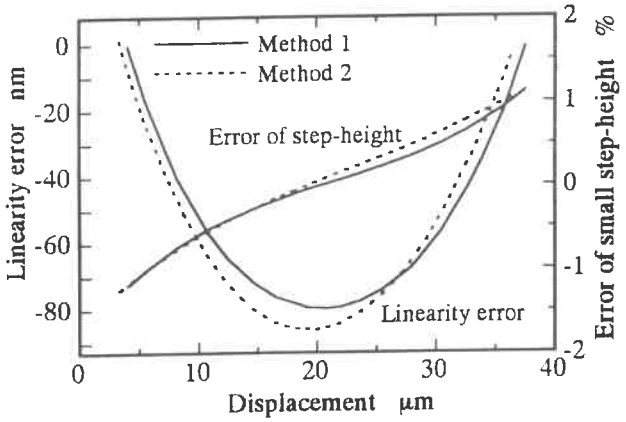

Figure 7 Averaged caliblation curve

In Figure 7, the derivative of each curve, for which the variation yields an error estimation of small step-height measurement, is also shown as a percentage. This figure shows that the error of the small step-height measured at different positions in the Z-direction varies from -1.2 % to 1.1 % of the step-height. This indicates that measurement data should be compensated using the calibration data in order to ensure high, accurate measurement.

4. CONCLUSIONS

To eliminate the influence of the linearity error of an interference microscope, we proposed a new in situ self-calibration technique that can accurately obtain the calibration curve by evaluating the derivative function using only the profile measurement data. Results from an inclined specimen and a step specimen have demonstrated that the proposed method is highly reliable and very effective for in situ self-calibration of an interference microscope.

ACKNOWLEDGMENT

This study was funded by a grant-in-aid for Scientific Research of Monbusho of Japan.

REFERENCES

[1] J.H.Bruning, D.R.Herriott, J.E.Gallagher, D.P.Rosenfeld, A.D.White, and D.J.Brangaccio : Digital Wavefront Measuring Interferometer for Testing Optical Surfaces and Lenses, APPLIED OPTICS, Vol.13, No.11, (1974), pp.2693-2703.

[2] P.Groot and L.Deck : Three-dimensional imaging by sub-Nyquist sampling of white-light interferograms, OPTICS LETTERS, Vol.18, No.17, (1993), pp.1462-1464.

[3] J.Schwider, R.Burow, K.-E.Elssner, J.Grzanna, R.Spolaczyk, and K.Merkel : Digital wave-front measuring interferometry: some systematic error sources, APPLIED OPTICS, Vol.22, No.21, (1983), pp.3421-3432.

[4] Yeou-Yen Cheng and James C.Wyant : Phase shifter calibration in phase-shifting interferometry, APPLIED OPTICS, Vol.24, No.18, (1985), pp.3049-3052.

[5] S.Kiyono, K.Morisima, T.Sugibuchi : Self calibration of the linearity error of displacement sensors, Proc. of ASPE 7th Annual Meeting, Florida, (1992), pp.305-308.

[6] S.Kiyono, S.Zhang : Self-Calibration of Precision Angle Sensors, Journal of The Japan Society for Precision Engineering, Vol.60, No.11, (1994), pp.1591-1595, (in Japanese).

[7] S.Kiyono, Z.Ge : Subnanometric calibration of a differential interferometer, Precision Engineering, Vol.19, No.2/3, (1996), pp.187-197.

[8] New View 100 Operation Manual OMP-0348K, Zygo Corporation.

A Model for Visualization of Roller Bearing Error Motion

Wolfgang Holzhauer
The Timken Company
Canton, OH

Introduction

A simple mathematical model of tapered roller bearing error motion is described. The model simulates a bearing with an outer raceway, inner raceway and three tapered rollers equally spaced. The rolling contact surfaces of the raceways and rollers are treated as circular cross-sections with variable, sinusoidal deviations from perfect roundness. The model treats each of the elements as a rigid body, and computes the radial and axial motion of the axis of rotation of the bearing as the bearing is rotated. The goal of the model is to use very simple inputs and modeling conditions to demonstrate the deterministic nature of rolling bearing error motion, and to demonstrate that these simple inputs can nonetheless result in motions that appear extremely complex. The model has also proven of interest in understanding fundamental aspects of rolling element bearing error motion as discussion points for the next revision of the ANSI/ASME B89.3.4 Axis of Rotation Standard[1], which is currently in progress.

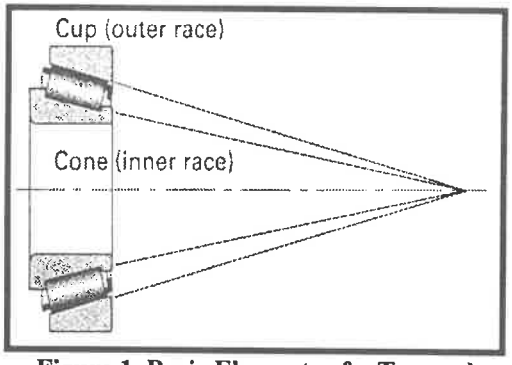

Figure 1 Basic Elements of a Tapered Roller Bearing With Common Apex Point

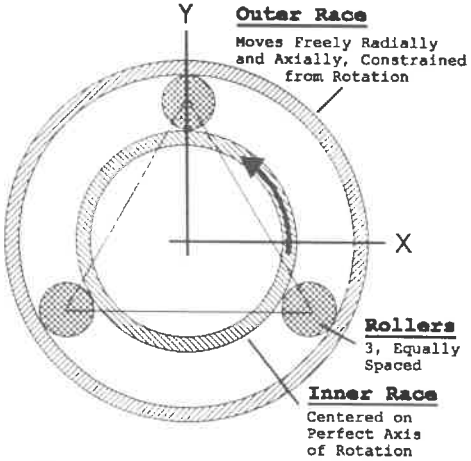

Figure 2 Model Bearing with Three Rollers

Tapered Roller Bearing Concepts

A tapered roller bearing consists of a conical inner and outer raceway, tapered rollers and a cage, which is used to separate and retain the rollers. As shown in Figure 1, pure rolling contact at the raceway and roller body surfaces is achieved by designing the bearing such that all of the conical elements share a common apex point. The inner ring also incorporates a conical thrust rib, which operates in contact with the spherical roller ends. A modern tapered roller bearing uses close to the maximum number of rollers that can physically fit around the periphery of the bearing, and the geometry of the internal contacting surfaces of the bearing includes features such as precision profiles and tightly controlled surfaces finish. None of these features of an actual bearing are considered in this basic model.

Model System

Figure 2 shows a diagram of the simplified bearing considered in the model. The inner race is rotated about it's geometric centerline, and the outer race is constrained from rotation, but allowed to move radially and axially. Theoretical deviations from perfect roundness are applied to each of the rolling contact surfaces (inner race, outer race, three roller bodies). In the work presented here, the roundness deviations are single wavelength sinusoids. These roundness deviations will result in variations in 2-point diameter for the rollers, and in variations in radius for the raceways. By rotating the model bearing one angular step at a time, the resulting motion of the outer raceway as a result of these roundness deviations can be calculated with straightforward trigonometric relationships.

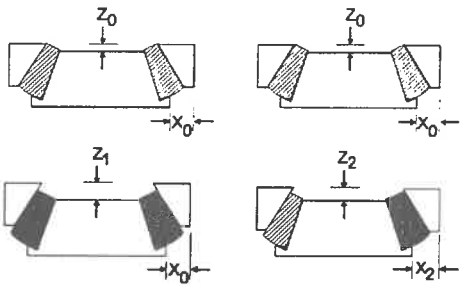

a) Equal increase in diameter of three rollers results in pure axial motion

b) Increase in diam. of one roller results in combined radial and axial motion

Figure 3 Axial and Radial Motions Caused by Instantaneous Changes in Diameter of (a) All or (b) One Roller. Larger Roller is Identified by Darker Shading.

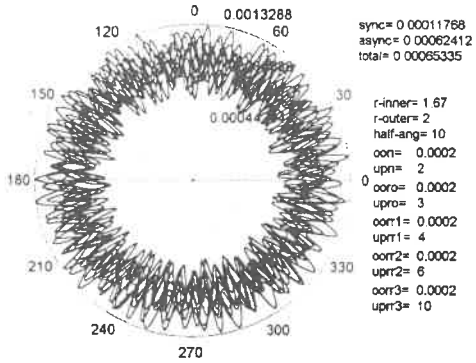

Figure 4 Error Motion Polar Plot for 10 Revolutions

A unique characteristic of a tapered roller bearing is the coupling of radial and axial forces and/or motions as a result of the tapered design. For example, if the instantaneous diameter of all three rollers in the bearing increases, axial motion of the outer race relative to the inner race can occur to accommodate the resulting geometric interference. This is shown in Figure 3a where dimension $Z_1 > Z_0$. In Figure 3b, an increase in instantaneous diameter of one roller will result in both radial and axial motion ($X_2 > X_0$ and $Z_2 > Z_0$).

Results

Figure 4 shows the error motion polar plot for a single, fixed sensitive direction for an example case in which the inner raceway mid-plane diameter is 1.67 units, the outer race mid-plane diameter is 2.00 units, the inner race has a 2 undulation per revolution (UPR) roundness deviation, the outer race has 3 UPR roundness deviation, and the rollers have 4, 6 and 10 UPR deviations respectively. All of the roundness deviations have a magnitude of 0.0002 units. Note that the units used are arbitrary: they can be inches, millimeters, etc. The plot represents 10 revolutions of the inner race. The synchronous, asynchronous and total error motion values are also shown on the plot.

The single sensitive direction polar plot in Figure 4 is the standardized [1] method of representing error motion data, and gives an excellent indication of the potential performance of a bearing or spindle on some machine tools or measuring instruments. However, it does not represent the complete motion of the bearing outer race relative to the rotating inner race. For this, the XY plot in Figure 5 is more useful. This plot shows the trajectory of a fixed point on the non-rotating outer race for ¼, ½, ¾ and 1 revolution of the inner race. It is evident that the non-rotating element of the bearing undergoes a variety of motions, including large excursions and rapid reversals of direction.

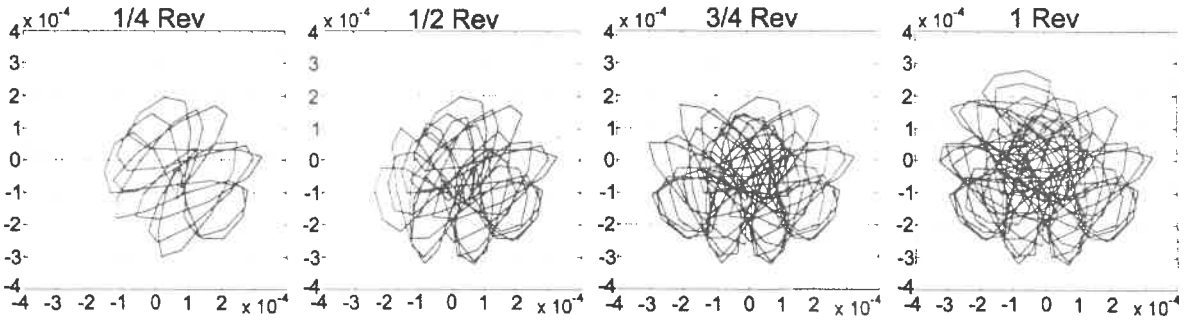

Figure 5 Error Motion XY Plot for ¼, ½, ¾ and 1 Revolution

While the radial motions represented in Figures 4 and 5 are taking place, axial motion also occurs in this model bearing. Figure 6 shows an XYZ plot of the trajectory of a fixed point on the outer race for one revolution of the inner race. The Z axis displacement is the result of sliding motion at the roller body/raceway contact

(assumed 10 degree half angle relative to bearing axis). Note that in this simple model with no inertia or sliding friction, the magnitude of axial motions can be quite large relative to the radial motions.

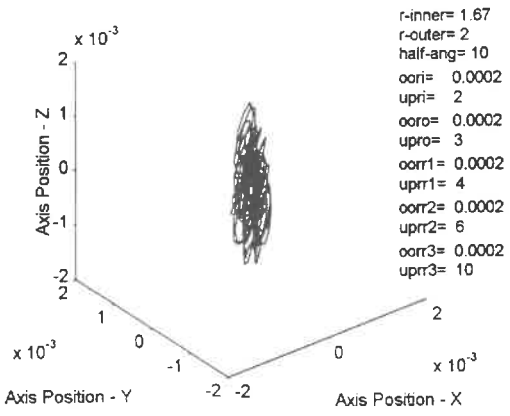

Figure 6 Error Motion XYZ Plot for 1 Revolution

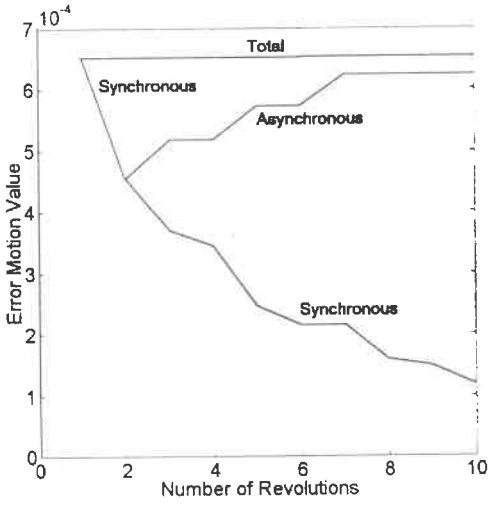

Figure 7 Error Motion Values Versus No. Of Revolutions

The model also shows behavior that has been observed experimentally on rolling element bearings. One example is the development of values of synchronous, asynchronous and total error motion values shown in Figure 7. Note that after the first two revolutions, the asynchronous error motion value increases, but that this increase sometimes occurs in steps. This phenomenon is also observed experimentally and can be explained by considering the definition of the asynchronous error motion value. This value is dependent on the largest excursions seen on the error motion polar plot. If during one or more revolutions of the bearing no excursions occur that are larger than those observed already, the asynchronous error motion value will remain constant. A stepwise increase then occurs in the subsequent revolution in which a larger excursion occurs. Also note that no asynchronous error motion value is plotted for 1 revolution, as the concept of asynchronous motion makes no sense for a single revolution (the same could be argued for the synchronous and total error motion values).

Figure 7 also reveals an interesting characteristic of a tapered roller bearing with three rollers equally spaced. As the number of revolutions increases, the synchronous error motion value decreases. Additional work with the model and with actual bearings has shown that the synchronous error motion value approaches zero after a sufficient number of revolutions. This occurs, however, at the expense of generating high values of asynchronous error motion.

Real Time Visualization

One of the most useful aspects of the model is in viewing the development of the error motion plots as the model bearing goes through it's simulated motions. A particularly useful representation of the data is to build the error motion XY or XYZ plot continuously, and display the most recent few data points in a different color from the rest of the plot. This method shows a short-term pattern driven by certain aspects of the part geometric deviations, and this pattern in turn moves around the plot area. The relative frequencies of these motions are determined by the bearing characteristic frequencies, and by the wavelength selected for the roundness deviation of each surface.

Fundamental Motions

The relatively complex-appearing error motion plots in Figure 4, 5 and 6 are actually comprised of some very basic motions. These motions are:

- Circular precession in the XY plane due to the 2 UPR component on the inner race.
- Axial motion in the Z direction, with zero motion in the XY plane, due to the 3 UPR component on the outer race.
- "Daisy" shaped patterns of three different frequencies in the XY plane, plus synchronized axial motions, due to the 4, 6 and 10 UPR roundness deviations of the three rollers.

These basic motions in XY and XYZ are plotted in Figures 8 and 9.

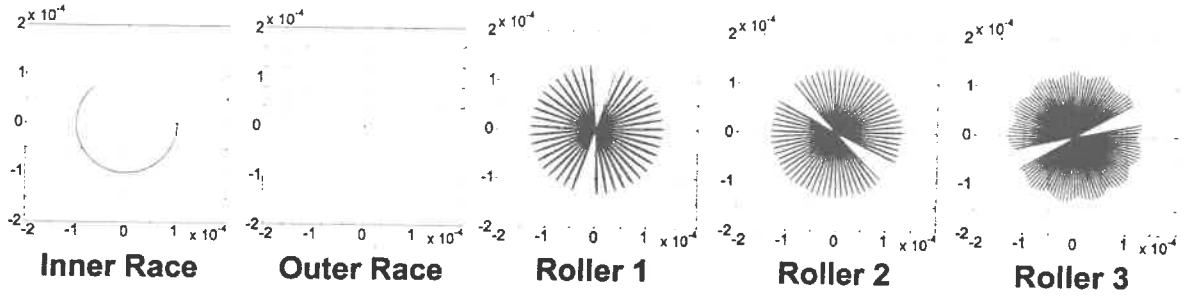

Figure 8 Error Motion XY Plots Showing Motions Generated by Each Bearing Element

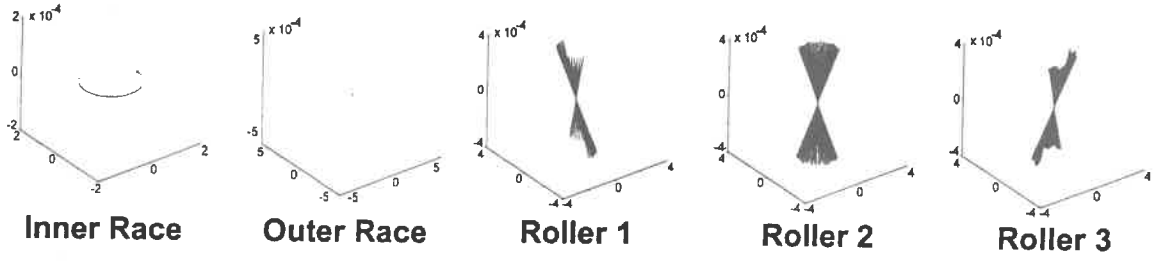

Figure 9 Error Motion XYZ Plots Showing Motions Generated by Each Bearing Element

Note in Figure 8 that the furthest right plot contains a false lower frequency which results from the selected angular increment in the calculations (1 degree angular increment) and the relatively high frequency of the motion. It is to be expected that the model reveals the same dangers of digitally sampling data as are encountered when sampling real data. The angular increment used in the model can be adjusted to minimize these effects if desired.

Conclusions

This model is clearly highly idealized and also restricted in the types of error motions that can be generated. The model does not consider tilt motion, the effect of the inner race thrust rib, slip, friction, inertia, component elasticity or more than three rollers. However, it has formed an excellent first step in the development of more sophisticated models that consider these factors. The simplified three roller model is also useful as a test bed for the development of new error motion parameters or concepts. Even though the idealized three-roller bearing is very simple, any generalized definitions and concepts proposed for understanding error motion should still be applicable to it. It has also proven useful for visualization of bearing error motion, and understanding the fundamental relationships between traditional single sensitive direction error motion polar plots and the XY and XYZ error motion trajectory plots shown here.

References

1. ANSI/ASME Standard B89.3.4M - 1985, "Axes of Rotation - Methods for Specifying and Testing," American Society of Mechanical Engineers, New York, NY, 1985.

GEOMETRIC ERROR CALIBRATION OF MULTI-AXIS MACHINES USING AN AUTO-ALIGNMENT LASER INTERFEROMETER

Jenq Shyong Chen
Department of Mechanical Engineering, National Chung Cheng University
160, San-Hsing, Ming-Hsiung, Chia-Yi, 621, Taiwan, R.O.C.
Tel:886-5-2428113, Fax:886-5-272-1522, e-mail: imejsc @ccunix.ccu.edu.tw

Introduction

Software error compensation technique has been proven to be a cost-effective method to enhance the machine accuracy. Volumetric error compensation of a multi-axis machine, however, requires the detailed information of machine geometric errors which are usually calibrated using laser interferometers. Commercial laser interferometer systems such as the HP5529A are expensive because it requires different optic sets for each kind of geometric error. Geometric calibration using commercial laser interferometer is also time-consuming because each error calibration requires a tedious work for initial optic setup and manual laser-path alignment. These commercial laser interferometers, designed major for single axis movement calibration, are also very difficult for a diagonal measurement where multiple axes are moved simultaneously. However, the diagonal measurement is found to be a better presentation of volumetric accuracy for a multi-axis machine.

This work will report the development and application of using an auto-alignment laser interferometer system to calibrate the geometric errors of multi-axis machines. The auto-alignment laser interferometer system is able do any diagonal displacement measurement without the necessary of laser beam alignment. One application of the auto-alignment laser interferometer technique is that geometric errors (including the angular roll errors) can be quickly calibrated or estimated from the displacement measurements of some determined diagonal lines in the machine working zone. Some experimental result will be disucssed.

System Configuration

The auto-alignment laser interferometer system is based on a Hewlett-Packard HP5529A laser interferometer system. Fig. 1 shows the configuration of this system implemented in a three-axis CNC machine. The system includes a laser head, an interferometer mirror, a retroreflector mirror, a fiber optic bundle, a lateral effect photodetector and computer interfaces. For a conventional laser interferometer system, the laser head, interferometer and retroreflector must be carefully aligned to parallel the motion line of a machine axis before calibration. In this modified system, the laser path between the laser head and interferometer is connected using a fiber optic bundle developed by POINT SOURCE LIMITED. The laser from the laser source to the interferometer is connected by a single mode and polarization preserving fiber optic. The laser from the interferometer to the receiver is connected by a step-index multimode optic fiber. Using the optic fiber, the alignment between the laser head and inteferometer can be eliminated.

Laser path alignment between the interferometer and reflector is achieved using a lateral effect photodetector and computer interface techniques. A lateral effect photodetector is attached on the interferometer as shown in Fig. 2a. Laser beam reflected back from the retroreflector will return to the interferometer. Part of the returned laser will be reflected by the interferometer and be projected on the surface of the lateral effect photodetector. During measurement, the interferometer will be programmed to move along one machine axis which is called the active motion. If active motion causes any relative lateral displacement between the interferometer and retroreflector, the laser spot position on the photodetector will be changed too, as shown in Fig. 2b. The PC continuously monitors the changing of the laser spot position and informs the CNC controller to coordinate the relative lateral displacements between the interferometer and retroreflector in order to make the laser spot on the surface of photodetector back to the initial position. The coordinated relative lateral displacements between the interferometer and retroreflector are called passive motion here. Through the control of passive motion, the alignment between the interferometer and retroreflector during measurement can be maintained.

System Evaluations

The reflected light from the beam splitter of the interferometer is used to align the laser path. Because the beam splitter is coated with anti-reflection coating, the intensity of the reflected laser projected on the photodetector is very low. Therefore, the noise level or the stability of the laser spot position is concerned. It is found that the position stability of the laser position caused by noise level is within 0.01mm which is good enough for most applications. Conventional laser interferometer system using manual alignment is very difficult to achieve this level. Fig. 3 shows the measurement results along a single axis measurement. The displacement errors are measured three times in a very short time period in order to eliminate the environmental effect. It shows that the modified system gives the same or slightly better performance in repeatability than the original HP5529A. It was probably because the air-turbulence-caused deterioration of the laser properties between the laser source and interferometer mirror was eliminated by the optic fiber transmission. Demonstration of 3D diagonal measurements is presented in the Fig. 4. One application of the diagonal displacement measurement capability is the volumetric accuracy evaluation of a multi-axis machine. Because the fiber optic cable will be swung during measuring, it is concerned that the measurement stability due to the swing effect of the optic fiber calbe. Fig 5 shows the measurement result of Y-axis displacement error using different feedrates (300mm/min, 1000mm/min, 3000mm/min, and 6000mm/min). It is shown that the swing effect of the cable is very limited, if the feedrate is below 3000mm/min.

Geometric Error Calibration

Another application of the auto-alignment laser interferometer system is that geometric errors of a multi-axis machine can be quickly calibrated from the diagonal measurement capability. Using this method, optic sets for angular, straightness and squareness measurements of a HP5529A system can be eliminated. Sophisticated training of optic setup and alignment is also not required, because only simple displacement measurement is needed. Geometric errors (including the angular roll errors) can be calibrated or estimated from the displacement measurements of some determined diagonal lines in the machine working zone. For example, pitch and yaw error can be calibrated from displacement measurements of parallel lines with a known offset distance between them. Fig. 6. shows the measurement results of pitch angular errors using the modified system and HP5529A system.

Other geometric errors such as straightness, squareness and roll error can also be calibrated from 2D diagonal displacement measurements at some determined planes. Squareness can be calibrated from the displacement measurements of two diagonal lines of a plane. As shown in Fig. 7, if there is no squareness error, the displacement errors of the diagonal line AB would be same as the errors of the diagonal line CD. However, the displacement errors of the line AB and CD would be different if there is squareness existed. Similarly, roll errors can be calibrated from the displacement measurements of diagonal lines located in two parallel planes. As shown in Fig. 8, if there is no roll error, the displacement errors of the line AB will be same as the errors of the line CD. However, displacement errors of the line AB and CD will be different if there are roll angular errors exited in the machine axis. Fig. 9 shows the comparison of the roll errors measured by the developed system and by an electronic level. It shows that the results are closed.

As demonstrated in the reference [1], straightness error can also be calibrated from the displacment errors of three diagonal line of a plane. However, this method involves an iteration calculation of the displacement errors. If the machine repeatability is not good, the iteration procedure could cause accumulated estimation error which makes this calibration method unreliable.

Conclusions

An auto-alignment laser interferometer system for machine tool calibration has been demonstrated. This system can do diagonal displacement measurements without the necessary of time-consuming laser path alignment procedure. Geometric errors of a multi-axis machine can be quickly calibrated from the diagonal measurement. It is expected that the geometric errors of a machine tool can be calibrated within one hour using the auto-alignement laser interferometer technique, compared with a time of several days using the traditional laser interferometer system. However, estimation of the straightness errors from the displacement measurement may be unreliable if machine repeatability is poor. In summary, benefits expected from this new technique are: 1) ease of setup and no alignment required for any diagonal measurement, and 2) single set of optics for all 21 geometric error calibration.

Acknowledgment

This work was supported by the National Science Council grant No. NSC86-2212-E-194-006.

Reference

[1]. Zhang, G., Ouyang, R., Lu, B., Hocken, R., Veale, R., and Donmez, A., "A displacement method for machine geometry calibration", Annals of the CIRP, Vol. 37/1/1988

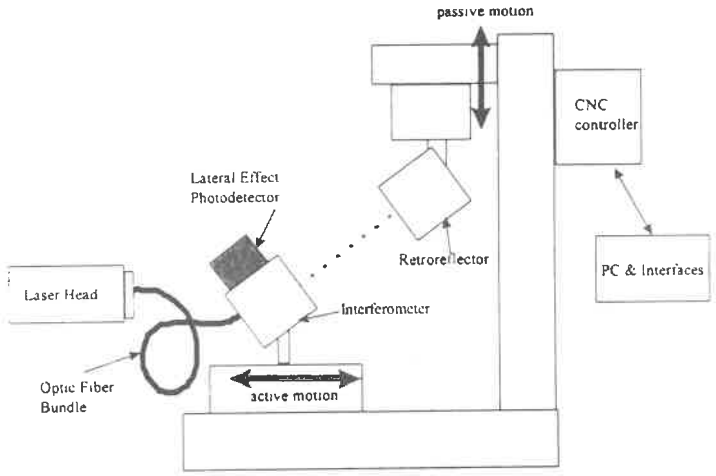

Fig. 1: The configuration of a auto-alignment laser interferometer

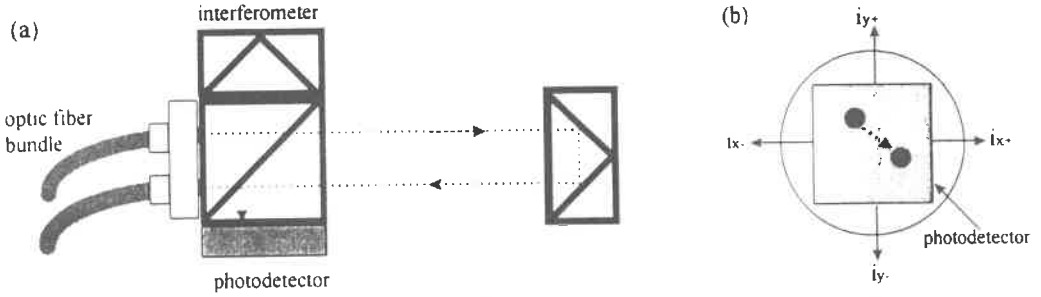

Fig. 2: Projection of the reflected back laser spot on the surface of the lateral effect photodector

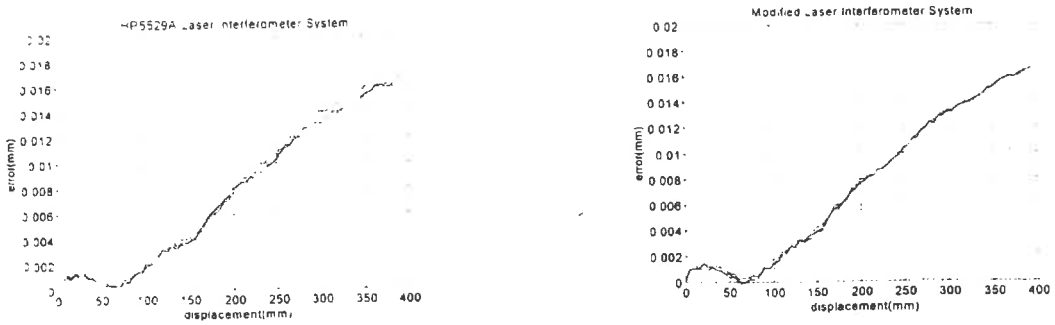

Fig. 3: Comparison of the modified system and the HP5529A

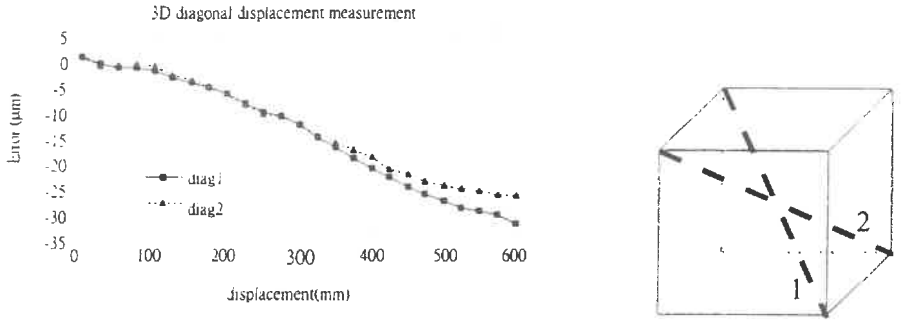

Fig. 4: Example of a diagonal displacement measurement

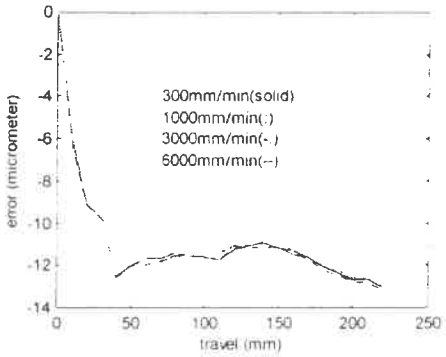

Fig. 5: Effects of machine feedrates

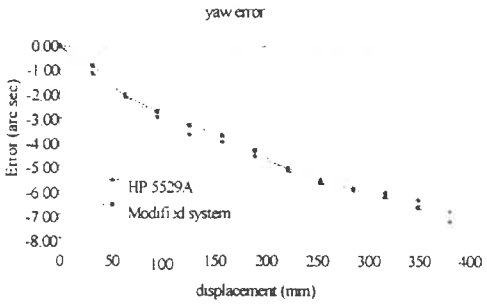

Fig. 6: Calibrated pitch angular error

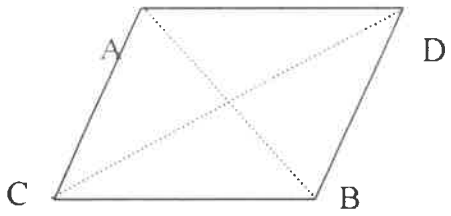

Fig. 7: Calibration of squareness

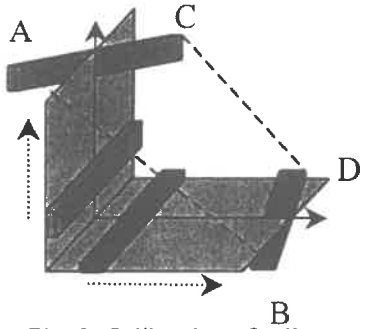

Fig. 8: Calibration of roll errors

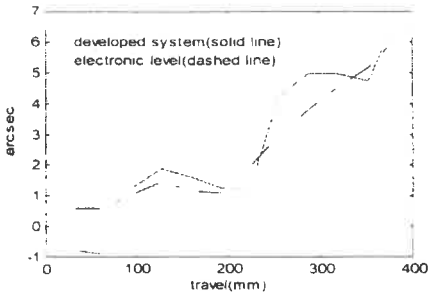

Fig. 9: Calibrated roll errors

PRECISION PROFILE MEASUREMENT OF ASPHERIC SURFACES BY IMPROVED RONCHI TEST

Seung-Woo Kim, Ho-Jae Lee
Korea Advanced Institute of Science and Technology, Department of Mechanical Engineering, Yusong-gu, Taejon, 305-701, Korea

Seong-Eun Lim,
Samsung Electronics, Core Technology Research Center, Suwon, 442-742, Korea

Abstract

We present an improved version of Ronchi test that is particularly intended for the precision profile measurement of aspheric surfaces of mold cores. A sinusoidal grating is used, instead of conventional rule grating, to obtain high quality lateral shear interferograms with only +1, 0, and -1 order diffraction terms. Undesirable higher order diffraction terms are inherently removed for better signal-to-noise ratio of measured interferograms. Further, the relative phases of interferograms are accurately computed by adopting phase-shifting technique along two orthogonal shear directions. Finally, the 3-dimensional profile of the aspheric surface under inspection is reconstructed using the wavefront extracted by a dual-path wavefront integration algorithm. As compared with the conventional Ronchi test, this improved version of Ronchi test provides a great improvement in measurement stability.

Keywords: Optical testing, aspheric surfaces, Ronchi test, lateral-shearing interferometer, sinusoidal gratings.

Introduction

Aspheric lenses are increasingly used in consumer products such as video cameras and compact disc pickups, as their mass production has become possible owing to recent remarkable innovations made in the ultraprecision plastic mold injection technology. However, still much work needs to be done for more effective manufacture of complex-shaped aspheric surfaces, especially in the area of precision profile measurement of fabricated mold cores and lenses. Traditionally various optical null tests have been widely used for optical surface quality assurance, but they are found not productive for aspheric surfaces due to the difficulty in preparing accurate aspheric reference surfaces. Instead, the principle of lateral-shearing interferometry draws much attention since it can operate without reference surfaces. The well-known Ronchi test is a special form of lateral-shearing interferometry in which necessary shearing is achieved by diffraction using a rule grating.[1]

Optical Setup and Measurement Theory

Figure 1 shows the optical setup of Ronchi test configured in this investigation. A collimated HeNe laser beam is focused by a microscope objective to form a point source at S_o. Then the diverging beam from S_o is directed to the aspheric test surface being measured and then reflected back through a beam splitter to converge to the point S_f that becomes the conjugate point of S_o. A sinusoidal rule grating is located at S_f to diffract the converging beam, and finally the -1, 0, and 1 order diffracted terms are imaged on a CCD array being overlapped to form Ronchigram.

The wavefront reflected from the test surface may be expressed as $w(x,y) = w_s(x,y) + w_a(x,y)$, i.e., the spherical term $w_s(x,y)$ and the non-spherical term $w_a(x,y)$. The spherical term may be explicitly written as $w_s(x,y) = (x^2 + y^2)/2d_2$ by adopting the Fresnel approximation, where d_2 is the distance from the surface to S_f. On the other hand, the non-spherical term $w_a(x,y)$ is to be directly measured to construct the whole wavefront $w(x,y)$. At the point S_f which corresponds the Gaussian image point of S_o, the spherical term cancels out and the complex amplitude is determined as [2]

$$g(u,v) = \exp[j\frac{\pi}{\lambda d_2}(u^2+v^2)]\iint_{P_1} f(x,y)\cdot\exp[j\frac{k}{d_2}(xu+yv)]dxdy \qquad (1)$$

where $f(x,y) = \exp[jkw_a(x,y)]$ and $k = 2\pi/\lambda$.

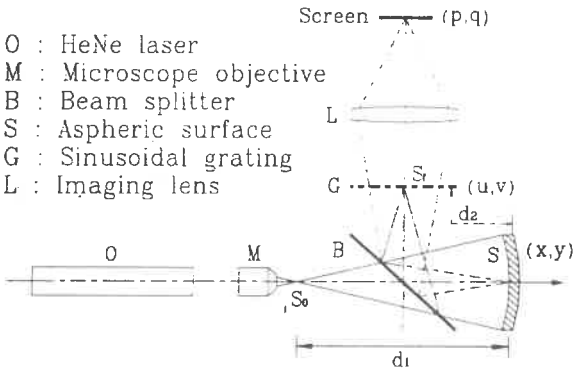

Figure 1. Optical setup for measurement of aspheric surfaces

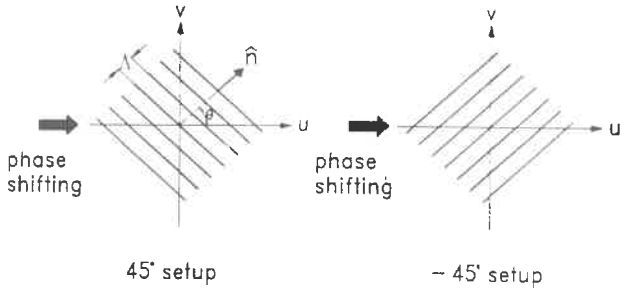

Figure 2. Alignment of sinusoidal grating

Figure 2 shows the orientation of the sinusoidal grating aligned in the uv-plane, in which Λ and $\bar{n}$ represent the pitch and the normal vector of the line grating, respectively. The transmittance of the grating is given by $t(u,v) = 1 + \cos[(2\pi/\Lambda)\bar{n}\cdot\bar{r}]$, which is obtained as

$$t(u,v) = 1 + \frac{1}{2}\left[\exp[j\frac{2\pi}{\Lambda}(u\cos\theta + v\sin\theta)] + \exp[-j\frac{2\pi}{\Lambda}(u\cos\theta + v\sin\theta)]\right] \qquad (2)$$

The complex amplitude of the beam right after the grating is modulated such as $g(u,v)\cdot t(u,v)$. The CCD array is placed on the conjugate plane of the test surface, thus the intensity distribution on the CCD array becomes the inverse Fourier transform of $g(u,v)\cdot t(u,v)$, which is worked out as

$$I(p,q) = I_0\left[I_{(0,1)}(p,q) + I_{(0,-1)}(p,q) + I_{(1,-1)}(p,q)\right] \qquad (3)$$

In the above, I_0 is the mean intensity, $I_{(0,1)}(p,q) = \cos\left[k\{w_a(p,q) - w_a(p-s_p, q-s_q)\}\right]$, $I_{(0,-1)}(p,q) = \cos\left[k\{w_a(p,q) - w_a(p+s_p, q+s_q)\}\right]$, $I_{(1,-1)}(p,q) = \cos\left[k\{w_a(p-s_p, q-s_q) - w_a(p+s_p, q+s_q)\}\right]$, $s_p = \lambda m d_2 \cos\theta/\Lambda$, $s_q = \lambda m d_2 \sin\theta/\Lambda$ where m is the magnification of the imaging lens. The intensity distribution in fact results from the interference occurring among the -1, 0, and 1 order

diffracted beams of Eq.(1).

Phase-shifting technique may be usefully adopted to analyze the Ronchigram of Eq.(3). If an equal amount of phase shift $2\pi / N$ is induced N times successively, the relative phase to be determined is related to the non-spherical wavefront such as [3]

$$\tan\phi(p,q) \equiv \sum_{n=1}^{N} I_n(p,q)\sin\Delta_n \Big/ \sum_{n=1}^{N} I_n(p,q)\cos\Delta_n = \tan\left[\frac{\partial w_a}{\partial p}s_p + \frac{\partial w_a}{\partial q}s_q\right] \qquad (4)$$

where $\Delta_n = (2\pi / N)(n-1)$. Therefore, once $\phi(p,q)$ is determined from Eq.(4), $w_a(p,q)$ is then computed through an appropriate integration process. For accurate computation of $w_a(p,q)$, it is necessary to incline the grating as shown in Figure 2 and also to implement phase-shifting technique twice with $\theta = +45°$ and $-45°$, respectively.
As the final step of the measurement, the surface profile is reconstructed from the measured wavefront $w(x,y) = w_s(x,y) + w_a(x,y)$. If it is assumed that the incident beam to the surface is in parallel with the optical axis as illustrated in Figure 3, the surface slope is related to the wavefront such as

$$\frac{\partial S}{\partial x} = \frac{1-\tan^2\vartheta_x}{2}\frac{\partial w}{\partial x} \quad \text{where} \quad \tan 2\vartheta_x = \frac{\partial w}{\partial x}. \qquad (5)$$

As for the general case when the incident beam is not in parallel with z-axis, the relationship between S and w becomes complicated to require numerical computation. Further description is omitted here for space limitation.

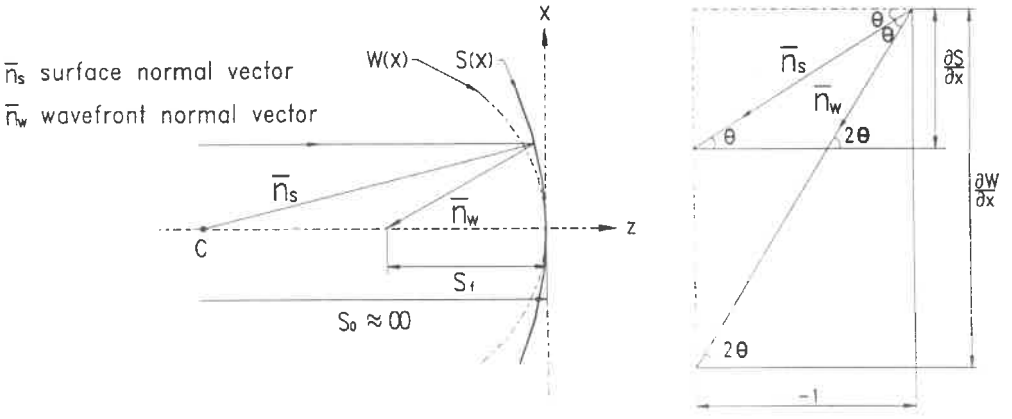

Figure 3. Relation between aspheric surface(S) and wavefront(W)

Experiment and Discussion

Figure 4 shows a typical Ronchigram and its corresponding profile of the test surface. Two different types of line gratings, one is the conventional rule grating of square transmittance fabricated by electron-beam lithography, while the other a sinusoidal grating made by holographic process on polyester film. Theory previously described predicts that the two films provide identical results, as higher order terms of diffraction than -1, 0, 1 do not affect the measurement. In practice, however, the square grating tends to generate more noises

deteriorating measuring accuracy. Figure 5 demonstrates a comparison of measurement results in that the sinusoidal grating provides a higher repeatability than the square grating in wavefront reconstruction.

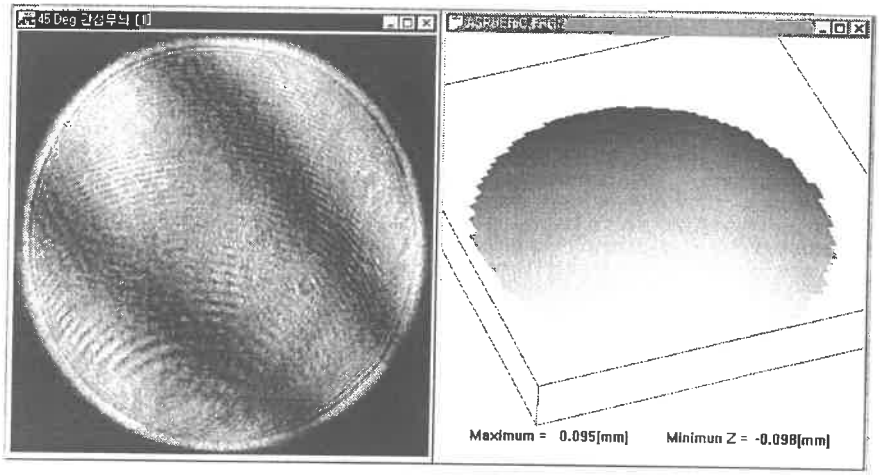

Figure 4. Ronchigram and reconstructed surface profile

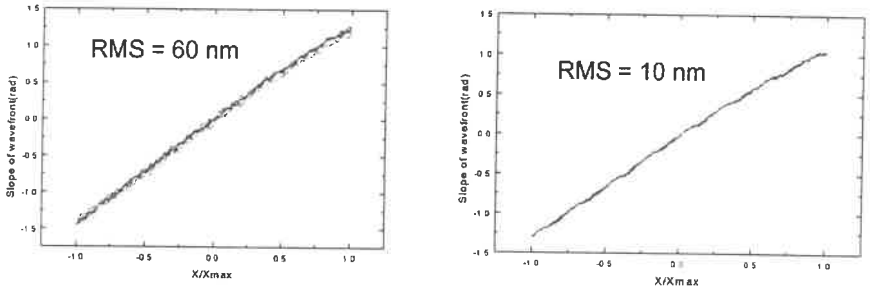

(a) square grating (b) sinusoidal grating

Figure 5. Reconstructed wavefront derivatives

Conclusion

An improved method of Ronchi test has been proposed with the intention of precision profile measurement of aspheric surfaces. Particular emphasis has been placed on generalization of measurement theory so that a flexibility of optical setup is gained in handling short-focal-length surfaces with large numerical aperture by using a point source laser beam instead of plane wave for illumination. In addition, a great enhancement in measuring accuracy has been achieved by compensating for the alignment errors of optical components through a well-established relationship between the measured fringe intensities and the surface profile.

References

[1] D. Malacara, "Optical shop testing," John Wiley & Sons, Inc., 2nd edition, 1992.
[2] A. VanderLugt, "Optical image processing," John Wiley & Sons, Inc.,1992.
[3] K. Omura, T. Yatagai, "Phase measuring Ronchi testing," Appl. Opt., 27, 523(1988).

Surface and Form On-Machine Metrology / Correction System for Ultraprecision Machining and Grinding

Gene Malkin
Precitech Inc.
Keene, NH 03431

Introduction

Modern methods of computer-assisted material processing, like diamond turning lathes and precision grinding machines [1], provide part surfaces with high-quality finish and of sub-micron form accuracy. Metrology control of these surfaces is a complicated and time consuming part of the manufacturing process, and is generally performed "off-line" on expensive stand-alone profilometry or interferometry devices [2].

The precision and repeatability of modern ultra-precise material processing machines are so high that in most cases the part form error originates not from machine inaccuracy but from the cutting process peculiarities, errors of tool path programming or from imperfect tool form. These errors can be investigated by using the cutting machine itself as a measuring device. This paper presents an on-machine technique for form error measurement and in-process corrective compensation.

System description

The system utilizes an ultra-precise air bearing Linear Variable Differential Transformer (LVDT) probe, mounted on a kinematic holder near the cutting tool. The kinematic holder allows the LVDT probe to be removed during the cutting process and subsequently replaced for measurement. The working linear range of the probe is ±40μm with 10nm resolution. The probe collects data by traversing the machined part surface with its ruby ball tip. All special hardware and software for the probing and tool path correction resides on the machine's controller and forms a system called *Ultracomp*™.

The input of the procedure is two blocks of data: initial tool path program, i.e. set of coordinates of tool origin (T on the scheme) along the tool path; and a set of coordinates of corresponding surface points S being processed (for each T_i point there is some S_i point)

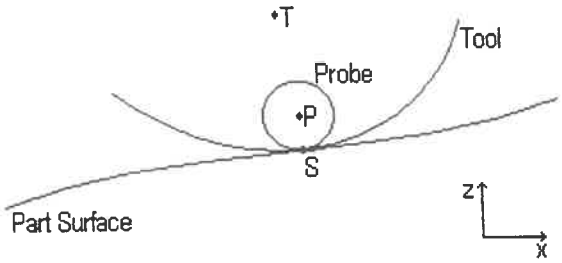

Knowing the probe ball geometry, the *Ultracomp*™ system estimates the position of the probe ball (P on the scheme) for contacting every surface point S and generates a theoretical probe path for each specific surface. The LVDT probe follows that theoretical path and measures its real (x;z)-position.

The measured data is smoothed and interpolated to present a measured probe position for the same x-coordinates. The next step is to make the measured and theoretical probe paths correspond. If the position of the probing ball in the machine coordinate system is known with some error, the measured data is shifted with respect to theoretical, and their "difference graph" exhibits some slope. The optimization procedures shift the measured data to remove all x- and z-offsets. The difference of the z-coordinates of the measured and theoretical data represents the first order of part form error. Finally, the form error graph is displayed on the controller screen.

If one assumes that the part form errors are produced only by the errors of tool path, the subtraction of those errors from tool z-coordinates in initial NC-program should compensate the part program and correct form errors.

A special calibration procedure has been developed for recording probe geometry. Detailed mapping of the probe's ruby tip can be done in minutes by probing a master spherical artifact (traceable to NIST) of known radius. This procedure is similar to the measurement of a machined part: a theoretical probe path along the artifact is calculated based on the nominal ruby tip radius. The LVDT collects data, this data is compared with a theoretical one and form error data is generated. An iterative process estimates the best sphere fit radius for the tip. These radius and shape deviations of the probe ball from the sphere are stored in a special calibration file that is used for probe path generation. Non-spherical irregularities of ruby balls used in *Ultracomp*™ were found to be less than 80nm.

Discussion

Examples of part generation, measurement and correction cycle are shown in figs.1-2 together with comparison part interferograms. It has been demonstrated that the on-machine metrology / correction system allows a decrease of overall part form error from several microns to submicron level within a single iteration.
There are three ranges of surface error, caused by different physical reasons:

- small-range surface errors (noise, vibration, resonances, etc.), that are non-repeatable and affect mostly surface roughness;
- medium-range errors (tool defects, e.g. waviness) bring repeatable local form defects;
- long-range form errors (e.g. tool form differs from theoretical one).

The *Ultracomp*™ on-machine metrology system has been proven to detect all three given types of surface errors. It displays the form error graph and allows the technician to study the various parameters of the workpiece without removing it from the machine. However, the most effective application of the system is the on-machine correction of the repeatable medium and long range errors. These errors may be caused by tool waviness, positive or negative rakes, cylindrical clearences, etc.

Methods of surface measurement, data processing and tool path correction described above are currently being used both for diamond turning and periphery grinding. However, grinding often produces its own specific form errors.

Form errors unique to grinding include:

1) A sharp negative part form error (hole) in the center that originates from the fact that central area of the part has smaller longitudinal speed and the grinding wheel forces continually vary;
2) A form error produced by the error in grinding wheel radius estimation.

Since an error of the first type strongly depends on various grinding process parameters (material, wheel properties, cutting speed, speed of spindle rotation, etc.), it can be overcome empirically by making a trial cut, measuring the part and generating a new path that should compensate for the error. The measurement / compensation technique described here has proved to be a very effective method for removing the center hole error.

Wheel radius problems are very common in grinding. Since the wear of the grinding wheel (i.e. change of its curvature radius) occurs quickly, the precise tool geometry during tool path generation is very difficult to consider.
It can be shown that for the pure spherical part, error Δ in tool radius produces the same form error $|\Delta|$ in part curvature (same sign for a concave part and opposite sign for a convex part). In many cases of aspheric parts it can be assumed that the part profile function can be presented as the sum of aspherical and spherical components and their ratio can be considered $<< 1$ for most of the part. If a best sphere fit radius for the measured part is known, then the data can "redistribute" form error according the following scheme:

"Real part profile" = "Design sphere" + "Design Asphere"+ "Form error" =
= "New best sphere fit" + "Design Asphere" + "New form error" (1).

Therefore the deviation of the best fit sphere radius from the design sphere radius gives the estimation of the grinding wheel wear. The *Ultracomp*™ system performs this analysis which helps an operator estimate the error of part global curvature and the wear of the grinding wheel or diamond tool.
There are cases in optical design when tolerances of the radius of curvature of spherical components are less severe than for aspheric components. If in that case the radius of the "new best fit sphere" (1) satisfies tolerance requirements, we can use the "new form error" for tool path correction. Since that error can be substantially less than the full form error, that simplifies the compensation process.

Summary

Method of on-machine part form and surface measurement and compensation implemented in the *Ultracomp*™ system have proved to be equally suitable for both single point diamond turning and precision grinding. The system provides simple and fast metrological control of machined ultra-precise axially symmetric surfaces. Moreover, it can substantially reduce or eliminate repeatable form errors and improve surface quality.

References

1. Alexander H. Slocum, "Precision Machine Design", Prentice Hall, 1992
2. Daniel Malacara "Optical Shop Testing" John Wiley and Sons, 2nd ed., 1992

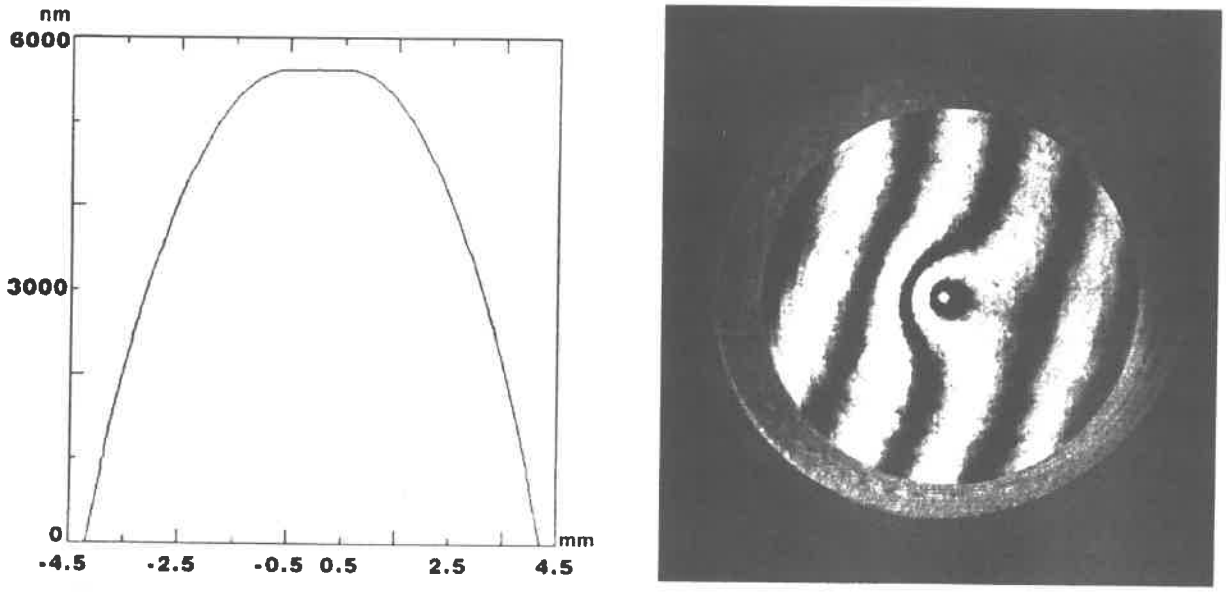

Fig. 1 The form error graph (left) of the diamond turned brass convex part (8mm radius of curvature) measured by the on-machine metrology system and the interferogram of the same part (right) for comparison. The on-machine system detects and eventually corrects not only the deviations from the spherical form seen on the interferogram, but also the general form error (error in part curvature) that is more than 5μm in this example.

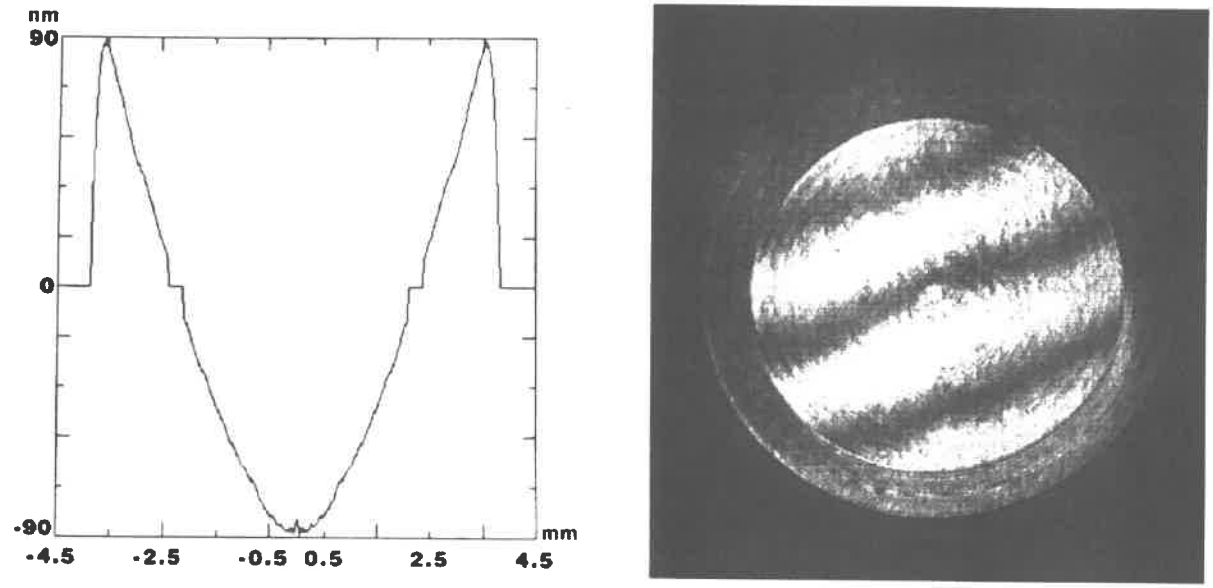

Fig. 2 The form error graph (left) and the interferogram (right) of the same part from fig.1 after the on-machine measurement and tool path correction have been performed. Total residual form error of the part is 180nm.

Development of Non-contact Measuring Machine for 3D Micro Pattern in Semiconductor Wafer using a New Optical Probe Implementing High Performance Optical Window

Heui Jae Pahk, Woo Jung Ahn
Dept. of Mechanical Design, Seoul National University, Seoul, Korea
Sung Wook Cho
Halla Optical Engineering, Seoul, Korea

1. Introduction

In recent years, quantitative measurement of 3 dimensional surface pattern has been increasingly applied in many science and engineering fields, and there have been several methods for the surface pattern measurement : Stylus based method, auto-focus based method, interferometric method, SEM(Scanning Electronic Microscope), and SPM(Scanning Probe Microscope), etc. In the case of semiconductor wafer, 3 dimensional pattern characteristics such as depth profile of chemically processed IC pattern was to be measured for the quality control of wafer manufacturing processes. Traditionally, SEM was used partly, but it caused inconvenience in wafer destruction and vacuum environment.

In this paper, a new type of non-contact/nondestructive measuring machine has been developed, comprising a new optical probe, precision stages, and controllers. The new optical probe has been designed and implemented around light illumination, optical lenses, optical window, and beam splitter. Efficient image processing algorithm has been developed in order to analyze the 3D micro pattern. The developed system has been successfully applied to measure the wafer surface, giving few nanometer vertical resolution.

2. Theoretical Backgrounds for the Optical Probe

2.1. Blur Image

The new optical probe, which is a key feature of the developed measuring machine, has been newly developed. Fig.1 shows the basic principle of the developed optical probe for the height measurement. Let I,II are the objects having δ height difference. When the objects I, II are transformed to image through the optics, the image A_1, A_2 are formed at each focal plane, whose distances are b_1,b_2 from the lens, respectively.

When a CCD plane is located at the focal plane of the object I (b_1 distance), a sharp image of size A_1 and a blurred image of size R are formed at the b_1 focal plane. The blurred image is traditionally ignored or avoided, but it is fully used for the height measurement in this research.

From the law of geometric optics, the following two equations are derived.

$$\frac{1}{a}+\frac{1}{b_1}=\frac{1}{f} \qquad \text{(Object I)} \tag{1}$$

$$\frac{1}{a-\delta}+\frac{1}{b_2}=\frac{1}{f} \qquad \text{(Object II)} \tag{2}$$

, where f is the focal length of the lens.

From the geometric similarity of triangles,

$$a : b_1 = S : A_1 \tag{3}$$

$$a-\delta : b_2 = S : A_2 \tag{4}$$

where S is the size of object.

From eq(3),(4), the relationship between the height difference(δ) and the blur image size(R) can be constructed. That is,

$$\delta = a - \frac{ab_2}{b_1 \frac{A_2}{A_1}} = a - \frac{ab_2 A_1}{b_1(A_1 + R)} \tag{5}$$

where a, b_1, b_2 are the distances from the lens, and A_1 is the image size of object I, and R is the size of the blur image.
Therefore when the sizes of object image(A) and blur image(R) are measured, the height data(δ) can be calculated from eq(5), if the coefficients are evaluated by the least squares technique.

2.2. Calibration Algorithm using Least Squares Technique

In order to obtain the accurate height data, δ, the calibration procedures are followed.
Prior to calibration, eq(5) can be arranged in simpler form, that is,

$$\delta = C_1 - \frac{C_2}{k} \tag{6}$$

where C_1 equals to a, C_2 is ab_2/b_1, and k is the ratio of image size A_2/A_1.
Based on measured data set (δ_i, k_i) for a master specimen, eq(6) can be expressed as follows.

$$k_i\delta_i = C_1 k_i - C_2 \tag{7}$$

For N data sets, the sum of squares of error, E, is

$$E = \sum_{i=1}^{N} (k_i\delta_i - C_1 k_i + C_2)^2 \tag{8}$$

Applying variational principle,

$$\frac{\partial E}{\partial C_1} = 2\sum_{i=1}^{N} (k_i\delta_i - C_1 k_i + C_2)(-k_i) = 0$$

$$\frac{\partial E}{\partial C_2} = 2\sum_{i=1}^{N} (k_i\delta_i - C_1 k_i + C_2)(1) = 0$$

Thus

$$C_1 = \frac{\begin{vmatrix} \sum k_i^2\delta_i & -\sum k_i \\ -\sum k_i\delta_i & N \end{vmatrix}}{\begin{vmatrix} \sum k_i^2 & -\sum k_i \\ -\sum k_i & N \end{vmatrix}} = \frac{N\sum k_i^2\delta_i - \sum k_i \sum k_i\delta_i}{N\sum k_i^2 - (\sum k_i)^2}$$

$$C_2 = \frac{\begin{vmatrix} \sum k_i^2 & \sum k_i^2\delta_i \\ -\sum k_i & -\sum k_i\delta_i \end{vmatrix}}{\begin{vmatrix} \sum k_i^2 & -\sum k_i \\ -\sum k_i & N \end{vmatrix}} = \frac{-\sum k_i\delta_i \sum k_i^2\delta_i + \sum k_i^2\delta_i \sum k_i}{N\sum k_i^2 - (\sum k_i)^2} \tag{9}$$

Therefore coefficients C_1, C_2 are evaluated using the least squares technique, completing relationship between the height data, δ, and the ratio of image size, $(A_1+R)/A_1$

2.3. Optical Window for Light Slit and Image Processing Algorithm

The optical window is inserted between the lenses and the splitter for making light slit and windowing the object size. Fig.2 shows the measured image of several step heights on a wafer surface. In the Fig.2, the sharp image is the image of reference step height, and the blur images are the images of step heights to be measured. Using the principles of the blur image, the step height data can be calculated along the vertical line. The object images are captured by a CCD camera associated with

magnifying optics system. The captured image is then processed to give the height data using image processing algorithm developed. The measured step height data are shown on the left of the figure. Therefore step height measurement has been implemented using the optical window and associated optical principles. Also, the feature of line scanning has been implemented.

3. Measurement System

The developed measuring machine consists of the optical part with illumination, mechanical part for motorized wide range scanning, and software part for operating measurement system.
Fig.3 shows the block diagram of optical and illumination part. The image frame grabber is implemented for capturing CCD camera image, and a light controller is also used for the illumination control. The whole optical image processing and illumination control are performed under Windows based image analysis and light control software developed.
For scanning wide range of wafer surface, a precision X-Y stage has been designed using air bearing, linear motor, optical scale, granite surface plate. Z-W-Theta stage also has been designed for the wafer handling and focus adjustment. Fig.4 shows the block diagram of mechanical motion control, where brushless linear motor, stepping motor, DC motor controllers are implemented. The whole motion control is operated by the Windows based motion control software developed. Thus it is possible to select specific measurement location within wafer surface by the menu driven software developed.
Fig.5 shows the non-contact measuring machine developed.

4. Practical Application to Wafer Surface

The developed measuring machine has been practically applied to DRAM wafer surface. The scanning area is chosen as 20um x 20um, and the optical probe line-scans the wafer surface at 0.1 um interval in the horizontal direction. Fig.6 shows the 3D plot of the measured wafer surface, giving height properties such as flatness. Three dimensional roughness parameters have been successfully evaluated by the developed measurement software, based on the optical measurement data. The measurement resolution has been achieved around few nanometers.

5. Conclusion

(1) A new measuring machine for 3D micro pattern of wafer surface has been developed, giving nondestructive measurement feature with less than 10 nanometer resolution.
(2) A new optical probe has been designed and implemented using the blur image of non-focused object. The feature of line-scanning capability of the optical probe has been found very much effective in practical measurement application.
(3) For scanning wide range of wafer surface, precision XY stage, Z-W-Theta stage have been designed, and the measurement region can be easily selected within whole wafer surface by user-interactive software developed.
(4) Variety of surface properties such as flatness, 3D roughness parameters can be evaluated by the measurement software developed, and is believed to replace SEM in many 3 dimensional pattern measurement, as the developed system does require neither vacuum environment nor specimen destruction

Reference

1. M. Subbarao, G.Surya, "Depth from Defocus: A Spatial Domain Approach", International Journal of Computer Vision, 13, 3, 271-294, 1994
2. M. Subbarao, Tae Choi, "Accurate Recovery of Three-Dimensional Shape from Image Focus, IEEE Trans. On Pattern Analysis and Machine Inteligence, Vol17, No.3, March 1995

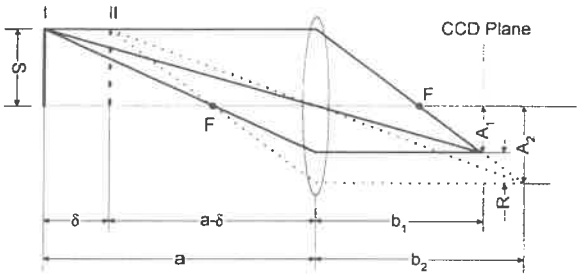

Fig.1 Basic Principle of the Optical Probe

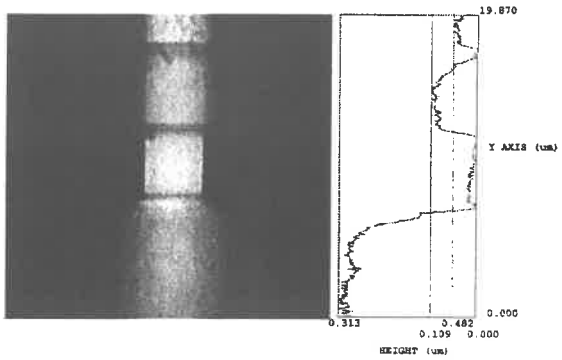

Fig.2 Image of Measured Area

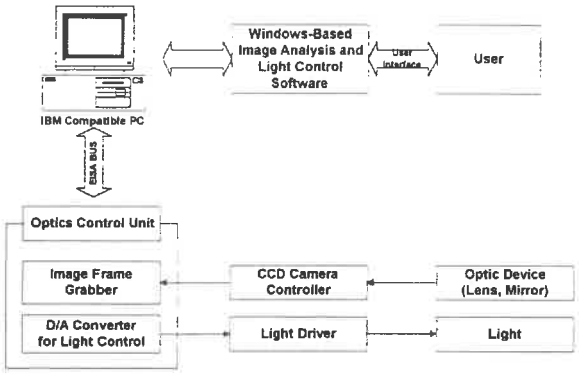

Fig.3 Block Diagram of optical and illumination part.

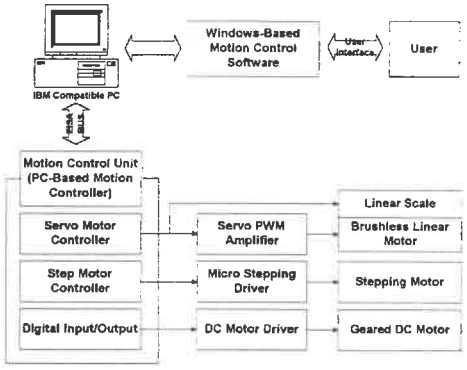

Fig.4 Block Diagram of Mechanical Motion Control

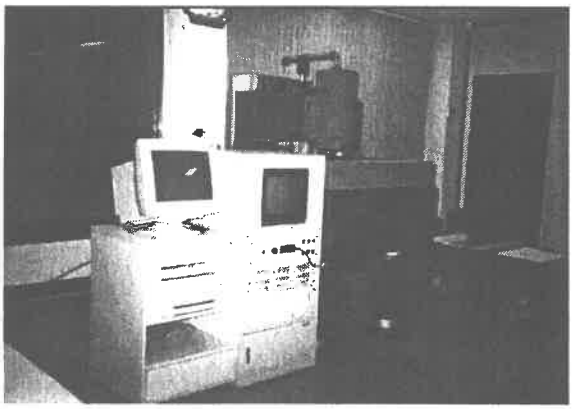

Fig.5 The Developed Non-contact Measuring Machine

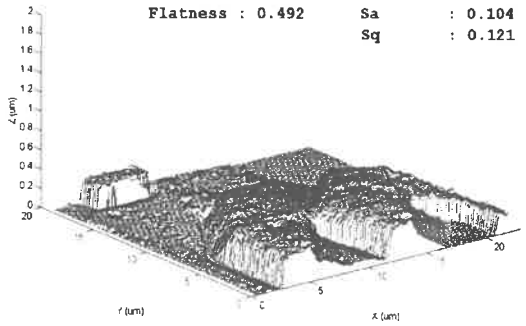

Fig.6 3D Plot of the Wafer Surface Measured

Development of a 2D probing system with nanometer resolution

Pril W.O., Struik K.G., Schellekens P.H.J.
Eindhoven university of technology
Eindhoven, the Netherlands

Abstract:
A newly developed 2D probing system for a small Coordinate Measuring Machine (CMM) with nanometer resolution and low probing force is presented. The instrument has been built and the first tests have been carried out, which will be presented here.
The probes measuring system is based on a Laser-Diode-Grating-Unit (LDGU). Used in CD-players, it is a cheap, mass produced component. The LDGU here measures two degrees of freedom of a mirror attached to the stylus: vertical translation and a tilt around one horizontal axis. The resolution has been measured to be 1 nm in vertical direction and 100 nm in one horizontal direction.
Special attention has been paid to the static and dynamic probing force to prevent indentations on the workpiece. The stylus with the attached mirror is kinematically suspended from the probe housing by three small leaf springs. The stiffness of the suspension is very low, allowing a static probing force of 1 μN. The dynamic measuring force when probing the workpiece can be orders higher than the static force, especially when the mass directly connected to the stylus is high. A very low moving mass of 4 mg limits the dynamic force to some mN or less, depending on, among others, contact velocities and probe ball diameter. This is small enough to prevent even very soft materials from being damaged. The possibility of measuring elastic samples, e.g., small plastic components, is another significant advantage of this low probing force.
Several precautions have been taken to prevent thermal drift. The probe housing is made from invar. The heat (80 mWatt) generated by the LDGU is conducted out of the construction by a thermal path that is to a large extent separated from the mechanical path.

Introduction

As miniaturization goes on, tolerances on dimensions become smaller and smaller. Often a Coordinate Measuring Machine (CMM) is used to check these dimensions because of its versatility and ease of use. However, for the most accurate parts, made e.g. on precision turning machines, two problems with the use of commercial CMM's arise:

- The CMM inaccuracy is 0.5 μm or more, which is comparable to the accuracy that can be reached with nowadays precision manufacturing techniques.
- Probing forces of normal CMM probes are too high for the materials that are often used for precision products. Measuring forces of 0.1 N or more are common. At the moment of probing, however, the (dynamic) forces are mostly much higher[1]. These forces may damage the surface of certain materials, such as aluminium, brass and even steel.

In our group two CMM's are being developed, one with an inaccuracy below 0.1 μm in a measuring volume of 1 dm^3 [2], the other especially for scanning, with a measuring volume of several cm^3 and a very fast z-axis with an accuracy in the nm region. Both CMM's require a newly developed probing system with high accuracy and low probing forces. A 2D probing system fulfilling these demands is described here. It is mainly intended for the scanning CMM, where two dimensions will satisfy in most cases. The second dimension is advantageous compared with 1D probes, because they may have problems detecting steep edges. In the meantime valuable experience can be gained for developing a full 3D version.

Working principle

In figure 1 the working principle of the probe system is shown. The stylus (S) is suspended elastically (c) to the probe house (details will follow). An optical measuring system was chosen because it is contactless and only a small mirror (M) has to be attached to the stylus. This is important because the smaller the moving mass of the probe, the smaller the probing forces will be as will be shown in the next paragraph. The measuring system uses a Laser Diode Grating Unit (LDGU) used in commercial CD-players[3]. Due to mass production this is a cheap but nevertheless accurate measuring tool. It contains a laserdiode (L), four photodiodes (D1...D4), and a grating (G). The light from the laser is focused by two lenses (L1 and L2) on the mirror and then reflected back into the LDGU. Passing through the grating the first order beam is split in two half beams which are imaged on D1 till D4. Depending on the imaging of the focal point of the half beams in front of or behind the diodes, D1 and D4 or D2 and D3 are illuminated. The Focal Error Signal (FES) is defined as[3]:

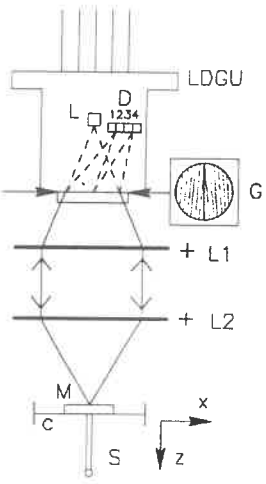

figure 1: working principle

$$FES = \frac{D1 + D4 - (D2 + D3)}{D1 + D2 + D3 + D4} \qquad (1)$$

where D1..D4 are the signals of the photodiodes. In the transitional zone the sensitivity for z-displacement of the mirror is very high. Besides z-position, the LDGU can also measure tilt of the mirror in one direction (RES: Radial Error Signal)[3]:

$$RES = \frac{D1 + D2 - D3 - D4}{D1 + D2 + D3 + D4} \qquad (2)$$

The focal lengths of L1 and L2 determine the sensitivities of the system:

$$S_{RES} \propto \frac{f_2}{f_1} \qquad S_{FES} \propto \left(\frac{f_1}{f_2}\right)^2 \qquad (3)$$

Two lenses with a small focal length of 9 mm were chosen, leading to high S_{FES} in comparison with S_{RES} and a compact design. The photo currents of the photodiodes are about a microampere which must be measured with an inaccuracy of a few nanoamperes. Therefore the wiring between the diodes and the preamplifiers may not be longer than a few centimeter, so preamplifiers were integrated in the probe system. Micropower opamps, consuming no more than about one mWatt each, are used to limit thermal drift. An SMD version of the IC makes them fit in the very limited space available in the probe system. Before the mechanical details will be discussed, first some remarks on probing forces will be made, because two important design parameters will be derived from this.

Probing forces

As mentioned earlier, the probing force is a big problem when using CMM's in precision metrology. In order to estimate how low the probing force should be to prevent plastic deformation, a model of the probing procedure was made, part of which is described by van Vliet[1]. It is also used to deduce design parameters. Three forces, originating from different events, can be distinguished:

- Collision force F_{col}. This force acts at the moment when probing the sample. The moving parts of the probe, i.e. stylus and moving part of the measuring system, have to be decelerated, which leads to forces between probe and sample. During this collision the probe may bounce once or several times.
- Overtravel force F_{ovt}. After receiving a stop signal from the probe, the CMM moves on a certain distance, called overtravel, which stretches the springs of the probe suspension leading to an elastic force between sample and probe. Because the maximum of F_{ovt} occurs when F_{col} has decreased to almost zero, both forces can be compared with the admissible force F_Y separately.
- Measuring force. This force works between sample and probe when the data point is taken. Its magnitude is usually adjustable. Although this is the force specified for most probe systems, it is not really important when considering damaging of the workpiece, because it is generally much smaller than the previously mentioned dynamic probing forces.

Both F_{col} and F_Y can be calculated using Hertzian spherical contact theory, described in e.g. Szabó[4] and van Vliet[1]. Derivation in other directions is not mentioned here because the forces in z-direction are most critical in our situation.

$$F_Y = 2.1\frac{R^2 Y^3}{E^{*2}} \quad [N]$$
$$\frac{1}{E^*} = \frac{1-\upsilon_1^2}{E_1} + \frac{1-\upsilon_2^2}{E_2} \quad [m^2/N] \tag{4}$$

$$F_{col} = \left(\frac{5mv^2}{4\alpha}\right)^{\frac{3}{5}} \ [N], \qquad \alpha = \left(\frac{9}{16E^{*2}R}\right)^{\frac{1}{3}} \ \left[m/N^{\frac{2}{3}}\right] \tag{5}$$

As can be seen in (5) F_{col} and F_Y are dependent from a number of parameters:

E_1, E_2	Young's moduli of probe ball and object material
υ_1, υ_2	Poisson moduli
Y	Yield strength of the workpiece (provided that the yield strength of the probe ball is higher). In practical situations comparable to $\sigma_{0,2}$.
R	Probe ball radius
v	probing speed
m	Moving mass of the probe

Because of the expected size of the workpiece it should be possible to measure with small probe ball diameters (e.g. 0.3 mm), which leads to an admissible probing force of one to several mN. For practical reasons v should be at least 1 mm/s, which limits the moving mass to several milligrams at most for reasonable object materials.

Assuming an overtravel of 5 µm, being the design value for our dm^3 CMM at a probing speed of 1 mm/sec, it follows from (4) that $c_z < 0.1\ N/mm$, where c_z is the stiffness by which the moving part of the probe is connected to the probe house. In spite of this small stiffness the eigenfrequency of the probe is still very high, namely 800 Hz.

Elastic Suspension

The stylus is suspended elastically to the probe house by three leaf springs (figure 2) to enable sufficient overtravel of the CMM. The stylus is connected to them by an intermediate part. The leaf springs give the stylus three degrees of freedom: translation in z-direction, and rotation along x- and y-axis. The rotations give rise to pseudo translations at the probe ball position in y and x respectively, so it can be moved in three directions. No other intermediates are needed for this suspension so that the moving mass can be kept small. Another advantage is the ease of manufacturing: because the leaf springs are all in one plane it can easily be etched from sheetmetal. Using elastic theory the stiffness in all directions can be calculated, providing that the displacements are small[5]:

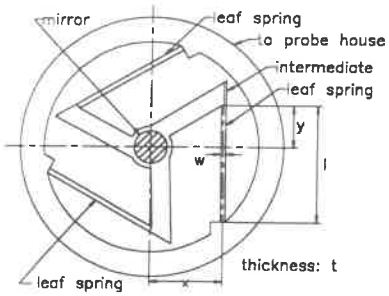

figure 2: elastic suspension

$$c_z = 3\frac{Ewt^3}{l^3}$$
$$c_{xy} = \frac{3Ewt^3}{ll_{st}^2}\left(\frac{1}{2(1+\upsilon)}\alpha_t - \frac{y}{l} + \frac{1}{12} + \frac{y^2}{l^2} + \frac{x^2}{l^2}\right) \qquad (6)$$

where E and υ are Young's and Poisson moduli, and t the thickness of the leaf springs. l_{st} is the stylus length and α_t is a torsional 'constant' depending on t/w. It approaches 1/3 for small t/w. Note that the stiffness is independent from the direction of probing in the xy-plane. In order to get F_{owl} below F_y, c_z and c_{xy} should both be smaller than 100 N/m, which is obtained by using 20 μm thick spring steel for the leaf springs.

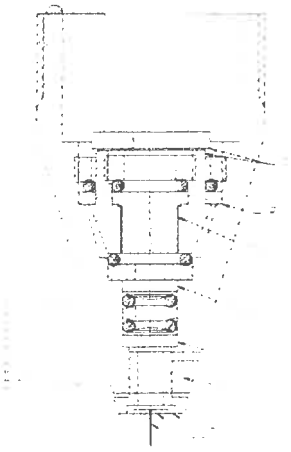

figure 3: construction

Mechanical design

LDGU (1), lenses (2,3) and a subassembly with leaf springs (4), mirror (5), and stylus (6) have to be positioned with nanometer stability (the numbers refer to figure 3). This is extremely difficult because the laserdiode in the LDGU dissipates about 80 mWatt. Therefore most parts were made from invar. To conduct the heat out of the construction an aluminum thermal path (7) was included, insulated by plastic (8) and air from the rest of the structure. Although the LDGU is fixed by the aluminum, no thermal length is bridged by it. Outside of the construction the heat should be transferred to the air by heatsinks, either passively, or actively by using Peltier elements.

An adjusting mechanism (9) was added to fix the mirror within the range of the measuring system. A lot of attention was paid to the outer dimensions: The probe system should be as narrow as possible so the tip can be seen from a reasonable angle.

Measurements

Measurements in z-direction were done, using a calibrated laser interferometer as a reference. A piezo actuator was used to move the stylus over a 3 μm distance. Due to the use of a C-frame support it is impossible to evaluate drift, because the expected considerable drift in the support cannot be distinguished from the drift in the probing system.

A better setup is being developed, but it's not yet available at the time of writing. The resolution, limited by the noise, is measured to be less than 1 nm. A 30 nm top-top non-linear effect is superimposed on the signal (figure 4), most probably caused by back scattering into the laserdiode or interference of the light on the photodiodes with stray light. For the time being the inaccuracy is limited to about 40 nm because of the non-linearity. Further research has to be done to find the origin of the effect and to correct it. It is expected that this will improve the accuracy to 10 nm (expected value).

The same experiment was repeated in x direction. The resolution in this direction is measured to be 100 nm.

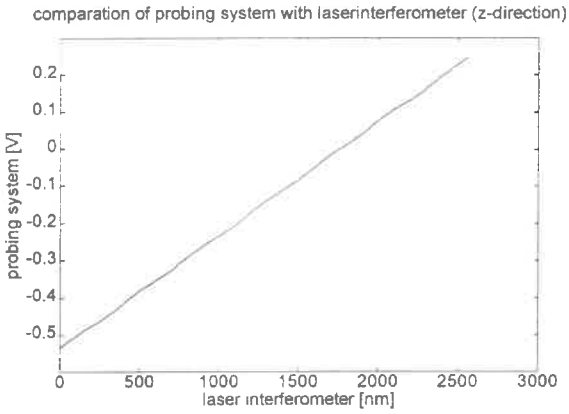

figure 4: comparison of probing system with laser interferometer

Conclusions

A 2D probing system was designed which combines high resolution with low probing force. The resolution has been measured to be 1 nm in z-direction and 100 nm in x-direction. Low masses in the design and a suspension with a low stiffness limit the dynamic probing force to several mN or less, depending on a number of parameters. This force is low enough to prevent damaging of the workpiece and influencing of the measurement. An interference effect seems to be superimposed on the FES signal so that the inaccuracy is limited to 40 nm. Further research has to be done to correct this and improve the accuracy to 10 nm.

---

[1] W.P. van Vliet, P.H. Schellekens; Annals of the CIRP **45**, 483-487,1996.

[2] M.M.P.A. Vemeulen, P.C.J.N. Rosielle, P.H.J. Schellekens. Proceedings from ASPE Annual Meeting **10**, 133-137, 1994.

[3] Sharp Technical information, model LTOH1OM, (1988).

[4] I. Szabó; Höhere Technische Mechanik (in German). Springer-Verlag Berlin Heidelberg New York, 1977.

[5] W.O. Pril: Ontwikkeling van een 3d-CMM-tastsysteem met nanometernauwkeurigheid (in Dutch); Thesis post-graduate course Mechatronic design 1995, ISBN 90-5282-479-7.

The Calculation of CMM Measurement Uncertainty via The Method of Simulation by Constraints

S.D. Phillips, B. Borchardt, D. Sawyer, W.T. Estler, D. Ward, K. Eberhardt, M.S. Levenson, M. McClain,
National Institute of Standards and Technology
B. Melvin, ICAMP Inc., T. Hopp, ZigZag Inc., Y. Shen, G. W. University

Introduction and Background: The calculation of task-specific measurement uncertainty when using coordinate measuring machines (CMMs) is an important and challenging task. By task-specific measurement uncertainty we mean the uncertainty of a particular feature inspected with a specific inspection plan and stated as prescribed by the ISO *Guide to the Expression of Uncertainty in Measurement*. The complete problem involves the assessment and propagation of numerous uncertainty sources including imperfect parts and extrinsic factors (see Fig. 1). One aspect of this problem which has attracted considerable attention is the assessment and propagation of uncertainties related to the measurement instrumentation, e.g. the CMM. Even this limited problem, (which assumes perfect parts, no extrinsic factors, and accurate software) represents a daunting task because CMMs can inspect an almost limitless variety of features, in a wide variety of locations and orientations on the CMM, using an infinite variety of sampling strategies (the number and locations of the probing points).

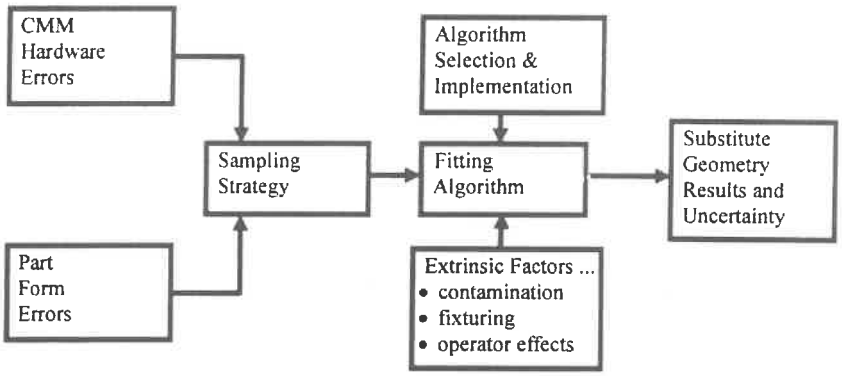

Figure 1. Schematic outlining the various factors affecting CMM measurements.

Historically, performance specifications embodied in national or international standards (which were designed to promote commerce) have been unable to provide useful estimations for task specific uncertainty, unless the part under inspection happened to be nearly identical to the calibrated artifact used in the performance evaluation. This has led to the development of the virtual instrument concept where software can propagate errors into the feature measurement under consideration. For CMMs this has involved the assessment of the individual rigid body parametric errors, i.e. the translational and rotational errors of each axis, and their propagation through the kinematic equations describing the CMM structure, to yield point coordinate errors. Point coordinates which contain these and other CMM hardware errors (e.g. due to the probe) are then run through the appropriate geometrical fitting algorithm to yield the error in the final feature.

Full Parametric Simulation (FPS): Recently, this process has been expedited (for small CMMs) by the use of calibrated ball plates measured in different positions and orientations from which one can extract the individual rigid body parametric errors. If all the parametric errors were known exactly and rigid body kinematic equations exactly described the CMM, then their propagation would determine the measurement error (the measured value minus the true value). However, since there is uncertainty in the calibration of the ball plate, and the kinematic description is only approximate, this calculation estimates the measurement bias of the feature due to the rigid body errors of the CMM. Recognizing that the parametric errors are not exactly determined, this uncertainty is assessed by simulating small perturbations about the measured mean parametric errors using many different measurement scenarios each with a slightly different parametric error description. The collection of calculated feature results (each of which will be slightly different reflecting a slightly different parametric state) is descriptive of the uncertainty in the feature due to the imperfect ball plate and the reproducibility of the CMM. This uncertainty can be combined with the estimated bias to yield the uncertainty in the feature due to the CMM; any additional sources of uncertainty such as part form errors or extrinsic effects must then be combined to produce a final uncertainty statement for the feature. This procedure, which in many situations can accurately describe the CMM's contribution

to the measurement uncertainty, has become known as the "virtual CMM"; however, we prefer the somewhat more descriptive name of "Full Parametric Simulation" (FPS). Its essential feature is that it requires a complete description of the CMM parametric errors.

Simulation by Constraints (SBC): We will now outline a generalization of this technique, of which FPS is a special case. Consider a three axis CMM. We call the "parametric state of the CMM" the particular values of the various rigid body parametric errors of the CMM. In general this unknown vector will include 18 functions (pitch, roll, yaw, etc.) and three scalars (squareness values). Mathematically, we can think of the parametric state of the CMM as being represented by a particular point in a large infinite dimensional state space. If we have no prior performance information about the CMM then we are completely ignorant of where in the state space the CMM actually lies; hence it could be said that our uncertainty about the parametric state fills all of state space. Suppose we learn that this CMM has measured a calibrated step gauge oriented along its X axis and that the largest error is less than 10 μm. From this information we can reasonably state that it is unlikely the X axis scale error >> 10 μm. Although it is possible that the various parametric errors combine with the X scale error in a manner such that they largely cancel each other out, this hypothesis becomes increasingly unlikely if we learn that additional step gauge measurements (oriented along the X axis but translated in the Z direction) continue to have errors less than 10 μm. Hence with a few measurements we can reasonably state that the X axis parametric scale error is bounded by $\eta \cdot 10$ μm, where η is greater than but on the order of unity. In terms of the state space, we can say that the subspace representing the X axis scale error is bounded. However, since there are no bounds on the other parametric errors, the region of state space which may contain the state of the CMM (and still be consistent with the known information) is still unbounded. Thus, in this example, our measurements form a constraint sufficient to bound one of the parametric errors but insufficient to provide a topologically bounded region in state space. Our goal is to obtain measurements which result in a topologically bounded region in state space. We call such a set of measurements a Bounding Measurement Set (BMS). Any calibration of the CMM must yield a BMS as a result of the calibration procedure, otherwise some error can have an arbitrarily large value. The points inside the bounded region of state space are known as "virtual states" because any one of them could be the "true" state of the CMM. The virtual states represent our ignorance, i.e. our uncertainty, about the exact state of the CMM. The boundaries of the virtual states represent our knowledge about the CMM, i.e. they summarize our information about the CMM, and all virtual states inside the boundaries are consistent with this information.

As a conceptual illustration of SBC, Fig. 2 depicts an idealized instrument which possesses only two error sources denoted α and β, both of which are scalars, e.g. these might be the relative scale error between two axes and a squareness error. In this idealized example, the state space is two dimensional and specifying the values of the two error sources uniquely locates the state of the CMM. Shown in the figure is the estimated state of the CMM (based on a full set of parametric measurements), the associated bounded region determined by FPS (this includes the true --but unknown -- state of the CMM. Also shown are two bounded regions derived from a BMS, i.e. multiple topologically bounded regions of state space may be derived from the BMS. (Fig. 2 illustrates a general case, however, in many situations there will be a symmetry of the bounded regions of virtual states permitted by BMS due to the symmetry in the kinematic equations and the BMS in terms of the error parameters α and β.)

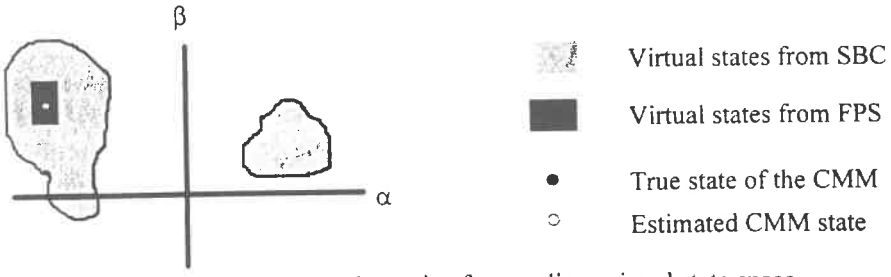

Figure 2. Schematic of a two dimensional state space

Central to the SBC method is that estimates of each parametric error are not required (as is the case for FPS). The only requirement is that sufficient measurements are taken to bound the parametric errors, i.e. a BMS. Hence SBC works with incomplete information about the state of the CMM whereas FPS uses a complete description of the CMM state. To illustrate the magnitude of this difference, a typical CMM might have each of its 18 functional parametric errors measured at a dozen points along each axis, plus three scalars (squareness values), resulting in

over 200 numbers to characterize its state. In contrast we will show that by using five numbers, i.e. five CMM performance evaluation test results, we can obtain very reasonable uncertainty estimates. Hence by using less than 5% of the amount of data needed for FPS, SBC can achieve useful results. The key to SBC is that the small amount of data utilized must be of high quality in the sense that it forms a good BMS.

SBC Using The ANSI/ASME B89.4.1 Standard: Ideally, the data used in the SBC method would be widely available to the user, as is the case for published performance specifications given by national or international standards. We will present the case of the US national standard which characterizes the geometric errors of a CMM, i.e. those involving the parametric errors, by five numbers: linear accuracy results for the X,Y, and Z axes, the volumetric performance, and the volumetric performance using an offset probe. With some assumptions (described later) these five values can form a BMS. Conceptually, SBC proceeds in the following manner: a random parametric state is selected from all of state space and the B89 performance tests are simulated using this state. If the simulated test results agree with the known five B89 values we label this a "good virtual state". If the simulated and known B89 results disagree the trial state is rejected and another random state is selected and tested. Continue this procedure until a large set containing several hundred good virtual states is obtained. This set represents a sampling of the topologically bounded regions in state space, and using these virtual states any part measurement under consideration can be simulated. The resulting collection of part feature results represents an estimate of the feature measurement uncertainty due to geometrical errors of the CMM. To test the uncertainty prediction of the SBC method we have measured a calibrated step gauge in 43 different positions and orientations throughout the workzone. In each position five different lengths were measured, and each length was measured three times. Figure 3 shows the SBC calculated expanded uncertainty ($k = 2$) and the actual measurement errors for the longest of the five lengths (this is 1000 mm for all positions except along the Z axis which is 700 mm), for a CMM with large uncorrected geometric errors. Figure 4 displays the same data as Fig. 3 but for a (parametric) error corrected CMM. For these two figures, as well as the eight similar figures (not shown) associated with the shorter length measurements, approximately 95% of the measurement errors are contained within the SBC calculated expanded uncertainty. We consider these results, based on a paucity of input information, to be quite reasonable.

Implementation Issues of SBC and the B89 BMS: Our implementation of the SBC method assumes that the parametric errors are analytic and slowly varying, e.g. the spatial frequency of the errors is restricted to less than 50 cycles/meter. Additionally, rather than picking prospective virtual states at random, we employ a reasonable initial guess and then use a gradient search method to locate good virtual states. (Some caution must be exercised to avoid a search that preferentially seeks only certain areas in state space, otherwise the search may miss disconnected regions of valid virtual states, see Fig 2). Using the B89 test results as a BMS also requires a few reasonable assumptions. Specifically the B89 tests are very weak at detecting straightness errors; consequently we employ a general kinematic relation between angular errors and straightness errors to bound this parametric error source. Similarly, only the linear term of the Z axis roll error (for a moving bridge machine) is constrained by the B89 tests; consequently we force the nonlinear terms to be smaller that the linear term in magnitude. This procedure can be somewhat justified both by experience and by the fact than the exact location in the workzone where the point-to-point Z roll test is performed is (in practice) determined by the user.

We have outlined the method of SBC for CMM uncertainty calculations. Using incomplete information about the CMM we are able to construct realistic point coordinate uncertainties which can, in turn, be used to calculate feature measurement uncertainty. Although feature measurement uncertainty is the desired objective, mathematically the challenge is to efficiently locate the good virtual states as these determine the point coordinate errors. The feature fitting algorithm can be considered simply a transformation from point coordinate errors to feature errors (see Fig. 1). The method is very general and can be applied to diverse systems, e.g. machine tools and laser trackers. Similarly, many different measurement schemes can be used for the BMS. The use of the B89.4.1 standard works well provided reasonable assumptions are made about straightness and Z roll errors. Finally, the standard could form a stronger constraint if measurements sensitive to straightness and the nonlinear component of Z roll were included and if the linear accuracy and volumetric performance values were stated as deviations from calibrated values instead of ranges. In the limit of taking more and more measurements the constraints become stronger. Ultimately only one set of parametric errors is consistent with the data, and we have reached the domain of FPS.

Acknowledgments: This work was funded in part by the Air Force CCG Program, NIST's Computational Metrology Project, and the Manufacturing Engineering Laboratory's NAMT Program.

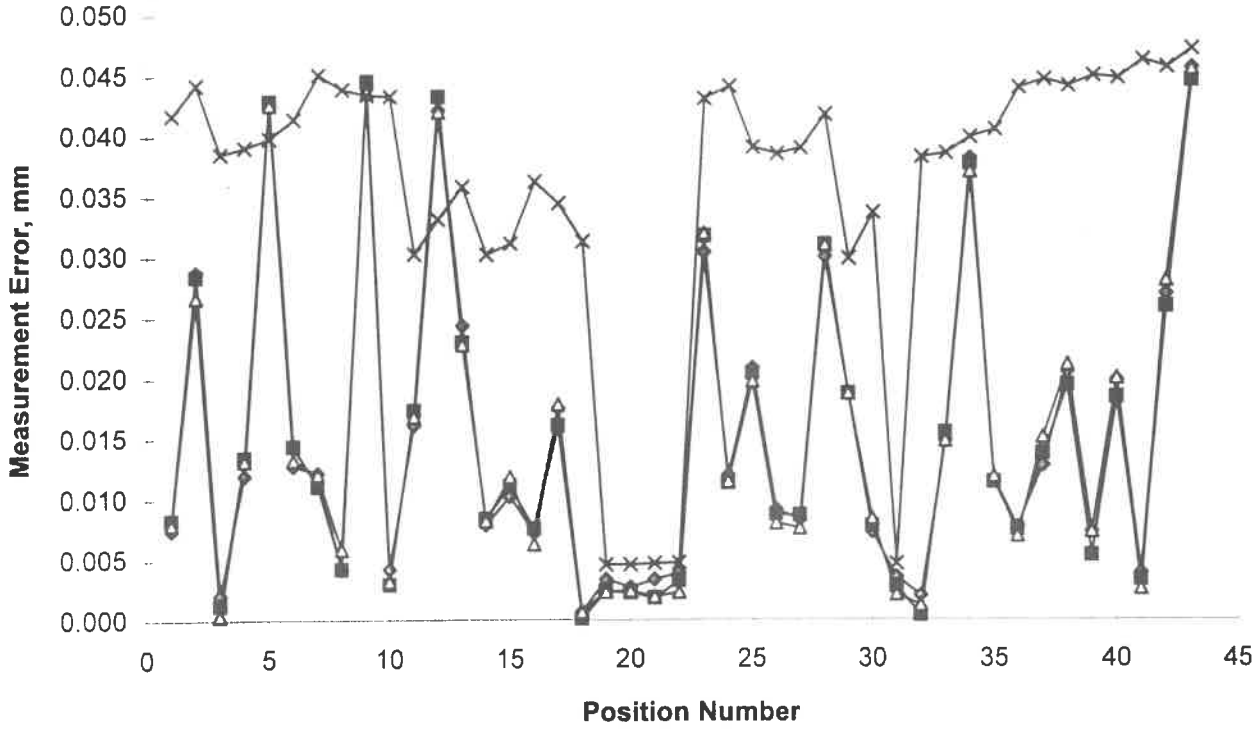

Figure 3. The calculated expanded uncertainty via the SBC method (shown as ×) of 43 point-to-point length measurements of a step gauge and three sets of measured deviations from the calibrated value (■, ◆, △). The constraints for this CMM are: X, Y, Z linear accuracy are 13.8 μm, 18.3 μm, 3.4 μm respectively, volumetric performance = 39.1 μm, volumetric performance with an offset probe = 55.0 μm/m.

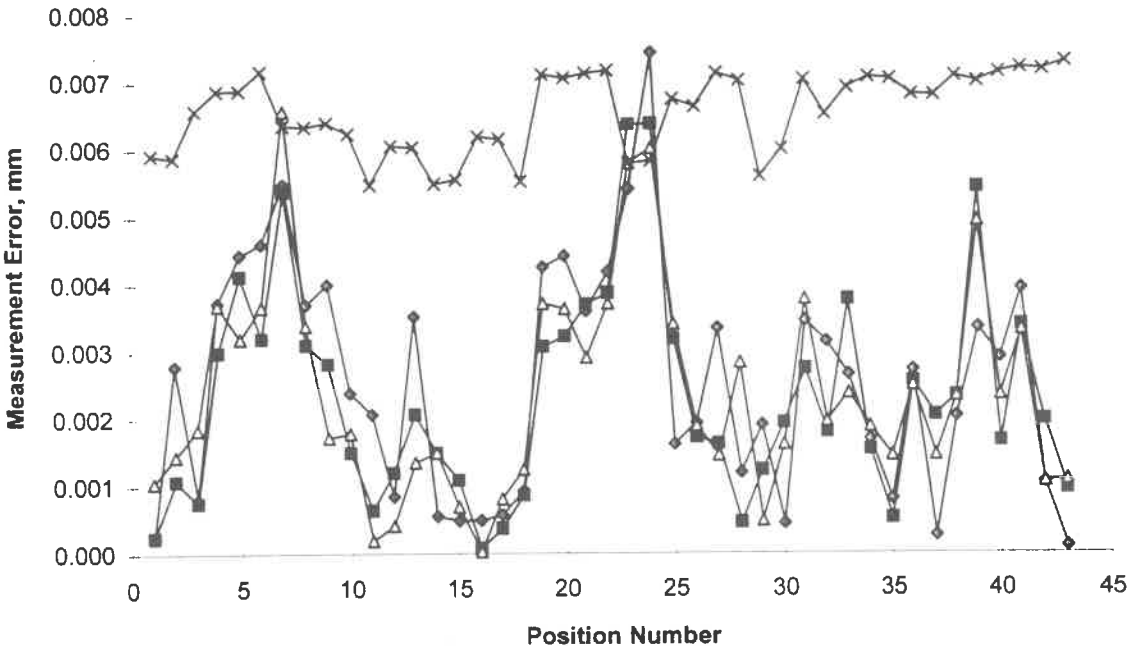

Figure 4. The calculated expanded uncertainty via the SBC method (shown as ×) of 43 point-to-point length measurements of a step gauge and three sets of measured deviations from the calibrated value (■, ◆, △). The constraints for this CMM are: X, Y, Z linear accuracy are 3.0 μm, 2.1 μm, 2.5 μm respectively, volumetric performance = 7.2 μm, volumetric performance with an offset probe = 7.1 μm/m.

Thermal Responses of Coordinate Measuring Machines

C. Nickles, T. Charlton
Brown & Sharpe Manufacturing Company
North Kingstown, RI

Coordinate measuring machines are being used with increasing frequency in environments that are thermally hostile to accurate measurement. The driving force for this change is the great benefit of more closely coupling precision measurement to manufacturing processes by gauging on the shop floor. The chief obstacles for this change are (a) objects only have their correct size at 20 C, (b) thermally-induced measurement errors represent differential expansion between the workpiece and measuring instrument elements, and (c) uncertainties associated with thermal correction techniques. The conflict between the movement of CMMs to the shop floor and the resulting thermally induced errors has led to a variety of claimed solutions for thermal problems. These include using mathematical compensation techniques, thermally insensitive machine components, localized temperature control methods, and error-budget uncertainty estimation. Unfortunately, no well-defined objective criteria exist for characterizing either the success or suitability of any of these possible solutions, or even the real magnitude of the problem.

To improve the quantitative discussion of these issues, we report on the development of a standard stimulated-response test for thermal effects. Our approach evolved out of our extensive experimentation with the thermal responses of CMMs and subsequent attempts to explain the results to diverse audiences. The current development addresses three essential features of characterizing thermal responses: the temperature "input" profile, the measurement task definition, and the simplified presentation of the results.

Temperature Cycle Selection

To "stimulate" differential thermal responses in the CMM and workpiece, we apply a specific environmental temperature profile as a function of time. By selecting an appropriate profile our goal is to produce test results representative of shop floor errors. Having experimented with sinusoids, step functions, impulses and various triangular pulses, we finally prefer a repeated diurnal cycle shown as Figure 1. Workpiece measurement accuracy is more widely and routinely degraded by diurnal cycling than by any other thermal effect. Users and researchers alike can readily accept the reality of this proposed cycle, if not its consequences. Further, this profile is reasonably easy to produce as if only combines linear ramps and constant dwells over a limited temperature range. Note that the specific details of one diurnal cycle was selected to qualitatively mimic a Summer workshop (middle Northern latitude) with two work shifts, including warming due to machinery power-up and solar ascension, cooling due to solar descension, and finally cooling due to machinery power-down.

We emphasize that standardizing on a temperature profile is essential to make possible direct comparison of results from different machine designs with different workpiece materials while using different techniques to handle the temperature effects.

Measurement Task Selection

The second essential feature of our work is the selection of a simple artifact as a surrogate workpiece, and the specification of the measurement sequence to be used. As with the temperature profile, dual goals of standardizing on one workpiece geometry are to facilitate reproducibility and comparative studies and to produce representative shop-floor results. Expanding on the excellent experience with planar ball plates (ref: Kunzman), we favor an inexpensive modified ball plate shown in Figure 2. The spheres roughly span a 300 mm cube. Key modifications are the addition of a perpendicular spar and the addition of a centralized clamping feature.

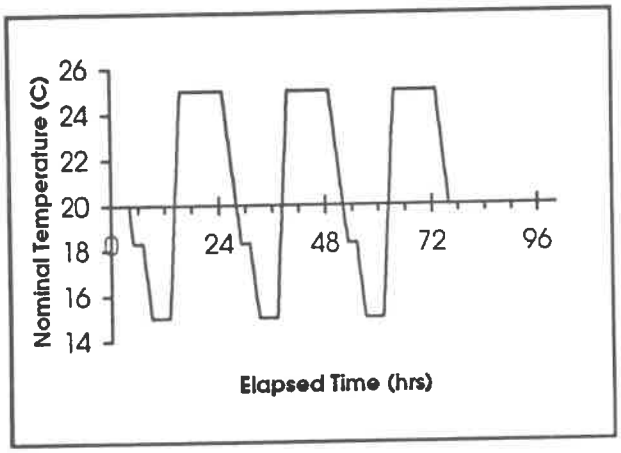

Figure 1. Standard Thermal Test Cycle

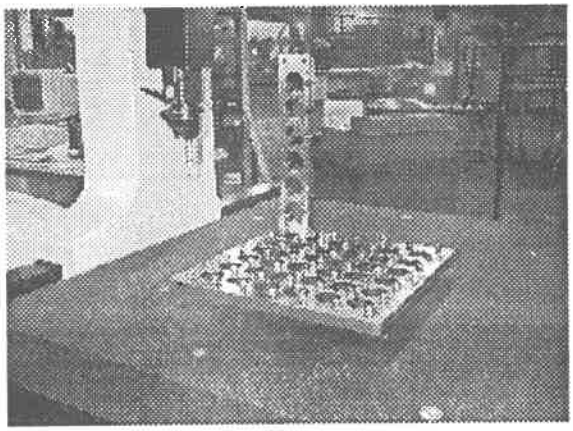

Figure 2. Thermal Test 3D Ball Plate

The addition of the spar allows measurement of the plate to incorporate some full three dimensional measurements in every orientation of the plate on the machine. This provides a sensitivity to changes in all of the machine axis squarenesses, which is a frequently unrecognized part of the thermal errors. Originally designed with kinematic location, our plate design now uses a single point clamping method. This change was made to reduce the influence of variable clamping forces and the resulting variable effects of different coefficients of expansion between the workpiece and the workpiece mounting surface. Such variability of thermal response due to fixturing of workpieces is extremely significant in practice. Unfortunately, no mounting method is reasonably representative of fixturing induced thermal response problems. Thus, it seems best to simply minimize these effects for a standard performance test, while emphasizing its importance.

To produce representative results for the application of CMMs it is important to report and compare functional results for workpiece materials with significantly different coefficients of expansion. Since the most significant engineering materials inspected on CMMs are steel and aluminum, plates of both of these materials were fabricated and used. Fortunately, these two materials cover a relatively wide range of expansion coefficients.

In applying this ball plate for thermal testing, we repeatedly measure the center coordinates of a fixed sequence of spheres using the CMM under test. Although the plate includes more spheres, we

eventually began to use only 12 spheres - a three by three grid in the plane and three on the spar - for our normal testing sequence. This represents our compromise between a more thorough sampling of the machine/workpiece geometry variation and a representative duration for a single execution of the measurement sequence. Measuring 12 spheres has a duration longer than would be found in transfer line applications (0.5-3 minutes), but shorter than many stand-alone inspection programs run on the shop floor (20-30 minutes.) The complete 12 sphere measurement sequence was repeated every 15 minutes.

Results Presentation

Finally, and perhaps most importantly, we report on our selection of methods for analyzing and presenting the large quantities of measurement data. We propose to use relatively simple quantities to characterize the thermal response of the workpiece-machine system and to estimate the thermal contribution to dimensional measurement uncertainty.

The record of the sphere centers is very analogous to a multi-point drift test, and the results of the test were initially presented in this manner. However, we concluded that the most meaningful (and easily explained) quantity is apparent variation in the distance between the spheres. This is analogous to a length measurement, whose variation with temperature is most easily understood. Also, it is analogous to measuring ball bars. Hence, reporting sphere center-to-center distance variations relates well to both widely used CMM performance standards. Further, by computing the distances between all pairs of spheres, of which there are 66 for 12 spheres, we mix together results from combinations of lengths (e.g., from crossed diagonals.) This provides sensitivity to changes in machine squarenesses, rotational errors, and straightnesses.

Having cleverly "reduced" the 36 raw coordinate variations to 66 time-varying distances, some further simplification is needed. Our approach is to scale all of the measured distances to a few standard lengths. In fact, for the data sets described here, all 66 distances were reduced to just two representative lengths. All distances between 100 mm and 300 mm, when initially measured at 20 C, were scaled up or down by the ratio of 200 mm to each initially measured distance. This effectively made all of these distances equal to 200 mm at 20 C. For lengths between 300 mm and 500 mm, the distances were scaled proportionally to 400 mm. The "standardized lengths" (200 mm and 400 mm) were then subtracted from all of the scaled time-varying distances. This produced two collections of thermal variations that were comparable within themselves. All of the distance variations for each standardized length could be plotted on a single graph, but just the centerline and envelope of the mass of data is much more informative. Consequently, we further reduced the results by determining the mean, minimum and maximum variations for each standard length at each measurement time. Typical results of this are presented as Figure 3.

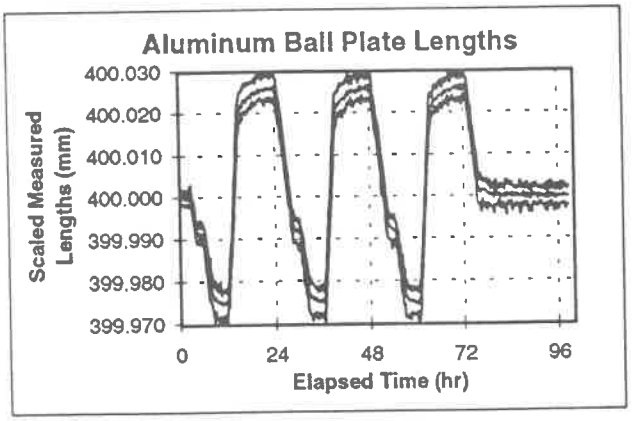

Figure 3. Standard Thermal Response Graph

PRECISION ENGINEERING AND STATISTICS: Is there any common ground?

Richard L. Rhorer and Janelle L. Rhorer

National Institute of Standards and Technology, Gaithersburg, MD
and Statistics Department, Iowa State University, Ames, IA

The term "Statistical Process Control (SPC)" is very well known in the field of precision manufacturing. Yet, precision engineers (very much involved in precision manufacturing) do not often incorporate SPC methodology in their work. Why? We present here a search for a common ground between precision engineering and statistics.

Background

There has been a concern in the precision engineering community about how some people use statistics. One view from the precision engineering position is illustrated by the quotations about statistical approaches in Evans*:

> "A basic finding from our experience in dealing with machining accuracy is that machine tools are deterministic. By this we mean that machine tool errors obey cause-and-effect relationships, and do not vary randomly for no reason. Further the causes are not esoteric and uncontrollable, but can be explained in terms of familiar engineering principles."

And, statistics are:

> "... at best an unwarranted distraction and at worst a cloak of respectability for bad metrology."

These views suggest we should concentrate on engineering principles and metrology. Yet, many modern manufacturing organizations use Statistical Process Control (SPC) methods for improving their processes, including improving the precision of their processes. The statistician using the SPC method is then playing the same role as that of the precision engineer: to improve the precision of the process. In this case the precision engineer and the statistician have the common goal of improving a process; however, they may approach the goal differently.

Statistics

The word "statistic" is typically thought of as simply the descriptive number given to represent an entire body of data, i.e. the percentage of defectives coming off a production line. Using a number of this type gives a description or summary of a large amount of data; however, statistics also involves the ability to make inferences about data that has not actually been observed. Statistics can be divided into three areas: 1. Data Analysis (the gathering, displaying, and summarizing of data), 2. Probability (the laws of chance), and 3. Statistical Inference (the science of drawing statistical conclusions from specific data using a knowledge of probability.) The authors believe that the

first area--Data Analysis--is certainly common ground between precision engineers and statisticians.

Example

An illustrative example uses data taken from a small classic NIST Special Publication by Dr. W.J. Youden**. Youden presents data of an experiment to determine the thickness of a page in a chemistry book by having many students measure the thickness of an arbitrary large number of pages with a ruler, and then divide by the number of pages. Each student gets a slightly different number. This data is used to arrive at a precise number for the thickness of a single page. We use Youden's data to illustrate data display methods that include stem-and-leaf plot, histograms, run charts, and control charts. Different display methods then aid in gathering different information from the data at hand.

A person from a precision engineering background might take an approach of first being concerned about how the measurements were taken:

-- how much pressure did each student use to compress the stack of pages before measuring the thickness with the scale?
-- how square was the edge of the stack and how parallel to the ruler?

The common ground between the statistical approach and the precision engineering approach begins with taking measurements and displaying the data. The precision engineer would probably analyze the measurement method carefully before trying to quantify any uncertainty and propose any improvement in the process. In hopes of making statistical inference from the sample of data to the entire population of interest, the statistician also considers the quality of the data collected by a particular method and the sources of error present, but primarily concentrates on the data.

Conclusions

In this example the SPC approach would use established data collection and display methods in searching for the most precise description of the thickness of a single page. This SPC type approach might lead to examining the metrology method more closely as well. In contrast, the precision engineering approach would involve first examining the metrology method based on metrology principles. Such an approach might lead to proposing a different metrology method before making the measurements. The common goal of the two approaches is to obtain a good estimate of the thickness of a typical page. Both approaches rely on good metrology and good data analysis, but they approach the problem in a different order.

*Precision Engineering: an Evolutionary View, C. Evans, Cranfield Press, 1989, page 21.

**Experimentation and Measurement, W.J. Youden, NIST Special Publication 672, 1961 and reprinted May 1994, page 31.

ULTRAPRECISION GRINDING OF HIGH ASPECT RATIO MICROPARTS

Hans H. Gatzen[1], J. Christoph Maetzig[2], and Lars P. Ruhbach[1]
[1] Institute for Microtechnology (imt), Hanover University, Hanover, Germany
[2] Now at Balzers Process-Systems, Alzenau, Germany

Abstract - Mechanical ultraprecision manufacturing technologies serve as an interesting alternative to fabricating structures by micromachining using thin film techniques. The main advantage of employing mechanical techniques is their capability of achieving a high aspect ratio between height and thickness of a microstructure. The paper describes investigations in how to accomplish the high aspect ratio profiling of an advanced ceramic workpiece. The test structure selected is a flexural resonator, the aspect ratio achieved is 50:1.

I. Introduction

Mechanical ultraprecision machining of ceramic microparts has been spearheaded by magnetic read/write heads for rigid disk or tape drive applications [1, 2]. Mechanical ultraprecision manufacturing technologies provide for an interesting alternative to fabricating structures by micromachining using thin film techniques. While the latter in general is only capable of creating very thin structures, mechanical ultraprecision machining allows to build components with high aspect ratios, i.e. parts with a height substantially greater than their length and width.

To accomplish high aspect ratio ultraprecision grinding, three key conditions have to be met. First, the ceramic workpiece material has to be free of subsurface damages like microcracks or residual stresses induced during preceding machining operations. Furthermore, the profiling has to be by ductile mode grinding in order not to compromise the workpiece quality by subsurface damages induced during the dicing process. This machining mode is also a precondition for achieving an optimal sidewall surface and edge quality [3, 4]. Finally, the dicing blade needs to be stabilized properly to avoid wheel walk which would inflict damage to the structure. For investigations on how to achieve high aspect ratios of a mechanical structure with little subsurface damage, a flexural resonator has been selected as a test structure. The mechanical processes applied are dicing and nanogrinding.

II. Test Specimen For High Aspect Ratio Profiling

For this high aspect ratio microgrinding study, Altic, an advanced ceramic consisting of 70% Al_2O_3 and 30% TiC has been chosen as workpiece material. Altic has been used successfully as a wafer material for data recording thin film heads. Through its excellent mechanical properties, like a Vickers Hardness of 2,000 HV, a Bending Strength of 880 MPa, and a Young's Modulus of 390,000 MPa .Altic is the ideal material for building the test specimen. The average grain size is 1.5 µm [5].

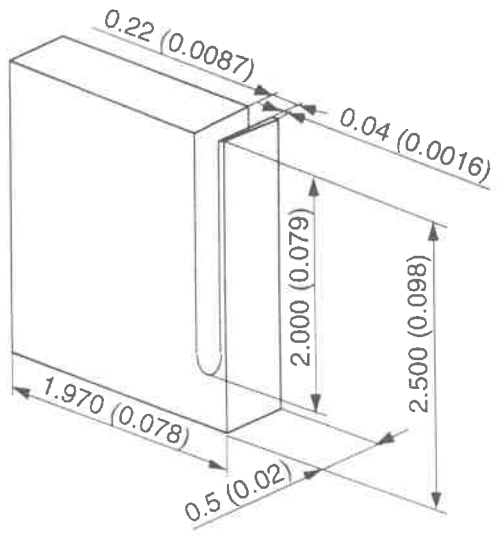

All dimensions in mm (in)

Fig. 1: Microresonator test structure.

Fig. 1 depicts the resonator test structure: a resonator tongue is created by cutting a groove into a ceramic block. Equation {1} describes the resonance frequency at the first bending mode of such a structure. The smaller the width of the tongue and the higher the aspect ratio between tongue length and tongue thickness chosen, the lower is the resonance frequency of such a system. To create a microresonator with a

resonance frequency at the upper audible range around and above 10 kHz, an aspect ratio of 50:1 is required. Therefore, such a microresonator is an excellent test object for high aspect ratio microprofiling.

$$f = \lambda^2 \cdot \frac{1}{2\pi} \sqrt{\frac{E \cdot h^2}{r \cdot 12 \cdot l^4}} \qquad \{1\}$$

- l - Resonator Length (Height)
- r - Material Density
- h - Resonator Thickness (Width)
- l - Characteristic Frequency
- E - Young's Modulus

III. Workpiece Surface Machining

Cutting a block of advanced ceramic to the workpiece's outer dimensions typically involves surface grinding, which is mostly accomplished by brittle fracture mode cutting. This type of cutting causes a substantial amount of subsurface damages by inducing microcracks in the workpiece. In advanced ceramics, the depth of the subsurface layer having suffered damages during surface grinding typically is 20 µm [6]. A material having suffered this kind of subsurface damage will not lend itself to any consecutive ultraprecision machining unless the damaged layer is completely removed. The surface layer therefore has to be removed before ultraprecision profiling may be attempted. For removing the damaged layer, as well as for creating a high quality workpiece surface, each of the block's surfaces is machined by nanogrinding [7]. Nanogrinding is an ultraprecision grinding process developed by the imt and is based on lapping kinematics. The nanogrinding machines (Peter Wolters, Type 3R40) are installed under laminar flow to avoid any plate contamination. While lapping uses loose abrasive grain for material removal, for nanogrinding diamond grain is completely embedded into a soft metallic plate. The diamond summits are aligned in a plane, thus forming a diamond brush. The workpiece is machined by ductile regime cutting, the depth of cut of an individual grain is in a range of 1 to 5 nm. The surface roughnesses of nanoground Altic blocks are R_a = 0.75 nm /R_z = 8 nm. Fig. 2 depicts an AFM image of an Altic block's nanoground surface. With the Altic block's damaged surface layer removed by nanogrinding, the workpiece is now properly prepared for a high aspect ratio profiling of the resonator tongue.

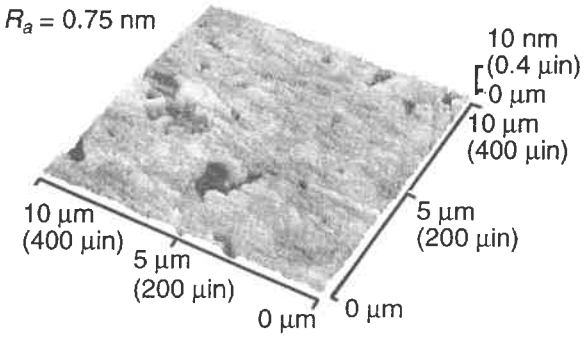

Fig. 2: Nanoground AltiC surface, surface topography measurement by AFM.

IV. High Aspect Ratio Ultraprecision Profiling

The grinding machine used in these tests is a single wheel dicing saw (Disco DAC-550) equipped with an air bearing spindle and an air slide, which allows minimum indexing step widths of 0.5 µm. To make full use of the machine accuracy, machine and tool deformation is minimized by holding both the room and the water coolant at a constant temperature of 21°C±1°C (70°F±1.8°F). The coolant is tap water with an additive to prevent rust and algae growth (Castrol Syntilo 9822). The cutting tools employed for the test specimen's fabrication are hubless type diamond blades. These blades may be resin bonded or metal bonded. In cutting hard and brittle ceramics, resin bonded wheels are superior to metal bonded ones. When the proper resin hardness is chosen, the diamond grains break out rather than get dull thus always providing new sharp diamond grains for cutting. Additionally, this process provides a space for the chips cut off from the work piece. Metal bonded blades, on the other hand, have a better radial wear behavior and therefore are mostly preferred for production. Since the diamond grains stay in the blade for a substantially greater period of time, they don't feature the superb self sharpening properties the resin bonded wheels excel in. For these investigations, blade accuracy is considered more important than blade durability; therefore resin bonded wheels have been chosen. As discussed previously, brittle fracture cutting is the most common cutting mode when surface grinding advanced ceramics. This also holds true for dicing and

profiling. Due to the subsurface damages this cutting mode is inducing, it is not feasible to use this particular cutting mode for ultraprecision machining. In case of a flexural resonator, subsurface damages also are not permitted since they will cause tongue breakage during operation. However, advanced ceramics may also be cut in a ductile mode. Reaching the ductile mode grinding regime requires a substantially higher induced energy than when cutting in the brittle fracture grinding mode. Furthermore, cutting conditions have to be chosen in a way that a submicron depth of cut is achieved. Blades used for microprofiling have to be very thin, which compromises blade stiffness. The blade thickness chosen for our tests is 200 µm (0.008 in). Insufficient blade thickness results in wheel walk: the groove the blade is cutting is not straight but veers off to one side. To minimize detrimental effects due to an insufficient blade thickness, two steps may be taken. The first measure is to minimize the blade exposure. This is accomplished by choosing a flange diameter minutely smaller than the difference between the blade diameter and the desired depth of cut. In our case, to achieve a depth of cut of 2 mm (0.080 in), a flange diameter of 50.6 mm (1.99 in) and a blade outer diameter of 55 mm (2.17 in) is used. The second one is to properly guide the blade. In our case, to provide for an optimal blade guidance when cutting the groove to profile the delicate resonator tongue, dummy blocks are attached to the workpiece at both the blade entry and blade exist side as shown in Fig. 3.

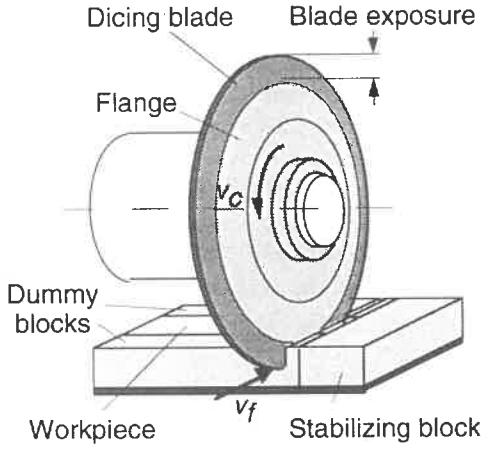

Fig. 3: Microprofiling machining set-up.

Furthermore, a stabilizer block stiffens up the tongue side of the workpiece to avoid is breakage during the cutting process. An adhesive (Aremco Crystal Bond 509) is used to attache workpiece and blocks to each other and to a carrier. For the majority of the tests, a resin bonded blade (Microkerf: 2.187-8-15H) with hard resin binder, a diamond grain size of 15 µm, and diamond concentration C100 (4.39 carat/ cm^3) has been chosen. This choice is based on previous investigations on how to achieve optimal cutting conditions when machining Altic [1]. In most cases, cutting or profiling of ceramics is done in a single run. However, cuts with a cutting depth greater than 1 mm (0.04 in) caused excessine forces at the workpiece resulting in a tongue breakage. Therefore, experiments were made to cut the groove in two steps, each step cutting half the groove depth. With this approach excellent results are achieved.

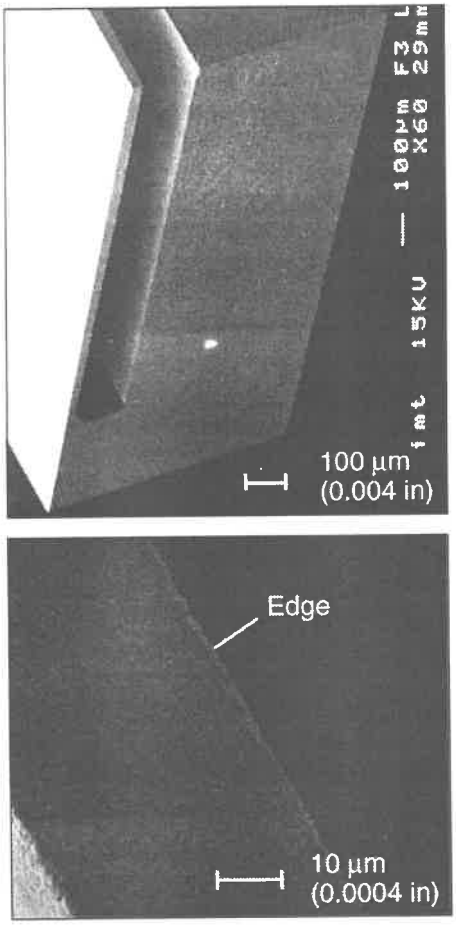

Fig. 4: SEM micrograph of resonator after tongue profiling/SEM micrograph of resonator tongue edge.

Fig. 4 depicts on its left side a micrograph of the resonator after cutting the tongue and on its right side the kerf's edge quality. The aspect ratio between tongue height and tongue thickness is 50:1. The cutting velocity is 86.4 m/s (30,000 RPM), the feed rate v_f = 3 mm/min (0.12 in /min). Before its use, a dicing blade has to be trued and sharpened. In general, a square shape of the dicing blade is desirable. However, for the given test structure a rounded kerf ground is required to avoid a stress concentration at the tongue's bottom due to a notch effect, which is likely to lead to breakage of the microstructure while oscillating in its sensor application. Therefore, the blade edges are rounded in a trueing process using a 45 µm grain size SiC block (Disco BGCA0113) moved circumferentially around the blade. For dressing a 35 µm grain size SiC block (Lunzer M50) is used. Fig. 5 presents the kerf's bottom created by such a blade.

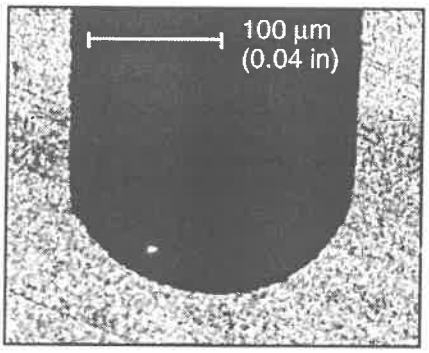

Fig. 5: Micrograph of the kerf radius.

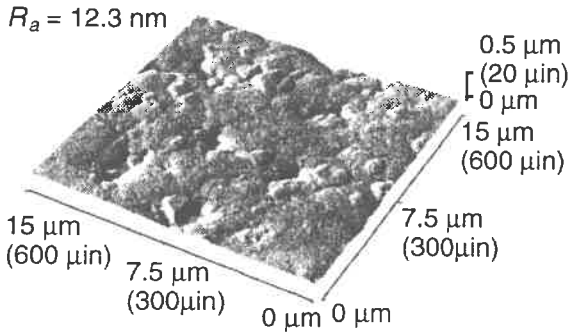

Fig. 6: Surface topography measurement by AFM of the kerf sidewall.

Fig. 6 depicts an AFM surface topography plot of the kerf's sidewall. Due to its contact with the blade's side wall, the kerf's sidewall is prone to suffering damages. There is also an indication that plastic deformation due to side wall friction causes a smoothening by plastic deformation.

V. Conclusion

A combination of nanogrinding and ultra-precision profiling allows the creation of a microstructure with high aspect ratios between structure height and structure thickness. Nanogrinding is used to remove subsurface damages at the workpieces' outer surfaces. The profiling result depends on choosing the machining parameters to achieve the ductile regime cutting, as well as avoiding wheel walk by properly stabilizing blade and worpiece. As a test structure, a flexural resonator has been machined, an aspect ratio between resonator tongue height and thickness of 50:1 has been accomplished by a two step cut with a depth of cut of 1 mm (0.040 in) each.

VI. References

[1] Gatzen, H. H.; Maetzig, J. C.; Schwabe, M. K.: "Precision Machining of Rigid Disk Drive Heads Sliders", IEEE Transactions of Magnetics, (1996), 32(3), p. 1843-1849

[2] Gatzen, H. H.: "Rigid Disk Recording Head Precision Engineering Requirements", 9th IPES/ 4th UME Braunschweig, Germany, (1997), Vol.1, p. 10-16

[3] Bifano, T. G.: "Ductile Regime Grinding: A New Technology for Machining Brittle Materials", Transactions of the ASME, (1991), Vol. 112, p. 184-189

[4] Komanduri, R.: "On Material Removal Mechanisms in Finishing of Advanced Ceramics and Glasses", Annals of the CIRP, (1996), Vol. 45/1, p. 509-513

[5] Source: Sumitomo Special Metals Co. Ltd. Japan

[6] Uhlmann, E. G.: "Tiefschleifen hochfester keramischer Werkstoffe" ("Creep Feed Grinding of Advanced Ceramics"), PhD Thesis, Berlin University (TU), (1994), p. 216-219

[7] Gatzen, H. H.; Maetzig, J. C.: "Nanogrinding", Received for Publication in: Journal of the American Society for Precision Engineering, (1997)

Direct Fabrication of Deep X-ray Lithography Masks by Micromechanical Milling

Craig Friedrich [a], Philip Coane [b], Jost Goettert [b], Niranjan Gopinathin [c]
[a] Michigan Technological University (MEEM), Houghton, MI
[b] Louisiana Tech University (IfM), Ruston, LA
[c] Read-Rite, Inc., Milpitas, CA

Introduction

Micromechanical milling has been shown to be a rapid and versatile method for the fabrication of microstructures in polymethyl methacrylate (PMMA) with lateral dimensions down to 4 micrometers [1-3]. These structures were micromilled in PMMA using custom-fabricated micromilling tools with a diameter of 22 micrometers [4]. To make the micromilling process more cost effective, it has been adapted for the fabrication of deep x-ray lithography masks. In deep x-ray lithography, the absorber pattern is transferred into the PMMA photoresist using x-rays as the illumination source.

Conventional deep x-ray lithography (DXRL) mask fabrication

Deep x-ray lithography masks must provide high contrast between the transmitted x-rays, through the *membrane*, and the absorbed x-rays, in the *absorber*, because exposures can take many hours. Membrane materials must offer high transparency to x-rays and are made of low absorption materials (low absolute absorption and thickness) such as beryllium, carbon, silicon, titanium, silicon nitride, or boron nitride. The higher atomic number membrane materials are usually a chemically etched, thin membrane, where the low atomic number materials are normally thicker. The absorber pattern is made of materials with high x-ray absorption such as tungsten, gold, or tantalum which have a high absorption coefficient for x-rays in the range of 2 keV to 30 keV.

Micromechanically Milled Masks

Micromilled masks have the same general characteristics as the lithography counterparts, but the materials and dimensions must be altered to allow for mechanical machining. The depth of the features depends on the diameter of the tool used and the desired result. Because the absorber thickness in most x-ray masks is on the order of 10 micrometers, the micromilling process may be a direct and rapid method for x-ray mask fabrication.

Micromilled mask materials

A mask structure capable of being machined must have a relatively thick *substrate* (transmission "membrane") because the flatness of the substrate, coupled with variations in the thickness, preclude the use of thin membranes as are commonly used in conventional masks. At the same time, the absorber deposited onto the substrate must be sufficiently opaque to x-rays, must be machinable with minimal cutting tool wear and adequate dimensional control, and must be deposited onto the substrate with adequate adhesion so as not to delaminate in the presence of the machining forces.

The first work used a single material as both the substrate and absorber. Aluminum was chosen and preliminary tests indicated a thickness of 6 micrometers for the substrate, and a total of 40 micrometers for the absorber gave reasonable contrast when exposed on the Institute for Micromanufacturing (IfM) beamline at the Center for Advanced Microstructures and Devices (CAMD). The drawback which precluded further development of this architecture was the time and care required to mill the aluminum foil down to a minimum thickness of 6 micrometers. Although attainable, it took great care and this detracted from the rapid intent of the process.

The next step was to investigate a low absorption substrate and a high absorption, sputtered

absorber. Because the substrate was subjected to machining, beryllium was not considered because of the toxicity of the oxide. The lowest atomic number structural material available was carbon. Test exposures were made with varying thicknesses of commercially available (Goodfellow) graphite sheets. It was found that a thickness of less than 250 micrometers gave sufficient transmission of the x-rays to allow for timely exposures (8 hours or less).

Work on an appropriate absorber was more extensive. Gold was the first material used, however sputtered gold was too ductile to leave a cleanly machined pattern. Other sputtered single layer absorbers were then tried. These were tantalum, titanium, tungsten, and molybdenum and were sputtered to a thickness of 5 micrometers (8 micrometers for molybdenum) over a 1000 - 2500 Angstrom- thick layer of chromium. The absorber adhesion was good, but cutting tool wear was excessive, particularly with the tantalum and tungsten. In addition, a thickness of 5 micrometers did not provide sufficient absorption and low contrast was observed in the exposed structures.

Because of the rapid tool wear, it was decided to use a thick layer of gold as the primary absorber and a thin layer of a harder metal on top to help reduce the burring of the gold. The best combination was gold covered with titanium. The sputtered gold layer was 8 micrometers thick and the sputtered titanium layer was 3 micrometers. A series of patterns, covering a total of more than 625 square millimeters, were micromilled to determine the quality of this mask combination. The total time required to mill the extensive patterns was about 4 hours. The machining parameters were a single axial pass at a depth of 36 micrometers (11 micrometer-thick absorber and 25 micrometers of overcut to account for any lack of blank flatness), a spindle speed of 10,000 rpm, and a feedrate of 30.5 micrometers per second with a 100-micrometer milling tool of tungsten carbide. The mask was exposed at CAMD and two results are shown in **Figures 1 and 2**.

Mask Absorber Quantification

The second phase of the study was to determine the precision of mask absorber features and the exposed pattern in the PMMA photoresist. There are two primary biases in the mask/exposure process. The first is the precision of the mask absorber definition and the second is the bias in transferring the absorber pattern into the photoresist.

The micromilling tools are held in a precision collet in the milling machine spindle. The tool has radial runout in the collet and there is also eccentricity between the tool shank and the cutting edges. To accurately machine trenches, which will leave narrow absorber features, this runout must be eliminated to the extent possible and the remaining error must be quantified so it can be compensated. Much of the runout can be removed by "tapping in" the tool using a video microscope. Typically, the remaining runout after this procedure is 3 to 5 micrometers, based on experience.

To quantify and compensate the remaining runout required two test cuts to be made in the mask blank, well away from the area to be patterned. Two parallel trenches, each 3 mm long, were milled into the absorber. The remaining absorber width was then measured with a WYKO RST-Plus at 80X. The wall width was measured at 20 points along the length and the mean was used to determine the effective tool diameter which was 109 micrometers (for a nominal tool diameter of 100 micrometers), with a standard deviation of 0.9 micrometers.

The effective tool diameter was then used as a process bias and five similar trenches were machined with the same feed, speed, and axial depth with a varying center spacing. The desired absorber widths between the trenches were 50, 20, 15, and 10 micrometers. Each absorber wall was measured at 20 points along the length and the results are shown in **Table 1.**

Exposure Quantification

The micromilled mask was then used to expose 300 micrometer-thick PMMA at the CAMD synchrotron under the same conditions mentioned previously. The result of the exposure and development is shown in **Figure 3.** The exposed wall widths were measured as previously described and the results are shown in **Table 2.** It can be seen that the exposed widths are consistently narrower than the measured

absorber widths. The mask absorber wall widths were again checked and it was found that the milling procedure left a slight taper in the absorber, particularly the gold, whereby the absorber thickness was less at the edge of the wall and quickly grew to full thickness a micrometer, or so, away from the wall edge. This variable thickness went unnoticed in the preliminary absorber width measurements but was observed in a more detailed inspection of the scanning electron micrographs. This created a second process bias which must be quantified to determine how repeatable it is and if the amount of taper is a function of the machining parameters (feed and speed).

One of the exposed samples was sectioned to determine the roughness in the vertical walls. A series of two-dimensional line scans were taken which covered the entire 3 mm length of the walls. The average mean roughness (Ra) was 0.17 micrometers with a standard deviation of 0.03, and the average peak-to-valley (Rt) was 1.42 micrometers with a standard deviation of 0.24. The relatively large peak-to-valley roughness was due to residual burring in the absorber which was transferred into the photoresist, but the relativley low average roughness indicated the burrs were random and occasional, and not overly prevalent. Similar wall roughness was measured in exposed PMMA using a conventional gold mask and the average mean roughness (Ra) was 0.08 micrometers with a standard deviation of 0.015, and the peak-to-valley roughness (Rt) was 0.51 micrometers with a standard deviation of 0.1 micrometers [6].

Acknowledgments

This work was supported by the Institute for Micromanufacturting under NSF grants OSR-9550481 and EEC-9420600 and the State of Louisiana under grant NSF/LEQSF(1995-98)-SI-01. Special thanks to Joe Blakesley and Jubin Shah for sputtering the absorbers.

References

1. Friedrich, C. and Vasile, M., "The micromilling process for high aspect ratio microstructures", ***Microsystem Technologies*** **(2)3**, pp.144-148, 1996.
2. Vasile, M., Friedrich, C., Kikkeri, B., and McElhannon, R., "Micron-scale machining:tool fabrication and initial results", ***Precision Engineering (19)2/3***, pp.180-186, 1996.
3. Friedrich, C., Coane, P., Goettert, J., and Gopinathin, N., "Metrology and quantification of micro-milled x-ray masks and exposures, *SPIE Vol. 3048* (in press), 1997.
4. Friedrich, C. and Vasile, M., "Development of the micromilling process for high aspect ratio microstructures", ***J. MEMS*** **(5)1**, pp.33-38, 1996.
5. Coane, P. and Friedrich, C., "Fabrication of composite x-ray masks by micromilling", *SPIE Vol. 2880*, pp.130-141, 1996.
6. Gopinathin, N., *Direct fabrication of x-ray masks for liga by micromilling*, MS Thesis, Louisiana Tech University, Ruston, LA, 1997.

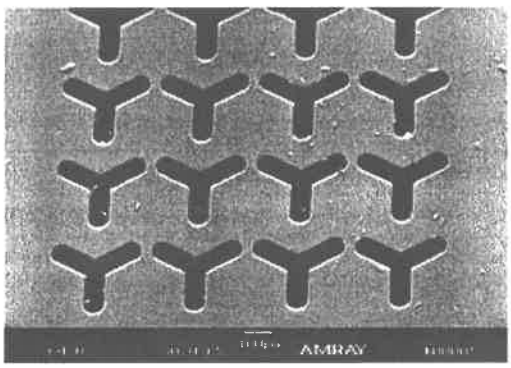

Figure 1. Portion of exposure in PMMA through Au-Ti micromilled mask. Scale bar = 100 um.

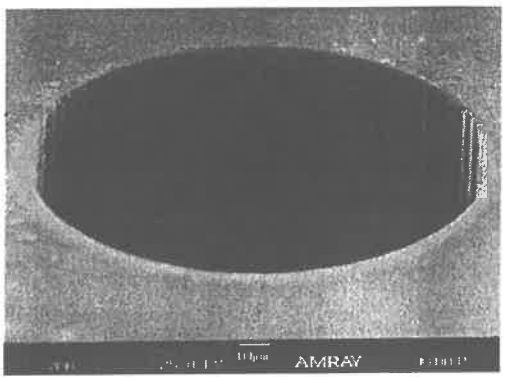

Figure 2. Portion of exposure in PMMA through Au-Ti micromilled mask. Scale bar = 10 um.

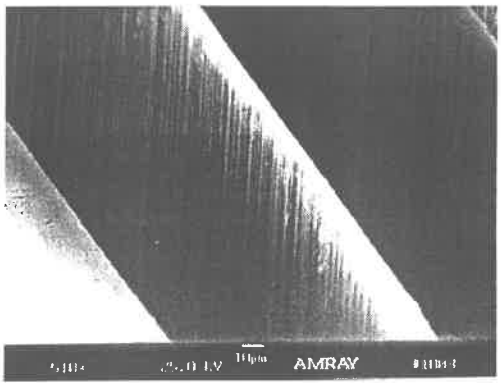

Figure 3. Closeup of 10-micrometer wide by 300-micrometer high exposed and developed wall. Scale bar = 10 um.

Table 1. Mask absorber width accuracy using tool runout characterization.

Nominal absorber wall width (um)	Measured absorber wall width (um)	Standard deviation (um)
50	50.4	0.5
20	20.7	0.4
15	15.4	0.8
10	11.1	0.5

Table 2. Exposed wall width accuracy in PMMA.
Large standard deviation is due to roughness from mask burrs.

Nominal absorber wall width (um)	Measured PMMA wall width (um)	Standard deviation (um)
50	48.2	1.4
20	16.0	1.8
15	13.6	1.3
10	9.6	0.8

THE MECHANISM OF MATERIAL REMOVAL IN GRINDING AND POLISHING SILICON MONO-CRYSTALS ON THE NANOMETRE SCALE

L. C. Zhang, H. Tanaka and I. Zarudi
Department of Mechanical and Mechatronic Engineering
The University of Sydney, NSW 2006, Australia

1. Introduction

Grinding and polishing are important machining processes in preparing high quality components of silicon mono-crystals for integrated circuits and electronic devices. These machining processes must be applied carefully to avoid surface and subsurface damages. It has been widely accepted that a 'damage-free' grinding or polishing of ceramics, such as alumina, can be achieved with certain processing conditions, under which sufficient number of independent slip systems are activated [1-3]. However, the mechanism of material removal associated with damage-free grinding or polishing of silicon has not been understood well. This paper aims to explore the mechanism using molecular dynamics (MD) simulation and experimental analysis.

2. Method

2.1 Molecular dynamics modelling

To reveal dynamically the deformation of silicon mono-crystals subjected to grinding and polishing on the nanometre scale, the three-dimensional molecular dynamics method is used to understand the deformation of the atomic lattice of silicon.

In grinding, an abrasive cutting edge is fixed on a grinding wheel so that the cutting of a diamond tip can be simulated approximately by a cutting process, as shown in Fig. 1, with a hemispherical diamond abrasive of radius R moving from the right to the left with the peripheral speed of a grinding wheel V_c. In polishing, however, abrasives are in a slurry and thus the motion of each abrasive has both a translation of speed V_t and a self-rotation of peripheral speed V_r during polishing. Such abrasive motion is simulated by the molecular dynamics model shown in Fig. 2 with an abrasive ball of diamond of radius R moving horizontally (translation) and rotating about its centre independently at the same time.

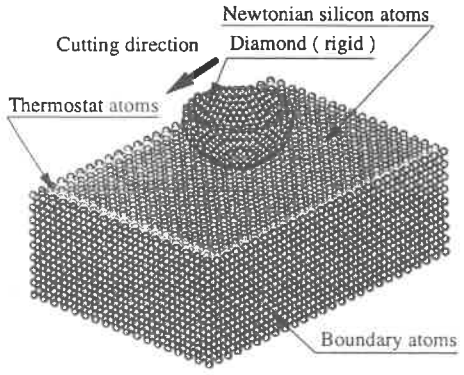

Figure 1 The initial MD model of cutting the (100) surface of a silicon mono-crystal. The indentation depth of the diamond tip is d_i.

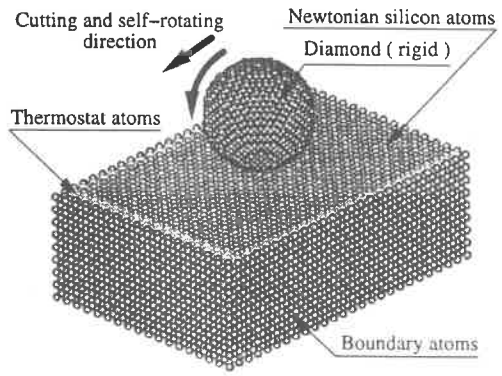

Figure 2 The initial MD model of polishing the (100) surface of a silicon mono-crystal. The indentation depth of the diamond ball is d_i.

To avoid the boundary effect, the dimension of the moving control volume (MCV) of the silicon specimen was taken as 9.23 $nm \times$ 13.57 $nm \times$ 4.34 nm. As usual [4-5], to eliminate the rigid body motion of the specimen and guarantee a reasonable heat conduction outwards the MCV,

layers of boundary atoms, which are fixed to the space, and layers of thermostat atoms, which absorb the heat at the MCV boundaries, are arranged to surround the Newtonian atoms of silicon in the MCV except its top surface (100) that is subjected to abrasion. According to the atomic structure of silicon, Tersoff potential was used to describe the interactions among silicon atoms but Morse potential was employed to reflect those among silicon and diamond atoms. Detailed information about Tersoff and Morse potential functions can be found in Refs. [3-6].

Another important factor in a successful molecular dynamics modelling is the reliability of the relationship between the kinetic energy and temperature of an atom. Currently, there are three models available [7], *ie*, Dulong-Petit model, which takes into account the independent lattice vibration, Einstein model, which is based on the consideration of the single characteristic frequency, and Debye model, which involves a range of frequencies. Our comparison with experiments shows that in the temperature regime encountered in the grinding and polishing processes to be discussed in this paper, Debye model is the best for silicon and Einstein model is the most applicable to diamond.

2.2 Experimental analysis

Experimental investigations were also carried out in two ways, *ie*, in polishing and grinding, to examine the variations of surface and subsurface microstructures of silicon mono-crystals with processing conditions and to understand the related mechanism revealed by MD analysis. In grinding, the (100) surfaces of silicon mono-crystals were ground in the <110> direction on a modified ultra-precision surface grinder, Minini Junior 90CNCM286 (loop stiffness = 80 *N/μm*), using a diamond wheel, SD4000L75BPF, of 305 *mm* in diameter rotating at 1500 *rpm*. The depth of cut of the grinding wheel was fixed at 100 *nm* but the table speed was varied from 0.02 *m/min* to 1 *m/min* to alter the nominal chip thickness. The coolant used was Syntilo 3 (99% water and 1 % mineral oil).

To prepare surfaces by polishing, the silicon mono-crystal specimens were first ground by loose abrasives of silicon carbide with a mean diameter of 50 *μm* and followed by a similar grinding with abrasives of 25 *μm* in diameter. After that, a series of fine polishing were carried out using alumina abrasives of mean diameters of 15 *μm*, 9 *μm*, 5 *μm* and 1 *μm*, respectively. A finishing polishing was carried out by ultra-fine particles of 25 *nm* in diameter. The polishing pressure applied was about 7.5 kPa. The arm (400 *mm* long) and disk of the polisher rotated at 40 *rpm* and 60 *rpm*, respectively. The finishing polishing took about 10 *hours*.

The topography of ground and polished surfaces were examined by a high resolution scanning electron microscope, JSM-6000F. The subsurface structure was investigated by a Transmission Electron Microscope, EM430, and a Scanning Transmission Electron Microscope, VGHB601.

3. Results

It found that there always existed a thin layer of amorphous silicon in a ground subsurface, as shown in Fig. 3. The thickness of the layer decreased with decreasing the nominal chip thickness. Dislocations of very low density were activated in the crystal silicon from the interface between the amorphous layer and the crystal substrate (Fig. 3a). When the nominal chip thickness or the depth of cut of cutting edges became extremely small, in the case of ultra-fine polishing in particular, no dislocation appeared. The residual amorphous layer became extremely thin and could not be detected even under a very high magnification shown in Fig. 4. In this case, 'truly' damage-free workpieces with perfect crystal structure were obtained. The mechanism of this phenomenon can be clearly elucidated by the atomic lattice deformation presented by the

molecular dynamics analysis. As shown in Figs. 5 and 6, the deformation of a silicon mono-crystal under grinding or polishing has the following distinct features:

(i) Phase transformation, from the original crystal structure of silicon to its amorphous state, happens almost simultaneously with the cutting edge penetration.

(ii) Chipping always takes place within the amorphous layer regardless of the appearance of dislocations in the crystal region. This means that the mechanism of material removal in grinding and polishing silicon mono-crystals is due to the viscous flow in the amorphous zone.

(iii) Re-crystallisation always occurs in the amorphous zone behind the cutting edge, from the bottom of the amorphous layer to the surface. As a result, the residual amorphous layer is always thinner. Under certain processing conditions (*eg*, small depth of cut and certain combination of translating and self-rotating speeds, *etc*), only a few atomic layer undergoes amorphous change during abrasion and a reverse phase transformation from amorphous to crystal may take place completely after abrasion. In this case, there will be no residual amorphous layer in the machined subsurface. In other words, a perfect crystal subsurface without any dislocations and amorphous change is generated.

(iv) In polishing, surface roughness may be improved by abrasive-rolling induced phase transformation without material removal. With an abrasive-indentation depth on the atomic scale, material removal may only occur *via* adhesion when abrasive-workmaterial interactions become sufficiently strong.

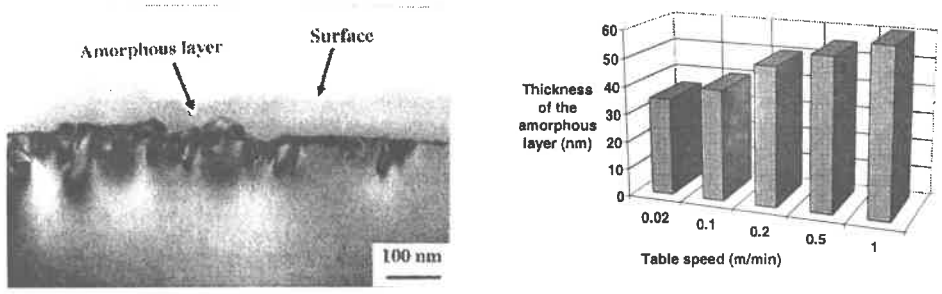

(a) (b)

Figure 3 Subsurface structure of a silicon mono-crystal after grinding, (a) phase change and dislocations (table speed = 0.02 *m/min*), (b) Thickness of amorphous layer *vs* table speed.

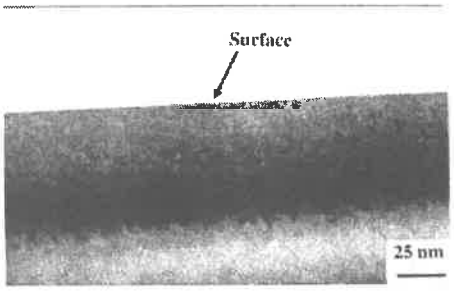

Figure 4 The 'perfect' subsurface structure of crystal obtained by the ultra-fine polishing process. The polished surface is (100). No dislocation exists. The residual amorphous layer cannot be detected. The ultra-fine polishing conditions used are presented in section *2.2* of this paper.

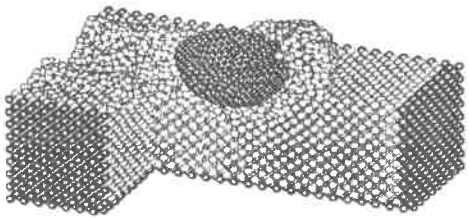

Figure 5 Chipping via viscous flow in the amorphous layer when cutting the (100) surface of a silicon mono-crystal. Note the thickness variation of the amorphous layer underneath and behind the diamond tip. Note also that no dislocations are generated. Cutting conditions are: $V_c = 200$ *m/s*, $d_i = 0.99$ *nm* and $R = 2.1$ *nm*.

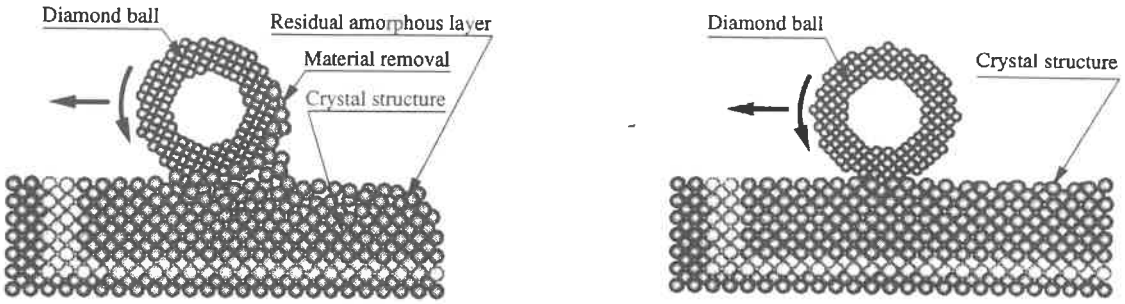

(a) (b)

Figure 6 A cross-sectional view of the instant change of subsurface structure in silicon during polishing, (a) with a residual amorphous layer (polishing conditions: R = 1.07 *nm*, d_i = 0.09 *nm*, V_t = 100 *m/s* and V_r = 50 *m/s*), (b) without any residual amorphous deformation or dislocations (R = 1.07 *nm*, d_i = 0.09 *nm*, V_t = 100 *m/s* and V_r = 100 *m/s*).

4. Conclusions

According to the above analysis, we obtain the following conclusions:

(1) The material removal of grinding and polishing silicon mono-crystals on the nanometre scale is due to the viscous flow within the amorphous layer. Below a certain limit of abrasive indentation depth (on the atomic scale), grinding cannot remove material, but polishing can do through the mechanism of adhesion when abrasive-workmaterial interaction is sufficiently strong.

(2) Dislocations are not important to material removal. If the depth of cut of each cutting edge is sufficiently small, a 'perfect' crystal subsurface can be produced.

(3) In nano-grinding and nano-polishing silicon mono-crystals, deformation via amorphous phase transformation and its associated viscous flow is more favourable than that via dislocation.

Acknowledgment

The authors would like to thank the continuous financial support from the Australian Research Council to this research. Dr Nicole Bordes at the Vislab of Sydney University helped in MD visualisation and Mr. A Leistner at CSIRO Lindfield helped in polishing specimens.

References

[1] I. Zarudi, L. C. Zhang and Y-W Mai, *J Materials Science*, **31** (1996) 905-914.

[2] I. Zarudi and L C Zhang, in: *Procs 10th ASPE Annual Meeting*, Austin, Texas, USA (1995) pp.163-166.

[3] I. Zarudi, L. C. Zhang and D. Cockayne, submitted to: *J Materials Processing Tech* (1997).

[4] L C Zhang and H Tanaka, Towards a deeper understanding of friction and wear on the atomic scale: a molecular dynamics analysis, *Wear*, in press (1997).

[5] H Tanaka and L C Zhang, in: *Progress of Cutting and Grinding*, edited by N Narutaki, et al, JSPE, Osaka, Japan (1997) pp.262-266.

[6] H. Tanaka and L C Zhang, in: *Advances in Abrasive Technology*, edited by L C Zhang and N Yasunaga, World Scientific, Singapore (1997) pp.43-47.

[7] C Kittel, *Introduction to Solid State Physics*, 7th edn, John Wiley & Sons Inc, New York (1996).

A Basic Study on Nanometer Cutting of Brittle Materials

Kohsaku ASAMOTO*, Katsushi FURUTANI, Naotake MOHRI
Toyota Technological Institute
12-1, Hisakata 2-chome, Tempaku-ku, Nagoya 468 JAPAN
Phone: +81-52-802-1111, Fax: +81-52-809-1721
* *Koyo Seiko Co. Ltd.* at present

Key words: nanometer cutting, brittle material, atomic force microscope (AFM), cantilever, frictional force microscope (FFM), wear, single crystal silicon

1. Introduction

In recent years, micromachining technology has been utilized in various fields [1]. The progress of technologies will require more precise machining.

Fine cutting with an atomic force microscope (AFM) suitable for observing in minute area has been studied by experiments and simulations [2][3]. In these studies, mechanical removal process is performed with the probe of the AFM for a cutting tool. Nanometer order shapes have been obtained by cutting in air. Single crystal silicon is usually used for a workpiece in these experiments because of its homogeneity. By cutting with the depth less than sub-micrometer order, silicon can be machined in the ductile mode with continuous chips [4].

The authors define the cutting brittle materials in the ductile mode with the nanometer roughness as the nanometer cutting.

In this paper, a measurement method of the wear of the probe tip is proposed at first. Then the influence of cutting conditions on the machinability of the nanometer cutting and the tendency of tool wear are experimentally investigated.

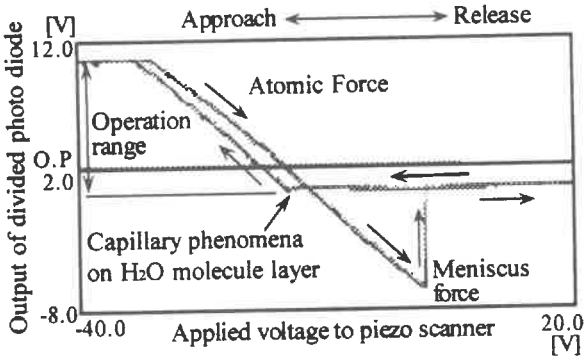

Fig. 1 Example of force curve in air

2. Determination of machining and measurement load

In the experiments, an AFM (SPM 9500 made by Shimadzu) is used to machine a workpiece and observe its shapes. A probe tip is made from Si_3N_4. It has a pyramid shape with the nominal radius of 20 nm . Since a cantilever is made by a leaf spring, the load of the tip on a workpiece can be changed by elevating the workpiece with a piezo scanner.

Before machining shapes, a force curve is measured to determine the machining and the measurement loads.

Fig. 1 shows an example of the force curve measured in air. The vertical and horizontal axes indicate the output of a divided photodiode and the applied voltage to the piezo scanner used for scanning motion in the *xy* plane, respectively. The output of the photodiode is proportional to the deflection of the cantilever in the *z* direction which depends on the load act on the tip. The positive deflection corresponds to the repulsive force between the tip and the specimen. The tip approaches the specimen when the applied voltage to the piezo is decreased. As the distance between the tip and the specimen is changed, the load act on the cantilever is changed by the capillary phenomena on H_2O molecule layer, the atomic force and the meniscus force as shown in Fig. 1. Since the displacement of the specimen is equal to the deflection of the cantilever by the atomic force on the linear part of the force curve, the load act on the cantilever can be

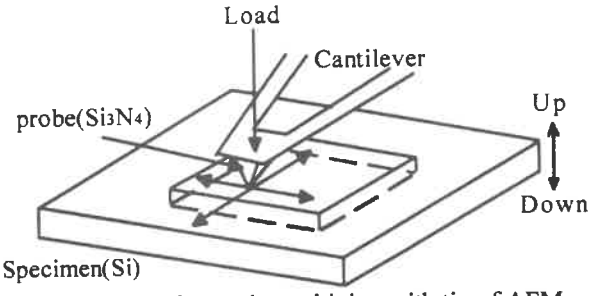

Fig. 2 Method of scratch machining with tip of AFM

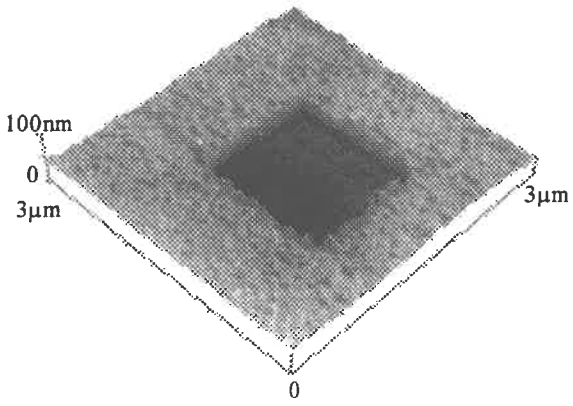

Fig. 3 Experimental result of machining measured with AFM

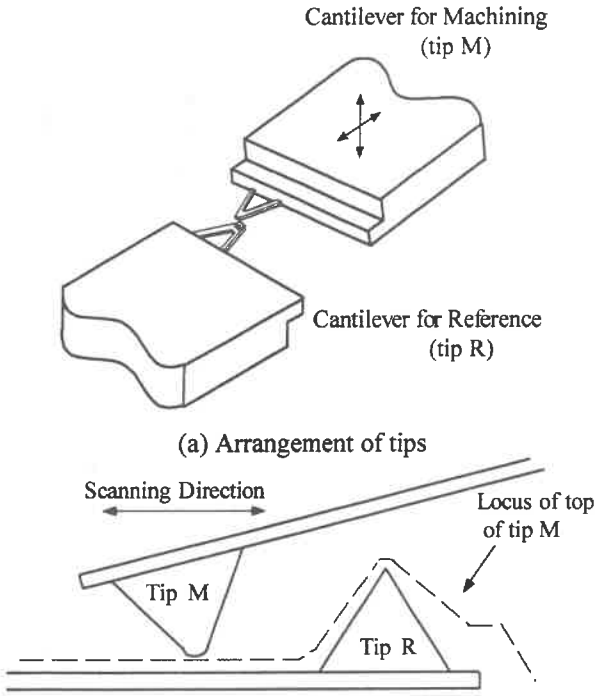

(b) Scanning motion of tip for machining

Fig. 4 Tip shape measurement by scanning over another tip

calculated by using the given spring constant [5]. By using this relation, the machining and measurement loads are determined as 196 nN and 9.8 nN, respectively.

Fig. 2 illustrates a method of scratch machining with the tip of the AFM. By scanning the tip in the x and y directions, shapes can be machined in the z direction.

Fig. 3 shows an experimental result of machining measured with the AFM. A silicon wafer cut along (100) plane is used for a workpiece after the RCA cleaning. The surface with nanometer roughness is obtained by scratching.

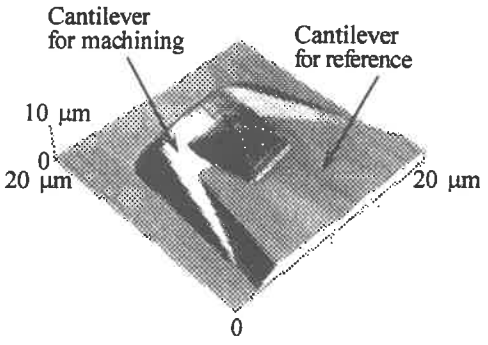

Fig. 5 Example of measurement of tip

3. Measurement of tip wear

3.1 Measurement method

The sharpness of a cutting tool affects the roughness of the machined surface in macro mechanical process.

Since a tip of the AFM is used for the cutting tool in this study, the tip shape should be measured after each scratching to avoid the influence of the tool shape.

In general, a specimen with uniform protrusions is used for a reference to estimate the wear of the tip. In this estimation, the decrease of the spacial frequency indicates the wear of the tip. However, the shape of the tip can not be directly measured by this method.

Fig. 4 illustrates the proposed measurement method of the tip shape. Two tips are faced each other: the tip for machining (tip M) and the tip for the reference (tip R). The sum of their curvature radiuses can be obtained by scanning the tip M over the tip R. When the radius of the tip R is much smaller than the that of the tip M, the radius of the tip M can be measured approximately. The progress of the tip wear can be quantitatively measured by observing the shape of the tips and comparing the shape with the initial shape.

Fig. 5 shows an example of the measurement of the tip. The odd shape of the tip M is observed near its boundary by the interaction between the tips M and R. However, there is no problem on the measurement of the top of the tip. The progress of the tip wear during machining can be observed as shown in Fig. 6.

3.2 Results of measurement

The measurement of the amount of the tip wear by the proposed method is introduced. Fig. 7 illustrates the principle of the tip wear measurement. At first, the

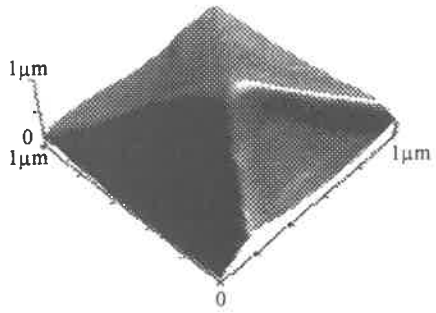

(a) Initial shape

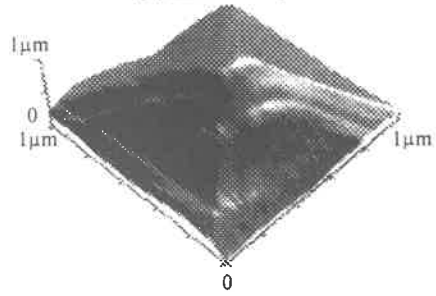

(b) After machining 5×10^4 μm^2

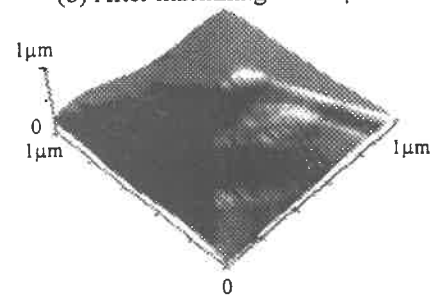

(b) After machining 1×10^5 μm^2

Fig. 6 Progress of tip wear during machining

area of a horizontal of the cross section A on a horizontal plane and the volume of the pyramid above the plane are calculated as the reference area and initial volume of the tip, respectively. After *n*th machining, the nth volume of the pyramid is calculated with the bottom area B which has the same area as the section A. Then the tip wear can be evaluated by comparing *n*th volume with the initial volume. Since the origin of measured shapes with AFMs always drifts and this method does not depend on the relative coordinates, the drift of the origin does not affect the measured amount of the wear.

Fig. 8 shows an example of the progress of the tip wear. It can be observed by the proposed method that the tip wear increases with a constant rate during machining. The adhesion of the chip on the tip causes the distribution of the measured wear. The distribution can be reduced by removing the chip.

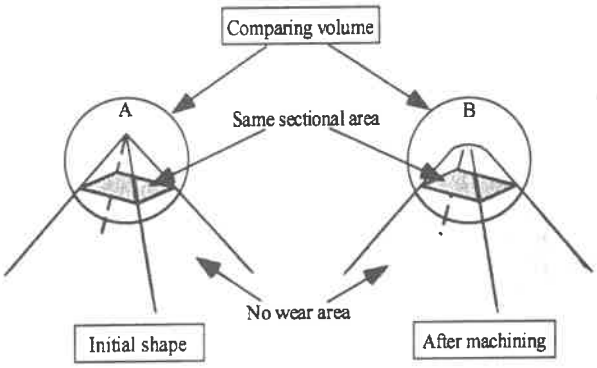

Fig. 7 Principle of tip wear measurement

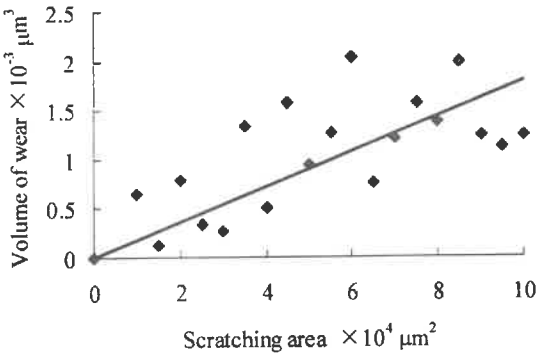

Fig. 8 Progress of tip wear

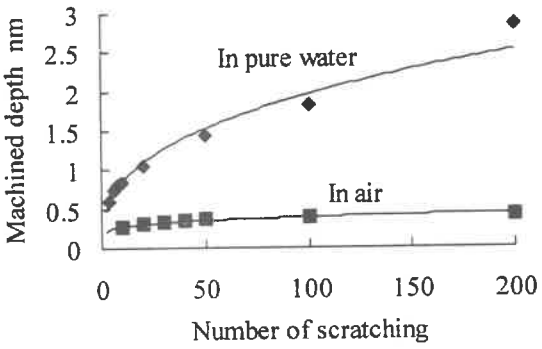

Fig. 9 Relationship between machined depth and number of scratching

4. Influence of surrounding conditions on cutting

4.1 Machined depth

To investigate the influence of surrounding conditions, the workpiece is scratched in air and in pure water under the low wear conditions of the tip.

Fig. 9 shows the relationship between the machined depth and the number of scratching. The same area with the dimensions of 0.5×0.5 μm is machined 200 times with scanning speed of 10 μm/s.

The machined depth in air is smaller than that in pure water. The machined depth in air is saturated after about 50th machining though the machined depth in pure water is still increasing. This tendency is almost the same under any conditions of the initial surface, ambient temperature and humidity.

4.2 Change of surface condition

The surface before and after machining is compared by using the frictional force microscope (FFM) mode.

Fig. 10 shows an AFM image of the surface and an FFM image near the boundary of the machined area after 200th machining in air. The AFM image indicates the machined rectangular area. By considering the machined depth and the result measured with the FFM image, the surface characteristics of the machined area is different from non machined area. Since there are adherent chips and oxide layers on the surface of the machined area, it is not sure that single crystal silicon can be machined with the tip of the AFM in air. The adherent chips on both the tip and the machined surface reduce the removal rate with the tip. In water, the chips hardly affect the sharpness of the tip or chemical reaction assists the removal of silicon.

5. Conclusions

Nanometer cutting has been carried out with an AFM. The following conclusions can be drawn through the experiments:

(1) The tip wear can be measured by the proposed method during scratch machining. The tip wear is proportional to the traveling distance of the tip in machining.

(2) The removed amount of silicon with the AFM in water is larger than that in air.

The influence of chemical reaction and other atmosphere will be investigated in future.

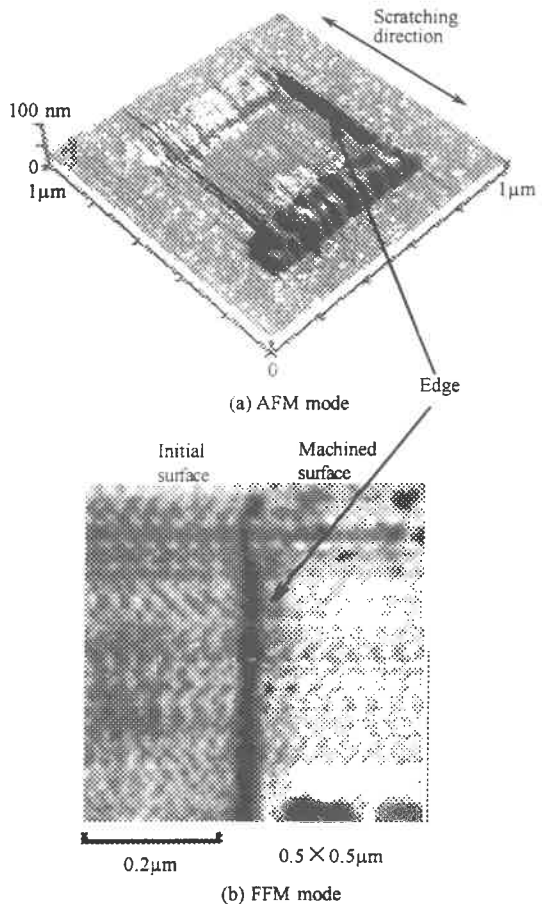

Fig. 10 AFM image of surface and FFM image near boundary of machined area after 200th machining in air

Acknowledgment

The authors wish to thank to Prof. S. Shimada of Osaka Univ., Prof. T. Inamura of Nagoya Inst. Technol., and Mr. R. Kokawa and Mr. Y. Yamakage of Shimadzu Corp.

References

[1] H. Fujita: A Decade of MEMS and Its Future, Proc. 10th IEEE Int. Workshop on Micro Electro Mech. Syst., Nagoya, Japan, pp. 1-8 (1997).

[2] S. Miyake, M. Ishii, T. Otake, N. Tsushima: Nanometer-scale Mechanical Processing of Muscovite Mica by Atomic Force Microscope, J. Jpn. Soc. Prec. Eng., 63, 3, pp. 426-430 (1997) [in Japanese].

[3] P. Markiewicz, M. C. Goh: Simulation of Atomic Force Microscope Tip-sample/ Sample-tip Reconstruction, J. Vac. Sci. Technol., B, 13, 3, pp. 1115-1118 (1995).

[4] S. Shimada, N. Ikawa, T. Inamura, N. Takezawa, H. Ohmori, T. Sata: Brittle-Ductile Transition Phenomena in Microindentation and Micromachining, Annals of the CIRP, 44, 1, pp. 523-526 (1995).

[5] B. Bhushan: Handbook of Micro/ Nano Tribology, CRC Press, (1995)

High-Precision Magnetic Levitation Stage for Photolithography

Won-jong Kim and David L. Trumper
Massachusetts Institute of Technology
Cambridge, MA 02139

1. Introduction

We have designed a permanent-magnet linear motor with Halbach magnet arrays to provide drive force as well as suspension force for a magnetically levitated wafer-stepper stage [1, 6]. Figure 1 shows a perspective view of the selected design concept for prototyping. Figure 2 is a photograph of such a prototype stage designed and implemented by the authors. The platen is levitated without contact by four novel permanent-magnet linear motors which provide both suspension and drive forces. By coordinating the forces applied by each motor, the stage can be accurately controlled in six degrees of freedom. The platen mass of 5.58 kg is supported against gravity by the combined forces of the four motors. Each motor consumes about 5.4 W to lift the platen. The present design has a travel of 50 mm in x and y, a travel of 400 μm in z, and is capable of milliradian-scale rotations about each of these three axes. Detailed fabrication issues of the stage can be found in [4] and are not repeated here. This electromechanical design and configuration has also been adopted in a scanning stage being under testing by Mike Holmes at the University of North Carolina-Charlotte [2].

This paper presents the working principle underlying the stage operation, and experimental data demonstrating the stage performance capabilities. In the following section, an overview of the magnetic levitation stage is given. Section 3 describes the real-time control of the stage. Test results are given and discussed in Section 4.

2. High-Precision Planar Magnetic Levitator

For our three-phase permanent-magnet linear motors, the parameters have the following values: magnet remanence, $\mu_0 M_0 = 1.29$ T, pitch $l = 25.6$ mm, and the nominal motor air gap $z_0 = 250$ μm. The magnet array thickness is $\Delta = l/4$ and the winding thickness is $\Gamma = l/5$.

To drive the motors, we implemented linear transconductance power amplifiers, with maximum current and voltage ratings of ± 1.5 A at $\pm$ 22 V. The nominal power dissipation per motor is 5.4 W at the 0.5-A nominal peak phase current. The suspension power coefficient of the stage is 7.2 mW/N^2.

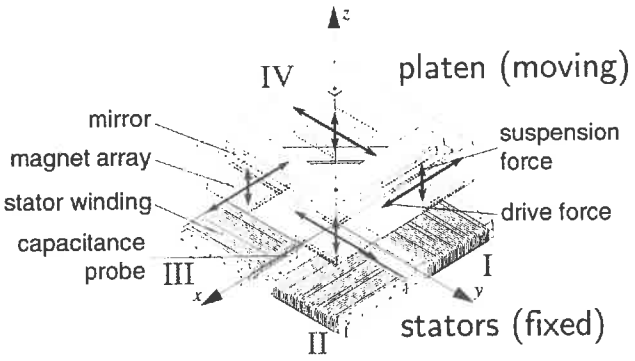

Figure 1: Perspective view of the selected design concept and force definitions of the levitator

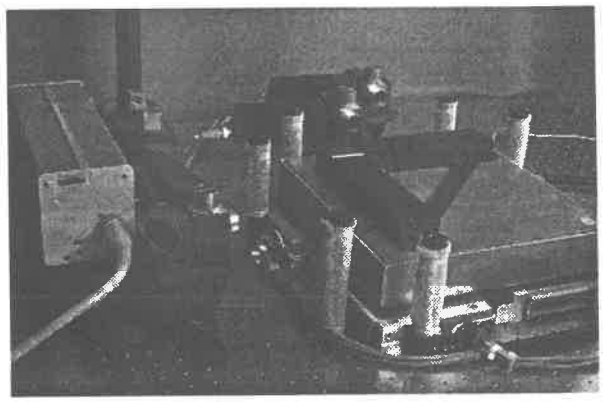

Figure 2: High-precision magnetic levitation stage for photolithography

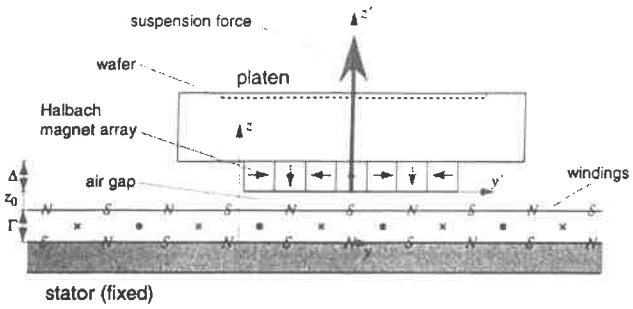

Figure 3: Suspension of the platen in dynamic equilibrium. Only peaks of winding currents are indicated as dots and crosses.

The resistance and the self-inductance of one-phase winding are 14.4 Ω and 3.44 mH.

Figure 3 depicts the dynamic equilibrium around which the levitator operates and is stabilized. These currents are shown as x's into the page and •'s out of the page. We also show the north (N) and south (S) poles generated by these currents. At a fixed time, if we generate the current sinusoidally distributed in the y-direction as in Figure 3, there is vertical repulsive force between the same magnetic poles of the magnet array and the current distribution (i.e., corresponding north to north and south to south). This vertical repulsive force lifts the platen against gravity. Since this equilibrium is unstable in the lateral direction (in the y-direction in the figure), however, we need active feedback control to stabilize the motion of the platen around this dynamic equilibrium. Conceptually, we can control the magnitude of the force by changing the magnitude of the current, and direction of the force by commutation. See [4, 6, 3] for more details.

The four motors in Figure 1 collaboratively generate all six-degree-of-freedom motions for focusing and alignment and large two-dimensional step and scanning motions for high-precision positioners such as a wafer stepper stage in semiconductor manufacturing. Two of the motors (I and III) drive the stage in the x-direction, and two of the motors (II and IV) drive the stage in the y-direction. The motor forces are coordinated appropriately to control the remaining degrees of freedom.

In the following section, we describe the real-time control of the magnetic levitator.

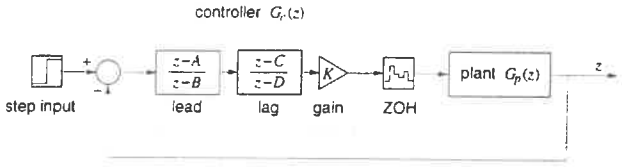

Figure 4: Decoupled lead-lag digital controller

3. Real-Time Digital Control

Figure 4 is a block diagram of the discrete-time lead-lag controller with $A = 0.96300$, $B = 0.68592$, $C = 0.99624$, and $D = 1$. The gains K for the six axes, x, y, z, ψ, θ, and ϕ are 2.2261×10^6 N/m, 2.2261×10^6 N/m, 2.3141×10^6 N/m, 2.2504×10^4 N/rad, 2.2504×10^4 N/rad, and 3.9804×10^4 N/rad, respectively. For small angular motions in our levitator, the Euler angles ψ, θ, and ϕ can be considered as rotational angles around the x-, y-, and z-axes, respectively. Because of the geometrical symmetry in x and y of the levitation system, they have identical controllers. The same is true for the controllers for ψ and θ.

Figure 5 shows a 5-μm step response in x with this lead-lag compensator. All the six-axis controllers are operational in this experiment. Note that the platen dynamics are coupled in all six degrees of freedom. Because of this coupling nature of the platen, there are perturbed motions in all other five axes. The step response also shows a 40-Hz frequency component which we believe to be a natural mode of the closed-loop system. The low damping shows that the system has only about 20° phase margin as compared with a design value 45°, and this response show correspondingly more ringing compared with the computer simulation. An unmodeled coupling effect is likely responsible for this phenomenon. The source of this coupling remains to be determined, and will be investigated in future work.

4. Test Results

We provide several test results in this section. Figure 6 shows the position regulation results by using the decoupled lead-lag controllers designed above. The platen's position is held at the origin in the global coordinate frame. The position noises in x- and y-axes are on the order of 5 nm rms. The

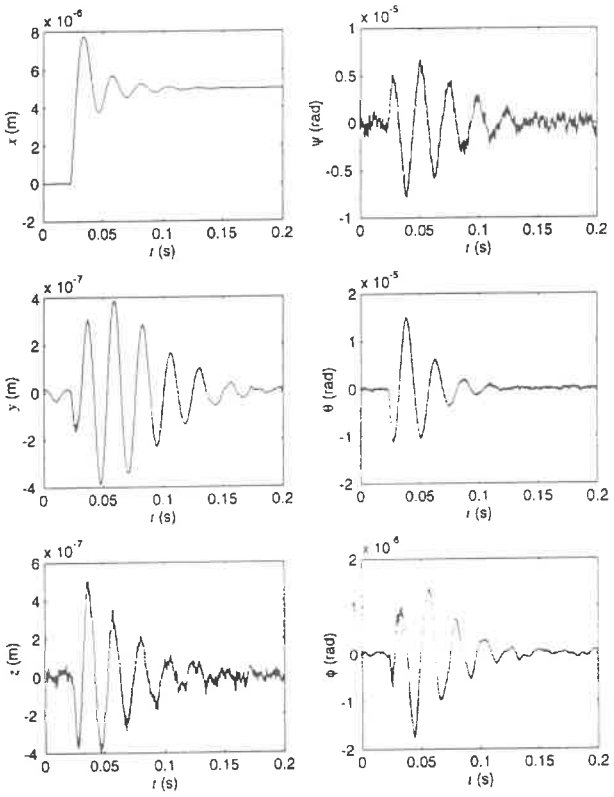

Figure 5: 5-μm step response in x with perturbed motions in the other five axes

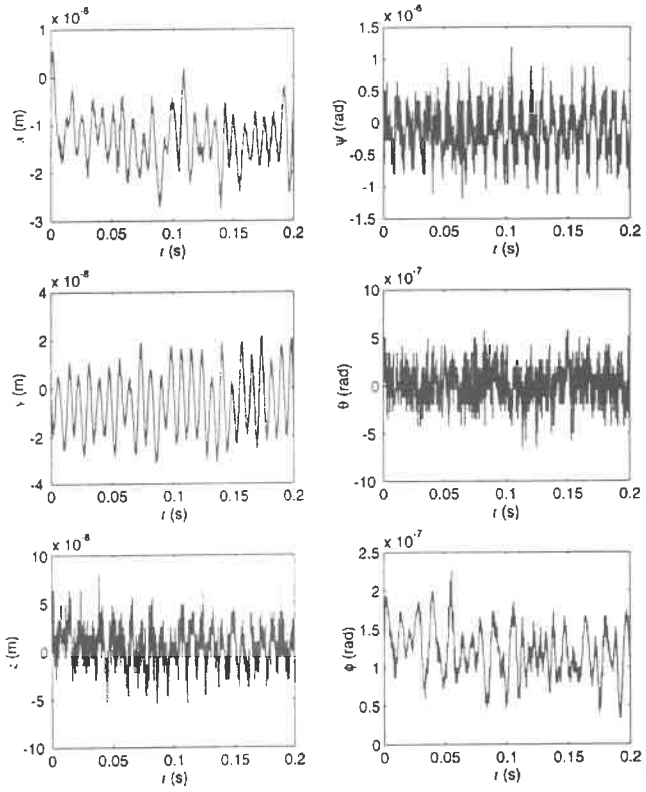

Figure 6: Position noises in six-degree-of-freedom position regulation with the six decoupled lead-lag compensators

position noise in ϕ is 0.05 μrad rms. The vertical displacement z shows a 70-nm-order position error envelope. The A/D converter electronics noise is primarily responsible for the poorer position noise in z, relative to x and y which are measured with sub-nanometer resolution via our laser interferometer system.

The testing result in Figure 6 also has a dominant 120-Hz noise. Lab floor vibration due to an HVAC equipment located in the next room is believed to generate this noise. The floor vibration of our lab includes other lower frequency components at 7.5 Hz, 8 Hz, 15 Hz, and 28 Hz. A more detailed trace of this floor vibration can be found in [5]. This vibration is attenuated by an air spring isolation system, but is still dominated in the error motions.

For the fastest motion generation, we accelerate the platen at the highest acceleration possible until the velocity reaches the maximum slew rate, hold this velocity for a time, then decelerate the platen at the same maximum acceleration to brake the platen motion. This is called a trapezoidal velocity profile. The platen thus follows a parabolic, a linear, and another parabolic reference trajectories. Figure 7 is a test result with a 20-mm step in the y-direction. The acceleration given to the platen is 10 m/s^2 (about 1 g). The command follows a 120-ms transition time for the 20-mm step.

We have also demonstrated that the stage can simulate motions of a wafer stepper. The platen makes step-and-settle motions described above in the positive y-direction, steps over in the positive x-direction, makes step-and-settle motions in the negative y-direction, and so on. The platen can also follow a circle with 30-mm diameter in one second. The purpose of this demonstration is to show the levitation system can generate any unified two-dimensional motions with predetermined paths.

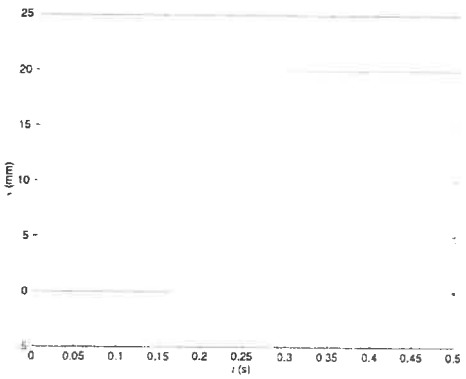

Figure 7: 20-mm step in y. The platen follows a trapezoidal velocity profile.

5. Conclusions

We have designed and implemented a world's first high-precision six-degree-of-freedom magnetic levitator with large two-dimensional motion capability for photolithography in semiconductor manufacturing. The magnetically levitated platen generates all the required small motions for focusing and alignments as well as large planar motions for wafer positioning. This magnetic levitation stage can be readily used in a clean room, since there is no wear particle generation and no lubrication is required. This design is also highly suitable for vacuum environments, since the heat generated in the motors is in the fixed frame and thus can be readily removed by material conduction.

Furthermore, there is no backlash because the levitation system uses no intermediate power transmission device like ball screws. Thanks to the lack of friction or backlash, the position accuracy depends primarily on sensors. Thus, the stage precision depends primarily on the fundamental limits of metrology and control. Another advantage is that no fine finishing of surfaces of mechanical parts, such as for bearings, is necessary. This simplifies the production process and reduces the manufacturing cost.

The magnetic levitation stage has been tested successfully. We implemented decoupled lead-lag digital controllers in a 320C40 digital signal processor. The sampling rate of the system is 5 kHz. The control loop for the levitator is able to be closed at a 50-Hz bandwidth. A mirror resonance at 400 Hz limits the ability to achieve higher bandwidth. Important experimental achievements include 5-nm rms position error in x and y, 30-nm rms position error in z, 20-mm steps following 120-ms references, and 1-g acceleration. We thus have demonstrated that the planar magnetic levitator is a promising candidate as the positioning stage in next-generation semiconductor manufacturing.

Acknowledgments

Portions of this work are part of a thesis submitted by W.-J. Kim [3] for the Doctor of Philosophy degree in Electrical Engineering and Computer Science at the Massachusetts Institute of Technology, Cambridge, Massachusetts. This work is supported in part by a contract from Sandia National Laboratories under Subcontract No. AH-4243 and in part by a Scholarship from Korean Ministry of Education to W.-J. Kim and a National Science Foundation Presidential Young Investigator Award (DDM-9496102) to D. L. Trumper.

References

[1] K. Halbach. Design of permanent multipole magnets with oriented rare earth cobalt material. *Nuclear Instruments and Methods*, 169(1):1–10, 1980.

[2] M. L. Holmes, R. J. Hocken, and D. L. Trumper. A long range scanning stage (the LORS project). In *Proceedings of 1997 ASPE Annual Meeting*, October 1997.

[3] W.-J. Kim. *High-Precision Planar Magnetic Levitation.* PhD thesis, Massachusetts Institute of Technology, June 1997.

[4] W.-J. Kim, D. L. Trumper, and J. B. Bryan. Linear-motor-levitated stage for photolithography. *Annals of the CIRP*, 46(1):447–450, August 1997.

[5] S. J. Ludwick. Modeling and control of a six degree of freedom magnetic/fluidic motion control stage. Master's thesis, Massachusetts Institute of Technology, February 1996.

[6] D. L. Trumper, W.-J. Kim, and M. E. Williams. Design and analysis framework for linear permanent-magnet machines. *IEEE Transactions on Industry Applications*, 32(2):371–379, March/April 1996.

A Long-Range Scanning Stage (The LORS Project)

Mike Holmes, Robert Hocken
Center for Precision Metrology, University of North Carolina,
Charlotte, NC, USA

David Trumper
Laboratory for Manufacturing and Productivity, Massachusetts Institute of Technology,
Cambridge, MA, USA

This extended abstract describes a magnetically-suspended six-degree-of-freedom precision motion control stage. This Long-Range Scanning (LORS) stage has travel in the horizontal plane of 25 mm x 25 mm along with 100 μm of vertical travel. Vertical position feedback is provided by three capacitance probe sensors while heterodyne laser interferometry is used for lateral position feedback. The performance objectives are a positioning resolution of 0.1nm, positioning repeatability of 1nm, and a positioning accuracy of 10nm. These performance objectives have been chosen to match the measurement requirements associated with present and future production needs for devices such as integrated circuits, photo-masks, and micromechanical actuators. The stage is presently operational in a preliminary fashion; full operation is expected shortly.

Keywords: magnetically suspended; precision motion control

Project Overview

The purpose of this research is to explore the use of magnetic bearings in precision motion control applications. In previous research[1,2], we demonstrated the utility of combining magnetic bearings with neutrally-buoyant oil flotation to achieve sub-nanometer positioning resolution. This project furthers those efforts by increasing the range of travel in the horizontal plane to 25 mm^2 and by placing an ambitious accuracy specification which if met, will make this stage one of the world's most accurate positioning stages. Scanned probe microscopy will be used to characterize the performance of the LORS stage. A two dimensional grid of crosses has been fabricated for use as a reference artifact and will be referred to hereafter as the **sample grid**. The sample grid was manufactured by Hewlett-Packard[3] and measured at PTB[4]. Our goal is to also measure the sample grid and to compare our results with those of PTB. Later the stage will be error mapped using techniques similar to those described by Ye et al[5]. Herein we summarize the results to date of this 2 $\frac{1}{2}$ year old project and present some photographs of the experimental setup.

The LORS Stage

The LORS stage, shown in figure 1, consists of a moving element (**platen**), a **machine frame**, and a **metrology head**. The bottom of the platen holds four permanent magnet arrays. A **reference block** is mounted to the top of the platen via three flexures[6]. The platen is buoyantly floated in oil to reduce bias currents in the motors and to provide

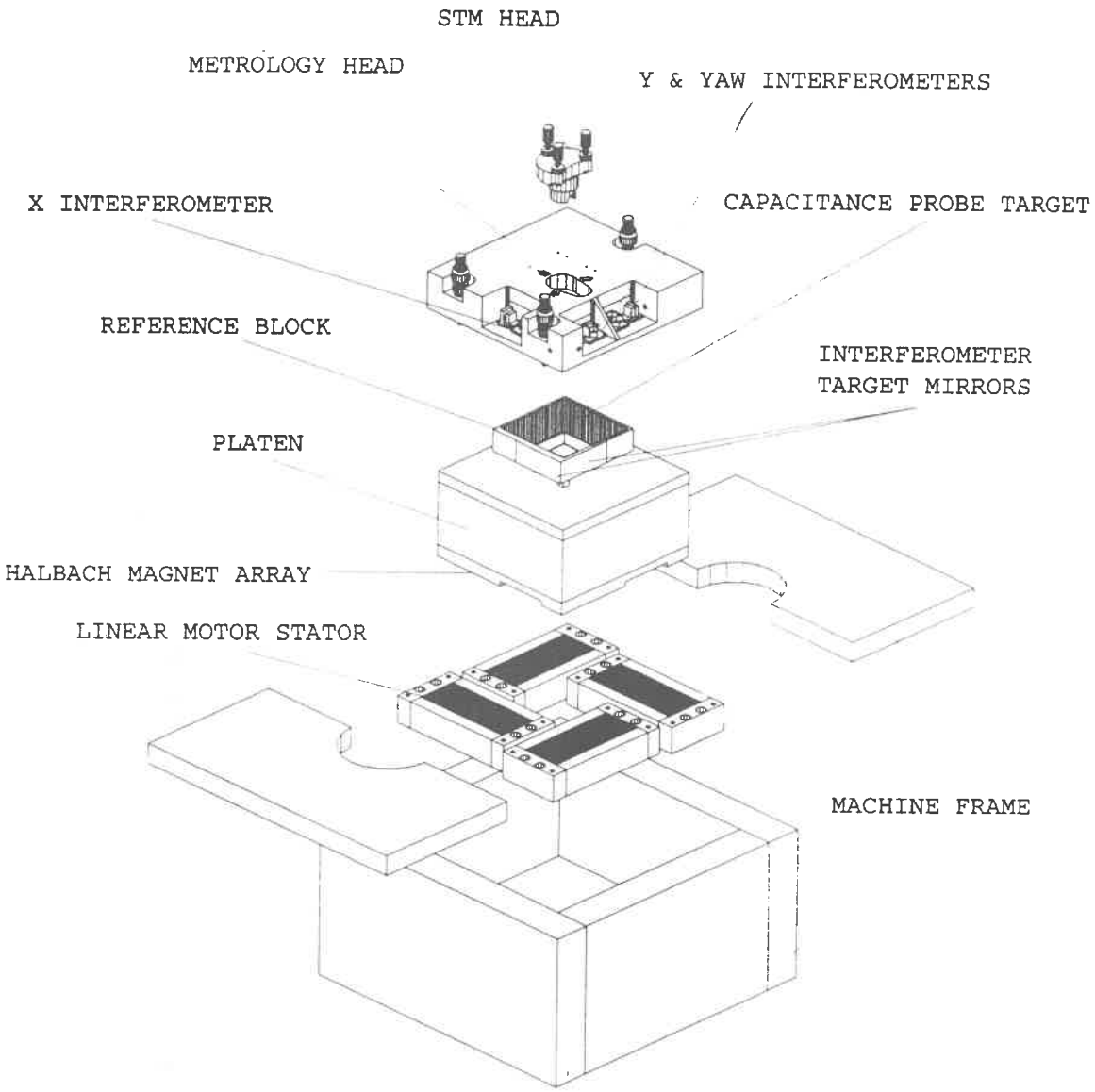

Figure 1: The LORS Stage (Exploded View)

viscous damping and high-frequency coupling. The stator windings are mounted in the machine frame opposite the magnet arrays. The reference block contains the reference surfaces for the position feedback sensors, namely, target mirrors for the interferometers and a conductor plane which acts as the target(s) for the capacitance probes. The sample to be imaged is supported by a sample holder which is kinematically mounted to the reference block. The metrology head is kinematically mounted to the top of the machine frame. The metrology head contains the feedback sensors, three 8-pass interferometers for lateral position feedback and three capacitance probes for vertical position feedback. The metrology head also provides support for the scanned probe microscope head. To reduce the effects of thermal drift, the metrology head and the reference block are made of Zerodur, with a coefficient of thermal expansion of[7] 0.05 μm/m/°C. The idea is to control the currents in the motors, thereby controlling the forces exerted on the platen, based on

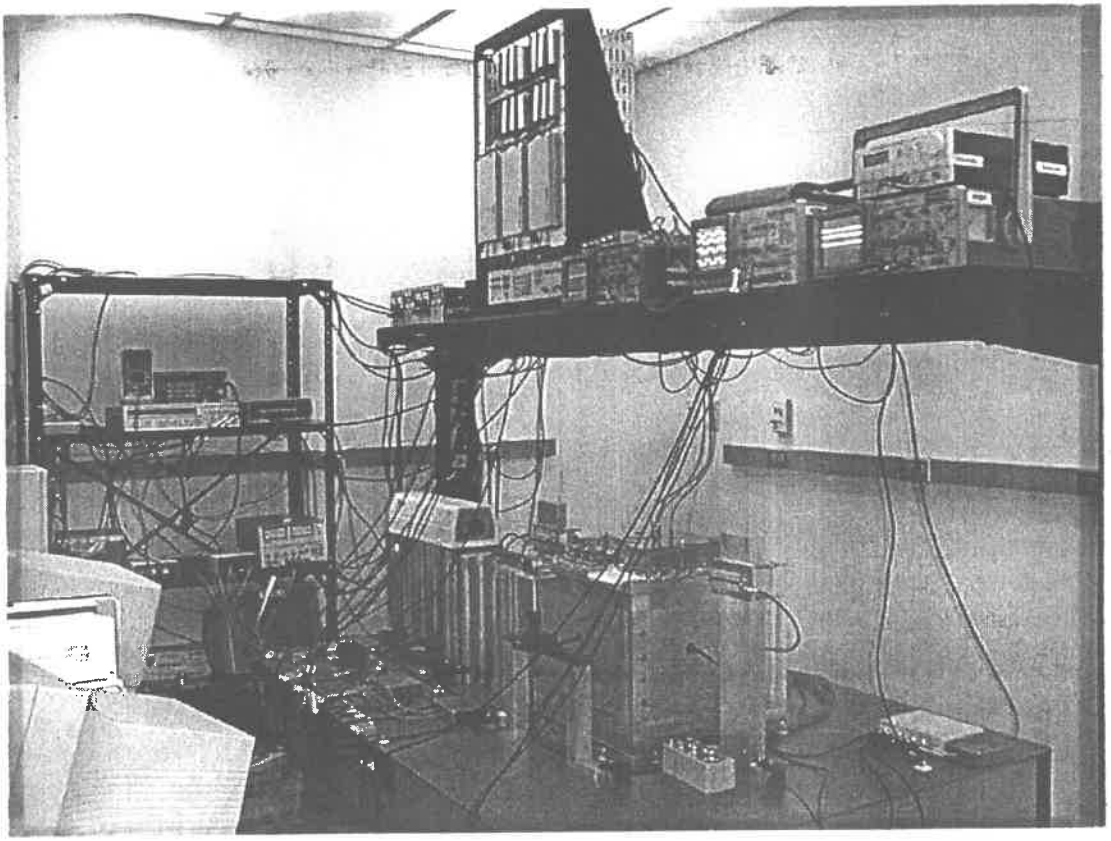

Figure 2: The LORS Project Support Hardware

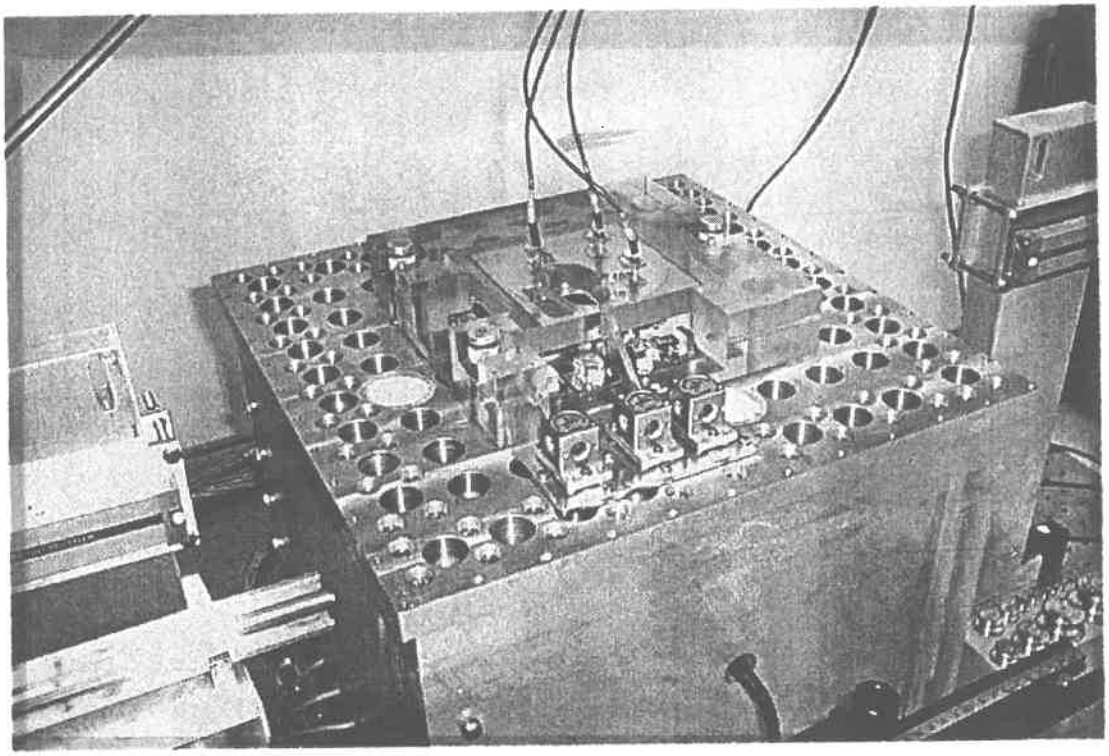

Figure 3: The LORS Stage

the position feedback from the interferometers and the capacitance probes. We will be able to image various samples which will be placed on the sample holder. The scanned probe interface mount is designed to support various types of scanned probe microscope heads (i.e., Atomic Force Microscopes (AFM) and Scanning Tunneling Microscopes (STM)).

Acknowledgments

This research is funded by the National Science Foundation under grant DMI-9414778. The ADE Corporation[8] is providing the capacitive gaging electronics and Zygo Corporation[9] is assisting with the metrology head and reference block fabrication. Hewlett-Packard Photomask fabricated the sample grid which will ultimately be used for performance characterization. The relative locations of the crosses on the sample grid have been measured by PTB. It is our intent to use their results as a comparison rule. Dr. Gerald Blessing of the National Institute of Standards and Technology did some initial experiments to determine the feasibility of using ultra-sonic probes to measure the initial position of the platen in the silicone oil. Also, Won-jong Kim at the Massachusetts Institute of Technology developed the theory underlying the linear motor design[10,11] and provided the impetus for using the chosen coil configuration.

References

[1] Holmes, M.L, Trumper, D.L., and Hocken, R. J., "Atomic-scale precision motion control stage (The Angstrom Stage)," *CIRP Ann.*, vol. 44, no. 1, pp.455-460, 1995.

[2] Holmes, M.L., and Trumper, D.L., "Magnetic/fluid-bearing stage for atomic-scale motion control (the Angstrom stage)," *Precision Eng.*, vol. 18, no. 1, pp. 38-49, Jan. 1996.

[3] Hewlett-Packard Photomask, 5301 Stevens Creek Blvd., Santa Clara, CA 95052-8059.

[4] Physikalisch Technische Bundesanstalt (PTB), Braunschweig, Germany.

[5] Ye, J., Takac, M., Berglund, C., Owen, G., and Pease, R., "An exact algorithm for self-calibration of two-dimensional precision metrology stages," *Precision Eng.*, vol. 20, no. 1, pp. 16-32, Jan. 1997.

[6] Smith, S.T., and Chetwynd, D.G., *FOUNDATIONS OF ULTRAPRECISION MECHANISM DESIGN*, Gordon and Breach Science Publishers, Yverdon, Switzerland, 1994.

[7] Slocum, A., *Precision Machine Design*, Prentice Hall, Englewoods Cliffs, NJ, 1992.

[8] ADE Technologies, 77 Rowe Street, Newton, Mass. 02166.

[9] Zygo Corporation, Laurel Brook Road, Middlefield, Conn. 06455.

[10] Trumper, D.L., Kim, W.J., and Williams, M.E., "Design and Analysis Framework for Linear Permanent-Magnet Machines," in press, *IEEE Trans. Ind. Applic.*, vol. 32, no. 2, Mar/Apr 1996.

[11] Kim, W.J., " High-Precision Planar Magnetic Levitation," Ph.D. Thesis, Electrical Engineering and Computer Science, Massachusetts Institute of Technology, June 1997.

A 3 DOF Z-tilts Micro Positioning System Using Electromagnetic Actuators With Air Bearings

Sung-Q Lee and Dae-Gab Gweon

Dept. of Mechanical Engineering

Korea Advanced Institute of Science and Technology

373-1 Kusung-Dong, Yusong-Gu, Taejon, 305-701, Korea

Abstract

A new 3 DOF (Z, pitch and roll motion) micro positioning system is developed. It uses electromagnetic actuator and air bearings. An Electromagnetic actuator can produce attraction force continuously and air bearings are used as the suspension and guidance with the clearance of several ten-μm in z-direction. Usually, active magnetic bearings with electromagnetic actuator can guide one degree of freedom and magnetic flux is very difficult to analysis. However, air bearing floating on the surface can guide three degrees of freedom, XYθ, moreover, can provide the counter force to the electromagnetic attraction force to make the z-directional positioning without affecting the magnetic flux of the electromagnet. With the control of current, equilibrium position between magnetic attraction force and air bearing thrust force can be controlled with inherently infinite resolutions. With the open loop control, this system provides 30 nm positioning resolution over the total range of 50 μm along the z-direction and 0.6 arcsec resolution over the total range of 100 arcsec in pitch and roll motion.

1. Introduction

A new 3 DOF (Z, pitch and roll motion) micro positioning system is developed. It uses electromagnetic actuator and air bearings. Electromagnetic actuator can produce attraction force continuously so that the resolution depends on measurement devices and D/A convert. Air bearings are used as the suspension and guidance with the clearance of several ten-μm in z-direction[1][2][3]. Usually, active magnetic bearings with electromagnetic actuator can guide one degree of freedom and magnetic flux is very difficult to analysis. However, air bearing floating on the surface can guide three degrees of freedom, XYθ, moreover, can provide the counter force to the electromagnetic attraction force to make the z-directional positioning without affecting the magnetic flux of the electromagnet[4][5].

The principle of this system is similar to the magnetic levitation system except it uses air bearings as suspension. Therefore, this system is

applicable to the magnetic levitation applications, wafer positioning system and another measurement systems which need fine Z-tilt motions.

2. System Configuration and Principle

This system is suspended by three air bearings which are radially disposed with 120 degrees pitch, about 57 mm radius and are wounded by coils to play the role of the electromagnetic actuator. From the combination of three actuators, Z-tilt motions can be obtained. (figure 1.)

Electromagnetic Parts

As in Figure2, magnetic flux is induced by the coils and closed along the base plate, air bearing and sensor holder. An Electromagnetic attraction force is induced between the base plate and sensor holder (h_o) or between the base plate and air bearing pad (h_g). However, since the h_g is several ten-μm which is much smaller than h_o, the attraction force is largely induced in the gap of h_o. Therefore attraction force is[1],

$$F_{attrac.} = (N I)^2 \mu_o A / (2 h_o)^2$$

where N is the number of coil turns, I, current, μ_o, permeability of free space, A, the cross section of effective area , h_o, the gap between the base plate and sensor holder, respectively. Within the Z-directional range, for h_o varies slightly, attraction force is only the function of current I.

Air bearing Parts

Two main performances of air bearings are bearing stiffness and load capacity. Design parameters to decide these performances are supply pressure, orifice diameter, the number of orifices, air gap size and the size of bearing. In this system, annular type air pads are used. To play the role of z-directional counter force to electromagnetic force, it is designed to have load capacity of 9kgf at 10μm h_o, 1kgf at 50μm with 4 orifices of 0.3 mm diameter. Since it is well known to design air bearings[1], it isn't difficult to design exactly. Theoretically load capacity has nonlinear characteristics versus h_g as shown in figure 3.[1] Accordingly, since the stiffness is not constant, open loop control may bring different errors at each point.

Principle of 3 DOF motion

An Electromagnet exerts 0-20kgf according to current I (0 - 2 Ampere) and air bearing's load capacity is 9kgf at 10μm h_o, 1kgf at 50μm as mentioned above. Therefore, with the control of current, equilibrium position between magnetic attraction force and air bearing thrust force can be controlled with inherently infinite resolutions. From the combination of three actuators, Z-tilt motions can be obtained. To decouple the coupling of three actuators, hinge mechanism is used(figure2).

3. Experimental Results

Figure 4 shows a schematic of the Z-tilt stage control. The overall system consists of a PC, D/A converters, current drivers, displacement measurement sensors, A/D converters and the system structure. The PC provides command input voltage (0-10 V) via the home-built D/A converters(12bit). The voltage is amplified by the current drivers (0-2 Ampere) and fed to the electromagnetic actuators. The actuation provides

the displacement required for the system positioning. The actual position information detected by the capacitance gages(probe 2805 with the sensitivity of 25μm/10V, ADE corp.) is also fed back to the PC via the 16 bit A/D converter (20ksamples/sec, AT-MIO-16XE50, National Instruments).

Figure 5 shows the experimental results of open loop control of one actuator remaining another two actuators at constant position. As in the figures, the system is commanded to move multi-step of 2μm. As can be seen from the figure, the system has noticeable open loop errors due to the effect of non-uniformity of bearing stiffness, and a small time varing fluctuating. Thus closed loop control must be performed. Though it uses hinge mechanism to decouple the each actuation motion, there are some coupling effects at each step. To obtain the resolution, it is commanded to move smaller step until distinguishable level. It is noticeable that resolutions are level of sensor noise. Therefore the resolution depends on sensor to a certain degree. With the open loop control, this system provides 30 nm positioning resolution over the total range of 50 μm along the z-direction(figure 6) and accordingly, 0.6 arcsec resolution over the total range of 103 arcsec in pitch and roll motion.

4. Conclusion

A new 3 DOF (Z, pitch and roll motion) micro positioning system is developed. It uses electromagnetic actuator and air bearings. An Electromagnetic actuator can produce the attraction force continuously 0-20kfg and air bearings are used as the suspension and guidance with the clearance of several ten-μm in z-direction. With the control of current, equilibrium position between magnetic attraction force and air bearing thrust force can be controlled with inherently infinite resolutions.

With the open loop control, this system provides 30 nm positioning resolution over the total range of 50 μm along the z-direction and 0.6 arcsec resolution over the total range of 103 arcsec in pitch and roll motion.

References

[1] Alexander H. Slocum, 1992, "Precision Machine Design", Prentice-Hall, pp551-628.

[2] S.A.Nasar and L.E.Unnewehr, 1983, "Electromechanics and Electric Machines", John Wiley and Sons, pp124-134.

[3] Francis. C. Moon, 1984, "Magneto-Solid Mechanics", John Wiley and Sons, pp275-279.

[4] Shigeo KATO, 1996, "Theoretical analysis of Damping Characteristics of Air-Lubricated Slideways", Int. J. JSPE, Vol. 30, No. 1, pp77-82.

[5] Yoshiyuki Tomita , Yasushi Koyanagawa and Fumiaki Satoh, 1996,"A Surface Motor-driven Precise Positioning System",Precision Engineering, Vol.16, No.3, pp184-191.

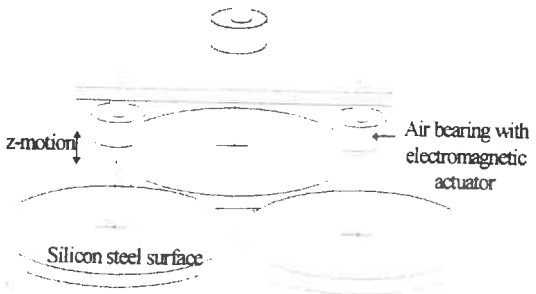

Fig. 1. The schematic of Z-tilts micro positioning system

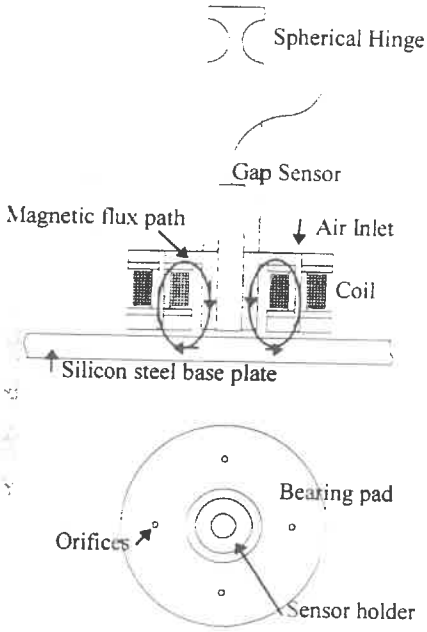

Fig. 2 Electromagnetic Actuator with Air Bearing

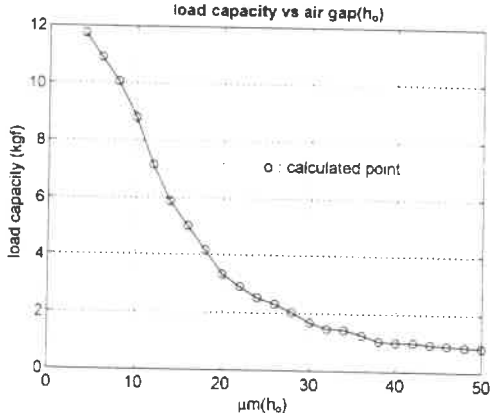

Fig. 3 Bearing's load capacity vs air gap(h_o)

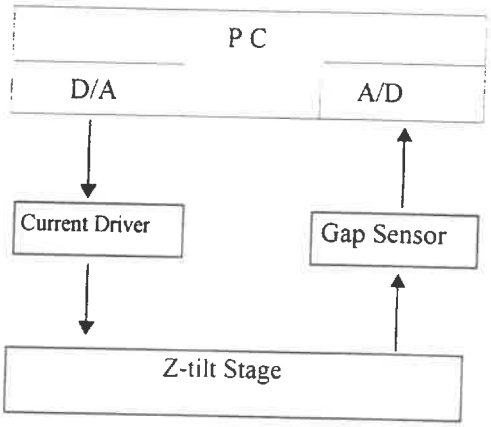

Fig. 4 Schematic of Experimental system

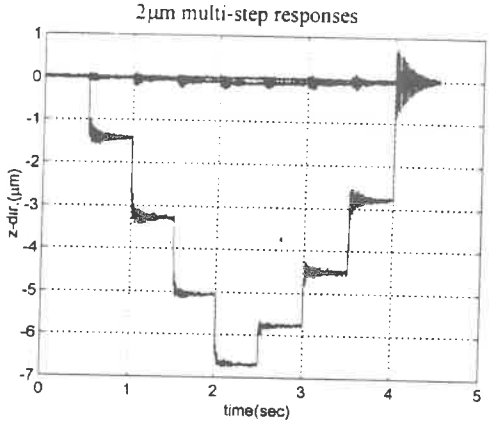

Fig. 5 Open loop multi-step responses

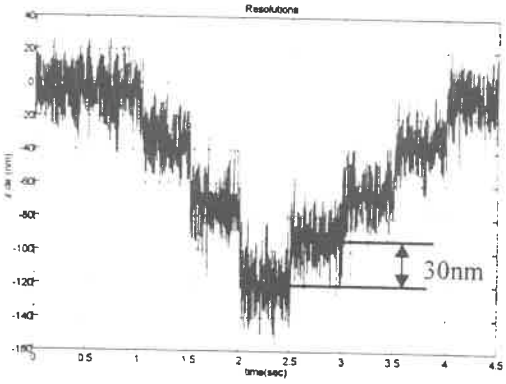

Fig. 6 Resolution of Z-tilt stage

A 1/100 Machine Tool to Fabricate 1/100 Micro Parts

Kazuhisa ISHII, Masayuki NAKAO and Yotaro HATAMURA
The University of Tokyo, Faculty of Eng., Dept. of Engineering Synthesis
7-3-1 Hongo, Bunkyo-ku, Tokyo 113 Japan

1. Introduction

"There's plenty of room at the bottom", in 1959, R. P. Feynman suggested plenty of possibilities for 3-dimensional miniaturized machine [1]. A micro mother machine is capable of producing smaller child machines. Currently, micromachining of micro parts mainly employs lithography technique. The technique has improved for semiconductor processing ; Dr. Feynman paid $ 1,000 for writing a page with 100 nm high characters using an electron beam exposure machine [2]. But this technique is for only thin-film deposited, 2-dimensional, plate-like structures, not for 3-dimensional ones. We want to fabricate complicated, 3-dimensional, micro structures using various materials, which is the same as conventional macro structures.

The authors challenged to design, construct, and evaluate a "1/100 machine tool," i.e. a machine tool which has by 1/100 a smaller size than conventional machines, to fabricate 1/100 micro parts. Through the evaluations we want to know : design constraints of the 1/100 machine tool, new mechanisms to be developed in future, new market using the machine tool and advantages of the miniatured machines. Miniaturized machine tools can save the machine cost and facility space : they can realize smaller positioning error induced by thermal expansion ; they can install in the special environment such as in vacuum or in clean air.

We need to develop some new mechanisms to realize the 1/100 machine tool : all parts of the 1/100 machine tool could not be miniaturized by 1/100. For example, a voice coil motor mechanism is developed for a table drive though a boll screw and AC motor is used in a conventional machine tool. Information on the development of such partial mechanisms, in addition the synthesized 1/100 machine tool, will be useful for future design of various micro elements.

2. Design of the 1/100 machine tool

Design requirement of the machine is "to realize a 1/100 sized machining center". The miniaturized machining center should have the same functions as conventional macro machining center : 3-axis translating table, spindle for tool rotation, auto-tool-changer and so on.

To satisfy the requirement, we should realize the following fourteen functions. The functions are required for machining centers regardless of size. But their realizations were difficult in miniature world, and had worked as design constraints for us. Next we decide the mechanism individually for fourteen functions as follows.

(1) table drive : by a voice coil motor
(2) table guide : by a parallel plates spring
(3) table positioning control : feedback controlled by deformation of the parallel plates spring using strain gauges attached on the plates
(4) spindle drive : by an air turbine using high pressured air
(5) spindle bearing : by a hydrodynamic bearing
(6) origin set-up : adjusted table position observing the workpiece and the tool in upper direction and front-side direction with two microscopic CCD cameras
(7) cutting tool : sharpened on a cutting edge to 0.1 μm using a ϕ 300 μm, purchased single crystal diamond endmill **, or using a ϕ 50-100 μm, homemade carbide endmill fabricated by Wire Electro-Discharged Grinding [3].
(8) tool change : * changing a rotor and a tool together which are glued, or ** by a micro chuck in the spindle
(9) chip removal : by air flow exhausted from a ϕ 100 μm glass pipe
(10) coolant flow : by air flow exhausted from a ϕ 100 μm glass pipe
(11) cutting force measurement : by a force sensor using strain gauges
(12) workpiece material : made of plastic materials or metals
(13) workpiece chuck : * glued on the plate, which is fixed on the table, or ** by a vacuum chuck
(14) workpiece transfer : ** supplied on a hoop sheet
* tentatively developed mechanism, ** still developing mechanism

3. Fabrication of the 1/100 machine tool

Fig. 1 shows the prototype of the 1/100 machine tool, which is 26×26×67 mm in size, 167 g in mass. The spindle is ϕ 12×16 mm in size, rotating at 138,000 r.p.m. maximum with a 0.1 μm radial vibration. The table

is 20×20×40 mm in size, and has 3 axes (x, y and z) translational linear drives with a 1 mm working range in x and y axis, and a 0.8 mm in z. The driving force of the table is 1 N maximum, and the rotating torque of the spindle is 0.1 mNm maximum.

Fig. 2 shows the homemade carbide endmill sized ϕ 50 μm×200 μm long with a 5 μm edge roundness. It was made by WEDG in rotating the tool. As applying voltage between the tool and the wire has not optimized yet, the tool surface looks relatively rough. The tool was glued with the rotor of the spindle in tool making : the axis of the tool is coincided with the axis of the spindle rotaion. It has a half circle shape in cross section.

4. Evaluation of the 1/100 machine tool

4.1 Evaluation of the mechanisms

Fig. 3 shows a resolution in x axis of the table. The figure indicates that steps of 80 nm are represented. The resolution should be 50 nm.

Fig. 4 shows a force (top) and force-induced displacement (bottom) under no control (left) or under position feedback control to keep an ordered position (right). When the force of about 1.1 mN worked the table, the table moved by 9 μm under no control, but by 0.5 μm under position feedback control. The control improved the rigidity from 120 N/m to 2,200 N/m.

4.2 Evaluation of the machine in cutting

Fig. 5 shows an optical view in cutting : 60,000 r.p.m. in spindle rotation, 30 μm /sec in feed rate, 30 μm in cutting depth and PPS (Poly-Phenylene Sulfide) for the workpiece material. Chips were not flown by air ; melted materials were stuck to the tool.

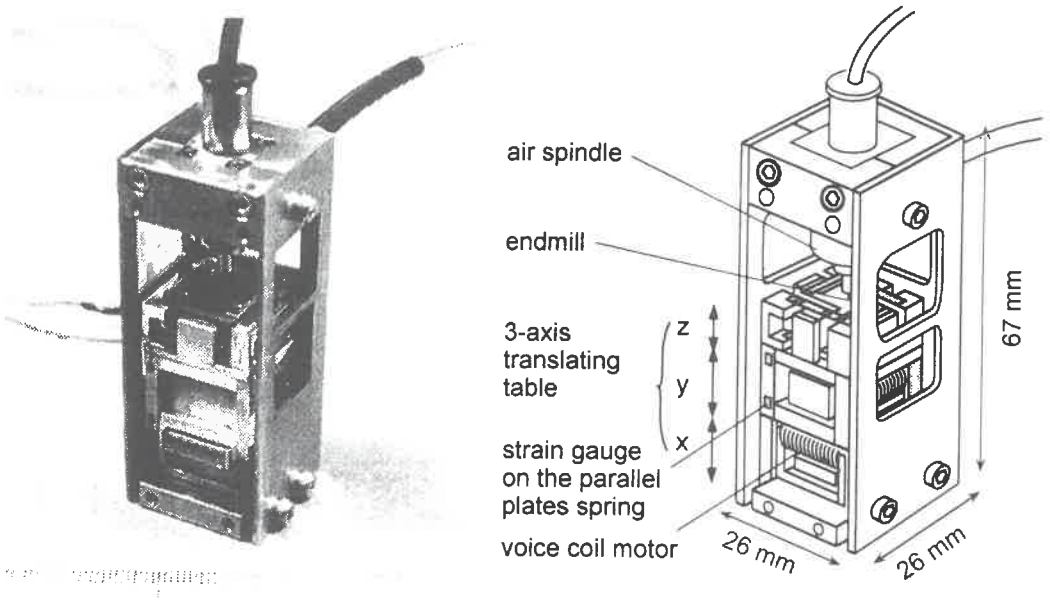

Fig.1 View of micro milling machine

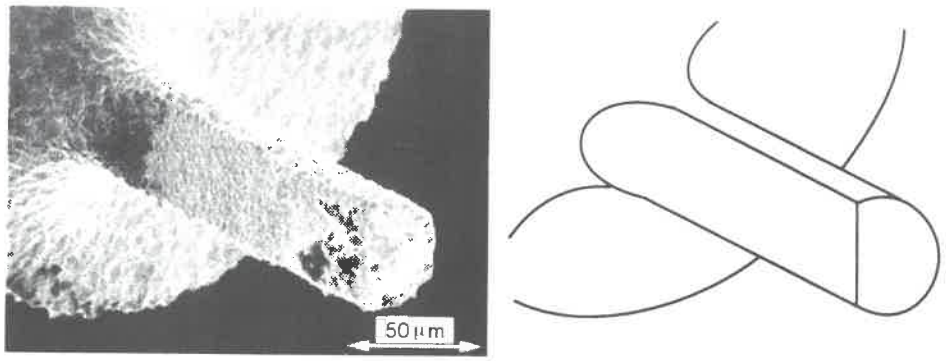

Fig.2 SEM view of carbide endmill

Fig. 6 shows a grooved workpiece using carbide endmill made by WEDG: 60,000 r.p.m. in spindle rotation, 60 μ m /sec in feed rate, 70 μ m in groove width, 10 μ m in groove depth and PMMA for the workpiece material. The tool was suddenly broken in cutting suddenly at the feed finish point of the groove ; Increased cutting force sholud break the endmill.

Fig. 7 shows another grooved workpiece using a diamond endmill : 60,000 r.p.m. in spindle rotation, 600 μ m /sec in feed rate, 380 μ m in groove width, 30 μ m in groove depth and PMMA for the workpiece material. Edge of the groove is free from the chips.

Fig. 8 shows the cutting force measured by a force sensor equipped between the workpiece and the table using (a) carbide endmill and (b) diamond endmill. Fig. 8 (a) indicates that the first slope was due to sensor deformation, the last vibration was due to air blow for chip removal, and the cutting force in stably cutting was about 1 mN. Fig. 8 (b) indicated that the cutting force was less than the resolution of the force sensor even though diameter of the endmill is larger than that of carbide endmill.

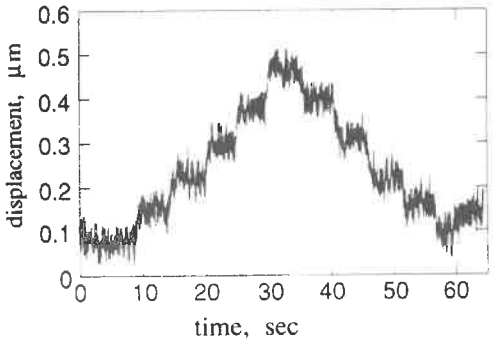

Fig. 3 Step movement in X axis of the table to measure a resolution

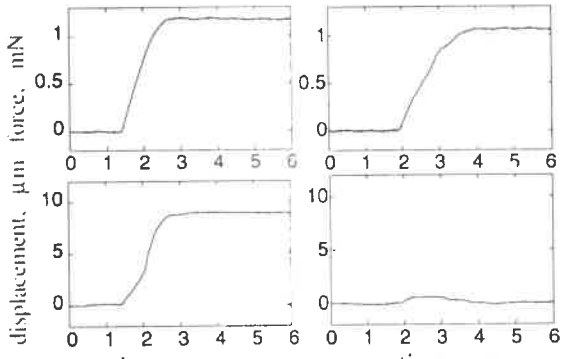

Fig. 4 Force-induced table displacement in X axis of the table

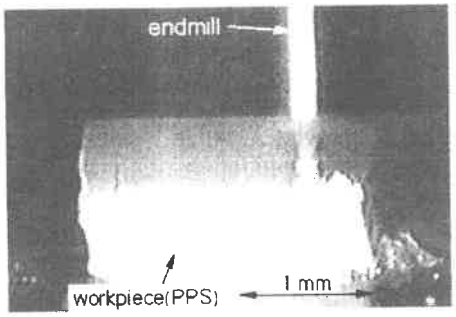

Fig. 5 View of milling process

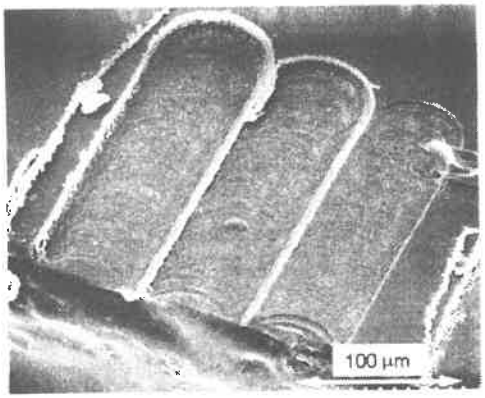

Fig. 6 SEM view of milled workpiece
Cutting condition: rotation: 60 krpm, feed rate: 60 μ m/sec depth: 10 μ m, width: 70 μ m, workpiece: PMMA

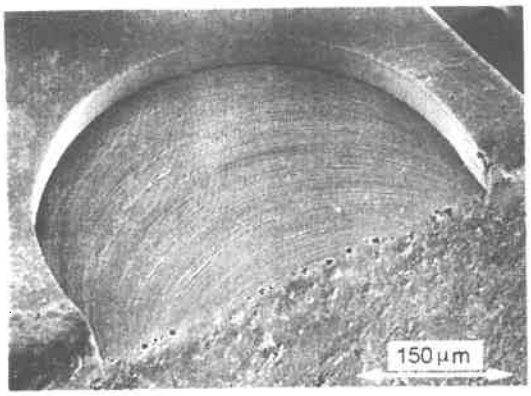

Fig. 7 SEM view of milled workpiece
Cutting condition: rotation: 60 krpm, feed rate: 600 μ m/sec depth : 30 μ m, width: 380 μ m, workpiece: PMMA

5. Discussion

We could not realize the four mechanisms by ourselves so far : (7) cutting tool (sharp cutting ridge), (8) tool change, (13) workpiece chuck and (14) workpiece transfer.

Sharp cutting ridge is indispensable for micro cutting. Because the tool cuts the workpiece by very low removal rate such as 0.06 μm per blade rotation and, a dull edge makes only burnishing, not cutting. The workpiece will melt, and finally will be strongly attached on the blade. The diamond tool realized no chip adhesion and no large cutting force, which suggests the importance of sharp cutting ridge.

Absence of tool change and workpiece chuck resulted in long adjusting time. Sometimes we suffered longer adjustment such as 30 minutes. Though the conventional machining process distributes the workpiece to the fixed machines, on the contrary, the micro machining process should distribute the machines to the fixed workpiece. Because fixing or releasing the workpiece / tool is difficult, the micro process prepares many but redundant machines.

Fig. 9 shows a layout of micro machining process. The machines are concentrated around the workpiece ; the workpiece is fixed without releasing during processing : a total environmental control is managed like an umbrella.

6. Summary

To fabricate 1/100 micro parts, a 1/100 machining tool was designed. The machine is composed of many newly developed mechanisms such as a voice coil motor suspended parallel plates spring because some mechanism were very difficult to be miniaturized. The fabricated machine is 26×26×67 mm in size, 167 g in mass. We could cut the plastic materials with ϕ 50 μm, carbide endmill fabricated by ourselves using Wire Electro-Discharged Grinding. But we still need a sharp cutting ridge such as a diamond endmill by a 0.1 μm edge roundness to cut a plastic material without any burnishing.

We would like to thank THK Co. Ltd. for designing and fabricating the spindle, Prof. T. Masuzawa and Mr. K. Egashira of I.I.S., the Univ. of Tokyo for valuably discussing on the tools made by WEDG.

Reference

[1] R.P. Feynman, "There's Plenty of Room at the Bottom." J. of Micro Electro Mechanical Systems, vol. 1, 1992, pp.60-66.

[2] Ed Regis, *Nano, The Emerging Science of Nanotechnology*, Brown and Company, Boston, MA, 1995.

[3] T. Masuzawa et.al., Wire Elactro-Discharge Grinding for Micro-Machining, Annals of CIRP vol. 34, 1985, pp. 431-434.

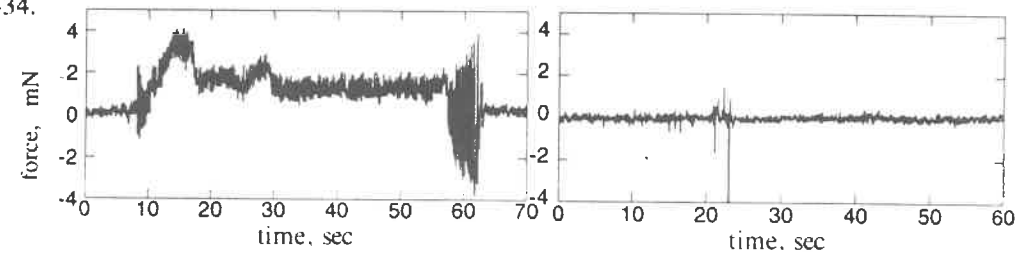

(a) using homemade carbide endmill (b) using diamond endmill

Fig. 8 Measured cutting force in cutting a straight groove
cutting condition : spindle rotation : 60,000 rpm, feed rate : 50 μm/sec,
cutting depth : 10 μm, cutting width: (a) 100 μm, (b) 380 μm, workpiece : PMMA

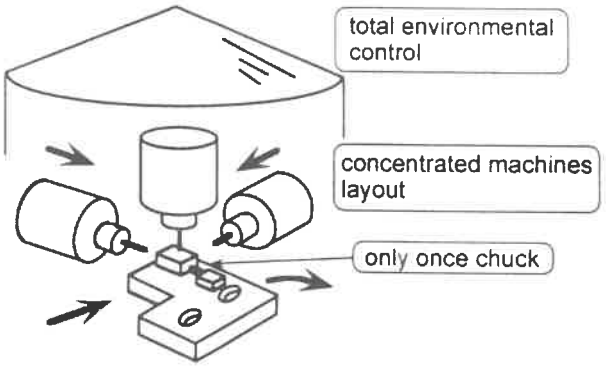

Fig. 9 A new layout of micro machining process

Assembly of micro systems in a large-chamber scanning electron microscope

Manfred Weck, Joachim Hümmler, Bernd Petersen

Fraunhofer Institute of Production Technology IPT
Aachen (Germany)

INTRODUCTION

More and more micro systems are available which are no longer built up monolithically in silicon, but consist of several different components. These components have to be assembled to form an overall system. Moreover, assembly is required whenever a micro system has to be connected to the outer world or housing is necessary. Today, assembly is usually done by hand with the help of tweezers and optical microscopes. It is obvious that this kind of manufacture is very cost-intensive. Only automation will lead to an efficient and precise assembly process.

PROCESS OBSERVATION IN MICRO ASSEMBLY

In order to better understand what is really happening in the micro world, observation is inevitably necessary. Especially in micro assembly, where precise positioning is essential, the operator must be able to have a close look at the process. Optical microscopy and scanning electron microscopy both offer a "live" view on the production process and are common means of magnification. However, there are some important differences.

An optical microscope is relatively compact and easy to handle. In fact, it is used in a number of applications where micro production is concerned, e.g. the assembly of a micro motor.[1] Compared to a scanning electron microscope (SEM) there are some disadvantages. For example, the lateral resolution and especially the depth of focus are much higher with the SEM. Furthermore, a SEM offers the possibility to work with a large distance between optics and sample (up to several centimeters). This is very important for the observation of micro assembly, as the SEM will leave enough room for a gripper to work below the optics. Another advantage of the SEM is the very clean production environment provided by the vacuum chamber.

The vacuum chamber of an ordinary SEM is very limited in size which in most cases will not allow to study micro production processes. In contrast to this, the large-chamber scanning electron microscope (LC-SEM) "Mira" (VisiTec) offers two exceptional features. First of all, it has a 2 m^3 vacuum chamber. This extraordinary large chamber leaves enough space for the installation of machines for micro production. For example at the Fraunhofer IPT cutting, laser welding and assembly have been performed and studied inside the LC-SEM. As a second feature, the electron source can be freely positioned. This allows to look at a production process from all directions while the process itself is left completely unaffected.

MECHANICAL GRIPPERS FOR MICRO ASSEMBLY IN A LC-SEM

In this case the chamber of a LC-SEM serves as environment for the assembly process. Therefore all materials of which the gripper is made have to be suitable for vacuum. For example, they must not release gases, as most plastics do. Another restriction is caused by the electron beam of the LC-SEM, which can easily be deflected by electric or magnetic fields. As this can result in image interferences, these fields have to be avoided. Materials that can be magnetized and electromagnetic drives must not be used in proximity to the electron beam.[2]

Several different grippers for micro assembly inside a LC-SEM have been developed and tested. Different types of drives, such as bimetallic strips, piezoelectric bimorph elements or shape memory alloys, have been examined. Very good performances were obtained with the gripper shown in figure 1.

The gripper´s body consists of a plate made of non-magnetic high quality steel (1.4301). Two metal stripes are attached to this body and form the arms of the gripper. They are 0.2 mm thick and are made of a copper-beryllium alloy (CuBe2). This material was chosen because it can not be magnetized and can be used as a spring (similar to spring steel). A third stripe forms a "U" and is fixed between the arms. With this design no abrasive articulations or lubricated bearings are necessary.[3]

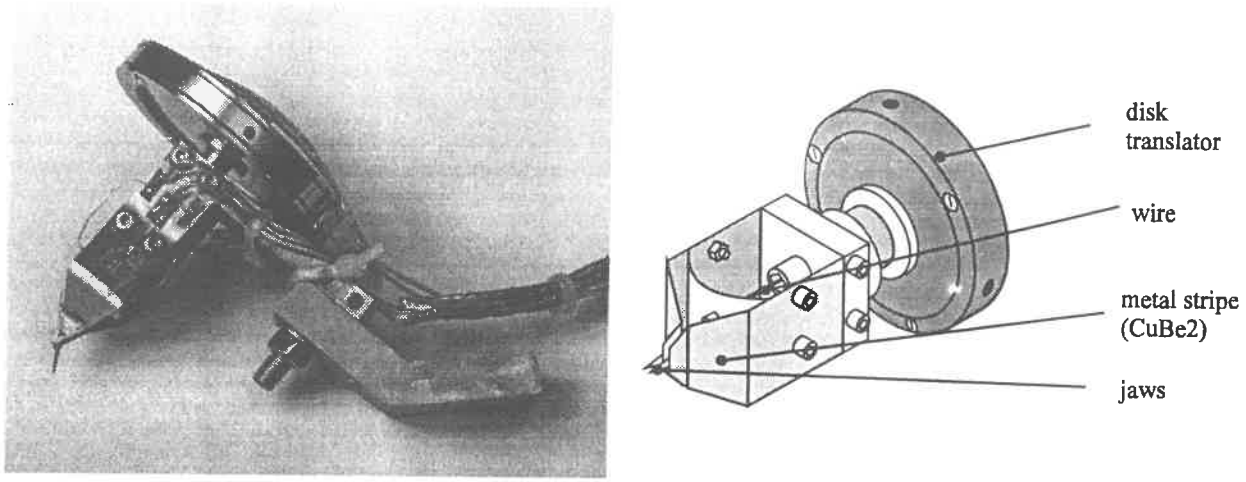

Fig. 1: Mechanical gripper for micro assembly inside a LC-SEM

In order to operate the gripper the "U" stripe has to be deformed by a force, which will cause the jaws to open. After releasing the "U", the gripper will return to its original position with the jaws closed again.[4] In order to avoid non-symmetrical movements of the jaws - e.g. open jaws but slightly tilted to one side - it is very important that the point of application of force is well in the center of the "U" stripe.

In order to prevent damages to the micro parts caused by a too high contact stress, the control of gripping force is very important. For this reason, resistance strain gauges were fixed to the inner and outer side of each arm. They were attached as near to the jaws as possible, for not being affected by the gripper´s deformation due to normal operation. When gripping an element, the arms of the gripper together with the resistance strain gauges will be deformed. Thus a change in electrical resistance is generated which allows to determine the change in gripping force.

A piezoelectric disk translator was used as drive for the gripper. It consists of two thin ceramic disks that are attached to each other. When connected to voltage one of them contracts while the other one expands which causes a bending of the whole disk. The thus generated force is transmitted to the "U" stripe via a thin wire. Piezoelectric elements allow very precise movements and enable the arms of the gripper to move in nanometer steps.

The jaws of the gripper were carefully attached to the end of the arms. For secure gripping it is very important that the jaws come together congruently when the gripper is closed. If this is not the case, a micro part might easily be flicked away when being gripped. Furthermore the jaws have to be very sharp in order to be able to grip elements with the size of only some micrometers. In this case tips of tweezers 50 µm wide and 10 µm thick were used as jaws. The material was titanium, which can not be magnetized.

The above presented gripper is able to move its arms in sub-µm steps and to open its jaws about 2 mm. It reacts almost instantly to any control signal. However, the normal hysteresis of the piezo elements causes a slight hysteresis in movement of the jaws. As for the detection of gripping force, a minimum resolution of 0.5 mN could be achieved.

ASSEMBLY INSIDE THE LC-SEM

An experimental assembly arrangement was set up inside the vacuum chamber of the LC-SEM. The gripper was mounted on a linear motion table in order to let it move up and down (Z-axis). Below the gripper, an assembly platform was arranged on which micro parts could be placed. The platform could be moved in the axes X and Y and rotated around the Z-axis. This arrangement allows to keep the focus of the LC-SEM on the jaws of the gripper all the time. No adjusting of the LC-SEM dependent on movements of the assembly platform is necessary, because with the jaws always visible, all steps of the assembly process can be well observed.

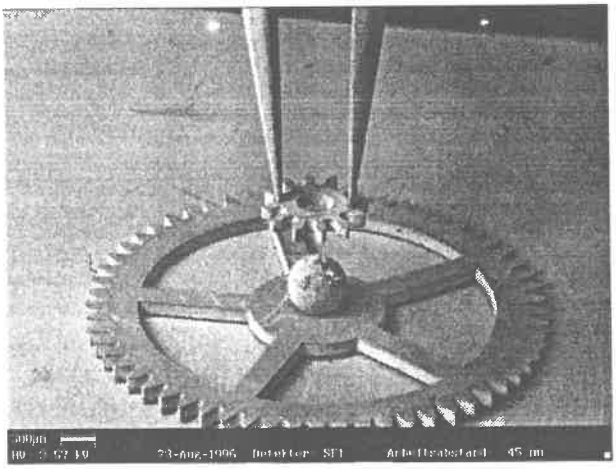

Fig. 2: Micro parts put on top of each other

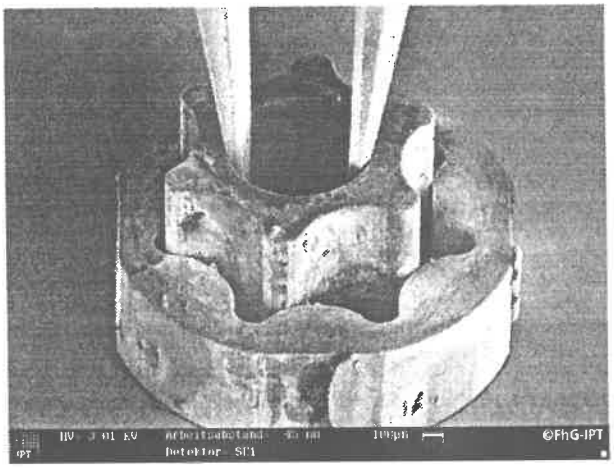

Fig. 3: Assembly of principal components of a micro gear pump

To begin with, some micro parts were put on top of each other in order to test the gripper. Figure 2 shows a gear wheel, a steel ball of 250 µm in diameter and a second gear wheel with a diameter of 500 µm. After that the two principal components of a micro gear pump were assembled (see figure 3). These components were made of hard metal. The outer diameter of the larger part was 2 mm, that of the smaller gear wheel was 1.4 mm. A very high accuracy in

the positioning of the components was necessary because they had to be put together creating a contact in six points with an average gap width of only 1.3 µm.

CONCLUSIONS

It was shown that the large-chamber scanning electron microscope (LC-SEM) is a useful experimental observation system for micro assembly and other micro production processes. It can help examining the phenomena of the micro world. Among other things, components of a micro gear pump were successfully assembled inside the LC-SEM using a remote controlled mechanical gripper. The gripper was designed especially for use in the LC-SEM and was equipped with resistance strain gauges for the control of gripping force. It is powered by piezo elements and can move its jaws in sub-µm steps. With a further integration of sensors in the gripper, the automation of micro assembly will become possible.

ACKNOWLEDGEMENTS

This work was supported by the Collaborative Research Center "Assembly of Hybrid Micro Systems", financed by the Deutsche Forschungsgemeinschaft DFG. The above mentioned micro gear pump was made available by Fraunhofer IPA, Stuttgart (Germany). It was developed for Hydraulik Nord GmbH, Parchim (Germany).

REFERENCES

1. W. Ehrfeld, "Assembly of Electromagnetic Milliactuators with LIGA Components", *2nd Japan-France Congress on Mechatronics*, Takamatsu, Kagawa (Japan), 1994
2. K.-H. Schmidt, "Mikro-Montage im Rasterelektronenmikroskop, dargestellt am Beispiel Nadelsensor", *38. Internationales Wissenschaftliches Kolloquium der TU Ilmenau*, Ilmenau (Germany), 1993
3. J. Dorner, "Braucht die Mikrosystemtechnik die Reinraumtechnik?", *38. Internationales Wissenschaftliches Kolloquium der TU Ilmenau*, Ilmenau (Germany), 1993
4. R. A. Russell, "A robotic system for performing sub-millimeter grasping and manipulation tasks", *Robotic and Autonomous Systems*, vol. 13, 1994

REVIEW OF NON-DESTRUCTIVE MEASURING METHODS FOR THE ASSESSMENT OF SURFACE INTEGRITY

A Survey of New Measuring Methods for Coatings, Layered Structures and Processed Surfaces

G. Goch [1,2], B. Schmitz [2], J.Geerkens [2], M. Reigl [1], P. Sprongl [2], R. Ritter [2]

[1] Abteilung Meß-, Regel- und Mikrotechnik, University of Ulm, Germany

[2] Institut für Lasertechnologien in der Medizin und Meßtechnik, Ulm, Germany

Abstract

Even though the near-surface areas of precisely manufactured parts represent only a few percent of the workpiece's volume, they influence its functional behaviour, quality and lifetime significantly. Therefore, sensors and measuring principles able to detect material changes, damages and process influences in the near-edge zone are of an increasing importance. However, they have to meet industrial purposes concerning accuracy, measuring time, robustness and costs. They should work non-destructively and should offer the suitability for a production process.
As the X-ray, sound propagation and Raman spectroscopy techniques were explained in detail in [1] by Brinksmeier, this contribution takes special emphasis on other non-destructive methods: photothermal, micromagnetic and SNAM-based microhardness measurement. They cover thin near-surface layers from the sub-micrometer to the millimeter-range. Namely the photothermal techniques including various detector-options have gained a substantial progress during the last five years, promising a broad spectrum of measuring abilities. Today, photothermics cover all kinds of layered-structure measurements concerning coatings (thickness, adhesion strength, local disturbances), hardness profiles, residual stresses, wear, thermal influences, and various manufacturing techniques, affecting the near-surface zone. The contribution concludes by the scanning near-field acoustic microscopy (SNAM), allowing simultaneously a surface and a new microindentational inspection.

1. Introduction

New capabilities in machining processes, a continuing miniaturization and tolerances down to the nanometer scale have lead to material treatments and depths of cut, affecting only very thin layers next to the surface. The more the over-all volume of a miniaturized product or its affected zone is scaled down in precision engineering, the more these near-surface areas influence its functional behaviour, quality and lifetime, even though they represent only a few percent of the workpiece's volume. Therefore, industrially applicable sensors and measuring principles, detecting material changes, damages and process influences in the near-edge zone, are of an increasing importance. However, they should work non-destructively and meet, at least, the actual standards concerning accuracy, measuring time, robustness and costs.

2. New measuring principles

Since the state-of-the-art of non-destructive measuring methods was summarized by E. Brinksmeier in 1989 [1], special interest is focused on measuring principles suitable for an installation in or near to a production line, i.e. others than pure laboratory instruments. Photothermal, micromagnetic and SNAM-based inspections (see sections 3, 4 and 5, resp.) belong to the indirect methods, correlating the material and structural properties of the near-edge zone with its thermal, electromagnetic or mechanical material parameters and their spatial distribution.
These measuring principles cover thin near-surface layers from the sub-µm- to the mm-range. Additionally, photothermics also include new materials like ceramics and special coatings. All these applications require new measuring and evaluation methods, able to discover new types of deviations (e.g. cracks, adhesion defects, material parameter profiles). Corresponding to the down-scaled thickness of the relevant near-surface layer, the requested measuring resolution and uncertainty must be reduced, too. Due to the importance of the edge zone and a widely stated lack of experiences processing new materials, there is an urgent need to improve manufacturing control, quality inspection and the wear-behaviour concerning all kinds of coatings, edge hardening, sub-surface damages and residual stresses.

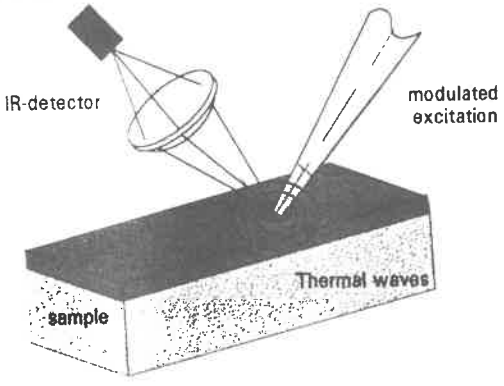

Fig.3-1: Excitation of thermal waves and their IR detection

3. Photothermal inspection of the near-surface zone

3.1. Physical principles

In a photothermal experiment, heat is generated by the interaction between an intensity-modulated tightly focused light beam (fig.3-1) and a sample. Thus, experiments with a resolution in a microscopic scale can be realized. The corresponding thermal response of the periodically heated object can be detected by different sensing devices. The detector signals imply information about the thermal material parameters, layer structures, type and distribution of hidden sub-surface defects. In order to reconstruct the depth and profiles of thermal changes, contrast signals as a function of the modulation frequency f are recorded (frequency sweep). Lateral scans across the sample detect local material deviations.

material	diffusion length for 1 Hz	diffusion length for 1 kHz
copper	6.0 mm	190 µm
steel 16MnCr5	2.0 mm	64 µm
air	2.6 mm	83 µm

Table 3-1: Thermal diffusion length for different materials and modulation frequencies

3.2. Theoretical Description of the Heat Diffusion Process

The basic equation (1) named thermal diffusion equation (TDE) enables to quantify photothermal signals. It describes the heat diffusion process, i.e. the temperature distribution with its spatial and time dependency after a thermal load (exciting laser) [2].

$$\frac{d}{d\underline{x}}\left(\kappa(\underline{x})\frac{d}{d\underline{x}}T(\underline{x},t)\right)-\rho(\underline{x})c(\underline{x})\frac{d}{dt}T(\underline{x},t)=-Q(\underline{x},t) \qquad (1)$$

It depends on the spatial distribution of the thermal parameters heat conductivity κ, specific heat c and density ρ. Therefore, general analytical solution can not be achieved, only for special cases regarding some restrictions. For a periodic excitation, thermal waves propagate within the sample. Their penetration depth is given by (2) as the thermal diffusion length μ, which is inverse proportional to the square root of the exciting frequency ω [3]:

$$\mu=\sqrt{\frac{2\alpha}{\omega}} \qquad \text{with the thermal diffusivity } \alpha=\kappa/(\rho c) \qquad (2)$$

Typical values for μ are shown in table 3-1. Thus, by varying the modulation frequency, photothermal detectors can 'look inside' a surface zone down to a variable depth, without contact, non-destructively, with a microscopic lateral resolution and very quickly.

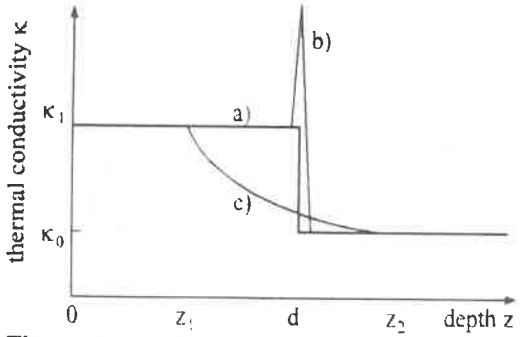

Fig. 3-2: Depth dependence of the thermal conductivity: a) coated system, b) coated system with a thermal contact resistance, c) thermal transition zone [8]

The analytical solutions of the TDE cover a wide range of applications. Each requires a specialized model concerning the objective near-surface properties, their correlation with thermal parameters, the theoretical heat propagation within the sample and the therefore expected signal response recorded by the photothermal detectors. For some applications, analytical models are available since several years, covering problems like layer thickness determination, adhesion strength inspection, diffusivity measurements or detection of local disturbances [3,6,8]. However, many other applications require an extended numerical treatment such as the finite-element method (FEM) or the finite-difference method (FDM) [4,5]. Measuring tasks concerning hardness depths and profiles, residual stresses, cracks, manufacturing traces, damages caused by material processing and defect identification belong to the latter application spectrum.

3.3. Layer Thickness and Adhesion Strength

For a non-homogeneous sample, the depth dependence of the thermal parameters (e.g. the thermal conductivity) may follow one of the shapes shown in fig. 3-2 [8]: a simple coating (fig. 3-2a), a thermal contact resistance (fig. 3-2b), modelling e.g. an adhesion defect or a delamination) as well as a continuous transition of the thermal conductivity (fig. 3-2c). This model, combined with a small and robust experimental set-up, has proved already its suitability in many industrial applications. As one example, fig 3-3 shows the calculated (lines) and measured (dots) photothermal phase signals, obtained from a Ni-coated copper sample. Modelling the passivation by a thermal contact resistance, the measurements are in a good agreement with the theory and with a destructive tensile test of the adherence force.

Special problems on adhesion strength occur at the coating of hard-metal or ceramic tool with wear-resistant layers like TiN. Investigations carried out by long-term cutting tests showed that photothermics may offer a regular inspection and prediction of the adhesion quality to be expected for a coating layer, even before this coating was performed.

3.4. Hardness and Residual Stress Measurement

Microstructural changes, as they appear in the steel hardening process occur together with modifications of the thermal properties, i.e. the increasing hardness in a near edge layer causes a decrease of the thermal conductivity in this zone. Theretore, hardness becomes detectable by photothermal means(fig. 3-4).

For the determination of hardness or compound layer thickness, the use of calibration curves (destructively obtained Vickers data versus photothermal data) offers a simple and practical approach.

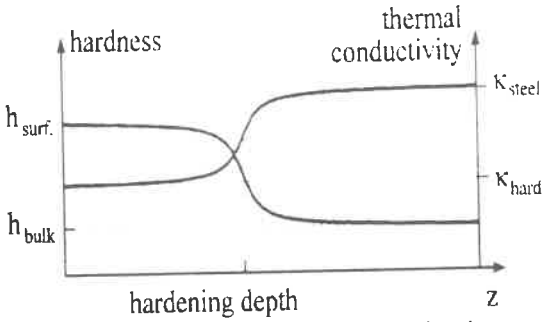

Fig. 3-4: Inverse relationship between hardness and the thermal conductivity

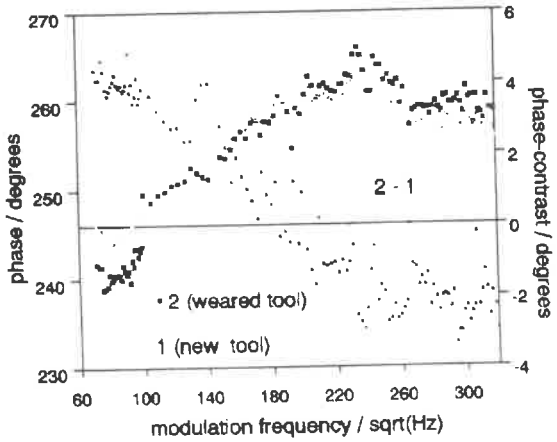

Fig. 3-5: left: Radiometric phase signals of drive shafts with tensile (2) and compressive(1) residual stress, turned with a weared (2) or a new tool (1); **right:** Phase contrast (difference) signal '2-1'

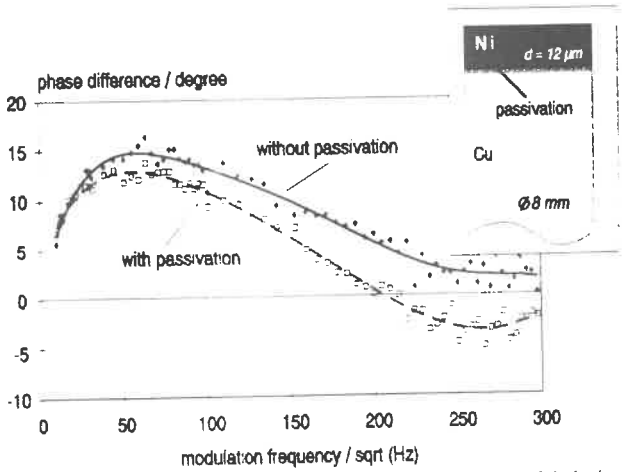

Fig. 3-3: Phase signal of a Ni-Cu sample with a high / low adhesive strength (without / with passivation)

In order to evaluate the shape of the hardness profile, several analytical and numerical models for a theoretical prediction of the photothermal signals were developed in the last five years [7]. The accuracy and application spectrum of these models increase with their mathematical complexity and computation time. Numerical methods like the FDM [6] also offer a 3-D evaluation of the photothermal signals.

Photothermics also enable to detect residual stress in a non-contact and non-destructive manner, in or near to production lines. Fig.3-5 summarizes radiometric measurements of two hard-turned shafts, one produced the with a new turning tool and a second one cutted with a weared tool. From X-ray measurements as described in [1], the actual surface stress values and orientation of part 1 (compressive) and 2 (tensile) were known. As a minimum result, the sign of an actual stress condition in a surface layer (i.e. compressive or tensile) can clearly be distinguished by contrast signals, which qualifies photothermal techniques for production control [9].

3.5. Photothermal Investigations of Advanced Ceramics

The final processing of ceramics induce micro-structural changes as well as the micro-cracks influence any heat propagation in the affected region. Therefore, photothermal measuring techniques yield information about the changed mechanical or structural properties of the surface and near surface region. The model-based reconstruction of thermal conductivity profiles from photothermal signals (fig. 3-5) enables to estimate the impacts on mechanically and laser treated ceramic surfaces. The results justify the assumption that the physical properties of the ceramic samples have been changed in the surroundings of the Vickers indentation (as a 'model' for grinding influences) or laser treated areas[b10]. The impacts yield changes of thermal properties and, hence, become detectable by photothermal techniques.

4. Micromagnetic measuring methods

Coercivity, saturation magnetization and magnetic remanence occurring on a hysteresis loop are significantly affected by hardness or mechanical deformation. These well known phenomena can be explained by a lattice distortion and strain, leading to an orientation change of magnetic dipoles, displacements of Bloch walls, formation / junction of Weiss's domains and Barkhausen-jumps. The resulting magnetic Barkhausen noise preferably occurs at the coercive force[10], thus, the recorded noise changes its maximum amplitude and position within the hysteresis loop.

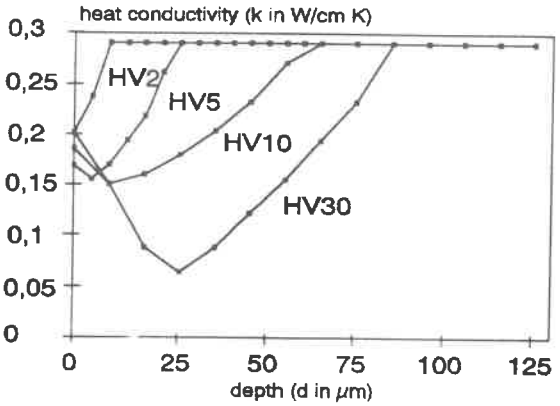

Fig. 3-5: Reconstructed heat conductivity profiles of ceramics, loaded with different forces(Vickers)

Conventionally, the hysteresis loop is measured with a transformer-like set-up, where the inspected object represents the core. Another, micromagnetic principle records an (amplitude-changed) Barkhausen noise as a function of a (changed) coercivity, reflecting the altered material properties in the near-surface zone. Exciting the sample periodically, the maximum noise amplitudes coincide with the (stress or hardness dependent) coercive force. A depth measurement from the mm- to the µm-range is achievable.

Similar to photothermal measurements, depth profiles of surface layer parameters can be evaluated by frequency sweeps of the exciting and analysing frequency [1]. On the other hand, the restriction to ferrous materials limits the scope of possible applications significantly, as e.g. all ceramics and non-ferrous objects cannot be inspected.

5. Contactless Topography and Microhardness Measurements Using SNAM

Among others, the Scanning Near-Field Acoustic Microscopy (SNAM) can be used as a contactless and non-destructive technique to inspect the topography, profile and roughness of a surface [11,12]. Recently finished projects proved that the same approach is suitable to measure microhardness of thin layers. The main advantage consists in the reduced preparation of the ground, milled or turned surfaces, where polishing is no longer necessary.

The scanning near-field acoustic microscopy belongs to the scanning probe techniques. A vibrating tip attached to a quartz tuning fork works as a distance sensor, damped by the air between the surface and the vibrating tip, which is pressed out and sucked in again periodically. In order to image the surface topography, the sensor scans across the surface in a constant distance (i.e. constant damping), of about 100 nm. Experimental comparisons showed a very good coincidence between mechanical and acoustical tracing.

The SNAM-microhardness approach leads to a three-step inspection procedure. First, the surface topography is imaged at a certain track. Second, the tip is pressed into the surface during its second scan along the same profile. Third, mapping the same line again and subtracting line 1 from line 2 results in the indentation profile alone.

6.References

[1]Brinksmeier,E.: State of-the-Art of Non-destructive Measurement of Sub-surface Material Properties and Damages, Prec. Eng. **11** (4), (1989), 211 - 224

[2]Carslaw, H.S.; Jaeger, J.C.: Conduction of Heat in Solids, Oxford Univ. Press, Oxford, (1959)

[3]Mandelis, A.(Ed.): Principles and Perspectives of Photothermal and Photoacoustic Phenomena, Elsevier, New York (1992)

[4]Goch, G.; Reigl, M.: Application of the Finite-Element Method and the Finite-Difference Method to Photothermal Inspections, J. Appl. Phys. **79** (11), (1996), 9084 - 9089

[5]Reigl, M.: Methods for the Quantification of Photothermal Signals, PhD thesis, University of Ulm, (1997) (in german)

[6] Seidel, U.; Haupt, K.; Walther, H.G.: Analysis of the detectability of buried inhomogeneities by means of photothermal microscopy, J.Appl.Phys. **75** (9), (1994), 4396-4401

[7] Lan, T.T.N.; Seidel, U.; Walther, H.G.: The determination of microstructural depth profiles by means of photothermal measurements: Theory, J.Appl.Phys. **77**, (1995), 4739-4745

[8] Schmitz, B.; Goch, G.: Charakterisierung von Oberflächen und randnahen Bereichen mit photothermischen Meßverfahren, Jahrbuch Oberflächentechnik, **52**, (1995), Ed. A. Zielonka, Hüthig Verlag, Heidelberg-Germany, 239-281

[9] Goch, G.; Schmitz, B.; Reigl, M.; Reick, M.; Geerkens, J.; Lechleiter, K.: Photothermische Sensorik zur berührungslosen Charakterisierung oberflächennaher Bereiche, VDI- Ber. **1255**, (1996) 113-118

[10] Crostak, H.A.; Bischoff, W.; Polaud B.: Induktive Prüfverfahren, at Survey **89/1** Angewandte Technik, Wegweiser für die zerstörungsfreie Prüfpraxis, (1989), 16-25

[11] Guethner, P., Fischer, U.CH., Dransfeld, K.: Scanning Near-Field Acoustic Microscopy, Appl. Phys. B **48**, (1989), 89-92

[12] Goch, G., Volk, R.: Contactless Surface Measurements with a New Acoustic Sensor, Annals CIRP **43** (1), (1994), 487-490

Six Axis Active Vibration Isolation and Payload Reaction Force Compensation System

M. Williams[1], P. Subrahmanyan[2], D.Trumper[2]

Abstract

"Successful precision engineering is the balance of robustness of the machine and how benign the environment can be made through isolation to minimize the strains caused by vibration that compromises a machine's accuracy."[1]

Photolithography equipment precision positioning capabilities have recently improved to the point where seismic level base disturbances comprise a much larger percentage of the total machine error budget. Additionally, the adverse effects of payload induced reaction forces limit the allowable stage acceleration and thus the wafer throughput of the machine. Current wafer stepper manufacturers have chosen to isolate the system from seismic disturbances and simultaneously profile stage motions to reduce reaction forces. This approach has allowed manufacturers to improve throughput, but is still limited in its capabilities.

We will present an integrated active seismic isolation system with the additional capability of compensating for payload reaction forces, in real time, in six degrees of freedom. The system is comprised of both active and passive elements to allow the isolation or control of disturbance forces in a band which extends from frequencies below 0.5 Hz and beyond any frequency of interest. These two distinct and separate sources of stepper vibration each require a unique controls approach. The vibration induced by stage motions are deterministic in nature and are easily compensated for with feedforward techniques. During wafer exposure, the primary source of vibration is from seismic level base disturbances. These vibrations are usually stochastic and broadband in nature. The fact that the stage motions are deterministic and that the isolation from ground is crucial only during wafer alignment and exposure allow us to hold the system reasonably stationary in inertial space.

In summary, this paper will present the mechanical design and the dual control approach implemented. Ground vibration transmissibility data will also be presented. Additionally, the performance of the system during stage accelerations will be presented. As lithography tools improve in performance, and the industry moves toward very high throughput platforms, these precision isolation and disturbance rejection issues become increasingly more critical.

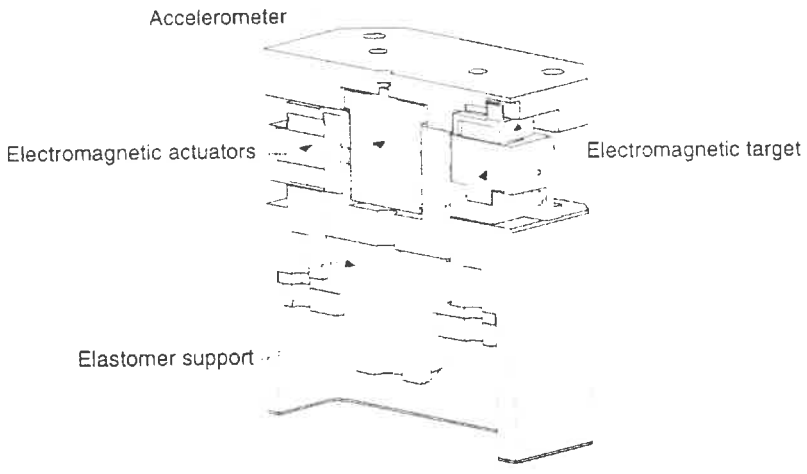

Figure 1: Cutaway view of one leg of the system

[1]Integrated Solutions Inc. 836 North Street Bldg 5, Tewksbury, Mass. 01876 williams@mail.insol.com
[2]Massachusetts Institute of Technology, Dept. of Mechanical Engineering, Cambridge, Mass 02139

Mechanical Design

The isolation system consists of a passive elastomeric mount that supports the mass of the system and also low pass filters seismic disturbance forces above approximately 10 Hz. The shape of the elastomer was chosen to more closely match the horizontal and vertical stiffness. Additionally, damping in the elastomeric mounts is hysteretic, so an increase in damping ratio does not lead to degradation of performance at higher frequencies.

In order to actively control disturbance forces at frequencies below the elastomers capabilities, the system utilizes sixteen variable reluctance tractive type force actuators to control acceleration in six degrees of freedom. These actuators were chosen for their high specific force and relatively large stroke. The system acceleration is sensed and fed back to a digital controller by six seismic accelerometers. These accelerometers were selected based on their high signal to noise ratio even at very low frequencies. Three of the accelerometers have a vertical orientation and sense $\ddot{Z}, \ddot{\theta}_x$, and $\ddot{\theta}_y$. The remaining three accelerometers are oriented horizontally and sense $\ddot{X}, \ddot{Y}$, and $\ddot{\theta}_z$.

The isolation system actuators are contained in the four supports at each corner of the stepper base. A more desirable arrangement is to use three legs separated by 120° and located closer to the plane that passes through the system center of gravity. This more desirable geometry results in an isolation system that has decoupled rotational and translational natural frequencies. The four support configuration was used to allow a direct substitution for the passive isolation system currently used. Figure 1 is a cutaway view of one of the isolation legs. In this figure, the placement of the elastomer, accelerometer, and actuators can be seen. As seen in Figure 2, the actuators are arranged such that the X and Y force pairs

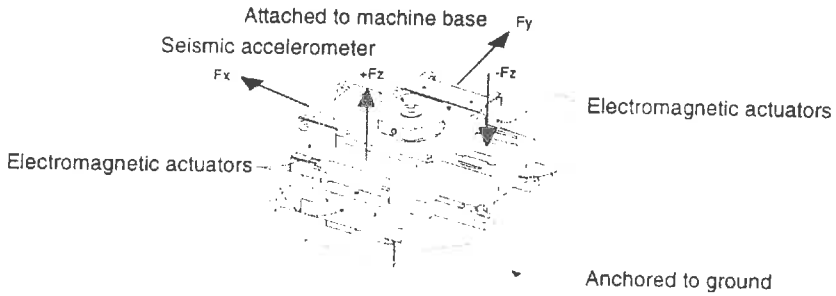

Figure 2: Forces provided at each leg location

are distributed amongst the four legs and the four Z bi-directional pairs are each located on a single leg. The eight pairs of actuators are symmetrically placed and are sized large enough to compensate for a 1-g acceleration of a 30 kg mass.

Modeling and Control Structure

The isolation system was designed based on a model of the stepper as a six degree of freedom rigid body supported by a series of well damped vertical and horizontal springs. The rigid body assumption is valid since the elastic modes of the structure are all well beyond the active control bandwidth. Due to the constraining forces of the static isolation mounts, the system axes of rotation are vertically offset from the centroid and result in tightly coupled equations of motion in $\ddot{X} - \ddot{\theta}_y$ and $\ddot{Y} - \ddot{\theta}_x$. This is not true horizontally since the constraining forces are symmetrical about the centroid. Therefore, the equations of motion for $\ddot{Z}$ and $\ddot{\theta}_z$ are decoupled. The control algorithm is based on this model and is designed to reduce the transmissibility at lower frequencies (a decade below the resonant frequency), suppress the resonant peak at the natural frequency of the mount, and join the passive transmissibility of the mount

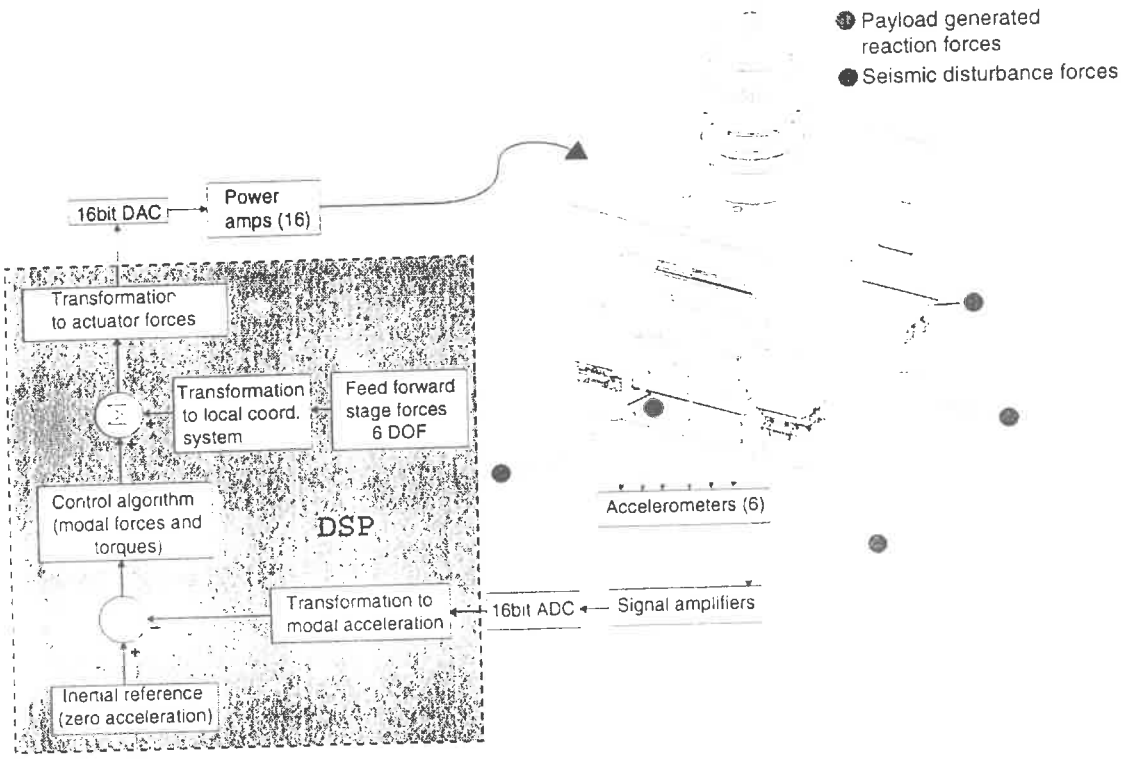

Figure 3: Control structure

about a decade greater than the resonant frequency. Figure 3 is a block diagram representation of the control system hardware and flow.

Results and Conclusions

Preliminary control implementation consisted of two poles. A pole at 1 Hz. to provide 90° phase margin at the low frequency crossover point, and a pole at 70 Hz for 90° phase margin at crossover a decade above resonance. Figure 4 shows the vertical seismic transmissibility of the system with and without active isolation. The figure clearly shows the resonance and the resulting amplification of base vibrations due to the passive mount. Active control is seen to attenuate base vibrations over the control bandwidth. Future work will focus on frequency shaping techniques to provide improved isolation characteristics [2].

In addition to seismic attenuation, the system can also reject payload generated reaction forces. Figure 5 shows the stepper acceleration in the X direction during a 20 mm step of the wafer stage. Without active control, the stepper oscillates at the natural frequency of the passive mount for ≈ 1.5 seconds. With active control the reaction forces are transferred to earth and the stepper is held "quiet" in inertial space.

In conclusion, preliminary results indicate that stage settling times for photolithographic steppers can be improved considerably using the active/passive control system described. Future work will implement MIMO time-optimal control to improve performance by coupling the stage control with the isolation control.

References

[1] D.B.DeBra, "Vibration Isolation of Precision Machine Tools and Instruments", ASPE short course notes, Cincinnatti, Ohio.,1994

[2] N.K.Gupta, "Frequency-shaped Cost Functionals: Extension of Linear Quadratic Gaussian Design Methods", AIAA Journal of Guidance and Control, Vol. 3, No. 6, 1980, pp 529-535

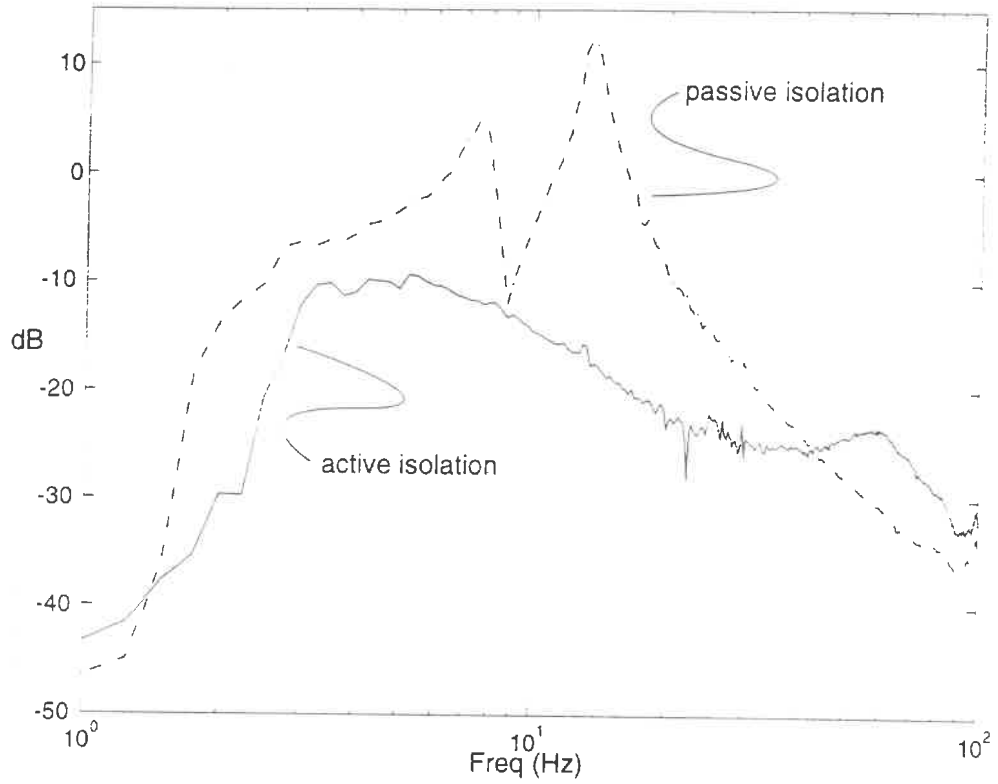

Figure 4: Vertical seismic transmissibility

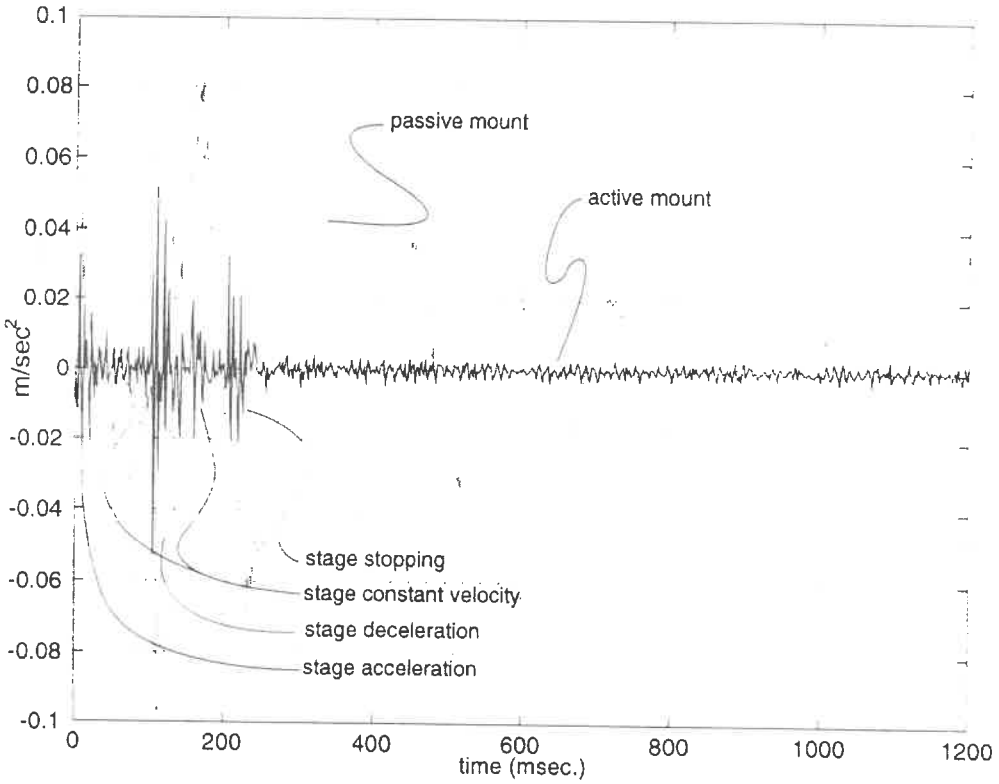

Figure 5: Payload disturbance force rejection

Compensation of Dynamic Vibrations and Spindle-Runout

Manfred Weck, Robert Hilbing

Fraunhofer Institute of Production Technology IPT

Aachen, Germany

Introduction

A primary intention with regard to chip-cutting surface processing of work pieces is to improve the finished surface quality of the work pieces. New approaches are needed to meet the increasingly stringent demands placed on machine tool manufacturers for cost-aware improvement of the machine systems.

Conventionally, machine vibrations are minimized by constructional optimization. This can entail high production costs. With the increased availability of electronic systems and, above all, considering the cost advantage of electronic control compared with mechanical construction optimization, active compensation of relative motion between tool and work piece caused by machine vibration has become an attractive approach to solve the problem. This can be achieved with a position-correcting device, the so-called actuator, on the tool to guide the latter such that the relative distance between the tool and the work piece always corresponds as exactly as possible to the setpoint specifications. Disturbance measurement and calculation of the compensating signal as well as the positioning correction itself require a length of time which is not negligible compared with the period duration of a typical machine vibration. Therefore a predictive projection of the disturbance waveform into the future is required, by the total time taken for measurement, calculation and position correction.

Basic principles

In principle, the possibilities for generating a signal suitable for influencing the vibrational behaviour of machines can be sectioned into control loop algorithms, echo compensation and prediction.

A conventional control loop algorithm is designed to minimize the control deviation with respect to the reference input in a closed loop, by applying a suitable setting variable to the drives and actuators of a machine. A problematic aspect is that the time required for measuring, calculation and position correction is of the order of magnitude of the period duration of the typically encountered, relevant dynamic machine disturbances with vibration frequencies up to 1000 Hz. This means that stable simple closed loop control is not possible.

For echo compensation, a compensatory correction signal is generated for the disturbance variable from the disturbance source signals, in order to achieve compensating position correction during the propagation time of the disturbance origin to the work piece processing location. The disadvantage is here that only complete coverage of all disturbances permits complete compensation.

In the third possible procedure, the correcting signal required to drive the compensator is generated from the disturbance signal itself. In contrast to echo compensation, this no longer requires any knowledge of the actual cause of the disturbance. However, because the principle requires that the compensator correction must be time-coincident with the appearance of the disturbance, but the necessary measurement, calculation and position correction take a finite time, this procedure needs a predictive projection of the disturbance waveform into the future, based on the actual course of the disturbance waveform in the past. Therefore autoregressive process models are used as they are exploited for efficient voice transmission in digital mobile radio communication with the GSM-standard.

In the process model, the human vocal system is represented by a tube of varying cross section to which acoustic pressure is applied by the glottis. The tube is terminated with the lips. Local discretisation of the tube produces the autoregressive digital model of the voice tract. The model of voice generation distinguishes between vowels and consonants. For voiced vowels (A,E,I,O,U) the glottis excites the

voice tract with short pulses, whereas unvoiced consonants (S, SH) are generated by applying noise to the voice tract. For voice encoding, the digital filter parameters and the excitation parameters are determined 20 times per second. The algorithms used for this purpose have been standardized in the digital mobile radiotelephone network.

Application: Vibration compensation in turning machinery

On comparing a consonant such as "SH" with a work piece-tool displacement waveform recorded for a turning machine, it is found that both signals have boosted amplitudes at certain frequencies. These are produced in voice signals by the resonances of the voice tract and for the turning machine by the resonances of the machine structure and the rotation speed dependent characteristic frequencies of the bearings or drive units. The process model assumed for prediction consists of an autoregressive digital filter excited by a noise signal. The filter replicates the resonant behaviour of the voice tract or machine structure. The analysis model which is the inverse of the process model is designated by the term Linear Predictive Coding (LPC) in voice processing systems. Short-term signal prediction by one digital sampling value is accomplished therewith. Multiple step prediction is directly obtainable therefrom by iteration.

Fig. 1 sketches the structural principle of a vibration compensating system for a lathe as set-up at the Fraunhofer IPT. The piezo-electric actuator can be seen interposed between the tool and the tool holder to make the position correction. The disturbance variable (deviation from the proper distance between tool and work piece) is measured with a non-contacting distance sensor and serves as input signal for the mathematical process model. The large measuring surface area of the sensor covering several square millimetres integrates over surface undulations which would otherwise falsify the measurement readings.

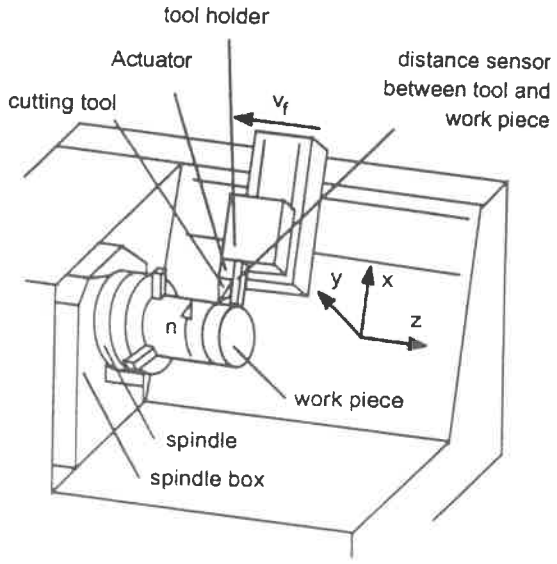

Fig. 1: Sketch showing the structural principle of a vibration compensation for a turning machine implemented in the Fraunhofer IPT.

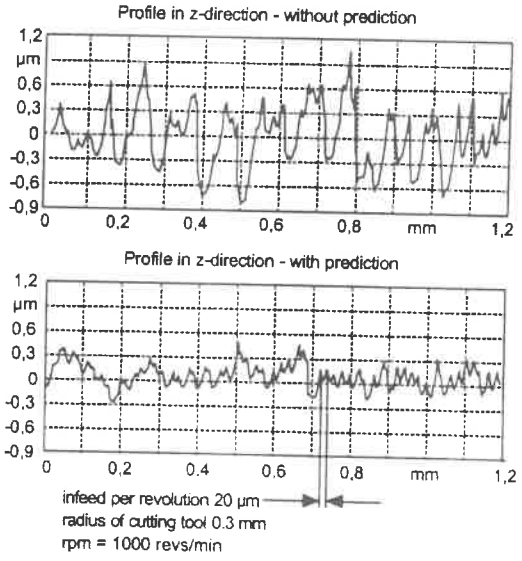

Fig. 2: Comparison of the surface structure for a turning process with and without prediction

The surface qualities achieved have improved significantly through the use of prediction. For quantisation of the improvement, the surface profile of the work piece was measured with a surface measuring instrument along the z-axis (feed axis). The result is shown in Fig. 2. With the compensation switched off (upper diagram) it is evident that after a few revolutions the tool penetrates deeply in an apparently stochastic manner so that the cutting edge form is clearly impressed. In contrast thereto, nearly all feed grooves are visible in the lower diagram. The amplitude is considerably reduced there, corresponding to a roughness reduction from R_a = 290 nm to R_a = 120 nm.

Application: Eccentric spindle rotation errors.

Eccentric spindle rotation errors are another important factor affecting the quality of the processed work pieces. They arise, for example, through inaccuracies in the spindle bearings and have the effect that the work piece is not truly round. This disturbance usually depends on the current rotation angle of the spindle and is non-statistical to a high degree. The associated dependence on the rotation speed has the consequence that the frequencies of this disturbance, e.g. 33 Hz for a rotation frequency of 1000 revolutions per minute, lie well below the frequencies of the dynamic disturbances considered so far.

A sensor mounted directly onto the tool to measure the relative movement between work piece and tool cannot be used to measure the deviations from roundness. Instead, a reference work piece is required which is rigidly attached to the spindle and has a high quality surface. Such a reference work piece may only have maximum form deviations considerably smaller than the desired form accuracy of the work piece which is to be processed. With the aid of a capacitive sensor, the relative movement of the reference surface in relation to the spindle box is measured in the sensitive direction. The deviation from ideal roundness found in this manner can be used to generate a compensation signal for active position correction.

The first practical implementations of this procedure at the Fraunhofer IPT confirm the fundamental feasibility of compensating deviations from roundness (Fig. 3). The very small round running error of 0.75 µm of a turning machine was further reduced by the described procedure to values around 0.45 µm.

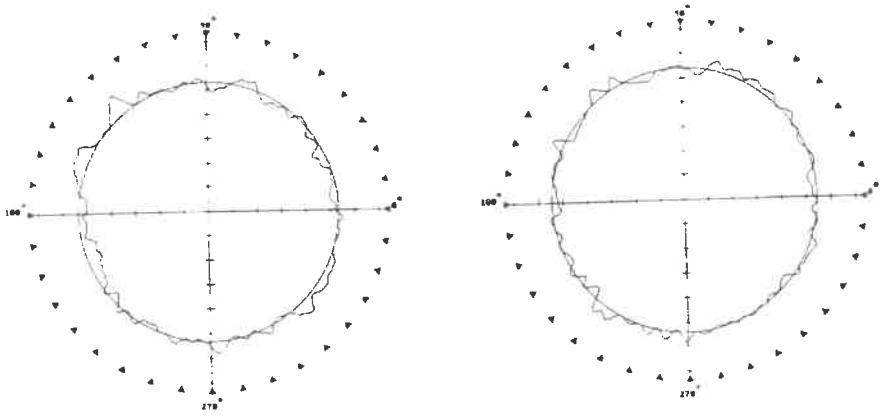

Fig. 3: Reduction of the roundness error by active position correction of the tool (scale subdivision: 0.50 µm / graduation)

Optimization: Using a force sensor

Capacitive sensors are only conditionally suitable for production process measurements because these sensors respond sensitively to cooling lubricants and ejected chip and because the measurements cannot be made directly at the working location, as the sensor has to be mounted adjacent to the tool. An alternative measuring method is to determine the processing forces arising in the position correcting direction. With the cutting parameters involved here, this passive force is approximately proportional to the actual chip thickness. Therefore by measuring the force it is possible to obtain the information about relative deviation of tool and work piece separation required for prediction.

A piezo-electric element is used as sensor for this purpose. It is attached in the force direction and generates an electric charge signal proportional to the applied force. Such a sensor is capable of measuring forces ranging from well below one Newton up to several kilo-Newton with high resolution and ade-

quate bandwidth. It is mounted together with the piezo-electric actuator in the same casing which is completely closed with respect to the exterior.

Thereby the aim is to keep the passive force as nearly constant as possible, because this will achieve uniform chip thickness. This is possible with a modification of the employed algorithms. One part of fig. 4 shows the frequency spectrum of the passive force in the course of normal processing. The typical boosted amplitudes at certain frequencies as characteristic for processing with continuous chip cutting are clearly recognisable. The spectrum becomes significantly flatter after switching-on the compensation algorithm; the disturbance frequency components are suppressed. The surface improvements achieved therewith correspond to a reduction of the roughness R_a by about 30 % compared with processing without compensation.

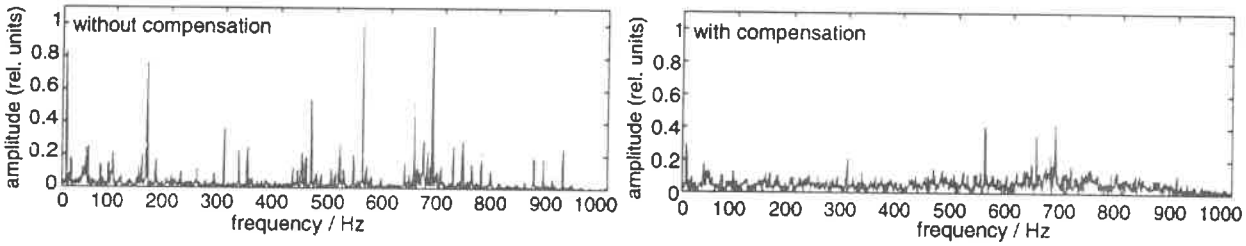

Fig. 4: Comparison of the frequency spectra for processing with and without force compensation

Conclusions and further prospects

In summary it can be said that new position correcting principles such as piezo-electric actuators provide the possibility of compensating high frequency vibrations typically encountered with machine tools, by active tool position correction. However, the propagation delay times of the measuring and positioning path require knowledge of the deviations which would appear without compensation earlier than their actual appearance. Predictive methods are already commonplace in other disciplines such as voice signal processing. It is possible to project vibrations into the future using echo compensation approaches or prediction methods. The investigations carried out for predicting and then compensating the deviations confirm the viability of such methods. By utilising special sensor systems, it is possible to include surface improvements in the production processes.

Apart from the chip-cutting processing machines considered here, special significance is attached to developing further applications in other fields. As far as the machine is concerned, industrial usability can be ensured in future by fixed integration of the sensor systems in the machine and actuators adapted to the production process. It is to be expected that the prediction accuracy can be improved further, by no longer approximating non-linear deviations with linear models, using non-linear prediction models and calculation algorithms instead. Special importance continues to be attached to enhancing the rugged stability of the compensation chain.

This work has been supported by the Volkswagen Foundation.

References

1 *Kammeyer, K. D., Kroschel, K.*: Digitale Signalverarbeitung, Teubner Studienbücher, 1989

2 *Weck, M.*: Werkzeugmaschinen, Fertigungssysteme Bd. 4, Meßtechnische Untersuchung und Beurteilung, 5th edition, VDI-Verlag, Düsseldorf 1996

3 *Haykin, S.*: Adaptive Filter Theory, 3rd edition, Prentice Hall, Upper Saddle River, 1996

In-Process Active Balancing of High-Speed Machine Tools

S.W. Dyer
Balance Dynamics Corporation
3915 Research Park Drive, Suite A-10
Ann Arbor, MI 48108

Research in the last fifteen years has highlighted many benefits of high-speed machining. Milling machines operating at speeds of 12,000 rpm up to 100,000 rpm allow for orders of magnitude increase in machining material removal rate for certain materials. Furthermore, higher spindle speeds lead to lower cutting forces and improved machining precision. Since the effect of mass unbalance is a function of spindle speed squared, however, spindle and tool/toolholder unbalance can cause vibration severe enough to damage sensitive spindle bearings and tools and nullify benefits of improved machining precision [1]. Unbalance forces can be of the same order of magnitude as cutting forces[2]. Spindle, tool, toolholder, and machine manufacturers have taken considerable steps to "pre-balance" all rotating components. However, when a tool is changed in a toolholder or a toolholder is changed in the spindle, even seemingly minor variations or misalignments can cause major problems at high speeds [3]. "Off-line" balancing technology does not address balancing of spindle/toolholder assemblies. Existing "in-process" balancing technology, though effective for precision grinding applications, is not suitable for high-speed rotation and responds too slowly to be cost effective for high-speed machining processes in which "chip-to-chip" time for tool changes takes only seconds. This paper presents actuation and control strategies and experimental results of a new technology for fast active balancing of high-speed machining spindles after tool changes. The balancing system utilized a balance ring mounted permanently to the nose of a spindle. Counterweight rotors were actively positioned relative to the spindle using a patent pending electromagnetic actuation device. An adaptive control strategy was developed which takes advantage of the input-output information available after each balance adjustment to perform on-line identification of machine dynamics at the operating speed. Experimental results show the effectiveness of the adaptive control system in rapidly controlling unbalance-induced vibration regardless of changes in machine dynamics due to variable mass tools. The active balancing systems also eliminated broad-band vibration harmonics present due to machine nonlinear dynamics at high synchronous vibration levels. Results indicate that active balancing of machine tools after each tool change promises to be a potent and cost-effective method of eliminating the detrimental effect of spindle/toolholder assembly unbalance on high-speed machining precision, productivity, and reliability.

1. Coleman, J. R., "No-Myth High-Speed Machining", Manufacturing Engineering, Oct. 1992.
2. Aronson, R. B., "The Balance Barrier", Manufacturing Engineering, Jan. 1997
3. Koepfer, C., "Tool Balancing on the Fly - It's Coming!", Modern Machine Shop, Oct. 1996

Key Words: Machining, balancing, vibration, vibration control, active control, rotating machinery, automatic balancing

A New Zero-Stiffness Magnetic Bearing for Vibration Isolation

G.J.P. Nijsse, J.W. Spronck, M.H.A. Leenders and H.F. van Beek

Delft University of Technology, Department of Mechanical Engineering,
Laboratory for Micro Engineering – Mekelweg 2, 2628 CD Delft, The Netherlands.
phone: +31-15-2785241, fax: +31-15-2781887, email: g.j.p.nijsse@wbmt.tudelft.nl

Abstract

This paper describes a new method to uncouple mechanical vibrations by means of a bearing with zero stiffness. The bearing force is independent of the position of the suspended object relative to the supporting construction. Therefore, the positioning accuracy of the suspended object is not influenced by disturbances like displacements, velocities and accelerations of the supporting construction. An additional control system — needed to compensate for the drift — enables position stability in the micrometer or even nanometer range. Moreover, this controller can impose any desired virtual stiffness between the support and the supported object.

Preliminary experiments show — in one degree of freedom — that bearing forces of about 185 N are possible, using small NdFeB permanent magnets (Ø25mm×10 mm) . By scaling the appropriate dimensions, a smaller or larger force is possible. Stiffness is zero at the central working point; around this point the stiffness increases with 11 N/mm every mm displacement. Thus, for a range of ± 5 μm, the maximum stiffness is as low as 55 N/m, resulting in a maximum resonance frequency of $\sqrt{55/18.9}/2\pi = 0.27$ Hz.

Research will be continued to investigate the possibilities to extend this principle of zero stiffness support to six degrees of freedom.

1 Introduction

In precision positioning systems, mechanical disturbances from the environment necessitate vibration isolation. In current applications damped tables (long springs, air pods) or active vibration reduction is used most commonly. However, these systems often are large and expensive.

1.1 Why zero stiffness?

In obtaining vibration isolation, the goal is to minimize the ratio $|z_m|/|z_w|$, as shown in figure 1. This can be done by minimizing $\omega = \sqrt{k/m}$. There are obviously two ways to minimize ω:

1. $m \to \infty$: this is not possible in practice, due to the limited load capacity of the bearing.
2. $k \to 0$: this method will be described in this paper.

The way to realize $k \approx 0$ is to construct a position-independent force. That means, to create a force $F \neq 0$ with $\partial F/\partial z = 0$ (in figure 1: $z = z_m - z_w$). When $c = 0$ the bearing force will be independent on the velocity and the acceleration of the supported mass relative to the supporting construction as well, because $\partial F/\partial \dot{z} = \partial F/\partial \ddot{z} = 0$.

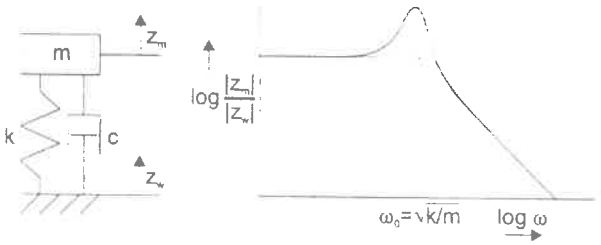

Figure 1: *Elementary spring-mass-damper system. To reduce the sensitivity for external vibrations, ω_0 has to be as low as possible.*

1.2 How to realize zero stiffness in practice?

There are a few possibilities to achieve an inherent zero stiffness bearing force:

1. Combination of mechanical springs with positive and negative stiffness. Disadvantages are the small assembly tolerances and the limited bandwidth due to the resonant frequency of the springs (usually between 10 Hz and 100 Hz for leaf springs).

2. Counterweight balancing. This method doesn't meet the needs of most bearing systems and does not give vibration isolation.

3. Lorentz actuator (also known as 'voice coil actuator'), where $F = B \cdot \ell \cdot I$ so $\partial F/\partial z = 0$, provided that $\partial B/\partial z = 0$. However, for larger bearing forces, energy dissipation and thus thermal problems become substantial.

4. Permanent magnet bearing unit. This new construction element will be described in this paper.

1.3 Possible applications of a zero stiffness bearing unit

In general, three categories of applications can be discerned:

1. Gravity compensation. An arbitrary bearing force can be applied to the object to compensate for $F = mg$ without adding stiffness or damping.

2. Vibration isolation. The new bearing unit is inherently insensitive to the relative distance between the supporting frame and the supported object (within a certain range).

3. Bearing and guidance systems that have a high demand on accuracy. With the new zero-stiffness bearing unit a very stable fine-positioning stage can be built on top of a coarse-positioning system.

The last item includes applications in which an object (e.g. a manipulator table) has to be positioned relative to a target (e.g. a lens), where no disturbing force is allowed on the target, e.g. in microscopes or IC lithography machines.

2 Working principle of the permanent magnet bearing unit

The working principle of the zero-stiffness permanent magnet bearing unit (ZSMB) is based on combining positive and negative stiffness of mutually repulsive and attracting permanent magnets, as depicted in figure 2 and 3. Thanks to modern magnet materials (e.g. rare earth metals) it is possible to generate a strong repulsive force without demagnetizing of the magnets. When properly designed, it is possible to create a working point where the stiffness in the bearing direction is virtually zero. Within some region, the stiffness can be very low, as is shown in figure 4. The lateral stiffness in the working point is negative, but can be kept small by carefully designing the magnet geometry.

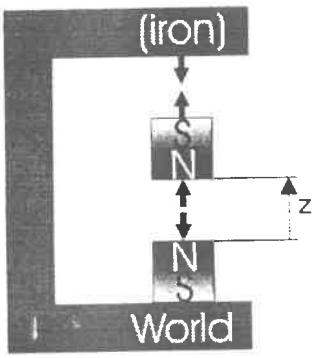

Figure 2: *Principle of the zero-stiffness bearing unit using permanent magnets. The attractive force (above) and repulsive force (below) create negative and positive stiffness, respectively and cause the total stiffness to be zero in a working point.*

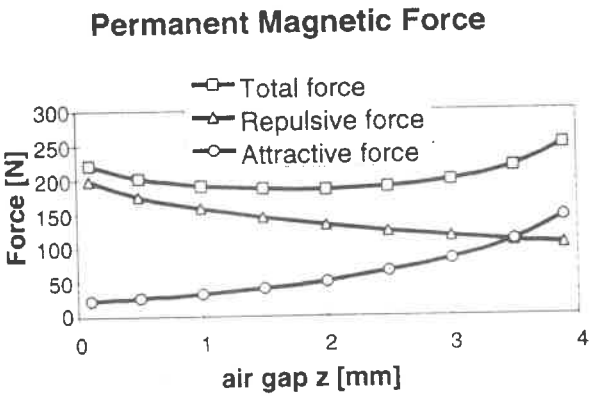

Figure 3: *When the attractive and repulsive forces of the permanent magnets are added up, the total force curve shows a minimum where the first derivative – the stiffness – is zero. The values in this figure are obtained from a Finite Element Analysis using the model shown in figure 6.*

The resulting bearing force is adjustable:

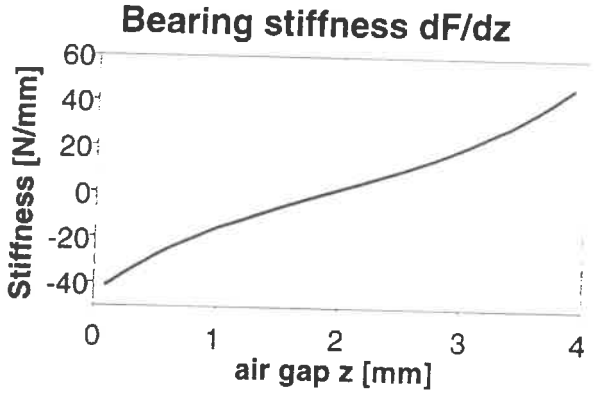

Figure 4: *The curve representing the first derivative of the total force (i.e. the stiffness), which is zero in a working point and near-zero in a small region.*

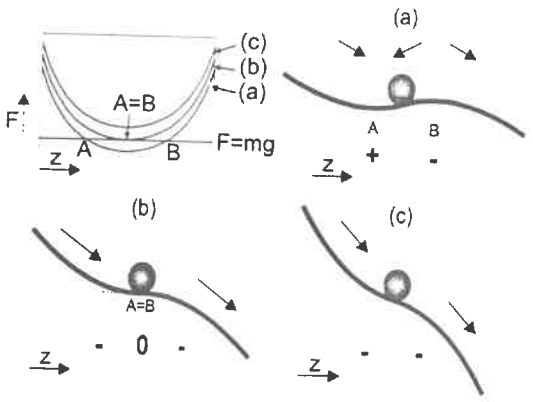

Figure 5: *Analogon for the stability in the working point. The horizontal ball movement corresponds to the displacement z in figures 2 through 4. (a) bearing force is smaller than weight → stable in A, unstable in B; (b) bearing force equals weight → neutral equilibrium only in the working point; (c) bearing force is larger than weight → unstable.*

1. by changing the air gap (for static adjustments), or

2. by an active control system, for example by adding a coil to generate an additional force on the supported object.

The latter adjustment can be applied to compensate not only for low-frequency drift, but also for higher-frequency disturbing forces that might act on the supported object from the outside. This way, it is possible to create a high (virtual) stiffness bearing without any mechanical coupling to the supporting base.

2.1 Stability of the bearing force

As can be seen in figure 3, when adding the attractive and repulsive force curve, there is a minimum in the total force. That is also the desired working point, because at that point $\partial F/\partial z = 0$. The neutral equilibrium in this point can be shown to be marginally stable. This can be explained as follows:

Suppose the weight of the supported object is slightly more than the minimum bearing force. Then there exist two intersections of the line $F = mg$ with the bearing force curve, of which one (A) is stable and the other (B) is unstable, see figure 5. This can be represented graphically by a rolling ball on a curved surface under the influence of gravity. The additional active controller can be considered as a rotating mechanism providing neutral equilibrium for the rolling ball, that is, A=B.

Summarizing, zero stiffness bearings enable supporting an object (around a certain working point) in such a way that:

- gravity is compensated for by the position-independent bearing force
- only inertia effects act on the object
- vibrations from the outer world with limited amplitude do not influence the object's position (except for acoustic coupling)
- arbitrary virtual stiffness relative to any other object is possible by means of active control, yet independent of the supporting construction

2.2 The ZSMB compared to the Lorentz actuator

Comparing the zero-stiffness permanent magnet bearing unit to the well-known Lorentz actuator or voice coil (generating a force proportional to the input current), the following qualifications can be formulated (+ means favorable):

	Lorentz act.	ZSMB
Maximum force	−	++
Force bandwidth	++	−
Isolation bandwidth	++	++
Energy dissipation	−−	++
Stiffness = 0	++	+

The ZSMB appears to be a good replacement for Lorentz actuators in low-frequency (bearing) applications. In other words, the ZSMB can be regarded as a DC module for a position-independent force, without energy dissipation. This position-independency makes it very suitable for modular use as well, i.e. superposition of the force with another force is possible without mechanical interaction.

3 Experimental setup

According to the principle of figure 2, a practical setup has been designed as shown in figure 6. The dimensions of the applied magnets are ∅25 mm × 10 mm The behavior was simulated using a Finite Element Analysis, resulting in the flux lines included in figure 6 and the force curves as shown in figure 3.

The slope of the stiffness curve around the working point is about 11 N/mm^2, so for a working region of ± 5 μm the maximum stiffness will be 55 N/m. That means that a mass of 18.9 kg (corresponding to the bearing force of 185 N) has a first resonance frequency lower than 0.27 Hz (for comparison: to achieve similar results with a spring, the minimal elongation should be $\frac{185}{55}\frac{\text{N}}{\text{N/m}} = 3.4$ m!).

Figure 7 gives a possible test setup to measure the relation between force and displacement experimentally. While the force sensor, attached to the middle magnet, is moved along the desired route, the force and the displacement are measured simultaneously. In this way the deflection of the sensor (e.g. a strain gauge type sensor) doesn't influence the measurement.

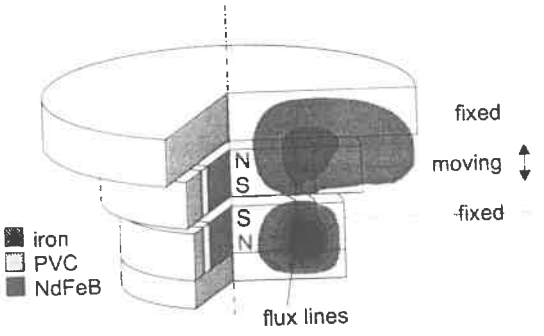

Figure 6: *Experimental setup, consisting of two permanent magnets with some flux guidance. The middle magnet is moving, the upper and lower part are fixed to the world. In the right half of the figure the flux lines are shown, as obtained from a FEM analysis.*

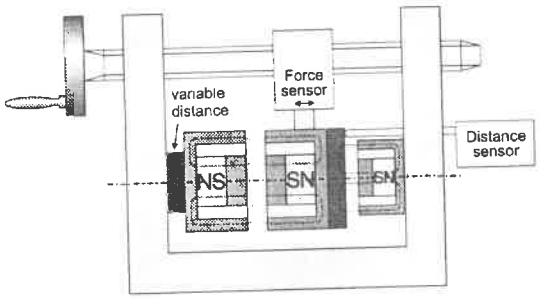

Figure 7: *Schematic test setup. The middle magnet is moved from left to right, while the displacement and the force are measured simultaneously, yielding the curve* $F = f(x)$.

4 Design of a 6-DoF ZSMB

For six-degrees-of-freedom the approach as sketched in figure 2 will not suffice, because of the lateral non-zero stiffness. Therefore, a more general method has to be used, analytically deriving the required bearing properties from the six-DoF zero-stiffness conditions.

It appears that, under certain conditions, it is indeed possible to realize a bearing system based on permanent magnets giving zero stiffness in all six degrees of freedom. It is obvious that active control will be necessary to prevent drift of the supported object, but this doesn't require high bandwidth.

5 Conclusions

1. With the help of permanent magnets it is possible to create a considerable bearing force, while the bearing stiffness is zero in a working point.
2. The zero stiffness permanent magnetic bearing is very suitable for vibration isolation and for applications in which the force coupling and the displacement coupling have to be separated.

6 Note

A Dutch patent application is in preparation.

Mechatronic Analysis and Design of High-Precision Drives

E. Kallenbach[+], P. Maißer[++], J. Lückel[+++], E. Saffert[+], C. Schäffel[+], H. Freudenberg[++], W. Kuhlbusch[+++]

[+] Technical University of Ilmenau, Faculty of Mechanical Engineering, Institute of Microsystems Technology, Mechatronics and Mechanics, P.O. Box 100565, D-98684 Ilmenau, Germany
[++] Institute of Mechatronics at Technical University of Chemnitz-Zwickau, Reichenhainer Strasse 88, D-09126 Chemnitz, Germany
[+++] University-GH Paderborn, Department 10 - Mechanical Engineering, Mechatronics Laboratory Paderborn Pohlweg 55, D-33098 Paderborn, Germany

Abstract
The paper describes the joint effort of three teams within the project Modeling, Simulation and Validation of Integrated Electromechanical Multi-Coordinate Drives. The project funded by the German Research Association lays the foundation for analysis and design tools that will assist engineers in the design of high-speed high-precision multi-coordinate drives.

1 Introduction

Increasing precision and faster processes are crucial factors in modern high technology. This area of technology requires, therefore, new drive concepts for motion in multiple coordinates with a positioning accuracy in the submicrometer range and high speed [1]. Applications include wafer lithography, measuring and inspection based on image processing, circuit testing, bonder heads, laser processing and many more.

2 Drive Structure

Figure 1 gives an overview of the drive design. An aero-statically supported stage carries symmetrically arranged magnetic circuits consisting each of two NdFeB-magnets and an iron yoke being closed by the iron stator. The moving magnet concept guaranties a high stiffness of the air-bearings which move on the stator that is manufactured with a high precision flat surface. The flat motor coils are again arranged symmetrically for the x- and y-axes. Opposite pairs of coils generate the force in the coordinate that is perpendicular to the coil arrangement. Different currents in opposite coils will generate a torque and allow thus to control the stage's angular position around the z-axis. The stage also carries a cross grid. It is scanned by an integrated measuring system for x, y and φ which is located in the center of the stator beneath the cross grid. A detailed description of the design including the force generation and the measuring system can be found in [1,4].

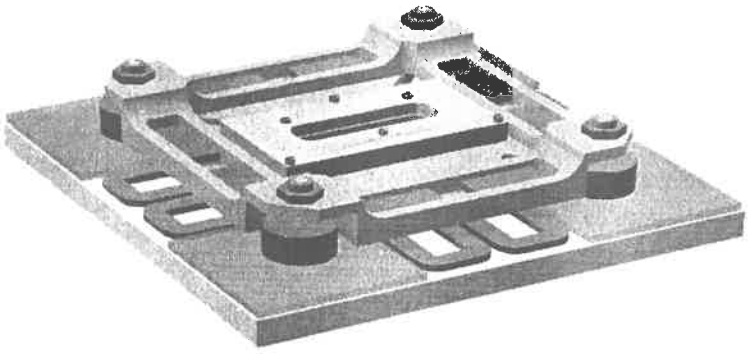

Figure 1. Mechanical structure of multi-coordinate drive

3 Modeling and Simulation of Mechatronic Systems

The simulation tool **alaska**, developed at the Institute of Mechatronics Chemnitz, Germany can be used for such problems [2]. **alaska** is based on a unified mathematical description of discrete electromechanical systems by using Lagrange's approach for multibody and electrical systems. A multibody system is a finite set of rigid/flexible bodies embedded in the three-dimensional Euclidean space. The bodies are coupled physically and/or geometrically to each other by force laws and constraints, respectively. The application of Lagrange's approach to electrical systems with lumped parameters is based on the concept of a multipole and its representation by abstract 2-poles as well as Kirchhoff's theory. Methods of graph theory are used to characterize topological properties of electrical networks. An electromechanical system can be understood as a finite set of physical objects with mechanical and/or electrical multipole-properties interacting among themselves by electrodynamic and/or electro-magneto-mechanical coupling.

The coupling of the mechanical and the electrical substructure will be described by constitutive equations containing mechanical and electrical generalized coordinates simultaneously. **alaska** automatically generates the equations of motion for the discrete electromechanical system. All of the electromechanical interactions are correctly taken into account. Even measurement systems, controllers and hydraulic/pneumatic components can be included in the modeling and simulation done with **alaska**. The (differential-) equations describing the dynamic behavior of such components are combined with the equations of motion of the electromechanical system. Sometimes the model-description language is not sufficient for the description of complex technical processes. In this case, **alaska** has an interface for using external FORTRAN-routines. The time-discrete behavior of controllers can also be described by such routines which is important for the simulation of real processes.

The dynamic behavior of a mechatronic system is influenced by its system components. If all system components and interactions can be described uniformly using only one simulation tool, then the dynamic behavior of the whole system and the influence of several components of the whole system can be analyzed. The main part of the mechanical substructure of the multi-coordinate drive is the stage. A rigid and a flexible model of the stage were generated. The flexible model is based on a complex FEM structure reduced to a structure with a few master nodes only. The reduced structure has the same elastic properties as the complex structure. A spatial force coupling element can be defined in alaska using the stiffness matrix of the reduced model. The multibody system model of the flexible stage contains 8 rigid bodies connected by this spatial force coupling element. A comparison of the multibody system model and the complex and reduced FEM model with respect to the eigenfrequencies gives a good agreement. The main part of the description of the electrical substructure in this special case is the calculation of the magnetic flux in the coils. This requires the calculation of the normal and tangential components of the magnetic induction between permanent magnets and yoke for any position of the stage. If boundary effects are neglected Maxwell's equations div B=0 and rot B=0 give a finite Fourier series as solution. The graph of the electrical network consists of 8 independent loops each containing a current generator and an inductance and a resistor. All current generators can be controlled separately. For a continuous stage movement the coils are supplied by commutated currents using suitable time dependent functions. The model of the measurement system contains the periodic sampling, filtering and transfer of measured values and the influence of disturbances. This model is implemented via a special routine. For controlled stage motion, state controllers with an integrated observer are implemented in the model. The modular structure of the whole model enables an easy exchange of submodels, for example the implementation of other controllers.

Simulations of the whole model allows to judge the dynamic behavior of the system and to investigate the influence of system components on it. The range of dimensions of the multi-coordinate drive is very different, the air gap of the bearings is in the range of µm, geometric dimensions of the stage are in the range of centimeters. This requires a high accuracy in the numerical analysis with a long integration time. In view of effective computation and using these models for a virtual prototyping a short integration time is of interest. For this aim the models of system components will be tuned, i.e. looking for simplified models with the dynamic behavior of complex models (simulation results with same exactness). In the near future symbolic codes of the models can be used for nonlinear optimization (optimal layout) and also with respect to the synthesis of new controllers.

4 Path Control

The aim of the control concept is to achieve high accuracy as well as good vibration damping for path oriented movements at high speed. To meet these demands possible disturbances must be considered in the control scheme. Disturbances may occur due to external forces or due to unmodeled system behavior of the plant.

The controller design consists of a structure optimization followed by an optimization of controller parameters. For the synthesis of the controller structure a symbolic model of the plant is used. The appropriate modeling depth of this symbolic model depends on the control accuracy required, but due to handling constraints it cannot be of any complexity.

4.1 Symbolic Design of the Controller Structure

The design starts at the main structure (figure 2) which is defined by a required accuracy of the controlled system as well as by the arrangement of actuators and sensors. Each controlled axis (x,y,φ) consists of a local state controller and a disturbance estimator. Furthermore a feed-forward control is included based not only on position but also on velocity and acceleration which are also provided by the path generator. The mathematical representations of some controller blocks are determined in a structure optimization process making use of a procedure based on the symbol-

manipulation program MAPLE. This procedure allows the symbolic coupling and analysis of linear state-space systems. The aim is to obtain feed-forward gains and filters for the observed disturbance which are nearly independent of the plant. The analysis of the reference and the disturbance transfer functions of the coupled system with an iteration process leads to an optimal controller structure. During the iteration the models of the disturbance estimator and the disturbance gains are varied. In this case the result is that the feed-forward gains are independent of any plant parameters if an estimator is used whose disturbance model consists of one or two integrators.

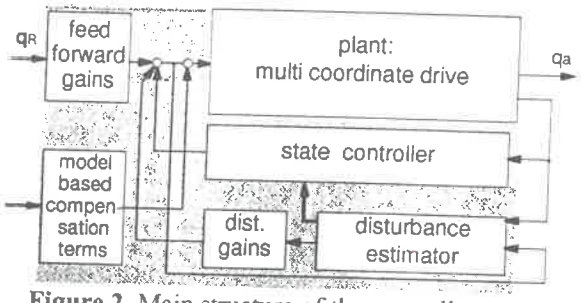

Figure 2. Main structure of the controller

Attention is also directed to the compensation of disturbance forces due to a non-symmetric stage mass distribution because of a working tool mounted on the stage. Since there is no mechanical anti-rotation lock the moment generated by the stage's acceleration will cause a rotation of the stage which is subsequently compensated by the φ-controller. This undesirable behavior can be prevented or at least considerably decreased by inserting a model based feed-forward control. This assumes that the parameters of the tool (mass, inertia, distance to the center of gravity of the stage) are well known and can be considered in the control scheme. If the tool parameters are unknown the disturbance estimators are used to adaptively determine them under the assumption that other disturbances can be neglected. In this case the inertia cannot be determined so that the tool's mass must be assumed as a concentrated mass. The detected forces are fed forward via the block *model based compensation terms* as shown in figure 1. The compensation of the nonlinear force-position-characteristic of the drive is done mainly by means of the inverse of a simplified trigonometric series which approximates the magnetic flux through the coils. The error caused by the simplification is detected and compensated by means of the disturbance estimator.

4.2 Optimization of the controller parameters

Once the controller structure is determined its parameters have to be optimized. For this the CAMeL tool [5] is used which was developed at the Mechatronics Laboratory Paderborn (MLaP). The free parameters are optimized using MOPO (multi objective parameter optimization [6]). This leads to a *pareto-optimal* solution minimizing a vectorial quality criterion. The objectives are calculated via nonlinear simulation of the closed loop system which is excited by a suitable step function By this any nonlinearity is considered including the limit of the servo unit. Besides the controlled quantity the tilt angles are used as objectives as well as the horizontal velocities to improve damping. During the optimization procedure the use of frequency and damping parameters turned out to be more efficient than the use of the feedback gains themselves. Moreover these controller parameters are good starting points for optimization of similar plants with other parameters.

4.3 Simulation Results

The effectiveness of the designed controller is underlined by the simulation results. Both the x- and the y-axis are excited by a path generator with the following maximal values: jerk 300 m/s^3, acceleration 6 m/s^2, and velocity 0.25 m/s. The movement follows a rounded square 30 by 30 mm. At any time the position error of both axis is less than 0.2 µm and even less than 0.02 µm if the acceleration torque caused by unsymmetric mass distribution is fed-forward. Figure 3 shows the corresponding rotation angles. In this simulation the tool mass amounts to nearly 10% of the stage mass.

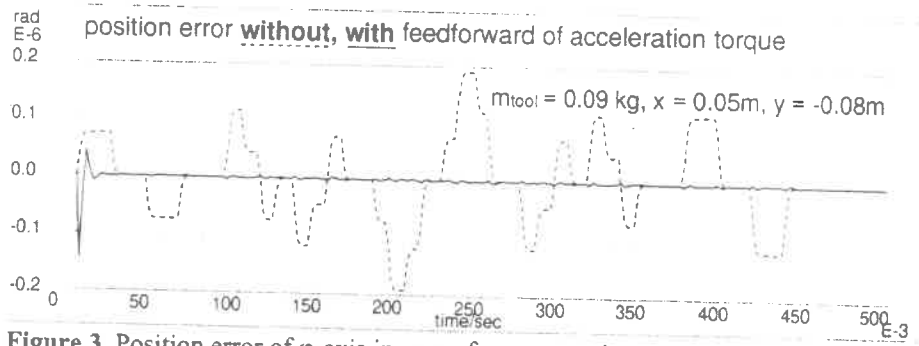

Figure 3. Position error of φ-axis in case of unsymmetric mass distribution

5 Control System Implementation

5.1 Hardware

The general structure of the control system shown in figure 4 is based on a dSPACE DSP system and no longer on a net of 7 transputers as reported in [4]. The greater number of analog outputs also provides for the individual control of all 8 coils of the drive. This enables a completely symmetric structure of the control software in particular for the generation of the torque that controls the drive's angular position. Also the comparatively weak power amplifiers based on power operational amplifiers were replaced by commercially available switched power amplifiers. They provide now ±20A with a significantly reduced power loss.

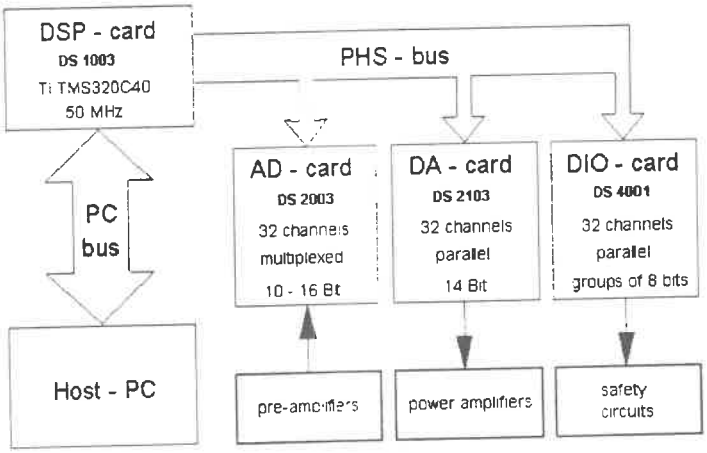

Figure 4. Hardware structure

5.2 Software

The control software used previously on the transputer hardware had to be rewritten completely. Fortunately, the generation of control software for the dSPACE system is quite comfortably supported by the MATLAB/SIMULINK extension REAL-TIME-WORKSHOP and the dSPACE REAL-TIME-INTERFACE on top of it which enable off-line simulation and testing as well as automatic code generation for the on-line program. The only alternative would have been a time consuming and error prone manual port of the OCCAM program to the programming language C. Therefore, it was attempted to implement all functions of the control system via the graphical interface. Figure 5 shows the hierarchical structure of the software.

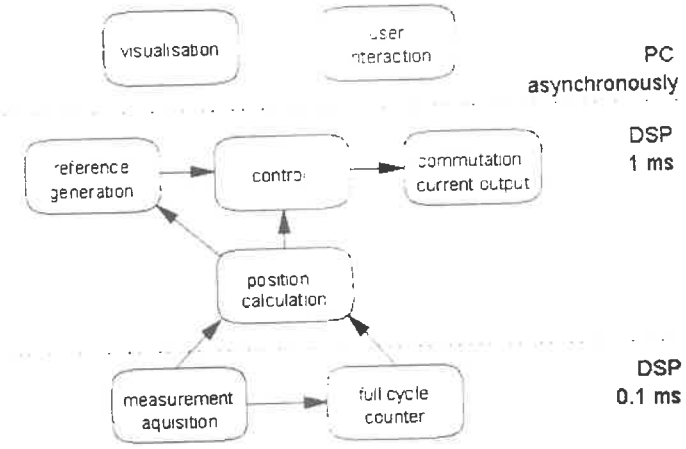

Figure 5. Software structure

6 Conclusion

Mechatronic analysis and design of high-precision drives can be done by integrating extended multi-body simulation with advanced symbolic control systems design implementing it on a rapid control systems prototyping platform. This approach results in short development cycles and paves the way towards an integrated design environment for mechatronic systems.

References

[1] E. Kallenbach, K. König, E. Saffert, C. Schäffel, M. Eccarius. Integrated Design of Shape and Function in Mechatronic Systems. Proc. 3rd Conf. Mechatronics and Robotics, Oct. 1995 Paderborn, pp. 44-51.

[2] O. Enge, G. Kielau, P. Maißer. Modelling and Simulation of Discrete Electromechanical Systems. Proc. 3rd Conf. Mechatronics and Robotics, Oct. 1995 Paderborn, Germany, pp. 302-318.

[3] C. Schäffel, E. Saffert, E. Kallenbach. Integrated Electrodynamic Multicoordinate Drives - Modern Components for Intelligent Motions. Proc. ASPE 1996 Annual Meeting, pp. 456-461.

[4] E. Saffert, C. Schäffel, E. Kallenbach. Control of an Integrated Multi-coordinate Drive. Proc. Mechatronics '96, Sept. 1996, Guimaraes, Portugal, vol.1 pp.151-156.

[5] R. Rutz, J. Richert. CAMeL - An Open CACSD Environment, IEEE Control Systems Magazine, April 1995.

[6] R. Kasper, J. Lückel, K.P. Jäker, J. Schröer. CACE Tool for Multi-Input, Multi-Output Systems using a New Vector Optimization Method. Int. Journal of Control 51 (1990), 5, pp. 963-993.

CURRENT AND FUTURE POSSIBILITIES OF NON-CONTACT NANO MACHINING BY COMBINATION OF LASER WITH SCANNING PROBE TECHNOLOGY

K. Dickmann, J. Jersch
University of Applied Sciences FH Muenster, FB Physikalische Technik, Laser Laboratory,
D – 48565 Steinfurt/GERMANY

Nano technology is of increasing interest for future oriented applications and bio technology. For the industrial production of nano components new nano handling systems as well as appropriate nano machining processes will be required. Various nano machining processes based on near field technology – known from Scanning Probe Microscopy (SPM) – have been developed in the past and will be introduced briefly in the following. However, this paper will mainly concentrate on a new laser machining process. FOLANT-process (Focusing of Laserradiation in the Nearfield of a Tip) is characterized by a couple of unique machining features and enables machining down to a few nanometers.

1. Introduction and current nano machining tools

Nowadays the potential of ion-beams, X-rays and electron beams for nano machining is well known. Another promising branch is based on SPM-technology. For example a simple known process utilizes the probe tip of a Scanning Tunneling Microscope (STM) for machining of nano structures by scratching into the material surface. Another contact nano machining process called "thermo mechanical writing" uses a laser heated tip from a Scanning Force Microscope (SFM). Nano structures for application in data storage are produced in polycarbonate by pressing the tip into the material. For industrial applications there is an increasing interest for non-contact nano machining processes. Thus, for example it is possible to create nano structures on metals when a short voltage peak is superimposed onto the tunneling voltage of an STM. It is also possible to modify magnetic surfaces with a resolution of some nanometers using magnetized probe tips. One of the optical nano machining methods is based on Scanning Nearfield Optical Microscopy (SNOM). Here laser radiation is guided through an optical fiber with an output aperture of some 10 nanometers onto the work piece. Nanostructures down to 50 nm can be obtained, when the fibre aperture is in the nearfield of the surface. Unfortunately, due to a reduced propagation of light, intensities are rather low and thus only machining of soft materials is possible. The listed disadvantages can be overcome by FOLANT-nano machining with considerable increased intensity and resolution[1-4].

2. Focusing of laserradiation in the nearfield of a SPM tip (FOLANT)

Based on various electrostatic ("lightning rod") and electrodynamic ("plasmon excitation") effects a considerable intensity enhancement of laser radiation occurs in the nearfiel of a probe tip, when the tip is lateral illuminated by a laser. This effect is already well known from Surface Enhancement Raman Scattering (SERS) and enables enhancement factors up to 10^6 mainly depending on the tip material and –geometry. Large enhancement is obtained from STM metal tips with a good conductivity (e.g. silver, gold) but still is sufficient for SFM silicon tips. The intensity enhancement also increases with the sharpness of the tip. Thus a curvature radius of < 100 nm is necessary for applications in nano machining of metals.

The intensity enhancement only occurs in a narrow zone of some nanometers (horizontal and vertical) around the probe tip. Thus, for nano machining it is necessary to approach the material surface in to the nearfield of the tip. However, this can be easy obtained by state of the art SPM-technology. Computer controlled SPMs with user friendly scanning software also simplify the machining of defined geometry.

3. Setup for nano machining

The entire experimental setup for nano machining is shown in Fig. 1. A commercial scanning probe device (STM, SFM) combined with a frequency-doubled Nd:YAG-laser (λ = 532 nm) was used. The pulse energy was < 0.1 mJ by a pulse duration of 5 ns. The optics were used for matching the polarization to the longitudinal tip axis and for prefocusing the radiation into the tip/sample-gap.

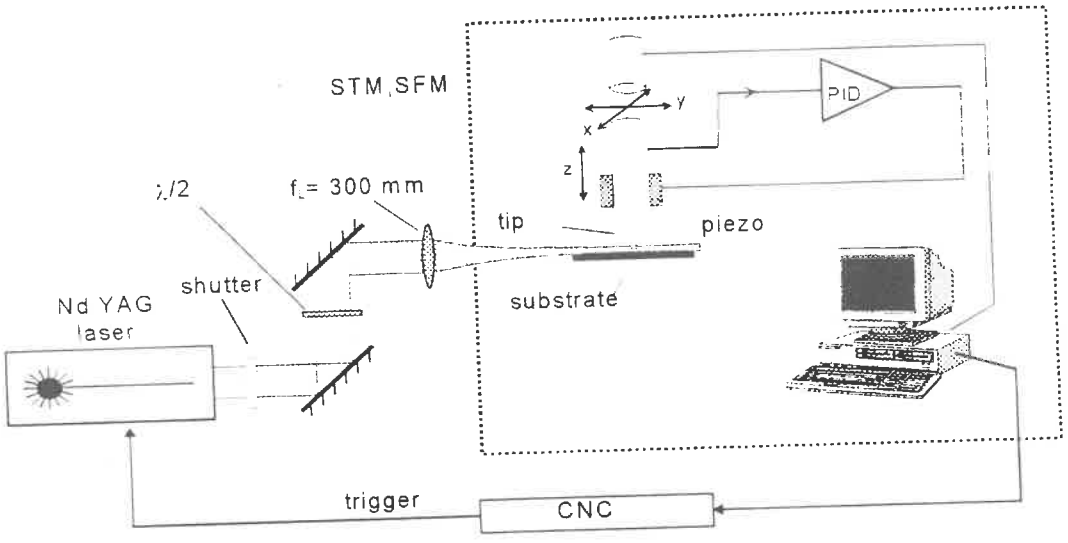

Fig. 1: Entire setup for nano machining in FOLANT configuration

4. Interaction processes and machining results

Various interaction processes of enhanced laser radiation with the substrate are possible, mainly depending on laser parameters (wavelength, pulse duration, pulse energy), substrate material and SPM-parameters (tip radius and -material, gap distance). We have determined thermal processes as well known from conventional laser material processing. We also believe in various non-thermal effects (e.g. "field evaporation").

The variety of process parameters optionally enable material removal from the substrate or deposition from the tip onto the substrate. The substrate variety ranges from metal to plastic. Thus nano-cutting, -drilling and -welding is possible. An overview of machining results is given in Fig. 2.

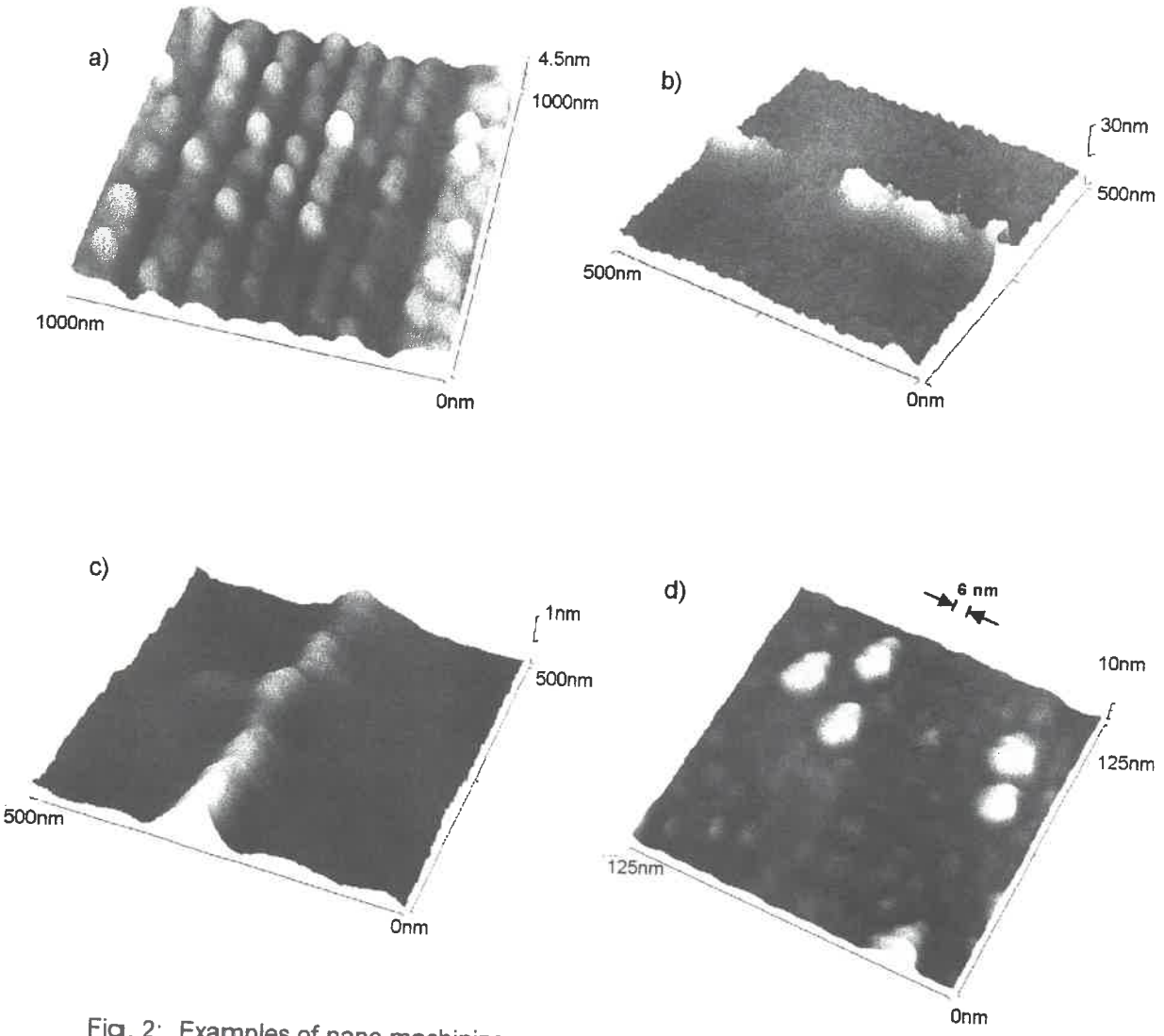

Fig. 2: Examples of nano machining

a) Parallel line cuts on a gold substrate

b) Line structures on a gold substrate by material deposition for demonstration the potential in nano joining

c) Nano structure on polycarbonate due to heating with a permanent surface modification

d) Nano holes on a gold substrate (so far as known, these are the smallest structures ever achieved by la laser)

5. Outlook

The described method is a promising alternative to other known nano machining processes. The original purpose of the development was the application in data storage technique. With FOLANT technique already today we are able to increase the data density by 10^4. Further increase up to 10^6 should be possible. Other applications can be found in mask repair of reticle for semiconductor industry, production of single electron transistors, production of X-ray fresnel optics and nano lithography. Since the introduced machining method is a basic technology, further applications will be found.

6. References

1. K. Dickmann, J. Jersch, Nanostrukturierung mit Laserstrahlung durch Feldverstärkung im Nahfeld einer RTM-Sondenspitze Laser und Optoelektronik 27 (3) 1995, p.76-83J.

2. J. Jersch, K. Dickmann, Nanostructure fabrication using laser field enhancement in the near field of a scanning tunneling microscope tip Appl. Phys. Lett. 68(6), 5 February 1996, p.868-870

3. K. Dickmann, J. Jersch, Nanostrukturierung mit Laserstrahlung Phys. Bl. 52 (1996) Nr.4. p. 363-365

4. J. Jersch, F. Demming, K. Dickmann, Nanostructuring with laser radiation in the nearfield of a tip from a scanning probe microscope Applied Physics A 64 (1), 29-32 (1997)

THERMAL EFFECTS OF BROAD BEAM NEUTRAL ION MACHINING

Helen E. Fawcett[1], Thomas G. Bifano[2], Donald Wroblewski[3]

Abstract

Broad beam neutral ion machining has been developed for a new manufacturing process for compact disc stampers: Precision Stamper Manufacturing (PSM). In this process, thermally induced degradation of the photoresist mask proved detrimental to the stamper quality, as can be seen from the following SEM micrographs.

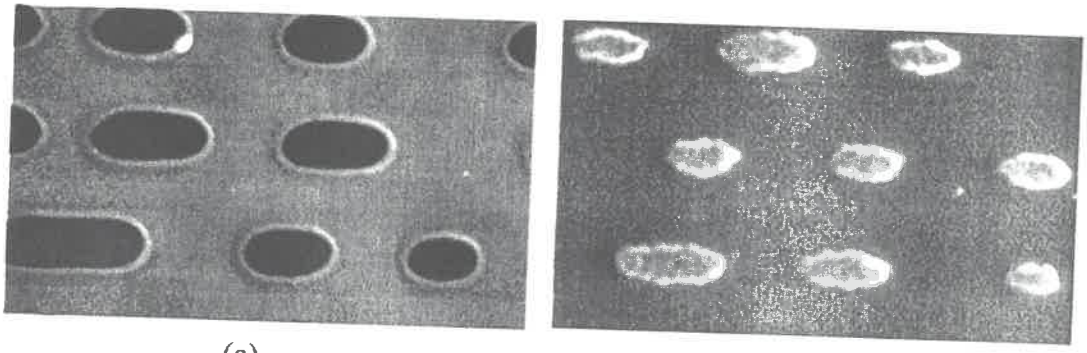

(a) (b)

Figure 1. Broad Beam Ion Machining (680 nm thick photoresist): These SEM micrographs show the relationship between: (a), photoresist mask material on a CVD SiC substrate after LBR exposure and development, but before ion machining; and (b), the CVD SiC substrate surface after broad beam ion machining. (Magnification: 10,000 X)

Vacuum compatible thermocouples were placed in the vacuum chamber at various locations to record and analyze the thermal effects of the ion machining process. Results indicated that the ion beam (plasma) temperature exceeded 300°C in 30 minutes of machining. A silicon wafer was used as the substrate being etched during this test, and the temperature on the backside of the wafer exceeded the flow temperature of the negative tone photoresist (170°C) within the first few minutes of machining.

Thermocouples were imbedded into a copper cooling fixture to allow the measurement of various temperatures including the top and bottom plates and the substrate for determining heat transfer coefficients. From these experiments, a model of substrate temperature in the vacuum chamber during ion machining was developed. The model can easily be modified for different ion sources and machining conditions and should prove to be of general utility for thermally sensitive ion machining processes. This paper will present the results of ion machining compact disc features (0.6 μm wide) over a 138 mm diameter stamper without any form of cooling and corresponding results when cooling is added to the system. The model developed for this cooling fixture will also provide an opportunity to "predict" temperatures that a substrate will encounter during neutral ion machining.

---

[1] MicroE, 8 Erie Drive, Natick, MA 01760-1313 Tel: (508) 903-5023 Fax: (508) 903-5005 email: fawcett_helen@micro-e.com.

[2] Precision Engineering Research Lab, Boston University, 110 Cummington St., Boston, MA 02215 Tel: (617) 353-5619 Fax: (617) 353-5866 email: tgb@enga.bu.edu.

[3] Aerospace and Mechanical Engineering Dept., Boston University, 110 Cummington St., Boston, MA 02215 Tel: (617) 353- Fax: (617) 353-5866 email: dew11@enga.bu.edu.

Introduction

The SEM micrographs shown in Figure 1 indicated that the photoresist had experienced thermal degradation during the ion machining process, therefore an initial experiment was conducted to quantify the thermal environment during machining. A shielded thermocouple was placed 1 inch above a silicon wafer that measured the plasma temperature (shown in Figure 2 as the thin line) and an exposed junction thermocouple was mounted under the wafer to measure substrate temperature (shown in Figure 2 as the thick line). It can be seen that without any cooling, the plasma and substrate temperatures during ion machining rapidly exceed the melting temperature of negative-tone photoresist (170°C).

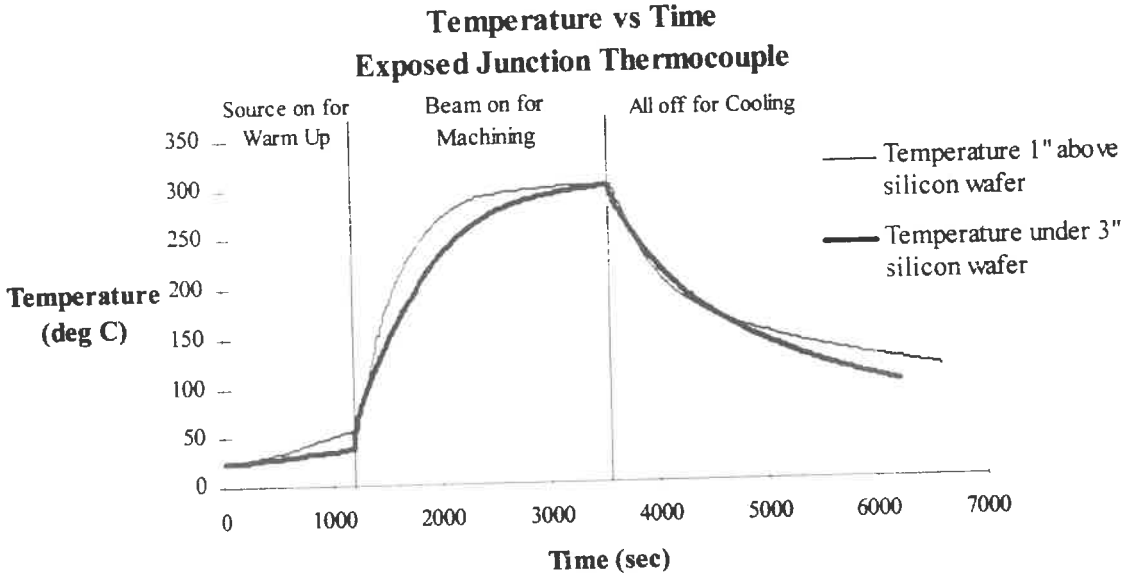

Figure 2. Thermal measurements 1 inch above and underneath a 3 inch silicon wafer.

Based upon the information shown in Figure 2, the need to characterize the substrate temperature before subjecting thermally sensitive material to the ion machining process became apparent. At the same time, the necessity of employing active cooling was evident in order to maintain the substrate temperature below 100°C ensuring that the photoresist mask would not degrade.

Heat Transfer Experiment

A lumped model describing the thermal energy flux during ion machining was developed. In concert with this modeling, a new copper chuck was designed and fabricated incorporating convective water cooling and allowing various temperatures to be measured for correlation with the thermal model. The chuck consisted of two parts: a copper top plate with integral flow channels to allow auxiliary convective cooling of the substrate, and a bottom plate of solid copper. A schematic of heat fluxes and stored energy in the substrate and the chuck is illustrated in Figure 3.

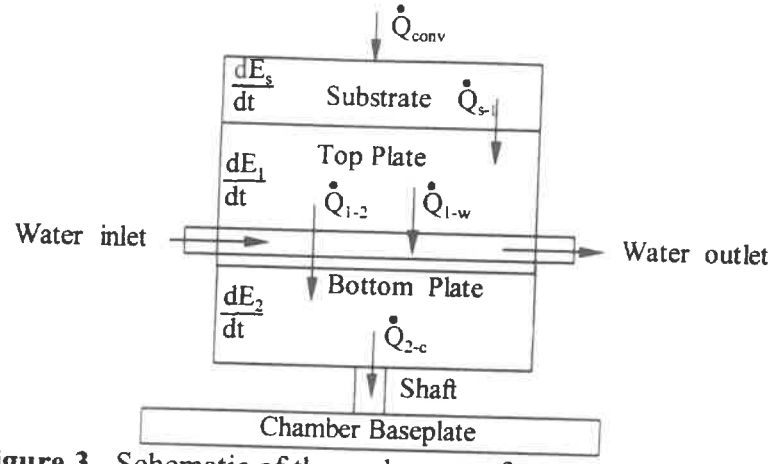

Figure 3. Schematic of thermal system for modeling analysis.

where Q_{conv} = convective heat flux from the ion plasma to the substrate

Q_{s-1} = heat flux from the substrate to the top plate (1)

Q_{1-w} = heat flux from the top plate (1) to the water

Q_{1-2} = heat flux from the top plate (1) to the bottom plate (2)

Q_{2-c} = heat flux from the bottom plate (2) to the chamber

$\frac{dE_s}{dt}$ = energy stored in substrate

$\frac{dE_1}{dt}$ = energy stored in top plate (1)

$\frac{dE_2}{dt}$ = energy stored in bottom plate (2)

The principal input of thermal energy for this system is convective heat flux from the Argon ion plasma to the substrate surface. A portion of this energy is stored in the substrate in the form of increased temperature. Heat flux out of the substrate is principally by conduction (through the substrate/chuck interface). The heat flux into the upper half of the chuck can be stored, convected to the water flowing through it, or conducted to the lower half of the chuck. Radiation from the substrate and chuck is assumed to be negligible based on a simple estimate of radiative heat flux using known bounds on substrate and chamber wall temperatures. A thermal energy balance on the substrate yields:

$$\dot{Q}_{conv} = \frac{dE_s}{dt} + \dot{Q}_{s-1} \tag{1}$$

The small thermal mass of substrate and its close coupling to the copper chuck allows stored heat in the substrate to be neglected.

Thus Equation 1 can be rewritten as:

$$h_i A_s (T_\infty - T_s) = \frac{(T_s - T_1)}{R_c} \tag{2}$$

where R_c = Thermal contact resistance at the substrate/chuck interface (K/W)
T_∞ = Plasma temperature (°C)
T_s = Substrate temperature (°C)
T_1 = Top plate temperature (°C)
A_s = Surface area of the substrate/chuck interface (m^2)
h_i = coefficient of the plasma's convective heat transfer (W/m^2 - K)

While time dependent quantities, T_s, T_1, and T_∞, can be measured, heat transfer coefficients, h_i, and R_c, are unknown. To estimate these heat transfer coefficients, ion machining experiments were conducted without a substrate. The energy equation for the chuck alone during ion machining is:

$$Q_{conv} = \frac{dE_1}{dt} + \frac{dE_2}{dt} + \dot{Q}_{2-c} + \dot{Q}_{1-w} \tag{3}$$

Once the heat transfer coefficients were evaluated, further simplifications to Equation 3 allowed an expression for the substrate temperature (T_s) to be obtained.

$$T_s \approx \frac{R_c h_i A_s T_\infty + T_{in}}{1 + R_c h_i A_s} \tag{4}$$

Equation 4 predicts T_s for steady state and is not a prediction for the time dependent temperature. It can be seen that the two critical parameters defining substrate temperature are interface contact resistance and the convective heat transfer coefficient. Only R_c can be modified substantially in the present system. Factors that decrease R_c and therefore decrease T_s include surface finish, contact pressure, and surface conditions. Also, interfacial vacuum compatible greases exist that increase thermal flux. Equation 4 required only three temperatures to be measured during an ion machining process, one of which is on the atmospheric side. The model can be used as an estimate of the temperature that an actual sample would encounter during ion machining.

Experiments were then conducted with a substrate on top of the cooling chuck. Figure 4 shows measured values for the substrate temperature (T_s), and the inlet water temperature (T_{in}): the plasma temperature (T_∞) was similar to that shown in Figure 2.

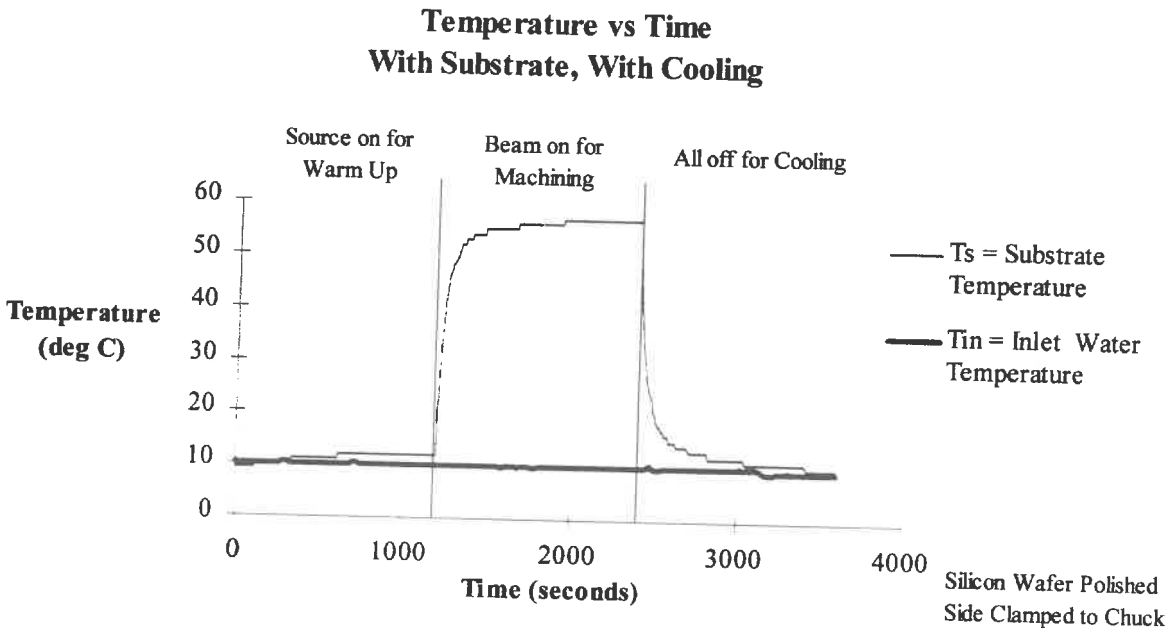

Figure 4. Temperature versus time for the plate with cooling and with a substrate on top. Shown in this figure are the temperatures of the inlet water temperature (T_{in}) and the substrate (T_s).

Machining Experiments

An electroless nickel stamper was used as the first to be machined with active cooling. SEM micrographs of the photoresist before and after the ion machining process with active cooling are shown in Figure 5.

ELECTROLESS NICKEL EN01 263e-6W
0001 20KU X20,000 1Pa WD30
ELECTROLESS NICKEL EN01 263e-6W
POST IN PRE-CLEAN
0001 10KU X20,000 1Pa WD28

(a.) (b.)

Figure 5. SEM micrographs of electroless nickel stamper. (a) photoresist exposed on electroless nickel stamper surface and (b) resulting feature on electroless nickel stamper after ion machining with active cooling. (Magnification: 20,000 X)

As can be seen from Figure 5, no distinguishable change in the CD feature integrity was observed. This stamper was then used to injection mold polycarbonate CD's from it in an attempt to characterize the quality of PSM compact discs when compared to those made through

attempt to characterize the quality of PSM compact discs when compared to those made through conventional processes. The following AFM results show comparable quality of feature transfer into the polycarbonate CD between PSM and conventional mastering processes.

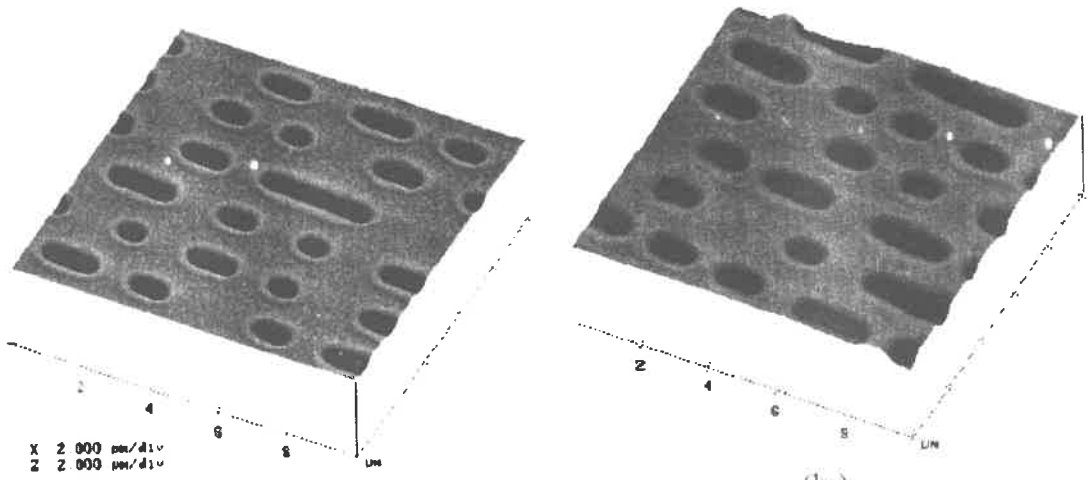

(a.) (b.)

Figure 6. AFM Comparison of CD replicas in polycarbonate. (a.) shows a replica molded from a conventional stamper and (b.) shows a replica molded from an electroless nickel PSM stamper.

Conclusions

The model and cooling chuck designed in this research fulfilled the objective of maintaining the temperature of the substrate below 100°C. The information in Figure 4 also shows that throughout 15 minutes of ion machining, the temperature of the substrate did not exceed 60°C. Since the machining time of the PSM process was limited to approximately 5 minutes, the thermal conditions were considered to be adequate for the process. The ability to machine stampers using the PSM process without the photoresist mask melting was achieved and the results of the thermal model and corresponding machining of the stampers will be presented.

Acknowledgments

This research was funded in part through the National Science Foundation Grant DMI 9500162 and Prism Corporation. We also wanted to thank the following people for their contributions to this research. Anlee Krupp who completed all of the SEM work, Steven Fawcett who worked on the design of the cooling chuck, Margo Velonis and all members of BU-PERL who helped with the thermal measurements, and Ion Tech, Inc for all their technical support.

References

[1] Fawcett, Helen E., May 1997, "Precision Manufacturing of Optical Storage Stampers," Ph. D. Dissertation.

[2] Lienhard, John H., 1981, A Heat Transfer Textbook: Second Edition. Prentice Hall, Inc., New Jersey.

[3] Melliar-Smith, C. M., "Ion etching for pattern delineation." *Journal of Vacuum Science and Technology* , Vol. 13, No. 5, p. 1008 - 1022.

[4] Pohlmann, Ken C., 1992, Volume 5: The Computer Music and Digital Audio Series: The Compact Disc Handbook 2nd Edition. A-R Editions, Inc., Wisconsin.

Near-field Photolithography to Realize High Resolution Smaller Than Light Wavelength ~ Stamp Photolithography

Shuji Tanaka*, Masayuki Nakao and Yotaro Hatamura
Department of Engineering Synthesis, The University of Tokyo
7-3-1 Hongo, Bunkyo-ku, Tokyo 113 Japan

1 Introduction

Lithographic techniques for micro device fabrication require high resolution, low cost, large throughput, high yield, accurate registration and so on.

A noncontact photolithographic technique has the advantages of large throughput, high yield and accurate registration, so that it is used mainly for the production of semiconductor integrated circuits. This technique, however, has the limit in resolution determined by the wavelength of exposure light because of diffraction limit. In order to realize higher resolution, shorter wavelength of exposure light is required. Patterning features with sizes less than 0.2 μm is, however, difficult even if deep ultraviolet light with wavelength of about 200 nm is used. Furthermore, a costly photolithographic device with a deep ultraviolet light source and an optical system for it results in large equipment investment and high production cost.

A conventional contact photolithographic technique is free from diffraction between a mask and a photoresist, and can realize high resolution smaller than the wavelength of exposure light. High yield is, however, difficult to realize without costly exchange or cleaning of a mask because of the damage to the mask caused by the contact with a photoresist. This technique is not also suited for registration, because the contact between a mask and a nonplanar surface is difficult.

An electron beam lithographic technique has the advantages of high resolution, high yield and accurate registration, while it also has the significant problems of throughput and cost.

As a photolithographic technique to complement the conventional ones, the authors propose a new near-field photolithographic technique to realize high resolution, large throughput and high yield at **low cost**. This technique, as Figure 1 shows, comprises the process of electron beam lithography to fabricate a master mold with a relief, replication of the master mold with a transparent replica material and near-field exposure with the replica mold, followed by etching or lift-off process.

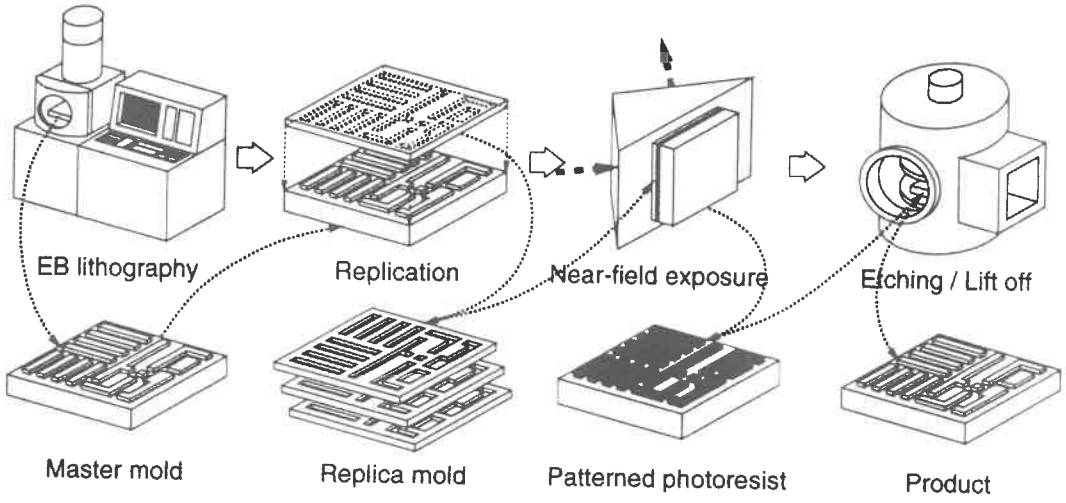

Figure 1 Process of the near-field photolithography

Figure 2 illustrates the method of the near-field exposure. A photoresist is attached or approximated to a relief on a transparent mold. The mold is illuminated through a prism in the condition of total internal reflection. The photoresist is exposured mainly to near-field light transmitted from the convex part of the

*Supported by JSPS Research Fellowships for Young Scientists

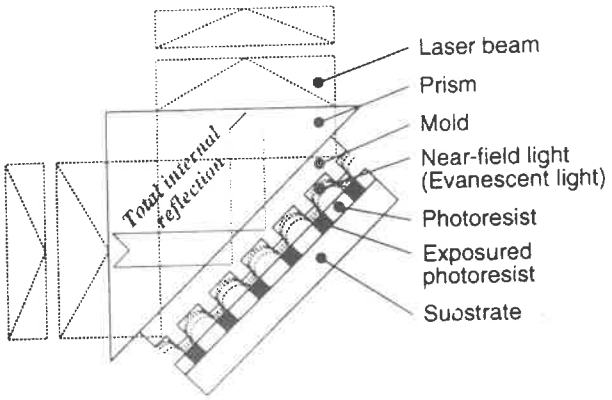

Figure 2 Method of the near-field exposure

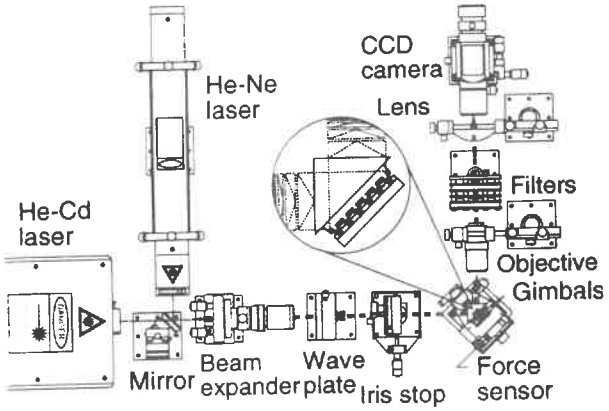

Figure 3 Schematic of the experimental device for the near-field exposure

relief. The authors call this technique "**Stamp Photolithography**", because the method of the exposure is like stamping.

The stamp photolithography can realize high resolution smaller than the wavelength of exposure light, because the exposure is performed in the near-field. A replica of a master mold fabricated at low cost serves as a disposable replica mold, which circumvents the reduction of yield caused by the damage to the mold at low cost. Furthermore, this technique does not require a light source with short wavelength or a high-performance optical system, so that the photolithographic device is inexpensive and a conventional photoresist can be used.

2 Experiment

An 80 μm thick replica film of acetyl cellulose is used for replication of a master mold with a relief fabricated by electron beam lithography. Figure 3 shows an experimental device for the near-field exposure. It is equipped with a He-Cd laser with wavelength of 441.6 nm (rated output: 10 mW, beam diameter: ϕ0.9 mm, TEM_{00}, linear polarization) to expose a G-line (wavelength: 446 nm) photoresist, and a He-Ne laser with wavelength of 632.8 nm to observe the position of a relief on the mold and the contact condition between a mold and a photoresist. The laser beam is expanded 10 times as large in diameter by a beam expander, polarized by a $1/2\lambda$ wave plate, narrowed down by an iris stop, and totally reflected in a prism with a replica mold on the slanting surface. A substrate with a spin-coated photoresist is fixed on a 0.2 mm thick gimbal plate, whose self-alignment mechanism allows the close contact between the mold and the photoresist. The contact force is measured by a force sensor (rated load: 50 N). The laser beam totally reflected in the prism is led to a CCD camera through an objective, filters and a lens. The CCD camera allows observing the position of the relief on the mold and the contact condition between the mold and the photoresist.

The authors conducted experiments along the process shown in Figure 1. First, the authors fabricated a master mold of silica glass with a relief of gratings with pitch of 100 nm $\sim$ 1 μm (width of 50 nm $\sim$ 500 nm) by electron beam lithography and fast atom beam etching. The depth of the relief is about 60 nm. Figure 4 shows an SEM view of the master mold.

Secondly, the authors replicated the master mold with a replica film of acetyl cellulose. The replica is easy to fabricate only by attaching the replica film dipped into methyl acetate to the master mold. Figure 5 shows an AFM view (a top view and a cross section) of the replica mold. The depth of the relief on the replica mold becomes shallower as the pitch of the grating decreases; the depth of the relief of the grating with pitch of 1 μm is about 50 nm, and that with pitch of 360 nm is about 15 nm.

Lastly, the authors attached the replica mold to the prism so that the grating is set parallel to the laser direction, put a Si substrate (about 5 mm square) with a spin-coated G-line positive photoresist (thickness: about 100 nm) against the replica mold by the contact force of 5 N observing the contact condition with the He-Ne laser and the CCD camera, and exposed the photoresist for 7 seconds. Figure 6 shows an optical microscope view of a pattern on the photoresist developed for 65 seconds at room temperature. Figure 7 shows an AFM view of the framed parts in Figure 6, and it corresponds with the AFM view of the replica mold in Figure 5. The grating pattern with pitch of 500 nm $\sim$ 1 μm (width of 250 nm $\sim$ 500 nm) was clearly printed, and that with pitch of 360 nm $\sim$ 400 nm (width of 180 nm $\sim$ 200 nm) was also printed, but

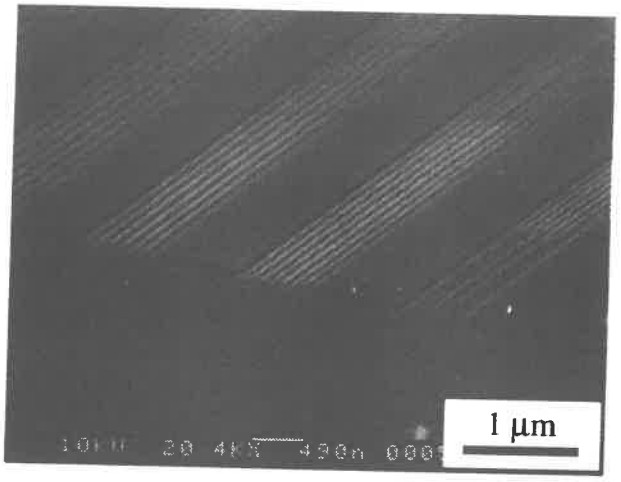

Figure 4 SEM view of the master mold

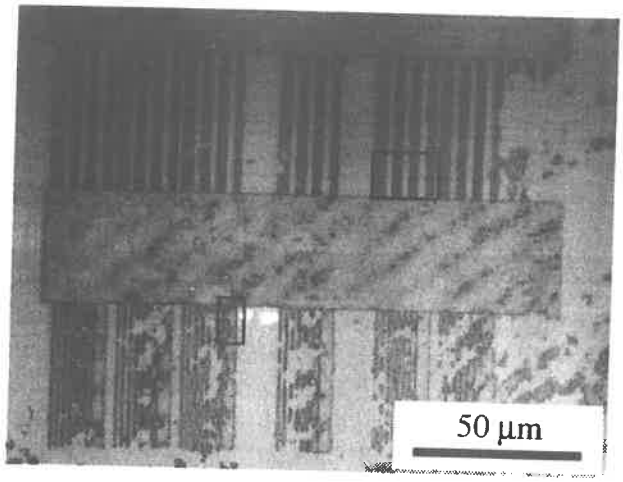

Figure 6 Optical microscope view of the pattern on the photoresist

not as clearly as in the first case. The grating pattern with pitch less than 360 nm was not printed in this experiment. The laser beam was p-polarized, because s-polarized laser beam extremely reduces the contrast of a printed pattern.

3 Discussion

The important conditions of the near-field exposure include the depth of a relief on a (replica) mold and the contact condition between a mold and a photoresist in addition to exposure time and polarization.

A deep relief on a mold enhances scattering light from the sides of the relief and lengthens the distance from the scattering light source to a photoresist, so that the scattering light interferes and many interference fringes are projected on to the photoresist. In another experiment with a mold of silica glass with a 700 nm deep relief, many interference fringes were observed on a photoresist [1].

A shallow relief on a mold, on the contrary, is elastically deformed and flattened by the contact with a photoresist. It is one of the probable causes that the grating pattern with pitch less than 360 nm was not printed in this experiment.

As for the contact condition between a mold and a photoresist, the close contact and the minimum deformation of a relief on a mold are necessary. It is thought that a replica material which allows a conformal contact with a photoresist without being pressurized to a photoresist can achieve a good contact between the mold and the photoresist.

Now the authors are fabricating new master molds and trying new replication methods to realize high resolution of 200 nm $\sim$ 300 nm.

4 Conclusion

The authors proposed the stamp photolithography to realize high resolution, large throughput and high yield at low cost. The grating pattern with pitch of 360 nm (width of 180 nm) was printed using exposure light with wavelength of 441.6 nm, and the high resolution smaller than the wavelength of exposure light was achieved. Future work will be to improve the feature of a relief on a mold and a replica material to realize higher resolution.

The authors would like to thank Dr. Masahiro Hatakeyama and Mr. Yasushi Tohma at Ebara Research Co., Ltd. for their assistance in electron beam lithography and fast atom beam etching. The authors also would like to thank Mr. Hideki Miyazaki at Research Center for Advanced Science and Technology, The University of Tokyo for his helpful advice.

References

[1] Shuji Tanaka, et al., Experiment of Simultaneous Patterning by Evanescent Light Lithography, Proceedings of The 74th JSME Spring Annual Meeting, 1997, Vol. IV, pp. 322-272

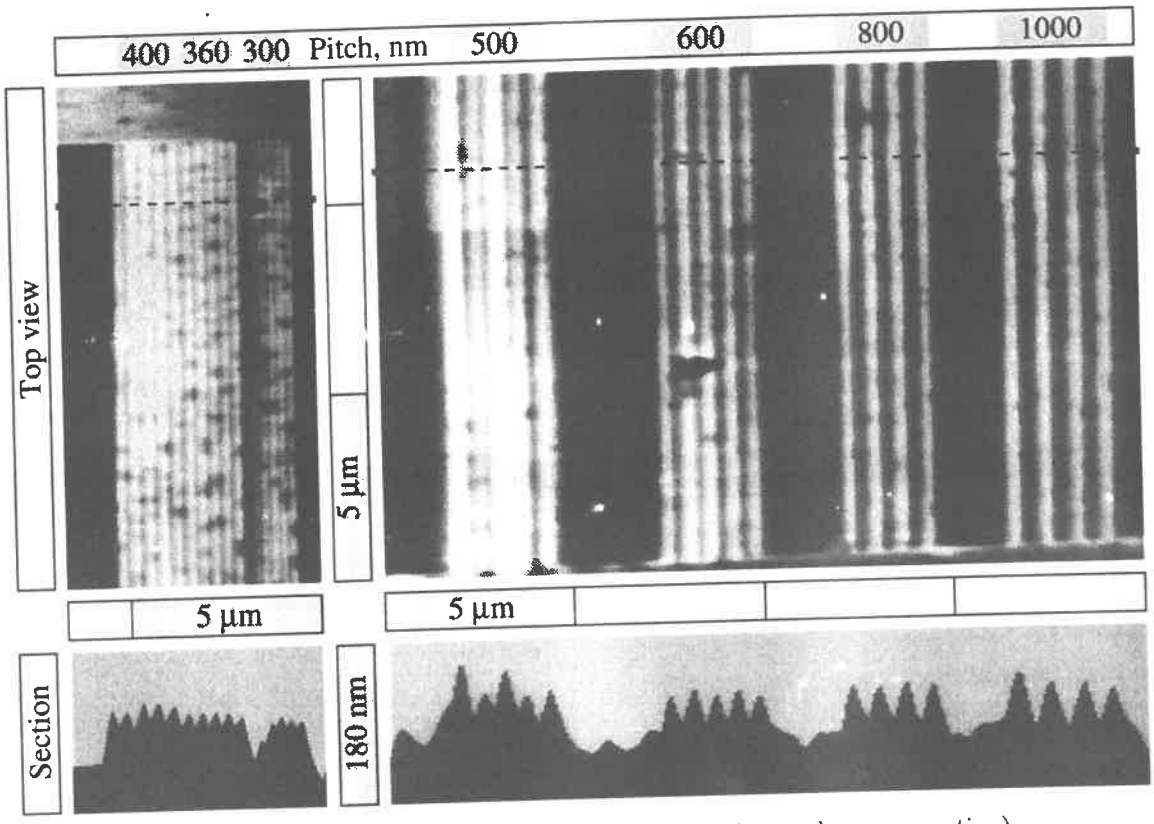

Figure 5 AFM view of the replica mold (a top view and a cross section)

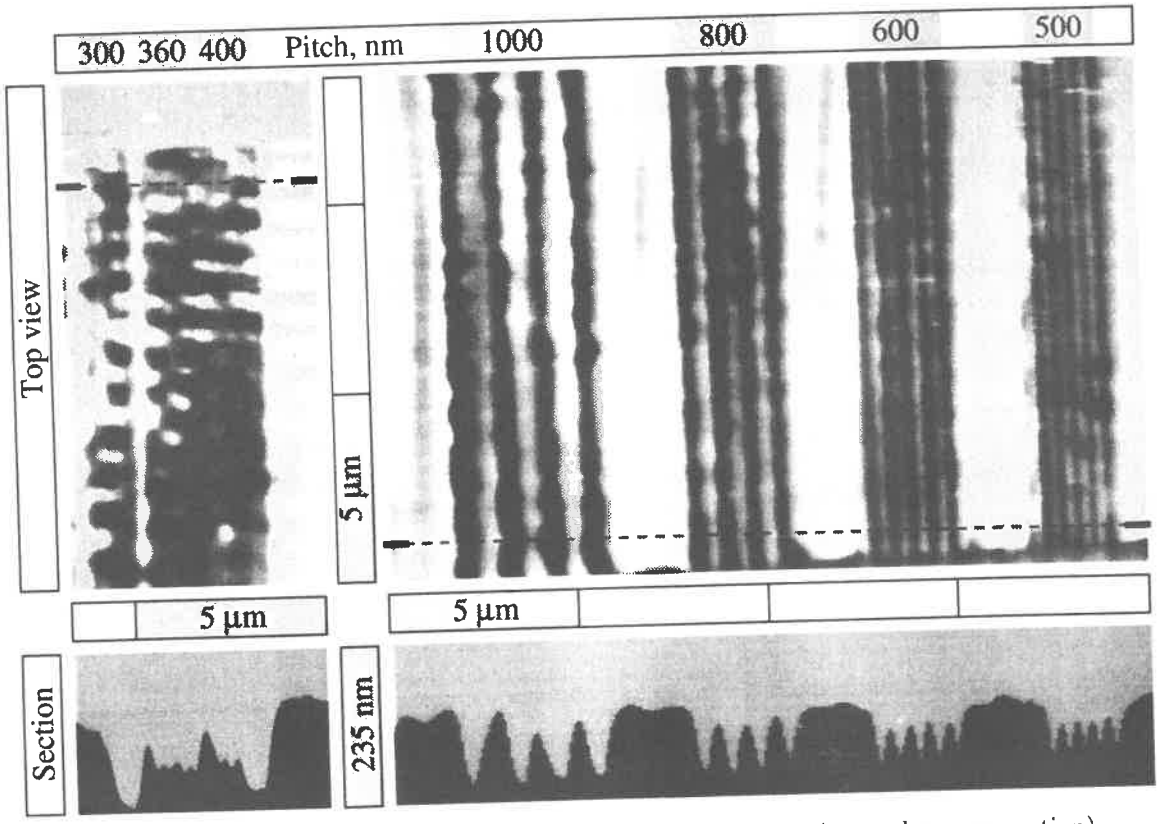

Figure 7 AFM view of the pattern on the photoresist (a top view and a cross section)

High Efficiency Fine Boring of Single Crystalline Silicon Ingot by Electrical Discharge Machining

Yoshiyuki UNO*, Akira OKADA*, Yasuhiro OKAMOTO* and Yoshiaki YAMADA**
* Okayama University, 3-1-1, Tsushimanaka, Okayama 700, JAPAN
** KASEN USA Corp., 9101 Southern Pines Blvd., Charlotte, NC 28273, USA

1. Introduction

Single crystalline silicon is one of the most important materials in the semiconductor industry because of its many excellent properties as semiconductor. In the manufacturing process of integrated circuits, plasma etching process is used for removing the oxidation film such as SiO_2.[1] In this process, graphite plate with many fine holes has been used as an electrode. Recently, it is examined to use single crystalline silicon as the electrode in order to minimize the contamination. Diamond grinding quill has generally been used for boring of silicon so far. However, it is difficult to machine accurately by the conventional methods, since the material removal is due to brittle fracture. In the diamond drilling method, the removal rate decreases and the loading of tool becomes severe with increasing of the machining depth. Furthermore, the chipping of workpiece occurs at the exit of hole. Therefore the usage of electrical discharge machining (EDM) is proposed for boring fine holes of single crystalline silicon. Then the possibility of high efficiency and high accuracy boring holes in silicon ingot by EDM is experimentally investigated.

2. Experimental Procedures

Fig.1 shows the schematic diagram of experimental apparatus. A copper pipe of 1 mm in diameter is used as an electrode, which rotates at 90 rpm. The uninflammable type fluid is spouted out from the tip of the electrode. Single crystalline silicon ingot used as an electrode in plasma etching process has low resistivity in the order of 0.01 Ω・cm, which makes it possible to machine silicon by EDM. Mild steel SS400 in JIS specification is also employed as a workpiece for comparison. Laser displacement sensor is set for in-process measurement of the electrode movement. The machining conditions are shown in **Table 1**. The polarity of electrode is kept plus through the experiment because the removal rate is higher than the reverse case.

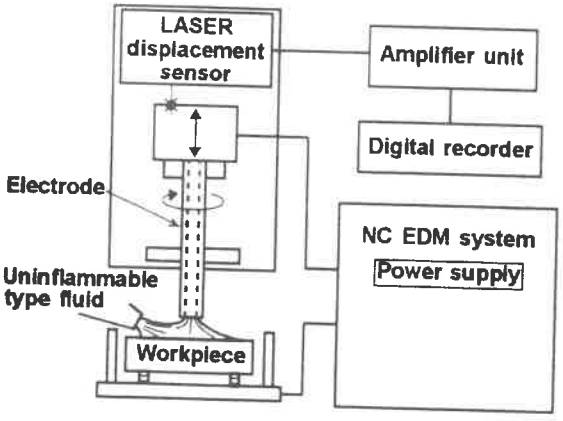

Fig.1 Schematic diagram of experimental apparatus

Table 1 Machining conditions

Polarity	Electrode(+)
Discharge current	Ip=2,6,15A
Pulse duration	τ p=4,8,12,20.28 μs
Duty factor	D.F.=50%
Capacity	C=380pF
Machining fluid	Uninflammable type

3. Results and Discussions

Fig.2 shows the relationships between the removal rate and the pulse duration in EDMing of silicon and mild steel. Here, the removal rate is expressed as the ratio of workpiece thickness to total machining time. As shown in the figure, the removal rate of silicon is about 4 to 8 times larger than that of steel when compared under the same machining conditions. In EDM, it is generally proved that the removal rate is controlled by the product of melting point θ m and heat conductivity λ, and low value of θ m $\cdot$ λ leads to high removal rate[2]. The value of θ m $\cdot$ λ for silicon is 14.1×10^5W/m, while that for steel is 1.04×10^5W/m. From this point of view, the removal rate of steel is expected much larger than that of silicon. However, the experimental result shows opposite tendency. It is recently reported by Saeki et al. that the Joule's heat generation played an important role in material removal in EDM of high resistance material[3]. Also in this case, it is considered that the Joule's heat generation in addition to heat conduction from arc column makes a great contribute to increasing the removal rate of silicon. On the other hand, the electrode wear of silicon is 1/15 to 1/7 compared with that of steel under the same conditions. Therefore, EDM is a very efficient method to machine single crystalline silicon.

Fig.3 shows an example of the displacement of electrode during machining time in EDMing of silicon. The machining process is divided into three distinct regions with the machining time: normal region, stagnation region and quick feed region. In normal region, the machining is stable and the machined depth increases linearly with the machining time. When the electrode advances around the exit of hole, the stagnation region appears. In this region, the electrode retracts suddenly and the machining becomes instable. After the stagnation region, the boring finished and the electrode advances at the rapid feed speed. **Fig.4** shows the SEM micrographs of the cross sections of machined hole. Good machined surface is generated around the entrance of the hole, while sticking of the insulator is observed on the wall of hole around the exit. The EPMA analysis pointed it out that the insulator contained silicon oxide and copper oxide. **Fig.5** is the explanation diagrams of these phenomena. As shown in (a), the exclusion of debris is smoothly performed through the gap between the workpiece and the electrode until the hole is penetrated. However, once the hole is penetrated as shown in (b), the exclusion of debris becomes difficult and they stagnate around the exit because the machining fluid leaks through the hole. The stagnation of debris causes the secondary discharge between the debris and the workpiece, and it makes the insulator stick on the wall of hole.

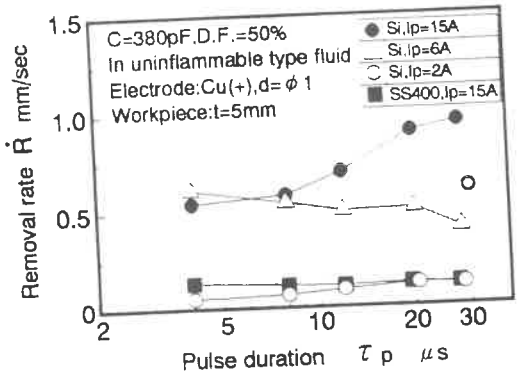

Fig.2 Relationship between removal rate and pulse duration

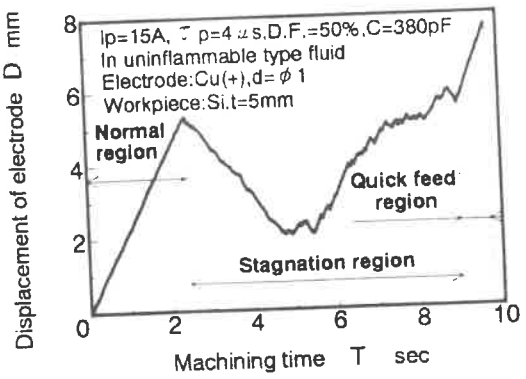

Fig.3 Displacement of electrode with machining time

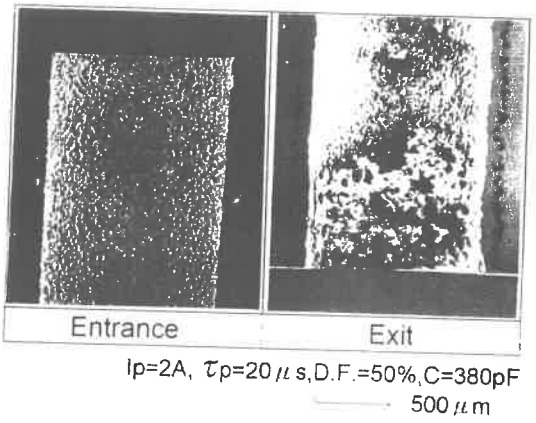

Fig.4 Cross sections of machined hole

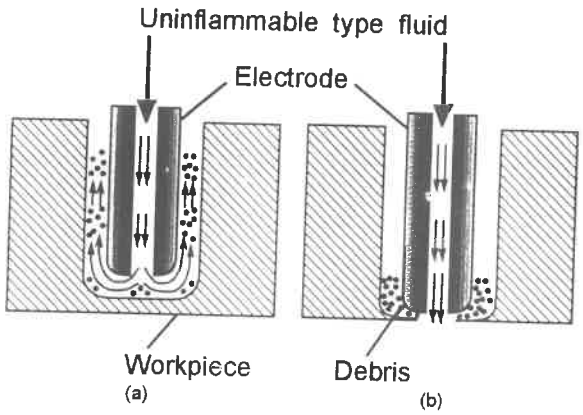

Fig.5 Exclusion of debris

4. Improvement Method of Machining Around Exit

In order to maintain the flow of the machining fluid well and make the exclusion of debris smooth even around the exit of hole, the improvement method is introduced as shown in **Fig.6**. In this method, the copper plate is attached under the silicon firmly. **Fig.7** shows the micrographs of machined hole generated with this method. Better hole can be obtained without sticking of the insulator and chipping around the exit. **Fig.8** shows the relationship between the displacement of electrode and the machining time. There is no stagnation region, which leads to better machined hole.

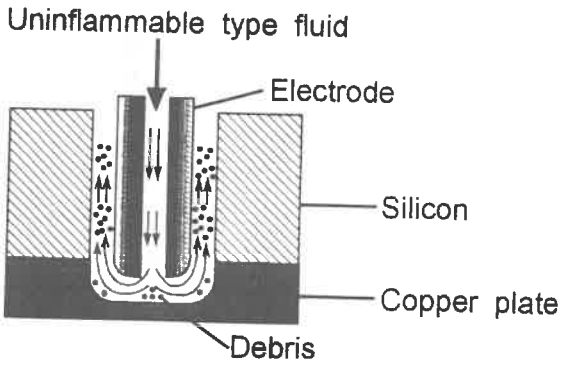

Fig.6 Improvement method of machining around the exit of hole

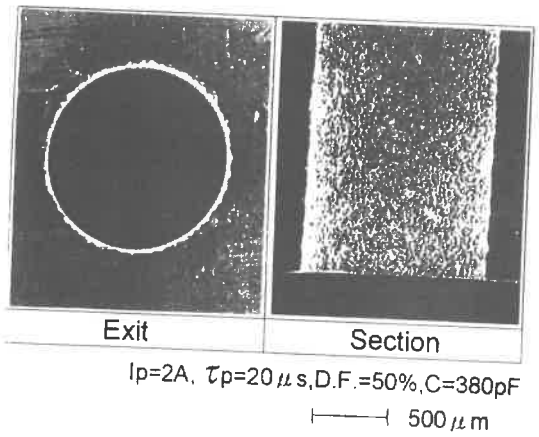

Fig.7 SEM micrographs of machined hole by improvement method

5. High Aspect Ratio Boring with EDM

Thicker electrode of silicon for plasma etching is required in order to reduce the arrangement time. We tried the deep boring of 200mm silicon which is the diameter length of 8" ingot. **Fig.9** shows the relationship between the displacement of electrode and the machining time.

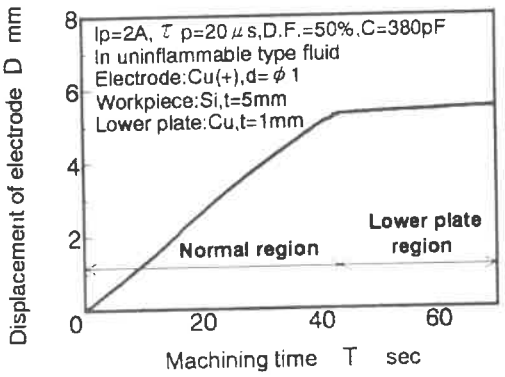

Fig.8 Relationship between displacement of electrode and machining time by improvement method

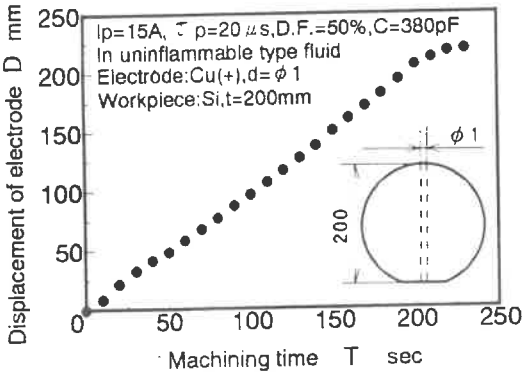

Fig.9 Relationship between displacement of electrode and machining time in high aspect ratio boring

Under this condition, stable machining is performed at the rate of 1mm per second and the straightness is maintained well. Judging from the experimental result, it seems that deeper hole than 200mm is possible to machine with this method. Generally speaking, it becomes difficult to machine in boring of deep hole because the loading of drill or the obstruction of debris with the depth of hole. However, it progresses at the constant speed and it is possible to bore the deep hole whose aspect ratio is about 200 in this method. From the above results, it proved that EDM is the suitable method for boring of single crystalline silicon.

6. Conclusions

Main conclusions obtained in this study are as follows:

(1) The removal rate of single crystalline silicon is much higher than that of steel, while the electrode wear is smaller.

(2) The exclusion of debris is difficult around the exit of hole, which leads to the inefficient stagnation region and the sticking of insulator made from silicon oxide and carbon oxide onto the wall of hole.

(3) The improvement method in which the copper plate is attached under the silicon firmly leads to better results.

(4) High aspect ratio boring of single crystalline silicon is efficiently attained by EDM.

Acknowledgment

The authors would like to express their thanks to Sin-Etsu Handotai Co. for supplying the precious workpieces of single crystalline silicon.

References

1) T.SUGANO: Plasma Process Technology for Semiconductor, SANGYO-TOSHO(1993)228.
2) N.SAITO: Principle of EDM and its Application,GIJUTSU-HYORONSHA(1994)38.
3) T.SAEKI et al.: Transient Workpiece Temperature Analysis in the EDM Processes of High Electric Resistance Materials Considering Joule's Heating, J. of JSPE, 62,3(1996)443.

Micro Devices Produced by Miniature Robots

*Hisayuki Aoyama, **Ken'ichiro Mizutani, **Tadahiro Miura,
#Kenji Murakami and **Futoshi Iwata

*Applied Micro Systems of Robotics Engineering
Dept. of Mechanical & Control Engineering
University of Electro-Communications
1-5-1, Chofu, Tokyo 182, Japan

**Dept. of Mechanical Engineering,
#Research Institute of Electronics
Shizuoka University
3-5-1, Hamamatsu, Shizuoka 432, Japan.

1.Introduction

Recently many new approaches have been developed to make the micro parts with the help of MEMS technology. One of them is an ultra precise machining techniques based on the mechanical tooling and another is on the electro-chemical technique which is widely used in LSI process. From the view point of micro-material processing, the former can be represented as a "*top-down*" approachinvolving material removal and the later is as a "*bottom-up*" approach with material deposition and etching. Such an ultra precise and a micro fabrication in micro realm need the multi-disciplinary experiences of several novel processes that can create complex micro structures.

In this report, many miniature robots of the beetle size with micro tools and workable in a vacuum chamber for the micro device fabrication will be described. Here the mechanical micro tooling and the local metal deposition control are to be combined. The small robot simply consists of piezoelements for source of motion and electromagnet for machine clamping so that it can provide stable locomotion with sub-micron resolution on any curved surface even in the high vacuum chamber[1]. Unique small tools which can be remotely controlled are mounted on the robots so that they can collaborate in doing microscopic operations[2],[3]

In the preliminary experiments, the local deposition patterning control of metals is carried out by two miniature robots. The precise deposition pattern is obtained by both the accurate positioning action of two miniature robots in lateral and the thickness control of deposition time. Then another miniature robot with a small manipulator is also ready for supplying different material grains into the heated pot. So this simple sequence can provide a set of unique micro deposition pattern with difference materials. Furthermore another small robot with a hopping micro tool of diamond is developed for the micro indention on the specified sample. The demonstrative results such as a batch of micro devices for the humidity sensor and micro pit holes are successfully achieved by the collaboration of miniature robots.

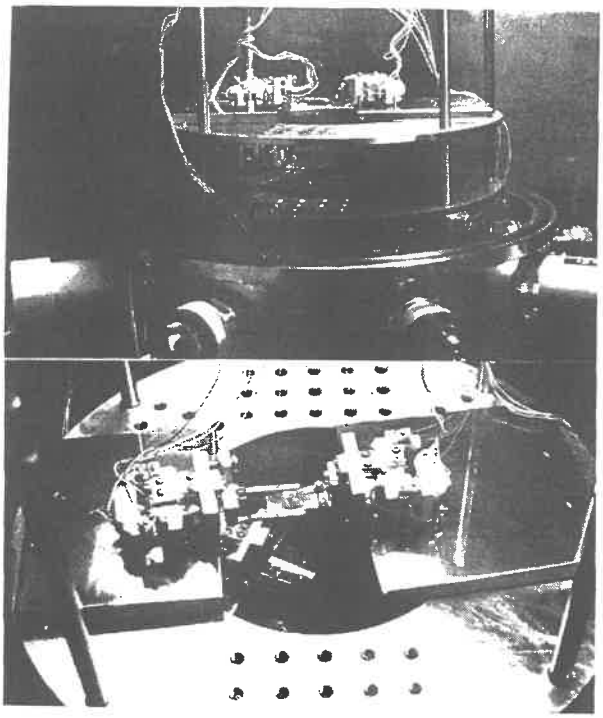

Fig.1 Experimental set-up
(3 miniature robots with mask, substrate and manipulator in the deposition chamber)

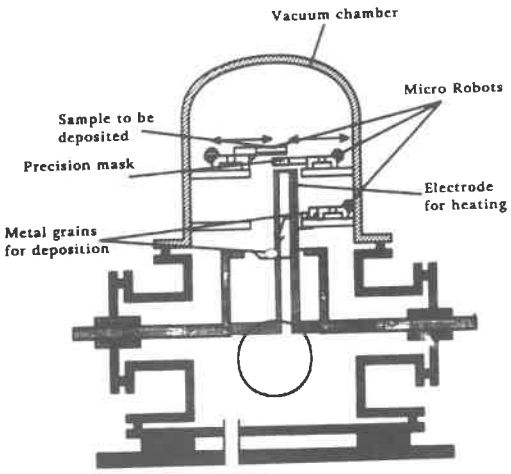

Fig.2 Layout of the experiemental facility

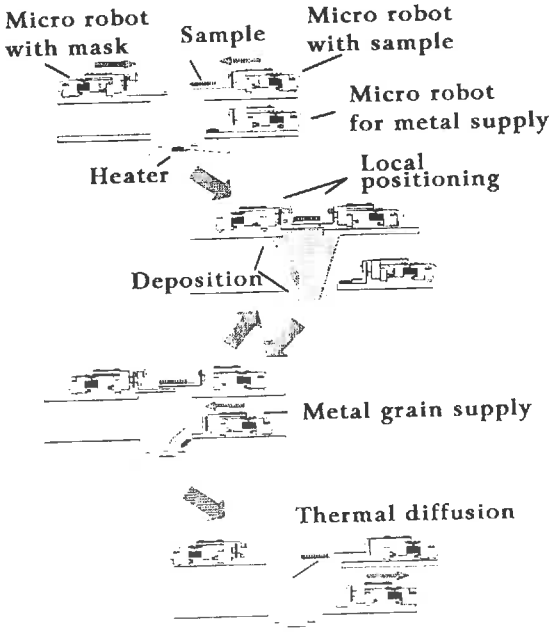

Fig.3 Process of flexible local deposition by miniature robots

2. Collaborative Work of Miniature Robots for Flexible Micro Patterning.

Figure 1 shows the experimental set-up that three mini-robots with a mask, a substrate and a small manipulator can work to control the local deposition process in the vacuum chamber. Each small robot is required to work there and controlled remotely by the responsible computer. There are two stages in the chamber, the upper stage for two small robots which are responsible for controlling the positions of the mask and the substrate precisely while the lower one is for the robot which will supply the metal grains into the heat pot as illustrated in **Fig.2** At first, the mask and the substrate can be overlaid and positioned at the initial point by two micro robots' collaboration so that they can move incrementaly with sub-micron resolution. At the bottom of the stage center, there is the heating pot for metal deposition and evaporated metal can go through the mask to the substrate. This arrangement provides local deposition patterns at any location of the substrate easily although the uncertainty of the pattern edge is determined by the layout of the deposition source, the mask and the substrate. On the lower stage, another mini-robot stands by for supplying different metal grains, for example Cu, Au and Al into the heat pot on demand so that the small amount of metal can be evaporated quickly. This process of small three robots action can be repeated to make the micro patterns anywhere as illustrated in **Fig.3**.

Experimental results to indicate the basic performance are shown in **Fig.4**. The set of the patterns of crossed arrow feature which are made of copper and aluminum have been deposited on the glass substrate with the same separation of 100 micron alternately in **Fig.4(a)**. The unique pattern which is possibly applied to the humidity sensor can be also patterned with the simple control sequence of micro robots as shown in **Fig.4(b)**. In the primary experiments, all of micro robots are maneuvered manually by the operators and the open loop positioning control manner based on the count of steps is used although the automatic production system are currently developed.

3. Hopping Tool for Micro Indention

In the conventional IC batch process, the photo lithography and etching techniques are widely used for material removal and patterning.We have been considered the possibility to combine the fine mechanical machining and the physical/chemical surface processing for the local micro fabrication. Here we may propose the hopping tool which is excited at the resonance frequency on the small robot and synchronized with the robot locomotion for dynamic micro-indenting to the thin film sample. The hopping tool consists of the micro tool

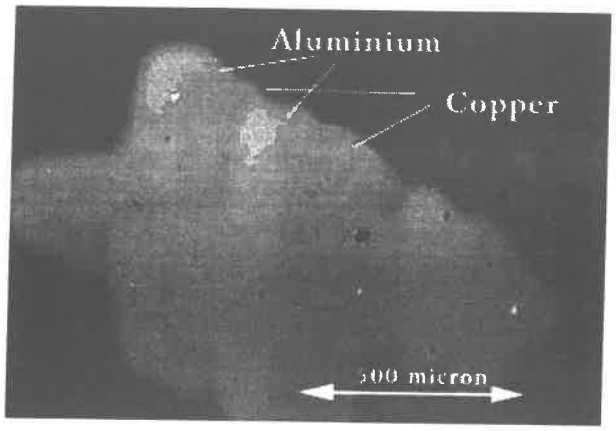

(a) Cross-arrow patterns of aluminum and copper

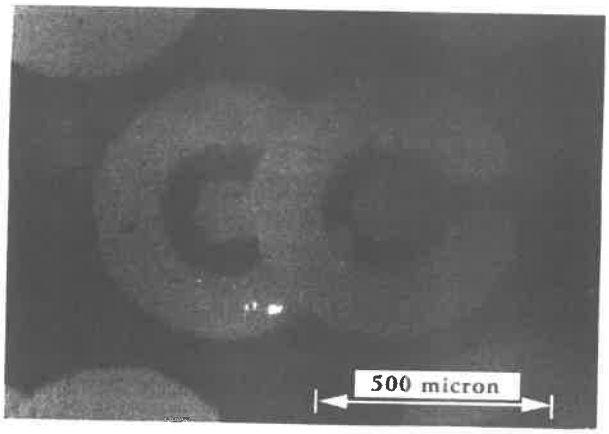

(b) Speical pattern for a humidity sensor

Fig.4 Experimental results made by the miniature robots

attached at the end of a cantilever and the piezo element as a resonator as illustrated in **Fig.5**. The distance between the tool end and the surface is adjusted by the micro screw so that the tool end can slightly contact to the surface. The mechanical frame of the tool hopping which is excited by the piezo is designed to resonate for expanding the tool stroke at the same frequency of the robot locomotion like an inchworm. This arrangement can make the dynamic micro indenting along the robot's path with the accurate stepwidth. The end of tool may be changeable for several kind of feature such as conical, quadrangular pyramid and hemisphere forms which are to be also ultra precisely machined as shown in **Fig.6**.

The typical experimental result is shown in **Fig.7(a)**, the photograph by an optical microscope, that is a set of indented pits by the conical diamond tool on the aluminum plate. We succeeded in making precise micro indentions with the separation of 10 micron. Another sample of SiO_2 sputtered Si substrate is also used as the target of hopping indention as shown in **Fig.7(b)**. Smaller pits of approximately 1 micron diameter can be achieved at every 10 micro separation. It is obvious that if greater indention force will be applied then the surface become cracked due to the nature of brittle material. However such tiny indenting force in this experiment is enough small to keep the ductile mode machining. It is expected that the thickness of SiO_2 thin film on Si is approximately ~200 angstrom. So the end of pit may be extended to the Si bulk although

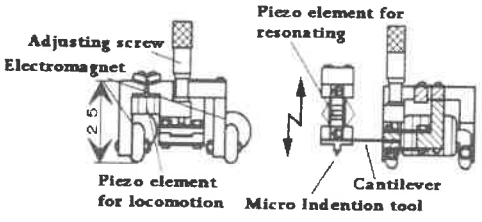

Fig.5 Micro robot with a hopping tool for micro indention

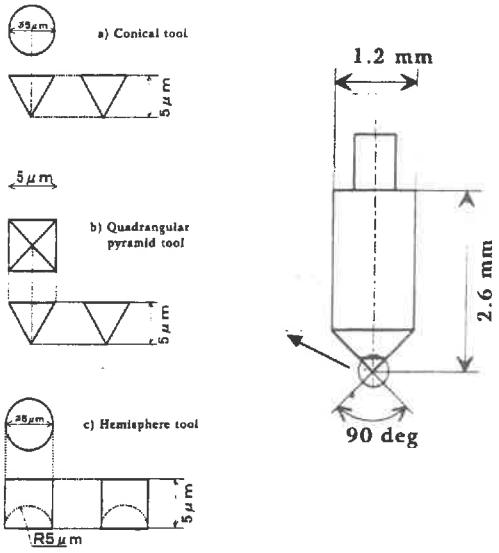

Fig.6 Micro tool top exchangeable for different indention.

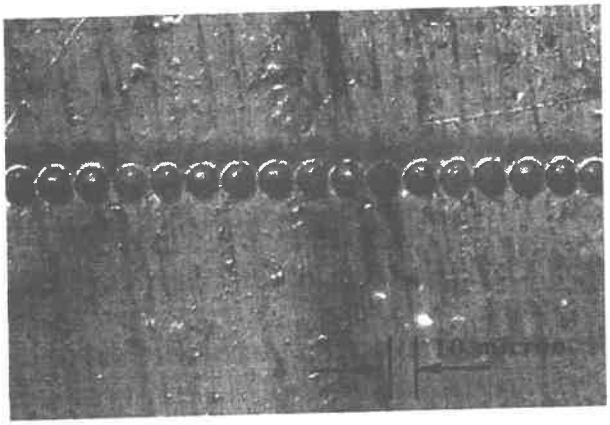

(a) Accurate indentions by the hopping tool of the robot on aluminum substrate

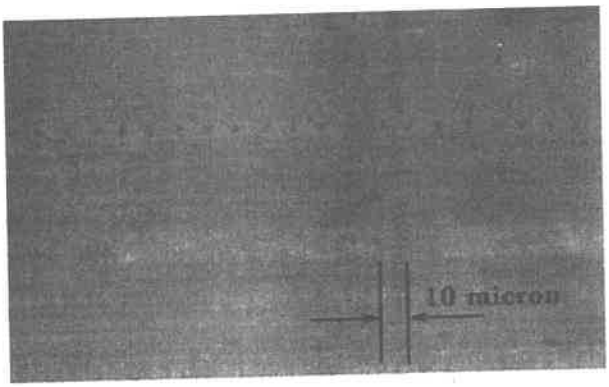

(b)Micro indentions on SiO_2 sputtered Si substrate

Fig.7 Dynamic micro indentions performed by the micro robot

we need much more detail investigation. It is feasible that some semiconductor devices can be produced by using this unique process performed by micro robots as shown in the conception of **Fig 8.** With the help of the thermal diffusion effect, it might be possible to get doped material around the indented hole so that the functional effect of such MOS-FET device can be produced.

4. Conclusion and Future Works

We proposed the new fabrication system which was the combination of the flexible micro deposition patterning as a physical process and the micro indention by the hopping tool of micro robot as a mechanical machining. Some experimental results such as a set of deposition metal and micro indention to the SiO_2 thin film were demonstrated. This micro robots system surely provides the potential application to a

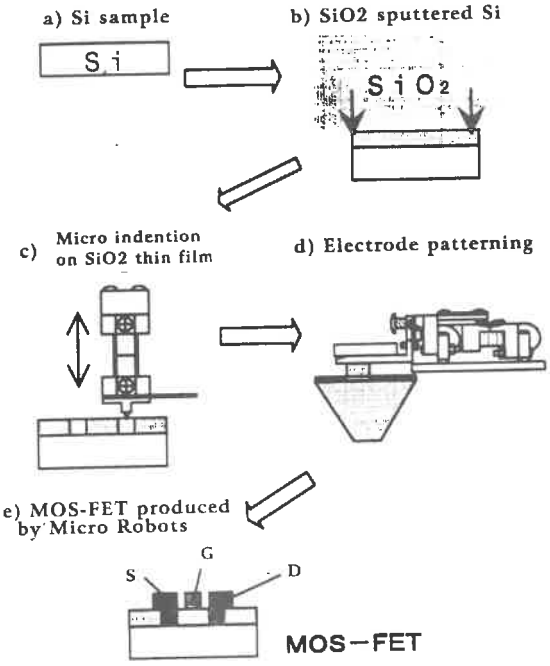

Fig.8 Micro fabrication process to make semiconductor devices by the micro robots

flexible micro device fabrication with cost saving benefit and low energy consumption . Currently we are on going development to establish "***Desktop Micro Robots Factory***" which can produce micro devices, assemble micro parts and could be installed into the conventional machine systems. Parts of this research were sponsored by Tateishi Science and Technology Fundation.

References

[1] H.Aoyama, K.Mizutani,F.Iwata and A.Sasaki; Micro-Pattern Control by Miniature Robots in Vapor Deposition Process, *Proc. of 10th ASPE Meeting*,(1995)pp.384-387

[2]H.Aoyama, F.Iwata and A.Sasaki; Collaboration Precise Operation by Two Miniature Robots - Single Diamond Cutting with Local Position Feedback, *Proc. of 9th ASPE Meeting* (1994)pp.238-241

[3]H.Aoyama, F.Iwata and A.Sasaki; Desktop Flexible Manufacturing System by Movable Miniature Robots-Miniature Robots with Micro Tool and Sensor, *Proc. of IEEE Int. Conf. on Robotics and Automation*, Vol.1(1995)pp.660-665

Authors Index

Ahn, Hyeong-Joon 406
Ahn, Jung-Hwan 215
Ahn, Woo Jung 434
Alayli, Y. 173
Aoyama, Hisayuki 529
Asamoto, Kohsaku 466
Ascanio, Gabriel 139, 283, 369
Atherton, Paul D. 328
Aziz, David J. 157
Badami, Vivek G. 153
Badrawy, S. 49
Barylski, Adam W. 287
Bernhard, David 49
Bhattacharya, R. N. 143
Bifano, Thomas G. 515
Birkicht, Albert. . . . . **
Blaedel, Kenneth L. 271
Bonis, Marc 173
Borchardt, Bruce R. 443
Bosse, H. 131
Bourdet, P. 82
Brinksmeier, Ekkard 33
Brooks, Charles W. 410
Brown, Christopher A. 118
Bruning, John H. 25
Caballero, Alberto 139
Cava, Carlos J. 283
Chang, C. M. . . . . **
Chang, In-Bae 406
Charlton, Thomas 447
Chen, Jenq Shyong. 422
Chicurel, Ricardo. 283
Cho, Sung Wook 434
Chou, Y. K. 451*
Chu, Xiohna . . . . . **
Chun, Keyoung Jin 345, 351
Coane, Philip. 458
Copeland, Nathan R. 410
Corbett, John. 365
Coyne, Dennis. 15
Cuttino, James F. 390, 394, 398
Daito,Masamichi 211
Daniel, Cecil M. 65
Davies, Matthew. A. 451*
Davis, Pete J. 271
Devitt, Andrew J. 377
Di Giacomo, Benedito 53
Díaz, Rufino. 139
Dickmann, K. 511
Ding ,Yao. 78
Dörrer, Peggy 319
Dow, Thomas A. 230
Drescher, Joseph D. 61
Duduch, Jaime G. 224
Dutterer, Brian S. 410
Dyer, Stephen W. 502*
Eberhardt, Keith R. 443
Edgeworth, Robert 90, 386
Estler, W. Tyler 29, 443
Evans, Christopher J. 29, 451*
Fähnle, Oliver W. 402
Fang, Fengzhou 220
Fawcett, Helen E. 515
Feautrier, Dominique. 82
Fleig, Jon F. 25,**
Frankena, H. J. 402
Frase, G. 131
Freudenberg, Heiko 507
Friedrich, Craig R. 458
Fu, Jiyou 78
Fujita, S. 211
Fukada, Shigeo 333
Furutani, Katsushi 307, 357, 466
Galindo, Enrique F. 369
Gao, Wei 57, 414
Gatzen, Hans H. 454
Gee, Anthony E. 365
Geerkens, J. 490
Gim, Taeweon 365
Goch, Gert. 490
Goettert, Jost. 458
Goho, Kenji 110
Gopinathin, Niranjan 458
Greene, Wade 187
Griffith, Lee 271
Gweon, Dae-Gab 337, 341, 478,**
Ha, Jae Y. 195
Hamaker, Chris 178
Han, Dong-Chul 351, 406
Hara, Seiichiro. 122
Hashiguchi, Makoto. 191
Hashimoto, Hiroshi 262
Hatamura, Yotaro 238, 242, 482, 521
Hatsuzawa, Takeshi 41
Hayashi, Akira 110
Henrio, J.C. 173
Hicks, Thomas R. 328
Hilbing, Robert. 498
Hirayama, Takao 311
Hoch, Pierre. 118
Hocken, Robert J. 386, 474
Holmes, Michael L. 386, 474

*Extended abstract not available at press time.

**Abstract unavailable at press time.

Holzhauer, Wolfgang 418
Hopp, T. 443
Horaguchi, Iwao 258
Horio, Ken-ichiro 199, 275
Hosokawa, Akira 203
Houston, J. E. 19*
Huang, Chin-Chou 361
Hümmler, Joachim 486
Imai, Kenichiro 262
Inaba, Fumio 211
Ishii, Kazuhisa 482
Itoh, Naoki 357
Iwata, Futoshi 529
Jarausch, Konrad 19*
Jared, Bradley H. 230
Jasinevicius, Renato G. 224
Jersch, J. 511
Joe, Yeo-Uk 165
Joung, Yoon 406
Jung, H. . . . . **
Jusko, Otto E. 131
Kaiser, Mark J. 69
Kakumanu, Thrinath S. 250
Kallenbach, Eberhard K. 507
Kamiya, Kazuhide 169
Kanai, Akira 211
Kanai, Masaya 414
Kasai, Toshio 199, 275
Kato, Ryoji 211
Kato, Shigeo 315
Kim, Hyung Min 86
Kim, Oui-Serg 406
Kim, S. M. 337
Kim, Seung-Woo 426
Kim, Tae H. 195
Kim, Won-jong 470
Kiriyama, Zenkichi 191
Kiyono, Satoshi 57, 414
Klein, Martin 21
Klein, Stephan 21
Knapp, Byron R. 246
Knight, P. Douglas, Jr. 106
Kohno, Tsuguo 183
Kondo, Sumihisa 203
Koteswara Rao, K. G. R. 299
Koyabu, Kunio 279
Kramer, Martin 157
Kroll, Jeremy 37
Kuhlbusch, W. 507
Kulawiec, Andrew W. 25
Kuppuswamy, G. 299
Lau, Kam C. . . . . **
Lawton, Kevin M. 149
Lee, Byung-Chai 86
Lee, G. 114
Lee, Ho-Jae 426
Lee, Jae Y. 195
Lee, Jin-Koo 165
Lee, Shuo-Jen . . . . . **
Lee, Sung-Q 341, 478
Lee, Taik Min 195
Leenders, M.H.A. 503
Levenson, M. S. 443
Li, Junqi 191
Li, Nan 37
Li, Zhen 73
Lim, HanSeok 215
Lim, Seong-Eun 426
Lin, Enhao 135
Liu, Shugui 73, 102
Lovingood, John 386
Lu, Y. S. 262
Lückel, Joachim 507
Lüdicke, Frank 131
Ma, Evan 143
Ma, Quanhe . . . . . **
Ma, Xin-hui 102
Maekawa, Katsuhiro 291
Mätzig, J. Christoph 454
Magara, Takuji 307
Mahdi, Mofid 303
Maißer, Peter 507
Malkin, Gene 430
Marinescu, Ioan D. 234
Marsh, Eric R. 207, 246, 295
Martin, Osborne A. 37
Martinez Orrego, Roxana 53
Martyniuk, Jerry 178
Matsumoto, Kiyoshi 242
Matsuo, Tetsuo 234
Matsuse, Atsuhiro 275
McClain, M. 443
McClimans, Donald P. . . . . **
McConnell, Malachy 328
Melvin, B. 443
Miller, Michele H. 250, 254
Mirro, Gene 178
Mishina, Satoshi 161
Mitsui, Kimiyuki 110
Mitsuishi, Mamoru 191
Miura, Tadahiro 529
Miyashiro, Hiroshi 169
Miyashita, Masakazu 211
Miyazawa, Kimio 161
Mizuhara, Kiyoshi 381
Mizutani, Ken'ichiro 529
Mohri, Naotake 307, 357, 466
Moon, Kee S. 126, 98
Moon, Sungho 94
Mou, Jong-I 114

Mu, Yunjun 135
Muñiz, Abdul 139
Murakami, Kenji 529
Muralikrishnan, Balasubramaniam 386
Na, Byung Chul 351
Nagalla, K. 37
Nagao, Takaaki 191
Nakao, Masayuki 238, 242, 482, 521
Namperumal, Ramesh 386
Natarajan, A. 143
Nava, Rigoberto 283
Nickles, C. 447
Nijsse, Gert-Jan P. 373, 503
Nomura, Takashi 169
O'Reilly, Thomas B. 295
Ogura, Ichiro 414
Ohira, Fumikazu 279
Ohno, Naohiro 183
Ohta, Kazushige 238
Okada, Akira 525
Okamoto, Yasuhiro 525
Okuda, Seiichi 169
Olson, Walter W. 65
Ozawa, Norimitsu 381
Pahk, Heui-Jae 434
Palomino, David M. 369
Pan, Y. L. . . . . **
Parks, Robert E. 29
Patterson, Steven R. 37, 106, 149, 153
Pereira, Paulo E. 386
Perkins, Jeffrey N. . . . . **
Petersen, Bernd 486
Phillips, Steven D. 443
Piscotty, Mark A. 271
Preuß, Werner 33
Pril, Wouter O. 438
Qu, Weimin 254
Radice, Josh 377
Reigl, M. 490
Reséndiz, Roberto U. 283
Rhead, P. 328
Rhorer, Janelle L. 452
Rhorer, Richard L. 410, 452
Ritter, R. 490
Robles, Guillermo 369
Ruhbach, Lars P. 454
Ruiz, Leopoldo 139
Russell, Phillip E. 19*
Saeki, Morihiko 203
Saffert, Eugen 507
Saito, Theodore T. 271
Sakai, Katsuhiko 311
Sanders, Benjamin 45
Sasajima, Kazuyuki 122
Sato, Yutaka 258
Sawyer, D. 443
Schäffel, Christoph 507
Schaut, Adam J. 207
Schellekens, Piet H. J. 438
Schinstock, Dale E. 187, 390
Schmidt, David M. 37
Schmitz, B. 490
Schmitz, Tony 49
Sekiguchi, Kazuhiro 199
Sethupathi, B. 37
Shao, L-Z. 29
Sharma, Aditya 386
Shen, Yin-Lin 94, 443
Shibatani, Kazuhiro 357
Shim, Jong Y. . . . . **
Shin, Dae Young 345
Shintani, Tadashi 315
Sotiropoulos, Nick 377
Spronck, Jo W. 373, 503
Sprongl, P. 490
Struik, Klaas G. 438
Subrahmanyan, P. 494
Sullivan, Paul J. 29
Sun, Z. N. 262
Sutherland, John W. 65
Takashima, Yasuhiro 238
Tanaka, H. 462
Tanaka, Shuji 521
Tang, W. 131
Tashiro, Hatsuzo 169
Thomas, Timothy N. 178
Todd, Michael W. 390, 398
Trumper, David L. 470, 474, 494
Tsukada, Tadao 122
Uda, Yutaka 183
Uno, Yoshiyuki 525
van Beek, H. Frank 503
van Brug, H. 402
van der Laan, C.J. 402
van Putten, P. F. A. M. 373
Venkatesh, Vellore C. 220
Vieira Porto, Arthur J. 224
Vieira Sato, Denise P. 53
Wan, De-an 135
Wang, Danping 173
Wang, Jianli 73
Wang, Wanjun 143
Wang, Yiding 98, 126
Ward, David E. 443
Weck, Manfred 486, 498
Weikert, Sascha 323
Wilhelm, Robert G. 37, 90
Williams, Mark 494
Wroblewski, Donald 515
Wu, Yan 394

Xu, Ying 328
Yamada, Hisashi 307
Yamada, Yoshiaki 525
Yamaguchi, Katsumi 258, 311
Yamanaka, Takashi 311
Yanagi, Kazuhisa 161
Yang, Fang 102
Yang, Min Yang 195
Yang, Yun-Won 165
Yasui, Heiji 203
Yazawa, Takanori 183
Yin, Ling 234
Yokotsuka, Tadashi 211
Yoshida, Y. 262
Yoshikawa, Kazuo 169
Zarudi, Irena 267, 462
Zhang, Guoxiong 73, 78
Zhang, Liangchi 267, 303, 462
Ziegert, John C. 45, 361
Zirn, Oliver 323